BEAUFORTIAN (JURASSIC – LOWER CRETACEOUS) SEQUENCE STRATIGRAPHY AND SEDIMENTOLOGY IN THE NATIONAL PETROLEUM RESERVE – ALASKA (NPRA)

David W. Houseknecht

U. S. Geological Survey, 956 National Center, Reston, Virginia 20192
dhouse@usgs.gov

ABSTRACT

Beaufortian strata (Jurassic – earliest Cretaceous) in NPRA have become a focus of exploration since the 1994 discovery of the nearby Alpine oil field. Interpretation of sequence stratigraphy and depositional facies from a regional 2-D seismic grid and well data has resulted in the definition of four major depositional sequence sets that each display unique stratal geometries and thickness trends across NPRA.

Sequence set K1 (Lower-Middle Jurassic) accumulated in a depocenter in northcentral NPRA. Constituent depositional sequences include lowstand (LST), transgressive (TST), and highstand (HST) systems tracts. Sequence set K2 (Oxfordian-Kimmeridgian) is a composite of higher-order depositional sequences that each reflects a forced regression, which caused widespread erosion across northcentral NPRA and accumulation of the derived sediment at the shelf margin in lowstand systems tracts. Subsequent flooding of the shelf resulted in deposition of transgressive systems tracts that commonly include well-winnowed, shoreface sandstones capped by a condensed section of fissile shale, forming good stratigraphic trapping potential. Sequence set K3 (Valanginian) displays relatively distal facies character, suggesting high relative sea level during most of the depositional history. An important exception is the presence of a transgressive systems tract at the base of K3 that contains winnowed, shoreface sandstones. Sequence set K4 (Hauterivian) is a shelf-margin wedge that developed as the result of tectonic uplift along the Barrow Arch. It comprises lowstand and transgressive systems tracts that display stratal geometries suggesting dynamic incision and synsedimentary collapse of the shelf margin.

Cores of Beaufortian strata from NPRA exploration wells display a variety of key stratigraphic surfaces and depositional facies. When integrated with the regional grid of public domain seismic data, these provide a unique opportunity for interpreting the sequence stratigraphy and depositional systems of oil-prospective strata in a frontier province.

INTRODUCTION

The primary focus of recent exploration in the the National Petroleum Reserve – Alaska (NPRA) and adjacent areas (Fig. 1) is stratigraphic traps within the Beaufortian megasequence, a Jurassic through Early Cretaceous (Neocomian) stratigraphic interval (Fig. 2) genetically linked to tectonic events that led to the opening of the Arctic Ocean (e.g., Hubbard and others, 1987). Renewed exploration in this region was stimulated by the 1994 discovery of the Alpine field, located on the Colville River delta immediately adjacent to the northeastern boundary of NPRA (Fig. 1). Brought on line in November 2000, the Alpine field contains more than 400 million barrels of recoverable, high gravity oil reservoired in Beaufortian strata (Hannon and others, 2000; Morris and others, 2000; Gingrich and others, 2001).

The objectives of this chapter are to (1) present a regional sequence stratigraphic framework for Beaufortian strata within NPRA, (2) summarize inferred depositional facies of those strata, and (3) provide an

Alaska North Slope Core Workshop, 2002

Copyright © 2012 Pacific Section, SEPM (Society for Sedimentary Geology)

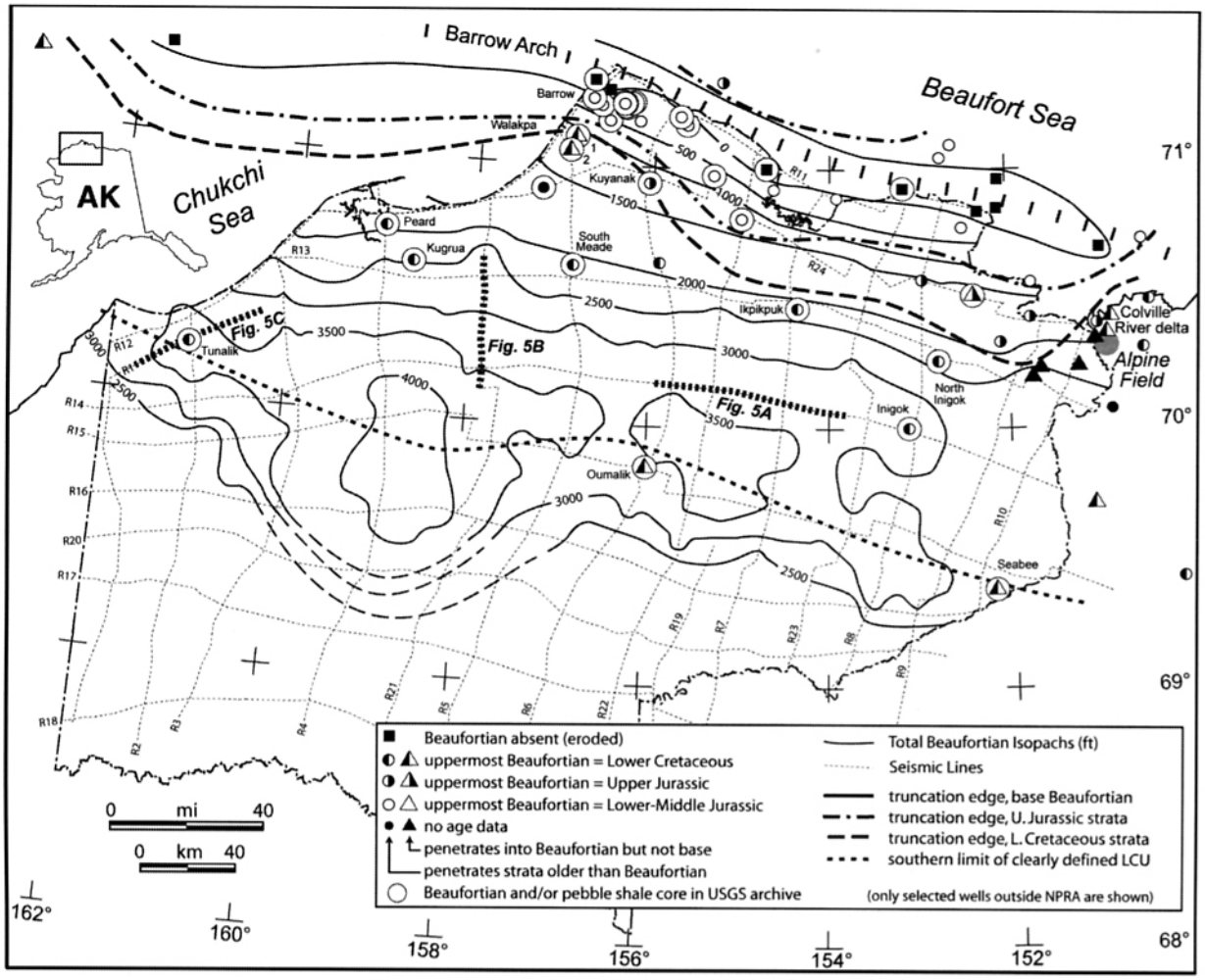

Figure 1. Map of the NPRA showing generalized total thickness of Beaufortian strata (derived from depth-converted seismic data); wells that penetrate Beaufortian strata with symbols indicating age of uppermost strata and core control; and approximate truncation edges of chronostratigraphic intervals. Ages are based on published literature plus new data presented here. Also shown are approximate locations of seismic line segments presented in Figure 5.

overview of cored Beaufortian intervals and demonstrate their utility in developing an understanding of both regional and local sequence stratigraphy. This chapter is an update of information published in Houseknecht (2001).

BEAUFORTIAN BACKGROUND

Stratigraphy

Literature addressing Beaufortian strata reflects contrasting levels of information available in NPRA as compared to adjacent areas of the Alaska North Slope. Earlier exploration efforts in NPRA, conducted mostly by the Federal Government during 1943-1953 and 1974-1982, resulted in an extensive grid of public domain, 2-D seismic data plus sparse and widely spaced well control. Consequently, the NPRA literature generally depicts Beaufortian strata as an undivided, Jurassic through lowermost Cretaceous (Neocomian) Kingak Shale (Fig. 2) that includes both regional and sub-regional unconformities (e.g., Bird, 1985, 1987, 1988, 1994; Hubbard and others, 1987; Kirschner and Rycerski, 1988; Mickey and Haga, 1987).

In contrast, literature stemming from exploration and development activities outside NPRA (particularly in the Kuparuk River field) reflects greater stratigraphic resolution resulting from denser well control. This literature also documents the presence of

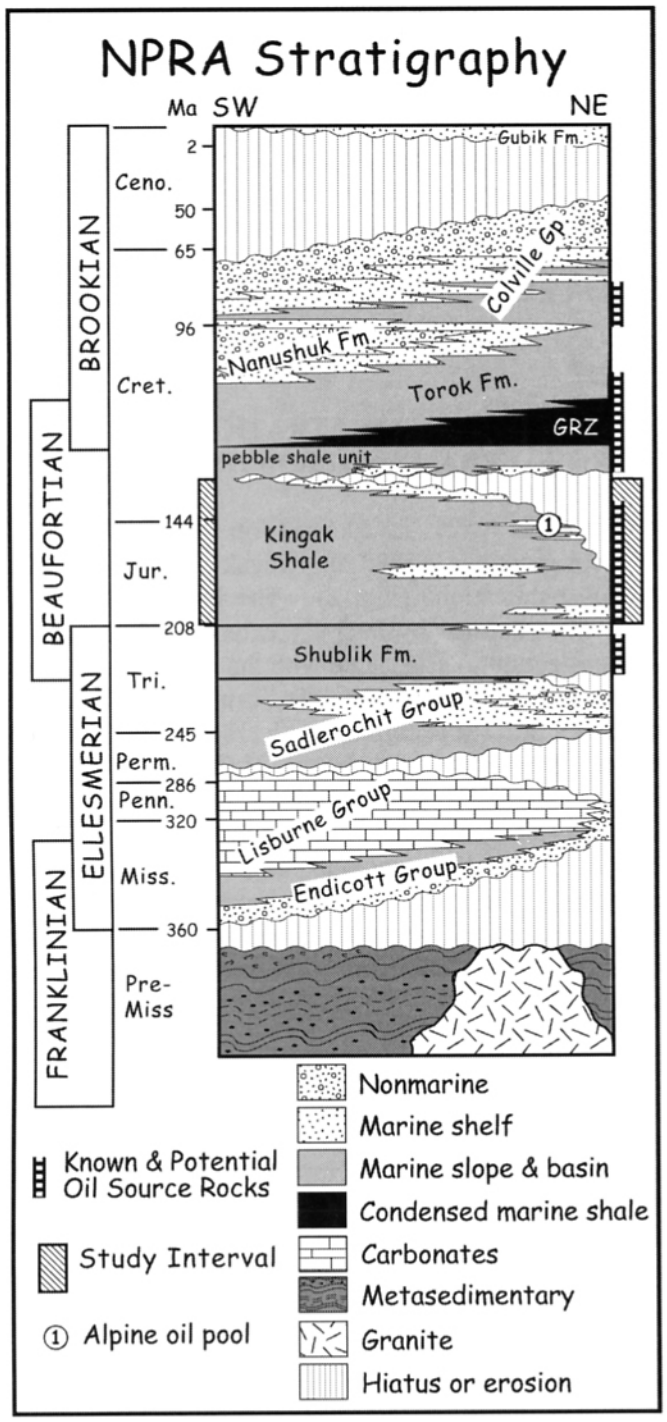

Figure 2. Stratigraphy in National Petroleum Reserve – Alaska showing stratigraphic positions of study interval, known oil source rocks, and Alpine oil pool.

local grabens that contain a more complete Neocomian section (e.g., Carman and Hardwick, 1983; Hubbard and others, 1987; Masterson and Paris, 1987; Masterson and Eggert, 1992). Consequently, Beaufortian strata have been variously sub-divided to include several units of approximately formation rank, including lower Kingak, upper Kingak, Miluveach, lower Kuparuk or Kuparuk A-B, upper Kuparuk or Kuparuk C, and Kalubik.

This chapter uses informal designations to represent inferred depositional sequence sets, and presents approximate correlations of those sequence sets to stratigraphic units recognized outside the NPRA. The information presented here is derived from work-in-progress and is subject to revision as additional data become available.

Previous Work

Previous regional studies have documented that Beaufortian strata are distinguished by a northern provenance and seismically defined clinoforms that indicate southward to southeastward offlap (e.g., Bird, 1985, 1987; Bird and Molenaar, 1992). The regional work of Hubbard and others (1987) presented a comprehensive interpretation that these strata record erosional and depositional effects of rifting associated with opening of the Arctic Ocean basin.

Much of the previous work on Beaufortian strata in NPRA emphasized the source rock potential of the Kingak Shale, although the presence of sandstone tongues, locally displaying good reservoir quality, also was documented by those studies (e.g., Bird, 1985, 1987, 1988, 1994; Magoon and Bird, 1988). The potential for these sandstone tongues to contain oil within NPRA was recognized, based on analogues from adjacent parts of the North Slope (e.g., Bird, 1995).

Outside NPRA, published work has focused on Beaufortian strata as important oil-reservoir intervals, primarily in the Kuparuk River field (Carman and Hardwick, 1983; Masterson and Paris, 1987; Werner, 1987; Masterson and Eggert, 1992). These studies not only documented the reservoir potential of Beaufortian sandstones, but also demonstrated the complexities of regional and local stratigraphy, and of trap types and geometries within Beaufortian strata. Recent presentations on the Alpine field have revealed information regarding sequence stratigraphy, reservoir quality, and source-rock potential of Beaufortian strata in the area of the Colville River delta (Hannon and others, 2000; Morris and others, 2000; Gingrich and others, 2001).

METHODS

Interpretation and mapping of Beaufortian stratigraphy and depositional sequences in NPRA is based primarily on a regional grid (Fig. 1) of 1974-

1981 vintage, public domain, 2-D seismic data (Miller and others, 2000). These data were reprocessed and converted to approximate depth following procedures similar to those summarized by Lee and others (1999). Depth-converted seismic data are used for the sequence stratigraphic interpretations so that stratal geometries are more realistically portrayed. However, the limited number and uneven spatial distribution of wells introduce a degree of uncertainty in the depth conversions, particularly in the south and west, far from wells that provide velocity control. It is estimated that the depth-converted data are accurate to approximately 10 percent.

Approximately 2,700 line miles were interpreted for this study. Interpretation was completed along the entire length of each line except where prohibited by poor data resolution and/or intense structural deformation. This generally excludes from interpretation the area south of line R20 except in westernmost NPRA, where interpretation along R1 was possible only north of line R14 (Fig. 1).

Seismically mappable units representing depositional sequences or sequence sets were defined and correlated throughout the study area. To the extent possible, depositional sequences were defined on seismic evidence of unconformities and their correlative conformities. However, the resolution of seismic data combined with the small-scale heterogeneity of some stratigraphic intervals resulted in the definition of sequences known to be composites in some cases. Within each sequence, seismic facies were interpreted using criteria summarized by Sangree and Widmier (1977). Thickness of stratigraphic intervals were derived from interpreted sections and exported to a geographic information system for isopach mapping.

Depositional sequences and sedimentary facies inferred from seismic expression were correlated directly to well data using synthetic seismograms. Once posted to wire-line log displays, the depths of some sequence boundaries were adjusted based on wire-line log response using criteria described by Van Wagoner and others (1990) and Posamentier and Allen (1999), and based on interpretation of sequence boundaries described in cores.

There are no known outcrops of the Beaufortian depositional sequence sets that have been mapped in the subsurface of NPRA, although Bird (1985, 1987) has shown that clinoform strata of similar age are discontinuously exposed about 100 miles to the east along the front of the Brooks Range. Strata of equivalent age that crop out in the Brooks Range foothills to the south are either (1) distal basinal facies that represent condensed sections (i.e., the Blankenship Member of the Otuk Formation; Mull and others, 1982) or (2) earliest foredeep facies shed northward from the ancestral Brooks Range (i.e., Okpikruak Formation; Moore and others, 1994). Neither shed much light on the nature of depositional sequences beneath NPRA, although the former provide important constraints on geochemistry and thickness of potential source rocks in distal Beaufortian strata.

BEAUFORTIAN STRATIGRAPHIC FRAMEWORK IN NPRA

This work is focused on the stratigraphic interval generally termed the Kingak Shale in previous NPRA publications (Fig. 2). The base of the study interval is defined by laterally extensive, high amplitude reflection(s) associated with the top of the Triassic Sag River Sandstone or Shublik Formation. The top of the study interval is defined by the regionally extensive Lower Cretaceous Unconformity (LCU). Although the specific seismic expression of the LCU varies across the study area, it is well defined by a combination of characteristics that include angular truncation of underlying strata (especially in northern NPRA) and close association with a regionally extensive, high amplitude reflection marking the overlying gamma-ray zone (GRZ, Fig. 2).

The Kingak Shale is a prism of strata whose thickness contours generally trend west-east (Fig. 1). A zone of maximum thickness (3,000 to >4,000 ft.) bisects NPRA from the Tunalik well to the vicinity of the Seabee well (Fig. 1). Northward from the zone of maximum thickness, the top of the Kingak Shale is defined by distinct truncation of reflections at the LCU and the formation thins gradually to a zero edge near the northern boundary of NPRA. This northward thinning reflects a combination of (1) onlap of the formation onto ancestral elements of the Barrow Arch, (2) erosion of the formation beneath the LCU as a result of uplift along the Barrow Arch, (3) onlap of depositional sequences onto sequence boundaries within the formation, and (4) erosion of depositional sequences beneath intra-formational, sequence-bounding unconformities within the formation.

Southward from the zone of maximum thickness, the top of the Kingak Shale appears in seismic data to be parallel to the overlying GRZ (disconformable or conformable?) and the formation thins in a geometry suggesting an "ultimate" (farthest basinward) shelf-margin clinoform. Irregularities in Kingak thickness near the southern limit of seismic

resolution may reflect variations in the thickness patterns of constituent depositional sequences (see subsequent sections) and/or local tectonic thickening that was not recognized as such during seismic interpretation.

The age of the uppermost strata within the formation generally increases northward, from earliest Cretaceous (Neocomian) in the zone of maximum thickness through late Jurassic to lower-middle Jurassic near the zero edge on the Barrow Arch (Fig. 1). This trend can be attributed to the northward beveling of the Kingak Shale beneath the LCU as illustrated schematically in Figure 3A. Uppermost strata of the Kingak Shale are inferred to be of Neocomian age throughout southern NPRA, although no constraining data exist south of the Tunalik, Oumalik, and Seabee wells (Fig. 1).

BEAUFORTIAN SEQUENCE STRATIGRAPHY IN NPRA

Basic properties of four depositional sequence sets (K1 through K4) defined and mapped in this study are summarized schematically in Figure 3. Although these four sequence sets display physical dimensions that are similar in magnitude, chronostratigraphic considerations together with facies analysis suggest they likely are not of equivalent magnitude in a sequence stratigraphic context. This issue is addressed further in subsequent sections.

Overall, the four depositional sequence sets define a generally southward offlapping succession of Beaufortian strata (Fig. 3A). Age constraints based on paleontology data from NPRA wells (Mickey and Haga, 1987; Magoon and others, 1988; previously unpublished data) permit approximate chronostratigraphic relations to be established for these sequence sets (Fig. 3B). These relations suggest that three of the four sequence sets are segregated by significant and widespread unconformities or disconformities that occur within the Beaufortian section (Fig. 2), including one in the lowermost Jurassic (sub-K1), a second in the middle Jurassic (between K1 and K2), and a third spanning the uppermost Jurassic-lowermost Cretaceous (between K2 and K3). The boundary between K3 and K4 appears to be erosional based on seismic evidence, although the resolution of public domain paleontology data is insufficient to suggest a widespread unconformity at that horizon. These sequence sets and their boundaries, independently defined on the basis of public domain seismic data and dated using published paleontology data, agree remarkably well with the sequences and unconformities recognized within the Beaufortian section by Hubbard and others (1987). Correlation of sequence sets K1 through K4 to the megasequences defined by Hubbard and others (1987) is shown in Figure 4. In addition to the regionally extensive unconformities or disconformities that serve as boundaries between sequence sets, higher-order, sequence-bounding unconformities occur within at least three of the sequence sets. These higher-order unconformities are discussed in subsequent sections.

Sequence Set K1

Description – The base of K1 across most of the study area is a high amplitude reflection that defines the contact between the Triassic Sag River Sandstone or Shublik Formation (Fig. 2) and the Kingak Shale (Fig. 5). The only exception occurs on the Barrow Arch in northernmost NPRA, where the base of the Kingak locally oversteps the Sag River and Shublik formations northward and rests directly on argillite of the basement complex. The top of K1 is a medium to high amplitude reflection that appears to be a downlap surface for basal reflections within sequence set K2 across much of the study area (Fig. 5A). However, in northwestern NPRA (north of dotted line in Fig. 6), the top of K1 displays attributes of an unconformity where K1 reflections are truncated at the base of K2.

Correlation with paleontology data from NPRA wells indicates that K1 is Lower to Middle Jurassic in age, and the youngest age commonly reported is Aalenian (Fig. 3). This sequence set is equivalent to the "Lower Kingak" of most literature.

An isopach map (Fig. 6) reveals a broad area in northcentral NPRA where sequence set K1 is 1,000 to >1,250 ft. thick, and this thick zone bulges to the south in central NPRA. Southward from this zone of maximum thickness, K1 thins rather abruptly in a radial pattern to less than 500 ft. in western NPRA and to less than 250 ft. in southeastern NPRA (Fig. 6). Northward from the zone of maximum thickness, K1 thins very gradually in the area where the K1-K2 contact appears on seismic data to be erosional. And, K1 thins abruptly to a zero edge along the trend of the Barrow Arch where it is beveled beneath the LCU (Fig. 6).

Within and north of the zone of maximum thickness, K1 displays internal reflections that are moderate to high amplitude, laterally continuous, and generally parallel to each other and to the base of K1 (Fig. 5A, west of mile 170; Fig. 5B). However, as K1 thins distally, those reflections abruptly roll over into

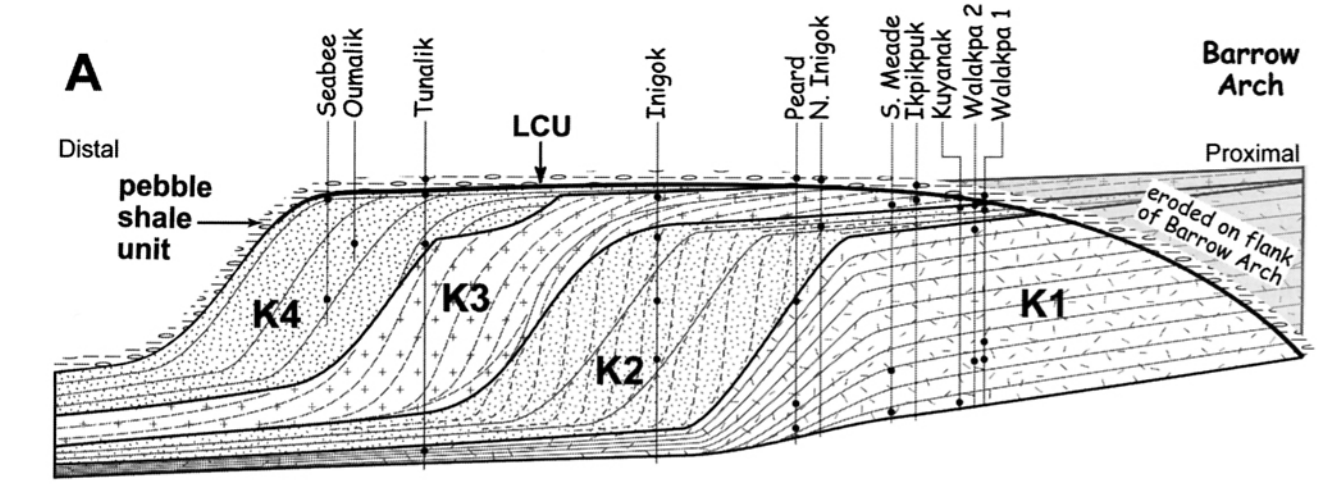
A
Seabee
Oumalik
Tunalik
LCU
Inigok
Peard
N. Inigok
S. Meade
Ikpikpuk
Kuyanak
Walakpa 2
Walakpa 1
Barrow Arch
Distal
Proximal
pebble shale unit
eroded on flank of Barrow Arch
K4
K3
K2
K1

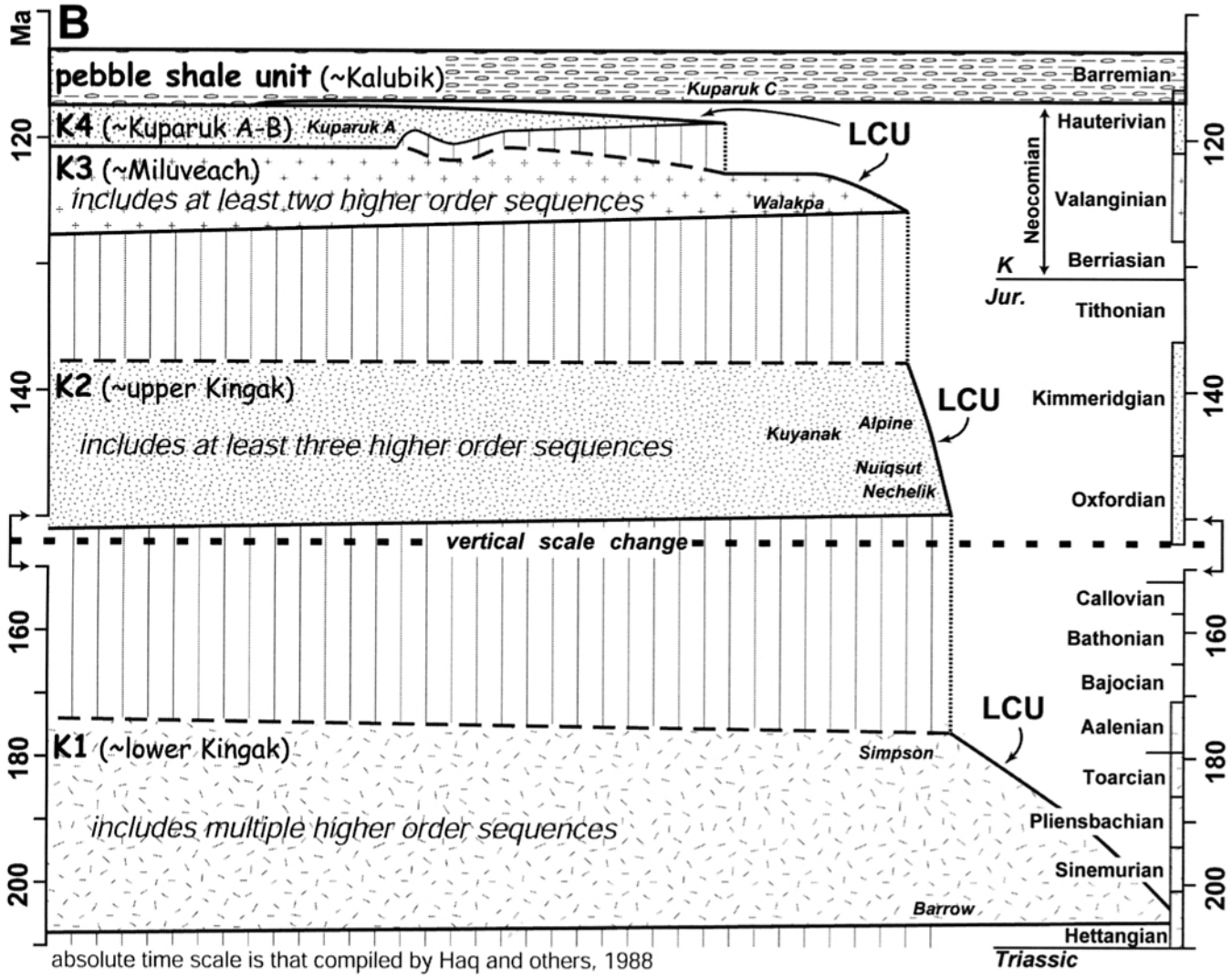
B
Ma
pebble shale unit (~Kalubik)
Kuparuk C
Barremian
K4 (~Kuparuk A-B)
Kuparuk A
LCU
Hauterivian
K3 (~Miluveach)
includes at least two higher order sequences
Walakpa
Neocomian
Valanginian
Berriasian
K
Jur.
Tithonian
K2 (~upper Kingak)
includes at least three higher order sequences
LCU
Kimmeridgian
Kuyanak
Alpine
Nuiqsut
Nechelik
Oxfordian
vertical scale change
Callovian
Bathonian
Bajocian
LCU
Aalenian
K1 (~lower Kingak)
Simpson
Toarcian
includes multiple higher order sequences
Pliensbachian
Sinemurian
Barrow
Hettangian
Triassic
120
140
160
180
200
absolute time scale is that compiled by Haq and others, 1988

← **Figure 3.** Schematic summary of inferred depositional sequence sets in Beaufortian strata of NPRA. *A*. Proximal (~north) to distal (~south) cross section of stratigraphic relationships among four Beaufortian depositional sequence sets, showing general aspects of internal stratal geometry. Note that the LCU bevels Beaufortian strata northward to a zero edge on the Barrow Arch. Selected wells are shown in positions relative to locations where they penetrate Beaufortian strata, and dots on wells represent approximate stratigraphic positions of cores in USGS archive. *B*. Chronostratigraphic depiction of Beaufortian sequence sets. Shown in parentheses are stratigraphic names widely applied to strata that are approximate age-equivalents of the four Beaufortian sequence sets. Names in italics show approximate positions of sandstones known to be reservoirs in some cases. Vertical lines denote time gaps between Beaufortian sequence sets. Note scale change near center of diagram. Time scale is that compiled by Haq and others (1988).

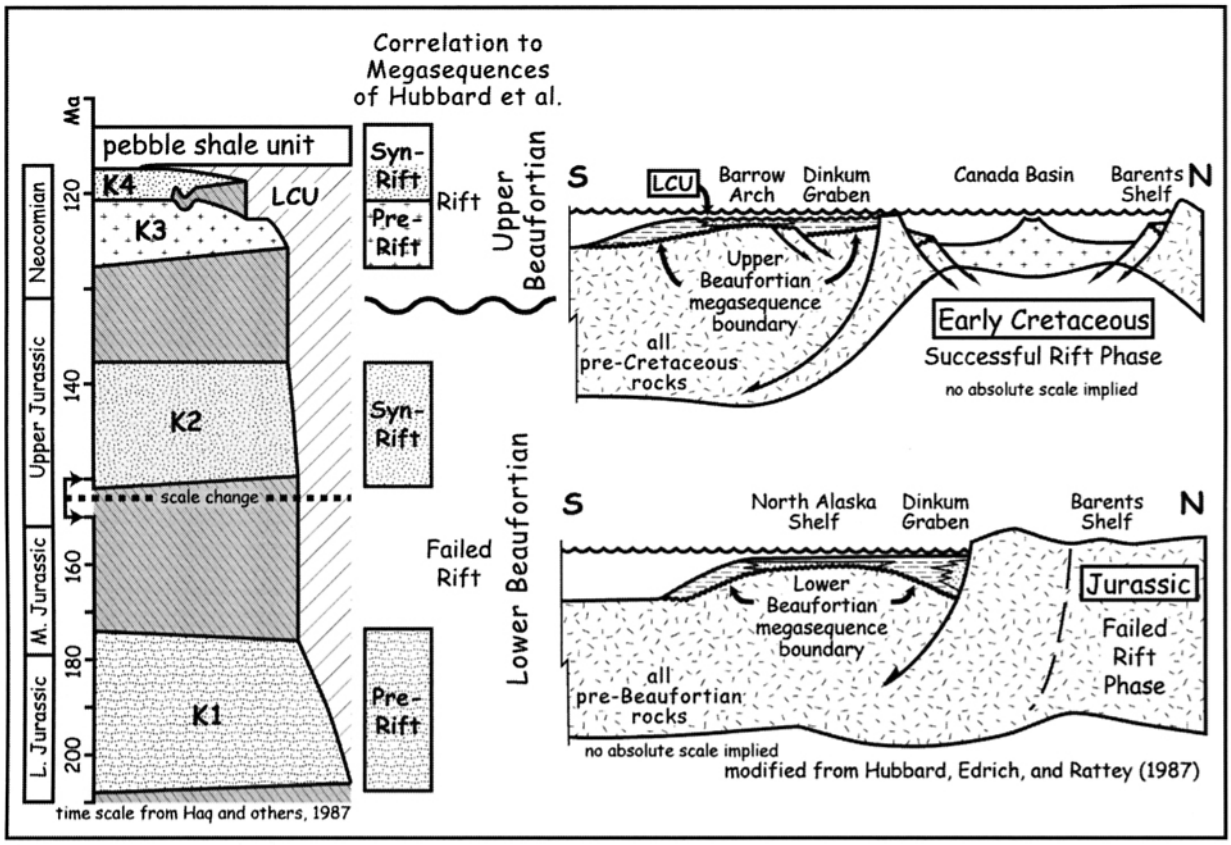

Figure 4. Correlation of sequence sets K1 through K4 of this study with Beaufortian megasequences and tectonic settings defined by Hubbard and others (1987).

clinoforms that dip (1-2°) radially to the southwest, south, and southeast in a pattern that is essentially perpendicular to the isopach contours (Fig. 6). The clinoforms downlap onto, and appear to coalesce with, the high amplitude reflection that marks the base of the study interval (Fig. 5A). These relationships are illustrated in the schematic cross section in Figure 3A.

Interpretation – Sequence set K1 is interpreted as a composite of numerous higher-order depositional sequences whose individual internal stratal geometries are too small to be resolved with seismic data available for this work. In northern NPRA, wire-line logs through K1 display at least six and perhaps as many as eight motifs that can be interpreted as individual depo-

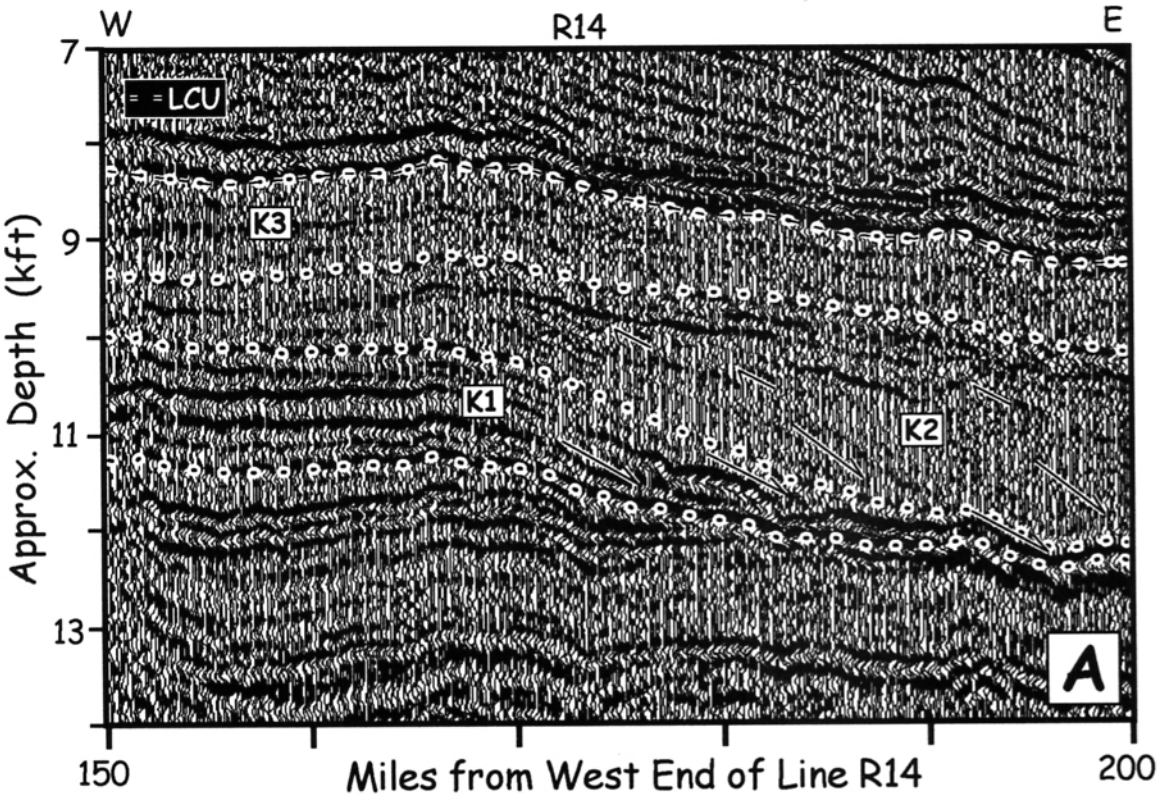
W
R14
E
7
9
11
13
Approx. Depth (kft)
LCU
K3
K1
K2
A
150
Miles from West End of Line R14
200

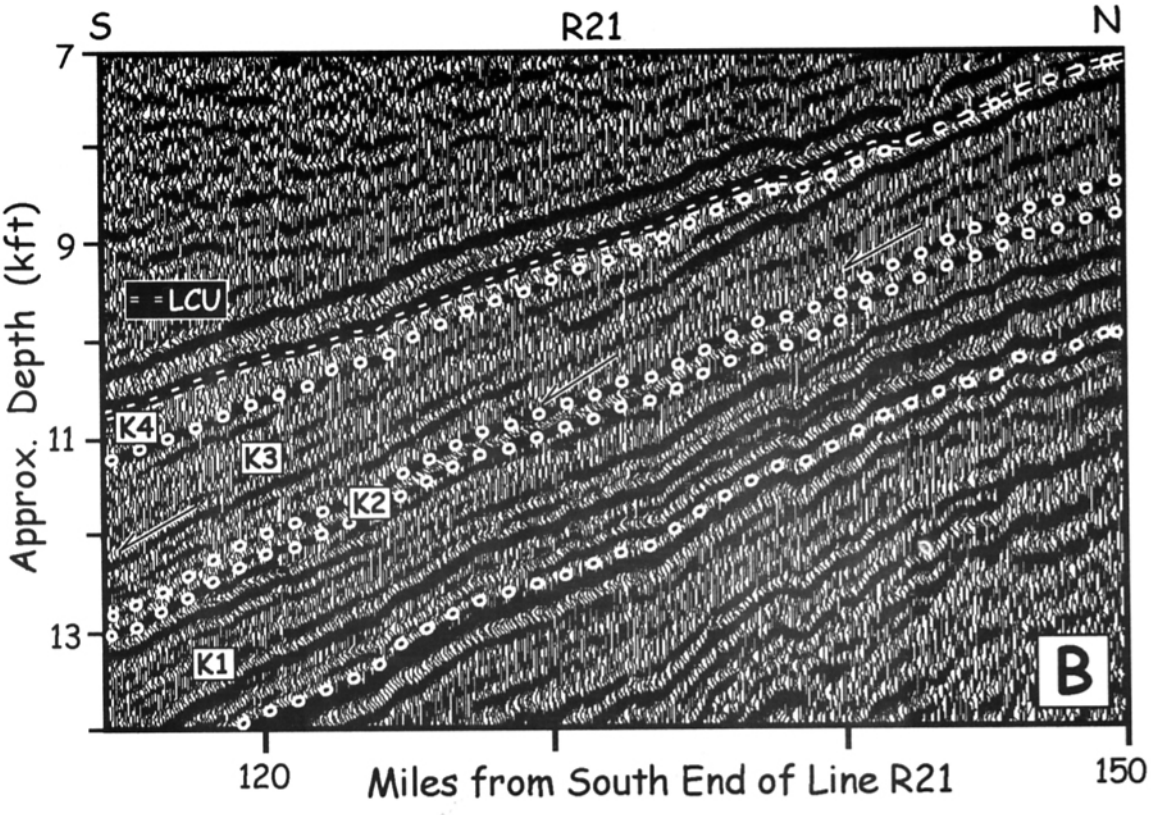
S
R21
N
7
9
11
13
Approx. Depth (kft)
LCU
K4
K3
K2
K1
B
120
Miles from South End of Line R21
150

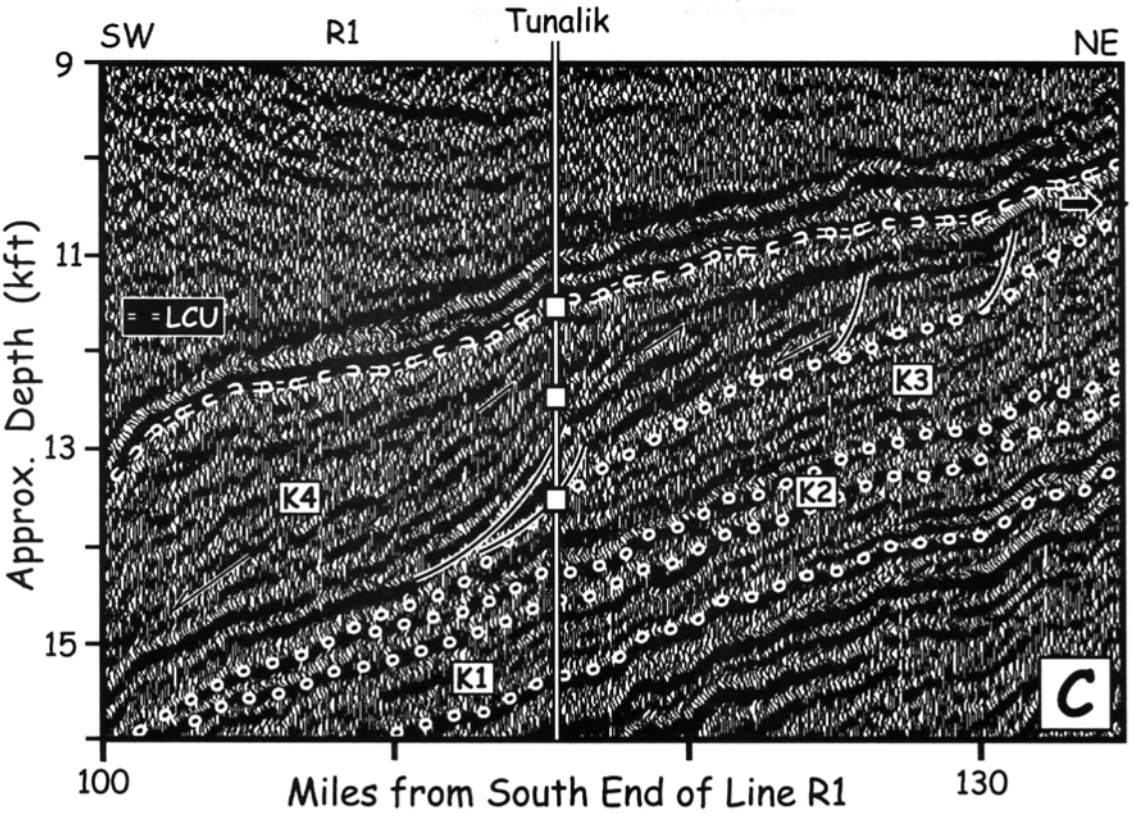

←↑ **Figure 5.** Representative seismic sections illustrating main attributes of Beaufortian depositional sequence sets. Locations of lines are shown in Figure 1. *A*. Segment of west-east line R14. In K1, the eastward transition from shelf to slope to basin is shown between miles 170 and 190. K2 thickens in a complementary manner above K1, and develops clinoforms that downlap basinward onto the top of K1. K3 at this location comprises gently south-dipping clinoforms, which appear to have no dip in this section parallel to their strike. No K4 strata are present in this section. *B*. Segment of south-north line R21. K1 displays medium to high amplitude, laterally continuous reflections typical of the shelf area in northern NPRA. K2 is thin and inferred to comprise mostly TSTs in this area. K3 displays gently south-dipping clinoforms typical of the study area. The northward tapering wedge and zero edge of K4 also are visible. *C*. Southwest-northeast segment of line R1 illustrates the abrupt basinward thickening of K4 at the shelf-margin. Note that the base of K4 truncates reflections in K3 and appears to cut into K2 at the left side of the figure. Internal stratal geometries suggest onlap (arrow at right), syndepositional normal faults (curved lines), downlap (single-barbed down arrows), toplap (single-barbed up arrows), internal truncations of reflections, and chaotic zones. Note seismically transparent zone that caps K4 along the entire length of this segment.

sitional sequences. For example, near the base of K1 an interval that includes the "Barrow sandstone" displays a coarsening-upward section capped by sandstones interpreted as a progradational succession of shoreface deposits inferred to be a lowstand systems tract (Fig. 7, Walakpa 1). This section is overlain by an abrupt fining from sandstone to siltstone that, in turn, is overlain by an abrupt fining from siltstone to shale with relatively high gamma-ray response ("warm shale"); together these are interpreted as a backstepping succession inferred to be a transgressive systems tract, with the shale corresponding to relatively condensed facies that include a maximum flooding surface. The interval is capped by a section that coarsens upward from shale to siltstone, which is interpreted as a progradational succession of distal shoreface deposits inferred to be a highstand systems tract. A synthetic seismogram through this interval displays a high amplitude reflection that corresponds to the shale inferred to include a maximum flooding surface. *During the workshop, examples of this type of sequence will be examined in cores from Walakpa 1 and Walakpa 2.*

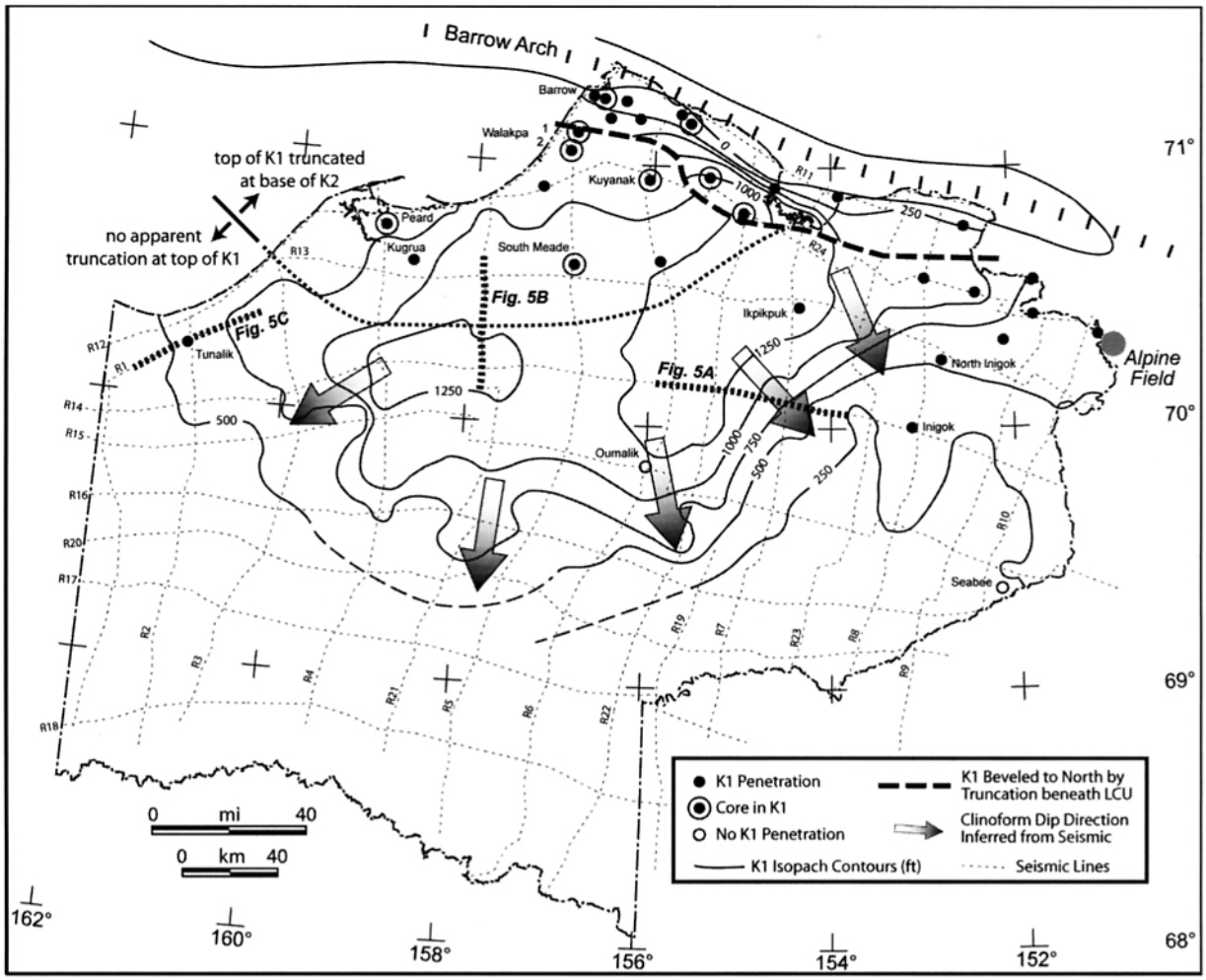

Figure 6. Map of the NPRA showing generalized thickness of Beaufortian sequence K1, well penetrations and cores of K1, inferred clinoform dip directions, and locations of seismic segments shown in Figure 5.

Less frequently, wire-line logs through K1 in northern NPRA display blocky sandstone patterns abruptly capped by shale with relatively high gamma-ray response. These blocky patterns are interpreted as shoreface or coastal channel (estuary or deltaic) deposits capped by relatively condensed facies that include a maximum flooding surface. In this case, a synthetic seismogram through the interval displays a high amplitude reflection that corresponds to the shale inferred to include a maximum flooding surface. These examples suggest that each laterally continuous, medium to high amplitude reflection within K1 may signify a low-velocity shale that represents a maximum flooding surface within an individual depositional sequence.

Farther south within the zone of maximum thickness (Fig. 6), wire-line logs through K1 display either subtle coarsening-upward sections capped with siltstone abruptly overlain by "warm shale," or monotonous sections of silty mudstone abruptly punctuated by "warm shale" (Fig. 7, Ikpikpuk). These intervals are interpreted as offshore to shelf successions that are the distal equivalents of the shoreface successions observed farther north. The "warm shales" are interpreted as relatively condensed facies that include maximum flooding surfaces.

The most distal well penetrations of K1 occur near the toe of the clinoforms in eastern NPRA (Fig. 6, North Inigok) and beyond the toe of the clinoforms (Fig. 6, Inigok). Wire-line logs through K1 at both locations display a "hot shale" (high gamma-ray response) within a thin interval of monotonous silty mudstone (Fig. 7, Inigok). The "hot shale" thickens from North Inigok to Inigok and is interpreted as a basinal condensed section.

Within the context of the interpretations presented above, the laterally extensive, moderate to high amplitude reflections that characterize K1 (Fig. 5) generally represent low velocity, condensed facies deposited during times when the shelf was flooded by

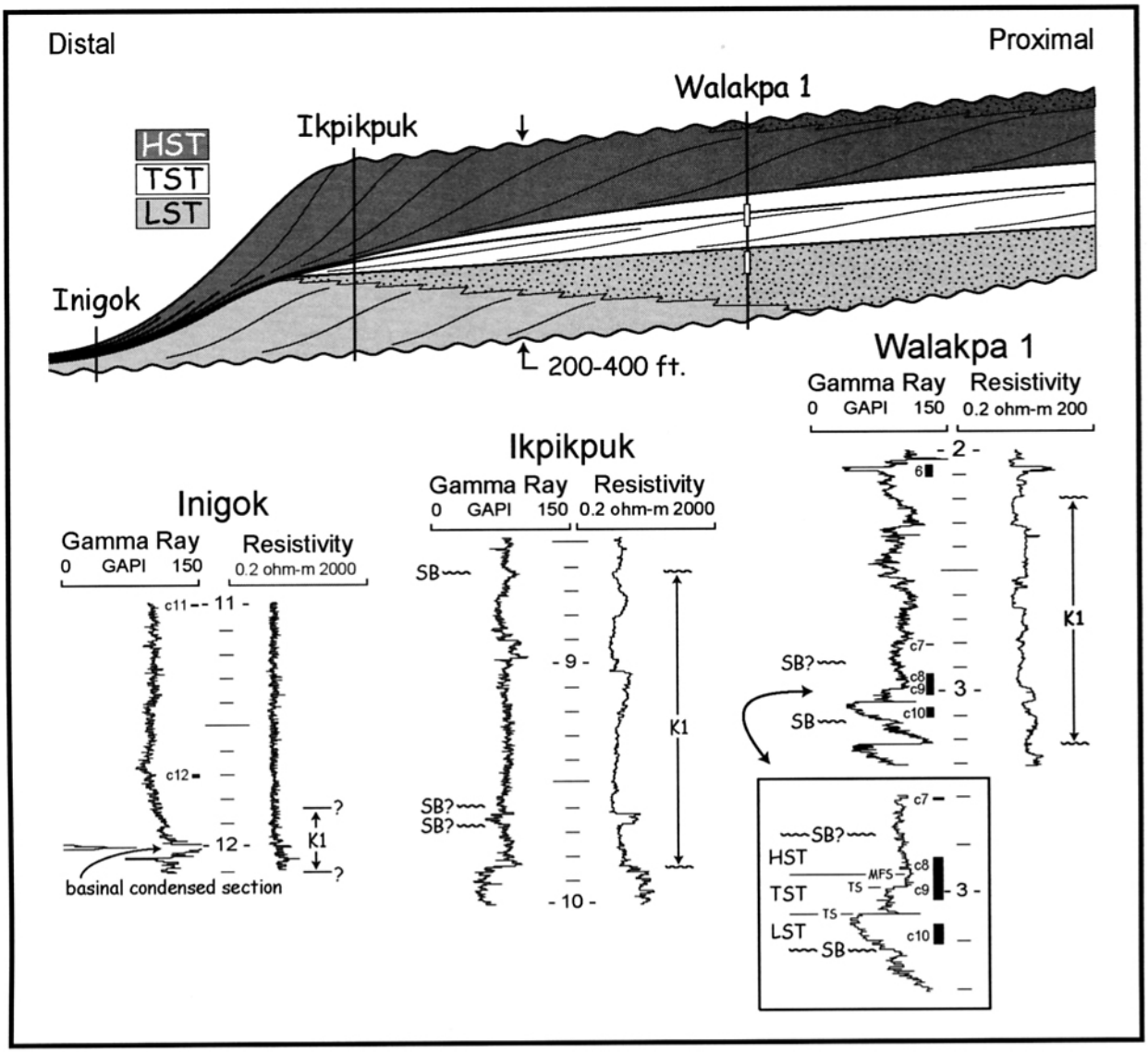

Figure 7. Schematic illustration of an individual depositional sequence within K1 and wire-line logs from wells inferred to penetrate various locations within depositional sequence. Core intervals are shown schematically in upper figure (white rectangles on wells) and accurately in log plots (c-prefix numbers denote cores in each well). Total K1 interval is shown for each well. Although one inferred depositional sequence is delineated in the expanded view of the Walakpa 1 well log, no attempt is made to correlate higher-order depositional sequences between wells. SB = sequence boundary; LST = lowstand systems tract; TST = transgressive systems tract; HST = highstand systems tract; TS = transgressive surface; MFS = maximum flooding surface. Wire-line log depth ticks are at 100 ft. intervals and numbers are X1000 ft. See Fig. 18 for key to symbols.

high relative sea level. On the shelf, these facies comprise "warm shales," each of which includes a maximum flooding surface. At the shelf margin, the "warm shales" grade basinward into "hot shales" as they downlap and coalesce into a basinal condensed section. The basinward increase in gamma-ray response likely reflects increased organic content and represents coalescence of time lines in a basinward direction. Collectively, the condensed facies that were draped across the shelf margin and deposited in the deeper basin comprise an important source rock interval that has long been recognized across the North Slope (e.g., Bird, 1985;Hubbard and others, 1987). The "Lower Kingak" has been mentioned in recent presentations (e.g., Hannon and others, 2000) as the probable source of the high gravity oil in Alpine field, and these condensed facies are likely candidates for that source rock.

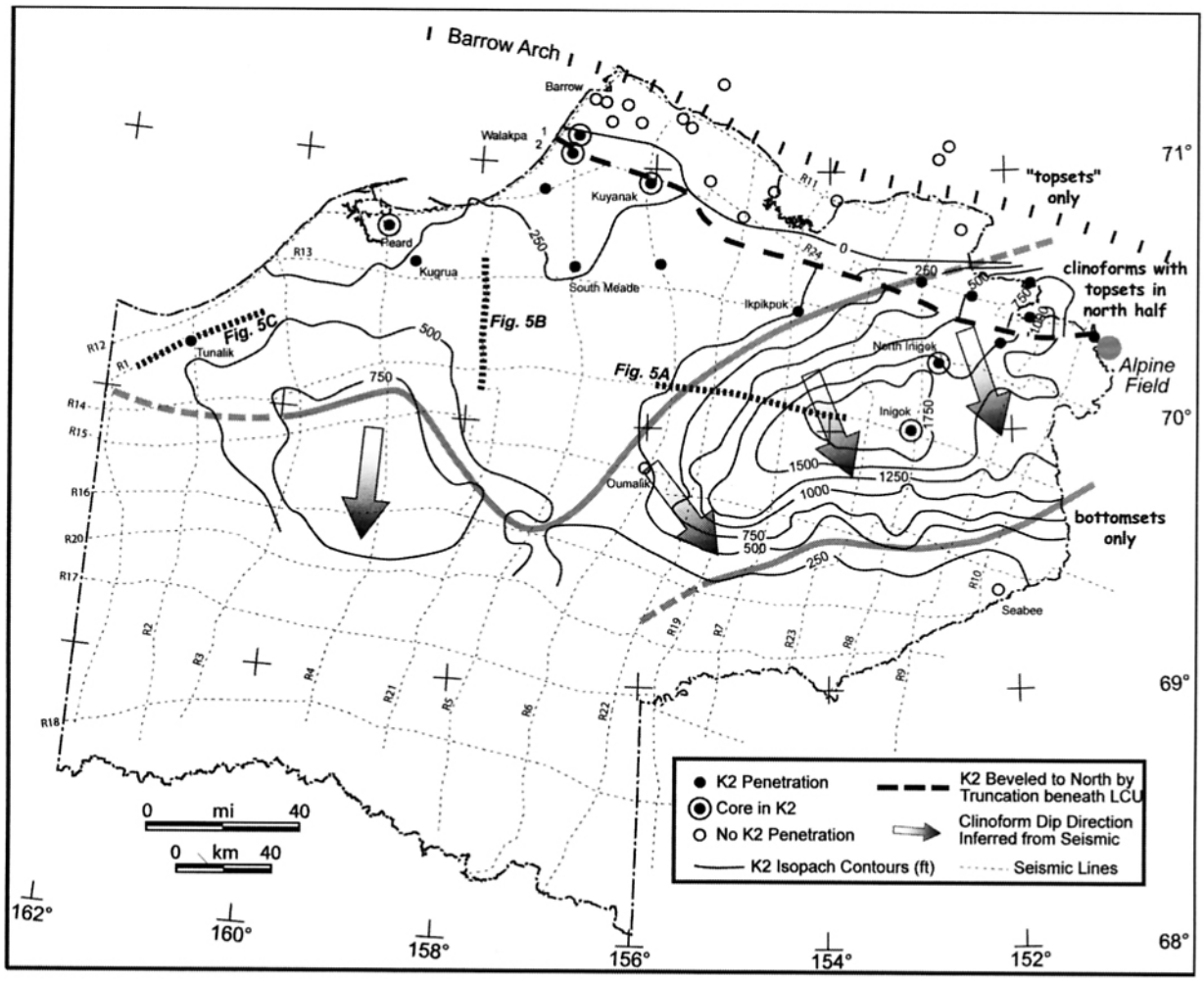

Figure 8. Map of the NPRA showing generalized thickness of Beaufortian sequence set K2, well penetrations and cores of K2, clinoform dip directions, and locations of seismic segments shown in Figure 5.

Sequence K1 represents the depositional construction of a clastic shelf primarily through progradation and aggradation of multiple depositional sequences through time under conditions of normal regression (as defined by Posamentier and Allen, 1999). The lobate shape of K1 and the radial dip of clinoforms (Fig. 5), together with the abrupt rollover of laterally extensive reflections into clinoforms at the shelf margin (schematically shown in Fig. 2A) suggest that this shelf was constructed as the result of long-lived sediment influx from a point source north of the Barrow area.

Sequence Set K2

Description – Across much of the study area (south of dotted line in Fig. 6) the base of K2 is a surface where internal reflections downlap onto the high amplitude reflection at the top of K1 (Fig. 5A). In northwestern NPRA (north of dotted line in Fig. 6), the base of K2 is defined by erosional truncation of K1 reflections and locally by northward onlap of K2 reflections onto that erosional surface. The top of K2 is defined by a reflection of laterally variable amplitude that serves as a subtle downlap surface for reflections within K3 (Fig. 5B). Internal reflection characteristics and geometries

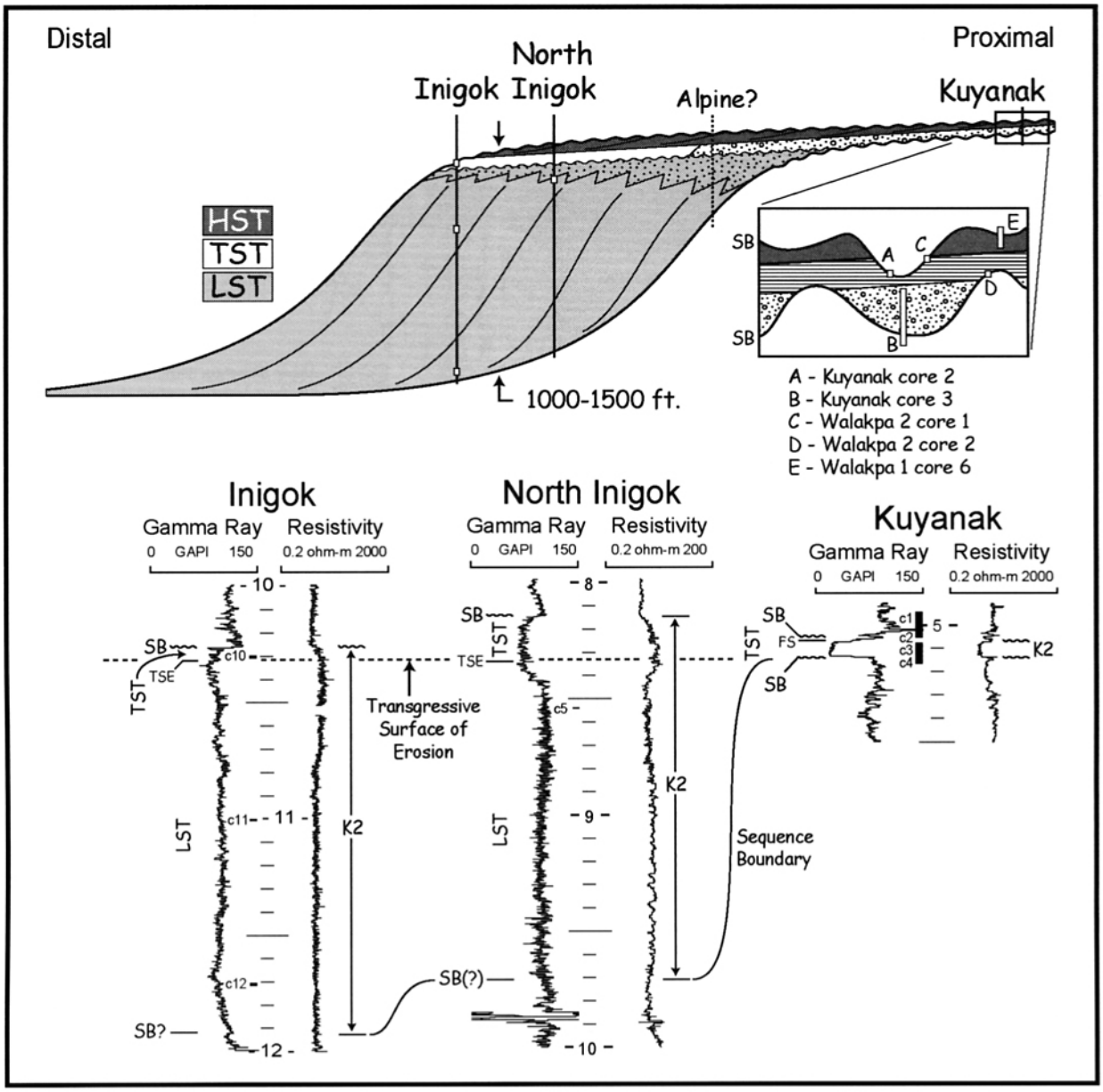

Figure 9. Schematic illustration of individual depositional sequence within K2 and wire-line logs from wells inferred to penetrate various locations within depositional sequence. Dotted line labeled "Alpine" shows inferred position within depositional sequence of stratigraphic interval containing main reservoir in Alpine field. Core intervals are shown schematially in upper figure (white rectangles on wells) and accurately in log plots (numbers with c-prefix denote core numbers in each well). Abbreviations same as in Fig. 7, plus TSE = transgressive surface of erosion. Wire-line log depth ticks are at 100 ft. intervals and numbers are X1000 ft. See Fig. 18 for key to symbols.

also are useful in defining the top of K2, and these are summarized below.

Correlation with paleontology data from NPRA wells indicates that K2 is Oxfordian to Kimmeridgian in age (Fig. 3). This sequence set is equivalent to the "Upper Kingak" of most workers.

An isopach map (Fig. 8) reveals a broad area in northcentral NPRA where sequence set K2 is less than 500 ft. thick, a depocenter in western NPRA where K2 attains a maximum thickness in excess of 750 ft., and a major depocenter in eastern NPRA where K2 attains a maximum thickness in excess of 1,750 ft.

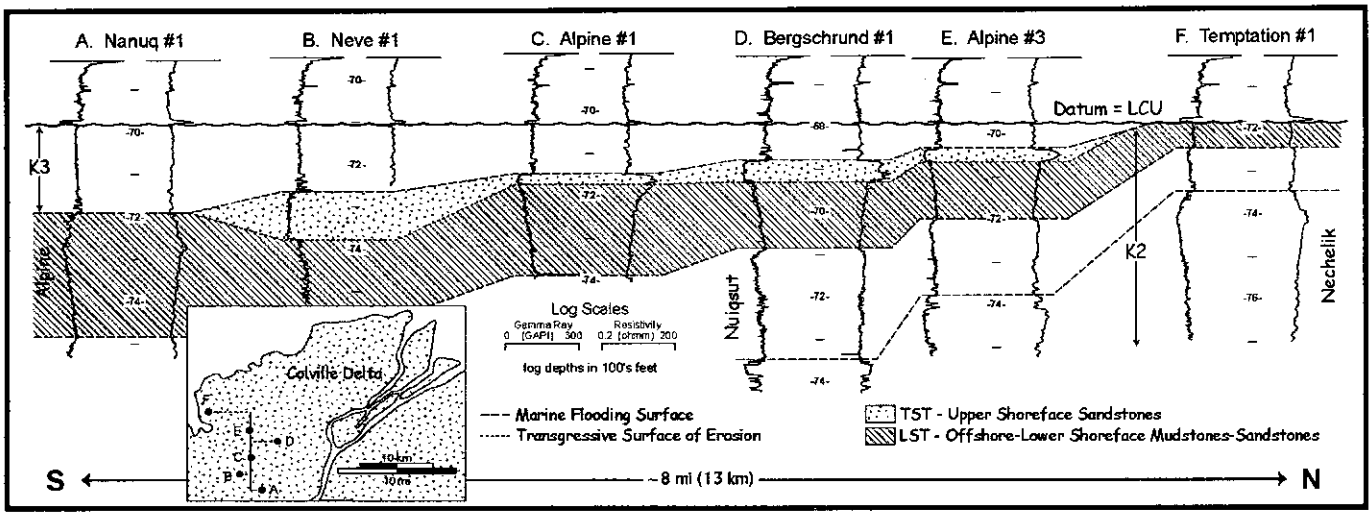

Figure 10. South-north wire-line log cross section through Alpine field. Location of Alpine field shown in Fig. 1. Stratigraphic intervals labeled Alpine, Nuiqsut, and Nechelik likely represent individual depositional sequences within sequence set K2. Inferred LST and TST are shown within Alpine interval. Marine flooding surfaces are also likely sequence boundaries. Main reservoir is inferred to be shoreface sandstone within TST. Datum is Lower Cretaceous Unconformity.

These thickness trends complement those of the underlying sequence set K1. That is, K2 is thin across the K1 shelf and K2 thickens abruptly basinward above the K1 shelf margin. K2 thins gradually to <500 ft. at the southern (basinward) margins of both depocenters (Fig. 8). Sequence set K2 thins abruptly to a zero edge along the trend of the Barrow Arch, where it is beveled beneath the LCU (Fig. 8).

Internally, sequence set K2 displays evidence of *at least* three higher-order depositional sequences that display similar seismic expressions. Within the broad area in northcentral NPRA where K2 is thin (<500 ft.), each of the higher-order sequences generally displays one predominant reflection that varies laterally from low to high amplitude and is underlain by a thin, seismically transparent zone (Fig. 5B). As the section thickens distally into the depocenters, the transparent zone thickens abruptly and develops clinoforms, and the reflection steps basinward across the clinoforms and then rolls over and sigmoidally downlaps the base of K2 (Fig. 5A). Within each higher-order sequence, the clinoforms dip steeply (3-4°), toplap the topset reflection, and downlap the basal sequence boundary where they coalesce into a medium to high amplitude bottom-set reflection distally. Clinoforms dip to the south in the western depocenter and to the southeast in the eastern depocenter (Fig. 8). Together, the three higher-order sequences form an offlapping pattern within K2, as illustrated schematically in Figure 3A.

Interpretation – Sequence set K2 is interpreted as three or more higher-order depositional sequences, each including a lowstand systems tract, a transgressive systems tract, and remnants of a highstand systems tract as illustrated schematically in Figure 9. Each depositional sequence contains a well-defined package of offlapping clinoforms. A typical wire-line log response through the distal part of a clinoform package (Fig. 9, Inigok) displays subtle patterns of coarsening upward (lower ~200 ft.) from "warm shale" to silty sandstone, fining upward (middle ~300-400 ft.) from silty sandstone to siltstone/mudstone, and siltstone/mudstone (upper ~400-500 ft.). The clinoform package is interpreted as a lowstand systems tract (LST) that represents rapid deposition of sediment on a marine slope during forced regression related to uplift and widespread erosion (probably subaerial) to form the unconformable sequence boundary to the north.

Overlying the LST and overstepping the LST in a northward (proximal) direction is a relatively thin (200-300 ft. or less) interval defined by a seismically transparent zone beneath a laterally extensive, medium to high amplitude reflection. Northward, this interval generally thins and onlaps the underlying sequence boundary. Locally, the reflection that defines this interval may display relief, may truncate underlying reflections, or may be truncated by overlying reflections. One well penetration of this interval in northern NPRA reveals a blocky, shoreface sandstone resting directly on the sequence boundary (e.g., Fig. 9,

Kuyanak) whereas other penetrations reveal black, fissile shale resting directly on the sequence boundary (e.g., Walakpa 2); *both cases will be examined in cores from Kuyanak and Walakpa 2 during the workshop.* This interval is interpreted as a transgressive systems tract (TST) whose constituent facies succession varies locally depending the geometry and relief of the underlying sequence bounding unconformity, which also appears to be transgressive surface of erosion in northern NPRA (Fig. 9).

At the base of the TST, shoreface sandstones displaying basal pebble lags and blocky log responses were deposited in topographically low areas. An additional possibility is that small displacement normal faults may have played a role in either the deposition or preservation of these shoreface sandstones, or perhaps in shaping the topography of the erosional surface on which the sandstones were deposited. The resolution of public domain data is insufficient to evaluate this possibility in NPRA, but the influence of faulting on deposition and preservation of Beaufortian sandstones in the Kuparuk River field has been documented (Masterson and Paris, 1987; Masterson and Eggert, 1992) and cannot be ruled out in the study area.

The porous, glauconitic sandstone in the Kuyanak well and the primary reservoir in the Alpine field (Figs. 9 and 10) are interpreted as examples of shoreface sandstones deposited on transgressive surfaces of erosion (i.e., ravinements) within higher order depositional sequences of K2. As illustrated in Figure 9, the "Kuyanak sand" likely was deposited in a proximal location where the transgressive surface of erosion and the basal sequence boundary are merged into a single surface, whereas the "Alpine sand" may have been deposited in a more distal, shelf-margin location where the transgressive surface of erosion caps a coarsening-upward parasequence of the LST, well above the basal sequence boundary. Descriptions of Alpine facies (Hannon and others, 2000; Morris and others, 2000) are consistent with interpretations of Kuyanak facies presented here, but a more definitive comparison must await the release of additional data and samples from the Alpine field.

Using data available in the public domain, two models are suggested for deposition of reservoir-quality sand in the K2 transgressive systems tracts. The "incision model" of Figure 11a depicts a broad erosional surface (sequence-bounding unconformity) dissected by a narrow incision cut by erosion (probably fluvial) during relative sea level lowstand. Subsequent transgression resulted in modification of the unconformity by shoreface erosion (ravinement) and local accumulation of winnowed shoreface sand in the incision. The overall depositional pattern envisioned in this model is that of an estuary. Evidence for this depositional geometry is derived primarily from 2-D seismic data in NPRA, as illustrated in Figure 12.

The "embayment model" of Figure 13a depicts a similar setting, except that a broad embayment replaces the incised channel. Evidence for this depositional geometry is derived from public domain maps of the Alpine field, which indicate sand-body geometry that is subequant and oriented approximately parallel to depositional strike. A possible example of this geometry is shown in 2-D seismic data from NPRA in Figure 14.

The incision and embayment depositional models may represent relatively proximal and distal depositional settings within a single depositional system. It seems logical that the northern part of NPRA (south flank of Barrow Arch) may have been characterized by incisions separated by broad interfluves and these may have graded southward into embayments or even open shelf depositional systems. The incision and embayment depositional models both suggest the following important implications: (1) The initial geometry of the depositional surface was sculpted by lowstand erosion, likely during forced regressions related to pulses of uplift on the Barrow Arch; (2) The ultimate geometry of the depositional surface was modified by transgressive shoreface erosion (i.e., ravinement); (3) Stratal geometry indicating the potential for shoreface sandstones ranges from subtle (embayments) to obvious (incisions) in public domain, 2-D seismic data in NPRA.

The northward convergence of multiple sequence boundaries in K2 makes it difficult to correlate specific surfaces and sandstones, considering the limited resolution of public domain data. It is possible, therefore, that some sandstone bodies may be composites of shoreface sandstones deposited within different depositional sequences. In other words, sequence-bounding unconformities may occur within the blocky sandstones.

As transgression proceeded to maximum flooding of the shelf, a condensed facies comprising dark grey to black, fissile shale was deposited (Figs. 11b and 13b). In areas of topographic lows on the ravinement/sequence boundary, this condensed facies caps shoreface sandstones and has excellent potential as a seal for any hydrocarbons in those sandstones (Alpine is a good example; Fig. 10). In areas of topographic highs on the ravinement/sequence boundary, the condensed facies rests directly on the sequence

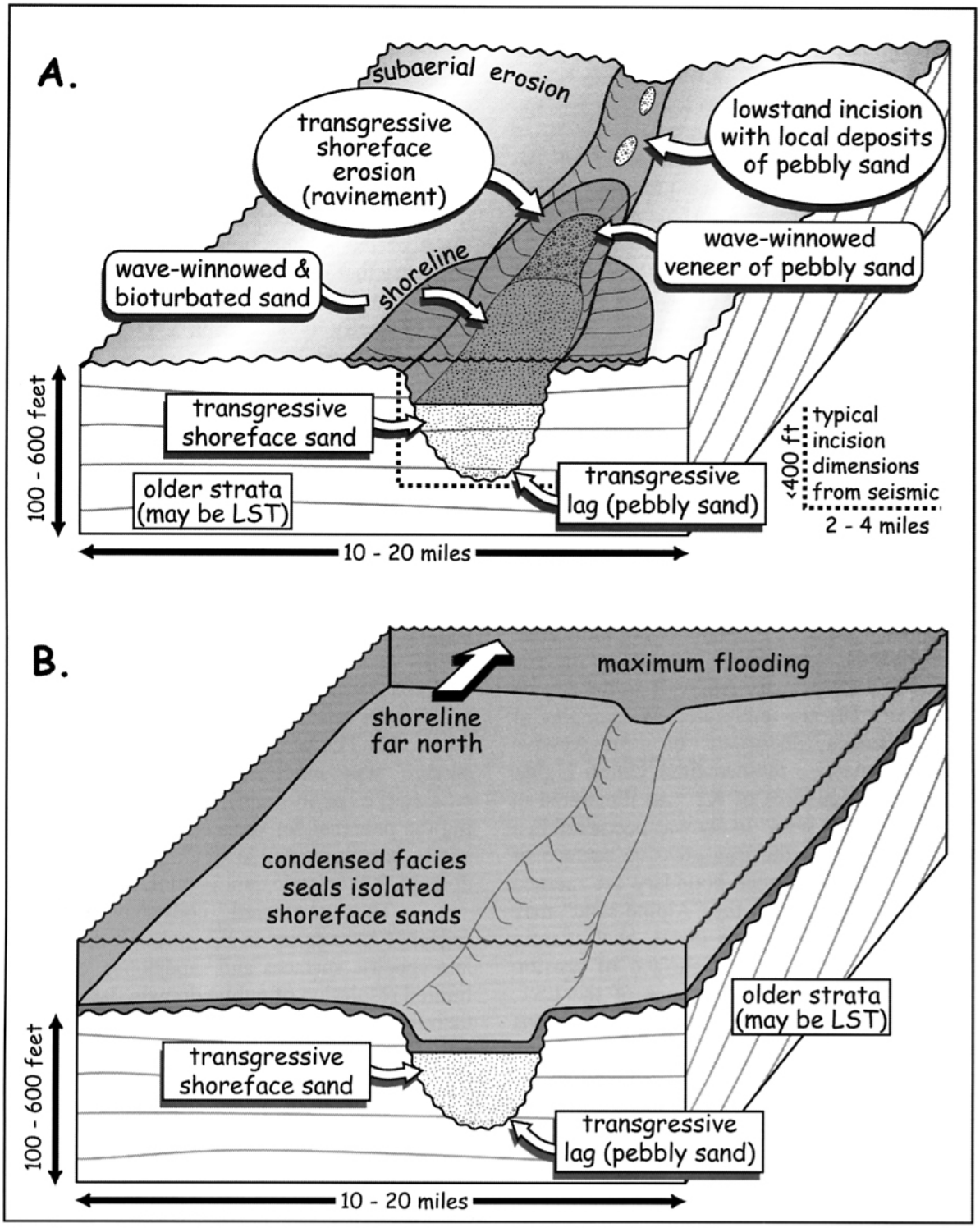

Figure 11. Incision model for deposition of shoreface sand within transgressive systems tract in sequence set K2. *A. (top)* Shoreface transgression showing deposition of shoreface sand. *B. (bottom)* Maximum transgression showing deposition of condensed mudstone.

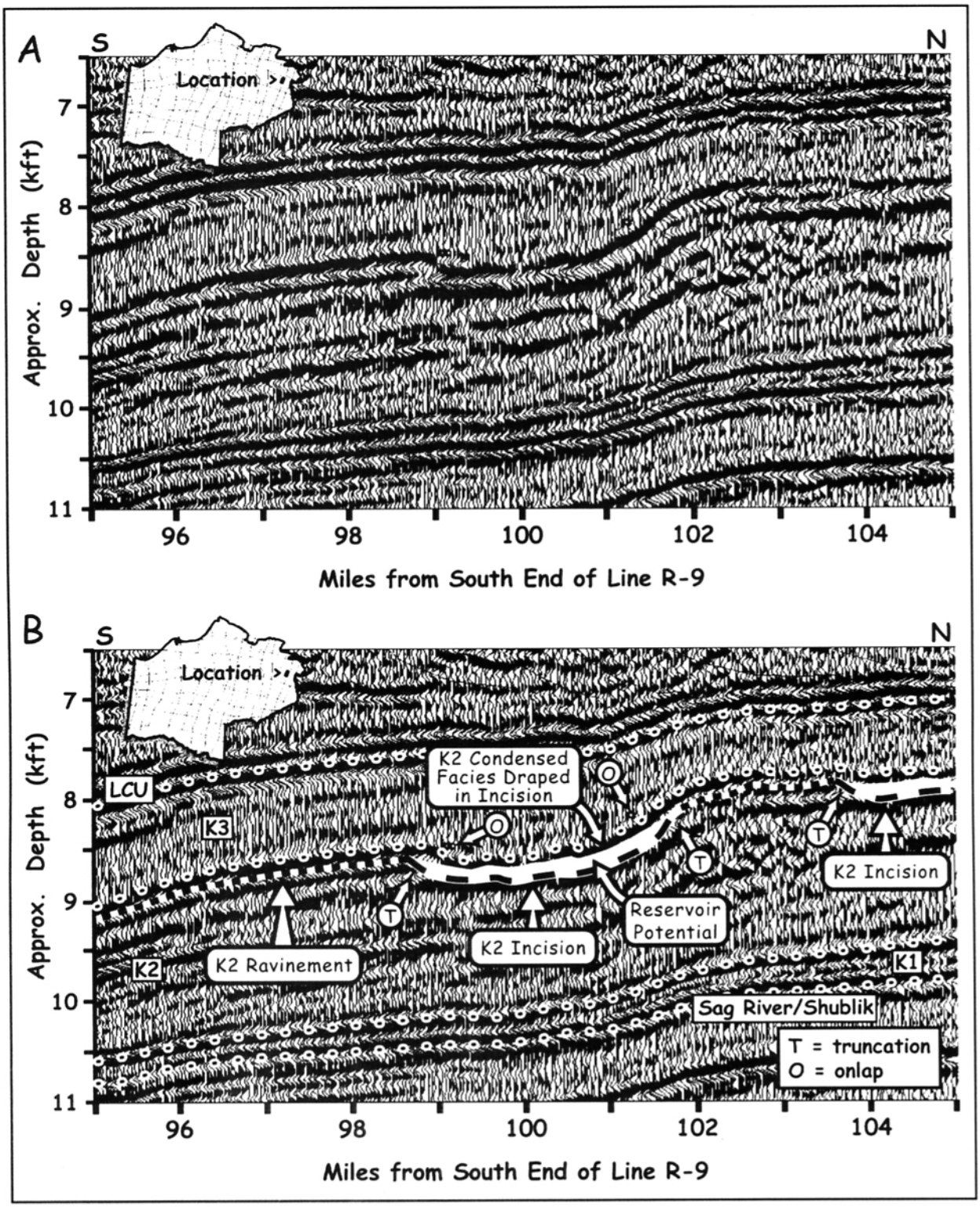

Figure 12. Segment of USGS seismic line R-9 illustrating feature interpreted to be incision in upper part of sequence set K2 in eastern NPRA. *A. (top)* Non-interpreted. *B. (bottom)* Interpreted.

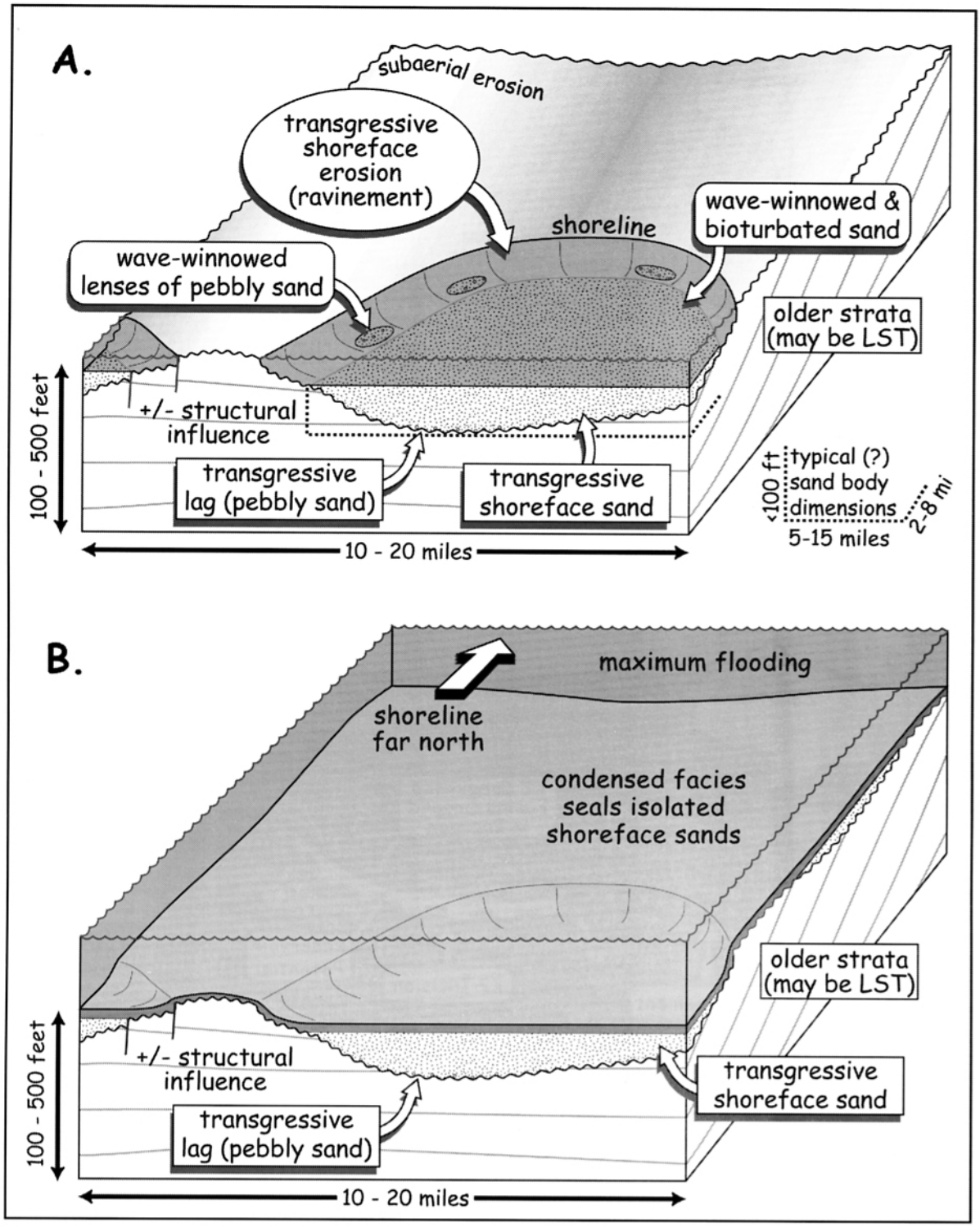

Figure 13. Embayment model for deposition of shoreface sand within transgressive systems tract in sequence set K2. *A. (top)* Shoreface transgression showing deposition of shoreface sand. *B. (bottom)* Maximum transgression showing deposition of condensed mudstone.

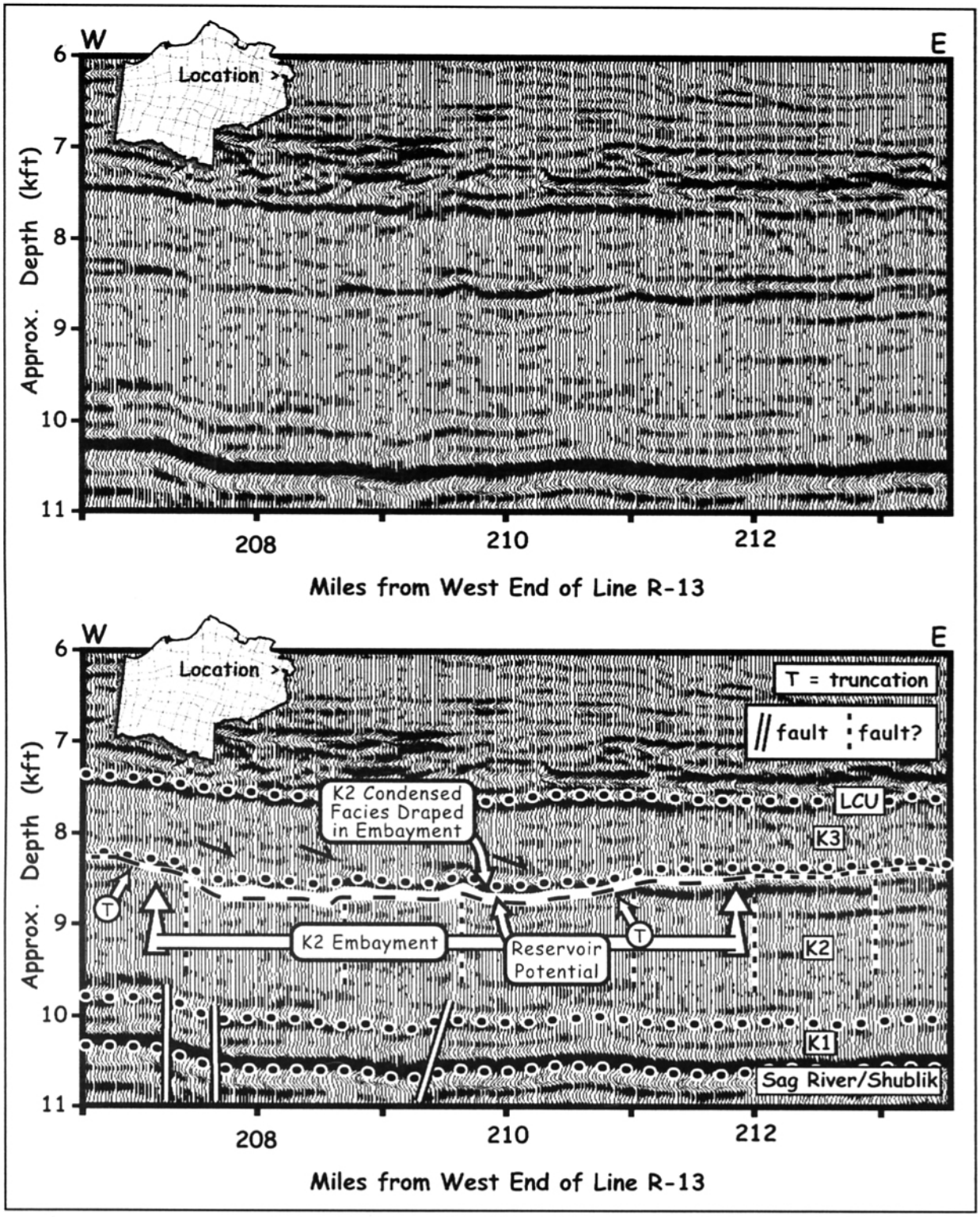

Figure 14. Segment of USGS seismic line R-13 illustrating feature interpreted to be embayment in upper part of sequence set K2 in eastern NPRA. *A. (top)* Non-interpreted. *B. (bottom)* Interpreted.

bounding unconformity (*e.g., Walakpa 2 core*). A maximum flooding surface is inferred to be present within this condensed facies.

Incompletely preserved above the TST is a generally coarsening upward succession of mudstones through muddy and silty sandstones, all thoroughly bioturbated, that represent offshore through lower shoreface deposits. *A good example of this succession will be examined in core from Walakpa 1, just beneath the "Walakpa sand."* This succession is interpreted as a highstand systems tract (HST) deposited during normal regression. Preservation of the HST is meager, particularly in northern NPRA, owing to widespread erosion of this succession during development of the succeeding sequence bounding unconformity(ies).

Sequence set K2 and its constituent higher-order sequences probably reflect repeated forced regressions (Posamentier and Allen, 1999) that caused widespread erosion across northcentral NPRA and accumulation of the derived sediment at the shelf margin in lowstand systems tracts. The forced regressions likely were caused by episodic tectonic uplift along the Barrow Arch during the "failed rift" events described by Hubbard and others (1987). Each forced regression was followed by flooding of the shelf as the result of a rise in relative sea level and the deposition of a transgressive systems tract.

Sequence Set K3

Description – The base of K3 is defined by a seismic reflection of laterally variable amplitude that serves as a subtle downlap surface for reflections within K3 (Fig. 5B). Across a broad area of northern NPRA, the top of K3 is defined by erosional truncation at the LCU (Fig. 15 – north of dashed line). South of that area, the top of K3 is an erosional surface defined by lateral termination of reflections within K3 (Fig. 5C).

Correlation with paleontology data from NPRA wells indicates that K3 is mostly Valanginian in age. This sequence may be equivalent to the Miluveach Formation and/or the lower part (A and/or B) of the Kuparuk (River) Formation (Carman and Hardwick, 1983; Hubbard and others, 1987; Masterson and Eggert, 1992).

An isopach map (Fig. 15) reveals a broad area in northern NPRA where sequence set K3 is beveled beneath the LCU, thinning northward from >1000 ft. to a zero edge, which trends from the Walakpa wells to the Colville River delta. South of that beveled zone, sequence set K3 displays two lobate depocenters, one in western NPRA where maximum thickness exceeds 1,750 ft. and a smaller one in eastern NPRA where maximum thickness exceeds 1,250 ft. (Fig. 15). The distal margins of both lobes display radial thinning to <750 ft.

Internally, sequence set K3 displays evidence of at least two higher-order sequences that display similar seismic expressions. In distal parts of the study area, the higher-order sequences include in their lower parts relatively thin intervals of reflections that onlap northward the basal sequence boundaries. Across the entire study area, including its northern-most limits, both of these higher-order sequences are characterized by low angle (<0.5°), ramp-like clinoforms defined by low to moderate amplitude reflections that display good lateral continuity (Fig. 5B). The older of the two higher-order sequences displays clinoform dips to the south-southeast and represents most of the volume of the eastern depocenter. The younger of the two higher-order sequences displays clinoform dips to the southwest and represents most of the volume of the western depocenter. In both cases, dip direction is generally perpendicular to thickness contours south of the LCU truncation line (Fig. 15). One notable exception to these characteristics is a local zone of relatively steep dipping (1-2°) clinoforms in the vicinity of the Kugrua and Peard wells in northwestern NPRA (Fig. 15).

Interpretation – Sequence set K3 is interpreted as two or more higher-order sequences that display similar characteristics. Although not resolvable on seismic data, a thin transgressive systems tract is inferred to occur at the base of K3 in northern NPRA, based on wire-line log and core data. In the Walakpa wells (Fig. 16), the gas reservoir is a sharp-based, blocky sandstone whose sedimentary structures and trace fossils indicate deposition in a shoreface environment. Micropaleontology data from core samples indicate that this sandstone is probably Valanginian in age, which suggests it is part of sequence K3. This shoreface sandstone likely represents a transgressive systems tract deposited during flooding of the shelf during a rise in relative sea level following a long interval of shelf exposure and erosion that formed the sequence bounding unconformity between K2 and K3. *This transgressive systems tract and its basal, reservoir-quality sandstone will be examined in cores from Walakpa 1 and 2.*

Wire-line logs elsewhere in northern NPRA display patterns that suggest the local presence of relatively sandy, proximal facies. For example, the

Ikpikpuk well penetrated a sandstone-rich K3 section displaying log motifs that suggest complex facies relationships within multiple depositional paraseq-uences (Fig. 16). Farther basinward, the Inigok log displays a sharp-topped, sandy successsion at the top of the underlying K2, which is overlain by a "warm shale" (~100 ft. thick) at the base of K3 (Fig. 16). The abrupt K2-K3 contact is interpreted as both the sequence boundary at the base of K3 and a transgressive flooding surface. The sequence boundary may be either a subtle unconformity or a correlative conformity, as there is no seismic evidence for erosion. Paleontological data available in the public domain indicate a time gap between Kimmeridgian at the top of K2 and Valanginian at the base of K3 in the North Inigok well (Fig. 17), but the presence of a similar gap in the Inigok well is equivocal. The "warm shale" at the base of K3 is interpreted as a thin transgressive systems tract that includes a maximum flooding surface at or near its top. This shale is interpreted as a relatively condensed facies deposited when the shelf was flooded by high relative sea level.

The overlying interval is a thick succession (up to 600 ft.) of monotonous to subtly coarsening-upward shale and silty shale that locally includes an interval of thin sandstone interbeds near its base (Fig. 16, Inigok). Sparse core control from the Inigok and South Meade wells indicate lithologies and trace fossils typical of offshore successions deposited well below maximum (storm) wave base. This is the interval that correlates to the low-dip clinoforms observed in seismic data, and it is interpreted as a highstand systems tract comprising a muddy and silty succession deposited on a gently dipping marine slope (ramp?). Seismic observations suggest that this facies is volumetrically predominant in K3 across much of NPRA.

The thin intervals of northward onlapping reflections in the lower part of each depositional sequence within K3 likely represent lowstand systems tracts. Although there is little well control in the distal parts of K3 sequences, the Tunalik log displays a K3 section comprising monotonous silty mudstone with one coarsening upward, sandstone-rich interval (Fig. 16). This succession may represent distal offshore and/or slope facies. The sandstone-rich interval may be a submarine fan lobe within a lowstand systems tract.

The local occurrence of relatively steep-dipping clinoforms within K3 is an anomaly worthy of brief discussion, as steeper clinoforms are thought to imply greater sand content (e.g., Galloway and Hobday, 1996). The Kugrua and Peard wells (Fig. 15) display a log response through K3 that is punctuated by multiple, thin (<100 ft.) successions of sandstone. Some coarsen upward and display sharp tops, whereas others coarsen upward and display fining-upward tops. These sandstones may represent lower shoreface sands associated with a depositional lobe that is sandier than K3 across most of NPRA.

The overall pattern of sedimentation indicated by K3 suggests progradation of at least two lobes of sediment under conditions of normal regression. The relatively distal character of most facies further suggests that relative sea level was high and that the study area was mostly an offshore system (distal shelf?) with perhaps indications of lower shoreface conditions in the northernmost areas of K3 preservation.

Sequence Set K4

Description – The base of K4 is an erosional surface defined by a medium to high amplitude reflection that cuts into K3 and K2 (Fig. 5C). Reflections within K3 and K2 terminate abruptly against the unconformity. In the proximal (northern) portion of K4, the top of the sequence is defined by the LCU. Basinward (Fig. 17, along and south of an approximate line between the Tunalik and Seabee wells), the top of K4 is defined by a high amplitude reflection that marks the contact between sandy successions near the top of K4 and the overlying pebble shale unit (Fig. 5C). Whether this contact is an unconformity or a correlative conformity in these distal parts of the basin is unknown.

Correlation with paleontology data from NPRA wells indicates that K4 is mostly Hauterivian in age (Fig. 3). This sequence may be equivalent to the lower part (A and/or B) of the Kuparuk (River) Formation (Carman and Hardwick, 1983; Hubbard and others, 1987; Masterson and Eggert, 1992).

An isopach map (Fig. 17) illustrates that K4 thickens gradually from a zero edge southward for 10 to 30 miles (to approximately 500 ft. thick), and then thickens abruptly to the south. Sequence K4 displays two depocenters, one in western NPRA where maximum thickness exceeds 2,000 ft. and one in eastern NPRA where maximum thickness exceeds 1,750 ft. (Fig. 17). The distal margins of these depocenters are poorly defined, as they occur at great depths where data resolution deteriorates and structural thickening introduces interpretation uncertainties.

Internally, sequence K4 displays seismic geometries that suggest a high degree of complexity on a relatively local scale, particularly in the area where the sequence thickens abruptly to the south. In the

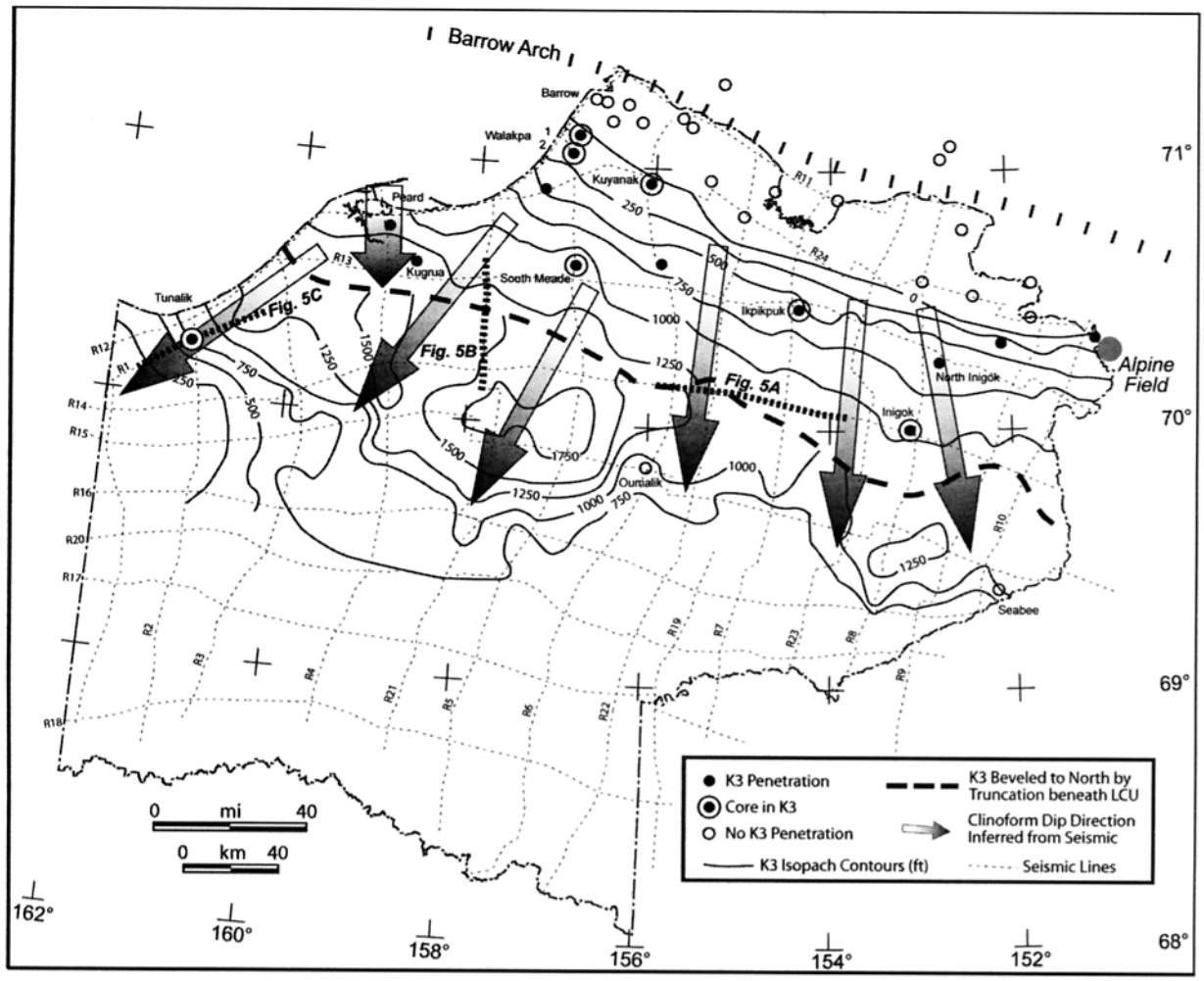

Figure 15. Map of the NPRA showing generalized thickness of Beaufortian sequence set K3, well penetrations and cores of K3, clinoform dip directions, and locations of seismic segments shown in Figure 4.

area of gradual thickening just south of the zero edge, medium to high amplitude reflections define clinoforms (average dip ~1°) that onlap in a proximal direction onto the basal sequence boundary and downlap in a distal direction onto the basal sequence boundary (Fig. 5C). Within the area of abrupt thickening, clinoforms dipping 1-3° are discernable and individual reflections are offset by normal faults in some places and deformed into chaotic geometries in other places (Fig. 5C). Extending from the zero edge southward across the thickest part of the depocenters, a relatively thick (up to 700 ft.) and laterally continuous, seismically transparent interval caps the sequence (Fig. 5C). Locally, chaotically deformed reflections in the underlying clinoform section are truncated by the transparent interval. Elsewhere, undeformed clinoforms toplap the transparent interval. The southern (distal) portions of the depocenters appear to be composed primarily of basinward-dipping clinoforms, but deterioration of seismic data precludes detailed characterization.

Interpretation – Interpretations of K4 rely heavily on information from the Tunalik well because a complete wire-line log suite and cores are available. Only two other wells have penetrated K4 in NPRA (Oumalik and Seabee; Fig. 17), and only partial wire-line logs are available from those penetrations.

Sequence K4 is interpreted as a single depositional sequence, including a lowstand systems tract capped by a transgressive systems tract as illustrated schematically in Figure 18. The sequence displays significant internal complexity inferred to be the result

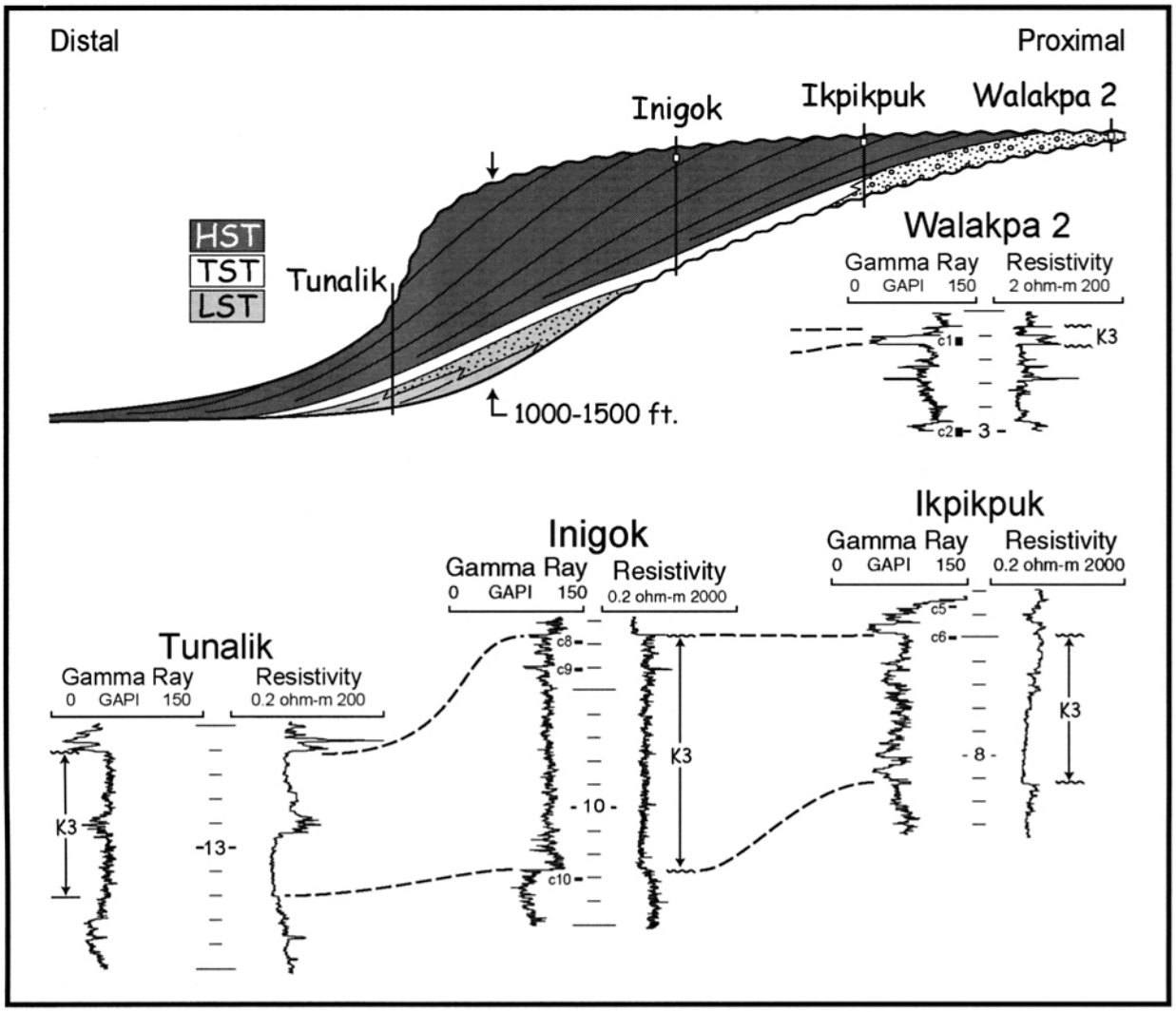

Figure 16. Schematic illustration of individual depositional sequence within K3 and wire-line logs from wells inferred to penetrate various locations within depositional sequence. Core intervals are shown schematically in upper figure (white rectangles on wells) and accurately in log plots (numbers with c-prefix denote core numbers in each well). Although total K3 interval is shown for each well, no attempt is made to correlate higher-order depositional sequences between wells. Wire-line log depth ticks are at 100 ft. intervals and numbers are X1000 ft. See Fig. 18 for key to symbols.

of repeated synsedimentary collapse of the shelf-margin.

The base of K4 is an erosion surface that, in the vicinity of the Tunalik well, cuts down into older Beaufortian sequences in two distinct steps (Fig. 18). The more proximal step is filled with strata that include moderate amplitude reflections that onlap the basal unconformity in a proximal direction and downlap the basal sequence boundary basinward (Fig. 18). These reflections are broadly convex upward and are interpreted as the early part of a lowstand systems tract.

The more distal (southern) step is filled with strata that display on seismic data an overall clinoform geometry complicated by a spectrum of synsedimentary deformation features. Some reflections appear to be offset by down-to-the-basin (south) normal faults and others are deformed into chaotic geometries. In fact, it is possible that a synsedimentary, listric normal fault forms the sequence boundary in part of this distal step. The Tunalik well penetrates this distal step and the wire-line log response displays a sandy section at the base of K4 overlain by a thick succession that generally

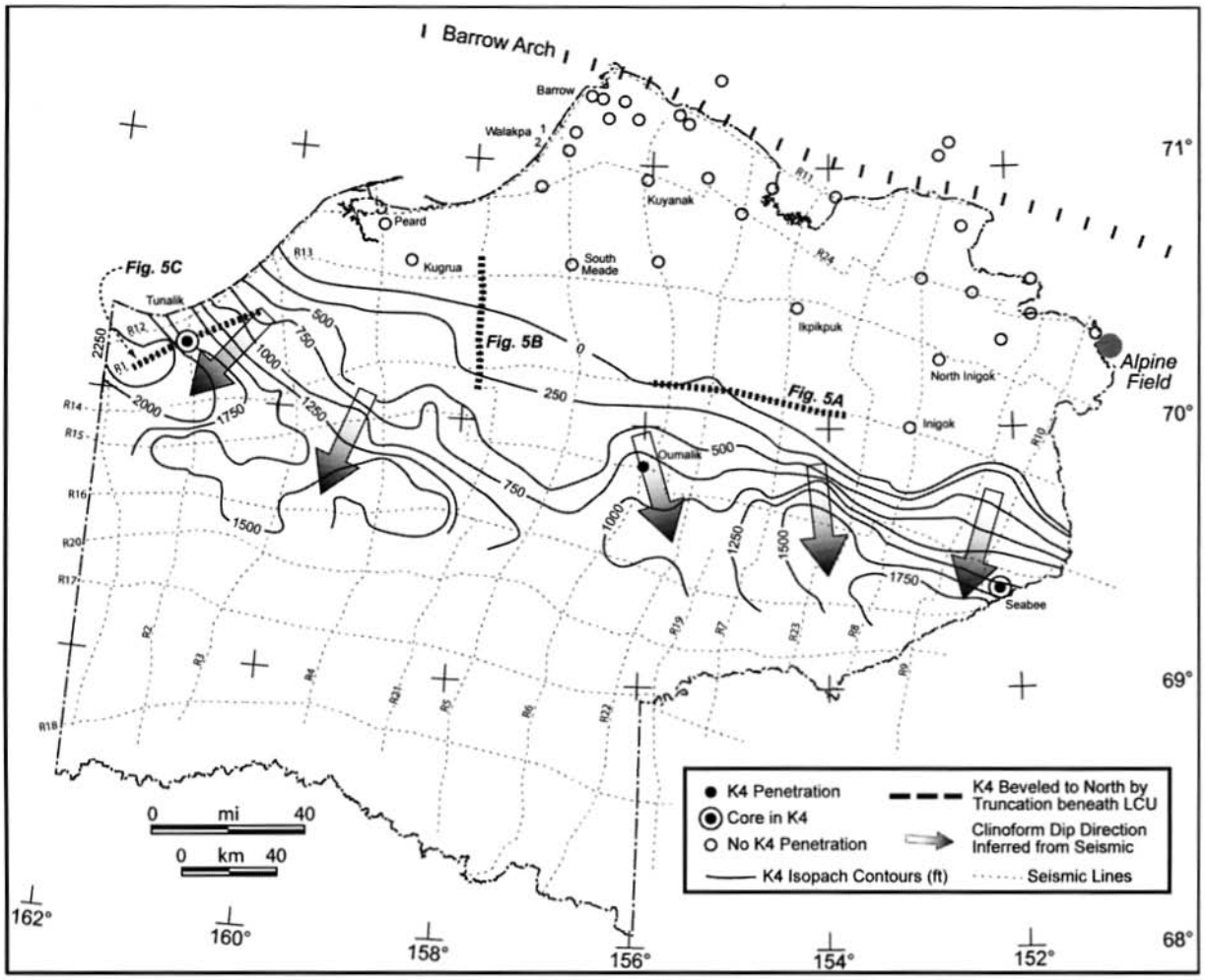

Figure 17. Map of the NPRA showing generalized thickness of Beaufortian sequence set K4, well penetrations and cores of K4, clinoform dip directions, and locations of seismic segments shown in Figure 5.

coarsens upward from silty mudstones to sandstone (Fig. 18). The sand-rich, upper part of this coarsening upward succession correlates to the lower half of the seismically transparent zone at the top of K4. A core through the basal, sand-rich section reveals intensely contorted shale and sandstone displaying megafauna and trace fossils that indicate shallow marine deposition (this core yielded foraminifera of "probable Valanginian" age). This section is interpreted as offshore to lower shoreface deposits of sequence K3 that slumped or collapsed into the base of sequence K4 as the shelf margin was deeply incised during formation of the K4 basal sequence boundary.

The thick, coarsening upward succession is interpreted as shoaling-upward deposits. Facies displayed in a core near the middle of the coarsening upward succession suggest more sand transport by unidirectional currents and less bioturbation than is commonly observed in shoreface deposits within the other Beaufortian sequences (K1-K3). Therefore, this succession is interpreted tentatively as prodelta through delta-front deposits. Collectively, these strata are interpreted as a lowstand systems tract deposited during forced regression, and they may represent a shelf-margin delta system.

The coarsening upward succession (LST) displays an abrupt top, which is overlain by a subtly coarsening upward interval more than 200 ft. thick that correlates to the upper half of the seismically transparent zone that caps K4 (Fig. 18). A core from this succession displays facies interpreted as the deposits of a wave-dominated shoreface. This succession is inferred to be a transgressive systems tract deposited as the shelf margin was flooded by a rise in relative sea level.

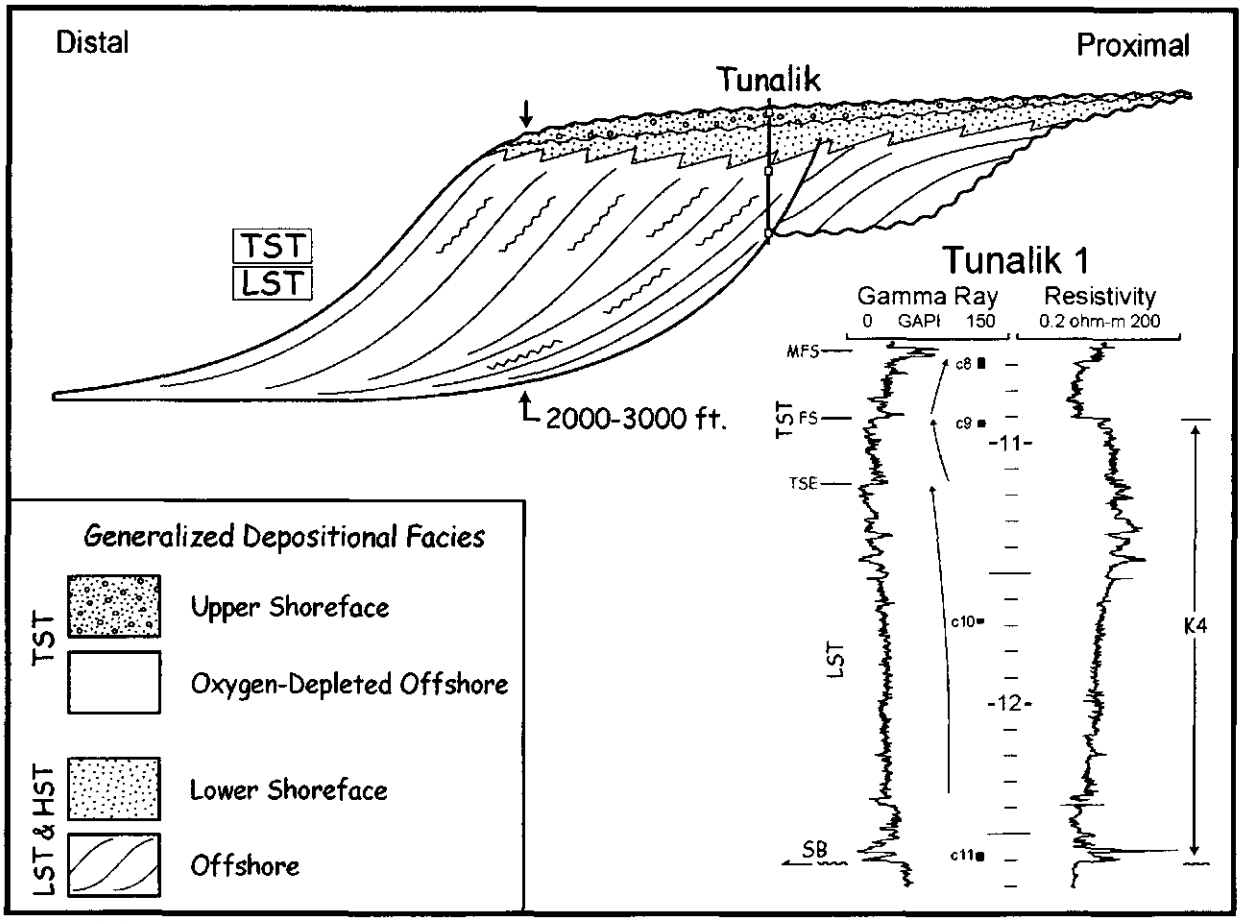

Figure 18. Schematic illustration of depositional sequence K4 and wire-line log from the Tunalik well. Core intervals are shown schematically in upper figure (white rectangles on wells) and accurately in log plot (numbers with c-prefix denote core numbers). Abbreviations same as Figs. 7 and 9. Wire-line log depth ticks are at 100 ft. intervals and numbers are X1000 ft. Arrows on log highlight overall coarsening and fining upwards successions.

Although sequence K4 has been interpreted as a single depositional sequence comprising a LST and a TST, it also is possible to interpret the two distinct steps within the LST as separate sequences. In fact, the overall geometry of those steps resembles the multiple, higher-order sequence boundaries formed under conditions of episodic fall in relative sea level described by Posamentier and Allen (1999, p. 35).

Sequence K4 clearly represents a forced regression that caused widespread erosion across northern NPRA and accumulation of the derived sediment at the shelf margin in a lowstand systems tract. It is suggested that the forced regression was caused by tectonic uplift along the Barrow Arch during the "successful rift" events described by Hubbard and others (1987). The uppermost part of K4 is a transgressive systems tract that reflects flooding of the shelf as the result of a rise in relative sea level.

SEDIMENTOLOGY OF BEAUFORTIAN STRATA

Depositional Facies

Cores of Beaufortian strata in NPRA display a spectrum of primary sedimentary structures and trace fossils that suggest deposition on a continental margin influenced predominantly by waves, and in environments ranging from offshore (shelf) through middle-upper shoreface. Therefore, most core intervals displayed in this workshop are interpreted within the context of well-documented shoreface analogues, and the main facies are described in the following sections. Because Beaufortian shoreface deposits in NPRA are so thoroughly bioturbated that few primary sedimentary structures are preserved, interpretations rely extensively on Pemberton (1992), both for facies

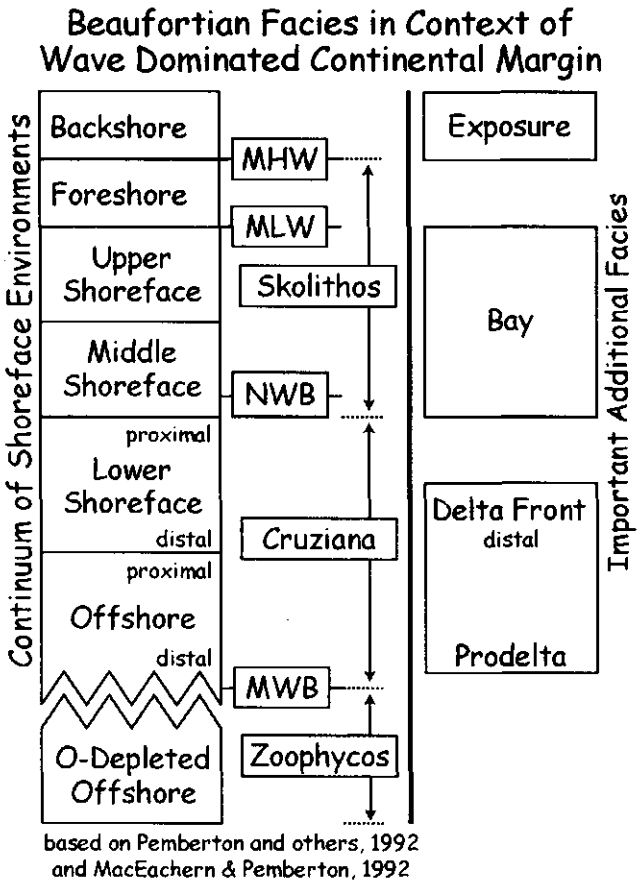

Figure 19. Idealized model of depositional facies inferred to be present in Beaufortian strata. Left side of model represents continuum of shoreface deposits and right side represents additional facies interpreted from NPRA cores. Approximate range of three major ichnofacies shown in center of figure. MHW = mean high water (high tide); MLW = mean low water (low tide); NWB = normal wave base (fair-weather); MWB = maximum wave base (storm). Based on MacEachern and Pemberton (1992) and Pemberton and others (1992b), with modifications (see text).

analogues and for trace fossil identification. A few additional facies, inferred to be locally present in NPRA cores, also are described below.

Facies successions observed in many NPRA cores can be placed into the idealized shoreface model shown on the left side of Figure 19 (based on MacEachern and Pemberton, 1992; and Pemberton and others, 1992b). This model summarizes the terminology used in this study, relates the ideal succession of shoreface deposits to diagnostic ichnofacies, and illustrates the approximate range of wave influence. An important element of this succession that has not been integrated into most shoreface models is the facies termed "oxygen-depleted offshore," which comprises fissile, dark grey to black shale that is commonly the primary facies of condensed sections. These facies do not fit conveniently into a generalized model because, although in some cases they may simply represent distal equivalents of more proximal shoreface deposits, in other cases they may represent relatively unusual geochemical conditions and therefore may not have recognized proximal facies equivalents. Additional depositional facies interpreted to be present in NPRA cores and not included in the genera-lized shoreface model also are shown on the right side of Figure 19.

Oxygen-Depleted Offshore Facies – This facies comprises dark grey to black, clay shales that typically display good fissility. Although bioturbation is rarely observed, the local occurrence of non-fissile claystone may suggest burrowing on a scale too fine to be observed in hand specimen. This facies locally contains pebbles of chert scattered randomly through the paper shale. Although total organic carbon (TOC) content varies between 1 and 10 percent, this facies tends to have consistently higher TOC values than other facies in the Beaufortian section. The oxygen-depleted offshore facies identified in NPRA cores may coalesce basinward to form the Blankenship member of the Otuk Formation (Mull and others, 1982).

This facies is interpreted as oxygen-depleted "offshore" deposits that represent a stratified water column at locations starved of clastic sediment influx. This condition may represent one or more of the following: (1) Deposition at the shelf margin and farther basinward during times of "normal" shoreface deposition landward; (2) Deposition on the shelf and farther basinward during times of high relative sea level, which accommodates upwelling of basinal water onto the shelf and starves the shelf of clastic influx by trapping sediment landward; (3) Deposition on the shelf and farther basinward due to stratification of the water column resulting from geochemical, oceanographic, or climatic influences.

Offshore Facies – This facies displays a spectrum of characteristics inferred to reflect gradation across a continuum of depositional conditions that have been termed distal (or lower) offshore through proximal (or upper) offshore by MacEachern and Pemberton (1992) and Pemberton and others (1992b). At one end of that spectrum, the *distal offshore* facies comprises silty mudstone and muddy siltstone with a few laminations of very fine-grained sandstone. It may display a horizontal fabric or appear massive. Laminations of silt and wispy clay indicate that the horizontal fabric

reflects primary bedding, although compacted horizontal trace fossils contribute to the fabric locally. This facies is sparsely to moderately bioturbated.

At the other end of the spectrum, the *proximal offshore* facies comprises muddy siltstone and silty mudstone, with thin zones of very fine-grained sandstone locally present. It is moderately to thoroughly bioturbated so that few primary laminations are visible. Most core intervals appear massive because of thorough bioturbation. A few intervals display a subtle horizontal fabric that appears to be more the result of a compacted, horizontal trace fossil assemblage than of primary bedding, although wispy clay laminations are common. Locally, thin interbeds of massive, very fine-grained sandstone displaying red-stained *Chondrites* are present.

The abundance of bioturbation increases by gradation from distal to proximal facies. Throughout the offshore facies, predominant trace fossils include *Chondrites*, *Planolites,* and *Helminthopsis*. Traces that are locally present include *Anconichnus* and *Asterosoma*. This assemblage is interpreted as a distal *Cruziana* ichnofacies (Pemberton and others, 1992a, b).

This facies is interpreted as the product of deposition in the offshore, completely below normal (fairweather) wave base and generally below maximum (storm) wave base. In various NPRA cores, the distal offshore facies grades into oxygen-depleted offshore deposits, and the proximal offshore facies grades into lower shoreface deposits.

Lower Shoreface Facies – This facies displays a spectrum of characteristics inferred to represent gradation across a continuum of depositional conditions. At one end of the spectrum, this facies comprises muddy siltstone and very fine grained, silty and muddy sandstone. At the other end of the spectrum, this facies comprises very fine grained, variably silty and muddy sandstone. Bioturbation is generally pervasive and complete, so that no primary sedimentary structures are preserved in most of the section. However, primary sedimentary structures are preserved locally in thin beds that display horizontal to low angle lamination. These beds tend to increase in abundance and thickness in going from finer-grained to coarser-grained subfacies.

Predominant trace fossils include *Anconichnus*, *Asterosoma*, *Chondrites*, *Helminthopsis*, *Planolites*, *Palaeophycus*, *Teichichnus*, *Terebellina*, and *Thalassinoides*. Trace fossils locally present include *Arenicolites*, *Diplocraterion*, *Rosselia*, *Skolithos*, and *Zoophycus*. Questionable trace fossils observed locally include *Ophiomorpha* and *Siphonichnus*.

The relative abundance and distribution of these trace fossils vary systematically and can be used to help define subfacies. In relatively fine-grained sections, predominant trace fossils are those considered to be indicators of deposit feeding organisms (e.g., *Anconichnus*, *Asterosoma*, *Chondrites*, *Planolites*, *Teichichnus*, and *Thalassinoides*), grazers (e.g., *Helminthopsis*), certain suspension feeders (e.g., *Terebellina*), and certain carnivores (e.g., *Palaeophycus*). In this association, trace fossils considered to be indicators of suspension feeders (e.g., *Arenicolites* and *Skolithos*) and escape burrows occur only in thin sandstone interbeds that display preserved horizontal to low angle laminations. Overall, this association is interpreted as a *Cruziana* ichnofacies that includes both fairweather and storm assemblages (Pemberton and others, 1992b).

Relatively coarse-grained parts of this facies, in contrast, display the same trace fossils but they tend to be more thoroughly integrated into a single assemblage. In other words, it is more common to observe vertical traces (e.g., *Skolithos*) indicative of suspension feeders occurring as an integral part of a diverse assemblage dominated by horizontal traces (e.g., *Anconichnus*, *Planolites*, *Teichichnus*) indicative of deposit feeders. This association is interpreted as a mixed *Skolithos-Cruziana* ichnofacies.

This facies is interpreted as the product of deposition on the lower shoreface, above maximum (storm) wave base and below normal (fairweather) wave base. Finer grained deposits that display *Cruziana* ichnofacies as the resident assemblage are lower-energy, distal subfacies whereas coarser grained deposits that display a mixed *Skolithos-Cruziana* ichnofacies are higher-energy, proximal subfacies. Sandstone interbeds displaying horizontal to low angle laminations and an opportunistic trace fossil assemblage are interpreted as storm beds that likely are hummocky cross stratified.

High Energy Lower Shoreface Facies – A core from sequence K4 in the Seabee well (Fig. 17) includes a distinct facies that warrants description. It comprises very fine-grained sandstone interbedded with silty mudstone. Most sandstone beds in this core display primary sedimentary structures and little or no bioturbation. Low angle laminations that display both concave-upward and convex-upward curvature are predominant, and these are interpreted as hummocky cross stratification (HCS). Ripple-scale cross-bedding is present in some sandstone beds. Unfortunately, the limited wire-line log data from the Beaufortian section

in the Seabee well precludes placing this facies into the context of log motifs.

Although bioturbation is relatively sparse, a rather robust assemblage including *Planolites*, *Palaeophycus*, *Teichichnus*, *Terebellina*, and *Thalassinoides* is conspicuous throughout this facies. *Rosselia*(?) also is present locally. This assemblage is interpreted as a *Cruziana* ichnofacies.

This facies is interpreted as the product of deposition on a high-energy lower shoreface. The pervasive preservation of HCS, together with the sparse and robust *Cruziana* ichnofacies, suggest deposition on a storm-dominated lower shoreface. Deposition likely occurred below normal (fair-weather) wave base and clearly occurred above maximum (storm) wave base. Relative to the lower shoreface deposits described previously, the preservation of primary sedimentary structures and sparse bioturbation may reflect either higher energy levels or higher rates of sedimentation.

Middle-Upper Shoreface Facies – This facies comprises very fine to fine-grained sandstone that locally coarsens to lower medium-grained sandstone. The sandstone generally is matrix-free and well sorted. It commonly occurs as a "blocky" sand that displays a sharp base, inferred to be erosional. The base of the sand typically includes chert pebbles, either as clasts randomly scattered through the sand or as a discrete pebble bed that is rarely more than 1 ft. thick. Chert pebbles also occur as randomly scattered clasts and, more rarely, as discrete beds within this facies well above its base. This facies is variably glauconitic, with glauconite content related to stratigraphic position. For example, this facies tends to be highly glauconitic within sequence K2 and mostly non-glauconitic within sequences K3 and K4. In many cored intervals, no primary sedimentary structures are preserved, owing to pervasive and complete bioturbation. Locally, horizontal to low angle laminations are preserved and thin trough cross beds are observed rarely.

The generally uniform texture and composition of the sand within this facies makes trace fossils difficult to distinguish. Diagnostic trace fossils that are clearly discernable and abundant include *Arenicolites*, *Diplocraterion*, and *Skolithos*. Within sequence K2, this facies contains locally abundant *Macaronichnus* (Clifton and Thompson, 1978; MacEachern and Pemberton, 1992; Bromley, 1996) and locally common *Ophiomorpha*. Rare trace fossils include *Palaeophycus* and *Teichichnus*. There are questionable occurrences of *Conichnus* and *Rosselia*. This facies locally displays abundant *Anconichnus* as a deeper tier (Bromley, 1996). Locally, *Anconichnus* is so pervasive that it obliterates most other trace fossils. This association is interpreted as a *Skolithos* ichnofacies.

This facies is interpreted as the product of deposition on the middle to upper shoreface, above normal (fair-weather) wave base and below the intertidal zone. The generally clean and well sorted nature of the sand, together with locally preserved horizontal to low angle lamination and cross-bedding suggest winnowing and deposition in the zone of shoaling and breaking waves. The occurrence throughout this facies of a *Skolithos* ichnofacies and the local abundance of *Macaronichnus* are consistent with a middle to upper shoreface setting (Clifton and Thompson, 1978; MacEachern and Pemberton, 1992).

In Beaufortian cores from NPRA, it may be significant that facies interpreted as middle-upper shoreface deposits have the following characteristics: (1) They typically rest on transgressive surfaces of erosion (i.e., ravinements) inferred also to be sequence boundaries in some cases; (2) They typically form the lowermost part of transgressive systems tracts; and (3) They tend to display higher porosity and permeability than the other facies. Although these observations may be influenced by the spatial distribution of Beaufortian cores (i.e., mostly in northern NPRA), they suggest that erosion and reworking during transgression may be a prerequisite to the development of reservoir-quality sandstones.

Prodelta-Distal Delta Front Facies – This faciess is tentatively inferred to be present within K4 on the basis of seismic character plus one short core from the Tunalik well. The facies comprises silty mudstone with thin sandstone interbeds. The mudstone is medium to dark grey with poorly defined fissility and with varying silt content. The sandstone interbeds range from thin laminations to 6-inch beds that display ripple scale cross-bedding, with distinct clay drapes on some of the ripple foresets. Although the single core through this facies comes from an overall coarsening-upward succession, as indicated by wire-line log response, both the thickness and distribution of the sandstone beds within the cored interval seem to be random. Evidence of small-scale deformation is common, and is interpreted as gravity slumping and loading.

This facies displays a trace fossil assemblage that is low in diversity and abundance relative to most facies described previously. Predominant trace fossils include *Planolites*, *Thalassinoides*, and *Teichichnus*. Although bioturbation locally disrupts individual laminations and thin beds, nowhere is the abundance of trace fossils sufficient to obliterate primary laminatons

and bedding across the width of a core. This association is interpreted as a *Cruziana* ichnofacies.

This facies is inferred to reflect higher rates of sedimentation compared to most facies described previously. Not only are primary sedimentary structures better preserved, but also most structures suggest deposition from unidirectional currents rather than waves. The trace fossil assemblage is consistent with an environment characterized by high rates of sediment accumulation and relatively high energy. All of these considerations, combined with the stratal geometry described previously (sequence K4, Tunalik area), suggest deposition on a marine slope in front of a prograding coastline. Therefore, these facies are interpreted as prodelta to distal delta front deposits. Alternatively, these facies could represent distal deposits of the high-energy lower shoreface deposits described previously.

Bay Facies – This facies comprises muddy siltstones through very fine-grained sandstones that typically display a horizontal fabric defined by laminations that are commonly discontinuous or burrow-disrupted. The facies ranges from dark grey to greenish grey to reddish grey in color. The facies is commonly associated with oxidized zones, inferred to be exposure surfaces (see below).

Although bioturbation typically is conspicuous, both the abundance and diversity of trace fossils are significantly less than in the fully marine facies described previously. The trace fossil assemblage consists mostly of *Teichichnus* and *Planolites*. In some core intervals, *Teichichnus* is the only trace fossil present.

The sedimentary structures indicate deposition in relatively low energy environments, the trace fossil assemblage suggests a stressed ecosystem that perhaps was not fully marine, and the close association with exposure surfaces suggests shallow water depths. This facies is therefore interpreted to represent deposition in coastal bays or similar environments.

Key Surfaces

In addition to the facies described above, cored Beaufortian strata display two distinct "facies" that typically represent a very small volume but are very important to sequence stratigraphic interpretations.

Exposure Surface – This facies is characterized by red color or a reddish stain in otherwise grey sediments, evidence of erosion of lithified or semilithified sediment, and fabrics that suggest pedogenic processes. In its most obvious cases, the red color is associated with siderite and iron oxide horizons that have sharp, erosional tops and that grade downward over several inches or feet into the indigenous colors (commonly grey) of facies described previously. In more subtle or questionable cases, the red color is a fabric-selective stain along trace fossils or other textural discontinuities. Clasts of the oxidized sediment commonly rest on the upper erosional surface. Some examples display angular cavities randomly scattered within the oxidized sediment and extending a foot or more below the upper erosional surface. Some of the angular cavities are filled with sediment like that above the erosional surface (presumably piped from above) whereas others are filled with drusy cements (both carbonate and silica cements have been observed). Some red horizons include trace fossils of the *Glossifungites* ichnofacies (see below).

This facies is inferred to represent subaerial erosional surfaces. Some of the examples displayed in NPRA cores correlate with sequence boundaries recognized regionally, whereas others do not. *Both types will be examined during the core workshop.*

Firmground – This facies represents "semilithified or firm substrates, typically consisting of dewatered cohesive muds, due either to subaerial exposure, or burial and subsequent exhumation" (MacEachern and others, 1992a, 1992b). This facies is recognized by the presence of a *Glossifungites* ichnofacies (MacEachern and others, 1992a, 1992b; Pemberton and others, 1992b), with or without an abrupt vertical change in depositional facies.

In NPRA cores of Beaufortian strata, inferred firmgrounds occur in two distinct settings. In one setting, *Thalassinoides* occurs immediately beneath transgressive surfaces of erosion as inferred from other sedimentological evidence. Several *Glossifungites* surfaces characterized by *Thalassinoides*, occurring in both oxidized and non-oxidized deposits, overlain by upper shoreface sandstones of a transgressive systems tract will be examined during the workshop. The other setting occurs within lower shoreface or, less commonly, offshore facies. In this case, the presence of a possible firmground is interpreted based on the abrupt occurrence of diagnostic trace fossils distinctly different than apparently indigenous trace fossils. For

Stratigraphic Unit	Key Surfaces	Depositional Facies	Walakpa 1	Walakpa 2	Kuyanak	Tunalik	Seabee	South Meade	North Inigok	Inigok	Ikpikpuk
pebble shale	sequence boundary psu/K3				X						
		oxygen-depleted offshore	X		X	X			X		
		middle-upper shoreface			X						
	Glossifungites firmground psu/K3				X						
K4	higher order sequence boundary within K4						X				
	slumped/faulted K3 at base K4					X					
		high energy lower shoreface					X				
		prodelta - distal delta front				X					
		middle-upper shoreface					X				
		lower-middle shoreface				X					
		offshore					X				
		O-depleted offshore					X				
K3	higher order sequence boundary within K3		X								
	exposure surface				X						
		middle-upper shoreface	X	X							
		lower shoreface (slump mass in K4)				X					
		offshore								X	X
		oxygen-depleted offshore	X								X
	sequence boundary K3/K2		X	X							
	Glossifungites firmground K3/K2		X	X	X						
K2	higher order sequence boundary within K2				X						
		middle-upper shoreface			X						
		lower shoreface	X		X						
		offshore	X		X				X	X	
		oxygen-depleted offshore		X				X		X	
	sequence boundary K2/K1			X							
K1	higher order sequence boundary within K1			X							
	marine flooding surface		X								
	exposure surface			X							
	Glossifungites firmground		X	X							
		bay		X							
		lower shoreface	X	X				X			
		offshore	X					X			

Table 1. For each major Beaufortian depositional sequence and the pebble shale unit, tabulation of key surfaces and depositional facies inferred to be present in cores from wells planned for display.

example, *Diplocraterion* and *Skolithos* may occur abruptly within lower shoreface sediments, cutting across an indigenous *Cruziana* ichnofacies. This likely represents erosion of sediment and habitation of the relatively firm substrate by a *Glossifungites* ichnofacies.

SUMMARY

Beaufortian (Jurassic through Early Cretacrous) strata in the NPRA include four major depositional sequence sets that each display unique stratal geometries and thickness trends. Cores from NPRA wells provide the opportunity to examine many important attributes of these sequences, including key surfaces and depositional facies (Table 1), within a regional context established through a grid of public domain, 2-D seismic data.

Sequence set K1 (Hettangian-Aalenian) is a composite of numerous higher-order depositional sequences whose progradation and aggradation through time constructed a clastic shelf in north-central NPRA. Cores from K1 illustrate the character of several key surfaces, and they display predominantly offshore through lower shoreface success-sions punctuated by evidence of exposure (Table 1 and Fig. 20).

Sequence set K2 (Oxfordian-Kimmeridgian) is a composite of at least three higher-order depositional sequences that developed as the result of episodic tectonic uplift along the Barrow Arch during "failed rift" events. Each higher-order sequence reflects a forced regression, which caused widespread erosion across northcentral NPRA and accumulation of sediment at the shelf margin in lowstand systems tracts, followed by flooding of the shelf as the result of a rise in relative sea level, which resulted in deposition of a transgressive systems tract. Cores from K2 illustrate attributes of sequence boundaries, including exposure surfaces and transgressive surfaces of erosion, and they display facies indicative of oxygen-depleted offshore through upper shoreface deposition. Cores from K2 are particularly important in constraining the sequence stratigraphic framework of oil-prospective sandstone reservoirs such as Alpine.

Sequence set K3 (Valanginian) is a composite of at least two higher-order depositional sequences that display relatively distal facies characteristics, suggesting high relative sea level during most of the depositional history. An important exception is the presence of a transgressive systems tract at the base of K3 that contains shoreface sandstones that are gas reservoirs in the Walakpa field. Cores from K3 dis-play a variety of sequence boundaries and deposi-tional facies that range from oxygen-depleted offshore through upper shoreface.

Sequence K4 (Hauterivian) is a shelf-margin wedge that developed as the result of tectonic uplift along the Barrow Arch during the "successful rift" events related to opening of the Arctic Ocean basin. This sequence comprises lowstand and transgressive systems tracts that display stratal geometries suggesting dynamic incision and synsedimentary collapse of the shelf margin. Facies within K4 suggest higher energy depositional systems and/or higher rates of sedimentation as compared to sequence sets K1 through K3. Cores from K4 display attributes of sequence boundaries and depositional facies that range from oxygen-depleted offshore through upper shoreface.

Throughout the Beaufortian section, the best potential for stratigraphic traps occurs in transgressive systems tracts containing high quality reservoir and seal facies. Well-winnowed, upper shoreface sandstones deposited in topographic lows on transgressive surfaces of erosion commonly occur at the base of TSTs. These sandstones are typically capped by a condensed section deposited in oxygen-depleted offshore environments as the shelf was flooded during high relative sea levels.

ACKNOWLEDGEMENTS

The staff of the U. S. Geological Survey Core Research Center, including Tom Michalski, Bill Linenberger, and Bill Whitus, provided outstanding support that enabled the integration of NPRA cores into this study. NPRA cores were slabbed by Chris Canacari and digitally photographed by Sara D'Agostino. Phil Nelson and Joyce Kibler provided petrophysical support. Rob Crangle and Max Borella provided digital drafting and GIS support. Bo Henk kindly helped with trace fossil identification and interpretation. Ken Bird, Chris Schenk, and Chris Swezey reviewed the manuscript. John Reeder of the Alaska Geological Materials Center provided access to Alpine core chips and other samples. Several industry geologists provided constructive feedback following presentations of this work at the Alaska Geological Society in January 2001 and at the NPRA core workshop in June 2001. I truly appreciate all these contributions!

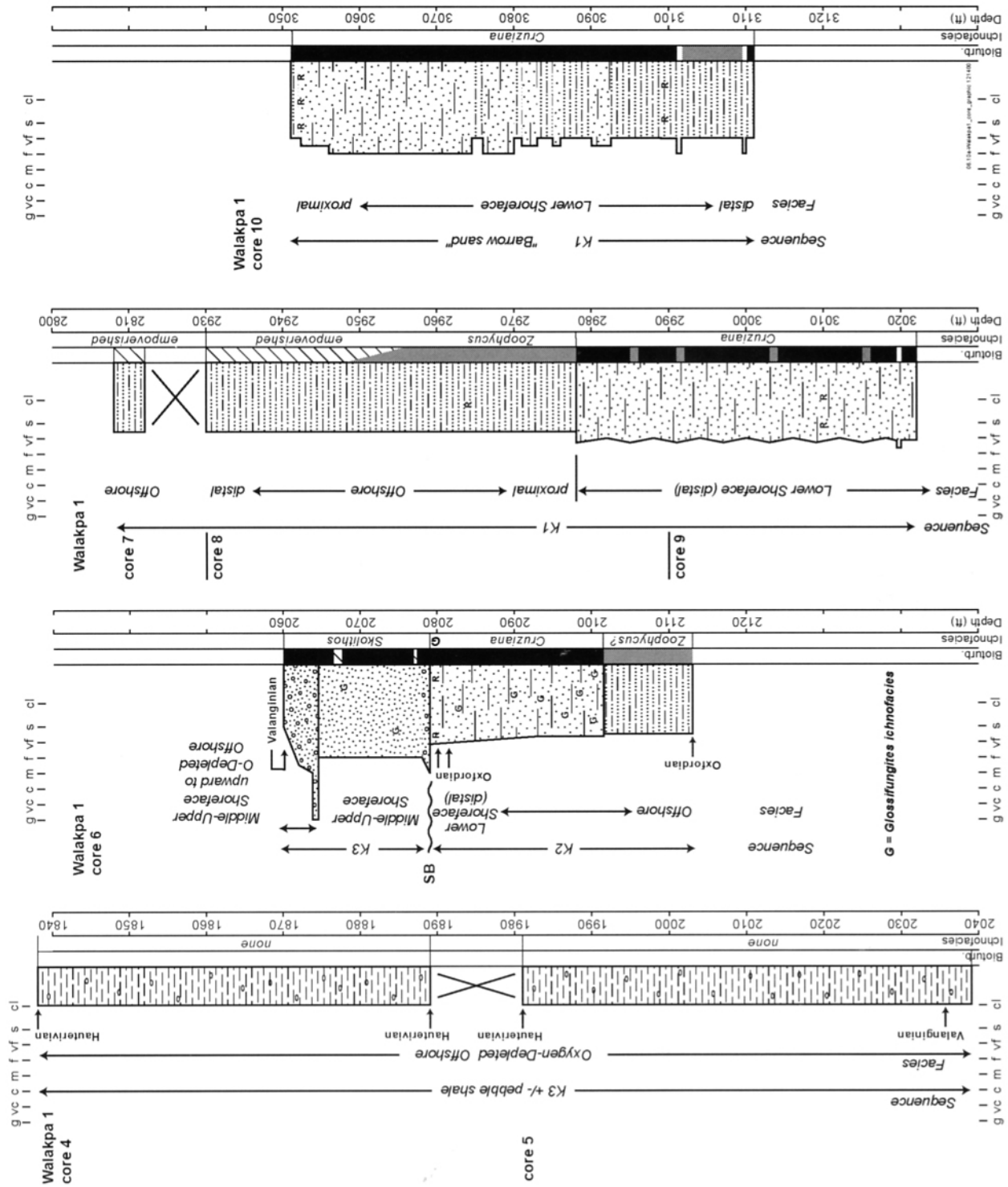

F Figure 20. Graphic measured sections of Beaufortian strata in NPRA cores. Key to measured sections included in Fig. 20D. *A*: Walakpa 1.

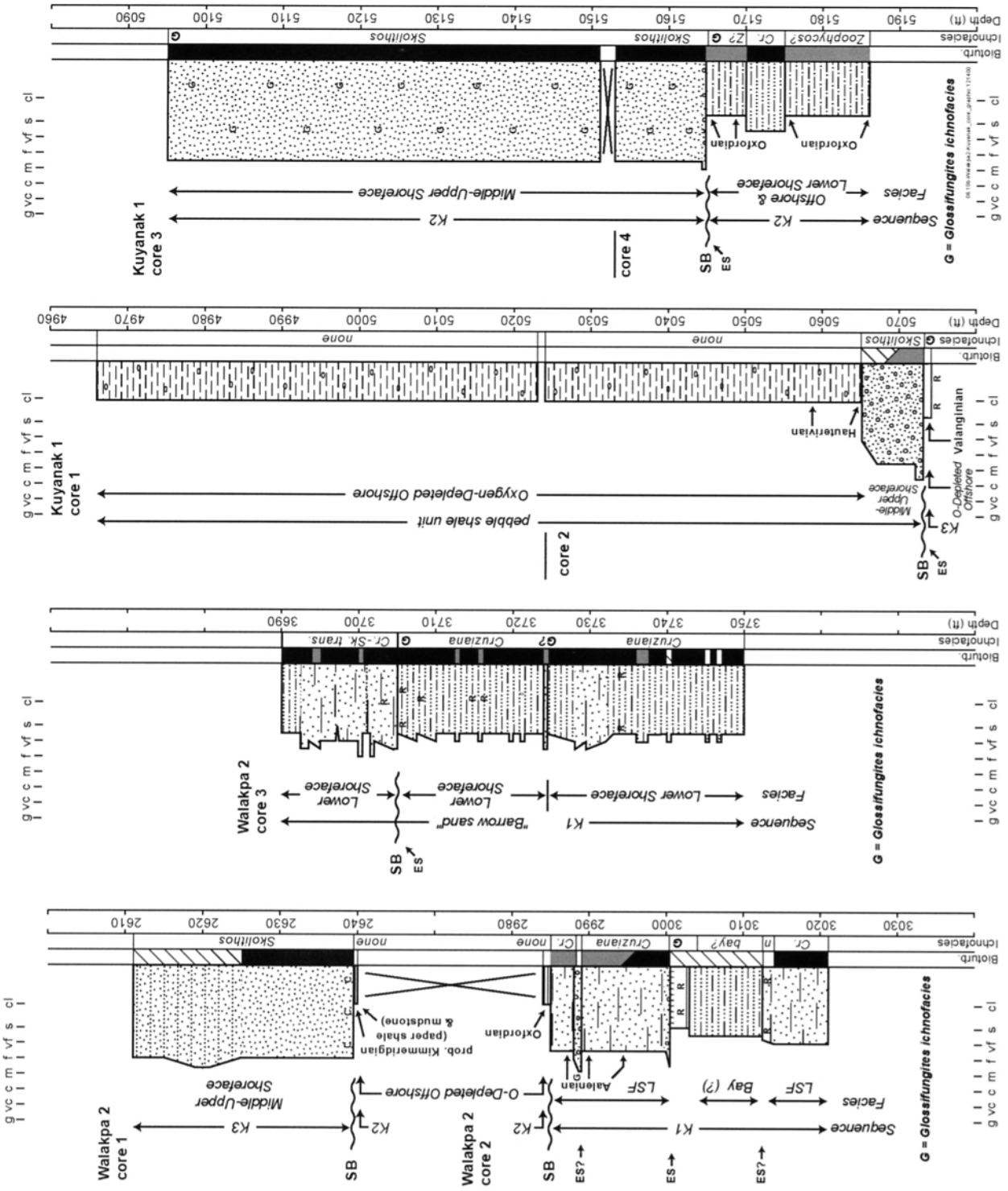

Figure 20. Graphic measured sections of Beaufortian strata in NPRA cores. Key to measured sections included in Fig. 20D – *Continued.*
B: Walakpa 2 and Kuyanak

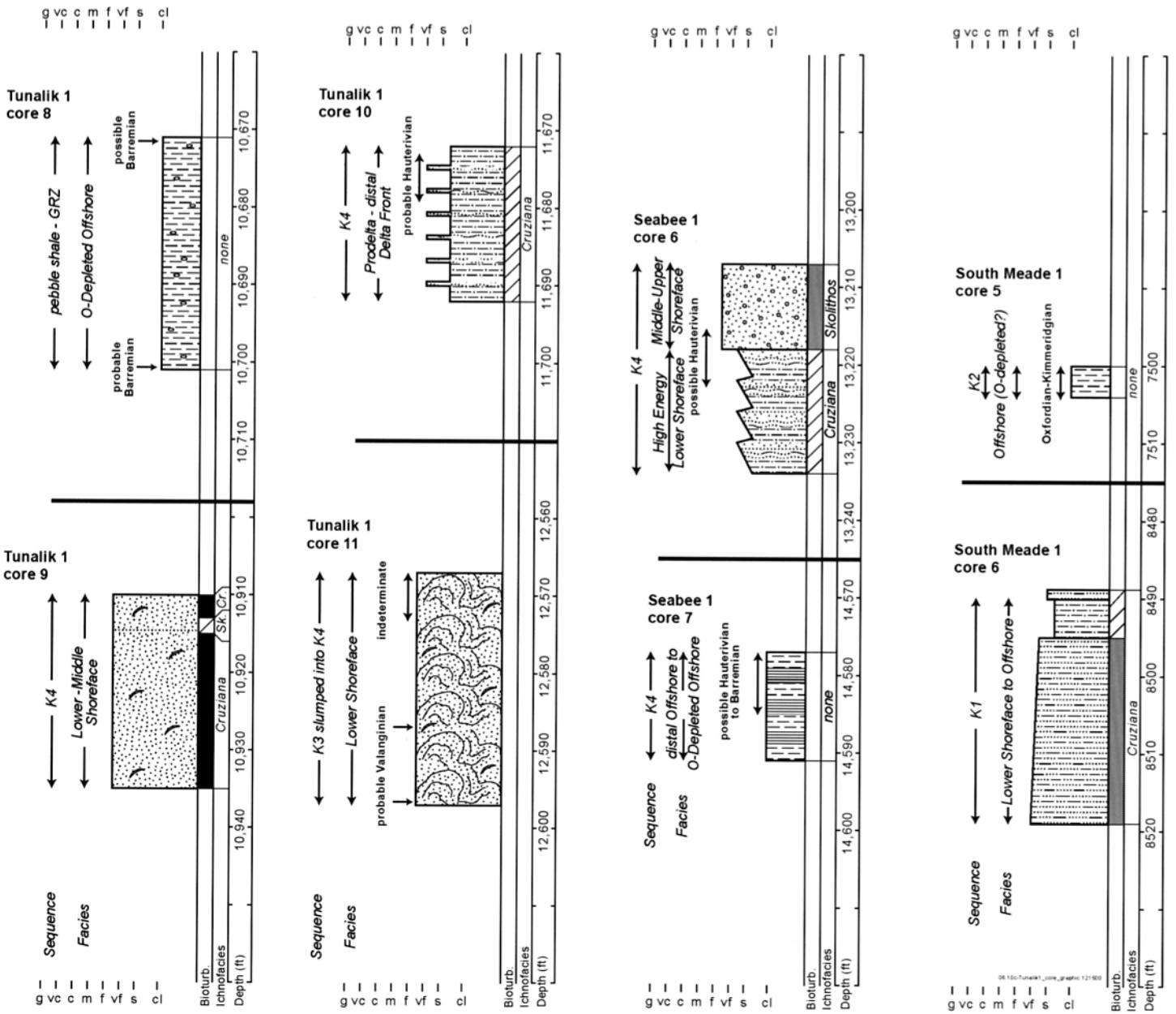

Figure 20. Graphic measured sections of Beaufortian strata in NPRA cores. Key to measured sections included in Fig. 20D – *Continued*. *C*: Tunalik, Seabee, and South Meade.

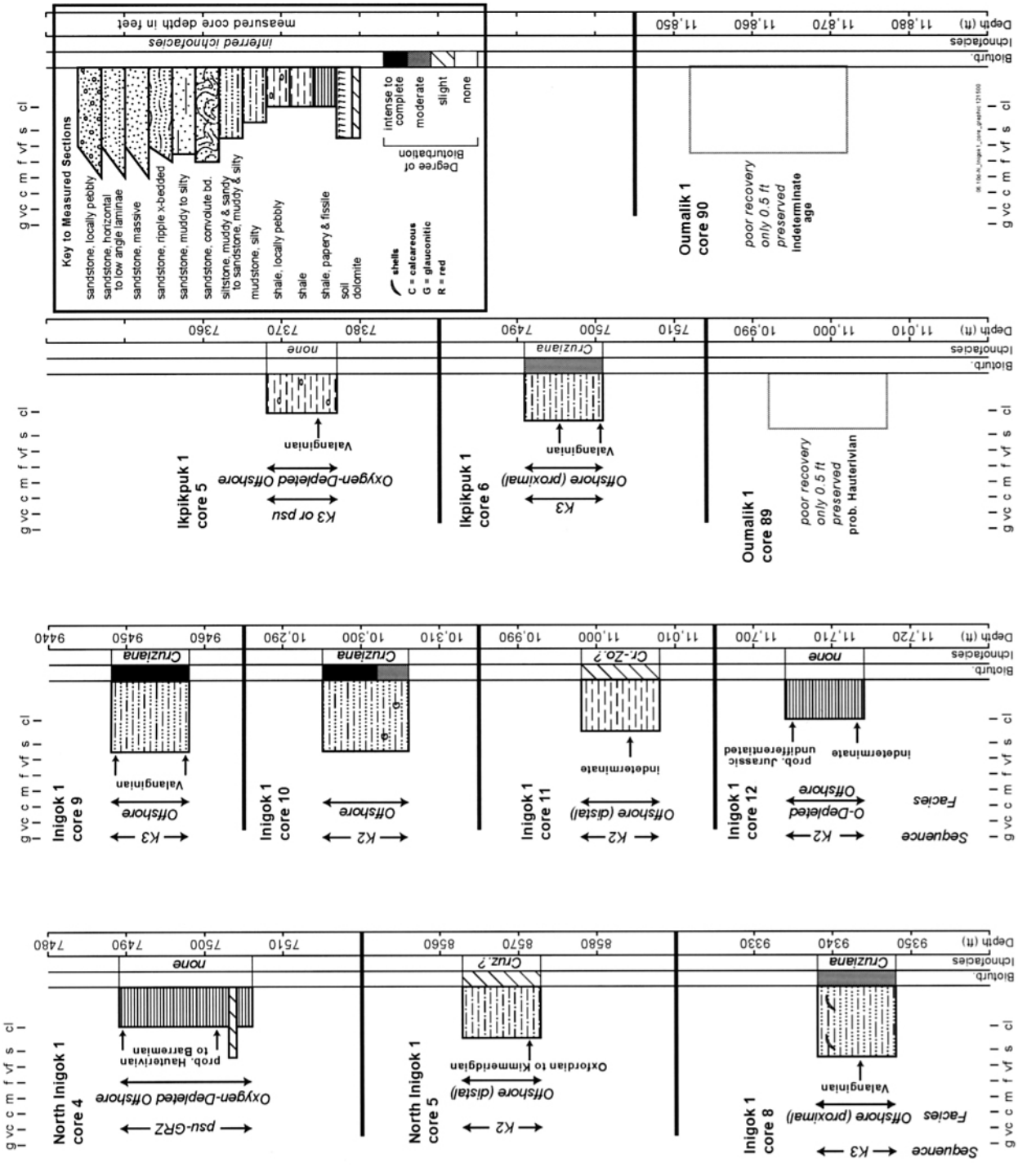

Figure 20. Graphic measured sections of Beaufortian strata in NPRA cores. Key to measured sections includcd in Fig. 20D – *Continued.* *D:* North Inigok, Ikpikpuk, and Oumalik.

REFERENCES

Bird, K.J., 1985, The framework geology of the North Slope of Alaska as related to oil – source rock correlations, *in* Magoon, L.B., and Claypool, G.E., eds., Alaska North Slope oil/rock correlation study: American Association of Petroleum Geologists Studies in Geology 20, p. 3-29.

Bird, K.J., 1987, The framework geology of the North Slope of Alaska as related to oil-source rock correlations, *in* Tailleur, I., and Weimer, P., eds., Alaskan North Slope Geology: SEPM Pacific Section and Alaska Geological Society, v. 50, p. 121-143.

Bird, K.J., 1988, Structure-contour and isopach maps of the National Petroleum Reserve in Alaska, *in* Gryc, G., ed., Geology and exploration of the National Petroleum Reserve in Alaska, 1974 to 1982, U.S. Geological Survey Professional Paper 1399, p. 355-377.

Bird, K.J., 1994, Ellesmerian(!) petroleum system, North Slope of Alaska, U.S.A., *in* Magoon, L.B., and Dow, W.G., eds., The petroleum system – from source to trap: American Association of Petroleum Geologists Memoir 60, p. 339-358.

Bird, K.J., 1995, Northern Alaska province (001), *in* Gautier, D.L., Dolton, G.L., Takahashi, K.I., and Varnes, K.L., eds., 1995 National Assessment of United States Oil and Gas Resources – Results, Methodology, and Supporting Data: U.S. Geological Survey Digital Data Serier DDS-30.

Bird, K.J., and Molenaar, C.M., 1992, The North Slope foreland basin, Alaska, *in* Macqueen, R.W., and Leckie, D.A., eds., Foreland basins and foldbelts: American Association of Petroleum Geologists Memoir 55, p. 363-393.

Bromley, R.G., 1996, Trace Fossils, 2nd ed., Chapman and Hall, New York, 361 p.

Carman, G.J., and Hardwick, P., 1983, Geology and regional setting of Kuparuk oil field, Alaska: American Association of Petroleum Geologists Bulletin, v. 67, p. 1014-1031.

Clifton, H.E., and Thompson, J.K., 1978, *Macaronichnus segregatis*: a feeding structure of shallow marine polychaetes: Journal of Sedimentary Petrology, v. 48, p. 1293-1301.

Galloway, W.E., and Hobday, D.K., 1996, Terrigenous Clastic Depositional Systems, 2nd ed., Springer, New York, 489 p.

Gingrich, D., Knock, D., and Masters, R., 2001, Geophysical interpretation methods applied at Alpine oil field: North Slope, Alaska: The Leading Edge, July 2001, p. 731-738.

Haga, H., and Mickey, M.B., 1999, Reworked palynomorph trends in Late Jurassic to Neocomian strata of the Colville delta region, Alaska: Alaska Division of Geological and Geophysical Surveys Report of Investigations 99-8, 14 p.

Hannon, R.C., Gingrich, D.A., Redman, S.R., Helmold, K.P., Campaign, W.J., and Dotson, C.B., 2000, The discovery and delineation of a new Alaskan reservoir: the Alpine field, North Slope, Alaska – U.S.A. (abstract): American Association of Petroleum Geologists, 2000 Annual Convention Official Program, p. A63.

Haq, B.U., Hardenbol, J., and Vail, P.R., 1988, Mesozoic and Cenozoic chronostratigraphy and cycles of sea-level change, *in* Wilgus, C.K., Hastings, B.S., Posamentier, H., Van Wagoner, J., Ross, C.A., and Kendall, C.G.S.C., eds., Sea-Level Changes: An Integrated Approach: SEPM Special Publication 42, p.71-108.

Houseknecht, D.W., 2001, Sequence stratigraphy and sedimentology of Beaufortian strata (Jurassic – Lower Cretaceous) in the National Petroleum Reserve – Alaska (NPRA), in Houseknecht, D.W. (editor), 2001, NPRA CORE WORKSHOP – Petroleum Plays and Systems in the National Petroleum Reserve – Alaska: SEPM Core Workshop No. 21, p. 57-88.

Hubbard, R.J., 1988, Age and significance of sequence boundaries on Jurassic and Early Cretaceous rifted continental margins: American Association of Petroleum Geologists Bulletin, v. 72, p. 49-72.

Hubbard, R.J., Edrich, S.P., and Rattey, R.P., 1987, Geologic evolution and hydrocarbon habitat of the 'Arctic Alaska microplate', *in* Tailleur, I., and Weimer, P., eds., Alaskan North Slope Geology: SEPM Pacific Section and Alaska Geological Society, v. 50, p. 797-830.

Kirschner, C.E., and Rycerski, B.A., 1988, Petroleum potential of representative stratigraphic and structural elements in the National Petroleum Reserve in Alaska, *in* Gryc, G., ed., Geology and exploration of the National Petroleum Reserve in Alaska, 1974 to 1982, U.S. Geological Survey Professional Paper 1399, p. 191-208.

Kornbrath, R.W., Myers, M.D., Krouskop, D.L., Meyer, J.F., Houle, J.A., Ryherd, T.J., and Richter, K.N., 1997, Petroleum Potential of the Eastern National Petroleum Reserve – Alaska: Alaska Division of Oil and Gas report, 30 p.

Lee, M.W., Agena, W.F., Grow, J.A., and Miller, J.J., 1999, Seismic processing and velocity assessments, *in* The oil and gas resource potential of the 1002 Area, Arctic National Wildlife Refuge, Alaska: U.S. Geological Survey Open File Report 98-34 (cd-rom), p. SP1-SP32.

MacEachern, J.A., and Pemberton, S.G., 1992, Ichnological aspects of Cretaceous shoreface successions and shoreface variability in the western interior seaway of North America, *in* Pemberton, S.G., ed., 1992, Applications of ichnology to petroleum exploration, SEPM Core Workshop 17, p. 55-84.

MacEachern, J.A., Raychaudhuri, I., and Pemberton, S.G., 1992, Stratigraphic applications of the Glossifungites ichnofacies: Delineating discontinuities in the rock record, *in* Pemberton, S.G., ed., 1992, Applications of ichnology to petroleum exploration, SEPM Core Workshop 17, p. 169-198.

MacEachern, J.A., Bechtel, D.J., and Pemberton, S.G., 1992, Ichnology and sedimentology of transgressive deposits, transgressively-related deposits and transgressive systems tracts in the Viking Formation of Alberta, *in* Pemberton, S.G., ed., 1992, Applications of ichnology to petroleum exploration, SEPM Core Workshop 17, p. 251-290.

Magoon, L.B., and Bird, K.J., 1987, Alaskan North Slope petroleum geochemistry for the Shublik Formation, Kingak Shale, pebble shale unit, and Torok Formation, *in* Tailleur, I., and Weimer, P., eds., Alaskan North Slope Geology: SEPM Pacific Section and Alaska Geological Society, v. 50, p. 145-160.

Magoon, L.B., and Bird, K.J., 1988, Evaluation of petroleum source rocks in the National Petroleum Reserve in Alaska, using organic-carbon content, hydrocarbon content, visual kerogen, and vitrinite reflectance, *in* Gryc, G., ed., Geology and exploration of the National Petroleum Reserve in Alaska, 1974 to 1982, U.S. Geological Survey Professional Paper 1399, p. 381-450.

Magoon, L.B., Bird, K.J., Claypool, G.E., Weitzman, D.E., and Thompson, R.H., 1988, Organic geochemistry, hydrocarbon occurrence, and stratigraphy of government-drilled wells, North Slope, Alaska, *in* Gryc, G., ed., Geology and exploration of the National Petroleum Reserve in Alaska, 1974 to 1982, U.S. Geological Survey Professional Paper 1399, p. 483-487.

Male, W.H., 1992, The sedimentology and ichnology of the Lower Cretaceous (Albian) Bluesky Formation in the Karr area of west-central Alberta, *in* Pemberton, S.G., ed., 1992, Applications of ichnology to petroleum exploration, SEPM Core Workshop 17, p. 33-55.

Masterson, W.D., and Eggert, J.T., 1992, Kuparuk River Field, North Slope, Alaska, *in* Beaumont, E.A., and Foster, N.H., eds., Atlas of Oil and Gas Fields: American Association of Petroleum Geologists Treatise of Petroleum Geology, p. 257-284.

Masterson, W.D., and Paris, C.E., 1987, Depositional history and reservoir description of the Kuparuk River Formation, North Slope, Alaska, *in* Tailleur, I., and Weimer, P., eds., Alaskan North Slope Geology: SEPM Pacific Section and Alaska Geological Society, v. 50, p. 95-107.

Mickey, M.B., and Haga, H., 1987, Jurassic – Neocomian biostratratigraphy, North Slope, Alaska, *in* Tailleur, I., and Weimer, P., eds., Alaskan North Slope Geology: SEPM Pacific Section and Alaska Geological Society, v. 50, p. 397-404.

Miller, J. J., Agena, W. F., Lee, M.W., Zihlman, F.N., Grow, J.A., Taylor, D.J., Killgore, M., Oliver, H. L., 2000, Regional seismic lines reprocessed using post-stack processing techniques; National Petroleum Reserve, Alaska, U.S. Geological Survey, Open-File Report , OF 00-0286, cd-rom.

Moore, T.E., Wallace, W.K., Bird, K.J., Karl, S.M., Mull, C.G., and Dillon, J.T., 1994, Geology of northern Alaska, *in* Plafker, G., and Berg, H.C., eds., The Geology of Alaska: Boulder, Colorado, Geological Society of America, The Geology of North America, v. G-1, p. 49-140.

Morris, W.R., Hannon, R.C., Helmold, K.P., Knock, D.G., and Posamentier, H.W., 2000, Jurassic Alpine sandstone, North Slope, Alaska: an example of shoreface deposition within a punctuated transgressive succession (abstract): American Association of Petroleum Geologists, 2000 Annual Convention Official Program, p. A102.

Morris, W.R., Hastings, D.S., Moothart, S.R., Helmold, K.P., and Faust, M.J., 2000, Sequence stratigraphic development and depositional framework of deep water slope apron systems, Tarn reservoir, North Slope, Alaska (abstract): American Association of Petroleum Geologists, 2000 Annual Convention Official Program, p. A101.

Mull, C.G., Tailleur, I.L, Mayfield, C.F., Ellersieck, I., and Curtis, S., 1982, New upper Paleozoic and lower Mesozoic stratigraphic units, central and western Brooks Range, Alaska: American Association of Petroleum Geologists Bulletin, v. 66, p. 348-362.

Pemberton, S.G., ed., 1992, Applications of ichnology to petroleum exploration, SEPM Core Workshop 17, 429 p.

Pemberton, S.G., Frey, R.W., Ranger, M.J., and MacEachern, J., 1992a, The conceptual framework of ichnology, *in* Pemberton, S.G., ed., 1992, Applications of ichnology to petroleum exploration, SEPM Core Workshop 17, p. 1-32.

Pemberton, S.G., Van Wagoner, J.C., and Wach, G.D., 1992b, Ichnofacies of a wave-dominated shoreline, *in* Pemberton, S.G., ed., 1992, Applications of ichnology to petroleum exploration, SEPM Core Workshop 17, p. 339-382.

Posamentier, H.W., and Allen, G.P., 1999, Siliciclastic Sequence Stratigraphy – Concepts and Applications: SEPM Concepts in Sedimentology and Paleontology no. 7, 210 p.

Sangree, J.B., and Widmier, J.M., 1977, Seismic stratigraphy and global changes of sea level, Part 9: Seismic interpretation of clastic depositional facies: *in* Payton, C.E. (ed.), Seismic Stratigraphy – applications to hydrocarbon exploration, American Association of Petroleum Geologists Memoir 26, p. 165-184.

Van Wagoner, J.C., Mitchum, R.M., Campion, K.M., and Rahmanian, V.D., 1990, Siliciclastic sequence stratigraphy in well logs, cores, and outcrops: Concepts for high-resolution correlation of time and facies: American Association of Petroleum Geologists Methods in Exploration Series, no. 7, 55 p.

Werner, M.R., 1987, West Sak and Ugnu sands: Low gravity oil zones of the Kuparuk River area, Alaska North Slope, *in* Tailleur, I., and Weimer, P., eds., Alaskan North Slope Geology: SEPM Pacific Section and Alaska Geological Society, v. 50, p. 109-118.

Thermal Structure of the Anadarko Basin[1]

Jaquidon Gallardo[2] and David D. Blackwell[3]

ABSTRACT

The Anadarko basin of Oklahoma is a two-stage Paleozoic cratonic basin with as much as 12 km (7.5 mi) or more of sedimentary fill. We present a present-day thermal model of the basin based on lithologic analysis at 3-m (10-ft) intervals in 63 wells, heat flow measurements at seven sites, and in-situ thermal conductivity calibration of the sediment section at two sites. We do not use BHT (bottom-hole temperature) information in the process, but we do, at the end of the process, compare the independently predicted temperatures to BHT information. The in-situ calibration of thermal conductivity was accomplished using detailed temperature logs and represents a new practical application for evaluating basin thermal characteristics. Shale exerts the most control on the temperature distribution because it is the most abundant lithology and has the lowest thermal conductivity. Shale comprises 47% by volume of rock in the basin and represents 75% of total thermal resistance, directly related to temperature gradient; therefore, shale dominates the thermal structure of the basin. Thus, the problems in sampling and in characterizing the in-situ thermal conductivity of shale from laboratory measurements represent a major limitation in basin thermal analysis; we use the in-situ calibration approach as a way to address the difficulty. The temperatures calculated do not mimic the structure of the sediments; i.e., the hottest area on a given age horizon in the lower Paleozoic is not in the most deeply buried part of the Anadarko basin. The combination of decreasing heat flow toward the Wichita Mountains and the facies changes in the Pennsylvanian units from marine shale (low thermal conductivity) in the basin to the granite wash (high thermal conductivity) toward the uplift results in the highest temperatures being displaced about 50 km (31 mi) northward into the basin. The pattern of vitrinite reflectance in the Woodford Shale is virtually identical to the present-day reconstructed temperature pattern; therefore, we conclude that the thermal pattern is and has been dominated by conductive heat transport.

©Copyright 1999. The American Association of Petroleum Geologists. All rights reserved.

[1]Manuscript received October 11, 1996; revised manuscript received June 16, 1998; final acceptance July 14, 1998.

[2]3704 Bryson Drive, Frisco, Texas 75035.

[3]Department of Geological Sciences, Southern Methodist University, Dallas, Texas 75275.

This paper is based on a master's thesis submitted to the Department of Geological Sciences at Southern Methodist University by Jaquidon Gallardo. Partial support for the study came from the Mobil Foundation. The following companies provided data for this project: American Stratigraphic Company; ARCO Oil and Gas Company; Arkla Exploration Company; Barby Energy Corporation; Enserch Exploration, Inc.; Exxon Company, USA; Forest Oil Corporation; The GHK Company; Meridian Oil, Inc.; Phillips Petroleum Company; Roden Oil Company; Samedan Oil Corporation; Santa Fe Minerals, Inc.; Sohio Petroleum Company; TXO Production Corporation; Union Oil Company of California; and Woods Petroleum Corporation. John L. Steele helped with the software development. Robert L. Laury and Roger Denison read an early version of the manuscript. Lloyd Gatewood generously allowed use of proprietary information for part of the interpretation. Charles F. Dodge and Earl Price also helped in obtaining the well data. Kenneth S. Johnson provided valuable assistance. Jay Maturese and Chris Eckhardt helped with the data collection, and Rene Greyvesteyn and Maria Richards prepared the figures. We received constructive reviews from Phil Armstrong, David Chapman, David Deming, and Jeffrey Nunn.

INTRODUCTION

Predicting the regional thermal structure of sedimentary basins is a topic of major interest to geologists because temperature is related to many processes that affect basins, such as tectonic setting, fluid motion, organic material maturation and diagenetic changes. The activities of the Geothermal Survey of North America indicate the interest in the subject (AAPG, 1976). More recently, the correlation of organic maturation and temperature has reemphasized the importance of knowing the thermal structure of a basin (Waples, 1980). Many approaches to study thermal structure have been proposed and results have been described by, for example, Sclater and Christie (1980), Chapman et al. (1984), Bodner and Sharp (1988), Deming et al. (1990), Brigaud et al. (1992), and Funnell et al. (1996), to list only a few. In almost every study, the basic thermal information has been bottom-hole temperature (BHT) data because of its ubiquity and because of the general lack of better temperature data.

The methodology employed by Chapman et al. (1984) typifies the approach of many other workers (Funnell et al., 1996; Lee et al., 1996). Thermal conductivity measurements are made on cuttings and the values are applied to formations. Gradient is calculated from BHT data. These two data sets are treated as known quantities from which to calculate surface heat flow.

Speece et al. (1985) employed matrix inversion techniques, corrected BHT data, and stratigraphic thickness data to calculate gradients for various formations and lithologies in the Michigan basin. The gradients associated with each lithology, in turn, were used to construct empirical temperature profiles of the wells in their data set. Speece et al. (1985) used one control well to test their empirical temperature-depth profiles. Comparisons of the empirical temperature-depth profiles to the BHT data resulted in residuals (differences between the predicted and actual BHT), which were used for interpretation.

The most sophisticated techniques have dealt with multiple data sets simultaneously and have attempted to include the effects of bias and error in the BHT measurements. Willet (1990) used a statistical inversion scheme to deal with the problem of the spatial significance of BHT variations, and Deming et al. (1990) used the method of variable bias for the same purpose.

In this paper, we take a different approach to determine thermal structure. We follow, in part, the approach used by Gosnold (1984) in assessing the geothermal resources of the Williston basin. Gosnold (1984) made basinwide estimates of surface heat flow and thermal conductivity from published measurements and used these values to calculate subsurface temperatures. The lateral thermal conductivity variations within each rock type in the Williston basin were assumed small compared to the thermal conductivity variations between the major rock types involved. Using the same assumption for thermal conductivity, we predict the thermal structure in the Anadarko basin in Oklahoma using (1) heat flow interpreted from conventional measurements, (2) lithologies determined at 3-m (10-ft) intervals for 63 wells, and (3) in-situ–calibrated thermal conductivity values. The procedure depends on heat flow measurements and equilibrium temperature logs made and described by Carter et al. (1998).

The only other published regional-scale thermal data for the Anadarko basin are represented on the geothermal gradient map of Oklahoma (Luza et al., 1984). This map was produced by calculating gradients from corrected BHT data. No attempt was made to account for thermal conductivity variations. BHT data used for the gradient map also were used by Harrison et al. (1983) to assess the geothermal resources of Oklahoma.

GEOLOGIC SETTING AND HISTORY

The Anadarko basin (Figure 1) encompasses the western one-half of Oklahoma, as well as parts of Kansas and Texas (Adler, 1971). The Anadarko basin is an asymmetric foreland basin (Evans, 1979) with its deepest part to the south at the edge of the tectonic uplift of the Wichita Mountains. The basin shallows northward and grades into a broad shelf in the northwestern part of Oklahoma and the Texas and Oklahoma panhandles (Figure 2). This study is confined to that part of the basin (about 70%) within Oklahoma (Figure 1). For reference in the following discussion, the generalized stratigraphy and stratigraphic nomenclature for the Anadarko basin are shown in Figures 2 and 3.

The structural features of southern Oklahoma have been interpreted as an aulacogen. Hoffman et al. (1974) proposed that a structural weakness developed in the lower Paleozoic. Burke and Dewey (1973) interpreted this structural zone as the failed arm of a triple junction located near the area presently occupied by Dallas, Texas. The rifting caused crustal thinning, which has controlled the subsequent history of the basin. This rifting and igneous activity in the Lower and Middle Cambrian constituted the first of four phases in Anadarko basin development (Denison, 1976). This phase culminated with the extrusion of the Carlton Rhyolite Group/Timbered Hills Group and emplacement of the associated Wichita Granite Group (Denison, 1982; Gilbert, 1983).

The second phase began with the transgression of Late Cambrian seas. Sediments deposited during this phase were dominated by shallow-water carbonates. The area of the aulacogen subsided more than the surrounding craton; consequently, the aulacogen received twice as much sediment as the surrounding craton. The subsidence rate had slowed by the beginning of the Silurian (Feinstein, 1981), so the Silurian and Devonian rocks (Figure 2) are relatively thin (Johnson et al., 1988; Johnson, 1989).

The third phase began in the Mississippian with tectonic activity related to the Ouachita-Marathon orogeny (Burgess, 1976) resulting in a transition to clastic deposition. The sediment deposited in the aulacogen was five times greater than that deposited on the surrounding craton during this deformation phase. The principal tectonic activity occurred in several pulses during Early to Late Pennsylvanian. The Wichita-Amarillo uplift began in the Morrowan and was accompanied by significant downwarping of the Anadarko basin. Carbonate and chert fan-deltas derived from the earlier-deposited Paleozoic rocks of the uplift were deposited first, followed by the fan-delta deposits known as "granite wash" (Figure 2) as the granitic Cambrian crystalline rocks were exposed. Brewer et al. (1983) have shown that the Wichita-Amarillo uplift has a component of overthrust motion resulting in 15 ±5 km (9 ±3 mi) of crustal shortening. The cessation of tectonic activity marked the beginning of the fourth, primarily Permian, phase, characterized by subsidence at a

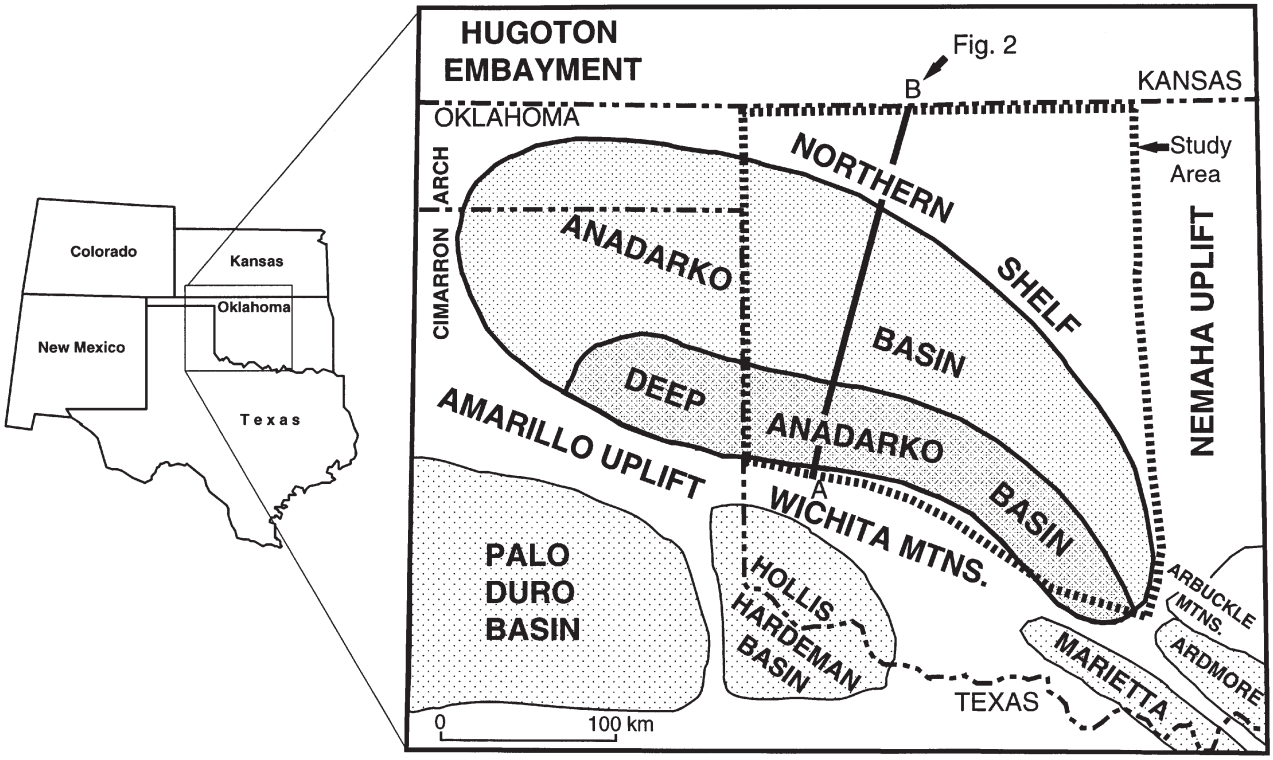

Figure 1—Study area limits (dashed box) and regional structural features. Line AB indicates cross section shown in Figure 2. From Johnson et al. (1988).

slower rate. Permian sediments include red beds and evaporites.

The thickness of the sediments deposited in this region is related to the type of underlying basement rock (Ham et al., 1964). Maximum sedimentary thicknesses occur in areas underlain by the Middle Cambrian basement rocks of the aulacogen. For example, 11.6 km (7.2 mi) of section is predicted in the deep Anadarko basin (Rowland, 1974). At the eastern end of the aulacogen, 10.4 km (6.5 mi) of sediments preserved in the Arbuckle anticline and the Ardmore basin also overlie a basement sequence of Middle Cambrian volcanic rocks. In contrast, the same sedimentary sequence is only about 3 km (2 mi) thick where it overlies Precambrian basement rocks of the craton. In addition, the types of sediments occurring within the aulacogen differ from those of the stable craton. The Arbuckle Group of Late Cambrian–Early Ordovician age consists mainly of limestone in the basin (aulacogen) and dolomite on the shelf (craton). Mississippian sediments are characterized by shales within the basin and limestones on the shelf. Pennsylvanian sediments are dominated by shales and sandstones in the basin, but contain more limestone on the shelf (Ham, 1969).

METHODS

Many workers (Carvalho and Vacquier, 1977; Carvalho et al., 1980; Chaturvedi and Lory, 1980; Lam et al., 1982) calculated temperatures assuming a constant gradient obtained from a single or multiple BHT measurements and the surface temperature; however, a constant gradient is an unrealistic representation of the true temperature distribution unless the entire sedimentary section has homogeneous thermal properties. This type of gradient assumption commonly is used to calculate heat flow and may lead to erroneous results. In contrast, this study makes no assumptions for temperature gradient. The approach for modeling thermal structure used in this study treats heat flow and thermal conductivity as known values and uses them to calculate temperature and gradient.

We make the assumption that heat flow is one-dimensional, a generally reasonable assumption in sedimentary basins where the heat from the basement travels vertically through layered sedimentary rocks to the surface. We also assume that heat flow does not vary with depth. This assumption is also reasonable for tectonically stable sedimentary basins unless there are significant fluid flow-effects in the area (Blackwell and Steele, 1989a). The following

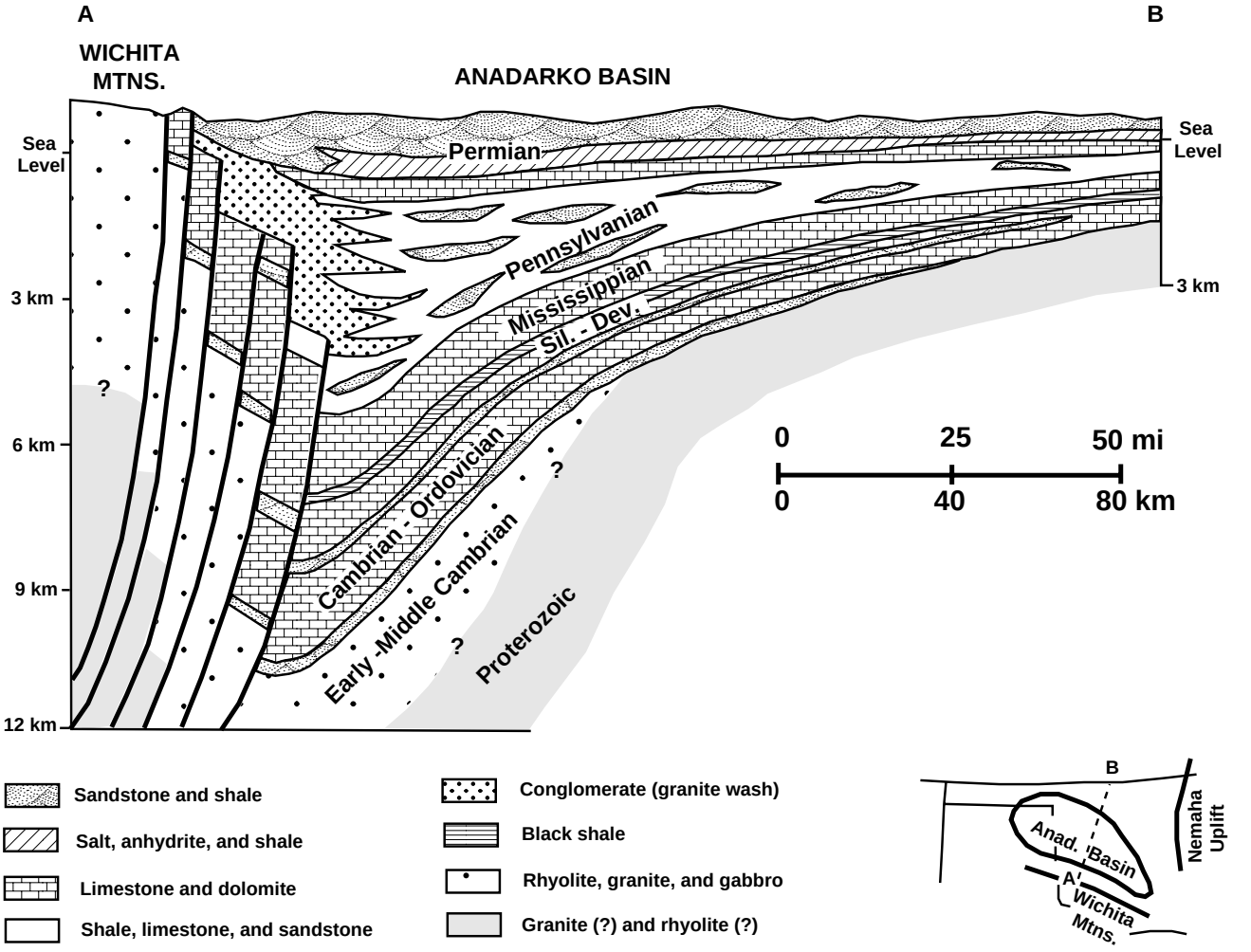

Figure 2—Simplified cross section of the Anadarko basin perpendicular to basin axis (Johnson, 1989). Location of the cross section is shown on the inset and in Figure 1.

formula can be derived from the one-dimensional heat flow equation (Gosnold, 1984):

$$T_z = T_o + \Sigma\left[z_i \times \left(Q/k_i\right)\right] \qquad (1)$$

where T_z is temperature at depth z, T_o is surface temperature, z_i is thickness of unit i, Q is heat flow, and k_i is thermal conductivity of unit i.

An empirical temperature profile of the sedimentary sequence can be constructed by summing the results of the incremental temperature calculations across individual units or layers of uniform conductivity. For a sedimentary section, this temperature change is calculated through each lithologic unit. The major types of sedimentary lithologies have characteristic thermal conductivity ranges, and lithologic units can be treated, in an average sense, as units of uniform conductivity. When these calculations are made for a number of vertical sections in an area, a three-dimensional representation of the temperature structure of the basin can be constructed, assuming variations in the parameters are regional in scale. The following section details how the data were obtained and analyzed for each of the variables needed to calculate T_z in equation 1 for this model.

DATA

Distribution

The index map of the study area (Figure 4) shows the southern limit of the Anadarko basin delineated by the frontal fault zone of the Wichita Mountains. On the eastern side, the main fault segments of the Nemaha uplift mark the limits of the

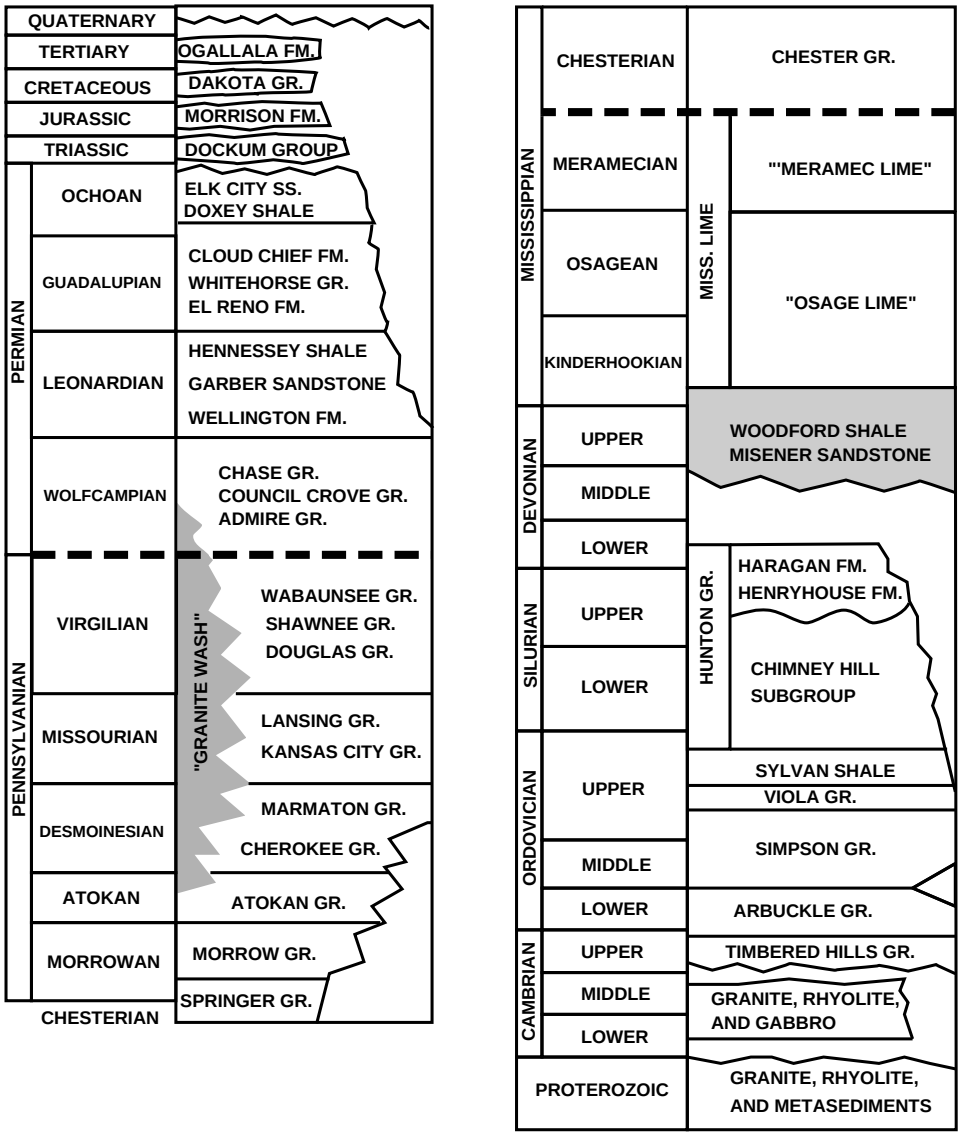

Figure 3—Generalized stratigraphic column for the Anadarko basin modified from Johnson and Cardott (1992). Thickness of individual units is not related to height of formation or group box. Horizons of temperature contour maps are shown by heavy dashed lines.

basin. A total of 63 wells were used for this study, giving a typical spacing of approximately 25–30 km (15–18 mi). Well names, locations, and other information about each well are listed in Appendix 1.

Because the Anadarko basin has been affected by only minor tectonic disturbances since the Permian, the temperature regime has had ample time to stabilize. Assuming one-dimensional heat flow, the average vertical distribution of the various rock types at each location controls the temperature in that area. This factor allows for the wide data spacing that has been used for this regional-scale study. In some areas, such as the vicinity of major faults, the one-dimensional temperature field assumption may be inaccurate, and temperatures may be different locally than those calculated here.

Surface Temperature

The mean annual surface temperature for Oklahoma ranges from 17.8°C (64.0°F) at the southern border of the state to 15.6°C (60.0°F) at the northern border (National Oceanic and Atmospheric Administration, 1980). All calculations used the average of these values, 16.7°C (62.0°F), as the assumed surface temperature (T_o). The maximum error introduced [1.1°C (2°F)] by using a single surface temperature throughout the basin is not significant compared to other sources of

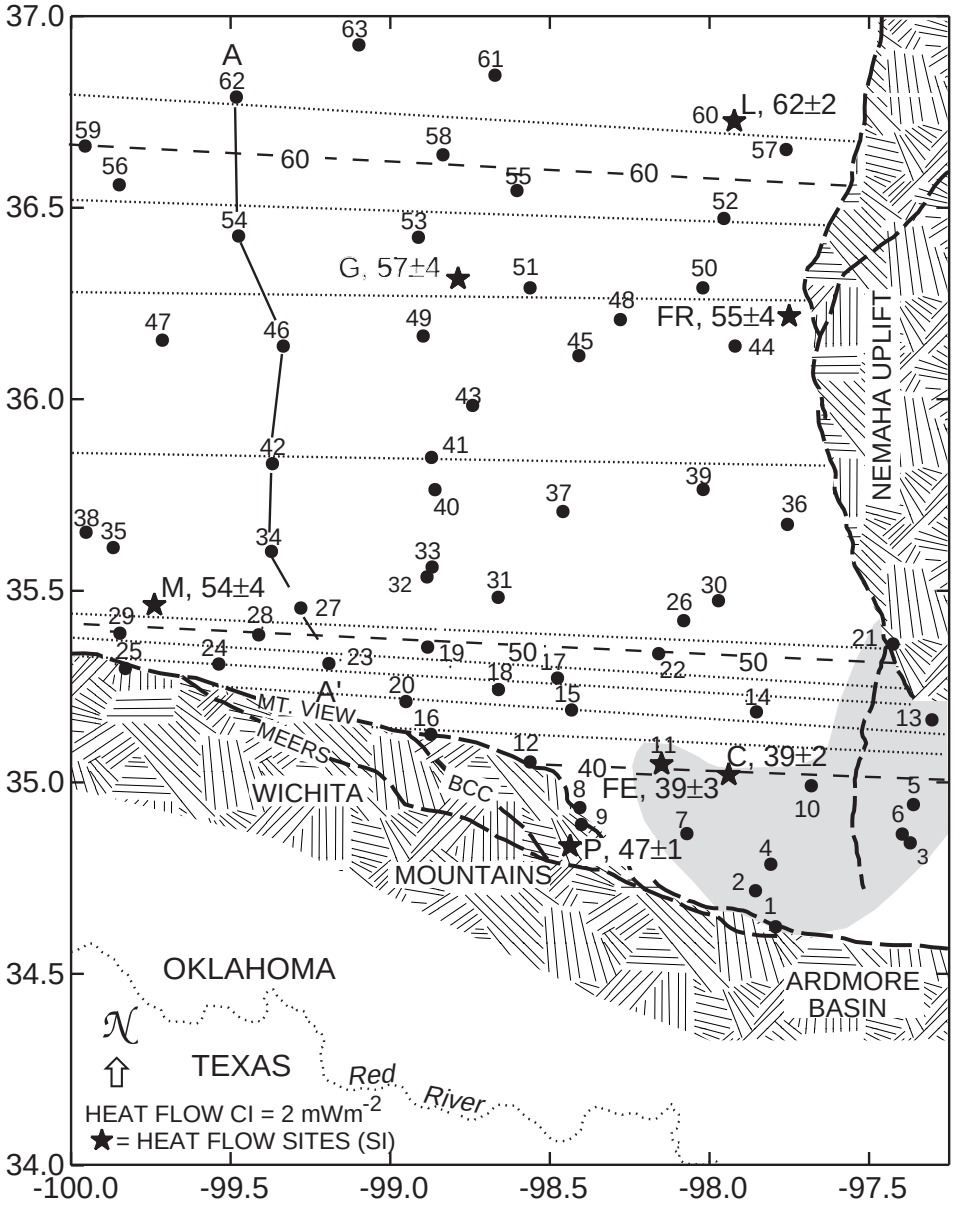

Figure 4—Map of well locations (dots), cross section A′A (Figure 11), and interpolated heat flow (dotted and dashed lines). Well sites are identified by numbers, and the location for each well is given in Appendix 1. Heat flow data are from Carter et al. (1998) for sites shown as stars. Wells in shaded area were modeled using red bed thermal conductivity of 1.7 W/m/K. All other wells were modeled using a red bed thermal conductivity of 2.0 W/m/K (Table 2). Test wells are well 60, the 2-14 LeForce (also heat flow site L), and well 11, the 1-28 Ferris (also heat flow site FE). Faults and boundaries are labeled. BCC = Blue Creek Canyon fault.

error. The surface temperature was the only input variable assumed to have no geographic variation.

Lithology

The greatest variation and source of error in the data comes from the interpretation of lithology and its relationship to thermal conductivity. To implement the temperature calculations for the Anadarko basin, the thickness of each lithologic unit having a unique thermal conductivity was needed. The practical approach in this study was to determine the lithology of each 3.05-m (10-ft) interval in studied wells using geophysical and sample logs. Well logs used in this study include spontaneous potential (SP), natural gamma-ray, density, neutron density, and resistivity. These logs all measure physical properties affected by other factors besides lithology, and hence do not necessarily determine lithology uniquely; therefore, some type of direct lithologic information was used in conjunction with the well logs to complete the lithology analyses. In general, sample logs were used in the northern shelf area of the basin. Deep-basin wells were selected for which mud logs could be obtained (generally the more recent wells).

For each well studied, the stratigraphic section was interpreted to the surface. Older wells generally were logged up to the bottom of surface casing

at 100–200 m (328–656 ft). In the deep basin, wells drilled in the last 25 yr were designed for deep targets, and logs for these holes usually start at 1500–2000 m (4920–6560 ft). In these instances, a section interpreted from a nearby older shallow well was spliced on top of the deep-well interpretation. In a few cases, a composite section was built for the near-surface interval from published sources (McNeal, 1953; Pate, 1959; Adkinson, 1960; Ham and Jordan, 1961; Adkinson and Sheldon, 1963; Jordan and Vosburg, 1963; Johnson, 1976). This approach was deemed reasonable because of the regional nature of this study.

Locating the most complete stratigraphic sections in the deep basin was also a problem. There are relatively few wells in the deep basin that even penetrate the entire Pennsylvanian section (Figure 2). Arbuckle Group information from an unpublished study by Lloyd Gatewood (1988, personal communication) was used in conjunction with the deepest well logs available to extrapolate the lithology interpretations to the base of the Arbuckle Group (Figure 3) approximating the basement (Gallardo, 1989). These extrapolations are thought to be reasonable because, on a regional scale, the lower Paleozoic formations are fairly uniform throughout the deep Anadarko basin.

For this study, thermal conductivity is based on gross lithology; therefore, all rocks were placed into one of the following lithologic categories: sandstone, limestone, dolomite, evaporite, granite wash, shale, or red beds. These limited categories are based on thermal conductivity differences to be explained in the following section. A category for siltstone would have been useful, but the logs generally did not permit the systematic identification of this lithology. This discussion will be limited to the interpretation of the stratigraphic section into this generalized classification scheme. The limited number of lithologic categories posed problems for mixed lithologies, such as sandy shale or dolomitic limestone. For each 3.05-m (10-ft) interval, units of mixed lithology were placed into the category of the dominant lithology. This poses more of a problem (i.e., introduces more error) when the mixed lithologies have significantly different thermal conductivities. We minimized this problem by using a small sampling interval. Interpreting lithology at this fine a resolution as a basis for determining thermal conductivity is in marked contrast to methods in which limited thermal conductivity measurements are applied to entire formations (e.g., Chapman et al., 1984; Funnell et al., 1996).

Characterization of the Permian section was particularly difficult and required a somewhat different approach. Much of the Permian section in the Anadarko basin is characterized by red shales with interbedded evaporites and other lithologies, often on a very fine vertical scale. These types of deposits are usually termed "red beds" (Dott and Batten, 1981; Bates and Jackson, 1984); therefore, in this study, "red bed" was the lithologic category assigned to all Permian units not specifically interpretable as one of the other individual lithologic categories. This interpretation included all shale units and many sections in the shallow parts of wells above the first casing depth where there was no lithologic information. This assumption is not strictly accurate, but it should not affect the results significantly due to the relatively thin stratigraphic section to which it was applied.

For this study, we distinguish between shale and Permian red beds because of the thermal conductivity difference between the two lithologies. This difference will be clearly illustrated by the calibration cases to be discussed in the following section and is further demonstrated by Carter et al. (1998). Although it is not strictly accurate, the arbitrary assumption was made that the shales change conductivity at the Permian–Pennsylvanian boundary. In the Anadarko basin, this boundary does not necessarily correspond to the lithologic change from red beds to the lower conductivity gray shales characterizing all older parts of the stratigraphic section (K. S. Johnson, 1988, personal communication). This lithologic change, in fact, is time-transgressive; furthermore, it is impossible to determine the difference between red beds and other shales from wireline-log character. A color change in the sample descriptions can be used, but color change is difficult to interpret, and sometimes is not noted. In some instances, the top of the Pennsylvanian (or Virgilian) was noted with listings of formation tops. More often, the Permian–Pennsylvanian boundary had to be interpolated from the formations noted nearest this boundary.

The granite wash was another difficult lithology to analyze. "Granite wash" refers to the arkosic conglomerate deposits derived from the rapid uplift and erosion of the Wichita Mountains. These deposits grade into quartz sandstones and shales northward from the Wichita Mountains. The descriptions on the sample or mud logs were relied upon to interpret granite wash intervals because well-log character is especially unreliable for this lithologic category. Of all the lithologic categories used in this study, this one is the most variable on a small and large scale, and the assumption of a single thermal conductivity is difficult to justify; however, the detailed evaluation of the properties of the granite wash lithologic category was beyond the scope of this study.

Weighted percentages of each lithology considered in this study were calculated for the entire basin from the raw data (Table 1). In the Anadarko basin, the dominant lithologies are different for sediments of different ages. The Permian is dominated

Table 1. Weighted Percentage of Lithology for Various Sections of the Anadarko Basin*

Lithology	Entire Basin	Permian	Penn.	Lower Paleozoic
Red beds	16.0	63.4	0.0	0.0
Shale	31.2	0.0	66.2	9.6
Sandstone	10.8	8.2	16.0	5.9
Granite wash	1.9	2.3	3.1	0.0
Limestone	27.4	8.9	14.3	59.1
Dolomite	8.8	1.2	0.4	25.4
Evaporite	4.1	15.9	0.0	0.0

*Lower Paleozoic values were calculated from thickness and lithology data for 50 of the wells that could be interpreted through the base of the Arbuckle Group. Penn. = Pennsylvanian.

by red beds, the Pennsylvanian by shales, and the remainder of the Paleozoic section by carbonates (Figure 2). Shale, including red beds composed mostly of shale, is by far the most abundant lithology in the Anadarko basin.

Thermal Conductivity

Thermal conductivity values of rocks cover a range of about one order of magnitude (Roy et al., 1981; Robertson, 1988). Conductivity can be measured in the laboratory; however, it must be demonstrated that such measurements represent the in-situ values (Blackwell and Steele, 1989b; Deming, 1994) because of inaccuracies associated with the sampling and measurement techniques, effects of anisotropy, etc. Laboratory measurements of thermal conductivity used as part of the process for this study are described by Carter et al. (1998). These measurements were made by the divided-bar method (Blackwell and Spafford, 1987) in the vertical direction on saturated core samples at room temperature. Published information (Robertson, 1988; Blackwell and Steele, 1989a) was also used to pick the best values for thermal conductivity.

We made two major assumptions concerning thermal conductivity as it relates to lithology. The first assumption was that each lithologic category could be assigned only one thermal conductivity value. We made a second assumption that these values for each lithology could be determined from a combination of laboratory measurements on a limited number of samples and, unique to this study, in-situ calibration of thermal conductivity using a few wells with detailed equilibrium temperature logs.

Of the many factors influencing the thermal conductivity of rocks, the most significant are lithology, porosity, fluid or gas content of the pores, and temperature (Robertson, 1988). Each lithology considered in this study has a characteristic thermal conductivity range based on its mineralogy. Porosity is probably the next most significant factor affecting the thermal conductivity of rocks. In sedimentary rocks, it can usually be assumed on a regional basis that the pore spaces are filled with low-conductivity water or brine. In general, porosity decreases with depth as the effects of compaction and cementation act on sedimentary rocks (Maxwell, 1964). So, as the porosity decreases, the effect of the low-conductivity fluid-filled pores becomes less, increasing the overall thermal conductivity of the rock. The porosity effect on conductivity is greatest at shallow depths where the porosity is relatively high, and decreases until negligible at great depth. There are exceptions to this generalization, such as if, for example, secondary porosity development or geopressure causes porosity to depart from a systematic decrease with depth.

In contrast to the general statement in the previous paragraph concerning the effect of porosity decrease with depth on thermal conductivity, empirical evidence indicates that shale conductivity is not affected much by porosity (Blackwell and Steele, 1989b; Carter et al., 1998). In uncompacted shales, the porosity may be as high as 70% (Friedman and Sanders, 1978). The high porosity causes the overall conductivity of the mud to be low, 0.7–1.0 W/m/K. Because the clay minerals are anisotropic, as compaction occurs with increasing depth, the clay particles become progressively oriented toward the lowest thermal conductivity direction for vertical heat flow. This effect offsets the increase in thermal conductivity that normally occurs with other lithologies because water is lost from the sediment; therefore, the conductivity variation with depth for shale may be relatively small (Blackwell and Steele, 1989b), even when large porosity changes occur. This situation is in marked contrast to the general prediction of increasing thermal conductivity with decreasing porosity usually made in basin modeling programs (see Sclater and Christie, 1980; Funnell et al., 1996).

Shale exerts more control on the overall thermal structure than any other lithology in the Anadarko basin because it is the most abundant lithology (Table 1) and has low thermal conductivity. The lithologies that have conductivities that are affected more significantly by porosity make a smaller contribution to the thermal structure; therefore, the porosity effect on conductivity is less pronounced for this basin than it might be in others. Estimates indicated that a porosity correction would make less than a 10% difference in the temperature predictions, and that the error introduced by not correcting for porosity would be confined primarily to the upper part of the section. The thermal conductivity of this upper section, mostly

Permian in age, has been calibrated by matching the models to actual temperature logs, which automatically compensates for the porosity effect. Conductivities of the remaining lithologies were selected based on in-situ values interpreted from measurements with porosity taken into account by the measurement process. For these reasons, no porosity correction to thermal conductivity has been made for this study.

Another important factor affecting thermal conductivity is temperature. The thermal conductivity of most rocks decreases with increasing temperature (Robertson, 1988). To account for this effect, the thermal conductivity values used for most lithologies were corrected for the ambient temperature based on temperature-thermal conductivity curves shown by Robertson (1988). No correction has been made for evaporites because they are volumetrically negligible and also occur at shallow depths and low temperatures. Shale has a consistently low thermal conductivity, and the in-situ values used here were determined by well calibration, so no temperature correction was made for either the shale or red bed categories.

The thermal conductivity data used for this study are summarized in Table 2. The measured values for Anadarko basin sandstones span a larger range than any other measured lithology (1.69 to 7.13 W/m/K). Some of the variability can be explained by differences in the mineralogy of the grains and cements and by differences in porosity. Clean quartz sandstones generally have the highest thermal conductivities because quartz has a higher thermal conductivity than feldspar and volcanic rock fragments. The lower values are found for siltstones and are due to the appreciable amounts of clay minerals in this rock type. The sandstone value selected for this study is the average of 125 samples with conductivities greater than 2.8 W/m/K. This value was determined by deleting the siltstone samples with the lowest values. The assumption was made that these siltstone samples contain more clay than quartz and were more likely to have been interpreted as shale from the well logs.

Granite wash is especially difficult to characterize by a single conductivity value. Feldspar lowers the conductivity of clastic rocks because it has a lower conductivity than quartz (Horai, 1971). The average of the five measurements on samples of granite wash is close to the average for sandstones. Because there were few samples on which to base an interpretation, a bulk value was selected for this study based on granite (Robertson, 1988), typical of the sediment source in the Wichita Mountains.

Limestone generally has a more uniform thermal conductivity than most clastic rocks because it is more likely to be monomineralic. The average value for 52 limestone samples (Ordovician–Pennsylvanian) from Oklahoma (Carter et al., 1998) has only a 2% standard error; therefore, the value selected for this study is close to the average of the measured samples.

Dolomite occurs in appreciable amounts in the lower Paleozoic section. The possibility for error in the dolomite conductivity value exists because of its common occurrence with lower thermal conductivity limestone. The value selected for this study is close to the average of the small number of measured samples.

Most evaporite lithologies have high thermal conductivities, as does dolomite, commonly found in the evaporite section. Anhydrite, gypsum, and salt are the primary evaporite minerals present in the Permian section of the basin. These lithologies have all been grouped together under the category of evaporite because their conductivities are similar, and it was impractical to separate them in the lithologic interpretations. The numerous evaporite units in the Middle Permian section are thin and

Table 2. Results of Thermal Conductivity Measurements and Analyses*

Lithology	Smokey Hill**	Oklahoma† N	Oklahoma† Avg. ±SE	This Study	Source
Red beds	2.00	0		2.0/1.7	Calibration
Shale	1.26	57	1.47 ±0.06	1.50	Calibration
Sandstone	2.47	141	4.01 ±0.10	4.21	Lab measurements
Granite wash		5	4.13 ±0.23	3.35	Typical granite
Limestone	2.94	52	2.96 ±0.05	2.90	Lab measurements
Dolomite	4.34	5	4.50 ±0.24	4.38	Published data
Evaporite	4.65	3	6.68 ±0.32	4.65	Published data

*Values listed (in W/m/K) are appropriate for room-temperature conditions.

**Sec. 32, T13S, R2W, Saline County, Kansas, data from Blackwell and Steele (1989a), a set of detailed thermal conductivity measurements for a mid-continent section of lithologies.

†Data from Carter et al. (1998). SE = standard error.

interbedded with red beds (Adkinson and Sheldon, 1963). Sections interpreted entirely as evaporites may contain high percentages of red beds (Jordan and Vosburg, 1963), as well as other lithologies (especially sandstone). To compensate for this fact, the thermal conductivity value selected for this category reflects the in-situ thermal conductivity for a composition of 70% anhydrite and 30% shale.

Core samples suitable to use for shale thermal conductivity measurements are difficult to obtain because shale separates along bedding surfaces. Cutting samples are generally available, but measurements of cuttings are inaccurate (Blackwell and Steele, 1989a). Cuttings are packed into a cylinder, and conductivity is measured as if the sample were solid (Sass et. al., 1971), but the measurement is affected by the extreme anisotropy of shale [see Deming (1994) for an approximate cuttings correction]. As a result, most shale conductivity values reported in the literature are too high (Blackwell and Steele, 1989b). The laboratory measurements made by Carter et al. (1998) were on dry core samples because the samples disaggregate upon saturation. Obviously, these measured values do not reflect in-situ thermal conductivities as well as measurements made on saturated samples.

A more accurate way to determine the in-situ thermal conductivity of shale is to calculate it [$k = Q/(dt/dz)$] from an interval gradient (Blackwell and Steele, 1989a; Demongodin et al., 1991) in a well where the heat flow is known from measurements in some other lithology. In our study, we did not apply the interval gradient method of determining shale conductivity to individual lithologic units. Because only one thermal conductivity value was used for each lithology basinwide, the best average conductivity was needed for this study; therefore, the best value for basinwide shale conductivity was determined by the best match to the temperature-depth logs of the calibration wells. This procedure is a generalization of the interval gradient method and is a unique approach used in this paper.

This procedure was also followed to calibrate the in-situ thermal conductivity of the red bed lithology. The rocks interpreted as red beds in the Permian section are made up mostly of shale. Based on the temperature logs, however, most of the Permian section has a lower average gradient (Carter et al., 1998) and, therefore, a higher average thermal conductivity than the underlying (mostly marine) shale section. This difference is caused by the presence of evaporites, as well as quartz sand, within the Permian shales. For this reason, red beds were considered a separate lithology from the lower conductivity shales that characterize the older part of the stratigraphic section.

Description of Thermal Conductivity Calibration Cases

To calibrate the in-situ thermal conductivity of the shale and red bed categories, the method described was applied to two wells from the study of Carter et al. (1998) where detailed temperature-depth logs (i.e., gradient information) and heat flow were available; therefore, values for three of the four variables in equation 1 (Q, z, T_o, and T_i) were known. Carter et al. (1998) made laboratory measurements of thermal conductivity on cores from these wells or adjacent wells for one or more intervals that can be characterized in the laboratory (sandstone or limestone sections). Gradient was determined for the interval from detailed temperature logs. Assuming one-dimensional heat flow, the interval gradient and the measured thermal conductivity were used to calculate surface heat flow for each well. This approach is the conventional way to measure heat flow. In this study, we used lithologic data interpreted from the geophysical and sample logs along with the Carter et al. (1998) heat flow and thermal conductivity data as values for the variables in equation 1. Using various test thermal conductivities in equation 1, temperature-depth profiles were calculated and compared to the measured temperature log. By matching the modeled results to the actual temperature logs using the criteria of the least cumulative temperature error and the best interval fits, the in-situ thermal conductivity values for the red bed and shale lithologic categories were determined. The thermal conductivity values selected for these lithologies (Table 2) produced the best match between the calculated and measured temperature logs of the calibration wells.

The Gungoll Exploration 2-14 LeForce Farms (Figure 5A; well 60 on Figure 4) was one calibration well. The temperature log was run 2 weeks after the well stopped producing and 4 months after the last drilling disturbance. The best average heat flow of 62 ±2 mW/m² (value range is standard error) was determined from the temperature gradient and thermal conductivity measurements in the Oswego Limestone (Marmaton Group, Figure 3). Lithologic information was interpreted from the dual-induction log to 1433 m (4700 ft). The dual-induction log and the mud log were used from that point to total depth in the Simpson Group at 1859 m (6100 ft). The lithology was extrapolated from well total depth to the base of the Arbuckle Group (L. Gatewood, 1989, personal communication).

The calculated temperature (Figure 5A) diverges only slightly from the observed temperature (difference of about 0.6°C) down to 756 m (2480 ft) at the base of the Permian/top of the

Pennsylvanian (Wolfcampian/Virgilian; see Figure 3) with an assumed red bed thermal conductivity value of 2.0 W/m/K; however, the predicted and observed gradient-depth curves do not correlate well in the Wolfcampian interval. The dual-induction log does not distinguish well between the shale and limestone units, and this ambiguity explains the lack of correlation seen in the gradient plot. This difficulty illustrates again the uncertain nature of interpreting lithology from geophysical logs alone, and demonstrates that gradient logs can be more accurate at predicting lithology than conventional geophysical logs (Blackwell and Steele, 1989b). Although this is another source of error, the overall fraction of limestone vs. red beds interpreted for this section appears to be fairly close to the actual relative amounts. The best temperature fit in the section above 756 m (2480 ft) gives a thermal conductivity value for red beds in this well of 2.0 W/m/K (Table 2).

For the Pennsylvanian section, two different thermal conductivity values for shale were tested for comparison. Model 1 used 1.5 W/m/K (Table 2) and model 2 used 1.7 W/m/K. In model 1, the shapes of the gradient curves match in the Pennsylvanian sections dominated by shale between 756 and 1228 m (2480 and 4030 ft), but the modeled gradient is systematically high by approximately 2°C/km (0.1°F/100 ft). This difference raises the cumulative error to 1.9°C at the base of the interval. If a shale thermal conductivity value of 1.7 W/m/K is assumed (model 2), the gradient error in this interval is corrected; however, the lower section, between 1228 m (4030 ft) and the end of the measured temperature log at 1533 m (5030 ft), contained a systematically low gradient by approximately 5°C/km (0.25°F/100 ft) in model 2 (Figure 5A). This problem illustrates the difficulty in assigning a single thermal conductivity value to each lithology. The shales clearly have different average thermal conductivity values for different parts of the sedimentary section in the LeForce well.

The Shell Oil Company 1-28 Ferris (Figure 5B; well 11 on Figure 4) was the second well used for calibration. A high-quality temperature log for this shut-in well was obtained with a downhole recording computer/memory tool to a depth of approximately 5182 m (17,000 ft). Heat flow was calculated from the gradients and thermal conductivities of two sandstone intervals (Carter et al., 1998). The best average heat flow for the Ferris well is 39 ±3 mW/m^2 (value range is standard error).

Lithology data were not available for the upper portion of the Ferris well. The lithology for this part of the hole was interpreted from the nearby Magnolia 1-A Lillian Miller in Sec. 14, T6N, R9W, approximately 6.4 km (4 mi) to the southeast. The dual induction log for the 1-28 Ferris well begins at 1067 m (3500 ft). At 2286 m (7500 ft), information from the neutron density log was added to the interpretation, and from 2438 m (8000 ft) to total depth, the mud log was also used. The well bottomed at 5601 m (18,376 ft) in the Springer Group.

Figure 5B shows the comparison between the temperature log and the model calculated with the thermal conductivity values chosen for this study. The best thermal conductivity value for the Permian red bed lithology in the 1-28 Ferris well is 1.7 W/m/K (Table 2). The cumulative error between calculated and measured temperatures is approximately 1.3°C (1%) for the entire section. The correlation between the predicted and observed gradient curves is excellent throughout the section, indicating correct interpretation of the lithology. The gradient correlation with lithology is emphasized in Figure 5B where the natural gamma-ray log is compared to the observed gradient log.

To summarize, thermal conductivity values for shale and Permian red beds were chosen by comparison to the gradient logs of the two calibration wells. Two different values for red bed conductivity are given in Table 2 corresponding to the best values for the two test wells, 1.7 W/m/K for the Ferris well and 2.0 W/m/K for the LeForce well. The Permian evaporites pinch out in the southeast part of the basin (K. S. Johnson, 1989, personal communication) and, indeed, the Permian section in the 1-A Lillian Miller well (used to interpret the lithology for the upper part of the 1-28 Ferris well) contains almost no evaporite units. Thus, we concluded that the red beds in the Ferris well also do not contain significant amounts of evaporite minerals. The lack of these higher conductivity minerals accounts for the lower average conductivity of the red bed lithology in this area. Even with the lower value, the red bed lithology, as it is interpreted in this study, still has a higher thermal conductivity than the older marine shale lithology. Because of the lower red bed conductivity value for this area, all wells in the southeastern corner of the basin, which also do not contain evaporite units, were modeled using the red bed thermal conductivity value 1.7 W/m/K. The shaded area in Figure 4 outlines these wells. For the remainder of the basin, the red bed thermal conductivity value of 2.0 W/m/K determined from the LeForce well was used in the calculations.

The best average shale thermal conductivity value determined from the Oklahoma test wells was 1.5 W/m/K. This value is higher than the value of 1.2 W/m/K found for Ordovician through Pennsylvanian shales in central and eastern Kansas by Blackwell and Steele (1989b). The Smokey Hill well results from their study are included in Table 2 for comparison. The best shale value determined

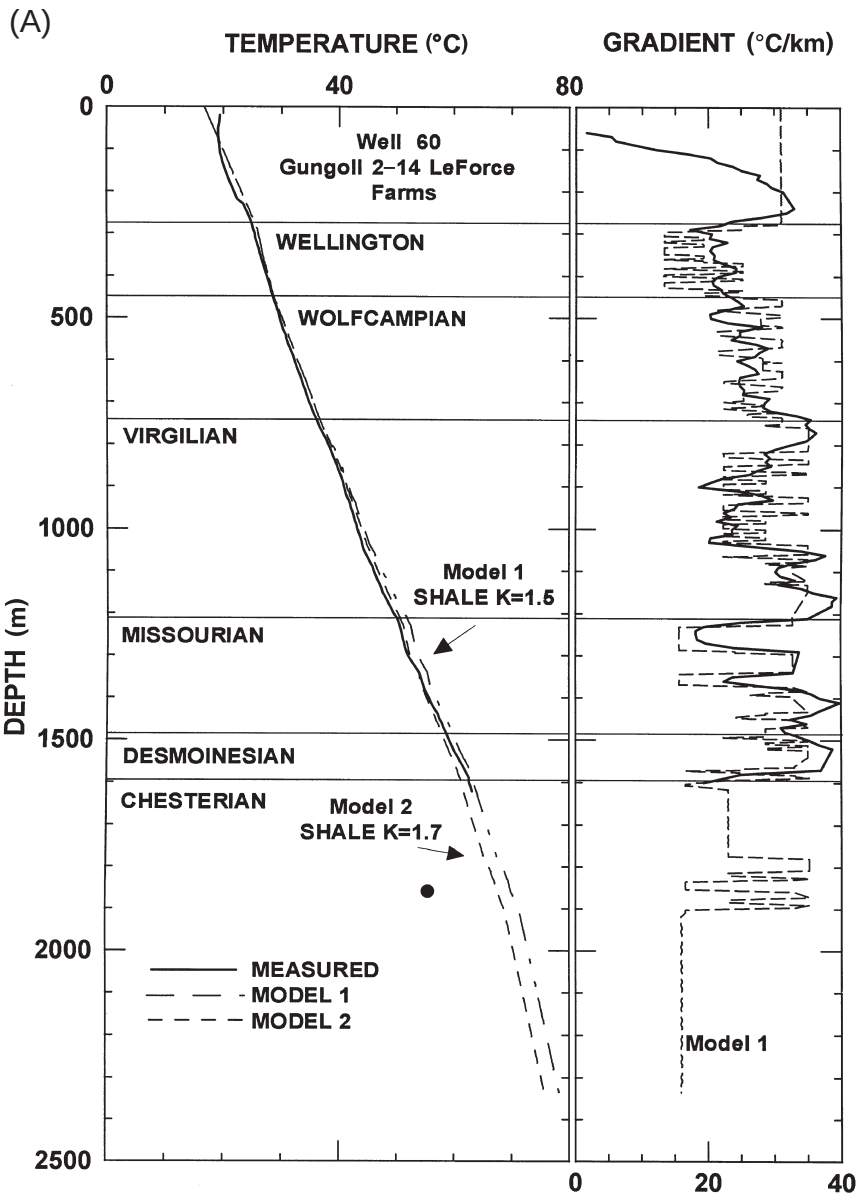

Figure 5—(A) Comparison of measured (solid line) and calculated (dashed line) temperature and gradient logs for well 60, the 2-14 LeForce well (Figure 4) calibration site. Thermal conductivity values in Table 2 (red beds 2.0 W/m/K, shales 1.5 W/m/K) are used for model 1. For model 2, shale value is 1.7 W/m/K. In the gradient panel, measured gradient is more irregular than model 1 gradient. Large dot is BHT (bottom-hole temperature). Data were filtered with a three-point running average of 10 m of log data and 3 m of model calculation results. Temperature data are from Carter et al. (1998). (B) Comparison of measured (solid line) and calculated (dashed line) temperature and gradient logs for well 11, the 1-28 Ferris well (Figure 4) calibration site using conductivity values in Table 2 (red beds 1.7 W/m/K). In the gradient panel, measured gradient is more irregular than model gradient. Natural gamma-ray log is shown in third panel. Large dots are BHT. Data filtered with three-point running average of 10 m of log data and 3 m of calculation results. Temperature data are from Carter et al. (1998).

for this study may be higher because the lithology referred to as shale in this analysis probably contains appreciable amounts of silt in the Anadarko basin (Adkinson, 1960), which could not be accounted for due to the limited resolution of the logs. Quartz and other nonlayered silicates raise the thermal conductivity of shales because their conductivities are higher than the layered silicates (Horai, 1971); furthermore, two different conductivity values fit different parts of the LeForce test well, so the single value used for this study applies only in an average sense. Obviously, local thermal conductivity contrasts within the sedimentary section are more complicated than can be addressed in this type of regional study.

Surface Heat Flow

Seven values of surface heat flow in the Anadarko basin were used for this study (Carter et al., 1998). The heat flow sites are indicated by stars in Figure 4. Carter et al. (1998) observed that the heat flow values vary somewhat systematically across the basin. Unfortunately, this sparse data set, with a particularly large gap in the central part of the basin, constitutes the only available heat flow information determined using conventional measurement techniques. So, in making the heat flow interpretation (shown by the dotted/dashed lines in Figure 4), we also considered the regional gravity data. The heat flow variation in the Anadarko basin

(B)

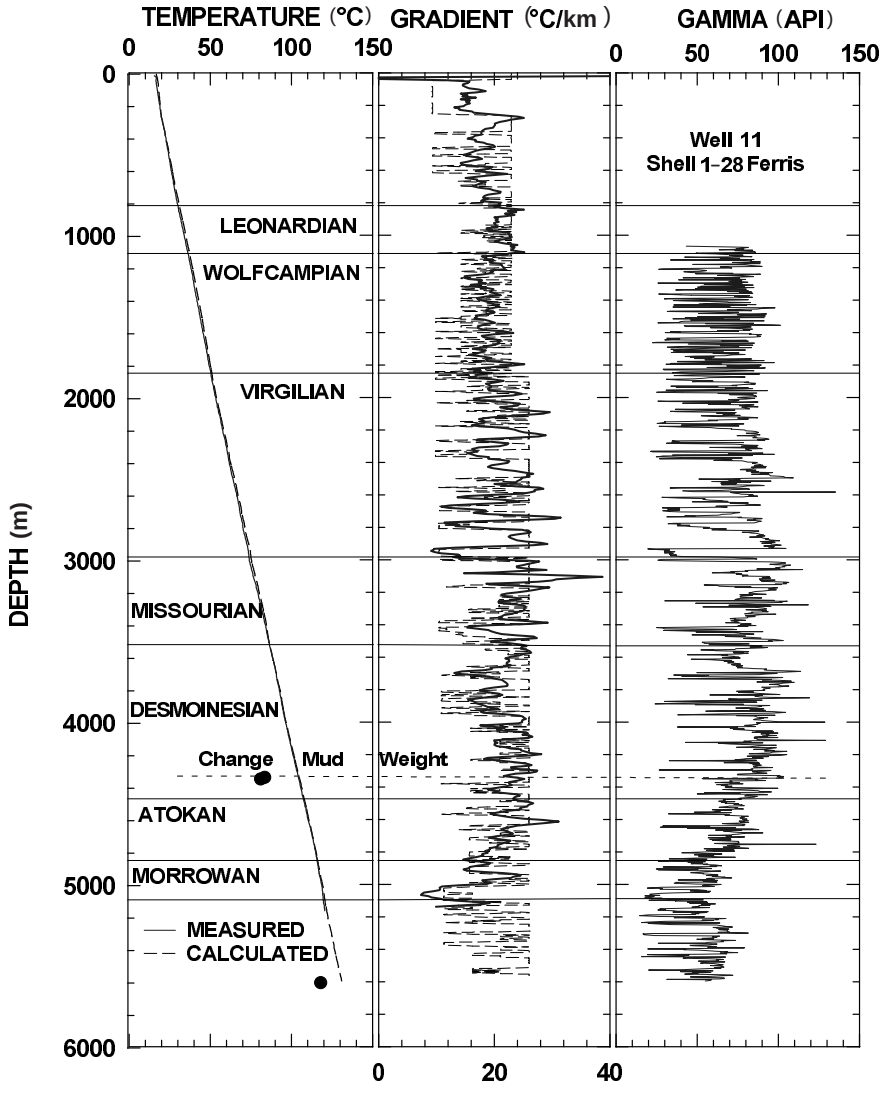

Figure 5—Continued.

is postulated to follow the trend of the gravity data (SEG, 1982). High Bouguer gravity values in the southern part of the basin are probably related to the basement lithology and thus imply basement continuity between the Arbuckle Mountains and the Wichita Mountains. The high gravity may be associated with more basic upper crust, which, in turn, would have a lower radioactive heat production leading to lower heat flow (Roy et al., 1972). Geophysical interpretations of the crust (Zhu and McMechan, 1989; Hsueh, 1991) are consistent with the proposed heat flow model.

The wells located within the area of high Bouguer gravity values have lower heat flow values than wells to the north. The Ferris well, located in the southeastern part of the basin, has a heat flow value of 39 ±3 mW/m^2. The southernmost heat flow site, the Perdasofpy well, is located within the frontal fault zone of the Anadarko basin. The Perdasofpy well is also within the area of high regional gravity values and has a heat flow value of 47 ±1 mW/m^2. The Mackey well to the west is just off the northwest edge of the high-gravity anomaly of the Wichita Mountains and has a higher heat flow value (54 ±4 mW/m^2) than the Ferris or Perdasofpy.

The Perdasofpy well cuts 975 m of Carlton Rhyolite and Wichita Granite underlain by 300 m of Navajoe Mountain Basalt-Spilite (Ham et al., 1964). One might assume that basic rocks similar to those found in the Perdasofpy well and exposed in the Wichita Mountains also underlie the Colbert Rhyolite exposures in the Arbuckle anticline (Ham et al., 1964). The geologic models (Gilbert, 1983) corroborate this hypothesis.

The heat flow appears to have little variation through the middle of the basin. The values on the basin shelf increase northward until the northernmost value is consistent with heat flow values measured in Kansas (Blackwell and Steele, 1989a). The heat flow contours shown on Figure 4, used to determine a heat flow value at each well site, are interpreted to lie in a west-northwest direction parallel to the gravity trend (SEG, 1982).

DISCUSSION OF TEMPERATURE CALCULATION RESULTS

Temperature Profiles

Temperature-depth profiles were calculated for all wells in the data set. Predicted temperature-depth profiles and gradient-depth profiles for two different parts of the Anadarko basin are shown in Figures 6 and 7 with stratigraphic units indicated. The depths of the stratigraphic units were obtained from the completion cards or logs for each of the wells, and some of the names shown on Figures 6 and 7 are not shown on the generalized stratigraphic column in Figure 3. The most important fact illustrated by these figures is the control of lithology (i.e., thermal conductivity) on temperature and gradient. On the gradient-depth plots, the high-conductivity, low-gradient rocks are easily distinguished from those with low conductivity and high gradients. This relationship is more difficult to see on the temperature-depth plots at this scale, but for every lateral shift on the gradient-depth plots, there is a corresponding change in the slope of the temperature-depth plot.

The vertical stratigraphic section of the Anadarko basin can be divided into three major divisions based on the dominant lithology for each depth range (Figure 2; Table 1). These stratigraphic divisions are the Permian section, dominated by red beds and evaporites, the Pennsylvanian section, dominated by shales, and the lower Paleozoic section, dominated by carbonates. The boundaries between these sections are noted by bold lines on Figures 6 and 7. The top of the Pennsylvanian can be identified on the gradient-depth plots in these figures by the difference in maximum gradients (intervals with peaks to the right) for the sections above and below that point. This change in gradient reflects the different thermal conductivity values used to model red beds of the Permian and shales below the top of the Pennsylvanian (Table 2). At the lower subdivision boundary, a shift to lower average gradients reflects the change to dominantly carbonate lithology. These changes in gradient can be seen directly in the observed temperature-depth curves from the Anadarko basin (Carter et al., 1998).

Although the differences are subtle, the three-part character of the basin also is evident on the temperature-depth plots because the average slopes of the temperature-depth profiles are different for each of the three sections. The differences are easiest to see in Figure 6. In Figure 7, the three-part character is obscured by the presence of granite wash in this deep-basin well. Within the Pennsylvanian section, the lateral facies change associated with the approach to the Wichita Mountains, the granite wash section, is important to the thermal structure of the basin. This point is discussed in more detail in the next section, but is easily illustrated by comparing the temperature-depth curves for two wells, one with an extensive section of granite wash and one without.

In Figure 8, the predicted temperature-depth profile for the Lone Star Gas 1 Bertha Rogers well (Figure 4, well 23) shows a temperature of 189°C (372°F) calculated at the top of the lower Paleozoic carbonates (see also Figure 10). This well contains a significant amount of granite wash, which lowers the gradient in the interval 1500–4500 m (4921–14764 ft) (steeper average slope, Figure 8). The profile for the GHK 1-2 Harrell well (Figure 4, well 27) has a predicted temperature of 220°C (428°F) at the top of the lower Paleozoic carbonates (see also Figure 10). The equivalent stratigraphic interval, 1500–4500 m (4921–14764 ft), in this well is dominated by low-conductivity shale resulting in a higher gradient (flatter average slope in Figure 8). The resulting temperature differences at the top of the lower Paleozoic carbonates will carry through to basement because this lower Paleozoic section is fairly uniform in lithology throughout the basin.

Horizon Maps of Temperature

Temperature maps were made from the calculated temperature results (equation 1) at the two boundaries between the three major lithologic divisions (dashed lines in Figure 3). The structure also is shown on these maps to provide a means of relating the temperature distribution to the lithologic distribution. The first mapped horizon is the top of the Pennsylvanian (Figure 9). As has been described in previous sections, this is the least well established horizon because it was determined from incomplete formation top data. Also, the boundary depicted in Figure 9 represents the difference in thermal conductivity between Permian red beds and lower conductivity shales occurring below them. The problems associated with this distinction have been explained previously. The structure and the predicted temperatures at this boundary have contours of similar

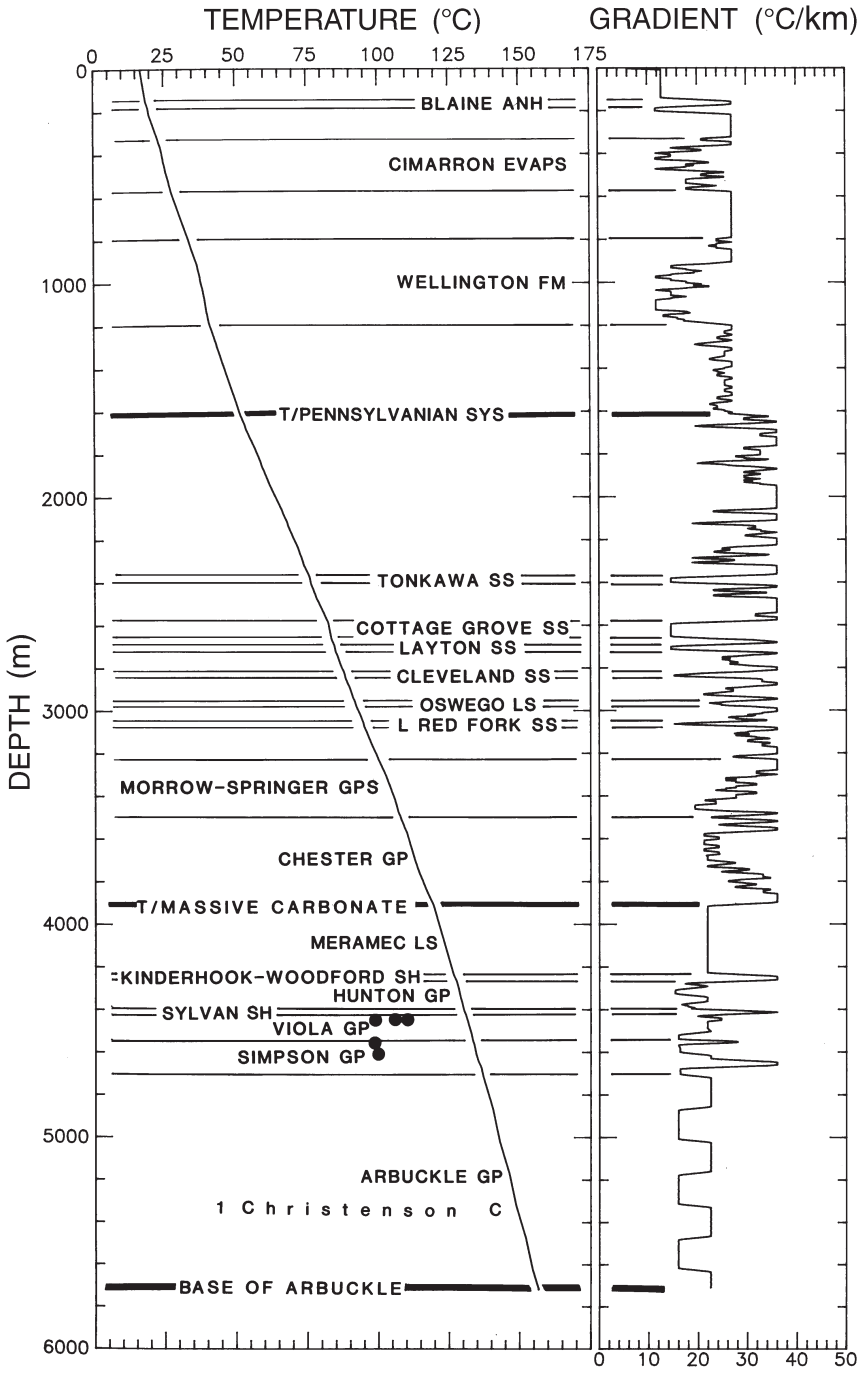

Figure 6—Calculated temperature-depth and gradient-depth model for a representative well in middle of basin, Texas Oil and Gas 1 Christenson C, Sec. 23, T16N, R16W, Dewey County (Figure 4, well 41). Stratigraphic names are shown. Large dots are bottom-hole temperatures at well total depth.

shape. The similarity is to be expected because the vertical lithologic distribution of rock types in the Permian section is comparable throughout most of the basin; therefore, the temperatures are controlled by the thickness of the section above this boundary. Typical thicknesses of the overlying Permian section range from 900 to 1800 m (3000 to 6000 ft) in the south to 400 to 800 m (1400 to 2800 ft) in the north, resulting in predicted temperatures at this horizon in the range of 40 to 60°C (104 to 140°F).

The most extensive evaporite deposits occur in the western part of the deep basin (Jordan and Vosburg, 1963). One might expect the lower gradient through these units to result in lower temperatures at this boundary where thick evaporite sections occur; however, the low-conductivity (high-gradient) red beds also are thicker in these

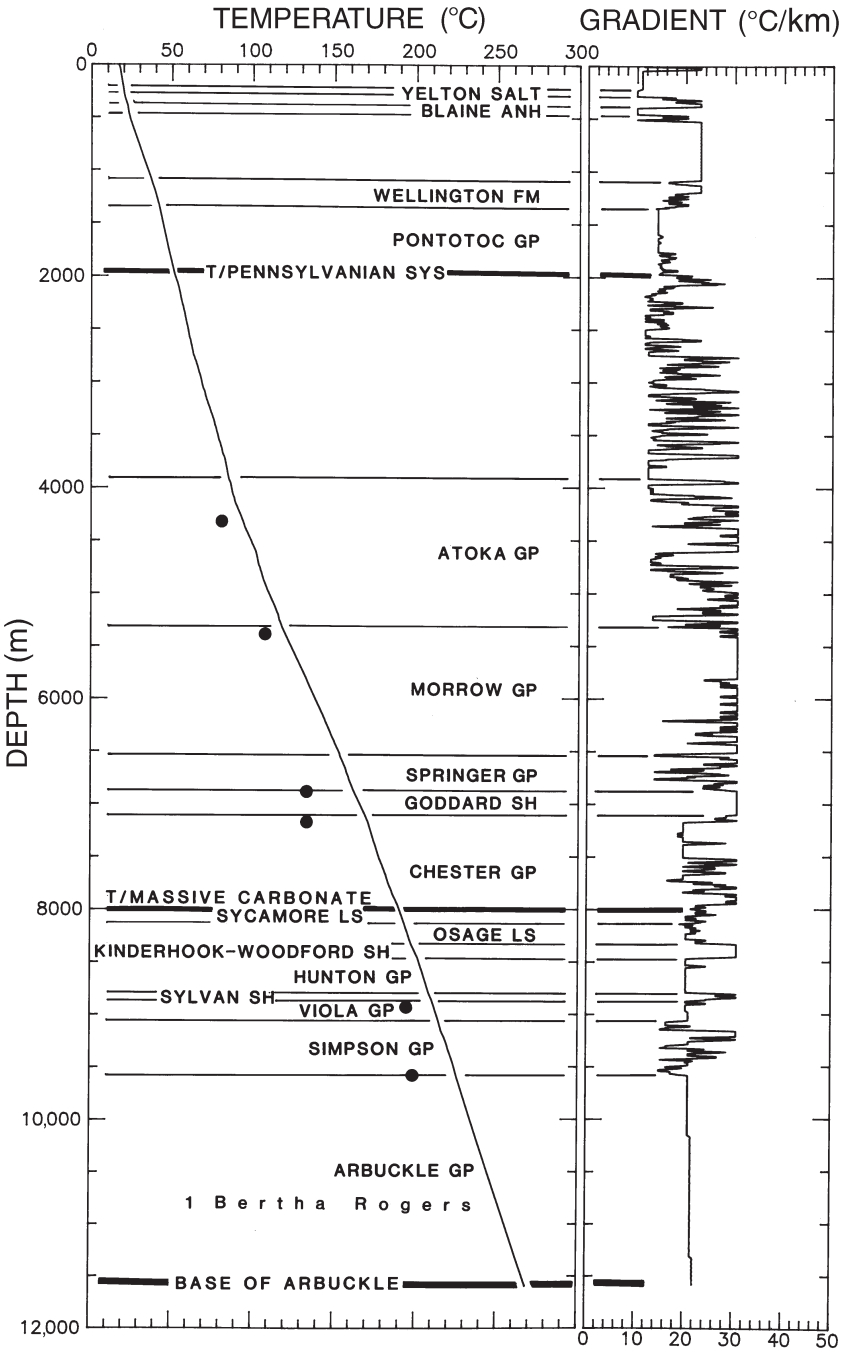

Figure 7—Calculated temperature-depth and gradient-depth model for a representative deep-basin well, Lone Star 1 Bertha Rogers, Sec. 27, T10N, R19W, Washita County (Figure 4, well 23). Stratigraphic names are shown. Pontotoc Group is approximately time equivalent to Chase, Council Grove, and Admire groups (Figure 3). Large dots are bottom-hole temperatures at well total depth.

areas. Thus, because the relative percentage of each rock type is similar for most of the basin, the overall temperature distribution reflects the thickness of the entire Permian section. The highest temperatures are displaced slightly north of the axis of the greatest thickness of Permian rocks due to the increase in regional heat flow to the north, away from the Wichita Mountains.

The next boundary illustrated (Figure 10) corresponds to the top of the lower Paleozoic carbonates (Figure 3). This boundary was established in the lithologic interpretations at the top of the massive carbonates. The Sycamore Limestone, the Meramec limestone, or the Mississippi lime was chosen rather than the top of the Chester Group because the Chester contains significant amounts of shale, especially in the deep basin. The elevation of this boundary increases northward across the basin from about –7300 to –1100 m (–23,951 to –3609 ft), with a corresponding temperature decrease from 220 to 60°C (428 to 140°F).

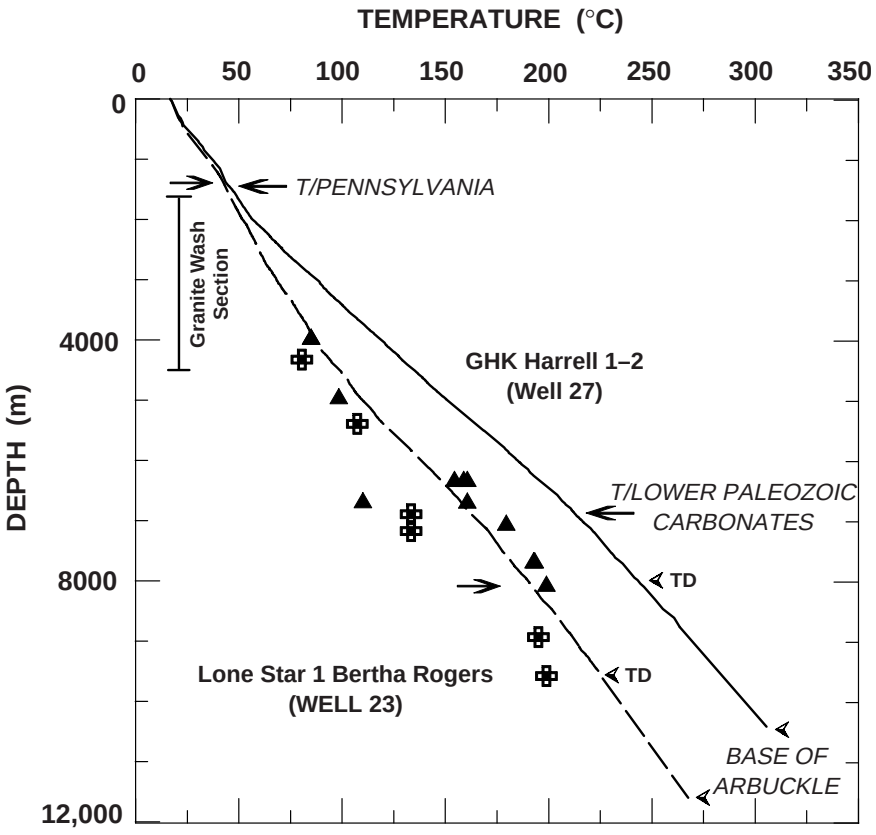

Figure 8—Comparison of predicted temperature-depth profiles for a well containing significant granite wash section (dashed line), the Lone Star 1 Bertha Rogers (Figure 4, well 23, Sec. 27, T10N, R19W, Washita County), and a well with equivalent section dominated by shale (solid line), GHK 1-2 Harrell (Figure 4, well 27, Sec. 2, T11N, R20W, Washita County). Granite wash occurs at 1500–4500 m in well 23. BHT (bottom-hole temperature) points are also shown (crosses = well 23, triangles = well 27).

The temperature map at the top of the lower Paleozoic carbonates (Figure 10) shows a different shape than the temperature map on the top of the Pennsylvanian (Figure 9). The deepest occurrence of this boundary is next to the frontal fault zone of the Wichita Mountains (Figure 10); however, the highest temperatures occur within the basin to the north of the frontal fault zone. Two reasons explain why the highest temperatures do not correspond to deepest burial as would be expected: (1) the lower heat flow to the south and (2) the fact that the Pennsylvanian section is not lithologically uniform across the basin. The presence of significant amounts of granite wash next to the Wichita Mountain front decreases the predicted gradients significantly through the Pennsylvanian section in that area, as illustrated in Figure 8. Low-conductivity shale (Table 2) dominates the Pennsylvanian section in other areas of the basin farther from the frontal fault zone.

A conspicuous data gap is apparent in the map in Figure 10; this gap occurs to the east of the area with the highest temperatures. The mapped boundary occurs at great depths in this area, and no well data were available. The total thickness of the sedimentary section may be approximately the same as to the west where the highest temperatures are predicted. If the section in this area with no data has a similar lithologic distribution as in the wells to its west, the temperatures should be similar; therefore, the shape of the contours for the high-temperature bull's-eye (Figure 10) may be more elliptical than indicated by this data set.

The high-temperature offset revealed in Figure 10 carries through the remainder of the stratigraphic section because the lower Paleozoic formations are relatively uniform across the basin. When temperatures are calculated at the base of the Arbuckle Group (Figure 3), a similar temperature pattern is seen (Gallardo, 1989). The highest temperature predicted in the basin is below the GHK 1-2 Harrell (Figure 4, well 27; see also Figures 8, 11). The well bottoms in the Hunton Group (Figure 3). Approximately 2400 m (7874 ft) of section were extrapolated from its total depth of –7449 m (–24,440 ft) to the base of the Arbuckle Group. The temperature at –9848 m (–32,310 ft) is predicted to be 305°C (581°F). The deepest well drilled in the Anadarko basin is the Lone Star 1 Bertha Rogers, (Figure 4, well 23; see also Figures 6, 8, 11). This well reaches a total depth of –8997 m (–29518 ft) in the Arbuckle Group, so only the remaining thickness, 2012 m (6600 ft), and lithology of the Arbuckle Group are extrapolated. At the base of

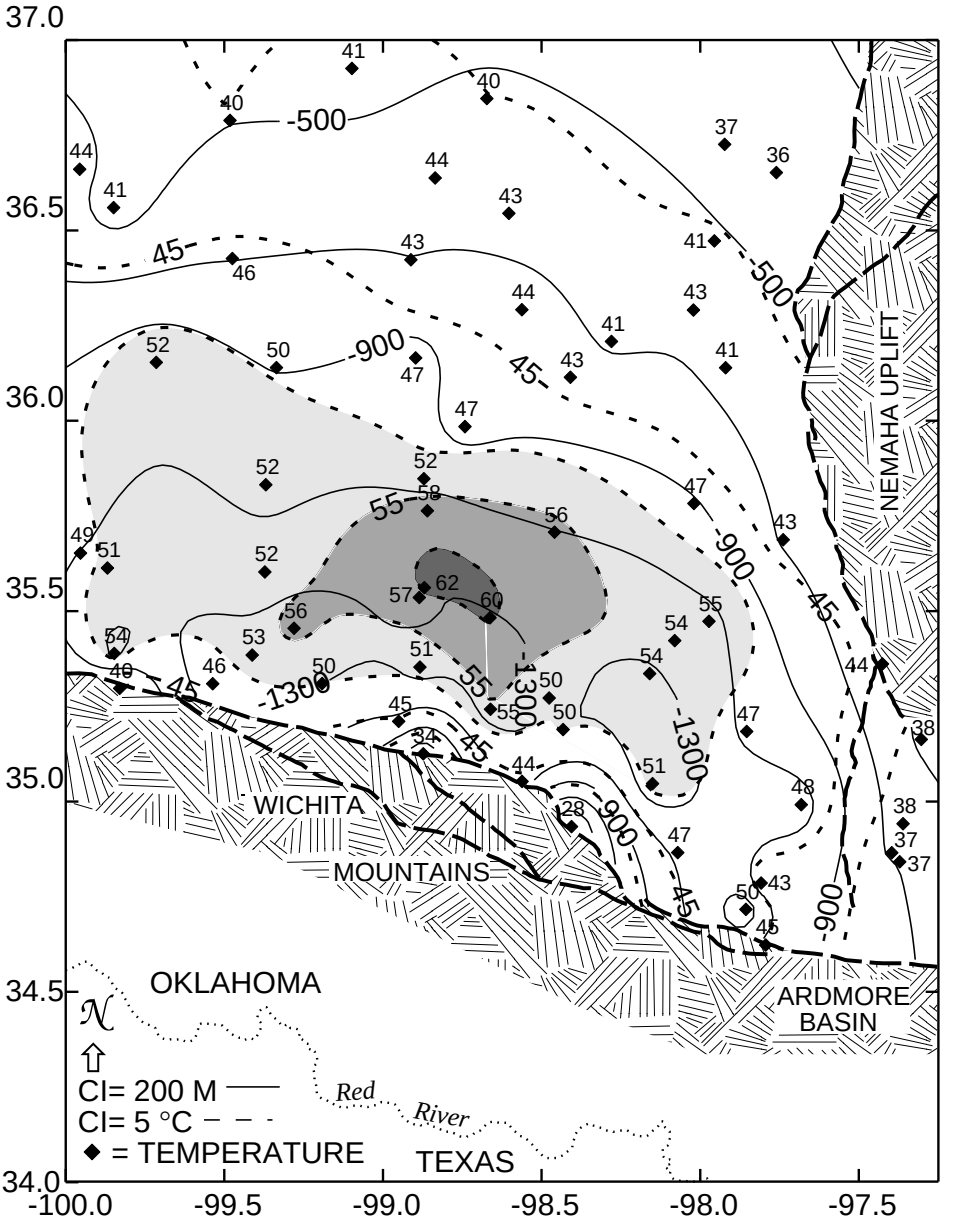

Figure 9—Structure contours (solid line, depth below sea level in meters) and predicted temperature (°C) contours (dashed line) on base of the Permian/top of the Pennsylvanian. Contour patterns are similar.

the Arbuckle Group, the Bertha Rogers well has a predicted temperature of 267°C (513°F) at an elevation of –11,009 m (–36,119 ft). The well immediately west of the Bertha Rogers is the Lone Star 1-28 Baden (Figure 4, well 24), the second deepest well drilled in the Anadarko basin (total depth is in the Viola Group). The Baden well has a predicted temperature of 252°C (486°F) at the base of the Arbuckle Group (Figure 3) extrapolated to be at a depth of –11,277 m (–36,998 ft). The Baden well has a lower predicted temperature at a greater depth than the Bertha Rogers well. The lower temperature is due to a slightly lower heat flow, as well as a granite wash section almost twice as thick [1344 m (4410 ft)] as that present in the Bertha Rogers well [814 m (2670 ft)].

Temperature Cross Section

As a further illustration of the results, Figure 11 shows a cross section for the western part of the basin perpendicular (north-south) to the basin axis (location in Figure 4). The cross section also shows the offset of the highest temperatures away from the deepest part of the basin evident in the map in Figure 10. Lower gradients through granite wash next to the mountain front to the south push the

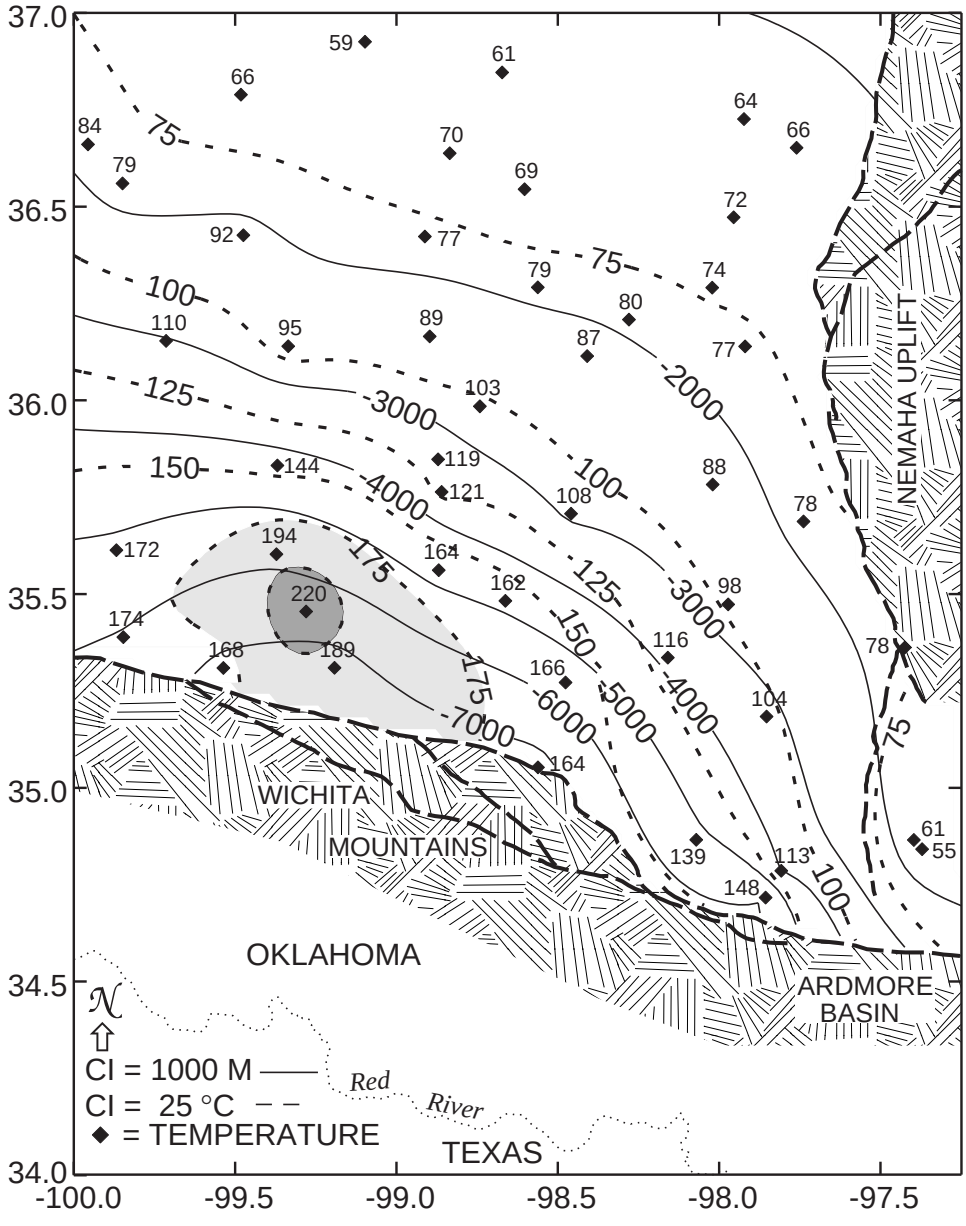

Figure 10—Structure contours (solid line, depth below sea level in meters) and predicted temperature (°C) contours (dashed line) at top of the lower Paleozoic carbonates. Highest temperatures are offset significantly from deepest occurrence of layer.

isotherms to greater depths (well 23), and thick shale sections with high gradients raise the isotherms at locations further north in the basin (well 27).

Woodford Shale Organic Maturation

Studies of the vitrinite reflectance of the Devonian Woodford Shale (Figure 3) in the Anadarko basin were done by Cardott and Lambert (1985) and Cardott (1989). The Woodford Shale is an important hydrocarbon source rock in this basin. Vitrinite reflectance is a measure of the thermal maturity of a source rock and generally is observed to increase with increasing depth; however, these studies showed the highest vitrinite reflectance values for the Woodford Shale to be offset from its deepest occurrence (Figure 12A). Because they are not associated with the deepest part of the basin, the highest vitrinite maturity values were attributed to a localized thermal event (Cardott and Lambert, 1985). The thermal event was interpreted to be the result of Pennsylvanian crustal thinning as inferred by Garner and Turcotte (1984).

The temperature map on the top of the Woodford Shale produced by this study (Figure 12B) shows the same type of offset as the vitrinite data. The highest

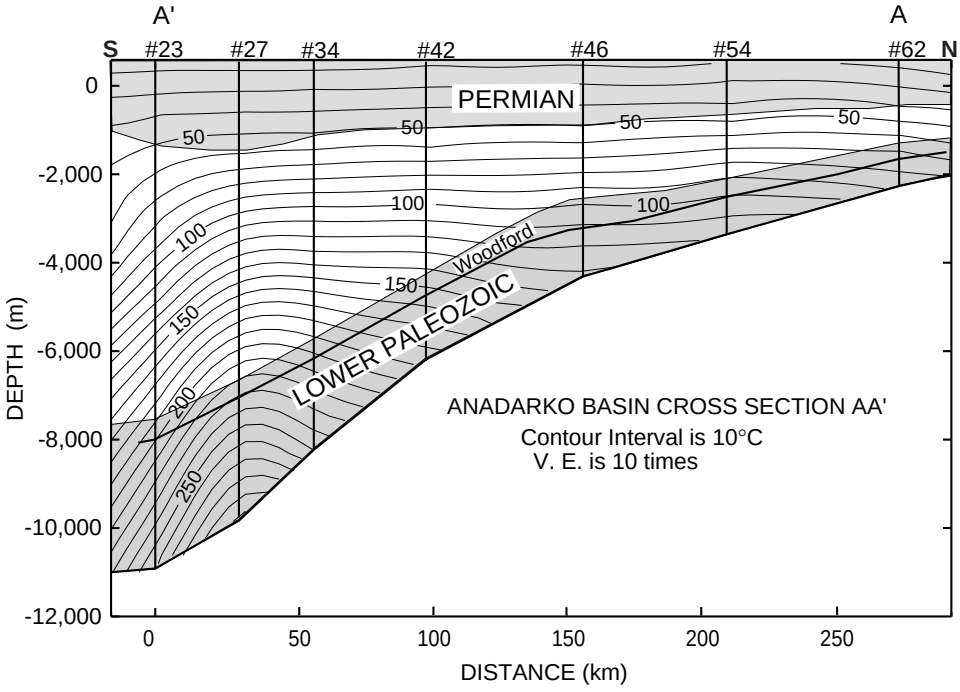

Figure 11—Predicted isotherms for cross section A′A (location on Figure 4). Well identification numbers from Figure 4 are given across the top. Lines between shaded intervals mark mapped boundaries at the top of the Pennsylvanian (Figure 9) and the top of the lower Paleozoic carbonates (Figure 10); bold line marks the top of the Woodford Shale (Figure 12).

temperatures are predicted in the same area as the highest vitrinite reflectance values rather than at the deepest occurrence of the formation. As previously explained, the offset is attributed to the lower heat flow and to the presence of granite wash in the deepest part of the basin. The situation is a normal consequence of the conductive thermal regime of the basin. Consequently, there is no need to postulate a paleothermal event to explain the present temperature pattern nor the pattern of vitrinite reflectance. Thus, the change in elastic thickness with time inferred by Garner and Turcotte (1984) may have a nonthermal cause. More details of the thermal and maturation history for three sites in the Anadarko basin are discussed by Carter et al. (1998).

Geopressure

The geothermal gradient map of Oklahoma (Luza et al., 1984) shows a region containing a geopressured zone in the Lower Pennsylvanian–Upper Mississippian section and shows high temperature gradients within this geopressured zone. Harrison et al. (1983) stated that gradients in rocks overlying geopressured zones are abnormally high due to the restriction of heat flow by the abnormally pressured zone. Higher gradients through geopressured zones along the northern Gulf of Mexico basin have been explained by excess pressure keeping the sediments from compacting. The result is higher porosity, which reduces thermal conductivity and, therefore, produces a higher gradient (Samuels, 1979).

The Ferris well, described in a previous section, penetrates the geopressured zone at approximately 4328 m (14,200 ft). The log header of the dual-induction log indicates that the mud weight was changed at this depth during the drilling. As Figure 5B illustrates, the gradient does not change at this depth. The model developed for this study predicted the gradients throughout the entire section of the Ferris well without making any adjustment in thermal conductivities for rocks within the geopressured zone; therefore, there is no evidence that the gradient in this well is affected by geopressure.

A possible explanation for the observation of higher gradients in the geopressured zone as noted on the geothermal gradient map (Luza et al., 1984) is simply that the temperatures were measured in thick shale sections. The top of the geopressured zone is approximately 150 m (492 ft) below the top of the Morrow group (Figure 3) at depths ranging from 2745 to 4570 m (9000 to 15,000 ft) (Luza et al., 1984). For the wells located within the geopressured area of the Anadarko basin that were used in this study, the Pennsylvanian section is composed of approximately 68% shale. The shales have low thermal conductivities, and gradients calculated from BHT measured in this part of the well section will be higher than gradients calculated from BHT measured in sections containing higher conductivity

rocks. In this case, the gradients are not anomalous, but instead reflect conductive heat flow in association with differences in thermal properties.

Another possible reason for apparent higher gradients in the geopressured zone could be that the measured BHT values are closer to equilibrium. In a geopressured zone, the formations are not as likely to be invaded and cooled by the drilling fluids as they are in normally pressured zones, so the measured BHTs may be closer to the actual formation temperature than, for example, temperatures predicted by the line shown in Figure 13. Temperatures measured under hydrostatic pressure conditions may be farther from equilibrium (i.e., lower), particularly if the formation is invaded by the drilling fluid; therefore, gradients predicted using the same BHT correction scheme across the transition to geopressure could be higher than the actual gradients.

Error

Because there are no correct answers to compare with the results except at the two test wells, the errors are hard to quantify. At the LeForce and Ferris calibration sites, the comparison is within ±2°C over a temperature change of 45 and 100°C respectively, or between 2 and 5%, so that the minimum error is ±5%. The important assumptions are values of the heat flow at each site and uniform thermal conductivity for each lithology throughout the basin. The heat flow errors are estimated by Carter et al. (1998) to be between ±5 and 10% depending on the site. The heat flow error translates directly into error in the temperature calculation. This heat flow error does not include errors introduced by interpolation of heat flow values in areas without nearby data, such as in the central part of the basin. The total heat flow variation is 25 mW/m^2, and the variation across the data gap in the center of the basin is from 3 to 15 mW/m^2, so that the error associated with the interpolation at any site is probably included within the ±10% associated with each heat flow point.

To some extent, the absolute magnitude of error related to the variation in thermal conductivity of shale as a function of position (the source of the largest uncertainty) should peak (about ±5%) at the top of the lower Paleozoic carbonates, and decrease below that boundary. Below the top of the lower Paleozoic carbonates, the error is primarily due to the original heat flow assumption, variations in porosity, dolomite:limestone ratios, and the temperature correction. Thus, the total error in temperature at the basement due to the heat flow and thermal conductivity uncertainty is approximately ≤15%.

All the errors except the random error of the heat flow determination are somewhat systematic and smaller between adjacent wells. Thus, the smaller scale patterns may be more accurate than basinwide patterns. The smoothness of the predicted temperature field suggests that the assumptions are reasonable for the regional scale of this investigation.

The objective of this paper is to illustrate a supplemental approach to conventional BHT/cuttings determination of the thermal regime in a sedimentary basin. One problem with the BHT/cuttings technique is that there is no evaluation of error by direct comparison to data of known error. The accuracy of the assumptions and thermal predictions can be significantly constrained and improved by combining the conventional approach with detailed heat flow and temperature gradient studies of a few wells per basin, allowing calibration of the inferred in-situ thermal conductivity values determined from cuttings measurements (or spot cores) and BHTs. To some extent, comparisons with maturation data do allow this check, but uncertainties in kinetics and heat flow history limit the constraining ability and may involve circular reasoning.

BHT Discussion

Because we propose in-situ thermal conductivity calibration and heat flow determination as an addition to the conventional steps in the thermal analysis of a basin, what about BHTs? To compare our modeled temperatures with BHT data where available, the log header BHT values were collected from the specific wells studied. Most of the logs lacked BHT series at fixed depths that could be extrapolated to equilibrium, and many logs lacked circulation time information or recorded temperatures did not change with time. All measurements were used, however, and the temperature difference between our predicted temperatures and each BHT point was calculated, with the results plotted as a function of depth in Figure 13.

BHT differences were available for 56 wells, of which 30 had more than three depths with BHT measurements. For the entire data set, the predicted temperatures average approximately 21°C higher than the measured BHT values. The cooling effect of drilling lowers the formation temperatures by tens of degrees. Also, in general, the error in BHT readings increases with the circulation time (Dowdle and Cobb, 1975), which, in turn, increases with depth. In the Anadarko basin, the mean difference between the predicted temperatures and BHT is approximately 25°C for wells with total depths in the range of 3658 to 9449 m (12,000 to 31,000 ft). On the shelf, the

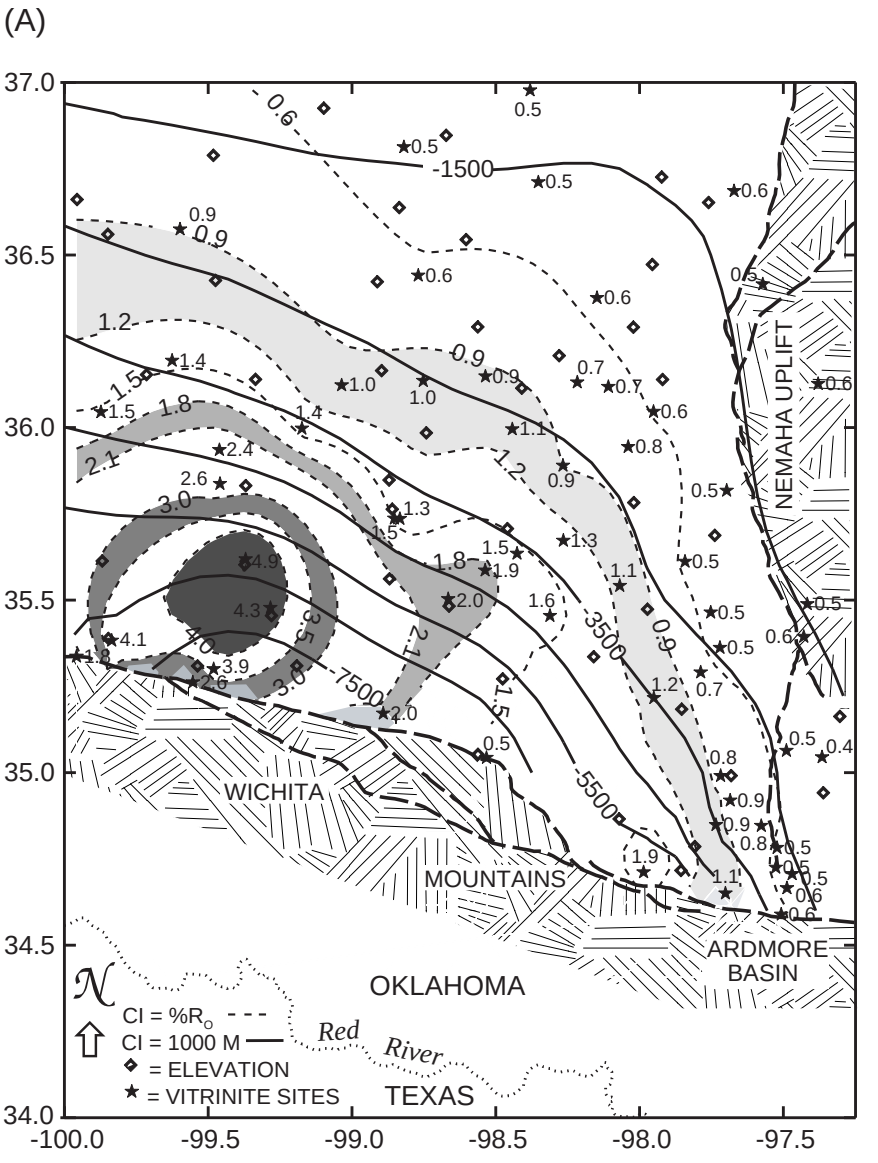

Figure 12—(A) Combined vitrinite isoreflectance and structure contours at the top of the Woodford Shale. Vitrinite reflectance contours in percent R_o (0.9, 1.8, etc.); contour interval is variable. Locations of vitrinite data points are shown with values from Cardott and Lambert (1985) and Cardott (1989). Vitrinite contours modified from Cardott (1989). Highest vitrinite values are offset from deepest occurrence of the Woodford Shale. (B) Combined vitrinite isoreflectance and predicted temperature map on the top of the Woodford Shale. Temperature control points, vitrinite control points, and temperature values are shown. Highest temperatures are offset from deepest occurrence of Woodford Shale and in same area as highest vitrinite reflectance values [compare to (A)].

average difference is approximately 18°C for wells with total depths ranging between 1829 and 4572 m (6000 and 15,000 ft). The difference between the basin and shelf averages may reflect the longer circulation times for the deeper wells or a greater error in the predicted temperature as depth increases.

Many methods have been suggested and used to correct BHT data, with the Horner plot being the most satisfactory technique employed (Dowdle and Cobb, 1975; Funnell et al., 1996); however, a Horner plot correction requires several BHT readings at the same depth taken at different known times after circulation has ceased, and so can be applied to only a small fraction of BHT measurements. Empirical corrections that can be applied to single BHT measurements (Harrison et al., 1983; Deming and Chapman, 1988; Lee et al., 1996) and averaging techniques (Deming et al., 1990; Willet, 1990) have been proposed for data unsuitable for Horner corrections.

To produce the geothermal gradient map of Oklahoma, Luza et al. (1984) used a BHT correction technique developed by Harrison et al. (1983). This empirical correction is shown as a heavy dashed line on Figure 13 and was established using "reliable" temperature-depth pairs obtained from bottom-hole pressure tests, temperature logs, and interpolations from "reliable" temperature measurements. The data cover the depth range from 600 to 4900 m (2000 to 15,000 ft) and indicate a maximum BHT correction of 18°C at a depth of approximately 3050 m (10,007 ft). Below 4000 m (12,000 ft), the reliability of the correction decreases due to an insufficient number

(B)

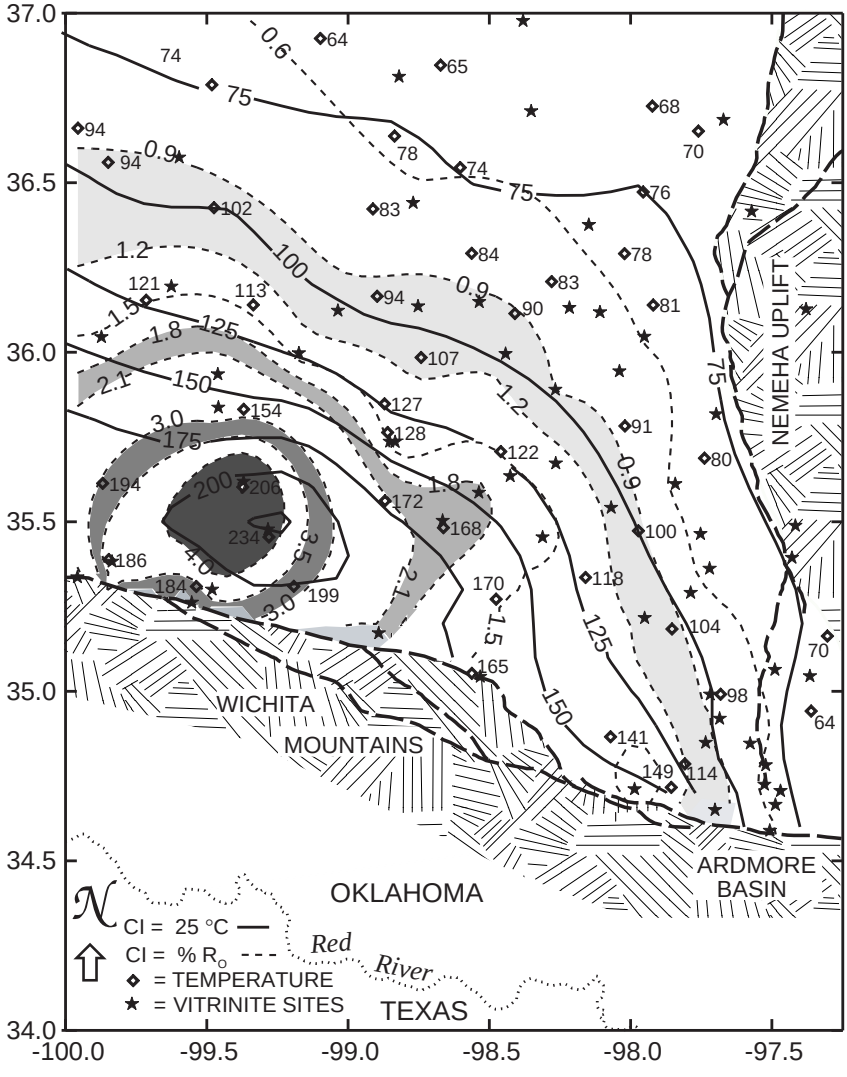

Figure 12—Continued.

of data points, with no data at all below 4900 m (15,000 ft).

Differences between the predicted temperatures and BHT values were averaged over 500-m (1640-ft) intervals (plotted as the diamonds on Figure 13) and compared with the Harrison et al. (1983) correction curve (the dashed line on Figure 13). The difference between the two curves is shown as the asterisks on Figure 13. Despite the typically wide scatter in the BHT data, the diamonds on Figure 13 show a statistically insignificant difference from the Oklahoma BHT correction curve developed by Harrison et al. (1983) except for the 2500–3000 m (8202–9843 ft) bin. A maximum difference of 4.4 ±1.3°C is found between 2500 and 3000 m (8202 and 9843 ft). The actual temperatures in the basin at 3000 m (9843 ft) are between 70 and 90°C (158 and 194°F), so 4.4°C is only 6–8% of the predicted 54–74°C increase. Between 3000 and 5000 m (8202 and 9843 ft) the average difference between our model and Harrison et al. (1983) is 8.1 ±3.5°C assuming a constant correction below 3000 m (9843 ft). At 5000 m (16,405 ft), actual temperatures range from 120 to 150°C (248 to 302°F), so again the difference between our model and the Harrison et al. (1983) correction curve is less than 5% of the predicted values. Thus, the methods appear statistically comparable above 5000 m (16,405 ft), the depth range where there is some control on the BHT correction.

Below 5000 m (16,405 ft) the average difference between BHT and our predicted values is 27.7 ±1.9°C [corresponding average depth of 6704 m (21,995 ft)] compared to 25.4 ±3.4°C between

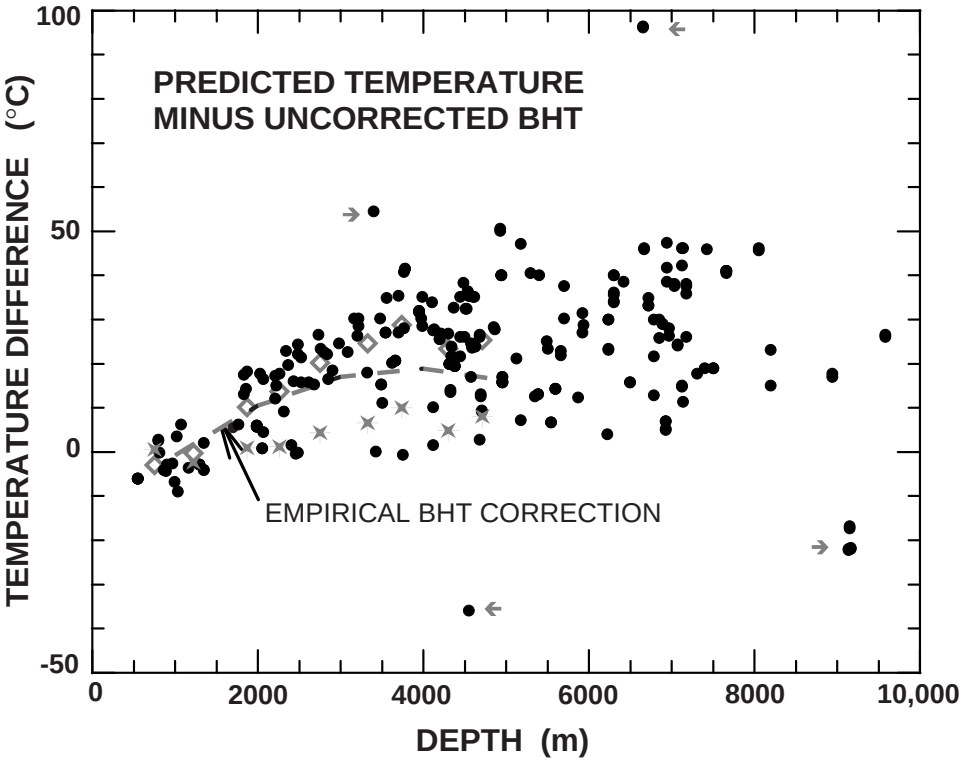

Figure 13—Plot of calculated minus observed BHT (bottom-hole temperature) for the wells studied. Empirical BHT correction curve from Harrison et al. (1983) is also plotted. Diamonds are 500-m average differences of predicted and observed BHTs. Stars are difference between the empirical correction curve and diamonds (see text). Points marked with short, thick (shaded) arrows were discarded in the analysis.

3000 and 5000 m (9843 and 16,405 ft) [average depth of 4707 m (15,443 ft)]. If the Harrison et al. (1983) empirical correction is assumed to stay the same, then the average difference in the two data sets would be about 10°C. Thus, statistically, and without a basis for estimating BHT corrections below 5000 m (16,405 ft), there is no evidence for a systematic difference between the two data sets.

CONCLUSIONS

In this study, the best value for basinwide shale conductivity (Table 2) was determined by the best match to the temperature-depth logs of the calibration wells. This procedure represents a generalization of the interval gradient method used in an individual well to evaluate the gradient in a difficult-to-sample lithology. Thus, we believe that the approach employed here of using temperature logs to calibrate in-situ thermal conductivities provides a significant improvement on the usual methods.

The range of shale and red bed conductivities illustrates the problems associated with determining the thermal properties of shales in situ. The variations in the mineralogy of fine-grained clastic rocks cause significant thermal conductivity differences, making predictions difficult. At the same time, it is difficult to impossible to obtain accurate laboratory data. Reliable data for shales are important because of the large contribution shale imparts to the thermal structure of a sedimentary basin due to its abundance. Clearly, more work is needed concerning characterization of the thermal properties of shales.

The result of the predicted temperature-BHT (bottom-hole temperature) comparison may be interpreted in a number of ways. For the depth interval 500–3500 m (1640–11,483 ft) there is no statistically significant difference between our model and Harrison et al.'s (1983), which may be interpreted to mean that the heat flow and thermal conductivity on which the predicted temperatures are based are correct. Inaccurate heat flow or thermal conductivity assumptions could result in significantly different temperature predictions or produce geographically systematic differences between the predictions and the BHT data. The BHT data were purposefully not used as a constraint on the temperature modeling in this study. The close correspondence of the Harrison et al. (1983) curve to the calculated differences between predicted temperatures and BHT suggests that there are no large biases in either data set. The estimates of error in the previous section probably are conservative in this case. Thus, the two data sets may appear to be redundant to some extent; however, one of the main points of

this paper is that using this approach as a supplement to a conventional BHT/cuttings study allows significant new information to be extracted, including an evaluation of the accuracy of the BHT/cuttings thermal model, an indication of the nature of heat transfer mechanisms in an area (nonconductive heat transfer leads to systematic differences in predicted and corrected BHT temperatures), and the accuracy of thermal conductivity estimates.

The approach proposed here can be used to test the predictions of a conductive thermal model against the observed BHT data in a manner that serves two purposes. The first purpose is to determine directly a limited number of "conventional" heat flow values in a basin, and the second purpose is to allow a test of the error or departure from conductive conditions in the basin as a whole using the BHT and cuttings information. The correspondence found here suggests that a deviation from the assumptions made in this study could be identified by systematic deviations of the predicted and observed equilibrium temperatures. To further constrain the results described here, additional detailed temperature logs, heat flow measurements, and higher quality BHT data are required.

No attempt has been made in this study to account for any fluid-flow effects in the Anadarko basin. We found no evidence for significant fluid flow in this basin (Jorgensen, 1989) at the present time. There might have been mass transfer from the basin during dewatering or hydrocarbon migration, but the agreement of the organic maturation indicators (Carter et al., 1998) with the thermal regime predicted here suggests that such events have had little significance on the regional thermal structure of the basin; furthermore, the temperature structure can be explained adequately by normal conductive heat flow when the thermal conductivity of the rocks is taken into account in the modeling. The presence of a geopressured zone does not appear to affect the temperature distribution in the basin. There is no evidence, in the form of systematic departures of observed and calculated temperatures, between areas with and without geopressured conditions.

The main factor limiting the use of "conventional" heat flow techniques in sedimentary basins has been the lack of detailed, precise temperature logs. The results of Carter et al. (1998) illustrated that useful temperature logs can be collected in the typical petroleum environment. Blackwell et al. (1998) described in more detail the types of wells that can be successfully logged for temperatures and discussed the technological advances that make equipment for temperature logging readily available in the commercial petroleum exploration and production setting.

Appendix 1. Data on Wells Studied*

Well No.	Well Name	County	Coordinates 1/4 Sec.	Sec.	T	R	Date	Top (m)	TD (m)	TD** Fm.	GL (m)	Lat.	Long.	API No.
1	Mid-America 1 Jones	Stephens	NENE	26	2	6	58	189	2749	>Deese	378	34°37.38′	97°47.60′	?
2	El Paso Natural Gas 1 Cramton	Grady	NWNESW	20	3	6	79	1006	7141	Simpson	383	34°43.01′	97°51.35′	3505120755
3	Midcontinent 1 Menefee	Garvin	SESESE	2	4	2	46	152	2222	Simpson	282	34°50.50′	97°22.26′	?
4	Pure B 1 Chapman	Grady	NWSWSW	26	4	6	?	579	5121	McLish	394	34°47.15′	97°48.46′	?
5	Harper-Turner 1 Ward	McClain	NWNWNE	1	5	2	?	158	2483	Brom Ss	353	34°56.50′	97°21.64′	?
6	Magnolia 1 Jacobs	McClain	NWSWNE	34	5	2	?	131	2268	Brom Ss	307	34°51.91′	97°23.78	?
7	Arco 1 Lucille	Grady	CNW/4	32	5	8	83	1250	7315	Arbuckle	390	34°51.95′	98°04.25′	3505121268
8	Shell 1 McDaniel	Caddo	NENWSW	6	5	11	54	152	1036	Springer?	396	34°56.05′	98°24.35′	?
9	Exxon 1 Apache Gas Unit	Caddo	NENESW	19	5	11	79	951	7532	Arbuckle	391	34°53.42′	98°24.09′	3501520698
10	Arkla 1-13 Mowdy	Grady	SWNESW	13	6	5	80	463	4374	Arbuckle	339	34°59.48′	97°40.88′	3505120990
11	Shell Oil 1-28 Ferris	Caddo	CSE	28	7	9	81	1067	5596	Springer	399	35°02.80′	98°09.01′	3501521199
12	Forest Oil 1 Tahpoodle	Caddo	CSENW	27	7	13	74	610	8199	Sylvan	433	35°03.17′	98°33.70′	3501520329
13	British American 1 State	Cleveland	NWSESE	16	8	1	?	213	2487	Oil Crk	350	35°09.78′	97°18.20′	?
14	Jordan 1 Hall	Grady	CSWNE	8	8	6	54	1067	4220	Brom Ss	382	35°11.03′	97°51.19′	?
15	Superior 51-11 Weller	Caddo	NWNWNE	11	8	12	48	43	5432	Miss Ches?	435	35°11.33′	98°25.94′	?
16	Frank Buttram 1 Smith	Washita	SESENW	34	8	16	52	76	3054	Atoka	466	35°07.50′	98°52.38′	?
17	Hassie Hunt Trust 1-A McAnally	Caddo	NWSENW	9	9	12	71	3048	6788	Brom Ss	458	35°16.31′	98°28.56′	3501520094
18	Deep Rock 1 Scott	Washita	CSENE	22	9	14	51	152	3664	Des Moines	485	35°14.53′	98°39.65′	?
19	GHK 1-10 Gars	Washita	CSW/4	10	9	16	81	1676	6965	>Springer	451	35°21.18′	98°53.00′	3503920366
20	Stanolind 1 State	Washita	NENESW	36	9	17	50	59	4116	Springer	473	35°12.63′	98°57.03′	?
21	Slick 1 Sudik	Cleveland	CNENE	8	10	2	30	610	2353	Wilcox	372	35°21.67′	97°25.53′	?
22	Denver Prod. & Refn. A 1 Schoolland	Caddo	CSESW	16	10	9	48	183	5210	Arbuckle	468	35°20.15′	98°09.55′	?
23	Lone Star Gas 1Bertha Rogers	Washita	CSE	27	10	19	73	1433	9583	Arbuckle	577	35°18.58′	99°11.51′	3514920020
24	Lone Star Gas 1-28 Baden	Beckham	SWNWSW	28	10	22	72	1576	9159	Viola	595	35°18.55′	99°32.20′	3500920102
25	Pure Oil 1 Taute	Beckham	CNWSE	34	10	25	49	72	2420	PC	590	35°17.84′	99°49.80′	?
26	Cities Service 1 Petree Ranch	Canadian	CSESE	18	11	8	49	137	3407	Chester	399	35°25.35′	98°04.83′	?
27	GHK 1-2 Harrell	Washita	CSE	2	11	20	81	1219	8016	Hunton	557	35°27.29′	99°16.80′	3514920098
28	GHK 1-34 Duncan	Beckham	NWNESE	34	11	21	82	1707	8921	Chester	595	35°23.09′	99°24.75′	3500920391
29	Union Oil 1-33 Annie Bruner	Beckham	NESWNE	33	11	25	70	30	7482	Hunton	627	35°23.33′	99°50.80′	3500920093
30	King Resources 1-32 Huchtemann	Canadian	SWNW	32	12	7	69	1524	3764	Arbuckle	422	35°28.41′	97°58.33′	?
31	GHK 1-27 Hayes	Custer	CSE/4	27	12	14	72	2155	5934	Viola	543	35°28.95′	98°39.75′	3503920055
32	V. A. Brill (Parker) 1 Newcomb	Custer	CNWNW	10	12	16	51	244	4221	Morrow	509	35°32.15′	98°53.13′	?
33	Roden Oil 35-1 Nickel	Custer	SWSWNE	35	13	16	70	1585	6419	Arbuckle	513	35°33.69′	98°52.15′	3503920045

Appendix 1. Continued.

Well No.	Well Name	County	Coordinates 1/4 Sec.	Sec.	T	R	Date	Top (m)	TD (m)	TD** Fm.	GL (m)	Lat.	Long.	API No.
34	GHK 1-18 Dugger	Custer	CW/2	18	13	20	80	1262	7175	Viola	564	35°36.16′	99°22.33′	3503920366
35	El Paso Natural Gas 1 Pierce	Roger Mills	CSW	9	13	25	74	1536	7148	Viola	724	35°36.80′	99°52.09′	3512920141
36	Jones, Shelburne et al. 1 Simpson	Canadian	CNESW	16	14	5	56	457	2530	Wilcox	363	35°41.25′	97°44.30′	?
37	Sante Fe Minerals 10-1 Pierce	Blaine	CNE	10	14	12	84	1524	4197	Sylvan	526	35°42.43′	98°27.55′	3501121984
38	Carter 1 Hartley	Roger Mills	NENENW	34	14	26	53	152	5352	Morrow	739	35°39.15′	99°57.20′	?
39	Camco Oil Trust 1 F. Parrington	Kingfisher	NWNWNE	14	15	8	53	1204	3089	Simpson	338	35°46.96′	98°01.20′	?
40	Magnolia 1 Jones	Custer	CSWNW	24	15	16	55	274	4578	Hunton	543	35°45.81′	98°51.60′	?
41	Texas Oil & Gas C 1 Christenson	Dewey	NWNWSE	23	16	16	76	1219	4609	Simpson	589	35°50.87′	98°52.25′	3504320723
42	Samedan 1 Walton	Dewey	NESW	30	16	20	73	2286	5547	Sylvan	603	35°49.91′	99°22.15′	3504320383
43	Oklahoma Nat. Gas 1 Green (Oakwood Unit)	Dewey	NWNWNW	6	17	14	46	920	3844	Simp Sd	579	35°59.07′	98°44.49′	?
44	Union Oil 1 Brown	Kingfisher	SWSENW	11	19	7	?	158	2481	Brom Den	341	36°08.36′	97°55.18′	?
45	Stanolind 1 Wildman	Blaine	NWNENE	19	19	11	48	799	3053	Simp Sd	390	36°06.86′	98°24.55′	?
46	Magnolia 1 Winter	Dewey	CSWNE	9	19	20	47	94	4210	Wilcox	682	36°08.37′	99°20.13′	?
47	Barnsdale (Sunray) 1 Hanan	Ellis	CSENW	1	19	24	50	137	4586	Simpson	782	36°09.21′	99°42.85′	?
48	White Eagle 1 Westfahl	Major	CNWSW	16	20	10	57	771	2713	Simpson	355	36°12.50′	98°16.77′	?
49	Continental 1 Kimball	Major	NWNWSW	34	20	16	52	296	3610	Arbuckle	512	36°09.91′	98°53.82′	?
50	Midcontinent 1 Lowenhaupt	Garfield	CSWSE	14	21	8	51	610	2429	Simpson	368	36°17.46′	98°01.28′	?
51	Gulf 1 Wichert	Major	CSESW	14	21	13	60	914	2907	Arbuckle	418	36°17.49′	98°33.73′	?
52	Benson-Montin 1 Schultz	Garfield	CSENW	16	23	7	57	366	2210	Wilcox	406	36°28.35′	97°57.31′	?
53	Sinclair 1 Spafford	Major	NESESW	33	23	16	59	792	2865	Arbuckle	458	36°25.36′	98°54.71′	?
54	Phillips A 1 Marshall	Woodward	NWNESW	32	23	21	74	1280	3493	Arbuckle	638	36°25.58′	99°28.47′	?
55	Amerada 1 Farris 1	Woods	CSWNW	21	24	13	55	823	2478	Arbuckle	429	36°32.68′	98°36.18′	?
56	Sinclair 1 D. L. Berry	Ellis	CSENW	14	24	25	50	198	3431	Arbuckle	710	35°33.60′	99°50.93′	?
57	Perkins Bros. 1 Fulmer	Grant	SESESW	8	25	5	57	579	1830	Simpson	314	36°39.12′	97°45.6′	?
58	Texas 1 McAntire	Woods	NWNWNE	20	25	15	56	823	2373	Arbuckle	473	36°38.25′	98°50.11′	?
59	Sunray Mid-Cont. 1 Klinger	Harper	CSENW	12	25	26	58	1219	3210	Arbuckle	698	36°39.65′	99°57.36′	?
60	Gungoll Exploration 2-14 LeForce Farms	Grant	CSESW	14	26	7	87	152	1859	Simp Sd	326	36°43.55′	97°55.38′	?
61	Beach & Talbot 1 Thornberry	Woods	CNWSE	21	27	14	52	588	2063	Arbuckle	441	36°48.19′	98°42.53′	?
62	Statex Pet. 1 Bennett	Harper	CNWSE	29	27	21	60	710	2228	Viola	528	36°47.32′	99°28.91′	?
63	Gulf 1 Zimmerman	Woods	SENWNW	12	28	18	54	762	2033	Arbuckle	597	36°55.52′	99°05.86′	?

*Well number corresponds to location on map shown in Figure 4. Top = top of the logged interval, TD = total depth, TD Fm. = formation or age of formation at depth, GL = ground level, BromSs = Bromide Sandstone, Oil Crk = Oil Creek, Miss Che? = Mississippi Chester? PC = Precambrian, Simp Sd = Simpson Sand.

**A > in front of the formation name means the well was deeper than this formation.

REFERENCES CITED

AAPG, 1976, Geothermal gradient map of North America: AAPG, scale 1:5,000,000, 2 sheets.

Adkinson, W. L., 1960, Subsurface cross section of Paleozoic rocks from Barber County, Kansas, to Caddo County, Oklahoma: U.S. Geological Survey Oil and Gas Investigation Chart OC-61. Scale: horizontal 1:380,160, vertical 1:2400.

Adkinson, W. L., and M. G. Sheldon, 1963, Sample descriptions and correlations for wells on a cross section from Barber County, Kansas, to Caddo County, Oklahoma: Oklahoma Geological Survey Guidebook 13, 139 p.

Adler, F. J., 1971, Anadarko basin and central Oklahoma area, *in* I. H. Cram, ed., Future petroleum provinces of the United States—their geology and potential: AAPG Memoir 15, v. 2, p. 1061–1070.

Bates, R. L., and J. A. Jackson, eds., 1984, Dictionary of geological terms: New York, American Geological Institute, 571 p.

Blackwell, D. D., and R. E. Spafford, 1987, Experimental methods in continental heat flow, *in* C. G. Sammis and T. L. Henyey, eds., Geophysics: field measurements, methods in experimental physics, geophysics: Orlando, Florida, Academic Press, v. 24, part B, p. 189–226.

Blackwell, D. D., and J. L. Steele, 1989a, Heat flow and geothermal potential of Kansas, *in* D. W. Steeples, ed., Geophysics in Kansas: Kansas Geological Survey Bulletin 226, p. 267–295.

Blackwell, D. D., and J. L. Steele, 1989b, Thermal conductivity of sedimentary rocks: measurement and significance, *in* N. D. Naeser and T. H. McCulloh, eds., Thermal history of sedimentary basins—methods and case histories: New York, Springer-Verlag, p. 13–36.

Blackwell, D. D., G. R. Beardsmore, R. K. Nishimari, and R. J. McMullen, Jr., 1998, High resolution temperature logs in a petroleum setting: examples and applications, *in* A. Forster and D. F. Merriam, eds., Geothermics in basin analysis: New York, Plenum Press, p. 1–34.

Bodner, D. P., and J. M. Sharp, Jr., 1988, Temperature variations in south Texas subsurface: AAPG Bulletin, v. 72, p. 21–32.

Brewer, J. A., R. Good, J. E. Oliver, L. D. Brown, and S. Kaufman, 1983, COCORP profiling across southern Oklahoma aulacogen: overthrusting of the Wichita mountains and compression within the Anadarko basin: Geology, v. 11, p. 109–114.

Brigaud, F., G. Vasseur, and G. Caillet, 1992, Thermal state in the north Viking graben (North Sea) determined from oil exploration well data: Geophysics, v. 57, p. 69–88.

Burgess, W. J., 1976, Geological evolution of the mid-continent and Gulf Coast areas—a plate tectonics view: Transactions, Gulf Coast Association of Geological Societies, v. 26, p. 132–143.

Burke, K., and J. F. Dewey, 1973, Plume generated triple junctions: key indicators in applying plate tectonics to old rocks: Journal of Geology, v. 81, p. 406–433.

Cardott, B. J., 1989, Thermal maturation of the Woodford Shale in the Anadarko basin, *in* K. S. Johnson, ed., Anadarko basin symposium, 1988: Oklahoma Geological Survey Circular 90, p. 32–46.

Cardott, B. J., and M. W. Lambert, 1985, Thermal maturation by vitrinite reflectance of Woodford Shale, Anadarko basin, Oklahoma: AAPG Bulletin, v. 69, p. 1982–1998.

Carter, L. S., S. A. Kelley, D. D. Blackwell, and N. Naeser, 1998, Heat flow and thermal history in the Anadarko basin, Oklahoma: AAPG Bulletin, v. 82, p. 291–316.

Carvalho, H. da S., and V. Vacquier, 1977, Method for determining terrestrial heat flow in oil fields: Geophysics, v. 42, p. 584–593.

Carvalho, H. da S., S. Purwoko, M. Thamrin, and V. Vacquier, 1980, Terrestrial heat flow in the Tertiary basin of central Sumatra: Tectonophysics, v. 69, p. 163–188.

Chapman, D. S., T. H. Keho, M. S. Bauer, and M. D. Picard, 1984, Heat flow in the Uinta basin determined from bottom hole temperature (BHT) data: Geophysics, v. 49, p. 453–466.

Chaturvedi, L., and J. K. Lory, 1980, A preliminary evaluation of geothermal potential of San Juan basin, New Mexico, using bottom hole temperatures from oil and gas wells: Geothermal Resources Council Transactions, v. 4, p. 21–24.

Deming, D., 1994, Estimation of the thermal conductivity anisotropy of rock with application to the determination of terrestrial heat flow: Journal of Geophysical Research, v. 99, p. 22,087–22,091.

Deming, D., and D. S. Chapman, 1988, Inversion of bottom-hole temperature data: the Pineview field, Utah-Wyoming thrust belt: Geophysics, v. 53, p. 707–720.

Deming, D., J. S. Hanor, and J. A. Nunn, 1990, Method of variable bias and its application to estimating subsurface temperature: Geophysical Research Letters, v. 17, p. 1949–1952.

Demongodin, L., B. Pinoteau, G. Vasseur, and R. Gable, 1991, Thermal conductivity and well logs: a case study in the Paris basin: Geophysical Journal International, v. 105, p. 675–691.

Denison, R. E., 1976, Evolution of the Anadarko basin (abs.): AAPG Bulletin, v. 60, p. 325.

Denison, R. E., 1982, Geologic cross section from the Arbuckle mountains to the Muenster arch, southern Oklahoma and Texas: Geological Society of America Map and Chart Series MC 28-R, 8 p.

Dott, R. H., and R. L. Batten, 1981, Evolution of the Earth: New York, McGraw-Hill, 573 p.

Dowdle, W. L., and W. M. Cobb, 1975, Static formation temperature from well logs—an empirical method: Journal of Petroleum Technology, v. 27, p. 1326–1330.

Evans, J. L., 1979, Major structural and stratigraphic features of the Anadarko basin, *in* N. J. Hyne, ed., Pennsylvanian sandstones of the mid-continent: Tulsa Geological Society Special Publication 1, p. 97–113.

Feinstein, S., 1981, Subsidence and thermal history of southern Oklahoma aulacogen: implications for petroleum exploration: AAPG Bulletin, v. 65, p. 2521–2533.

Friedman, G. M., and J. E. Sanders, 1978, Principles of sedimentology: New York, John Wiley, 792 p.

Funnell, R., D. Chapman, R. Allis, and P. Armstrong, 1996, Thermal state of the Taranaki basin, New Zealand: Journal of Geophysical Research, v. 101, p. 25,197–25,215.

Gallardo, J. D., 1989, Empirical model of temperature structure, Anadarko basin, Oklahoma: Master's thesis, Southern Methodist University, Dallas, Texas, 186 p.

Garner, D. L., and D. L. Turcotte, 1984, The thermal and mechanical evolution of the Anadarko basin: Tectonophysics, v. 107, p. 1–24.

Gilbert, M. C., 1983, Timing and chemistry of igneous events associated with the southern Oklahoma aulacogen: Tectonophysics, v. 94, p. 439–455.

Gosnold, W. D., 1984, Geothermal resources in the Williston basin, North Dakota: Geothermal Resources Council Transactions, v. 8, p. 431–436.

Ham, W. E., 1969, Regional geology of the Arbuckle mountains, Oklahoma: Oklahoma Geological Survey Guidebook 17, 52 p.

Ham, W. E., and L. Jordan, 1961, A Permian stratigraphic section in west-central Oklahoma: Oklahoma Geology Notes, v. 21, p. 4–9.

Ham, W. E., R. E. Denison, and C. H. Merritt, 1964, Basement rocks and structural evolution of southern Oklahoma: Oklahoma Geological Survey Bulletin 95, 302 p.

Harrison, W. E., K. V. Luza, M. L. Prater, and P. K. Cheung, 1983, Geothermal resource assessment in Oklahoma: Oklahoma Geological Survey Special Publication 83-1, 42 p.

Hoffman, P. F., J. F. Dewey, and K. Burke, 1974, Aulacogens and their genetic relation to geosynclines, with a Proterozoic example from Great Slave Lake, N.W.T., *in* R. H. Dott, Jr., and R. H. Shaver, eds., Modern and ancient geosynclinal sedimentation: SEPM Special Publication 19, p. 38–55.

Horai, K., 1971, Thermal conductivity of rock-forming minerals: Journal of Geophysical Research, v. 76, p. 1278–1308.

Hsueh, F., 1991, Application of ray trace modeling to a large scale seismic experiment in Oklahoma: Master's thesis, University of Texas at El Paso, El Paso, Texas, 94 p.

Johnson, K. S., 1976, Evaluation of Permian salt deposits in the Texas panhandle and western Oklahoma for underground storage of radioactive wastes: Oak Ridge National Laboratory, report no. Y/OWI/SUB-4494/1, 75 p.

Johnson, K. S., 1989, Geologic evolution of the Anadarko basin, *in* K. S. Johnson, ed., Anadarko basin symposium, 1988: Oklahoma Geological Survey Circular 90, p. 3–12.

Johnson, K. S., and B. J. Cardott, 1992, Geologic framework and hydrocarbon source rocks of Oklahoma, *in* K. S. Johnson and B. J. Cardott, eds., Source rocks in the southern mid-continent, 1990 symposium: Oklahoma Geological Survey Circular 93, p. 21–37.

Johnson, K. S., T. W. Amsden, R. E. Denison, S. P. Dutton, A. G. Goldstein, B. Rascoe, Jr., P. K. Sutherland, and D. M. Thompson, 1988, Southern midcontinent region, *in* L. L. Sloss, ed., Sedimentary cover—North American craton; U.S.: Boulder, Geological Society of America, The Geology of North America, v. D-2, p. 307–359.

Jordan, L., and D. L. Vosburg, 1963, Permian salt and associated evaporites in the Anadarko basin of the western Oklahoma-Texas panhandle region: Oklahoma Geological Survey Bulletin 102, 76 p.

Jorgensen, D. G., 1989, Paleohydrology of the Anadarko basin, central United States, *in* K. S. Johnson, ed., Anadarko basin symposium, 1988: Oklahoma Geological Survey Circular 90, p. 176–193.

Lam, H. L., F. W. Jones, and C. Lambert, 1982, Geothermal gradients in the Hinton area of west-central Alberta: Canadian Journal of Earth Science, v. 19, p. 755–766.

Lee, Y., D. Deming, and K. F. Chen, 1996, Heat flow and heat production in the Arkoma basin and Oklahoma platform, southeastern Oklahoma: Journal of Geophysical Research, v. 101, p. 25,387–25,401.

Luza, K. V., W. E. Harrison, G. A. Laguros, M. L. Prater, and P. K. Cheung, 1984, Geothermal resources and temperature gradients of Oklahoma: Oklahoma Geological Survey Map GM-27, scale 1:500,000.

Maxwell, J. C., 1964, Influence of depth, temperature, and geologic age on porosity of quartzose sandstone: AAPG Bulletin, v. 48, p. 697–709.

McNeal, R. P., 1953, Subsurface geology of south-central Anadarko basin, Oklahoma: AAPG Bulletin, v. 37, p. 2677–2704.

National Oceanic and Atmospheric Administration, 1980, Climates of the states: National Oceanic and Atmospheric Administration, v. 2, 1175 p.

Pate, J. D., 1959, Stratigraphic traps along north shelf of Anadarko basin, Oklahoma: AAPG Bulletin, v. 43, p. 39–59.

Robertson, E. C., 1988, Thermal properties of rocks: U.S. Geological Survey Open-File Report 88-441, 106 p.

Rowland, T. L., 1974, Lone Star 1 Rogers unit captures world depth record: Oklahoma Geology Notes, v. 34, p. 185–189.

Roy, R. F., D. D. Blackwell, and E. R. Decker, 1972, Continental heat flow, *in* E. C. Robertson, ed., The nature of the solid earth: McGraw-Hill, p. 506–543.

Roy, R. F., A. E. Beck, and Y. S. Touloukian, 1981, Thermophysical properties of rocks, *in* Y. S. Touloukian and C. Y. Ho, eds., Physical properties of rocks and minerals: New York, McGraw-Hill/CINDAS Data Series on Material Properties,v. II-2, p. 409–426.

Samuels, G., 1979, Geopressure energy resource evaluation: Oak Ridge National Laboratory, report no. ORNL/PPA-79/2, 72 p.

Sass, J. H., A. H. Lachenbruch, and R. J. Munroe, 1971, Thermal conductivity of rocks from measurements on fragments and its application to heat flow determinations: Journal of Geophysical Research, v. 76, p. 3391–3401.

Sclater, J. G., and P. A. F. Christie, 1980, Continental stretching: an explanation of the post-mid-Cretaceous subsidence of the central North Sea basin: Journal of Geophysical Research, v. 85, p. 3711–3739.

SEG, 1982, Gravity anomaly map of the United States: Tulsa, Society of Exploration Geophysicists, scale 1:2,500,000, 2 sheets.

Speece, M. A., T. D. Bowen, J. L. Folcik, and H. N. Pollack, 1985, Analysis of temperatures in sedimentary basins: the Michigan basin: Geophysics, v. 50, p. 1318–1334.

Waples, D. W., 1980, Time and temperature in petroleum formation: application of Lopatin's method to petroleum exploration: AAPG Bulletin, v. 64, p. 916–926.

Willet, S. D., 1990, Stochastic inversion of thermal data in a sedimentary basin: resolving spatial variability: Geophysical Journal International, v. 103, p. 321–339.

Zhu, X., and G. A. McMechan, 1989, 2-D tomographic imaging of velocities in the Wichita uplift-Anadarko basin of southwestern Oklahoma: Bulletin of the Seismological Society of America, v. 79, p. 873–887.

ABOUT THE AUTHORS

Jaquidon D. Gallardo



Jaquidon D. Gallardo received a B.S. degree in geology from Wichita State University and an M.S. degree in geology from Southern Methodist University. She spent several years as a cartographer and imagery analyst for the Defense Mapping Agency (now the National Imagery and Mapping Agency). She is currently employed by Raytheon Systems Company as a systems engineer. Jaquidon is a member of AAPG, the Dallas Geological Society, and the American Society for Photogrammetry and Remote Sensing.

David D. Blackwell

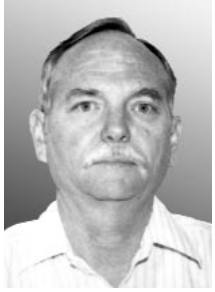

David D. Blackwell received a B.S. degree in geology and mathematics from Southern Methodist University (SMU) (1963) and a Ph.D. in geophysics from Harvard University in 1967. After a year of postgraduate work at Caltech, he joined the faculty at SMU where he is now W. B. Hamilton Professor of Geophysics. He is a member of AAPG, Society of Exploration Geophysicists, American Geophysical Union, Geological Society of America, and the Geothermal Resources Council, of which he is a past-president. His research focuses on the thermal field of the lithosphere and the factors that influence it.

Zagorski, William A., Martin Emery, and Jeffrey L. Ventura, 2017, The Marcellus Shale Play: Its Discovery and Emergence as a Major Global Hydrocarbon Accumulation, *in* R. K. Merrill and C. A. Sternbach, eds., Giant fields of the decade 2000–2010: AAPG Memoir 113, p. 55–90.

5

The Marcellus Shale Play: Its Discovery and Emergence as a Major Global Hydrocarbon Accumulation

William A. Zagorski

Range Resources Corporation, 3000 Town Center Boulevard, Canonsburg, Pennsylvania 15317, U.S.A. (e-mail: bzagorski@rangeresources.com)

Martin Emery

Chisholm Energy Holdings, LLC., 801 Cherry Street, Suite 1222, Unit 20, Fort Worth, Texas 76102, U.S.A. (e-mail: memery@chisholmenergy.com)

Jeffrey L. Ventura

Range Resources Corporation, 100 Throckmorton Street, Suite 1222, Fort Worth, Texas 76102, U.S.A. (e-mail: jventura@rangeresources.com)

ABSTRACT

The Middle Devonian Marcellus shale play has emerged as a major world-class hydrocarbon accumulation. It has rapidly evolved into a major shale gas target in North America and represents one of the largest and most prolific shale plays in the world with a prospective area of approximately 114,000 km^2 (44,000 mi^2). Two major core areas have emerged, each with a unique combination of controlling geologic factors. Production from the Marcellus play reached 16 billion cubic feet of gas equivalent per day (BCFepd) in 2015, and it has been recognized as the largest producing gas field in the United States since 2012.

The organic-rich black shales comprising the Marcellus shale were deposited in a foreland basin that roughly parallels the present-day Allegheny structural front. The Marcellus shale accumulated within an environment favorable to the production, deposition, and preservation of organic-rich sediments. The key geologic and technical factors that regionally define the Marcellus play core areas include organic richness, thermal maturity, degree of overpressure, pay thickness, porosity, permeability, gas in place, degree of natural fracturing, mineralogy, depth, structural style, lateral target selection, completion design, and important rock mechanics issues such as the ability to be fractured, rock brittleness versus ductility, and the ability to generate complex fractures. Structural setting and deformation styles are critical to address natural fracture trends, potential geologic hazards such as faulting and fracturing in structurally complex areas, and fracture stimulation containment issues.

Copyright ©2017 by The American Association of Petroleum Geologists.
DOI:10.1306/13572001M1133491

Since the Marcellus shale unconventional shale gas reservoir discovery in 2004 until May 2015, more than 8600 horizontal Marcellus shale wells had been drilled in Pennsylvania, West Virginia, and limited portions of eastern Ohio. Many decades of future drilling potential remain due to the enormous extent of the Marcellus shale play. Horizontal Marcellus wells report initial production rates ranging from less than 1 MMCFe/day to over 47.6 MMCFe /day. Despite the large number of wells drilled and completed to date and production of 16 BCFepd in 2015, the play is still in its infancy due to its vast geographic extent and production potential.

The Marcellus shale represents a continuous-type gas accumulation and when fully developed will comprise a large continuous field or series of fields. Over its productive trend, the Marcellus shale play has significant additional reserve potential in the overlying organic shales in the Devonian Age Rhinestreet, Geneseo, and Burket units as well as deeper potential in the Ordovician Age Utica/Point Pleasant units. Estimates of recoverable reserves from the world's largest gas fields combine their reserve estimates for all key productive units in the field/play trend. Likewise, estimates of in-place gas resources for the Marcellus play range from 2322 tcf for the Marcellus (Hamilton Group) to over 3698 tcf for the combined Devonian Age Marcellus-Geneseo-Rhinestreet system. This represents the largest technically accessible in-place gas resources in the world.

INTRODUCTION

The Middle Devonian Marcellus shale in the Appalachian basin of the northeastern United States represents the premier unconventional natural gas resource of North America. The organic-rich sediments that comprise the Marcellus shale were deposited in a foreland basin setting. The Marcellus shale formation is positioned in the lower portion of the Hamilton group (Middle Devonian), which is bounded above by the Tully Limestone and below by the Onondaga Limestone. Immediately above the Marcellus and Tully intervals are the organic-rich and productive Rhinestreet, Geneseo, and Burkett shales, which are an important, yet largely untapped, part of the Marcellus play.

The Appalachian basin has been an important shale gas producing province since the early 1800s. Since 2004, the organic-rich Marcellus shale, a major source rock, became a major successful hydrocarbon reservoir target for drilling. The modern era of Marcellus shale production began in October 2004 when the Range Resources Renz Unit No. 1 well in Mount Pleasant Township of Washington County, Pennsylvania, was completed using a large Barnett shale–style slick-water fracture stimulation treatment. The play was successfully tested horizontally in 2007, resulting in the establishment of production rates that encouraged industry and generated public interest in the Marcellus shale. The play has attracted the attention of independents, major oil companies, and international partners as discoveries continue to expand the scope of the play and highlight the formation's reservoir characteristics and long-term economic potential. As of May 2015, more than 70 companies had acquired lease positions and drilled over 8616 horizontal wells across a broad play area encompassing a prospective region of over 114,000 km^2 (44,000 mi^2) across Pennsylvania, West Virginia, New York, Maryland, and Ohio. Production from the Marcellus reached 16 BCFe/day in 2015 and is expected to exceed 20 BCFe/day by 2020.

Prospective limits of the Marcellus shale play are defined to the north, south, and east by the outcrop belt of the unit and to the west by insufficient thermal maturity combined with thinning of the Marcellus shale. Key geologic parameters controlling the productive capability of the Marcellus shale include thickness, total organic content, porosity, permeability, thermal maturity, degree of overpressure, depth, gas show characteristics, and rock mechanics. The wide area of prospective acreage, favorable geologic setting, and excellent production performance confirm the Marcellus shale play's enormous reserve potential.

There are enormous volumes of gas present within the Appalachian Basin Marcellus shale play. We estimate total in-place gas resources of 2322 tcf for the Marcellus and 3698 tcf for the combined upper Devonian shale and Marcellus system. Not yet calculated are the potential reserves underlying the Marcellus play in the deeper Ordovician Point Pleasant-Utica gas petroleum system. When compared to the gas-in-place (GIP) estimates for the top 15 gas fields in the world, the Marcellus gas play has nearly double the gas in place of the North Pars field.

In 2013, the Marcellus shale became the largest producing gas field in the United States. Production reached approximately 16 BCFe/day in 2015 and is

expected to reach over 20 BCFe/day by 2020. Recoverable reserve estimates for the Marcellus shale range from 87 tcf and 3.5 billion bbl of natural gas liquids (Milici, 2005) to as high as 867 tcf (Engelder, 2009). Most recent estimates of the Marcellus generally fall within the range of 160 to 489 tcf (Engelder, 2009).

PETROLEUM DEVELOPMENT HISTORY OF THE APPALACHIAN BASIN: PRE–MARCELLUS SHALE ERA

The Appalachian basin represents an historically significant producing province recognized as the birthplace of the modern U.S. petroleum industry (Figure 1). In 1859, the Drake well discovery in Titusville, Pennsylvania, initiated a robust petroleum industry that grew to worldwide prominence. The Drake discovery and subsequent activity initially focused on the development of oil reservoirs from shallow upper Devonian sandstone reservoirs that were deposited along a broad arcuate trend extending from western New York through large portions of Pennsylvania and West Virginia. Shallow oil and gas was developed from various Mississippian-age targets in eastern Ohio, western West Virginia, and Kentucky. Shallow oil and gas exploration continued until the early 1900s, when secondary recovery projects and methods became increasingly important. Significant exploration for natural gas was initiated in Pennsylvania and western West Virginia in the late 1800s, yielding significant natural discoveries that were critical starting points for our modern natural gas industry.

The giant Lima Indiana oil field was discovered in the Trenton Limestone in northwestern Ohio in 1884 and quickly expanded into adjacent Indiana and Illinois. Production from the Lima Indiana field is estimated at over 485 million barrels of oil and over 1 tcf associated gas. Another giant gas field, the Big

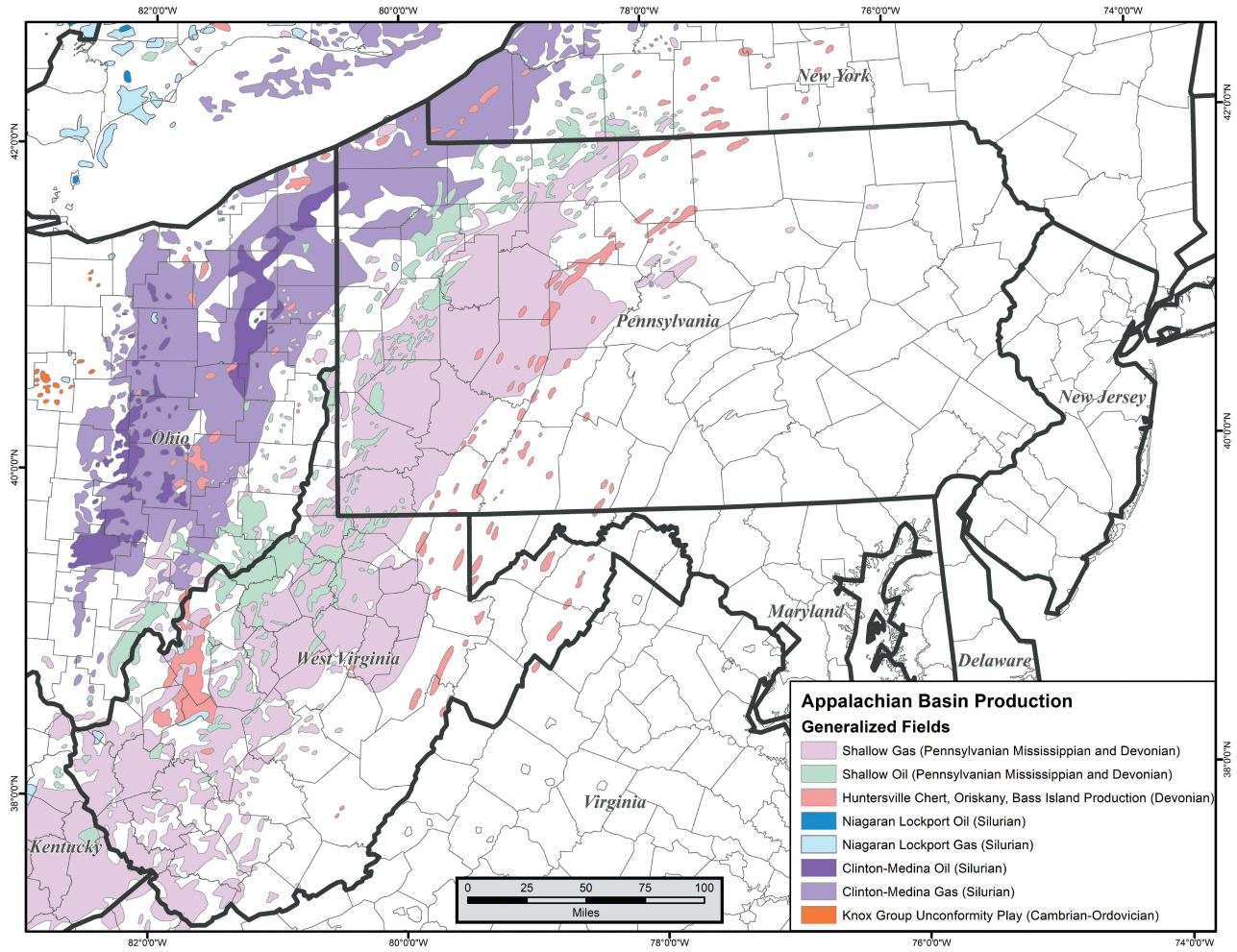

Figure 1. Appalachian basin conventional targets, circa 1990.

Sandy field, was discovered in Kentucky in 1921 and quickly expanded into West Virginia and Virginia. The Big Sandy field was one of the first significant commercial giant accumulations from upper Devonian source rocks. Production from the Big Sandy field is expected to exceed 3 tcf. From 1930 to 1980, industry focused on exploration for the lower Devonian–age Huntersville chert and Oriskany sandstone along several broad northeast to southwest trending anticlines that extend from New York southward into Pennsylvania and West Virginia. This phase of exploration yielded several major fields and many other smaller pools as well as some of the basin's most prolific individual gas wells. Most of the larger of these fields were later converted to active gas storage fields. Primary production from the lower Devonian–age Huntersville chert and Oriskany sandstone fields is estimated at over 1.4 tcf (Flaherty, 1992; Harper, 1992).

A major lower Silurian–age stratigraphic target, the Clinton Medina sandstone, was discovered in Ohio in 1887 and expanded from eastern Ohio into northwestern Pennsylvania and western New York from the 1940s well into the late 1990s. Significant Cambrian Ordovician production associated with the Knox unconformity production was established in the late 1960s in Ohio (Morrow County) and continues today. Prior to 2004 and the emergence of the Marcellus play, the last big conventional industry play in the Appalachian basin was a major resurgence of interest in the Ordovician Trenton Black River interval when several major gas discoveries were developed in central New York and to a lesser degree central West Virginia and Ohio.

Prior to the discovery and commercialization of the Marcellus, the estimated total cumulative and recoverable production from the Appalachian basin's key petroleum systems as defined by the USGS (Ryder et al., 2011) was 69.8 tcf and 3.5 bbl of oil. This study did not account for the full potential of the Marcellus shale or the deeper unconventional play in the Ordovician–age Utica Point Pleasant formations. These estimates are important benchmarks to compare the size and scope of historic conventional plays in the Appalachian basin to the potential now being developed from Marcellus shale.

HISTORY OF APPALACHIAN BASIN UNCONVENTIONAL SHALE DEVELOPMENT

The Appalachian basin has a unique history related to unconventional gas development (Figure 2). Shale gas development in the Appalachian basin began in the early 1800s. The discovery and commercial use of natural gas from upper Devonian shales was first reported in 1825 in Fredonia, New York, which is widely recognized as the birthplace of the natural gas industry (Lash, 2014). This discovery and expansion of operations significantly predates the early North American oil discoveries in Ontario in 1858 and the Drake oil discovery in Titusville, Pennsylvania, in 1859. By 1860, there were several shallow shale gas fields established over a broad fairway along the Lake Erie shoreline extending from Fredonia, New York, southwest to Sandusky, Ohio (Harper, 2008). These fields produced from organic-rich black shale formations, including the upper Devonian Dunkirk, Rhinestreet, and Middlesex formations and, to a lesser extent, the middle Devonian Marcellus formation. Similar unconventional shale gas resources were developed in the middle Ordovician upper Trenton interval in north-central New York along the southern Lake Ontario shoreline between 1888 and 1940 (Robinson, 1985). In both plays, these relatively shallow wells were used mainly for domestic and light industrial purposes that were extensively developed until the mid-1900s. Initial reported gas volumes for these fields were low and are not considered commercial by modern standards. Nonetheless, these discoveries represent important milestones in the development of unconventional gas resources in North America.

North America's first giant unconventional shale discovery in the Appalachian basin, the Big Sandy field, was discovered in early 1920s in northeastern Kentucky (Hunter, 1935). The primary target is the upper Devonian Huron shale combined with contributions from the Cleveland shale, Rhinestreet shale, and Marcellus shale intervals at depths ranging from 609 m (2000 ft) to over 1829 m (6000 ft) in West Virginia and Virginia. Two key characteristics of the Big Sandy field are a low-pressure gradient combined with a well-established open natural fracture network. These characteristics significantly differentiate Big Sandy field from modern shale plays such as the Barnett, Fayetteville, Haynesville, and the Marcellus, which characteristically display higher pressure gradients combined with lower-density open natural fracture networks. More than 21,000 wells, mostly vertical, have been drilled in the Big Sandy field in eastern Kentucky, southern West Virginia, southern Ohio, and southwest Virginia. The Big Sandy field is considered a giant field with an estimated recovery exceeding 3 tcf.

The Big Sandy field was critically important in aiding understanding of production mechanisms and drivers from unconventional resources. This field was the subject of extensive joint government and industry research from the early 1970s through the early 1990s. These studies provided an excellent basin-wide framework for understanding the extent and various mechanisms governing known shale gas producing areas

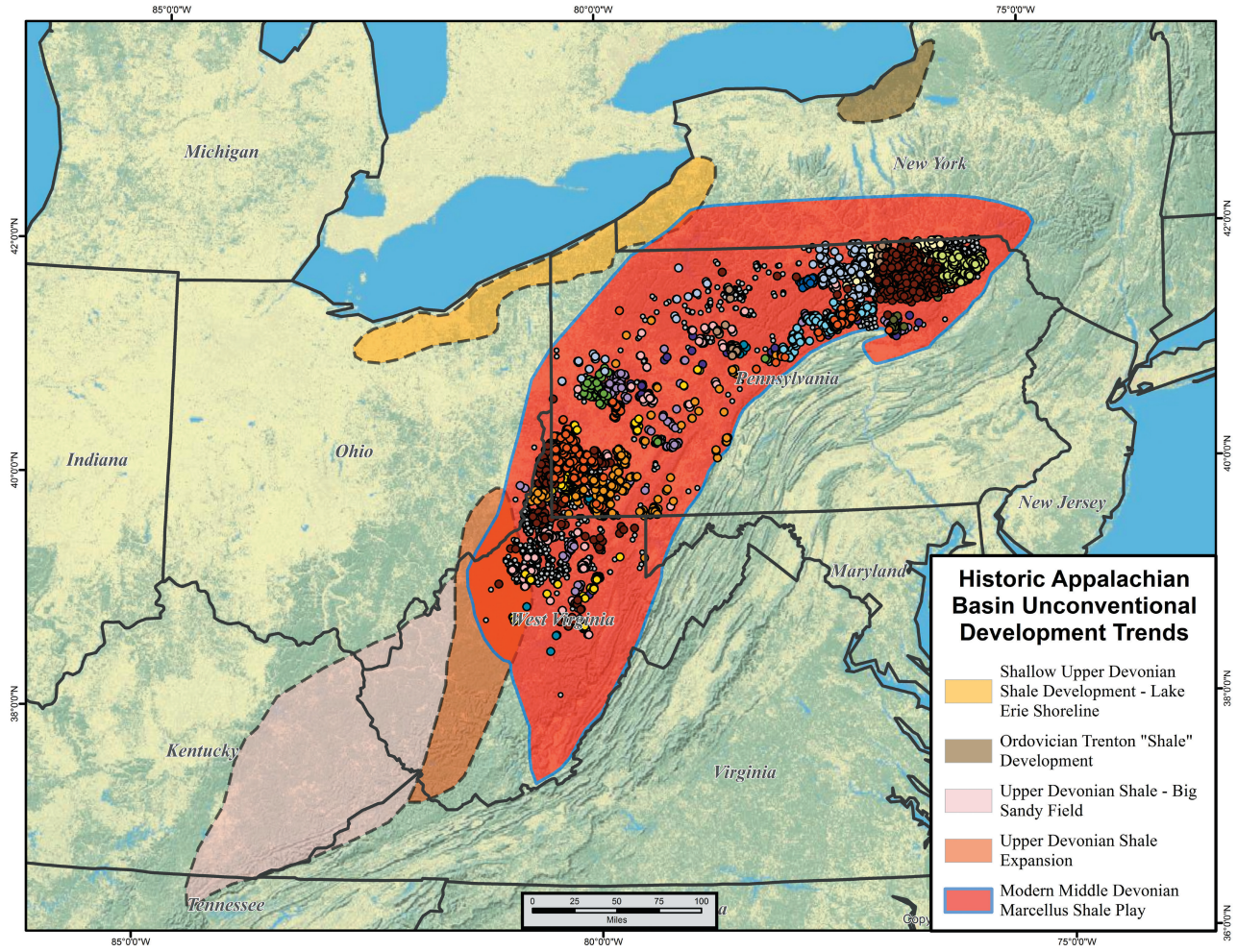

Figure 2. Map depicting major unconventional production trends in the Appalachian basin, key discovery wells, and Marcellus play activity (modified from Zagorski et al., 2012).

at that time and helped provide the path for new Devonian shale discoveries that expanded the Big Sandy field further eastward into central West Virginia. This research also identified the Antrim shale and New Albany shales as potential unconventional plays, both of which were successfully developed by industry prior to the discovery of the Barnett shale and the Marcellus.

COMMERCIAL DEVELOPMENT OF THE MARCELLUS SHALE

Prior to 2004, the Marcellus shale was considered a major Appalachian basin source rock with pervasive natural shows but only a minor exploration target. Earliest low-volume production from the Marcellus can be dated to around 1900 from very shallow depths in northern New York, which were suitable only for domestic purposes. The Marcellus interval was sometimes completed as a secondary pay zone in the West Virginia portion of the Big Sandy field. From the 1930s through the 1960s in Pennsylvania and New York, there was early interest in the Marcellus during the drilling of early gas discoveries in the underlying Huntersville Chert and Oriskany sandstone. Often, these early Huntersville chert and Oriskany sandstone wells reported significant natural gas shows in the Marcellus shale. These initial shows, while reporting high flow rates, blew down very quickly, indicating limited wellbore connectivity to porosity, permeability, and natural fracturing. A few early Marcellus completions were attempted in northern and northeastern Pennsylvania, usually through natural completions or by explosive shot.

Identification of the Marcellus shale as a potential reservoir by the Eastern Gas Shale Project (EGSP) encouraged several operators to pursue testing of this

interval in the late 1970s and early 1980s. Several completions of the Marcellus shale researched and even financed as a result of the U.S. Department of Energy (DOE)–funded Eastern Gas Shale Project (EGSP) were conducted across south-central New York and southwestern Pennsylvania from 1979 through 1982. These wells were extensively studied but achieved only marginal rates of production that were unsuited for large-scale development. These early Marcellus tests in New York were all completed using foam-based fracture treatments (Van Tyne, 1993).

In Pennsylvania, one of the earliest successful tests of the Marcellus shale was drilled and completed in 1979 in Allegheny County. In Washington County, Pennsylvania, three wells were drilled in 1982. In Allegheny and Washington Counties of Pennsylvania, two of these four early tests of the Marcellus were stimulated with carbon dioxide or nitrogen foam–based treatments and showed very poor test rates. Two of these early tests were completed with small-volume slick-water treatments, which yielded more measureable rates and pressures. While these early water based fracture treatments were clearly more effective than the foam treatments, these initial treatments were simply not large enough to establish the rates of production needed to achieve play commerciality on a broad scale. This initial testing phase failed to reach commercial play expectations because of technological limitations and a lack of understanding of how hydraulic fracturing technology can be effectively applied in areas where natural fracture networks were lacking and where significant over pressure was present.

There continued to be limited testing of the Marcellus shale in Pennsylvania, West Virginia, and New York after 2000 as interest in the Barnett grew. These tests also repeated either the foam-based treatments of the past or very-small-scale hydraulic fracture treatments, neither of which were comparable in size and scale to the standard completion treatments being applied to vertical wells in the emergent Barnett shale play in the Fort Worth basin in Texas since 1997.

2004: FIRST COMMERCIAL DEVELOPMENT OF THE MARCELLUS SHALE

The modern era of Marcellus shale gas development began in October 2004 with the successful vertical completion of the Marcellus interval by Range Resources Corporation in Washington County, Pennsylvania. Here, the company had previously drilled an unsuccessful deep exploration well, the Renz Unit 1 to test deeper Devonian and Silurian targets below the Marcellus on a seismic-defined structural closure associated with a left lateral strike-slip fault system. During the drilling of the Renz Unit well in 2003, several large gas shows were observed in the Marcellus shale. In 2003, Range and other companies were initiating significant shifts in corporate strategy, transitioning from traditional, higher-risk exploration to identifying and testing large-scale and repeatable resource plays. By the end of 2003 and early 2004, horizontal drilling in the Barnett shale had successfully evolved. The Barnett shale quickly became the largest proven gas field in the United States, eventually ramping up to over 6.33 BCFe/day in November 2011 (Powell and Brackett, 2015).

The new exploration paradigm became where the next Barnett-type play/field could be found. Operators were looking throughout North America for new shale gas plays, including the Appalachian basin. The Marcellus shale play in the Appalachian basin and the Renz Unit wellbore then became the focus of an extensive technical analysis by Range Resources. The Barnett and Marcellus plays were compared in terms of geographic extent, depth, thermal maturity, thickness, pressure, reported gas shows, organic content, and gas in place. Range's technical team reviewed old well reports for the numerous well penetrations of the Marcellus in Pennsylvania and nearby areas that documented the distribution and intensity of gas shows in the Marcellus, particularly in southwestern Pennsylvania. A number of these gas shows were identified in some old wells offsetting Range's available Renz wellbore, some dating back to the 1940s. This initial research suggested that the Marcellus could contain significantly larger resource potential than the Barnett, as the Marcellus covers a much larger geographic area than the Barnett.

In early 2004, Range had an opportunity to test the Marcellus in the Renz Unit well combined with a substantial acreage position. Conventional wisdom then was to not test the Marcellus. Unsuccessful attempts to commercialize the play had been tried before in the 1940s and in the 1970s through 1997. Operators of these earlier, unsuccessful, attempts tried various stimulation treatments, usually foam-based treatments or very small gelled water fracture stimulations, in an attempt to unlock hydrocarbons from the Marcellus. These treatments were very small and mere fractions of the scale successfully applied to the Barnett. The explorationist's viewpoint countered that the Marcellus had great gas shows, and its broad prospective play was significantly larger than the Barnett, so it should be approached and tested using the same completion approach successfully applied to the Barnett shale.

On October 23, 2004, a large Barnett-style water frac consisting of 3,569,500 L (943,000 gal) of water and 167,800 kg (370,000 lbs) of sand was used to treat a 27 m (90 ft) gross interval of the Marcellus organic shale in the Renz Unit 1 well (Figure 3). The well was flow tested on October 24, 2004, at an initial rate of 0.300



Figure 3. Photo of Renz Unit 1 large-scale hydraulic fracturing treatment of the Marcellus shale on October 23, 2004 (modified from Ventura, 2013). Photo courtesy of Range Resources Corporation.

MMCFe/day. This rate favorably compared to Barnett vertical tests and marked the discovery of the modern Marcellus shale play. The Renz Unit 1 completion established the production rates needed to encourage both industry and public interest in the Marcellus shale. After a year shut-in period, the Renz Unit 1 was turned on line at an initial rate of 0.800 MMCFe/day. The Marcellus pressure build-up test showed a clearly overpressured gradient of 0.65 psi/ft, confirming the suspected analog to the Barnett shale play. With the establishment of commercial production rates, the modern era of the Marcellus gas play in Appalachian basin had started.

EARLY VERTICAL/HORIZONTAL DEVELOPMENT, 2005 THROUGH 2007

Development of the Marcellus play progressed slowly following the Renz Unit discovery. There was limited drilling and testing (both vertical and horizontal) within the play over the next couple of years. In 2005, Range drilled two successful vertical delineation wells offsetting the Renz Unit. In 2005 and 2006, Range drilled three operationally successful horizontal wells in the Marcellus shale. However, the initial rates for these first three horizontal wells were not commercial compared to current Barnett horizontal wells. Compared to the successful vertical completions, these early Marcellus horizontal tests were expensive and problematic, largely due to a combination of lack of services and insufficient field experience drilling and completing the Marcellus as a horizontal play.

Activity in the Marcellus play slowly accelerated in 2006 as 28, mostly vertical, Marcellus wells were drilled along a wide fairway that encompassed north-central West Virginia, through most of Pennsylvania, and into southern New York. A landmark vertical Marcellus discovery well was drilled in 2006 in Susquehanna County, Pennsylvania, by Cabot Oil and Gas. The discovery well, the Cabot Oil and Gas Teel 5, was the first new oil and gas well to be drilled in Susquehanna County in 34 years and the fifth well ever drilled in that county. The Teel well initial unrestricted production test rate was reported to be 7 MMCFe/day (Cabot, 2009). A major challenge was there simply was no industry experience in drilling and completing horizontal wells in the Marcellus like there was in the Barnett and emergent Fayetteville

plays. A major change was needed to advance the commercialization of the Marcellus into its next successful phase. The largest complicating factor facing all of the early Marcellus pioneers was the lack of services, equipment, and infrastructure and operational experience in the basin to perform multiple-stage slick-water hydraulic fracture treatments.

Drilling activity and success in the Marcellus play increased significantly in 2007. Key step-out and exploration wells were drilled across northeastern and southwestern Pennsylvania. Most significant were the first economically successful horizontal completions in Washington County, Pennsylvania, by Range Resources. In early 2007, while the technical challenges of drilling and completion were slowly being solved, production results lagged, with production rates not exceeding those from vertical wells. After drilling three disappointing horizontal wells in the Marcellus, Range Resources made changes in the lateral target selection and completion approach. The fourth horizontal well, the Gulla 9H, tested 3.2 MMCFe/day after fracture stimulation (Figure 4)



Figure 4. Photo of drilling operations on the Gulla 9H, the key 2007 Marcellus horizontal well located in Washington County, Pennsylvania (modified from Ventura, 2013). Photo courtesy of Range Resources Corporation.

and was the breakthrough horizontal well for the Marcellus shale play.

Later in 2007, Range drilled and completed three more successful horizontal wells, testing 3.7 MMCFe/day, then 4.3 MMCFe/day and 4.7 MMCFe/day. These successful horizontal completions provided the repeatability needed to advance the emerging Marcellus play. Range issued a press release on December 10, 2007, announcing the results of the successful Marcellus horizontal wells. Immediately afterward, investment analyst Ross Smith/ITG (now Warburg Pincus) released an exciting report to industry and the financial community about the horizontal breakthroughs in the Marcellus and the exciting potential of the play, comparing it to the Barnett Shale (RSEG, 2007). The gold rush phase of the play now moved into full gear as a lease acquisition boom started.

MARCELLUS BOOM: 2008 THROUGH 2010

The year 2008 was the breakout year for the Marcellus shale play. Over 130 horizontal completed Marcellus wells were reported, marking the major industry shift from vertical wells to predominantly horizontal development, which was a major milestone. In early 2008, Dr. Terry Engelder and Dr. Gary Lash gave their initial estimate of recoverable Marcellus reserves (50 tcf), which provided early tangible clues of how large a field it promised to be when compared to the world's largest gas fields. By late 2009, more than 70 companies had acquired significant lease positions and drilled numerous horizontal wells, establishing a broad play area for the Marcellus across Pennsylvania, West Virginia, New York, Maryland, and Ohio. By 2009, the industry recognized core productive areas of the Marcellus that consist of the original discovery area in southwestern and northeastern Pennsylvania. Over 2280 Marcellus horizontal tests were drilled between 2008 and 2010, and by year-end 2010, over 80 drilling rigs were reported as active in West Virginia and Pennsylvania.

2010 THROUGH PRESENT DAY

By 2010 and 2011, the Marcellus play had attracted the attention of major independents, major oil companies, and international partners. From 2010 onward, core producing areas had become increasingly delineated in northeastern and southwestern Pennsylvania as well as northern West Virginia. By year-end 2011, the Marcellus rig count peaked at over 100 horizontal rigs. By 2012, the Marcellus play was recognized as the

largest and most economical gas play in United States. Improvements in well quality and performance since 2011 have significantly impacted the play and allowed the Marcellus to weather a large downturn in gas commodity prices. Major factors driving these improvements in well performance were a focus on only the core areas with high gas-in-place, optimal reservoir conditions, and an improved understanding of the critical role of lateral target selection. Major technical improvements in drilling, completion, and engineering designs resulted and led to significant increases in the average lateral length drilled, wells being drilled quicker, and an increase in the number of stages completed, both because of lateral length and shorter stage spacing. Initial potential rates per well reached as high as 43 MMCFe/day in southwestern Pennsylvania and as high as 47.6 MMCFe/day in northeastern Pennsylvania. All these factors combined to significantly increase production rates from the play that offset a rig count decline that began in 2012.

By year-end 2014, over 8616 horizontal Marcellus wells had been drilled in Pennsylvania and West Virginia. Figure 5 depicts the scope of Marcellus shale development through 2015 and shows the initial comparison to the Barnett shale play. Marcellus production grew to a rate of over 16 BCFe/day in 2015. This is the largest unconventional gas play in North America and currently provides approximately 18% of the gas used daily in the United States. Due to temporary pipeline constraints, infrastructure and takeaway capacity have become increasingly important. Drops in product prices and temporary pipeline takeaway capacity issues became key concerns in 2014 and 2015.

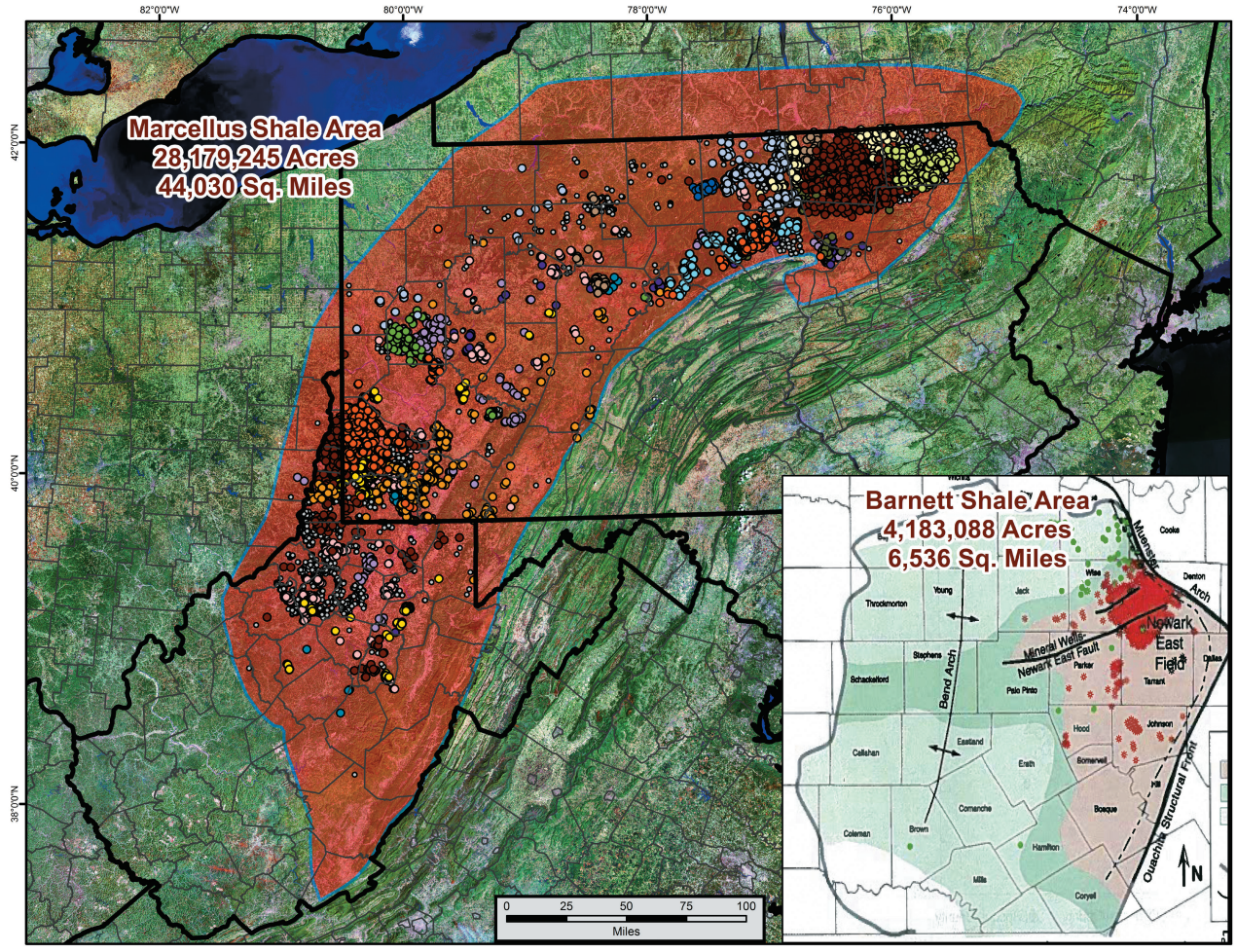

Figure 5. Map showing prospective regions of the Marcellus play compared with prospective area of the Barnett Shale in Texas. Both maps matched to scale (Barnett map from Pollastro et al., 2007, reprinted with permission from AAPG, whose permission is required for further use) (modified from Zagorski, 2010).

STRATIGRAPHIC FRAMEWORK

Figure 6 is a type log of the Marcellus shale in southwestern Pennsylvania showing the stratigraphic nomenclature utilized in Pennsylvania to describe the Marcellus shale play. The middle Devonian Marcellus shale formation lies within the lower portion of the Hamilton group, bounded above by the middle Devonian Tully limestone and below by the lower Devonian Onondaga limestone (Onesquethaw group). The Marcellus can be divided into two main members, the lower Marcellus/Union Springs shale and the upper Marcellus/Oatka Creek shale, which are separated by the Cherry Valley/Purcell limestone.

Based on analysis of log and core data, the productive units of the Marcellus are mainly comprised of quartz, clay, calcite, pyrite, plagioclase feldspar, and dolomite. In addition to its mineral content, the Marcellus contains high amounts of organic material ranging from 1 to over 18.7 (wt.%) TOC. TOC can constitute almost a third of the whole rock volume. Common clay minerals include illite/mica with minor amounts of chlorite. Data from X-ray diffraction (XRD) suggest the Marcellus ranges in character from a noncalcareous mudstone to a slightly calcareous mudstone with localized zones of highly calcareous mudstone and/or limestone. Since the majority of porosity, permeability, and reservoir storage volume is associated with the organics, the TOC content is a

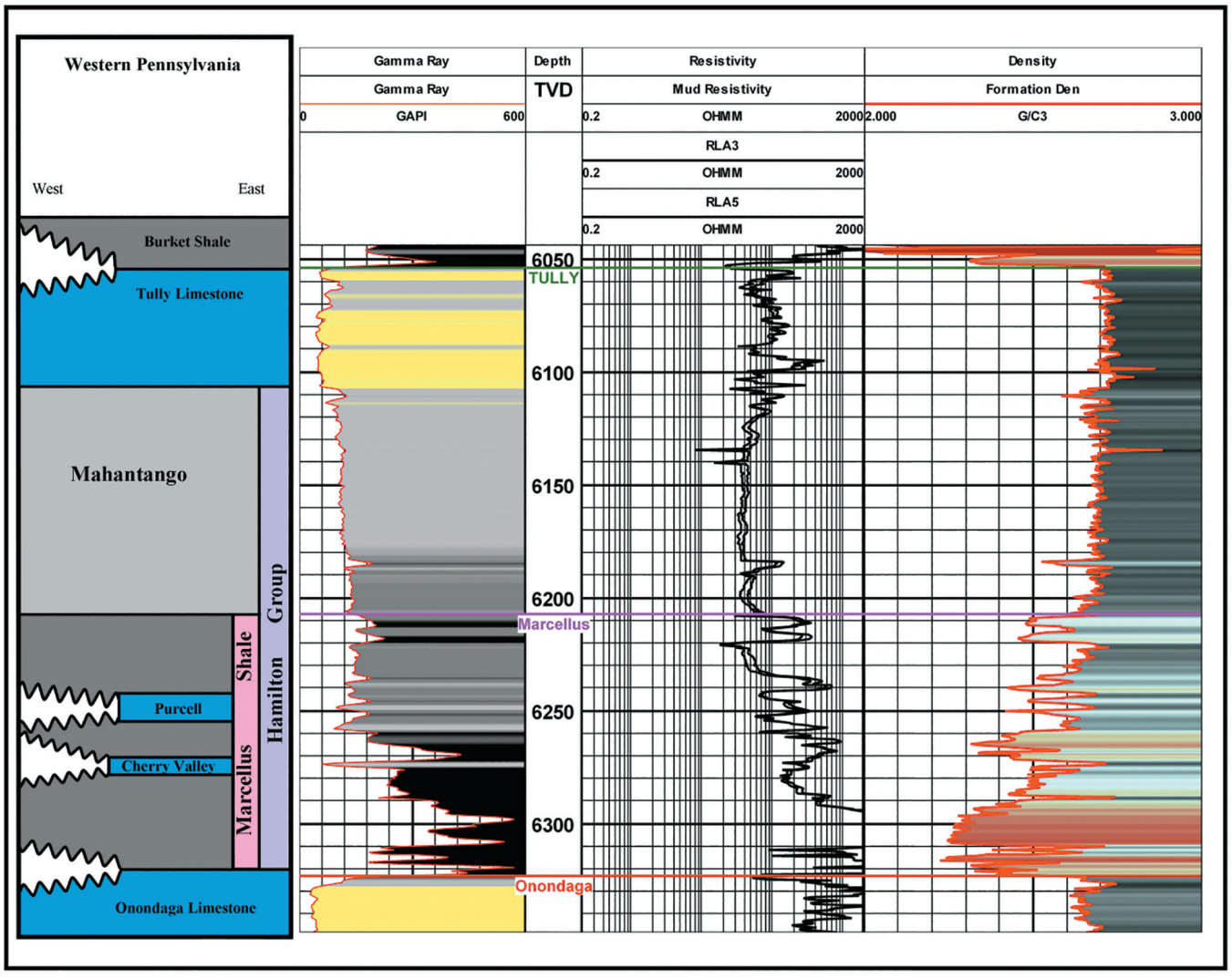

Figure 6. A typical gamma ray log of the Marcellus shale interval in southwestern Pennsylvania with selected thin-section and SEM images showing the complex mineralogy and high organic content of key Marcellus shale play intervals. G/C3 = matrix density *r* matrix (in grams per cubic centimeter); GAPI = gamma ray API units; SEM = scanning electron microscope; TVD = true vertical depth (in ft); RLA3 = borehole corrected resistivity in OHMM; RLA5 = borehole corrected resistivity in OHMM.

key reservoir element. Increased clay content is generally believed to marginalize reservoir potential and performance. Pyrite volume is high based on focused ion beam/scanning electron microscopy (FIB/SEM) data. Both the northeastern and southwestern core areas of the Marcellus have the highest volume of organic material and lower clay volumes. Calcite-filled fractures are common in the Marcellus, increasing in size and intensity from west to east. Barite nodules are common in core and outcrop. Fluid sensitivity studies indicate the Marcellus has low sensitivity to freshwater and saltwater. Using recycled production water in fracture treatments is now an industry standard practice in the Marcellus play. Understanding the variation in mineralogy and organic content within varying lithofacies in the Marcellus shale and the lithofacies stratigraphic distribution are critical to lateral placement in the Marcellus shale for optimal productivity. Target intervals, usually within the lower Union Springs member, contain high TOC and high organic porosity. Understanding the mechanical properties of lithofacies with differing mineralogy and organic content is essential for effective hydraulic stimulation of the Marcellus.

EARLY STRATIGRAPHIC RESEARCH

Paleogeographic reconstruction by Ettensohn (1985b), Woodrow and Sevon (1985), and Blakey (2005) depict that the organic-rich deposition occurred in a large nearly enclosed three-sided embayment that likely would have served to enhance oceanic organic productivity. Figure 7 depicts the paleogeographic reconstruction by Blakey (2005) of the Appalachian area at about 385 Ma. The arid conditions that were believed present during deposition of the organic-rich facies led to probable sediment starvation, as evidenced by the decrease in noneolian siliciclastic deposition in the organic-rich facies, preventing dilution of the

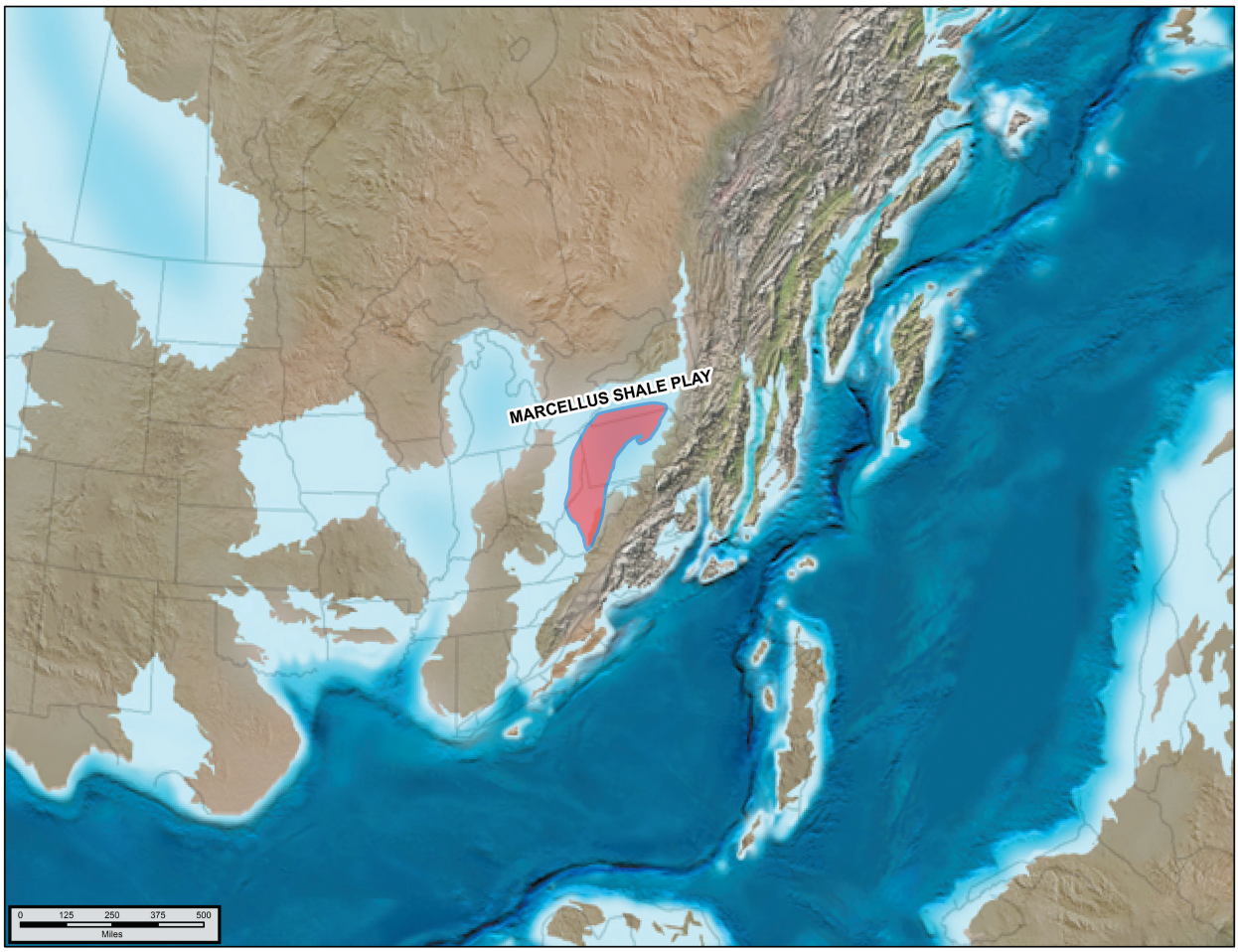

Figure 7. Middle Devonian paleogeography depicting the outline of the Marcellus shale play located within the restricted Marcellus shale depositional basin (modified from Blakey, 2005).

accumulating organic material. Ettensohn (1985a, b, 1992, 2004) assigned the period of deposition of the Marcellus shale to be the second of four tectonically related depositional phases associated with the Devonian Acadian Orogeny. Each of Ettensohn's four tectophases of the Acadian Orogeny represent regressive episodes that were further subdivided into four stages: (1) the beginning of tectonism and rapid subsidence leading to the accumulation of black shales, (2) deposition of gray shales and siltstones due to impending collision and regression, (3) collision causing widespread uplift and regional disconformities, and (4) widespread accumulation of limestone during a tectonically quiet transgressive period. During deposition of the Marcellus, the central Appalachian basin is interpreted to have been located between 15° and 30° south latitude (Ettensohn, 1992) with a dry tropical or savannah-like climate where rainfall was seasonal with extended dry conditions.

The creation, deposition, and preservation of the organic-rich Marcellus sediments was controlled by three primary factors: (1) primary photosynthetic production, (2) bacterial decomposition, and (3) bulk sedimentation rate (Sageman et al., 2003). The traditional interpretation of deposition of the organic-rich members of the Marcellus is a preservation model of organic enrichment where there is a permanently stratified water column with anoxic or euxinic (anoxic-sulfidic) bottom water conditions that allowed for the preservation of organic material (Demaison and Moore, 1980). This preservation model is best reflected in Ettensohn's proposed model of a nearly permanent pycnocline (Ettensohn, 1992).

Unconformity surfaces below and above the Marcellus are interpreted to become conformable to the southeast, into the deeper parts of the basin (Hamilton-Smith, 1993). A major Middle Devonian unconformity that lies above the Tully limestone (Hamilton-Smith, 1993) progressively removes stratigraphically older units from east to west. Westward toward the Cincinnati arch, this regional unconformity truncates the entire Tully, Hamilton and progressively older formations.

RECENT STRATIGRAPHIC RESEARCH

Recent stratigraphic and sedimentologic research is developing better and more detailed depositional models of the varying lithofacies within the Marcellus shale and other unconventional reservoir mudstones. The ongoing research allows better understanding and prediction of where the more organic-rich parts, which contain greater in-place hydrocarbons, are positioned stratigraphically. Recent workers dispute the original theory of deep-water deposition with consistent anoxia. Werne et al. (2002) and Sageman et al. (2003) proposed that the Marcellus organic-rich members were deposited without a permanent pycnocline and with possible seasonal fluctuations. MacQuaker et al. (2009) investigated the Marcellus at bed scale levels and found sedimentary structures inconsistent with a continuous deep-water anoxic model, including rip-up clasts and ripple lamina. He proposed that the organic-rich mudstones were not deposited in waters that were persistently anoxic; rather, the seafloor was occasionally reworked, which would have led to destruction of a portion of the organics. Boyce and Carr (2010) proposed that possible small local microanoxic environments played a role in the deposition of the organic-rich members based on local variations in the black shale units and thin limestones. The lower part of the Union Springs member seems to have been deposited below wave base and has the highest TOC content. The upper Union Springs member oscillated between anoxic and dysoxic conditions based on decreasing concentrations of U and Mo and increasing concentration of Mn (Wendt et al., 2015). Elevated U and Mo concentrations and the lack of bioturbation in the lower Union Springs indicate euxinic to anoxic bottom water conditions (Wendt et al., 2015).

Lash (2008) interprets the Cherry Valley and the Purcell limestones to be stratigraphically equivalent, while other authors, including de Witt et al. (1993) and Werne et al. (2002), correlate Cherry Valley and Purcell as separate. Lash and Engelder (2009) assign two third-order transgressive-regressive sequences to the Marcellus formation. The lower sequence includes the upper part of the underlying Onondaga formation, Union Springs, and Cherry Valley Members. The upper sequence includes the upper part of the Cherry Valley member, the Oatka Creek member, and the Stafford limestone member of the Skaneateles formation. The sequence stratigraphic framework of Lash and Engelder (2009) allows prediction of the key reservoir organic-rich shale lithofacies of the condensed sections positioned around the maximum flooding surfaces. The Union Springs member is thin or absent to the west and northwest, where a ravinement surface at the base of the upper Marcellus sequence exists. Kohl et al. (2014) interpret a forced regression and falling stage systems tract in the upper part of the Union Springs member. Lash (2008) identifies several unconformities to be present within the Marcellus shale within distal areas of the Appalachian basin, including western New York and northwestern Pennsylvania. These include unconformities that are the upper sequence boundaries for the Union Springs and Oatka

Creek shales. Lash (2009) documents that the entire Union Spring shale has been removed by a regional disconformity in some of these areas.

STRUCTURAL SETTING

Regional structural features influencing the Marcellus shale hydrocarbon system include the position of the Rome trough and related basement faulting patterns, strike-slip faulting and lateral ramps in Allegheny thrust fault systems, the presence (or absence) of the underlying Silurian Salina salt and associated decollement surfaces, and regional fold development and amplitude, which influence the degree of natural fracturing in the Marcellus shale. The major structural features of the Appalachian basin and key shale production trends of the Appalachian basin are depicted in Figures 8 and 9. Regional structural elements of the Appalachian basin from west to east include the Waverly arch and Cincinnati arch to the west, the Cambridge arch and Burning Springs anticline further eastward, the Rome trough, and the anticlinal fold belts in the Appalachian plateau and Valley and Ridge provinces.

The majority of Marcellus shale development lies in the Appalachian plateau physiographic province. This province is characterized by generally gentle structures and an overall lack of intense faulting toward the western portions of the province. Structural complexity increases to the east toward the structural front where high-amplitude detached, salt-cored anticlines trend northeast–southwest. The structural front represents the boundary between the plateau and the Valley and Ridge provinces, where the Devonian section rises quickly to the surface and crops out. The Valley

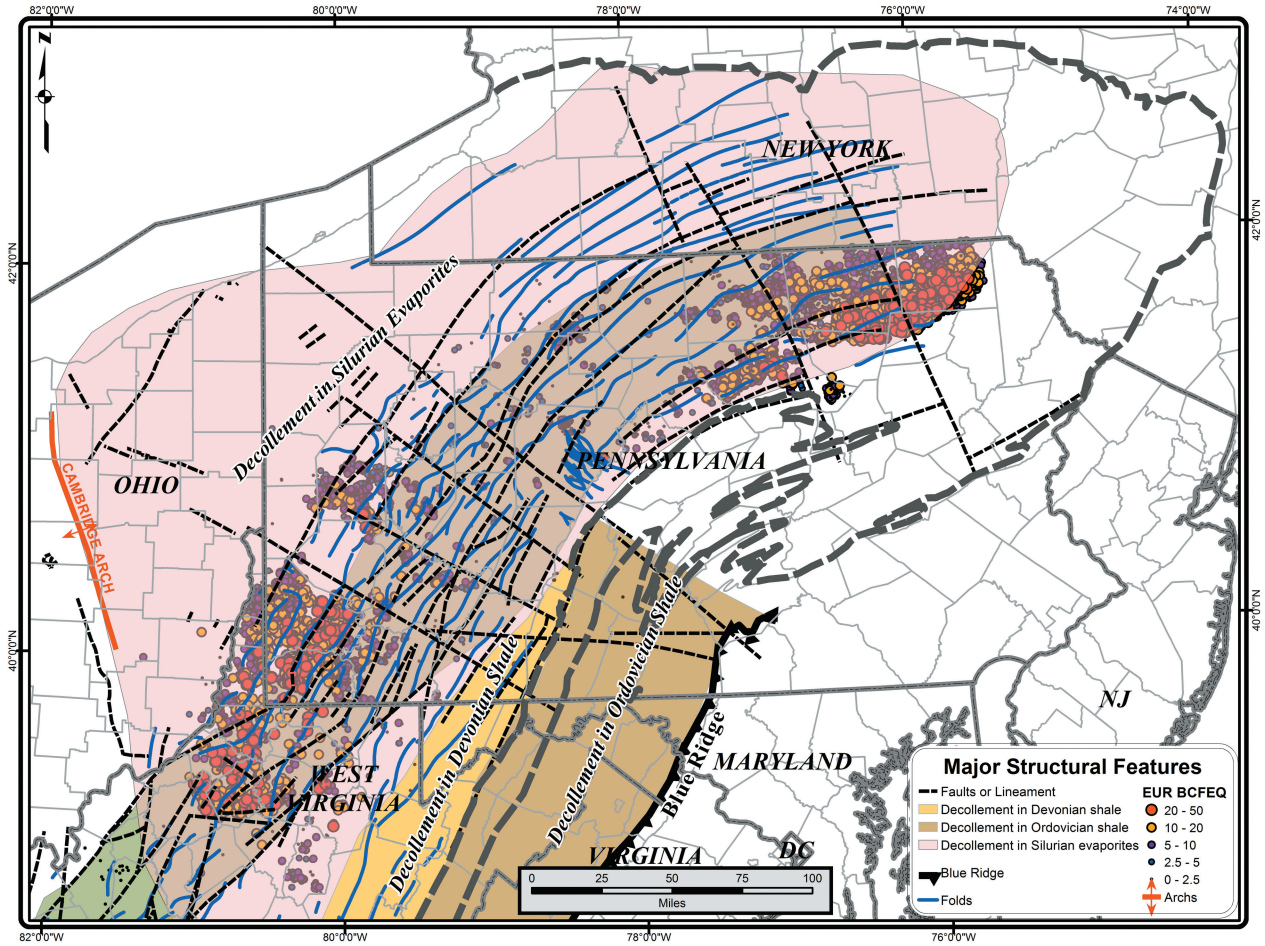

Figure 8. Map showing the primary structural features of the Appalachian basin that influence the Marcellus shale play. Key decollement trends from Colton (1970), Frey (1973), and Sanford (1993) are shown together with Marcellus well control (modified from Zagorski et al., 2012, and Schumaker, 1996). DC = District of Columbia; DE = Delaware; NJ = New Jersey.

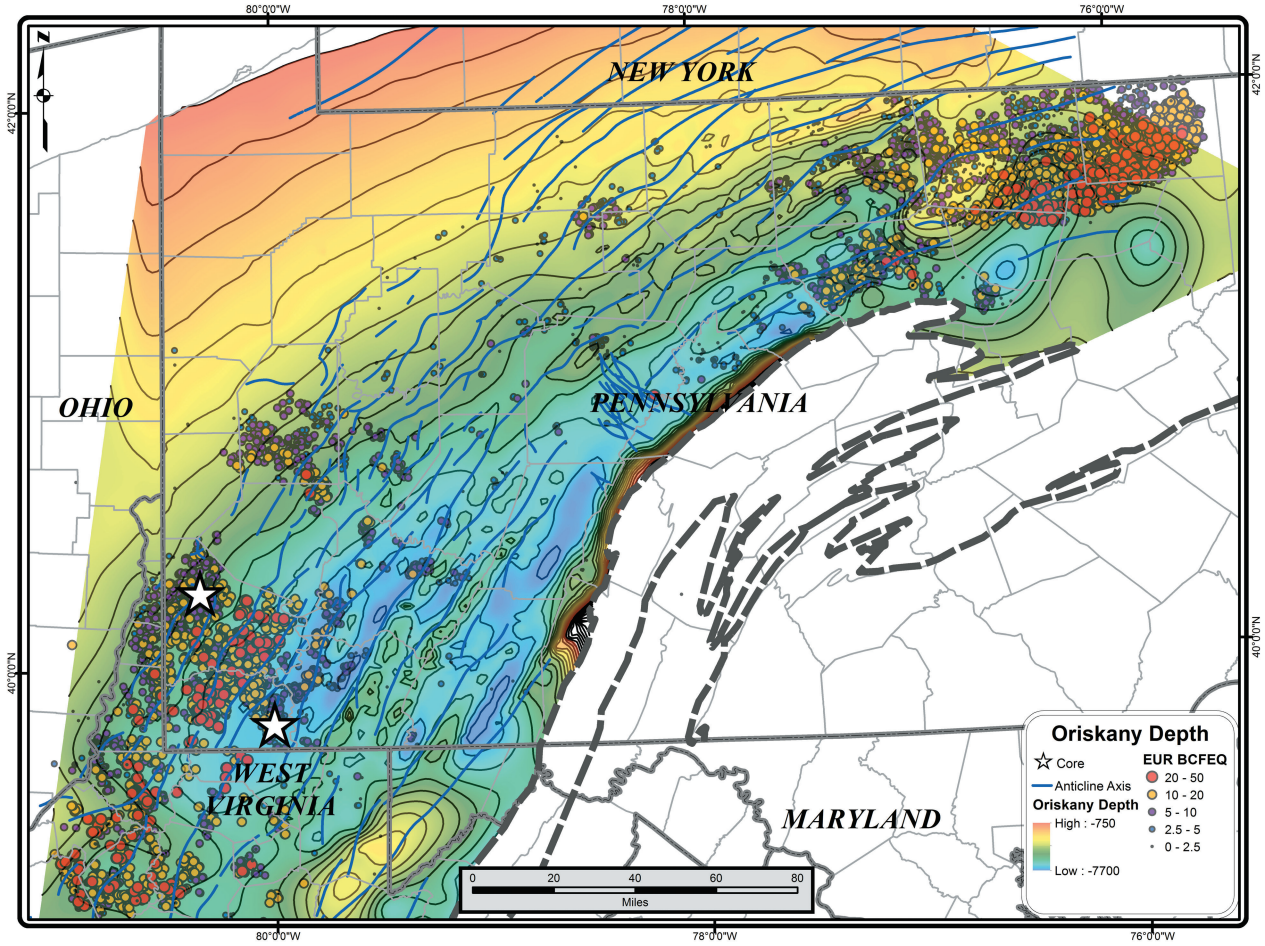

Figure 9. A map showing the subsea depth of the top of the Oriskany sandstone and major structural features. Core locations refer to Marcellus core examples referred to later in this text. (modified from Zagorski et al., 2013). DC = District of Columbia; DE = Delaware; NJ = New Jersey.

and Ridge provinces represent the most structurally challenging area in which the Marcellus shale is present. The area is structurally complex with high-amplitude detached folds, repeated and overturned beds, and multiple thrust faults detached in multiple decollement levels but mainly sourced in the highly ductile Salina salt beds.

IMPACT OF BASEMENT FAULTING

A key component of the Marcellus play is the strong influence basement faulting has on various key aspects of the play, including thickness, thermal maturity, reservoir quality, BTU content, organic content, clay content, and mechanical properties. Figure 8 depicts the basement structure of the Appalachian basin together with major interpreted basement-related faults, the projected position of the Rome trough, and key Devonian shale and Marcellus shale production trends. Major basement faults fall into two classifications: (1) strike parallel to the basin and related to the Rome trough and (2) faults trending perpendicular to the strike of the basin and interpreted as transform faults or cross-strike discontinuities (CSDs) (Harper and Laughrey, 1987). These basement faults represent zones of weakness believed to have been reactivated several times during the Paleozoic period (Negus-DeWyss, 1979; Lee, 1980; Shumaker, 1993).

The Rome trough represents a major structural feature of the Appalachian basin and is comprised of a failed rift system that formed in the middle Cambrian period. The Rome trough has been extensively studied in West Virginia and eastern Kentucky and extends into Pennsylvania and New York (Shumaker, 1996; Harper and Laughrey, 1987; Scanlin and Engelder, 2003; Kulander and Ryder, 2005). Shumaker (1993) showed several areas where the Rome trough affected

sedimentation of key Devonian organic shale members and where reactivation of basement faults provided for enhanced areas of natural fracturing. Within the Marcellus shale play, Kulander and Ryder (2005) defined the boundaries of the Rome trough in southwestern Pennsylvania through a series of regional cross-sections and regional two-dimensional reconnaissance seismic profiles. The Rome trough appears to delineate areas of maximum depositional thickness of key organic shale beds in the Marcellus shale as well as overlying beds such as the Tully. In addition, it is a critical feature related both to the burial and thermal maturity history of the Marcellus shale. The position of the Rome trough system is related closely to the highest observed pressure gradients in the Marcellus shale.

Offsetting the Rome trough strike-parallel basement faults are a series of cross-striking basement faults, which are likely transform faults created during rifting episodes in the Cambrian and Ordovician periods (Harper and Laughrey, 1987). These have been investigated based on lineament studies, remote sensing analysis, surface drainage patterns, aeromagnetic and gravity studies, and structural mapping. The surface expressions of these strike normal faults were called cross-strike structural discontinuities (CSDs) by Wheeler (1980). The two most significant include the Tyrone-Mt. Union lineament (Rodgers and Anderson, 1984; Canich and Gold, 1977) and the Pittsburgh-Washington lineament (Lavin et al., 1982). Rodgers and Anderson (1984) reported that an increase in natural fracturing and also enhanced hydrocarbon and fluid migration occurred along the Tyrone-Mt. Union lineament. Both of these features appear to be critical elements in the Marcellus play. Within the Appalachian basin, these cross-strike features often have a detrimental effect on oil and gas production from many reservoirs, with field terminations occurring at or near the cross-strike features. In some areas of the Marcellus play, the effect on the CSDs appears to be neutral or even additive, as is the case in southwestern Pennsylvania. Other areas of the Marcellus play, such as Clearfield County, observe a more negative association with Marcellus productivity. The CSDs probably allowed migration of mature source rock hydrocarbons to shallower reservoirs. Marcellus-sourced hydrocarbons could have had access to upper Devonian conventional reservoirs along the CSDs and the associated fracturing, and the Marcellus was depleted of hydrocarbons and pressure along the structural discontinuity. Lateral ramps in the Allegheny compressional system also could have allowed access of Marcellus hydrocarbons to younger reservoirs either through fault juxtaposition or migration along the lateral thrust fault.

ORGANIC CONTENT

The Marcellus shale is a world class source rock. The total organic carbon (TOC) content in the Marcellus shale ranges from less than 1% to over 18% (wt.%) based on review of regional core and log data. The macerals deposited in the Marcellus sediment are predominantly marine algal and prone to generate oil (type II). Minimum TOC threshold values for good source rocks and prospective shale gas plays are considered to be typically 2% (wt.%) or higher (Jarvie, 2005). The Marcellus shale has some of the highest TOC of modern thermogenic-style source rock plays. Studies by Reed (2008) suggest calculated original TOC contents in the Marcellus shale to be in the 4 to 20% (wt.%) range. One of the best indirect measurements of TOC content in the Marcellus shale is its gamma ray count. The spectral gamma ray log data show that most of the natural gamma radiation in the Marcellus shale is due to uranium, which is preserved only in sediments deposited in euxinic to anoxic environments where organic matter accumulates and is preserved. Schmoker (1981a, b) documented a direct correlation between the organic content of Appalachian shales and the wire-line log gamma ray intensity. Significantly high TOC content (5% or greater) can be identified with gamma ray counts of 200 API or greater. In southwestern Pennsylvania and northern West Virginia, peak gamma ray counts in excess of 300 to 400 API are not uncommon and reflect the higher uranium content and TOC in this portion of the play. Within the Marcellus shale play, TOC can be directly related to organic porosity, which results from the maturation and conversion of kerogen to hydrocarbons and the cracking of liquid hydrocarbons to pyrobitumen.

THERMAL MATURITY

Figure 10 is the thermal maturity map of the Marcellus shale compiled using a combination of publically available and proprietary measured vitrinite reflectance values and calculated R_o data. Thermal maturity patterns in the Marcellus generally increase in a southeasterly direction, ranging from 0.5% R_o equivalent in northwestern Pennsylvania to greater than 3.5% R_o equivalent in northeastern Pennsylvania. Recent Marcellus shale drilling activity and results indicate that most significant hydrocarbon potential and production occur approximately southeast of the 1.0% R_o equivalent maturity contour in the western portions of Pennsylvania, West Virginia, eastern Ohio, and southern New York. Based on the drilling results released to date, at

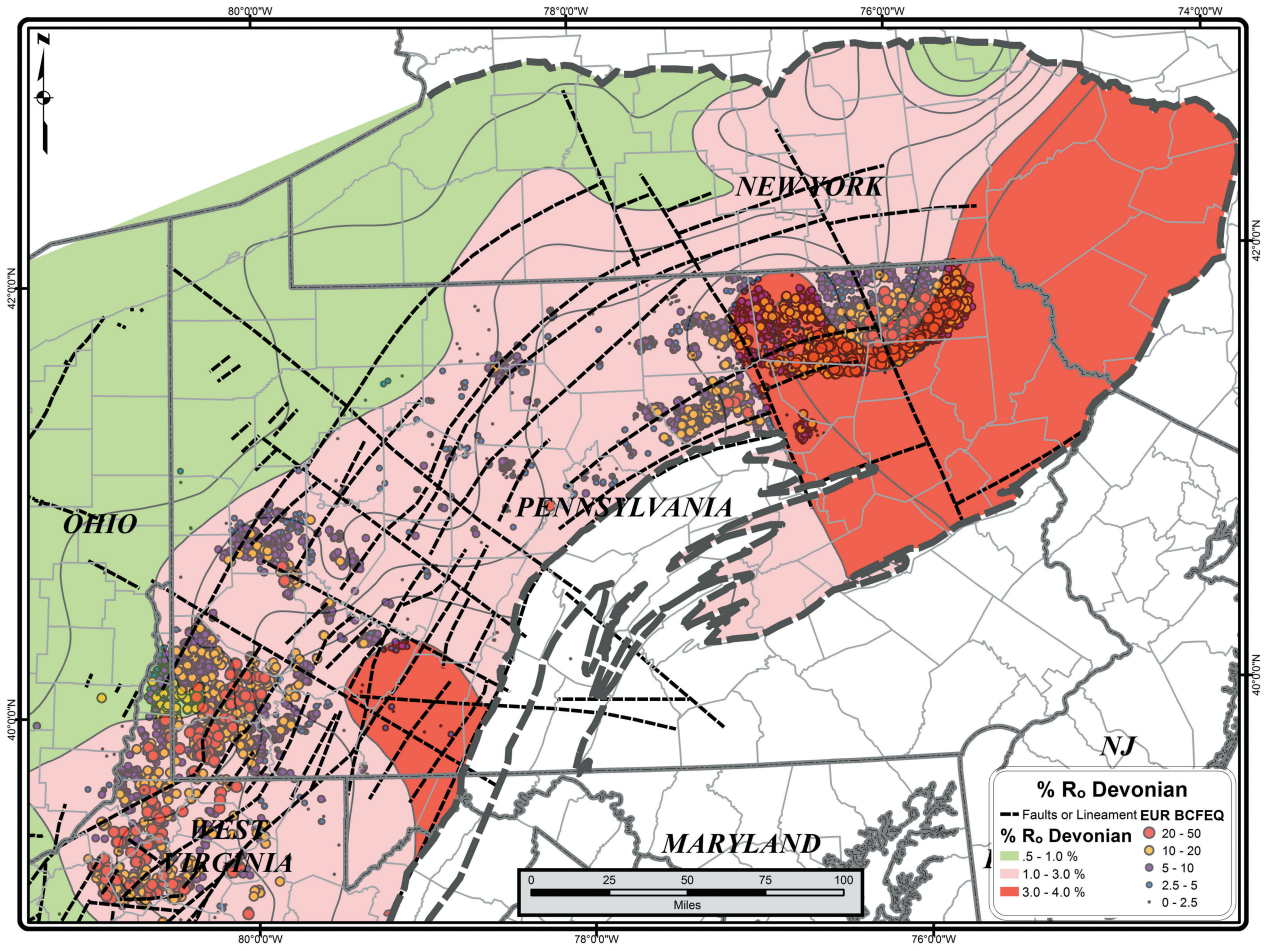

Figure 10. A map showing the thermal maturity trends for the Marcellus shale play and major basement faults (modified from Repetski, 2008, and Zagorski et al., 2013). DC = District of Columbia; DE = Delaware; NJ = New Jersey.

thermal maturity values of greater than 3.5% R_o equivalent, the productive potential of the Marcellus shale significantly decreases. Also shown on Figure 10 are major basement fault patterns and the Rome trough. Several major cross-striking basement faults appear to relate to discontinuities in the observed thermal maturity patterns. In addition, the Marcellus shale play in northeastern Pennsylvania appears to have been subjected to greater depths of burial as well as increased sedimentation and subsidence rates (Faill, 1985), which clearly influenced thermal maturity patterns.

Thermal maturity is a critical play element for the Marcellus shale. Thermal maturity studies for the Appalachian basin (Rowan, 2006) assume that the measured and estimated R_o values in the Marcellus shale require greater depths of burial and higher temperatures than those presently observed. The Rome trough and associated basement faults were critical to reaching the needed burial depths and pressures. The northwestern boundary of the Rome trough likely represents a hinge zone where rapid burial of the Marcellus allowed it to reach the current observed thermal maturity levels.

The two emerging core areas developing in the Marcellus shale play have somewhat different thermal maturity characteristics. In the southwestern area, the established production to date from the Marcellus occurs in a thermal maturity range of 1.0 to 2.8% R_o, with commercial gas discoveries occurring both in a dry gas window to the east and a combination gas/gas condensate play to the west. Here, Btu contents in the Marcellus are around 1000 to the east and approach 1400 in the western areas near the 1.0% R_o contour. The established productive areas of the Marcellus shale in the northeastern part of the play have a higher thermal maturity profile, with most production occurring between R_o values of 2.0 to over 3.0%. Here, the Btu values are in the range of 1000 Btu to 1080 Btu.

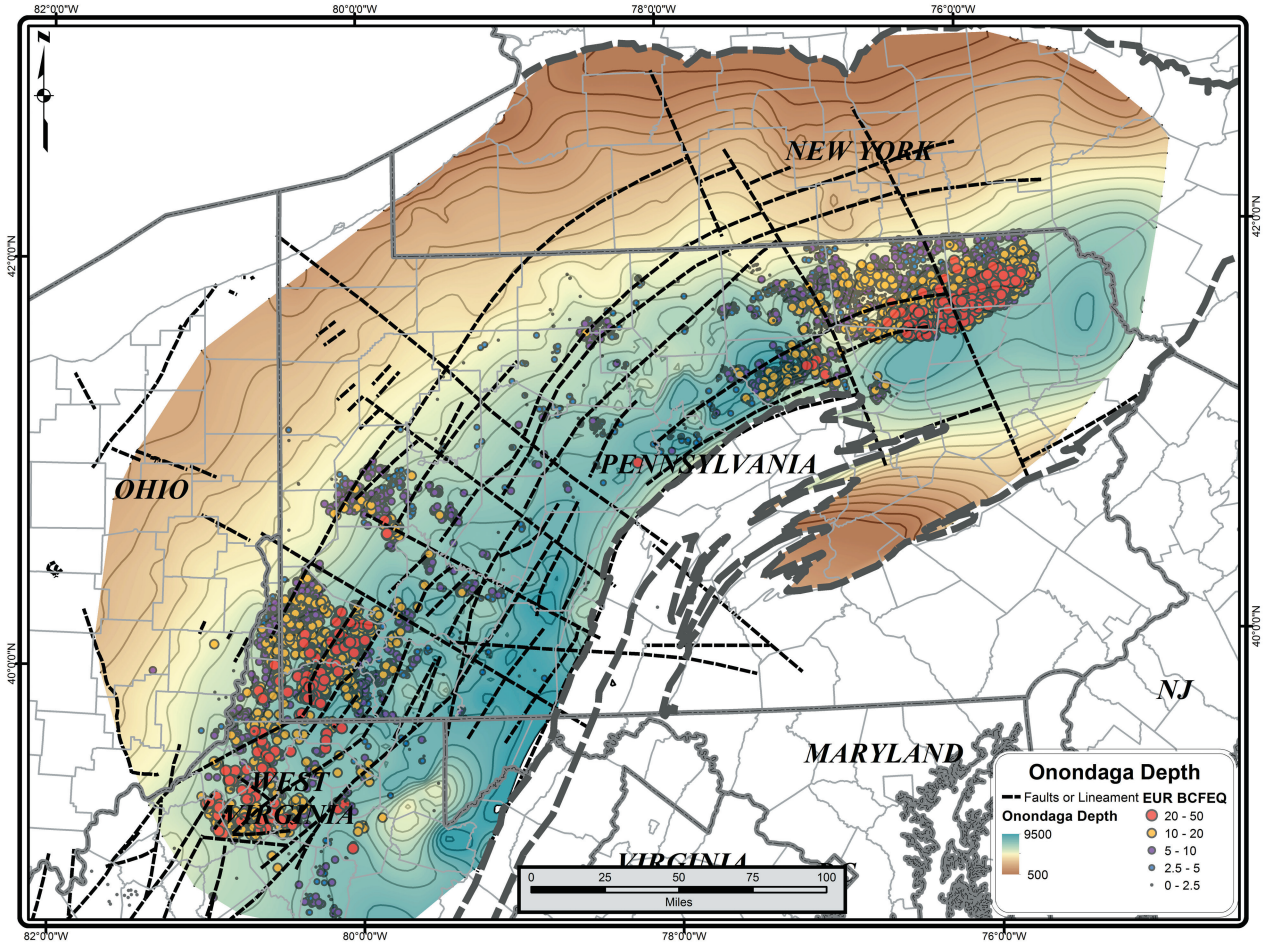

Figure 11. A map showing the drilling depths in TVD to the base of the Marcellus shale and major basement faults (modified from Zagorski et al., 2012). DC = District of Columbia; DE = Delaware; NJ = New Jersey.

DRILLING DEPTHS

Figure 11 shows the range of required drilling depths (TVD) to the base of the Marcellus across its main productive fairway. The map and distribution of depth data illustrate a key structural framework of the Appalachian basin that represents a strongly asymmetric trough. The majority of commercial production established to date from the Marcellus has been within a general depth fairway of 1375 to 2750 m (4500 to 9000 ft). The maximum drilling depths are encountered in synclines just basinward of the structural front. In general, increased depth results in higher gas-in-place values due to increases in both thermal maturity and overpressure. Encouraging horizontal production tests have been made in the Marcellus as shallow as 1158 m (3800 ft) TVD in northwestern Pennsylvania and as deep as 3048 m (10,000 ft) TVD in the Bedford syncline area. These both are in noncore areas but should be considered as future prospective play areas.

OVERPRESSURE

A key parameter influencing the Marcellus play is overpressure. A near-normal or overpressure gradient is essential for effective large-scale water fracs. Effective fracture stimulation is a critical play element needed to unlock hydrocarbons from the Marcellus, Utica, Eagleford, Haynesville and other modern shale plays in North America. Each displays overpressure gradients in its core areas. In the Marcellus shale play, pressure gradients range from 0.40 to over 0.80 psi/ft. The pressure generation mechanism is the conversion of liquid hydrocarbons to gas combined with uplift or unroofing. In general, the core productive areas have the highest pressure gradients. Marcellus pressure gradient trends are shown in Figure 12. Normal to overpressure gradients are observed across most of the Marcellus shale play in north-central West Virginia and northward into most of Pennsylvania and the southern tier of New York. Pressure gradients in

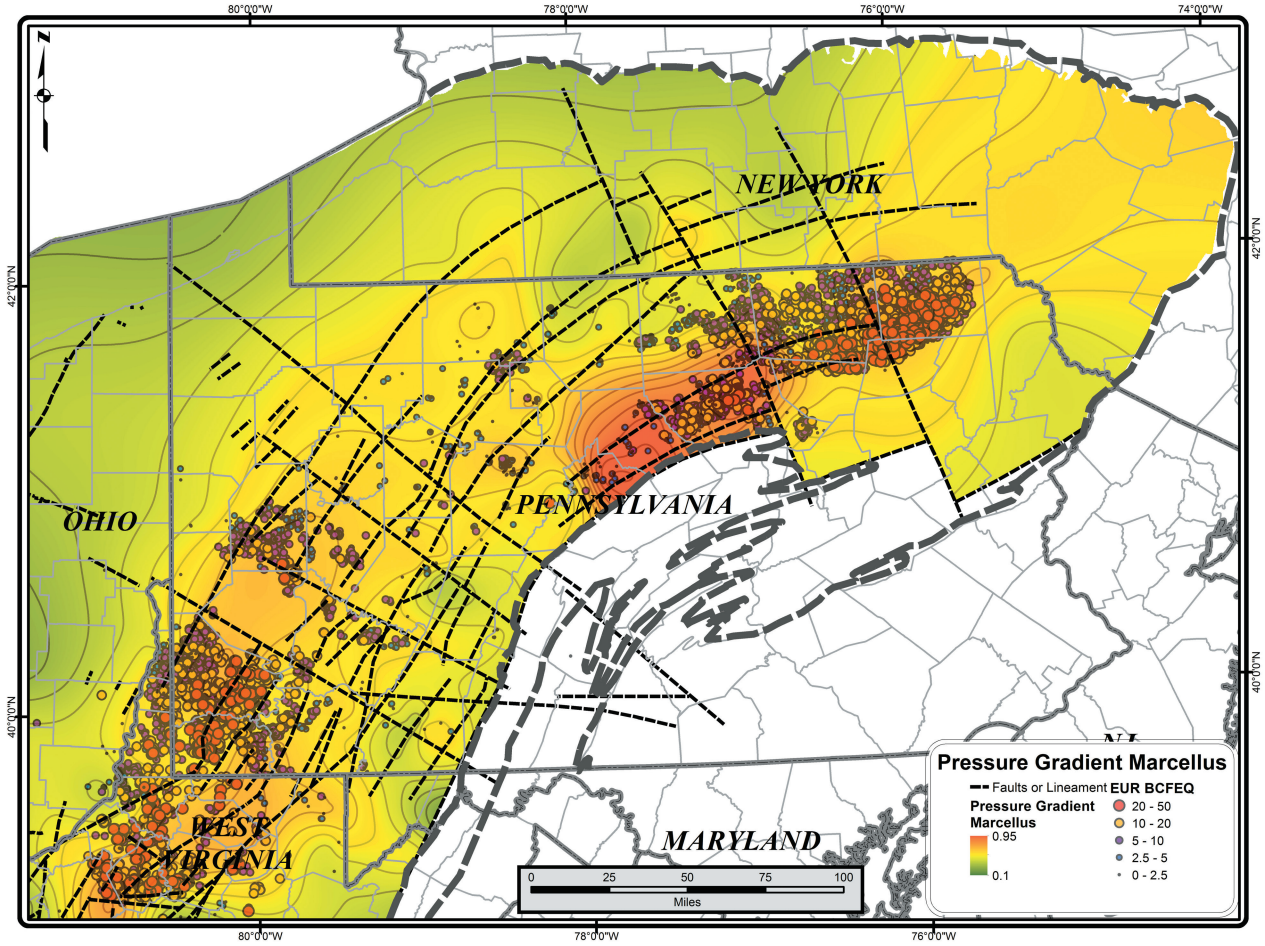

Figure 12. A map showing the pressure gradient trends for the Marcellus shale play and major basement faults (modified from Zagorski et al., 2011). DC = District of Columbia; DE = Delaware; NJ = New Jersey.

these areas are projected to range from approximately 0.43 to more than 0.80 psi/ft. The position of the Rome trough system is closely related to the areas of highest observed pressure gradients in the Marcellus shale.

In addition, the development of overpressure appears to be directly related to burial history and thermal maturity and can be seen to be clearly associated with areas where thermal maturity of greater than 0.9 to 1.0% equivalent R_o is observed. The overpressure mechanism is most likely conversion of liquid hydrocarbon to dry gas within a fixed pore space, which generated the observed high 0.6 to 0.8 psi/ft gradients. The original Marcellus pressure cell was then uplifted to its present depth without the full dissipation of the pressure cell due to the overall low permeability of the Marcellus and upper Devonian shale systems. The seal was not perfect and via migration through natural fractures, the Marcellus and overlying upper Devonian shale represent the likely source for the majority of shallower Devonian- and Mississippian-age conventional reservoirs. The coincidence of the Marcellus shale overpressure trends and the Rome trough is striking, particularly with the onset of the gas window of the Marcellus.

The normal and overpressured Marcellus areas in the Appalachian basin have been largely retained over geologic time, which helped to preserve both natural gas volumes and the overpressured cell generated during thermal maturation and uplift. Interestingly, except for source rocks such as the Marcellus and Utica Point Pleasant shales, the majority of conventional reservoir zones in the Appalachians basin are modestly underpressured, especially in areas where the Silurian Salina beds are absent.

One possible theory proposed to explain the presence of overpressure in Pennsylvania as well as northern and southern West Virginia is the close association between the presence of the deeper Silurian Salina formation to the highest degree of overpressure in the Marcellus. The Marcellus is overpressured where the Salina formation is present and significantly underpressured where the Salina formation is absent. This relationship between the presence of the Salina formation and the overpressured portion of the Marcellus

shale might be related to two factors. The first is that the evaporites of the Salina are the preferential structural detachment where the Salina is present. The thrust detachment jumped to the Marcellus and younger Devonian source-rock shales where the Salina formation is absent and probably compromised any pressure cells that had developed. The second factor may be that the thermal conductance of the salt in the Salina provided higher thermal stress to the Marcellus shale. The Marcellus is mostly in the gas window above Salina evaporites where the liquid hydrocarbons have been converted to gas and generated and overpressure cell. Here, during Alleghenian thrusting, much of the early and basinal accommodation was provided by the deformation of the Salina and then to a lesser extent the overlying Devonian shales. In the no-salt areas south of the Burning Springs feature and especially in southern West Virginia and Kentucky, the organic Devonian shale acted as the most ductile beds and hence experienced much more deformation and natural fracturing.

The presence of a regional decollement in the Salina group evaporites has been proposed (Gwinn, 1964; Shumaker, 1996; Milici and Swezey, 2006) for the area underlain by the thick Salina salt. This Salina decollement created an allochthonous block that was transported generally westward along low-angle detachment thrust faults. Shumaker (1996) also proposed that south of the Salina pinch-out, the basal detachment zone occurred within the Devonian shale (Rhinestreet, Huron, and Marcellus) interval. It is proposed that this detachment and extensive movement in the Devonian section led to severe compromise of seals within and above the Marcellus and subsequent loss of hydrocarbons and pressure.

MARCELLUS THICKNESS TRENDS

Most current industry drilling activity is associated with areas having greater than 15 m (50 ft) of gross Marcellus shale thickness. Figure 13 depicts the gross

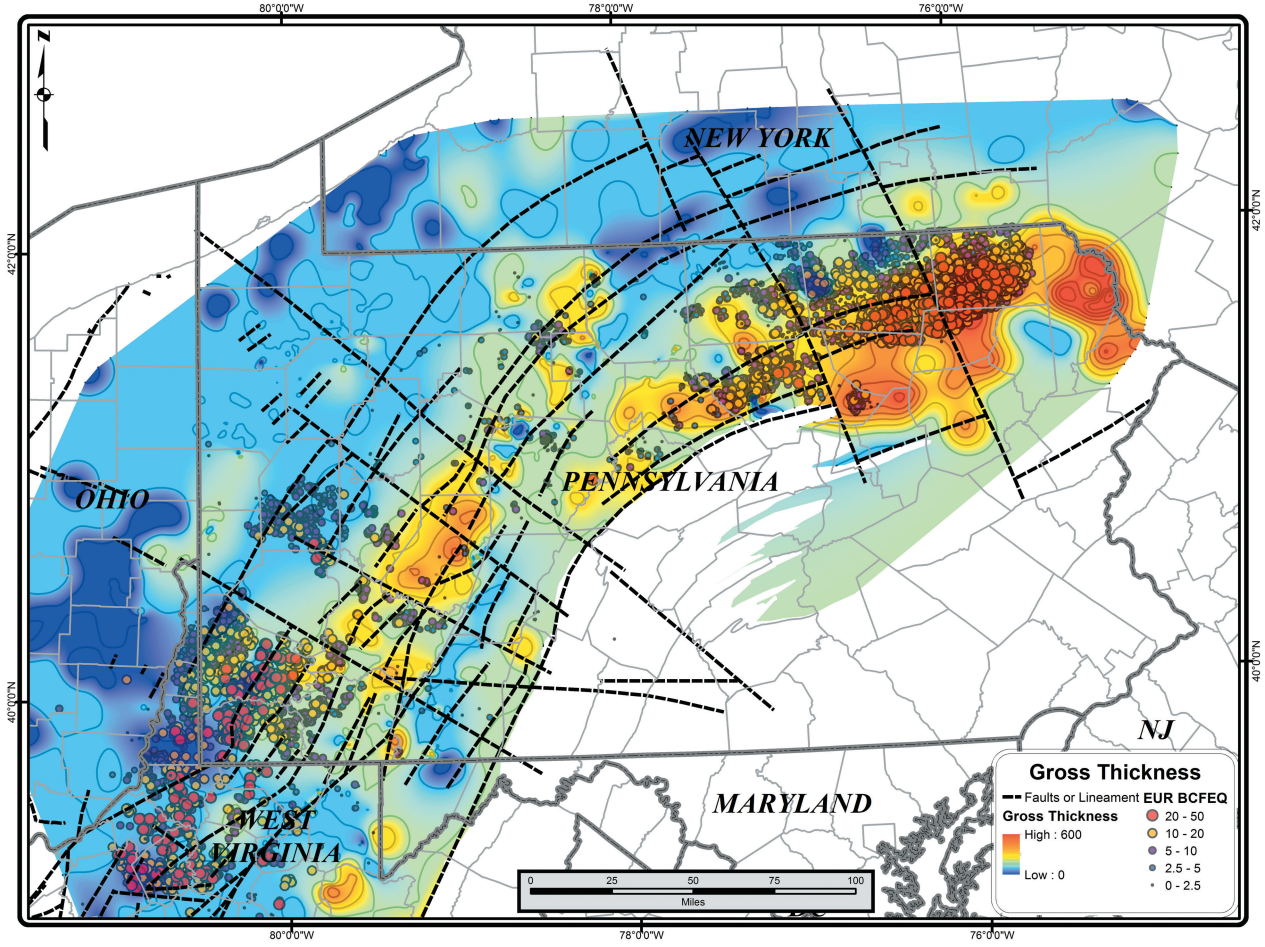

Figure 13. A map showing the gross thickness trends for the Marcellus shale and major basement faults (modified from Zagorski et al., 2012). DC = District of Columbia; DE = Delaware; NJ = New Jersey.

thickness of the Marcellus shale across the Appalachian basin together with major mapped basement fault trends. This map shows a general eastward thickening of the Marcellus shale within, or near, the Rome trough. The gross thickness of the Marcellus as mapped is defined by the top of the first occurrence of organic shale near the base of the Mahantango formation to the top of the Onondaga limestone. Gross thickness of the Marcellus increases generally eastward from the zero isopach in eastern Ohio and western West Virginia to a maximum thickness of more than 107 m (350 ft) in northeastern Pennsylvania. The gross thickness map has not been corrected for potential repeated sections or areas that encounter significant bed dips. The trend of thickening in the Marcellus generally parallels the Appalachian structural front. The gross depositional patterns of the Marcellus shale are highly influenced by basement fault patterns. They show general strike-parallel thickening within the Rome trough feature and related strike-parallel basement faults. Additionally, abrupt depositional terminations appear to exist at, or near, the cross-striking basement faults.

The generalized cross-section shown in Figure 14 illustrates the significant stratigraphic changes that occur across the Marcellus shale play. On a regional basis, the entire section thickens considerably to the northeast, suggesting significantly higher sedimentation rates associated with the early Catskill delta compared with the southwestern play region. Also shown on the regional cross-section is the position of key maximum flooding surfaces in the Union Springs and Oatka Creek members of the Marcellus shale, which records episodes of maximum organic deposition and preservation in the condensed sections. These maximum flooding surfaces can be traced across the entire play and represent key pay intervals. Thicker gross Marcellus shale also relates to higher gas-in-place along isomaturity trends.

POROSITY, PERMEABILITY, AND PORE TYPES

High organic content, organic-sourced porosity, permeability, and overpressure are key gas productivity factors for the Marcellus shale. Organic content can be accurately estimated by gamma ray and density log data calibrated with core measurements. The high organic facies of the Marcellus is the key reservoir unit in terms of hydrocarbon storage. Porosity within

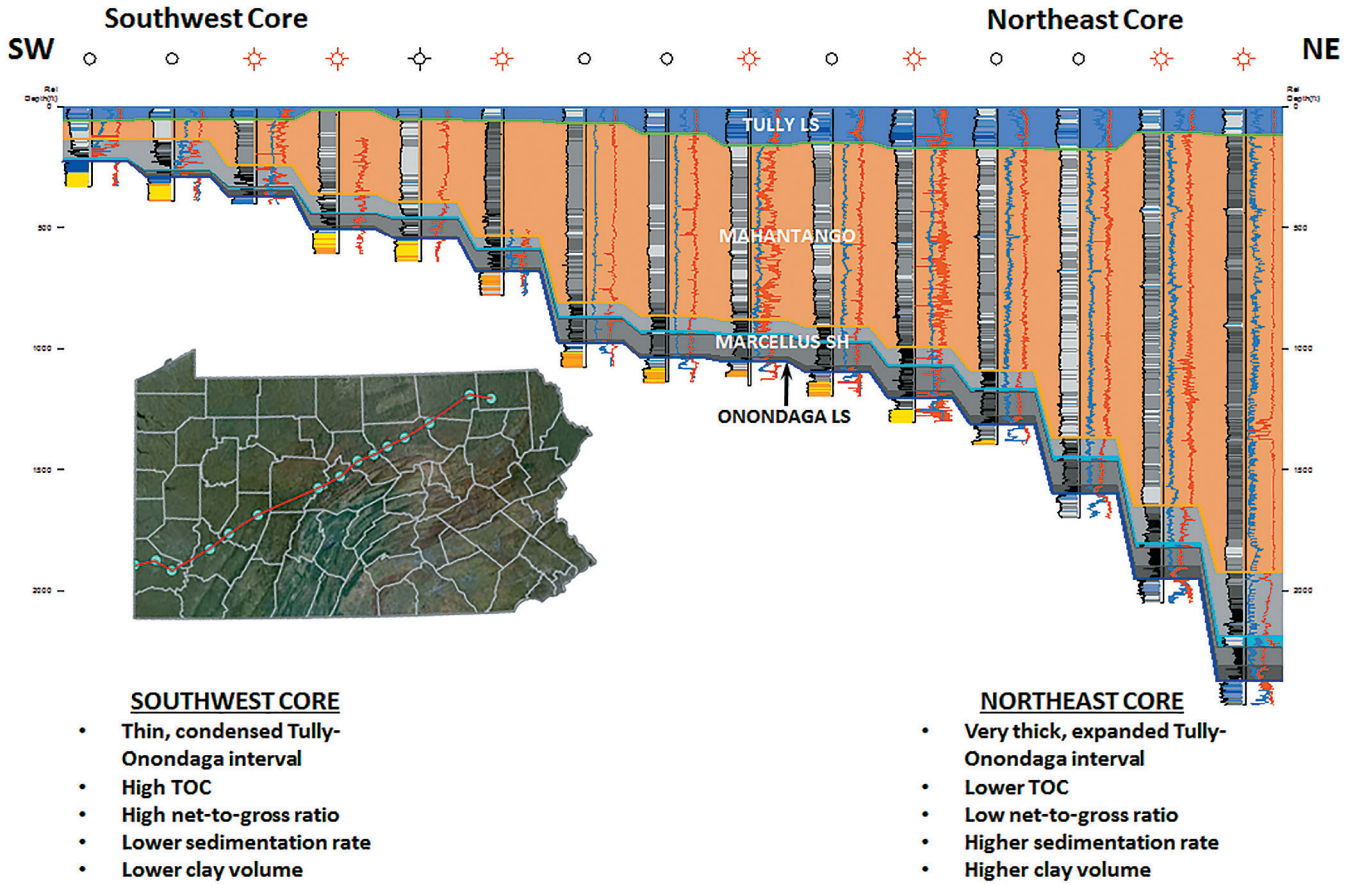

Figure 14. Marcellus regional cross-section.

organic matter, either partially converted kerogen, bitumen, or pyrobitumen, is key for hydrocarbon storage in the Marcellus shale because the organic pores contain both absorbed and free gas with little to no water saturation. The organic content varies between approximately 2 and 18 (wt.%) average in southwestern Pennsylvania to approximately 4 to 10 (wt.%) average in north central Pennsylvania. Organic content and the development of intraorganic porosity are key factors that affect Marcellus shale gas-in-place and productivity. The observed intraorganic porosity displays a high degree of connectivity (Figure 15) and is responsible for a significant portion of the Marcellus shale's productivity and gas-in-place. Intraorganic pores range from less than 10 to more than 200 nm. Other pore types include intergranular, intercrystalline, and microcracks.

Core data and calibrated log data confirm that good porosity and permeability are present in the organic-rich lithofacies of the Marcellus shale across a large area. Core and log data acquired across the Marcellus shale play exhibit porosities ranging from 2 to 18% and permeability ranging from 130 to over 2000 nanodarcies (nd). Most workers consider minimum values of commercial permeability in gas shales to be in excess of 100 nd. Shale gas reservoirs with average permeability values of more than 500 nd are considered very high for unconventional shale plays. As such, observed ranges of permeability in the Marcellus shale play appear exceptional and unique compared with other North American gas shale plays.

The regional distribution of organic material and porosity and permeability can be mapped using gamma ray feet calculations as a proxy. As shown in Figure 16, gamma ray feet distribution patterns are concentrated in the northeastern and southwestern areas of the Marcellus shale play. Again, regional basement fracture trends clearly influence the distribution of organic matter throughout the play fairway. This regional mapping approach combined with the distribution of Marcellus shale estimated ultimate recovery (EUR) data highlights the location of the core producing regions of the Marcellus shale play.

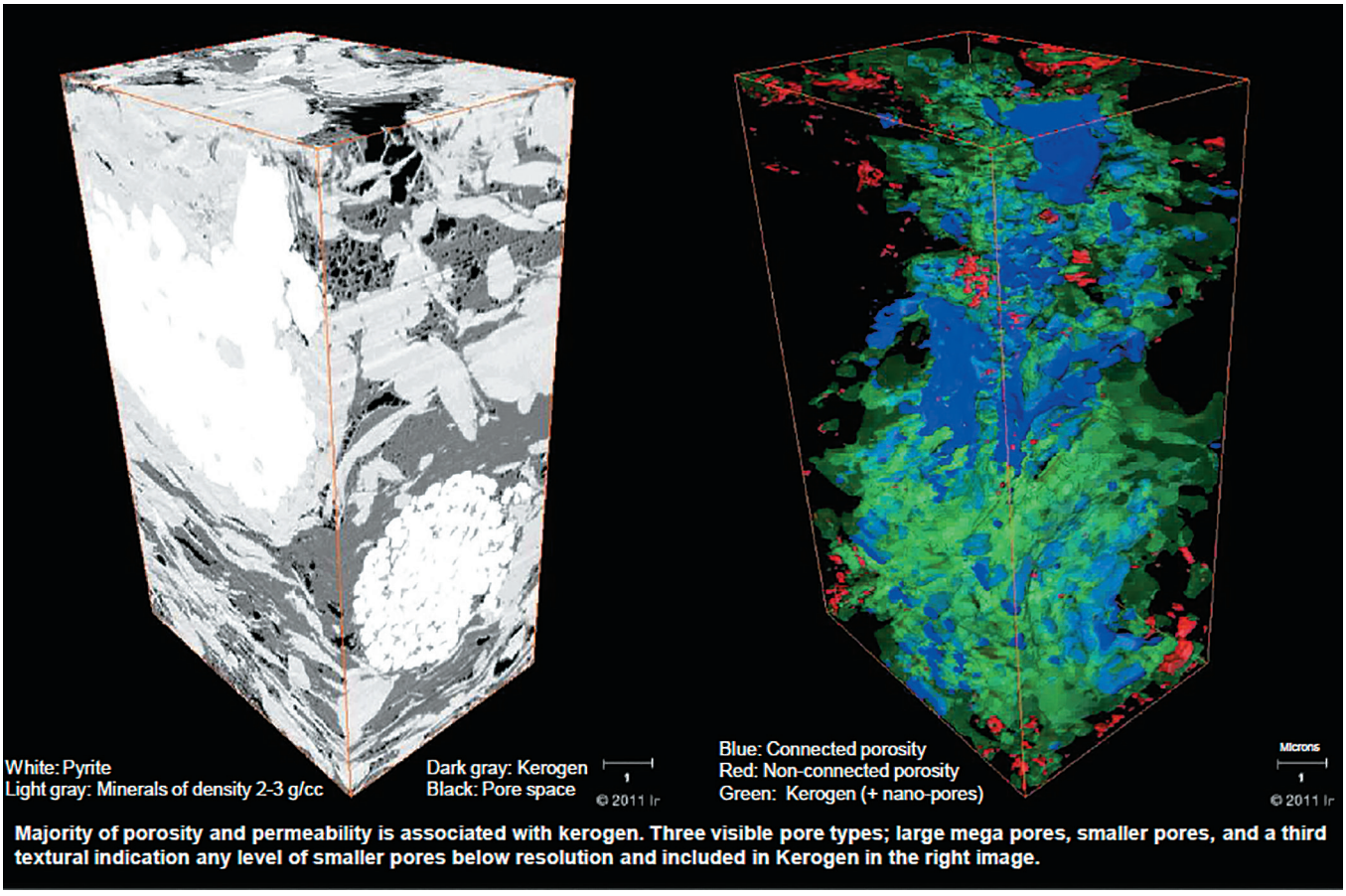

Figure 15. Three-dimensional FIB/SEM imagery of Marcellus pay interval in wet gas/liquid–rich area of southwestern Pennsylvania. Note well-developed and large pore size and high degree of connected porosity with nanopore network (modified from Yang et al., 2013).

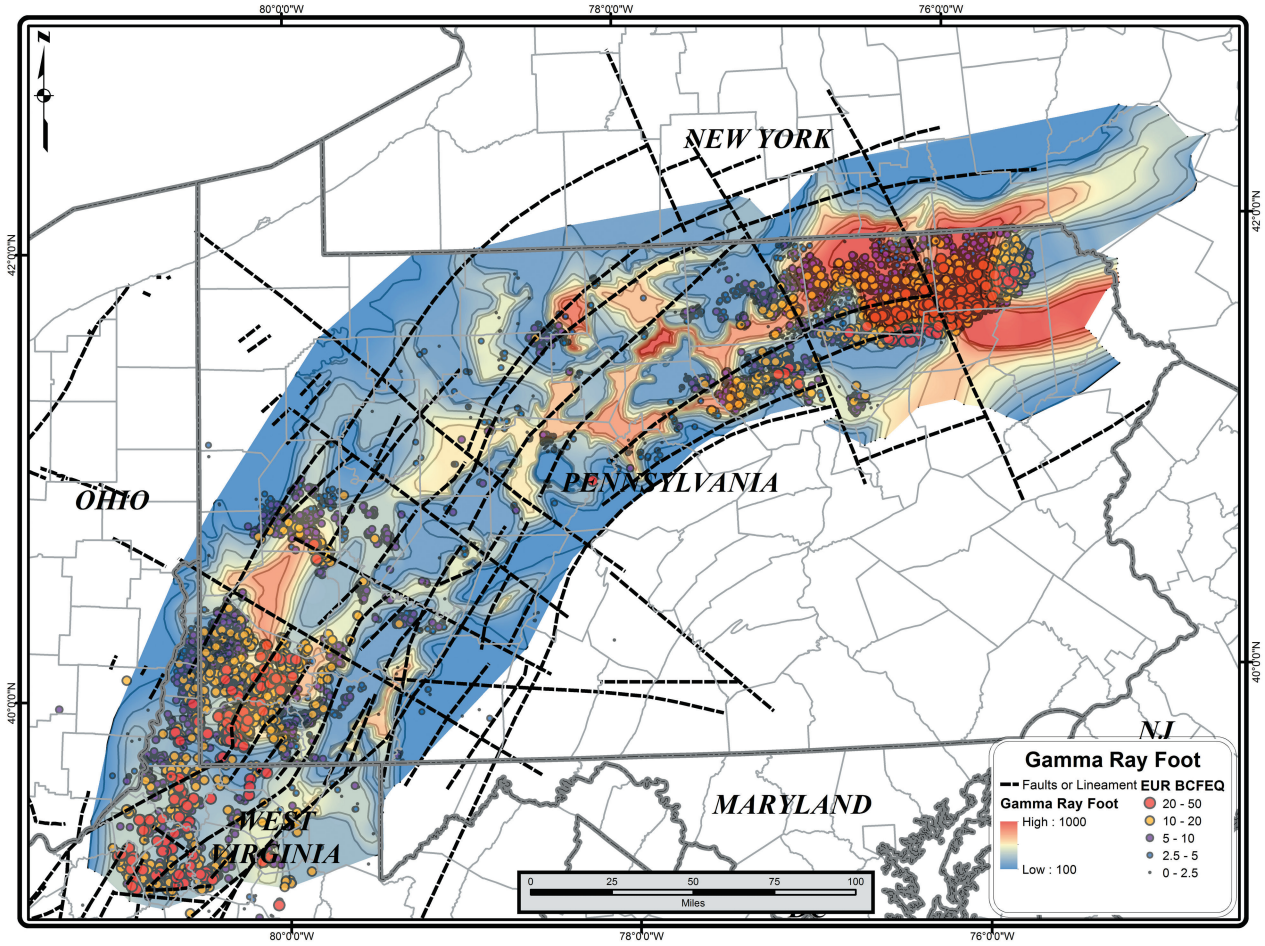

Figure 16. A map showing the total gamma ray feet (a proxy for total organic volume of total organic pore volume) for the Marcellus shale play and major basement faults (modified from Zagorski et al., 2013). DC = District of Columbia; DE = Delaware; NJ = New Jersey.

NATURAL FRACTURING

Natural fractures represent an important element of the Marcellus shale play on both a local and a field level. There is a major regional natural fracture network present in the Marcellus shale as documented by various core and outcrop studies. These regional fracture or joint sets are designated J1 (east-northeast trending) and J2 (north-northwest trending) by Engelder et al. (2009). The Devonian organic black shales exhibit predominately at the J1 set of joints. Natural fractures influence Marcellus production, but their role appears more subtle, suggesting that while they potentially significantly contribute to well performance, their role is less critical in defining commercial production. Interestingly, in highly fractured regions, it appears the higher degree of natural fracturing significantly negatively impacts well performance. Low Marcellus interval velocity anisotropy from three-dimensional seismic data and the predominately J2 orientation of the joint sets correspond to higher Marcellus productivity (Inks et al., 2015). Based on available well performance data and extensive log and core data, it is evident that the Marcellus shale is regionally more strongly controlled by key reservoir characteristics such as thickness, porosity, permeability, gas-in-place, pressure gradient, and the ability to be fractured. There are several areas in southwestern Pennsylvania where higher observed initial test rates can be demonstrated to be related to the presence of natural fracture systems. However, it appears that once natural fracturing systems develop to a point where effective stimulation is compromised or the reservoir seal is compromised over time, their role changes from one of enhancement to one of detriment.

Nearly all horizontal wells drilled in the Marcellus shale play are oriented along a northwest by southeast azimuth. The current shear max (SHmax) direction for the Appalachian basin is observed to be northeast-southwest based on numerous studies by

the EGSP, the world stress map, microseismic studies, and observed direction of drilling-induced fractures or bore-hole breakout observed in cores and formation microimaging (FMI) logs for the Marcellus shale and other EGSP wells. These are shown in Figure 17. As such, the northwest by southeast azimuth is the primary orientation for most horizontal Marcellus wells.

On a broad scale, most current activity in southwestern Pennsylvania and northern West Virginia is situated in relatively uncomplicated structural trends. Open natural fractures are rarely observed in whole cores of the Marcellus or in FMI logs. Most observed natural fractures appear to be healed and calcite filled. FMI logs run primarily in southwest Pennsylvania in the Devonian shale interval tend to favor a strong northwest by southeast orientation for healed fractures. Analysis of FMI patterns on several wells across the Marcellus play show the following types of fracture patterns: drilling-induced fractures, which trend northeast to southwest, paralleling the inferred SHmax direction (or conversely, bore-hole breakout oriented northwest to southeast in the higher–pore pressure Marcellus); healed fractures defined by high resistivity patterns trend primarily in a northwest to southeast direction paralleling the J2 set proposed by Engelder et al. (2009); and many of the fracture patterns observed earlier in the EGSP cores. Possible faults and fractures with varying orientations show good representation of the proposed J1 and J2 joint and fracture sets. Other orientations also are well represented and are believed to represent features associated with slickensides (low-angle) and high-angle faults and fractures.

The effect of increased folding and faulting to the east can be depicted on the two cores shown in Figure 18. The core in the westernmost area (Washington County, Pennsylvania) demonstrates the presence of natural fracturing, but fracture density and width are low. This differs from the significantly higher fracture density and fracture width exhibited by the core of the well located near the Fayette anticline in eastern Greene County, Pennsylvania. This comparison illustrates the significant increase in natural fracturing observed in the many

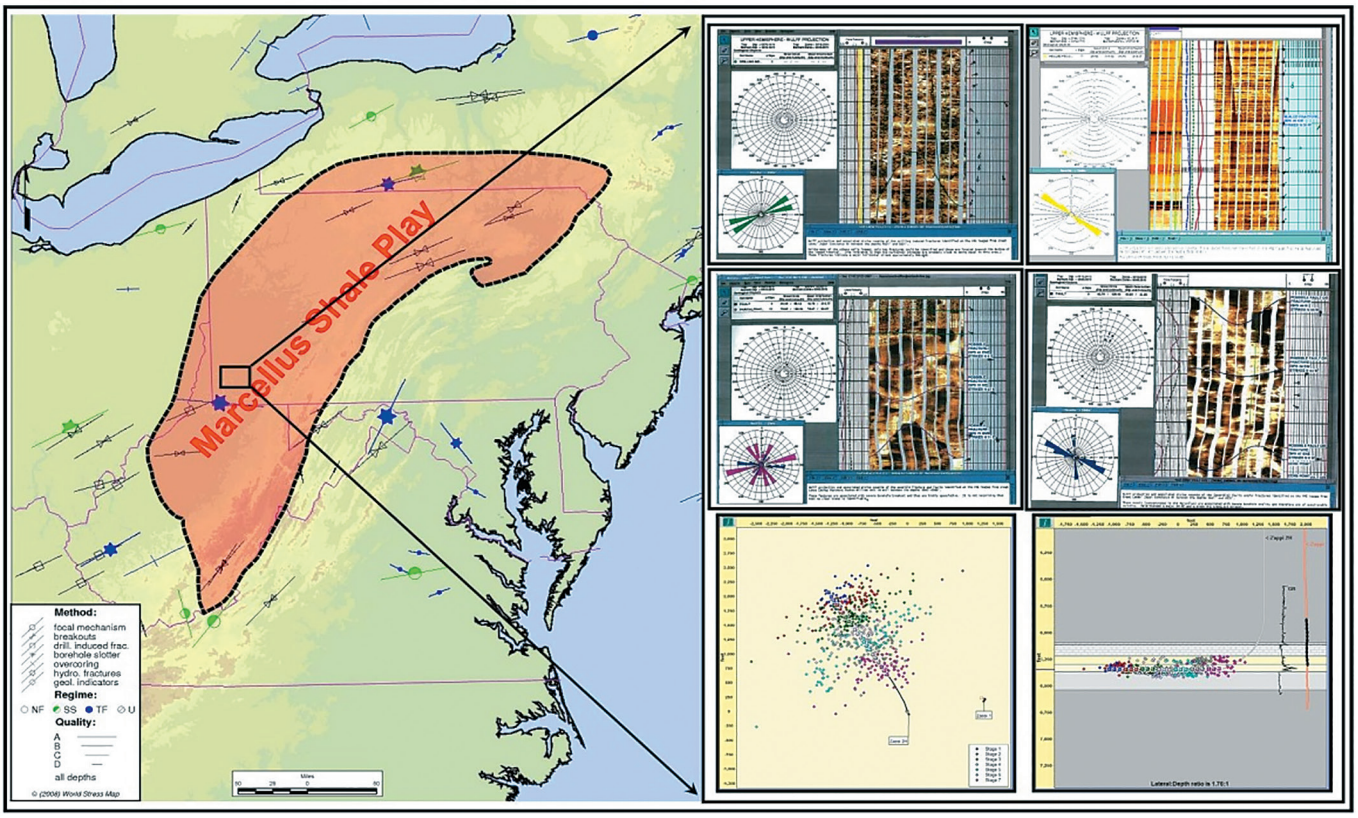

Figure 17. A stress map (modified from Heidbach et al., 2007) showing the observed SHmax trends, observed FMI features, and sample microseismic observations from the Marcellus shale play in southwestern Pennsylvania. Attached FMI images include (1) drilling-induced fractures (green), (2) healed natural fractures (yellow), (3) partially healed fractures (purple), and (4) possible faults (blue). Microseismic examples show the primary fracture growth direction in a northeast to southwest direction and good observed containment between the Tully limestone and Onondaga limestone intervals bounding the Marcellus shale (modified from Zagorski et al., 2012). FMI = formation microimaging; Drill. induced frac. = drilling-induced fracture; geol. indicators = geologic indicators; NF = normal faulted regime; SS = strike-slip faulted regime; TF = thrust faulted regime; U = unfaulted regime.

cores taken in the Marcellus shale interval. This appears to have a regional detrimental effect on Marcellus well productivity in the southwestern portions of the play.

CORE AREAS

Since the Marcellus play's vertical and horizontal commercialization in 2004 and 2007, two major core areas have developed along a 1295 km^2 (500 mi^2) southwest to northeast trending fairway (Figure 5). The prospective play area encompasses approximately 114,000 km^2 (44,030 mi^2) and includes large portions of Pennsylvania and northern West Virginia, as well as limited portions of eastern-most Ohio. Establishment of core producing areas is critical to effective development of unconventional shale plays. While the geographic extent of modern shale gas plays is enormous, as is their in-place reserve potential, they each possess wide variations in production capabilities, and the core areas are the portions that are most economically viable. Only a limited portion of each play has the optimal reserve potential and reservoir characteristics needed for economic development. This is highly dependent, both geographically and temporally, on gas and oil prices, rock quality, completion efficiencies, and the level of technologic advancement and understanding of each play. These core areas are typically estimated at 15 to 25% of any one play's geographic extent.

In the Marcellus play, productive potential of core versus noncore areas can vary by 100% or more on an EUR per 1000 ft (305 m) basis. Two major core areas have developed across the play trend: southwestern Pennsylvania and northern West Virginia and northeastern Pennsylvania. Interestingly, the initial discovery areas in southwestern and northeastern Pennsylvania

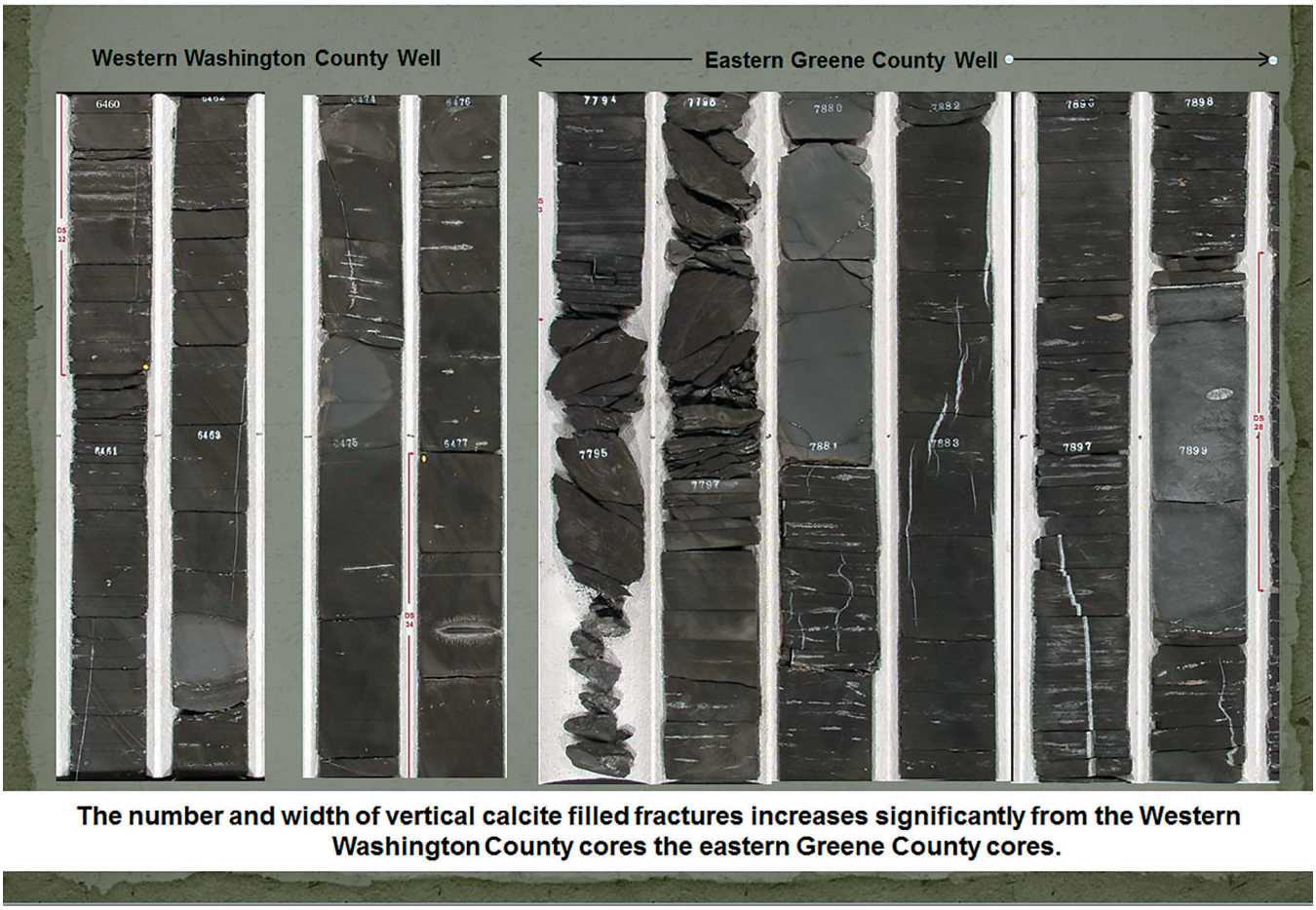

Figure 18. Comparison of two Marcellus cores in southwestern Pennsylvania showing increased natural fracturing from west to east. Core locations shown on Figure 9 and are in detail area on Figure 17 (modified from Zagorski et al., 2013).

that were most successful evolved to be the core areas within the Marcellus play. These core areas of the Marcellus play each display unique combinations of controlling geologic factors. Thickness, depth, net-to-gross ratios, organic content, intraorganic porosity, overpressure, thermal maturity, structural position, and degree of natural fracturing represent key factors. In addition to the core areas themselves, between these two established core areas, there are large underexplored areas that have excellent future potential for Marcellus development. Gas takeaway capacity has influenced the rate of exploration and development in this play to date. Several pipeline expansion projects will become operational after 2017 that will influence future exploration and development patterns in the Marcellus play.

SOUTHWESTERN CORE AREA

The southwest core area of the Marcellus play encompasses large areas of southwestern Pennsylvania and northern West Virginia. Shown on Figure 19 are the horizontal well control and thermal maturity R_o trends. The southwestern play area was established by Range Resources Corporation's 2004 Renz Unit 1 vertical completion and the successful Range Gulla 9H horizontal test in 2007. Horizontal results in this area range from less than 1 MMCFe/day for early tests to over 43 MMCFe/day. Estimated ultimate recoveries calculated from reported production data in Pennsylvania and West Virginia range from 2 to over 20 BCF of gas equivalent per horizontal well. On a EUR per 1000 ft basis, projected recoveries range from 1.0 to over 4.5 BCF/1000 ft. Gas-in-place calculations for the southwestern portion of the play range from 40 to more than 150 BCF/mi^2. Natural gas liquids (NGL) production is significant throughout much of this core area, with 281,000 to 1 million barrels or greater of recoverable NGL per lateral in key areas.

In this region, drilling depths in the Marcellus range from 1371 to 2439 m (4500 to 8000 ft), and the Marcellus has a gross thickness ranging from 15 to 30 m (50 to 100 ft). Some of the highest observed total organic content percentages, porosity, and permeability in the Marcellus play are observed in the southwestern core area. Here, the Marcellus is represented by a relatively thinner, but more condensed, sedimentary section with very high total organic content, a high net-to-gross pay ratio, and overall higher porosity and permeability. Key pay intervals are represented as maximum flooding surfaces within the Marcellus interval. Log and core data for the southwestern core portion of the play shows higher volumes of carbonate content and reduced clay volumes. This reflects lower sedimentation rates and a relatively distal position from sediment sources. Marcellus depositional patterns appear to be strongly influenced by basement faulting. Sedimentation rates appear low compared to other parts of the play, favoring the concentration of organic matter in the Marcellus shale. Typical log suites run in southwestern Pennsylvania display elevated gamma ray counts in the Marcellus shale compared with the northeastern part of the play. In the southwestern core area, key characteristics include high porosity and permeability, as well as high resistivity compared to the same intervals in the northeastern portion of the play. The key pore type in the Marcellus in the southeastern play is intraorganic porosity. Other pore types include intercrystalline/intergranular between pyrite crystals (which are significant in the southwest part of the play) and between platey clay crystals/grains. Silica (quartz), organic material, carbonates, and pyrite predominate in the southwestern play area.

Within the southwestern core areas of Marcellus play, thermal maturity observed is in the 1.0 to 2.8% R_o range. In the western-most portions of the southwestern play, thermal maturity is lower, and significant NGL production has been established. Pressure gradients in the southwest core range between 0.45 and 0.70 psi/ft. These overpressure trends closely coincide with the position of the Rome trough and thermal maturity levels of 1.0% R_o or higher. The best observed results are located in less tectonically disturbed areas west of the major fold belt structures of the Allegheny front (Chestnut ridge). Core, log, seismic, microseismic, and other data suggest that natural fracturing, while present throughout the Marcellus system, changes from a potential positive enhancer of reservoir quality in the west to a probable detriment to reservoir quality to the east. The thickness of the underlying Salina formation is considerably thinner in the southwestern core areas compared to the northeastern core area, suggesting that a higher regional level of natural fracturing present in the southwestern portions of the play translates into lower reservoir quality with less efficient completion potential. This is coincident with observed fold wavelength and intensity.

NORTHEASTERN CORE AREA

The northeastern core area of the Marcellus play encompasses large areas of northeastern Pennsylvania. Shown on Figure 20 are the horizontal well control and thermal maturity R_o trends. The northeastern play area was established by Cabot Oil & Gas Corporation's Ely 1 Unit vertical completion in December 2006 and subsequent horizontal tests completed in 2008. Horizontal results in this area range from less than 1 MMCFe/day from early tests to over 47.6 MMCFe/day.

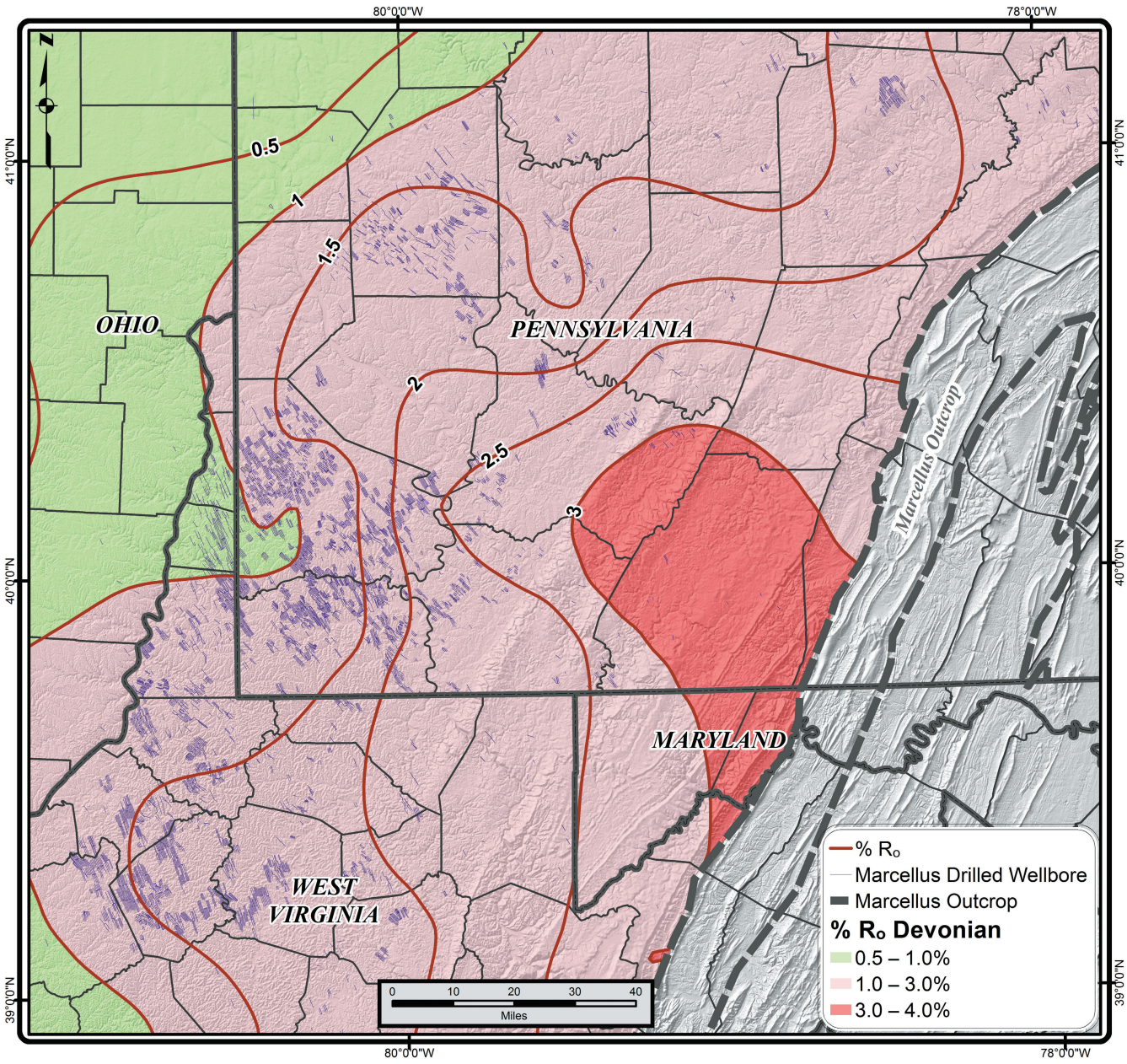

Figure 19. Map depicting Marcellus shale play southwestern core area, thermal maturity trends, and horizontal well development as of early 2016.

EUR calculations based on reported production data in Pennsylvania range from 2 to over 30 BCF per lateral. On a EUR per 1000 ft basis, projected recoveries range from 1.0 to over 5.0 BCF/1000 ft. Gas-in-place calculations for the northeastern portion of the play range from less than 75 to over 200 BCF/mi^2. Production from the northeast core area of the Marcellus is dry gas only with no liquid production.

In the northeastern core area, Marcellus typical TVD drilling depths range from 1067 to 2744 m (3500 to 9000 ft). The Marcellus attains a gross pay interval of 60 to 105 m (200 to 350 ft). Here, regional sedimentation rates appear to have been higher, favoring the additional clastic material concurrent with the deposition and preservation of organic matter. Well log and core data (Figure 14) show an expanded sedimentary section associated with greater levels of sediment influx. This is accompanied by an increase in clay deposition and overall reductions in carbonate content, suggesting a closer proximity to the source area compared with the southwestern Marcellus core area. The Marcellus here is represented by a relatively thick sedimentary section with fair-to-high total organic content and reduced net-to-gross pay ratios. Porosity and permeability values are somewhat lower

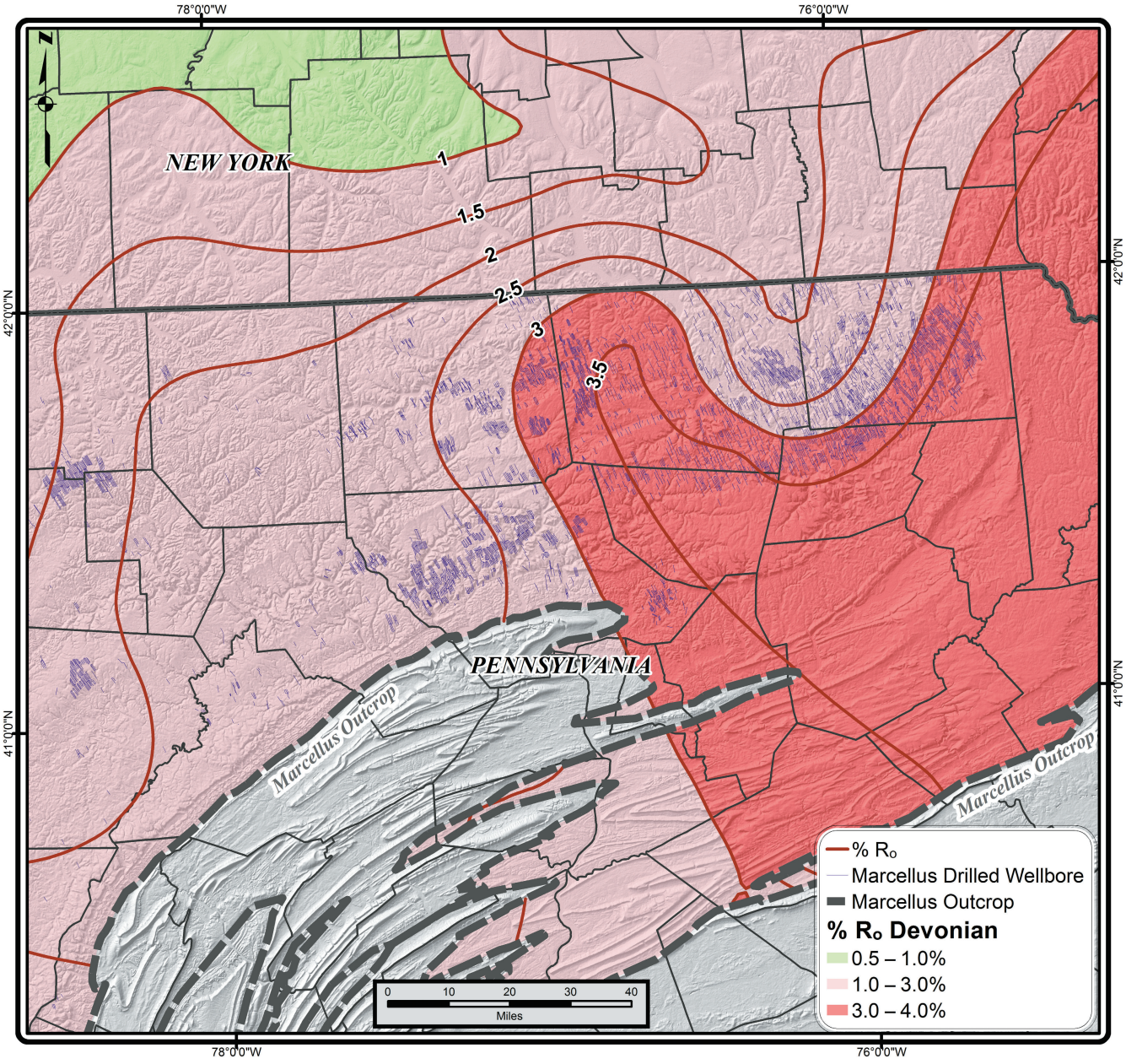

Figure 20. Map depicting Marcellus shale play northeasters core area, thermal maturity trends, and horizontal well development as of early 2016.

than the southern core region. Key pay intervals are represented as maximum flooding surfaces within the Marcellus interval. The key pore type in the Marcellus in the northeastern portion of the play is intraorganic porosity. Other pore types include intercrystalline/intergranular between pyrite crystals and platey clay crystals/grains. Silica (quartz), organic material, carbonates, and pyrite predominate in the northeast play area.

Within the northeastern portion of the Marcellus play, thermal maturity for established production is in the range of 2.0 to greater than 3.0% R_o. This suggests greater depth of burial history than the southwestern core area. Marcellus production in the northeastern play area is in the dry gas window with a BTU content of 1000 to 1050 due to the elevated thermal maturity levels. Eastern commercial limits to the Marcellus play in the northeastern area are well defined and are related to areas where the Marcellus has reached a thermal maturity level of greater than 3.3 to 3.5% R_o combined with increased structural complexity. In addition, the eastern limit appears to coincide with the eastern limits of Salina deposition. Pressure gradients in the northeast core range from 0.50 to more than 0.82 psi/ft. These are significantly higher than in the southwestern

core and represent the highest overpressure observed in the Marcellus play to date. In the northeastern core area, the Marcellus is generally more structurally complicated, with higher fold amplitudes and wavelength. Unlike the southwestern core area, significant Marcellus production is being developed relatively close to the Allegheny front. This may be attributed to broader fold wavelengths and a lesser degree of deformation at the Marcellus level caused by a tectonically thickened section of salt beds in the underlying Salina formation. However, the same dual role of natural fracturing and faulting is observed. In areas with extensive faulting and fracturing, the Marcellus is marginally productive, probably due to a breach of the Marcellus pressure cell and expulsion of gas and pressure from the Marcellus.

MARCELLUS SHALE RESOURCE POTENTIAL

There are enormous volumes of gas present within the Marcellus shale play. In 2013, the Marcellus shale became the largest producing gas field in the United States. Production reached approximately 16 BCFe /day in 2015 and is expected to reach over 20 BCFe /day by 2020. The Marcellus represents a continuous-type gas accumulation and when fully developed will be comprised of a large continuous field or series of fields. Engelder and Lash (2007) provided early recognition of the world-class potential of this resource at 50 tcf recoverable, which was quickly revised as the play grew. More recent estimates of the recoverable reserve potential range from 87 tcf and 3.5 billion bbl (USGS) to higher estimates of 489 tcf (Engelder, 2009). Other recent estimates fall within this general range.

Modern core and log analyses now show the Marcellus shale to have abundant to exceptional gas-in-place. A regional gas-in-place (GIP) map for the Marcellus play incorporating log, core, and pressure data is shown in Figure 21. This map assumes 1000 Btu, so in the liquids-rich regions, we are underestimating the total hydrocarbon-in-place. Gas-in-place estimates for the entire Marcellus play range from 40 to over 200 BCF/mi^2. Most development of the Marcellus shale is within areas of GIP greater than

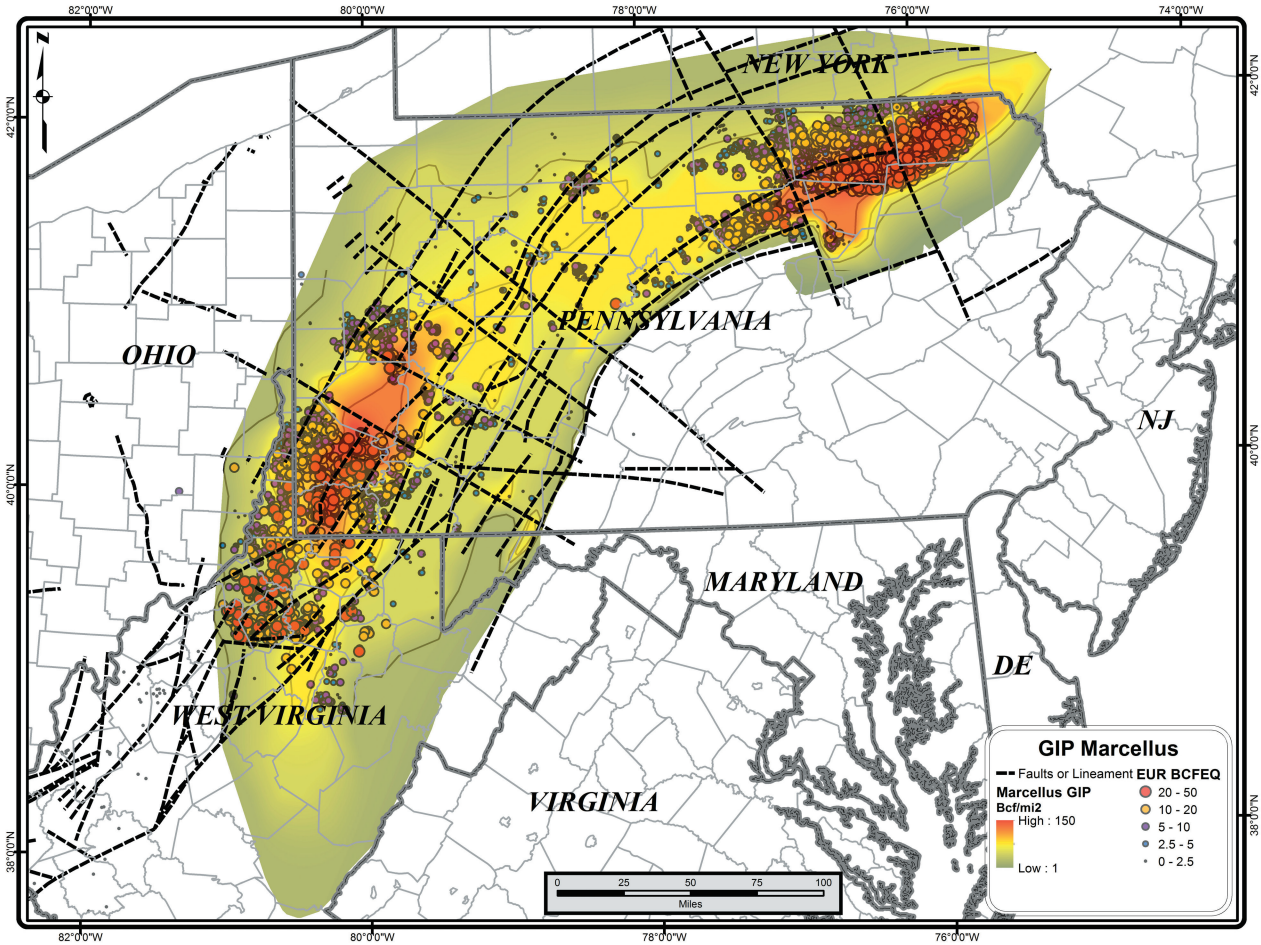

Figure 21. A map showing the gas-in-place trends for the Marcellus shale play and major basement faults. DC = District of Columbia; DE = Delaware; NJ = New Jersey.

50 BCF/mi^2. It is the authors' opinion that GIP values are being underestimated in the northeastern portion of the play, where some of the highest EUR wells are being drilled, yet GIP values are 100 to 200 BCF/mi^2. In the southwestern portion of the play, GIP values are also believed to be underestimated based on the higher hydrocarbon density and the 1100 to 1400 Btu value of the gas combined with the production of natural gas liquids. Initial nuclear magnetic resonance (NMR) log studies by Range Resources Corporation (RRC) and Schlumberger suggest similar findings when comparing standard log gas-in-place analysis with GIP calculations using NMR data. Other issues when calculating gas-in-place are accurate estimates (or lack) of pressure gradients, the negative effects of depletion and well interference, the significant contribution of adsorbed gas due to the high organic content of the Marcellus, and the effects of ethane absorption isotherms in liquids-rich areas.

When considering a giant field, it isn't just one horizon; it's all horizons comprising the play/field. The Marcellus play has significant stacked resource potential across most of its extent. There is excellent potential in the younger upper Devonian shale (Burket, Geneseo, Middlesex, and Rhinestreet) that lies above the Marcellus and from the deeper Ordovician-age Utica/Point Pleasant shale. Both of these associated plays have been successfully tested horizontally and have been steadily developed since 2010. The shallower upper Devonian shale units above the Marcellus and Tully intervals have now reached a level of testing, development, and characterization that supports the inclusion of these related/penetrated intervals to the resource assessment of the Marcellus play (Wrightstone, 2015). We believe that in the future when an adequate level of testing and characterization has been completed the deeper resource potential of the Ordovician-age Utica/Point Pleasant interval will be added to the resources/reserve estimates of the Appalachian basin Marcellus play.

Gas-in-place maps of the Marcellus, Burket/Geneseo/Rhinestreet, and combined Marcellus/Burket/Geneseo/Rhinestreet intervals are shown on Figures 21, 22, and 23. Using these maps and the

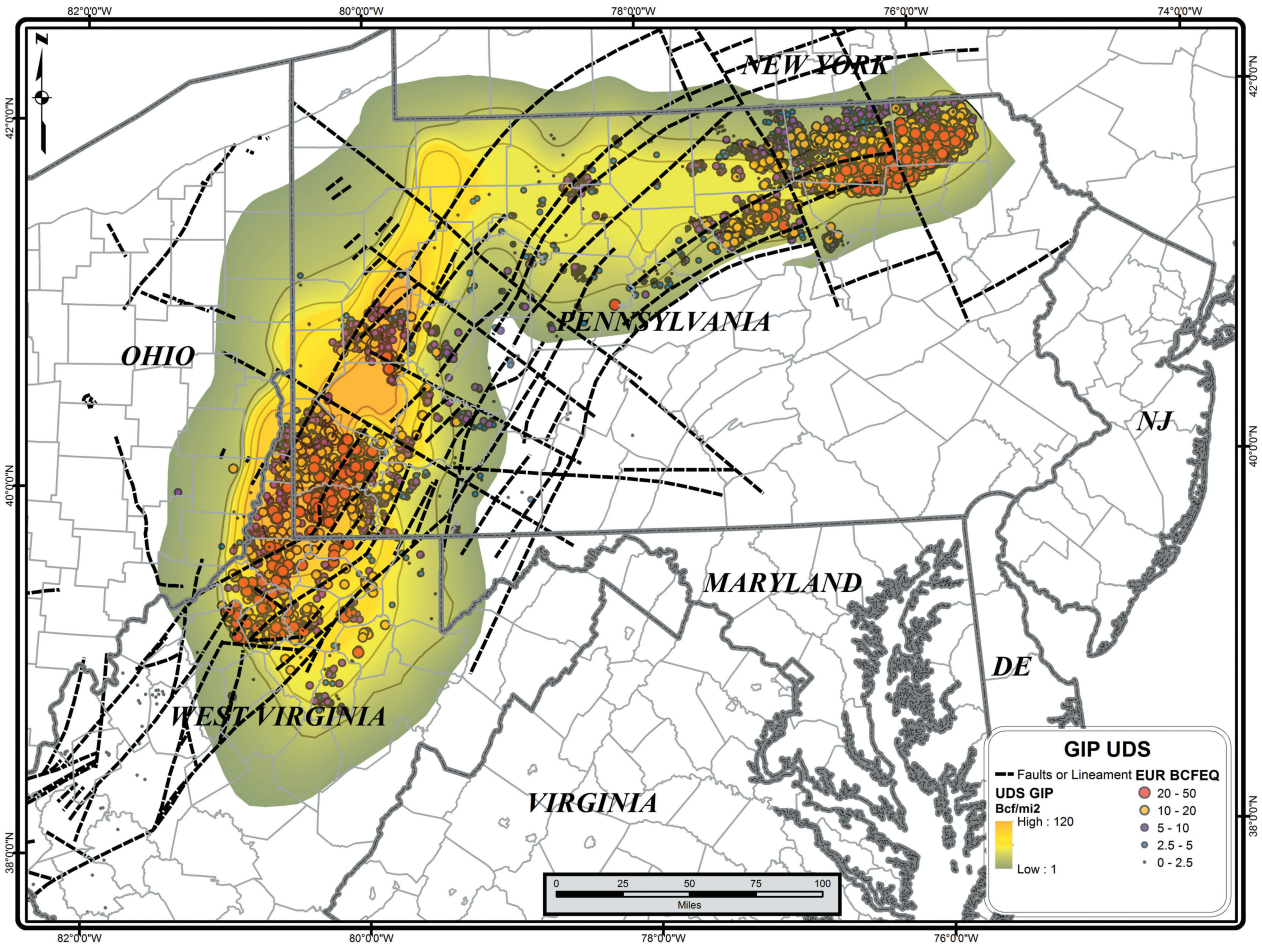

Figure 22. A map showing the gas-in-place trends for the middle Devonian Rhinestreet through Burkett shale interval and major basement faults. DC = District of Columbia; DE = Delaware; NJ = New Jersey.

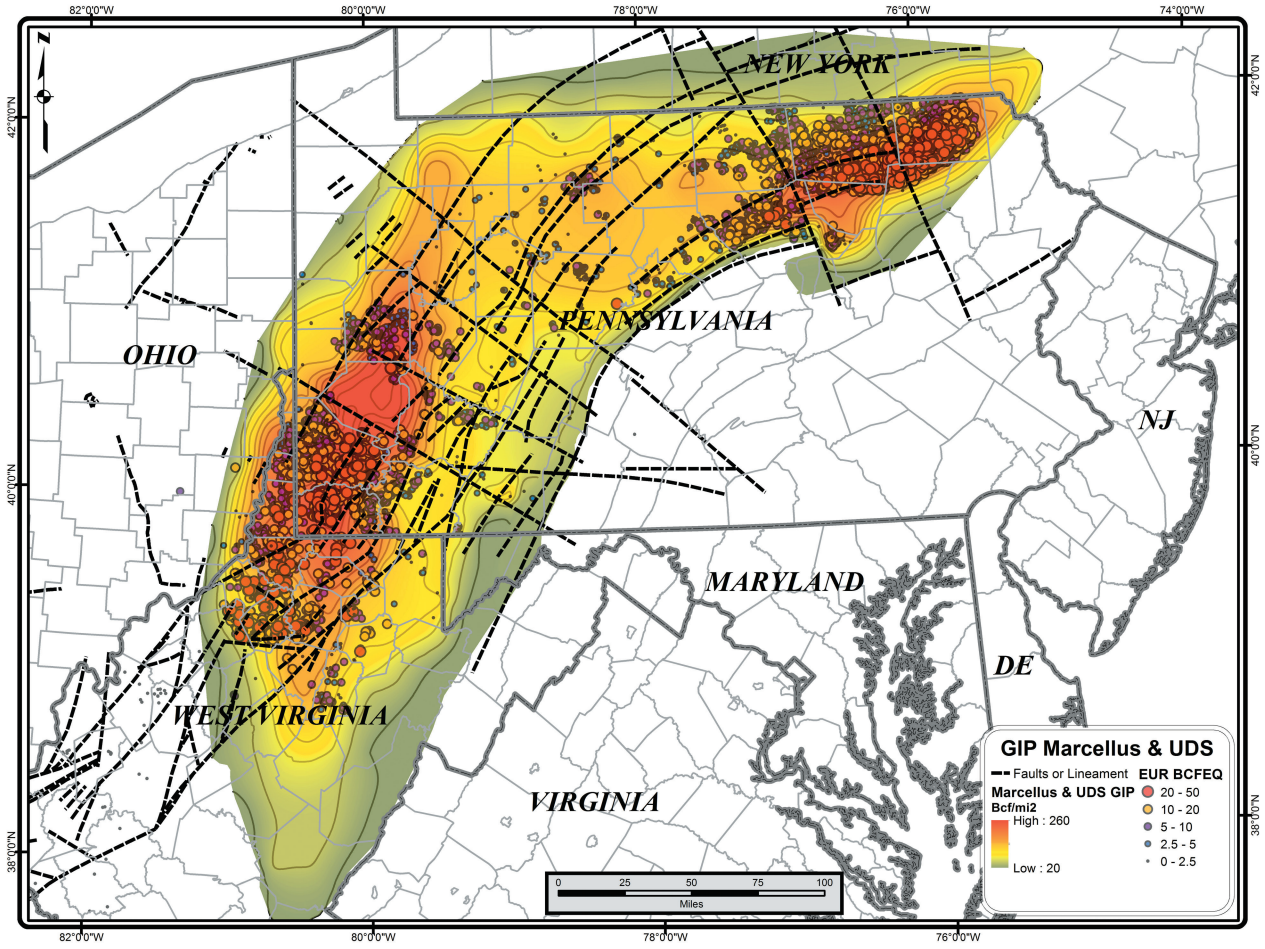

Figure 23. A map showing the gas-in-place trends for the combined Marcellus shale/Rhinestreet/Burket play and major basement faults. DC = District of Columbia; DE = Delaware; NJ = New Jersey.

regional play extents for the Marcellus and shallower upper Devonian shales suggests total in-place-gas resources of 2686 tcf for the Marcellus, 1012 tcf for the shallower Burket/Geneseo/Rhinestreet (upper Devonian shales), and 3698 tcf for the combined Marcellus /upper Devonian shale system. This calculated total GIP does not yet include the deeper Utica/Point Pleasant interval that, based on the very limited testing to date, may be highly productive across portions of the mapped Marcellus shale play. When compared to the gas-in-place estimates for the majority of top gas fields in the world, the Marcellus and the combined Marcellus /upper Devonian shales easily demonstrate in-place resources greater than the North Pars field. Another interesting comparison is that the total gas-in-place estimated for the combined Marcellus/upper Devonian shale (3698 tcf) is almost as great as the calculated gas-in-place for all of the conventional gas fields (3847 tcf).

The map in Figure 24 and Table 1 depicts the top 15 gas fields in the world together with their estimated in-place reserves and estimated recoverable reserves (Sandrea, 2006a; Sandrea, 2006b). Estimated reserve potential ranges from 40 to 1400 tcf. On a recoverable reserve basis, the Marcellus play comes in at number 2 behind the South Pars/North Dome field in Iran and Qatar. When compared on the basis of in-place reserves, the Marcellus clearly is significantly larger than all of the conventional giant fields. When the range of the recent reserve estimates for the Marcellus is compared against these top worldwide fields, the scope of the Marcellus play is clearly apparent.

ECONOMIC IMPACT OF THE MARCELLUS SHALE

Results from Marcellus wells continue to improve despite a declining rig count since 2012 and drops in commodity prices in 2014. When the Marcellus was first commercialized, conventional wisdom was that the EURs for the Marcellus wells might be 2.5 to 3.5

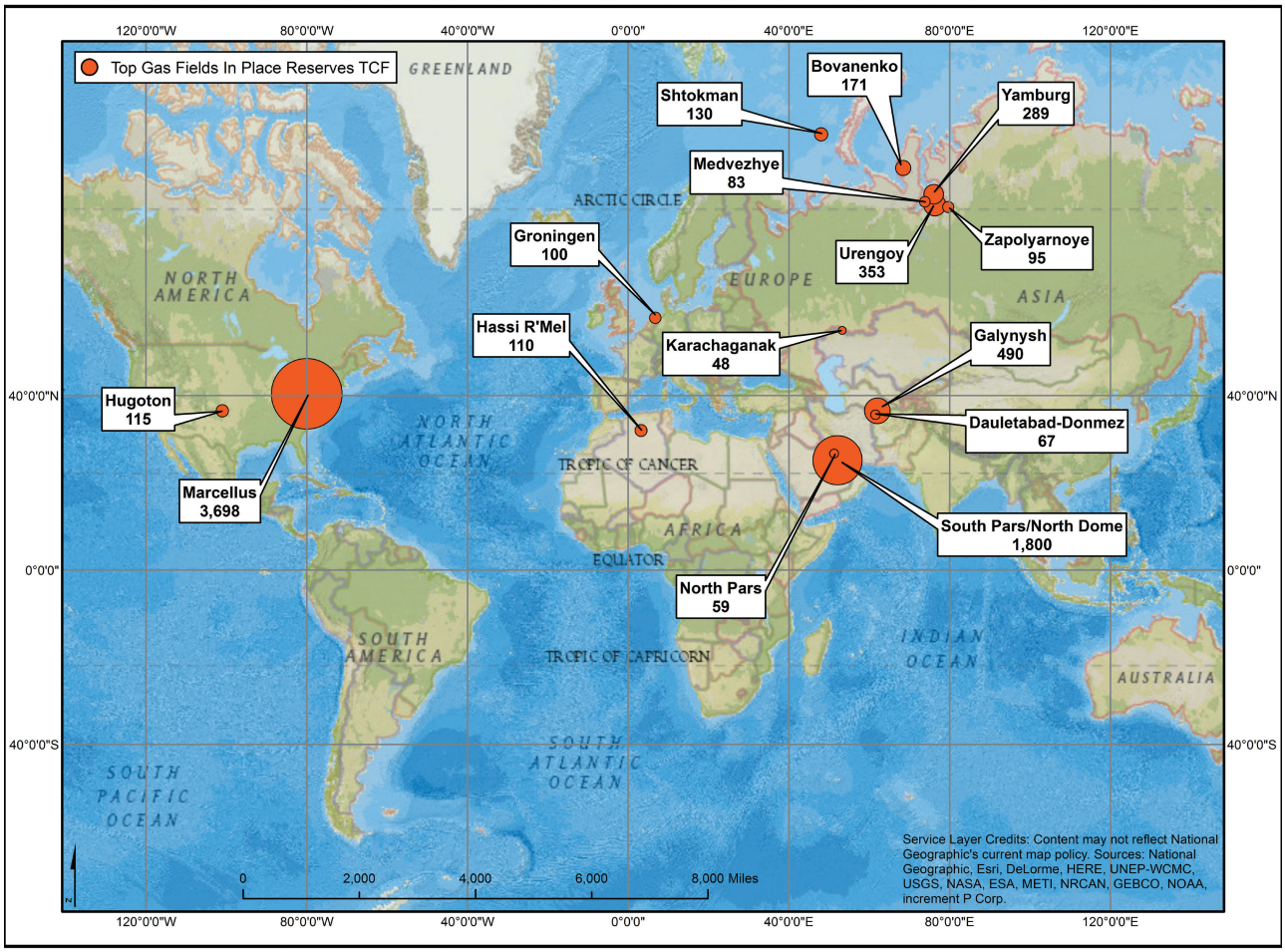

Figure 24. Map depicting the largest gas fields in the world and comparisons of in-place gas reserves and projected recoverable reserves (Marcellus reserve estimates from this study; Engelder [2009] and Wrightstone [2015]; worldwide reserve estimates from Sandrea [2006]).

BCF of gas equivalent per well, using the Barnett shale play as an analog. Drilling efficiency improvements, improved lateral targeting, optimizing completions, and longer laterals combined to drive the Marcellus shale well average EUR to 8.9 BCF of gas equivalent per well in 2014. This current study documents technical accessible in-place gas reserves in the Marcellus ranging from 2322 to 3698 tcf. This demonstrates the Marcellus gas system to be largest documented in-place gas reserves in the world. Marcellus liquids production now is supplying the northeastern United States, and Marcellus NGLs will soon be exported internationally. The Marcellus is transforming how natural gas moves across the United States. Instead of bringing Rocky Mountain gas east, the Marcellus gas now displaces gas from the Rockies Express pipeline.

The Marcellus play has been transformative to industry, economy, and environment. In 1979, the gas reserve life index in the United States was roughly estimated at about 10 years. Today, it is estimated to be at least 100 years, and some projections estimate over 200 years of reserve life. In less than a decade, the United States went from a country that was short of gas to one of the largest-producing nations in the world. Due to the abundance of natural gas, U.S. prices are now extraordinarily competitive. The price of natural gas in the United States as of early 2016 was approximately $2.40/MCF (million cubic feet). By comparison, in Europe, the cost of gas is $6.00 to $7.00/MCF, and in places around the world—including Japan and China—the price for gas is about $7.00 to $8.00/MCF. This abundance and low price has led to the rebirth of American manufacturing. The petrochemical industry overseas was using naphtha derived from crude oil as its main feedstock to manufacture products such as ethylene and plastics. Now, many are considering converting to ethane processed from natural gas as feedstock instead of naphtha. This is allowing some

Table 1. Summary of gas-in-place and recoverable reserves for top 15 gas fields worldwide.

Ranking	Field Name	Country	Size (km^3)	In-Place Reserves (tcf)	Recoverable Reserves (tcf)
1	South Pars/North Dome	Iran and Qatar	35,000	1800	1235
2	Marcellus	United States	148,000	3698	489
3	Urengoy	Russia	6300	353	222
4	Yamburg	Russia	3900	289	138
5	Hassi R' Mel	Algeria	3500	110	123
6	Shtokman	Russia	3100	130	110
7	Galynysh	Turkmenistan	2800	490	98
8	Zapolyarnoye	Russia	2700	95	95
9	Hugoton[a]	United States	2300	115	81
10	Gronigen	Netherlands	2100	100	73
11	Bovanenko	Russia	2000	171	70
12	Medvezhye	Russia	1900	83	68
13	North Pars	Iran	1400	59	48
14	Dauletabad-Donmez[a]	Turkmenistan	1300	67	47
15	Karachaganak	Kazakhstan	1300	48	46
	Total GIP: All Fields			**7608**	
	Total GIP: Marcellus/UDS System			**3698**	
	Total GIP: Conventional Systems Only			**3910**	

[a]Published gas-in-place data not available. Gas-in-place estimated based on published recoverable reserves is assumed to be 70% of total GIP.

petrochemical industries to move back to the United States. Thanks to lower energy prices, the United States has provided an estimated $113 billion annual utility savings for domestic consumers.

The United States is now supplying about 84% of its energy needs. In contrast, in the mid-1970s, the consensus was that the United States was running out of oil and natural gas. But with the development of domestic resources such the Permian basin as well as Bakken and Eagleford plays, oil imports have dropped to levels of roughly 40%. This reduced dependency on foreign oil is due almost solely to the ingenious work of America's oil and gas industry. The success has been so significant that some projections suggest that by 2025, North America may be energy secure. The abundance of low-cost natural gas is changing how we generate electricity. These developments have had positive impacts not only on the cost of electricity but also on the quality of our environment. In 2003, natural gas supplied about 17% of power generation and in 2015, it reached about 30%. Coal historically has provided a large energy source to generate electricity in the United States, but now its share has decreased from 51 to 37%, with natural gas now providing a much bigger share of the fuel used for power generation.

Natural gas has many positive environmental benefits. It produces no sulfur dioxide, no nitrous oxide, and no mercury. It doesn't contain the particulates that burning coal releases and has about half the $C0_2$ content and therefore is a significantly better fuel environmentally and for public health. Based on a recent U. S. Environmental Protection Agency (EPA) reports, there has been a 14% decrease in toxic air emissions from the last reporting period in the mid-Atlantic region. Importantly, $C0_2$ reduction in the United States has been about two times what the entire world reduction has been over the past 20 years.

Finally, the Marcellus story is still unfolding. Our current estimates of gas-in-place and recoverable reserves are still evolving. Future technological breakthroughs not yet considered could further impact the ultimate recovery from this play. In addition, the potential for additional in-place and recoverable gas reserves from the Utica/Point Pleasant interval appears very promising across much of the Marcellus play area. Perhaps that will be the next giant unconventional discovery story of the current decade.

ACKNOWLEDGMENTS

The authors thank the senior management of Range Resources Corporation for their support and permission to publish. Special thanks go to Ray Walker, Alan

Farquharson, and John Applegath of Range Resources for their long-term vision and consistent encouragement in the process of unlocking and understanding the Marcellus shale play. Special thanks also to the excellent long-term research and mapping support provided by Range Resources Geoscience staff with special mention of Brad Hina, Chuck Moyer, Douglas Bowman, James Morris, Jared Van Meter, Nathan Dowey, Doug Odham, Mark Limbruner, Chris Pounds, Toni Eilerts, Steve Poe, Carl Dokter, Doug Odham, Taylor McClain, Matt Weber, Magell Candelaria, Josh Kuhn, and Chaoqing Yang. We also wish to acknowledge Mike Forrest and Jim Funk for their excellent long-term support and critical peer review. Sincere thanks and acknowledgment for the critical engineering and operational contributions and support from Range's engineering groups, with special mention of Mike Middlebrook, Dennis Degner, Don Robinson, Brad Grandstaff, Ken Brown, Joe Frantz, Zhong He, Greg Frazier, and Andrew Tullis. We also gratefully acknowledge the efforts of Core Lab, Geomark, Halliburton, Ingrain, Schlumberger, and Terra Tek for their excellent technical contributions to the understanding of this giant play.

REFERENCES CITED

Blakey, R., 2005, Global paleogeography, accessed October 10, 2015, http://jan.ucc.nau.edu/~rcb7/globaltext2.html.

Boyce, M., and T. Carr, 2010, Stratigraphy and petrophysics of the middle Devonian black shale interval in West Virginia and southwest Pennsylvania: AAPG ACE Conference Poster Proceedings, accessed January 9, 2017, http://www.searchanddiscovery.com/pdfz/documents/2010/10265boyce/ndx_boyce.pdf.html.

Cabot Oil and Gas, 2009, Cabot Oil & Gas Corporation discussion handout: Enercom 2009 Oil & Gas Conference of August 10, 2009, accessed January 9, 2016, http:www.cabotog.com/pdfs/Londonoil&gasconference09_presentation.pdf.

Canich, M. R., and D. P. Gold, 1977, A study of the Tyrone-Mt. Union lineament by remote sensing techniques and field methods: State College, Pennsylvania, Office of Remote Sensing and Earth Resources (ORDER) Technical Report 120-137, Pennsylvania State University, p. 59.

Colton, G. W., 1970, The Valley and Ridge and Appalachian Plateau: Stratigraphy and sedimentation; The Appalachian basin. Its depositional sequences and their geologic relationships, *in* G. W. Fisher, F. J. Pettijohn, and J. C. Reed Jr., eds., Studies of Appalachian geology: Central and southern: New York, New York, Interscience Publishers, p. 5–47.

Demaison, G. J., and G. T. Moore, 1980, Anoxic environments and oil source bed genesis: AAPG Bulletin, v. 64, p. 1179–1209.

de Witt, W., Jr., J. B. Roen, and L. G. Wallace, 1993, Stratigraphy of Devonian black shales and associated rocks in the Appalachian basin, *in* J. B. Roen and R. C. Kepferle, eds., Petroleum geology of the Devonian and Mississippian black shale of eastern North America: USGS Bulletin 1909, p. M1–M16.

Engelder, T., 2009, Marcellus 2008: Report card on breakout year for gas production in the Appalachian basin: Fort Worth Basin Oil and Gas Magazine, August, p. 18–22.

Engelder, T., G. G. Lash, and R. S. Uzcategui, 2009, Joint sets that enhance production from middle and upper Devonian gas shales of the Appalachian basin: AAPG Bulletin, v. 93, no. 7, p. 857–889.

Ettensohn, F. R., 1985a, The Catskill Delta complex and the Acadian Orogeny: A model, *in* D. W. Woodrow and W. D. Sevon, eds., The Catskill Delta: Geological Society of America Special Paper 201, p. 39–49.

Ettensohn, F. R., 1985b, Controls on development of Catskill Delta complex basis facies, *in* D. W. Woodrow and W. D. Sevon, eds., The Catskill Delta: Geological Society of America Special Paper 201, p. 65–77.

Ettensohn, F. R., 1992, Controls on the origin of the Devonian–Mississippian oil and gas shales, east-central United States: Fuel, v. 71, p. 1487–1492.

Ettensohn, F. R., 2004, Modeling the nature and development of major Paleozoic clastic wedges in the Appalachian basin, USA: Journal of Geodynamics, v. 37, p. 657–681.

Faill, R. T., 1985, The Acadian orogeny and the Catskill Delta, *in* D. W. Woodrow and W. D. Sevon, eds., The Catskill Delta: Geological Society of America Special Paper 201, p. 15–37.

Flaherty, K. J., 1992, Fractured middle Devonian Huntersville Chert and lower Devonian Oriskany sandstone, *in* John B. Roen and Brian J. Walker, eds., The Appalachian Oil and Natural Gas Research Contortium: The atlas of major Appalachian gas plays, p. 103–108.

Frey, M. G., 1973, Influence of Salina salt on structure in New York-Pennsylvania part of the Appalachian plateau: AAPG Bulletin, v. 57, no. 6, p. 1027–1037.

Gwinn, V. E., 1964, Thin-skinned tectonics in the Plateau and northwestern Valley and Ridge provinces of the central Appalachians: Geological Society of America Bulletin, v. 75, no. 9, p. 863–900.

Hamilton-Smith, T., 1993, Stratigraphic effects of the Acadian orogeny in the autochthonous Appalachian basin, *in* D. C. Roy and J. W. Skehan (eds.), The Acadian orogeny: Recent studies in New England, maritime Canada, and the authochthonous foreland: Geological Society of America, Special Paper, v. 275, p. 153–164.

Harper, J. A., 1992, Lower Devonian Oriskany sandstone structural play, *in* Gas Research Institute: The atlas of major Appalachian gas plays, p. 109–117.

Harper, J. A., 2008, The Marcellus shale: An old "new" gas reservoir in Pennsylvania: Pennsylvania Geology, v. 38, no. 1, p. 2–13.

Harper, J. A., and C. D. Laughrey, 1987, Geology of the oil and gas fields of southwestern Pennsylvania: Commonwealth of Pennsylvania Mineral Resource Report no. 87, p. 91–97.

Heidbach, O., K. Fuchs, B. Muller, J. Reinecker, B. Sperner, M. Tingay, et al., eds., 2007, The world stress map: Release

2005: Paris, Commission for the Geological Map of the World.

Hunter, C. D., 1935, Natural gas in Eastern Kentucky, *in* Henry A. Ley, ed., Geology of Natural Gas: AAPG Special Publication 7, p. 915–947.

Inks, T. L., T. Engelder, E. Jenner, B. Golob, J. S. Hocum, and D. G. O'Brien, 2015, Marcellus fracture characterization using P-wave azimuthal velocity attributes: Comparison with production and outcrop data: Interpretation, v. 3, no. 3, p. SU1–SU15.

Jarvie, D. M., R. J. Hill, and R. M. Pollastro, 2005, Assessment of the gas potential and yields from shales: The Barnett shale model, *in* Brian J. Cardott, ed., Unconventional Energy Resources in the Southern Midcontinent, 2004 symposium: Oklahoma Geological Survey Circular 110, p. 37–50.

Kohl, D., R. Slingerland, M. Arthur, R. Bracht, and T. Engelder, 2014, Sequence stratigraphy and depositional environments of the Shamokin (Union Springs) member, Marcellus formation, and associated strata in the middle Appalachian basin: AAPG Bulletin, v. 98, no. 3, p. 483–513.

Kulander, C. S., and R. T. Ryder, 2005, Regional seismic lines across the Rome trough and Allegheny plateau of northern West Virginia, western Maryland, and southwestern Pennsylvania, USGS Geologic Investigations Series Map I-2791, accessed January 9, 2017, https://pubs.er.usgs.gov/publication/pp1708E.5.1.

Lash, G. G., 2008, Stratigraphy and fracture history of the middle & upper Devonian succession, western New York: Significance to basin evolution and hydrocarbon exploration: Pittsburgh Association of Petroleum Geologists unpublished field trip guide, p. 85.

Lash, G. G., and Terry Engelder, 2009, The middle Devonian Marcellus shale: A record of eustacy and basin dynamics (abs.): AAPG Annual Convention and Exhibition, accessed September 21, 2016, http://www.searchanddiscovery.com/abstracts/html/2009/annual/abstracts/lash.htm.

Lash, G. G., 2009, Sequence stratigraphic framework of the middle Devonian Marcellus shale (abs.): AAPG 2009 Eastern Section Meeting, accessed September 21, 2016, http://www.searchanddiscovery.com/abstracts/html/2009/eastern/abstracts/lash.htm.

Lash, G. G., and T. Engelder, 2008, Marcellus shale subsurface stratigraphy and thickness trends: Eastern New York to northeastern West Virginia (abs.): AAPG Eastern Section Meeting and http://www.papgrocks.org/lash_p.pdf.

Lash, G. G., and T. Engelder, 2011, Thickness trends and sequence stratigraphy of the middle Devonian Marcellus formation, Appalachian basin: Implications for Acadian foreland basin evolution: AAPG Bulletin, v. 95, no. 1, p. 61–103.

Lash, G. G., and E. P. Lash, 2014, Early history of the natural gas industry, Fredonia, New York: Search and Discovery Article #70000.

Lavin, P. M., D. L. Chaffin, and W. F. Davis, 1982, Major lineaments and the Lake Erie–Maryland crustal block: Tectonics, v. 1, p. 431–440.

Lee, K. D., 1980, Subsurface structure of the eastern Kentucky gas field: Unpublished M.S. thesis, West Virginia University, 52 p.

Macquaker, J., D. McIlroy, S. J. Davies, and M. A. Keller, 2009, Not anoxia! How do you preserve organic matter then? (abs.): AAPG Annual Convention and Exhibition.

Milici, R. C., 2005, Assessment of undiscovered natural gas resources in Devonian black shales, Appalachian basin, eastern U.S.A.: USGS Open-file report, accessed September 15, 2009, http://pubs.usgs.gov/of/2005/1268/2005-1268.ppt#313.

Milici, R. C., and C. S. Swezey, 2006, Assessment of Appalachian Basin oil and gas resources: Devonian shale–Middle and Upper Paleozoic total petroleum system: USGS Open-file Report, accessed January 9, 2017, https://pubs.usgs.gov/of/2006/1237/of2006-1237.pdf, 70 p.

Murphy, A. E., 2000, Physical and biochemical mechanisms of black shale deposition, and their implications for ecological and evolutionary change in the Devonian Appalachian basin: Unpublished Ph.D. dissertation, Northwestern University, 363 p.

Negus-deWyss, J., 1979, The eastern Kentucky gas field: A geological study of the relationship of oil shale gas occurrence to structure, stratigraphy, lithology, and inorganic geochemical parameters: Unpublished Ph.D. dissertation, West Virginia University, 199 p.

Pollastro, R. M, D. M. Jarvie, R. J. Hill, and C. W. Adams, 2007, Geologic framework of the Mississippian Barnett shale, Barnett-Paleozoic total petroleum system, Bend arch-Fort Worth basin, Texas: AAPG Bulletin, v. 91 no. 4, p. 405–436.

Powell, M. E., and W. Brackett, 2009, Best Barnett shale wells based on peak month daily average: Powell Barnett Shale Newsletter, July, p. 9.

Powell, M. E., and W. Brackett, 2015, Best Barnett shale wells based on peak month daily average: Powell Barnett Shale Newsletter, August 21, p. 9.

Range Resources Corporation, 2010, Range Resources company presentation, August: accessed August 2010, Unpublished internal document, Range Resources Corporation.

Reed, J. R., and D. Dunbar, 2008, Using ArcGIS to estimate thermogenic gas generation volumes by upper and middle Devonian shales in the Appalachian basin (abs.): AAPG Eastern Section Meeting, 2008.

Repetski, J. E., R. T. Ryder, J. A. Harper, and M. H. Trippi, 2002, Thermal maturity patterns (CAI and $\%R_o$) in the Ordovician and Devonian rocks of the Appalachian basin in Pennsylvania: U.S. Geological Survey Open-File Report 2002-302, 57 p.

Repetski, J. E., R. T. Ryder, K. L. Avary, and M. H. Trippi, 2005, Thermal maturity patterns (CAI and $\%R_o$) in the Ordovician and Devonian rocks of the Appalachian basin in West Virginia: U.S. Geological Survey Open-File Report 2005-1078, 72 p.

Repetski, J. E., R. T. Ryder, D. J. Weary, A. G. Harris, and M. H. Trippi, 2008, Thermal maturity patterns (CAI and $\%R_o$) in the Ordovician and Devonian rocks of the Appalachian

basin: A major revision of USGS Map I-917 using new subsurface collections: U.S. Geological Survey Scientific Investigations Map 3006.

Robinson, J. E., 1985, Development of gas-bearing reservoirs in the Trenton limestone formation of New York: New York State Energy and Development Authority (NYSERDA) Report: New York, The Authority, p. 85-18.

Rodgers, M. R., and T. H. Anderson, 1984, Tyrone-Mt. Union cross-strike lineament of Pennsylvania: A major Paleozoic basement fracture and uplift boundary: AAPG Bulletin, v. 68, p. 92–105.

Rowan, E. L., 2006, Burial and thermal history of the central Appalachian basin, based on three 2-D models of Ohio, Pennsylvania, and West Virginia: USGS Open File Report 2006-1019, accessed January 10, 2017, https://pubs.er.usgs.gov/publication/ofr20061019.

Rowan, E. L., R. T. Ryder, J. L. Repetski, M. H. Trippi, and L. F. Ruppert, 2004, Initial results of a 2D burial/thermal history model: Central Appalachian basin, Ohio and West Virginia: USGS Open File Report 2004-1445, 37 p.

RSEG (Ross Smith Energy Group, Ltd.), 2007, The Marcellus shale: Get your lease on: RSEG Alert December 12, 7 p.

Ryder, R. T., M. H. Trippi, C. S. Swezey, R. C. Milici, J. E. Repetski, L. F. Ruppert, et al., 2011, A regional perspective of the Devonian shale and Ordovician Utica shale total petroleum systems of the Appalachian basin: AAPG Search and Discovery Article #90131, accessed September 21, 2016, http://www.searchanddiscovery.com/pdfz/abstracts/pdf/2011/eastern/abstracts/ndx_ryder.pdf.html.

Sageman, B. B., A. E. Murphy, J. P. Werne, C. A. Ver Straeten, D. J. Hollander, and T. W. Lyons, 2003, A tale of shales: The relative role of production, decomposition, and dilution in the accumulation of organic-rich strata; Middle–upper Devonian, Appalachian basin: Chemical Geology, v. 195, p. 229–273.

Sandrea, R., 2006a, Global natural gas reserves: A heuristic viewpoint (part 1 of 2): Middle East Economic Survey, v. 49, no. 11, accessed January 10, 2017, http://archives.mees.com/issues/298/articles/12167.

Sandrea, R., 2006b, Global natural gas reserves: A heuristic viewpoint (part 2 of 2): Middle East Economic Survey, v. 49, no. 11, accessed May 1, 2007, http://www.mees.com/postedarticles/oped/v49n12-5OD01.htm.

Sanford, B. V., 1993, St. Lawrence platform-economic geology, *in* D. F. Stott and J. D. Aitken, eds., Sedimentary cover of the craton in Canada: Boulder, Colorado, Geological Society of America, p. 787–798.

Scanlin, M. A., and T. Engelder, 2003, The basement versus the no-basement hypothesis for folding within the Appalachian plateau: Detachment sheet: American Journal of Science, v. 303, p. 519–563.

Schmoker, J. W., 1981a, Determination of organic-matter content of Appalachian Devonian shales from gamma-ray logs: AAPG Bulletin, v. 65, no. 7, p. 1285–1298.

Schmoker, J. W., 1981b, Organic-matter content of Appalachian Devonian shales determined by use of wire-line logs: Summary of work done 1976–80: U.S. Geological Survey, accessed January 9, 2017, https://pubs.er.usgs.gov/publication/ofr81181.

Shumaker, R. C., 1993, Structural parameters that affect Devonian shale gas production in West Virginia and eastern Kentucky, *in* J. B. Roen and R. C. Kepferle, eds., Petroleum geology of the Devonian and Mississippian black shale of eastern North America: USGS Bulletin 1909, p. K1–K38.

Shumaker, R. C., 1996, Structural history of the Appalachian basin, *in* J. B. Roen and B. J. Walker, eds., The atlas of major Appalachian gas plays: Morgantown, West Virginia, West Virginia Geological Survey, p. 8–10.

Van Tyne, A. M., 1993, Detailed study of Devonian black shales encountered in nine wells in western New York state, *in* J. B. Roen and R. C. Kepferle, eds., Petroleum geology of the Devonian and Mississippian black shale of eastern North America: USGS Bulletin 1909, p. M1–M16.

Ventura, J. L., 2013, Range's path to discovery and commercialization of the Marcellus shale:

The largest producing gas field in the United States: Search and Discovery Article 110165, 2013 Michael T. Halbouty Presentation and Award, AAPG National Conference, Pittsburgh, Pennsylvania.

Ventura, J. L., et al., 2013, The Discovery of the Marcellus shale Play, An Operator's Experience: URTeC Conference Proceedings, accessed January 9, 2017, http://library.seg.org/doi/abs/10.1190/urtec2013-077.

Wendt, A. K., M. A. Arthur, R. Slingerland, D. Kohl, R. Bracht, and T. Engelder, 2015, Geochemistry and depositional history of the Union Springs member, Marcellus formation in central Pennsylvania: Interpretation, v. 3, no. 3, p. SV17–SV33.

Werne, J. P., B. B. Sageman, T. W. Lyons, and D. J. Hollander, 2002, An integrated assessment of a "type euxinic" deposit: Evidence for multiple controls on black shale deposits in the middle Devonian Oatka Creek formation: American Journal of Science, v. 302, p. 110–143.

Wheeler, R. L., 1980, Cross-strike structural discontinuities: Possible exploration tool for natural gas in Appalachian overthrust belt: AAPG Bulletin, v. 64, no. 12, p. 2166–2178.

Williams, H., and R. D. Hatcher, 1982, Suspect terranes and accretionary history of the Appalachian orogen: Geology, v. 10, p. 530–536.

Woodrow, D. L., and W. D. Sevon, eds., 1985, The Catskill delta: Geological Society of America, Special Paper, 246 p.

Wrightstone, G. R., 2015, Burket/Geneseo shale: Appalachia's little brother to the Marcellus and Utica: PAPG Eastern Section Meeting.

Yang C., D. Bowman, J. Morris, and W. Zagorski, 2013, Marcellus shale asset optimization through increased geological understanding: Search and Discovery Article 41144, accessed September 20, 2016, http://www.searchanddiscovery.com/pdfz/documents/2013/41144yang/ndx_yang.pdf.html.

Zagorski, W. A., 2010, The Appalachian Marcellus shale play: Discovery thinking, timing and technology: Search and Discovery Article 110138, accessed September 20, 2016, http://www.searchanddiscovery.com/pdfz/documents/2010/110138zagorski/ndx_zagorski.pdf.html.

Zagorski, W. A., G. R. Wrightstone, and D. C. Bowman, 2012, The Appalachian basin Marcellus gas play: Its history of development, geologic controls on production, and future potential as a world-class reservoir, *in* J. A. Breyer, ed., Shale reservoirs: Giant resources for the 21st century: AAPG Memoir 97, p. 172–200.

Zagorski, W. A., D. C. Bowman, M. Emery, and G. R. Wrightstone, 2011, An overview of some key factors controlling well productivity in core areas of the Appalachian basin Marcellus shale play: 2011 AAPG National Conference, Houston, Texas.

Zagorski, W. A., D. Bowman, J. Morris, and C. Yang, 2013, Marcellus shale: Geologic considerations for an evolving North American liquids-rich play: Search and Discovery Article 110166 , accessed January 9, 2017, http://www.searchanddiscovery.com/pdfz/abstracts/pdf/2015/90229playmaker/abstracts/ndx_zagorski.pdf.html.

Discovery of the Utica Shale: Update on an Evolving Giant*

William A. Zagorski[1] and Taylor G. McClain[1]

Search and Discovery Article #10965 (2017)**
Posted June 26, 2017

*Adapted from oral presentation given at 2017 AAPG Annual Convention & Exhibition, Houston, Texas, April 2-5, 2017
**Datapages © 2017 Serial rights given by author. For all other rights contact author directly.

[1]Range Resources Corporation (bzagorski@rangeresources.com)

Abstract

The Utica-Point Pleasant play has grown rapidly since horizontal discovery and commercialization in PA (2010) and Ohio (2011) with current production of approximately 5 BCFE/d and an active rig count of 25 as of early 2017. The U.S. portion of the play covers a large extent within the Appalachian Basin, including parts of Pennsylvania, Ohio and West Virginia. While modern horizontal drilling is focused on the organic-rich Point Pleasant Member in Eastern Ohio and Southwestern Pennsylvania, a long history of testing and development can be traced back to several key attempts to commercialize the play in both the US and Canadian portions of the Appalachian Basin beginning in 1858 in Ontario and in 1888 in northern New York. Early industry focus of the modern horizontal play was in the wet-gas and oil windows, as some touted the liquids content and possible similarity of the Utica-Point Pleasant to the evolving Eagle Ford oil play of Texas. However, current activity trends are focusing deeper and deeper into the highly over-pressured dry gas portions of the play. Key productivity drivers for the play include pore pressure gradient, depth, thermal maturity, TOC content, porosity & permeability, frac containment, gas in place, facies changes in key reservoir targets, and the regional influence of basement faulting. Although significant evolution and understanding of the play has been achieved since modern commercialization, many concepts and drivers have yet to be completely understood. Play extents are not yet fully realized and future growth potential remains quite significant.

Discovery of the Utica Shale: Update on an Evolving Giant

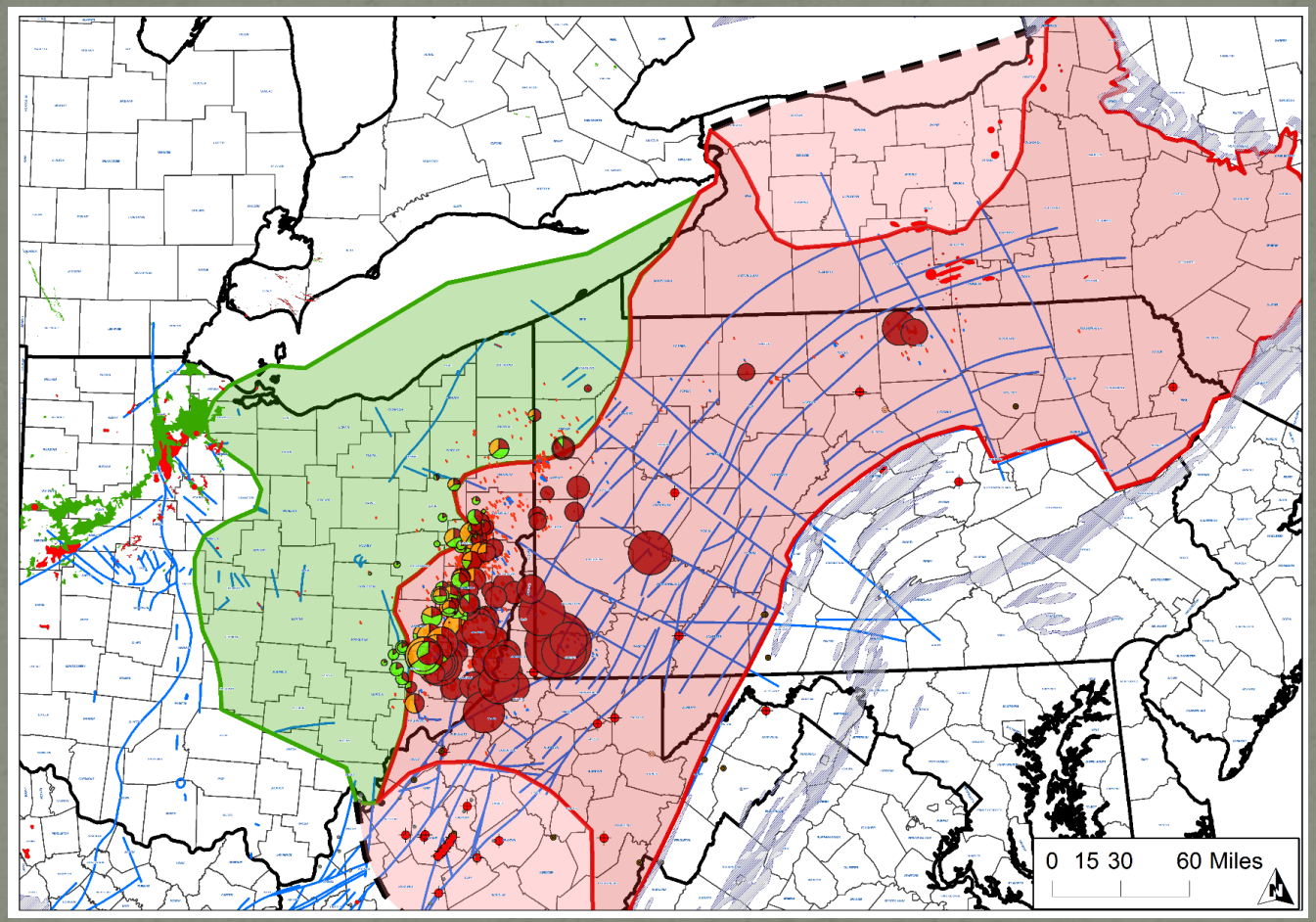

RANGE RESOURCES®

AAPG Discovery Thinking Session – April 5, 2017
William A. Zagorski & Taylor G. McClain
Range Resources Corporation

Present Day Extent Utica Point Pleasant Play

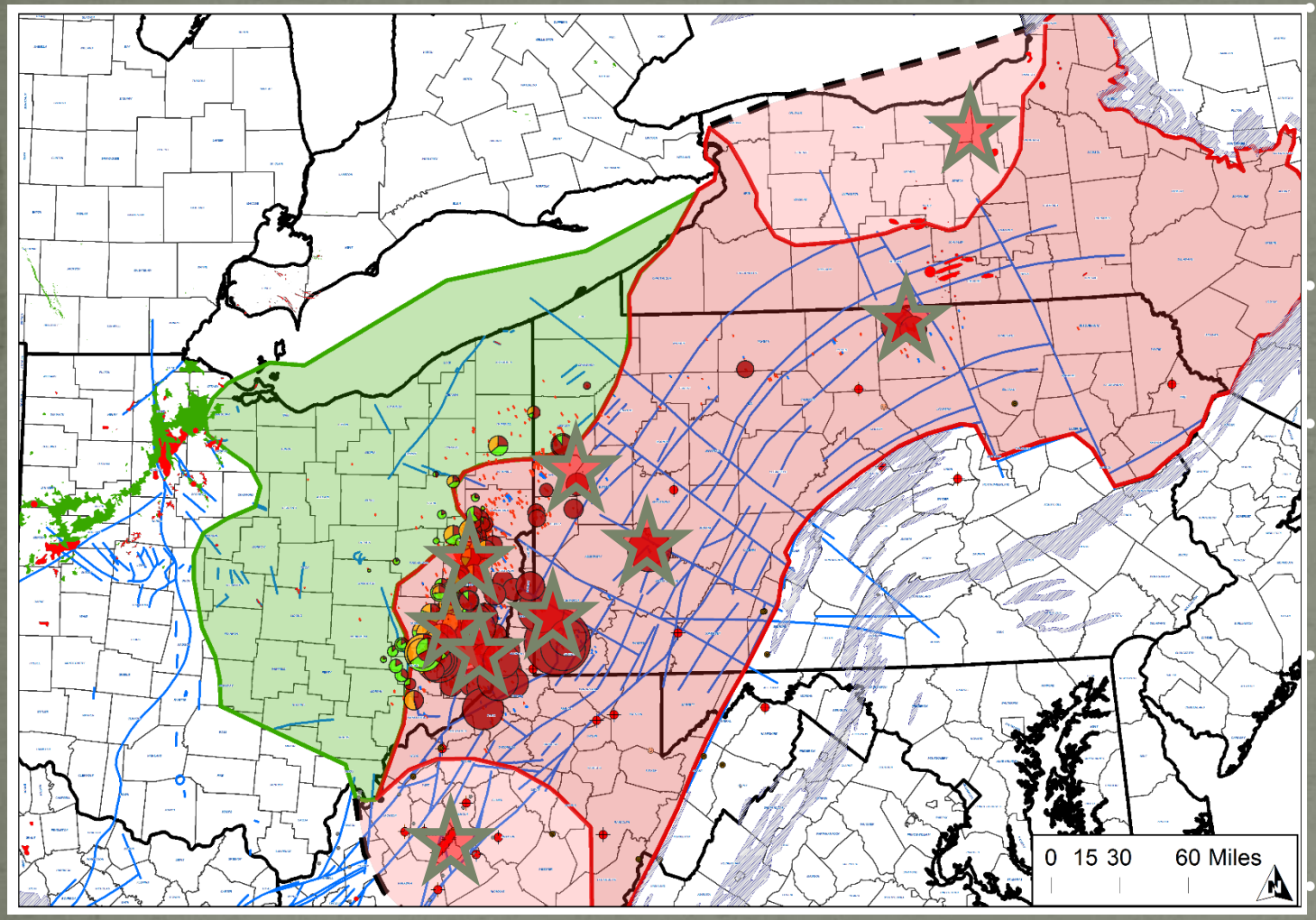

Play Boundaries – USGS (2009)
Proposed Extensions - This study.

Milestone Fields/Wells

- Current production from Utica-Point Pleasant Play is 5 BCFE/day.
- 25 Rigs running as of early 2017.
- Current focus is on deeper dry gas portion of the play.
- Modern horizontal play commercialized in 2010.
- However interest in the play started much earlier……

Early Utica Oil Production – Ontario
1859 – 1863 - Collingwood Oil Shale Extraction



In 1859 – Craigleith Shale Oil Works - Reported oil production from member of Collingwood Shale. North American oil discoveries in 1858 and 1859 made the operation uneconomic by 1863.



Source: Wikipedia

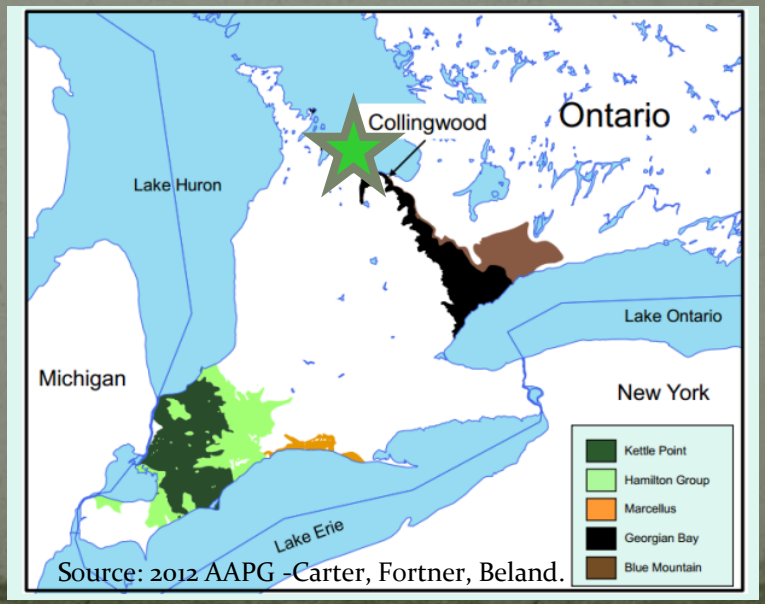

Source: 2012 AAPG -Carter, Fortner, Beland.

Early New York Trenton Gas Production



Source: Zagorski 2007

- 1888 Sandy Creek Field.
- Wells were shallow 600' to 2,800' in the Trenton FM.
- Flow rates and pressures initially high but were low volume producers.
- Early recognition as a shale gas play by several geologists.
- Activity waned after 1940.
- Renewed interest in late 1990's.

Previous Work

"That the gas is confined to the shale partings and shale layers can be observed at any well during the drilling of the Trenton. The drill first strikes a hard, dense limestone layer which is usually only a few inches thick but is hard to penetrate. As the drill breaks through this layer the gas rushes forth, sometimes under enormous pressure which may even blow the tools out of the hole. When drilling is again resumed it is invariably found that the layer under the hard dense limestone is a calcareous shale… No increase in volume is realized until another hard dense limestone is reached. Unquestionably the limestone acts as a cap rock."

Early geologic review of play.

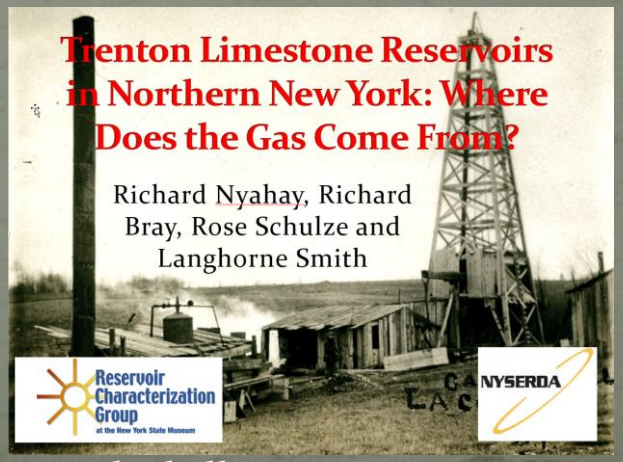

Early drilling NY Trenton Gas

Example Well Records – Note Gas Shows and Pressures!

Bottom of Oswego 1885'
Top of Trenton 2540
Present depth 2670'

Gas at 415' Niagara

Gas at 1748' Oswego

Gas at 2670' Trenton

Rig burned, will build new rig according to Boyce and drill deeper.

October 1 log

October 27 12' more

See Gillette's letter of Nov. 7

"When shut in, pressure lifted 633 feet of casing and drive pipe out of hole and scattered it about the land. One 80-foot length was thrown 600 feet from the well."

-Scout card from well in Pulaski Field

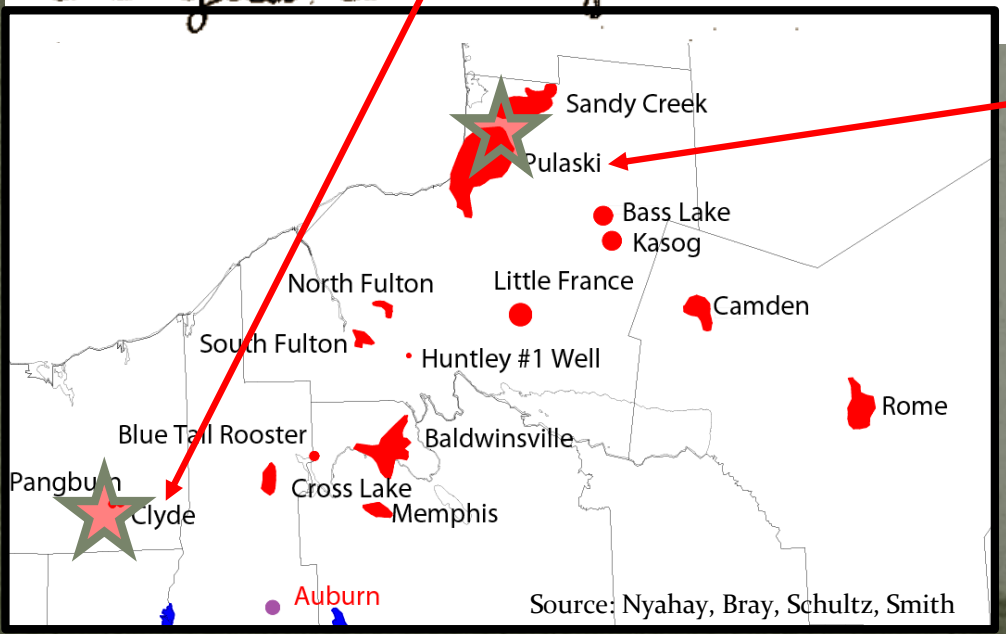

Source: Nyahay, Bray, Schultz, Smith

Bender Gas Well Contacted Powerful Gas Pocket at One O'clock This Morning

Explosion Skyrockets Two Ton Drill, Disrupts Cable and Fires Rock to Top of Derrick--Work Proceeds for a Main Vein.

The Bender gas well, which is being drilled on the Harvey Dunn farm near this village, struck a pocket of gas this morning at 1 o'clock that hoisted the 3,800 pound drill, dislodged the cable from its track and sent a volume of rock and water into the air to an altitude about the height of the towering derrick.

This is the fourth time within the week that pockets of gas have been struck. Yesterday morning a pocket, capable of flowing 50,000 cubic feet of gas daily, blew in at 8:45 o'clock. Each succeeding strike comes with greater force and the explosions increase in noise. Excitement this morning is running high at the well. Engineer Cady is supervising the two shifts of workmen who have resumed operations to drill on until the main vein is hit. The well is now down 950 feet.

The young gusher that came to light at 1 a. m. today has permeated the air about the premises with a strong odor—sample of the real stuff. The gas is strong enough that some of the workmen complain of it making their heads ache. The flow of gas, from the six inch hole, can be felt on the hand when held six to eight feet above the platform, visitors report.

The monotony of just drilling has reached a different stage—for the workmen stand ready to hustle for their lives with each re-curring explosion. Engineer Cady is highly jubilant over the prospects of the well to date and ventures his belief that within a week they will tap a major vein.

Warning is given to any visitor to the premises that smoking is absolutely forbidden.

Gusher Blows in at 10:15 Today

Modern NY Trenton Gas Fields – Lake Ontario Shoreline

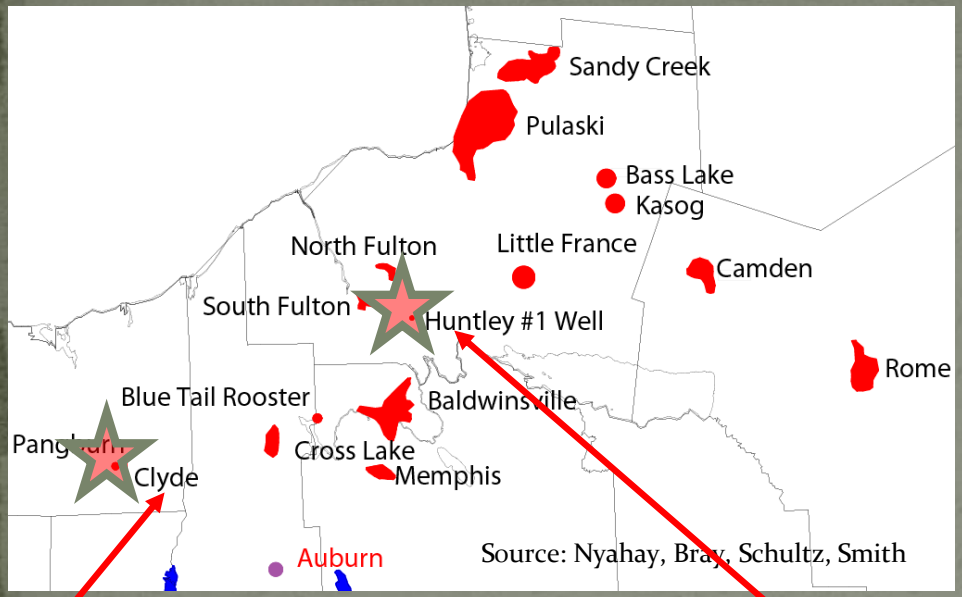

- After 1999 exploration efforts in the Trenton Black River play led to renewed interest in this play.
- Play was recognized as a source rock/unconventional type play and was successfully tested in 2003.
- Play concept was to target fractured zones defined by 2D/3D seismic and drill and complete natural.
- Testing of the play stopped after 2007 as regulations in NY discouraged horizontal drilling and large scale hydraulic fracturing.



Source: Zagorski 2003

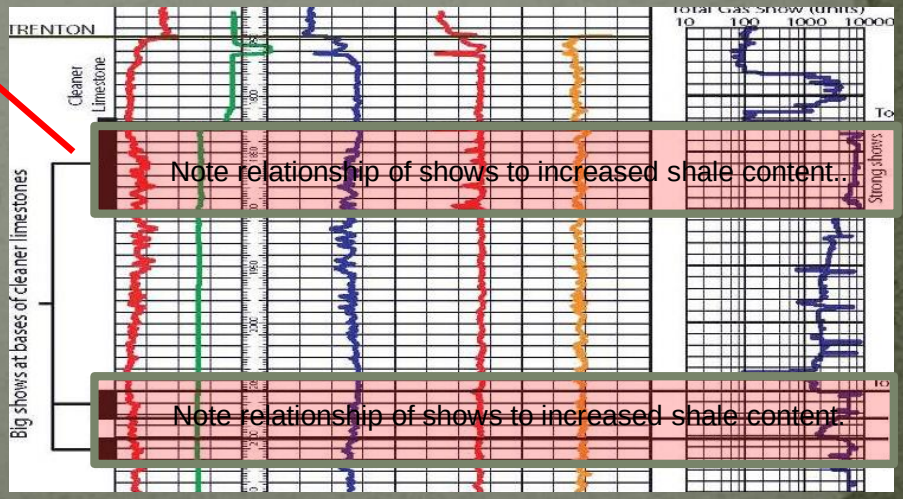

Source: Nyahay, Bray, Schultz, Smith

Huntley #1

Trenton Black River Over Pressure Play – Cottontree Field - WV

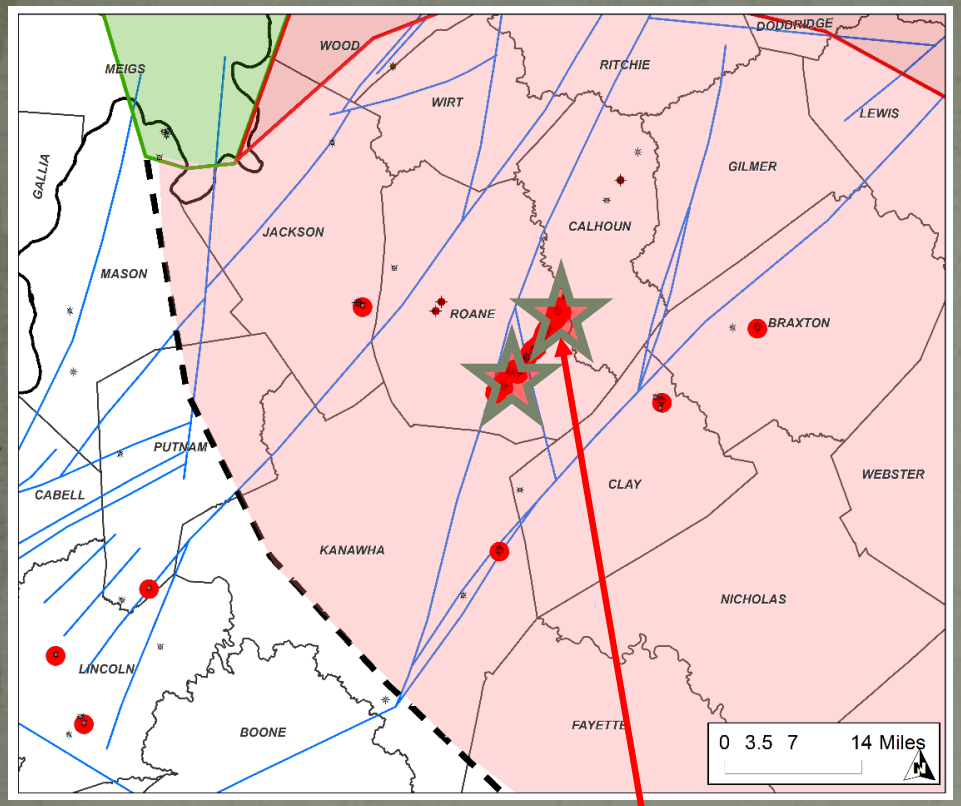

- Discovery was Cottontree Field in Roane County, WV.
- Original drilling targeted highly fractured areas in search of dolomitized Trenton Black River carbonates using mainly 2D seismic coverage.
- Reservoir is highly over pressured. Pervasive gas shows in section even in dry holes.
- Several other tests drilled in WV but all looking for fractures not source rock plays.
- Similar to Utica Point Pleasant play but thicker and less organic rich.



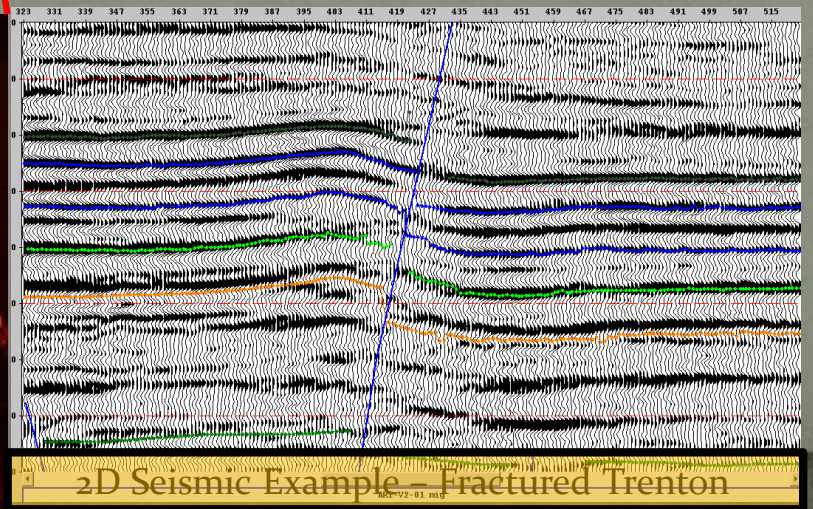

2D Seismic Example – Fractured Trenton

- Play not considered source rock play initially.

2000 -Emerging Deep Play in SW PA – Encouraging Shows

Key 2003 test showing significant gas shows in Utica Point Pleasant

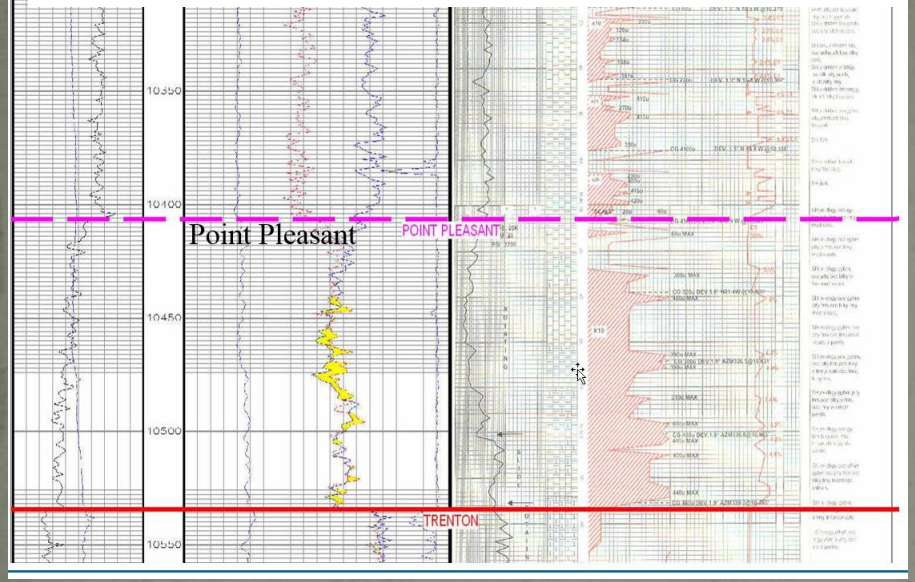

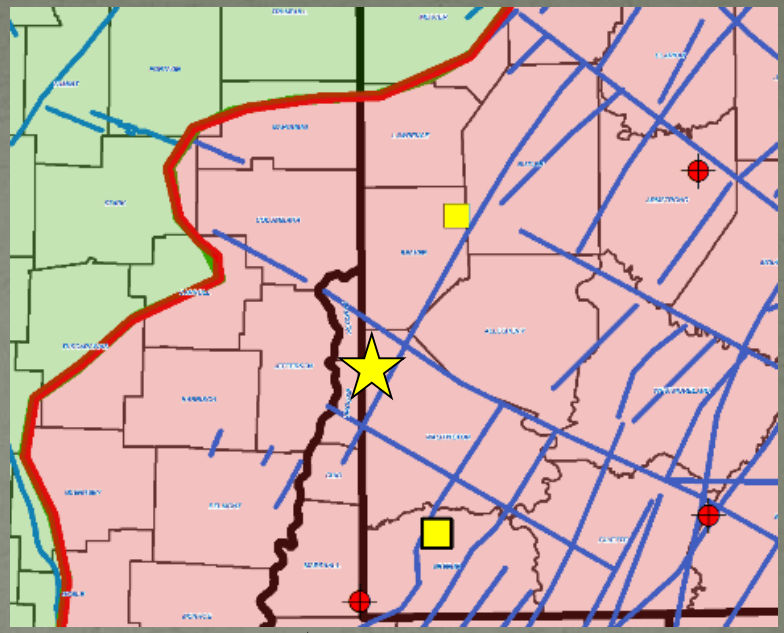

Key deep test in 2006 confirming reservoir quality and significant GIP

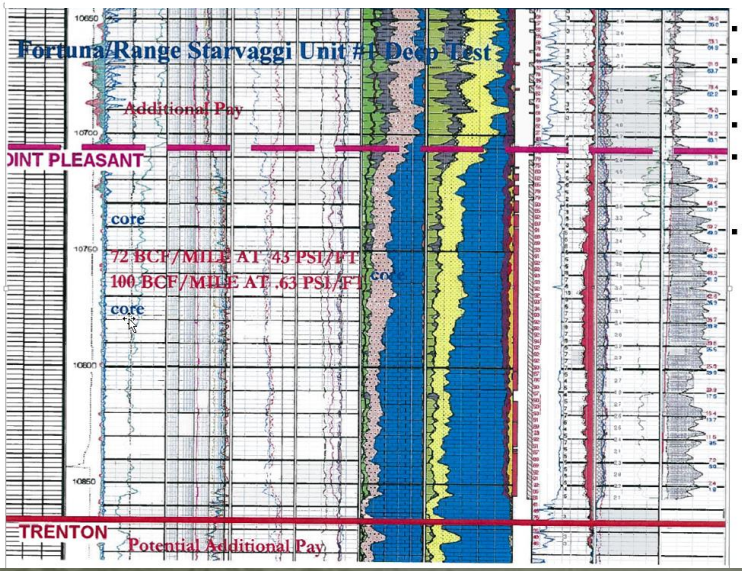

- Drilled 7/2006
- Washington Co
- TBR test
- Sidewall Cored
- Gas Shows throughout interval
- Organic content confirmed

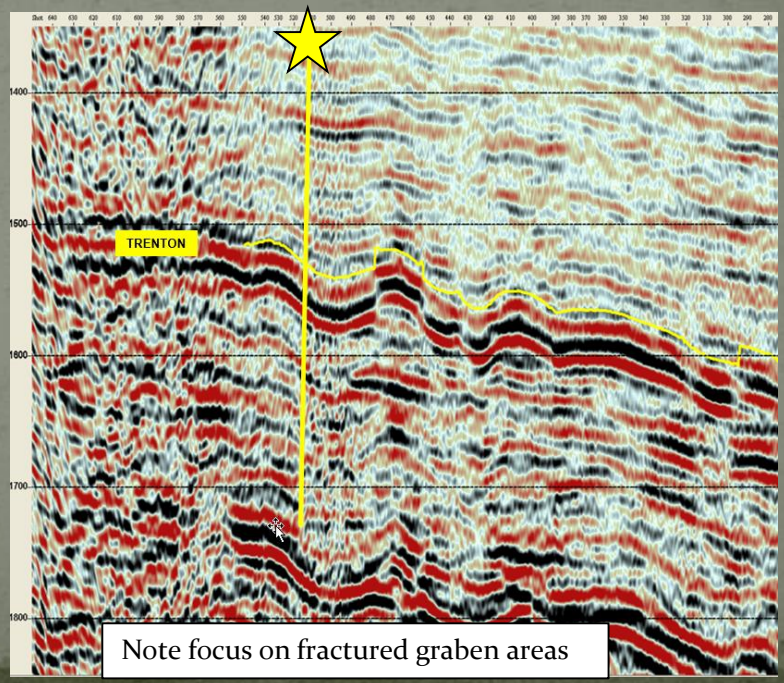

Note focus on fractured graben areas

Early NW Pennsylvania Deep Shows – Not Widely Known

World's Deepest Cable-Tool Test Is Completed

*by John T. Galey**

THE deepest cable-tool hole in the world, so far as can be ascertained, has recently been completed by Manufacturers Light and Heat Co. on the Jesse G. Hockenberry farm, Mercer Township, Butler County, Pennsylvania. This wildcat was abandoned, after it showed considerable salt water, at 10,096 ft. in what is considered to be an Upper Cambrian sand. Stratigraphically, the test is the deepest yet drilled in Western Pennsylvania, Eastern Ohio, or



View of rig which drilled the 10,096-ft. deep test in Butler County, Pennsylvania. Inset: Charles E. Bennett, president, The Manufacturers Light & Heat Co., which firm drilled the deep test here described

Drilling Difficulties

There were only two major obstacles to be overcome in drilling, and these were encountered commencing at a depth of 8,510 ft. and extending to 8,710 ft. where 11 gas pockets with various degrees of explosive force were struck. Some of these gas pockets would make gas at the rate of from 5 to 10 million cubic feet of gas per day, but would last only a matter of a few minutes. The gas pockets all occurred in soft shale and after each one, it was necessary to clean out the hole before new hole could be made. At a depth of 8,710 ft. in the last of three gas pockets the tools were stuck. They were jarred for 80 hours in hope of switching off the drilling line. Acid was dumped into the hole in an attempt to weaken the line and the tools again jarred. The process was repeated and finally

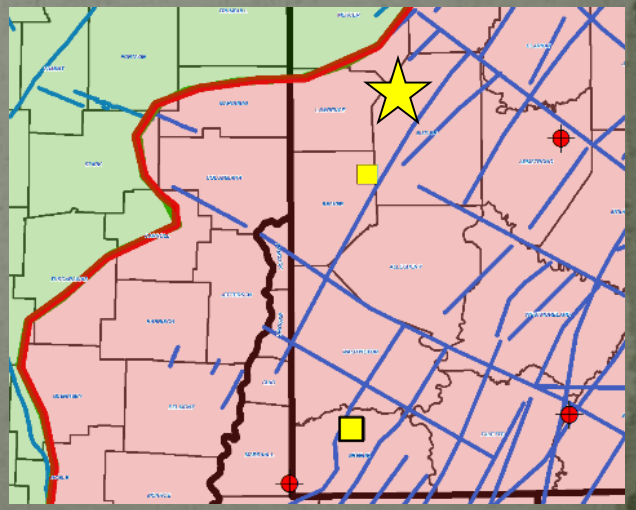

Note report from famous AAPG explorer John T. Galey!
The volumes reported in the article did not make it to the official well records.

My source – Surprise email in 2008 from D. Beardsley.....
Another famous AAPG explorer.....remember the Trenton Black River play.....Cottontree? NY Steuben County discoveries?

RRC Zahn Horizontal Discovery – 2010 Beaver County, PA

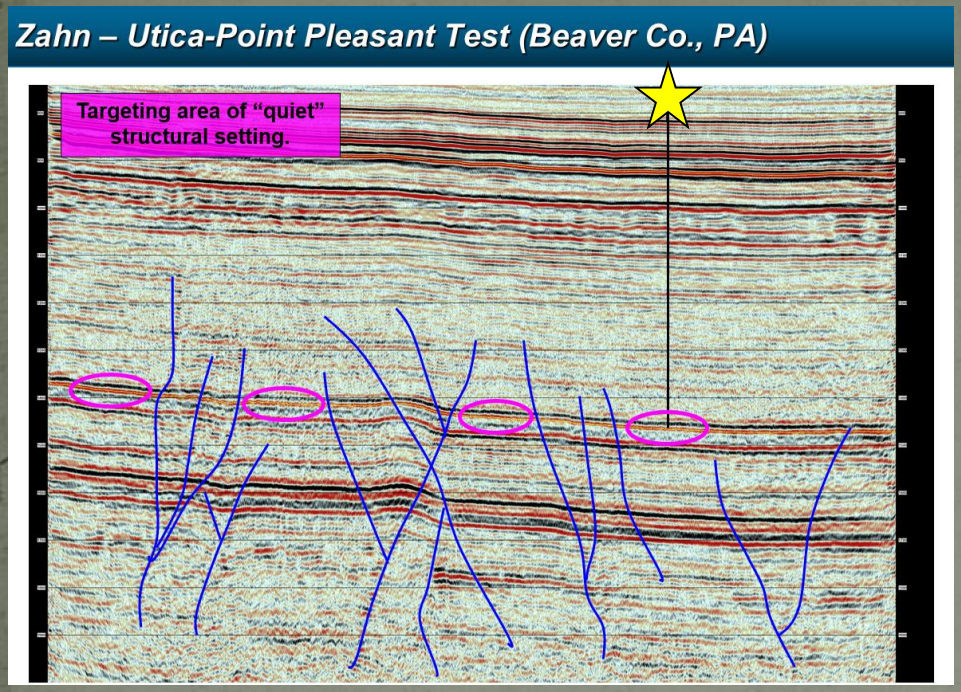

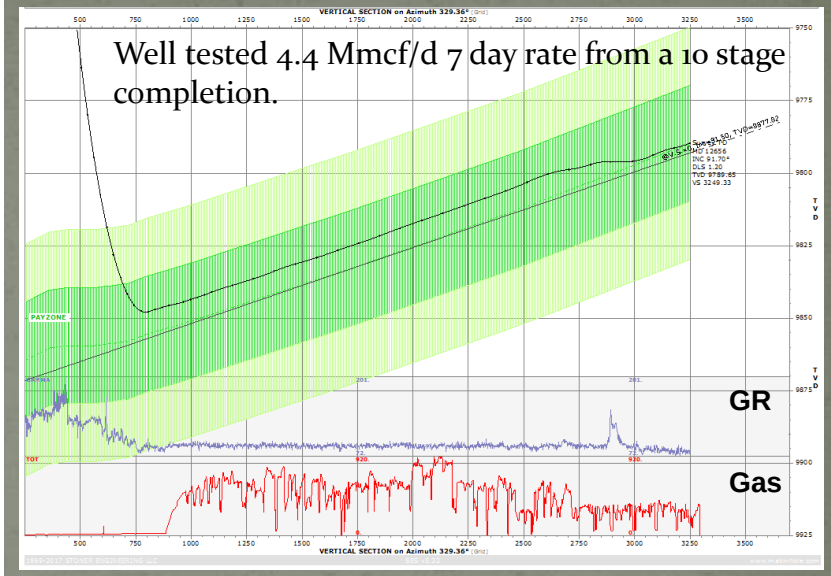

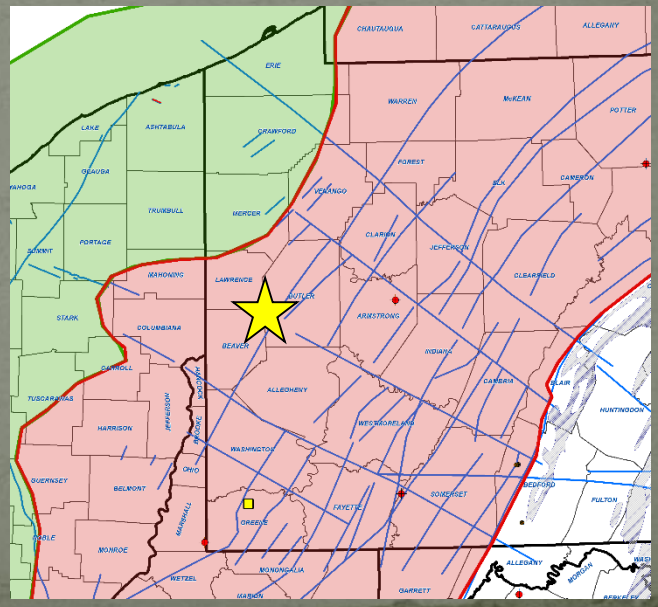

RRC Zahn represented first successful horizontal completion of the Utica Point Pleasant in the USA.

Utica-Point Pleasant Play Activity as of 2010

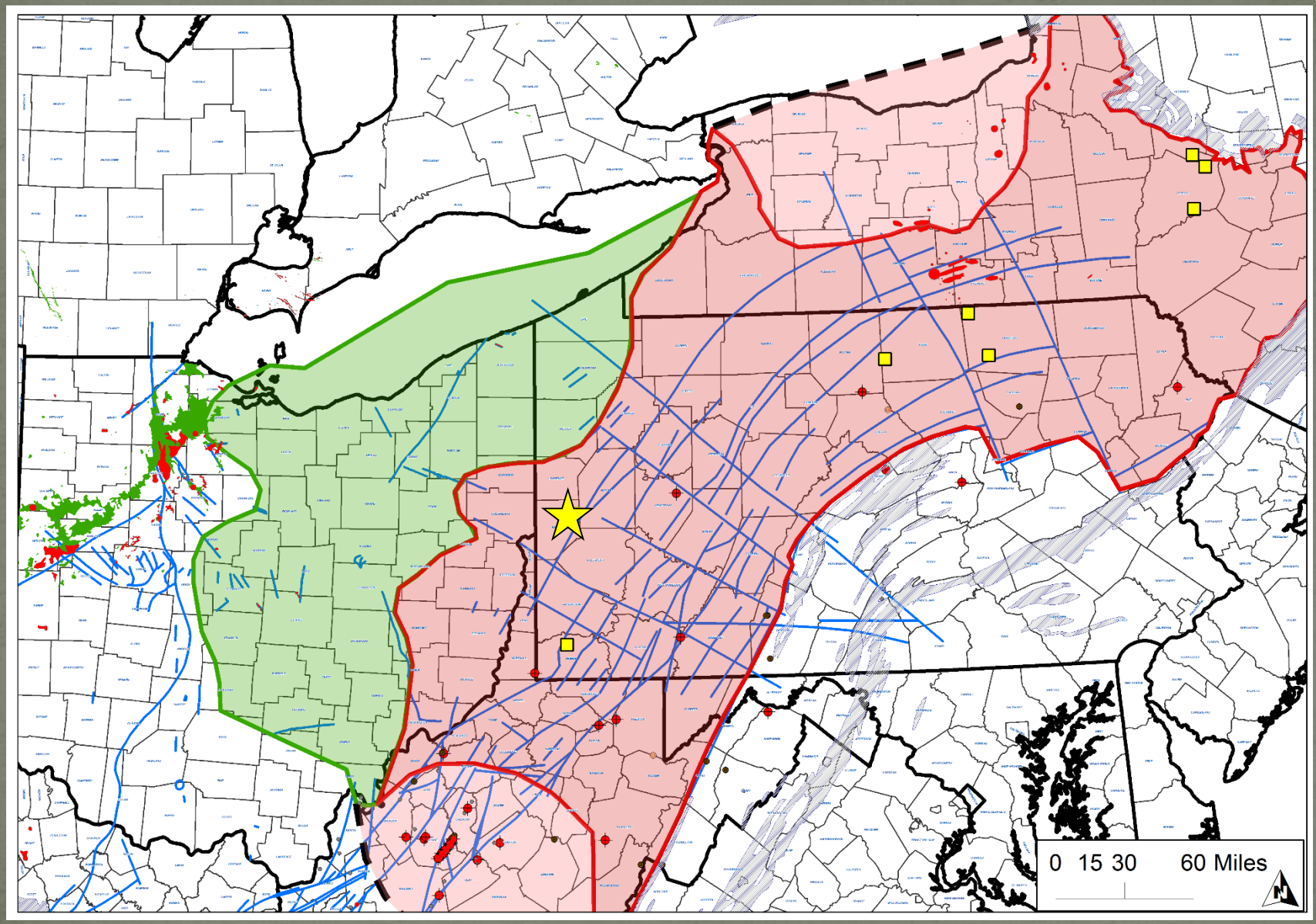

Unlike the Barnett and Marcellus plays, early vertical tests between 2004-2009 were unsuccessful.

Undergraduate Idea - Study the Utica Shale

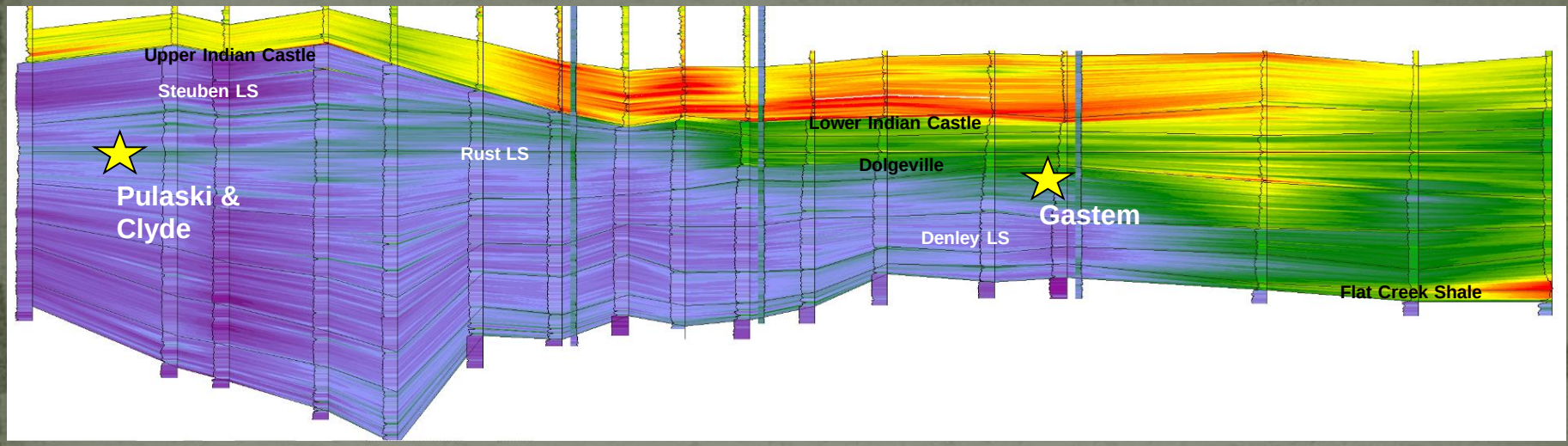

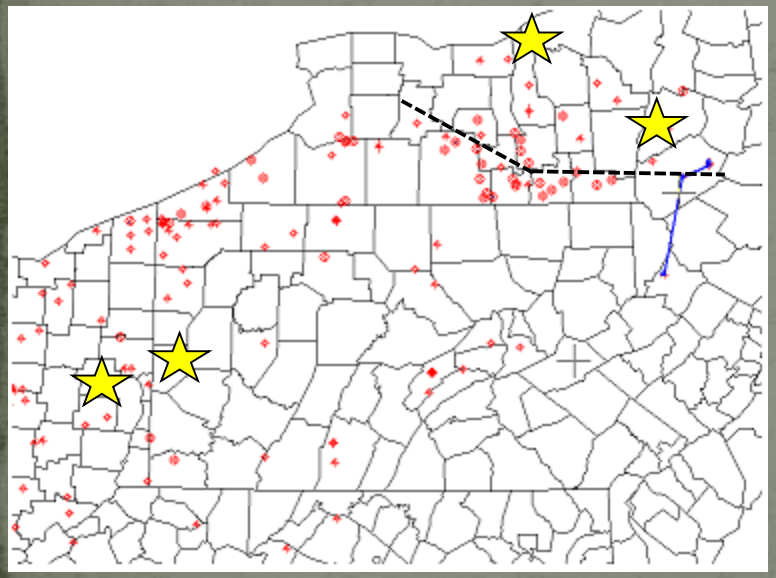

Study area and well dataset

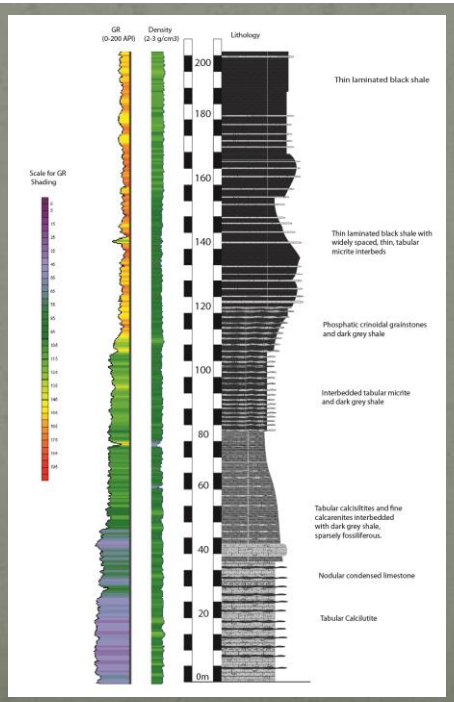

GR log tied to outcrop section

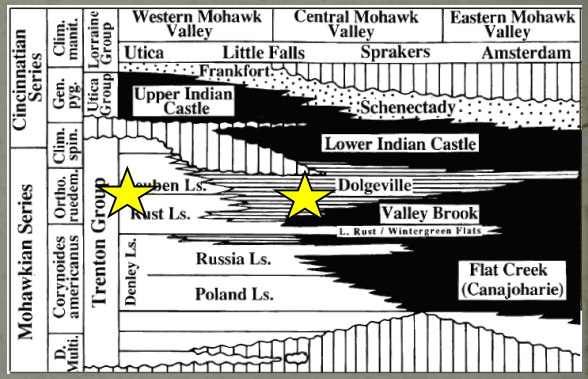

- Completed PSU undergrad thesis study of Utica using publications and outcrops in New York State and Central PA to tie into subsurface.
- Initially compared to Marcellus, focus on areas of thick high-GR black shale.

Critical Thinking Moment – Focus on the Point Pleasant!

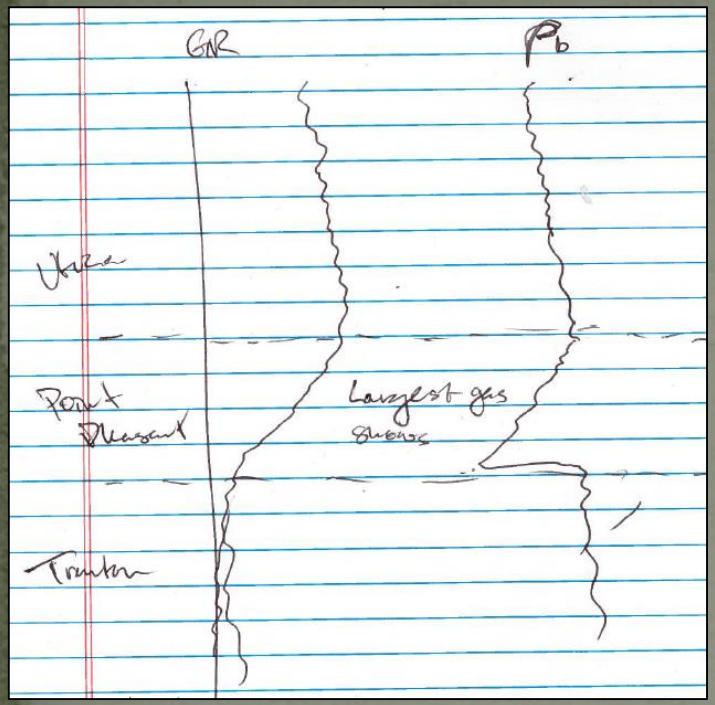

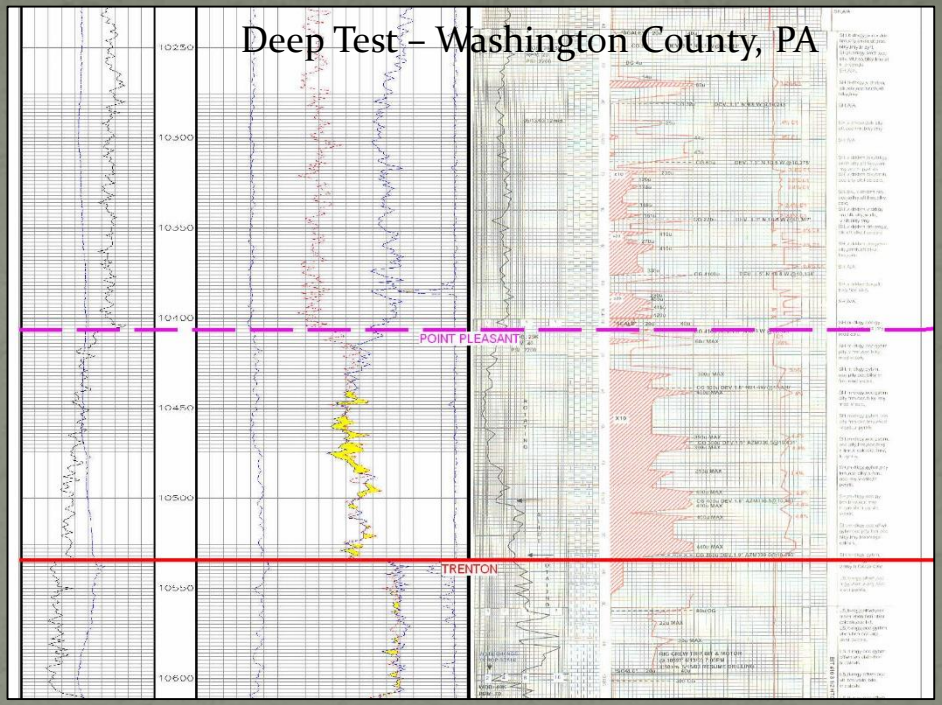

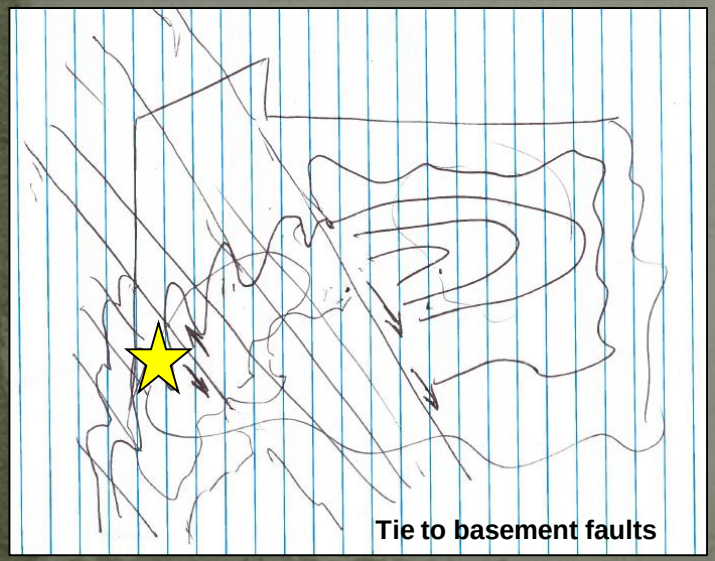

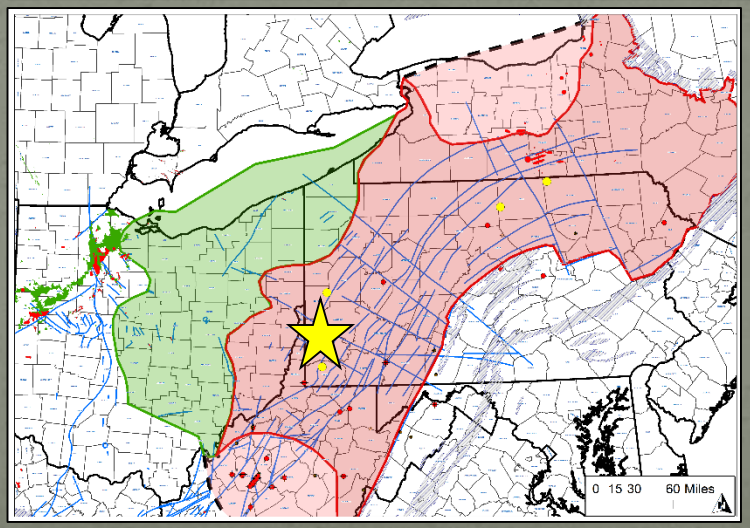

- Focus on density log, look for low bulk density signature.
- Ties to highest TOC and gas shows.

Developing A Stratigraphic Framework

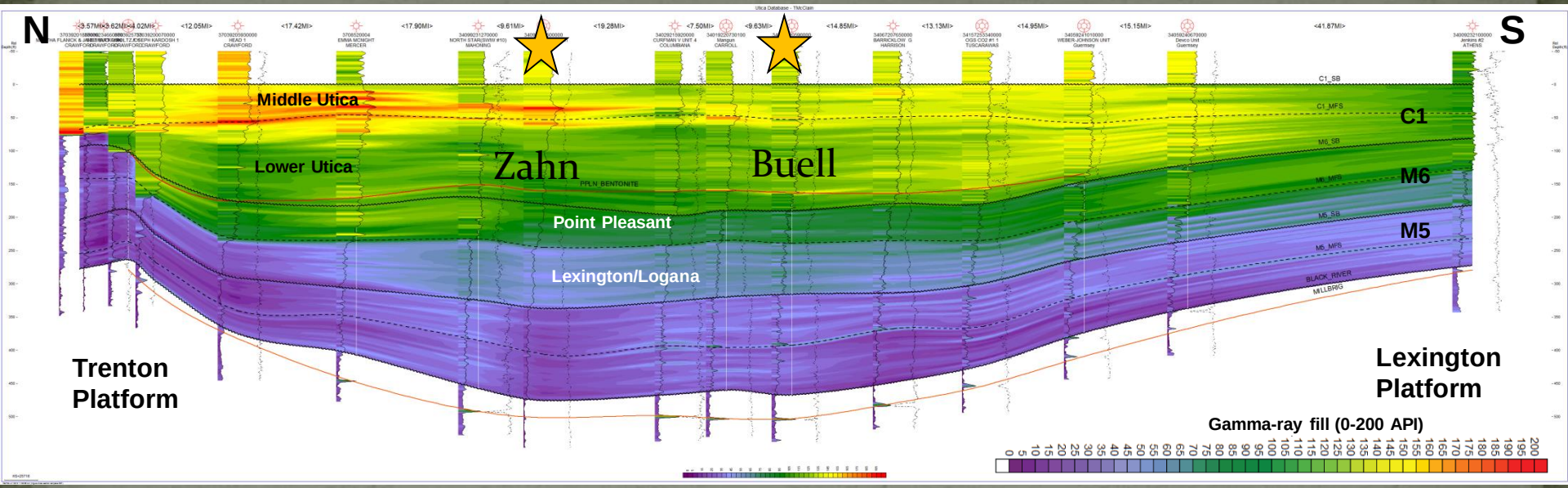

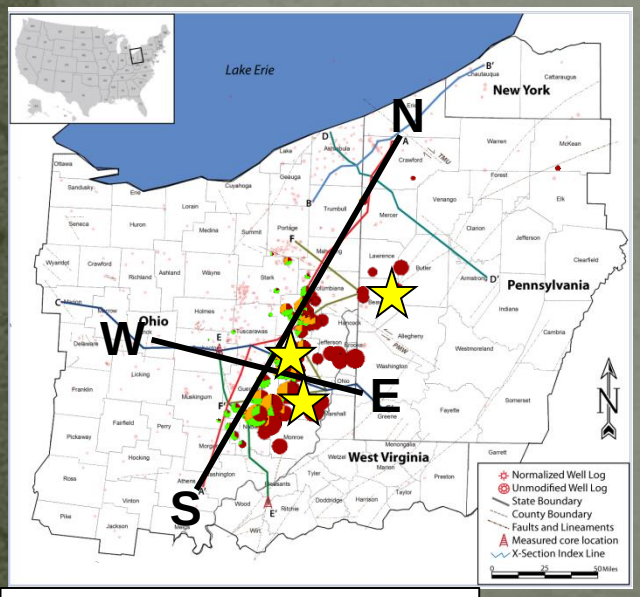

IP rates reported as of early 2013

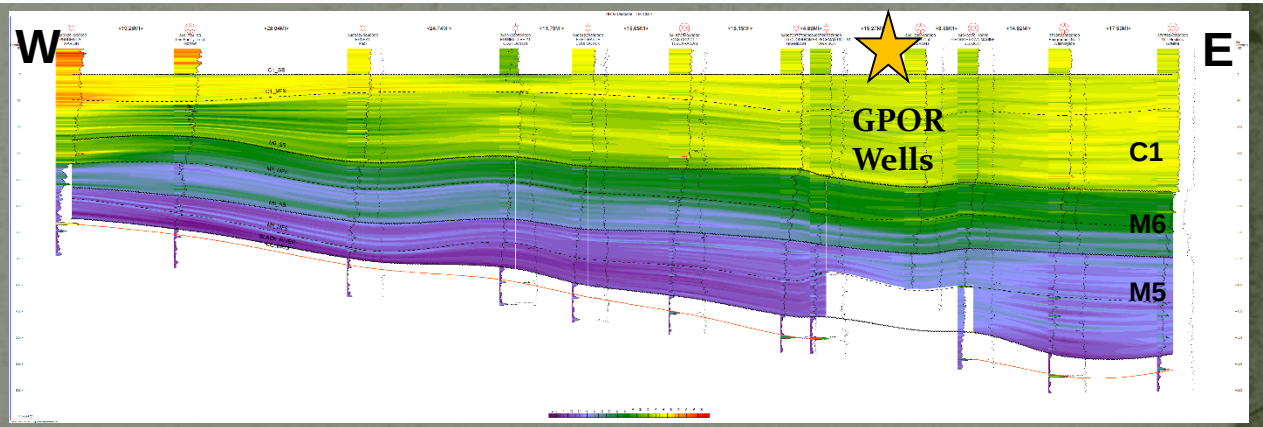

- Detailed correlation of sequence stratigraphy on smaller scale.
- Investigated the distribution of the organic-rich facies and tied to production test rates.
- Identified key reservoir facies and sequences (M5, M6, C1).

Comparing Production Trends to Sequence Stratigraphy

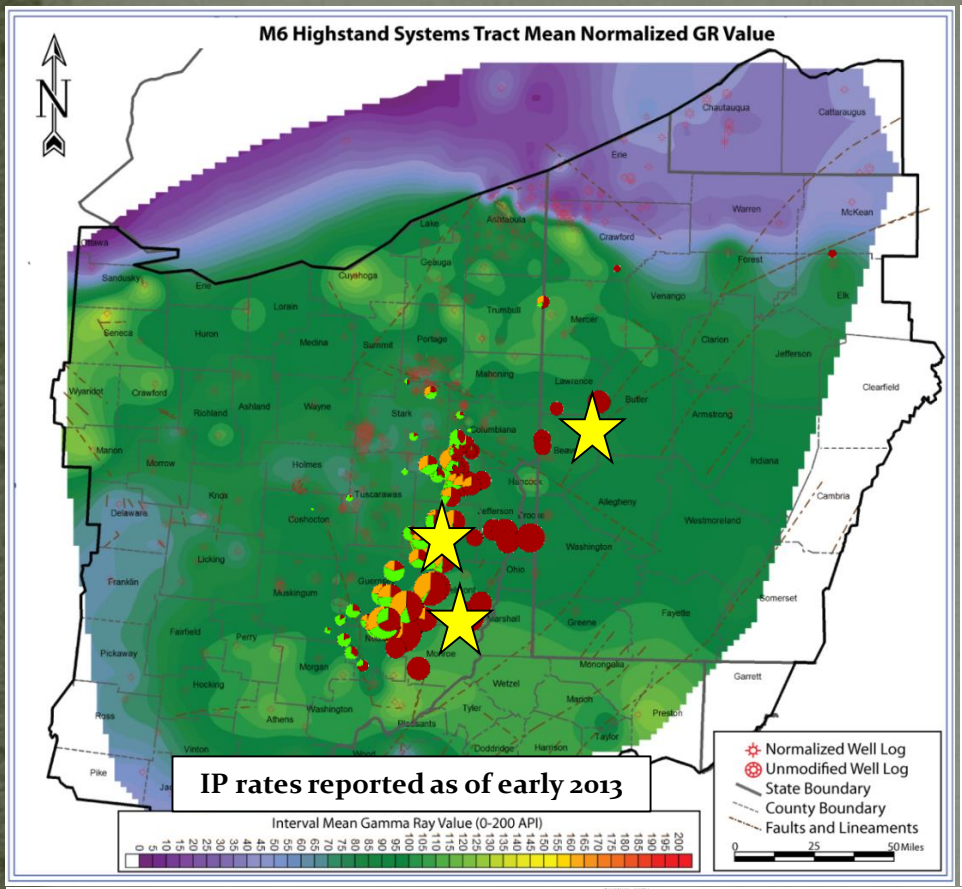

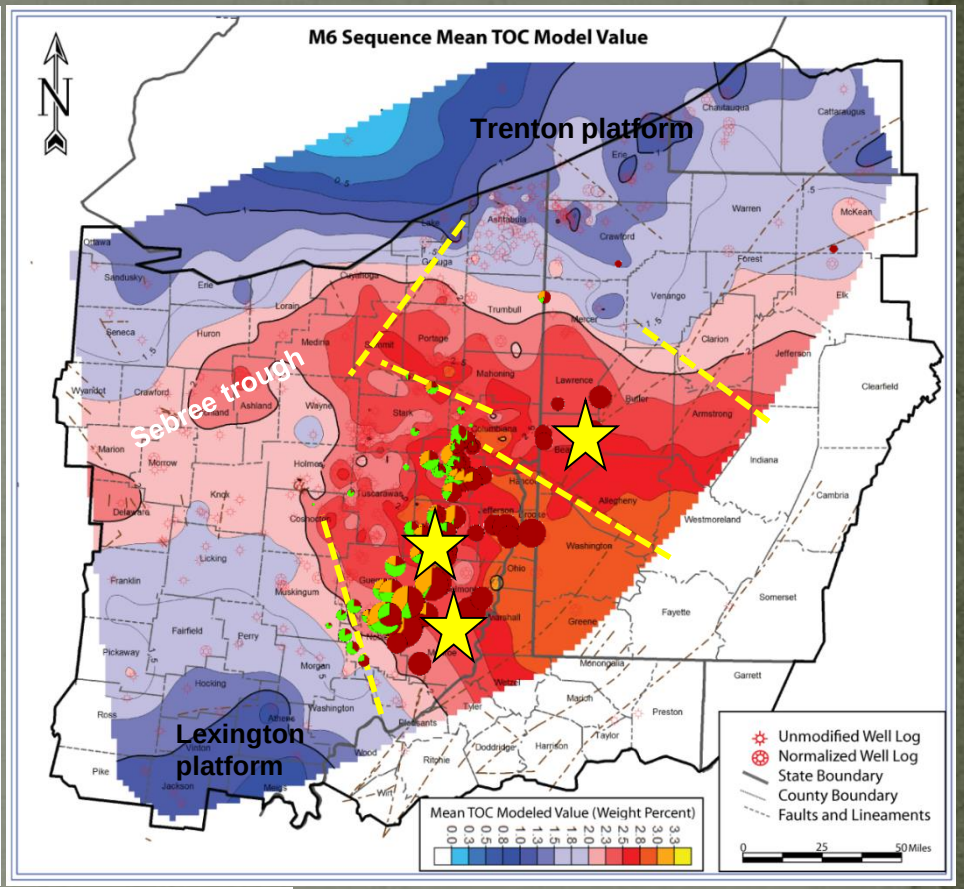

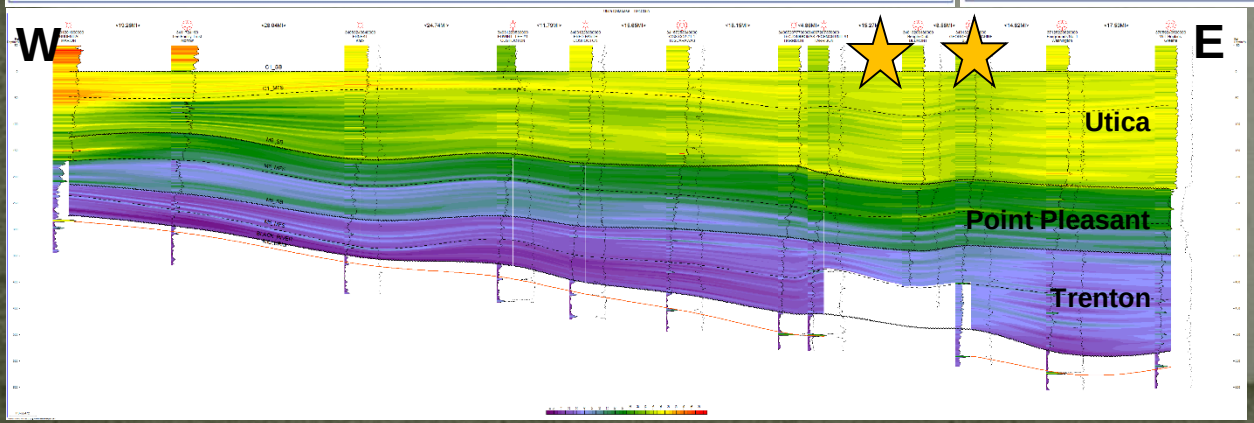

- Observed poor tie between GR and production rates.
- Observed strong tie with density/TOC! Content.
- Noted the strong influence of basement faulting on the play.

Comparing Production Trends To Thermal Maturity

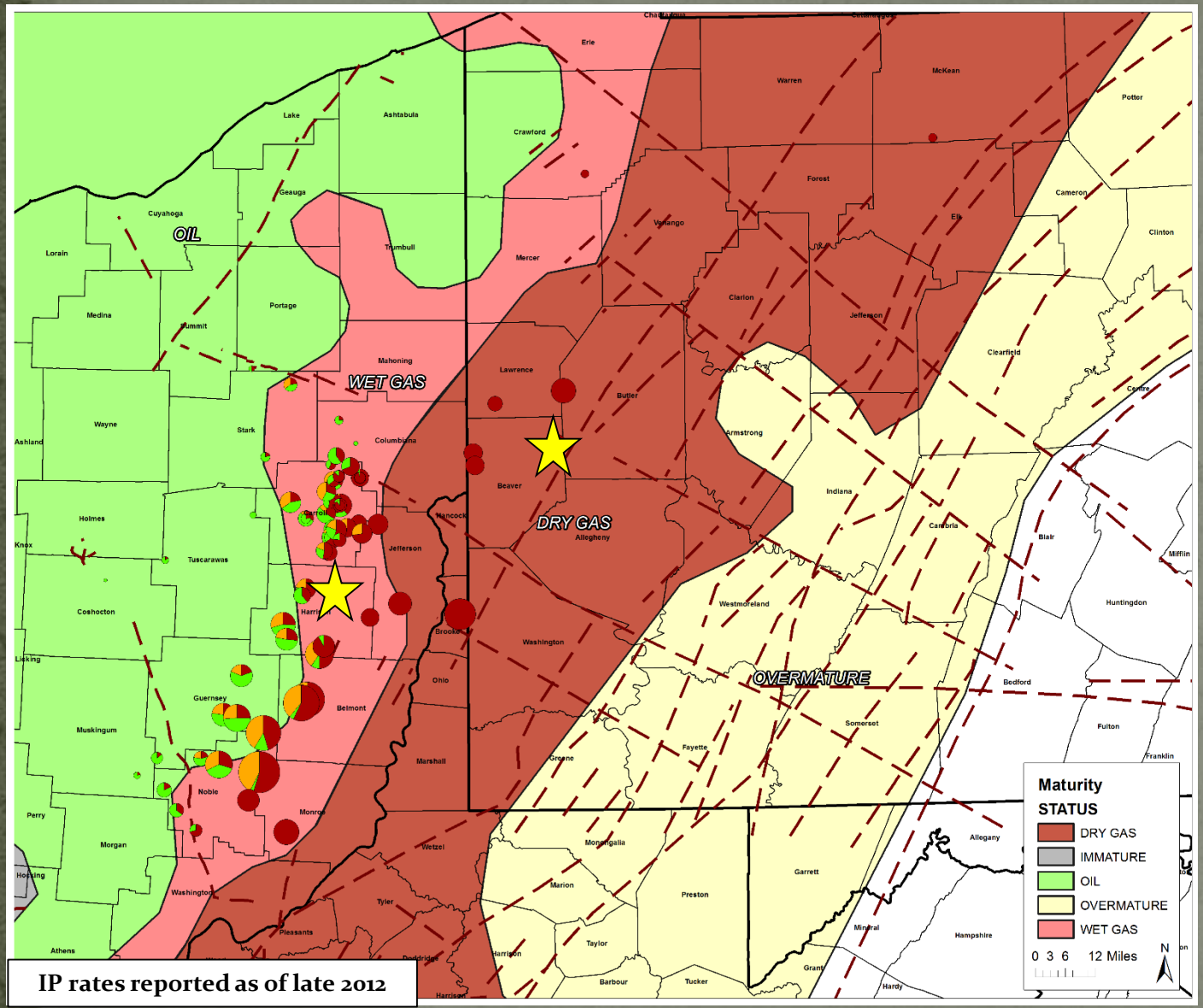

IP rates reported as of late 2012

Modified from Hulver 1997, Rowan 2006, Patchen et al 2006

- Thermal maturity is a key parameter to productivity in shale plays.
- Early thinking of the Utica Play touted liquids content and possible analog to the evolving Eagle Ford oil play of TX.
- Initial challenge was to accurately predict and project the the liquids rich play fairway.
- Early CAI/Ro work predicts NE-SW trending liquids window in Eastern OH and extending into Northwest PA.

Transition of Play From Liquids To Deeper Dry Gas

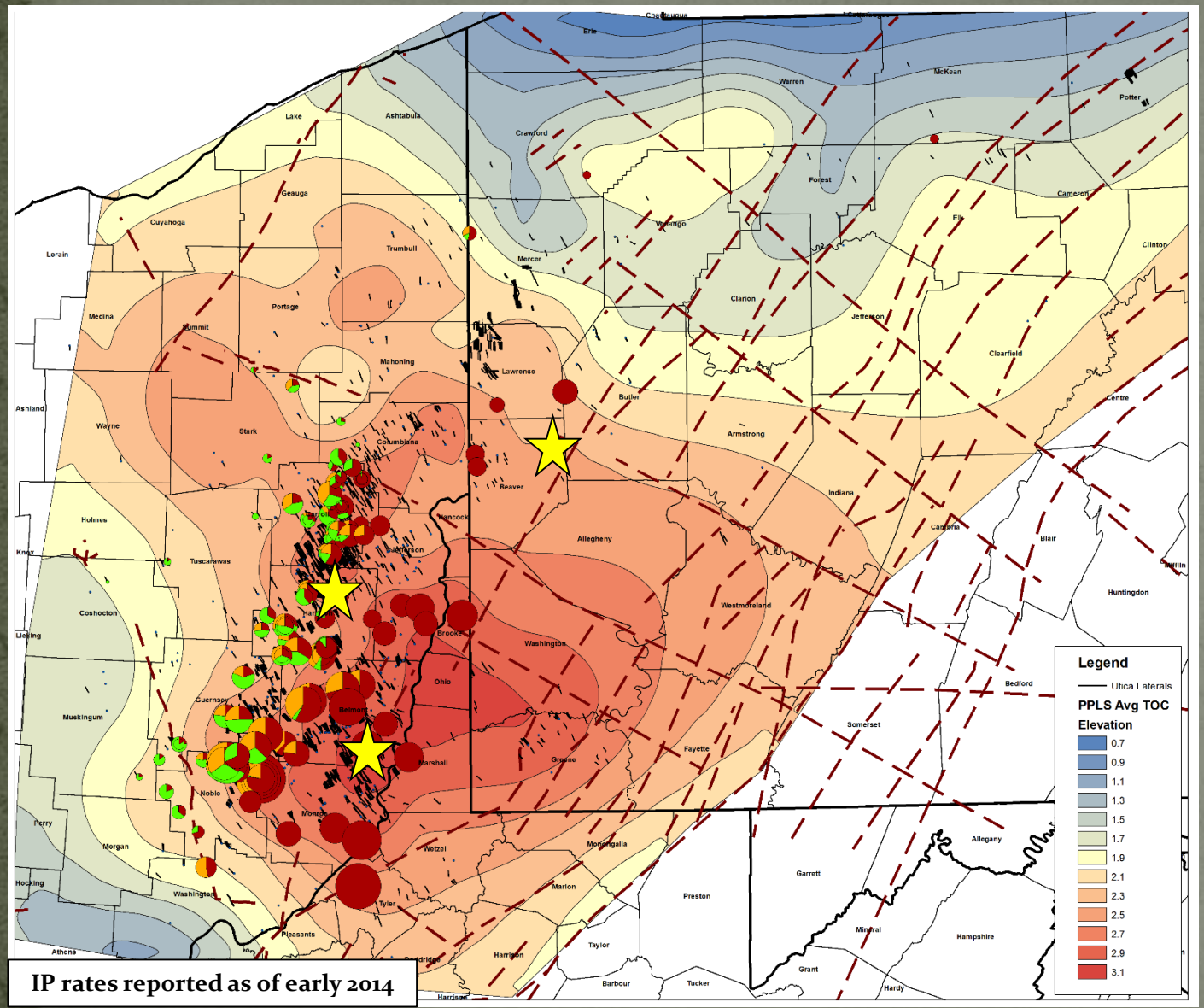

IP rates reported as of early 2014

- Tests in Eastern OH demonstrated 40% higher IP rates than in initial industry focus areas.
- A strong correlation between highest IP rates and areas of highest average Point Pleasant TOC is observed.
- By 2014 industry activity was testing deeper dry gas window advancing the productive areas of the play to south and east.
- Reservoir mapping projected the play to extend into SW PA.

What Else is Driving This Play? – Over-Pressure!

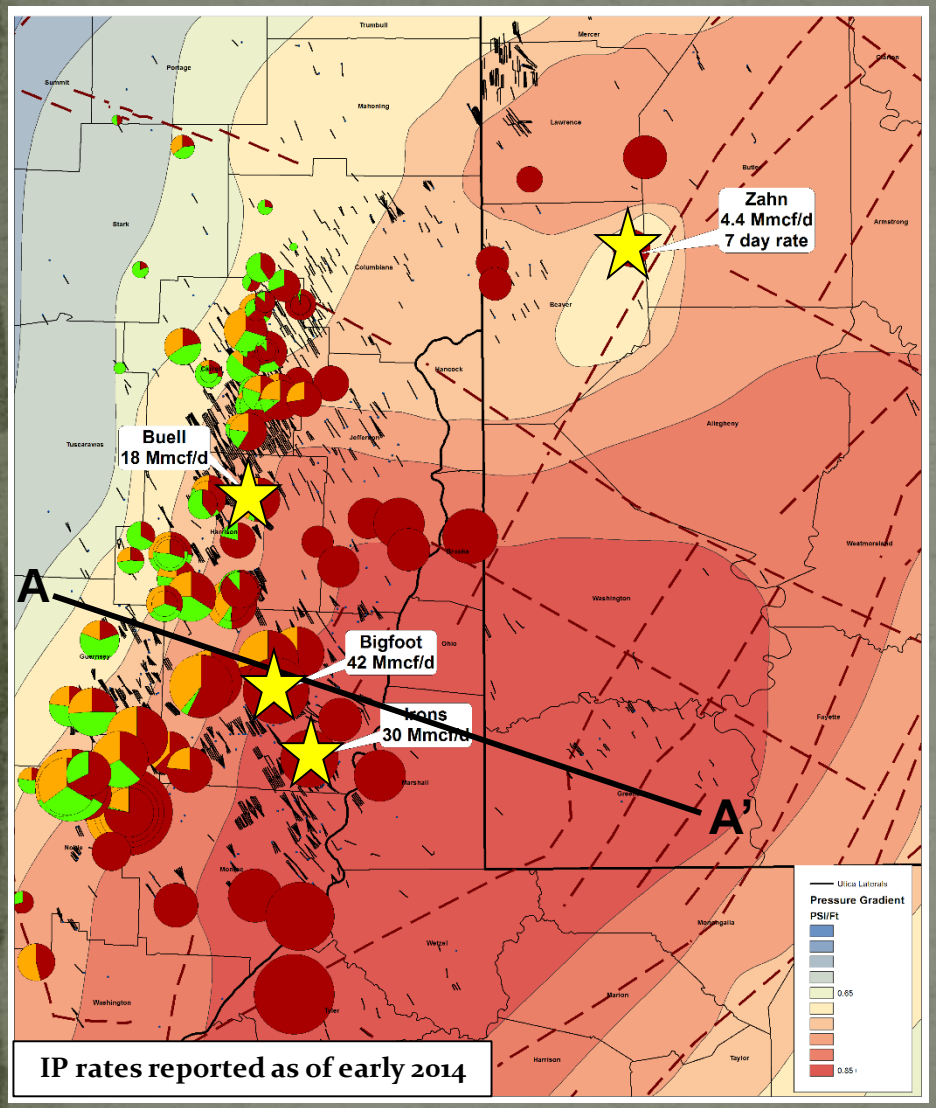

Note clear association of increasing productivity with increased pressure gradient.

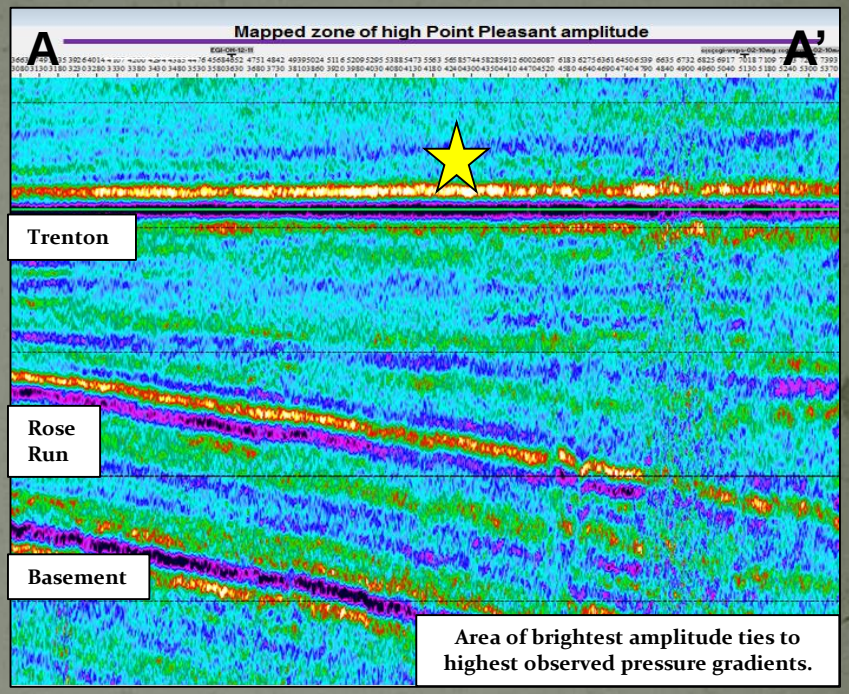

- Correlated production volumes to pressure gradient trends.
- Noted trend of increasing pressure gradient with increasing depth.
- Correlated seismic attributes to observed pressure trends.
- Best wells are associated with gradients of greater than 0.8 psi/ft.

Comparing Reservoir Thickness to Reservoir Quality

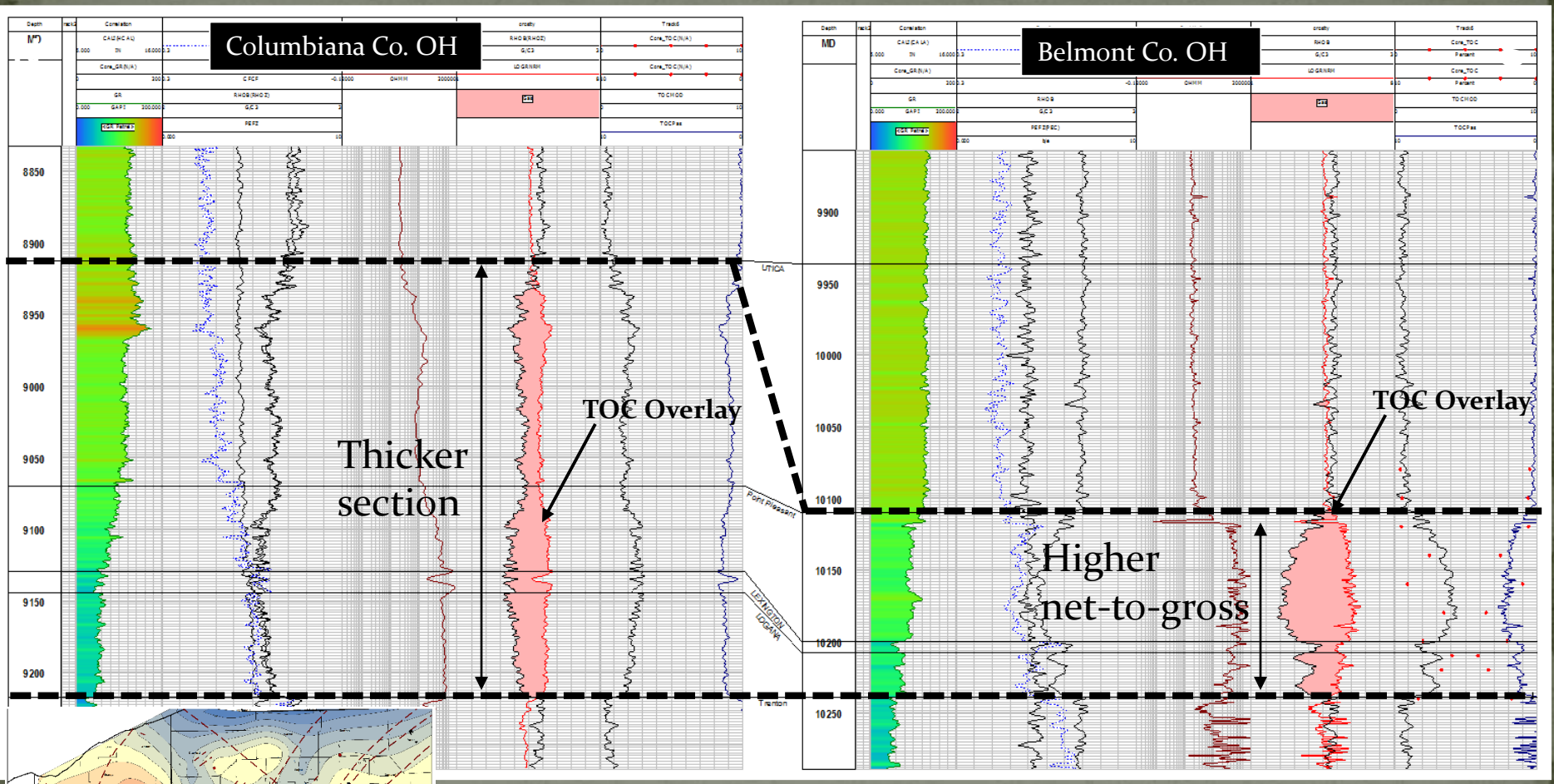

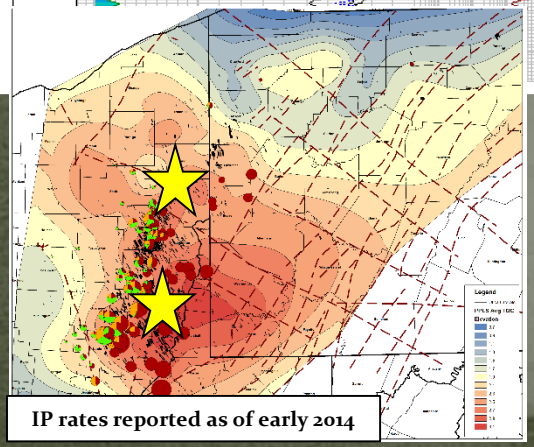

IP rates reported as of early 2014

- Wells to north contain thicker section of lower reservoir quality rock.
- High rate wells to south show condensed section of higher quality reservoir rock.

Stratigraphy Matters! Key Play Driver – Reservoir Quality and Frac Containment

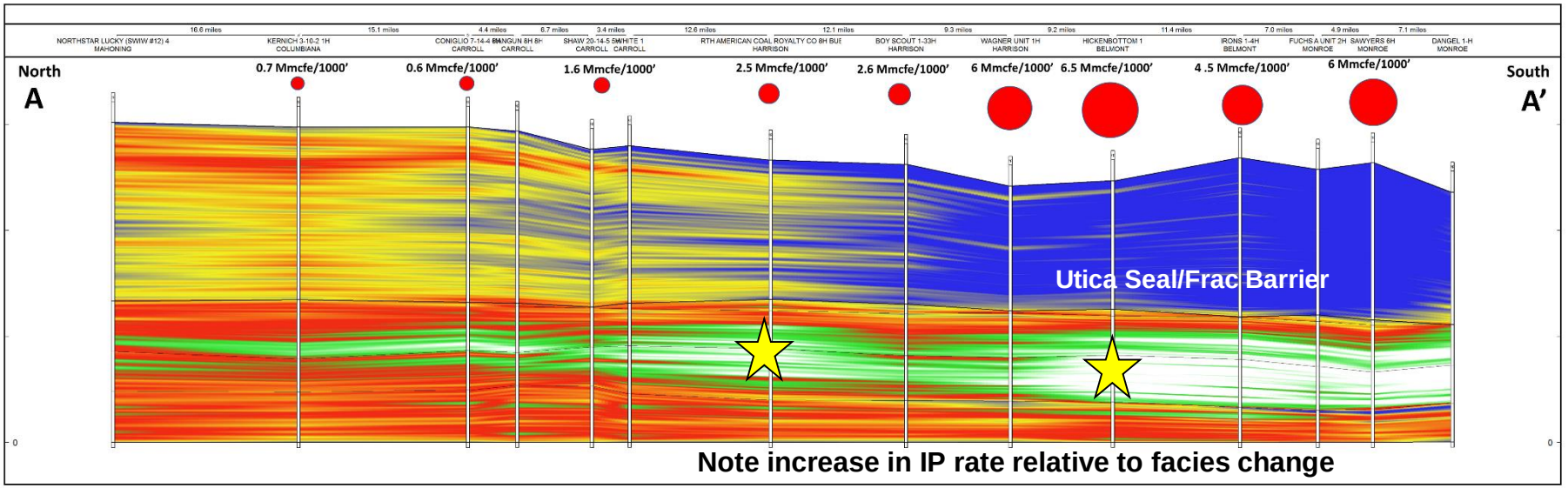

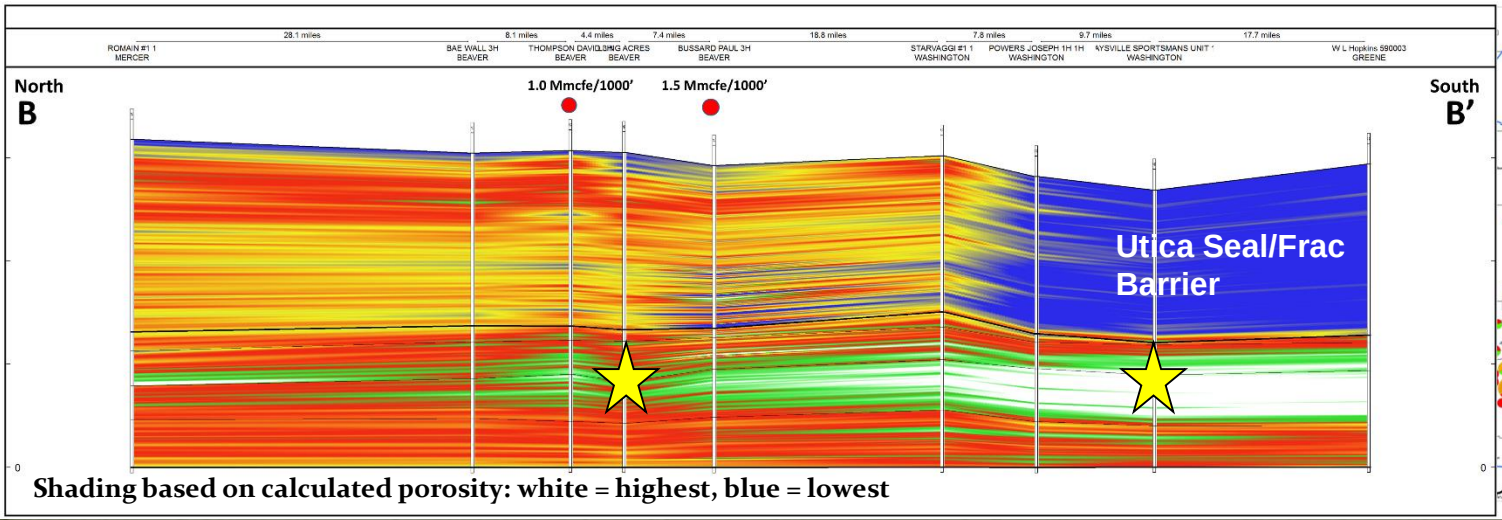

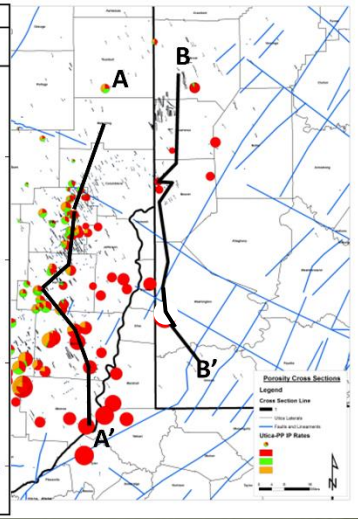

Regional cross sections showing facies change from organic rich Utica shale to non organic seal and IP's.

Examples of Frac Containment Using Reservoir Modeling

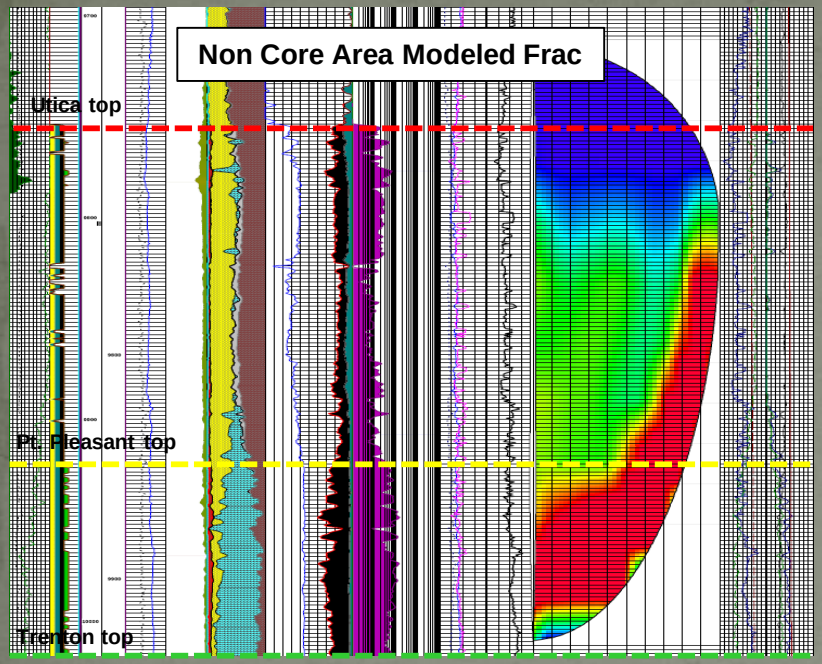

Example frac model of Utica seal area.

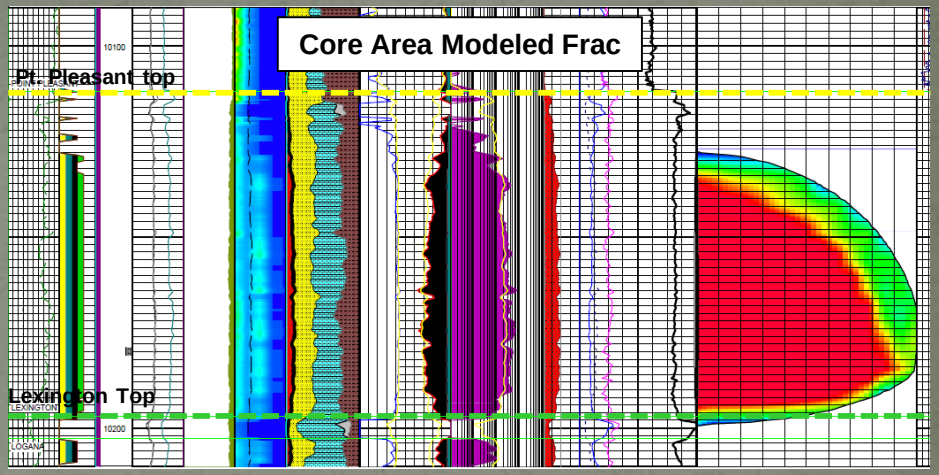



Microseismic confirms majority of the frac energy stays within the Point Pleasant

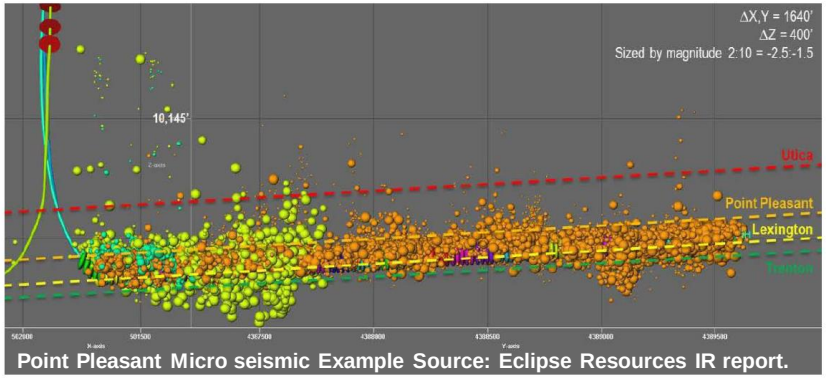

Point Pleasant Micro seismic Example Source: Eclipse Resources IR report.

- Frac containment is a key driver when comparing IP/1000' rates and EUR estimates.
- Areas with the best Point Pleasant to Utica rock property contrasts and the highest pressure gradients are optimal.
- Optimizing proppant placement across the highest pressure, highest porosity intervals is critical.

2014 - Dry Gas Play Expands Into PA and WV

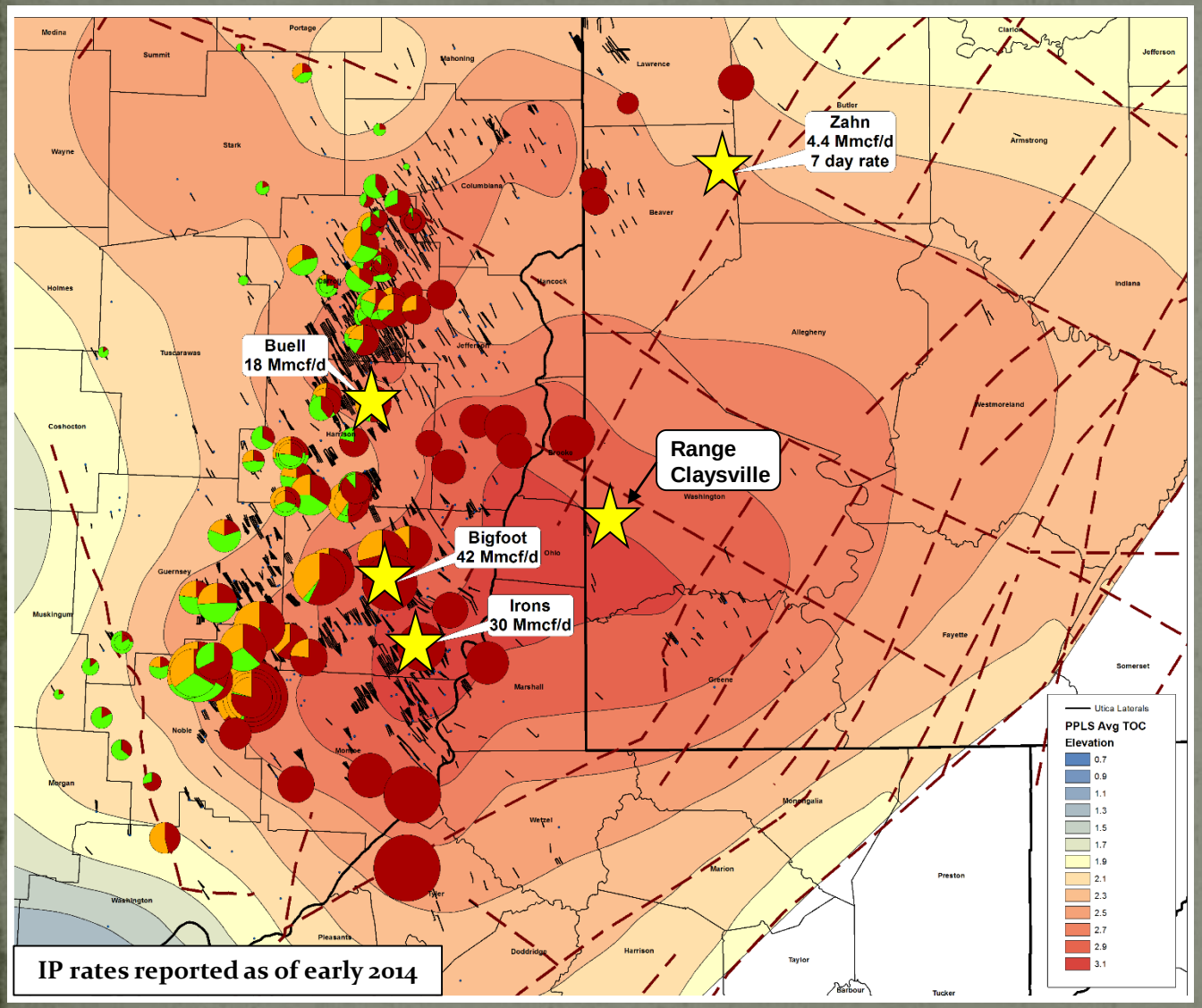

Note increase of IP/1000 rates as play grows eastward.

- By 2014, industry testing had extended the dry gas play into the WV Panhandle and PA.
- Established the relationship between overpressure/TVD, frac containment to facies change, and the projection of key reservoir quality indicators into SWPA.
- Exceptional flow rates were being reported from key wells in eastern Ohio.
- Range Resources first successful horizontal test of SWPA dry gas Utica Point Pleasant play was drilled and completed in late 2014.

Utica – Point Pleasant Reservoir Characteristics, SWPA

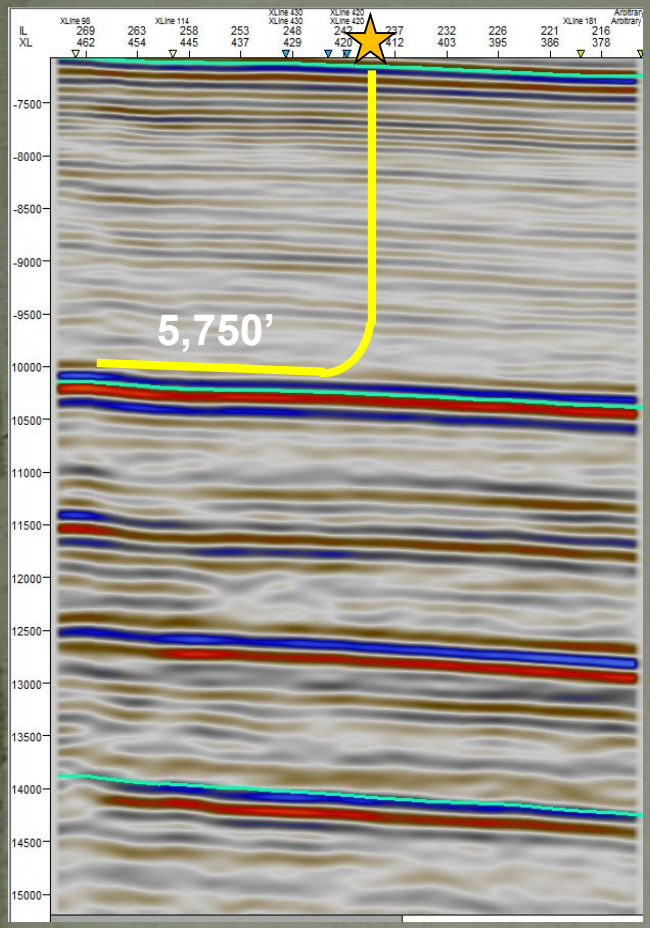

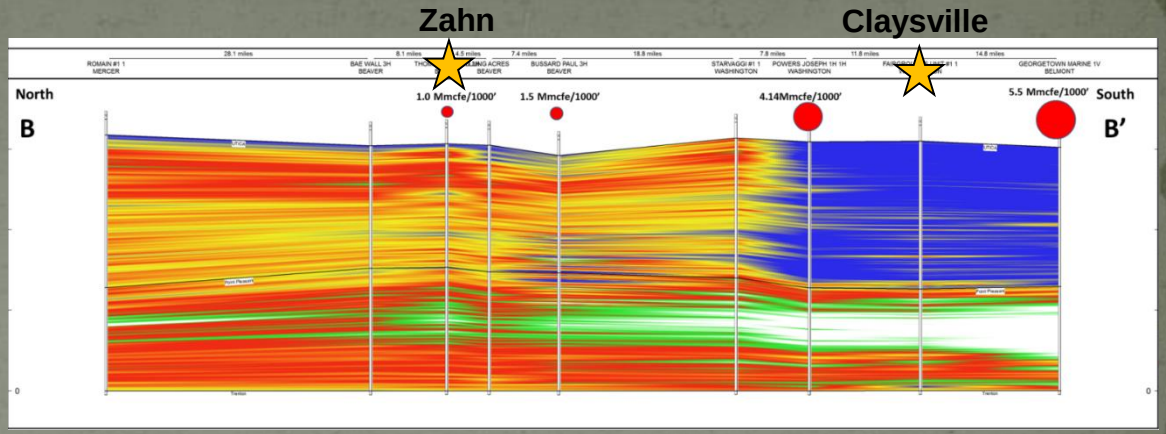

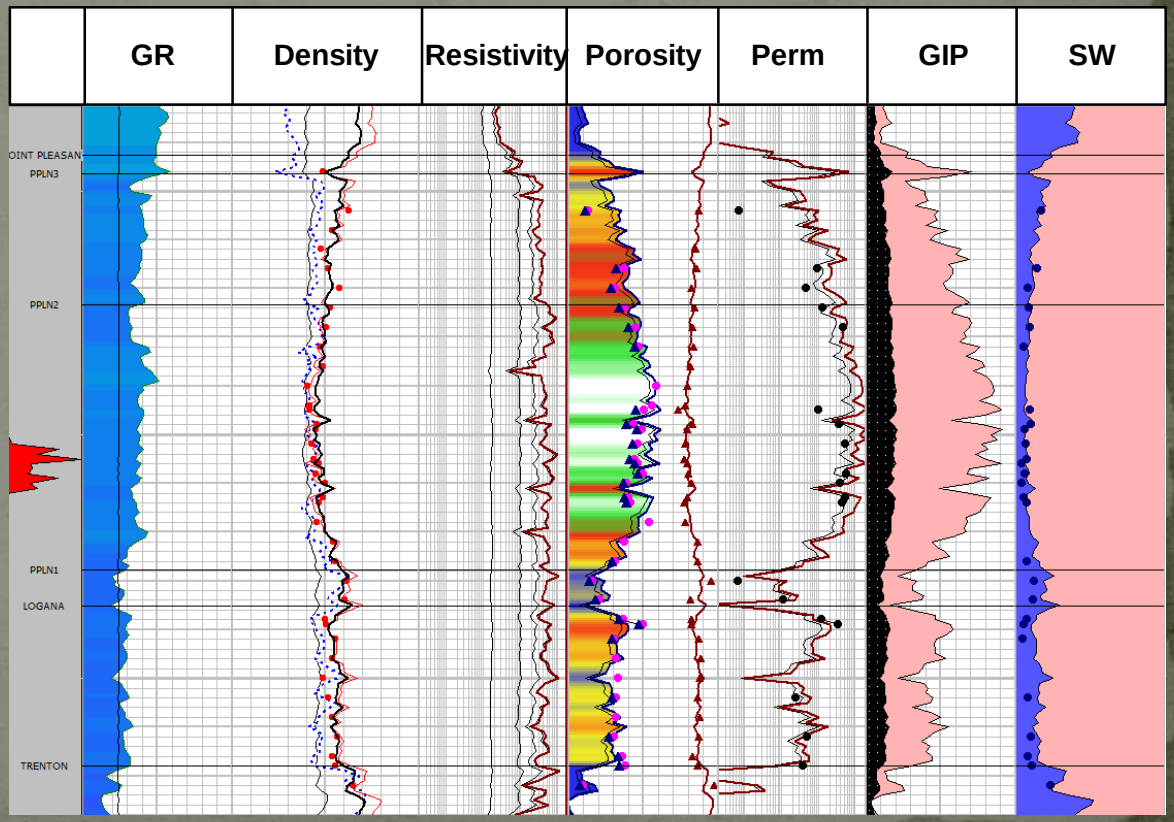

- Targeted and drilled structurally quiet area defined by 3D seismic coverage.

- Log and core data show excellent reservoir characteristics in the Point Pleasant target.

Claysville Sportsman’s Club Point Pleasant section

Key Point Pleasant Reservoir Quality Indicators

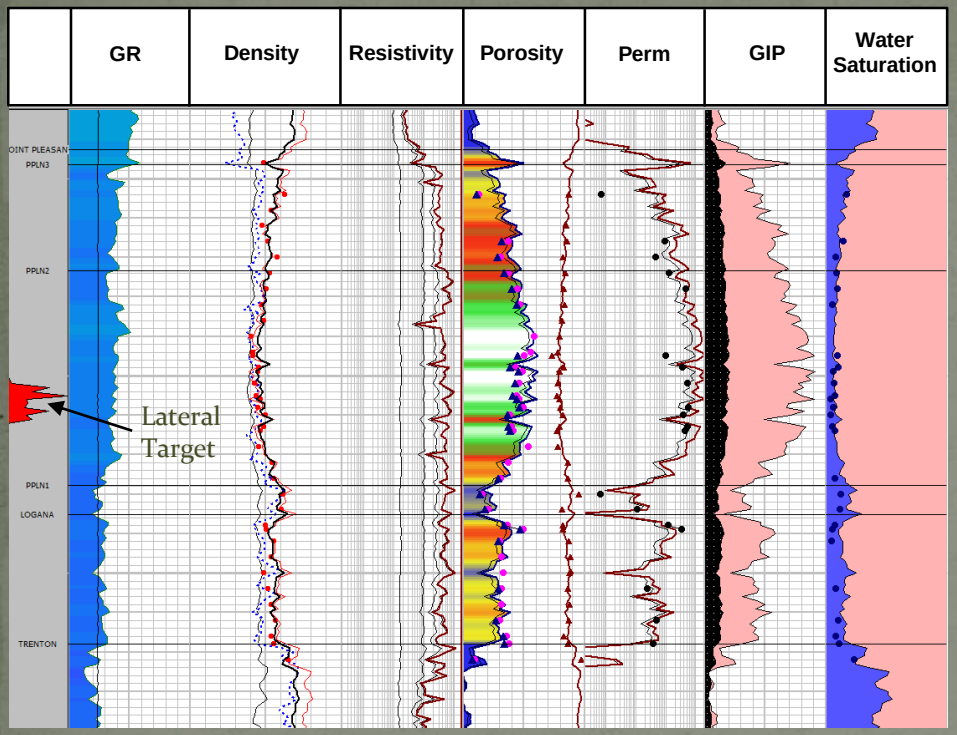

	GAS IN PLACE ANALYSIS: Claysville Sportsman 11H				
		Bulk Density (g/cc)	Gas Content (scf/ton)	GIP (scf/acre-ft)	GIP (BCF/section)
Utica to Trenton	Free Gas	2.64	240.4	863,811	140.9
	Sorbed Gas		23.5	84,488	13.8
	Total Gas in Place		263.9	948,299	154.7
	GAS IN PLACE ANALYSIS: Claysville Sportsman 11H				
		Bulk Density (g/cc)	Gas Content (scf/ton)	GIP (scf/acre-ft)	GIP (BCF/section)
Utica	Free Gas	2.73	148.2	549,663	46.3
	Sorbed Gas		9.9	36,534	3.1
	Total Gas in Place		158.1	586,197	49.3
	GAS IN PLACE ANALYSIS: Claysville Sportsman 11H				
		Bulk Density (g/cc)	Gas Content (scf/ton)	GIP (scf/acre-ft)	GIP (BCF/section)
Point Pleasant	Free Gas	2.56	338.5	1,177,676	93.0
	Sorbed Gas		38.1	132,404	10.5
	Total Gas in Place		376.5	1,310,080	103.5

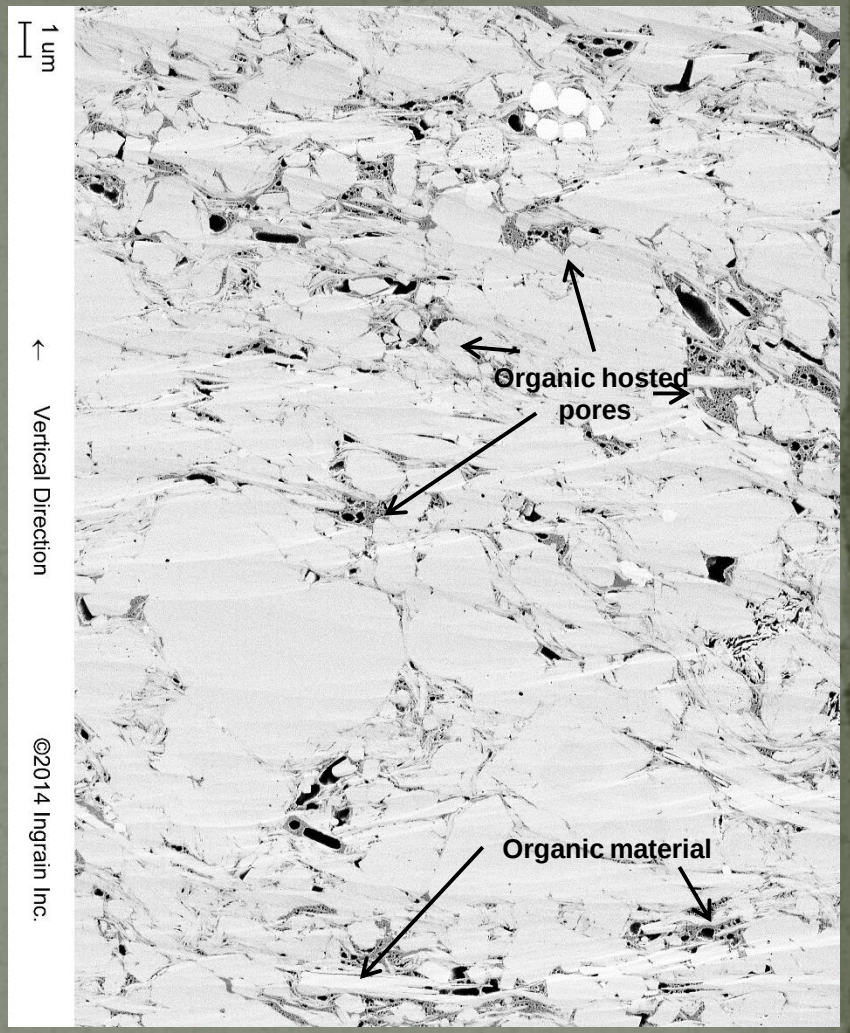

FIB SEM examples from lateral target interval.

Note TOC content and well developed pore network.

Selection of Point Pleasant Lateral Target

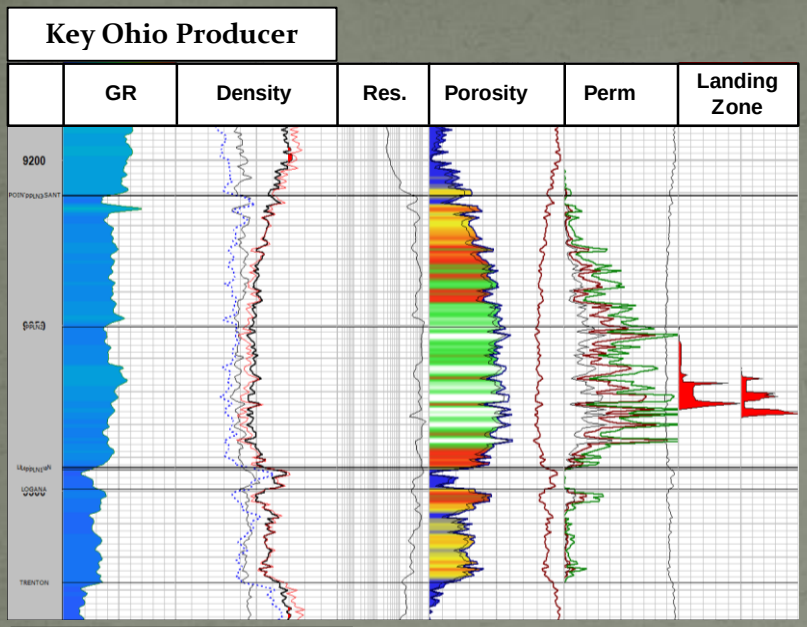

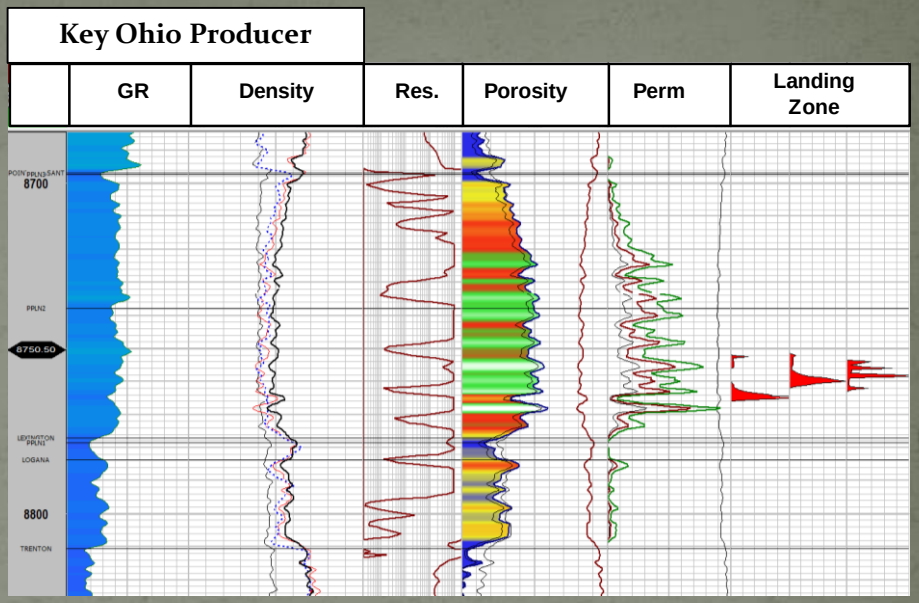

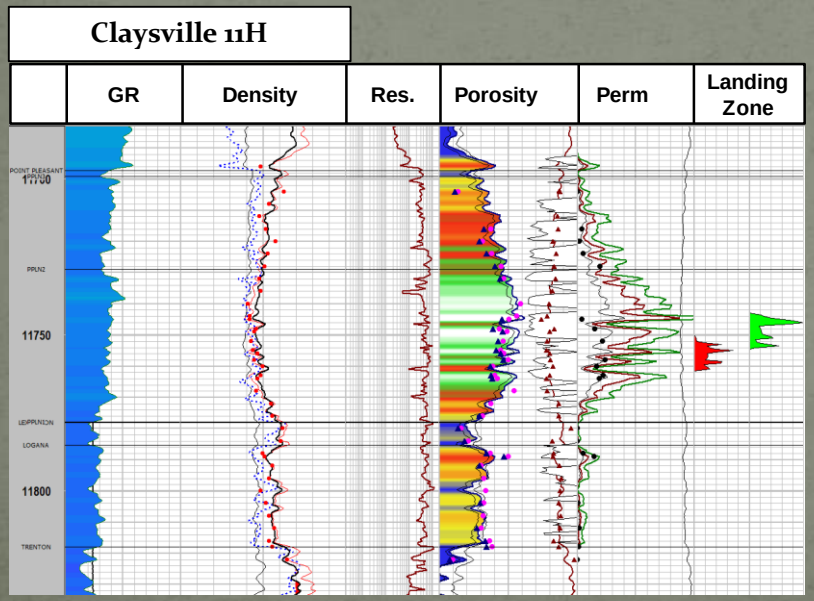

- Re-interpreted offsetting well MWD data to evaluate landing target.
- Compared lateral target to production data and EUR/1000 metrics.
- Observed correlation between highest production and targeting highest porosity zone.

1st High-Volume Horizontal in Southwest Pennsylvania



2014 Claysville 11H Flowback – tested 59 Mmcf/d and 5,800 psi initial pressure.

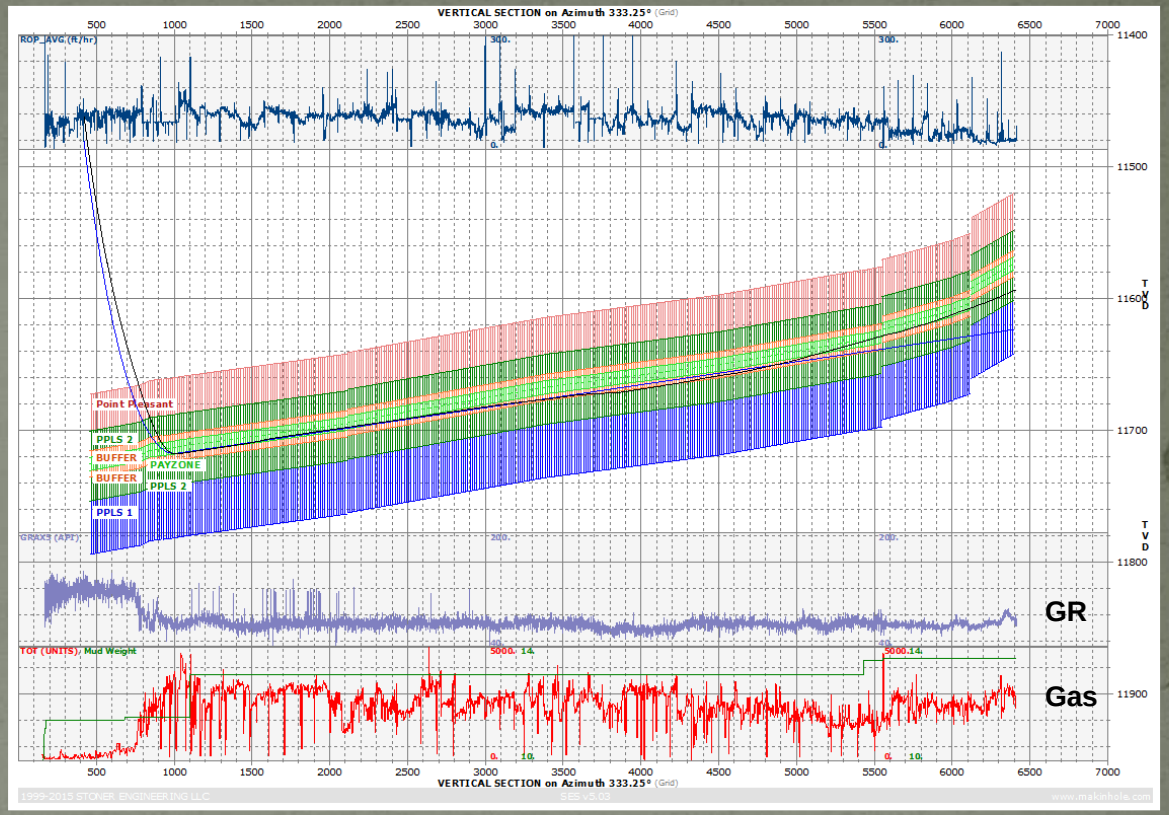

- Drilled pilot hole and horizontal in Q3 2014.
- Maintained strong gas shows throughout lateral.
- No significant well control issues.
- Key horizontal well establishing commerciality of the Point Pleasant dry gas play in SWPA.

Utica - Point Pleasant Play – Present Day

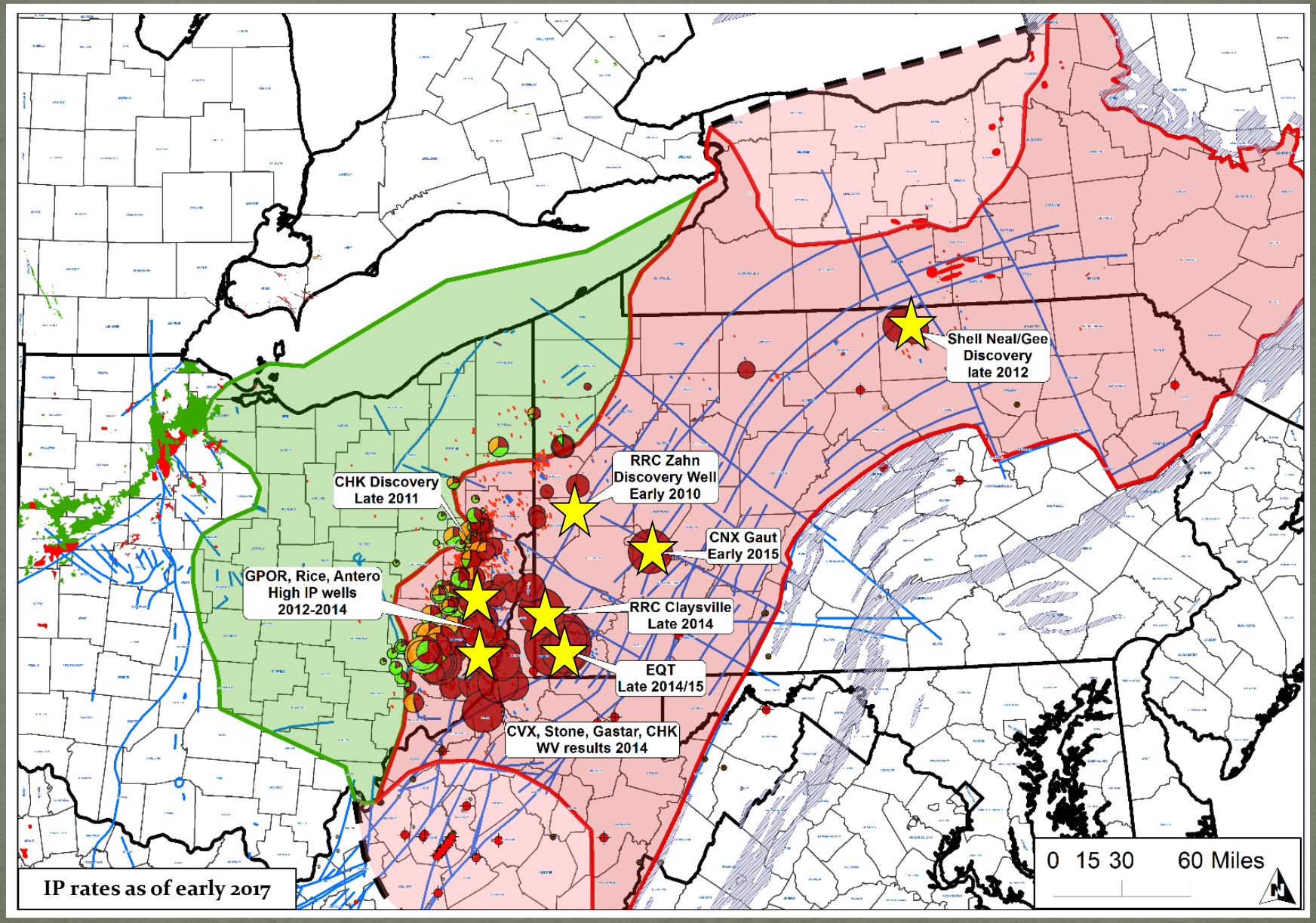

Since 2013 there has been significant expansion of play into Pennsylvania, Northeast Pennsylvania, and West Virginia.

What Is The Role of Natural Fracturing?

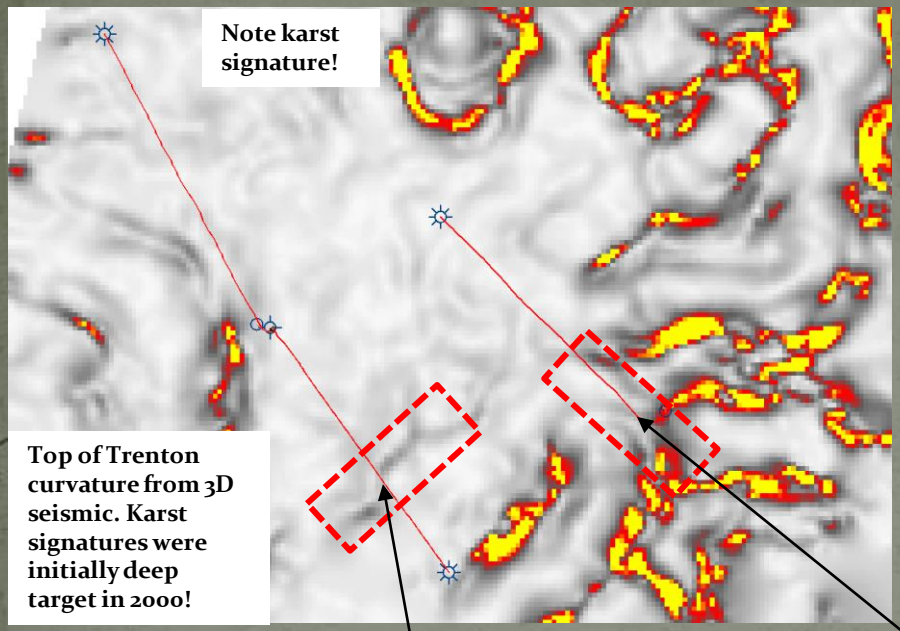

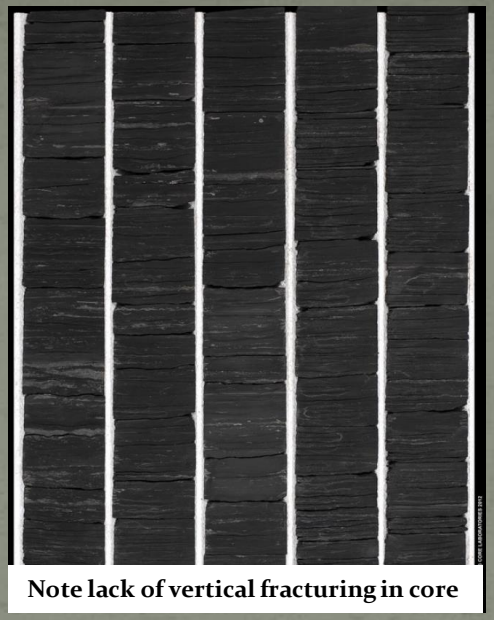
Note lack of vertical fracturing in core

- Fractures rare in core and vertical FMI but observed in seismic, drilling, and production.
- Level of fracturing significantly less than that observed in Marcellus.

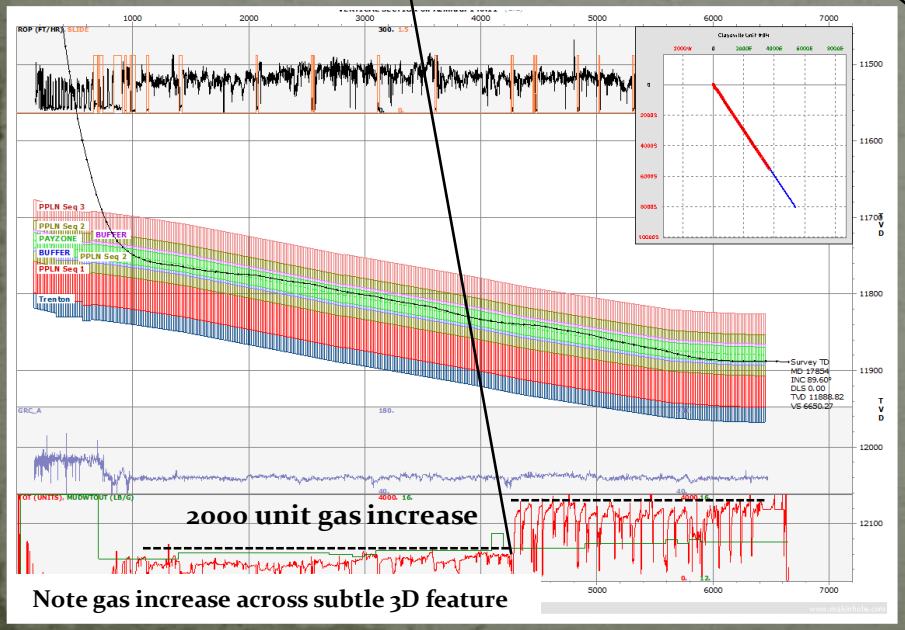

Note gas increase across subtle 3D feature

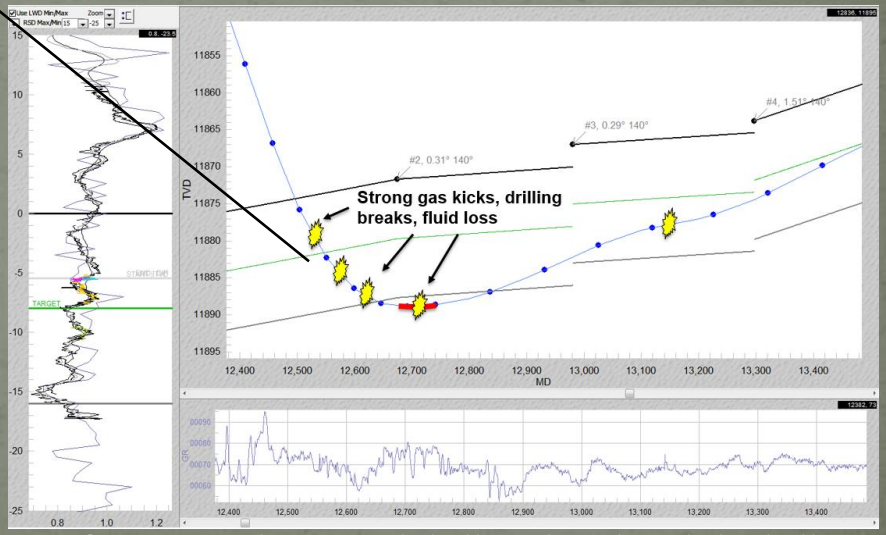

Significant gas shows and drilling breaks while drilling through fractured interval identified on seismic.

Future Considerations, Concepts, Ideas

- What is the influence of fracturing and faulting?
- Have the core areas been fully established and defined?
- What other play concepts need to be tested?
- What about the Utica Interval?
- Can the oil window be commercialized?
- What is the eastern thermal maturity limit of play?
- Are there any technological limitations?
- Should we be looking at old areas with new approaches?
- Lots of exploration challenges and opportunities to cover in the future.

- Thank you!!!

RANGE RESOURCES®

Petroleum Systems in the World's Richest Petroliferous Basin, Los Angeles, California*

K.E. Peters[1], L.S. Ramos[2], J.E. Zumberge[3] and T.L. Wright[4]

Search and Discovery Article #80386 (2014)**
Posted July 7, 2014

*Adapted from oral presentation at Session Honoring 50 Years of Wallace Dow's Contributions to Petroleum Geochemistry and Source Rock Characterization, AAPG Annual Convention and Exhibition, Houston, Texas, April 6-9, 2014
Other presentations from this session and posted on Search and Discovery are Article #80375 (2014) by Wallace Dow, Article #80385 (2014) by Robert Sterling and Anne Grau, and Article #80387 (2014) by Prasanta Mukhopadhy.
**AAPG©2014 Serial rights given by author. For all other rights contact author directly.

[1]Schlumberger, Mill Valley, California, US (KPeters2@slb.com)
[2]Infometrix, Inc. Bothell, Washington, US
[3]GeoMark Research, Houston, Texas, US
[4]Chevron (retired), San Anselmo, California, US

Abstract

Based on a training set of 112 nonbiodegraded or mildly biodegraded crude oil samples, a chemometric decision tree was constructed which identifies five tribes and 12 genetic oil families in the Los Angeles basin. The decision tree classified more than 50 additional samples that were affected by severe thermal maturation or biodegradation. The families occur in different parts of the basin and exhibit different bulk properties, such as API gravity, sulfur and metal content. Unlike previous publications, which propose that these differences result from maturation or biodegradation of similar oil, this work shows that these properties are largely controlled by different source rock organofacies. The character of the source rock was inferred from the geochemistry of each family and their distinct stratigraphic occurrence. Carbon isotope ratios for saturate and aromatic fractions indicate marine Neogene source rocks. Tribes 1–2 consist of five oil families found mainly east of the Newport-Inglewood Fault Zone (NIFZ). These oils show evidence of proximal, clay-rich source rock deposited under suboxic conditions with more higher-plant and especially angiosperm input than Tribes 3–6 (e.g., elevated C_{19} tricyclic terpane, oleanane/hopane, C_{31}R/hopane, and C_{24}/C_{23} tricyclic terpane ratios). Tribes 1–2 originated from upper Miocene (Delmontian) shale in the Central Trough. Tribes 3–6 originated from distal, clay-poor source rock deposited under anoxic conditions with less angiosperm input. Tribes 3–6 also show elevated bisnorhopane/hopane, supporting anoxic conditions. Tribe 3 consists of three families generated

from upper Miocene (Middle-Upper Puente) marl source rock west of the NIFZ. These oils occur from Torrance in the north to the giant Wilmington and Huntington Beach fields in the south. Tribe 4 consists of two families west of the NIFZ that likely originated from middle-upper Miocene (Mohnian) marl source rock. The oils range from Playa del Rey in the north to Wilmington field in the south. Tribe 5 occurs southwest of the NIFZ mainly in the Wilmington and Huntington Beach fields and originated from middle-upper Miocene (Lower Puente) nodular shale with significant higher-plant plant input. Tribe 6 occurs northwest of the NIFZ from Beverly Hills in the north to the El Segundo field in the south. These oils were generated from middle-upper Miocene (Lower Modelo) nodular shale equivalent with significant higher-plant plant input.

References Cited

Blake, G.H., 1991, Review of the Neogene biostratigraphy and stratigraphy of the Los Angeles basin and implications for basin evolution, *in* Active Margin Basins: AAPG Memoir 52, p. 135-184.

Jeffrey, A.W.A., H.M. Alimi, and P.D. Jenden, 1991, Geochemistry of Los Angeles basin oil and gas systems, *in* Active Margin Basins: AAPG Memoir 52, p. 197-219.

Peters, K.E., Moldowan, J.M., 1993. The Biomarker Guide: Prentice Hall, Englewood Cliffs, New Jersey. 363p.

Philippi, G.T., 1965, On the depth, time and mechanism of petroleum generation: Geochim. et Cosmochim. Acta, v. 29, p. 1021-1-49

Sofer, Z., 1984, Stable carbon isotope composition of crude oils: Application to source depositional environments and petroleum alteration: AAPG Bulletin, v. 68, p. 31-49.

Walker, A.L., T.H. McCulloh, N.F. Petersen, and R.J. Stewart, 1983, Anomalously low reflectance of vitrinite in comparison with other petroleum source-rock maturation indices from the Miocene Modelo formation in the Los Angeles basin, Califorinia, *in* C.M. Isaacs and R.E. Garrison, eds., Petroleum Generation and Occurrence in the Miocene Monterey Formation, Californa: Pacific Section, SEPM, p. 185-190.

Wright, T.L., 1991, Structural geology and tectonic evolution of the Los Angeles Basin, California, *in* Active Margin Basins: AAPG Memoir 52, p. 35-134.

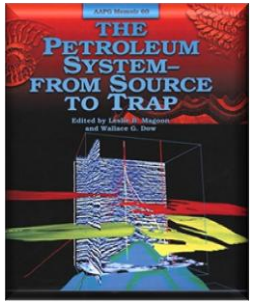

Petroleum Geochemistry and Source Rock Characterization:
Honoring 50 Years of Wallace Dow's Contributions



APRIL 8, 2014
HOUSTON, TX

Petroleum Systems in the World's Richest Petroliferous Basin, Los Angeles, California

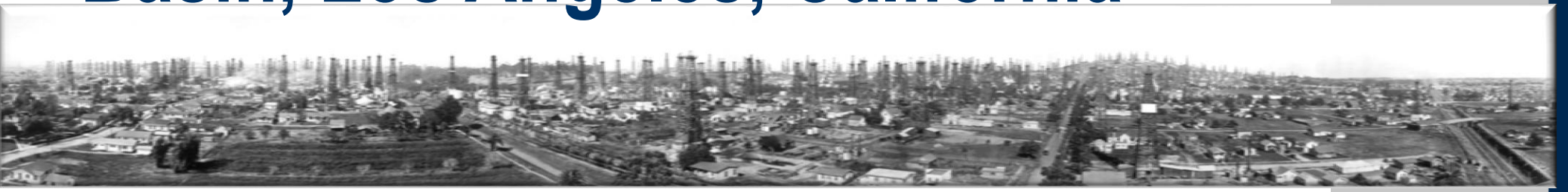

K.E. Peters[1,2], L.S. Ramos[3], J.E. Zumberge[4], T.L. Wright[5]

[1] Schlumberger Information Solutions, Mill Valley, CA 94941; kpeters2@slb.com
[2] Dept. Geology & Environmental Sciences, Stanford University, Stanford, CA 94305
[3] Infometrix, Inc., Bothell, WA 98011
[4] GeoMark Research, Houston, TX 77095
[5] Chevron U.S.A. (retired)

Acknowledgements

- *Tess Menotti (maps of sample locations)*
- *Les Magoon (general discussions)*

Signal Hill, California, c 1923

Significant Characteristics of the Los Angeles Basin

- **World's richest basin; classic transform-margin basin.**
- **Since 1880, ~67 fields were discovered, e.g., supergiant Wilmington, Long Beach, and Huntington Beach fields.**
- **Little exploration since the early 1970's; significant potential remains in deep, especially offshore areas.**
- **Current Paradigm – Variations in oil quality are caused by differing *maturity, migration, and/or source oxicity, not by different organic matter* (Jeffrey et al., 1991).**

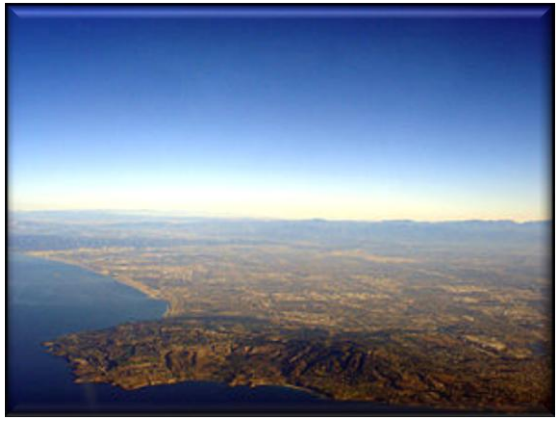

Purpose of the Los Angeles Basin Study

- **Measure biomarker and isotope ratios for ~150 crude oil samples from the basin to evaluate genetic relationships.**
- **Assess the extent of biodegradation for each sample to identify a "training set" where source-related biomarker or isotope ratios are unaffected.**
- **Identify oil families; create a chemometric (multivariate statistics) decision tree to classify new samples.**
- **Map the distribution of oil families; use biomarker and isotope ratios to infer their source-rock organofacies.**

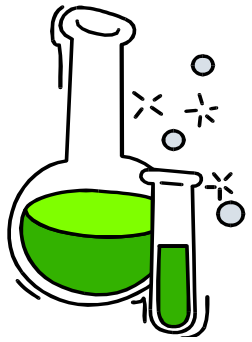

Map Shows Families and Base Mohnian (~14 Ma) >12,000 Ft.

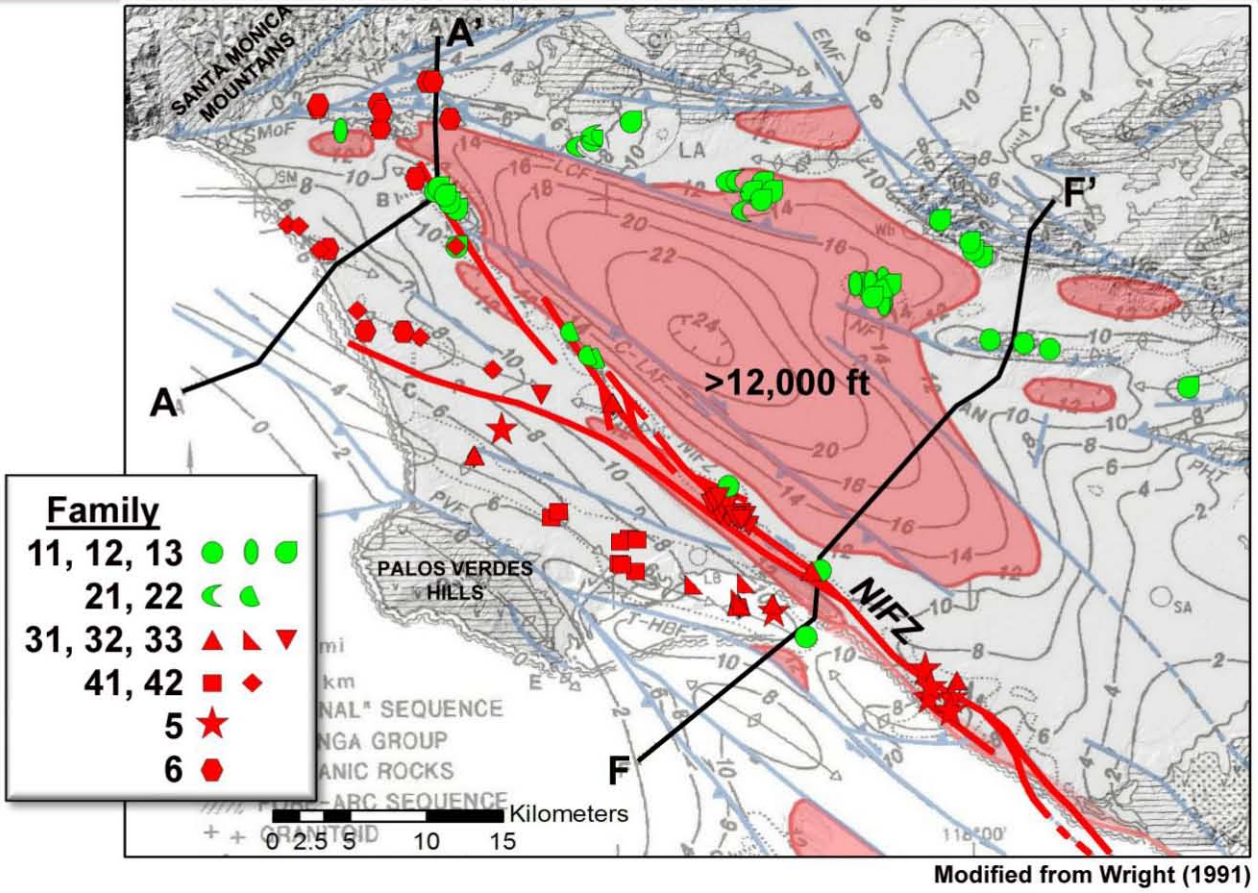

Presenter's notes: Base Mohnian is a late middle Miocene horizon; NIFZ = Newport-Inglewood Fault Zone

Oil Families: 24 *Source-Related* Biomarker & Isotope Ratios

Oil Sample	Biodegradation*	Terpanes																Steranes				Isotopes		
		C_{19}/C_{23}	C_{22}/C_{21}	C_{24}/C_{23}	C_{26}/C_{25}	C_{26}/Ts	Tet/C_{23}	$C_{27}T/C_{27}$	C_{28}/H	C_{29}/H	X/H	Ol/H	$C_{31}R/H$	Ga/31R	$C_{35}S/C_{34}S$	$C_{27}Ts/Tm$	$C_{29}Ts/Tm$	S/H	$\%C_{27}$	$\%C_{28}$	$\%C_{29}$	S1/S6	$\delta^{13}C_{sat}$	$\delta^{13}C_{aro}$	CV
ElS5	0	0.0350	0.2470	0.7517	0.7903	1.8274	0.1190	0.0378	0.3835	0.5460	0.0192	0.1162	0.2847	0.1006	0.9857	0.4668	0.2008	1.7745	31.1369	41.6277	27.2354	0.1793	-25.02	-23.68	-0.92
LB6	4	0.0332	0.1781	0.6544	1.1647	2.6412	0.1335	0.0590	0.4458	0.5961	0.0167	0.1319	0.2269	0.6705	0.8730	0.3510	0.1628	1.8849	29.7768	44.5270	25.6962	0.1514	-23.88	-22.94	-2.16
BvH7	3	0.0263	0.2458	0.9474	0.8300	2.6974	0.1033	0.0329	0.2743	0.5091	0.0256	0.1405	0.2452	0.2843	0.9021	0.5314	0.2110	1.6759	30.0511	43.9406	26.0083	0.2100	-23.87	-23.16	-2.67
BvH26	0	0.0202	0.2926	0.7979	0.8203	2.0286	0.1268	0.0560	0.3661	0.5678	0.0151	0.1439	0.2741	0.2774	0.9107	0.4159	0.1811	1.3432	31.9467	39.9842	28.0690	0.0125	-25.06	-23.67	-0.80
CvH2	0	0.0237	0.2735	0.8494	0.9053	2.0887	0.1302	0.0499	0.1838	0.5275	0.0216	0.1478	0.2242	0.4121	0.6551	0.5258	0.1826	1.2655	30.6225	39.4825	29.8950	0.1942	-24.95	-23.64	-1.01
SwN28	1	0.0202	0.2647	0.7878	0.8106	2.0852	0.1262	0.0559	0.3621	0.5702	0.0139	0.1472	0.2723	0.4088	0.9618	0.3826	0.1758	1.5505	30.6532	40.9345	28.4122	0.1608	-25.04	-23.73	-0.98
Wht42	4	0.0555	0.2478	0.8727	1.0259	2.8864	0.0908	0.0815	0.2331	0.4251	0.0319	0.2837	0.1736	0.6051	0.6676	0.7019	0.2142	1.3942	32.0455	40.8963	27.0582	0.2966	-23.68	-23.05	-2.91
Wil78	5	0.0169	0.2394	0.7959	0.7684	3.8077	0.0926	0.0514	0.4284	0.7302	0.0286	0.1976	0.3393	0.5113	0.9033	0.3726	0.1649	0.7196	32.7066	41.3216	25.9717	1.1362	-23.66	-22.96	-2.76
Wil79	4	0.0166	0.2464	0.8045	0.7615	3.6745	0.0908	0.0573	0.3370	0.6352	0.0256	0.1622	0.2890	0.5523	0.9238	0.4197	0.1587	1.0619	33.0806	40.7143	26.2051	0.4414	-23.59	-22.91	-2.83

*0-10 biodegradation scale of Peters and Moldowan (1993)

Training Set: No Biodegradation of Steranes or Terpanes

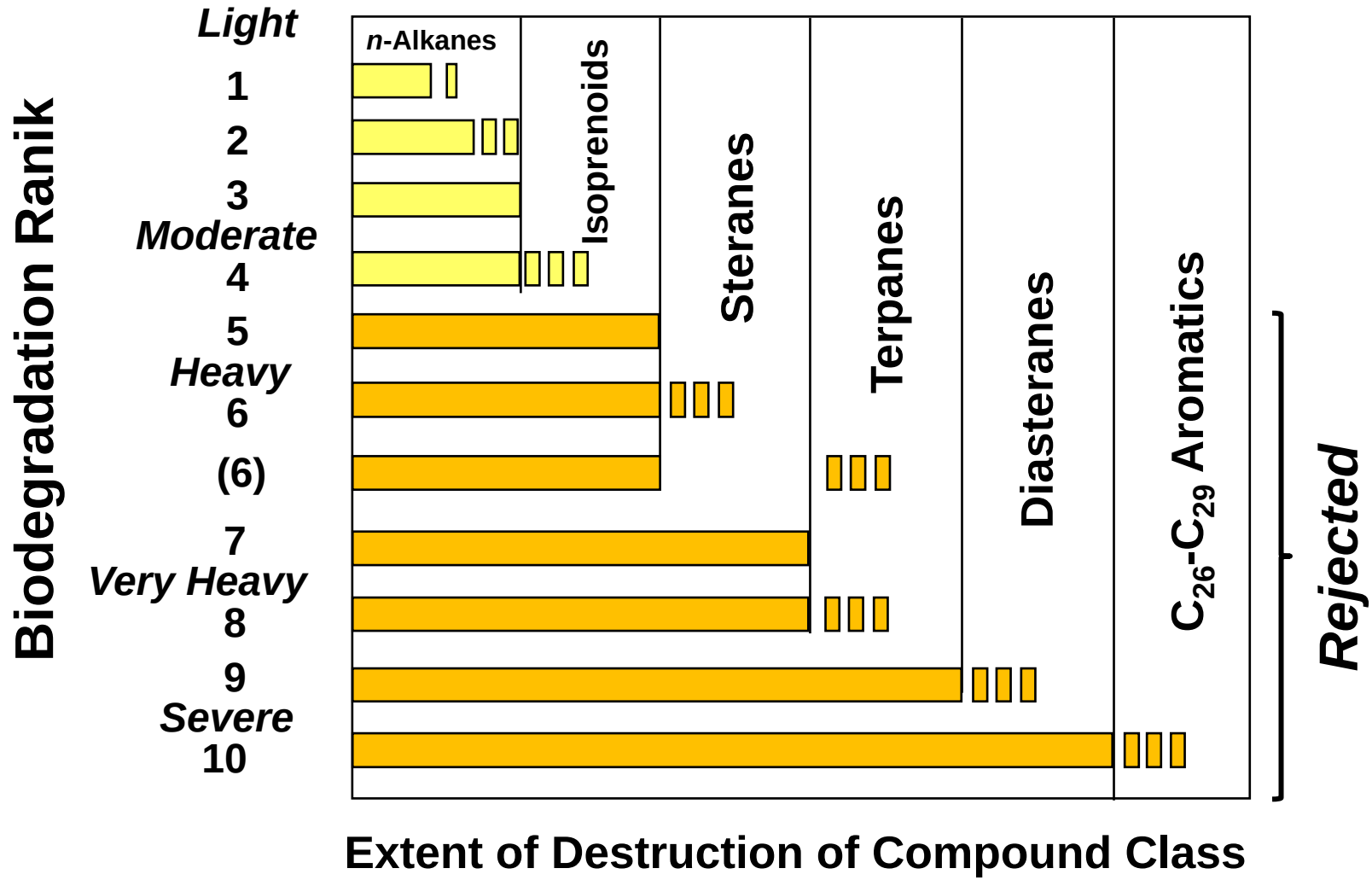

Peters and Moldowan (1993)

Oil Having Biodegradation Rank 5 or More was Rejected

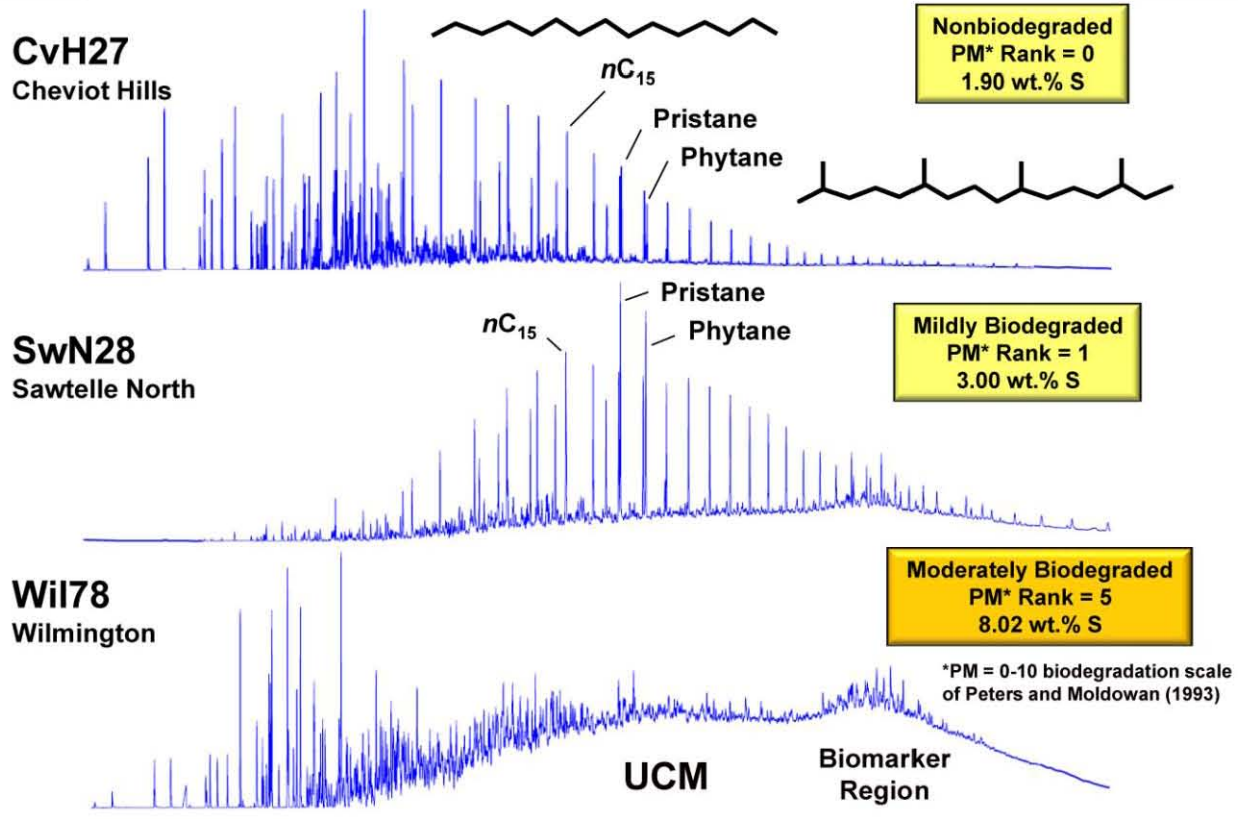

Presenter's notes: CvH27S, SwN28S = family 6 west of Newport-Inglewood Fault Zone
Wil78S = not classified (heavy biodegradation)

6 Tribes: East/West of Newport-Inglewood Fault Zone (NIFZ)

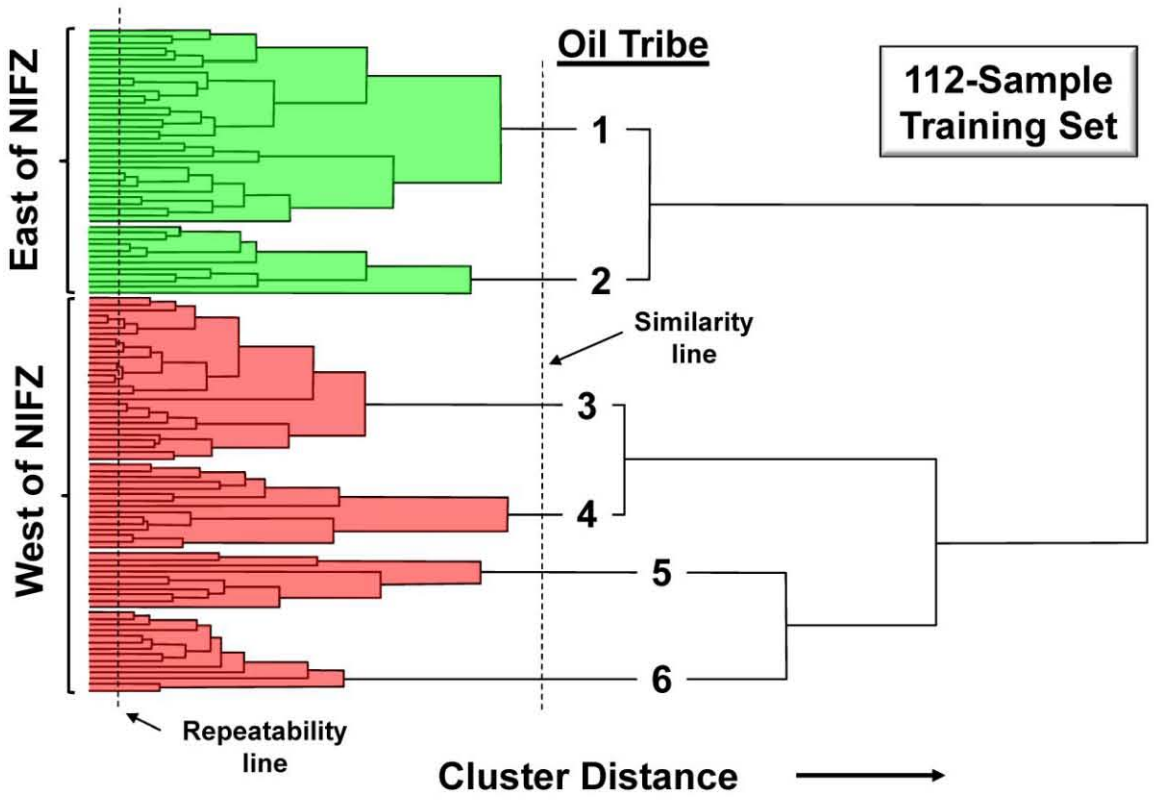

Presenter's notes: Four oils from LB 498, LB499, LB500, and LB501 from different wells, but about the same depth (2518-3060 ft), occur in the middle of Tribe 3 and represent a better assessment of repeatability that four analyses of the same sample.

All Samples Have a Miocene Isotopic Signature (^{13}C-Rich)

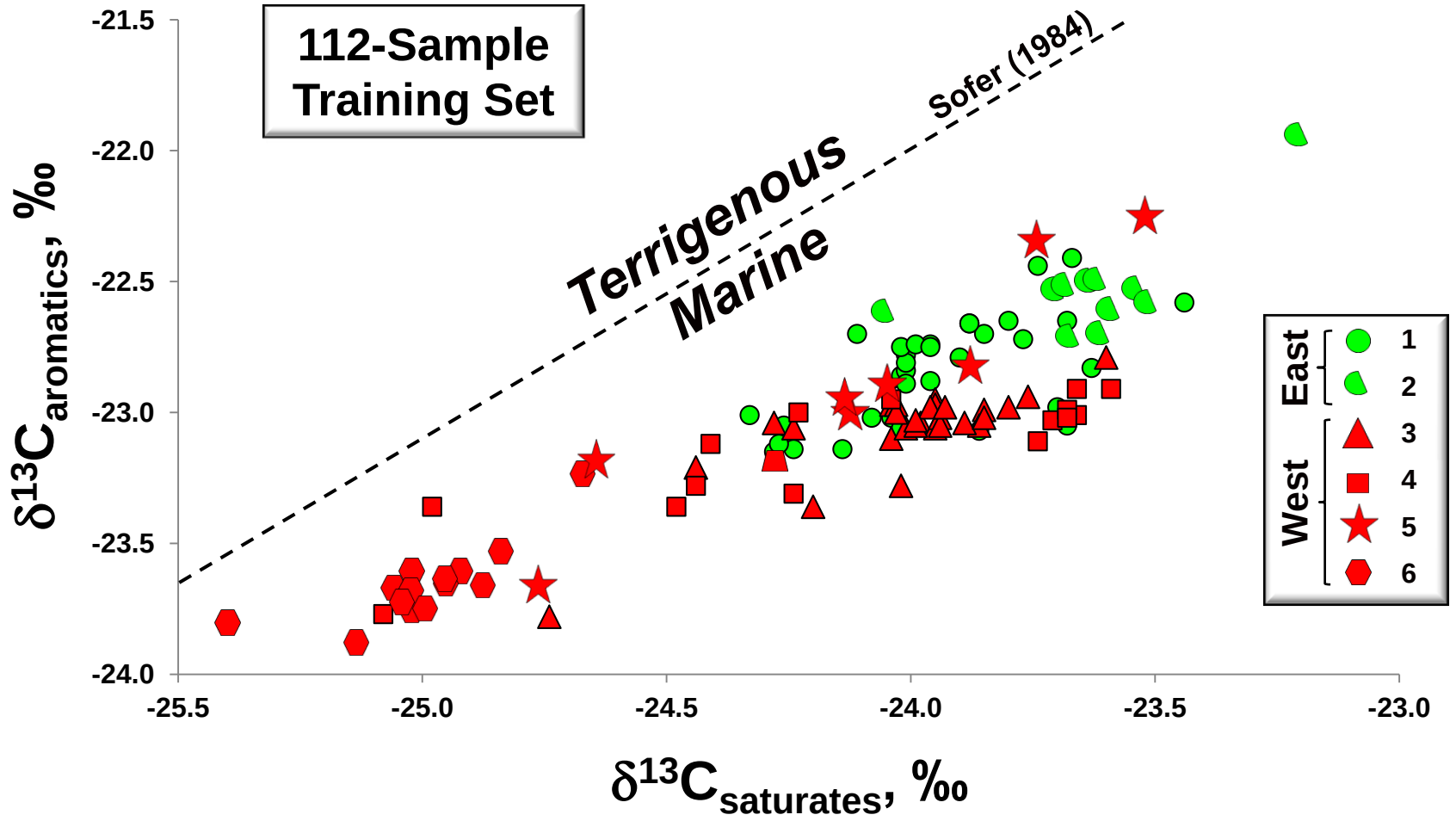

Tribes 1 and 2 are Enriched in Higher-Plant Biomarkers



Nerium oleander

Families East/West of Newport-Inglewood Fault Zone (NIFZ)

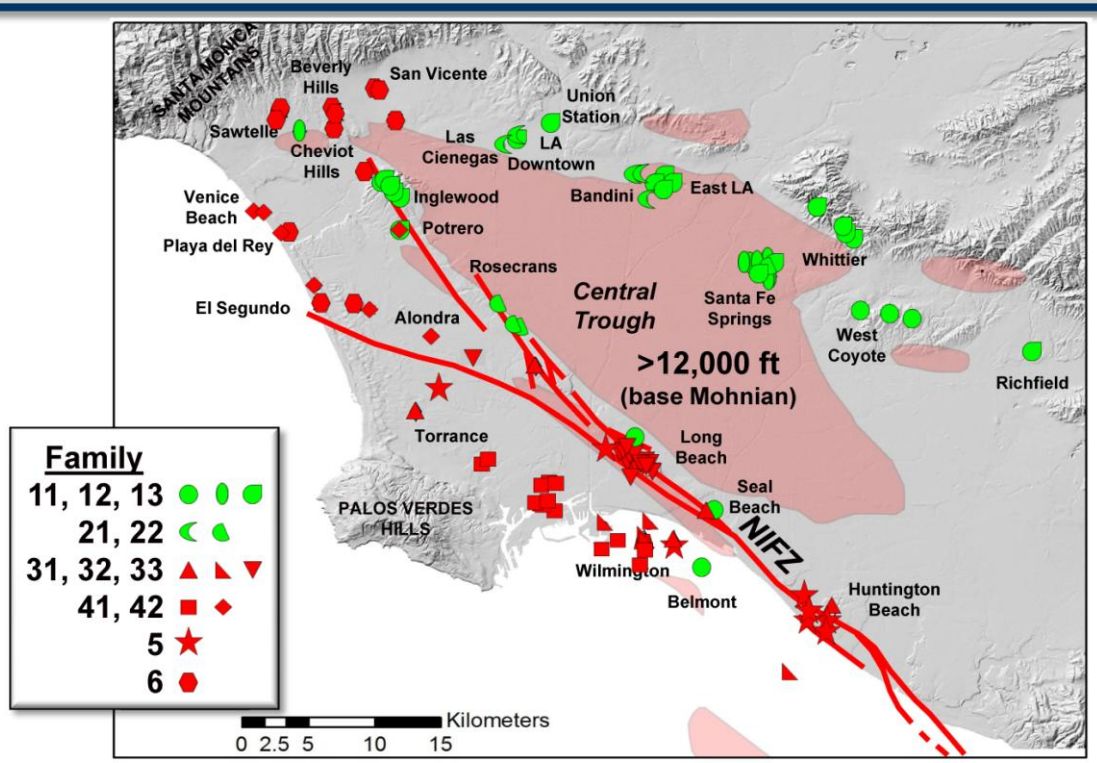

Presenter's notes: The central trough north of the NIFZ trends N50°W. Maximum width between Dominguez and Santa Fe Springs oil fields is about 8 mi (14 km). The American Petrofina Central Core Hole #1, located 1 mi (3.2 km) northeast of the Rosecrans oil field, reaches Delmontian or lowermost Repetto at TD of 20,700 ft (6311 m). Base of Mohnian from Wright (1991) is late middle Miocene horizon, ca. 14 Ma.

Families in Tribe 1 Originated from Source Rock East of NIFZ

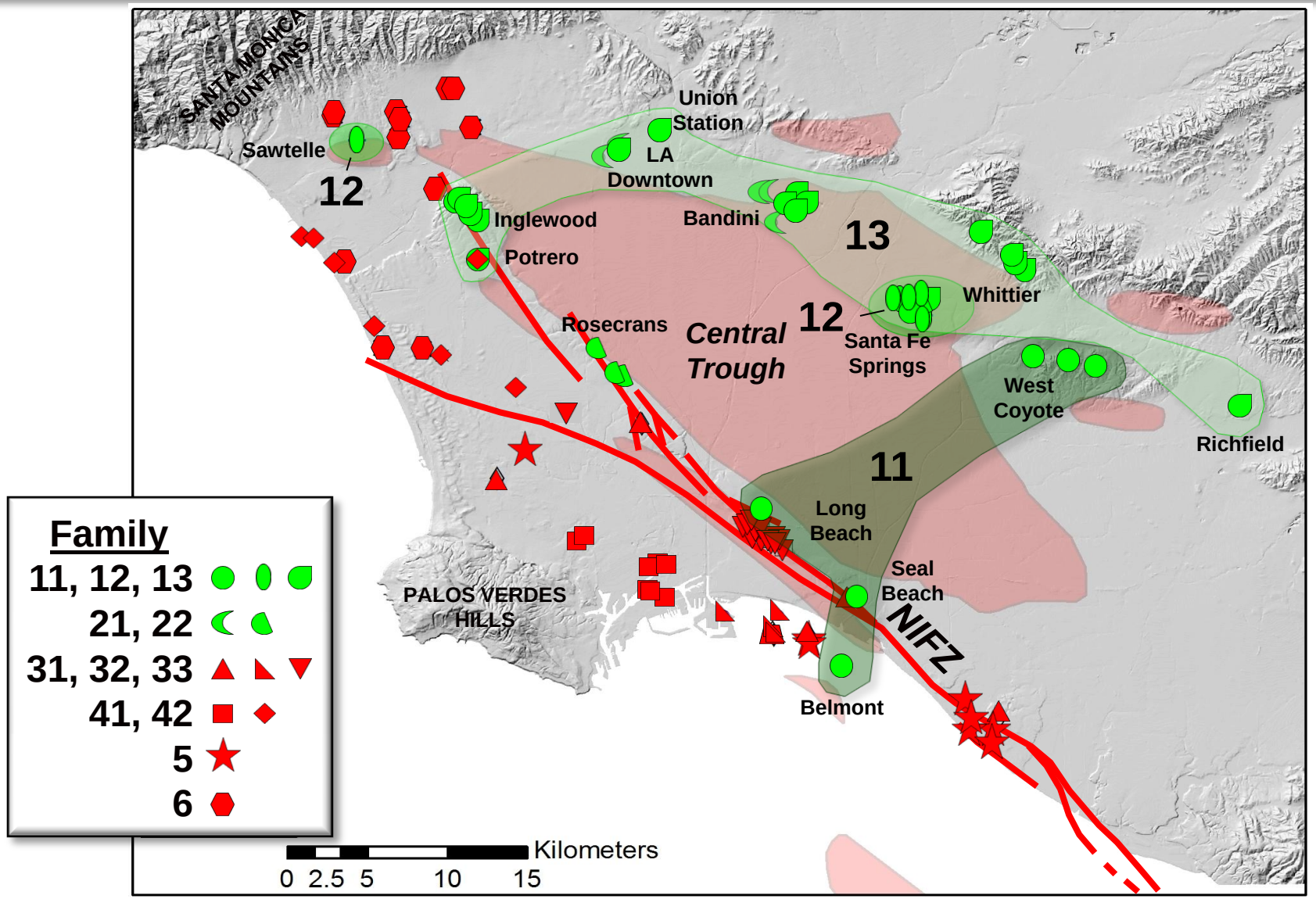

Families in Tribe 1 Originated from Source Rock East of NIFZ

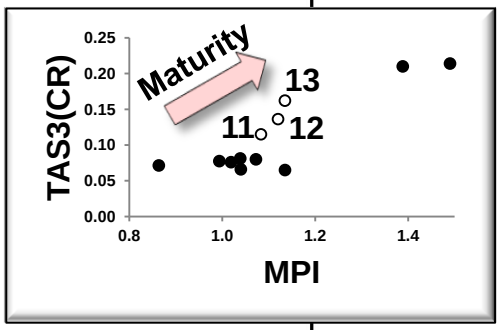

Family

11, 12, 13	● ● ●
21, 22	◐ ◐
31, 32, 33	▲ ◣ ▼
41, 42	■ ◆
5	★
6	⬢

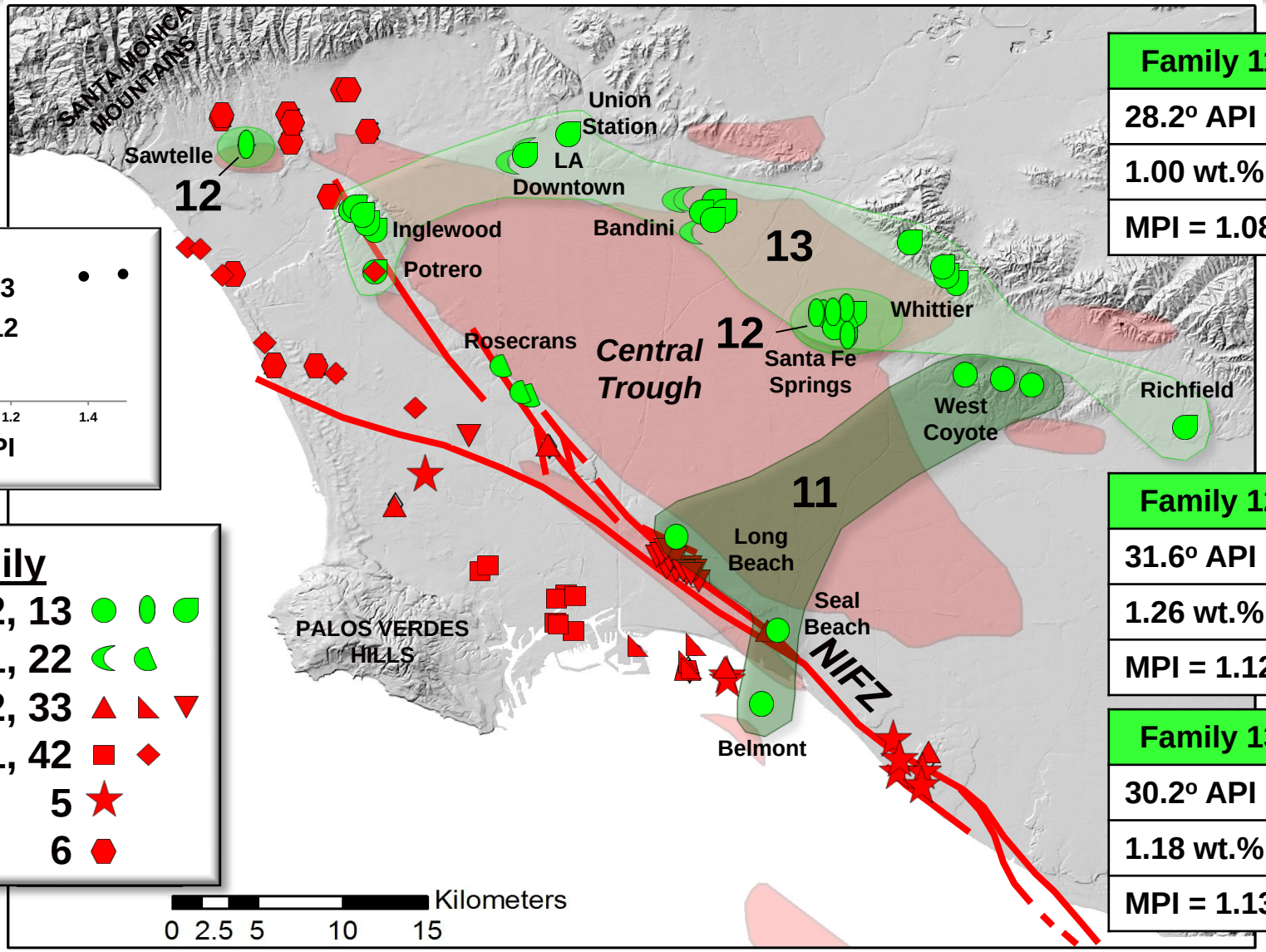

Family 11
28.2° API
1.00 wt.% S
MPI = 1.08

Family 12
31.6° API
1.26 wt.% S
MPI = 1.12

Family 13
30.2° API
1.18 wt.% S
MPI = 1.13

Families in Tribe 2 Originated from Source Rock East of NIFZ

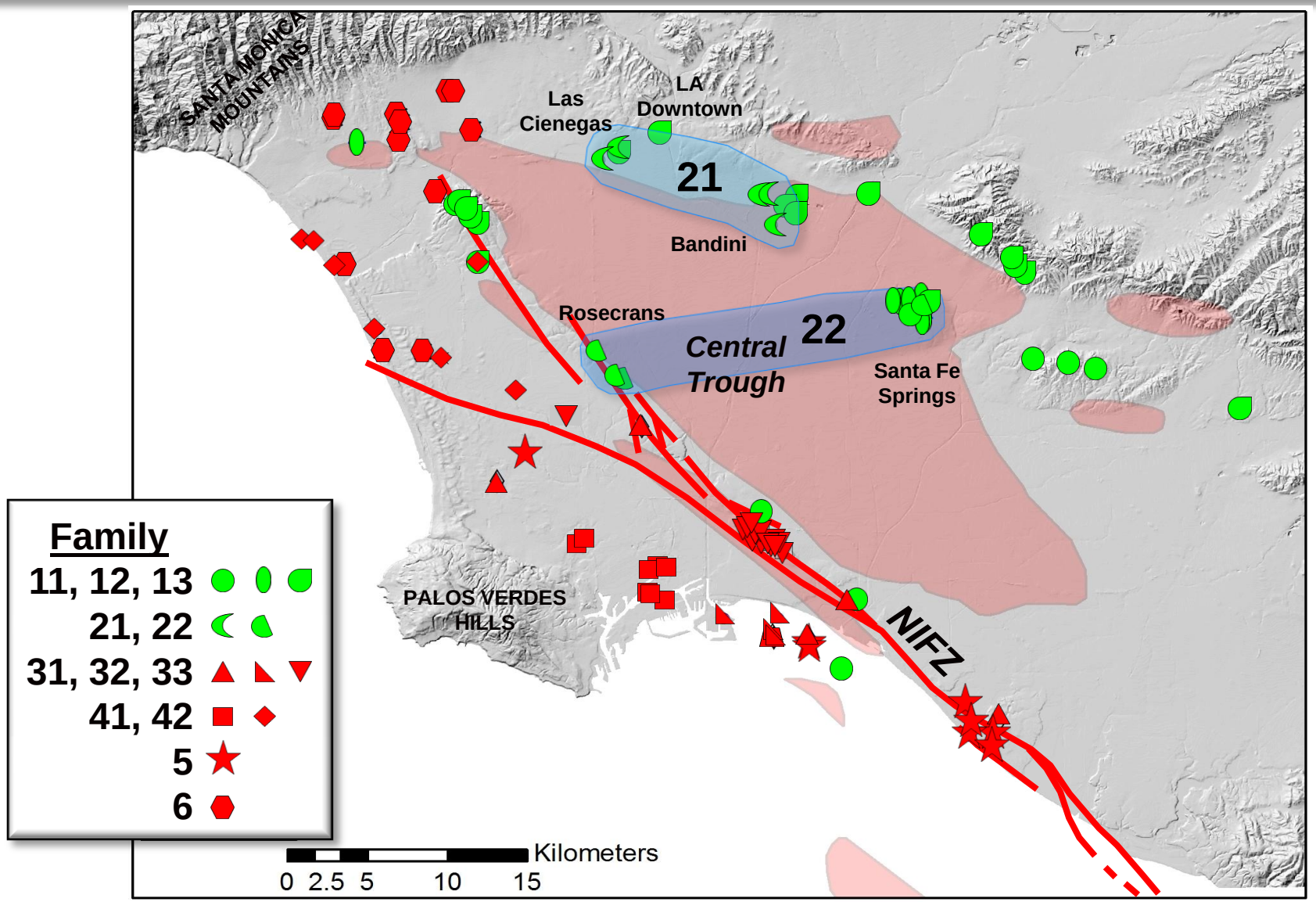

Families in Tribe 2 Originated from Source Rock East of NIFZ

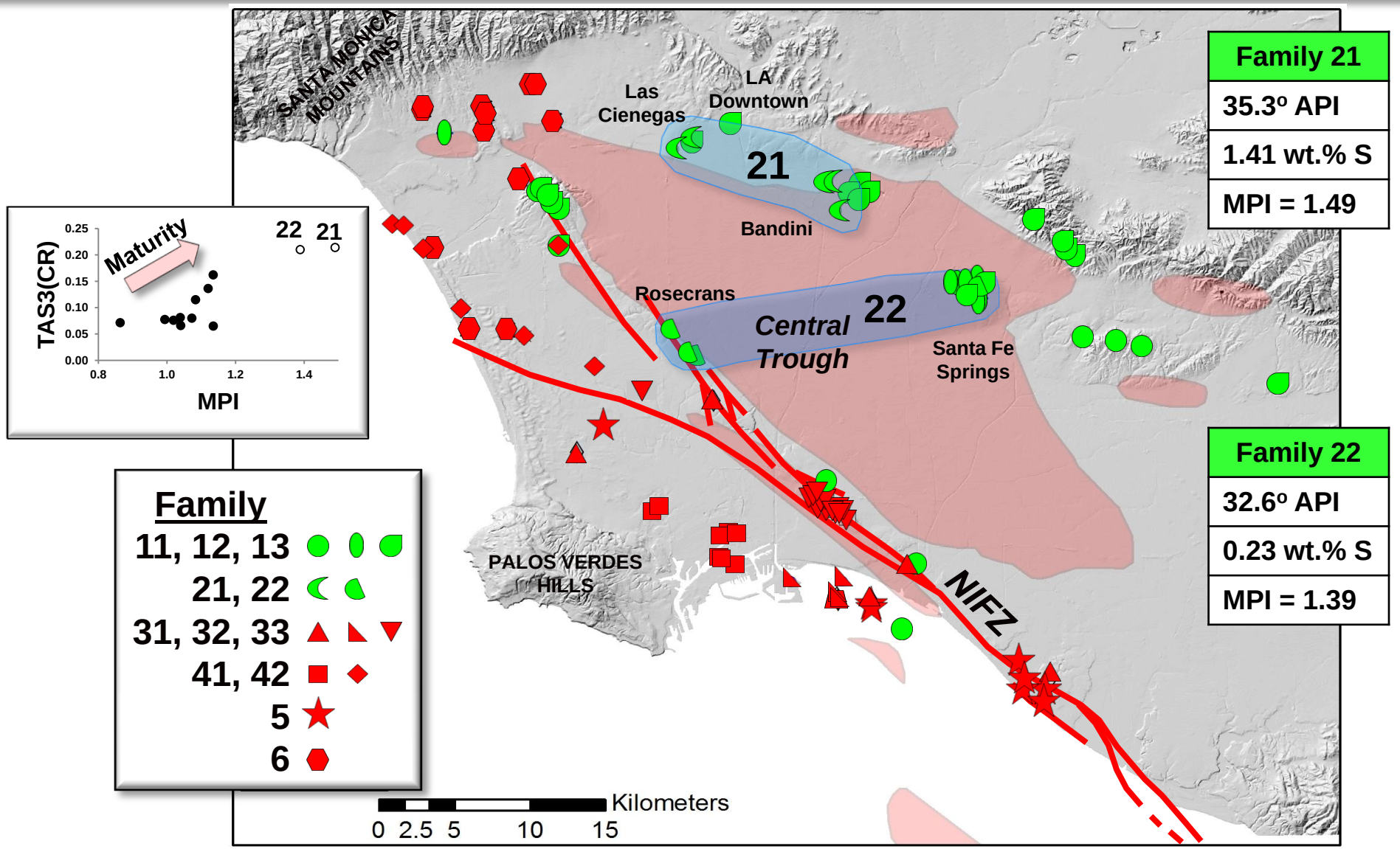

Tribe 3 Families Originated from Source Rock West of NIFZ

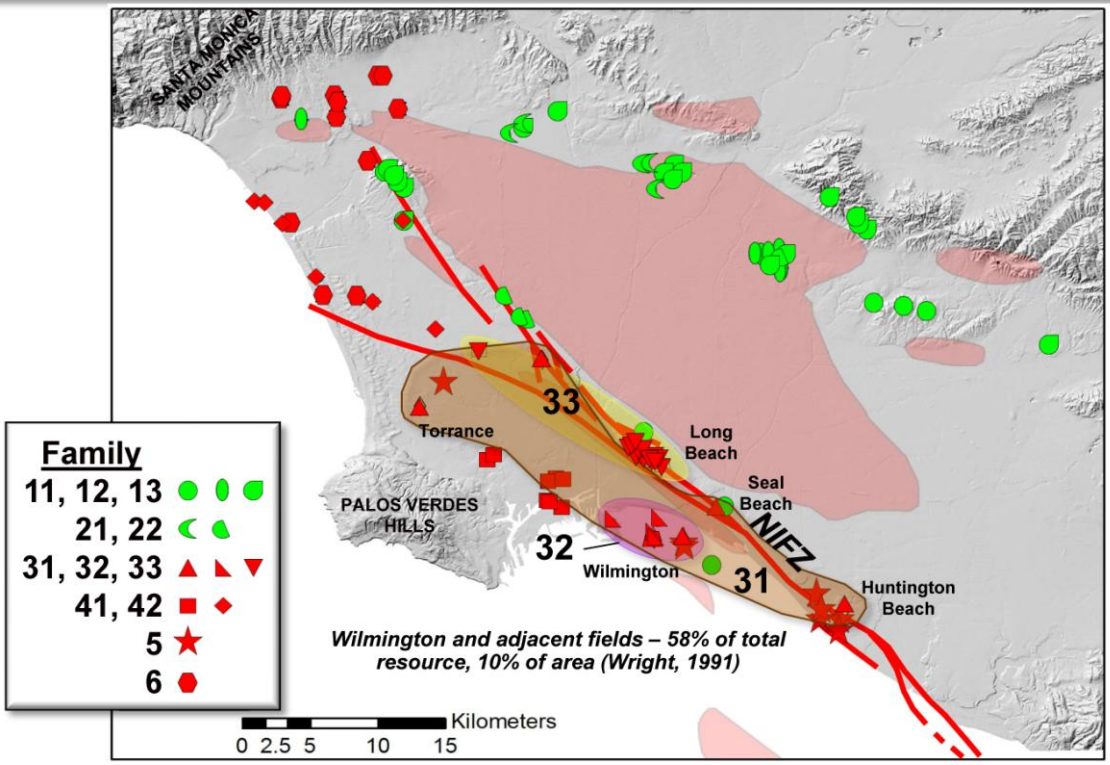

Presenter's Notes: "Wilmington and adjacent oil fields – Long Beach, Seal Beach, and Huntington Beach will yield 5.2 GBO, about 58% of the basin's total resource; yet the area encompassed by these fields occupies no more than 10% of the basin. Here all the factors are optimal." Wright (1991). Thick localized Monterey source rock and high geothermal gradient 3.29^{o}F/100 ft (60°C/km) at Wilmington (Beyer, 1988).

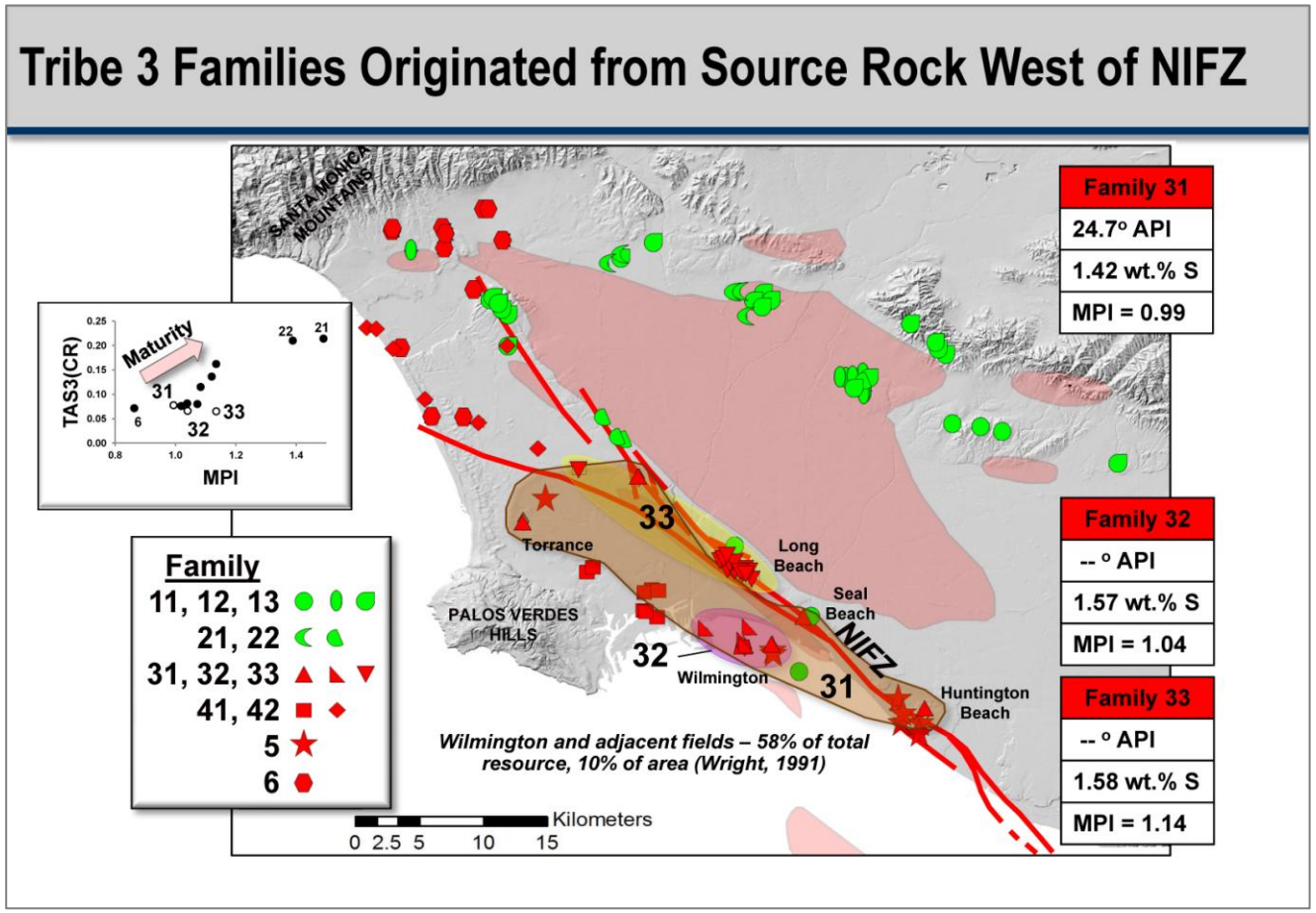

Presenter's Notes: "Wilmington and adjacent oil fields – Long Beach, Seal Beach, and Huntington Beach will yield 5.2 GBO, about 58% of the basin's total resource; yet the area encompassed by these fields occupies no more than 10% of the basin. Here all the factors are optimal." Wright (1994). Thick localized Monterey source rock and high geothermal gradient 3.29^{o}F/100 ft (60°C/km) at Wilmington (Beyer, 1988). The present-day average geothermal gradient in the Los Angeles basin is ~2.15^{o}F/100 ft (39.1^{o}C/km; Bostick et al., 1978 in Jeffrey et al., 1991).

Tribe 4 Families Originated from Source Rock West of NIFZ

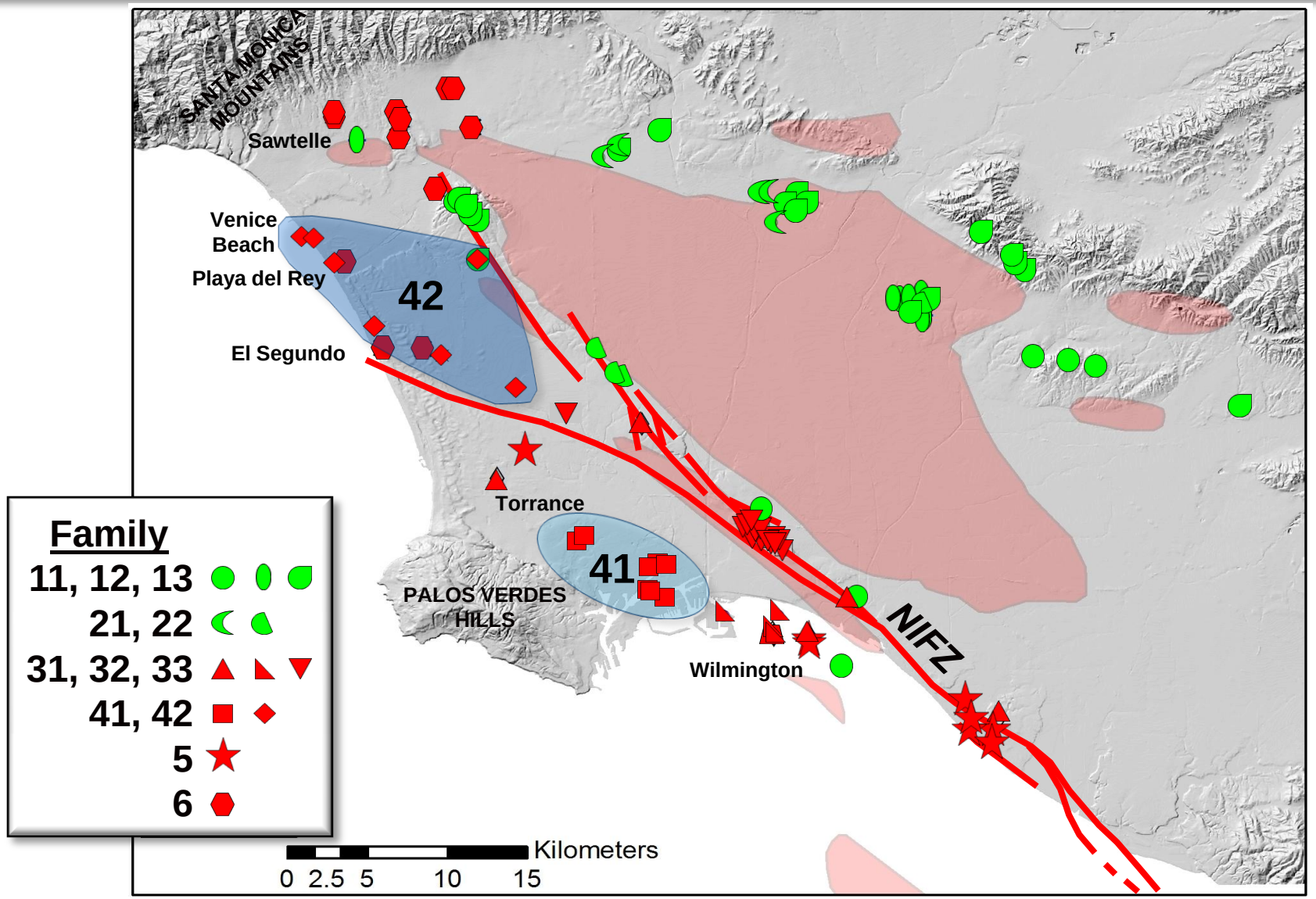

Tribe 4 Families Originated from Source Rock West of NIFZ

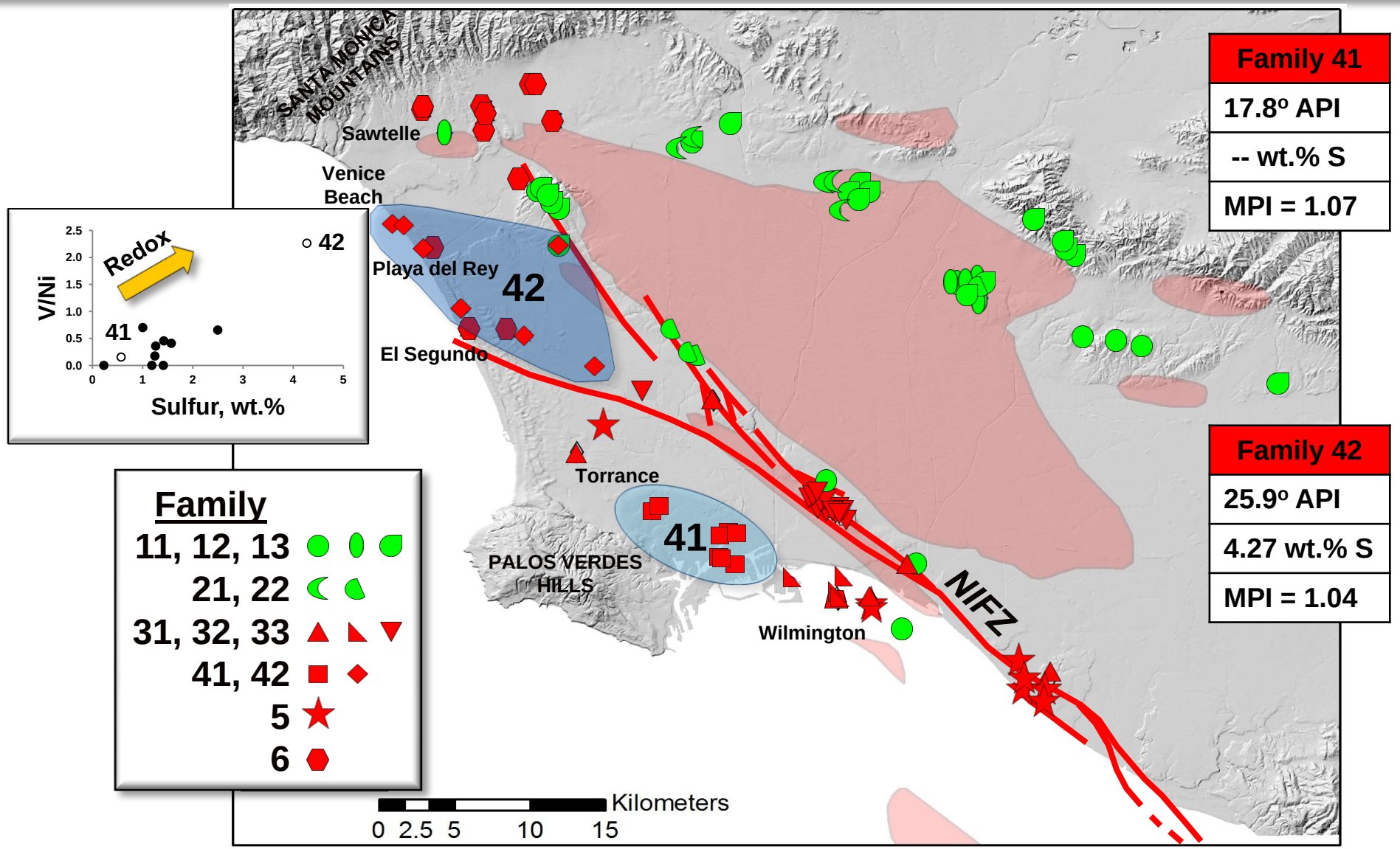

Tribes 5 and 6 Originated from Source Rocks West of NIFZ

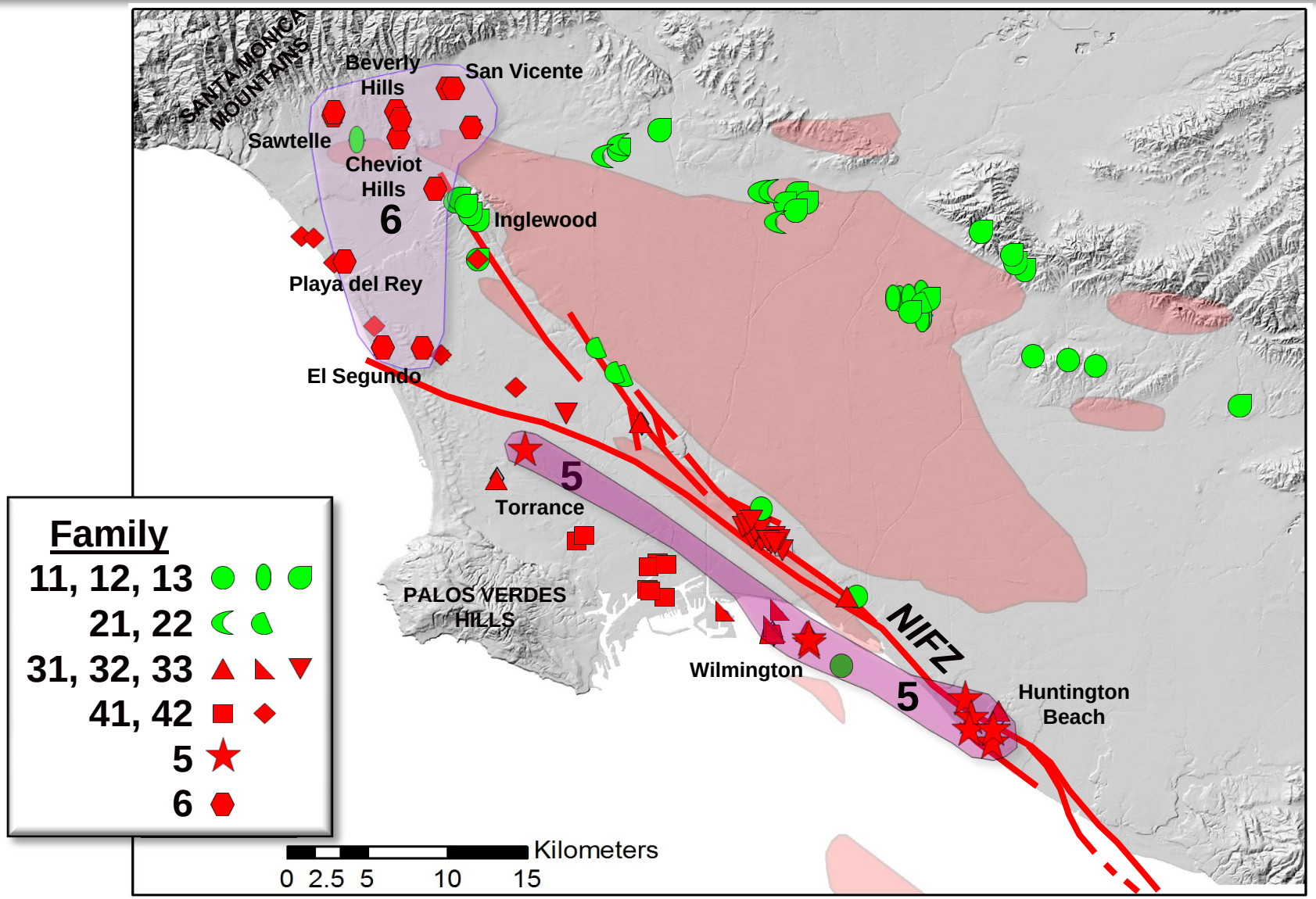

Tribes 5 and 6 Originated from Source Rocks West of NIFZ

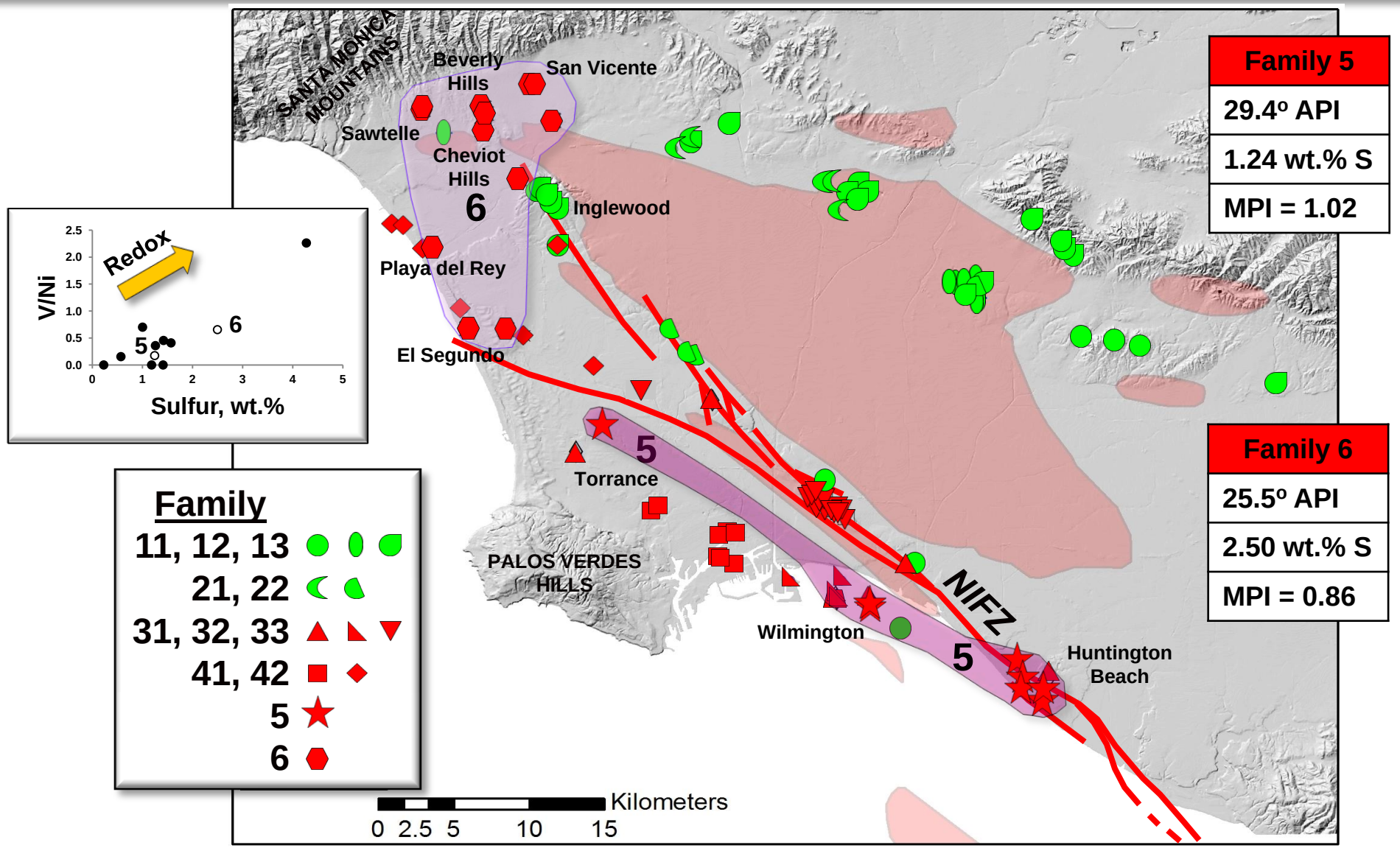

Chemometric Decision Tree Classifies New Oil Samples

112-Sample Training Set
Six Tribes; 12 Families

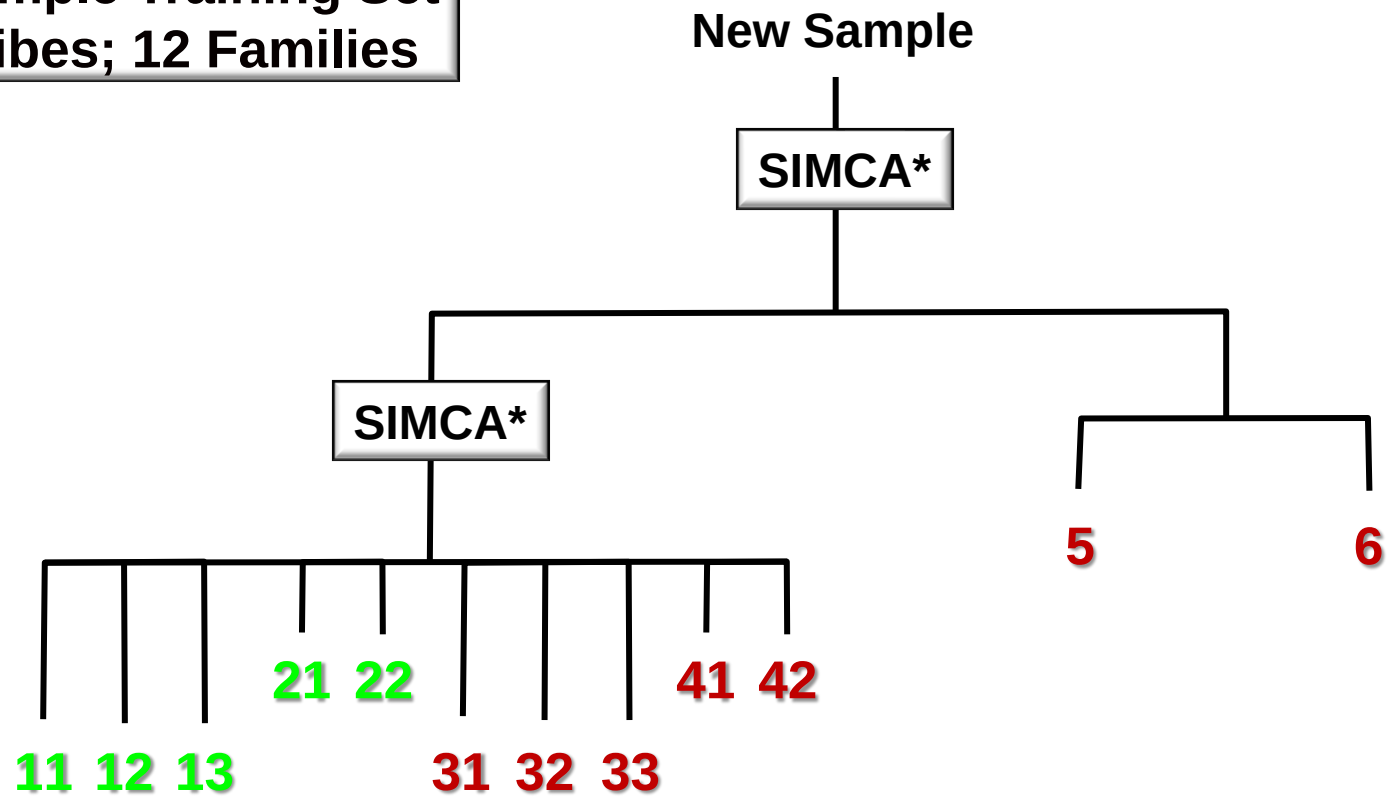

*Soft independent modeling of class analogy

Some Biodegraded or Anomalous Samples Can be Classified

Sample	Longitude	Latitude	Biod. Rank	Family	Confidence*
Saw481	-118.4555	34.05864	6	6	0.814
Wil78	-118.2464	33.78629	5	41	0.987
Wil85	-118.2361	33.78633	5	41	0.935
HB462	-118.044	33.66256	5	32	0.923
Wil531	-118.1796	33.75942	5	41	0.958
Wil532	-118.1625	33.74057	5	41	0.985
Wil533	-118.1624	33.74132	5	41	0.992
Wil536	-118.1942	33.75238	5	41	0.960
Wil592	-118.1577	33.7532	5	41	0.989
LB6	-118.1896	33.82376	4	5	0.971
LB506	-118.1694	33.80556	1	33	0.969

* If the probability cutoff for family membership is set to 0.99, then 99% of samples will be properly predicted.

Chemometric Decision Tree Classifies 11 New Oil Samples

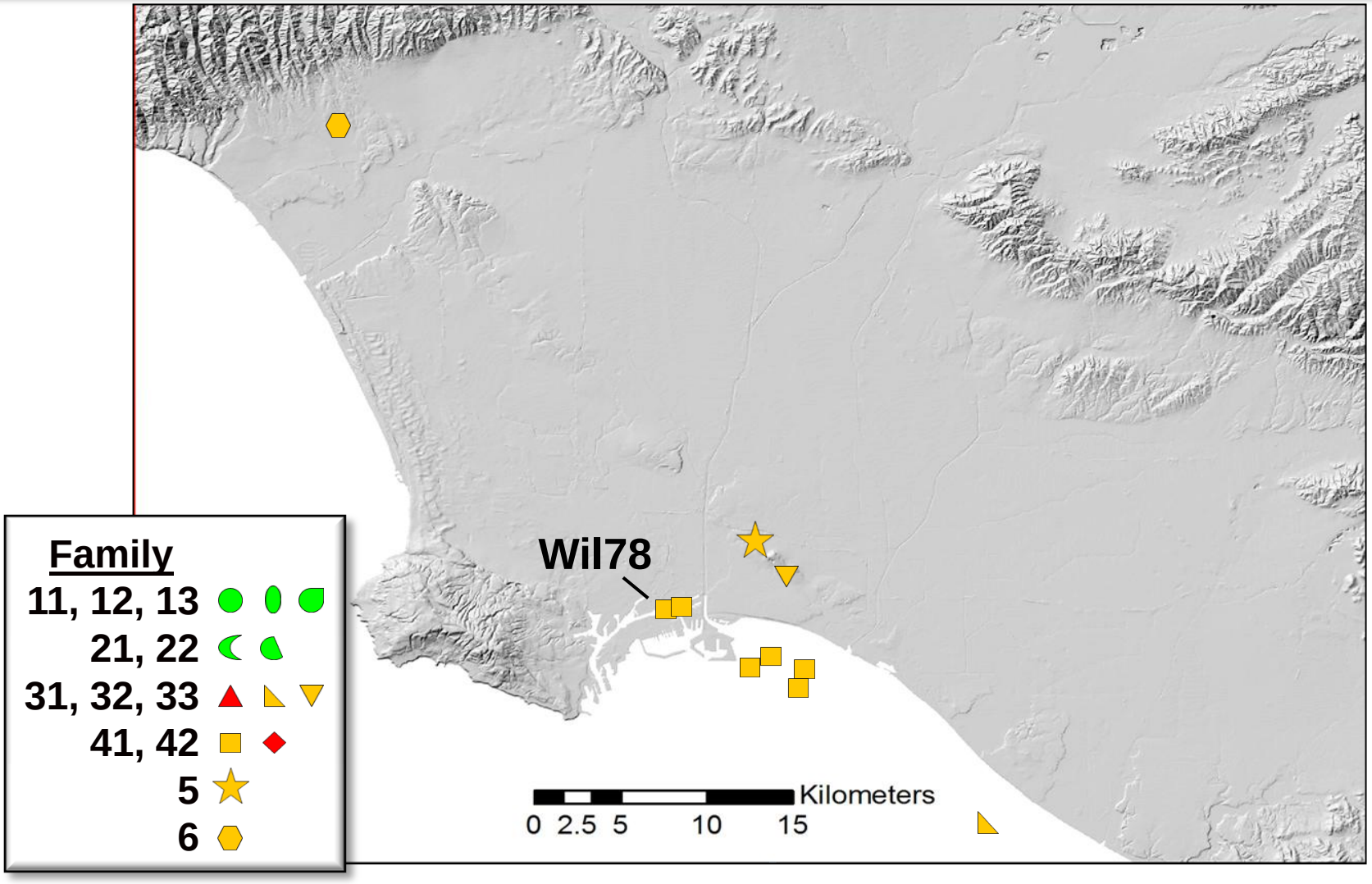

Cross Sections Reveal Stratigraphy of Some Oil Families

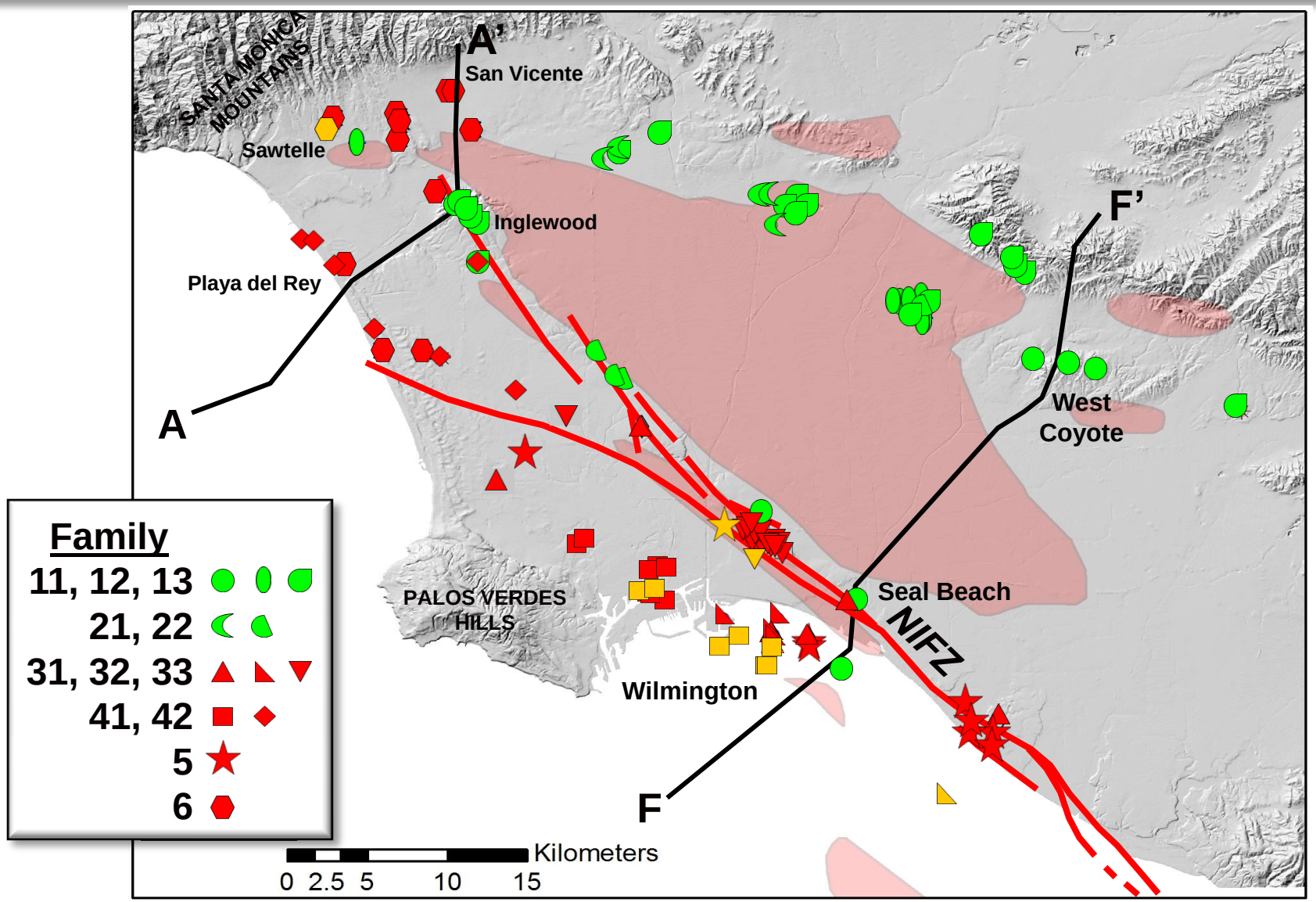

A-A' Section Reveals Stratigraphy of Tribe 6 and Family 13

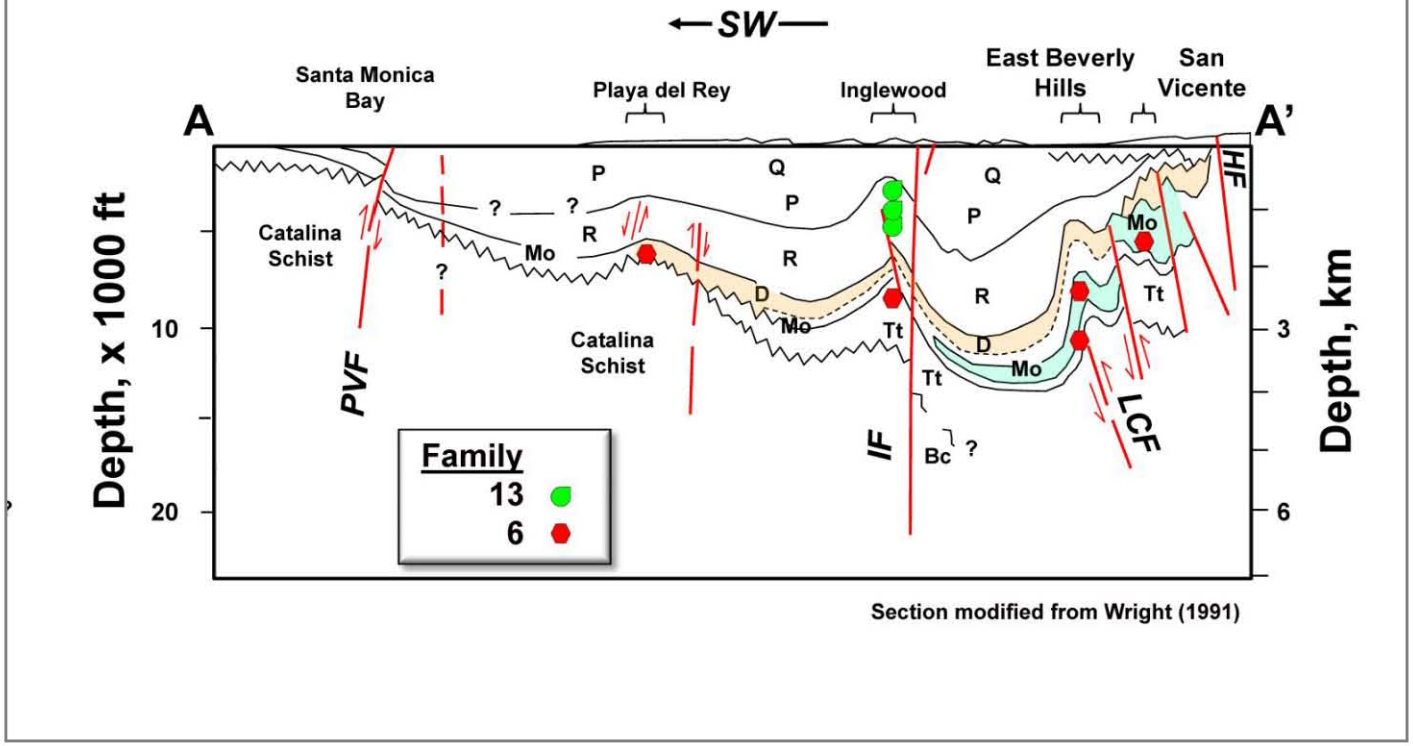

Presenter's notes: P = Pico Formation, R = Repetto Formation, D = Delmontian, Mo = Mohnian, M = undifferentiated Delmontian-Mohnian, Tm = Monterey Formation, L = Luisian, Tt = Topanga Formation, Pg = Paleogene, K = Cretaceous, Bc = undifferentiated metamorphic basement complex; u, m, l = upper, middle, lower; NIFZ = Newport-Inglewood Fault Zone.

F-F' Section Reveals Stratigraphy of Families 5, 11, 31, 32

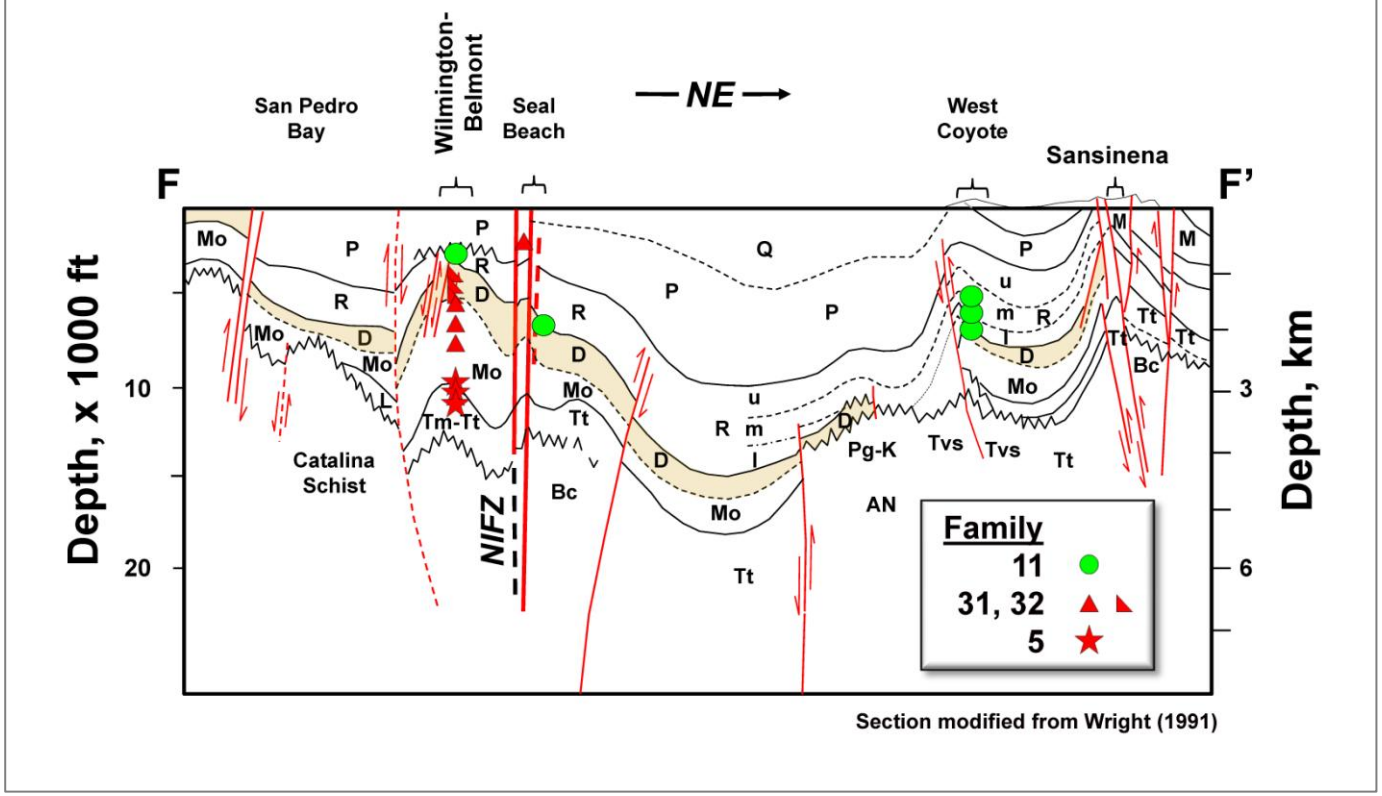

Presenter's notes: P = Pico Formation, R = Repetto Formation, D = Delmontian, Mo = Mohnian, M = undifferentiated Delmontian-Mohnian, Tm = Monterey Formation, L = Luisian, Tt = Topanga Formation, Pg = Paleogene, K = Cretaceous, Bc = undifferentiated metamorphic basement complex; u, m, l = upper, middle, lower; NIFZ = Newport-Inglewood Fault Zone. Family 11 *west* of NIFZ at Belmont offshore (Bel542S) at 4954 ft.

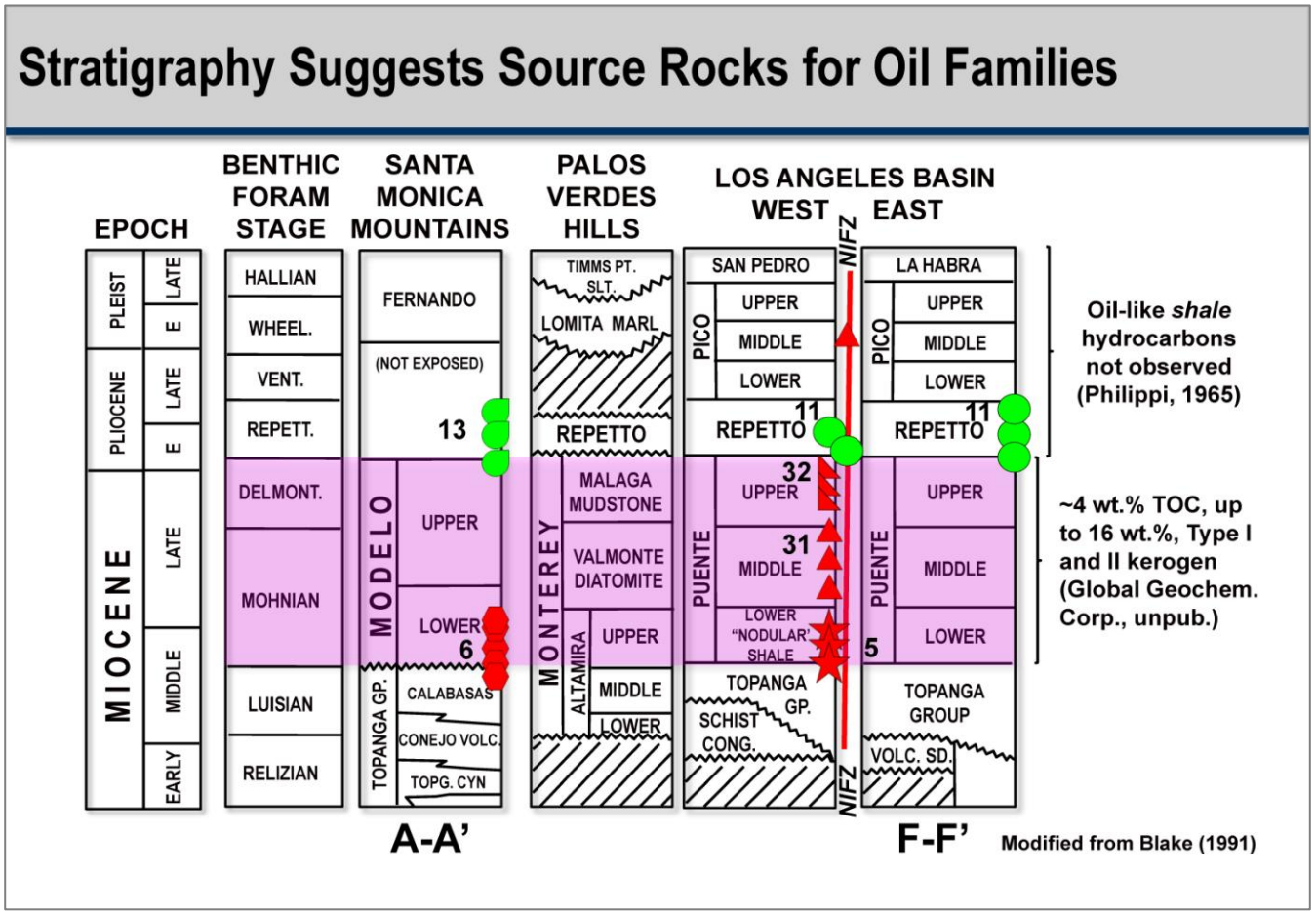

Presenter's notes: Santa Monica Mountains (NW and NE basin) – Modelo Fm is Mohnian-Delmontian: brown to brownish gray diatomaceous shale with interbedded ss. Phosphatic "nodular shale" contains up to 10 wt.% TOC (Walker et al., 1983); marine, slightly reducing

Monterey Shale (Divisions D and E; i.e., Mohnian-Delmontian) contains 2-18 wt.% TOC with an average of 4 wt.%, marine anoxic conditions – major source (Philippi, 1965). Palos Verdes Hills – Monterey Fm is Topanga-Puente.

Conclusions: Los Angeles Basin Geochemistry

- **At least six Miocene petroleum systems (12 families) occur in different parts of the basin.**
- **The Newport-Inglewood fault separates tribes 1-2 (families 11, 12, 13, 21, 22) to the east from tribes 3-6 (families 31-33, 41-42, 5, 6) to the west.**
- **Biomarkers, isotopes, and stratigraphic occurrence help to identify source rocks for the oil families.**
- ***Source rock samples for oil-source rock correlation and kinetic modeling would be useful.***

Thanks for Your Attention!



Presenter's notes: "Tribute to the Roughnecks" by Cindy Jackson stands atop Signal Hill; Long Beach in distance. Alamitos #1 Signal Hill; photo by Tom Lorenson. Alamitos #1 was completed June 25, 1921, at 3114 ft, flowing 590 bbl of oil/day. EUR is 700,000 bbl. The oilfield still produces 1.5 million bbl each year.

Source Rock Can be Inferred from Stratigraphy-Biomarkers

- **Suboxic Upper Miocene (Delmontian) shale with significant angiosperm input generated Tribes 1-2 at moderate-high maturity in the Central Trough east of NIFZ.**
- **Anoxic Upper Miocene (M.-U. Puente) marl source rock generated Tribe 3 west of NIFZ.**
- **Anoxic Mohnian(?) marl generated Tribe 4 west of NIFZ.**
- **Anoxic M.-U. Miocene (L. Puente “nodular shale”) marl with significant terrigenous plant input generated Tribe 5 southwest of NIFZ.**
- **Anoxic M.-U. Miocene (L. Modelo “nodular shale”) marl with significant terrigenous plant input generated Tribe 6 at low maturity northwest of NIFZ.**

References

- Blake, G.H., 1991, Review of the Neogene biostratigraphy and stratigraphy of the Los Angeles basin and implications for basin evolution: AAPG Memoir 52, 135-184.
- Jeffrey, A.W.A. et al., 1991, Geochemistry of Los Angeles basin oil and gas systems: AAPG Memoir 52, 197-219.
- McCulloh, T.H. et al., 1994, How oil composition relates to kerogen facies in the world's most petroliferous basin: AAPG Search and Discovery Article #90986, AAPG Annual Convention, Denver, CO, June 12-15, 1994.
- Wright, T.L., 1991, Structural geology and tectonic evolution of the Los Angeles Basin, California: AAPG Memoir 52, 35-134.

Source Rock Character Can be Inferred from Oil Biomarkers

	Family	No.	Shale		Carbonate	Reducing Conditions		Marine	Terrigenous	Angiosperms
			Ts/Tm	C_{24}/C_{23} TT	C_{29}/C_{30}	C_{35}/C_{34}S	BNH/H	C_{26}/Ts	C_{29}/C_{27} St	OI/H
East of NIFZ	11	6	0.50 0.03	0.77 0.03	0.49 0.00	0.81 0.08	0.17 0.01	4.24 0.01	0.75 0.03	0.14 0.01
	12	8	0.55 0.04	0.86 0.03	0.46 0.02	0.71 0.03	0.18 0.01	4.04 0.17	0.77 0.33	0.22 0.01
	13	19	0.63 0.09	0.94 0.08	0.45 0.02	0.76 0.09	0.21 0.04	3.57 0.43	0.80 0.03	0.26 0.07
	21	5	0.83 0.22	0.88 0.05	0.42 0.03	0.64 0.09	0.21 0.08	3.35 0.36	0.83 0.04	0.52 0.12
	22	6	0.59 0.04	0.90 0.03	0.43 0.01	0.61 0.03	0.15 0.02	3.75 0.11	0.78 0.03	0.30 0.01
West of NIFZ	31	8	0.42 0.04	0.74 0.04	0.53 0.03	0.87 0.06	0.32 0.08	3.66 0.38	0.76 0.02	0.13 0.02
	32	5	0.42 0.02	0.72 0.04	0.56 0.01	0.88 0.02	0.34 0.02	3.44 0.18	0.83 0.01	0.14 0.01
	33	15	0.33 0.01	0.70 0.05	0.57 0.02	0.89 0.07	0.28 0.01	4.00 0.19	0.79 0.02	0.12 0.02
	41	8	0.41 0.07	0.85 0.06	0.57 0.07	0.95 0.05	0.32 0.05	3.53 0.19	0.75 0.03	0.14 0.02
	42	8	0.43 0.02	0.98 0.09	0.50 0.03	0.99 0.13	0.32 0.20	3.34 0.37	0.72 0.04	0.14 0.02
	5	10	0.42 0.14	0.74 0.06	0.54 0.04	0.83 0.10	0.55 0.32	2.90 0.18	0.91 0.06	0.17 0.02
	6	14	0.44 0.05	0.78 0.03	0.54 0.02	0.88 0.13	0.32 0.10	2.10 0.25	0.90 0.06	0.14 0.02

Several Petroleum Systems Exist in the Los Angeles Basin

- Four essential elements and two processes and all related petroleum that originated from *one* pod of active source rock

Source rock
Reservoir rock
Seal rock
Overburden rock

Essential Elements

Trap Formation
Generation-Migration-Accumulation

Processes

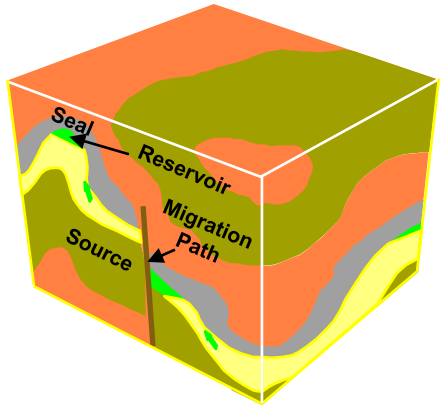

5

Ducros, M., W. Sassi, R. Vially, T. Euzen, and V. Crombez, 2017, 2-D Basin Modeling of the Western Canada Sedimentary Basin across the Montney-Doig System: Implications for Hydrocarbon Migration Pathways and Unconventional Resources Potential, *in* Mahdi A. AbuAli, Isabelle Moretti, and Hege M. Nordgård Bolås, eds., Petroleum Systems Analysis—Case Studies: AAPG Memoir 114, p. 117–134.

2-D Basin Modeling of the Western Canada Sedimentary Basin across the Montney-Doig System: Implications for Hydrocarbon Migration Pathways and Unconventional Resources Potential

Mathieu Ducros, William Sassi, and Roland Vially

IFP Énergies nouvelles, 1 et 4 Avenue de Bois-Préau, 92852 Rueil-Malmaison Cedex, France (e-mails: mathieu.ducros@ifpen.fr; william.sassi@ifpen.fr; roland.vially@ifpen.fr)

Tristan Euzen

IFP Technologies (Canada) Inc., Suite 810, 744 4th Avenue S.W., Calgary, AB, Canada (e-mail: tristan.euzen@ifp-canada.com)

Vincent Crombez

IFP Énergies nouvelles, 1 et 4 Avenue de Bois-Préau, 92852 Rueil-Malmaison Cedex, France and Sorbonne Universités, UPMC Univ Paris 06, CNRS-UMR 7193, ISTeP, 75252 Paris Cedex, France (e-mail: crombez.v@gmail.com)

ABSTRACT

Basin and petroleum system modeling tools can aid in assessing unconventional resources. The present study gives an overview of the petroleum system of the Western Canada Sedimentary Basin (WCSB) through the modeling of a representative regional geologic cross section. A special emphasis is given on the Triassic Montney and Doig formations, which host the largest known unconventional play in Canada. Our model simulated the large diversity of plays that are found in the WCSB: self-sourced and tight reservoirs as well as conventional reservoirs with conventional and biodegraded oils. Results of this study strengthen the hypothesis of long-distance (>100 km [>62 mi]) migration for a major part of the hydrocarbons generated by the Gordondale and Doig Phosphate source rocks from the western to the eastern part of the basin. They also show that hydrocarbons generated within the Montney formation did not migrate far from their source rock due to very low permeabilities. Although the quantification of expelled versus generated hydrocarbons is still in its infancy, our results suggest that as much as half of the hydrocarbons generated in the Montney-Doig formations might still be retained in their source rock. Extending such a model in three dimensions might help improving the assessment of the volumes and distributions

Copyright © 2017 by The American Association of Petroleum Geologists.
DOI:10.1306/13602027M1143703

of dry gas, liquid-rich gas, and oil present in the low-permeability Montney and Doig formations.

INTRODUCTION

During the last decade, the focus of the North American oil and gas industry has shifted toward the exploration and production of unconventional resources. In 2013, shale gas represented 40% of the total natural gas volume produced in the United States. In recent years, this unconventional rush has started to spread over Canada and, although at a slower pace, around the world.

Unconventional plays encompass a variety of very low-permeability reservoirs that require horizontal drilling and multistage fracturing technologies to produce economic volumes of hydrocarbons. These reservoirs are generally found within or in close association with source rock intervals and are called self-contained source-reservoir systems by Jarvie et al. (2007). The assessment of these new petroleum resources trapped in low-permeability source rocks and tight reservoirs requires dedicated basin analysis studies to achieve in-depth understanding of the petroleum system. To this end, advanced basin modeling tools are being adapted to better account for key petrophysical and thermo-mechanical rock properties, such as organic porosity and gas adsorption on organic matter (Romero-Sarmiento et al., 2013).

In the Western Canada Sedimentary Basin (WCSB), the Montney-Doig succession is the host of both conventional and unconventional petroleum accumulations. Conventional oil and gas trapped in proximal deposits and turbiditic reservoirs have been produced for decades. In recent years, organic-rich fine-grained sediments from the distal part of the basin have become the most active unconventional plays in Canada. The present study aims at giving a first overview of the complete petroleum system with a special emphasis on the Triassic Montney and Doig formations, through the modeling of a representative section across the WCSB.

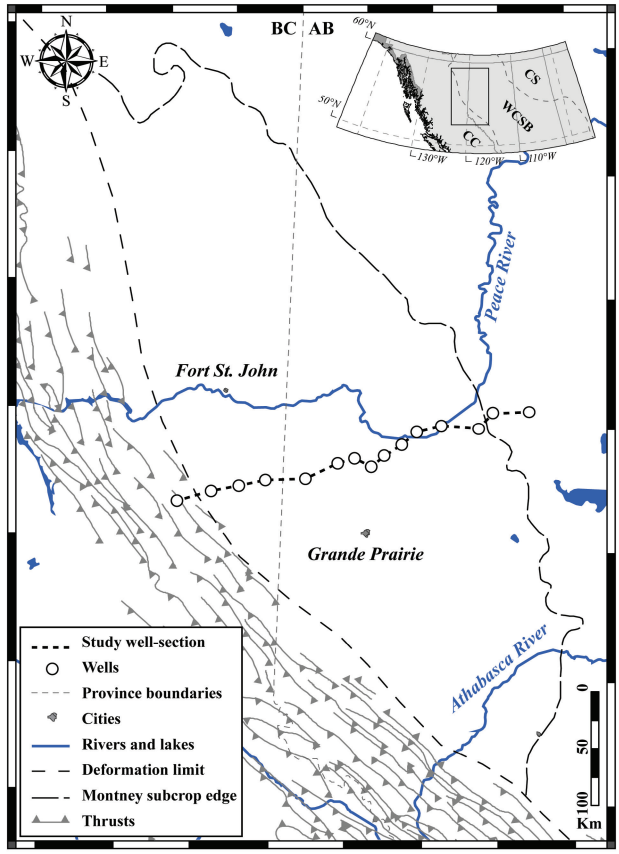

Figure 1. Location of the studied section. Thrusts from Reed et al. (2005), deformation limit from Price (1994), and Montney formation subcrop edge from Edwards et al. (1994). On the small map: location of the study area within the Western Canadian Sedimentary Basin. CC = Canadian Cordillera; WCSB = Western Canadian Sedimentary Basin; CS = Canadian Shield; AB = Alberta; BC = British Columbia.

GEOLOGICAL SETTINGS

The WCSB is a foreland basin that extends from southern Saskatchewan through Alberta to northeastern British Columbia (Figure 1). It is limited to the east by the Precambrian Canadian Shield and to the west by the Canadian Cordillera. The sedimentary succession of the basin can be subdivided into two major periods (Price et al., 1972; Ziegler et al., 1983; Mossop and Shetsen, 1994): during the Paleozoic to early Mesozoic time, the sedimentation took place on the western margin of a stable craton and was dominated by carbonate deposits: from the mid-Jurassic to the Paleocene, a clastic sedimentary wedge was induced by the formation of the Canadian Cordillera and its associated foreland basin. From the Paleocene onward, the WCSB has been dominated by erosion and sediment bypass due to the exhumation of the basin. Two major unconformities formed during the Columbian Orogeny (Early Laramide) in the Late Jurassic and in the Early Cretaceous, and during the Laramide Orogeny (Laramide sensu stricto) in the Late Cretaceous to Early Tertiary (Ricketts, 1986).

The Triassic succession of the WCSB was deposited during a transition period from a passive to an active margin setting and corresponds to a mix of siliciclastic, evaporitic, and carbonate sedimentation. The Triassic rests unconformably on the Permian Belloy formation, and its lower boundary corresponds to a Late Permian unconformity associated with the

amalgamation of Pangea followed by a major transgression (Henderson, 1997). The upper boundary of the Triassic is a major unconformity related to the onset of the formation of the Canadian Cordillera (Columbian Orogeny). In the eastern part of the study area, this unconformity rests directly on the Montney formation, which is capped by the organic-rich shale of the Nordegg formation. In the western part of the study area, the Montney and Doig formations are overlaid by the proximal, sandy deposits of the Middle Triassic Halfway formation.

The Montney and Doig formations form an overall prograding clastic ramp that was deposited during the Early to Middle Triassic (Davies, 1997). In the proximal, eastern part of the basin, the Montney formation consists of foreshore, tidal, and shoreface sandstone, siltstone, and coquina bed deposits that form stratigraphic traps below the Jurassic unconformity. In the distal, western part of the basin, the Montney Formation entails offshore-transition and offshore organic–rich siltstones as well as turbiditic deposits. In this area, the Montney formation is capped by the Lower Doig organic-rich phosphatic zone, underlying dolomitic-rich siltstone and sandstone of the Doig formation.

In this work, the studied section is located 60 km (37 mi) north of Grande Prairie in the foreland basin of the Canadian Cordillera (Figure 2). This section, oriented east-northeast–west-southwest, is 320 km

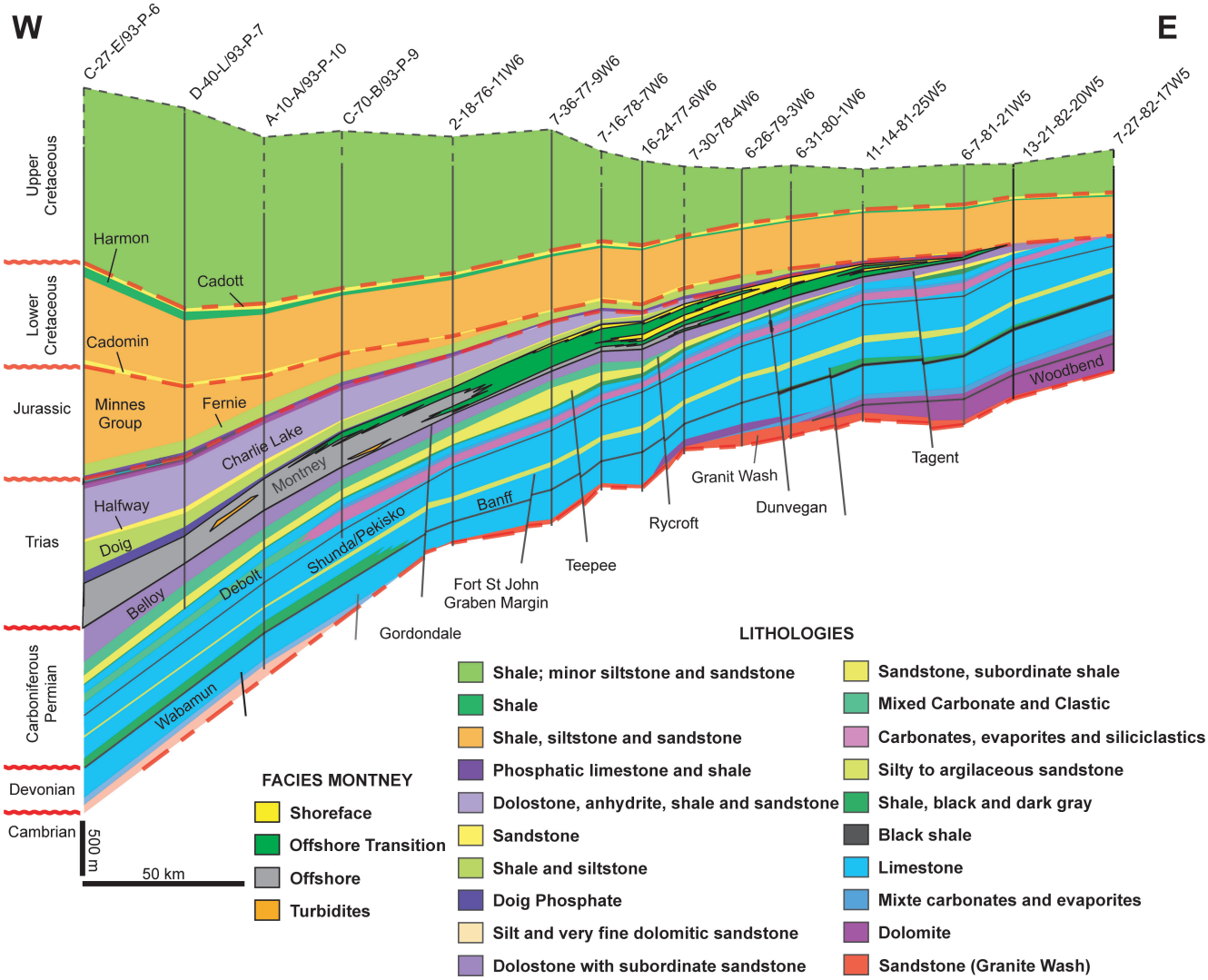

Figure 2. Cross section used in the basin model. It presents the main stratigraphic intervals and the corresponding lithologies included in the model. A special care was given to describe the facies transition in the Montney formation, from the proximal setting in the Eastern part to the distal setting in the Western part. The location of the faults is based on a structural map published by Berger et al. (2008).

(199 mi) long and is interpreted using 15 wells from Alberta and British Columbia.

PETROLEUM SYSTEM MODELING

Geometry and Burial History

The present-day geometry of the 2-D basin model of this study, which consists in 35 stratigraphic intervals (Table 1), is based on a master cross section from the Geological Atlas of the WCSB (Creaney and Allan, 1990; Mossop and Shetsen, 1994; Higley et al., 2005; Proverbs et al., 2010). Table 1 shows the stratigraphy and the lithologies used to construct the 2-D basin model.

The back-stripping method integrated in the TemisFlow™ software (version 2013) of Beicip-Franlab was applied to reconstruct the past geometries of the WCSB (e.g., Doligez et al., 1987; Burrus et al., 1996; Allen and Allen, 2005). The sedimentary layers are sequentially removed out of the cross section, and each individual bed of the remaining sedimentary pile is decompacted using lithology-dependent porosity versus depth relationships. This geometric reconstruction also takes into account possible mechanical rebounds due to known erosion events during the basin history.

In our basin history reconstruction, three erosion periods were taken into account. The oldest has no significant impact on the petroleum system since the source rocks had certainly not generated hydrocarbons then. The second one corresponds to the sub-Mannville unconformity (Early Cretaceous). Since this event occurred before the maximum burial depth was reached, limited effects are expected on thermal maturation. The last erosion took place during the Laramide Orogeny, in the Late Cretaceous to Early Tertiary. It can be considered as a critical event that controls the petroleum system. The estimated thickness of eroded sediments associated with the Laramide Orogeny can range from 4000 m (13,123 ft) close to the Rocky Mountains (Roure et al., 2011) to less than 400 m (1312 ft) near the Precambrian shield in Saskatchewan (Ness, 2001; Higley et al., 2005; Roure et al., 2011). Figure 3 shows the reconstructed burial history curve at the location of well C-70-B/93-P-9.

Source Rocks

The main potential hydrocarbon sources, summarized in Table 2, are the Devonian Duvernay formation, the Upper Devonian/Lower Mississippian Exshaw formation, the Triassic Montney and Doig formations, the carbonates of the Nordegg Member (Gordondale source rock), and the coals of the Mannville Group (Creaney and Allan, 1990; Higley et al., 2005).

Behar et al. (1997) and Vandenbroucke et al. (1999) studied the kerogens of the Duvernay and Exshaw formations, and the corresponding kinetic schemes were derived from their laboratory experiments. For the other source rocks, kerogen properties were chosen based on known properties of representative geochemical characteristics and depositional environment conditions such as those described in Creaney and Allan (1990) and Higley et al. (2005).

Source rocks' richness in organic carbon (Table 3) was estimated and adapted based on a previous modeling work by Higley et al. (2005) and on measured total organic carbon (TOC) from Rock-Eval data in the well A-10-A/93-P-10.

Erosions and Thermal Conditions

Petroleum system modeling requires setting the thermal boundary conditions to compute temperature over time in the whole model. Values of the surface temperature and heat flow from below the basement of the basin are required. The maximum temperature reached by each strata and estimated using vitrinite reflectance or Rock-Eval T_{max} is a function of both maximum burial depth and past thermal regime. When major uplift and erosion occur after maximum burial, such as in the WCSB, it becomes difficult to estimate the relative contribution of burial and heat flow on past temperature. Consequently several scenarios, consistent with the available data (present-day temperatures, vitrinite reflectance data, and Rock-Eval T_{max}), were simulated by increasing or decreasing the amount of eroded thickness and respectively decreasing or increasing the basal heat flow. Analyses of the thermal results in the different scenarios of eroded thicknesses show that it is possible to select the most consistent geological scenario. Profile of eroded thickness along the cross section consistent with the geological events was kept, and heat flow at the base of the sediments was adjusted to fit temperatures and vitrinite reflectance data. Furthermore, the heat flow in the model may also impact on the prediction of oil biodegradation, and the amount of uplift and erosion will influence pressure distribution.

Table 1. Ages of the 35 stratigraphic intervals used for the Western Canada Sedimentary Basin 2-D model. The model starts with the Granite Wash formation in the Early Devonian and goes up to the present day.

Ages (Ma)		Era/System	Stratigraphic Unit	Petroleum System Element
57.8	0.0	Cenozoic	Erosion	400–4000 m (1312–13,123 ft)
65.5	57.8		Hiatus	
79.5	65.5		Hiatus	
97.5	79.5		Colorado group (4 subdivisions)	Seal and reservoirs
102.0	97.5		Hiatus	
103.0	102.0		Cadott	Reservoirs
105.0	103.0	Cretaceous	Harmon	Seal
118.0	105.0		Mannville (3 subdivisions)	Source rock (coals) and reservoirs
119.0	118.0		Cadomin	Reservoirs
135.0	119.0		Erosion	500–2500 m (1640–8202 ft)
145.0	135.0		Minnes group (2 subdivisions)	
155.0	145.0		Minnes group (2 subdivisions)	
193.0	155.0	Jurassic	Fernie	
199.0	193.0		Nordegg (Gordondale)	Seal and source rock
213.0	199.0		Erosion	0–500 m (0–1640 ft)
227.0	213.0		Pardonnet	
229.0	227.0		Baldonnel	Reservoirs
235.0	229.0		Charlie Lake	Reservoirs
237.0	235.0	Triassic	Halfway	
242.0	237.0		Doig	Source rock
247.0	242.0		Doig Phospshate	Seal and source rock
250.0	247.0		Montney (6 subdivisions)	Source rock and reservoir
252.0	250.0		Hiatus	
299.0	252.0	Permian	Belloy	Reservoirs
307.0	299.0		Hiatus	
331.0	307.0		Taylor Flat	
335.0	331.0	Carboniferous	Kiskatinaw & Golata	
342.0	335.0		Debolt (3 subdivisions)	
347.0	342.0		Shunda and Pekisko	
357.0	347.0		Banff (2 subdivisions)	Reservoirs
367.0	357.0		Exshaw + Lower Banff	Seal and source rock (Exshaw)
372.2	367.0		Wabamun	
378.5	372.2	Devonian	Winterburn	
382.7	378.5		Woodbend	Source rock (Duvernay)
419.0	382.7		Granite Wash	Reservoirs

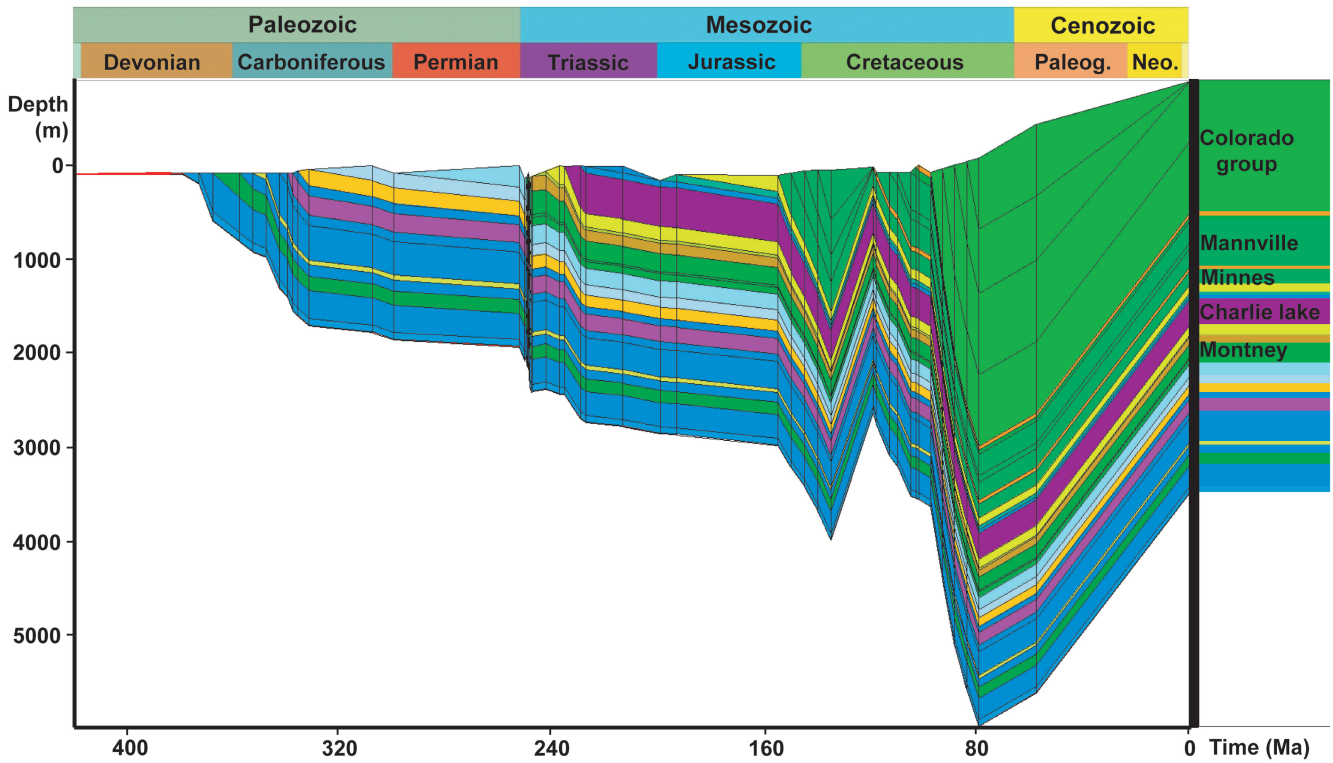

Figure 3. Burial history at the location of well C-70-B/93-P-9. It shows that the basin evolved from sedimentation on the margin of a stable craton during the Paleozoic to early Mesozoic time to foreland sedimentation during the Canadian Cordillera's Orogeny from the mid-Jurassic to Paleocene. The Foreland Basin development was associated with two major erosions that occurred during the Columbian Orogeny (Early Laramide) in the Late Jurassic to Early Cretaceous and during the Laramide Orogeny (Laramide sensu stricto) in the Late Cretaceous to Early Tertiary (ages of geological events from Ricketts, 1986).

Table 2. Major modeled source rocks and initial input parameters.

Source Rock	System	Kinetics Used in the Model	Measured Richness	Thickness (m [ft])
Mannville Coal	Cretaceous	Type III (Vandenbroucke et al., 1999)	HI: 211 mg/g TOC: 1–5%	20–120 [66–394]
Gordondale	Jurassic	Type IIS (Modified from Behar et al., 1997)	HI: 566 mg/g TOC: 5–16%	0–35 [0–115]
Doig	Triassic	Type II (Modified from Behar et al., 1997)	HI: 611 mg/g TOC: 5%	0–150 [0–492]
Doig Phosphate	Triassic	Type IIS (Modified from Behar et al., 1997)	HI: 566 mg/g TOC: 8%	0–100 [0–328]
Montney	Triassic	Type III (Vandenbroucke et al., 1999)	HI: 211 mg/g TOC: 1–4%	0–300 [0–984]
Exshaw	Devonian	Exshaw (Type II)	HI: 425 mg/g TOC: 9.6%	0–50 [0–164]
Duvernay	Devonian	Duvernay (Type II)	HI: 518 mg/g TOC: 5.8%	0–200 [0–656]

Surface temperatures used in the model (Table 4) are the same than those of the USGS model and are based on Wygrala's work (1986) that describes the evolution of surface temperature of each point of the globe over time. Maximum burial, reached before the last erosion, is one of the major controlling factors of the petroleum system of the WCSB. Temperatures were first calibrated by adjusting the present-day heat flow at the base of

Table 3. Initial total organic carbon (TOC) values used in the model.

Formation	Initial TOC (wt.%)
Mannville	2.5
Gordondale	10.0
Doig	1.8
Doig Phosphate	6.2
Montney	1.4–3.4
Duvernay	9.6
Exshaw	5.8

Table 4. Surface temperatures used in the model. These temperatures are based on Wygrala (1986).

Age (Ma)	Temperature (°C [°F])
0.0	5.0 [41]
57.8	15.0 [59]
102.0	24.0 [75.2]
199.0	20.0 [68]
419.0	24.0 [75.2]

the sediments. To obtain a good match between simulated temperatures and measured temperatures, a variable heat flow was used along the section (Figure 4). Heat flow appears to be higher in the central part of the basin, which is consistent with results from Bachu and Burwash (1994). Figure 5 shows that simulated present-day temperature gradients are consistent with temperature measured in wells of the modeled cross section.

Once the present-day temperatures were fitted, past heat flow (from the beginning of the simulation to the last erosion event) was adjusted to match the measured values of vitrinite reflectance (Figure 4). Figure 6 shows that the model achieved a very good match in all the wells. An increase of the basal heat flow of about 20 mW/m² between past and present-day heat flow gave a good solution to fit both vitrinite reflectance and temperature. The relevance and origin of such a huge increase of heat flow must be further investigated in the literature about the crust evolution over time. Alternatively, heat flow variations in the model might be narrowed by reducing the eroded thickness and increasing the past heat

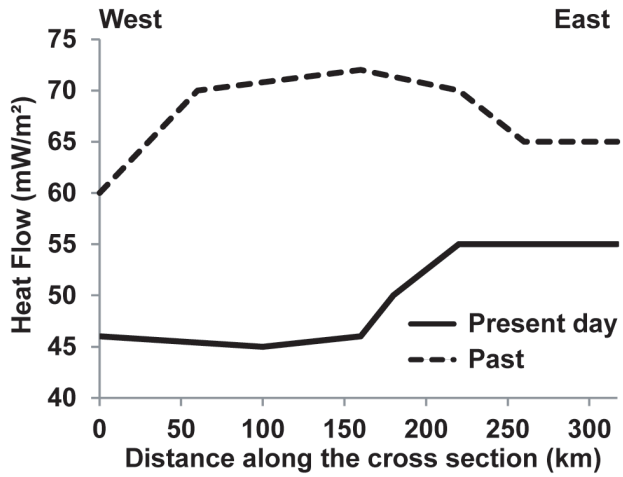

Figure 4. Calibrated present-day (dashed) and past (from the starting age to the last major erosion in the early Paleogene) heat flow (mW/m²) along the section (from west to east, distances are in km).

flow. However, it is not possible to discriminate the relative contribution of burial versus heat flow with the available data.

Pressure Calibration

After thermal calibration, which controls source rocks maturity in the basin, pressure calibration is another key step in the workflow of petroleum system modeling, as pressure gradients play a major role in the hydrocarbons migration processes.

The present-day pressure field in the basin contains several zones that exhibit subhydrostatic fluid pressures (Corbet and Bethke, 1992; Bachu, 1995; Bachu and Underschultz, 1995; Parks and Toth, 1995). Contrary to the present-day pressure field, simulated past overpressures (above hydrostatic trend) are related to the rapid sediment deposition that occurred during the Late Cretaceous (Colorado Group). Many factors may contribute to the development of abnormal fluid pressure, such as subsidence and uplift, sedimentation rates and compaction, diagenesis and permeability evolution, and hydrocarbon generation. Consequently, the history of the pressure field in the WCSB is complex since the basin contains at least six major source rocks, experiences three major phases of erosions, and contains very tight layers. Figure 7 shows that pressure trends simulated in the model are relatively consistent with well data, although considerable scattering may occur in available pressure measurements.

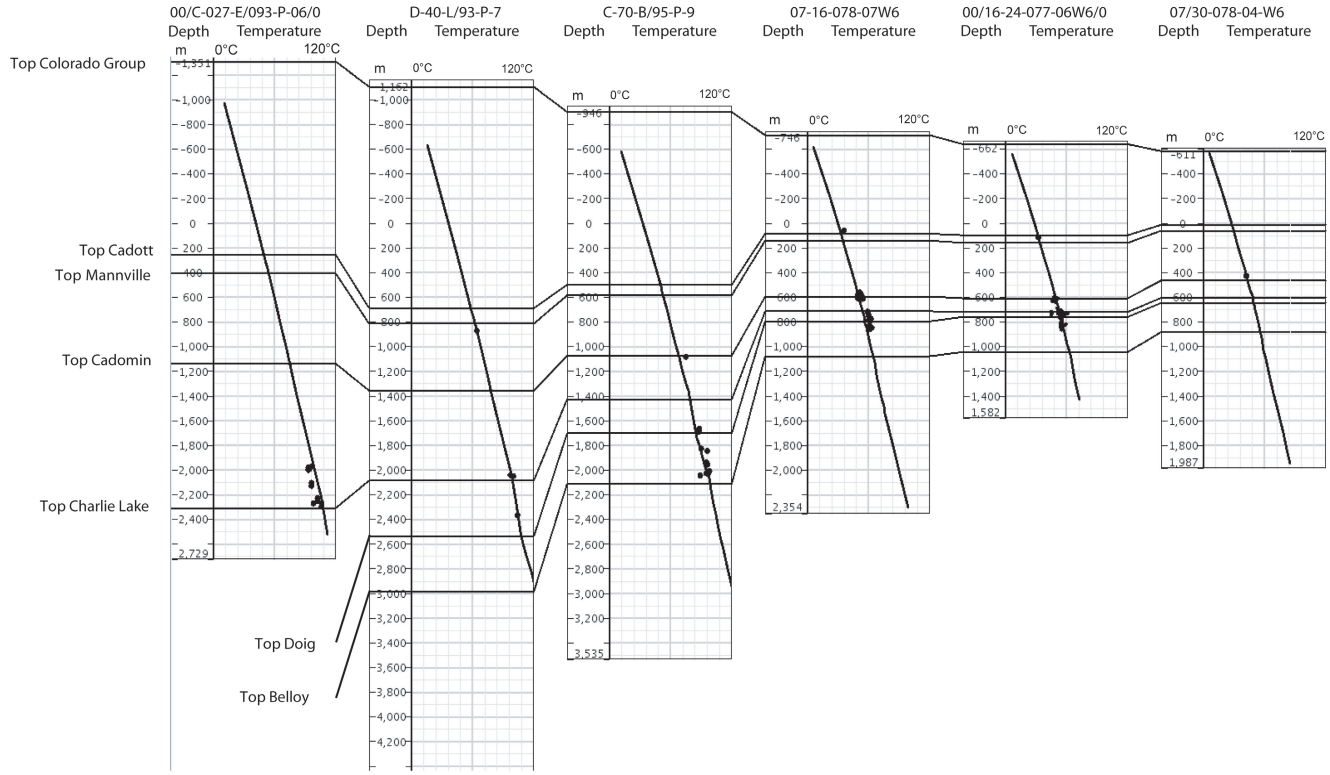

Figure 5. Comparison between measured and simulated temperatures (°C) after thermal calibration (wells are sorted from west to east).

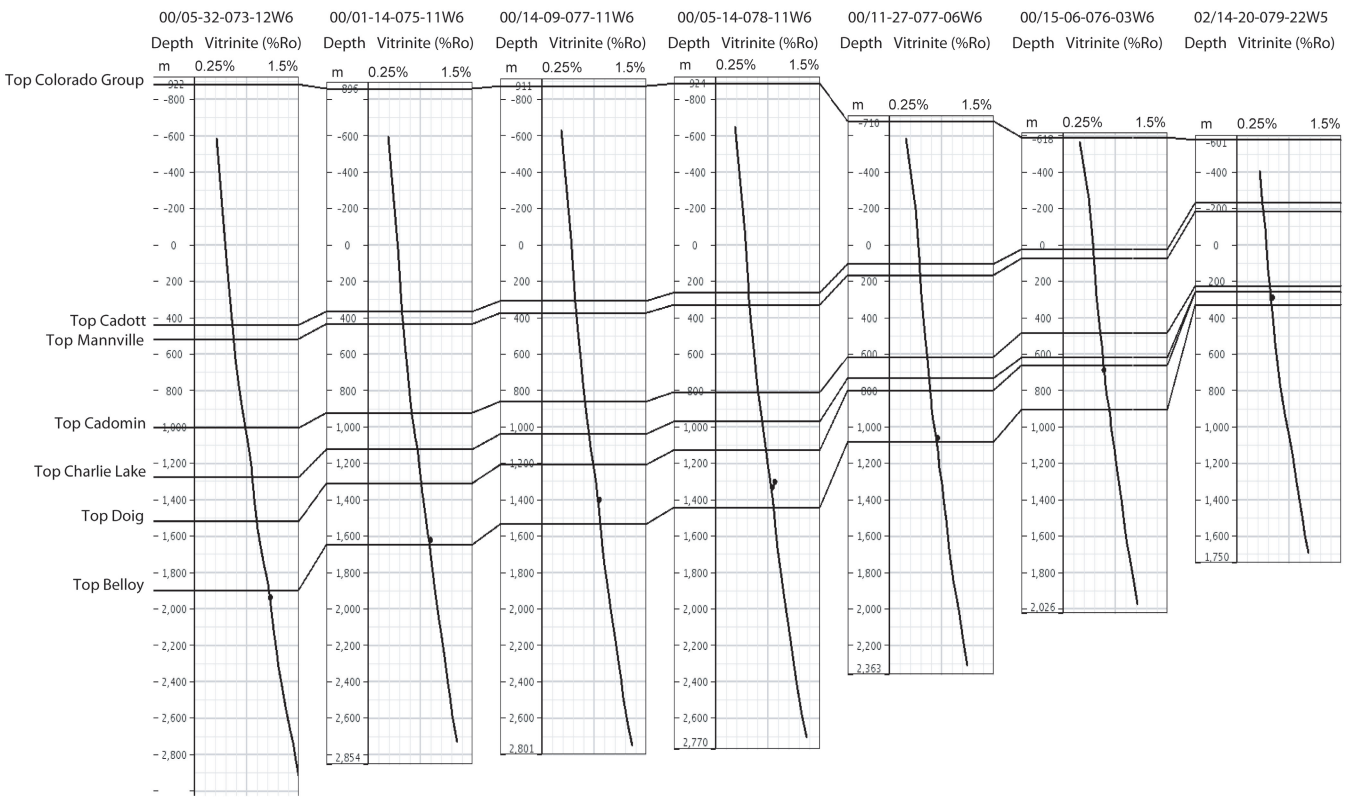

Figure 6. Comparison between measured and simulated vitrinite reflectance (%R_o) after thermal calibration (wells are sorted from west to east).

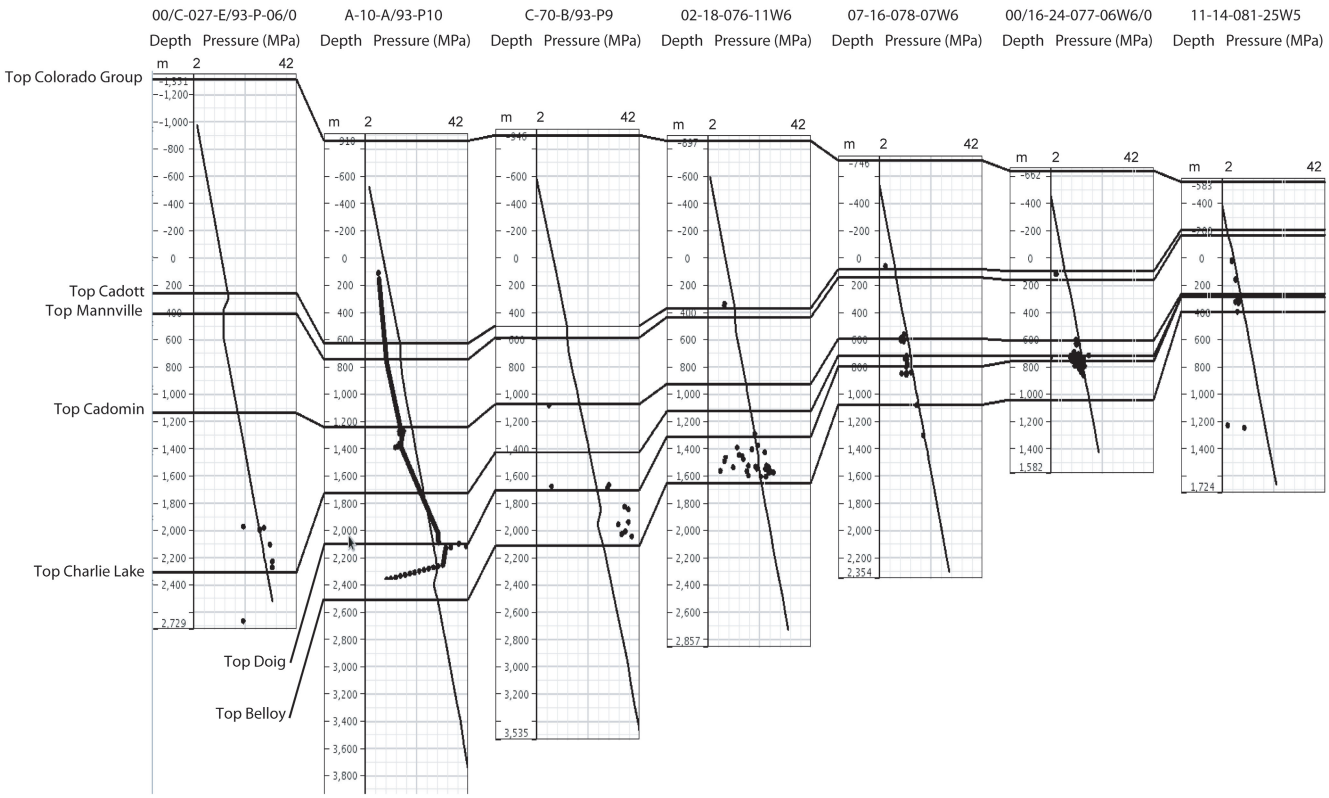

Figure 7. Comparison between measured and simulated present-day pressures (MPa, wells are sorted from west to east). In some wells (i.e., 2-18-076-11W6), all available values cannot be considered as representative of the true pressure given their scattering (sometimes more than 20 MPa of difference at almost the same depth).

RESULTS AND DISCUSSION

Maturity of Triassic Source Rocks

Our model shows that all source rocks are more mature in the western part of the basin due to higher maximum burial depths (Figure 8). Triassic source rocks only reach maturity in the western part of the basin and become overmature close to the cordillera deformation front. The source rock quality also impacts on maturity. For instance, the Doig source rock (type II) is shallower than the Montney formation (type II/III) but generated more of its hydrocarbon potential due to higher reactivity of the organic matter. Likewise, the Gordondale source rock (type IIS) overlying the Triassic is more mature than the Montney source rock due to higher sulfur content, which makes it more reactive.

Figure 9, which illustrates temperature and vitrinite reflectance evolution through geological time in the western part of the Montney formation, shows that Triassic source rocks started to generate hydrocarbon (vitrinite reflectance [$\%R_o$] $> 0.9\%$) during the Middle to Late Cretaceous. It mainly corresponds to the deposition of the Colorado Group that resulted in the maximum burial of Triassic source rocks.

Pressure

Available pressure measurements show that the basin is mostly underpressured at present day (Corbet and Bethke, 1992; Bachu, 1995; Bachu and Underschultz, 1995; Parks and Toth, 1995). It is clearly illustrated by the simulation results that show that although the basin was highly overpressured before the Laramide Orogeny (Figure 10), it has completely released its pressure at present day (Figure 11). The western part of the basin is mostly under or close to hydrostatic pressure in the shallower part of the sedimentary column (Colorado Group) but is highly overpressured in formations with high hydrocarbon saturation (Charlie Lake, Doig, and Montney formations). These formations correspond to producing units, and pressure exceeding hydrostatic pressure is related to the generation of hydrocarbons.

In accordance with previous results from Bekele (1999), the analysis of the pressure evolution over

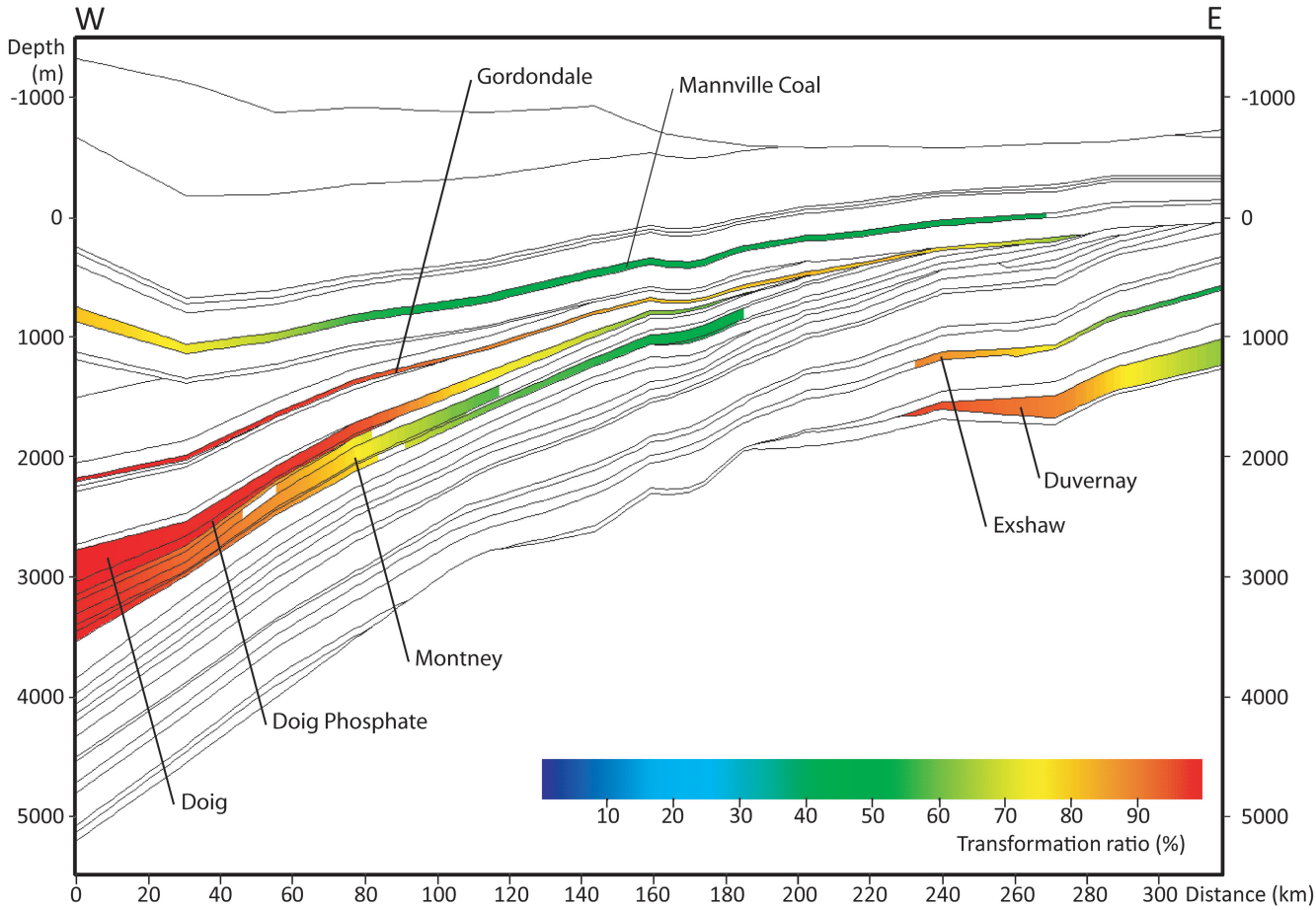

Figure 8. Simulated transformation ratio (TR) in the basin. All source rocks are more mature west of the basin. Triassic source rocks are only mature in the western part of the basin. Although they are shallower, the Doig and Gordondale source rocks are more mature than the Montney source rocks due to a higher thermal reactivity of their organic matter.

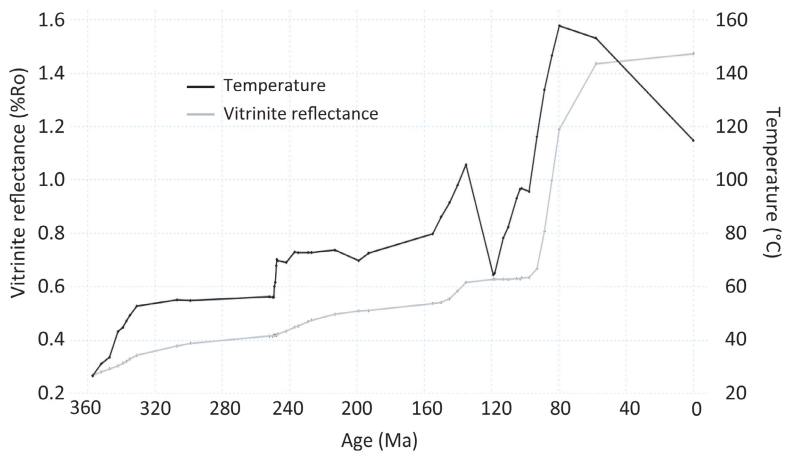

Figure 9. Evolution of temperature (continuous line) and vitrinite reflectance (gray line) through geological time at 2818 m (9245 ft) of present-day burial (MD) in well 100/05-32-073-12W6.

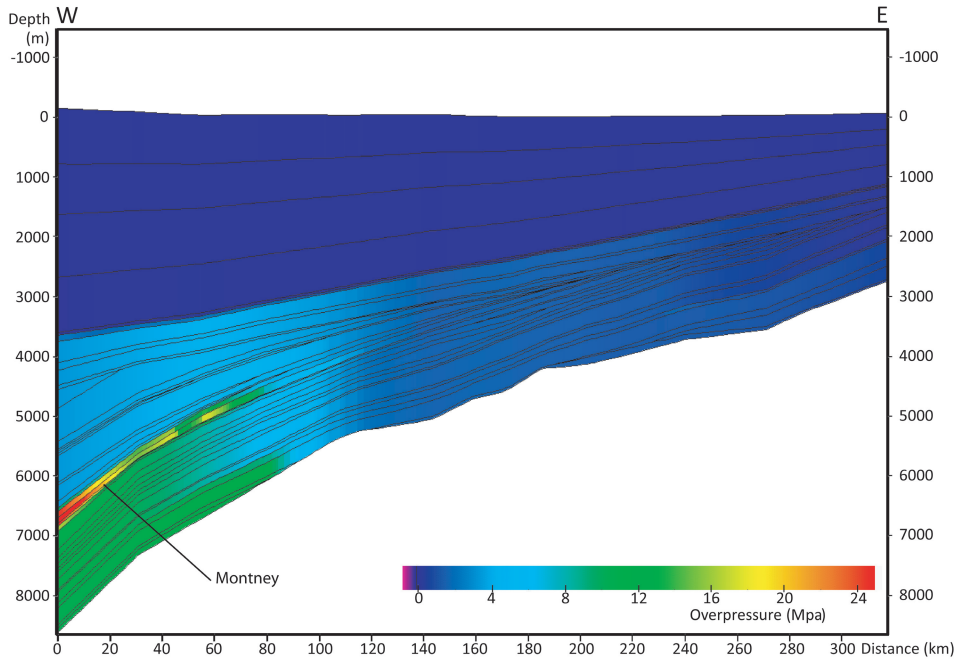

Figure 10. Simulated overpressures before the erosion related to the Canadian Cordillera Orogeny (MPa). The strong overpressures in the Montney formation are due to deep burial, generation of hydrocarbons, and low permeability.

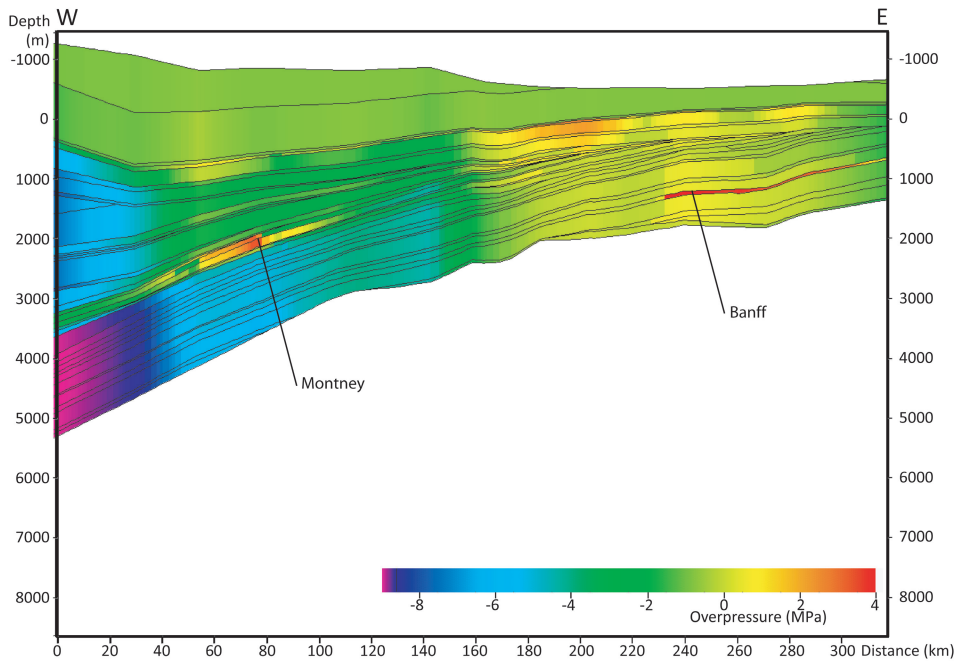

Figure 11. Simulated overpressures at present day (MPa). Overpressures generated during the deposition of the Colorado Group are completely released. Red cells are overpressured and correspond to hydrocarbon-rich layers, yellow zones are close to hydrostatic pressure, and green and blue zones are underpressured. The basin can be divided into two regions: the underpressured western part and the almost hydrostatic eastern part.

time in the basin (Figure 12) shows that abnormal or large overpressure was not developed until the Lower Cretaceous. It started to increase during the deposition of the Colorado Group and the onset of hydrocarbons generation. This pressure build up is mostly due to compaction disequilibrium, which is the consequence of the rapid deposition of a large amount of sediments. Indeed, it created a great sediment load on low-permeability sediments that had to expel water to reach a mechanical compaction equilibrium. However, the excess of water could not easily escape due to the very low permeability of the Triassic formations, resulting in an overpressured system (~10 MPa). This period also corresponds to the onset of hydrocarbon generation in the low-permeability Montney formation that resulted in even higher overpressures (~20 MPa

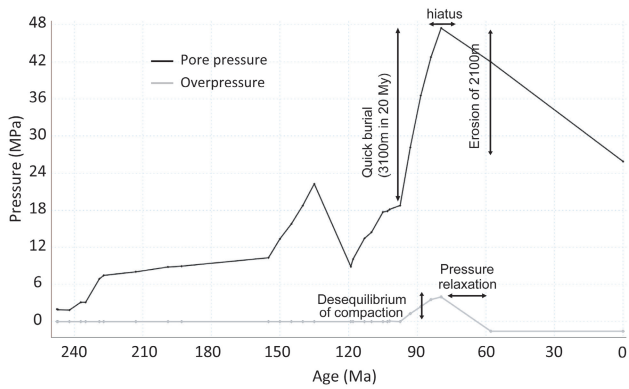

Figure 12. Example of water pressure (continuous line) and overpressure (gray line) evolution through geological time in the Montney Formation nearby well C-70-B/93-P-9.

overpressure in the Montney formation). Overpressures are higher in the western part of the basin due to both fast sedimentation rate (3000 m [9843 ft] in 20 m.y. in the west versus 1800 m [5906 ft] in the east) and higher hydrocarbon generation (higher maturity).

The uplift and erosion of the Canadian Cordillera that followed resulted in a decrease of the sediment load. This break in the sedimentation also enabled water to escape from overpressured layers during 20 m.y., even at low water flows. Then, due to the inverse dip between the surface topography and the bedding of deep formations (Triassic and older) after the uplift of the Canadian Cordillera, some abnormally low pressures (pressure under the vertical hydrostatic pressure) can be observed in the deep basin in units below impermeable layers. These anomalously low pressures result mainly from the equilibration of pressures due to the same mechanism as for an artesian groundwater. They are also partly explained by the fact the porosity slightly increased due to a mechanical rebound (rock elasticity) after the last erosion period. Since rock permeability was already low, there is a slight decompaction disequilibrium participating in the creation of pressures below the hydrostatic trend. An important consequence of the evolution toward these anomalous pressures within petroleum source rocks is that they significantly modified the history of oil charge, creating down-dip hydrocarbons migration.

Analysis of simulated water pressure evolution along the wells' paths shows two main changes in the pressure trend: at the base of the Colorado group and at the top of the Montney formation (Figure 13). They are due to the presence of a permeability barrier that creates a mechanism of artesian groundwater after the Laramide Orogeny. Overpressures that are observed below the top of the Doig formation can be directly related to hydrocarbon presence. This information is of great interest for exploration since overpressures can be related to hydrocarbon occurrence instead of water pressure.

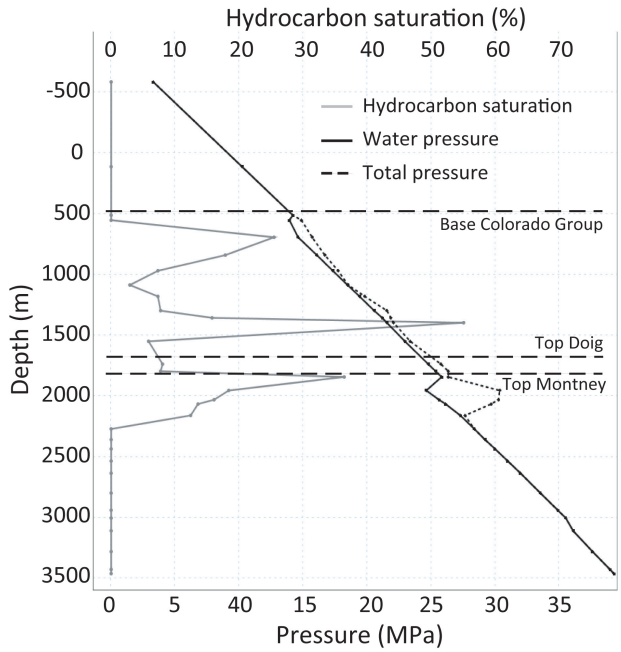

Figure 13. Vertical evolution of water pressure (continuous black line), hydrocarbon pressure (dashed line), and hydrocarbon saturation (gray line) along well C-70-B/93-P-9. This graph illustrates that overpressures are associated with source rock formations and hydrocarbon generation.

The possible hydraulic fracturing that can have occurred in the Triassic formations, which experienced high mechanical stresses during the deposition of the Colorado Group and the following uplift and erosion of the Canadian Cordillera, was not accounted for in the model. This mechanism could lead to an earlier release of water pressure in the system and to vertical migration of hydrocarbons generated in the Montney formation in the overlying units. Including major structural elements and hydraulic fracturing mechanisms would further help improve our understanding of the petroleum system and should be addressed in the future.

Migration

Simulated Hydrocarbon Accumulations: The WCSB hosts a large variety of oil and gas play types including tight and source rock reservoirs, as well as conventional plays with gas, light oil, heavy oil, and bitumen. The distribution of hydrocarbon saturations within our model properly reproduces this variability and illustrates possible migration pathways and accumulations (Figure 14). In our simulation, major hydrocarbon accumulations occur in the following reservoirs:

- Lower Cretaceous sandstones (1 in Figure 14)
- The Charlie Lake formation, westward from the Doig Phosphate subcrop edge (2 in Figure 14)

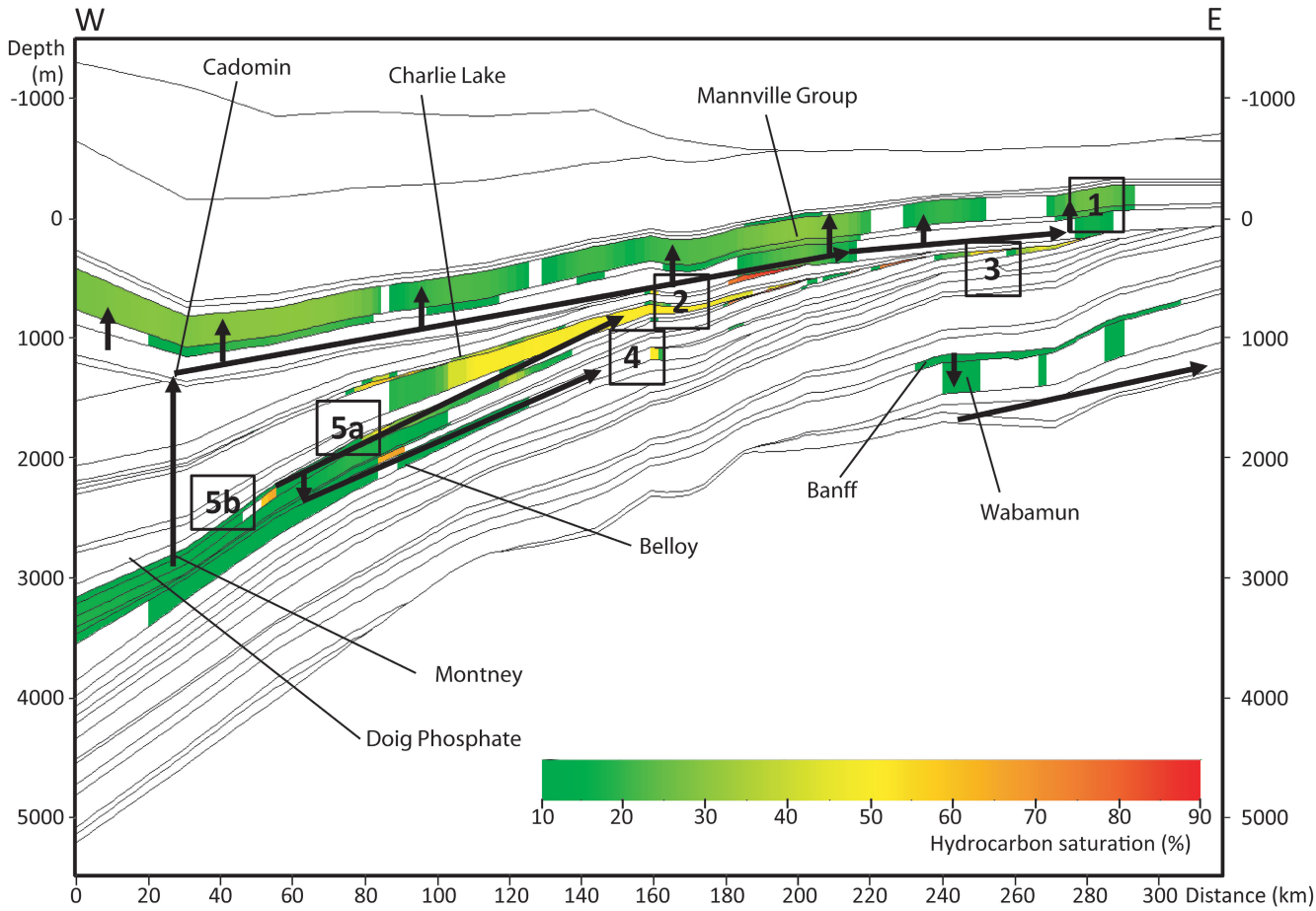

Figure 14. Simulated hydrocarbon saturation (%) in the Western Canada Sedimentary Basin. Main hydrocarbon accumulations are located in: (1) Lower Cretaceous reservoirs of the Mannville Groupat Peace River, (2) Charlie Lake reservoirs west of Peace River oil sands, (3) Charlie Lake and Montney stratigraphic reservoirs along their subcrop edges, (4) Belloy reservoirs, (5a) tight plays of the Montney and Doig formations, and (5b) turbiditic reservoirs of the Montney formation. Hydrocarbon migration pathways are represented by arrows. Hydrocarbons generated in the Montney formation mostly migrated laterally toward tight reservoirs of the Montney formation or in reservoirs of the underlying Belloy formation. Hydrocarbons generated early in the Gordondale and Doig formations migrated vertically (–135 to –119 Ma). Then, migration was mostly lateral toward the eastern part of the basin (–97.5 to –57.8 Ma). Vertical migration from Cadomin and Triassic reservoirs east of the Doig subcrop to Upper Mannville reservoirs occured from –79.5 Ma to present day.

- Stratigraphic traps in the Montney formation below the Triassic unconformity (3 in Figure 14)
- The Belloy formation, westward from the Doig subcrop edge (4 in Figure 14)
- Tight reservoirs and organic-rich fine-grained sediments of the Montney and Doig formations (5a in Figure 14)
- Turbiditic sandstones of the Montney formation (5b in Figure 14).

Little or no accumulation was sourced by the Duvernay and Exshaw source rocks along the section of our model. This is due to the fact that most of the reservoirs sourced by these source rocks are located further east in the basin (at the eastern edge of the model toward the Peace River, Wabasca, and Athabasca fields).

Simulation results clearly show hydrocarbon accumulations in tight reservoirs of the Montney formation. In such petroleum systems, facies and petrophysical property variations play a key role in the hydrocarbon migration and distribution since accumulations are the result of low migration velocity.

Migration and charge of the WCSB (Figure 14) involves vertical and lateral long-distance oil migrations, multiple oil mixing from different source rocks, oil degradation, and even per-descensum migration (e.g., gas from Montney formation to Belloy formation or oil from Doig formation to Montney formation). Some authors investigated the oil source and alteration of known fields based mostly on geochemical data (Creaney and Allan, 1990; Allan and Creaney, 1991; Adams et al., 2012) and brought new understanding

on the petroleum system. However, as stressed by Adams et al. (2012), it is challenging to clearly evaluate the contribution of each source due to the lack of regional and extensive source rock characterization and to the alteration and differences of maturity of the different oil charges. Basin modeling provides a powerful tool to understand how accumulations formed by tracking migration of hydrocarbons from sources to reservoirs. Possible biodegradation of hydrocarbon was investigated by comparing the relative timing of reservoir filling versus thermal evolution. It shows that only the most eastern part of our modeled section undergone biodegradation.

Plays of the Montney Formation: Although hydrocarbons in the Montney formation were generated early in the basin history according to the model (between −88.5 and −57.8 Ma), they did not migrate far from their source and mostly accumulated in tight or turbiditic reservoirs within the Montney formation itself. However, in the proximal part of the unconventional Montney play, westward from the Doig Phosphate subcrop edge, the hydrocarbons accumulated in the upper part of the Montney formation were mostly sourced by the upper Doig formation (Doig and Doig Phosphate) according to our model (5a on Figure 14 and Figure 15C). They do not correspond to the classical definition of hydrocarbon accumulation but rather to continuous petroleum saturations or regional pervasive petroleum accumulations that can be oil or gas saturated ("basin-centered systems"; Law, 2002, 1893 p) characterized by an absence of downdip water contact, seal and conventional trap, very low reservoir permeabilities, and the proximity of a source rock (e.g., Law, 2002; Ramirez and Aguilera, 2012). Those hydrocarbon accumulations correspond to a hydrocarbon front of migration moving very slowly due to extremely low permeabilities. They do not present an oil–water contact, making conventional methods of resource assessment ineffective. In our model, hydrocarbon accumulations dominantly consist of liquids (>70%) due to late filling from overlying cooler formations but vary from dry gas in the western part to very light hydrocarbons in the eastern part. The more we go toward distal parts of the Montney formation, the more the hydrocarbons originate from the Montney itself and the more these hydrocarbons are gas rich. Indeed, analysis of hydrocarbons migration generated by the Montney source rock shows relatively short-distance migration compared to oil generated elsewhere in the basin (Figure 14). Vertical migration from the Montney formation is difficult due to the overlying Doig Phosphate layer that acts as a seal. Hydrocarbon flow is then only possible slowly toward the east because of very low permeabilities (>0.005 mD) as pointed out by several authors (e.g., Kuppe et al., 2012). Consequently hydrocarbons generated in the Montney,

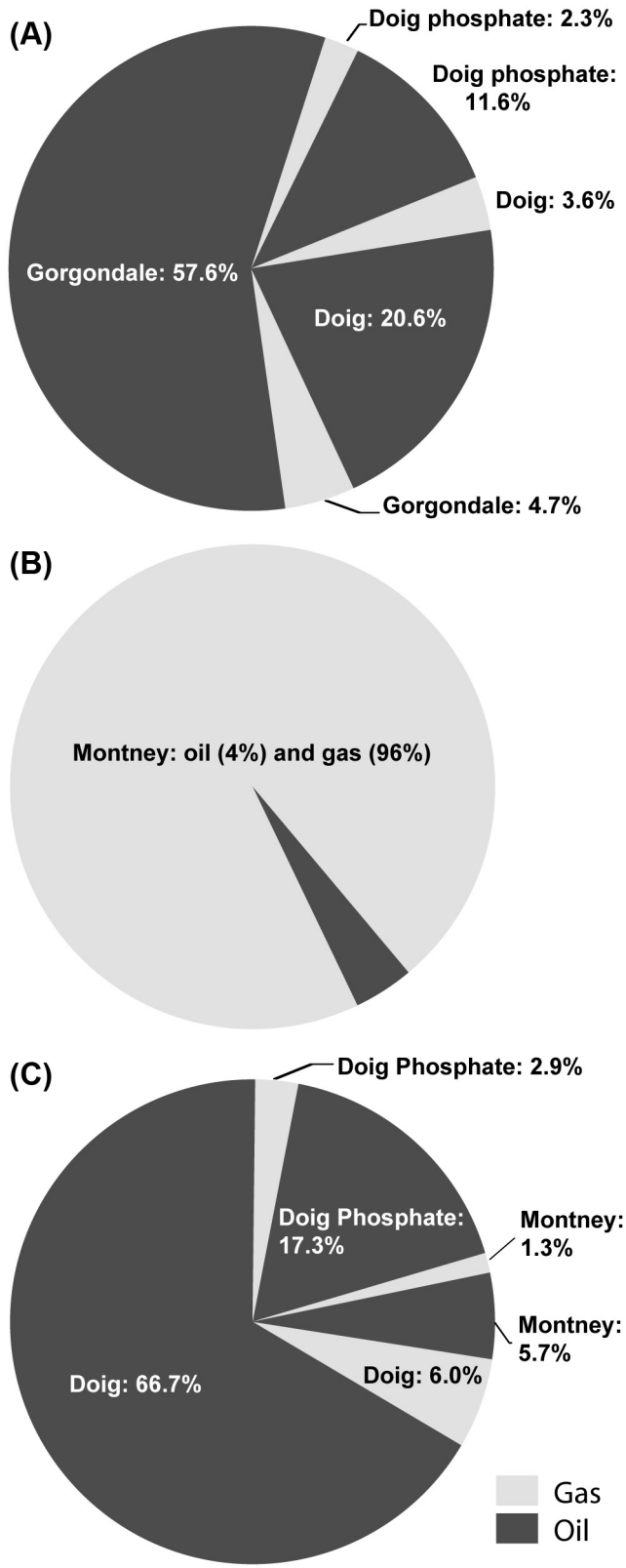

Figure 15. Origin of hydrocarbons (%) according to the petroleum system model: (A) in tight plays of the proximal part of the Upper Montney formation (5a on Figure 14); (B) in turbiditic reservoirs of the Montney formation (5b on Figure 14); (C) in Charlie Lake and Montney formations along their subcrop edges (2 and 3 on Figure 14).

mostly gas or condensates, accumulate in tight turbiditic reservoirs (<0.05 mD) or even in the underlying reservoirs of the Belloy formation (Figure 15B). Since those hydrocarbons remained trapped in deep reservoirs, most of them experienced secondary cracking (cracking of oil into gas and coke). Accordingly, most Montney resources should correspond to very mature hydrocarbons (gas and condensates) and should show traces of solid residual organic matter.

Stratigraphic Traps of Charlie Lake and Montney Formations: According to the simulation results, early generated oil from the Gordondale and Doig Phosphate source rocks could have migrated farther to the east in the underlying Charlie Lake and Montney formations and filled reservoirs along their subcrop edges (Figure 15A). These results are consistent with those obtained by Ejezie (2006), who found that these reservoirs are sourced primarily from the Gordondale source rock. Results also suggest that hydrocarbons trapped in these reservoirs should be of good quality (no biodegradation) since pasteurization temperature is reached before the reservoir is filled with hydrocarbon. Indeed, hydrocarbon charge started during the deposition of the Colorado Group (Upper Cretaceous).

Organic Porosity and Methane Adsorption: Porosity is created by the maturation of organic matter, and source rocks can retain hydrocarbons generated in situ in this organic porosity (e.g., Loucks et al., 2009). In some basins (e.g., Fort Worth Basin, Texas), this porosity can even represent more than 50% of the rock porosity. Moreover, mechanisms of gas adsorption also participate in hydrocarbon retention in source rocks (e.g., Langmuir, 1918; Lu et al., 1995). Thus, it is important to estimate hydrocarbon quantity that could be adsorbed in WCSB source rocks. Recent basin modeling capabilities for unconventional resources assessment (Romero-Sarmiento et al., 2013) were used to estimate both methane retention (Figure 16) and organic porosity creation (Figure 17) in the WCSB.

Organic porosity is strongly related to source rock richness in organic material, to maturity, and to source rock quality. It is evaluated by computing the volume released during the transformation of solid organic matter into hydrocarbons (oil and gas). Other factors

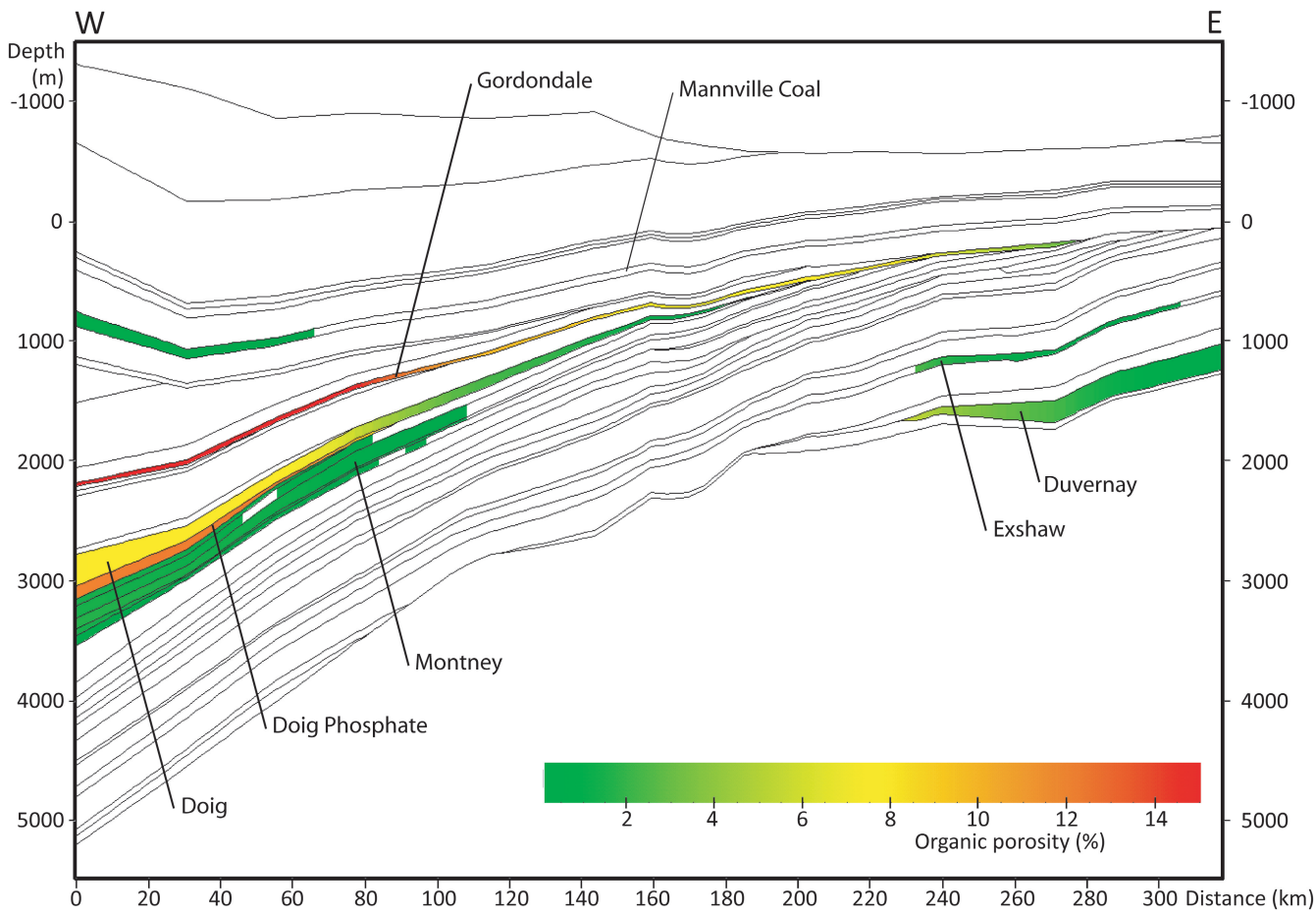

Figure 16. Simulated porosity created in the organic matter (%).

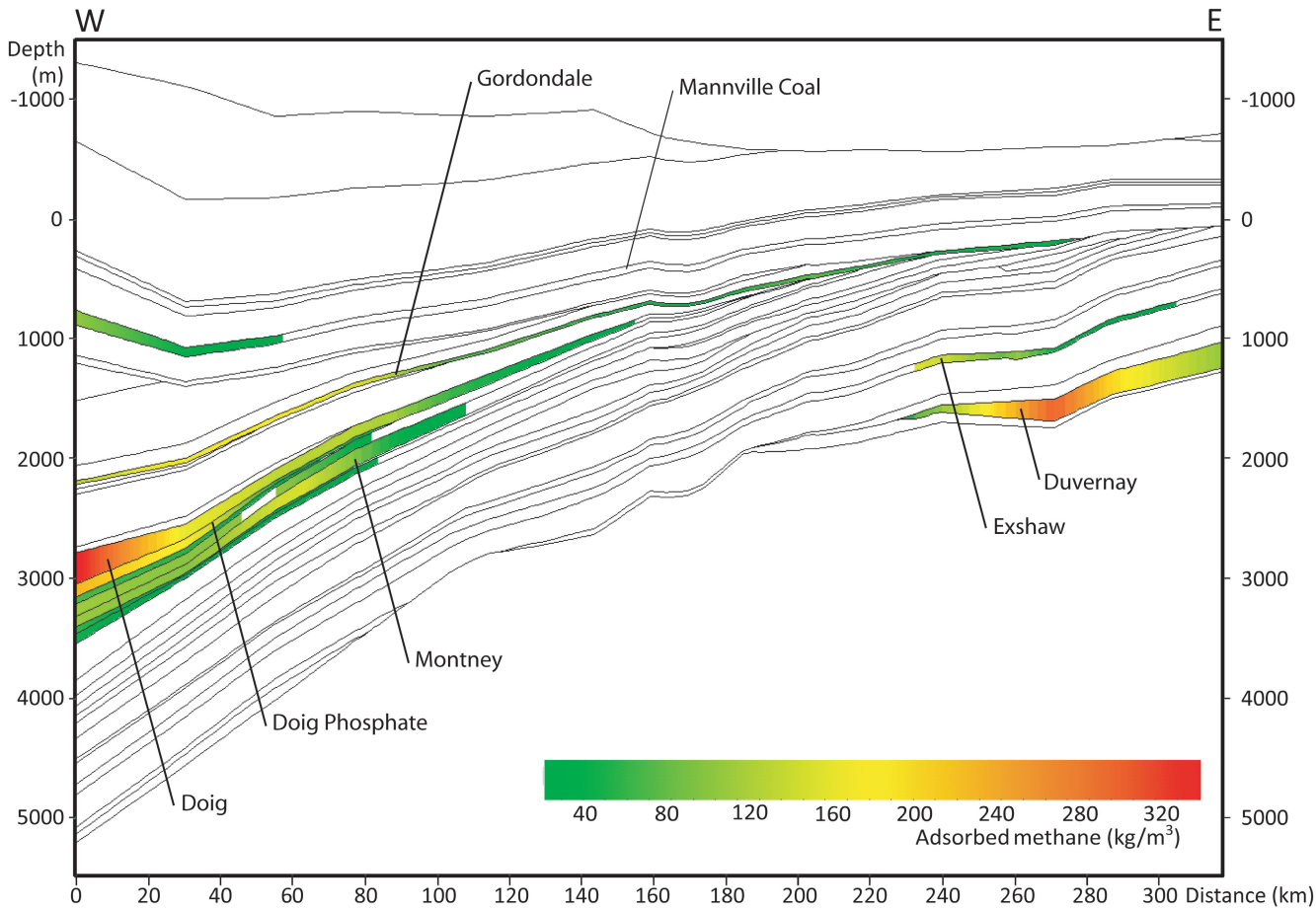

Figure 17. Simulated mass of adsorbed methane (kg/m²).

such as compaction and mineralogy may also affect organic porosity, but they are not taken into account in this model. Therefore, values are only indicative and correspond to maximum values that can be expected.

Organic porosity in Montney, Exshaw, and Mannville Coals hardly reaches 1%, which can be considered almost negligible contribution to porosity even in the low-porosity shale plays of the Montney formation (4–7% porosity). Duvernay has organic porosity values that could reach 3% and thus contribute significantly to oil retention in the source rock. More promising are the Doig Phosphate and Gordondale source rocks that show porosity of respectively 4 to 5% and 2 to 9% in the more mature zones. This porosity would represent a major contribution to hydrocarbon accumulation in the source rock.

Methane adsorption at the surface of organic matter depends on pressure (positively), temperature (negatively), TOC, and generated methane. Optimal conditions for adsorbed methane occur in the Gordondale, the Duvernay, and the Doig Phosphate. However, quantities of hydrocarbons trapped under the adsorbed state are much lower than those retained in the organic porosity (less than one fifth). Interestingly, according to simulation results and with the assumption of no organic porosity compaction, there could be as much retained hydrocarbons as expelled hydrocarbons. These results, given the large amount of oil in conventional plays, and even with the above mentioned limitations, confirm the potential for unconventional resources not only in Triassic formations of the WCSB but also in the Gordondale (Lower Jurassic) and Duvernay (Devonian) formations.

CONCLUSIONS

The present study aimed to give a first overview of the petroleum system of the WCSB through the modeling of a representative section crossing the north of the WCSB using the TemisFlow™ software. The model was constructed and calibrated based on available well data. Thermal calibration results propose heat flow values ranging from 45 to 72 mW/m² and eroded thickness up to 2200 m (7218 ft). The main results of our work are:

(1) All source rocks reached their maximum transformation rate just before the last major erosion (early Paleogene), which corresponds to their maximum burial. Only the deepest and most reactive (lower activation energy) source rocks (Gordondale and Phosphatic Doig) could have started to generate hydrocarbons before the erosion of the Minnes Group (Upper Jurassic). The early Paleogene also corresponds to maximum overpressure in source rocks due to the peak of hydrocarbon generation.
(2) Analysis of both available pressure measurements and computed pressures suggests that present-day overpressures are entirely due to hydrocarbon accumulation, not to compaction disequilibrium.
(3) Our model was able to reproduce the large diversity of plays that are found in the WCSB: tight reservoirs, shale plays, and conventional reservoirs with conventional and biodegraded oils. It strengthens the hypothesis of long-distance (>100 km [>62 mi]) migration of hydrocarbons from Gordondale and Doig Phosphate source rocks to Lower Cretaceous Mannville sandstones as well as to Triassic Charlie Lake and Montney reservoirs at their subcrop edges, as proposed by Higley et al. (2009) and supported by Berbesi et al. (2012).
(4) Montney sourced hydrocarbons did not migrate far from their source rock due to very low permeabilities. They can be found mostly in turbiditic reservoirs (gas) and fine-grained distal deposits within the Montney formation and in the underlying Belloy formation (mostly gas). Hydrocarbon accumulations in tight reservoirs of the Montney formation do not present any oil-water contact, making classical assessment of hydrocarbon in place ineffective.
(5) According to our results, there could be as much retained hydrocarbons in source rocks as expelled hydrocarbons (including adsorbed gas and free hydrocarbons in organic and matrix porosity). This could represent huge amounts of oil and gas still in the source rocks. Most promising targets for such plays would be associated to Duvernay, Doig Phosphate, and Gordondale source rocks and some parts of the Montney formation.

Although our model provides an overview of key aspects of the petroleum system, it does not account for the potential contribution from source rocks outside and lateral migrations across the two-dimensional plane of the simulated section. Furthermore, possible vertical migrations through faults were not included in the model. Extending our model in three dimensions and including major structural elements would further help improving our understanding of the petroleum system and provide a basis for process-based assessment of unconventional resources in place.

REFERENCES

Adams, J., S. Larter, B. Bennett, and H. Huang, 2012, Oil charge migration in the peace river oil sands and surrounding region: GeoConvention 2012, accessed March 1, 2017, http://www.geoconvention.com/archives/2012/270_GC2012_Oil_Charge_Migration_in_the_Peace_River_Oil_Sands.pdf.

Allan, J., and S. Creaney, 1991, Oil families of the Western Canada Basin: Bulletin of Canadian Petroleum Geology, v. 39, p. 107–122.

Allen, P. A. & J. R. Allen, 2005, Basin analysis: principles & applications: Blackwell Science., Oxford, UK, 549 pp.

Bachu, S., and R. A. Burwash, 1994, Geothermal regime in the Western Canada Sedimentary Basin, *in* G. D. Mossop and I. Shetsen, compilers, Geological atlas of the Western Canada Sedimentary Basin. Canadian Society of Petroleum Geologists and Alberta Research Council, Chapter 30, accessed March 1, 2017, http://www.ags.gov.ab.ca/publications/wcsb_atlas/atlas.html.

Bachu, S., 1995, Synthesis and model of formation-water flow, Alberta Basin, Canada: AAPG Bulletin, v. 79, no. 8, p. 1159–1178.

Bachu, S., and J. R. Underschultz, 1995, Large-scale underpressuring in the Mississippian–Cretaceous succession, southwestern Alberta Basin: AAPG Bulletin, v. 79, no. 7, p. 989–1004.

Beaton, A. P., J. G. Pawlowicz, S. D. A. Anderson, H. Berhane, and C. D. Rokosh, 2010, Organic petrography of the Montney formation in Alberta: Shale Gas Data Release, ERCB/AGS Open File Report 2010-07, accessed March 1, 2017, http://ags.aer.ca/document/OFR/OFR_2010_05.PDF.

Behar, F., M. Vandenbroucke, Y. Tang, F. Marquis, and J. Espitalié, 1997, Thermal cracking of kerogen in open and closed systems: Determination of kinetic parameters and stoichiometric coefficients for oil and gas generation: Organic Geochemistry, v. 26, p. 321–339.

Bekele, E. B., 1999, Anomalous pressures and fluid migration within the Alberta Basin, Canada: Thesis submitted to the University of Minnesota in partial fulfilment of the requirements for the degree of doctoral of philosophy, 202 p.

Berbesi, L. A., R. di Primio, Z. Anka, B. Horsfield, and D. K. Higley, 2012, Source rock contributions to the Lower Cretaceous oil accumulations in Alberta: A basin modeling study: AAPG Bulletin, v. 96, no. 7, p. 1211–1234.

Berger, Z., M. Boast, and M. Mushayandebvu, 2008, The contribution of integrated HRAM studies to exploration and exploitation of unconventional plays in North America Part 1: The Peace River Arch: Reservoir, v. 35, no. 10, p. 42–47.

Burrus, J., K. Osadetz, S. Wolf, B. Doligez, K. Visser, and D. Dearborn, 1996, A two-dimensional regional basin model of Williston basin hydrocarbon system: AAPG Bulletin, v. 80, no. 2, p. 265–291.

Corbet, T. F., and C. M. Bethke, 1992, Disequilibrium fluid pressures and groundwater flow in the Western Canada Sedimentary Basin: Journal of Geophysical Research, v. 97, no. B5, p. 7203–7217.

Creaney, S., and J. Allan, 1990, Hydrocarbon generation and migration in the Western Canada Sedimentary Basin, *in* J. Brooks, ed., Classic petroleum provinces: Geological Society Special Publication, v. 50, p. 189–202.

Creaney, S., J. Allan, K. S. Cole, M. G. Fowler, P. W. Brooks, K. Osadetz, et al., 1994, Petroleum generation in the Western Canada Sedimentary Basin, *in* G. D. Mossop and I. Shetsen, compilers, Geological atlas of the Western Canada Sedimentary Basin, Canadian Society of Petroleum Geologists and Alberta Research Council, Special Report 4, Chapter 31, accessed March 1, 2017, http://www.ags.gov.ab.ca/publications/wcsb_atlas/atlas.html, p. 455–468.

Davies, G. R., 1997, The Triassic of the Western Canada Sedimentary Basin: Tectonic and stratigraphic framework, paleogeography, paleoclimate and biota: Bulletin of Canadian Petroleum Geology, v. 45, no. 4, p. 434–460.

Doligez, B., P. Ungerer, P. Y. Chénet, J. Burrus, F. Bessis, and G. Bessereau, 1987, Numerical modeling of sedimentation, heat transfer, hydrocarbon formation and fluids migration in the Viking graben, North sea, *in* J. Brooks and K. Gleenie, eds., Petroleum geology of north-west Europe: London, Graham and Trotman, p. 1039–1048.

Edwards, D. E., J. E. Barclay, D. W. Gibson, G. E. Kvill, and E. Halton, 1994, Chapter 16, Triassic Strata of the Western Canada Sedimentary Basin, *in* G. D. Mossop and I. Shetsen, compilers, Geological Atlas of the Western Canada Sedimentary Basin: Canadian Society of Petroleum Geologists and Alberta Research Council, p. 259–273.

Ejezie, N., 2006, Triassic oil families and possible source rocks, Peace River Embayment area, Alberta, Canada, M. Sc. Thesis: Calgary, Alberta, University of Calgary, 162 p.

Henderson, C. M., 1997, Uppermost Permian conodonts and the Permian-Triassic boundary in the Western Canada Sedimentary Basin: Bulletin of Canadian Petroleum Geology, v. 45, no. 4, p. 693–707.

Higley, D. K., H. Mitchell, L. N. R. Roberts, and D. W. Steinshouer, 2005, 1-D/3-D geological model of the Western Canada Sedimentary Basin: The Rocky Mountain Association of Geologists, v. 42, no. 2, p. 1–13.

Higley, D. K., M. D. Lewan, L. N. R. Roberts, and M. Henry, 2009, Timing and petroleum sources for the Lower Cretaceous Mannville Group oil sands of northern Alberta based on 4D-modeling: AAPG Bulletin, v. 93, p. 203–213.

Jarvie, D. M., R. J. Hill, T. E. Ruble, and R. M. Pollastro, 2007, Unconventional shale-gas systems: The Mississippian Barnett Shale of north-central Texas as one model for thermogenic shale-gas assessment: AAPG Bulletin, v. 91, p. 475–499.

Kuppe, F., S. Haysom, and G. Nevokshonoff, 2012, Liquids rich unconventional Montney reservoir: The geology and the forecast: SPE 162824, v. 2, p. 1407–1435.

Langmuir, I., 1918, The adsorption of gases on plane surfaces of glass, mica and platinum: Journal of the American Chemical Society, v. 40, p. 1403–1461.

Law, B. E., 2002, Basin-centered gas systems: AAPG Bulletin, v. 86, no. 11, p. 1891–1919.

Loucks, R. G., R. M. Reed, S. C. Ruppel, and D. M. Jarvie, 2009, Morphology, genesis and distribution of nanometer-scale pores in siliceous mudstones of the Mississippian Barnett Shale: Journal of Sedimentary Research, v. 79, p. 848–861.

Lu, X-C., F-C. Li, and A. T. Watson, 1995, Adsorption measurements in Devonian shales: Fuel, v. 74, p. 599–603.

Mossop, G. D., and I. Shetsen, compilers, 1994, Geological Atlas of the Western Canada Sedimentary Basin. Canadian Society of Petroleum Geologists and Alberta Research Council, accessed March 1, 2017, http://www.ags.gov.ab.ca/publications/wcsb_atlas/atlas.html, 507 p.

Ness, S. M., 2001, The application of basin analysis to the Triassic succession, Alberta Basin: An investigation of burial and thermal history and evolution of hydrocarbons in Triassic rocks. M. Sc. Thesis: Calgary, Alberta, University of Calgary, 179 p.

Parks, K. P., and J. Toth, 1995, Field evidence for erosion-induced underpressuring in Upper Cretaceous and Tertiary strata, West Central Alberta, Canada: Bulletin of Canadian Petroleum Geology, v. 43, no. 3. p. 281–292.

Proverbs, I. P., L. B. Kerrie, and C. Fratton, 2010, Integrated sedimentology, ichnology and petrography of unconventional gas reservoirs of the Montney formation, Dawson Creek Region, Northeastern B.C.: GeoCanada, accessed March 1, 2017, http://cseg.ca/assets/files/resources/abstracts/2010/core/0798_GC2010_Integrated_Sedimentology.pdf.

Price, R. A., H. R. Balkwill, H. A. K. Charlesworth, D. B. Cook, and P. S. Simony, 1972, The Canadian Rockies and tectonic evolution of the southeastern Canadian Cordillera: International Geological Congress, 129 p.

Price, R., 1994, Chapter 2, Cordilleran tectonics and the evolution of the Western Canada Sedimentary Basin, *in* G. D. Mossop and I. Shetsen, compilers, Geological Atlas of the Western Canada Sedimentary Basin: CSPG and Alberta Research Council, p. 13–24.

Ramirez, J. F., and R. Aguilera, 2012, Updip water blockage in the Nikanassin basin centered gas accumulation, Western Canada Sedimentary Basin: SPE 162774, v. 2, p. 1189–1200.

Reed Jr., J. C., J. O. Wheeler, and B. E. Tucholke, 2005, Decade of North American Geology Geologic Map of North America—Perspectives and explanation: Geological Society of America, Boulder, Colorado, 32 p.

Ricketts, B. D., 1986, Styles of alluvial fan–braid plain sedimentation in orogenic foredeeps—Examples from Canadian Cordillera Orogen: Bulletin of Canadian Petroleum Geology, v. 34, no. 1, p. 1–16.

Romero-Sarmiento, M. F., M. Ducros, B. Carpentier, F. Lorant, M. C. Cacas, S. Pegaz-Fiornet, et al., 2013, Quantitative evaluation of TOC, organic porosity and gas retention distribution in a gas shale play using petroleum system modeling: Application to the Mississippian Barnett Shale: Marine and Petroleum Geology, v. 45, p. 315–330.

Roure, F., P. Andriessen, J. P. Callot, J. L. Faure, H. Ferket, E. Gonzales, et al., 2011, The use of palaeo-thermo-barometers and coupled thermal, fluid flow and pore-fluid pressure modeling for hydrocarbon and reservoir prediction in fold and thrust belts, *in* G. P. Goffey, ed., Hydrocarbons in contractional belts: Geological Society of London, Special Publication 348, p. 87–114.

Vandenbroucke, M., F. Behar, and J. L. Rudkiewicz, 1999, Kinetic modeling of petroleum formation and cracking: Implications from the high pressure/high temperature Elgin Field (U.K., North Sea): Organic Geochemistry, v. 30, no. 9, p. 1105–1125.

Wygrala, B., 1986, Integrated study of an oil field in the southern Po Basin, northern Italy, Ph.D. thesis: Germany, University of Cologne, 332 p.

Ziegler, A., C. Scotese, and S. Barrett, 1983, Mesozoic and Cenozoic paleogeographic maps: Tidal Friction and the Earth's Rotation II, p. 240–252.

[AV]Second White Specks Formation: New Concepts for Understanding Fractured Reservoirs*

Paul MacKay[1]

Search and Discovery Article #110218 (2015)**
Posted September 7, 2015

*Adapted from presentation at the AAPG DPA Playmaker, Calgary, Alberta, March 31, 2015
**Datapages©2015 Serial rights given by author. For all other rights contact author directly.

[1]CEO & President, Shale Petroleum Ltd., Calgary, Alberta (http://www.shalepetroleum.com; info@shalepetroleum.com)

Abstract

The Upper Cretaceous Second White Specks Formation is a fractured, marine, interbedded shale, siltstone, and fine-grained sandstone. This unit is part of the Colorado Group (Alberta Group), which also includes the Cardium and Viking formations and was deposited in the Cretaceous Seaway during a relatively quiet tectonic period of the building of the western Canadian Cordillera. The Second White Specks has been characterized as a zone with numerous hydrocarbon shows, but to date it has not shown the repeatable success needed to establish a resource play.

Despite the lack of repeatability, there have been a few notable individual wells within the zone that have produced over one million barrels of liquid petroleum from vertical drill holes. In these cases the well appears to have intersected a regional natural fracture system that has delivered significant volumes of hydrocarbons. In resource plays there is an ongoing debate over the merits of matrix permeability versus the permeability of the natural fracture system. In the case of the Second White Specks Formation, the natural fracture system dominates the permeability system.

A paradox in the exploration/production endeavor is that wells are positioned and drilled to find hydrocarbon storage but are completed to maximize rate and deliverability. In this procedure the natural delivery system is ignored (natural fractures) in the belief that well stimulation and induced hydraulic fractures can replicate or improve upon the natural system. Flow from the rock is a complex interplay of varying fracture apertures, access to the hydrocarbon-generating system, development of elevated fluid pressures, fluid compatibility, and resistance to flow within the rock. Successful wells appear to access large natural fluid pathway systems such that the mega-fracture network connects effectively with the micro-fracture system.

Selected References

Clarke, H., L. Eisner, P. Styles and P. Turner, 2014, Felt seismicity associated with shale gas hydraulic fracturing: The first documented example in Europe: Geophysical Research Letters, v. 41/23, p. 8308-8314.

Sieminski, A., 2014, Oil and gas outlook:For Independent Petroleum Association of America November 13, 2014 Palm Beach, FL: Energy Information Administration (EIA), 25p. Website accessed August 11, 2015, http://www.eia.gov/pressroom/presentations/sieminski_11132014.pdf.

Styles, P., I.Stimpson, R. Westood, S. Toon, L. Eisner, H. Clarke, and P. Turner, Seismicity induced by Shale Gas Hydraulic Stimulation: PreeseHall, Blackpool, United Kingdom. Website accessed August 10, 2015, http://www.seismo.ethz.ch/research/groups/schatzalp/Download/Styles.pdf.

Website

Department of Energy and Climate Change: https://gov.uk/oil-and-gas-uk-field-data. Website accessed August 10, 2015.

Second White Specks Formation

New concepts for understanding fractured reservoirs.

Paul MacKay
Shale Petroleum Ltd.

June 2015

AAPG Playmakers' Forum



Shale Petroleum

AAPG

Canada's Energy Geoscientists

cspg.org

Life Cycle of a Resource Play

Definition Mode
Early Entrant
Low Land Cost
Innovator

De-Risk Mode
Competitive
High Land Cost
Implement Technology

Manufacture Mode
Entry through Corporate Acquisition
Low Cost Operator
Continuous Improvement

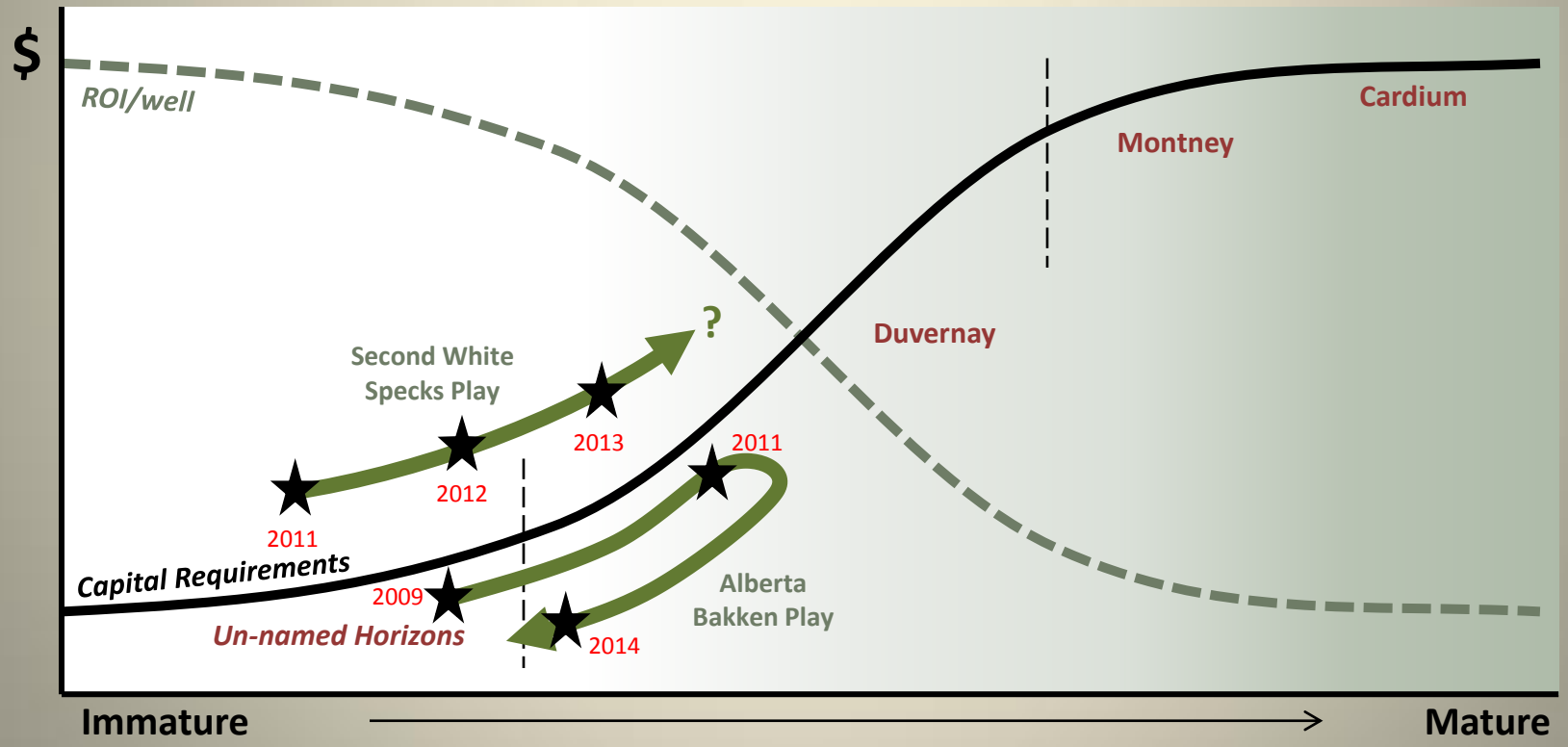

Understanding **Procedure**

The Production of Hydrocarbons from Fine-Grained Rock

A fundamental change in theory and practice

- Technical Challenges:
  - How do I know that my company is current with technology?
  - How do I know if my contractor is current?
  - Who is doing the latest research and are they a benefit to me or will they slow me down?
- Social Challenges:
  - What is a social license?
  - Is there a new regulatory system (Frac Procedures)?

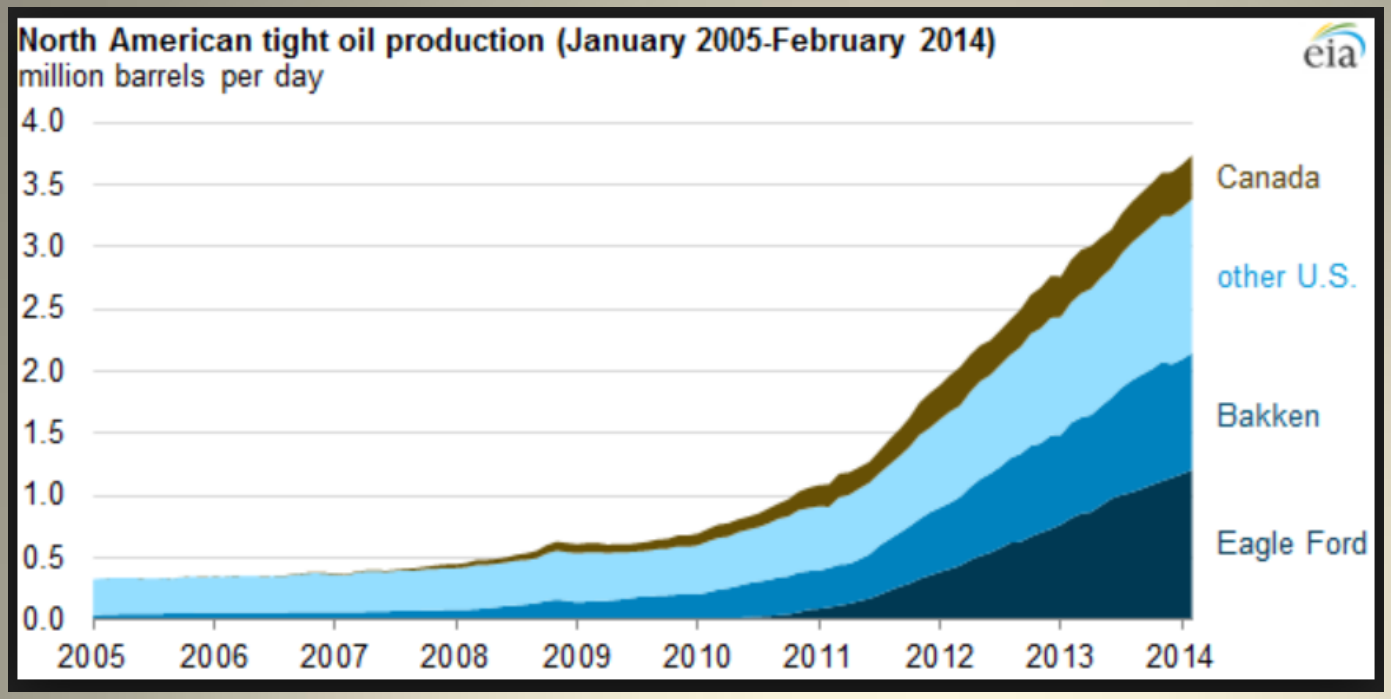

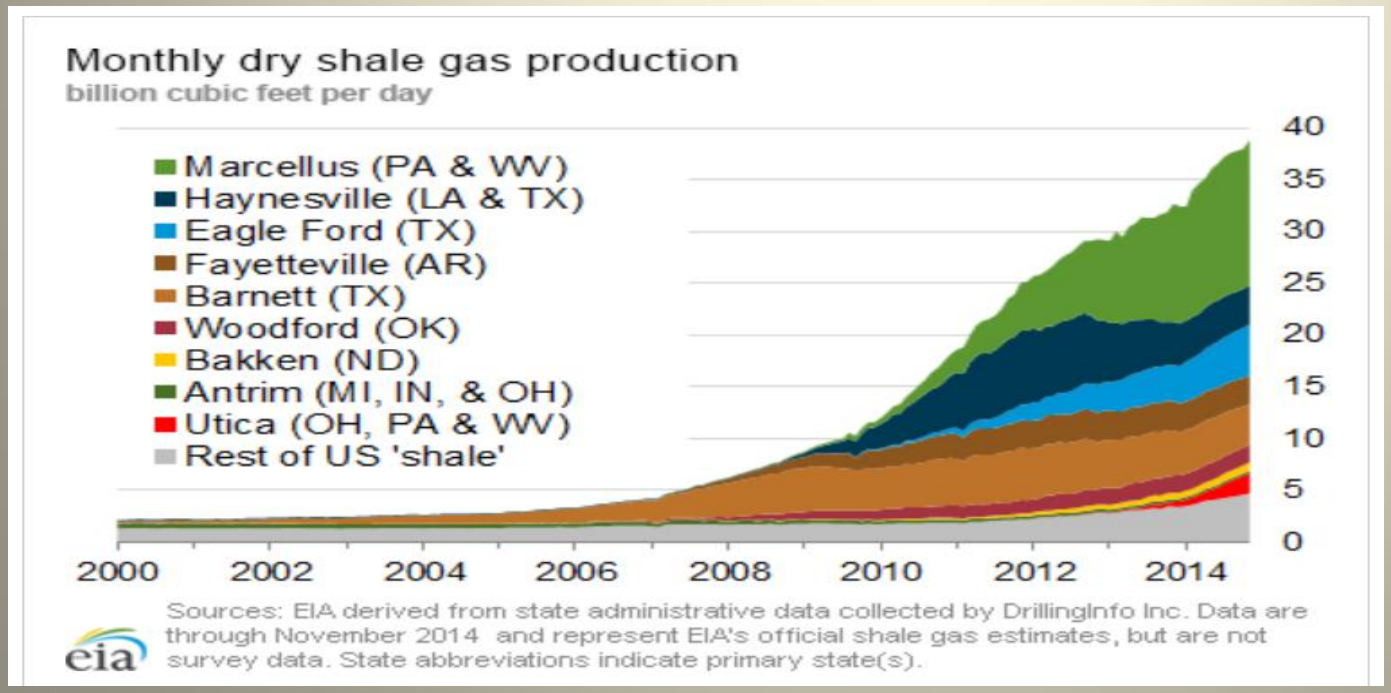

Commodity Prices

vs.

Time

Spot Prices vs. Rigs Graph | Rigs Table

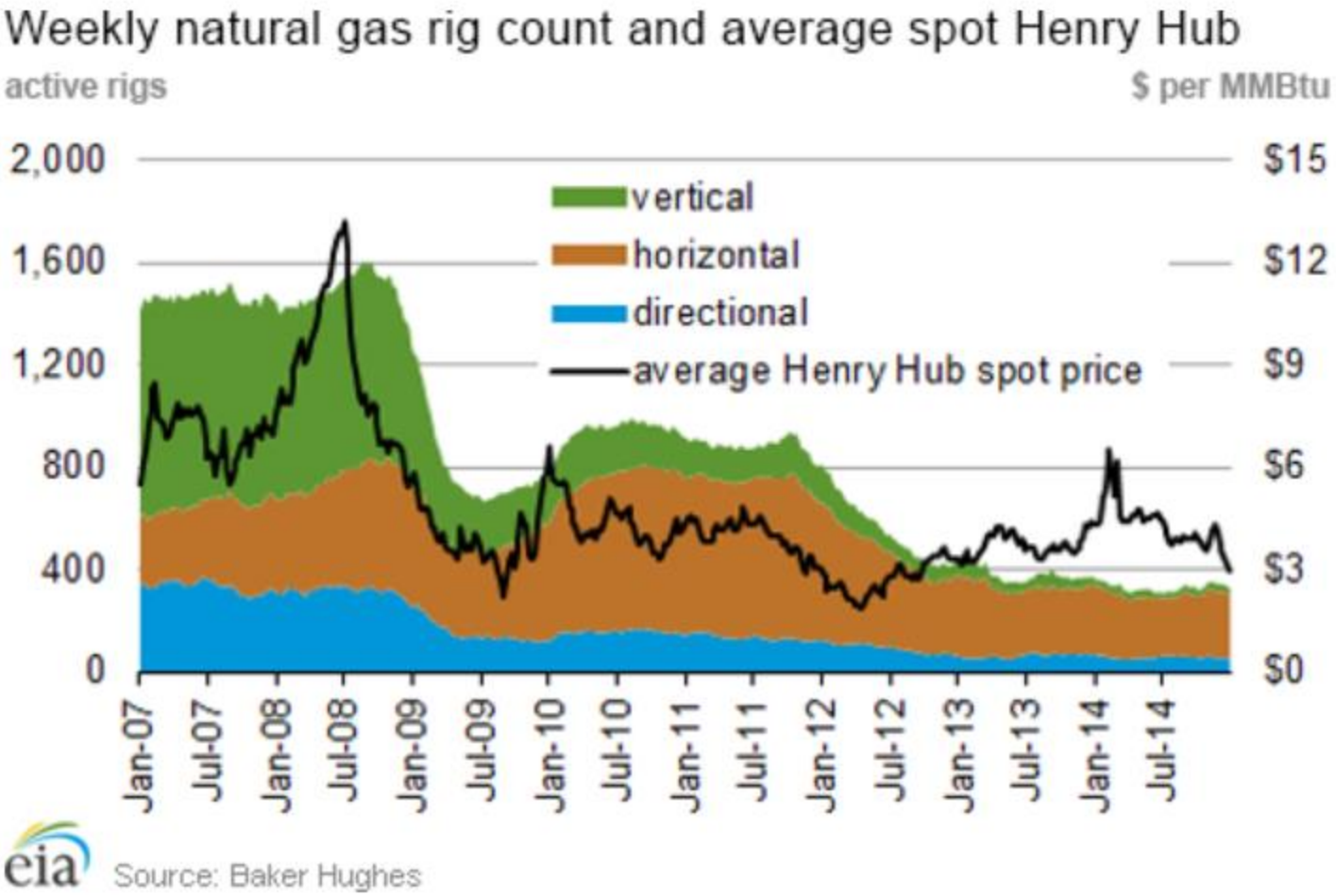

United States Sources of Carbon Dioxide

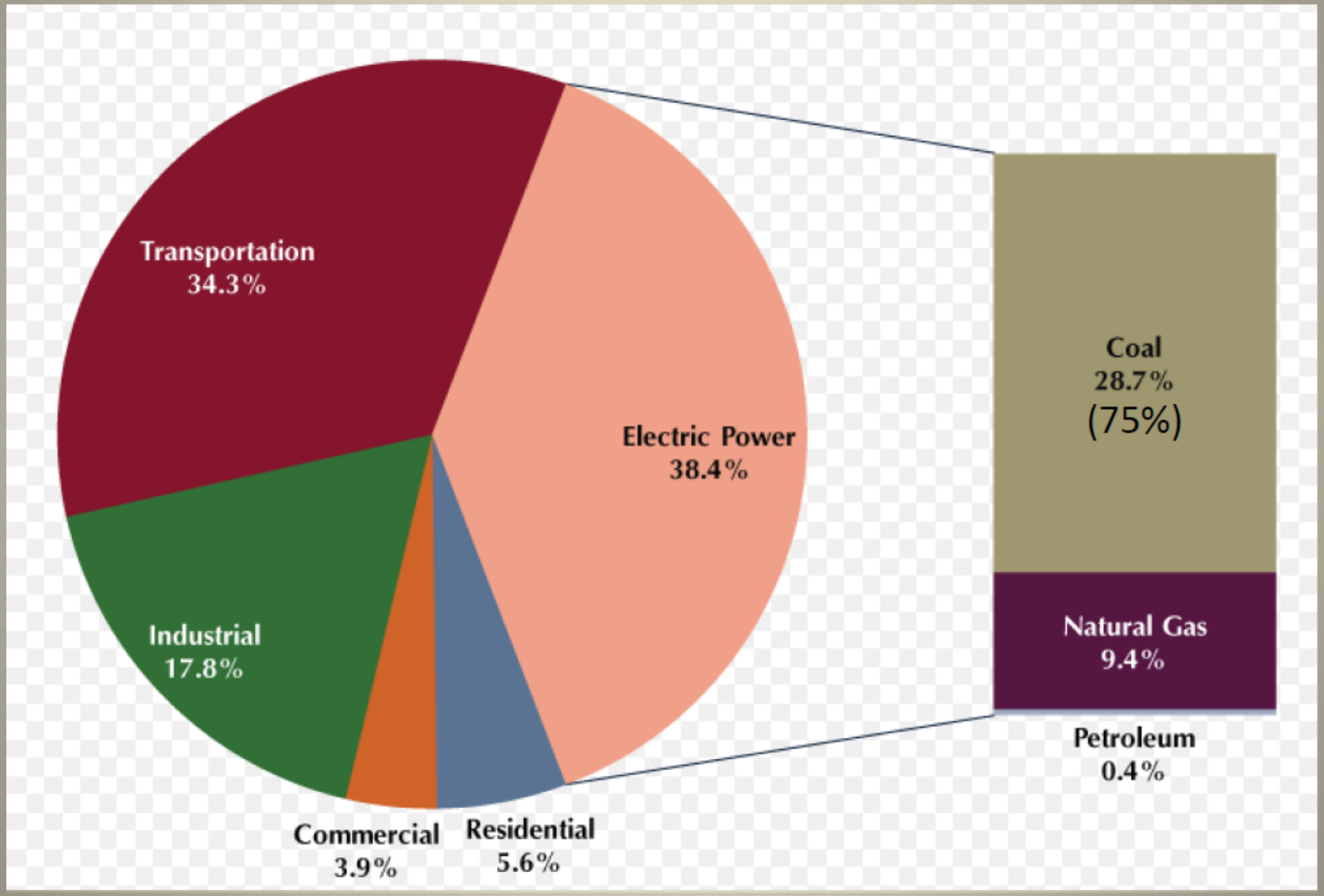

The new technical order

Conventional Reservoirs

1. Porosity dictates reserves
2. Reserves define NAV
3. Highly competitive
4. Defined expl./dev. cycle
5. Small land position req'd.
6. Defined roles for staff
7. Dislocation to surface issues
8. Efficient drilling requires understanding

Unconventional Reservoirs

1. Porosity is poorly defined
2. Cash Flow define NPV
3. Collaborative amongst the companies
4. Expl. is not defined
5. Large land base req'd.
6. Integrated team
7. Surface issues are germane
8. Efficient drilling requires procedure

The Fundamental Question:

How do fluids move through the crust?

- Requires a pathway
- Requires increased Fluid Pressure

Nano-permeability

vs.

Fracture systems

Buoyancy Forces are equal to the density contrast between the generated hydrocarbons and formation water. Generally these are not strong enough to overcome the frictional forces resisting flow (pore entry pressures).

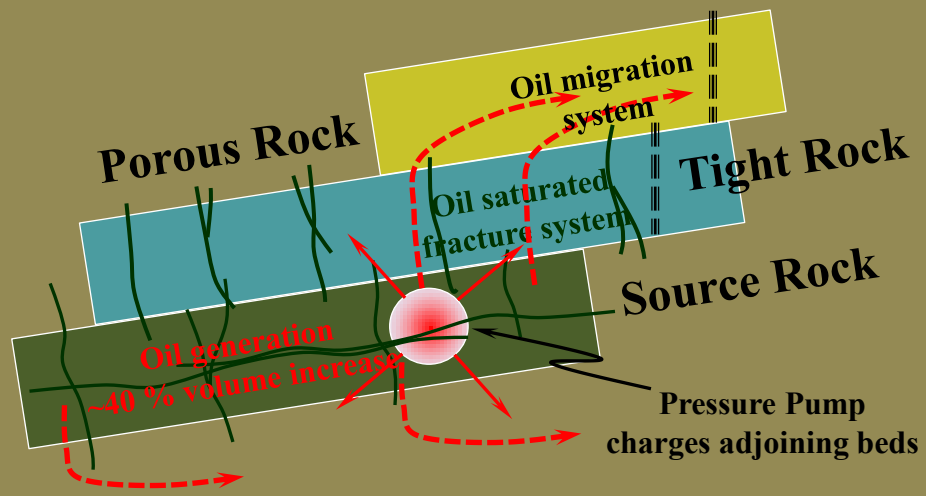

Cardium Horizontal Well Results (2012) Garrington

- ~120 wells
- 88 wells with reported deviation surveys
- 8 wells missed Cardium sandstone by more than 5 metres

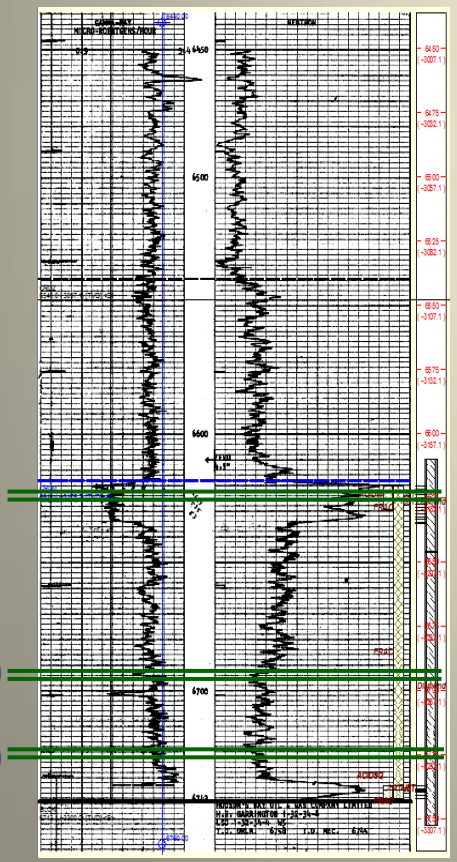

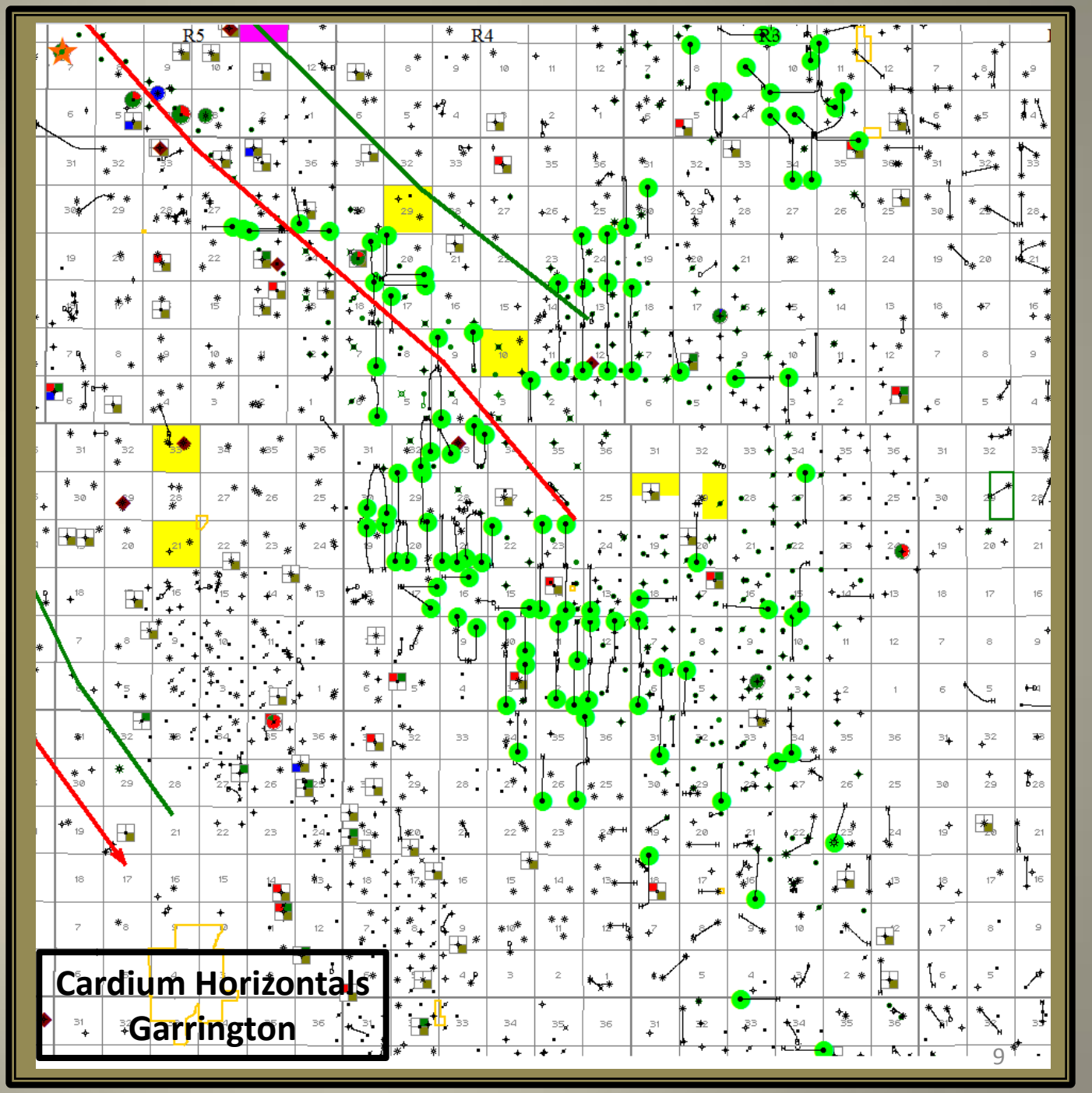

Production Data

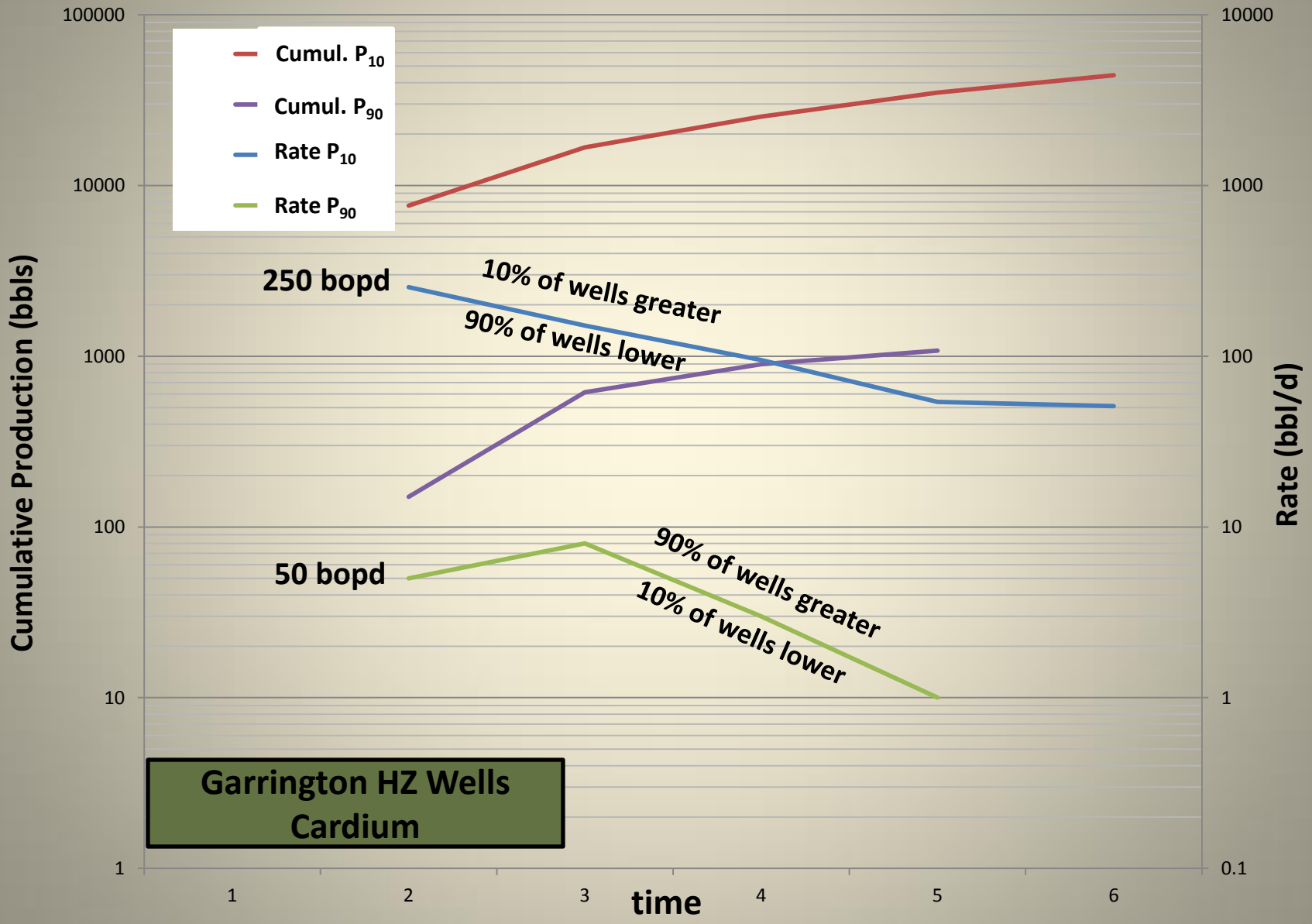

Averaged decline curve

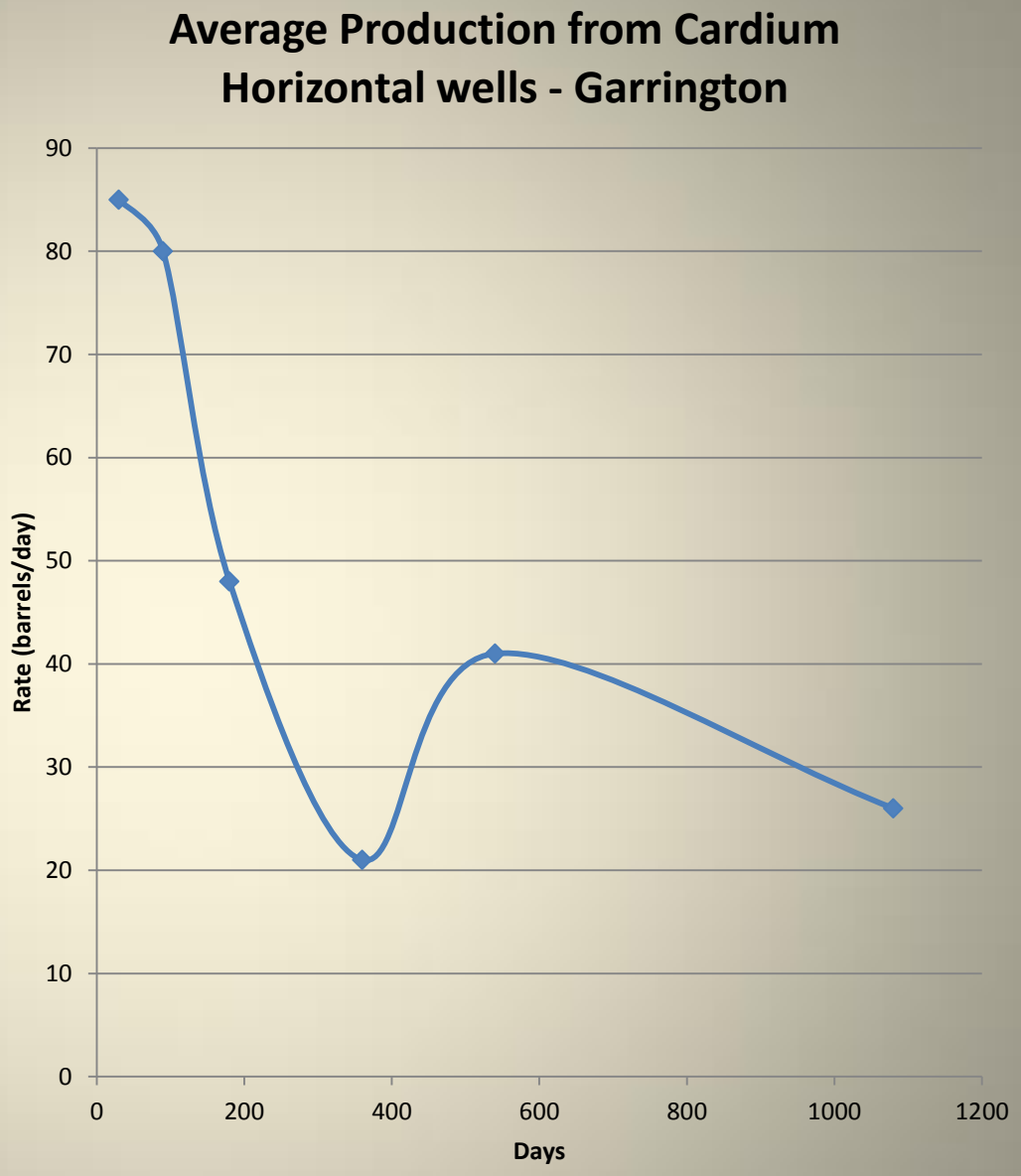

Explanation:

- All horizontal wells in the Cardium from the Garrington Area
- IP(30), IP(90), IP(180), IP(360), IP(540), IP(1080)
- Back Calculate the average rate
- Use Arithmetic Average

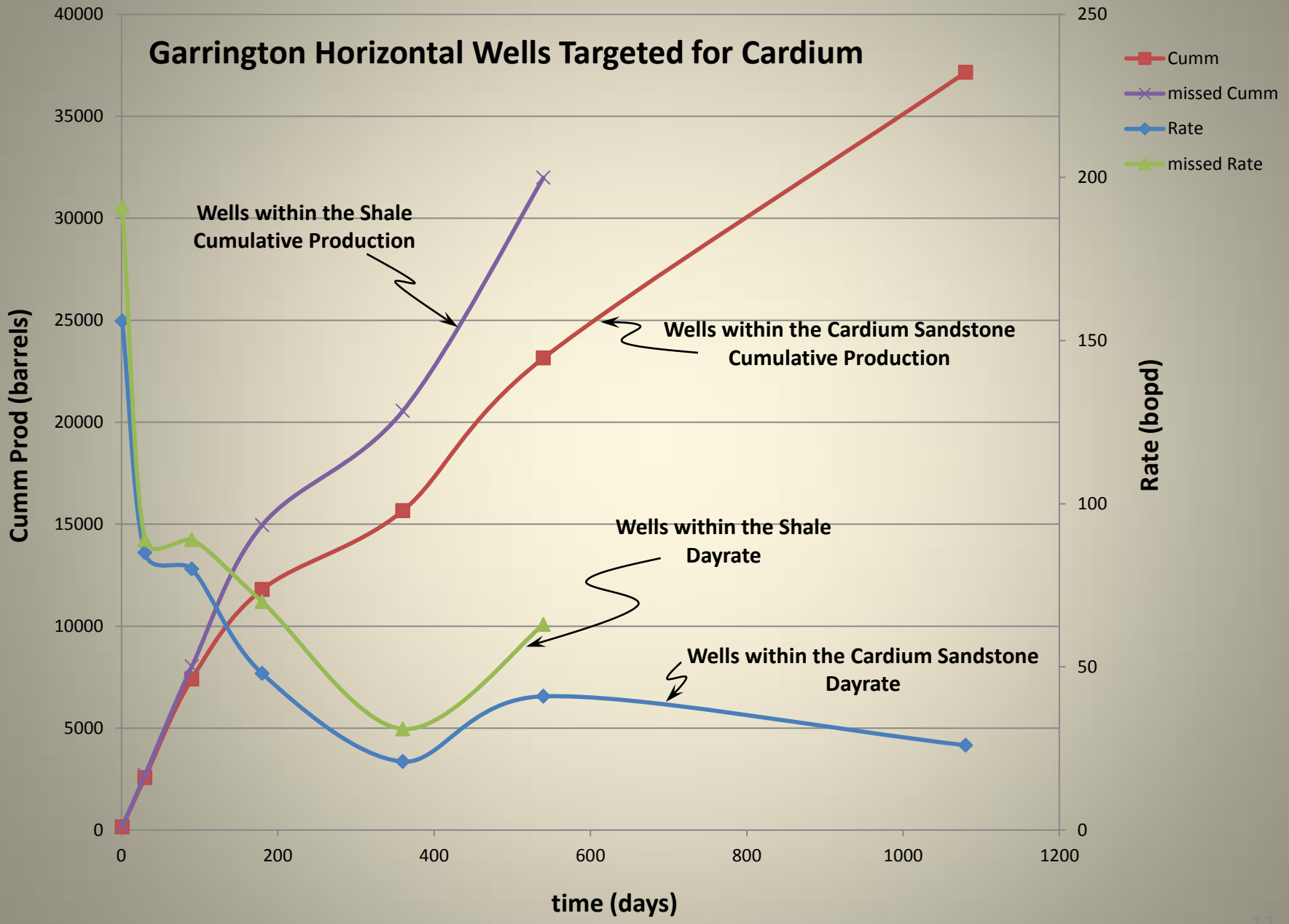
Garrington Horizontal Wells Targeted for Cardium
Cumm Prod (barrels)
Rate (bopd)
time (days)
Cumm
missed Cumm
Rate
missed Rate
Wells within the Shale Cumulative Production
Wells within the Cardium Sandstone Cumulative Production
Wells within the Shale Dayrate
Wells within the Cardium Sandstone Dayrate
40000
35000
30000
25000
20000
15000
10000
5000
0
250
200
150
100
50
0
0
200
400
600
800
1000
1200

Linear Transport Laws

Ohms Law

$$I = \frac{V}{R}$$

Darcy's Law

$$Q = \frac{-kA}{\mu}\frac{(P_b - P_a)}{L}$$

Linear Transport Laws

Ohms Law

$$I = \frac{V}{R}$$

$$\text{Flow} = \frac{\text{Driving Force}}{\text{Friction}}$$

Darcy's Law

Friction

Driving Force

$$Q = \frac{-kA}{\mu}\frac{(P_b - P_a)}{L}$$

Flow

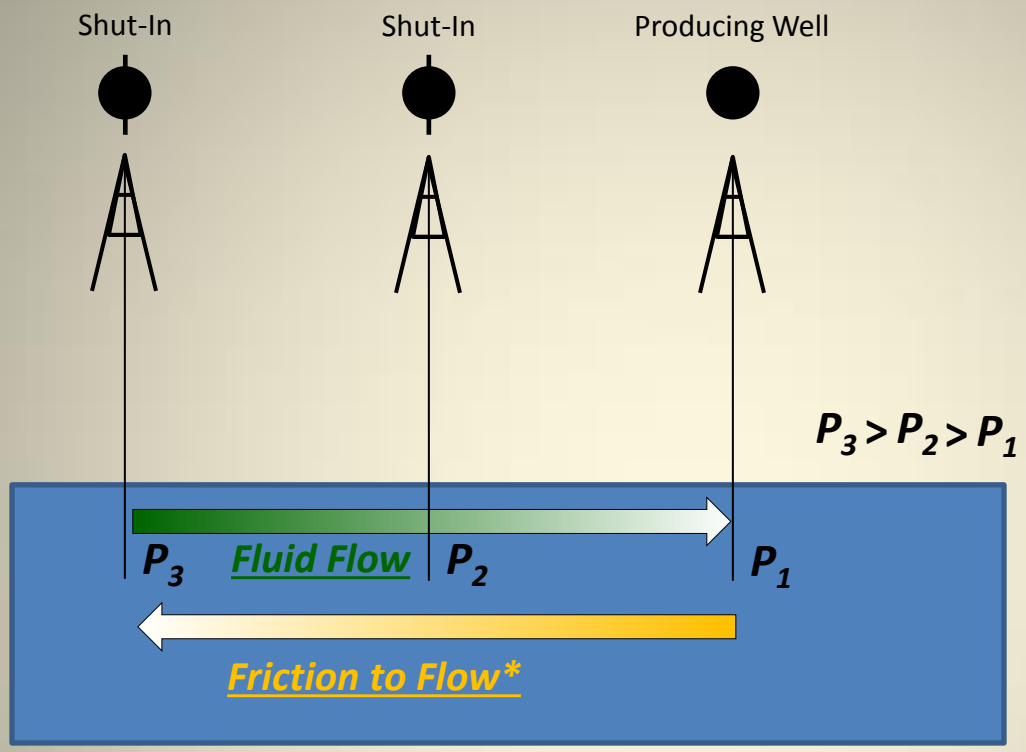

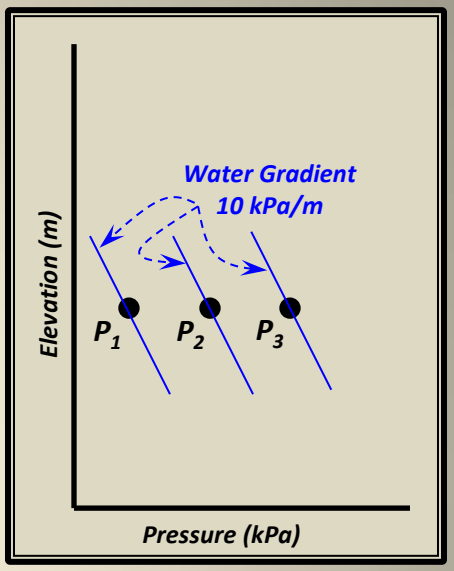

* System will not equilibrate to common water gradient due to friction

$$\vec{Q} = \frac{-\vec{k}A}{\mu}\frac{(P_b - P_a)}{L}$$

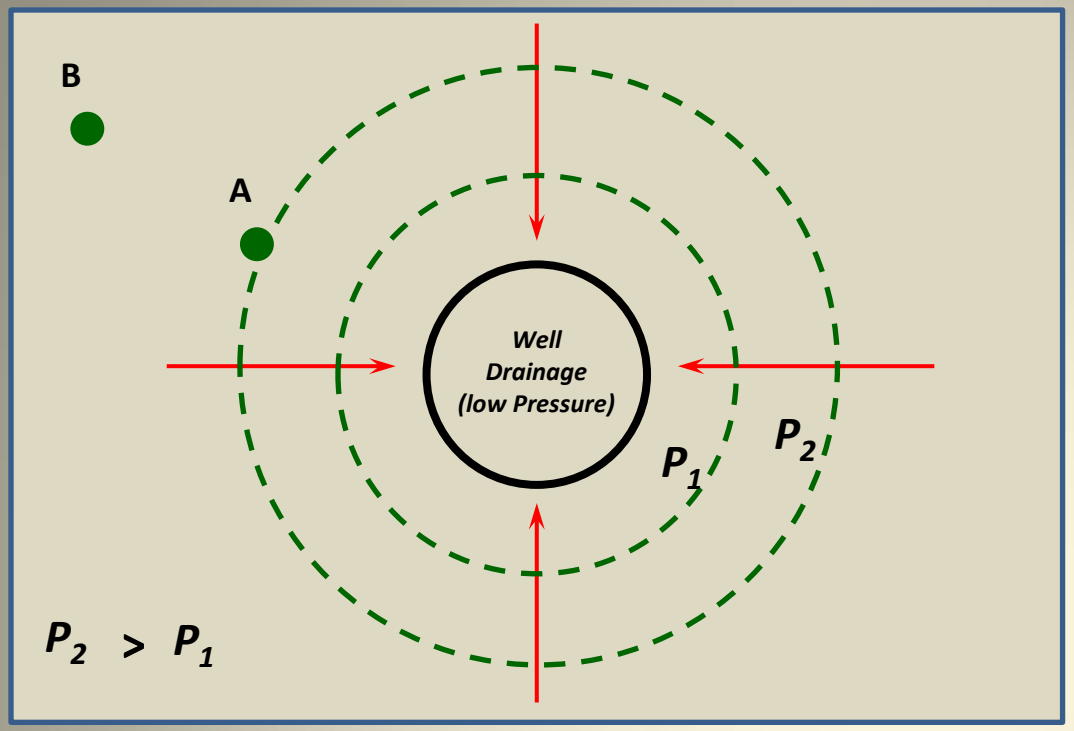

Flow in a Homogeneous Isotropic Reservoir

Radial Flow:

- Particle A will reach the well bore before particle B
- Pressure Front radiates from the well bore as a function of the radius of the well bore
- Drainage is along straight lines towards the well bore

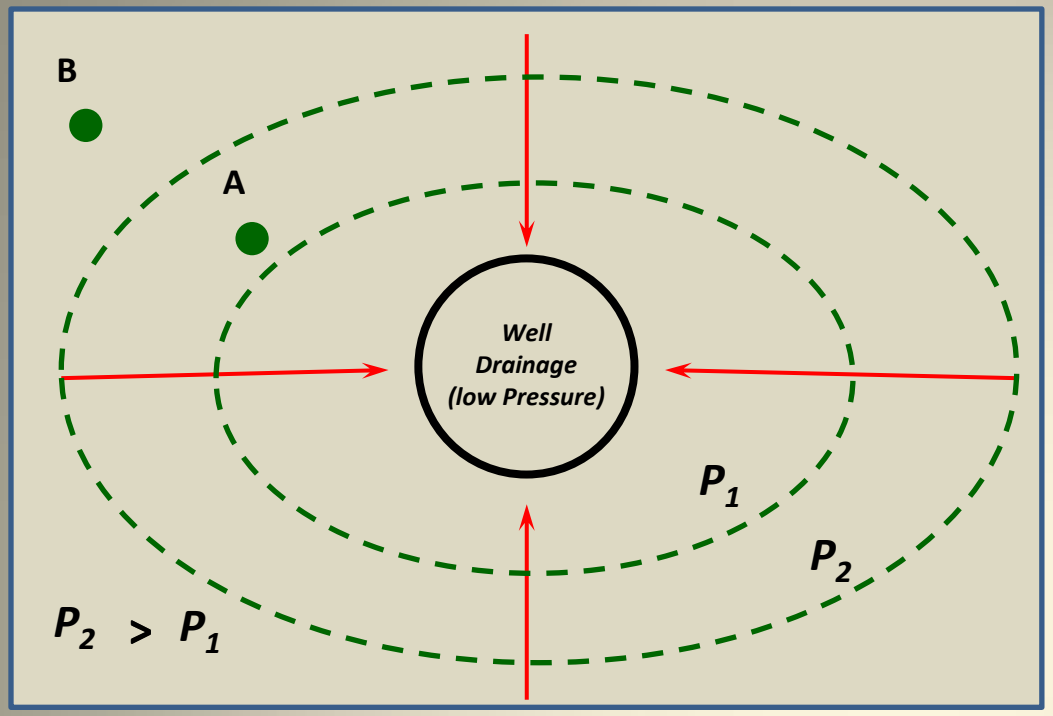

Flow in a Two Porosity (permeability) system

Elliptical Flow:

- Particle A will reach the well bore before particle B
- Pressure Front radiates from the well bore as a function of the radius of the well bore and the difference in permeability between k_{hmax} and k_{hmin}
- Drainage is along lines perpendicular to the pressure front creating smooth curve drainage trajectory to the well bore

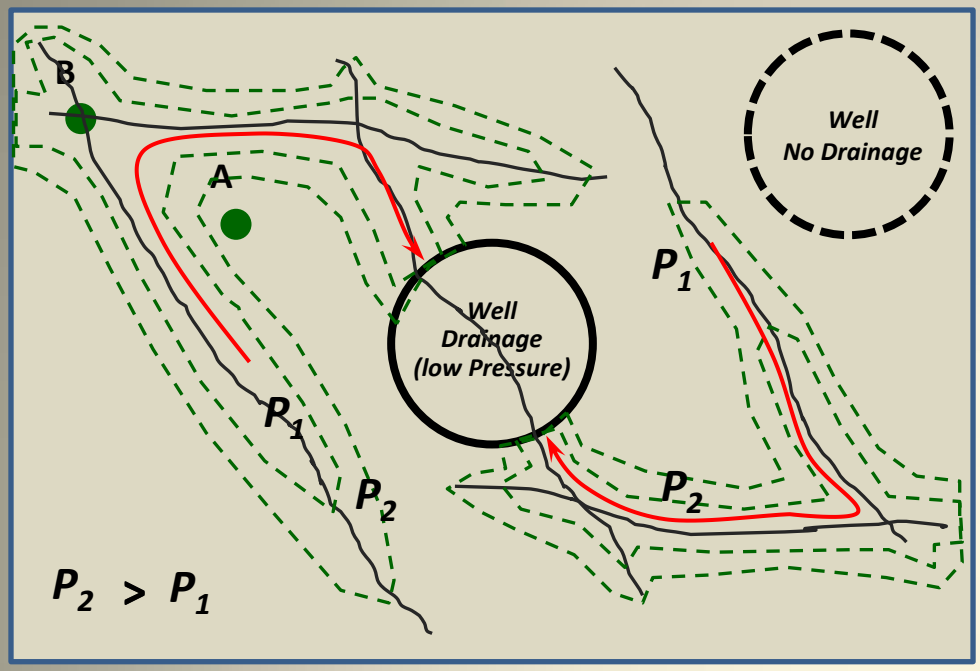

Flow along Fractures

Fracture Flow:

- Particle B will reach the well bore before particle A
- Pressure Front radiates from the fractures and is a complex relationship between the matrix permeability and the fracture permeability
- Drainage is along tortuous paths in the reservoir and distance is difficult to determine
- A well not connected to fractures likely will not have flow

How does a Shale Reservoir work?

Fractured Reservoir Model

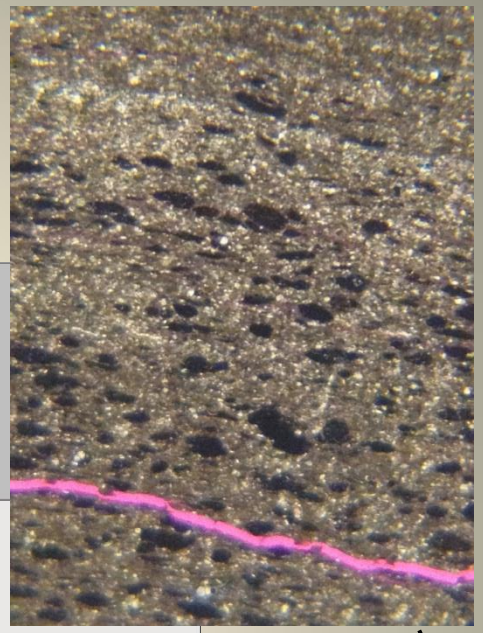

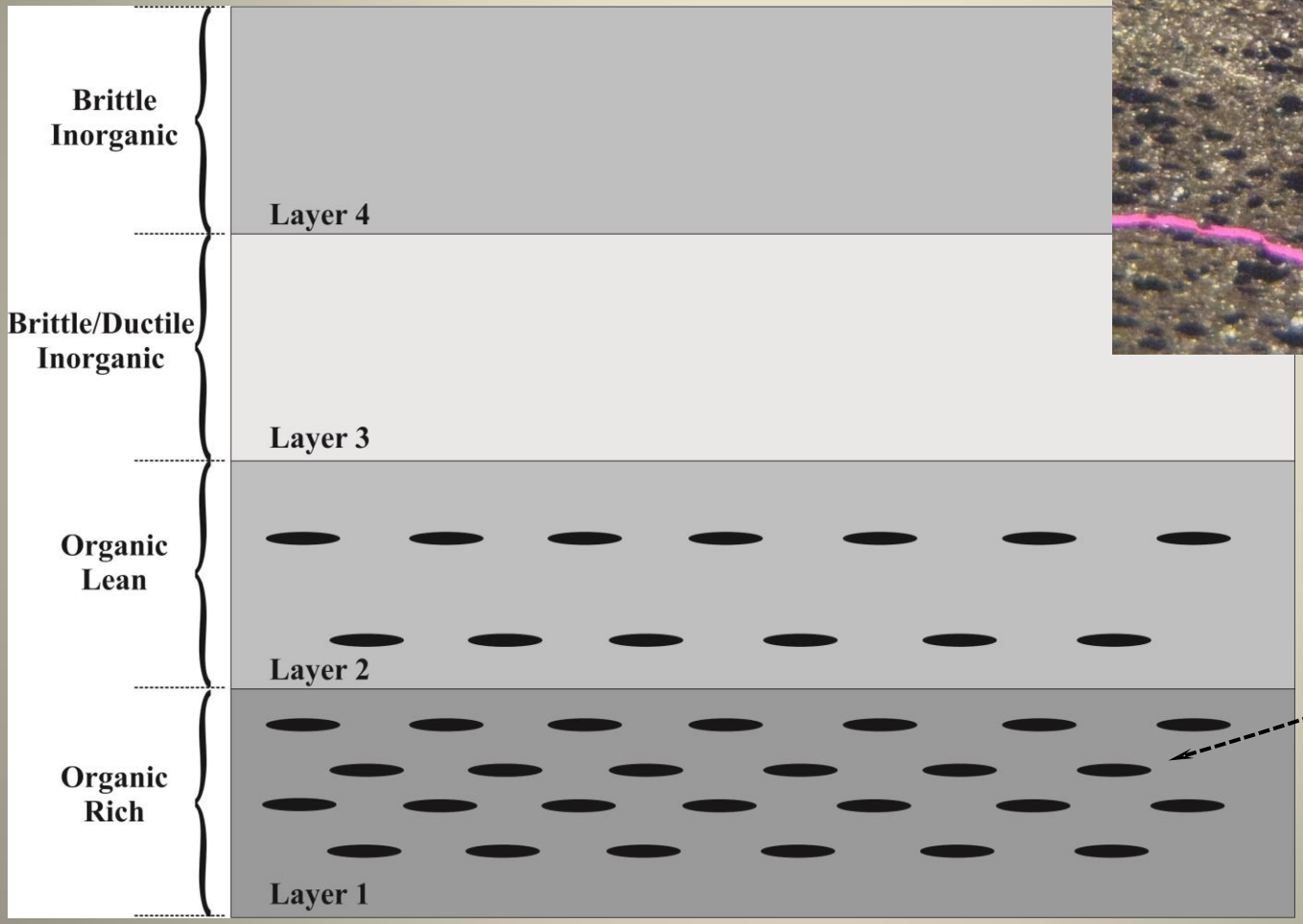

Fractured Reservoir Model

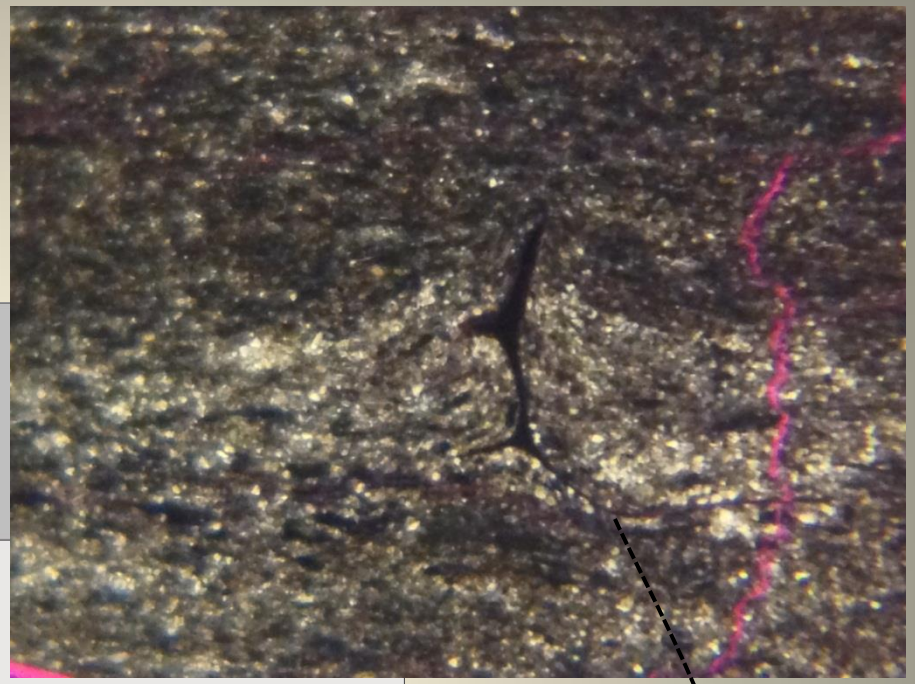

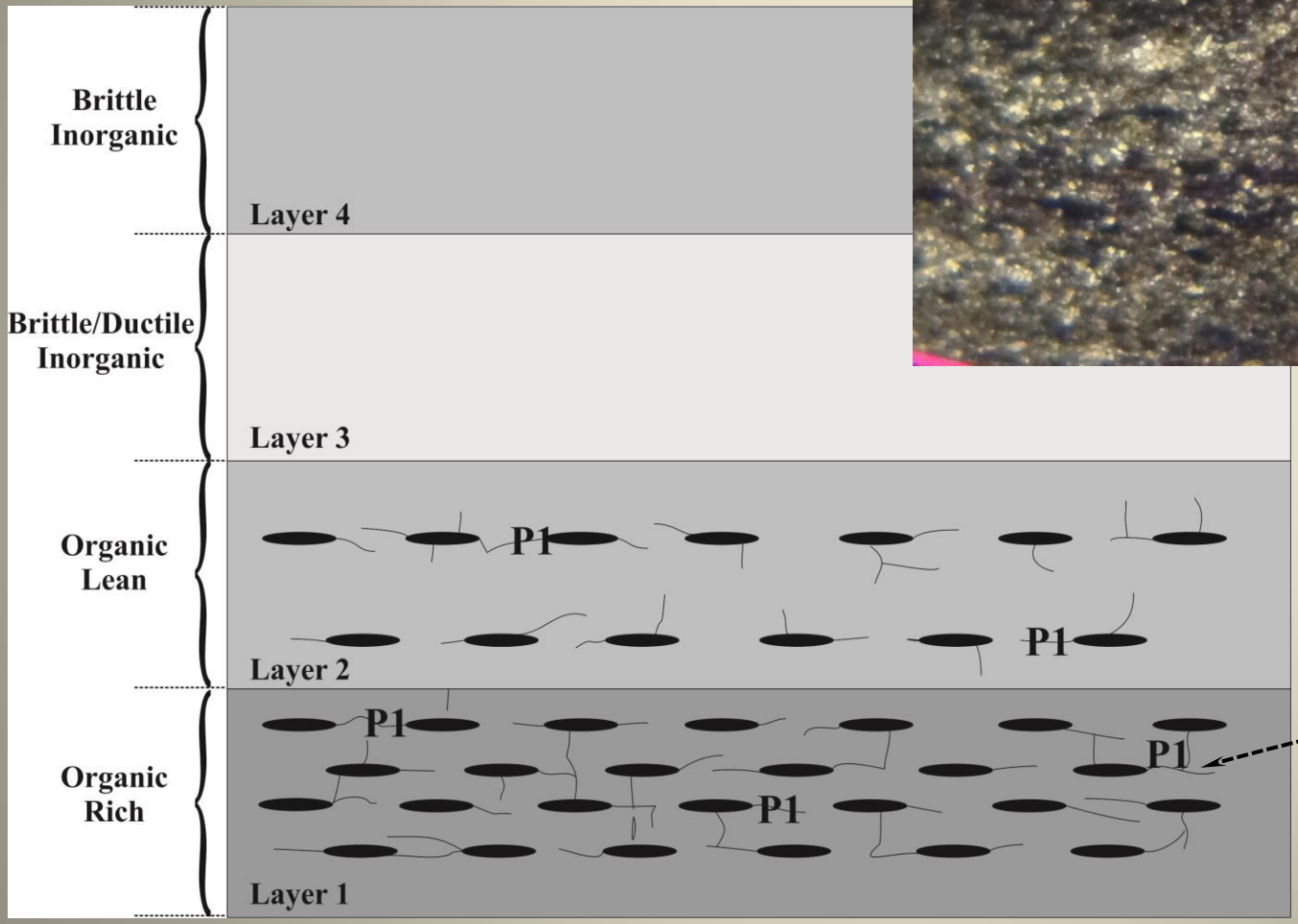

Hydrocarbon generation and micro-fracture development

Second White Specks – Highwood River

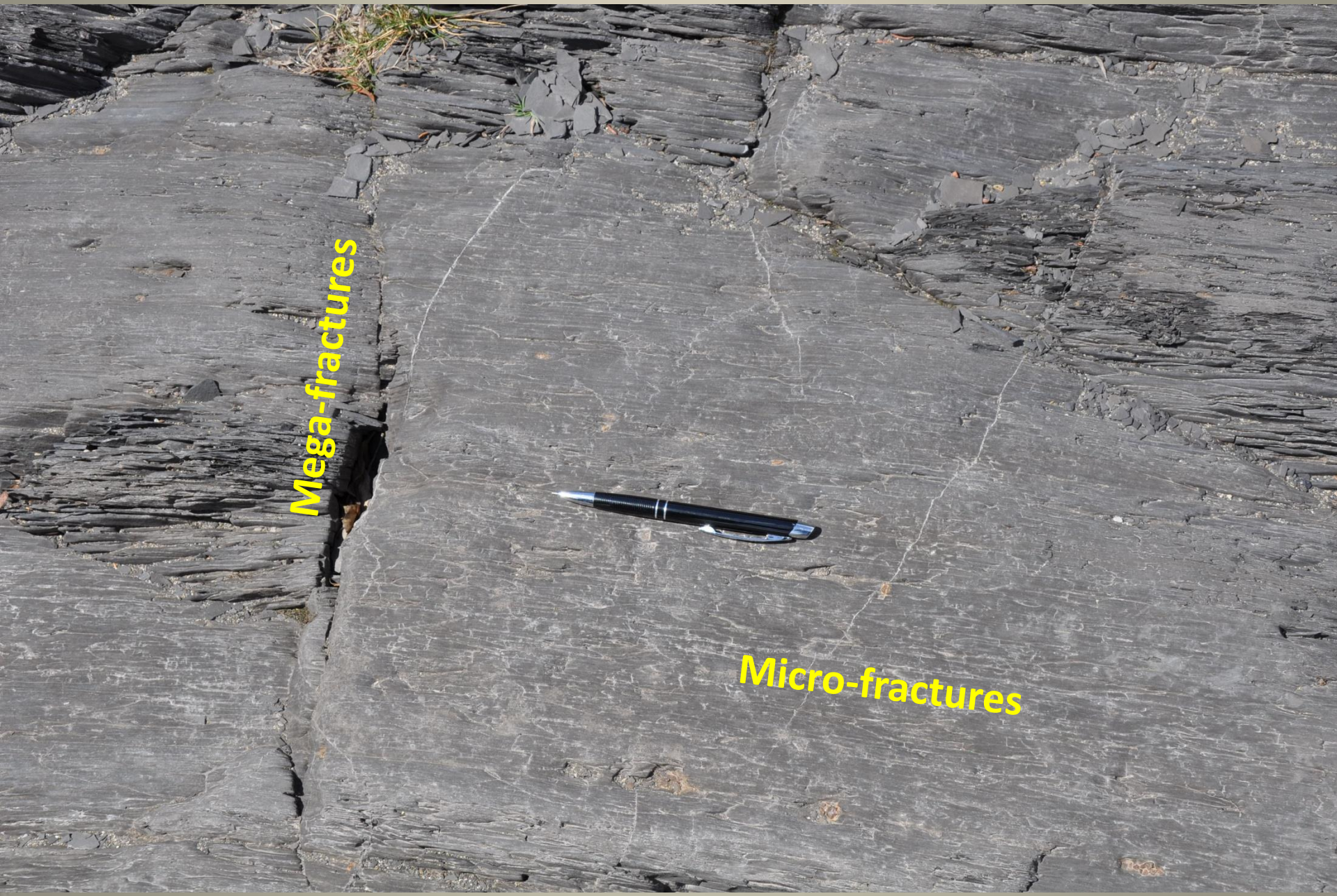

Fractured Reservoir Model

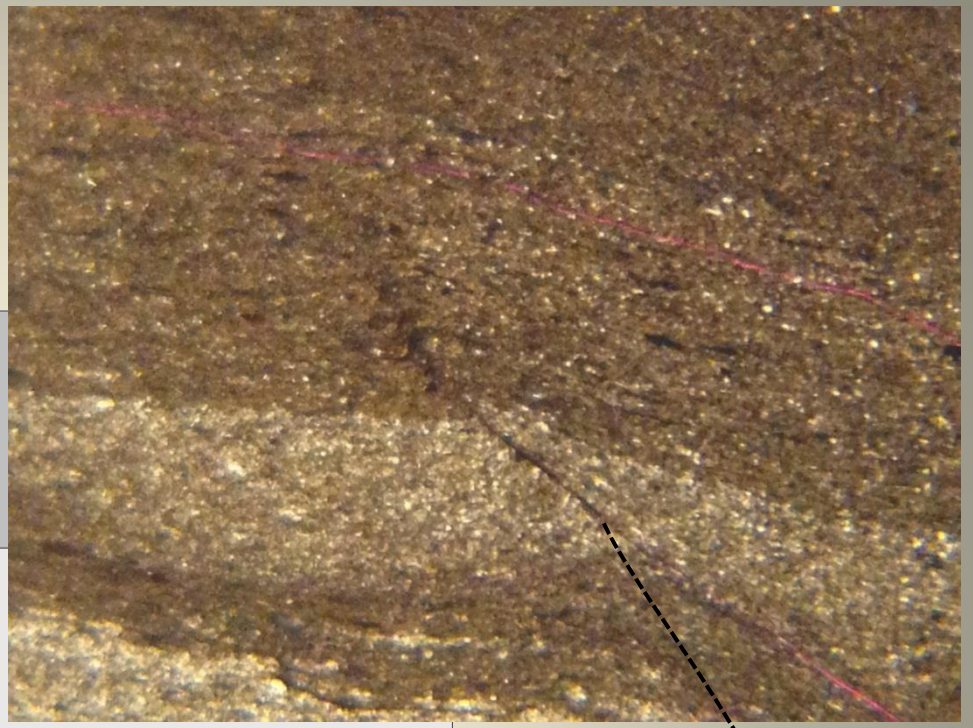

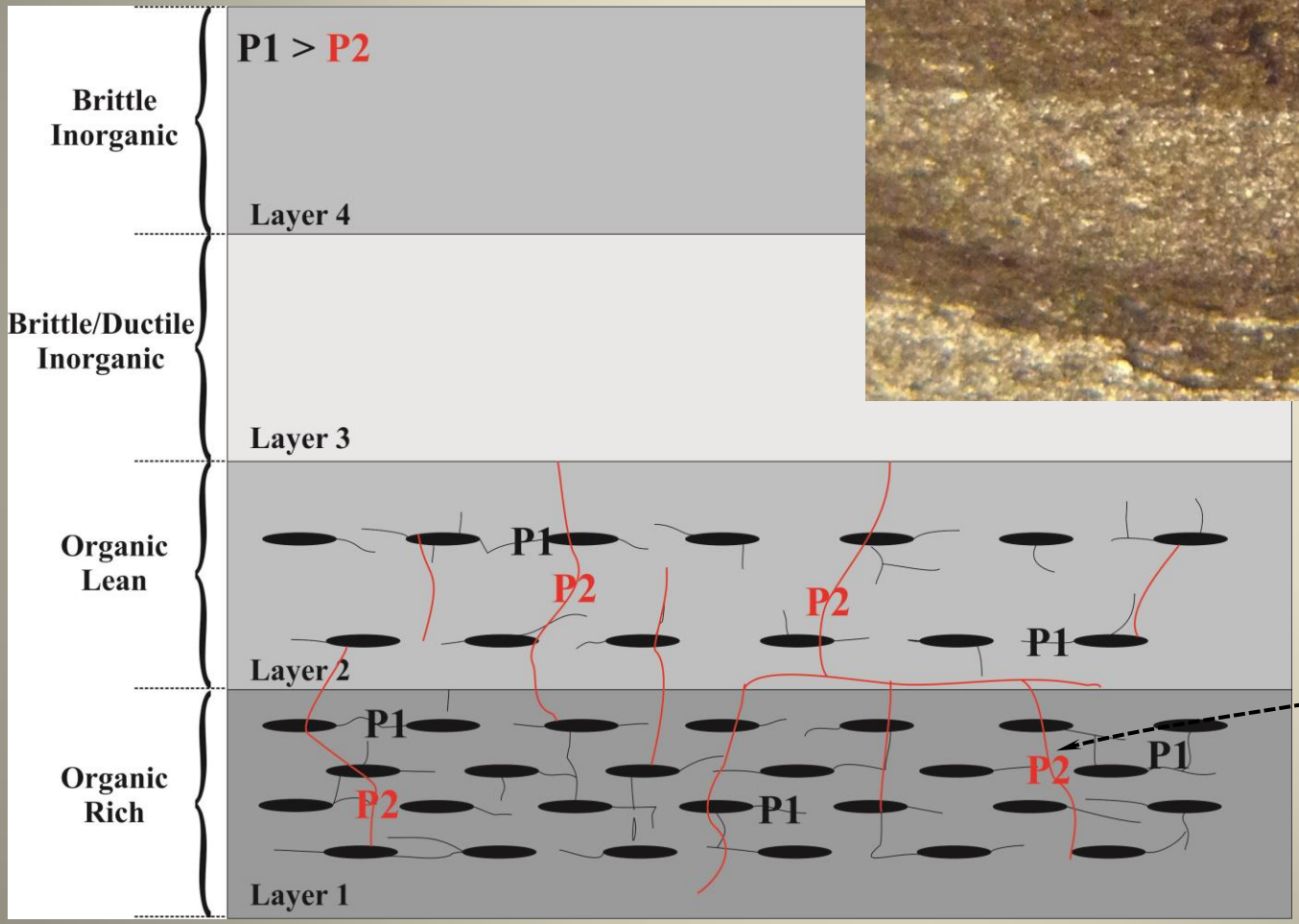

Continued hydrocarbon generation and fluid migration

Second White Specks (Upper Cretaceous)



Fractured Reservoir Model

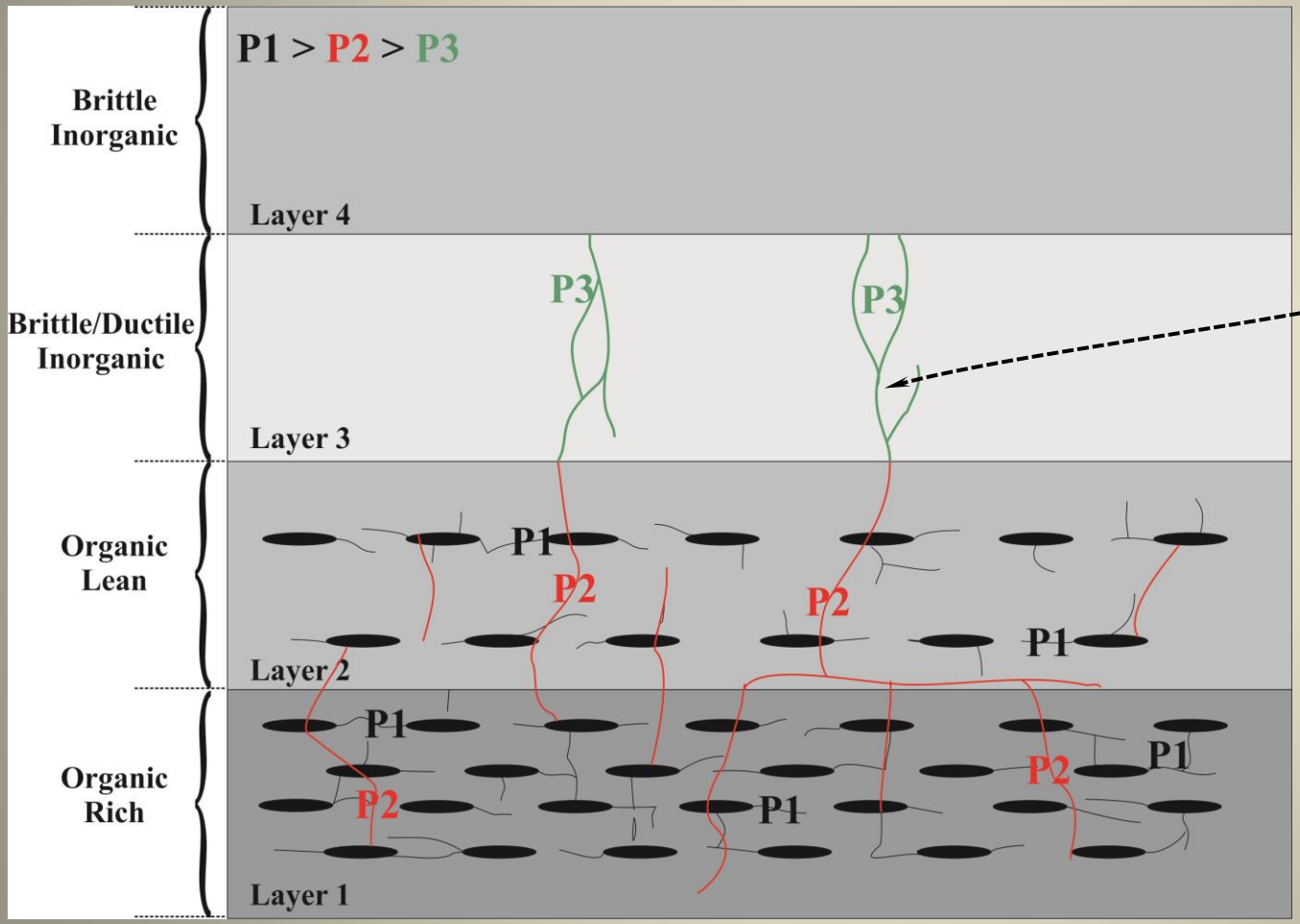

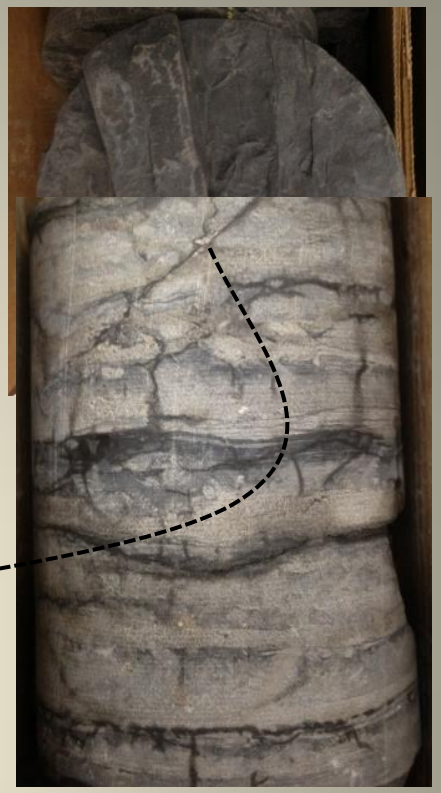

Continued hydrocarbon generation and fluid migration
Vertical migration into meso-fractures

Fractured Reservoir Model





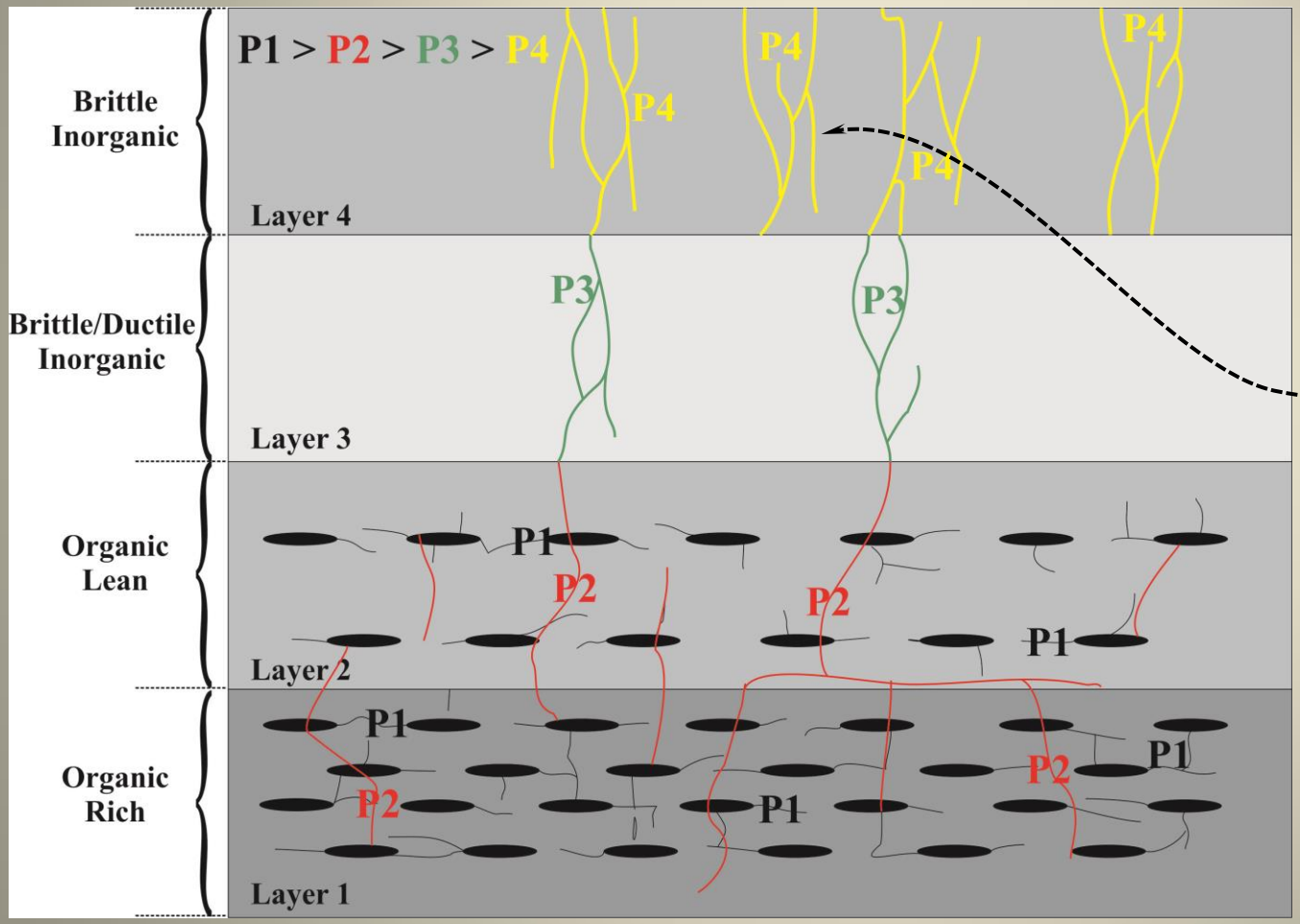

Continued hydrocarbon generation and fluid migration
More Brittle Zones form macro-fractures

Second White Specks – Highwood River

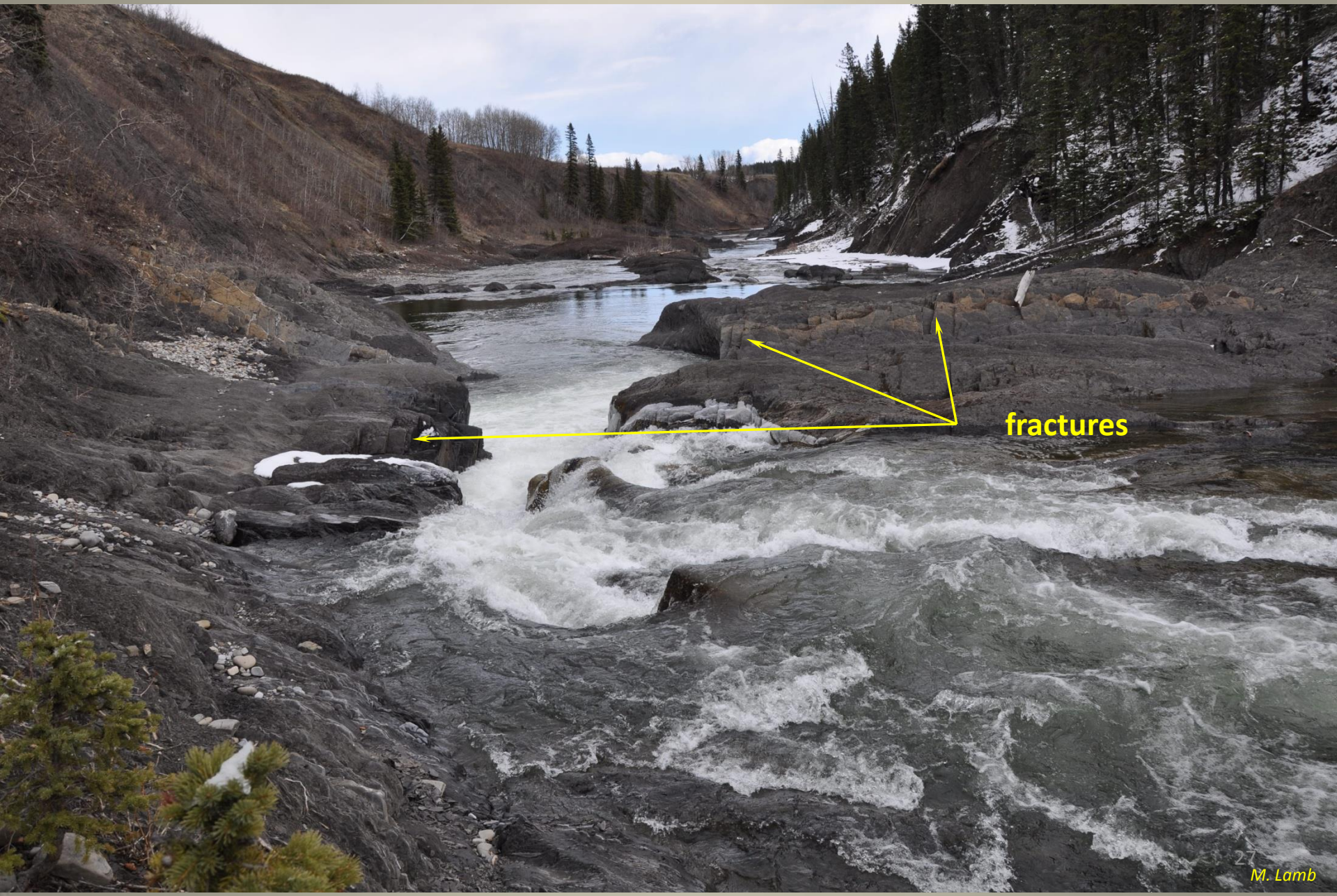

M. Lamb

Fractured Reservoir Model

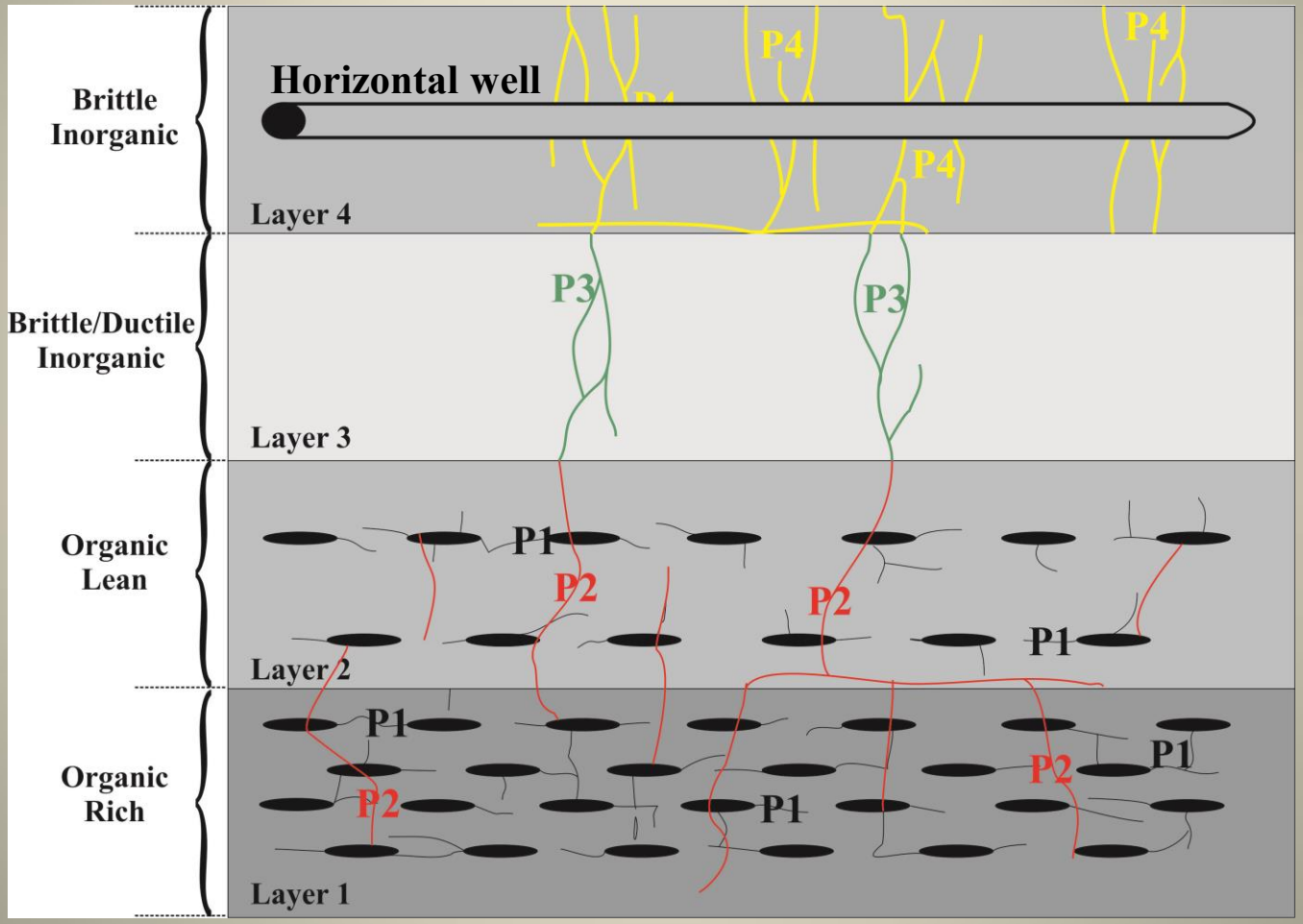

Fractured Reservoir Model

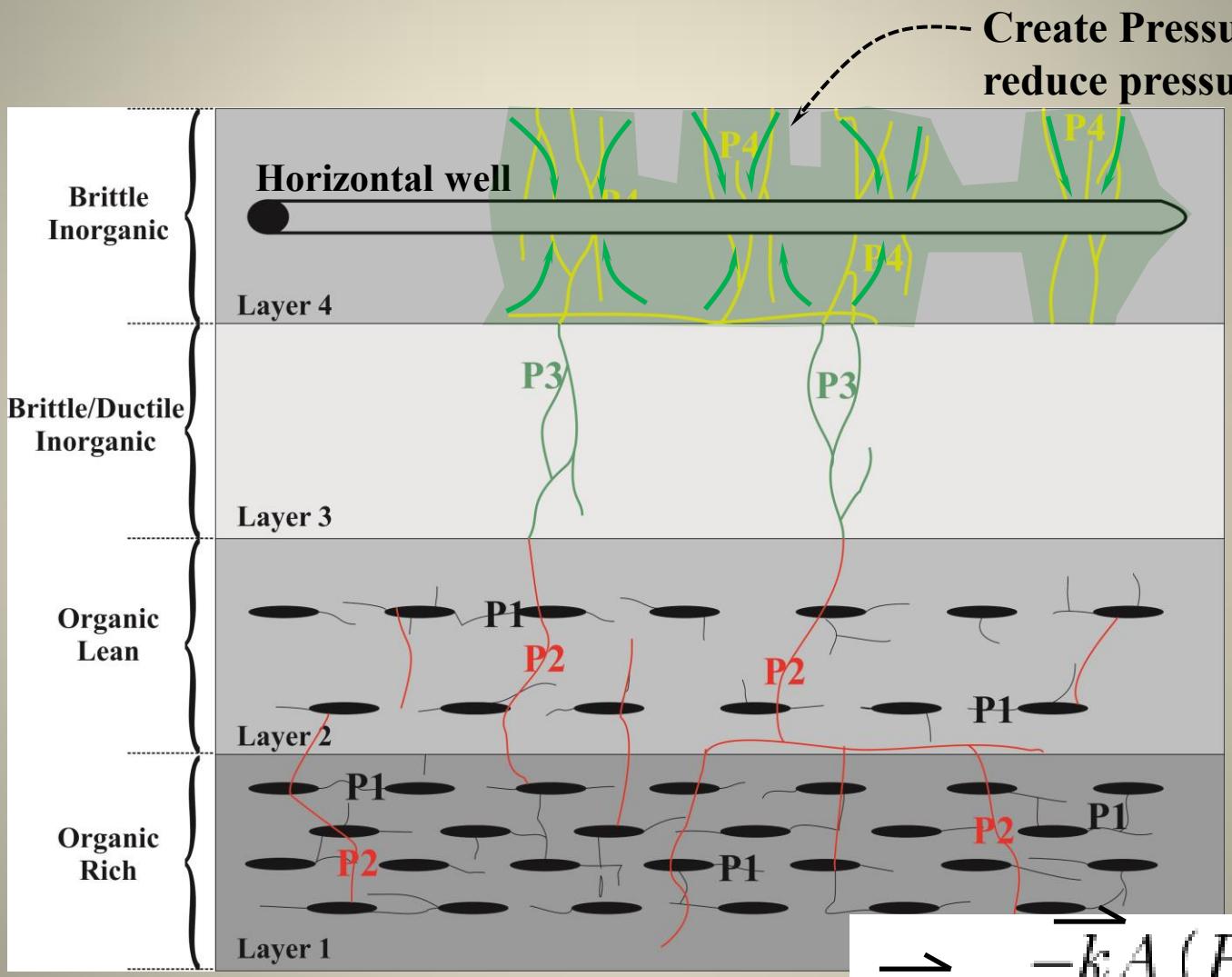

$$\vec{Q} = \frac{-kA}{\mu}\frac{(P_b - P_a)}{L}$$

Fractured Reservoir Model

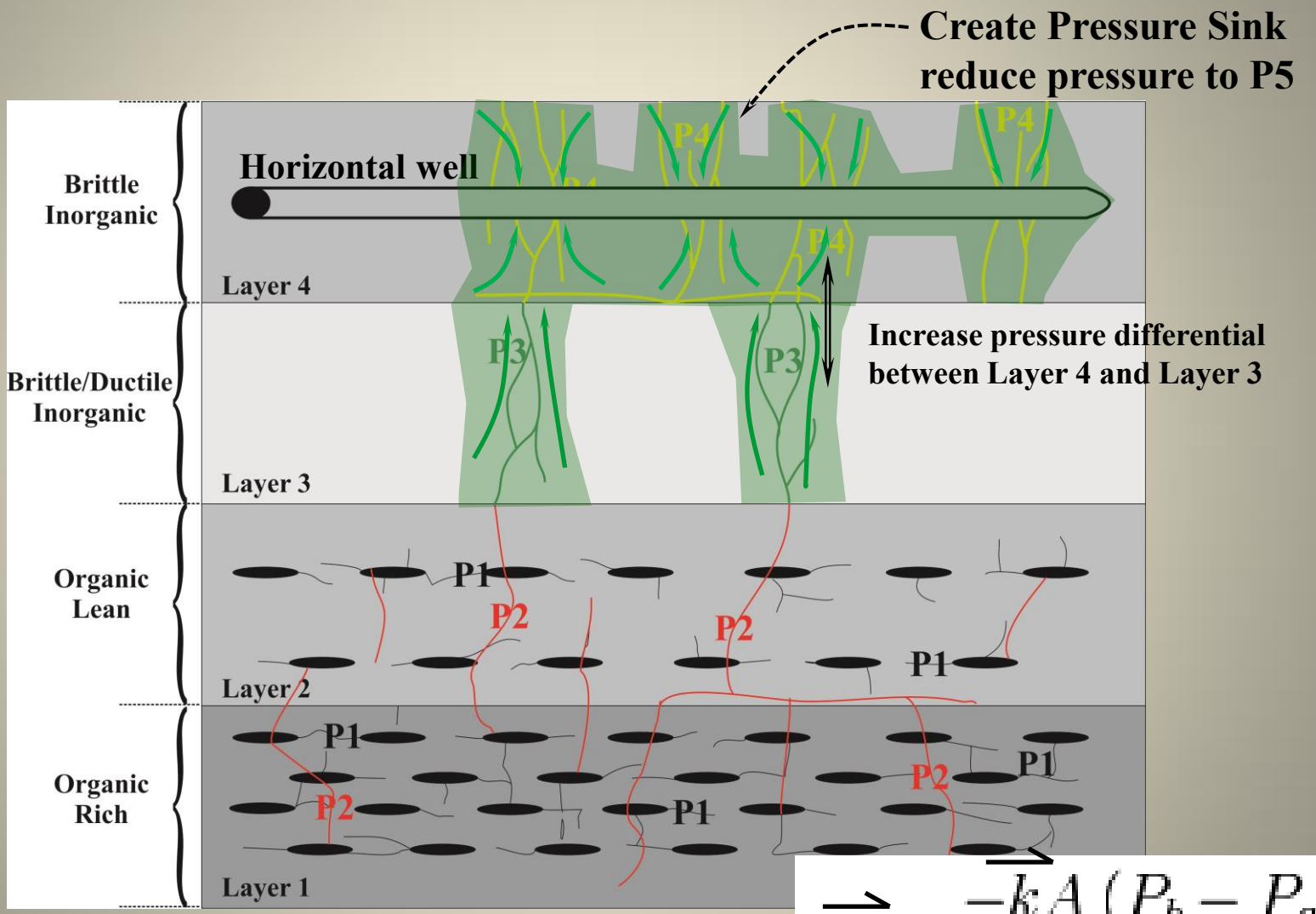

$$\vec{Q} = \frac{-kA}{\mu}\frac{(P_b - P_a)}{L}$$

Fractured Reservoir Model

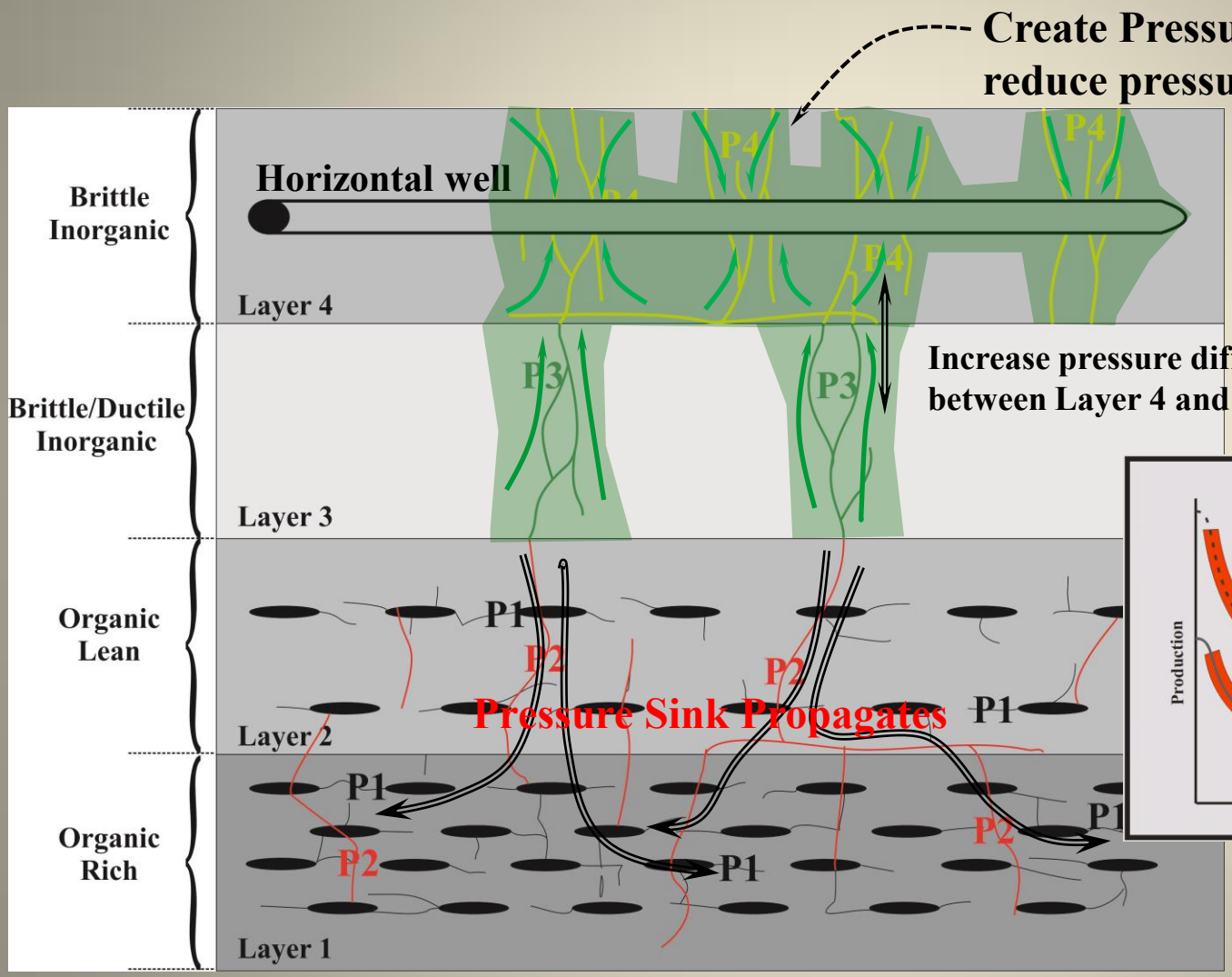

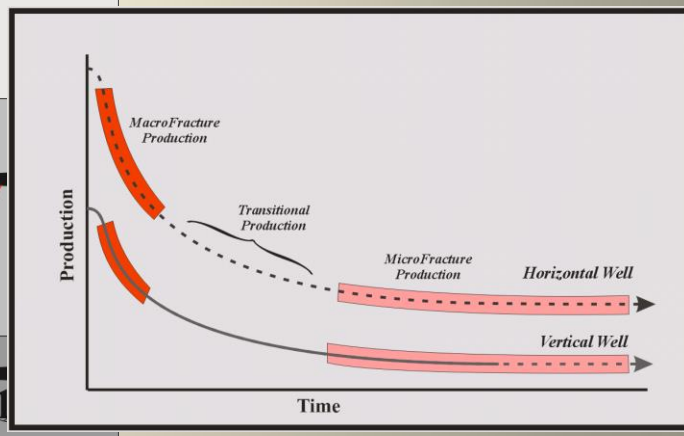

$$\vec{Q} = \frac{-\vec{k}A}{\mu}\frac{(P_b - P_a)}{L}$$

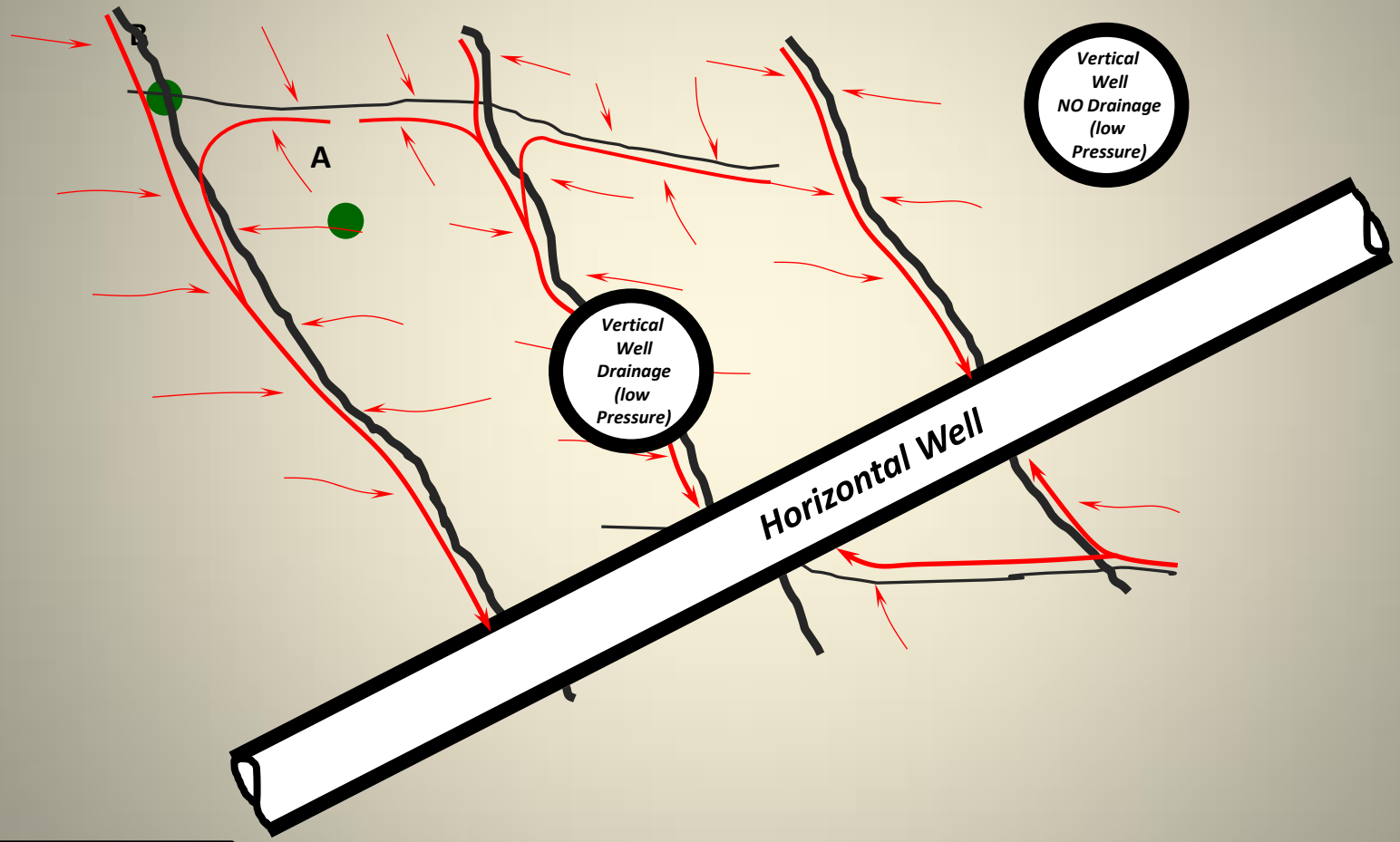

Conceptual View of a Fractured Reservoir

Plan View

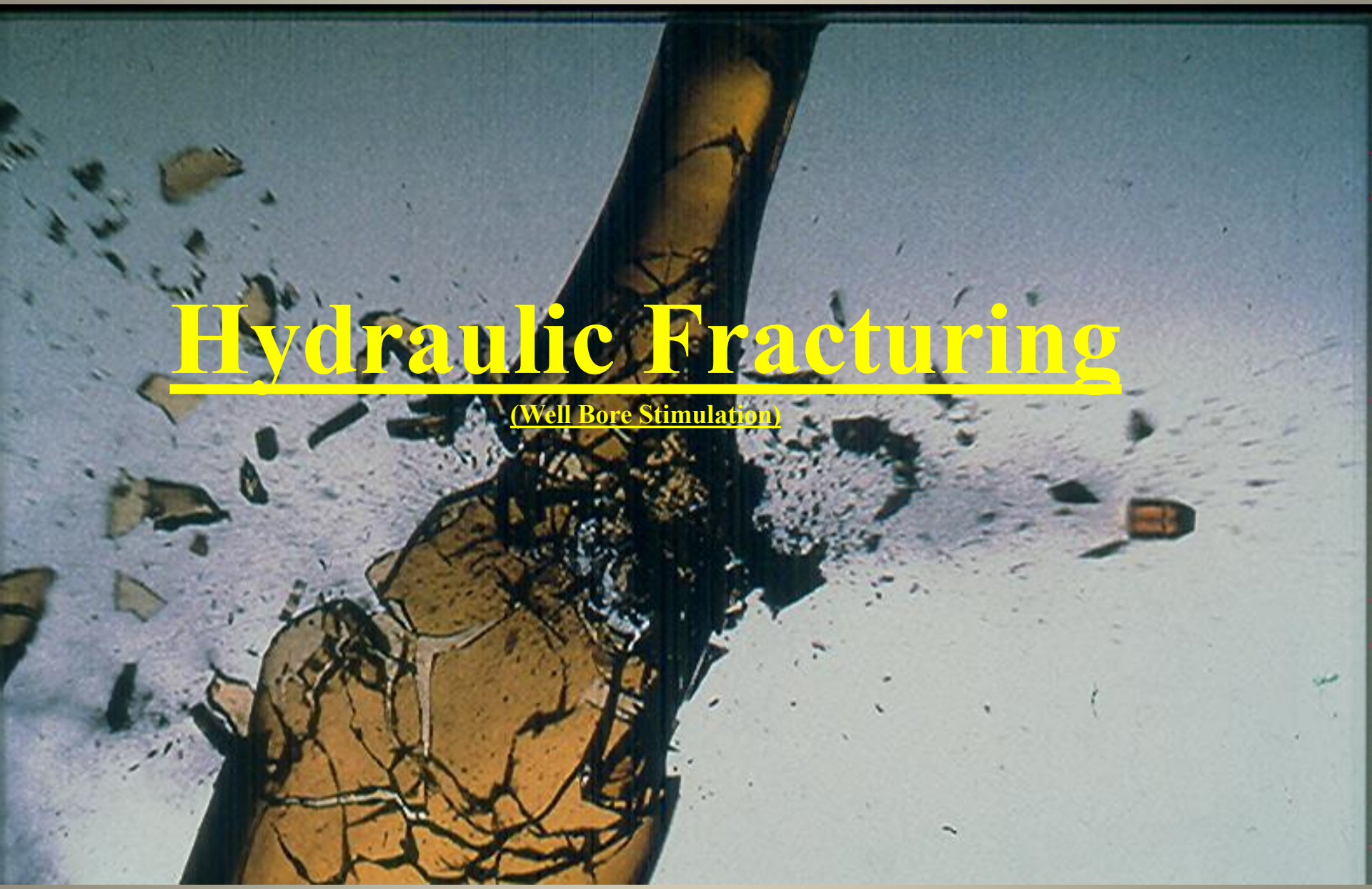

Hydraulic Fracturing

(Well Bore Stimulation)

The Role of Proppant



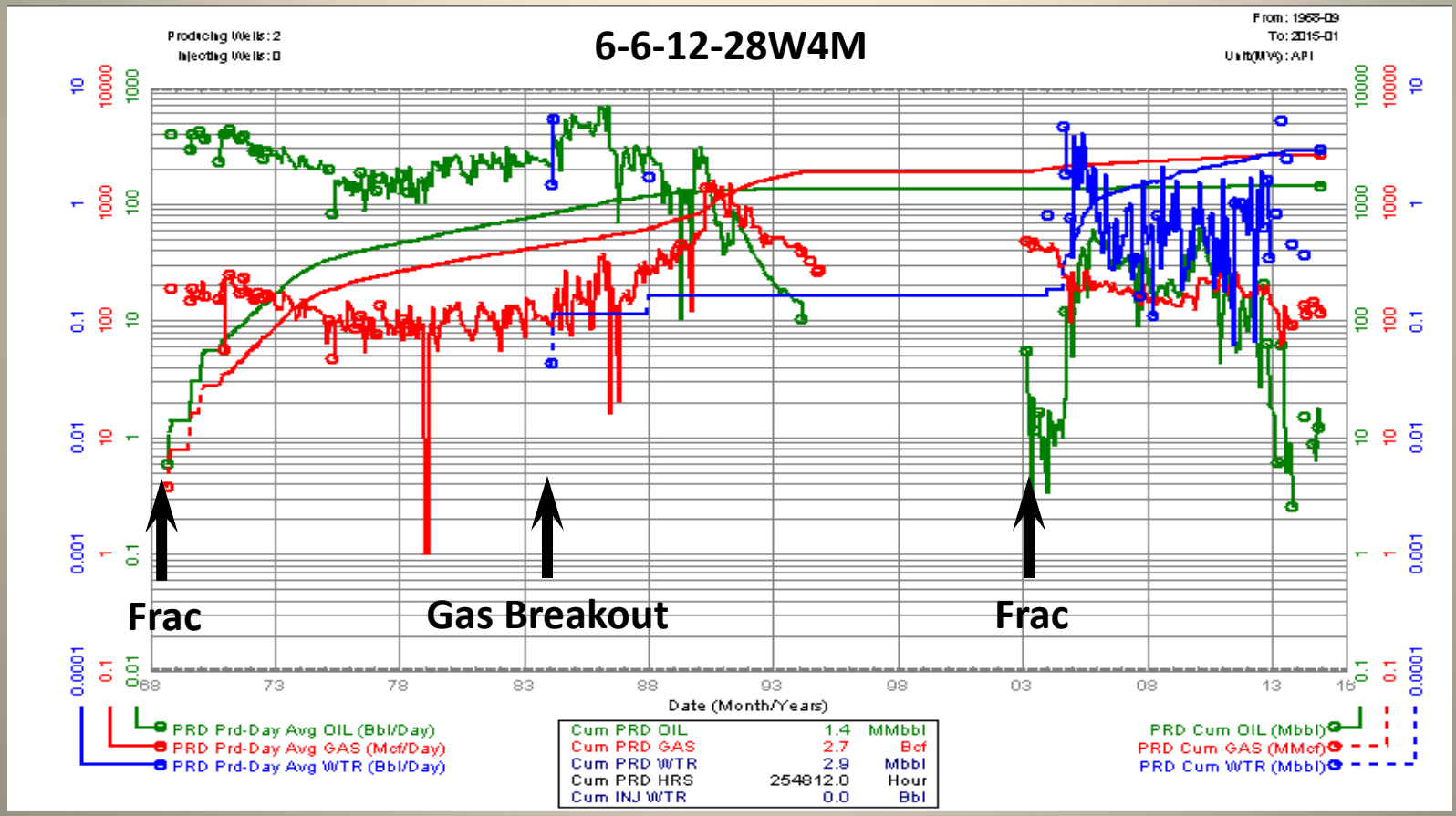

Issues

1. Ground water protection
2. Water use
3. Airborne Emissions
4. Use of a variety of industrial chemicals
5. Industrial Impact
   - Site fluid storage and containment
   - Trucking
   - Noise
6. Induced Seismicity

Problems

- Pavillion, WY, 2010 – EPA detect petroleum in drinking water (liability not determined)
- Leroy Twp, PN, 2011 – Operational failure led to surface spill
- Mamm Ck, CO, 2006-2011 – frac fluid migrated to ground water – faulty design
- Grande Prairie, AB, 2011 – frac fluid contamination of ground water – faulty operation
- Blackpool, UK, - earthquake linked to frac operation
- Horn River, BC – earthquake linked to Frac operation

Induced seismicity – Blackpool, UK

- Cuadrilla Resources conducts multistage hydraulic frac: April, 2011
- Induced a series of microseismic events with the largest at M=2.3
- UK Government responds to public complaint and puts Moratorium on hydraulic fracturing
- Moratorium lifted in 2014
- Lancashire has 40,000 signatures asking to reject Cuadrilla's application to hydraulically fracture stimulate its well
- A motion to call a moratorium on "Fracking" was rejected in the House of Commons 308 votes to 52 votes

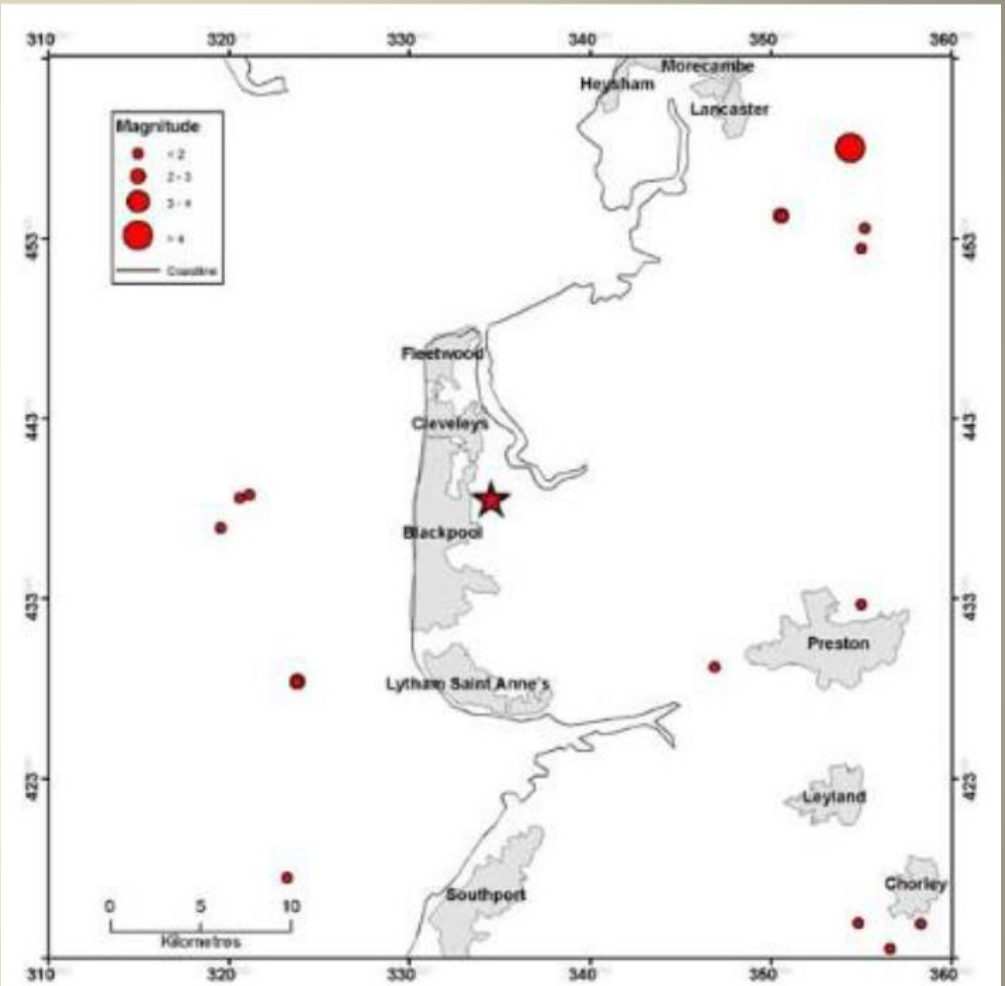

Figure 5. Seismic activity in a 50 km square centred on the epicentre of the magnitude 2.3 earthquake.

Situation in the United Kingdom

(a cautionary tale)

35% of all energy consumed in the UK is from Natural Gas

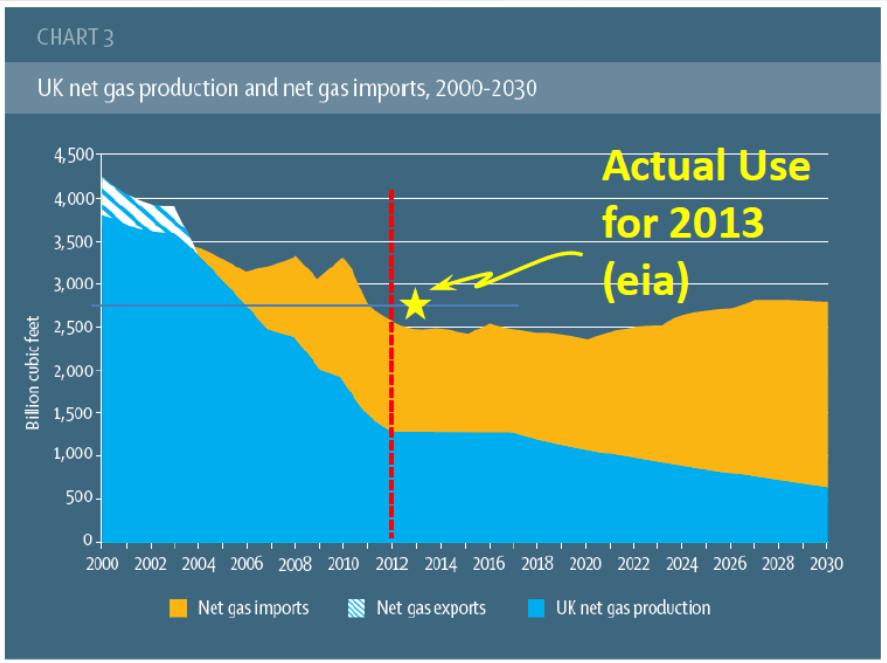

Source: Department of Energy and Climate Change, Production projections, extracted 15 March 2013 https://www.gov.uk/oil-and-gas-uk-field-data. NB: Figures given in billion cubic metres are converted to billion cubic feet.

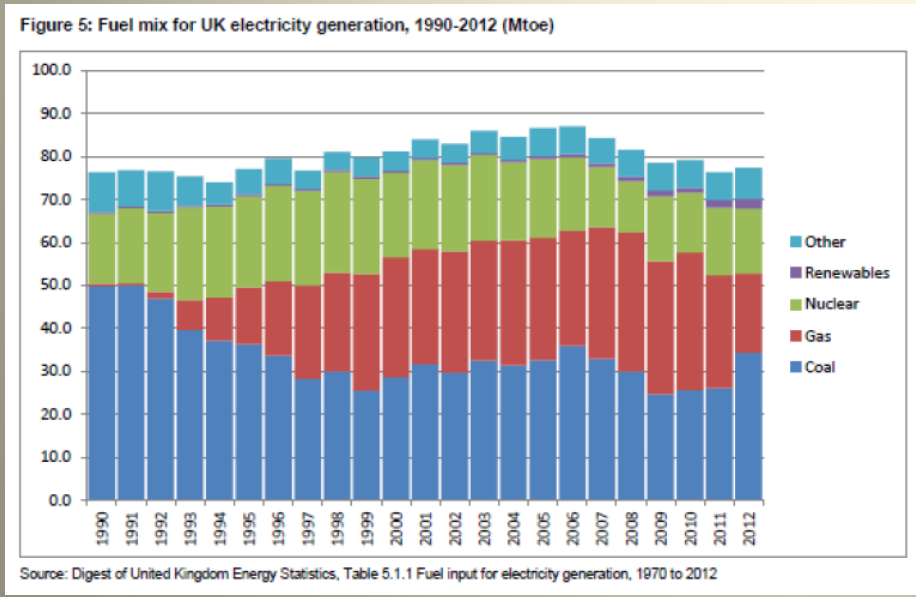

Source: Digest of United Kingdom Energy Statistics, Table 5.1.1 Fuel input for electricity generation, 1970 to 2012

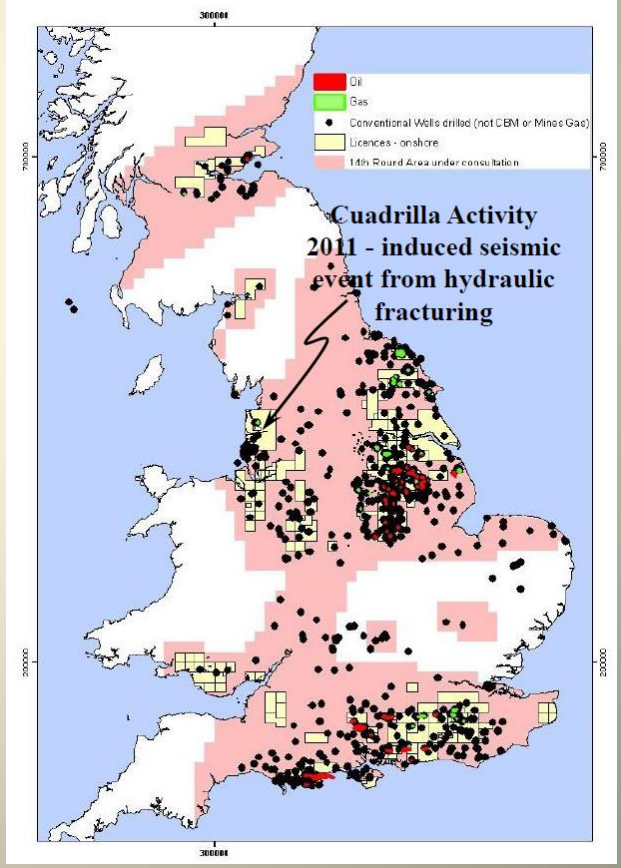

Demand for Affordable Energy
Advancing Technology
and the
Nature of Trial and Error







The Social Contract
And the Public's
Level of Scientific Literacy
Cost of Mistakes

Modeling petroleum generation in the Paleozoic of the Carnarvon Basin, Western Australia: Implications for prospectivity

K. Ameed R. Ghori, Arthur J. Mory, and Robert P. Iasky

ABSTRACT

Maturity and petroleum generation modeling of the Paleozoic succession in the Carnarvon Basin shows that most potential source rock intervals reached their maximum generation migration during the Carboniferous–Permian and could have charged traps developed during rifting in the middle Carboniferous to Early Permian except for the Peedamullah Shelf, where generation peaked during the Cretaceous. However, identification of such traps is challenging because it is difficult to differentiate between the deformation associated with middle Carboniferous–Early Permian rifting and that of the Early Cretaceous breakup rifting. Given the presence of suitable reservoir and sealing units in most of the Paleozoic, the prime risks for this section are the volume of available source rock, trap integrity because of the long period of preservation required, and relative timing of generation vs. trap formation, such that charging of younger traps requires secondary migration.

The best Paleozoic oil-prone source beds identified in the Carnarvon Basin are thin beds in carbonate-dominated Silurian and Devonian units on the Gascoyne Platform, but Devonian source beds are restricted to the northern parts of the platform. The maturity of these units progressively increases from immature in the south-southeast to mature in the north-northwest, following increasing depth of burial in that direction. The best gas-prone source beds lie within the Lower Permian of the Merlinleigh Subbasin, and their maturity ranges from immature along the margins of the subbasin to overmature toward the center. Within the Upper Permian, the best source beds for oil and gas are in the Peedamullah Shelf, where they range from immature in the southeast to mature in the northwest.

Copyright ©2005. The American Association of Petroleum Geologists. All rights reserved.

Manuscript received December 29, 2003; provisional acceptance May 25, 2004; revised manuscript received August 2, 2004; final acceptance August 15, 2004.

DOI:10.1306/08150403134

AUTHORS

K. Ameed R. Ghori ~ *Geological Survey of Western Australia, Department of Industry and Resources, Mineral House, 100 Plain Street, East Perth, Western Australia 6004, Australia; ameed.ghori@doir.wa.gov.au*

Ameed has M.Sc. degrees in geology from the University of Karachi (1968) and the Curtin University of Technology, Perth, Western Australia (1994). He specializes in petroleum geochemistry and has worked on Pakistani, Libyan, Australian, and Ugandan basins. Ameed joined the Geological Survey of Western Australia as a senior geologist in 1994; he is a member of AAPG, the Formation Evaluation Society of Western Australia, and the Petroleum Exploration Society of Australia.

Arthur J. Mory ~ *Geological Survey of Western Australia, Department of Industry and Resources, Mineral House, 100 Plain Street, East Perth, Western Australia 6004, Australia; arthur.mory@doir.wa.gov.au*

Arthur graduated from the University of Sydney (B.Sc., 1976; Ph.D., 1980) and joined the Geological Survey of Western Australia in 1980. He has published articles on stratigraphy and sedimentology of all major onshore basins in the state and is a member of the Petroleum Exploration Society of Australia and the Geological Society of America.

Robert P. Iasky ~ *Geological Survey of Western Australia, Department of Industry and Resources, Mineral House, 100 Plain Street, East Perth, Western Australia 6004, Australia; robert.iasky@doir.wa.gov.au*

Robert graduated from the Western Australia Institute of Technology (B.App.Sc., 1978; Grad.Dip.Sc., 1979) and Curtin University of Technology, Perth, Western Australia (M.App.Sc., 1991) majoring in geophysics. He joined the Geological Survey of Western Australia in 1981 and maintains an active interest in structural interpretation of basins in the state, particularly the Perth, southern Carnarvon, and Officer basins. He is a member of Australian Society of Exploration Geophysicists and Petroleum Exploration Society of Australia.

ACKNOWLEDGEMENTS

Reviews by John B. Curtis, Ernest A. Mancini, and Qingming Yang greatly improved this manuscript. This paper is published with the permission of the director of the Geological Survey of Western Australia.

DATASHARE 15

Tables 1–3 are accessible in an electronic version on the AAPG Web site as Datashare 15 at <www.aapg.org/datashare/index.html>.

Commercial Paleozoic petroleum has yet to be discovered in the Paleozoic of the Carnarvon Basin, but the assessment of this part of the basin is limited because few, if any, of the exploration wells drilled to date were valid tests of these objectives.

INTRODUCTION

One of the major exploration risks in the poorly explored Paleozoic succession of the Carnarvon Basin (Figure 1) is the preservation of any trapped hydrocarbons throughout its complex tectonic history. Marked contrasts in the distribution of strata between subbasins reflect variations in geological evolution and consequent burial, thermal, and generation histories that profoundly affect their prospectivity. In particular, the depositional history of the onshore Cambrian to Middle Devonian Gascoyne Platform (Iasky and Mory, 1999; Iasky et al., 2003; Mory et al., 2003) has little in common with the eastern, mostly Permian, depocenter adjacent to Precambrian basement (Merlinleigh and Byro subbasins; Crostella and Iasky, 1997; Iasky et al., 1998) (Figure 2). In most offshore portions of the basins, the Paleozoic is too deep to be evaluated from well data, except near the Peedamullah Shelf, where the succession onlaps Precambrian basement to the southeast. Geohistory modeling was used to evaluate the timing of petroleum generation and the relative importance of variations in thermal and burial history in the individual subbasins.

The study attempts to evaluate Paleozoic petroleum formation and preservation risk using basin modeling constrained by subsurface geological and geochemical information. Wells and geological cross sections were reconstructed to show burial and thermal histories with likely timing of petroleum generation migration across the basin using BasinMod® software of Platte River Associates. Modeling was performed in three steps: (1) one-dimensional modeling of single well locations, using version 7.06 of BasinMod 1-D; (2) one-dimensional modeling of multiwell locations, in version 7.06 of BasinView; and (3) two-dimensional modeling of a geological cross section using version 4.17 of BasinMod 2-D.

GEOLOGICAL HISTORY

Cambrian to Middle Devonian

Cambrian–earliest Ordovician deposition inferred across the basin (Iasky et al., 2003) has limited significance to the prospectivity of the basin because it is deep and has a patchy distribution, whereas extensive Silurian carbonate-shale facies of the Ajana, Yaringa, and Coburn formations (Dirk Hartog Group), with locally moderate to good source potential, overlie the Middle to Upper Ordovician red beds (Tumblagooda Sandstone) with good reservoir potential. These facies extend across the Gascoyne Platform, probably also

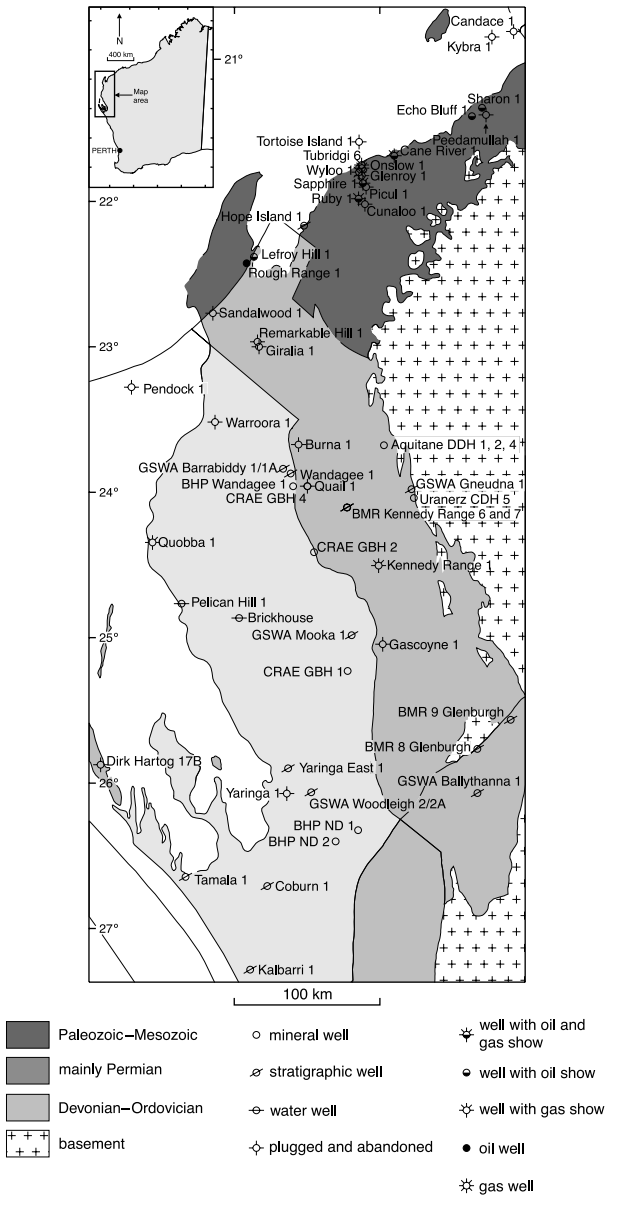

Figure 1. Location map of subbasins and wells. CRAE = Conzinc Riotinto of Australia Exploration Company; CDH = core drill hole; DDH = diamond drill hole; BMR = Bureau of Mineral Resources; BHP = Broken Hill Proprietary Company.

over the Peedamullah Shelf, and possibly the western part of the Merlinleigh and Byro subbasins. By comparison, after a short hiatus at the end of the Silurian, Early Devonian deposition can only be demonstrated on the Gascoyne Platform. Carbonate and siliciclastic (Faure Formation) deposition in the Early Devonian was followed by coarse-grained siliciclastics (Kopke Sandstone) and then a mixed carbonate, clastic, and evaporitic succession (Sweeney Mia Formation), which may have continued into the early Middle Devonian.

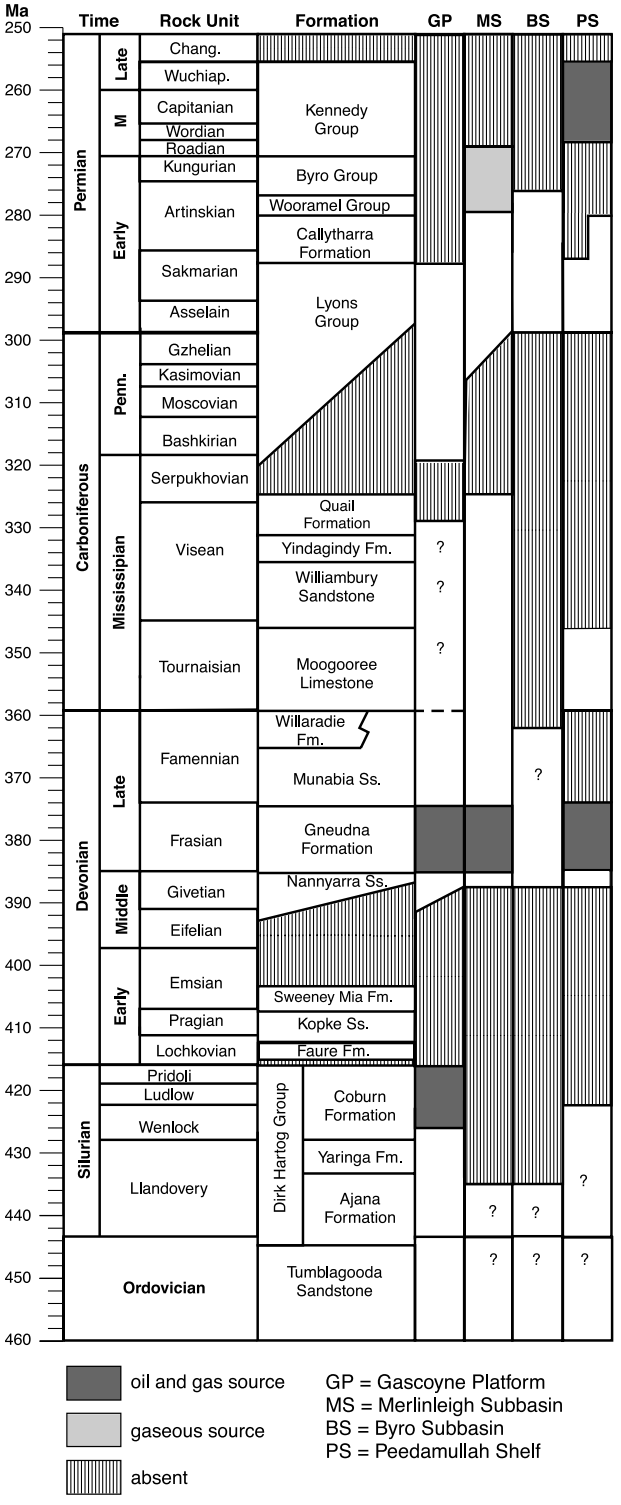

Figure 2. Generalized time stratigraphy and source rock type for the Gascoyne Platform, Merlinleigh and Byro subbasins, and Peedamullah Shelf (timescale after Gradstein et al., 2004).

Middle Devonian to Early Carboniferous

Following a period of minor erosion, deposition recommenced in the Eifelian with shallow-marine transgressive sand (Nannyarra Sandstone) followed by Givetian–Frasnian shallow-marine to intertidal carbonates and fine-grained siliciclastics (Gneudna Formation). During the Famennian, clastic deposition became dominant (Munabia Sandstone and Willaradie Formation), but by the Early Carboniferous (Tournaisian), shallow-marine carbonate deposition (Moogooree Limestone) was reestablished. In the late Tournaisian to Serpukhovian, siliciclastic and carbonate deposition alternated (Williambury Sandstone and Yindagindy and Quail formations). Deposition in this period in the basin was restricted to the Merlinleigh Subbasin and possibly in northern part of Gascoyne Platform, as well as across the Peedamullah Shelf, where the youngest of the units present is the Moogooree Limestone. Late Devonian deposition can also be inferred in the Byro and Coolcalalaya subbasins, where rocks of this age are known from just three shallow boreholes (Mory et al., 1998).

Middle Carboniferous to Permian

Deposition during this period did not extend over the central and southern parts of the Gascoyne Platform as inferred from the low maturity of pre-Carboniferous strata there. Marine glacigene deposition (Lyons Group) in the Serpukhovian–Sakmarian followed a major middle Carboniferous tectonic episode of uplift. These deposits are overlain by predominantly shallow-marine clastics (Callytharra Formation and Wooramel, Byro, and Kennedy groups). On the Peedamullah Shelf, there was a significant hiatus during the Sakmarian–Wordian, but parts of the Upper Permian are present there, whereas deposition continued without a significant break to the end of the Roadian in the Merlinleigh and Byro subbasins.

PETROLEUM GENERATION HISTORY

Source Rocks

Paleozoic oil-prone source rocks are associated with carbonate facies and are part of the Australia–wide Larapintine 2 and 3 petroleum supersystems deposited when Australia was in low tropical latitudes. Permian source rocks are part of the Gondwanan 1 and 2 petroleum supersystems deposited when Australia was in high southerly latitudes. Australia-wide, the latter two systems are dominated by clastic nonmarine facies with gas-prone and coaly source rocks (Bradshaw, 1993; Bradshaw et al., 1994). The concept of these supersystems was first applied by Bradshaw (1993) with a considerably broader application than the systems originally defined by Magoon and Dow (1991) and encompasses a continentwide family of similar source rocks instead of a single pod, as well as numerous individual petroleum systems.

In the Carnarvon Basin, the best quality source rocks have been identified in the Silurian Coburn Formation (Dirk Hartog Group), Devonian Gneudna Formation, and Permian Wooramel, Byro, and Kennedy groups from total organic carbon (TOC) and Rock-Eval data (Table 1 [available as Datashare 15 at www.aapg.org/datashare]; Figure 3a–e), as well as pyrolysis–gas chromatography, extract gas chromatography–mass spectrometry, and organic petrology (Ghori 1996; 1997; 1998a, b; 1999; 2002). Maturity data show that most of the sections drilled to date are no more than mid-mature (Table 2 [available as Datashare 15 at www.aapg.org/datashare]; Figure 3f–h). In the Merlinleigh Subbasin, however, the three deepest wells (Kennedy Range 1, Quail 1, and Remarkable Hill 1; Figure 1) penetrated overmature sections.

To date, good to excellent Silurian and Devonian source beds have been recognized only in fully cored wells because they are generally thin and consequently hard to identify from cuttings samples, particularly from carbonate facies. By comparison, shale beds in the more clastic parts of the Silurian and Devonian are more easily identifiable but so far have proved to be organically lean.

Within the lower Paleozoic of the Gascoyne Platform, the best Silurian source beds are present in Yaringa East 1 (deepening), with organic richness of up to more than 7% TOC, potential yields ($S_1 + S_2$) of up to 38 mg/g, and hydrogen indices of up to 505 (Figure 3a, e). The best Devonian source beds are present in Geological Survey of Western Australia (GSWA) Barrabiddy 1A, with organic richness of up to 13% TOC, potential yields ($S_1 + S_2$) of up to 40 mg/g, and hydrogen indices of up to 267 (Figure 3b, e). Pyrolysis–gas chromatography and extract analyses confirm that these organic facies are oil prone, and that they were deposited in reducing environments (Ghori, 1998b, 2002).

Within the upper Paleozoic of the Merlinleigh Subbasin and Peedamullah Shelf, Lower Permian source beds in the 380-m (1250-ft)-thick Artinskian Wooramel Group have fair to very good source potential

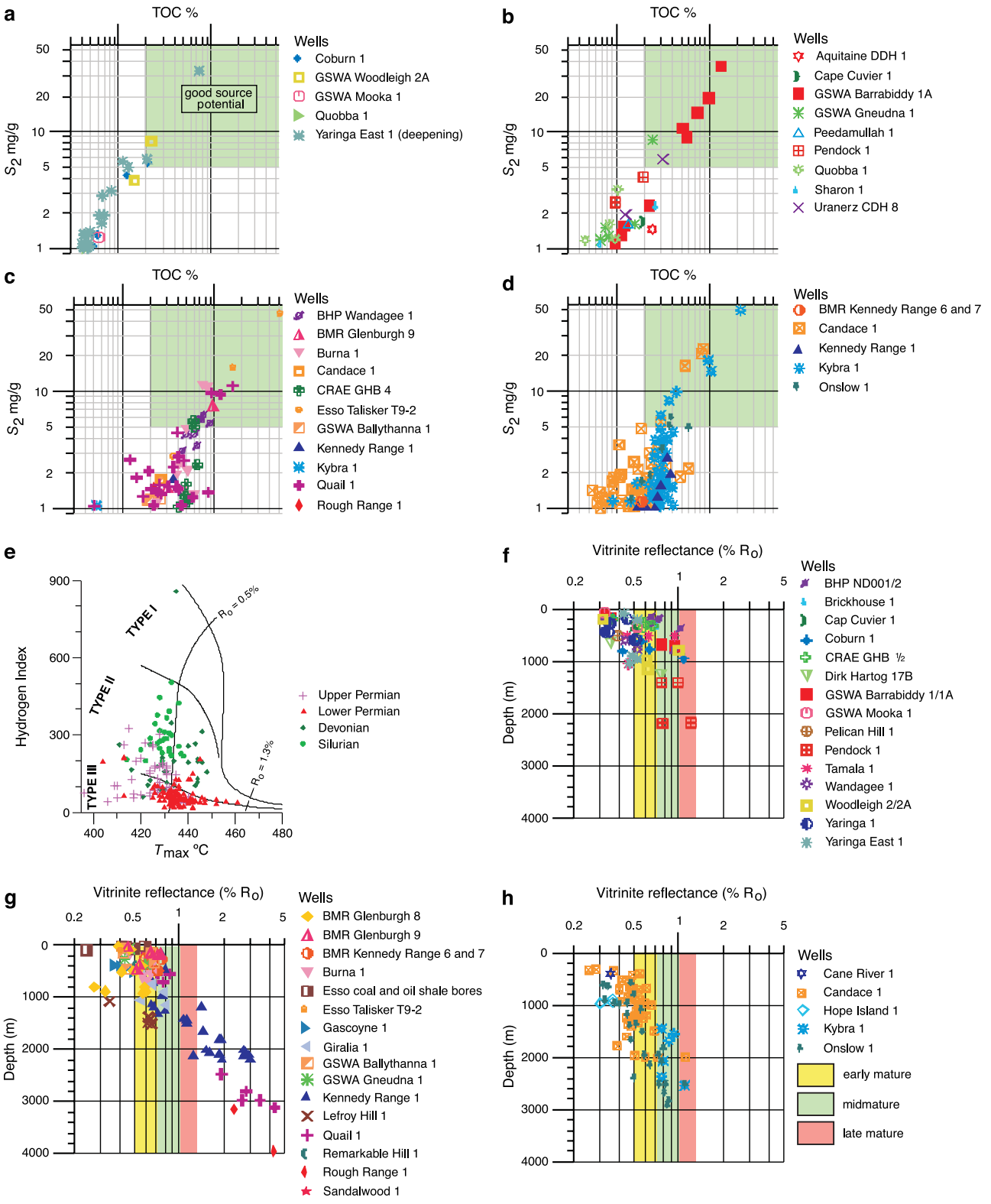

Figure 3. Petroleum-generating potential, kerogen type, and vitrinite reflectance vs. depth plots: (a) Silurian Dirk Hartog Group; (b) Devonian Gneudna Formation; (c) Lower Permian Wooramel and Byro groups; (d) Upper Permian Kennedy Group; (e) kerogen type; (f) Gascoyne Platform; (g) Merlinleigh Subbasin; and (h) Peedamullah Shelf.

(Figure 3c, e). Analyzed samples are organic rich, containing up to 16% TOC and 12 mg/g ($S_1 + S_2$) potential yields, with predominantly gas-generating kerogen. Within the Byro Group, good to fair predominantly gas-generating source rock intervals are present, but the unit is immature and not fully penetrated in the studied wells except Kennedy Range 1, where it ranges from immature to overmature. Upper Permian source beds (Kennedy Group) were intersected in Candace 1 and Kybra 1 (Figure 3d, e), with up to 8% TOC, potential yields ($S_1 + S_2$) up to 23 mg/g, and hydrogen indices up to 300.

Present-Day Temperatures

Present-day geothermal gradients were determined from a least-square fit of well bottomhole temperatures (BHT) plotted against depth. The temperatures at the minimum and maximum depths according to this linear relationship were used to calculate the gradient to avoid seasonal variation in surface temperatures. The average recorded gradient is 3.5°C/100 m in the Exmouth Subbasin, 3.2°C/100 m on the Gascoyne Platform, 3.0°C/100 m in the Merlinleigh Subbasin, and 3.1°C/100 m over the Peedamullah Shelf. The Exmouth Subbasin was included to evaluate the effect of the thick offshore Mesozoic–Cenozoic succession, because there is an increase in temperature gradient from east to west, from the predominantly Paleozoic (onshore) to Mesozoic–Cenozoic basins (offshore). In the modeling, present-day heat flows were constrained by estimated BHTs, which are generally 10% lower than the recorded values, using the Horner plot or increasing by 10%, depending on the type of BHTs data available for individual wells.

Apatite Fission-Track Analysis

Apatite fission-track analysis (AFTA) is useful in understanding the geothermal history of host rocks because fission-track ages are largely a function of track annealing in response to increasing temperature between approximately 50 and 120°C, whereas track length reflects the style of cooling. When combined with reflectance data, AFTA constrains paleotemperatures and periods of cooling from peak temperatures. Reflectance data provide control over a wider paleotemperature range, especially when the apatite fission tracks are totally annealed (above ~110°C; corresponding to an R_o range of 0.7–0.9%). In such a situation, AFTA constrains minimum paleotemperature estimates (Green et al., 1986; H. J. Gibson, S. J. Marshallsea, and P. G. F. Watson, 1998, unpublished work).

The geothermal history of the Carnarvon Basin is constrained by 20 AFTA determinations of Ordovician to Cretaceous samples selected to determine the significance of the middle Carboniferous, Permian, Triassic–Jurassic, and earliest Cretaceous depositional breaks and a minor Middle Devonian break. The data from the Gascoyne Platform show three major, regionally synchronous, paleothermal cooling episodes, with cooling beginning some time between 280 and 250 Ma (Permian), 180 and 145 Ma (Jurassic), and 55 and 10 Ma (Cenozoic; H. J. Gibson, S. J. Marshallsea, and P. G. F. Watson, 1998, unpublished work). By comparison, data from the Merlinleigh Subbasin indicate two paleothermal episodes, with cooling beginning at some time between 140 and 110 Ma (Early Cretaceous) and 20 and 5 Ma (late Tertiary) (K. A. Hegarty, M. E. Moore, and P. G. F. Watson, 1998, unpublished work). On the Peedamullah Shelf, there is a major paleothermal episode in the Jurassic between 160 and 150 Ma and in the Cretaceous after 120 Ma (H. J. Gibson, C. O'Brien, and P. G. F. Watson, 2000, unpublished work).

For these paleothermal episodes, present and paleotemperatures and the onset of cooling determined from AFTA and vitrinite reflectance data are summarized in Table 3. The magnitudes of paleotemperatures for each episode are consistent, with the highest paleotemperatures during the earliest episodes (generally >110°C) and the lowest paleotemperatures during the last episode of heating (generally <70°C; Table 3 [available as Datashare 15 at www.aapg.org/datashare]). The maximum paleotemperatures and maturities in the Paleozoic succession at the studied locations were reached early in the thermal history of the basin (late Paleozoic), except in wells on the Peedamullah Shelf, although there is some variation across the region.

Figure 4 demonstrates the age constraints on the regional paleothermal cooling episodes based on AFTA determinations of Cretaceous to Ordovician samples from eight wells and outcrop. The spread of the cooling limits confirms that there were at least five discrete regional thermal maximum episodes of Tertiary, Cretaceous, Jurassic, Permian, and Carboniferous ages. These regional thermal episodes encompass uplifting of the Gascoyne Platform during the Carboniferous, uplifting of the northern Perth Basin during the Late Permian, Jurassic rifting, breakup along Australia's northwest margin during the Early Cretaceous, and Miocene compression associated with the collision between the Australian and Indonesian plates. These

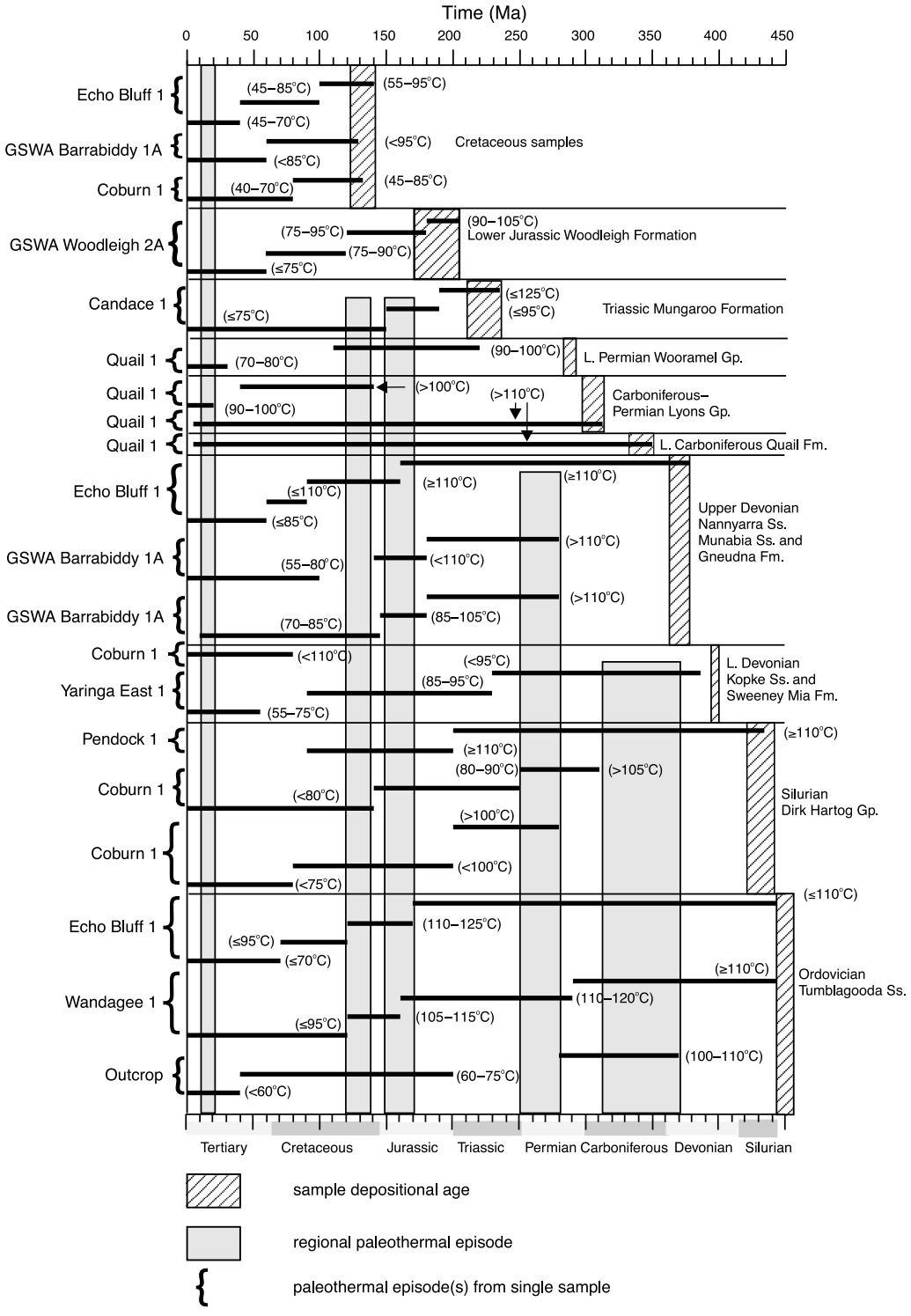

Figure 4. Timing of paleothermal episodes from AFTA, showing individual sample depositional ages, range of maximum paleotemperatures, and cooling events, sampled wells, and regional paleothermal cooling episodes.

events are discussed in depth mostly for the northern Carnarvon Basin by Veevers (1988), Boote and Kirk (1989), Malcolm et al. (1991), Westphal and Aigner (1997), and Keep et al. (1998), and for the Merlinleigh Subbasin and Gascoyne Platform by Iasky et al. (1998, 2003) and Iasky and Mory (1999).

BASIN MODELING

One-dimensional modeling of four representative wells across the region (Coburn 1, GSWA Barrabiddy 1A, Quail 1, and Onslow 1) was used to reconstruct the possible timing of petroleum generation for likely

Silurian–Upper Permian source rocks (Figure 5). The constraints on modeling peak generation of likely Silurian, Devonian, and Permian source rocks in these wells include time stratigraphy, formation tops, and estimates of missing sections (Figure 6). Regional maturity trends of several stratigraphic levels were calculated from one-dimensional modeling of 39 wells and 62 pseudowells based on seismic data (Figure 7). The burial histories of these wells were reconstructed from preserved major stratigraphic units and their lithologies. Finally, the maturity across the basin was calculated by two-dimensional modeling of two geological cross sections, constructed from the wells used in the one-dimensional modeling and seismic data (Figure 8).

The models were adjusted to account for stratigraphy, lithologies, regional geology, source rock characteristics, present-day temperatures from corrected BHTs, present-day maturity from reflectance data, T_{max}, and maximum paleotemperatures and their timing from AFTA. The following options of Platte River BasinMod were used in modeling: Bmod 2-D fluid-flow compaction, power function for permeability calculation, and transient heat flow with 25 and 20°C present-day sediment surface temperatures for onshore and offshore wells, respectively. The calculated maturities and timing of petroleum generation are based on Lawrence Livermore National Laboratory vitrinite and kerogen kinetics, respectively.

Figure 5 shows the modeled transformation ratio and generation rate vs. time as a function of burial history for wells that have maximum data to characterized source rocks and modeled maturity for formation tops and bottoms that contain likely Silurian–Upper Permian source rocks. On the Gascoyne Platform, Silurian source beds in the Coburn Formation (Dirk Hartog Group) are at the early stages of oil generation, and their generation rate peaked during the Carboniferous–Permian in Coburn 1 (Figure 5a). By comparison, Devonian source beds (Gneudna Formation) are within the oil-generative window, and their generation rate peaked during the Permian in GSWA Barrabiddy 1A (Figure 5b). Within Quail 1 in the Merlinleigh Subbasin, Devonian source beds (Gneudna Formation) are overmature, and their generation rate peaked during the Carboniferous, whereas Lower Permian source beds (Wooramel Group) are immature (Figure 5c). On the Peedamullah Shelf, Upper Permian source beds (Kennedy Group) in Onslow 1 are within the oil-generative window, and their generation rate peaked during the Cretaceous (Figure 5d).

Silurian Maturity and Generation Timing

On the Gascoyne Platform, the measured maturity of Silurian samples ranges from immature to overmature, and many are mature for oil generation (Figure 3f). The regional maturity at the top of the Silurian Dirk Hartog Group increases northward in the Gascoyne Platform (Figure 7a), probably because of increasingly deeper burial; it was intersected at 182 m (597 ft) in Kalbarri 1 in the south, and at 1850 m (6070 ft) in Pendock 1 in the north. The petroleum generation history for the Dirk Hartog Group in Coburn 1 on the Gascoyne Platform (Figure 5a) indicates that the Silurian is marginally mature and had a low rate of oil generation, which peaked during the Early Permian.

Devonian Maturity and Generation Timing

The succession is overmature for oil generation in the Merlinleigh Subbasin, where there is a thick Permian succession, but its maturity decreases southwest from Pendock 1 on the Gascoyne Platform and northeast toward Echo Bluff 1 on the onshore Peedamullah Shelf (Figure 7b). The Gneudna Formation is mature on the Gascoyne Platform in GSWA Barrabiddy 1A and Pendock 1. Devonian source rock in GSWA Barrabiddy 1A is within the oil-generative window, and oil generation peaked during the Late Permian (Figures 5b, 7b). Within the Merlinleigh Subbasin, Devonian source rock is overmature and reached optimum generation during the Carboniferous–Permian (Figure 5c).

Permian Maturity and Generation Timing

In the Merlinleigh Subbasin, the Wooramel Group is marginally mature in the northwest and immature in the south. The only exception is in Kennedy Range 1, (Figure 3g) where both vitrinite reflectance and Rock-Eval T_{max} indicate an abnormally high thermal maturity. In that well, there is an abrupt increase in the maturity below 1400 m (4600 ft) in the middle of the Byro Group, probably because of local intrusion, so that the section below 1400 m (4600 ft) is midmature to overmature. Within the northern Merlinleigh Subbasin and Peedamullah Shelf, the Permian is overlain by a Mesozoic–Cenozoic succession and is comparatively more mature, with the base of the succession ranging from early mature to overmature. On the Peedamullah Shelf, Upper Permian source rock in Onslow 1 is within the oil-generative window, and its generation rate peaked during the Cretaceous (Figure 5d). Figure 7c

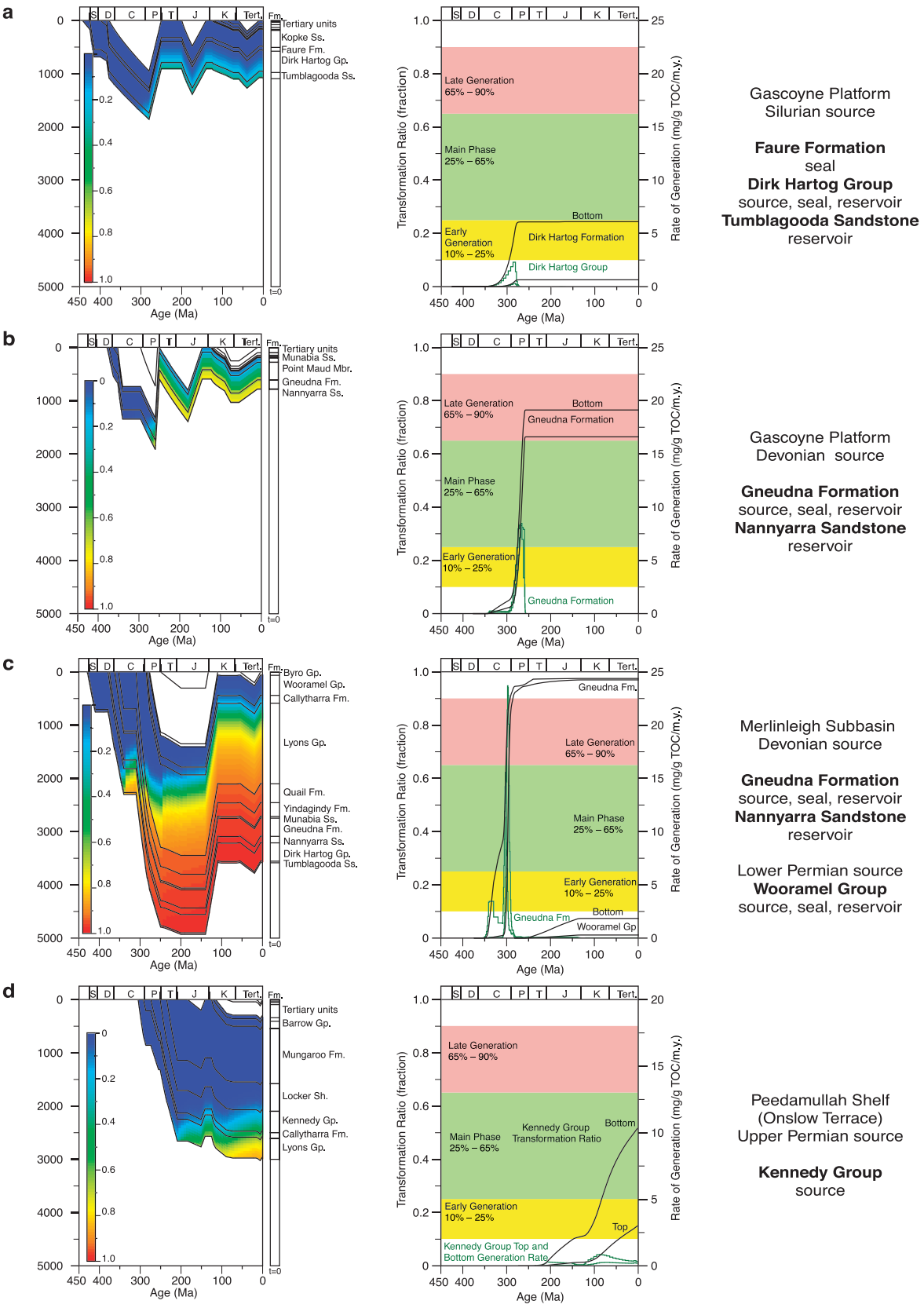

Gascoyne Platform
Silurian source

Faure Formation
seal
Dirk Hartog Group
source, seal, reservoir
Tumblagooda Sandstone
reservoir

Gascoyne Platform
Devonian source

Gneudna Formation
source, seal, reservoir
Nannyarra Sandstone
reservoir

Merlinleigh Subbasin
Devonian source

Gneudna Formation
source, seal, reservoir
Nannyarra Sandstone
reservoir

Lower Permian source
Wooramel Group
source, seal, reservoir

Peedamullah Shelf
(Onslow Terrace)
Upper Permian source

Kennedy Group
source

Figure 5. Petroleum charge timing as a function of generation history and rate vs. time for the (a) Silurian Dirk Hartog Group in Coburn 1; (b) Devonian Gneudna Formation in GSWA Barrabiddy 1A; (c) Lower Permian Wooramel Group in Quail 1; (d) Upper Permian Kennedy Group in Onslow 1.

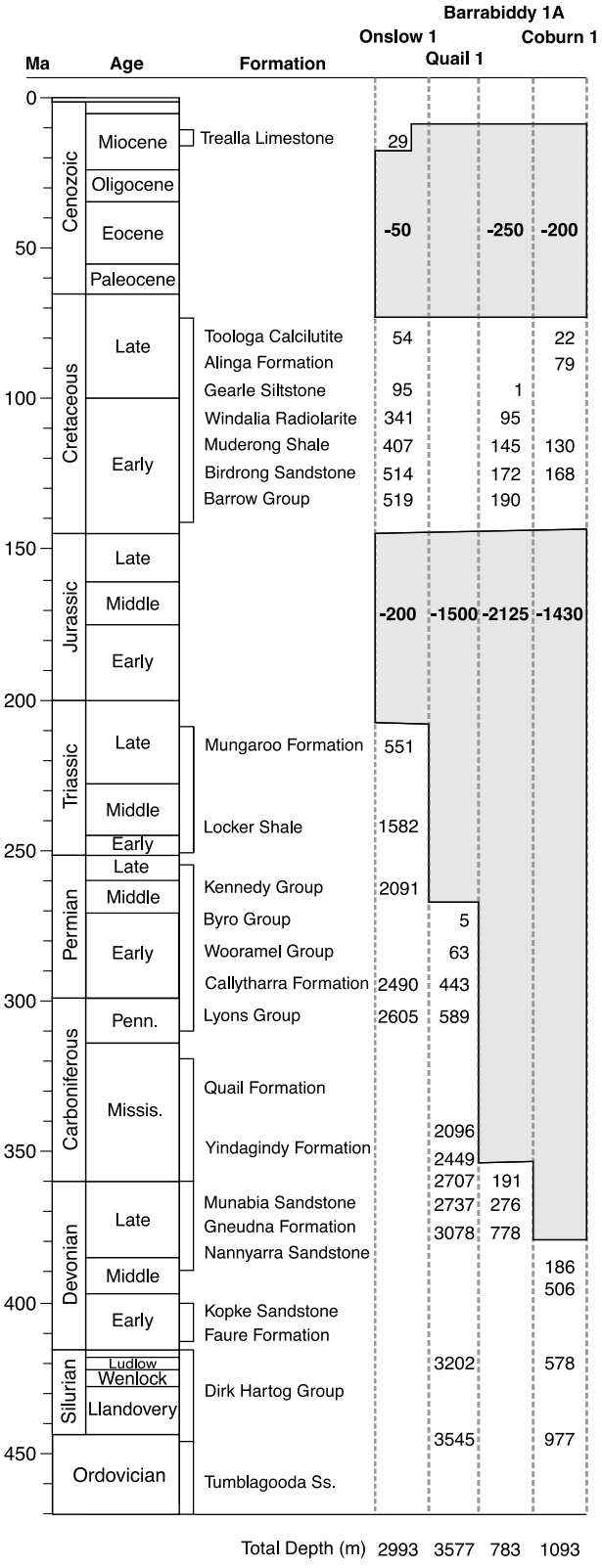

Figure 6. Time stratigraphy, formation tops, and missing rock thickness used to model time of petroleum generation in Onslow 1, Quail 1, GSWA Barrabiddy 1A, and Coburn 1.

shows the regional maturity at the top of the Permian (Wooramel, Byro, and Kennedy groups), whereas Figure 3h shows measured maturity in wells drilled on the Peedamullah Shelf.

POTENTIAL PETROLEUM SYSTEMS

The available geochemical data are insufficient to differentiate the numerous petroleum shows on the Peedamullah Shelf or the few in the Gascoyne Platform and Permian depocenter into discrete families or to correlate them with recognized source rocks of the study area to define possible petroleum systems (Magoon and Dow, 1994). However, the regional stratigraphic distribution of likely source, reservoir, and seal rocks limits the number of possible petroleum systems to those charged by the Silurian Coburn Formation (Dirk Hartog Group), Devonian Gneudna Formation, Lower Permian Wooramel and Byro groups, and Upper Permian Kennedy Group.

Two-dimensional modeling of geological sections was undertaken to evaluate the likelihood of active petroleum systems in the Gascoyne Platform, Merlinleigh Subbasin, and Peedamullah Shelf. For the Gascoyne Platform and Merlinleigh Subbasin, the model was constrained by data from six wells (Figure 8a, b), and for the Peedamullah Shelf, the model was constrained by data from eight wells (Figure 8c, d). The modeling indicates possible charge from Silurian and Devonian source rocks in parts of the Gascoyne Platform, Lower Permian source rocks in parts of the Merlinleigh Subbasin, and Upper Permian source rocks in the Peedamullah Shelf.

Figure 9 summarizes the essential elements of petroleum systems for the Gascoyne Platform, Merlinleigh Subbasin, and Peedamullah Shelf. Possible lower Paleozoic petroleum systems in the southern Gascoyne Platform would incorporate seal and source rocks in the Dirk Hartog Group and reservoirs in the underlying Tumblagooda Sandstone, or source and reservoir rocks in the Dirk Hartog Group, sealed by the overlying Devonian Faure Formation. In the northern Gascoyne Platform, the best possibility of a productive petroleum system is within the Devonian, because seal, source, and reservoir rocks are present in the Gneudna Formation, and there is an additional reservoir in the underlying Nannyarra Sandstone (Figure 9a).

In the Merlinleigh Subbasin, the Lower Permian Wooramel Group contains significant elements of a

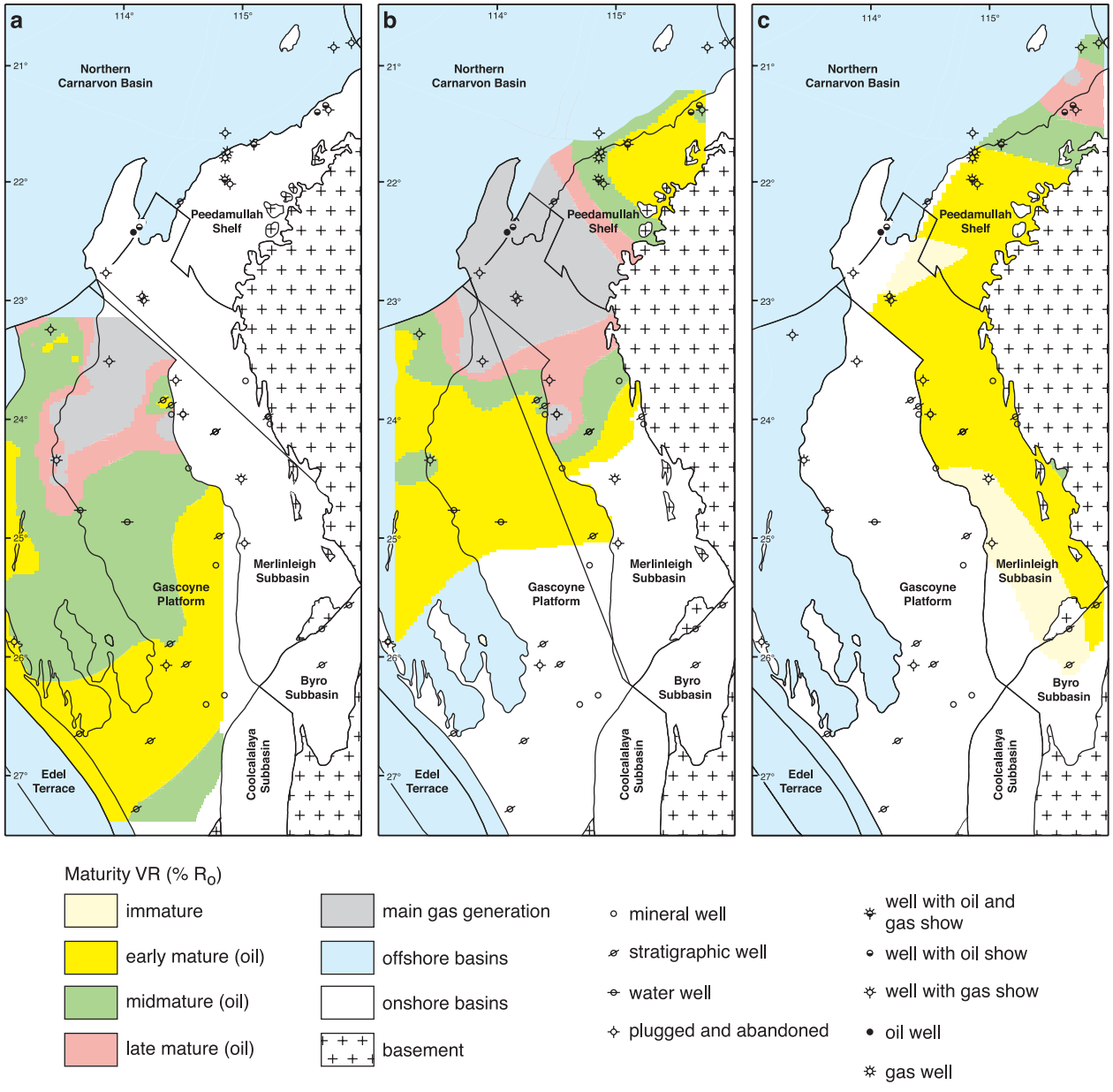

Figure 7. Present-day reflectance maturity at top (a) Silurian; (b) Devonian; (c) Permian; see Figure 1 for well names.

petroleum system: organic-rich shale; sandstone with excellent reservoir characteristics (Havord, 1998; Baker et al., 2000); and potential sealing units (I. Lavering, 1982, unpublished work; Percival and Cooney, 1985; Crostella, 1995). In the eastern part of the subbasin, a petroleum system may form with seal and source in the Devonian Gneudna Formation and the underlying Nannyarra Sandstone as a reservoir (Figure 9b). In the Peedamullah Shelf, a potential petroleum system exists in the Permian–Triassic (Figure 9c), as demonstrated by the presence of petroleum shows believed to be of Paleozoic origin (Crostella et al., 2000).

In the Merlinleigh Subbasin, there were significant tectonic events in the middle Carboniferous–Early Permian, Early Cretaceous, and Tertiary (Mory and Iasky, 1997). On the Gascoyne Platform, by comparison, AFTA and reflectance data indicate paleothermal cooling episodes during the Permian, Late Jurassic, and Tertiary (H. J. Gibson, S. J. Marshallsea, and P. G. F. Watson, 1998, unpublished work). Of these events, middle Carboniferous–Lower Permian rifting appears to have immediately preceded possible petroleum generation migration during the Carboniferous–Permian and Late Permian from Silurian–Devonian and Lower Permian source rocks, respectively.

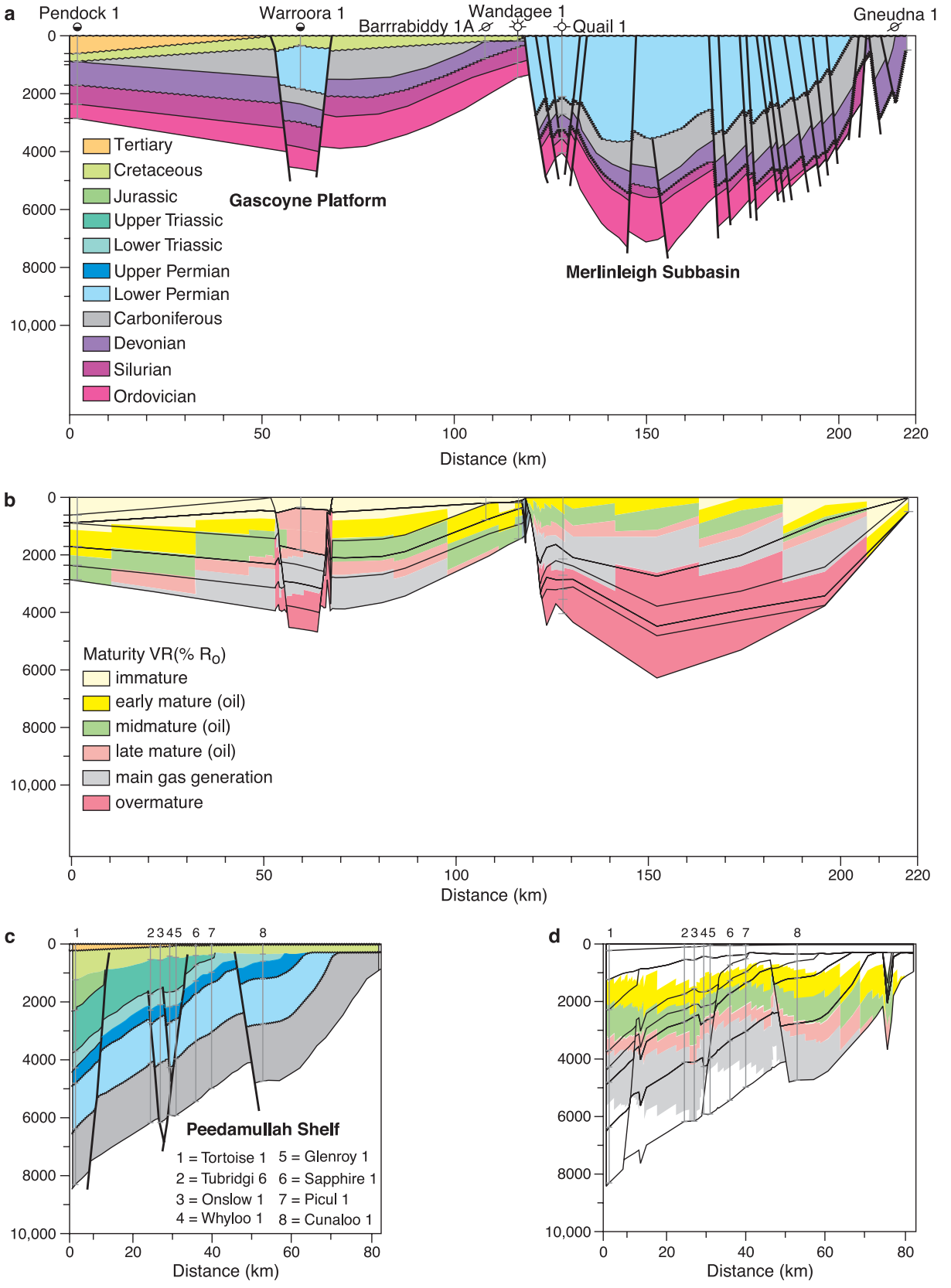

Figure 8. Present-day maturity of geological cross sections: (a) section modeled: Pendock 1 to GSWA Gneudna 1; (b) maturity of section from Pendock 1 to GSWA Gneudna 1; (c) section modeled: Tortoise 1 to Cunaloo 1; (d) maturity of section from Tortoise 1 to Cunaloo 1. See Figure 1 for well locations.

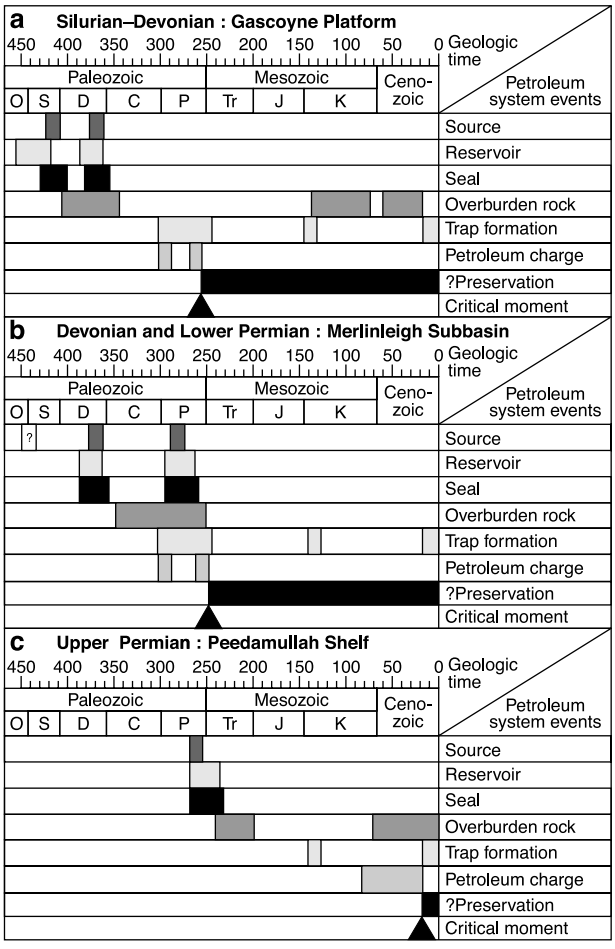

Figure 9. Petroleum system essential elements: (a) Gascoyne Platform; (b) Merlinleigh Subbasin; and (c) Peedamullah Shelf.

To date, no significant Paleozoic petroleum has been discovered in the Carnarvon Basin. Nevertheless, exploration is limited because there have been few, if any, valid tests of Paleozoic objectives (Crostella, 1995, 1996; Iasky et al., 2003).

CONCLUSIONS

Petroleum shows, geochemical analyses, and geohistory modeling constrained by apatite fission-track analysis, maturity data, and present-day temperatures imply four Paleozoic petroleum systems charged by source rocks identified in the Silurian Coburn Formation, Devonian Gneudna Formation, Lower Permian Wooramel Group, and Upper Permian Kennedy Group.

The best oil-prone Silurian source beds in the Coburn Formation in Yaringa East 1 (deepening) on the southern Gascoyne Platform have organic richness of up to 7% TOC, potential yield ($S_1 + S_2$) of up to 38 mg/g, and hydrogen index of up to 505. The best Devonian source beds have organic richness of up to 14% TOC, potential yield ($S_1 + S_2$) of up to 40 mg/g, and hydrogen index of up to 267 and are present in the Gneudna Formation in GSWA Barrabiddy 1A on the northern Gascoyne Platform. Silurian and Devonian source beds, identified so far, lie in carbonate facies, are thinly laminated, and are limited in volume.

The best Lower Permian source beds have organic richness of up to 16% TOC, potential yield ($S_1 + S_2$) of up to 12 mg/g, and contain predominantly gas-generating kerogen. They are widespread in the Lower Permian Wooramel Group of the Merlinleigh Subbasin. The best Upper Permian source beds are from the Peedamullah Shelf, where they have organic richness of up to 9% TOC, potential yield ($S_1 + S_2$) of up to 23 mg/g, and hydrogen index of up to 300.

Geohistory modeling indicates that petroleum generation migration from Silurian and Devonian source beds peaked during the Carboniferous–Permian, whereas that for Lower Permian source beds peaked during the Late Permian, except on the Peedamullah Shelf where it peaked during the Cretaceous. Such hydrocarbons could have charged existing structures (middle Carboniferous–Early Permian), which, if breached by later tectonism, could have remigrated into younger structures of breakup and/or Miocene age.

The petroleum prospectivity of the Ordovician to Middle Devonian succession is uncertain on the southern Gascoyne Platform because the thin source beds documented to date in the Silurian Coburn Formation are at most marginally mature, and overlying Mesozoic and younger rocks are immature. Farther north, the lower Paleozoic succession is buried below Devonian–Permian strata at depths unlikely to be drilled in the near future. For the Middle Devonian to early Carboniferous succession, prospectivity is regarded as good, at least on the Gascoyne Platform, and possibly also in the northeastern Merlinleigh Subbasin, where marine shale and carbonate of the Gneudna Formation is expected to have acted as source and seal for the Nannyarra Sandstone. The middle Carboniferous to Permian succession is considered to be the most prospective in the Merlinleigh Subbasin because it includes source, seal, and reservoir intervals in close proximity in the Wooramel Group. The source potential of the Upper Permian Kennedy Group is relevant only for the Peedamullah Shelf because this unit is immature in the Merlinleigh Subbasin.

The complex and varied depositional and erosional histories of the studied subbasins were affected by

five discrete regional thermal maximum episodes, as recognized from vitrinite reflectance, AFTA, and geology, within the Tertiary, Cretaceous, Jurassic, Permian, and Carboniferous. With a long and complex evolution, the major exploration risk in the Paleozoic of the Carnarvon Basin is preservation. Commercial Paleozoic petroleum has yet to be found in the Paleozoic part of the basin, but exploration has been limited with few, if any, valid tests.

REFERENCES CITED

Baker, J. C., P. J. Havord, K. R. Martin, and K. A. R. Ghori, 2000, Diagenesis and petrophysics of the Early Permian Moogooloo Sandstone, southern Carnarvon Basin, Western Australia: AAPG Bulletin, v. 84, no. 2, p. 250–265.

Boote, D. R. D., and R. B. Kirk, 1989, Depositional wedge cycles of evolving plate margin, western and northwestern Australia: AAPG Bulletin, v. 73, no. 2, p. 216–243.

Bradshaw, M., 1993, Australian petroleum systems: Petroleum Exploration Society of Australia Journal, v. 21, p. 43–53.

Bradshaw, M. T., J. Bradshaw, A. P. Murray, D. J. Needham, L. Spencer, R. E. Summons, J. Wilmot, and S. Winn, 1994, Petroleum systems in West Australian basins, *in* P. G. Purcell and R. R. Purcell, eds., The sedimentary basins of Western Australia: Proceedings of Petroleum Exploration Society of Australia, Perth, 1994, p. 93–118.

Crostella, A., 1995, The structural evolution and the hydrocarbons potential of the Merlinleigh and Byro sub-basins, Carnarvon Basin, Western Australia: Western Australia Geological Survey Report 45, 36 p.

Crostella, A., 1996, North West Cape petroleum exploration analysis of results to early 1995: Western Australia Geological Survey Record 1996/3, 45 p.

Crostella, A., and R. P. Iasky, 1997, Structural interpretation and hydrocarbon potential of the Giralia area, Carnarvon Basin, Western Australia: Western Australia Geological Survey Report 52, 38 p.

Crostella, A., R. P. Iasky, K. A. Blundell, A. R. Yasin, and K. A. R Ghori, 2000, Petroleum potential of the Peedamullah Shelf and Onslow Terrace, northern Carnarvon Basin, Western Australia: Western Australia Geological Survey Report 73, 119 p.

Ghori, K. A. R., 1996, Petroleum source rocks, Merlinleigh and Byro sub-basins, Carnarvon Basin, Western Australia: Western Australia Geological Survey Record 1995/5, 102 p.

Ghori, K. A. R., 1997, Palaeozoic source rock facies and maturation history of the southern Merlinleigh Sub-basin, Carnarvon Basin, Western Australia, *in* J. V. C. Howes and R. A. Noble, eds., Petroleum system of SE Asia and Australasia: Proceedings of Indonesian Petroleum Association, Jakarta, Indonesia, 1997, p. 175–190.

Ghori, K. A. R., 1998a, Petroleum generating potential and thermal history of the Palaeozoic, Carnarvon Basin, Western Australia, *in* P. G. Purcell and R. R. Purcell, eds., The sedimentary basins of Western Australia: Proceedings of West Australian Basins Symposium, Western Australia, Perth, 1998, p. 553–567.

Ghori, K. A. R., 1998b, Geochemistry of the Devonian, Barrabiddy 1A, Carnarvon Basin, Western Australia: Petroleum Exploration Society of Australia Journal, v. 26, p. 136–146.

Ghori, K. A. R., 1999, Silurian–Devonian petroleum source-rock potential and thermal history, Carnarvon Basin, Western Australia: Western Australia Geological Survey Report 72, 88 p.

Ghori, K. A. R., 2002, High-quality oil-prone source rocks within carbonates of the Silurian Dirk Hartog Group, Gascoyne Platform, Western Australia: Western Australia Geological Survey Annual Review 2000-01, p. 58–62.

Gradstein, F. M., J. G. Ogg, A. G. Smith, W. Bleeker, and L. J. Lucas, 2004, A new geologic time scale, with special reference to Precambrian and Neogene: Episodes, v. 27, no. 2, p. 83–100.

Green, P. F., I. R. Duddy, A. J. W. Gleadow, P. R. Tingate, and G. M. Laslett, 1986, Thermal annealing of fission tracks in apatite: 1. A quantitative description: Chemical Geology, v. 59, p. 237–253.

Havord, P. J., 1998, Assessment and prediction of petroleum reservoir quality in the Moogooloo Sandstone and Keogh Formation, southern Carnarvon Basin, Western Australia: Western Australia Geological Survey Record 1998/4, 68 p.

Iasky, R. P., and A. J. Mory, 1999, Geology and petroleum potential of the Gascoyne Platform, southern Carnarvon Basin, Western Australia: Western Australia Geological Survey Report 69, 46 p.

Iasky, R. P., A. J. Mory, K. A. R. Ghori, and S. I. Shevchenko, 1998, Structure and petroleum potential of the southern Merlinleigh Sub-basin, Carnarvon Basin, Western Australia: Western Australia Geological Survey Report 61, 63 p.

Iasky, R. P., C. D'Ercole, K. A. R. Ghori, A. J. Mory, and A. Lockwood, 2003, Structure and petroleum prospectivity of the Gascoyne Platform, Western Australia: Western Australia Geological Survey Report 87, 56 p.

Keep, M., C. M. Powell, and P. W. Baillie, 1998, Neogene deformation of the North West Shelf, Australia, *in* P. G. Purcell and R. R. Purcell, eds., The sedimentary basins of Western Australia: Proceedings of West Australian Basins Symposium, Western Australia, Perth, 1998, p. 81–91.

Magoon, L. B., and W. G. Dow, 1991, The petroleum system—From source to trap (abs.): AAPG Bulletin, v. 75, no. 3, p. 627.

Magoon, L. B., and W. G. Dow, 1994, The petroleum system—From source to trap: AAPG Memoir 60, 655 p.

Malcolm, R. J., M. C. Pott, and E. Delfos, 1991, A new tectonostratigraphic synthesis of the North West Cape area: Australian Petroleum Exploration Association Journal, v. 31, part 1, p. 154–176.

Mory, A. J., and R. P. Iasky, 1997, Integrating seismic, gravity and aeromagnetic data in the structural interpretation of the Merlinleigh Sub-basin, Western Australia: Australian Petroleum Production and Exploration Association Journal, v. 37, part 1, p. 33–41.

Mory, A. J., R. P. Iasky, and S. I. Shevchenko, 1998, The Coolcalalaya Sub-basin: A forgotten frontier 'between' the Perth and Carnarvon Basin, *in* P. G. Purcell and R. R. Purcell, eds., The sedimentary basins of Western Australia: Proceedings of West Australian Basins Symposium, Western Australia, Perth, 1998, p. 613–622.

Mory, A. J., R. P. Iasky, and K. A. R. Ghori, 2003, A summary of the geological evolution and petroleum potential of the southern Carnarvon Basin, Western Australia: Western Australia Geological Survey Report 86, 26 p.

Percival, J. G., and P. M. Cooney, 1985, Petroleum geology of the Merlinleigh Sub-basin, Western Australia: Australian Petroleum Exploration Association Journal, v. 25, part 1, p. 190–203.

Veevers, J. J., 1988, Morphotectonics of Australia's northwestern margin—A review, *in* P. G. Purcell and R. R. Purcell, eds., The North West Shelf Australia: Proceedings of North West Shelf Symposium, Perth, West Australia, 1998, p. 19–27.

Westphal, H., and T. Aigner, 1997, Seismic stratigraphy and subsidence analysis in the Barrow-Dampier Sub-basin, northwest Australia: AAPG Bulletin, v. 81, no. 10, p. 1721–1749.

The Next 100 Years of Global Energy: Part I
Energy Security and Energy Poverty*

Scott W. Tinker[1]

Search and Discovery Article #70268 (2017)**
Posted June 28, 2017

*Adapted from oral presentation given at Forum, "The Next 100 Years of Global Energy Use: Resources, Impacts and Economics," at AAPG Annual Convention and Exhibition, Houston, Texas, April 4, 2017
**Datapages © 2017. Serial rights given by author. For all other rights contact author directly.

[1]Director, Bureau of Economic Geology, The University of Texas at Austin (scott.tinker@beg.utexas.edu)

Preface

Forum Topics

• Energy Security and Energy Poverty	Scott W. Tinker
• Global Population, Energy Demand and Future Technology	E. Koonin
• Global Petroleum Resources and Transportation Fuel Options	Cindy Yeilding
• Global Power Fuel Mix and Carbon Transition	Mark Snell
• Energy Density, Fake and True News about Energy and Environment	Jesse Ausubel
• The Grand Energy Challenge: Energy Diversity and Economic Realities	Kenneth Medlock

Outline

Energy Security
Energy Poverty
Energy Reality

Summary

1. Oil, natural gas, and coal are secure sources of energy and will remain vital well into the 21st Century.
2. Secure energy is required to lift humanity from poverty.
3. Secure energy—affordable, available, reliable, sustainable—underpins economies and is required for investment in the environment.

Selected References

BP, 2016, Statistical Review of World Energy. Website accessed June 1, 2017, http://www.bp.com/en/global/corporate/energy-economics/statistical-review-of-world-energy.html.

Bureau of Economic Geology (BEG), 2017, Shale Resources, Reserves and Production Group. Website accessed June 13, 2017, http://www.beg.utexas.edu/research/programs/shale.

Department of Energy (DOE), 2014, The Water-Energy Nexus: Challenges and Opportunities (July). Website accessed June 1, 2017, https://www.energy.gov/under-secretary-science-and-energy/downloads/water-energy-nexus-challenges-and-opportunities.

Energy Information Administration (U.S.) (EIA), 2015, Monthly Energy Review—May 2015. Website accessed June 1, 2017, https://www.slideshare.net/CFCC15/energy-policy-greenhouse-gas-reduction-and-climate-negotiations.

EIA, 2016, Lower 48 states shale plays (June). Website accessed June 1, 2017, https://www.eia.gov/maps/images/shale_gas_lower48.pdf.

International Energy Agency (IEA), 2015, World Energy Outlook 2015. Website accessed June 1, 2017, https://www.iea.org/newsroom/news/2015/november/world-energy-outlook-2015.html.

IEA, 2016, World Energy Investment 2016. Website accessed June 1, 2017, https://www.iea.org/newsroom/news/2016/september/world-energy-investment-2016.html.

Sweeney, J., 2015, Energy Efficiency Obstacles and Opportunities: an Overview. Website accessed June 1, 2017, https://www.slideshare.net/CFCC15/energy-policy-greenhouse-gas-reduction-and-climate-negotiations.

Tinker, S.W., Director, 2011, *Switch: Discover the Future of Energy* (Film for viewing and on DVD and the web). Website accessed June 1, 2017, http://www.switchenergyproject.com/screenings.

Tinker, S.W., 2013, Energy 360: Leaving our corners for the radical middle: New Zealand sets an example: Earth (September), p. 8–9.

Tinker, S.W., H. Lynch, M. Carpenter, and M. Hoover, 2013, Global energy and the role of geosciences: A North American perspective , in M.E. Bickford, editor, The Impact of the Geological Sciences on Society: GSA Special Paper 501, p. 21-51.

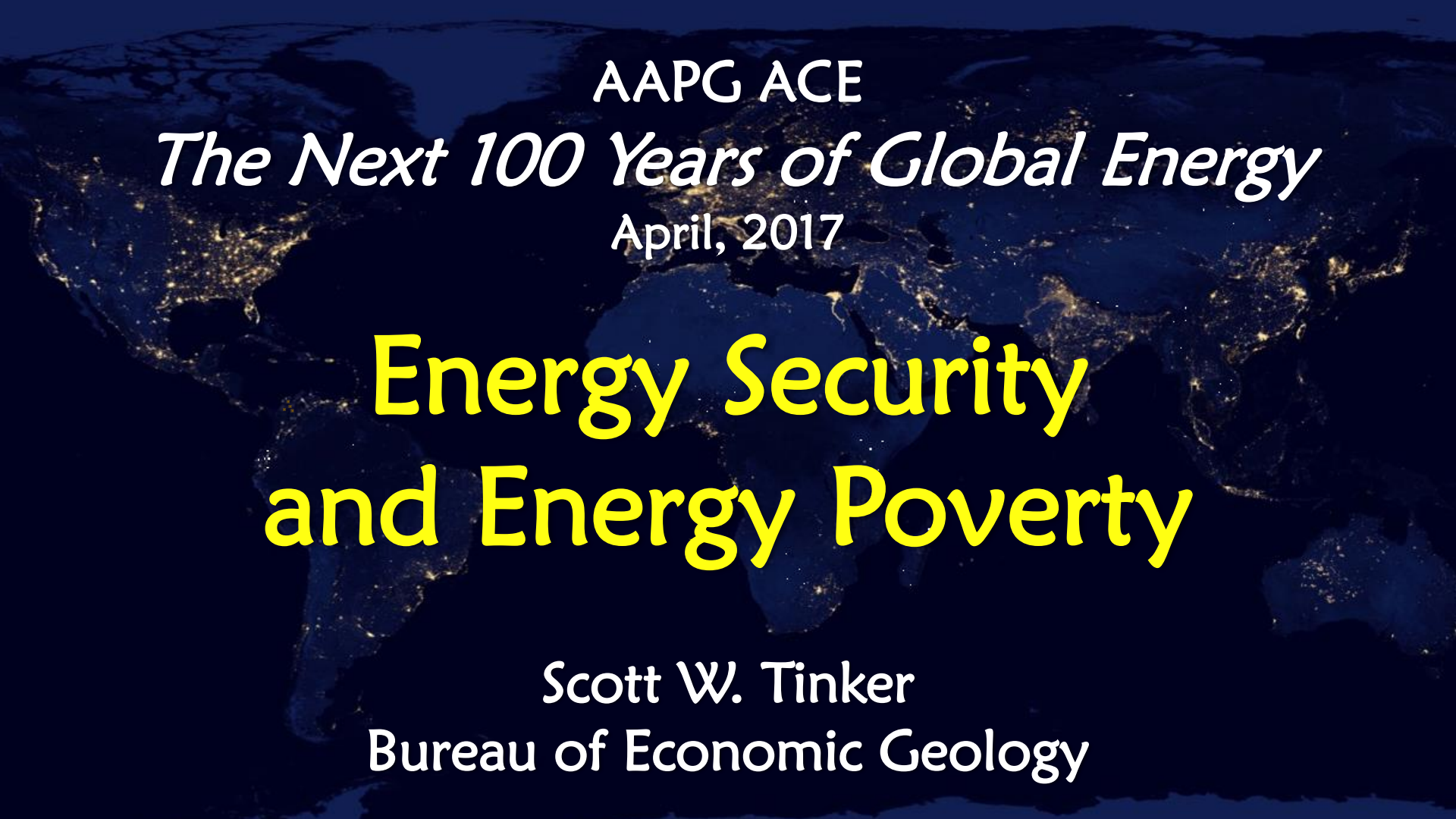

AAPG ACE

The Next 100 Years of Global Energy

April, 2017

Energy Security and Energy Poverty

Scott W. Tinker
Bureau of Economic Geology

Outline

- Energy Security
- Energy Poverty
- Energy Reality

U.S. Primary Energy Demand

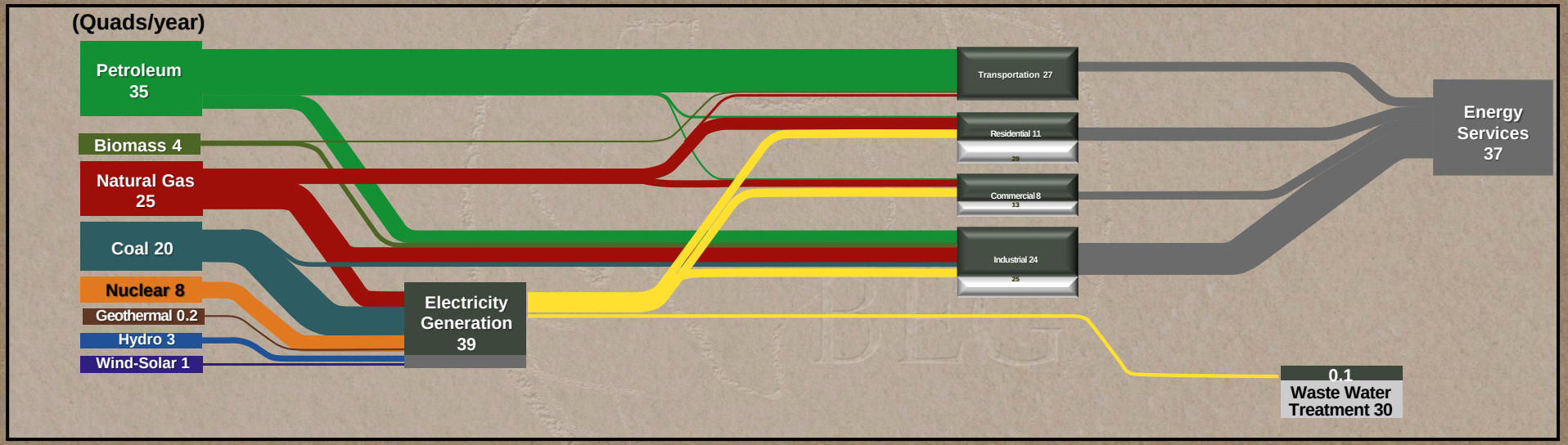

The Water-Energy Nexus: Challenges and Opportunities, DOE, July, 2014

The Next 100 Years of Energy

Population, Energy Demand and Future Technology	Steven E. Koonin
Petroleum Resources and Transportation Fuel Options	Cindy Yeilding
Power Fuel Mix and Carbon Transition	Mark Snell
Energy Density, Fake & True News about Energy and Environment	Jesse Ausubel
Energy Challenge: Diversity and Economic Realities	Kenneth Medlock

The Next 100 Years of Energy

Population, Energy Demand and Future Technology

Petroleum Resources and Transportation Fuel Options

Power Fuel Mix and Carbon Transition

Energy Density, Fake & True News about Energy and Environment

Energy Challenge: Diversity and Economic Realities

Energy Security

Affordable

- Cost: per unit of energy
- Price Volatility: stable or fluctuating
- Infrastructure: cost to build the plant

Available

- Access: substantial resources

Reliable

- Intermittent: source consistent or variable
- Safe: natural/human causes

Sustainable

- Clean: air and atmospheric emissions
- Dense: energy per area, weight and volume
- Dry: fresh water use/risk

Energy Security Challenges

Transportation

I. **Oil**
   - **Available, affordable, reliable**
   - Land use, water, emissions

II. **Natural Gas (CNG, LPG, LNG, GTL)**
   - **Available, affordable, reliable**
   - Dirtier than certain electric fuels

III. **Electricity**
   - **Benefits depend on fuel source**
   - Mining, expensive, chemicals, range

IV. **Biofuels**
   - Scale, land use, water, cost

V. **Hydrogen**







From Tinker et. al. 2013, GSA Special Publication

Energy Security Challenges

Electricity Generation

I. **Coal**
   - Available, affordable, reliable
   - Mining, water, air emissions, CO_2

II. **Natural Gas**
   - Available, affordable, reliable
   - Water, methane and CO_2

III. **Nuclear**
   - Available, affordable, reliable, sustainable
   - Radioactive waste, safety







From Tinker et. al. 2013, GSA Special Publication

Energy Security Challenges

Electricity Generation

IV. **Hydro**
- Affordable
- Water and topography

V. **Geothermal**
- Reliable, sustainable
- Energy density

VI. **Wind**
- Affordable, sustainable
- Intermittent, land and visual, transmission

VII. **Solar**
- Available, sustainable
- Expensive, intermittent, inefficient









From Tinker et. al. 2013, GSA Special Publication

Energy Security

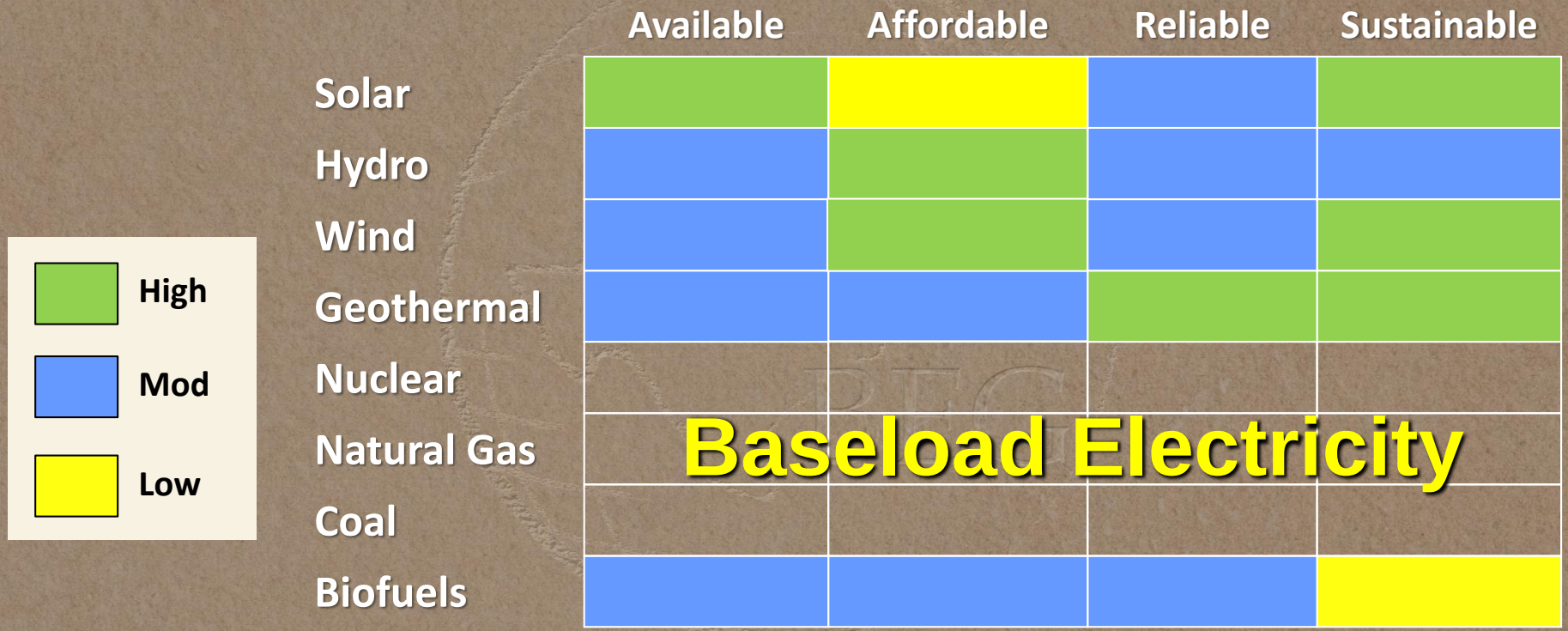

Tinker informal survey of experts

Energy Security

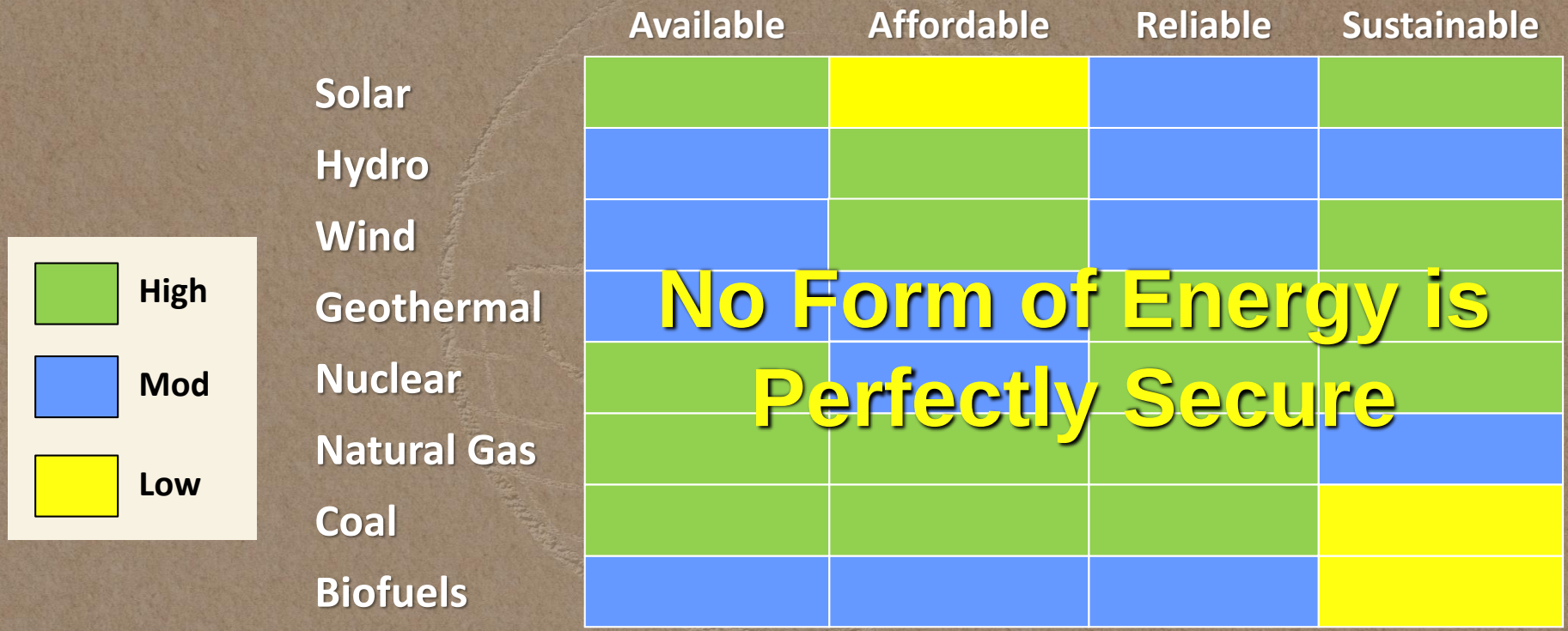

Tinker informal survey of experts

Outline

- Energy Security
- Energy Poverty
- Energy Reality

Electricity and Poverty

Poverty and electricity access in selected developing countries, circles sized by total population

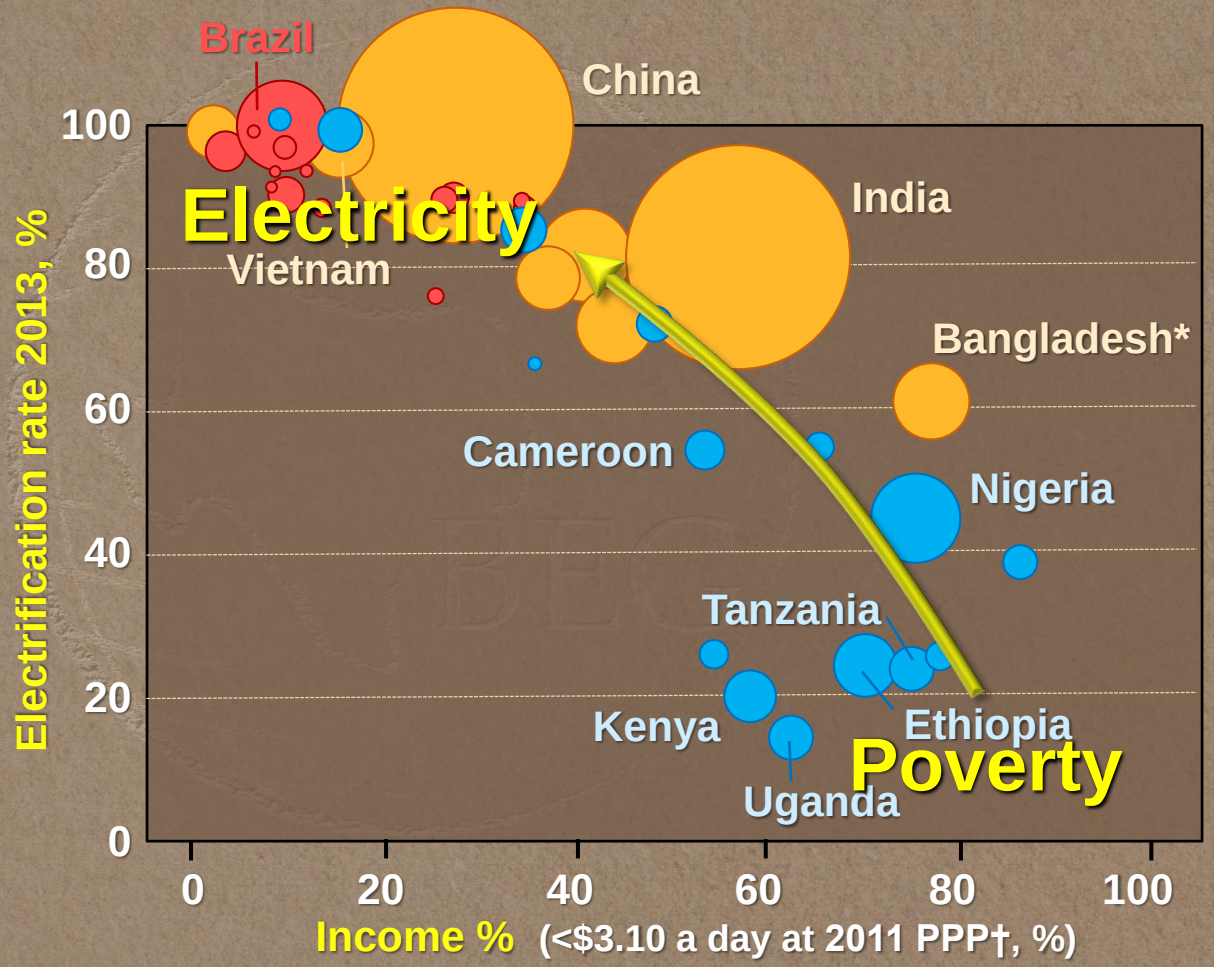

Africa

Asia

Latin America

* Bangladesh uses 2005 PPP and $2 a day poverty line

† Purchasing power parity

Sources: World Bank; IEA; World Energy Outlook 2015









Photos Tinker, Ecuador, 2017


Photos Lynch, Ecuador, 2017

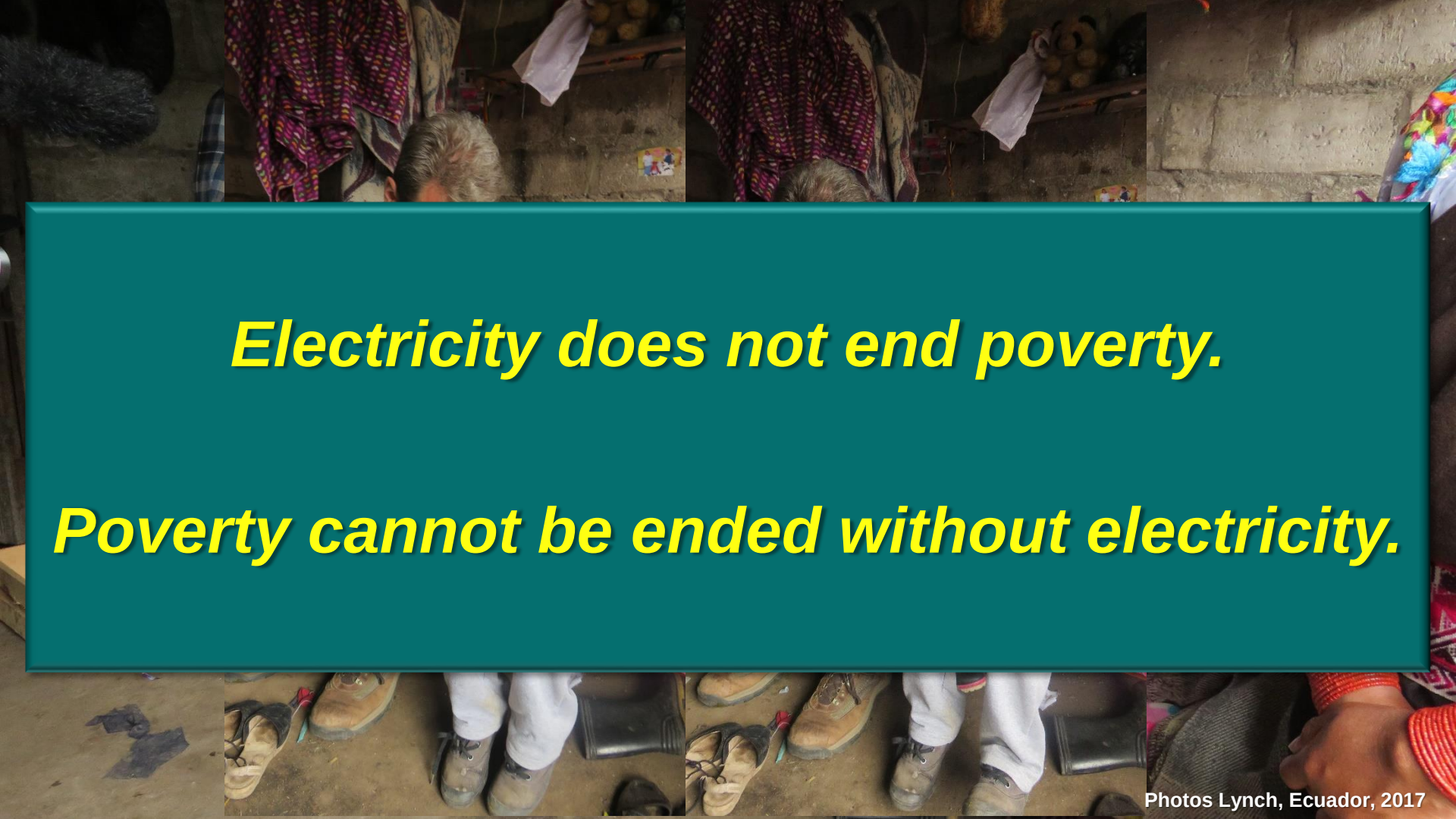
Electricity does not end poverty.
Poverty cannot be ended without electricity.
Photos Lynch, Ecuador, 2017

Limited Access to Electricity Restricts Standard of Living

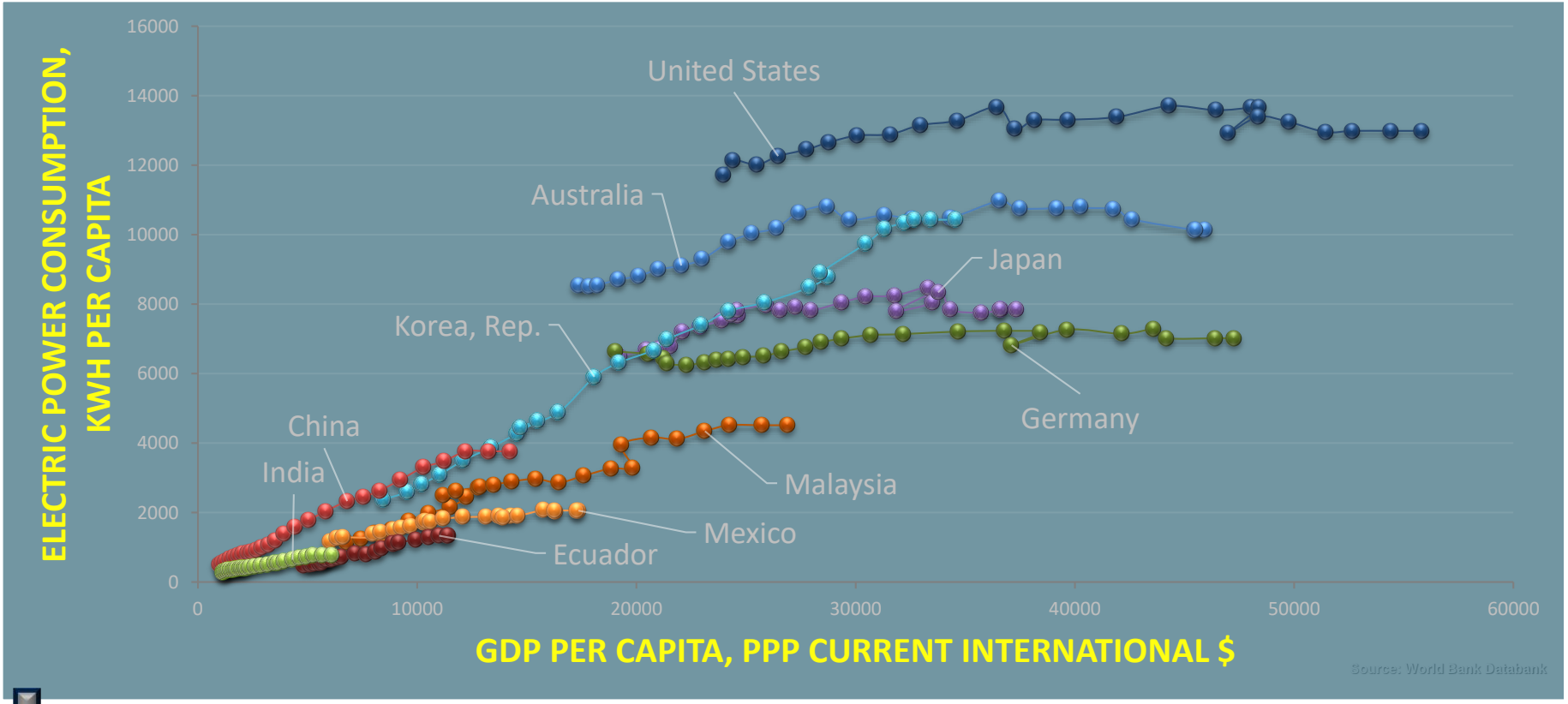

Limited Access to Electricity Restricts Standard of Living

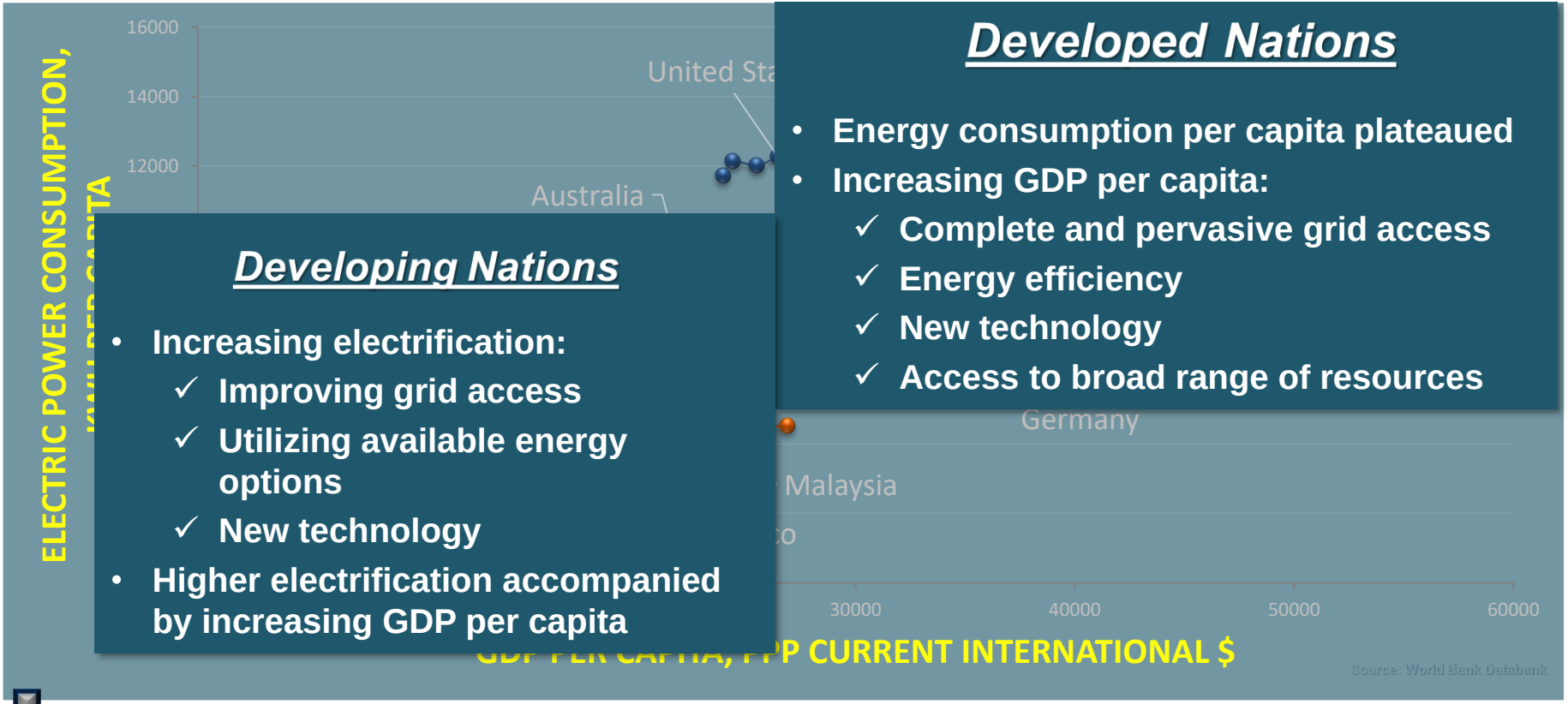

Developed Nations

- Energy consumption per capita plateaued
- Increasing GDP per capita:
  - ✓ Complete and pervasive grid access
  - ✓ Energy efficiency
  - ✓ New technology
  - ✓ Access to broad range of resources

Developing Nations

- Increasing electrification:
  - ✓ Improving grid access
  - ✓ Utilizing available energy options
  - ✓ New technology
- Higher electrification accompanied by increasing GDP per capita

'92 '93 '94 '95 '96 '97 '98 '99 2000 '01 '02 '03 '04 '05 '06 '07 '08 '09 2010 '11 '12 '13

Limited Access to Electricity Propagates Inequality



1990 '92 '93 '94 '95 '96 '97 '98 '99 2000 '01 '02 '03 '04 '05 '06 '07 '08 '09 2010 '11 '12 '13

Limited Access to Electricity Propagates Inequality

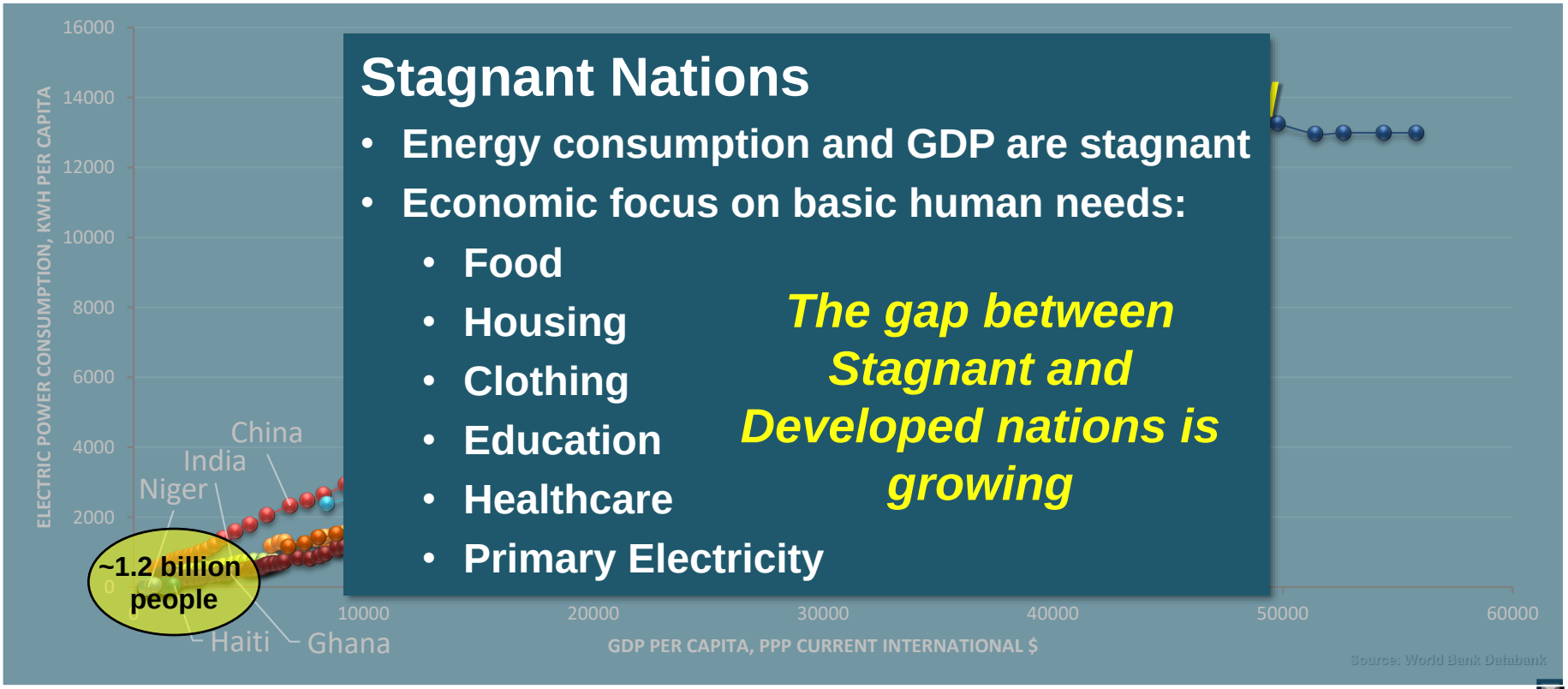

Stagnant Nations

- Energy consumption and GDP are stagnant
- Economic focus on basic human needs:
  - Food
  - Housing
  - Clothing
  - Education
  - Healthcare
  - Primary Electricity

The gap between Stagnant and Developed nations is growing

1990 '92 '93 '94 '95 '96 '97 '98 '99 2000 '01 '02 '03 '04 '05 '06 '07 '08 '09 2010 '11 '12 '13

Limited Access to Electricity Propagates Inequality

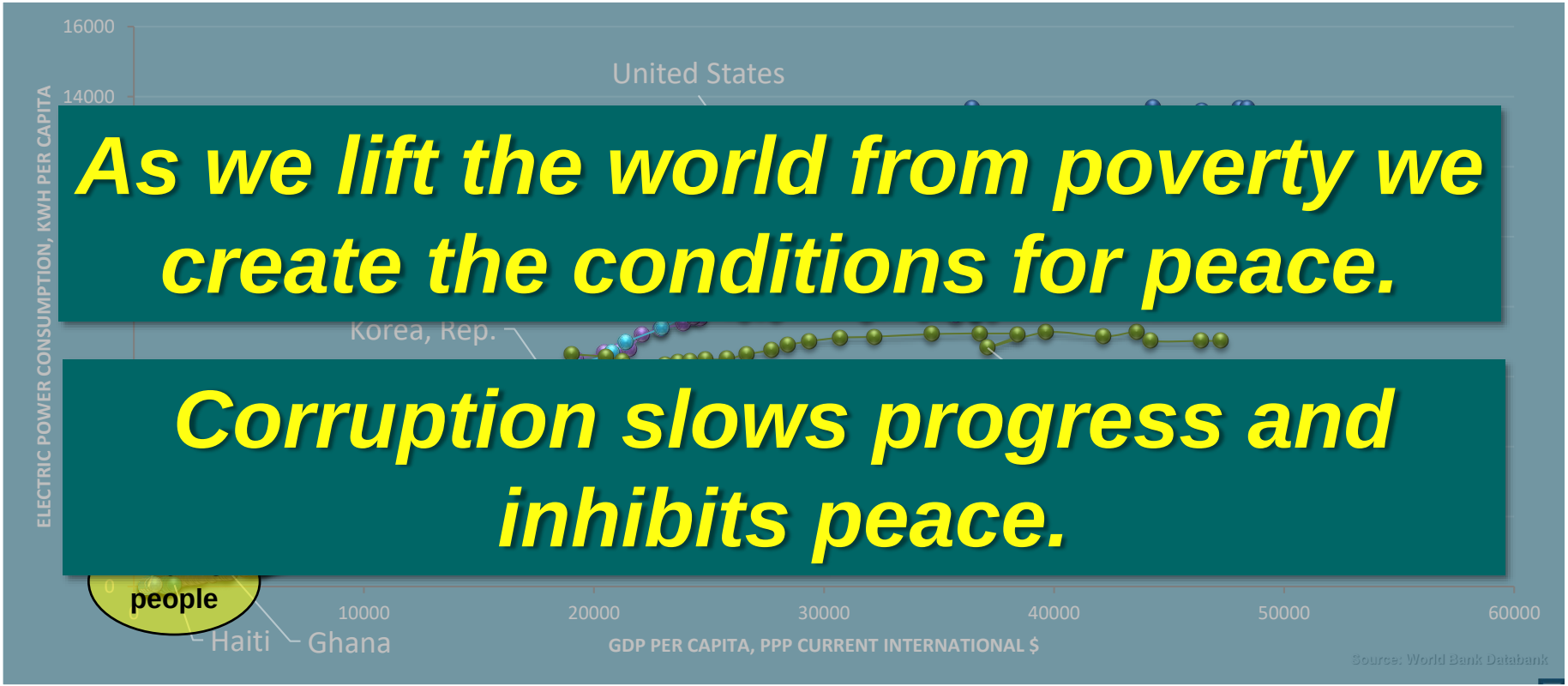

As we lift the world from poverty we create the conditions for peace.

Corruption slows progress and inhibits peace.

1990 '92 '93 '94 '95 '96 '97 '98 '99 2000 '01 '02 '03 '04 '05 '06 '07 '08 '09 2010 '11 '12 '13

Limited Access to Electricity Propagates Inequality

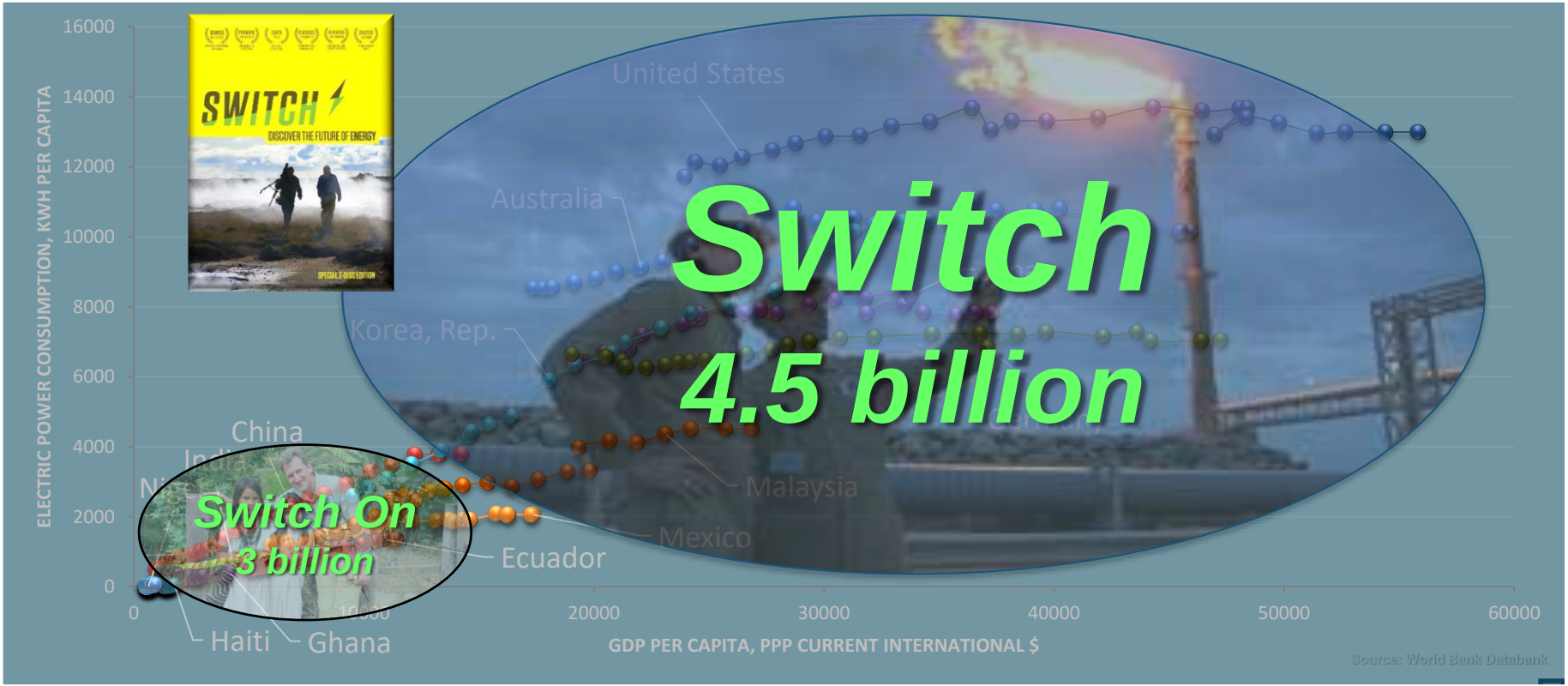

1990 '92 '93 '94 '95 '96 '97 '98 '99 2000 '01 '02 '03 '04 '05 '06 '07 '08 '09 2010 '11 '12 '13

It's Time to Power the People



Photos Tinker, Ecuador, 2017

Outline

- Energy Security
- Energy Poverty
- Energy Reality

BEG Shale Resource, Reserve and Production Studies

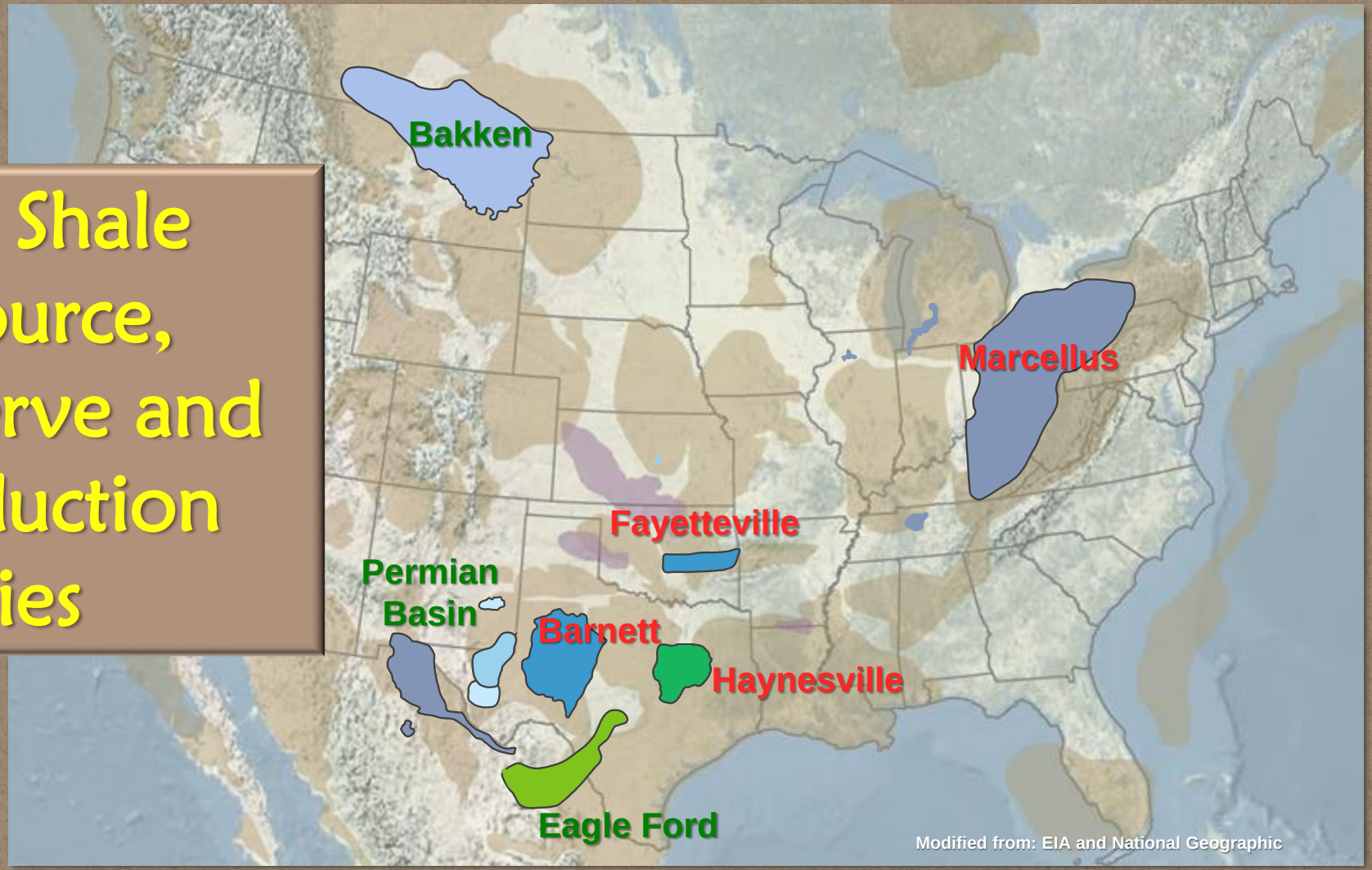

BEG Shale Resources and
Reserves Team

U.S. Shale Gas

Tinker 2017

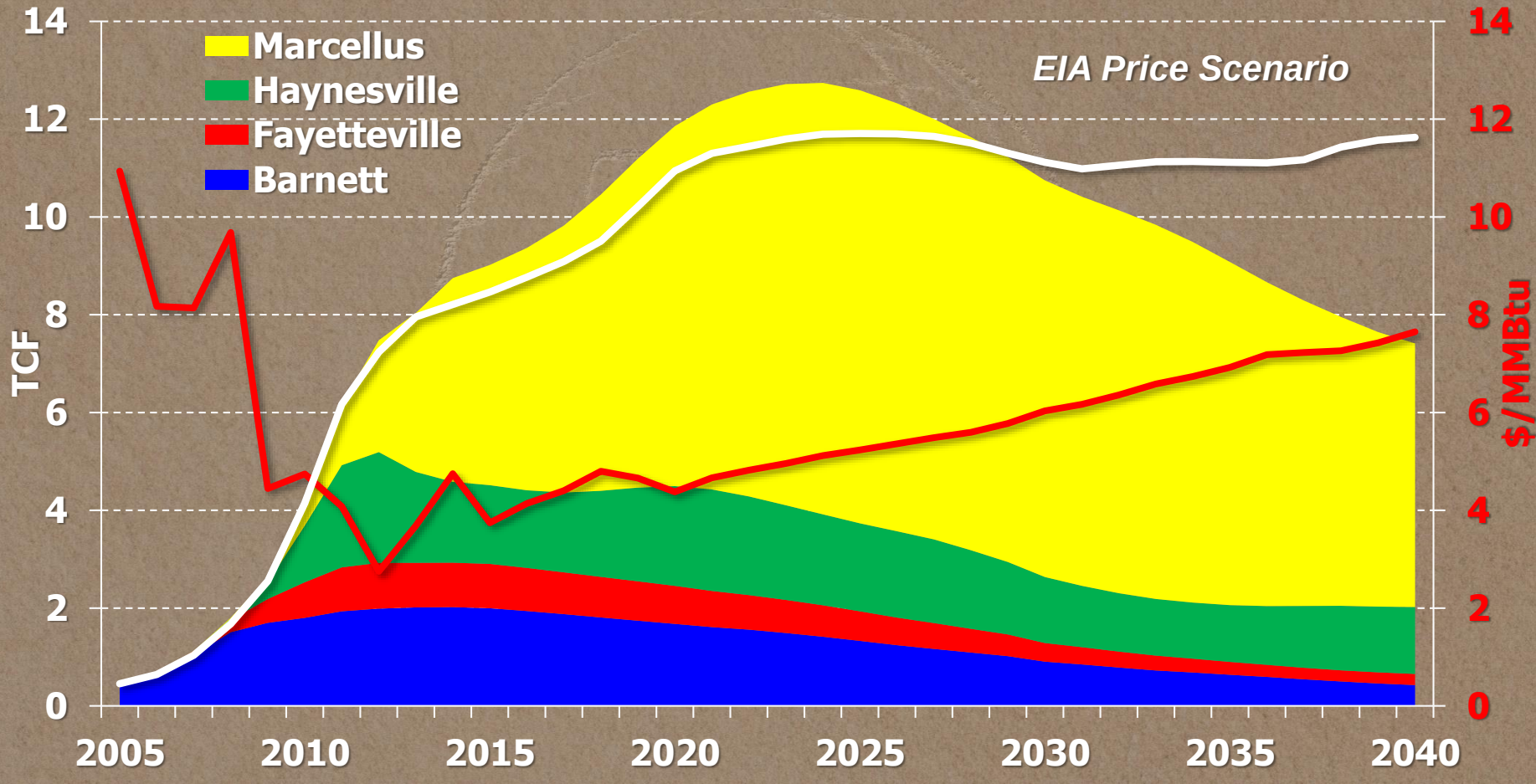

U.S. Shale Gas

Formation	$OGIP_{free}$	Prod. through 2045			RF (P50)
		P10	P50	P90	
Barnett	444	37	47	57	11%
Fayetteville	80	12	18	23	23%
Haynesville	489	33	52	72	11%
Marcellus	2071	-	183	-	9%
	3084		**300**		**10%**

U.S. Electric Generation Shares (2005-15)

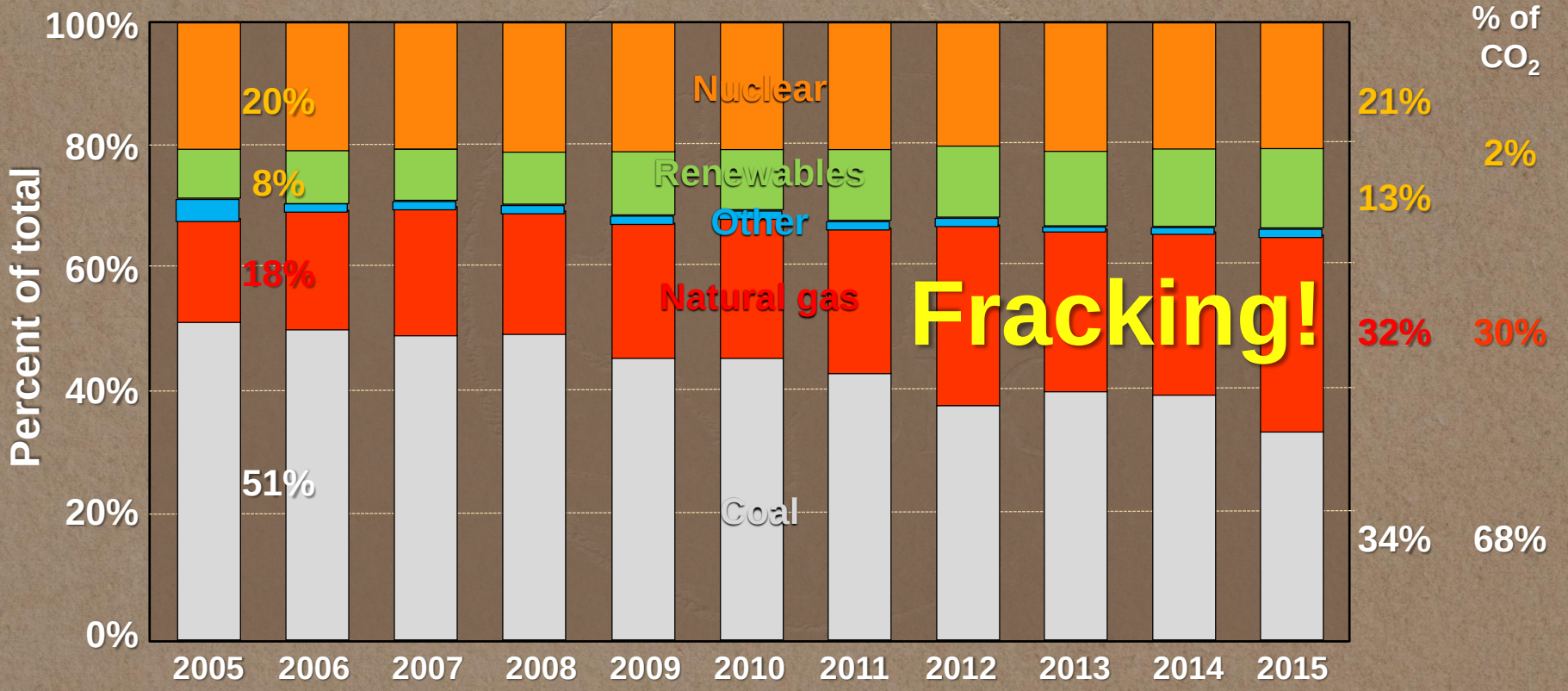

Source: EIA

Electric Power Sector U.S. Carbon Dioxide Emissions

Tinker 2017

Clean Power Plan

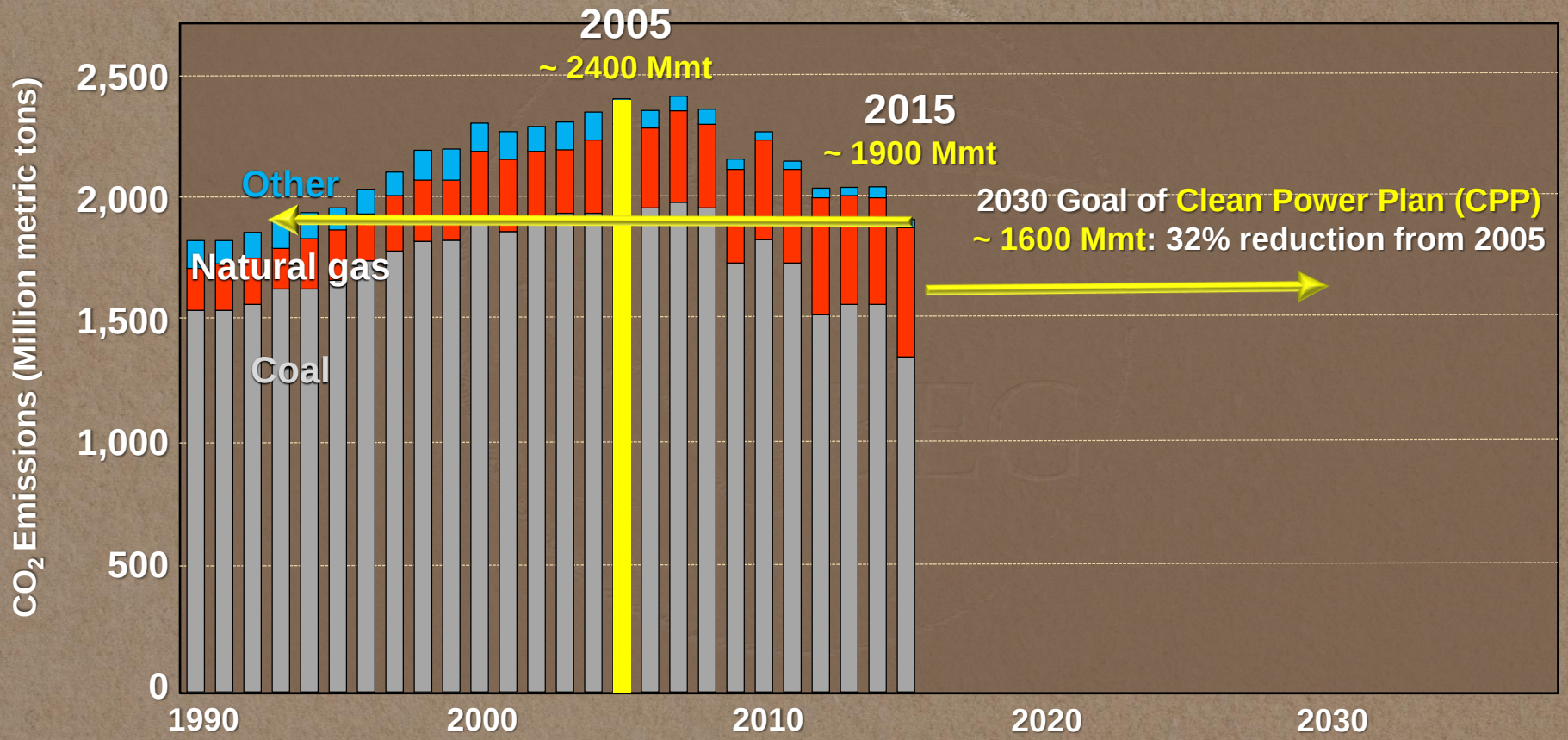

Source: EIA

QAe4743

Electric Power Sector U.S. Carbon Dioxide Emissions

Tinker 2017

Clean Power Plan

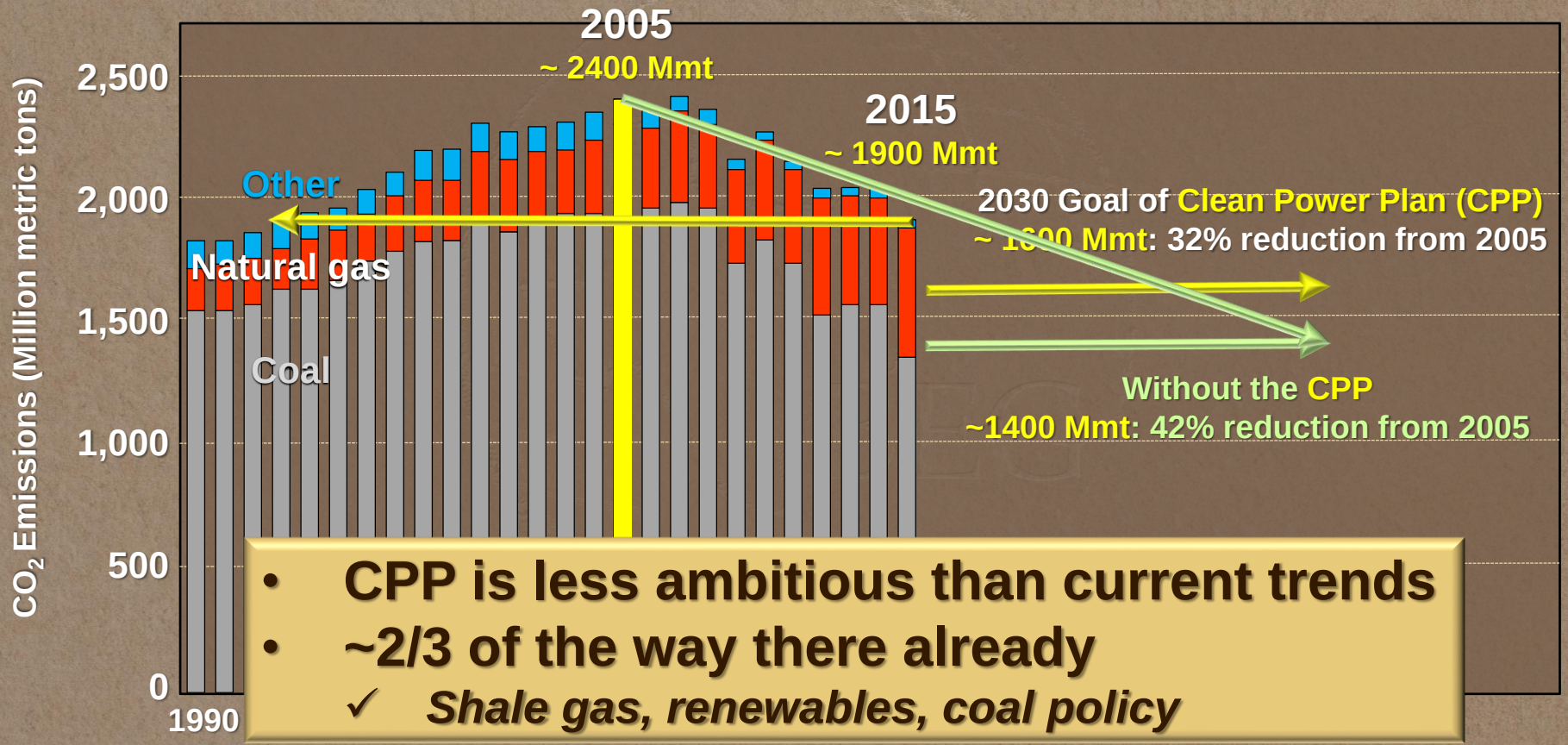

- CPP is less ambitious than current trends
- ~2/3 of the way there already
  - ✓ *Shale gas, renewables, coal policy*

Source: EIA

QAe4743

US Energy Mix

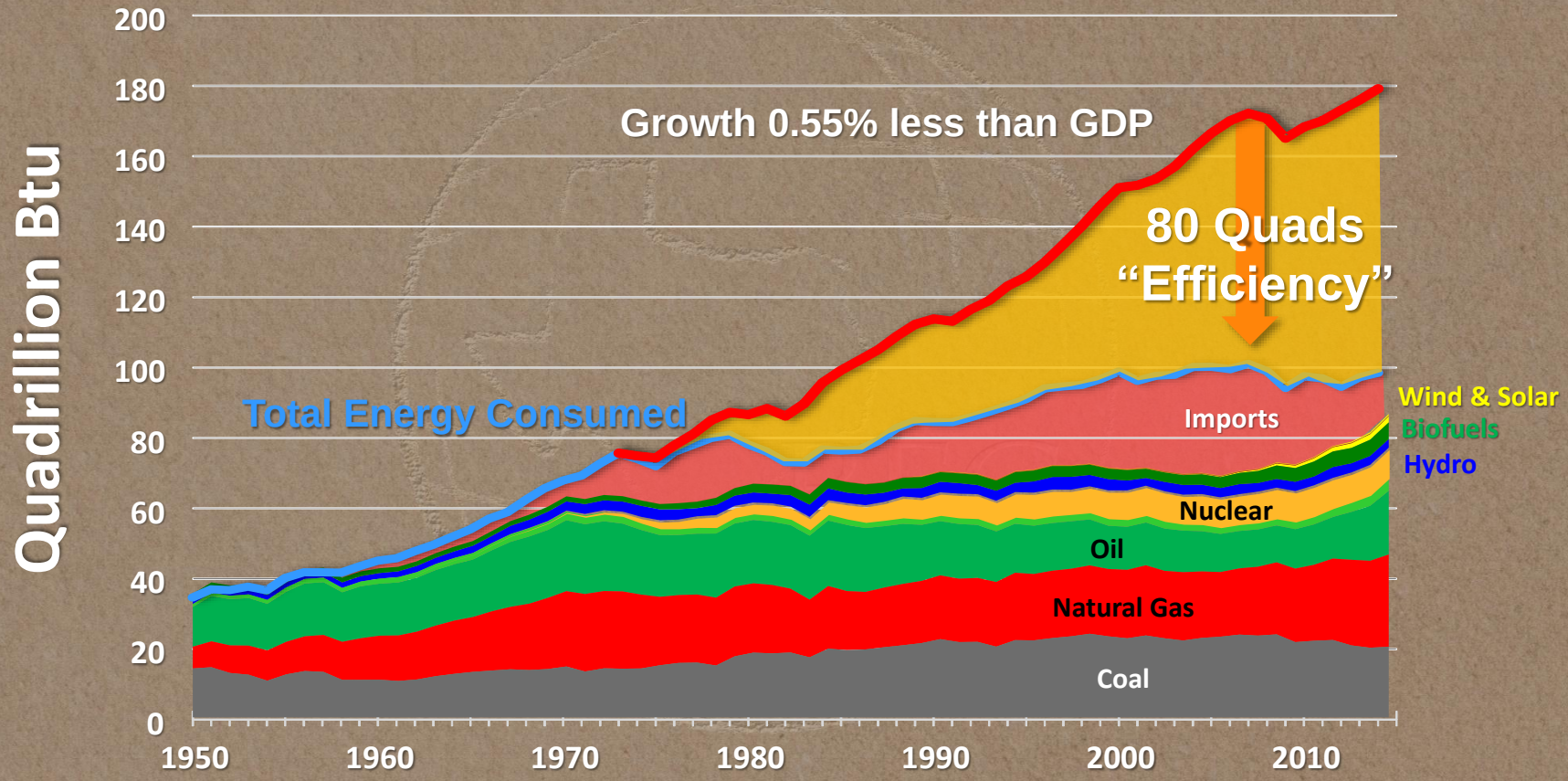

After Jim Sweeney, 2015. Data: EIA, Monthly Energy Review

Energy

U. S. Energy Demand

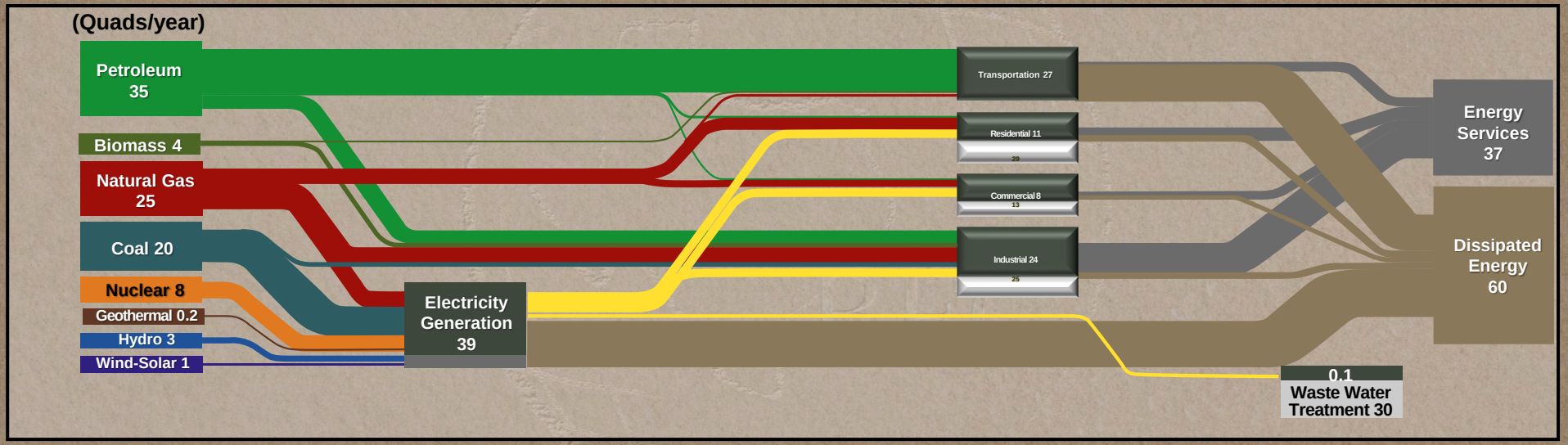

The Water-Energy Nexus: Challenges and Opportunities, DOE, July, 2014

Tinker 2017

The Global Energy Mix

Million Tonnes Oil Equivalent

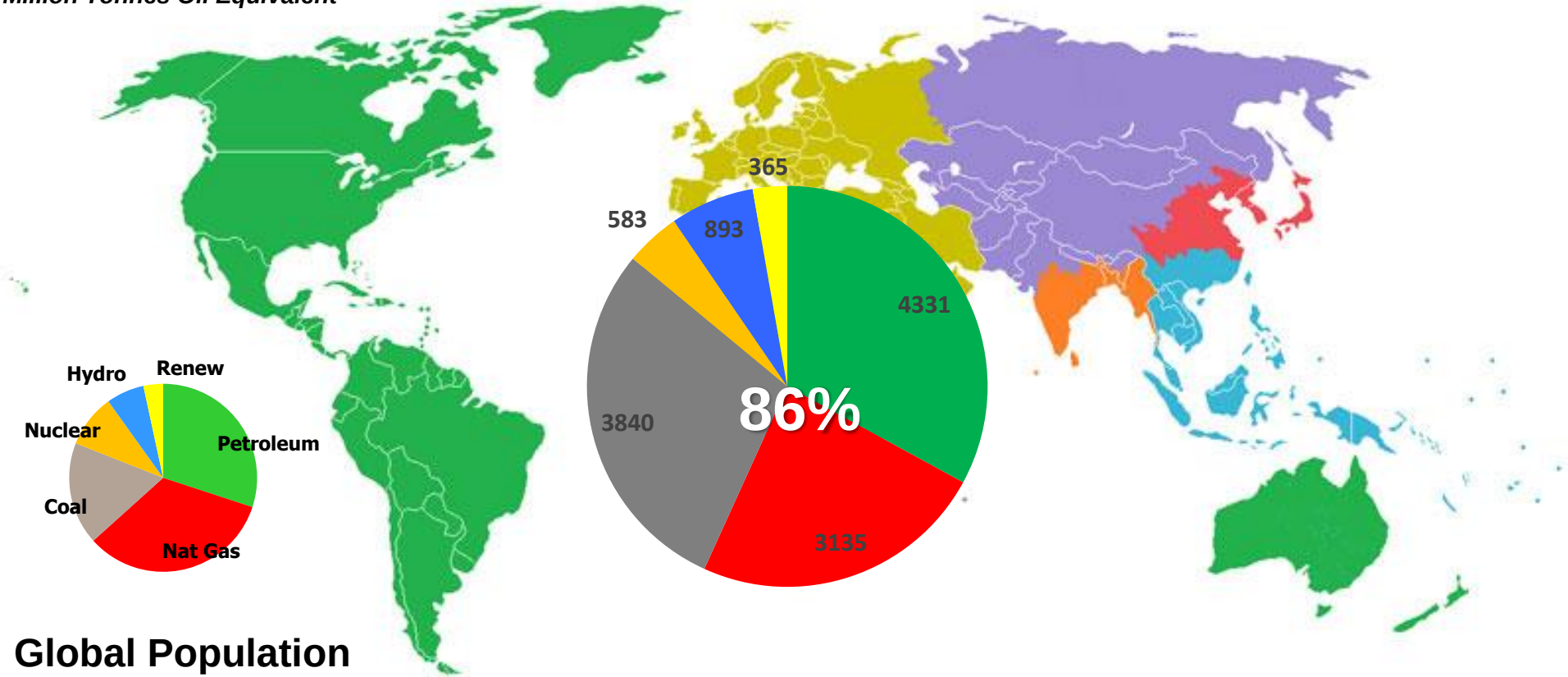

Global Population

Each color on the map represents ~ 1 billion people

Data: BP Statistical View of World Energy (2016)

The Global Energy Mix

Tinker 2017

Million Tonnes Oil Equivalent

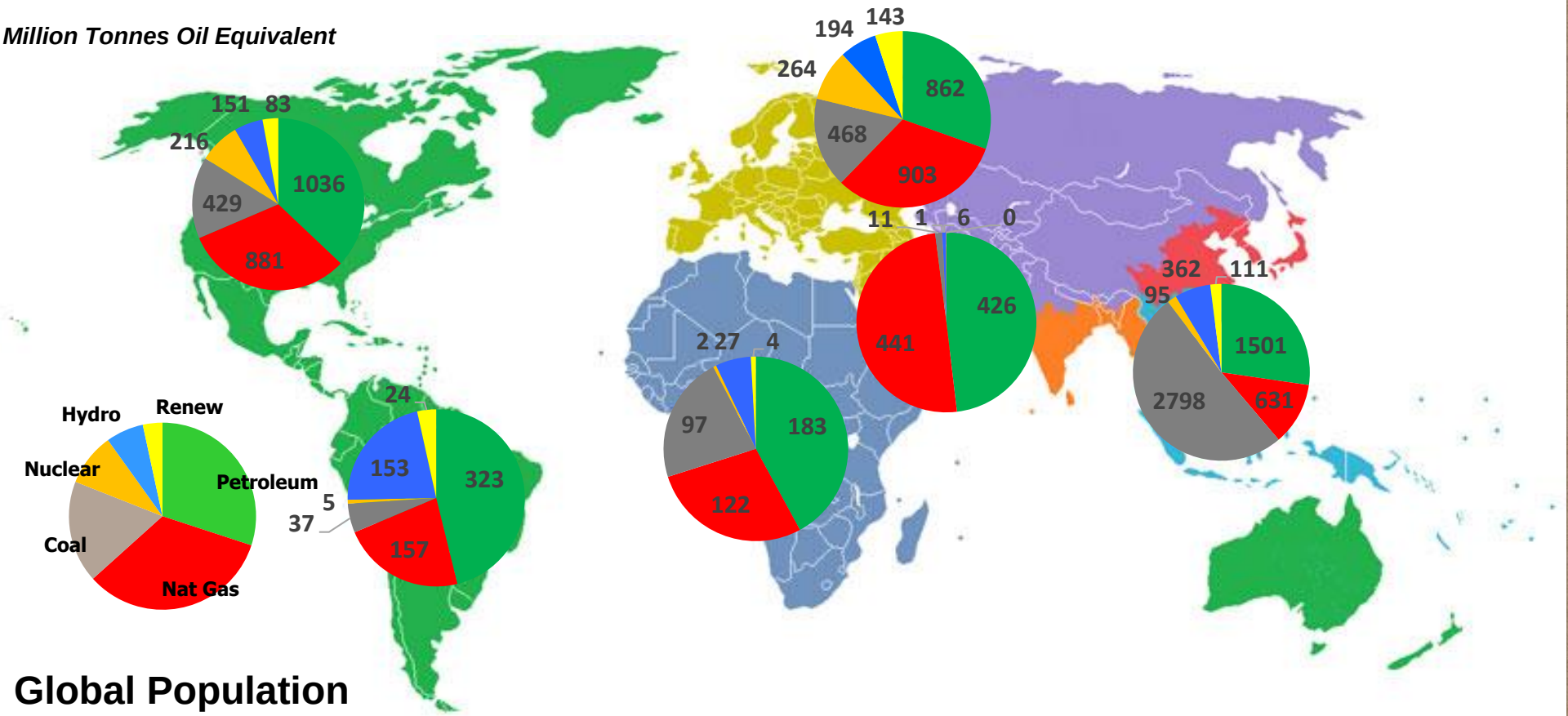

Global Population

Each color on the map represents ~ 1 billion people

Data: BP Statistical View of World Energy (2016)

The Global Energy Mix Scaled to Consumption

Tinker 2017

Million Tonnes Oil Equivalent

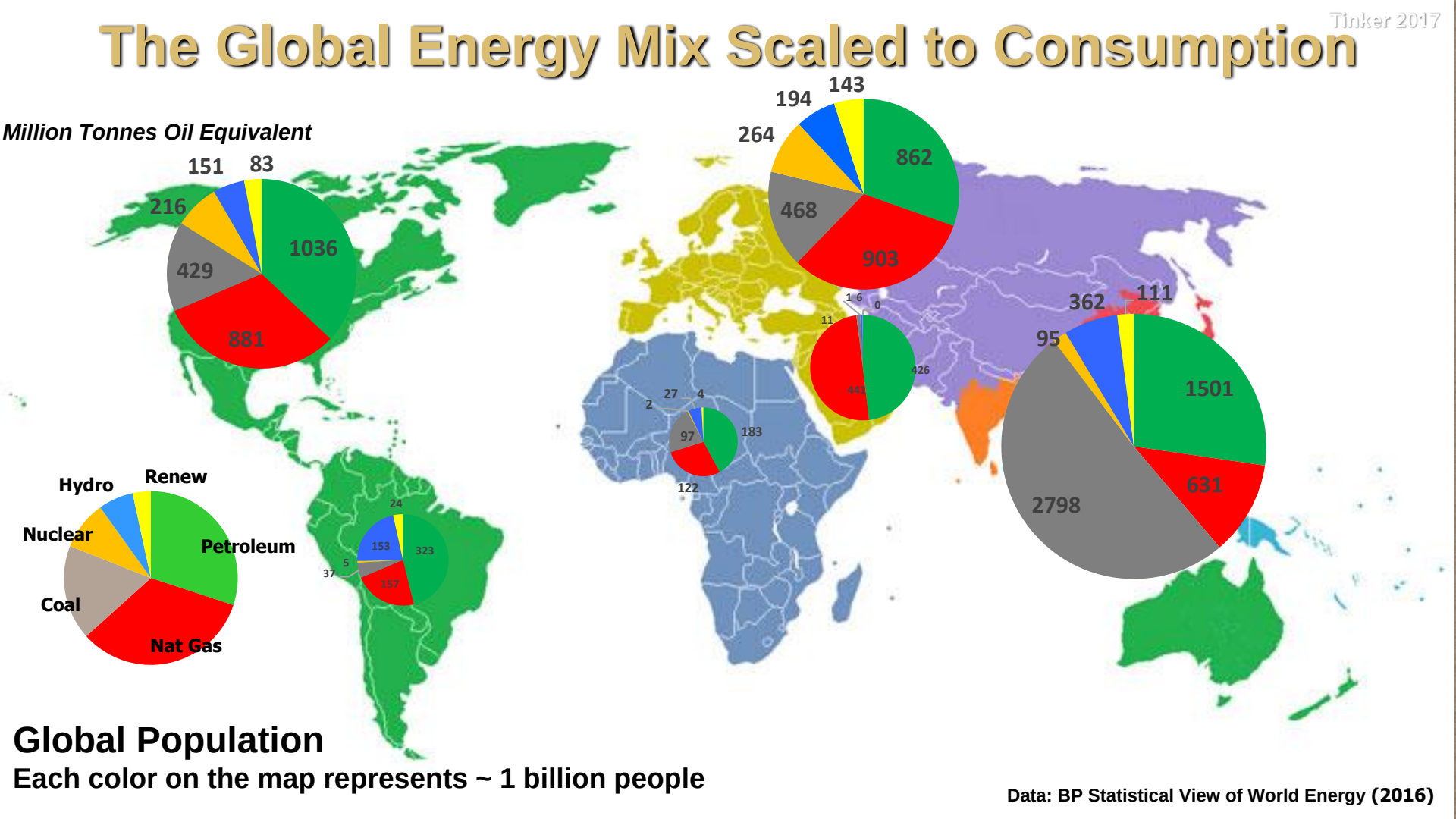

Global Population

Each color on the map represents ~ 1 billion people

Data: BP Statistical View of World Energy (2016)

Global Energy Mix

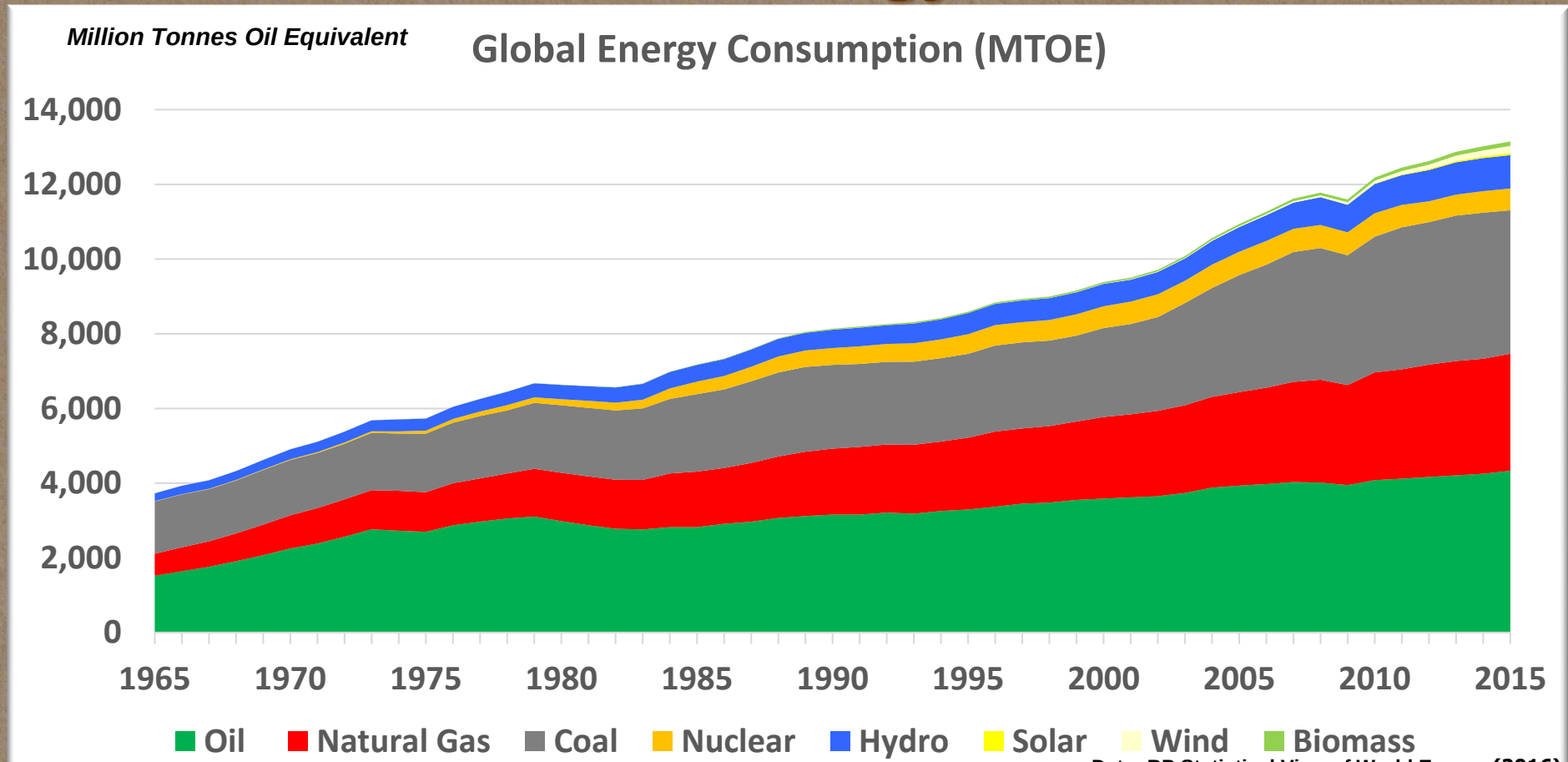

CO_2 Emissions

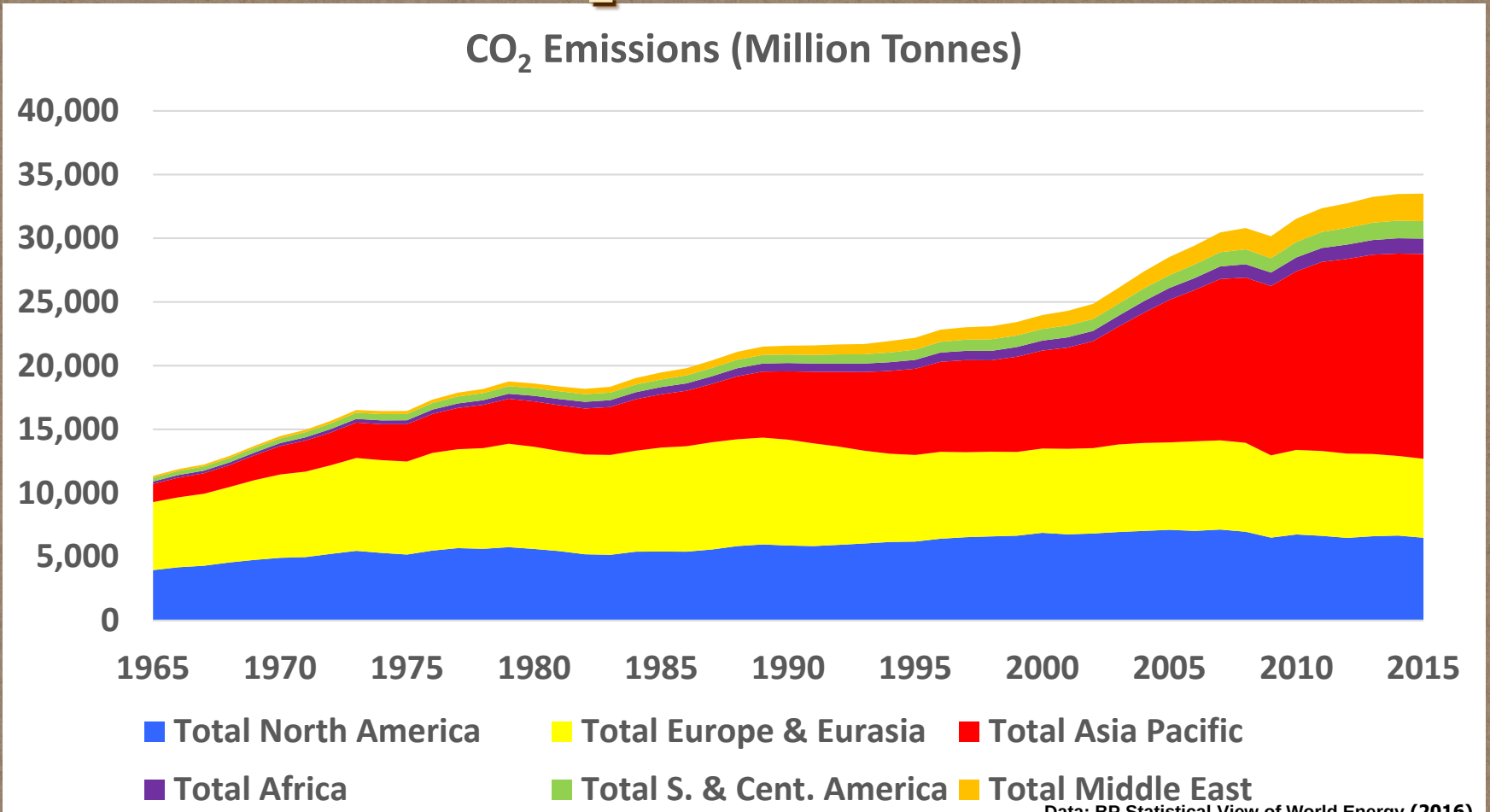

Data: BP Statistical View of World Energy (2016)

Global Energy Mix

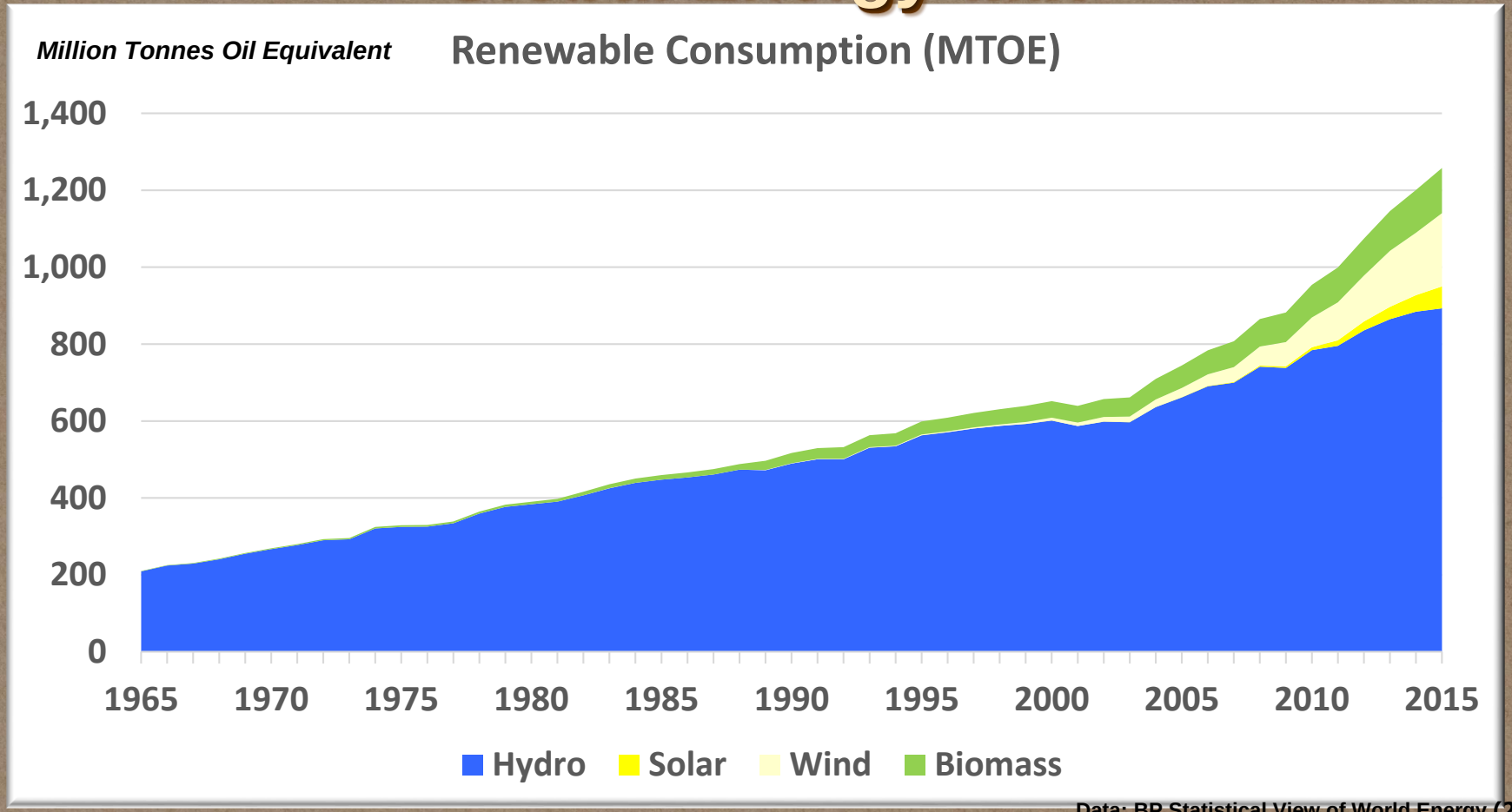

Data: BP Statistical View of World Energy (2016)

Global Energy Mix

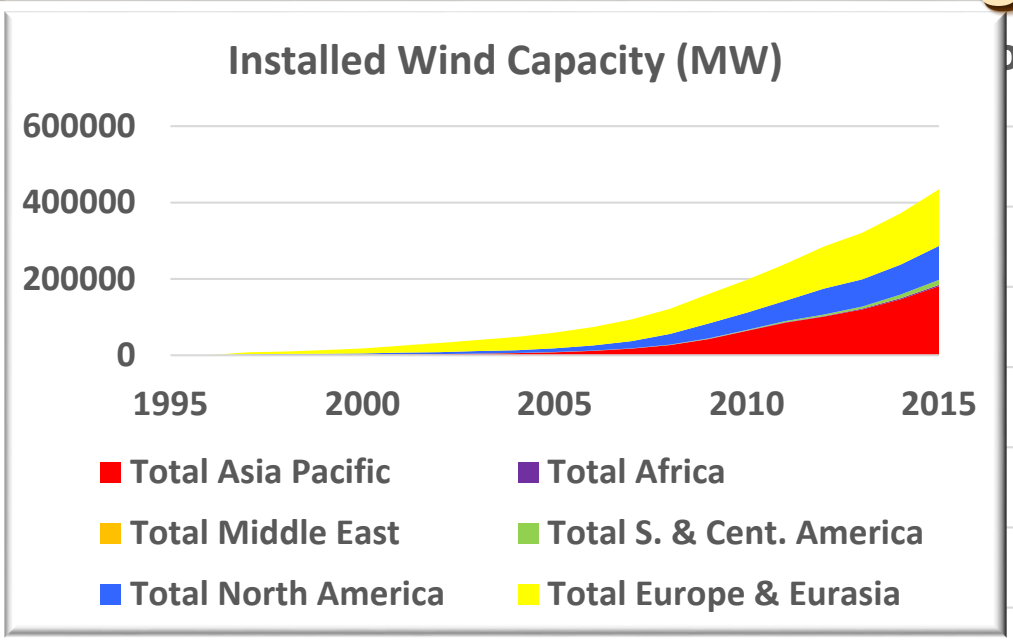

Data: BP Statistical View of World Energy (2016)

Global Energy Mix

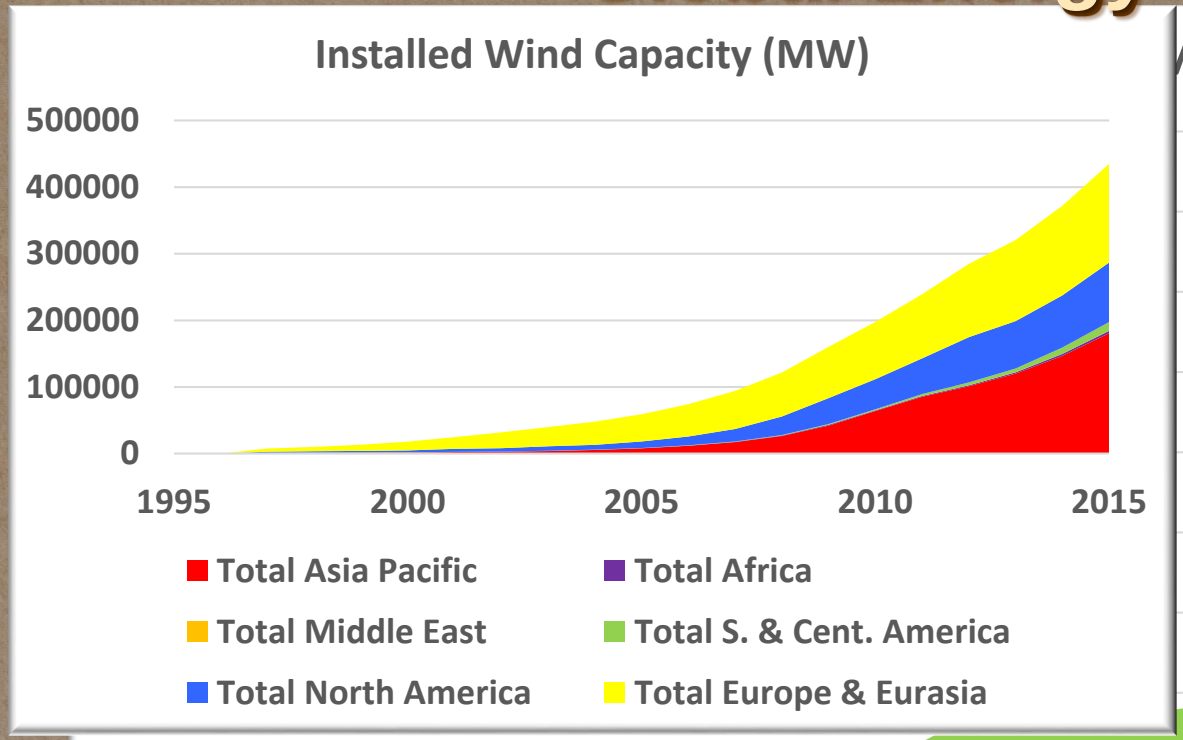

Data: BP Statistical View of World Energy (2016)

Tinker 2017

Global Energy Mix

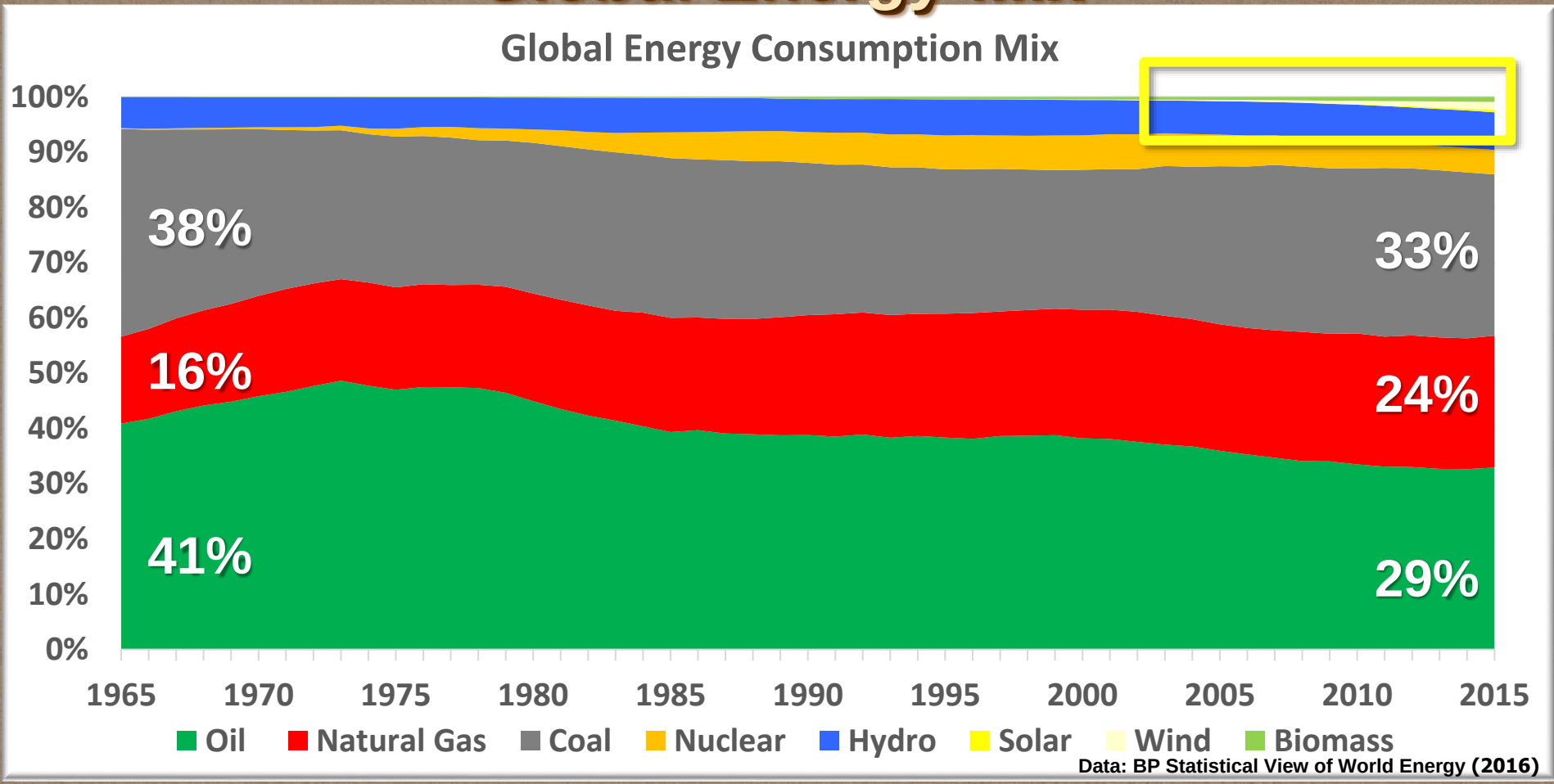

Total Energy Supply

Global Investment 2015 USD $ Billion

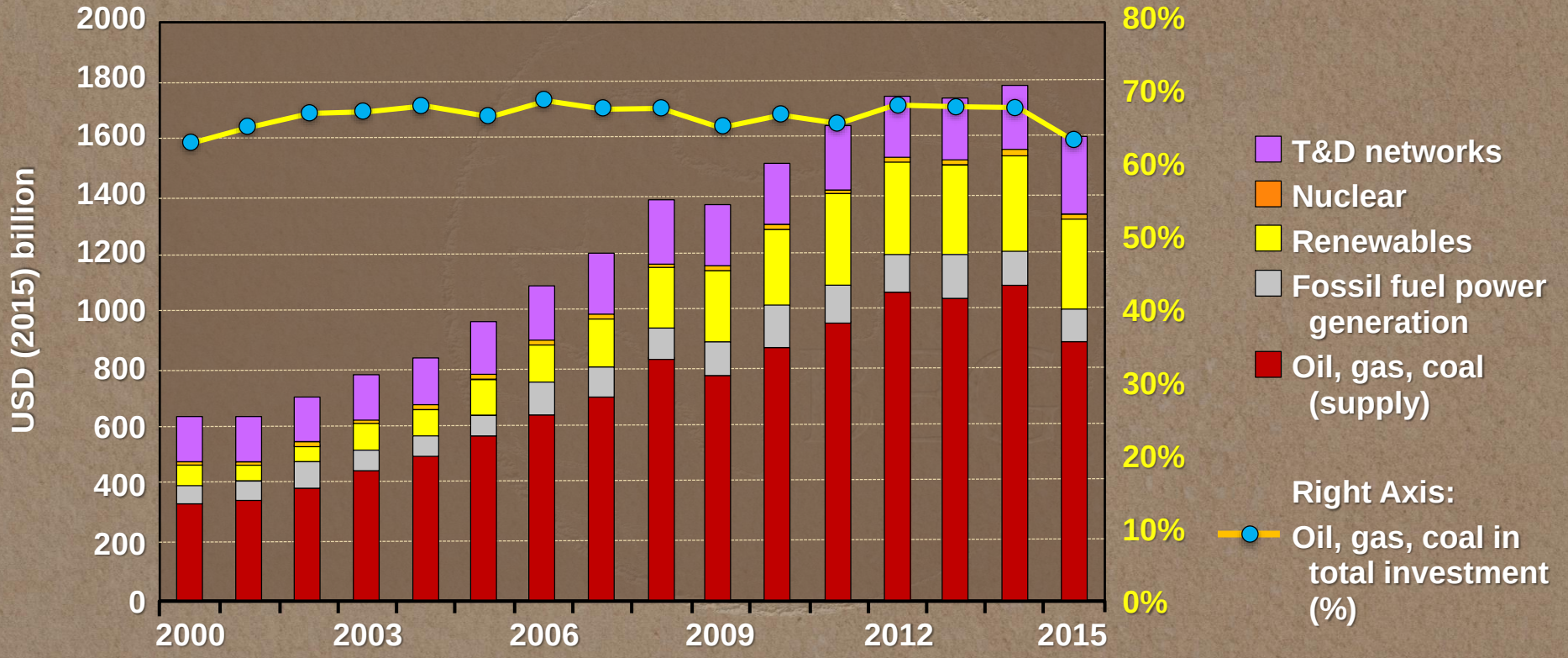

Source: IEA – World Energy Investment, 2016

Total Energy Supply

Global Investment 2015 USD $ Billion

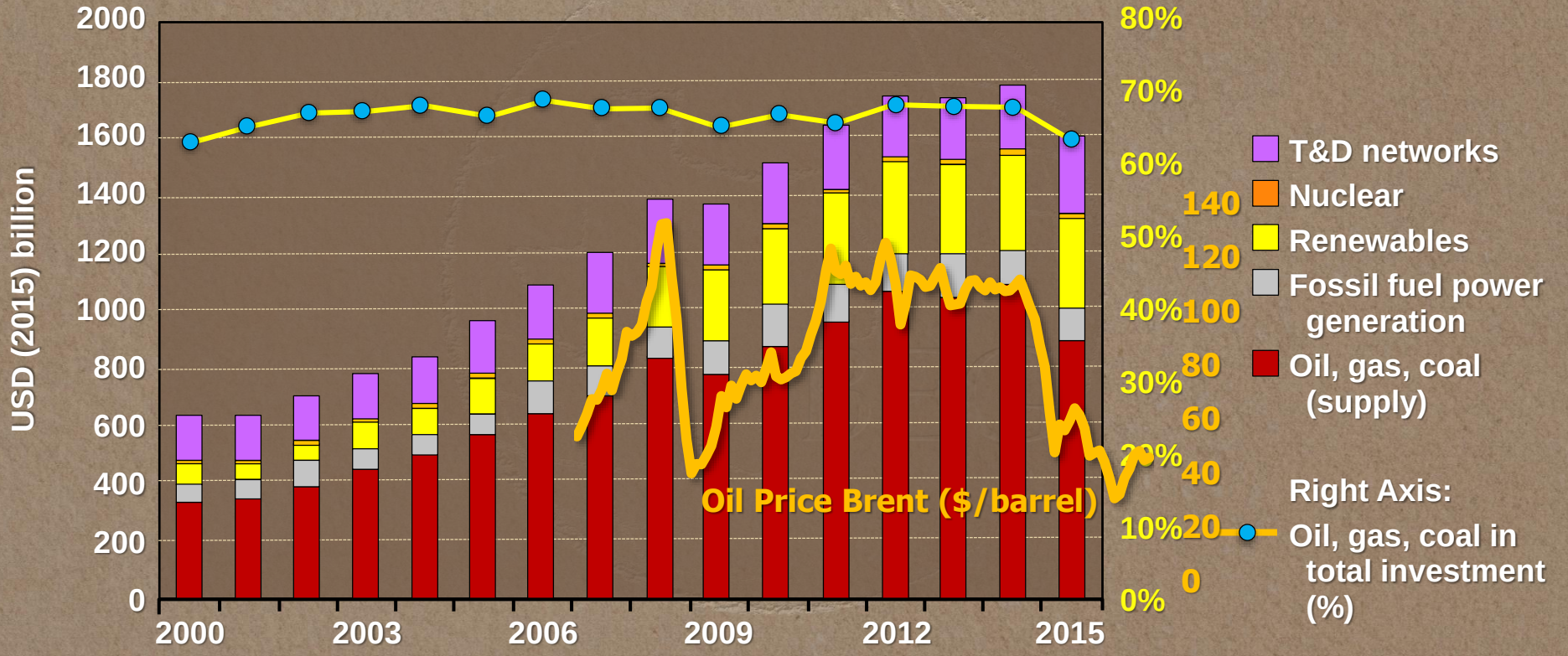

Source: IEA – World Energy Investment, 2016

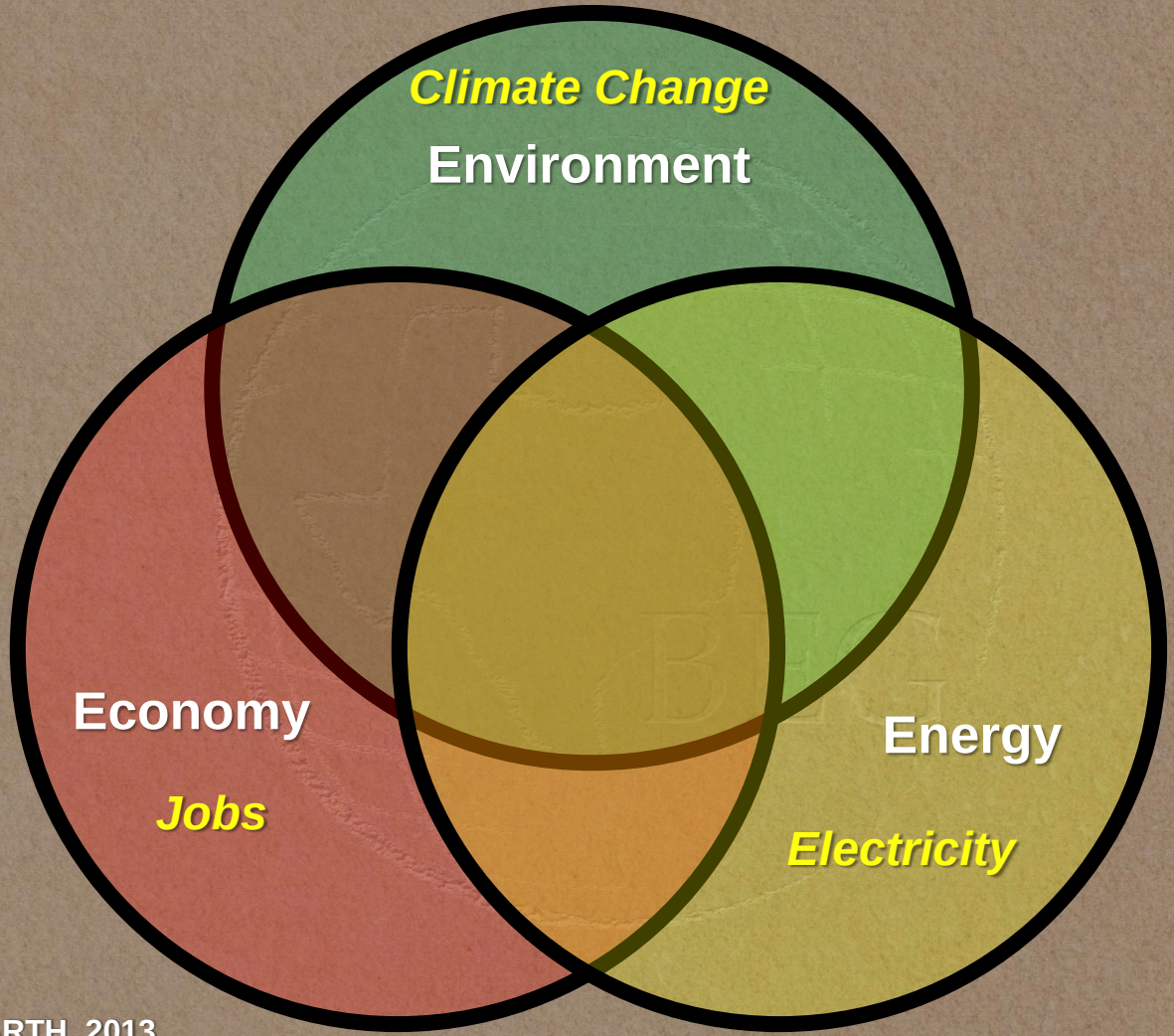

Source: Tinker, EARTH, 2013

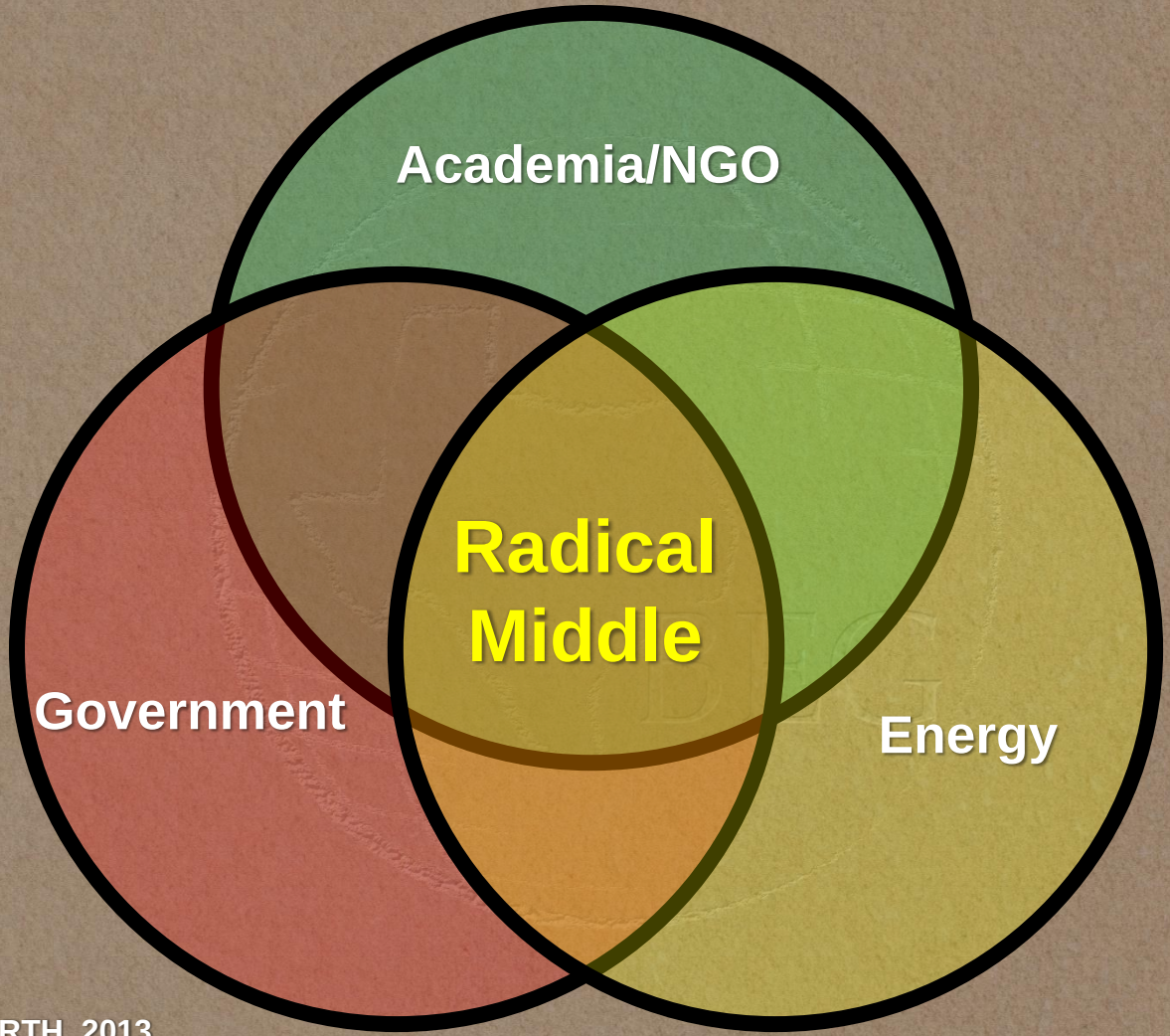

Source: Tinker, EARTH, 2013

Tinker's Top Take Away's

1. Oil, natural gas and coal are secure sources of energy, and will remain vital well into the 21st Century.
2. Secure energy is required to lift humanity from poverty.
3. Secure energy—affordable, available, reliable, sustainable—underpins economies and is required for investment in the environment.


Thanks!

7

Stoneburner Richard K., 2017, The Eagle Ford Shale Field in the Gulf Coast Basin of South Texas, U.S.A.: A "Perfect" Unconventional Giant Oil Field, *in* R. K. Merrill and C. A. Sternbach, eds., Giant Fields of the Decade 2000–2010: AAPG Memoir 113, p. 121–140.

The Eagle Ford Shale Field in the Gulf Coast Basin of South Texas, U.S.A.: A "Perfect" Unconventional Giant Oil Field

Richard K. Stoneburner

Pine Brook Partners, 1301 McKinney Street, Suite 3550, Houston, Texas, U.S.A. 77010 (e-mail: dstoneburner@pinebrookpartners.com)

ABSTRACT

The Eagle Ford shale Formation (Upper Cretaceous) in the Gulf Coast basin of south Texas was first commercially produced in 2008 and has since achieved production and reserve growth that is virtually unprecedented in the history of onshore North American oil and gas development. Through December 2014, the field had cumulative production of approximately 1.1 billion bbl of oil and condensate and 4.8 trillion cubic ft of natural gas (TCFG). Average daily production during 2014 was approximately 1.3 million bbl of oil and condensate per day and 4.9 billion cubic ft per day of natural gas (BCFGD). The horizontal rig count in October 2014 was approximately 200, resulting in approximately 300 wells drilled per month (RigData). While the entire resource potential of the Eagle Ford is still quite subjective, it has been estimated to be as high 25 to 30 billion bbl of oil equivalent (BBOE).

The Eagle Ford shale covers a vast area that spans approximately 7 million ac (2,832,799 ha) of continuous prospective reservoir and therefore should be considered as one oil and gas accumulation, or field. As a result of the aerial extent of the field occurring at depths ranging from approximately 5000 ft (1524 m) to the north to approximately 13,000 ft (3962 m) to the south, the product mix covers the entire spectrum from low gravity–low gas oil-ratio oil to dry gas, and everything in between.

The Eagle Ford Formation lies above the Buda limestone and beneath the Austin chalk over the entire field area. The formation varies in thickness from approximately 250 ft (76 m) to as much as 600 ft (183 m) and is composed of a variety of facies. The primary reservoir facies, herein referred to as the Hawkville facies, is the primary reservoir and is located near the base of the formation. The Hawkville facies, named for the field area located in LaSalle and McMullen Counties where the net reservoir thickness is found to be in excess of 300 ft (91 m), is a calcareous mudstone that was deposited in an anoxic environment as part of the Cretaceous seaway that traversed north to south through west-central United States and Canada. Long known as a source for oil and gas production from other Cretaceous reservoirs such as the Buda, Austin chalk, Olmos, and others, the Eagle Ford has moderate to high total organic

Copyright ©2017 by The American Association of Petroleum Geologists.
DOI:10.1306/13572003M1133682

content (TOC) ranging from 3 to 5% and thermal maturities based on vitronite reflectance ranging from approximately 0.7 to 1.3.

Operationally, the field has proven to be one that has been relatively benign from a drilling perspective. The Tertiary is at the surface and is a sand-dominated section extending to as deep as approximately 8000 ft (2438 m) near the down dip limits of the field and results in excellent rates of penetration. The Cretaceous Midway, Taylor, and Austin formations also provide consistent drilling conditions. Wells in the field that are in the measured depth range of 15,000 to 18,000 ft (4572 to 5486 m) are commonly drilled from spud to total depth in 8 to 12 days or less. Completion operations are similarly advantaged. The reservoir is extremely brittle and is very receptive to the high-rate hydraulic fracturing processes that are necessary to establish commercial production, with a very low percentage of screened out fracture stimulation stages. Production operations vary widely based on product type, gas-to-oil ratio, and the volatility of the liquid. However, to date, there have not been material changes in the gas-to-oil ratio of the producing wells that would suggest degradation of ultimate recoveries based on bubble point or dew point effects.

The regulatory and community effects have also been relatively benign in terms of impediments to the development of the field. The state of Texas and the oil and gas industry have a long history of working in a collaborative manner. Very early in the field's history, the Eagle Task Force, led by railroad commissioner David Porter, was organized with members from the state bureaucracy, industry, and community with the intent of promoting economic activity, establishing best practices across the play, and reacting to issues that affected the constituencies within the group. One of the most significant issues is water usage, which is a common issue in all unconventional development that utilizes isolated multistage hydraulic fracturing. One of the benefits to the field is the presence of the Carrizo aquifer, which underlies a vast majority of the field. The Carrizo is a fresh-water aquifer that has proven to be an excellent source of water without experiencing material depletion, primarily because of its extremely large amount of available water and because it is actively replenished except in times of severe drought.

HISTORY OF UNCONVENTIONAL SHALE EXPLORATION AND DEVELOPMENT

A discussion of unconventional shale exploration can start in only one place, and that is the Barnett shale in the Fort Worth Basin. Likewise, there is only one person that should be involved in that initial discussion, and that is George Mitchell.

George's company, Mitchell Energy, had been exploiting the Fort Worth Basin, in an area specifically known as the Boonsville Bend Conglomerate field, for over three decades when he made the decision to test the Barnett shale to determine if it could produce hydrocarbons commercially. The decision to do so was a combination of both economic necessity and scientific curiosity. The necessity aspect was a function of a depleting natural gas asset across Wise and Denton Counties in conjunction with a contractual obligation to deliver gas under a long-term contract. The scientific aspect was a function of George Mitchell being a geologic visionary who became convinced, and maybe a bit obsessed, that the Barnett could become a commercial gas reservoir.

The initial test of the Barnett was in 1981 when Mitchell completed the C.W. Slay 1 in Wise County. The well, fracture stimulated with nitrogen foam, was noncommercial but did validate the most basic premise, which was that natural gas could be produced from the Barnett.

It has been estimated that over the next two decades Mitchell Energy spent approximately $250 million drilling and completing Barnett shale wells and was woefully short of getting a return on that investment. The biggest breakthrough for Mitchell came in 1997, when a Mitchell Energy petroleum engineer, Nick Steinsberger, suggested that a slickwater frac might be the most effective means of stimulating the reservoir (Gold, 2014). Slickwater fracs had been widely used in other conventional low-permeability reservoirs such as the Cotton valley sands in east Texas but had not been tried yet in the Barnett. The result was both a dramatic increase in productivity and a significant decrease in total well cost. Prior to this time, Mitchell had a monopoly on the Barnett. However, it became apparent to the industry that a new play had been proven and by 2001, there were more wells drilled by other operators than by Mitchell.

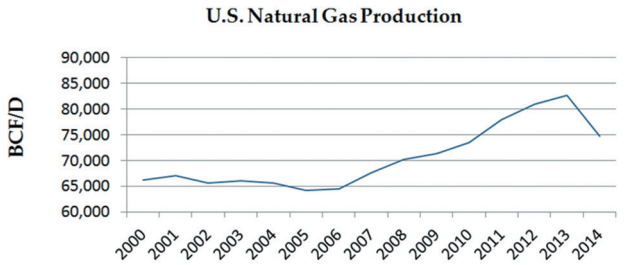

Figure 1. U.S. natural gas production vs. time (2000–2014) (EIA, 2015).

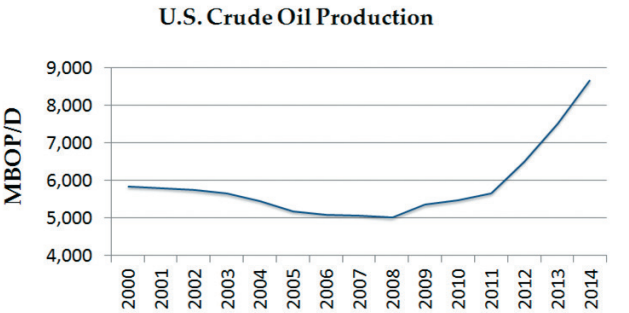

Figure 2. U.S. crude oil production vs. time (2000–2014) (EIA, 2015).

In 2002, Devon Energy became convinced that the Barnett shale was for real and acquired Mitchell Energy for $3.5 billion. Shortly after the acquisition, Devon concluded that horizontal drilling should dramatically improve the commerciality of the play due to the low permeability of the reservoir and the cultural challenges of drilling in the play's largely urban area. Conceptually, they were entirely correct. However, the challenge became stimulating the horizontal lateral and having confidence in both where the stimulation went and how much of the wellbore was actually stimulated to the point of achieving flow.

After several years of trying a wide variety of completion techniques, the concept of cementing casing in the lateral and employing the isolated multistage hydraulic fracturing method of completion, often referred to as plug and perf, was proven. Not only did the results in the Barnett improve dramatically but it became the catalyst for successful exploration and development of other shale gas reservoirs.

Figure 1 is a graph showing total U.S.A. natural gas production from 2002 through 2014 and the New York Mercantile Exchange (NYMEX) price for natural gas. The growth from 2006 until 2009, which saw an unprecedented collapse of natural gas prices, was coincident with the advent of isolated multistage hydraulic fracturing in horizontally drilled shale reservoirs. Even though growth has diminished dramatically over the past 5 years, the resource is in place and can provide the country adequate supplies of natural gas for many decades to come.

While natural gas exploration peaked from 2006 through 2009, the industry began taking the lessons learned from shale gas exploration and began exploring for more liquids-rich shale reservoirs. Beginning with the Bakken and Eagle Ford and followed by the Niobrara, Permian, and others, the growth of U.S.A. oil production from oil and condensate shale reservoirs has proven to be equally as prolific as that from shale gas reservoirs. Figure 2 displays the growth in oil and condensate production from 2004 to 2014, whereby total daily production increased by ~100%.

The impact of the shale reservoirs, both oil and natural gas, can be seen not only by the previous graphs but also by the ranking of the most prolific producing fields in the U.S.A. Figure 3 is the ranking of the top 10 natural gas fields of 2014 by annual production, and Figure 4

2013 Rank	Field Name	Location	2013 Proved Reserves	2013 Estimated Production	Discovery Year
1	MARCELLUS SHALE AREA	PA & WV	-	2,836,043	2008
2	NEWARK EAST (BARNETT SHALE)	TX	-	1,951,750	1981
3	B-43 AREA (FAYETTEVILLE SHALE)	AR	-	1,025,153	2005
4	SAN JUAN BASIN GAS AREA	CO & NM	-	1,024,962	1927
5	HAYNESVILLE SHALE UNIT	LA	-	1,425,661	2008
6	PINEDALE	WY	-	568,153	1955
7	CARTHAGE	TX	-	653,093	1936
8	JONAH	WY	-	239,233	1977
9	WATTENBERG	CO	-	304,540	1970
10	PRUDHOE BAY	AK	-	147,554	1967
	Group 1 -10 Volume Subtotal		**144,614,724**	**10,176,142**	

Figure 3. Top 10 U.S. natural gas fields by 2013 total production (EIA, 2015).

2013 Rank	Field Name	Location	2013 Proved Reserves	2013 Estimated Production	Discovery Year
1	EAGLEVILLE (EAGLE FORD SHALE)	TX	-	238,050	2009
2	SPRABERRY TREND AREA	TX	-	99,787	1949
3	PRUDHOE BAY	AK	-	79,080	1967
4	WATTENBERG	CO	-	47,259	1970
5	BRISCOE RANCH (EAGLE FORD SHALE)	TX	-	62,046	1962
6	KUPARUK RIVER	AK	-	29,487	1969
7	MISSISSIPPI CANYON BLK 778 (THUNDER HORSE)	Fed Gulf	-	15,833	1999
8	WASSON	TX	-	19,996	1937
9	BELRIDGE SOUTH	CA	-	23,703	1911
10	GREEN CANYON BLK 699 (ATLANTIS)	Fed Gulf	-	27,346	1998
	Group 1-10 Volume Subtotal		**9,659,688**	**642,587**	

Figure 4. Top 10 U.S. oil fields by 2013 total production (EIA, 2015).

is the ranking of the top 10 oil fields. Five of the top 10 natural gas fields are shale reservoirs, and five of the top 10 oil/condensate reservoirs are shale reservoirs.

HISTORY OF THE EAGLE FORD DISCOVERY AND DEVELOPMENT

It was simply a matter of time before the Eagle Ford shale, a well-known source rock throughout south Texas, became an exploration target. In fact, multiple companies were testing the concept during 2008. The differentiating factors between the companies that were involved in the play appeared to be a combination of completion techniques and geological variability.

Some of the first attempts to establish commercial production from the Eagle Ford were by Newfield and The Exploration Company (TXCO). Newfield completed a 2700 ft (823 m) horizontal lateral well in March 2008 in Maverick County with a small one-stage fracture stimulation that resulted in an initial production rate of 81 thousand cubic feet of gas per day (MCFGD) and 2 barrels of oil per day (BOPD). TXCO completed a 4800 ft (1463 m) open-hole horizontal lateral in May 2008 in Zavala County for 61 BOPD. In July 2008, Cornerstone E & P completed a 1600 ft (488 m) horizontal lateral in Maverick County with a four-stage fracture stimulation that resulted in a rate of 40 BOPD. Anadarko completed two wells in August and October 2008 in Dimmit County: the first was a 2900 ft (884 m) lateral that tested at a rate of 337 MCFGD and 37 BOPD, and the second was a 3100 ft (945 m) lateral that tested at a rate of 192 MCFGD and 43 BOPD. As intimated above, all of these wells suffered from at least one of two limiting factors: inferior reservoir quality and/or thickness and inadequate fracture stimulation.

The exploration of the Eagle Ford by Petrohawk began in January 2008 when Petrohawk's geological staff joined forces with Gregg Robertson, a very successful geologist with a tremendous amount of experience working the Cretaceous trend of south Texas. Together they began a concerted evaluation of the subsurface across the entire Texas Gulf Coast region with the intent of identifying the type of reservoir characteristics in the Eagle Ford that were known to be requisite for a commercially productive shale reservoir.

Within several months of initiating this effort, an area had been identified that was clearly anomalous. Not only was there the appearance of outstanding petrophysical properties in the Eagle Ford, but the thickness of the reservoir was more than anywhere else along the entire trend of the Eagle Ford. Even though the well control was sparse, you can see in Figure 5 a well log with over 250 ft (76 m) of what appeared to be continuous reservoir-quality rock in the Eagle Ford at a depth of approximately 11,000 ft (3353 m).

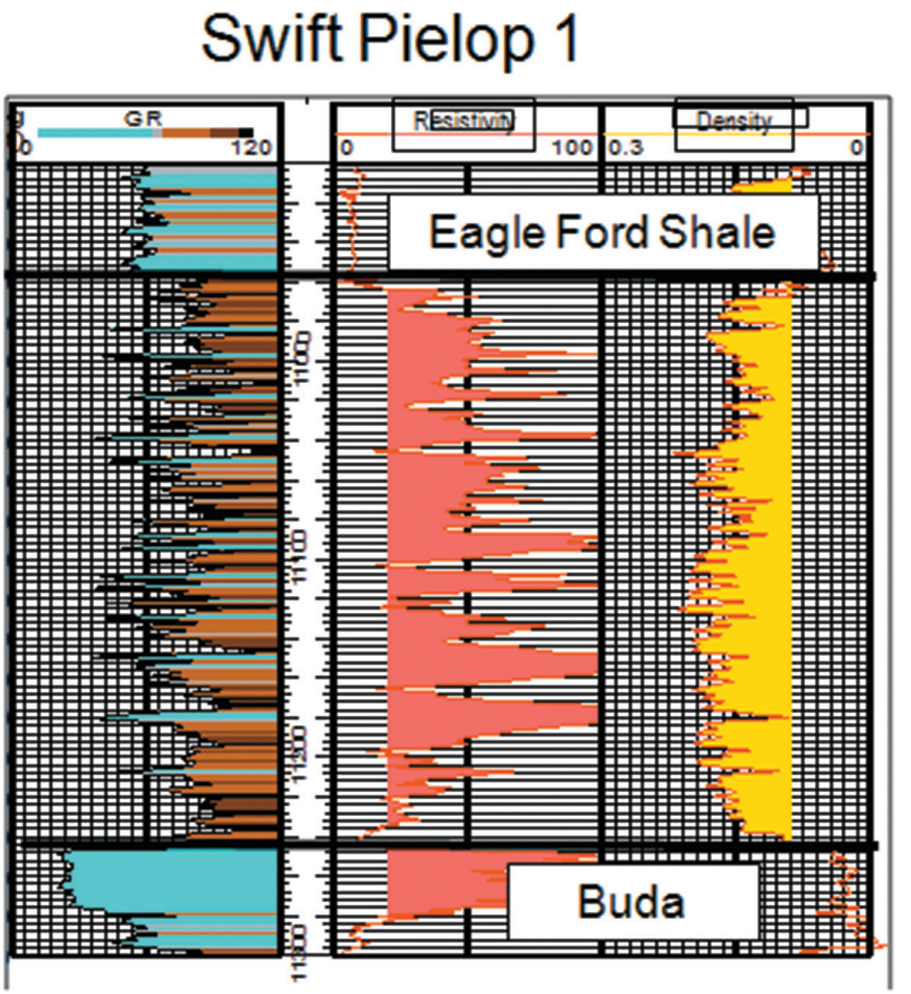

Figure 5. Open-hole log Swift #1 Pielop; LaSalle County, Texas, U.S.A. (Stoneburner, 2014).



Figure 6. Regional map of south Texas with location of Cretaceous shelf margins and key well control (Stoneburner, 2014).

As shown in Figure 6, the area around this well, located in LaSalle and McMullen Counties, was actually between the Edwards and Sligo shelf margins where a natural mini-basin had formed to allow for lower Eagle Ford reservoir thicknesses two to three times greater than what had been observed anywhere else along the trend.

While these findings were extremely supportive of the play concept, the question of shale geochemistry was still uncertain. Prior to the discovery of the Eagle Ford, all of the commercial shale gas reservoirs had been from rocks that were Paloezoic in age (with the exception of the Jurassic-aged Haynesville, which was just beginning to emerge as a shale reservoir), and knowledge of the thermal maturity of a Cretaceous shale reservoir seemed to be a component of the play that was needed to reduce the risk.

To mitigate this point, the exploration team located drill cuttings at the Bureau of Economic Geology from a well located in the mini-basin, the Phillips 1 LaSalle. Samples of the cuttings were sent to a lab to be analyzed for certain geochemical properties, most notably vitinite reflectance (Ro) and total organic carbon (TOC). The results of the analysis strongly supported the Eagle Ford being a thermogenic reservoir with R_o being in the range of 1.1 (gas condensate window) and TOC in the 3 to 5% range, which was consistent with readings from other commercial shale reservoirs.

These data in conjunction with the petrophysical support provided a level of confidence for the company to initiate a leasing effort. The challenge to that, however, was that the lack of subsurface control made the establishment of a buy outline quite problematic. The answer to that dilemma was found with the utilization of a fairly robust two-dimensional seismic grid. As shown in Figure 7, seismic data quickly verified that the seismic signature of the Eagle Ford was such that it became a straightforward exercise to confidently build an isochron map that allowed the construction of a buy outline that approximated the area where the lower Eagle reservoir was greater than approximately 150 ft (46 m).

The leasing effort began in April 2008. Due to sparse existing production in the area and the presence of many large ranches, over 160,000 ac (64,750 ha) were leased within a 3-month time frame. The STS 241 1H was spudded on July 8 in LaSalle County and reached total depth on August 23. A 10-stage hydraulic fracture stimulation over an approximately 3200 ft (975 m) horizontal lateral was pumped in early October. The well tested at a rate of 7.6 MMCFGD and 240 BCPD and became the first commercial Eagle Ford completion. The Dora Martin 1H, also located in LaSalle County, was completed in January 2009 approximately 10 mi (16 km) to the southwest at a rate of 8.3 MMCFGD from a 12-stage hydraulic fracture stimulation over an approximately 4200 ft (1280 m) horizontal lateral and the Donnell Minerals 1H, located in McMullen County, was completed approximately 10 mi (16 km) to the northeast at a rate of 398 BOPD and 3.4 MMCFGD from a 10-stage hydraulic fracture stimulation over an approximately 3600 ft (1097 m) horizontal lateral. In April 2010, EOG announced its successful exploration in the Eagle Ford with the completion of its Milton 1H in April 2009,

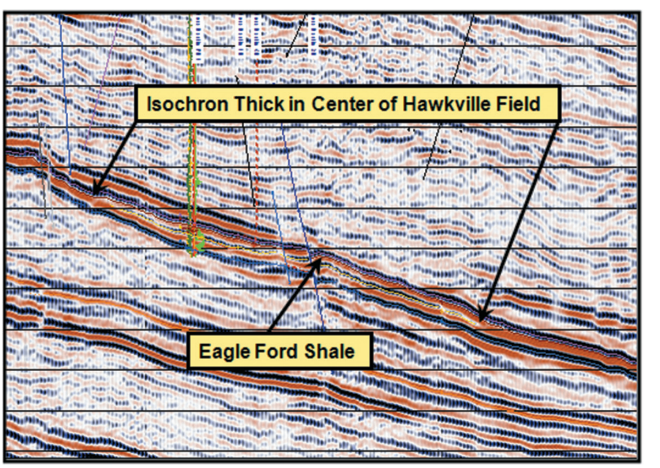

Figure 7. 2-D seismic line through the Hawkville field area (Stoneburner, 2014).

located in Karnes County, at a rate of 608 BOPD from an approximately 1800 ft (549 m) horizontal lateral. With the completion of the Milton 1H, located over 100 mi (161 km) northeast from the STS 241 1H, the Eagle Ford was validated as a potentially incredibly large oil and gas resource.

Further validation of the size of the resource is reflected in Figures 8 through 10, which represent the growth of oil and condensate production, natural gas production, and number of drilling permits issued from 2008 through 2014.

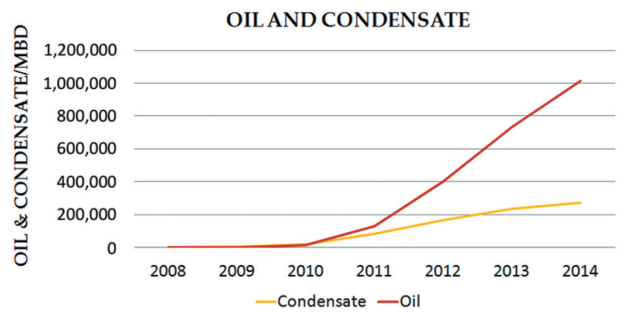

Figure 8. Eagle Ford oil and condensate production vs. time (2008–2014) (Texas Railroad Commission, 2017).

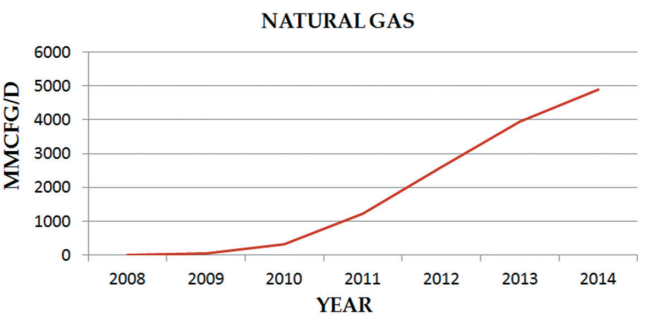

Figure 9. Eagle Ford oil natural gas production vs. time (2008–2014) (Texas Railroad Commission, 2017).

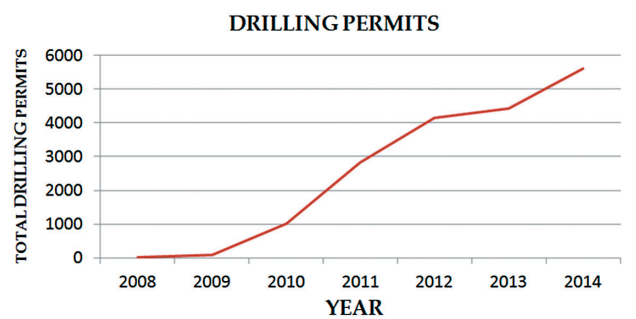

Figure 10. Eagle Ford drilling permits vs. time (2008–2014) (Texas Railroad Commission, 2017).

UPPER CRETACEOUS STRATIGRAPHY

The Cretaceous period along the Gulf Coast was dominated by a series of carbonate platforms that were amalgamated into a single platform called the Comanche shelf. The shelf is characterized by a series of stacked, prograding carbonate platforms separated by transgressive, organic-rich facies. The Sligo limestone was the initial carbonate development on the Comanche shelf. It formed as a shallow, rimmed carbonate platform that was very a broad, restricted interior platform with a narrow, high-energy well-circulated outer platform that had a well-defined margin and gently dipping foreslope (Workman, 2013). The Sligo carbonate development was followed by a rapid marine transgression, resulting in the deposition of the organic-rich Pearsall shale. Figure 11 shows relationships between the Glen Rose, Edwards, Georgetown, and Buda limestones. They represented another period of carbonate shelf deposition during late Albian to early Cenomonian that amalgamated into what is locally referred to as the Stuart City reef complex at the margin of the Comanche shelf. This period of platform and reef carbonate deposition was once again followed by a rapid transgression, resulting in the deposition of the Eagle Ford shale

With the exception of minor outcrops in the San Antonio area, Eagle Ford outcrops are limited in south Texas. As a result, much of the descriptions, stratigraphic divisions, and correlations have been done using wire-line and core data. Figure 12 provides a summary and comparison of the Eagle Ford and equivalent units in south and east Texas. Cusack et al. (2010) subdivided the Eagle Ford in south Texas into the upper and lower Eagle Ford.

The lower Eagle Ford was deposited during a second-order transgressive systems tract and attains a maximum thickness of over 91 m (300 ft) in the Hawkville field area in LaSalle and McMullen Counties. This interval thins to the southeast toward the Sligo shelf margin and northeastward toward the San Marcos arch, as shown in Figure 13. It consists predominately of dark-gray mudrocks with TOC values between 1.0 and 8.3% and high gamma ray values typically between 90 and 135 API units (Hentz and Ruppel, 2010, sourced from Workman, 2013). Light-gray calcareous mudrocks, marls, and limestones with low gamma ray values also occur locally.

The upper Eagle Ford was deposited during a marine transgression and is generally restricted to areas southwest of the San Marcos arch. It reaches a maximum thickness of 146 m (480 ft) in the Maverick Basin. It also thins to the southeast toward the Sligo and Edwards shelf margins and to the northeast toward the San Marcos arch. It consists primarily of light-gray calcareous

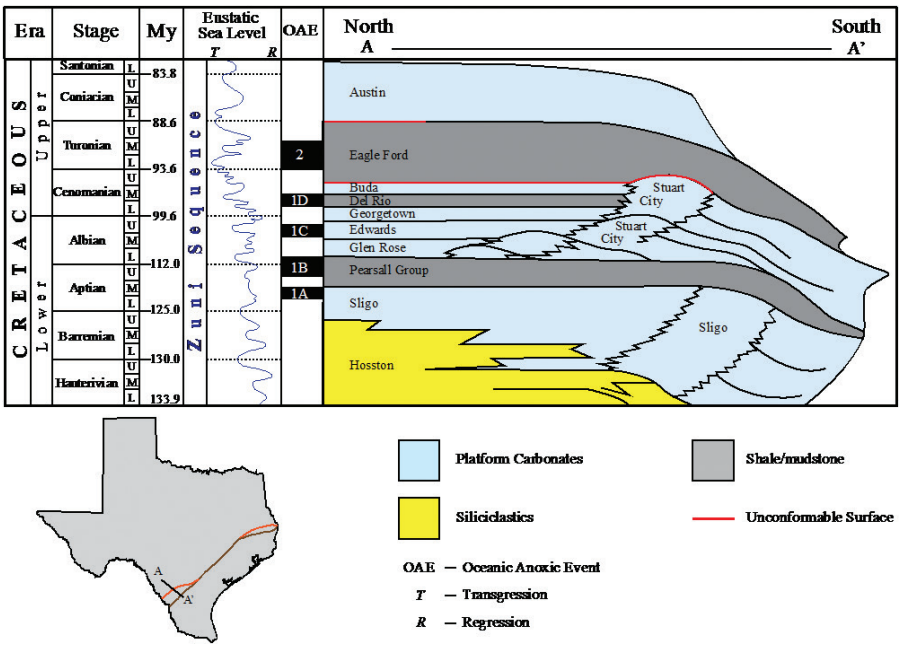

Figure 11. Diagrammatic representation of the evolution and architecture of Cretaceous carbonate platforms in the Northern Gulf Coast (reprinted with permission from Workman, 2013, whose permission is required for further use).

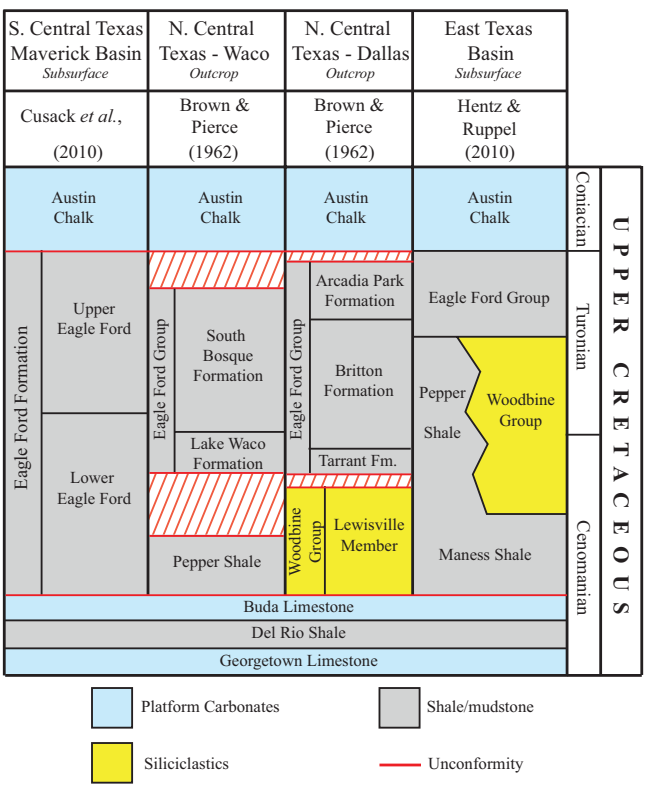

Figure 12. Summary and comparison of nomenclature for the Eagle Ford and equivalent units in South Texas and east Texas (reprinted with permission from Workman, 2013, whose permission is required for further use).

mudrocks with low organic content and low gamma ray values between 35 and 60 API units (Hentz and Ruppel, 2010, sourced from Workman, 2013). Thin beds of organic, dark-gray noncalcareous mudrocks with gamma ray values as high as 120 API units are locally present.

Figure 14 represents the mineralogical content of the Eagle Ford taken from a core provided by Core Laboratories. The entire section is dominated by calcite with lesser amounts of quartz, dolomite, various clay minerals, and kerogen. The primary difference between the upper and lower Eagle Ford is the percentage of kerogen, which has a direct relationship with effective porosity and permeability as a result of the conversion of kerogen to hydrocarbon product.

STRUCTURAL ELEMENTS AFFECTING THE EAGLE FORD

The Eagle Ford has been structurally influenced by a variety of features across the entirety of the state. Figure 15 is a map of the state of Texas with (1) the outcrop highlighted, (2) the subsurface representation of the Cretaceous Comanche shelf, and (3) a number of structural elements that significantly affect on the deposition and reservoir development of the Eagle Ford.

Mesozoic tectonism led to the development of the predominant structural and geologic features in the study area and surrounding regions. These features greatly influenced the deposition and spatial distribution of the carbonate facies in the Eagle Ford. A good example of that influence is the regional variations in thickness of the Eagle Ford, with thins toward and over the arches and thickening into the bordering embayments.

The San Marcos arch is a southern subsurface expression of the Llano uplift and is characterized as a low-amplitude, south to southeast plunging anticline, as shown in Figure 15. During the upper Cretaceous, the arch formed a topographic high in central Texas that experienced less subsidence than the flanking east Texas and Gulf Coast/Maverick Basin areas did (Laubach and Jackson, 1990, sourced from Workman, 2010). This decrease in subsidence established shallow-marine platform environments over the arch with numerous internal unconformities.

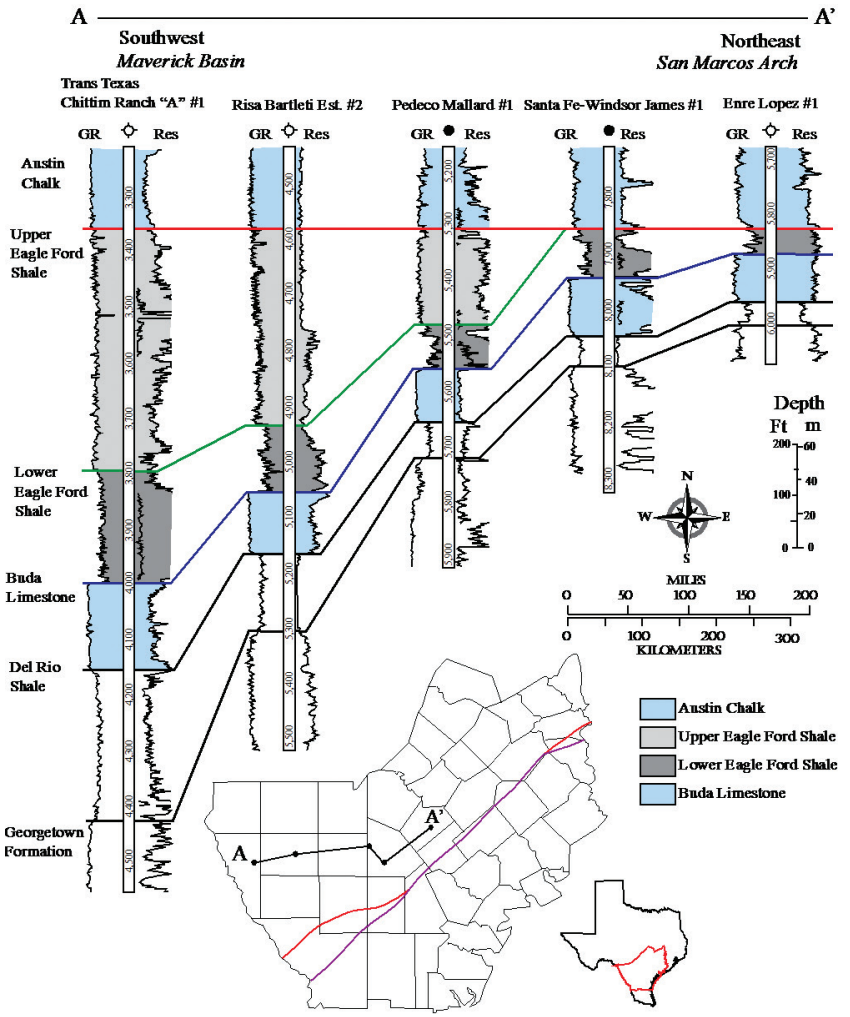

Figure 13. Strike oriented cross section (A—A') illustrating thickness and stratigraphic trends of the Eagle Ford and related sections from the Maverick Basin to the San Marcos Arch area (reprinted with permission from Workman, 2013, whose permission is required for further use).

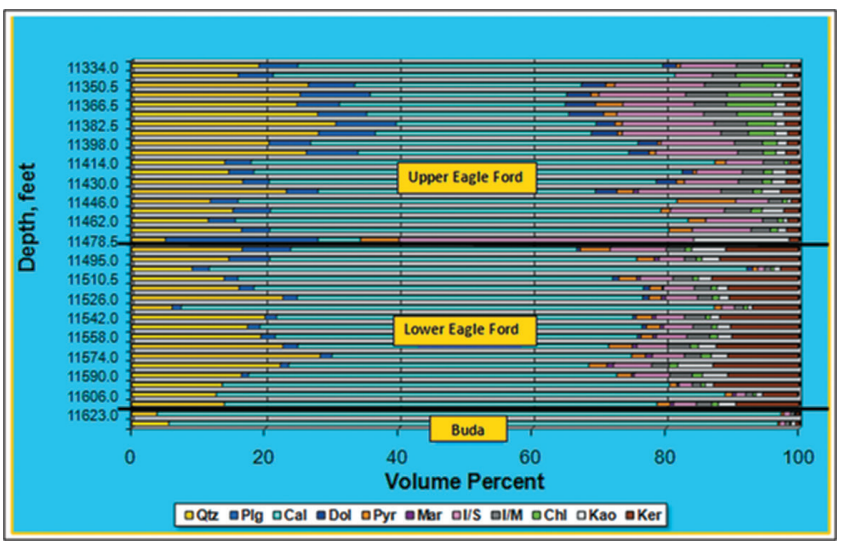

Figure 14. Mineralogical diagram from Eagle Ford core (Stoneburner, 2014).

The Maverick Basin is an intrashelf depocenter that developed on the southeast flank of the Edwards platform, which is also shown in Figure 15. The increased sedimentation within the Basin resulted from prolonged subsidence and the development of accommodation for the sediments. Sediment loading and thermal subsidence was the result and is associated with underlying basement structures that formed during the failed Rio Grande rifting event (Hull, 2011, sourced from Workman, 2013). Movement of the underlying Louann salt began soon after it was deposited and is believed to have continued through the Paleogene, which compounded the effects of thermal subsidence in the Maverick Basin.

Between the Maverick Basin and the San Marcos arch is what is commonly referred to as the Gulf Coast Basin area of the Eagle Ford. Numerous structural features are present in this area, most notably the Atascosa and Karnes troughs, which are regionally significant graben features. They were initiated during the late Albain and continued into the Eocene and likely resulted from salt withdrawal and sediment loading. These graben systems experienced contemporaneous growth with Cretaceous sedimentation and accumulated thickened Eagle ford sections (Corbett, 2010, sourced from Workman, 2013).

SUBSURFACE MAPPING

Figure 16 is a regional structure map of the top of the Eagle Ford. The region is dominated by monclinal dip to the southeast. There is not any large-scale faulting that manifests itself at this regional scale. However, as is shown in Figure 15, the Karnes and Atascosa troughs are two areas with faulting that is readily mappable from subsurface data. Additionally, there is a moderate amount of localized faulting, with both up to the coast faults and down to the coast faults present. The other notable feature in Figure 16 is the expression of the Chittum anticline in the western area of the map in the vicinity of the Red

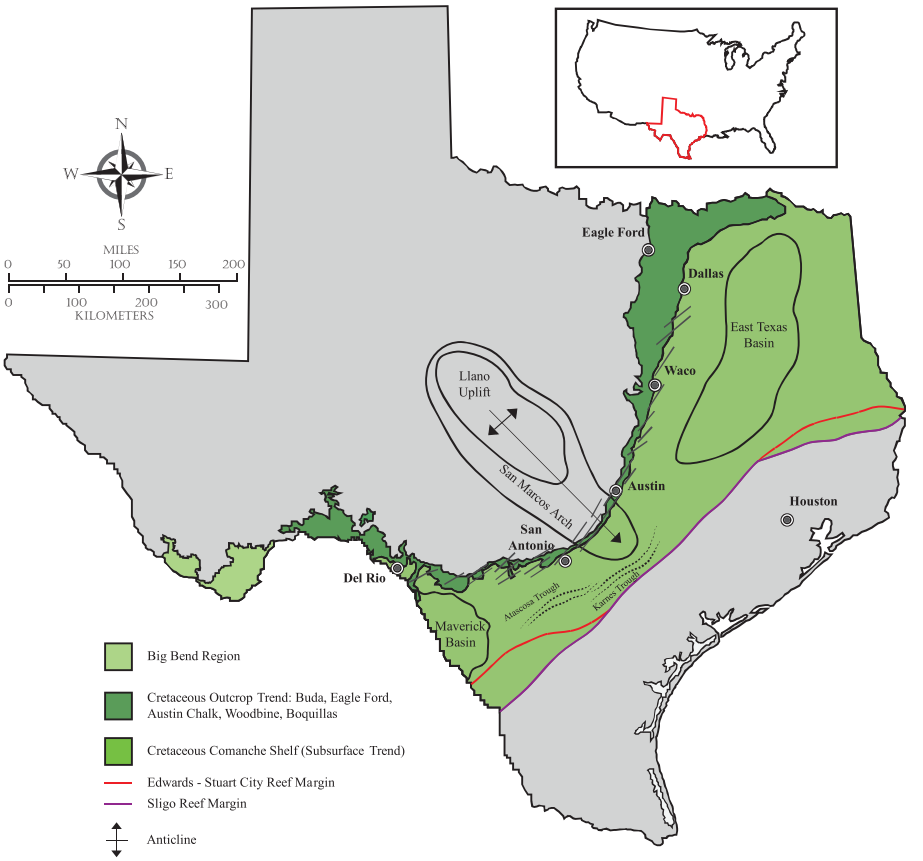

Figure 15. Map of Texas that shows prominent structural and geologic features (reprinted with permission from Workman, 2013, whose permission is required for further use).

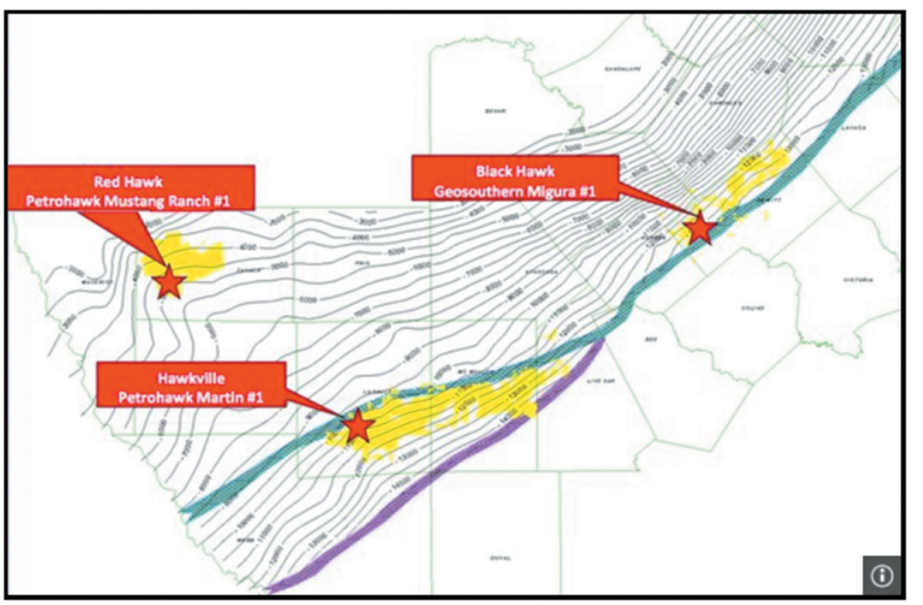

Figure 16. Regional structure map top of the Eagle Ford shale (PetroHawk, 2017).

Hawk prospect. The anticline represents the boundary between the Maverick Basin to the west and the Gulf Coast Basin to the east.

Figure 17 is a regional net isopach map of the lower Eagle Ford reservoir, commonly referred to as the Hawkville facies. The Hawkville area is the location of the discovery well, and it contains the thickest development of the Hawkville facies in the entire trend areas with in excess of 300 ft of net reservoir. The anomalously thick section is a result of it being located in a minibasin between the Edwards shelf margin, denoted by blue-stippled trend, and the Sligo shelf margin, denoted by purple-stippled trend. Updip of the Edwards shelf margin, the reservoir gradually thins and eventually has insufficient thickness for commercial reserves. The Red Hawk area, as discussed above, is on the flank of the Maverick Basin and represents another area of thickening of the Hawkville facies.

PALEOGEOGRAPHY AND DEPOSITIONAL ENVIRONMENT OF THE UPPER CRETACEOUS

Early Mesozoic tectonism initiated the fragmentation of Pangea and the opening of the proto-Gulf of Mexico. At this time, the northern Gulf Coast was situated within the Caribbean province of the Tehyan seaway and paralleled the pantropic equatorial belt, as shown in Figure 18 (Scott, 1993, in Workman, 2013). The North American plate drifted northward as seafloor spreading continued to open the Gulf of Mexico. During the Cretaceous period, the Gulf Coast region was located near the junction of the southern end of the western Interior seaway and the westernmost part of the Tethys Ocean, also shown in Figure 18.

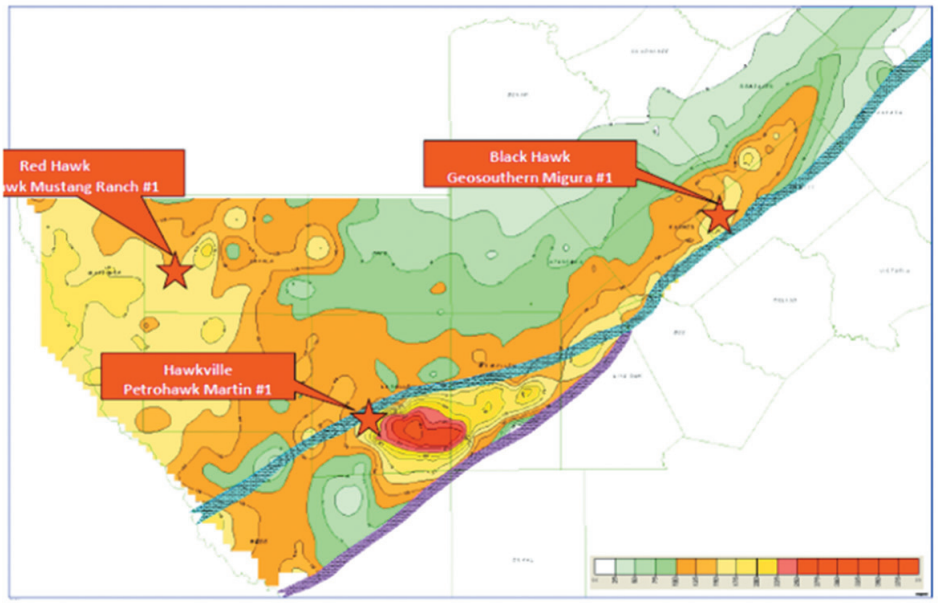

Figure 17. Regional net isopach map of lower Eagle Ford reservoir or Hawkville facies (PetroHawk, 2017).

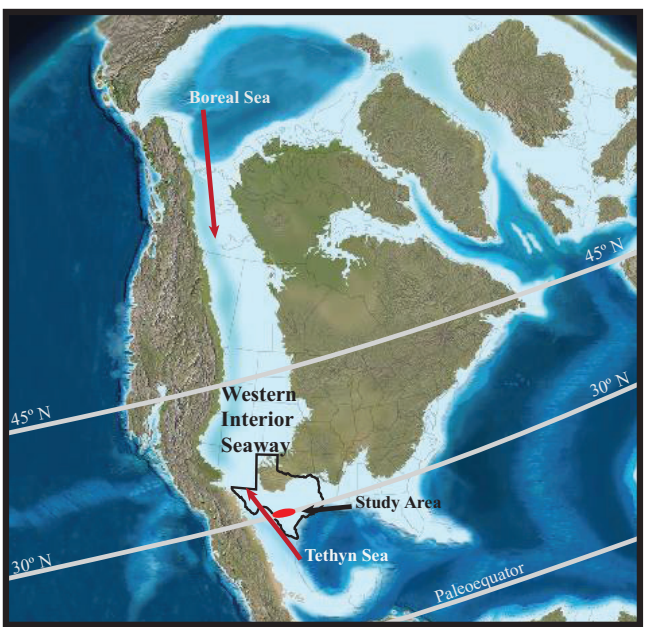

Figure 18. Late Cretaceous (85 Ma) paleogeographic map of North America (reprinted with permission from Workman, 2013, whose permission is required for further use).

The Cretaceous was also characterized by marine transgressive and regressive cycles (Figure 19) with the most significant transgressive events corresponding to worldwide phases of bottom-water anoxia, otherwise known as oceanic anoxic events, or OAE. OAE were first recognized in association with deposition of the Pearsall shale during the Aptian–Albian and the deposition of the Eagle Ford shale during the Cenomanian–Turonian (Schlanger and Jenkyns, 1976, sourced from Workman, 2013). Global OAE correspond to worldwide deposits of thick organic-rich black shales. The OAE associated with the Eagle Ford is characterized by large-scale pulses of magmatic activity during the late Cretaceous (Turgeon and Creaser, 2008).

Figure 20 is a subsurface cross-section from the northern flank of the Maverick Basin, through the Stuart City/Edwards shelf margin and terminating near the Sligo shelf margin. During the period of maximum transgression, such as existed during lower Eagle Ford deposition, deep-water organic deposits filled the Basin, resulting in sediments exhibiting the primary reservoir facies of the Eagle Ford, which was a result of this facies containing the highest total organic content. The upper Eagle Ford is still dominated by marine shale deposits, but the TOC has moderated, and the resultant porosity and permeability as a result of the conversion of kerogen has moderated as well. The return to carbonate-dominated platform deposits occurred with the deposition of the Austin chalk.

PETROPHYSICS OF THE EAGLE FORD RESERVOIR FACIES

Understanding the nano-level composition of a shale reservoir, and what that implies in terms of reservoir characteristics, is one of the most important aspects in the exploration and appraisal of shale reservoirs. Virtually every discovery of a commercial shale reservoir began with the evaluation of a whole core taken from the initial exploratory well drilled. The analysis of a shale reservoir goes way beyond the approach to evaluating conventional reservoirs, whose primary focus was porosity, permeability, and water saturations with lesser need to understand the mineralogical, geochemical, and geomechanical attributes of the rock. While the details of the core analysis are beyond the scope of this chapter, it is clear that tests, measurements, readings, and images extracted from the whole core were critical to ascertaining whether the rock was capable

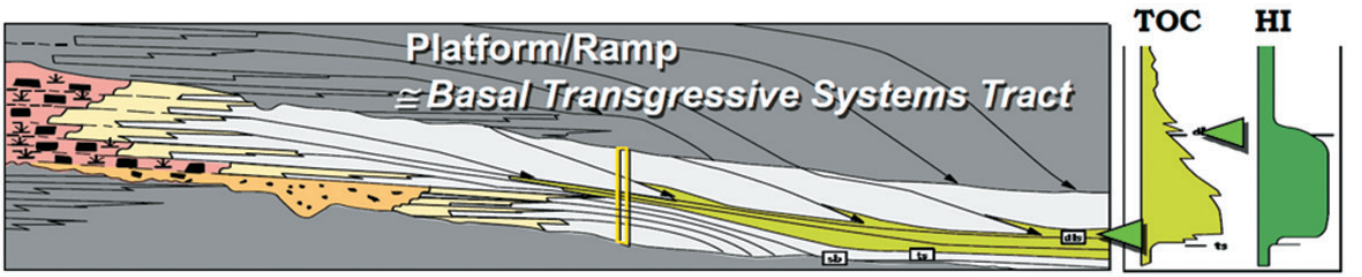

Figure 19. Diagrammatic cross section of Comanche style platform and transgressive depositional model (Passey et al., 2012, reprinted with permission from Q. Passey, whose permission is required for further use).

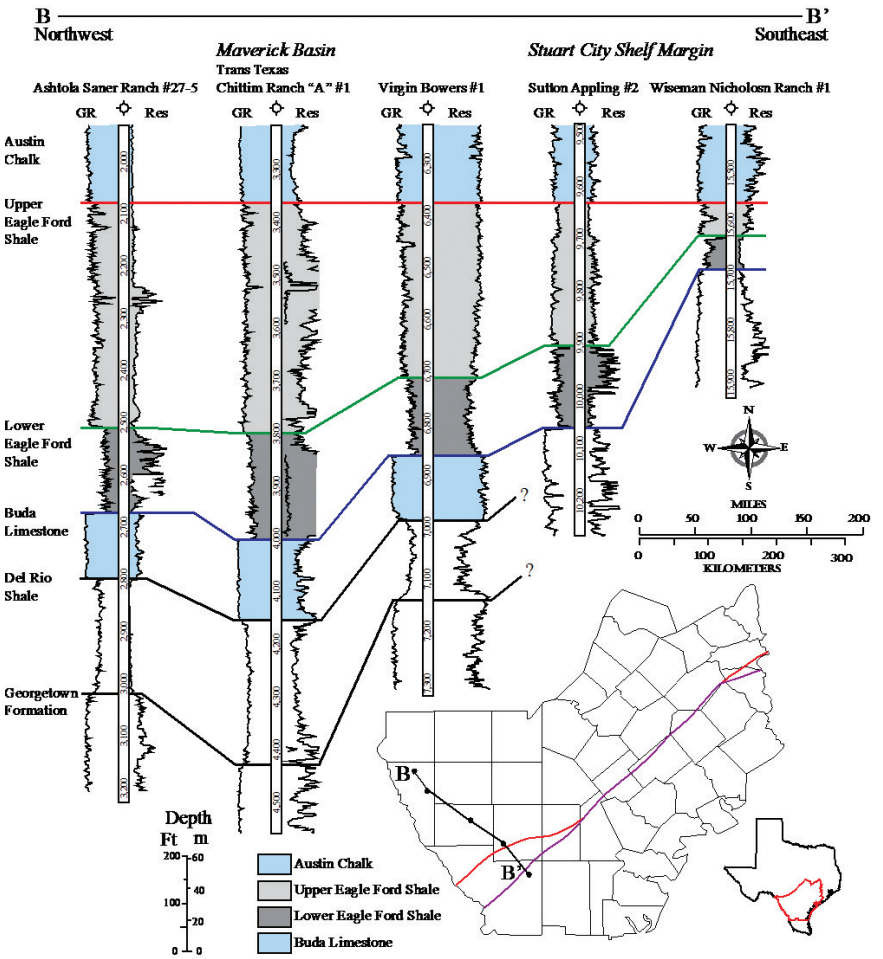

Figure 20. Dip oriented cross section (B—B') showing thickness and stratigraphic trends of the Eagle Ford and related sections from the Maverick Basin to the Sligo shelf margin (reprinted with permission from Workman, 2013, whose permission is required for further use).

DRILLING, COMPLETION, AND PRODUCTION PRACTICES FOR HORIZONTAL EAGLE FORD WELLS

of producing commercial volumes of hydrocarbons and, equally important, what type of hydrocarbons it would likely produce.

Once the exploration and early appraisal of a play is complete, the acquisition of whole core data diminishes, if not ceases entirely, as the cost of acquisition becomes prohibitive when compared with the added benefit. However, this phase of geologic reconnaissance is driven by the calibration of the existing core database to the existing subsurface database. The utilization of cross-plot analyses of certain metrics such as porosity, hydrocarbon-filled porosity, TOC, Young's modulus, and Poisson's ratio as well as many other attributes allows the use of more widespread subsurface data to become calibrated to the core specific data, thereby providing a much more robust data set to be utilized in the geologic modeling process. Figure 21 is a representative set of log curves that can be utilized to calibrate the data from both core and open-hole logs. The solid curves represent the open-hole log data, and the multicolored dots represent core-derived data for the particular readings such as TOC, permeability, porosity, water saturation, and mineralogy. The combined uses of these data have been instrumental in gaining a more complete understanding of the nature of the rock.

As is the case with most every large-scale resource play that has been under development during the past decade, remarkable strides have been made in all phases of the engineering processes.

The Eagle Ford covers a wide range of depths at which the reservoir is encountered, from as shallow

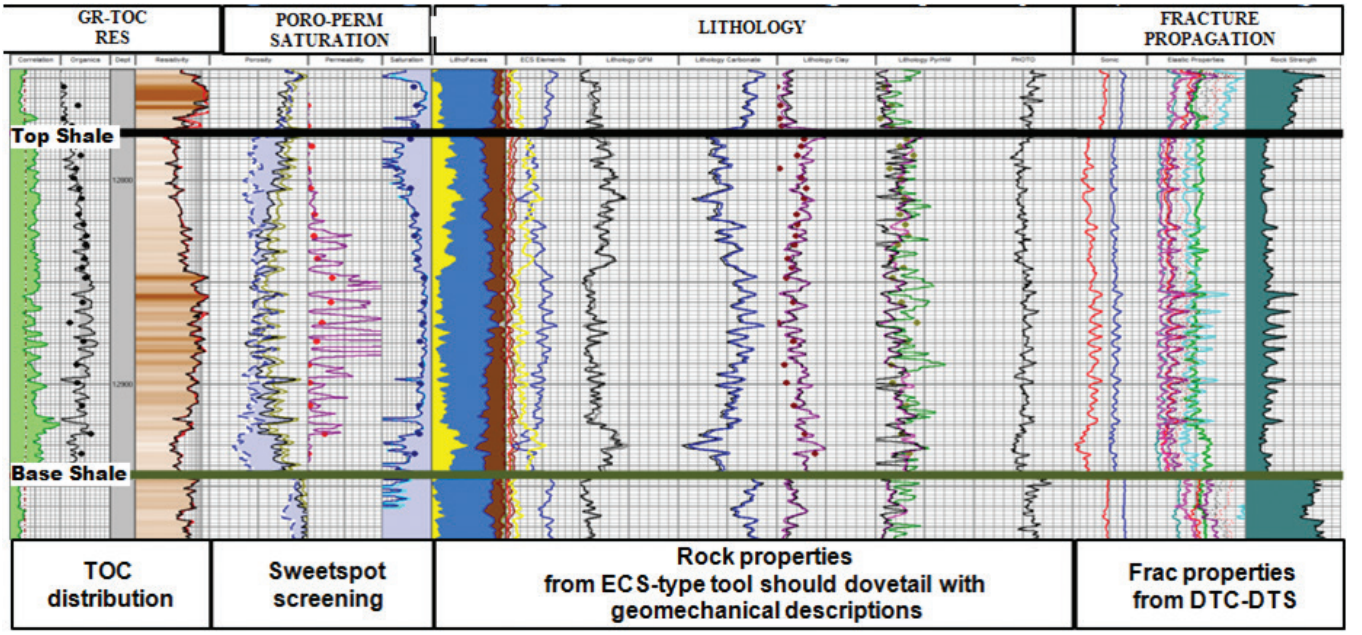

Figure 21. Petrophysical data derived from open-hole logs in conjunction with data derived from whole core analysis (Stoneburner, 2014).

as ~5000 ft (~1520 m) to as deep as ~13,000 ft (~3960 m). Additionally, both normal and abnormal reservoir pressure exist within the trend. However, even in light of such a wide range of depths and pressures, the Eagle Ford drilling operations have proven to be as accommodating a drilling environment as exists in the realm of shale plays. The following is a summary of most drilling operations as they have evolved over the past 7 years:

- Drill 12 3/4-in. (32.4 cm) surface hole to the base of the fresh water bearing Carrizo sand (ranging from ,3000 to ,5500 ft [,910 to ,1670 m]) and set 9 5/8-in. (24.5 cm) surface casing. This is often done with a spudder rig prior to mobilizing the actual rig that will drill the well to total depth.
- Mobilize drilling rig with top drive unit to drill 8 3/4-in. (22.2 cm) hole out from under the surface casing to total depth with oil-based mud and set 7-in. (17.8 cm) production casing.

There are a few areas where contingent strings need to be set should abnormal pressure, lost circulation, unstable hole conditions, or other drilling-related issues cause the need for intermediate casing to be run. The most notable of these areas is in the far eastern area of the play where the upper Eagle Ford has a tendency to create unstable hole conditions. However, in the vast majority of the play, a two-string program is all that is necessary.

Completion operations have also proven to be relatively risk free. The reservoir is extremely brittle and generally very receptive to the isolated multistage hydraulic fracturing process. Early in the development of the play, most operators would validate their fracture stimulation coverage by acquiring microseismic data such as those shown in Figures 22 and 23. In these images, it is apparent that the areal coverage of each stage was consistent in creating a significant amount of SRV, or stimulated reservoir volume. While early in the play companies tried a variety of fluid systems ranging from slickwater, hybrid systems utilizing slickwater and gel to all cross-linked gel, the vast majority of operators are currently pumping slickwater and Ottawa sand, even though in some of the deeper, higher-pressure wells, resin-coated sand or ceramic proppant is recommended.

Another variable in the completion recipe is the amount of sand that is pumped. The trend over the past few years has been to dramatically increase the proppant load from less than 1000 lb/lateral ft (305 lb/lateral m) to as much as 3000 lb/lateral ft (914 lb/lateral m). Figure 24 is a plot of pound per lateral foot on the *x*-axis and a lateral-normalized test rate of BOE per day per 1000 ft (305 m) on the *y*-axis. As can be seen on the plot, there is a definitive trend of increasing productivity with increasing proppant load. The variable that is not apparent is whether the increased cost of the proppant diminishes the rate of return or

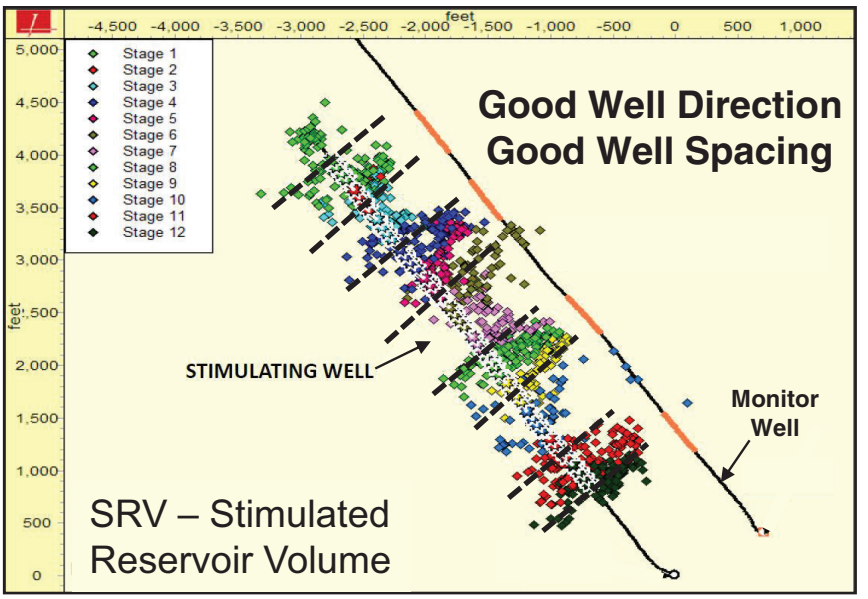

Figures 22. Microseismic data in aerial view and plan view (Stegent, 2011, reprinted with permission from N. Stegent, whose permission is required for further use).

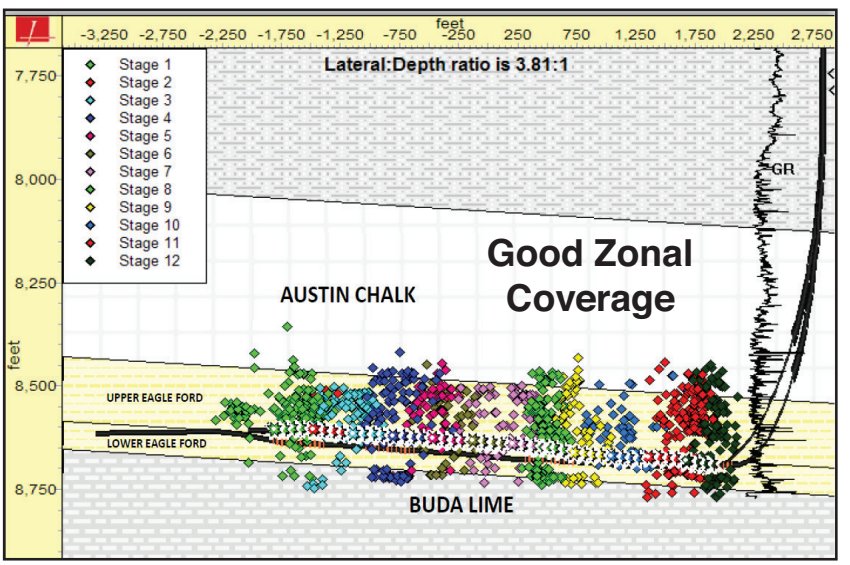

Figures 23. Microseismic data in aerial view and plan view (Stegent, 2011, reprinted with permission from N. Stegent, whose permission is required for further use).

if the increased productivity increases the rate of return. Considering that proppant, particularly regular-strength proppant such as Ottawa sand, is a relatively small component of the cost of a completion, it is most likely that the increased proppant load results in improved economics.

Another trend that is taking place in the industry, and particularly in the Eagle Ford, is the concept of geometric completions as opposed to engineered completions. Figures 25 and 26 are generalized representations of both approaches. In a geometric completion, the lateral is indiscriminately divided into equal stages, generally in the 200 to 250 ft (61 to 76 m) range, with a set number of perforation clusters equally spaced apart, generally in the 50 to 75 ft (15 to 23 m) range. The rational for the geometric concept is that it is imperative to stimulate as much of the wellbore as possible and that this would be the most efficient method of doing that. In an engineered, or sometimes referred to as a geologic, completion, open-hole logs are run in the lateral to gain more knowledge as to the petrophysical and geomechanical properties of the reservoir. The log suite will typically be comprised of a quad combo, including a gamma ray, resistivity, density-neutron, and dipole sonic. These logs would then quantitatively define which areas of the lateral were the most prospective and contrarily would identify which areas were least prospective. The most influential data from the log suite is the dipole sonic, which is capable of identifying geomechanical heterogeneity in the lateral by focusing on sections of the wellbore that should be most receptive to hydraulic fracturing and eliminating those sections of the wellbore that appear to be much less receptive to hydraulic fracturing. By utilizing reservoir analysis in the lateral and designing the fracture stimulation accordingly, it is believed that the wellbore will become more economic as a result.

Production engineering also plays a key role in an economically successful shale play. Several of those practices are briefly discussed below:

- Choke management, sometimes referred to as restricted rate production: Many shale reservoirs, particularly those that are abnormally pressured, benefit from limiting the drawdown on the reservoir, which in turn minimizes the degradation of the permeability that was created by the hydraulic

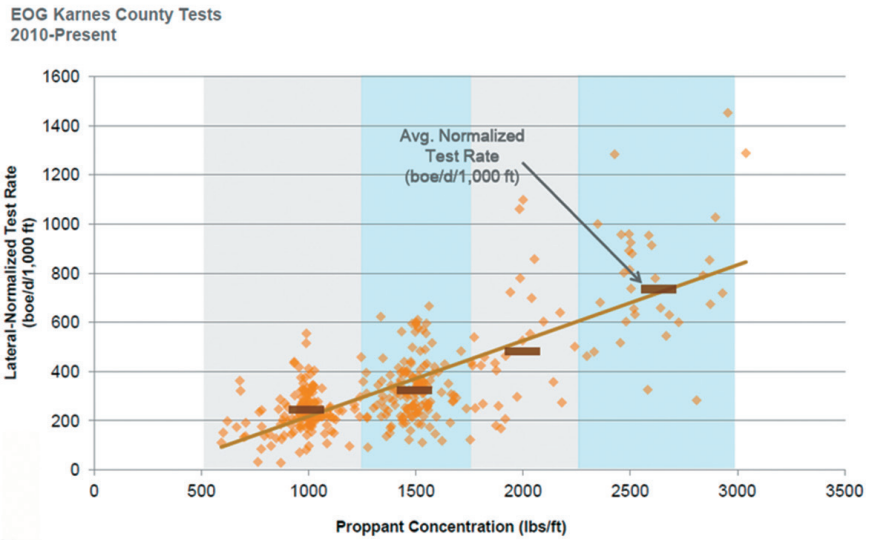

Figure 24. Test rate of EOG wells in Karnes County normalized to 1000 BOPD/d/1000 lateral ft vs. proppant concentration in #/lateral ft.

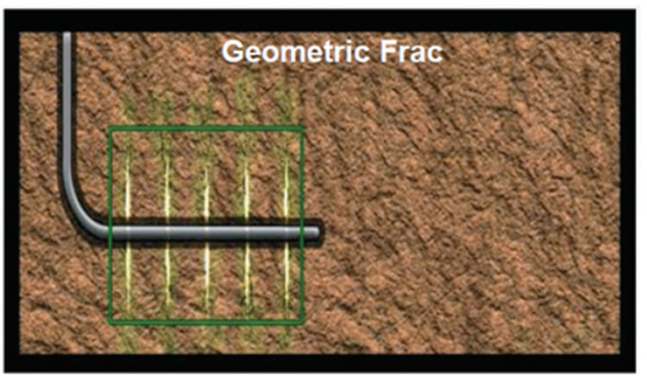

Figure 25. Diagrammatic representation of geometrically designed isolated multi-stage hydraulic fracturing and engineered designed isolated multi-stage hydraulic fracturing (Banks, 2014).

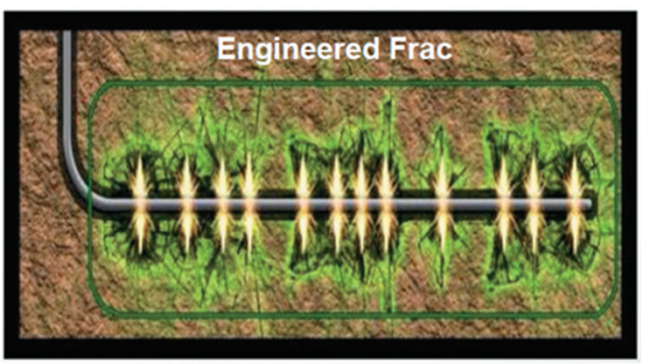

Figure 26. Diagrammatic representation of geometrically designed isolated multi-stage hydraulic fracturing and engineered designed isolated multi-stage hydraulic fracturing (Banks, 2014).

fracturing process. While it has not been universally accepted as a beneficial production practice in the Eagle Ford, it is one that is emplyed by a number of operators.

- Artificial lift: The unique aspect of artificial lift in the Eagle Ford is a function of the wide range of depths, pressures, and gas-to-oil ratios that exist across the play. As a result of the variability of reservoir conditions, a wide range of lift mechanisms are employed, with rod pump and gas lift being the most common.

Another aspect of the Eagle Ford that has caused uncertainty as what are best production practices is the question of how reaching the bubble point or dew point of the reservoir will affect ultimate recovery. While this subject is well beyond the scope of this chapter, a few examples of these effects display the variability that exists in the reservoir. Figure 27 is a plot of eight downspaced wells in Dimmit County with gas–oil ratio (GOR) on the *y*-axis and time on the *x*-axis. The plot shows a definitive increase in GOR with time. Figure 28 show two plots of GOR versus time for two wells in Karnes County, one being an oil well and one being a rich gas well. In both instances, there is no discernible change in GOR, which would suggest that the bubble point and dew point effects have not occurred.

RESERVE AND RESOURCE POTENTIAL OF THE EAGLE FORD

With over 10,000 wells on production from the Eagle Ford, the evaluation of reserves and resource for the play can be based on a reasonable amount of technical data and therefore should be considered to be reasonably certain assumptions.

One source of credible analysis for the resource associated with the Eagle Ford is ITG and Associates, a research firm located in Calgary, Canada. ITG is widely considered to be one of the foremost engineering firms specializing in unconventional reservoir analysis. The following are several conclusions the company published in its analysis of the data through 2014:

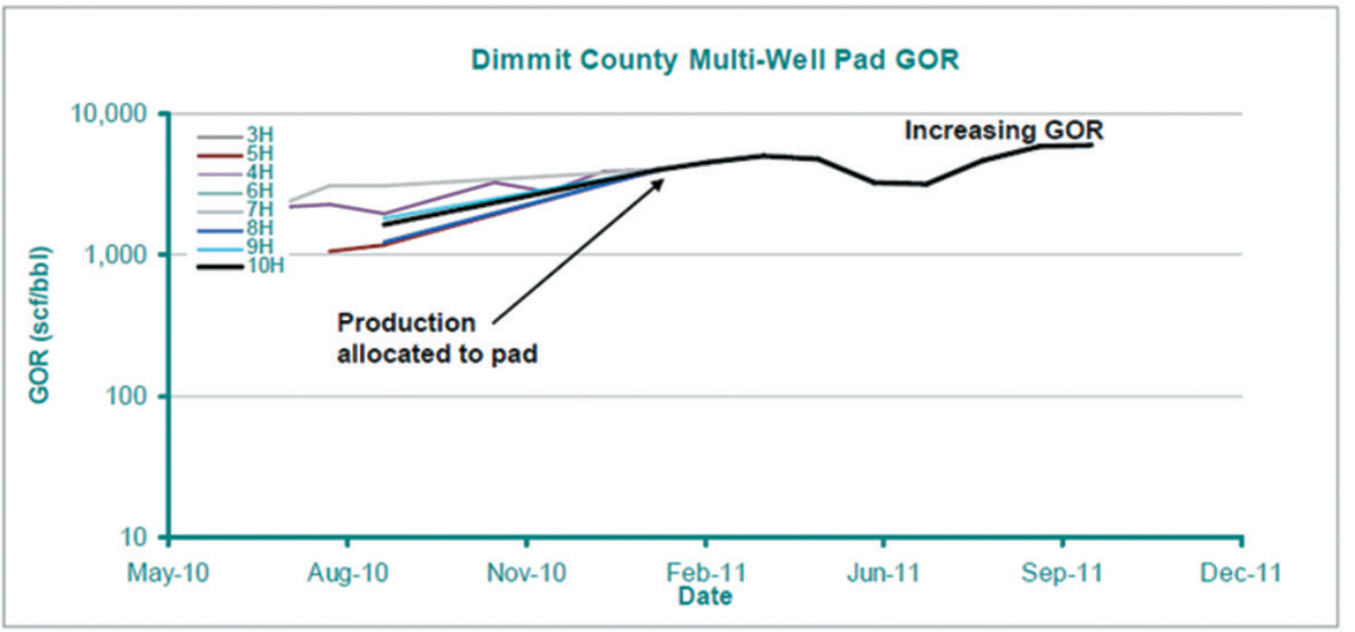

Figure 27. Gas–oil ratio vs. time of Eagle Ford wells in Dimmitt County, Texas.

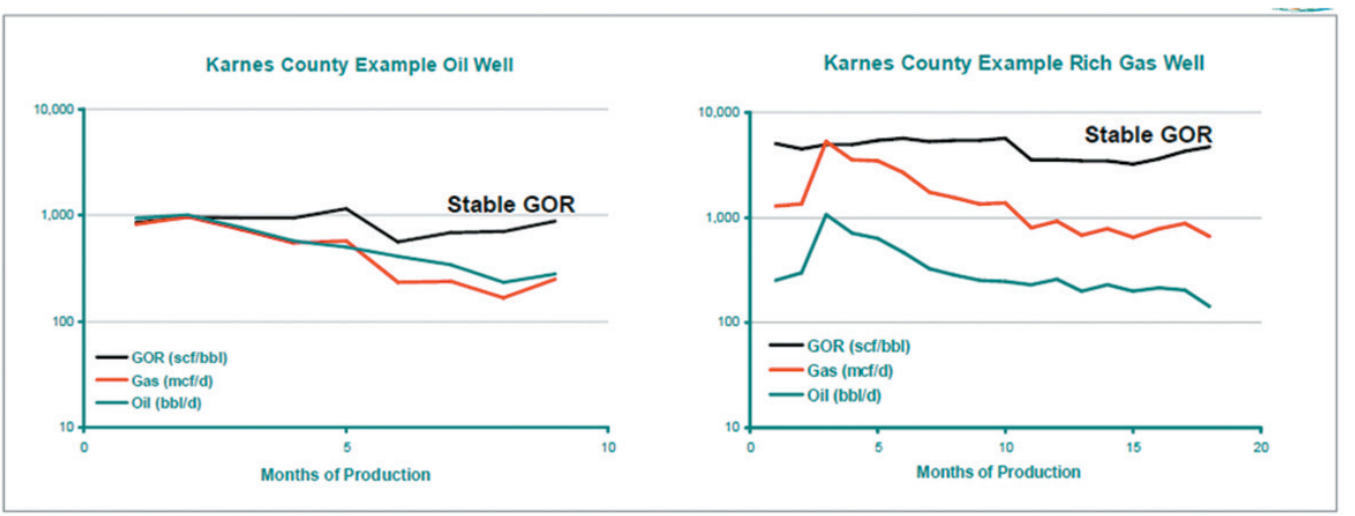

Figure 28. Gas–oil ratio vs. time of Eagle Ford wells in Karnes County, Texas.

- The Eagle Ford has been adding approximately 170,000 BOPD per month
- ITG analyzed decline curves from 10,119 Eagle Ford wells in order to calculate the economics of those wells
- Calculated break-even price across the entire play to average $65/barrel West Texas Intermediate (WTI)
- If the NYMEX gas price were to remain flat at $4.00, the break-even price would be reduced to $53/barrel WTI
- The remaining resource in the Eagle Ford is approximately 26 billion BOE

Gong (2013) divided the Eagle Ford into eight distinct regions, as shown in Figure 29. Within each region, the highest established well density (HEWD) within each region was determined, with those densities ranging from 2.0 wells/section (320 ac [129 ha] spacing) to 11.2 wells/section (57 acre [23 ha] spacing).

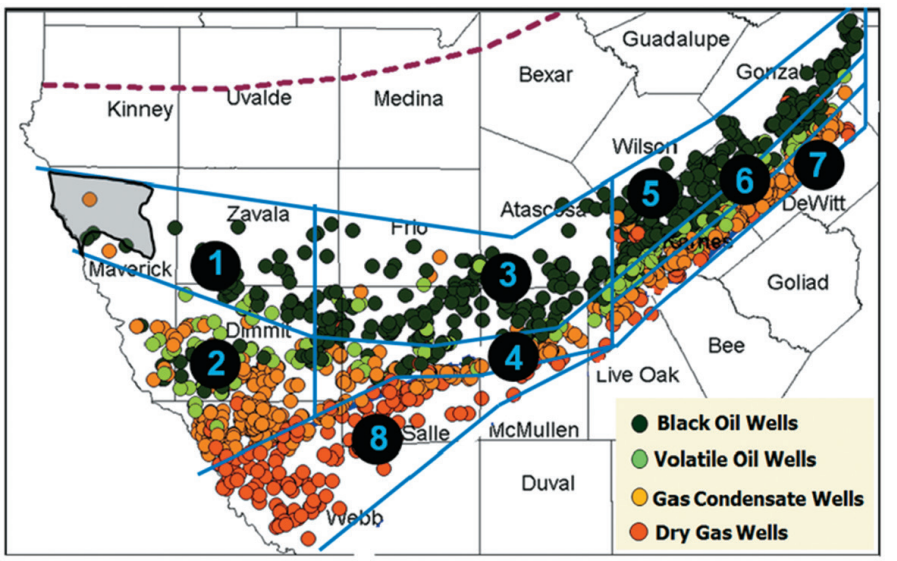

Figure 29. Fluid type changes from black oil to dry gas from north to south (Gong, 2013, reprinted with permission from X. Gong, whose permission is required for further use).

Figure 30 is a table assigning the total acres for each region, specifying which acres are allocated to proven/contingent resource and which are allocated to prospective resource, and a calculation of the well count for each area and resource type based on the HEWD.

An assignment of technically recoverable resource over 20 years (TRR20) for each region was made based on a Monte Carlo based analysis. The methodology in concluding the distribution of TRR20 by region included, but was not limited to, analysis of the following parameters of the reservoir by region:

- Percentiles of thickness of upper and lower Eagle Ford
- Percentiles of initial reservoir pressure
- Percentiles of matrix permeability
- Percentiles of fracture permeability by region
- Percentiles of bubble point pressure for black oil
- Percentiles of dew point pressure for volatile oil and condensate
- Percentiles of recovery factor for oil, condensate, and gas

These parameters then led to the generation of type probabilistic decline curves by region that resulted in the TRR20 volumes summarized in Figure 31.

Figure 32 calculates the reserves and resources for the Eagle Ford based on the per-well resource in Figure 28 multiplied by the total number of wells to be drilled in each region represented in Figure 27. That calculation, assuming a P90 result, implies a total resource of 2.95 billion barrels of oil and 34.3 tcf. Assuming a P50 result the resource is 8.25 billion barrels of oil and 90.57 tcf, and assuming a P10 result the resource is 23.53 billion barrels of oil and 266.17 tcf.

While it is difficult to compare ITG's resource of 26 billion BOE to the range Gong (2013) calculated primarily because ITG takes the wells to commercial limits while Gong cuts it off at 20 years, it is

Table 3.31— Summary of P_{50} Well Count for Reserves and Resources

Production Region	PR1	PR2	PR3	PR4	PR5	PR6	PR7	PR8	Total
Area (Acres)	799,836	942,734	1,617,410	584,070	977,484	338,000	478,888	1,201,185	6,939,607
Reserves/Contingent Area (Acres)	173,590	550,944	1,017,488	414,105	675,539	318,336	370,863	565,281	4,086,146
Prospective Area (Acres)	626,246	391,790	599,922	169,965	301,945	19,664	108,025	635,904	2,853,461
Current Well spacing (Acres/Well)	206	57	160	96	57	61	106	320	
Drilling Efficiency Factor	0.7875	0.7875	0.7875	0.7875	0.7875	0.7875	0.7875	0.7875	
Existing Well Count	102	839	913	428	1020	561	310	229	4,402
Reserves Well Count	235	2,035	2,710	965	2,710	1,545	730	365	11,295
Contingent Well Count	327	4,738	1,385	2,004	5,603	2,004	1,715	797	18,572
Prospective Well Count	2,394	5,413	2,953	1,394	4,172	254	803	1,565	18,947
Total Well Count	3,058	13,025	7,961	4,813	13,505	4,364	3,558	2,956	53,216

Figure 30. Summary of P50 well count by region (Gong, 2013, reprinted with permission from X. Gong, whose permission is required for further use).

Table 3.29— Summary of TRR20 Oil and Gas for All Production Regions										
	Oil TRR20, STB					Gas TRR20, BCF				
Production Regions	P_{90}	P_{50}	P_{10}	Mean	SD	P_{90}	P_{50}	P_{10}	Mean	SD
PR1	23,059	72,345	199,612	100,688	96,760	0.04	0.19	0.71	0.32	0.38
PR2	26,699	124,438	382,868	173,595	169,270	0.48	2.43	8.16	3.62	3.89
PR3	71,994	199,662	488,506	254,858	226,309	0.14	0.55	1.73	0.81	0.94
PR4	27,941	93,645	282,178	133,376	129,414	0.48	1.97	6.54	2.97	3.27
PR5	84,686	204,650	457,435	247,402	172,769	0.16	0.54	1.57	0.75	0.70
PR6	136,613	318,489	925,599	453,708	412,886	0.51	1.66	6.35	2.79	3.35
PR7	28,227	151,288	653,800	269,239	318,648	0.54	2.70	11.35	4.75	5.89
PR8						0.84	2.42	6.39	3.25	3.11

Figure 31. Summary of Monte Carlo distribution of TRR20 by region (Gong, 2013, reprinted with permission from X. Gong, whose permission is required for further use).

Table 3.36— Reserves and Resources of the Eagle Ford Play						
	Oil, BBO			Gas, TCF		
	P_{90}	P_{50}	P_{10}	P_{90}	P_{50}	P_{10}
Cumulative	0.264	0.264	0.264	1.37	1.37	1.37
Existing Reserves	0.59	0.74	0.89	5.50	7.89	10.28
Undeveloped Reserves	1.71	2.75	4.25	13.64	23.32	37.01
Total Reserves	2.30	3.49	5.14	19.13	31.21	47.28
Contingent Resources	0.92	4.52	14.59	11.25	47.93	155.19
Prospective Resources	2.03	3.72	8.93	23.05	42.63	110.98
Total Resources	2.95	8.25	23.53	34.30	90.57	266.17

Figure 32. Summary of Monte Carlo distribution of total resources by region (Gong, 2013, reprinted with permission from X. Gong, whose permissions is required for further use.).

interesting to compare the two. Gong's P50 BOE, assuming the same 22.5:1 revenue-based gas conversion that ITG assumes, is 12.27 billion BOE, and the P90 is 35.3 billion BOE, putting the ITG resource of 26 roughly between those two and probably much closer to the P50 if the Gong resource were not assuming a 20-year life.

REGULATORY AND COMMUNITY ISSUES ASSOCIATED WITH EAGLE FORD DEVELOPMENT

The oil and gas regulatory environment in Texas has long been recognized as being rational and well intentioned to both the industry and to other stakeholders, specifically the mineral owners and the communities in which the operations are taking place. It is this long history of oil and gas exploration and production that has helped establish the Eagle Ford play as one that provides an operating environment that is conducive to all parties involved.

One development that helped establish trust and collaborative relationship between the operators, the regulators, and the community was the establishment of the Eagle Ford Task Force by Texas railroad commissioner David Porter in 2010. This group, the members of which Porter picked himself, is comprised of 24 individuals from all facets of the play with five from the upstream sector, two from the midstream sector, four from the service sector, seven from state and local government, two from environmental NGOs, and four from institutions. By having such a diverse collection of stakeholders, the task force felt empowered to study the effects of the play from virtually all facets and encourage a range of findings that were not biased toward any one sector. The task force met 10 times from July 2010 to November 2011 to study the following issues related to developing the Eagle Ford shale:

- Infrastructure: roads, pipelines, and housing
- Water quality and quantity
- Railroad Commission regulations
- Economic benefits
- Flaring and air emissions
- Health, education, and social services
- Landowner, mineral owner, and royalty owner issues

One of the most controversial elements of all unconventional resource development that depends

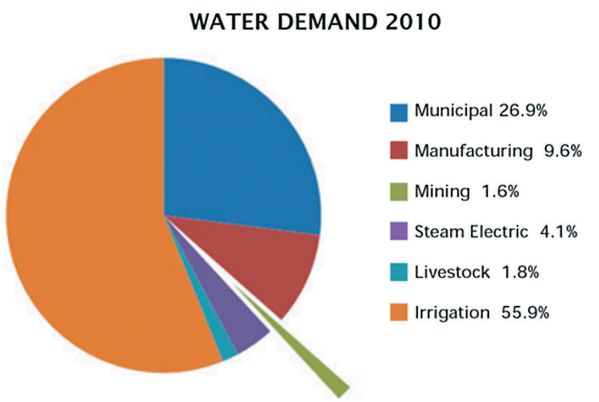

Figure 33. Pie chart depicting water demand in the State of Texas for 2010 as per the Texas Water Development Board, as presented in the 2012 State Water Plan (modified from Texas Railroad Commission, 2017).

on isolate multistage hydraulic fracturing is water usage. Because of the relatively arid nature of south Texas, the primary source of water for hydraulic fracturing needs to be from the subsurface. Fortunately, a world-class fresh-water aquifer called the Carrizo sandstone exists under a large portion of the play. Figure 33 is a pie chart showing the region's water usage from the Carrizo. As can be seen, mining (which includes not only oil and gas operations but coal mining operations as well) comprised only 1.6% of the total usage in 2010. While that volume has increased as the level of activity has increased, it is still a very small percentage of the water drawn from this critically important water resource.

One of the foremost experts of water usage in south Texas is Dr. Darrell Brownlow, who testified before the task force and offered the following findings regarding the use of subsurface water, particularly the Carrizo Formation which is a Wilcox aged sandstone.

Projected south-central Texas water usage for the year 2060 would be 1.27 million acre-ft (.953 million hectare-meter) of water:

- Municipality use at 637,236 acre-ft (477,927 hectare-meter), or 50.1%
- Agricultural irrigation use at 301,679 acre-ft (226,259 hectare-meter), or 23.7%
- Steam-electric power generation use at 109,776 acre-ft (82,332 hectare-meter), or 8.6%
- Industrial needs use at 67,016 acre-ft (50,262 hectare-meter), or 5.9%
- Livestock use at 25,954 acre-ft (19,466 hectare-meter), or 2.0%
- Oil and gas and other mining use at 18,644 acre-ft (13,983 hectare-meter), or 1.5%

Brownlow quantified his estimates of industry's annual water usage related to Eagle Ford operations:

- Average water usage for drilling and hydraulically fracturing a well in the Eagle Ford shale is 15 acre-ft (11.25 hectare-meter), or 116,000 bbl of water with approximately 0.5 acre-ft (.38 hectare-meter) required for drilling (162,500 gal [615,129 L] of water) and 14.5 acre-ft (10.9 hectare-meter) are required for hydraulic fracturing (over 4.7 million gal [17,791,435 L] of water).
- He estimated that between 20,000 and 25,000 new wells would be drilled over the next 10 to 20 years, resulting in 300,000 to 375,000 acre-ft (225,000 to 281,250 hectare-meter) of cumulative future water use.
- His estimate does not take into account or address the use of recycled water. He added that via the industry's recycling efforts, many operators could decrease that by one-third to an average of 10 acre-ft (7.5 hectare-meter), or 77,000 bbl, of water per well.

Brownlow spoke to specific usage from the subsurface aquifer, most specifically the Carrizo:

- Annual groundwater pumpage from the portion of the Carrizo aquifer located in the area of Eagle Ford development is 285,000 acre-ft (213,750 hectare-meter)
- Total groundwater pumpage from all aquifers located in the area of Eagle Ford development is 426,000 acre-ft (319,500 hectare-meter) per year
- He emphasized that if hydraulic fracturing-related water use in the Eagle Ford shale equals 15,000 acre-ft (11,250 hectare-meter), then the industry's current annual Carrizo usage is approximately 5%

Another aspect related to water usage is the maintenance of water quality. The Texas Railroad Commission is in the process of amending its rules for injection and disposal wells, well integrity, wellhead control, waste management, and water recycling. All of these issues are of paramount importance to the state, local communities, and industry.

Economic benefits are another significant result of the development of the Eagle Ford shale. During a task force meeting on April 18, 2012, the director of local government assistance and economic development for the Texas comptroller of public accounts, Robert Wood, reported that employment in the oil and gas industry, including the refining of oil, manufacturing of chemicals, and related manufacturing sectors, increased by 11% from 2010 to 2011, compared to a growth rate of 2% for all industries. He added that wage and salary income in the oil and gas industry increased by 18% from 2010 to 2011, versus just 2% for all industries. He further reported that the average 2011 income for workers in the oil and gas industry was $117,000, compared to the all-industry average of $49,000.

CONCLUSIONS

It is clear that the discovery of the Eagle Ford shale oil and gas resource has been an incredibly important event in the state of Texas and the United States. In addition, it has had repercussions throughout the world. The growth of production to over 2.1 million BOED in just in the course of just over 6 years is an unprecedented level of growth. What made that growth possible is a combination of factors that collectively resulted in the success of the play:

- Superior petrophysical and geomechanical properties of the reservoir rock
- Abnormal pressure reservoir conditions
- A range of hydrocarbon product that covered every generating window from dry gas to low-GOR black oil
- Very large area of commercial production
- A high percentage of unleased acreage in an area of sophisticated, oil- and gas-literate mineral owners, providing ready access for operators to acquire meaningful acreage positions
- A large source of accessible fresh water without causing stress to the community or environment
- A regulatory environment that encouraged and allowed for development that was properly engineered, environmentally prudent, and aligned with local and state authorities as well as stakeholders

All of these factors support the contention that the Eagle Ford play could be considered the "perfect" unconventional giant oil field.

REFERENCES CITED

Banks, B., 2014, Gaining efficiencies in monetizing Eagle Ford pay: 2014 DUG Eagle Ford Conference, Proceedings, accessed February 15, 2017, http://www.adstrategiesconference.com/dugef-conf14.

Corbett, K., 2010, Eagleford Shale exploration models: Depositional controls on reservoir properties: AAPG Search and Discovery Article #10242, accessed October 3, 2016, http://www.searchanddiscovery.com/pdfz/documents/2010/10242corbett/ndx_corbett.pdf.html.

Cusack, C., J. Beeson, D. Stoneburner, and G. Robertson, 2010, The discovery, reservoir attributes, and significance of the Hawkville Field and Eagle Ford Shale trend, Texas: Gulf Coast Association of Geological Societies Transactions, v. 60, p. 165–179.

EIA, 2015, Top 100 U.S. Oil and Gas Fields: U.S. Department of Energy. U.S. Energy Information Administration, accessed February 15, 2017, http://www.eia.gov/naturalgas/crudeoilreserves/top100/pdf/top100.pdf.

Gold, R., 2014, The boom, how fracking ignited the American energy revolution and changed the world: New York, Simon & Schuster Paperbacks, 84 p.

Gong, X., 2013, Assessment of Eagle Ford Shale Oil and Gas Resources: Ph.D. Dissertation, Texas A&M University, 159 p.

Hentz, T. F., and S. C. Ruppel, 2010, Regional lithostratigraphy of the Eagle Ford Shale: Maverick Basin to East Texas Basin: Gulf Coast Association of Geological Societies Transactions, v. 60, p. 325–337.

Hull, D. C., 2011, Stratigraphic architecture, depositional systems, and reservoir characteristics of the Pearsall shale-gas system, Lower Cretaceous, South Texas: M.S. Thesis, University of Texas at Austin, 192 p.

Laubach, S. E., and M. L. W. Jackson, 1990, Origin of arches in the northwestern Gulf of Mexico basin: Geology, v. 18, p. 595–598.

Passey, Q. R., K. M. Bohacs, W. L. Esch, R. Klimentidis, and S. Sinha, 2012, My source rock is now my reservoir: Geologic and petrophysical characterization of shale-gas reservoirs: AAPG Distinguished Lecture, 2012, accessed February 15, 2017, http://www4.unileoben.ac.at/fileadmin/shares/unileoben/erdoelgeologie/docs/AAPG_2012_European_Distinguished_Lecture_Quinn_Passey.pdf.

PetroHawk, 2017, Eagle Ford Shale: PetroHawk Energy Corporation, accessed February 15, 2017, http://eaglefordshale.com/companies/petrohawk-energy/.

Schlanger, S. O., and H. C. Jenkyns, 1976, Cretaceous oceanic anoxic events: Causes and consequences: Geologie en Mijnbouw, v. 55, p. 179–184.

Scott, R. W., 1993, Cretaceous carbonate platform, U.S. Gulf coast, *in* J. A. Simo, R. W. Scott, and J. P. Masse, eds., Cretaceous carbonate platforms: AAPG Memoir 56, p. 97–109.

Stegent, Neil, P. E., 2011, Let's Put Engineering Back into Fracture Stimulation!: Norman, Oklahoma: Oklahoma Geological Society Presentation, accessed February 15, 2017, http://ogs.ou.edu/docs/meetings/OGS-workshop-shales_moving_forward_2011-stegent.pdf.

Stoneburner, R.K., 2014, The Discovery, Reservoir Attributes, and Significance of the Hawkville Field and Eagle Ford Shale Trend: Implications for Future Development, accessed February 15, 2017, http://www.searchanddiscovery.com/documents/2014/20251stoneburner/ndx_stoneburner.pdf.

Texas Railroad Commission, 2017, Eagle Ford Shale Information: Railroad Commission of Texas, accessed February 15, 2017, http://www.rrc.state.tx.us/oil-gas/major-oil-gas-formations/eagle-ford-shale/

Turgeon, S. C., and R. A. Creaser, 2008, Cretaceous oceanic anoxic event 2 triggered by a massive magmatic episode: Nature, v. 454, p. 323–327.

Workman, S. J., 2013, Integrating depositional facies and sequence stratigraphy in characterizing unconventional reservoirs: Eagle Ford Shale, south Texas: M.S. thesis, accessed February 15, 2017, http://scholarworks.wmich.edu/cgi/viewcontent.cgi?article=1154&context=masters_theses.

An overview of the petroleum systems of the northern deep-water Gulf of Mexico

Paul Weimer, Renaud Bouroullec, James Adson, and Stephen P. J. Cossey

ABSTRACT

The northern deep-water Gulf of Mexico is one of the most active deep-water petroleum provinces in the world. This paper introduces the regional geologic setting for the northern deep-water Gulf of Mexico and briefly discusses the importance of technology in developing the area's resources. Exploration has focused on four major geologic provinces: Basins, Subsalt, Fold Belt, and Abyssal Plain. These provinces formed from the complex interactions between Mesozoic–Cenozoic sedimentation and tectonics. Improved understanding of the geology of these provinces has largely been accomplished by improvements in seismic acquisition and processing. In addition, advances in drilling technology have permitted drilling and field development in increasingly greater water depths.

The 226 oil and gas fields and discoveries in the northern deep-water Gulf of Mexico are summarized in terms of their exploration and development history, producing facility, ages of reservoirs (Upper Jurassic, upper Paleocene–lower Eocene, Oligocene, lower Miocene–upper Pleistocene), and trap type (structural, combined structural-stratigraphic, and stratigraphic). In addition, the interpreted regional distribution of Upper Jurassic and possible Lower Cretaceous source, source rocks is shown, in part based on the 26 wells that have penetrated these source rocks.

The eight papers in this special issue review the geology of the Mississippi Canyon and northern Atwater Valley protraction areas. The first five papers review the subregional structural setting and the evolution of its tectonics and petroleum systems. The final three papers summarize the geologic evolution of two economically important intraslope basins—Thunder Horse and Mensa—in terms of their stratigraphy, structural evolution, and petroleum

Copyright ©2017. The American Association of Petroleum Geologists. All rights reserved.

Manuscript received October 18, 2008; provisional acceptance February 9, 2009; revised manuscript received May 14, 2015; revised manuscript provisional acceptance April 23, 2015; 2nd revised manuscript received May 5, 2015; final acceptance September 1, 2016.
DOI:10.1306/09011608136

AUTHORS

PAUL WEIMER ~ *Energy and Applied Minerals Research Center, Department of Geological Sciences, University of Colorado, Boulder, Colorado 80309; paul.weimer@colorado.edu*

Paul Weimer holds the Bruce D. Benson Endowed Chair in the Department of Geological Sciences at the University of Colorado and serves as the director of the Energy and Minerals Applied Research Center. His recent research activities include the study of the petroleum systems of deep-water margins, creating animations for public outreach, and co-chairing the 100th AAPG Anniversary Committee.

RENAUD BOUROULLEC ~ *Petroleum Geosciences, TNO, Princetonlaan 6, 3584 CB Utrecht, The Netherlands; renaud.bouroullec@tno.nl*

Renaud Bouroullec received his B.Sc. degree from the Université de Bretagne Occidentale, Brest, France (1994); his M.Sc. degree from the Université de Rennes 1, France (1996); and his Ph.D. from Imperial College, London (2001). After graduation, he conducted postdoctoral research at the Energy and Minerals Applied Research Center at the University of Colorado, Boulder, and then joined the Bureau of Economic Geology at The University of Texas at Austin, where he was principal investigator of the Laser-Assisted Analogs for Siliciclastic Reservoirs Consortium. He then joined the Chevron Center of Research Excellence, Department of Geology, Colorado School of Mines, as a research assistant professor. Currently, he is a senior researcher and Basin Analysis Team coordinator at TNO, the Netherlands Organisation for Applied Scientific Research.

JAMES ADSON ~ *Energy and Applied Minerals Research Center, Department of Geological Sciences, University of Colorado, Boulder, Colorado 80309; present address: Level 3 Communications, 1025 Eldorado Boulevard, Broomfield, Colorado 80021; james.adson@colorado.edu*

Jim Adson works as a senior Internet security analyst at Level 3 Communications. He received his B.A. from Temple University in

Tokyo in 2010 in Far East languages. He worked as an animator of Colorado geology from 2011 to 2016 at the Interactive Geology Project at the University of Colorado.

Stephen P. J. Cossey ~ *Cossey and Associates, Inc., P.O. Box 1510, Durango, Colorado 81302; cosseygeo@aol.com*

Stephen P. J. Cossey is a geologist with over 37 years of experience with Conoco (1978 to 1983) and with Sohio/BP (1983 to 1995). From 1990 to 1992, he was at BP Research in Sunbury, United Kingdom, and helped to start their deep-water research program. In 1995, he started the consulting company Cossey and Associates, Inc., specializing in the exploration, development, and modeling of deep-water clastic reservoirs, with emphasis on the Gulf of Mexico.

ACKNOWLEDGMENTS

We thank AAPG Editor Mike Sweet and past elected editors Gretchen Gillis and Steve Laubach for their support in assembling this issue. This *AAPG Bulletin* issue includes many of the research results from the University of Colorado Gulf of Mexico Research Consortium Phase III. Work was done from late 1999 to early 2005; 12 M.S. degrees were awarded for the research, and 3 research scientists were supported. Our sincerest thanks go to the following companies for their support and technical input: AEC, Agip, Amerada Hess, Anadarko, BP, Burlington, Chevron, Conoco, Devon, Dominion, Enterprise, ExxonMobil, Helis, Kerr McGee, Maersk, Marathon, Maxus, Murphy, Nexen, Norsk Hydro, Ocean Energy, Occidental, PanCanadian, Pemex, Petrobras, Phillips, Shell, Texaco, Total, Unocal, Vastar, and Woodside. Members of the sponsoring companies have given us input that has improved some of the interpretation.

We thank the following companies and individuals who made this study possible. Seismic data have been kindly provided by WesternGeco Geophysical (Jerry Peterson), now Schlumberger (Ian Bryant, Daniel Domeracki); PGS Geophysical (Mark Wilkinson); and TGS Geophysical (John Adamick). Bob Wentland was essential in helping to arrange the donation of some of these data sets. Software donations were from IHS (Petra, SMT), Landmark Graphics

systems. These two basins contain two of the larger oil and gas fields, respectively, in the northern deep-water Gulf of Mexico.

INTRODUCTION

The northern deep-water Gulf of Mexico (i.e., >457 m [1500 ft] water depth) is one of the most active deep-water areas in the world for petroleum exploration and development (Figure 1). The geology of the area is extremely complex, comprising a thick Cenozoic sedimentary fill (>15,000 m [50,000 ft]) and a structural setting including multilevel allochthonous salt systems, extensional and contractional faults, and large, salt-cored fold belts. In the early 1980s, only a few wells in this area had been drilled in water depths greater than 457 m (1500 ft); 30 yr later, there are 226 discoveries and fields in these depths (Tables 1–5).

The northern deep-water Gulf of Mexico is noteworthy for three reasons. First, its petroleum is an important part of the US energy supply. In 2015, the US Energy Information Administration predicted daily oil production of 1.52 million bbl, approximately 16% of the daily production in the United States (Yen, 2016). Production is expected to increase to approximately 1.9 million BOE/day by 2016 and then stay at that level for the next 5 yr (Beaubouef, 2015; Yen, 2016). Second, the northern deep-water Gulf of Mexico serves as a geologic analog to help us understand other deep-water basins. Third, its geologic complexity spurred many technological advances; workers have had to invent new techniques in seismic imaging, drilling, and development.

This theme issue of the *AAPG Bulletin* consists of eight papers that address the different components of the petroleum systems for one part of the northeastern deep-water Gulf of Mexico—specifically in the Mississippi Canyon and Atwater Valley protraction areas. This introductory paper is intended for geoscientists who are not familiar with the details of the northern Gulf of Mexico. We explain the advances in technology that have led to economic success. We also summarize the area's geology, exploration provinces, and exploration plays to give the regional context of the seven following papers that focus on the eastern part of the northern Gulf of Mexico.

IMPROVING TECHNOLOGY FOR EXPLORATION AND DEVELOPMENT

Drilling in Deep Water

Two geologic attributes found in the north-central deep-water Gulf of Mexico and only a few other deep-water basins create significant challenges in drilling. First, overpressured sediments

occur directly below the sea floor and continue downward in the shallow subsurface (Day-Stirrat et al., 2012). These shallow, overpressured sediments are likely caused by clay, specifically smectite (N. Braunsdorf, 2015, personal communication). Second, the sand-bearing, near-surface sedimentary section (upper 1000 m [3300 ft]) can be out of equilibrium with the surrounding overpressured muds. Undercompacted, near-surface sands, deposited late in the basin's history (in some cases during the past few tens of thousands of years), create flow problems during drilling (i.e., large volumes of water released into the well bore from overpressured sands, termed "shallow-water flow"). Other shallow drilling problems include overpressured gas-charged sands and near-surface faults. All of these shallow-subsurface drilling challenges, when identified, can often be avoided or at least mitigated.

Deep-water exploration and development have many challenges, which have been addressed by innovative drilling technology. These challenges include (1) routine drilling in water depths 458 to 3050 m (1650 to 10,000 ft) and beyond; (2) safely securing development platforms during hurricanes and storms; (3) adapting for high-velocity loop and eddy currents that induce vortex vibration and motion to marine risers; (4) near-surface drilling hazards; (5) drilling through thick, allochthonous salt masses (up to 3 km [9840 ft] thick) with unpredictable layers of enclosed nonsalt sediments; (6) abrupt and unpredictable pressure changes at the base of salt, which are extremely difficult to predict and remediate; (7) underpressured porous and permeable sands (i.e., thief zones), with a loss of circulation leading to a significant loss of drilling fluid; (8) high temperatures, high pressures, and low permeability in ultradeep reservoirs; and (9) biodegraded oil, creating asphaltenes and waxes that impede drilling circulation in pipes.

With successful exploration in increasing water depths, drilling and development facilities have evolved from simple jackup rigs to tension-leg platforms, floating production storage offloading units (FPSOs), floating platforms, and subsea tiebacks (Figure 2). The vast amount of drilling in the northern deep-water Gulf of Mexico has led to several record-breaking achievements for exploration and production (Figure 2). Exploration drilling is becoming more common in ultradeep water, where 40 fields and discoveries have been drilled in water depths greater than 2135 m (7000 ft) (Table 1). Long-distance subsea tiebacks, a technology first developed in the North Sea, are now common in some areas of the northern deep-water Gulf of Mexico; 143 of the 226 fields and discoveries are or will be produced by subsea tiebacks (Tables 2–5), and this technology will increasingly be used. The deepest subsea tieback is the Tobago field in 2945 m (9656 ft) of water for the Perdido SPAR hub in Alaminos Canyon; two separate fields have been tied back to one production facility (Figure 2; Table 4). With ongoing development, these water-depth records for development are broken every few years. The deepest water depth for

(Connie Johnson, Bill Keach), Paradigm (Duane Dopkins), and Platte River (China and Jay Leonard). Digital wire-line logs were donated from A2D (Bill Ross, Linda Santiago). Art Waterman (PaleoData, Inc.) kindly allowed the use of his proprietary biostratigraphic data. A special thanks to IHS and Pete Stark for creating the graph in Figure 23. Finally, we are indebted to Norman Rosen, executive director of the Gulf Coast Section SEPM Foundation; Kate Kipper, executive director of the Gulf Coast Association of Geological Societies; ION Geophysical; Springer-Verlag; and CGG (Mathhew Bognar) for their permission to reprint their figures.

The input from the following colleagues was absolutely essential to the completion of this paper: Jon Blickwede, Mary Broussard, Robin Broussard, Steve Burt, Andrew Cook, Richard Denne, Scott Douglas, Shirley Dutton, Mike Fauquier, Mike Fein, Chelsea Fenn, Ted Godo, Alfredo Guzman, Sverre Henricksen, Peter Etherman, Dan Huffman, Mike Jobe, Ian Kane, Jack Leedy, Ann Marchand, Tim McGinty, Alonso Navarro, Henry Pettingill, Andy Pulham, David Reiter, Toby Roesler, Kurt Rovang, Kris Schwendeman, Colin Stabler, Cheree Stover, John Wagner, Art Waterman, Paul Wieg, Larry Zarra, and Eric Zimmerman. To all of them, we express our sincerest gratitude.

The inclusion of two sections above was only possible with the input of Rick Lindsey, who patiently walked us through the discussion of seismic acquisition and processing, and Larry Zarra and Tim Diggs, who helped us summarize the reservoir quality accurately. For all three of them, 100,000 thanks.

We thank the following individuals for their careful reviews, which greatly improved the final content: Shirley Dutton, Laurie Lamar, Mike Leibovitz, Rick Lindsay, Robert Loucks, Ira Pasternak, David Sawyer, Kris Schwendeman, Craig Shipp, Derek Smalls, M. S. Wacker, and Larry Zarra. We alone are responsible for the interpretation presented here.

EDITOR'S NOTE

Color versions of Figures 1–24 can be seen in the online version of this paper.

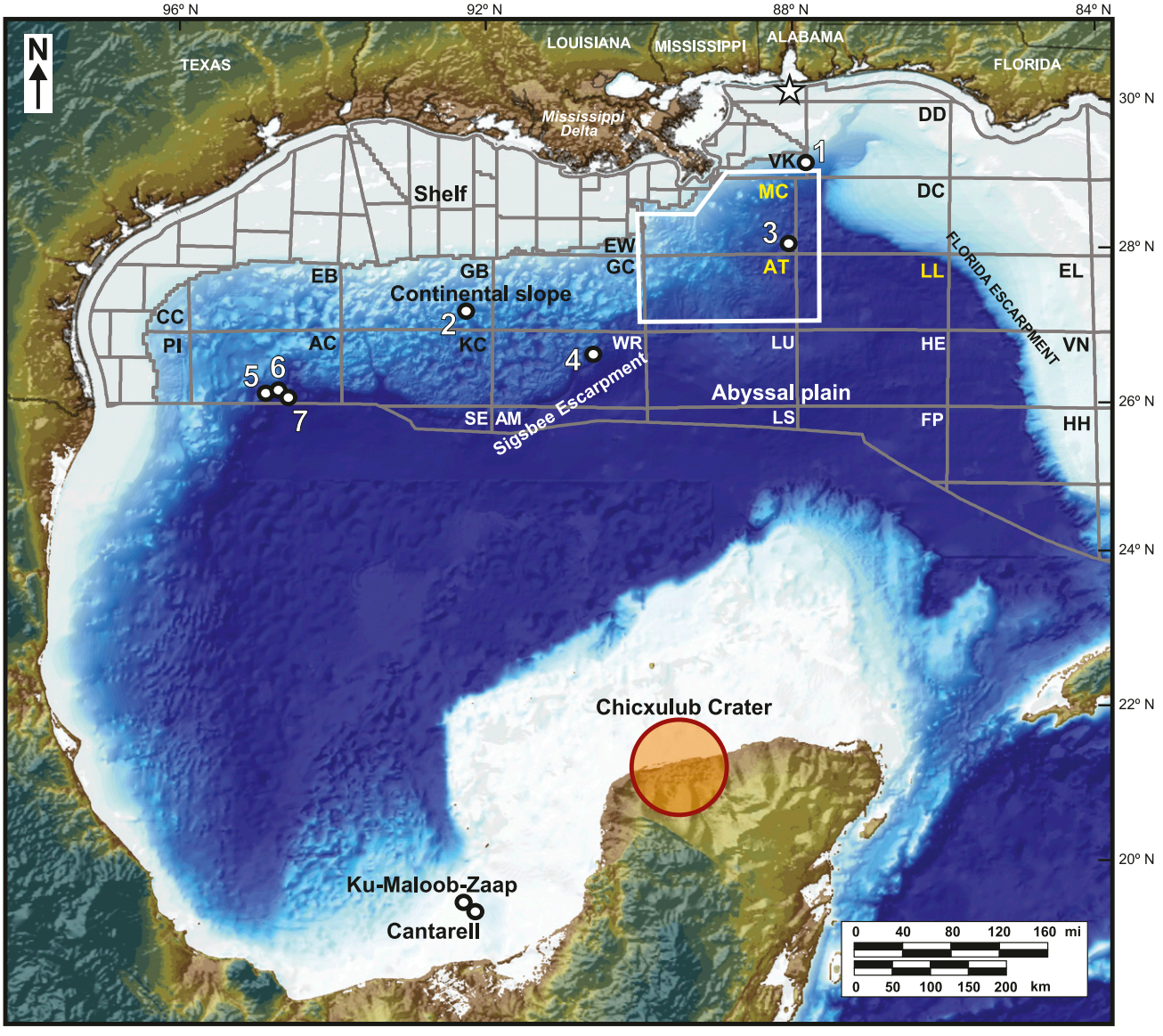

Figure 1. Regional shaded bathymetric map of the Gulf of Mexico, with protraction boundaries. Outline of study area is shown by a white polygon. Circles indicate wells discussed in the text and shown in Figure 2. The location of the Fairway field in Mobile Bay is shown by a white star. Locations of Chicxulub crater and the supergiant Cantarell and Ku-Maloob-Zaap fields are shown. Base map is courtesy of Trey Meckel and Wayne Clark. Abbreviations for protraction areas: AC = Alaminos Canyon; AM = Amery Terrace; AT = Atwater Valley; CC = Corpus Christi; DC = DeSoto Canyon; DD = Destin Dome; EB = East Breaks; EL = Elbow; EW = Ewing Bank; FP = Florida Plain; GB = Garden Banks; GC = Green Canyon; HE = Henderson; HH = Howell Hook; KC = Keathley Canyon; LL = Lloyd Ridge; LS = Lund South; LU = Lund; MC = Mississippi Canyon; PI = Post Isabel; SE = Sigsbee Escarpment; VK = Viosca Knoll; VN = Vernon; WR = Walker Ridge.

exploration drilling in the Gulf of Mexico was 3300 m (10,010 ft) in Alaminos Canyon 951 in 2003.

The technology for the new deep-water floating rigs (semisubmersible or drillship) has continued to improve to address the upcoming challenges. Many of the newest deep-water rigs have two independently operated drill floors on the rig (termed dual activity), with more capability to drill deeper, allowing a total drill-string length of 12,200 m (40,000 ft) in water depths up to 3660 m (12,000 ft). Although commonly used in many deep-water basins globally, only two FPSOs in the Gulf of Mexico have been used in the development of the Cascade and Chinook fields in Walker Ridge (8877 ft [2706 m]) and the Stones field (9576 ft [2919 m]) in Walker Ridge 508. These fields are also the deepest water for FPSOs in the world (Offshore Technology, 2015).

Table 1. Fields and Discoveries in Water Depths Greater Than 7000 ft (2134 m), Northern Deep-Water Gulf of Mexico

Field Number in Figure 5A	Field Name	Location Abbreviation	Discovery Year	Water Depth (ft [m])	Operator
216	Maximino DL	Mexico	2014	9984 (3043)	Pemex
203	Tobago	AC 859	2004	9636 (2937)	Shell
195	Stones	WR 508	2005	9576 (2919)	Shell
215	Maximino	Mexico	2012	9574 (2918)	Pemex
217	Supremus	Mexico	2013	9426 (2873)	Pemex
201	Silvertip	AC 815	2004	9356 (2852)	Shell
219	Cratos	Mexico	2015	9213 (2808)	Pemex
224	Atlas	LL 50	2003	9000 (2743)	Anadarko
226	Cheyenne	LL 399	2004	8987 (2739)	Anadarko
213	Chinook	WR 469	2003	8826 (2690)	Petrobras
223	Atlas NW	LL 5	2004	8810 (2685)	Anadarko
221	Jubilee	AT 349	2003	8800 (2682)	Anadarko
225	Jubilee Extension	LL 309	2005	8774 (2674)	Anadarko
189	Phobos	SE 39	2013	8500 (2591)	Anadarko
214	Exploratus	Mexico	2014	8488 (2587)	Pemex
220	Vortex	AT 261	2002	8340 (2542)	Anadarko
222	Mondo NW Extension	LL 1	2005	8340 (2542)	Anadarko
218	Trion	Mexico	2012	8304 (2531)	Pemex
212	Cascade	WR 206	2002	8203 (2500)	Petrobras
10	Spiderman	DC 621	2003	8100 (2469)	Anadarko
202	Great White	AC 857	2002	8009 (2441)	Shell
211	Q	MC 961	2005	7925 (2415)	Statoil
204	Merganser	AT 37	2002	7900 (2408)	Anadarko
9	San Jacinto	DC 618	2004	7850 (2393)	ENI
136	Callisto	MC 876	2001	7800 (2377)	Anadarko
200	Logan	WR 969	2011	7750 (2362)	Statoil
119	Na Kika–Coulomb	MC 657	1988	7600 (2316)	Shell
114	Rydberg	MC 525	2014	7479 (2279)	Shell
8	Vicksburg	DC 353	2007	7457 (2273)	Shell
122	Troubadour	MC 699	2013	7438 (2267)	Noble
169	Hadrian–Hadrian South	KC 919	2009	7425 (2263)	ExxonMobil
101	Appomattox	MC 392	2010	7290 (2222)	Shell
99	Camden Hills	MC 348	1999	7213 (2198)	ATP
121	Big Bend	MC 698	2012	7200 (2194)	Noble
168	Lucius	KC 875	2009	7100 (2164)	Anadarko
197	Julia	WR 627	2007	7087 (2159)	ExxonMobil
98	Aconcagua	MC 305	1999	7039 (2145)	ATP
112	Na Kika–Fourier	MC 522	1989	7000 (2134)	BP
118	Na Kika–East Anstey	MC 607	1998	7000 (2134)	BP
199	Jack	WR 759	2004	7000 (2134)	Chevron

Locations of fields are shown in Figures 5, 10, and 11.

Abbreviations: AC = Alaminos Canyon; AT = Atwater Valley; DC = DeSoto Canyon; KC = Keathley Canyon; LL = Lloyd Ridge; MC = Mississippi Canyon; SE = Sigsbee Escarpment; WR = Walker Ridge.

Table 2. Fields and Discoveries in Basins Province, Northern Deep-Water Gulf of Mexico

Field Number	Field Name	Location Abbreviation	Discovery Year	Water Depth (ft [m])	Operator	Status	Onstream	Production Type	Age of Reservoir	Trap Type(s)
1	Madison	AC 24	1998	4854 (1479)	ExxonMobil	Producing	2002	SS	l. Pliocene	Three-way closure against salt flank
2	Hoover	AC 25	1997	4806 (1465)	ExxonMobil	Producing	2000	SPAR	l. Pliocene	Four-way closure (compactional drape)
3	Diana South	AC 65	1996	4679 (1426)	ExxonMobil	Abandoned, 2015	2000	SS	l. Pliocene	Three-way closure against salt flank
4	Dalmatian North	DC 4	2008	5876 (1791)	Murphy	Producing	2014	SS	m. Miocene	Stratigraphic
5	Dalmatian	DC 48	2008	5876 (1791)	Murphy	Producing	2014	SS	m. Miocene	Stratigraphic
6	Dalmatian South	DC 134	2012	6394 (1949)	Murphy		2016	SS	l. Miocene	Stratigraphic
7	Shiloh	DC 269	2003	7509 (2289)	Shell	Appraisal	Projected 2020	SS	L. Jurassic	Three-way closure against salt flank
8	Vicksburg	DC 353	2007	7457 (2273)	Shell	Appraisal	Projected 2020	SS	L. Jurassic	Three-way closure against salt flank
9	San Jacinto	DC 618	2004	7850 (2393)	ENI	Abandoned, 2011	2007	SS	l. Miocene	Four-way closure (compactional drape)
10	Spiderman	DC 621	2003	8100 (2469)	Anadarko	Abandoned, 2015	2007	SS	l. Miocene	Four-way closure (compactional drape)
11	Lost Ark	EB 421	2001	2740 (1749)	Noble	Abandoned, 2009	2002	SS	l. Pliocene	Three-way closure against fault–stratigraphic
12	SW Horseshoe	EB 430	2000	2285 (696)	Walter	Producing	2005	SS	l. Pliocene	Three-way closure against fault
13	Balboa	EB 597	2001	3373 (1028)	Apache	Producing	2010	SS	l. Pliocene	Two-way closure between faults–onlap
14	North Boomvang	EB 599	2001	3153 (961)	Anadarko	Producing	2007	SS	l. Pliocene–e. Pleistocene	Three-way closure against fault
15	Nansen	EB 602	1999	3686 (1123)	Anadarko	Producing	2002	SPAR	l. Pliocene–e. Pleistocene	Three-way closure against fault
16	Tomahawk	EB 623	2003	3514 (1071)	Marubeni	Producing	2004	SS	m. Miocene	Three-way fault closure against fault–stratigraphic
17	Boomvang	EB 643	1997	3539 (1079)	Anadarko	Producing	2002	SPAR	l. Pliocene–e. Pleistocene	Faulted high over salt ridge

(*continued*)

Table 2. Continued

Field Number	Field Name	Location Abbreviation	Discovery Year	Water Depth (ft [m])	Operator	Status	Onstream	Production Type	Age of Reservoir	Trap Type(s)
18	Navajo–Northwest	EB 646	2001	4114 (1254)	Anadarko	Producing	2002	SS	l. Pliocene–e. Pleistocene	Three-way closure against fault
19	Diana	EB 945	1990	4670 (1423)	ExxonMobil	Abandoned, 2015	2000	SS	l. Pliocene	Three-way closure against salt flank–stratigraphic
20	Marshall	EB 949	1998	4376 (1334)	ExxonMobil	Producing	2001	SS	e. Pliocene	Three-way closure against salt flank–stratigraphic
21	Rockefeller	EB 992	1996	4872 (1424)	ExxonMobil	Abandoned 2015	2009	SS	e. Pliocene	Four-way closure (compactional drape)
22	Ewing Bank 878	EW 878	2000	1523 (464)	Walter	Producing	2001	SS	e. Pliocene	Three-way closure against fault
23	Morpeth–Klamath	EW 921	1992	1747 (532)	ENI	Producing	1998	TLP	l. Miocene–e. Pliocene	Three-way closure against fault–stratigraphic
24	Prince	EW 958	1994	1502 (457)	Enven	Producing	2001	SS	e. Pliocene	Stratigraphic
25	Arnold	EW 963	1996	1752 (534)	Marathon	Producing	1998	SS	e. Pleistocene	Three-way closure against fault
26	Black Widow	EW 966	1998	1840 (560)	Apache	Producing	2000	SS	e. Pleistocene	Three-way closure fault–dip
27	Manta Ray	EW 1006	2003	1854 (565)	Walter	Abandoned, 2003	1999	SS	e. Pleistocene	Three-way closure against salt flank
28	Northwestern	GB 200	1998	1750 (533)	Hess	Producing	2000	SS	l. Pliocene–e. Pleistocene	Three-way closure against salt flank
29	Cottonwood	GB 244	2001	2000 (610)	Petrobras	Producing	2007	SS	e. Pliocene	Three-way closure against fault
30	Power Play	GB 258–302	2006	2310 (704)	W&T	Producing	2008	SS	l. Pliocene	Three-way closure against salt–fault
31	Baldpate	GB 260	1991	1650 (502)	Hess	Producing	1998	FP	e. Pliocene–e. Pleistocene	Three-way closure against salt
32	Pyrenees	GB 293	2009	2100 (640)	W&T	Abandoned, 2015	2012	SS	e. Pliocene	Three-way closure against salt
33	Sargent	GB 339	2008	2240 (683)	Deep Gulf Energy	Producing	2010	SS	l. Pleistocene	Stratigraphic
34	Habanero	GB 341	1999	2001 (610)	Shell	Producing	2003	SS	e. Pliocene	Three-way closure against salt

(*continued*)

Table 2. Continued

Field Number	Field Name	Location Abbreviation	Discovery Year	Water Depth (ft [m])	Operator	Status	Onstream	Production Type	Age of Reservoir	Trap Type(s)
35	Llano	GB 386	1989	2294 (699)	Shell	Producing	2004	SS	l. Miocene–e. Pliocene	Three-way closure against salt
36	Auger	GB 426	1987	2863 (873)	Shell	Producing	1994	TLP	e. Pliocene–e. Pleistocene	Three-way closure against fault–stratigraphic
37	Cardamom	GB 427	1995	2873 (876)	Shell	Producing	2014	SS	l. Pliocene–e. Pleistocene	Three-way closure against fault–stratigraphic
38	Geauxpher–Noonan	GB 462–506	2008	2820 (859)	ERT	Producing	2009	SS	e. Pleistocene	Three-way closure against fault
39	Bushwood	GB 463	2009	2700 (823)	Apache	Appraisal	Projected 2017		e. Pleistocene	Three-way closure against fault
40	Danny	GB 506	2007	2700 (823)	ERT	Producing	2010	SS	e. Pliocene	Three-way closure against fault
41	Ozona Deep	GB 515	2001	3280 (999)	Marathon	Development	Projected 2017	SS	l. Miocene	Three-way closure against salt flank
42	Serrano	GB 516	1996	3400 (1036)	Shell	Abandoned, 2004	2001	SS	e. Pliocene–e. Pleistocene	Stratigraphic
43	Oregano	GB 559	1999	3400 (1036)	Shell	Producing	2001	SS	e. Pliocene–e. Pleistocene	Three-way closure against fault–stratigraphic
44	Macaroni	GB 602	1995	3700 (1128)	Shell	Producing	1999	SS	e. Pliocene–e. Pleistocene	Three-way closure against fault–stratigraphic
45	Winter	GB 605	2009	3400 (1036)	W&T	Appraisal			l. Pleistocene	Stratigraphic
46	Dawson Deep	GB 625	2004	2900 (884)	Anadarko	Producing	2006	SS	l. Pliocene–e. Pleistocene	Faulted closure against salt overhang
47	Durango	GB 667	2001	3150 (960)	Anadarko	Producing	2004	SS	e. Pleistocene	Three-way closure against salt flank–fault–stratigraphic
48	Gunnison	GB 668	2000	3131 (954)	Anadarko	Producing	2003	SPAR	e. Pleistocene	Three-way closure against salt flank–fault–stratigraphic
49	Dawson	GB 669	2001	3000 (914)	Anadarko	Producing	2004	SS	e. Pleistocene	Three-way closure against salt flank–fault–stratigraphic

(*continued*)

Table 2. Continued

Field Number	Field Name	Location Abbreviation	Discovery Year	Water Depth (ft [m])	Operator	Status	Onstream	Production Type	Age of Reservoir	Trap Type(s)
50	Magnolia	GB 783	1999	4700 (1432)	ConocoPhillips	Producing	2004	TLP	e. Pleistocene	Three-way closure against fault–stratigraphic
51	Katmai	GC 40	2014	2100 (640)	Noble	Appraisal			e.–m. Miocene	Four-way closure against faults
52	Rocky	GC 110	1987	1785 (544)	Marubeni	Producing	1995	SS	l. Pliocene?	Three-way closure against salt flank
53	Angus	GC 113	1997	2000 (610)	Marubeni	Producing	1999	SS	e. Pleistocene	Three-way closure against salt flank
54	Popeye	GC 116	1985	2067 (630)	Shell	Producing	1996	SS	e. Pleistocene	Three-way closure against fault
55	Manatee	GC 155	1998	1940 (591)	Marubeni	Producing	2002	SS	l. Pliocene	Three-way closure against salt–stratigraphic
56	Brutus–Ru	GC 158	1989	2985 (910)	Shell	Producing	2001	TLP	l. Pliocene–e. Pleistocene	Three-way closure against salt–fault–stratigraphic
57	Jolliet	GC 184	1981	1750 (533)	MC Offshore	Producing	1989	TLP	Pleistocene	Three-way closure against fault
58	Lorien	GC 199	2003	2179 (664)	Noble	Producing	2006	SS	l. Miocene	Stratigraphic
59	Genesis	GC 205	1988	2628 (801)	Chevron	Producing	1999	FPS	e. Pleistocene	Three-way closure against salt–stratigraphic
60	Phoenix	GC 236	1998	1969 (600)	Helix (ERT)	Producing	2010	FPU	e. Pliocene	Three-way closure against salt flank
61	Aspen	GC 243	2001	3063 (934)	Walter	Producing	2002	SS	l. Miocene	Three-way closure against salt weld
62	Droshky	GC 244	2007	2900 (884)	Marathon	Producing	2010	SS	l. Miocene	Three-way structural-stratigraphic against salt
63	Troika–Wasatch	GC 244	1994	2679 (816)	Marathon	Producing	1997	SS	e. Pliocene	Three-way closure against salt flank
64	Glider	GC 248	1996	3300 (1006)	Shell	Producing	2004	SS	Pliocene	Three-way pinchout against salt–stratigraphic faults
65	Allegheny	GC 254	1992	3225 (983)	ENI	Producing	1999	TLP	e. Pliocene	Three-way closure against fault–weld

(*continued*)

Table 2. Continued

Field Number	Field Name	Location Abbreviation	Discovery Year	Water Depth (ft [m])	Operator	Status	Onstream	Production Type	Age of Reservoir	Trap Type(s)
66	Allegheny South	GC 298	2005	3280 (999)	ENI	Producing	2005	SS	l. Pliocene–e. Pleistocene	Three-way closure against salt–stratigraphic
67	Clipper	GC 300	2005	3452 (1052)	Bennu	Producing	2013	SS	e. Pleistocene	Three-way closure against salt–stratigraphic
68	Front Runner	GC 338	2000	3500 (1067)	Murphy	Producing	2004	SPAR	Pliocene	Three-way closure against salt–stratigraphic
69	Front Runner South	GC 339	2001	3500 (1067)	Murphy	Producing	2005	SS	Pliocene	Three-way closure against fault–stratigraphic
70	Quatrain	GC 382	2002	3500 (1067)	Murphy	Producing	2005	SS	Pliocene	Three-way closure against fault–stratigraphic
71	Pegasus	GC 385	2005	3491 (1064)	ENI	Producing	2008	SS	e. Pleistocene	Three-way closure against fault–stratigraphic
72	Samurai	GC 432	2009	3400 (1036)	Murphy	Appraisal			e.–m. Miocene	Four-way closure (faulted)
73	Condor	GC 448	2008	3266 (995)	Deep Gulf Energy	Producing	2011	SS	e. Pleistocene	Three-way closure against salt–faults
74	King Kong	GC 472	1989	3799 (1158)	ENI	Abandoned, 2005	2002	SS	e. Pliocene	Three-way closure against fault
75	Wide Berth	GC 490	2009	3700 (1128)	Apache	Producing	2012		e. Pleistocene	Two-way fault–stratigraphic–dip
76	Ness Deep	GC 507	2001	3950 (1204)	Hess	Appraisal		SS	l. Miocene	Three-way closure against salt weld
77	Yosemite	GC 516	2001	4452 (1357)	ENI	Abandoned, 2012	2002	SS	l. Pliocene	Three-way closure against fault–stratigraphic
78	K2 North–K2	GC 518–562	2004	4000 (1219)	Anadarko	Producing	2006	SS	e.–m. Miocene	Three-way closure against salt–stratigraphic
79	Marco Polo	GC 608	2000	4300 (1311)	Anadarko	Producing	2004	TLP	Pliocene	Three-way closure against fault–salt flank
80	Holstein	GC 644	1999	4292 (1308)	Plains E&P	Producing	2004	SPAR	l. Pliocene to e. Pleistocene	Three-way closure against faults–stratigraphic
81	Daniel Boone	GC 646	2004	4230 (1289)	W&T	Abandoned, 2015	2009	SS	Pliocene	Three-way closure against fault–salt flank

(*continued*)

Table 2. Continued

Field Number	Field Name	Location Abbreviation	Discovery Year	Water Depth (ft [m])	Operator	Status	Onstream	Production Type	Age of Reservoir	Trap Type(s)
82	Constitution	GC 680	2003	5100 (1554)	Anadarko	Producing	2006	SPAR	e. Pliocene–l. Pliocene	Three-way closure against salt–fault
83	Ticonderoga	GC 768	2004	5250 (1600)	Anadarko	Producing	2006	SS	e. Pliocene-l. Pliocene	Three-way closure against salt–fault
84	Pompano II	MC 28	1986	1864 (568)	Stone	Producing	1996	SS	l. Miocene–Pliocene	Three-way closure against fault and stratigraphic traps
85	Cardona–Cardona South	MC 29	2014	2135 (651)	Stone	Producing	2014	SS	l. Miocene	Three-way closure against salt flank
86	Mississippi Canyon 72	MC 72	2008	2013 (613)	LLOG	Producing	2009	SS	l. Miocene	Stratigraphic
87	Otis	MC 79	2014	3950 (1204)	LLOG	Producing	2016	SS	l. Miocene	Stratigraphic
88	King–King West	MC 84	1993	5386 (1642)	BP	Producing	2002	SS	l. Miocene	Three-way closure against fault
89	Horn Mountain	MC 126	1999	5400 (1646)	Plains E&P	Producing	2002	SPAR	l. Miocene	Three-way closure against fault
90	Mississippi Canyon 161	MC 161	2005	2924 (800)	Stone	Producing	2008	SS	e. Pliocene	Three-way closure against fault
91	Mandy	MC 199	2010	2096 (639)	LLOG	Producing	2012	SS	e. Pliocene	Four-way closure against fault
92	King's Peak 1	MC 217	1992	6541 (1994)	BP	Producing	2002	SS	l. Miocene	Stratigraphic
93	Matterhorn	MC 243	1991	2862 (872)	W&T	Producing	2003	TLP	e. Pliocene	Three-way closure along salt flank
94	Rigel	MC 252	1999	5200 (1585)	ENI	Abandoned, 2011	2006	SS	l. Miocene	Stratigraphic
95	Neidermeyer	MC 253	2013	3400 (1036)	LLOG	Producing	2015	SS	m. Miocene	Four-way closure (extensional–turtle)
96	Seventeen Hands	MC 299	2000	5400 (1646)	ENI	Abandoned, 2011	2006	SS	l. Miocene	Stratigraphic
97	Marmalard	MC 300	2012	5781 (1762)	LLOG	Producing	2015	SS	m. Miocene	Three-way closure against fault
98	Aconcagua	MC 305	1999	7039 (2145)	ATP	Abandoned, 2013	2002	SS	l. Miocene	Three-way closure against fault

(*continued*)

Table 2. Continued

Field Number	Field Name	Location Abbreviation	Discovery Year	Water Depth (ft [m])	Operator	Status	Onstream	Production Type	Age of Reservoir	Trap Type(s)
99	Camden Hills	MC 348	1999	7213 (2198)	ATP	Abandoned, 2010	2002	SS	l. Miocene	Stratigraphic
100	Na Kika–Kepler	MC 383	1987	5800 (1768)	BP	Producing	2004	SS	l. Miocene	Stratigraphic
101	Appomattox	MC 392	2010	7290 (2222)	Shell	Appraisal	Projected 2020	SS	L. Jurassic	Three-way closure against fault
102	La Femme	MC 427	2004	5800 (1768)	LLOG	Appraisal			l. Miocene	Stratigraphic
103	Na Kika–Ariel	MC 429	1995	6200 (1890)	BP	Producing	2004	SS	l. Miocene	Stratigraphic
104	Son of Bluto II	MC 431	2012	5013 (1528)	LLOG	Producing	2015	SS	l. Miocene	Stratigraphic
105	Appaloosa	MC 459	2008	2500 (762)	ENI	Producing	2011	SS	l. Pliocene	Three-way closure against salt flank
106	Zia	MC 496	1997	1800 (549)	Marubeni	Producing	2003	SS	l. Miocene	Three-way closure against fault–stratigraphic
107	Longhorn	MC 502–546	2006	2461 (750)	ENI	Producing	2009	SS	e. Pliocene	Four-way closure against fault
108	Who Dat	MC 503	2007	3099 (944)	LLOG	Producing	2011	FPS	l. Miocene–e. Pliocene	Three-way closure against salt flank
109	Wrigley	MC 506	2005	3700 (1128)	W&T	Producing	2007	SS	l. Miocene	Stratigraphic
110	Santiago-Santa Cruz	MC 519–563	2011	6500 (1981)	Noble	Producing	2012	SS	m. Miocene	Three-way closure against fault
111	Na Kika–Herschel	MC 520	1997	6800 (2073)	BP	Producing	2004	SS	l. Miocene	Three-way closure against fault
112	Na Kika–Fourier	MC 522	1989	7000 (2134)	BP	Producing	2004	SS	l. Miocene	Stratigraphic
113	Rydberg	MC 525	2014	7479 (2279)	Shell	Appraisal	Projected 2020	SS	L. Jurassic	Three-way closure against fault
114	Medusa North	MC 538	2003	2185 (666)	Murphy	Producing	2005	SS	e. Pliocene	Three-way closure against salt flank
115	Isabela	MC 562	2007	6500 (1981)	BP	Producing	2012	SS	m. Miocene	Four-way dosure against fault
116	Medusa	MC 582	1999	2125 (648)	Murphy	Producing	2002	SPAR	e. Pliocene	Three-way closure against salt flank
117	Ulysses	MC 583	2002	2487 (758)	ENI	Producing	2005	SS	e. Pliocene	Stratigraphic
118	Na Kika–East Anstey	MC 607	1998	7000 (2134)	BP	Abandoned, 2010	2004	SS	l. Miocene	Three-way closure against salt flank

(*continued*)

Table 2. Continued

Field Number	Field Name	Location Abbreviation	Discovery Year	Water Depth (ft [m])	Operator	Status	Onstream	Production Type	Age of Reservoir	Trap Type(s)
119	Na Kika–Coulomb	MC 657	1988	7600 (2316)	Shell	Producing	2004	SS	m. Miocene	Three-way closure against salt flank
120	Blind Faith	MC 696	2001	6900 (2103)	Chevron	Producing	2008	Semi	m. Miocene	Four-way closure (extensional–turtle)
121	Big Bend	MC 698	2012	7200 (2194)	Noble	Producing	2015	SS	m. Miocene	Three-way closure against salt flank
122	Troubadour	MC 699	2013	7438 (2267)	Noble	Appraisal	Projected 2017		l. Miocene	Stratigraphic
123	Biddy Ball	MC 705	1999	1000 (305)	LLOG	Producing	Restart–2015	SS	l. Pleistocene	Three-way closure against fault
124	Valley Forge	MC 707	2004	1538 (469)	LLOG	Producing	2008	SS	e. Pliocene	Three-way closure against salt flank
125	Pluto–BS&T	MC 718	1995	2748 (837)	Mariner	Abandoned, 2008	1999	SS	m. Miocene	Three-way closure against fault
126	Mensa	MC 731	1986	5300 (1615)	Shell	Producing	2000	SS	l. Miocene	Four-way closure (faulted)
127	Goose	MC 751	2003	1548 (472)	LLOG	Producing	Restart–2015	SS	e. Pliocene	Three-way closure against salt flank
128	Anduin West	MC 754	2008	2696 (822)	ATP	Abandoned, 2012	2010	SS	l. Miocene	Three-way closure against fault
129	Anduin	MC 755	2005	2400 (731)	ATP	Abandoned, 2013	2007	SS	l. Miocene	Three-way closure against fault
130	Goldfinger	MC 771	2004	5423 (1653)	ENI	Producing	2005	SS	l. Miocene	Stratigraphic
131	Triton	MC 772	2002	5610 (1710)	ENI	Producing	2005	SS	l. Miocene–e. Pliocene	Three-way closure against fault
132	Devils Tower	MC 773	1999	5607 (1709)	ENI	Producing	2004	SPAR	l. Miocene–e. Pliocene	Three-way closure against salt flank
133	Dantzler	MC 782	2013	6613 (2016)	Noble	Producing	2015	SS	l. Miocene	Three-way closure against salt flank
134	Gladden	MC 800	2008	3116 (950)	LLOG	Producing	2011	SS	e. Pliocene	Three-way closure against salt flank
135	Mississippi Canyon 837	MC 837	2001	1520 (463)	Walter	Producing	2003	SS	e. Pleistocene	Three-way closure against fault

(*continued*)

Table 2. Continued

Field Number	Field Name	Location Abbreviation	Discovery Year	Water Depth (ft [m])	Operator	Status	Onstream	Production Type	Age of Reservoir	Trap Type(s)
136	Callisto	MC 876	2001	7800 (2377)	Anadarko	Abandoned, 2015	2007	SS	l. Miocene	Three-way closure against fault
137	Europa	MC 935	1994	3900 (1189)	Shell	Producing	2000	SS	l. Miocene–e. Pliocene	Three-way closure against salt flank
138	Tahoe–SE Tahoe	VK 783–827	1984	1500 (457)	W&T	Producing	1994	SS	m. Miocene	Three-way closure against fault
139	Petronius	VK 786	1995	1754 (535)	Chevron	Producing	2000	CT	m. Miocene	Three-way closure against fault
140	Neptune–Thor	VK 826	1984	1866 (569)	Anadarko	Producing	1997	SPAR	m. Miocene	Three-way closure against fault
141	Perseus	VK 830	2003	3376 (1029)	Chevron	Producing	2005	DT	m. Miocene	Stratigraphic
142	Einset	VK 873	1998	3500 (1067)	Shell	Producing	2002	SS	l. Miocene	Stratigraphic
143	Nile	VK 914	1997	3534 (1077)	BP	Producing	2001	SS	m. Miocene	Stratigraphic
144	Dorado	VK 915	2002	4023 (1226)	BP	Producing	2009	SS	m. Miocene	Four-way closure over salt (compactional drape)
145	Marlin	VK 915	1993	3384 (1031)	Plains E&P	Producing	1999	TLP	m. Miocene	Four-way closure over salt (compactional drape)
146	South Dorado	VK 915	2003	3494 (1065)	BP	Producing	2004	SS	m. Miocene	Four-way closure over salt (compactional drape)
147	Ram–Powell	VK 956	1985	3214 (980)	Shell	Producing	1997	TLP	m. Miocene	Stratigraphic
148	Swordfish	VK 961	2001	4677 (1425)	Noble	Producing	2005	SS	m. Miocene	Stratigraphic
149	Fastball	VK 1003	1999	3000 (914)	W&T	Abandoned, 2014	2009	SS	m. Miocene	Three-way closure against fault–stratigraphic

Locations of fields are shown in Figures 5, 10, and 11.

Location abbreviations: AC = Alaminos Canyon; DC = DeSoto Canyon; EB = East Breaks; EW = Ewing Bank; GB = Garden Banks; GC = Green Canyon; MC = Mississippi Canyon; VK = Viosca Knoll. Production type abbreviations: CT = compliant tower; DT = dry tree; FP = floating production; FPS = floating production storage; FPU = floating production unit; Semi = semisubmersible; SS = subsea tieback; TLP = tension leg platform. Age of reservoir abbreviations: e. = early; l./L. = late/Late; m. = middle.

Table 3. Fields and Discoveries in the Subsalt Province, Northern Deep-Water Gulf of Mexico

Field Number	Field Name	Location Abbreviation	Discovery Year	Water Depth (ft [m])	Operator	Status	Onstream	Production Type	Age of Reservoir	Trap Type(s)
150	Telemark	AT 63	2000	4385 (1336)	Bennu	Development	2010	MinDOC	e.–m. Miocene	Three-way closure against base of salt
151	North Platte	GB 959	2012	4871 (1485)	Cobalt	Appraisal			l. Paleocene–e. Eocene	Four-way closure (contractional fold)
152	Boris	GC 282	2001	2393 (729)	ERT	Producing	2003	SS	e. Pliocene	Three-way closure against base of salt
153	Stampede	GC 468	2005	3440 (1048)	Hess	Development	Projected 2018	TLP	m. Miocene	Four-way closure (extensional fold–turtle)
154	Tahiti	GC 640	2002	4017 (1224)	Chevron	Producing	2009	SPAR	e.–m. Miocene	Three-way closure against base of salt
155	Holstein Deep	GC 643	2006	3830 (1167)	Plains E&P	Producing	2016	FPS	e. Miocene	Three-way closure against base of salt
156	Genghis Khan	GC 652	2005	4300 (1311)	BHP Billiton	Producing	2007	SS	e.–m. Miocene	Three-way closure against base of salt
157	West Tonga–Caesar	GC 726	2007	4700 (1432)	Anadarko	Producing	2012	SS	m. Miocene	Three-way closure against base of salt
158	Anchor	GC 807	2014	5183 (1580)	Chevron	Appraisal			l. Paleocene–e. Eocene	Three-way closure against base of salt
159	Heidelberg	GC 903	2009	5000 (1524)	Anadarko	Producing	2016		m. Miocene	Three-way closure against base of salt
160	Guadalupe	KC 10	2014	3992 (1217)	Chevron	Appraisal			l. Paleocene–e. Eocene	Four-way closure (contractional fold)
161	Gila	KC 93	2013	4900 (1493)	BP	Appraisal			l. Paleocene–e. Eocene	Four-way closure (contractional fold)
162	Tiber	KC 102	2009	4155 (1266)	BP	Appraisal			l. Paleocene–e. Eocene	Four-way closure (contractional fold)
163	Kaskida	KC 292	2006	5860 (1786)	BP	Appraisal		FPS	l. Paleocene–e. Eocene	Three-way closure against base of salt
164	Leon	KC 642	2014	6117 (1864)	Repsol	Appraisal			l. Paleocene–e. Eocene	Four-way closure (contractional fold)
165	Moccasin	KC 736	2011	6739 (2054)	Chevron	Appraisal			l. Paleocene–e. Eocene	Four-way closure (contractional fold)

(*continued*)

Table 3. Continued

Field Number	Field Name	Location Abbreviation	Discovery Year	Water Depth (ft [m])	Operator	Status	Onstream	Production Type	Age of Reservoir	Trap Type(s)
166	Sicily	KC 814	2015	6716 (2047)	Chevron	Appraisal			l. Paleocene–e. Eocene	Four-way closure (contractional fold)
167	Buckskin	KC 872	2009	6920 (2109)	Chevron	Appraisal			l. Paleocene–e. Eocene	Four-way closure (contractional fold)
168	Lucius	KC 875	2009	7100 (2164)	Anadarko	Producing	2015	SPAR	l. Miocene–e. Pliocene	Three-way closure against salt keel
169	Hadrian–Hadrian South	KC 919	2009	7425 (2263)	ExxonMobil	Producing	2015	SS	l. Miocene–e. Pliocene	Three-way closure against salt keel
170	Mica–Mickey	MC 211	1990	4314 (1315)	ExxonMobil	Producing	2001	SS	l. Miocene	Four-way closure (fault bounded)
171	Raton–Raton South–Gemini	MC 248–292	2006	3400 (1036)	Noble	Producing	2008	SS	l. Miocene	Stratigraphic
172	Tubular Bells	MC 725	2003	4300 (1311)	Hess	Producing	2014	FPS	m. Miocene	Three-way closure against base of salt
173	Thunder Hawk	MC 734	2004	5724 (1745)	Murphy	Producing	2009	Semi	m. Miocene	Three-way closure against base of salt
174	West Boreas	MC 762	2004	3112 (948)	Shell	Producing	2014	SS	l. Miocene	Three-way closure against base of salt
175	King	MC 764	1997	2940 (896)	Shell	Producing	2000	SS	l. Miocene	Three-way closure against base of salt
176	Princess	MC 765	2000	3650 (1112)	Shell	Producing	2002	SS	l. Miocene	Three-way closure against base of salt
177	Kodiak	MC 771	2008	5000 (1524)	Deep Gulf Energy II	Producing	2016	SS	m. Miocene	Four-way closure (extensional fold–turtle)
178	Thunder Horse North	MC 776	2000	5640 (1719)	BP	Producing	2009	SS	m. Miocene	Three-way closure against base of salt
179	Thunder Horse	MC 778	1999	6103 (1860)	BP	Producing	2008	Semi	m. Miocene	Four-way closure (extensional fold–turtle)
180	Deimos	MC 806	2002	3000 (914)	Shell	Producing	2005	SS	m.–l. Miocene	Three-way closure against fault
181	Mars	MC 807	1989	2990 (911)	Shell	Producing	1996	TLP	l. Miocene	Three-way closure against base of salt

(*continued*)

Table 3. Continued

Field Number	Field Name	Location Abbreviation	Discovery Year	Water Depth (ft [m])	Operator	Status	Onstream	Production Type	Age of Reservoir	Trap Type(s)
182	Ursa	MC 810	1991	3800 (1158)	Shell	Producing	1999	TLP	l. Miocene	Three-way closure against base of salt
183	Crosby	MC 899	1997	4400 (1341)	Shell	Producing	2001	SS	l. Miocene	Three-way closure against base of salt
184	Mirage	MC 941	1991	3914 (1193)	Bennu	Producing	2010	MinDOC	m. Miocene	Three-way closure against base of salt
185	Morgus	MC 942	1999	3937 (1200)	Bennu	Producing	2012	SS	m. Miocene	Three-way closure against base of salt
186	Gunflint	MC 948	2008	6100 (1859)	Noble	Appraisal	2016	SS	m. Miocene	Four-way closure (extensional fold–turtle)
187	Vito	MC 984	2009	4038 (1231)	Shell	Appraisal			e. Miocene	Four-way closure (extensional fold–turtle)
188	Power Nap	MC 986	2015	4200 (1280)	Shell	Appraisal			e. Miocene	Three-way closure against base of salt
189	Phobos	SE 39	2013	8500 (2591)	Anadarko	Appraisal			l. Paleocene–e. Eocene	Four-way closure (contractional fold)
190	Big Foot	WR 29	2005	5330 (1624)	Chevron	Producing	2015	TLP	l. Paleocene–e. Eocene-m. Miocene	Three-way closure against base of salt
191	Shenandoah	WR 52	2009	5750 (1753)	Anadarko	Appraisal			l. Paleocene–e. Eocene	Four-way closure against salt keel
192	Yucatan	WR 95	2015	5945 (1812)	Chevron	Appraisal			l. Paleocene–e. Eocene	Three-way closure against salt weld
193	Coronado	WR 98	2008	5722 (1744)	Chevron	Appraisal			l. Paleocene–e. Eocene	Three-way closure against base of salt
194	Yeti	WR 160	2015	5924 (1806)	Statoil	Appraisal			m. Miocene	Three-way closure against base of salt
195	Stones	WR 508	2005	9576 (2919)	Shell	Producing	2016	FPS	l. Paleocene–e. Eocene	Four-way closure (contractional fold)
196	Tucker	WR 543	2006	6778 (2066)	Statoil	Appraisal			l. Paleocene–e. Eocene	Three-way closure against fault–salt
197	Julia	WR 627	2007	7087 (2157)	ExxonMobil	Appraisal	2016	SS, FPS	l. Paleocene–e. Eocene	Four-way closure (contractional fold)

(*continued*)

Table 3. Continued

Field Number	Field Name	Location Abbreviation	Discovery Year	Water Depth (ft [m])	Operator	Status	Production Onstream	Production Type	Age of Reservoir	Trap Type(s)
198	St. Malo	WR 678	2003	6900 (2103)	Chevron	Producing	2014	FPS	l. Paleocene–e. Eocene	Four-way closure (contractional fold)
199	Jack	WR 759	2004	7000 (2134)	Chevron	Producing	2014	FPS	l. Paleocene–e. Eocene	Four-way closure (contractional fold)
200	Logan	WR 969	2011	7750 (2362)	Statoil	Appraisal			l. Paleocene–e. Eocene	Four-way closure (contractional fold)

Locations of fields are shown in Figures 5, 10, and 11.

Location abbreviations: AT = Atwater Valley; GB = Garden Banks; GC = Green Canyon; KC = Keathley Canyon; MC = Mississippi Canyon; SE = Sigsbee Escarpment; WR = Walker Ridge. Production type abbreviations: FPS = floating production storage; MinDOC = Minimum Deep-Water Operating Concept; Semi = semisubmersible; SS = subsea tieback; TLP = tension leg platform. Age of reservoir abbreviations: e. = early; l. = late; m. = middle.

Future challenges in deep-water technology must address routine development in water depths greater than 2745 m (9000 ft). To operate economically in these water depths, companies must have reliable production facilities and systems. For example, fluids in pipelines must flow continuously, which is an extremely challenging problem, because pipeline blockages can be caused by waxes, asphaltenes, and gas hydrates at the lower temperatures of deep water. Another ongoing problem is dealing with the separation and sequestration of CO_2 gas, which will be a major challenge in the future.

Seismic Acquisition and Processing

Improvements in both seismic acquisition and processing have been crucial to the continued successful exploration and development in the northern deep-water Gulf of Mexico. The improved seismic imaging has allowed for more accurate definition of the structure and stratigraphy below shallow allochthonous salt and has opened an entire new exploration province. Shallow allochthonous salt presents major challenges for seismic imaging, primarily because the long offset seismic signals do not penetrate through salt. The critical angle is reached at relatively low incidence angles, typically little more than 30°, at the top of salt. Consequently, seismic energy gets refracted along the salt–sediment interface. Imprecise knowledge of depth of base of salt also results in imaging problems. The result is that a limited range of receivers collect seismic wavelets that have passed through the salt. Fewer active reflections result in noisier data. That is, the effective "fold" of the data is less than the acquisition geometry predicts.

Because of the strong velocity contrast of salt (~14,600 ft/s [4790 m/s]) with subjacent and overlying sediments (6000–8000 ft/s [1970–2625 m/s]), the seismic wavefront travels almost twice as fast in the salt as in the surrounding sediment. That phenomenon causes the wavelet to change shape as it travels through the salt. Different ray paths through the salt, as demanded by different shot and receiver locations, cause the signal to exit the base of salt at different times and at different places. Unless the signals are corrected perfectly for the different ray paths, which would require a priori knowledge of the salt body geometry, wavelets of different shapes and

times are summed together. The result is destructive interference, which translates to a reduction in high frequencies, and therefore, lower resolution.

There has been a distinct evolution in improved acquisition and updated streamer technologies. Initially, narrow azimuth towed streamer (NAZ) data with prestack depth migration (PSDM) processing were used for imaging the geology below salt; NAZ typically uses one boat (source of sound) towing 6-km (3.7-mi)–long streamers. A typical crossline aperture is 0.5 km (0.3 mi), with an inline aspect ratio of 1:16 and typically 60-fold data. By 2006, wide azimuth towed streamer (WAZ) became common in multiclient acquisition; WAZ may use up to four source boats with multiple streamer arrays. Typical crossline aperture is 4 km, with an inline aspect ratio of 1:2 and 160-fold data. The increase in spatial distribution of the data improves the signal-to-noise ratio, provides natural attenuation of some multiples, and potentially allows oblique ray paths unavailable with NAZ acquisition. Additionally, new streamer technologies are being introduced to reduce noise, provide deeper penetration, and sharpen imaging of the subsurface. However, the tradeoff is that WAZ data tend to have poorer resolution in the shallower part of the subsurface.

Seismic surveys are now routinely processed to depth with the multiple processing algorithms available. Each processing algorithm has different strengths and different levels of resolution. Wave equation migration (WEM) is current technology. Reverse time migration (RTM) is a special kind of WEM requiring a more precise velocity model; RTM can produce excellent results when a better velocity model is known. It is primarily used for imaging the structural geology below salt at depth; RTM can preserve lower frequencies than other processing. Kirchoff PSDM is older technology but is considered to better retain the amplitude information than other processing. Beam migration is perhaps state of the art, because it combines the better features of the earlier algorithms and, possibly, better images the steeper dips of salt edge and sediment. The latest versions of modern migration algorithms include anisotropic parameters. These data are closer to true depth and accurate geometric shapes—assuming that the anisotropy model, like the velocity model, is correct.

Finally, WAZ data can be processed into multiple output volumes, relating to the source-receiver azimuth. These products are the equivalent of multiple shoots in varying azimuths. And, as such, they image complex structures differently. Where one azimuth may image the dipping base of salt, another might better image a steep salt face not in the plane of the first azimuth.

REGIONAL SETTING

Geology as an Analog

The northern deep-water Gulf of Mexico serves as a crucial geologic analog for the exploration and development of many other deep-water basins. To date, approximately 70% of the deep-water reserves in the world are found in sedimentary basins with mobile substrates (i.e., salt, shale), similar to the Gulf of Mexico (updated from Worrall et al., 2001). These basins have four salient characteristics: (1) numerous extensional and contractional structures creating potential traps, (2) drainage of moderate to large areas of continents so that there is abundant overburden and vast volumes of sand for reservoirs, (3) stacked reservoir sands that are deposited in intraslope basins or at the base of slope, and (4) a petroleum system characterized by older, deeper source rocks, whose generation and migration are a fairly recent phenomenon geologically.

The continental slope and abyssal plain of the northern deep-water Gulf of Mexico were developed by the complex set of interacting processes that create a suite of unique features. A bathymetric map of the slope shows highly irregular topography in the central and western part of the continental slope (Figure 1). The slope has a more uniform bathymetry to the northeast, and the gradient increases substantially to the southeast along the Florida Escarpment, where slope gradients range from 10° to 40° (locally 90°).

Two factors are critical in understanding the geology of the northern deep-water Gulf of Mexico and the controls on its petroleum systems: (1) major siliciclastic sedimentation during the Cenozoic (Figures 3–5) and (2) complex tectonics caused by high sedimentation rates and the mobile substrates (Figure 3). The interaction of these two factors has created complex petroleum systems, where migration pathways are constantly evolving and changing because of the ongoing deformation (McBride et al., 1998a;

Table 4. Fields and Discoveries in Fold Belt Province, Northern Deep-Water Gulf of Mexico

Field Number	Field Name	Location Abbreviation	Discovery Year	Water Depth (ft [m])	Operator	Status	Onstream	Production Type	Age of Reservoir	Trap Type(s)
201	Silvertip	AC 815	2004	9356 (2852)	Shell	Producing	2010	SS	Oligocene	Four-way closure (contractional fold)
202	Great White	AC 857	2002	8009 (2441)	Shell	Producing	2010	SPAR	l. Paleocene–e. Eocene, Oligocene	Four-way closure (contractional fold)
203	Tobago	AC 859	2004	9636 (2937)	Shell	Producing	2011	SS	l. Paleocene–e. Eocene, Oligocene	Four-way closure (contractional fold)
204	Merganser	AT 37	2002	7900 (2408)	Anadarko	Abandoned, 2014	2007	SS	l. Miocene	Three-way closure against flank of salt
205	Bass Lite	AT 426	2001	6623 (2019)	Apache	Producing	2008	SS	l. Pleistocene	Three-way closure against salt–fault–stratigraphic
206	Neptune	AT 575	1995	6162 (1878)	BHP	Producing	2008	TLP	e.–m. Miocene	Four-way closure (contractional fold)
207	Shenzi	GC 654	2002	4400 (1341)	BHP	Producing	2009	TLP	e. Miocene	Four-way closure (contractional fold)
208	Atlantis	GC 699	1998	6133 (1869)	BP	Producing	2007	Semi	e.–m. Miocene	Four-way closure (contractional fold)
209	Parmer	GC 823	2004	4130 (1259)	Stone	Appraisal	Projected 2016	FPS	e.–m. Miocene	Four-way closure (contractional fold)
210	Mad Dog	GC 826	1999	4400 (1341)	BP	Producing	2005	SPAR	e.–m. Miocene	Four-way closure (contractional fold)
211	Q	MC 961	2005	7925 (2415)	Statoil	Abandoned, 2010	2007	SS	m. Miocene	Three-way closure against fault
212	Cascade	WR 206	2002	8203 (2500)	Petrobras	Producing	2012	FPSO	l. Paleocene–e. Eocene	Four-way closure (contractional fold)
213	Chinook	WR 469	2003	8826 (2690)	Petrobras	Producing	2012	SS	l. Paleocene–e. Eocene	Four-way closure (contractional fold)
214	Exploratus	Mexico	2014	8488 (2587)	Pemex	Appraisal			l. Paleocene–e. Eocene	Four-way closure (contractional fold)
215	Maximino	Mexico	2012	9574 (2918)	Pemex	Appraisal			l. Paleocene–e. Eocene	Four-way closure (contractional fold)
216	Maximino DL	Mexico	2014	9984 (3043)	Pemex	Appraisal			l. Paleocene–e. Eocene	Four-way closure (contractional fold)

(*continued*)

Table 4. Continued

Field Number	Field Name	Location Abbreviation	Discovery Year	Water Depth (ft [m])	Operator	Status	Onstream	Production Type	Age of Reservoir	Trap Type(s)
217	Supremus	Mexico	2013	9426 (2873)	Pemex	Appraisal			Oligocene	Four-way closure (contractional fold)
218	Trion*	Mexico	2012	8304 (2531)	Pemex	Appraisal			l. Paleocene–e. Eocene	Four-way closure (contractional fold)
219	Cratos	Mexico	2015	9213 (2808)	Pemex	Appraisal			l. Paleocene–e. Eocene	Four-way closure (contractional fold)

Locations of fields are shown in Figures 5, 10, and 11.
Location abbreviations: AC = Alaminos Canyon; AT = Atwater Valley; GC = Green Canyon; MC = Mississippi Canyon; WR = Walker Ridge. Production type abbreviations: FPS = floating production storage; FPSO = floating production storage offloading; Semi = semisubmersible; SS = subsea tieback; TLP = tension leg platform. Age of reservoir abbreviations: e. = early; l. = late; m. = middle.
*The Trion discovery is not technically in the Fold Belt province (see Figure 18), but it is included here because of its proximity.

Colling et al., 2001; Stover et al., 2001; Mount et al., 2006; Pilcher et al., 2011; Gibson, 2012).

Geologic Evolution of the Northern Deep-Water Gulf of Mexico

The geologic evolution of the northern deep-water Gulf of Mexico is illustrated in regional seismic profiles (Figures 3, 6), a series of chronostratigraphic and tectonic charts (Figures 7–9), and seven sequential maps that show the regional distribution of reservoirs in producing fields and discoveries by their ages (Figure 10).

Rifting developed during the Bajocian–Bathonian, and Louann Salt was deposited during the Middle Jurassic (Callovian) (Figures 6–8). During the Late Jurassic, the modern, deep northern Gulf of Mexico subsided rapidly during sea-floor spreading (Figure 8). Locally, in the northeastern deep-water Gulf of Mexico, the Norphlet Formation, an eolian sandstone, developed across the Middle Ground arch before the regional subsidence (Figures 7, 8, 10A). Two of the major source rocks in the deep water were deposited during this period: Oxfordian and Tithonian source rock (Figures 7, 8). The first allochthonous salt was initially emplaced during the Kimmeridgian in the northwest in the present area of the Perdido fold belt (D. Worrall, 2012, personal communication; Figure 8).

During the Berriasian–Valanginan, a third possible source rock was deposited locally in the eastern Gulf of Mexico (Figure 7). From the latest Valanginian through the Barremian, a major allochthonous salt layer was rafted basinward and translated the original Upper Jurassic and lowermost Cretaceous strata (Hudec et al., 2013). The initial contractional folds in the Keathley–Walker and Mississippi Fan fold belts developed within the downdip parts of this allochthonous salt layer (Figures 5, 6, 8). The Early Cretaceous emplacement of this salt layer is significant, because much of the subsequent Cenozoic salt tectonics were related to its initial deformation. Regionally, it is likely that this allochthonous salt emplacement continued later in time, possibly into the Late Cretaceous.

The Upper Cretaceous strata are dominated by interbedded, fine-grained shales and carbonates to the northeast; they are more shale rich centrally and to the northwest (Weimer et al., 2016a). One major

Table 5. Fields and Discoveries in Abyssal Plain Province, Northern Deep-Water Gulf of Mexico

Field Number	Field Name	Location Abbreviation	Discovery Year	Water Depth (ft [m])	Operator	Status	Onstream	Production Type	Age of Reservoir	Trap Type(s)
220	Vortex	AT 261	2002	8340 (2542)	Anadarko	Abandoned, 2011	2007	SS	l. Miocene	Four-way closure (compactional drape)
221	Jubilee	AT 349	2003	8800 (2682)	Anadarko	Abandoned, 2015	2007	SS	l. Miocene	Four-way closure (compactional drape)
222	Mondo NW Extension	LL 1	2005	8340 (2542)	Anadarko	Abandoned, 2015	2007	SS	l. Miocene	Four-way closure (Fault bounded)
223	Atlas NW	LL 5	2004	8810 (2685)	Anadarko	Abandoned, 2009	2007	SS	l. Miocene	Four-way closure (compactional drape)
224	Atlas	LL 50	2003	9000 (2743)	Anadarko	Abandoned, 2009	2007	SS	l. Miocene	Four-way closure (compactional drape)
225	Jubilee Extension	LL 309	2005	8774 (2674)	Anadarko	Abandoned, 2015	2007	SS	l. Miocene	Four-way closure (compactional drape)
226	Cheyenne	LL 399	2004	8987 (2739)	Anadarko	Abandoned, 2015	2007	SS	l. Miocene	Four-way closure (compactional drape)

Locations of fields are shown in Figures 5, 10, and 11.
Location abbreviations: AT = Atwater Valley; LL = Lloyd Ridge. Production type abbreviation: SS = subsea. Age of reservoir abbreviation: l. = late.

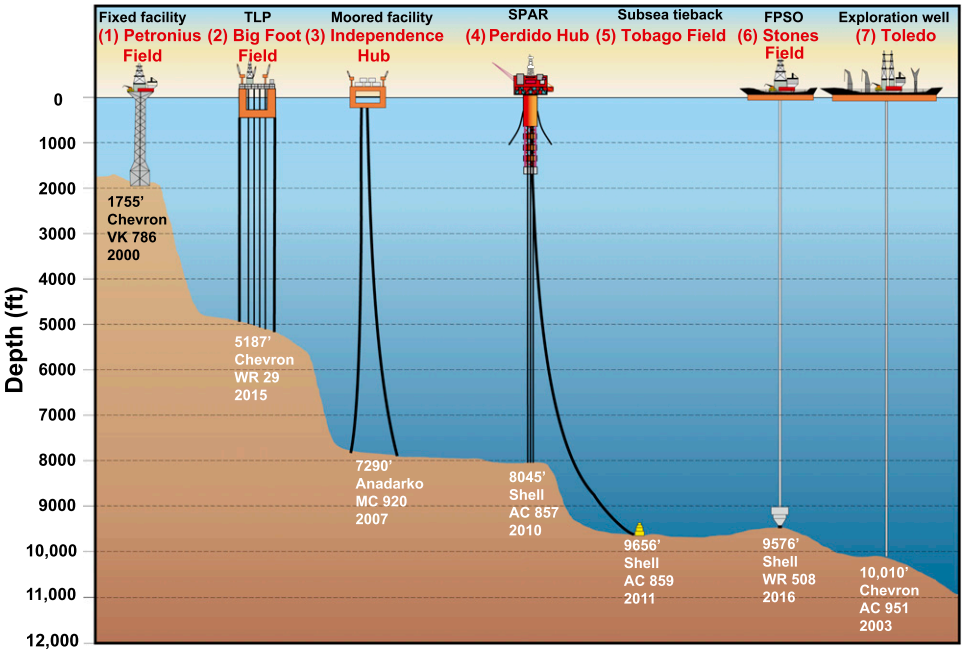

Figure 2. Schematic diagram showing the world-record water depths for exploration and development facilities. See Figure 1 for location of facilities. Note that the deepest water exploration well in the Gulf of Mexico is (7) Toledo, Alaminos Canyon (AC) block 951 (10,010 ft [3051 m]). Globally, the deepest water exploration well is the Raya-1 well in 11,191 ft (3411 m), Pelotas Basin, Uruguay. A SPAR is a type of floating oil platform typically used in very deep waters and is named for logs used as buoys in shipping that are moored in place vertically. Updated from Weimer and Pettingill (2007). FPSO = floating production storage offloading; MC = Mississippi Canyon; TLP = tension-leg platform; VK = Viosca Knoll; WR = Walker Ridge.

sandstone unit, the downdip equivalent to the productive, updip shallow-marine Tuscaloosa sandstone, was deposited during the Cenomanian to earliest Turonian (Figures 7, 8). This sandstone has been penetrated in two wells: Tiber (WR 102) and Baha 2 (AC 600) (Figure 7; Horn, 2011; Scott et al., 2012, 2014).

A unique geologic event at the end of the Cretaceous, the meteorite impact at Chicxulub in the northwestern Yucatan platform to the south in Mexico, had a major effect on the geologic evolution of the Gulf of Mexico. The Yucatan platform was a carbonate province, and the bolide impact generated an instantaneous, extensive collapse of the platform margin and created carbonate-rich debris flows, which form some of the reservoirs for the supergiant Cantarell and Ku-Maloob-Zaap Complexes (Figure 1; Magoon et al., 2001; Ricoy, 2005; Mitra et al., 2006).

Regionally, extensive carbonate debris flows and turbidity flows were generated and transported across the northern deep-water Gulf of Mexico onto the slope. The seismic stratigraphic expression of the

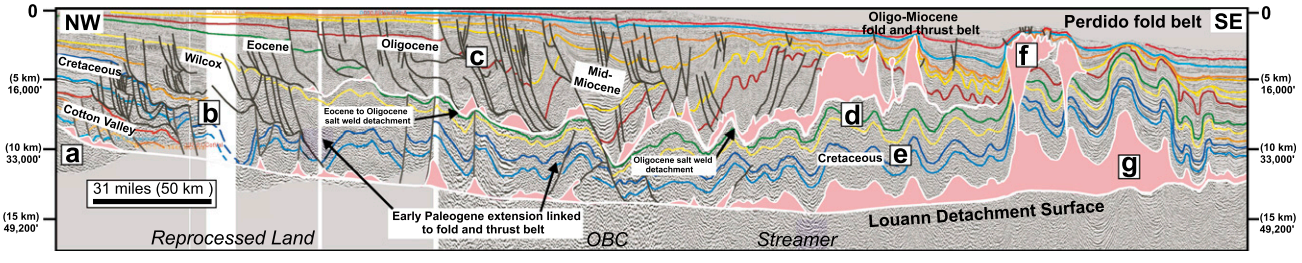

Figure 3. Regional seismic profile (in depth) from the Texas coastal plain (left) across shelf, slope, and abyssal plain, showing the complexity of the Mesozoic–Cenozoic strata of the northwestern Gulf of Mexico. Marine data were collected from ocean bottom cables (OBC). The profile crosses the four deep-water provinces: Basins, Subsalt, Fold Belt, and Abyssal Plain. From the north (left), note the (a) original level of autochthonous (Middle Jurassic) salt, (b) different level of normal faults, (c) expansion of Oligocene–Miocene sediments, (d) Oligocene salt-weld detachment and associated structures, (e) extensive structures interpreted below the salt and salt weld, (f) shallow allochthonous salt in lower slope, and (g) Perdido fold belt with early allochthonous salt. See Figure 5B for location of the profile. After Radovich et al. (2007). Reproduced with permission of Barbara Radovich, Ion Geophysical, and the Gulf Coast Section SEPM Foundation, and any other use requires their permission.

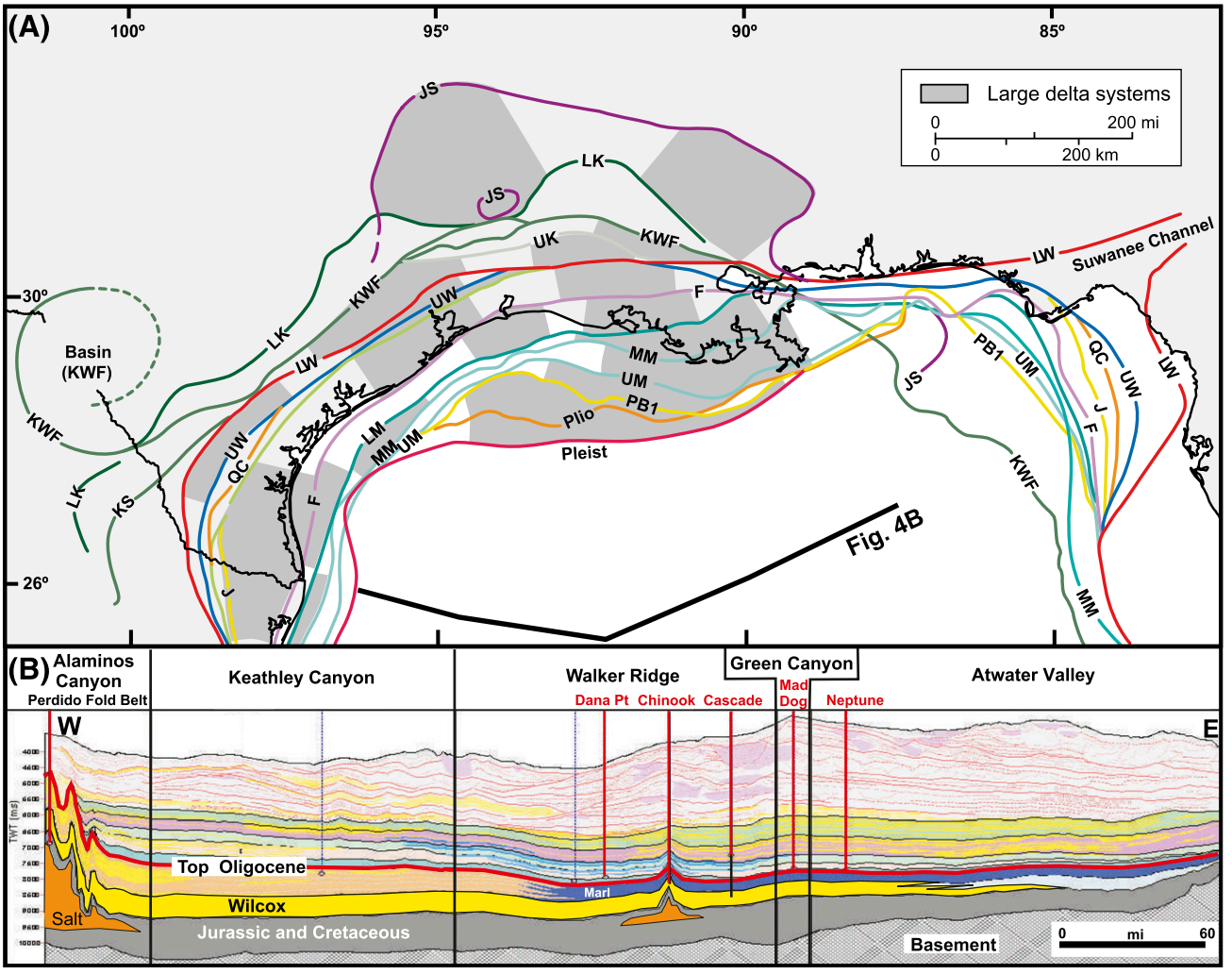

Figure 4. (A) Map showing the distribution of large Mesozoic and Cenozoic deltas and shelf margins, northern Gulf of Mexico (GOM). After Galloway (2008). Approximate location of (B) is shown. Reprinted with permission of Springer-Verlag. (B) Regional seismic profile basinward of the Sigsbee Escarpment in the Abyssal Plain province, showing the regional distribution of sediments in deep water. Distinct wedges of the Cenozoic strata can be seen. Paleogene strata are largely present in the western deep GOM, whereas the Neogene depocenter sits to the center and east. These depocenters mirror the locations of the shallow-marine depocenters preserved in the present onshore and shelf. After Zarra (2007a). Reprinted with permission of the Gulf Coast Section SEPM Foundation, and any other use requires their permission. F = Frio; J = Jackson; JS = Jurassic Smackover; KS = Sligo; KWF = Washita–Fredericksburg; LK = Lower Cretaceous = Hosston; LM = lower Miocene; LW = lower Wilcox; MM = middle Miocene; PB1 = *Buliminella* 1; Pleist = Pleistocene; Plio = Pliocene; Pt = Point; QC = Queen City; TWT = two-way traveltime; UK = Upper Cretaceous; UM = upper Miocene; UW = upper Wilcox.

impact on the deep-water strata has been documented by Scott et al. (2012, 2014) and Sanford (2015), and the wireline characteristics for all penetrations are shown in Weimer et al. (2016b); 58 wells have penetrated this deposit and have found a variable thickness (0 to 204 m [0 to 669 ft]) of the deposit (Tables 6–8). Scott et al. (2012, 2014) noted that this deposit eroded significant parts of the underlying strata. The minimum stratigraphic level of erosion across the northern deep-water Gulf of Mexico was at the mid Campanian level (Richard Denne, 2014, personal communication). The greatest amount of eroded section penetrated in wells was in the Atwater Valley 336 well, where erosion extended down to the Upper Jurassic strata, which overlie the Lower Cretaceous allochthon (Weimer et al., 2016b).

This impact deposit likely affected the stratigraphic evolution of the area for several million years. The deposit possibly affected the evolution of the salt, which in turn affected the distribution of the

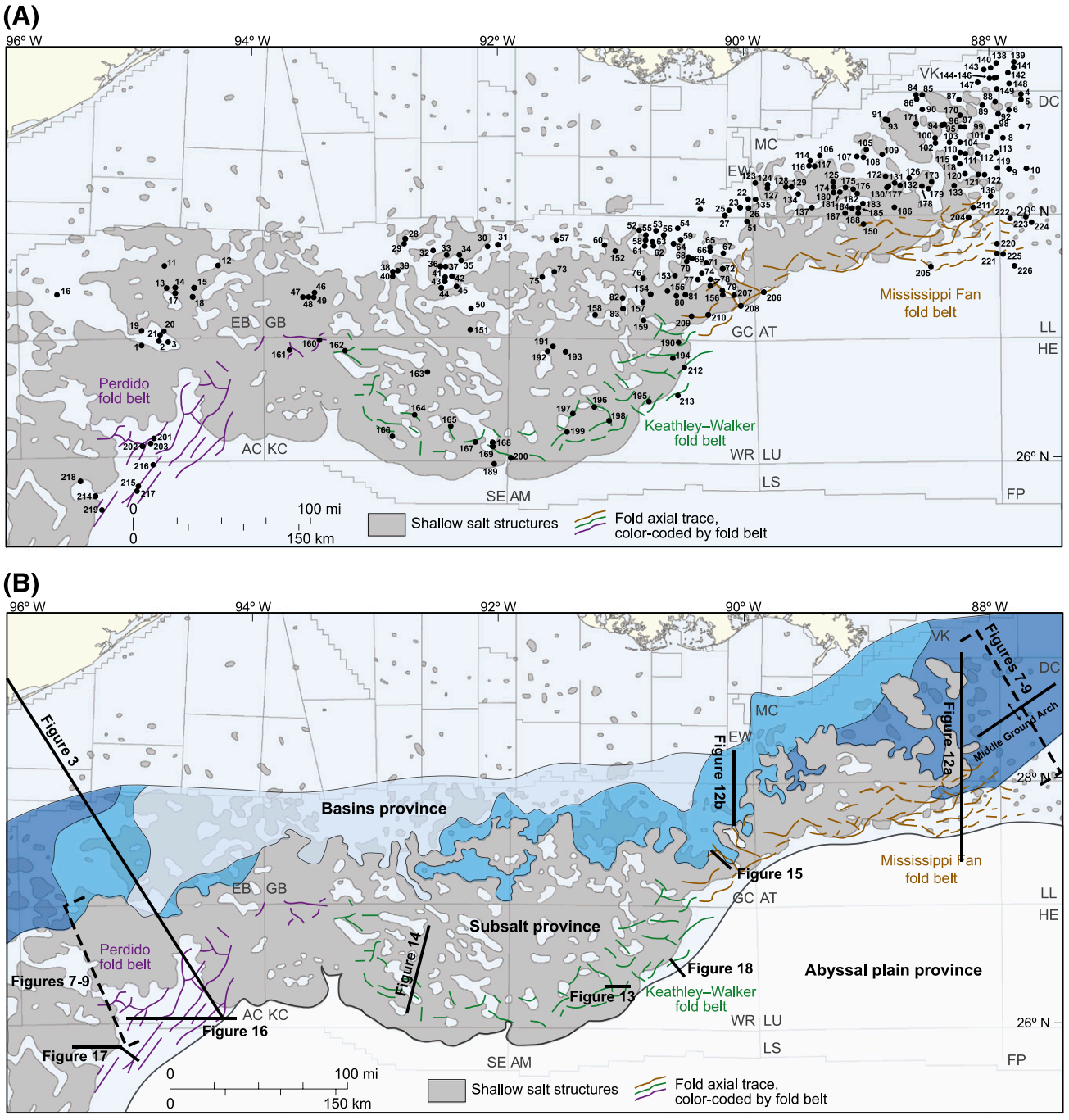

Figure 5. (A) Regional map of the northern deep-water Gulf of Mexico showing the protraction boundaries, locations of major structural features, and the 226 fields and discoveries (black dots) in greater than 1500-ft (457-m) water depth. Numbers correspond to fields listed in Tables 2–5. (B) Regional map of the northern deep-water Gulf of Mexico showing the protraction boundaries, locations of major structural features, tectonic-exploration provinces (Basins, Subsalt, Fold Belt, and Abyssal Plain), and age of stratigraphic fill in the Basins province: dark blue = Miocene; medium blue = Pliocene; light blue = Pleistocene. Area used for the schematic cross sections in Figures 7–9 is shown by the dashed brackets. Locations are shown for Figures 3 and 12–18. Provinces and ages are modified from Zarra (2007a). Base map is adapted from Hudec et al. (2013), including distribution of shallow salt and trends for the Perdido, Keathley–Walker Ridge, and Mississippi Fan fold belts. Trends of fold axes for Perdido fold belt in Mexican water is adapted from Figure 17. Abbreviations for protraction areas: AC = Alaminos Canyon; AM = Amery Terrace; AT = Atwater Valley; DC = DeSoto Canyon; EB = East Breaks; EW = Ewing Bank; FP = Florida Plain; GB = Garden Banks; GC = Green Canyon; HE = Henderson; KC = Keathley Canyon; LL = Lloyd Ridge; LS = Lund South; LU = Lund; MC = Mississippi Canyon; SE = Sigsbee Escarpment; VK = Viosca Knoll; WR = Walker Ridge. Note: A color version can be seen in the online version.

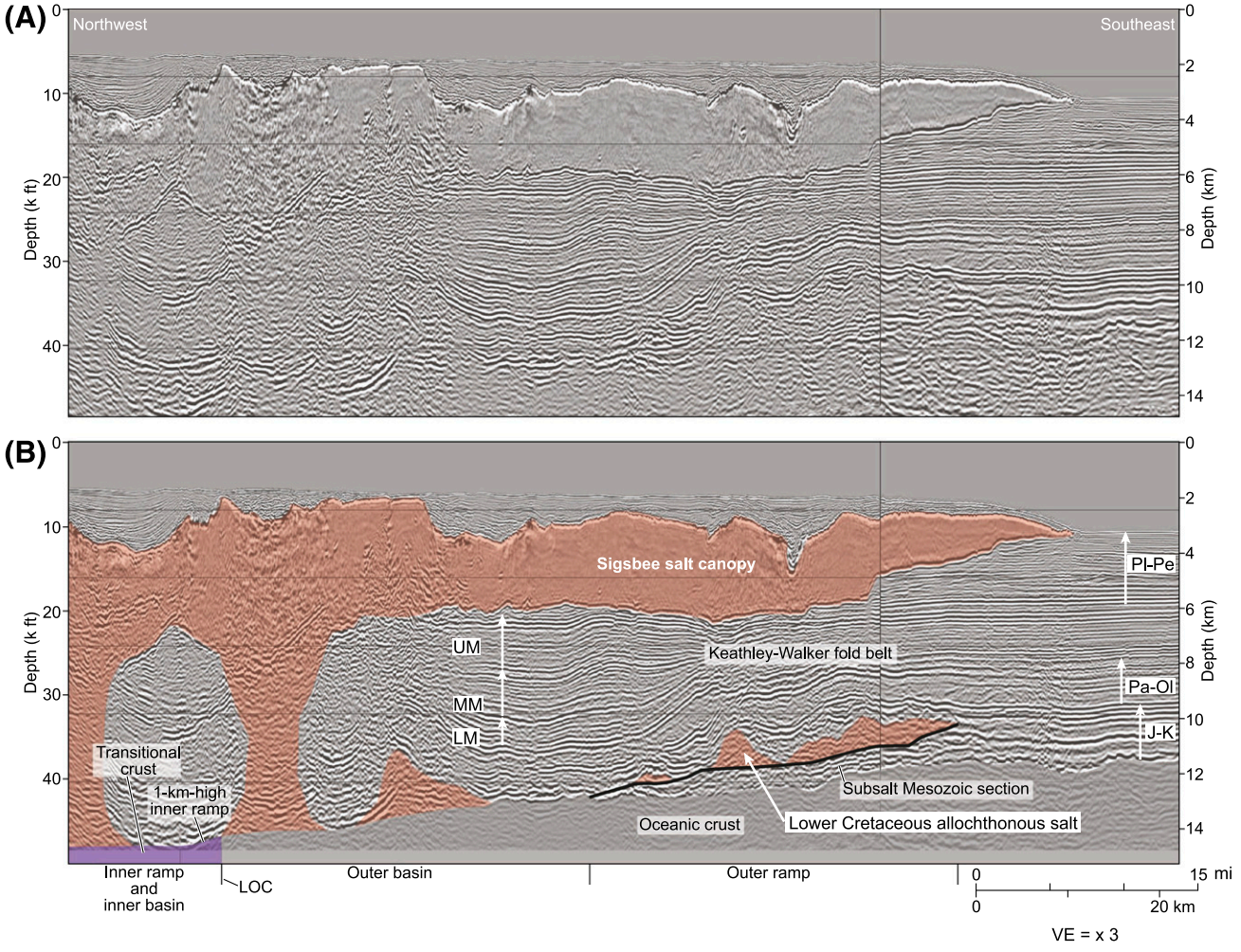

Figure 6. Regional seismic profile across Walker Ridge–Keathley Canyon: (A) uninterpreted; (B) interpreted. Shallow allochthonous salt overlies the Lower Cretaceous allochthonous level. Approximate ages of key horizons are shown. See text for detail. Modified from Hudec et al. (2013). Seismic data image proprietary to and provided courtesy of CGG. Reprinted with permission of CGG and Matthew Bognar. J = Jurassic; K = Cretaceous; LM = lower Miocene; LOC = limit of normal oceanic crust; MM = middle Miocene; Ol = Oligocene; Pa = Paleogene; Pe = Pleistocene; Pl = Pliocene; UM = upper Miocene; VE = vertical exaggeration.

overlying Wilcox sandstones across the entire area (Scott et al., 2012, 2014).

During the Paleocene, there was a marked increase in rates of sedimentation in the northern deep-water Gulf of Mexico (Figures 4, 9, 10A). Siliciclastic sediments were derived from highlands created from the Laramide orogeny in the Rocky Mountains to the northwest and deposited in a series of sand-rich shorelines during the Paleogene (Figure 4). Two major deep-water reservoir deposits are equivalent to the petroleum-productive shallow-marine sandstones. First, the Wilcox Formation (upper Paleocene–lower Eocene) forms the reservoir in 23 fields and discoveries in the United States and 5 additional discoveries in Mexico (Figures 9, 10A; Tables 3, 4). Second, the Frio Formation (Oligocene) forms the reservoir in the two fields in the United States (Great White, Silvertip) and one in the Mexican area (Supremus) (Figure 10A; Table 4).

At the beginning of the Miocene, two significant events affected the regional sedimentation. First, the drainage area for sediment expanded to the east and included the western Appalachian Mountains. These additional drainages caused the shallow-marine depocenters to shift to the east into the central Gulf of Mexico (Figures 4, 10B). Second, the rates of sedimentation greatly increased, causing large volumes of sediment to be deposited overlying the deeper salt. This extensive loading of sediment significantly impacted the tectonics in two ways: (1) the Lower

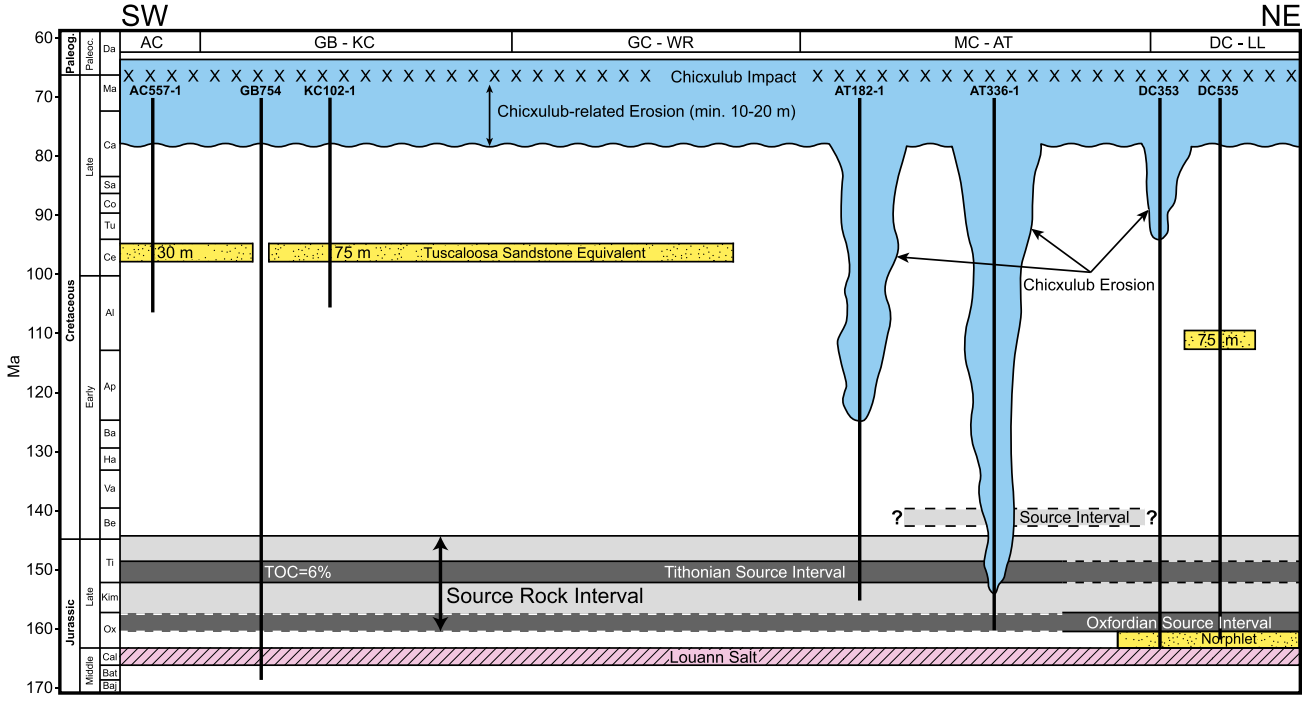

Figure 7. Regional chronostratigraphic chart across the northern deep-water Gulf of Mexico showing the stratigraphic evolution of the Middle Jurassic through Upper Cretaceous section. See Figure 5B for general area included in the cross section. Seven key wells and their depths of penetration are projected onto the section. Norphlet eolian sandstone is penetrated in the DeSoto Canyon (DC) 353 Vicksburg discovery well and three additional discoveries. Two main source intervals, centered on the Tithonian (Ti) and Oxfordian (Ox), are shown in dark gray; light gray shows other possible source intervals. The dashed lines indicate where the lithofacies of the source intervals may not contribute to oil generation. Total organic carbon (TOC) values for the source intervals of the Garden Banks (GB) 754 well are plotted (adapted from Cole et al., 2001b). Note that considerable thickness variation exists in the Upper Jurassic and Lower Cretaceous sections resulting from salt tectonics. The DC 535 well penetrated Albian sandstone unit, and two wells (Alaminos Canyon [AC] 557 and Keathley Canyon [KC] 102) that penetrate the deep-water Tuscaloosa (and their thickness at penetration) are shown. The X's at the top Cretaceous indicate the instantaneous gravity-flow deposit layer deposited from the Chicxulub meteorite in Mexico. Blue (in online version) indicates the depth of erosion from the Chicxulub gravity-flow deposit at the top Cretaceous, as indicated by the wells that penetrated the section (Denne et al., 2013). Protraction area abbreviations: AT = Atwater Valley; GC = Green Canyon; LL = Lloyd Ridge; MC = Mississippi Canyon; WR = Walker Ridge. Geologic age abbreviations: Al = Albian; Ap = Aptian; Ba = Barremian; Baj = Bajocian; Bat = Bathonian; Be = Berriasian; Ca = Callovian; Ce = Cenomanian; Co = Coniacian; Da = Danian; Ha = Hauterivian; Kim = Kimmeridgian; Ma = Maestrichtian; Paleoc. = Paleocene; Paleog. = Paleogene; Sa = Santonian; Tu = Turonian; Va = Valanginian.

Cretaceous allochthon began to deform, creating the emplacement of the shallow-salt features present in the slope (Figures 3, 6), such as extensive series of salt diapirs and intraslope basins developed, and where many reservoir sands were deposited, and (2) the associated salt migration downdip resulted in increased deformation in the Keathley–Walker and Mississippi Fan fold belts (Figure 6). During the middle to late Miocene, numerous fold-belt structures developed, and fold limbs steepened considerably, increasing the structural closures that are now being explored and developed (see below). Finally, continued sediment loading at high depositional rates throughout the Neogene–Pleistocene created the irregular bathymetry on the slope that we see today in shallow allochthonous salt features (bathymetric highs) and intraslope basins (bathymetric lows) (Figure 1).

The evolution of the shallow-marine and downdip deep-marine depocenters during the Neogene is shown in Figures 4, 9, and 10B–G. The location of the fields and discoveries is only a general proxy for the location of the deep-marine depocenters (Figure 10). During the early Miocene, the shallow-marine depocenter was in the north-central Gulf of Mexico (Figure 4); the downdip-equivalent deep-water reservoir sands are primarily located in southern Green Canyon (Figure 10B). During the middle to

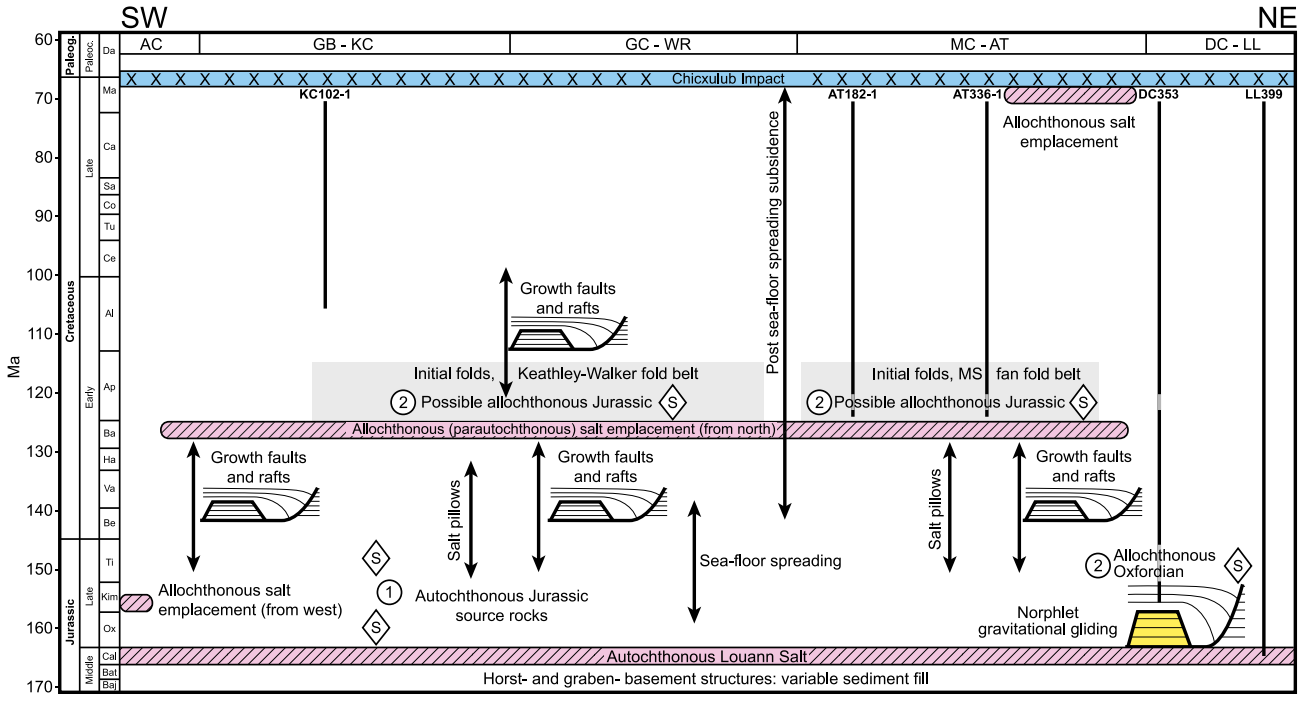

Figure 8. Tectonic events chart for the Jurassic and Cretaceous section shown in the chronostratigraphic chart in Figure 7. Five key wells and their depths of penetration are projected onto the section. Bajocian and Bathonian strata are present in the inherited rift topography, below the Callovian autochthonous Louann salt. Emplacement of allochthonous salt happened at three discrete times: Kimmeridgian (Kim) (western Gulf of Mexico [GOM]), Early Cretaceous (regional in GOM), and locally at the top Cretaceous in the eastern GOM. Early salt pillows, growth faults, and raft systems developed during the Late Jurassic and continued during the Cretaceous. The initial stages of deformation of the Keathley–Walker fold belt and Mississippi Fan fold belt occurred on top of the Lower Cretaceous allochthonous salt layer. Source intervals (shown by numbers in circles) are indicated by diamonds (with S). To the east, the Oxfordian (Ox) source interval was translated laterally on top of the Norphlet sandstone raft (e.g., DeSoto Canyon [DC] 353). The Norphlet sandstone was not present in the Lloyd Ridge (LL) 399 well, which did penetrate Louann salt. The Ox and Kim source intervals were emplaced on top of the Lower Cretaceous nappe and provide much of the oil in the deep water. Note that the Atwater Valley (AT) 182 and 336 wells penetrate the Jurassic source intervals where they overlie the Lower Cretaceous allochthonous salt. Protraction area abbreviations: AC = Alaminos Canyon; GB = Garden Banks; GC = Green Canyon; KC = Keathley Canyon; MC = Mississippi Canyon; WR = Walker Ridge. Geologic age abbreviations: Al = Albian; Ap = Aptian; Ba = Barremian; Baj = Bajocian; Bat = Bathonian; Be = Berriasian; Ca = Callovian; Ce = Cenomanian; Co = Coniacian; Da = Danian; Ha = Hauterivian; Ma = Maestrichtian; Paleoc. = Paleocene; Paleog. = Paleogene; Sa = Santonian; Ti = Tithonian; Tu = Turonian; Va = Valanginian.

late Miocene, the main shallow-marine depocenter shifted to the east, and the downdip-equivalent reservoirs are primarily found in Mississippi Canyon, eastern Green Canyon, Viosca Knoll, and eastern DeSoto Canyon protraction areas (Figures 9; 10C, D). During the early Pliocene, the shallow-marine depocenter shifted westward to the central part of the northern Gulf of Mexico, and deep-water reservoirs are primarily found in Green Canyon, western Garden Banks, and western Mississippi Canyon protraction areas (Figures 9; 10E, F). During the late Pliocene, the shallow-marine depocenter continued to shift westward, with the deep-water reservoirs found in East Breaks, Garden Banks, and Green Canyon (Figures 9, 10G). During the early Pleistocene, reservoir sands are primarily East Breaks, Garden Banks, and Green Canyon. Only a few reservoirs produce from the upper Pleistocene sediments (Figures 9, 10G).

EXPLORATION AND TECTONIC PROVINCES

The distribution of the general geologic and exploration provinces of the northern deep-water Gulf of Mexico is shown in Figure 5. Zarra (2007a) defined four main provinces based on the ages of strata and styles of deformation: Basins, Subsalt, Fold Belt, and Abyssal Plain (Figure 5B). The geology of each province is summarized here, including a summary of the fields, the ages of the reservoirs (Figure 10; Tables

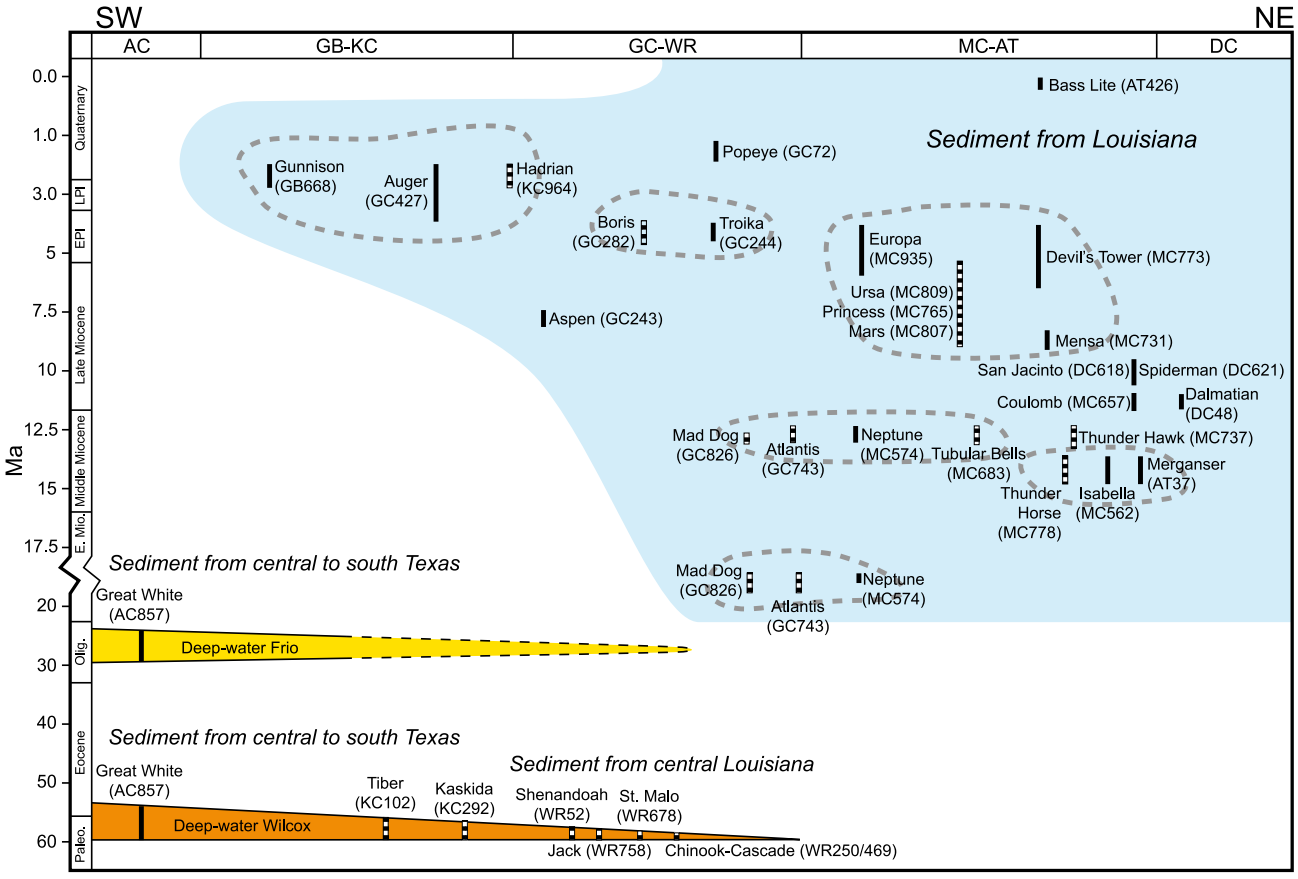

Figure 9. Regional chronostratigraphic chart across the northern deep-water Gulf of Mexico showing the stratigraphic evolution of the Cenozoic. Note the change in scale at 20 Ma. See Figure 5B for the general area included in the cross section and wells. The changing locations of the depocenters are highlighted by the ages of the reservoirs in different key fields; subsalt fields are shown by dashed lines, and suprasalt fields are shown by solid lines. See Figure 4 for detailed distribution of sediment in deep water in the abyssal plain. Protraction area abbreviations: AC = Alaminos Canyon; AT = Atwater Valley; DC = DeSoto Canyon; GB = Garden Banks; GC = Green Canyon; KC = Keathley Canyon; MC = Mississippi Canyon; WR = Walker Ridge. Geologic age abbreviations: E. Mio. = Early Miocene, EPl = Early Pliocene; LPl = Late Pliocene; Olig. = Oligocene; Paleoc. = Paleocene.

2–5), the trap type of each field (Figure 11; Tables 2–5), and representative seismic profiles (Figures 12–18). In classifying the traps, it is important to note that nearly all fields in the northern deep-water Gulf of Mexico have a stratigraphic component to their trap, including those fields with four-way closure.

In addition, because of the structural complexity, some of these provinces overlap, making this classification difficult. For example, the Mississippi Fan fold belt extends below the salt in southeastern Green Canyon where four fields are present (Figures 5, 11). In this case, we included these fields in the Fold Belt province (Table 4). In contrast, all discoveries in the Keathley–Walker fold belt are included in the Subsalt province, except for Chinook and Cascade fields, which lie basinward of the Subsalt province (Figures 5, 11; Table 4). Those fields that sit below salt but are immediately adjacent to the Basins province are included in the Subsalt province (Figures 5, 11; Table 3).

Basins Province

The Basins province (Table 2) rests in the modern upper to middle slope and largely consists of thick Neogene suprasalt sediments that overlie shallow allochthonous salt or have been welded to strata that once underlaid the welded-out basins (Figures 3, 5, 12). To the northeast, the original sedimentary basins are largely undeformed in the slope, indicating relatively thinner original salt thickness and decreased subsequent related deformation.

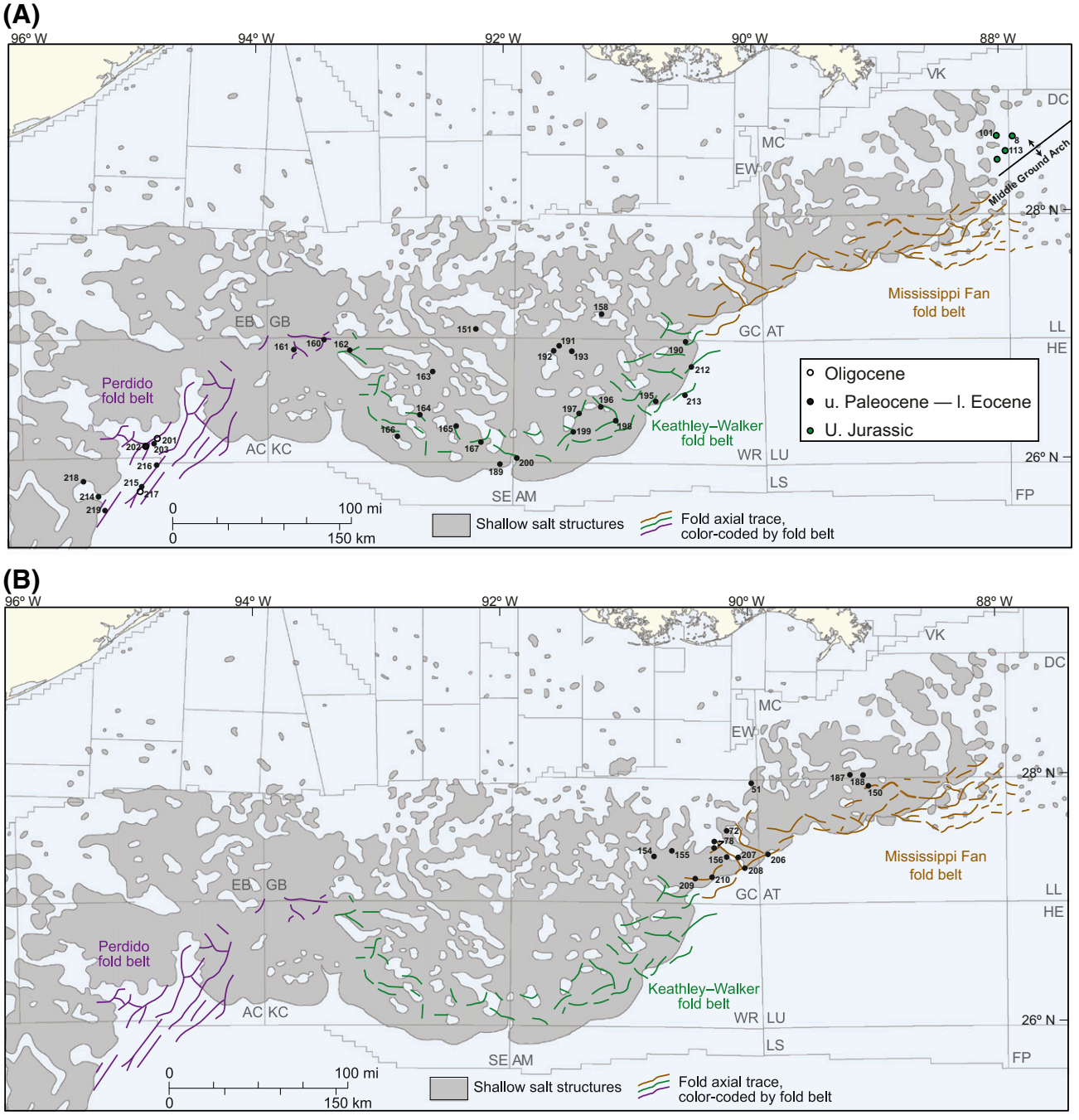

Figure 10. Sequential maps showing the distribution of reservoir ages for fields and discoveries in the northern deep-water Gulf of Mexico for (A) Late Jurassic (Oxfordian; 163.5 to 157.3 Ma), late Paleocene–early Eocene (60.0 to 51.8 Ma), and Oligocene (29 to 27 Ma); (B) early Miocene (23.0 to 16.0 Ma); (C) middle Miocene (16.0 to 11.6 Ma); (D) late Miocene (11.6 to 5.3 Ma); (E) early Pliocene (5.3 to 3.6 Ma); (F) late Pliocene (3.6 to 2.6 Ma); and (G) Quaternary (2.6 to 0.0 Ma). Black dots show locations of fields and discoveries. Numbers correspond to fields listed in Tables 2–5. Abbreviations of protraction area boundaries: AC = Alaminos Canyon; AM = Amery Terrace; AT = Atwater Valley; DC = DeSoto Canyon; EB = East Breaks; EW = Ewing Bank; FP = Florida Plain; GB = Garden Banks; GC = Green Canyon; HE = Henderson; KC = Keathley Canyon; LL = Lloyd Ridge; LS = Lund South; LU = Lund; MC = Mississippi Canyon; SE = Sigsbee Escarpment; VK = Viosca Knoll; WR = Walker Ridge. Geologic age abbreviations: l. = late; u./U. = upper/Upper.

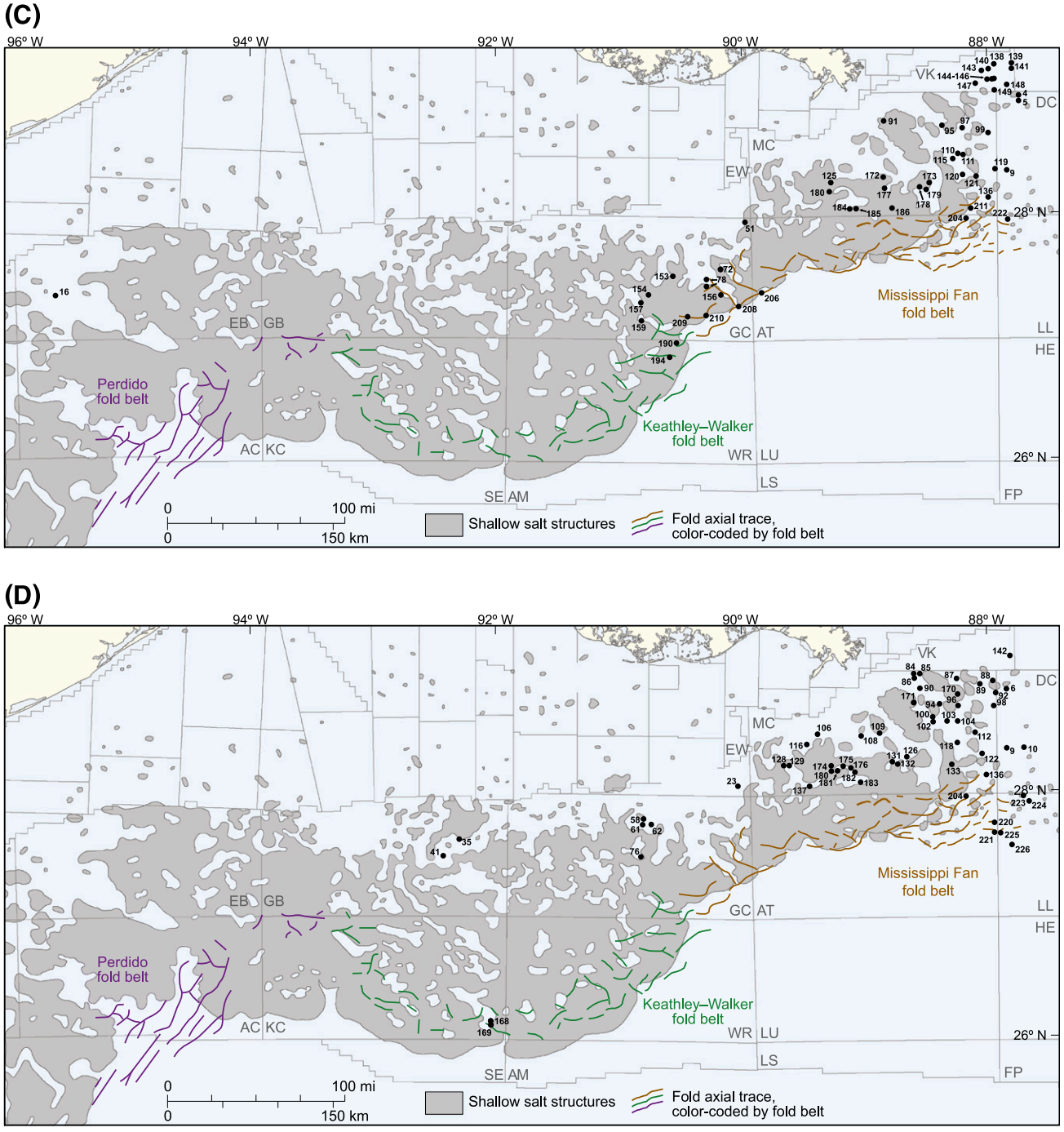

Figure 10. Continued.

The Neogene sedimentary fill is younger in the central part of the province and older to the east and west, as indicated by the different shades of blue in Figure 5B. These different ages of sedimentary fill are caused by the regional shifting of the shallow-marine depocenters during the Cenozoic (Galloway et al., 2000, 2011; Galloway, 2008; Figures 4, 10). The structural geology varies regionally, ranging from little to no deformation to the northeast to areas of extensive salt migration and intraslope basin formation in the central upper slope (Figure 5B). Salt structures vary as well, including diapirs, shallow tongues, and deep remnants such as pillows and rollers. Finally, both normal and reverse faulting is present in the

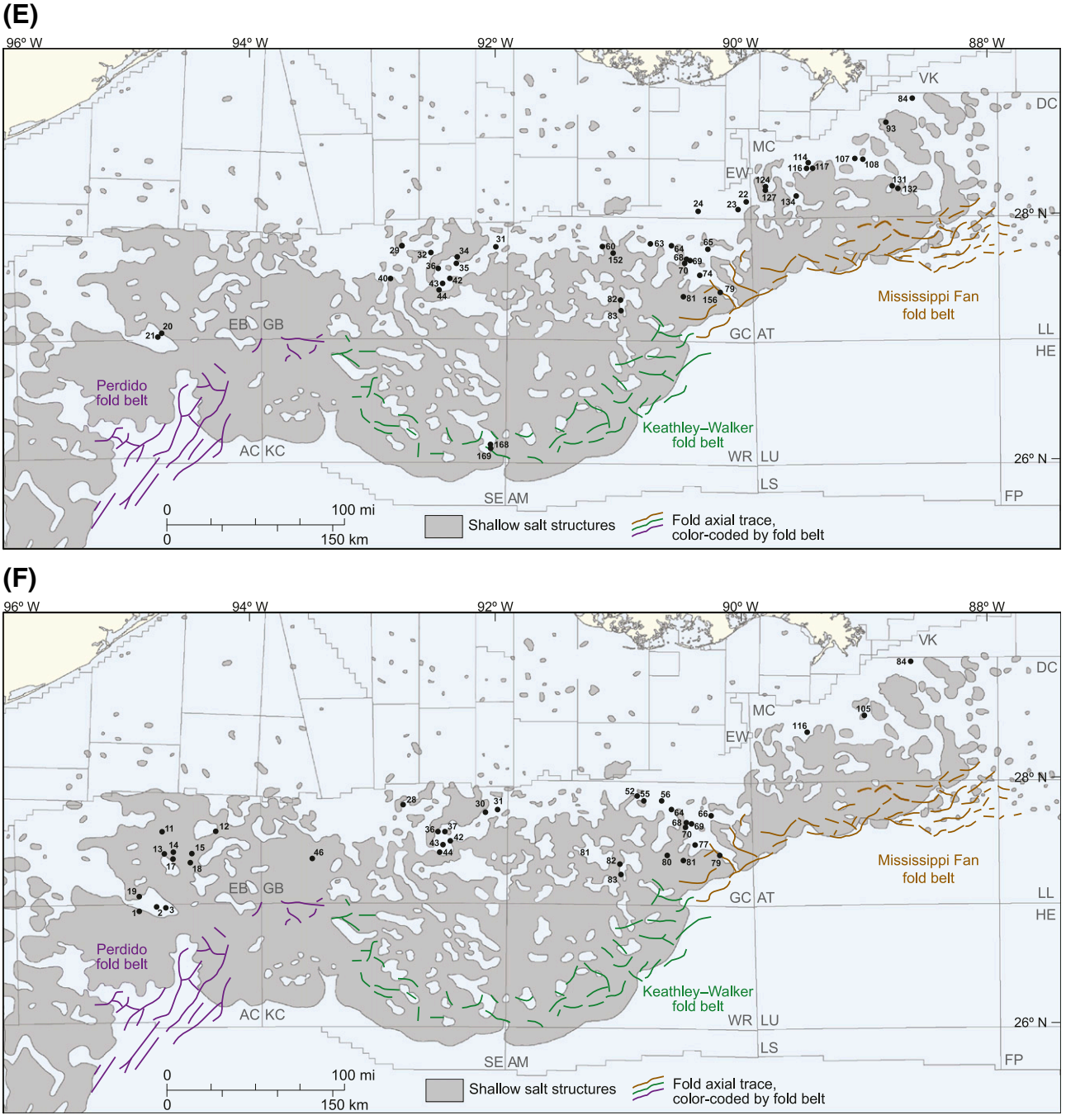

Figure 10. Continued.

upper slope (Figure 12; McBride et al., 1998a; Mount et al., 2006, 2007; Pilcher et al., 2011).

The Basins province includes 149 fields (Figures 5, 10, 11; Table 2). Most of the traps developed in association with sediment loading and salt deformation, primarily on the salt-diapir flanks and/or associated with salt-related faults. Three broad trap types are recognized (Figure 11). First, four-way closure exists in 15 fields: (1) extensional anticline turtles (2 fields), (2) fault bounded (6 fields), and (3) compactional drape overlying a deeper structure (7 fields). Second, 103 fields have three-way closures with combined structural-stratigraphic traps, which include (1) termination against a fault (51 fields) and (2) reservoir onlap pinchout along the flanks of salt bodies (52 fields). (In fact, many of the fields have

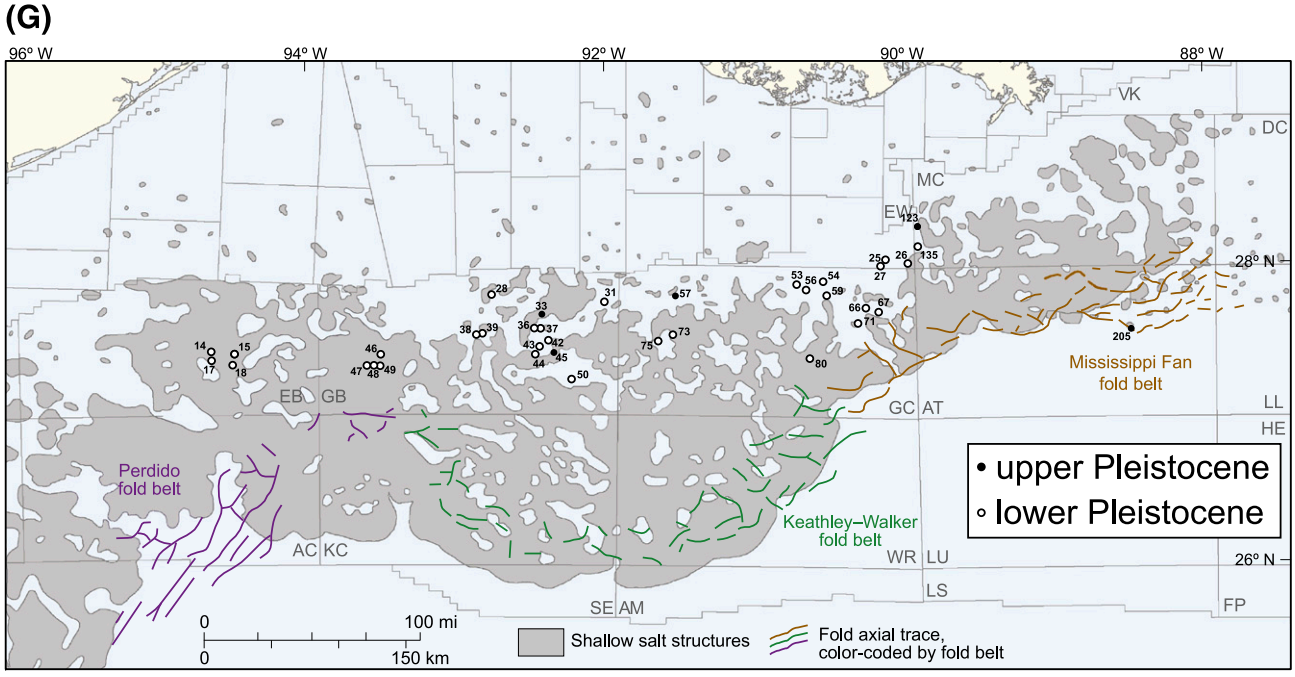

Figure 10. Continued.

multiple trapping elements, e.g., dominantly pinchout against salt flanks with minor faulting.) Third, 28 fields have stratigraphic traps that consist of onlap onto the slope or salt (Table 2). Note that nearly all of the fields (27 of 28) with stratigraphic traps in the northern deep-water Gulf of Mexico are present in the Basins province, and the fields are primarily Miocene in age. One field produces from a trap that is a fault-bounded two-way closure.

Reservoirs are primarily middle Miocene through Pleistocene in age (Figures 10C–G; Table 2). Reservoirs primarily consist of single to multistory channel-fill sands, amalgamated and layered sheet sands, and, to a lesser degree, thin-bedded sands in levees. Note that 105 of the 151 fields and discoveries produce or will produce by subsea tieback to nearby permanent facilities (see figure 2 in Weimer et al., 2017d, this issue).

To the northeast, four fields contain Upper Jurassic (Oxfordian) eolian sandstone reservoirs (Appomattox, Fort Sumter, Vicksburg [A, B] Rydberg; Figure 10A; Tables 2, 6). The reservoirs are equivalent to the producing eolian sandstone reservoirs in the Mobile Bay area near the present-day shoreline (Figure 1; Story, 1998). The fields overlie rafted stratal blocks over the Louann salt (Godo et al., 2011; Godo, in press; Pilcher et al., 2014; Figure 8), and traps consist of three-way closure against faults and four-way closure (Figures 7, 11; Table 2). These discoveries indicate that this particular area remained a relative high along the Middle Ground arch immediately after oceanic spreading began, in contrast to surrounding areas. This area then subsided rapidly during the late Oxfordian. Appraisal drilling of these discoveries for possible field development is ongoing. These four discoveries open up the possibility of exploration in Upper Jurassic shallow-marine to continental reservoirs as well as in Upper Triassic rift-related strata.

Subsalt Province

The Subsalt province (Table 3) contains shallow allochthonous salt bodies, most of which have bathymetric expression (Figures 1, 3, 5). The term primarily refers to "subsalt" prospects that are imaged below the allochthonous salt and thus present significant challenges in seismic imaging. Substantial resources have been dedicated to the acquisition and processing for higher-resolution seismic data for exploration.

The Subsalt province is simplistically viewed as a nearly continuous shallow-salt feature (Figure 5). In actuality, allochthonous salt has considerable variation in its thickness, styles, and timing of formation (Hudec

Table 6. Wells That Penetrated Upper Jurassic Strata, Northern Deep-Water Gulf of Mexico: Exploration Target, Thickness of Top Cretaceous–Paleogene Deposit, (after Denne et al., 2013), Well Status

Well Number in Figure 19	Location Abbreviation	Field, Well Name	Exploration Target	Approximate Top Cretaceous Erosion (m [ft]) or Thickness of KPg Deposit (After Denne et al., 2013)	Status
1	AT 26	Big Horn	MS Fan fold belt	0	Dry hole
2	AT 182-1	Sturgis-1	MS Fan fold belt	0	Noncommercial
3	AT 336	Showboat	MS Fan fold belt	23 (75)	Dry Hole
4	DC 178	Titan	Norphlet	6 (20)	Dry Hole
5	DC 231	Perseus	Norphlet	NA	Dry Hole
6	DC 268	Antietam	Norphlet	13 (43)	Noncommercial
7	DC 269	Shiloh	Norphlet	21 (69)	Noncommercial
8	DC 353	Vicksburg B	Norphlet	20 (66)	Development
9	DC 353	Vicksburg A	Norphlet	NA	Tight Hole
10	DC 398	Gettysburg	Norphlet	NA	Dry Hole
11	DC 486	Fredricksburg	Norphlet	20 (66)	Dry Hole
12	DC 529	Petersburg	Norphlet	NA	Dry hole
13	DC 535	Raptor	Norphlet	9 (29)	Dry hole
14	DC 726	Sake	Smackover	NA	Dry Hole
15	DC 757	Madagascar	Norphlet	NA	Dry Hole
16	DC 843	Swordfish	Norphlet	9 (29)	Dry Hole
17	DC 927	Coral	Smackover	12 (39)	Dry Hole
18	EW 922	Wrigley	Salt weld (Overturned)	67 (220)	Dry hole
19	GB 754	Norton	Shallow salt	21 (69)	Dry Hole
20	LL 399	Cheyenne-deep	Smackover	16 (52)	u. Mio-produced 2007–2015
21	MC 348	Appomattox 3, 3ST	Norphlet	NA	Development
22	MC 391	Appomattox 1, 1ST	Norphlet	NA	Development
23	MC 392	Appomattox 1A/1S	Norphlet	27 (88)	Development
24	MC 393	Corinth	Norphlet	12 (39)	Dry Hole
25	MC 525	Rydberg	Norphlet	NA	Development
26	MC 566	Fort Sumter	Norphlet	NA	Appraisal

Abbreviations: AT = Atwater Valley; DC = DeSoto Canyon; EW = Ewing Bank; GB = Garden Banks; KPg = top Cretaceous–Paleogene; LL = Lloyd Ridge; MC = Mississippi Canyon; MS = Mississippi; u. Mio = upper Miocene; NA = not available.

et al., 2013). These extensive salt features have often merged through time but originally developed from different types of salt structures. Strata below the shallow salt are Middle Jurassic through early Pleistocene in age, depending on the timing of the development of the allochthonous salt systems. The subsalt sediments were originally deposited into the relatively unconfined abyssal plain or into intraslope fairways formed during salt evacuation.

Table 3 summarizes the 51 fields and discoveries in the Subsalt province that are considered to be commercial. Two key structural styles create the traps. First, the Keathley–Walker fold belt extends across the southern part of the province (Figures 5, 6, 13, 14). Traps for 15 fields are contractional folds (Figure 11; e.g., St. Malo, Figure 13; Leon, Figure 14; Table 3). Second, the wide variation in salt styles creates two kinds of general traps—those detached

Table 7. Wells That Penetrated Lower Cretaceous Strata, Northern Deep-Water Gulf of Mexico: Exploration Target, Age at Total Depth, Thickness of Top Cretaceous–Paleogene Deposit (After Denne et al., 2013), Well Status

Well Number in Figure 19	Location Abbreviation	Field, Well Name	Exploration Target	Approximate Top Cretaceous Erosion (m [ft]), or Thickness of KPg Deposit (After Denne et al., 2013)	Status	Oldest Cretaceous Strata Penetrated
27	AC 557	Baha 2	Perdido fold belt	204 (669)	Dry hole	Hauterivian
28	AT 182–1S	Sturgis	MS Fan fold belt	24 (79)	Noncommercial	Aptian
29	AT 187	Sierra	Under salt (overturned)	NA	Dry hole	Aptian
30	KC 875–1	Lucius	Keathley–Walker fold belt	27 (88)	Producing	Barremian
31	KC 875–2	Lucius	Keathley–Walker fold belt	23 (75)	Producing	Barremian
32	KC 919–1	Hadrian	Keathley–Walker fold belt	5 (16)	Producing	Albian

Abbreviations: AC = Alaminos Canyon; AT = Atwater Valley; KC = Keathley Canyon; KPg = top Cretaceous–Paleogene; MS = Mississippi; NA = not available.

from the salt and those attached to the salt (Mount et al., 2006, 2007; Weimer et al., 2006; Pilcher et al., 2011). Detached traps underlie the allochthonous salt and formed prior to the emplacement of the shallow Neogene salt. Trap styles include four-way closures created from (1) turtle structures (five fields; Figure 11; Table 3; see figure 77 in Weimer et al., 2017d, this issue) and (2) one fault-bounded field (Mica field, Table 3). One accumulation with a stratigraphic trap is present at Raton–Raton South–Gemini complex (Figure 11; Table 3). In contrast, fields with attached traps have three-way closure against salt or salt weld, which also acts as the updip seal (27 fields; Figure 11; Kaskida, Figure 14; K2–K2 North, Genghis Kahn, Figure 15; Table 3).

Reservoirs become younger from west to east (Figure 9). To the west and south, reservoirs are upper Paleocene–lower Eocene, that is, the downdip equivalent of the prolific updip Wilcox Formation in onshore Texas (Zarra, 2007a); 21 fields have reservoirs of this age. In contrast, to the east, 29 fields have reservoirs that are primarily Miocene, and one field includes lower Pliocene reservoirs.

Reservoirs primarily consist of amalgamated channel-fill and sheet sandstones (lobes) deposited in both unconfined and confined basins and slope fairways. The upper Paleocene–lower Eocene Wilcox Formation was deposited in a largely unconfined, base-of-slope setting (Zarra, 2007a). Curiously, the Wilcox strata thin over the crest of the structures that were created by the Early Cretaceous salt emplacement (North Platte, Figure 13; Figure 14).

In contrast, for the fields with Miocene–lower Pliocene reservoirs, sands were deposited in intraslope basins, either adjacent to or against the shallow-salt features. With ongoing deformation, the salt was emplaced later and overrides the reservoir (e.g., Kaskida, Figure 14; K2 North and Genghis Khan, Figure 15; Mars and Ursa fields, Meckel et al., 2002).

It is worth noting that if the shallow allochthonous salt were not present, many of these detached structures probably would have been drilled 10 to 15 yr earlier, because many of the structures are not particularly complex (Figures 6, 13, 14). However, this is not true in the attached traps that developed during the emplacement of shallow-salt bodies. For these fields, salt is part of the trap and seal (Figure 15).

Fold Belt Province

The northern deep-water Gulf of Mexico holds three subregional fold belts: (from west to east) Perdido, Keathley–Walker, and the Mississippi Fan (Figures 3, 5). (The Keathley–Walker fold belt completely underlies the salt and is included above in the Subsalt province.) These fold belts have different structural styles, timing of deformation, ages of potential

Table 8. Wells That Penetrated Upper Cretaceous Strata, Northern Deep-Water Gulf of Mexico: Exploration Target, Age at Total Depth, Thickness of Top Cretaceous–Paleogene Deposit (After Denne et al., 2013), Well Status

Well Number in Figure 19	Location Abbreviation	Field, Well Name	Exploration Target	Approximate Top Cretaceous Erosion (m [ft]), or Thickness of KPg Deposit (After Denne et al., 2013)	Status	Oldest Cretaceous Strata Penetrated
33	AT 63	Telemark	MS Fan fold belt	>40 (131)	Producing	TDed in KPg deposit
34	AT 398	Bonsai	MS Fan fold belt	>15 (49)	Dry hole	TDed in KPg deposit
35	AT 428	Palamino	MS Fan fold belt	>20 (66)	Dry hole	TDed in KPg deposit
36	GB 840	Vienna	Salt feature	>15 (49)	Dry hole	TDed in KPg deposit
37	GB 989	Salida	Keathley–Walker fold belt	>2 (6)	Dry hole	TDed in KPg deposit
38	GC 639	Tahiti West	Overturned subsalt feature	>40 (131)	Dry hole	TDed in KPg deposit
39	GC 653	Shenzi	MS Fan fold belt	90 (295)	Producing	Turonian
40	GC 826	Mad Dog	MS Fan fold belt	>18 (59)	Producing	TDed in KPg deposit
41	GC 847	Turtle Lake	MS Fan fold belt	>55 (180)	Dry hole	TDed in KPg deposit
42	GC 866	Puma	Overturned salt carapace	39 (128)	Dry hole	Campanian/Salt
43	KC 102	Tiber	Keathley–Walker fold belt	90 (295)	Appraisal	Albian (?)
44	KC 596–1	Bass	Keathley–Walker fold belt	100 (328)	Dry hole	Campanian
45	KC 681	Sardinia	Keathley–Walker fold belt	>30 (98)	Dry hole	TDed in KPg deposit
46	KC 774	Ponza	Keathley–Walker fold belt	85 (279)	Dry hole	Santonian
47	KC 919–2	Hadrian	Keathley–Walker fold belt	>20 (66)	Producing	TDed in KPg deposit
48	MC 84	Horn	Salt diapir	27 (88)	Producing	Cenomanian
49	MC 379	Chin Music	Overturned salt carapace	46 (151)	Dry Hole	TDed in Campanian
50	MC 876	Callisto	MS Fan fold belt	–	Produced 2007–2015	TDed in KPg deposit (logs didn't reach the deposit)
51	VK 915	Dorado	Salt feature	>13 (43)	Producing	TDed in KPg deposit
52	VK 826	Neptune	Salt feature	60 (197)	Producing	Tded in Cenomanian/Anhydrite
53	WR 52–1	Shenandoah	Keathley–Walker fold belt	>30 (98)	Appraisal	TDed in KPg deposit
54	WR 95	Yucatan	Keathley–Walker fold belt	>9 (29)	Appraisal	TDed in KPg deposit
55	WR 155	Atlas Deep	Keathley–Walker fold belt	>9 (29)	Dry hole	TDed in KPg deposit
56	WR 316	Lewis	Keathley–Walker fold belt	14 (46)	Dry hole	TDed in KPg deposit
57	WR 584–1	Julia	Keathley–Walker fold belt	>21 (69)	Appraisal	TDed in KPg deposit
58	WR 969	Logan	Keathley–Walker fold belt	155 (508)	Appraisal	Hauterivian*

* Logan penetrated a shallower Cretaceous section that overlies allochthonous salt. Well total depth (TDed) in Paleocene.

Abbreviations: AT = Atwater Valley; GB = Garden Banks; GC = Green Canyon; KC = Keathley Canyon; KPg = top Cretaceous–Paleogene; MC = Mississippi Canyon; VK = Viosca Knoll; WR = Walker Ridge.

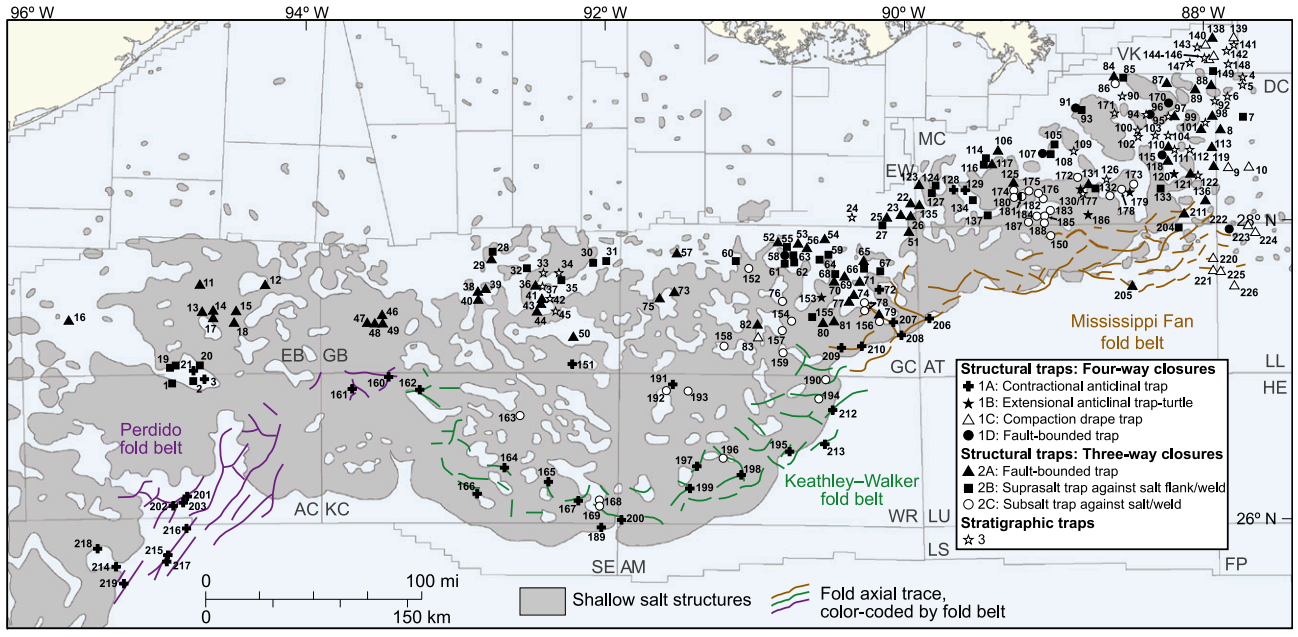

Figure 11. Regional map showing the relationship of kinds of trap styles in the northern Gulf of Mexico to the tectonic provinces. Eight kinds of traps are recognized (see Tables 2–5 for fields and Figure 5A for the name of each field). For trap classification, see figure 3 in Weimer et al. (2017d, this issue) and figure 5 in Bouroullec et al. (2017a, this issue). Abbreviations for protraction areas: AC = Alaminos Canyon; AM = Amery Terrace; AT = Atwater Valley; DC = DeSoto Canyon; EB = East Breaks; EW = Ewing Bank; FP = Florida Plain; GB = Garden Banks; GC = Green Canyon; HE = Henderson; KC = Keathley Canyon; LL = Lloyd Ridge; LS = Lund South; LU = Lund; MC = Mississippi Canyon; SE = Sigsbee Escarpment; VK = Viosca Knoll; WR = Walker Ridge.

reservoirs, and natures of salt. Discoveries have been made in both the Perdido and Mississippi Fan fold belts (Table 4).

The Perdido fold belt is characterized by northeast-trending folds, with minor faulting along their flanks (Figures 3, 16, 17; Trudgill et al., 1999; Camerlo and Benson, 2006; Zarra, 2007a). The northeastern part extends below the allochthonous salt. These folds are cored with allochthonous Upper Jurassic salt (D. Worrall, 2012, personal communication; Figures 8, 16). The fold belt formed primarily during the latest Oligocene, although there was minor growth during the Eocene. Traps in the Great White and Tobago producing fields are four-way closures; at Silvertip field, the trap is a dipping three-way closure that is slightly fault bounded (Eikrem et al., 2010). All fields have a stratigraphic component to their traps. At the Great White field, the reservoirs are deep-water Wilcox (upper Paleocene–lower Eocene) and deep-water Frio (Oligocene; Figures 5, 8; Zarra, 2007b; Eikrem et al., 2010); at Tobago field, the Wilcox forms the reservoir. In the Silvertip field, the reservoirs are Oligocene (Figures 5, 8; Eikrem et al., 2010). These three fields produce from the Perdido SPAR facility in 2438 m (8045 ft) water depth—the world record for SPAR (Figure 2). Tobago and Silvertip fields produce via subsea tieback to the SPAR. Tobago produces from the deepest water depth from tiebacks (9636 ft [2937 m]). Note that most of the Perdido fold belt rests in the Mexican deep water to the southwest, where Pemex has made six discoveries during the past 4 yr (Figures 5, 17; Cratos, Exploratus, Maximino, Maximino-DL, Supremus, Trion; Colmenares, 2014).

The Mississippi Fan fold belt developed primarily during the middle to late Miocene and consists of slightly asymmetric folds with primary vergence to the north (Figures 5, 12; Morris and Weimer, 2004a, b; see figure 20 in Bouroullec and Weimer, 2017, this issue; figures 3, 4 in Bouroullec et al., 2017b, this issue). This fold belt is cored by the Lower Cretaceous allochthonous salt layer that developed from the Middle Jurassic autochthonous salt layer (Figures 8, 12; Moore et al., 2001). Traps for the five western fields are four-way closures (Atlantis, Mad Dog, Neptune, Parmer, Shenzi; Figure 11). For the three eastern fields (Bass Lite, Merganser, Q), traps are combined three-way closures. For the seven fields (except Bass Lite), the reservoirs are lower to middle

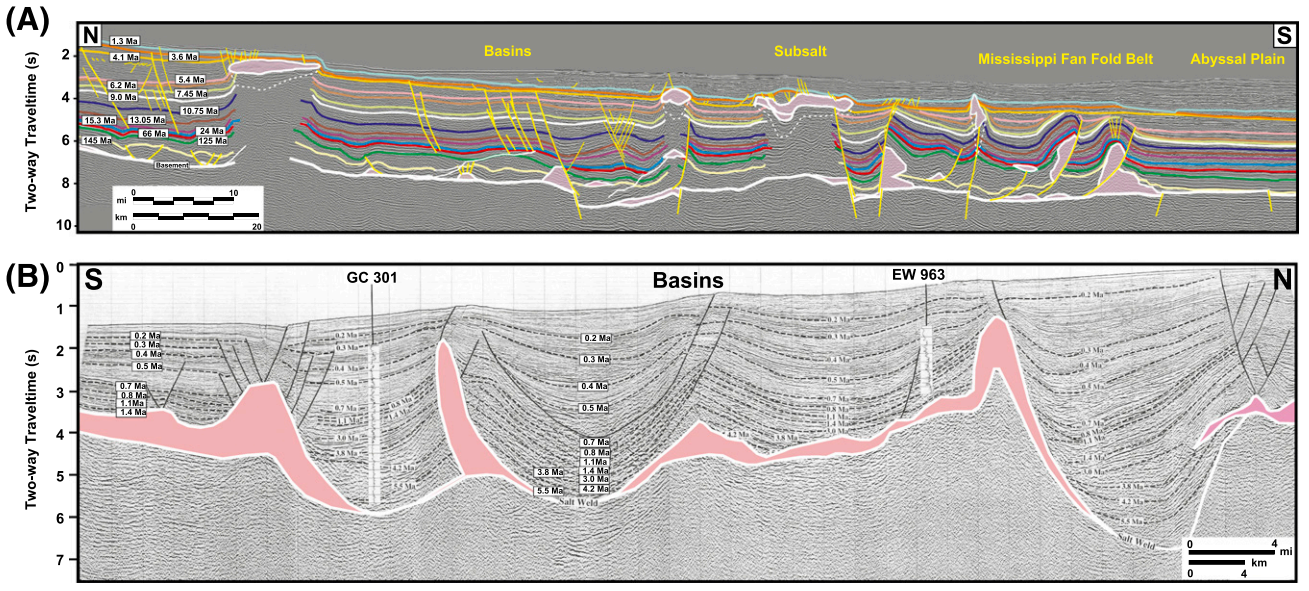

Figure 12. Regional seismic profiles across the Basins province. (A) Interpreted profile in eastern Mississippi Canyon and northern Atwater Valley across the Basins province (undeformed strata), Subsalt province (isolated shallow and deep salt structures), Fold Belt province (eastern part of the salt-cored Mississippi Fan fold belt), and Abyssal Plain province (south of fold belt). After Bouroullec et al. (2004). Reproduced with permission of the Gulf Coast Association of Geological Societies. (B) Interpreted profile from eastern Green Canyon (Basins province) across counterregional and reverse faults, faults, and shallow-salt structures. Prominent weld surface is shown. See Figure 5B for location of profiles. After McBride et al. (1998b). Reproduced with permission of AAPG.

Miocene sands that were deposited in an unconfined, base-of-slope setting (Mander et al., 2012; Walker et al., 2012). Bass Lite produces from an upper Pleistocene channel-fill sand.

Finally, the Cascade and Chinook fields are part of the Keathley–Walker fold belt system (discussed above) but rest outside of the Subsalt province (Figures 5, 18). Traps are four-way closures that are cut by faults near their crest. Reservoirs are Wilcox sandstone (Figure 10; Table 4). The Cascade field is produced by an FPSO, and Chinook is produced by a subsea tieback.

Abyssal Plain Province

The Abyssal Plain province (Table 5) rests outboard (south) of the Subsalt, Fold Belt, and Basins provinces (Figures 4, 6A). The boundary of the Subsalt province is abrupt and is marked by the edge of the Sigsbee Escarpment. This province lies directly basinward of the Fold Belt province. To the east, the boundary is transitional with the Basins province. The Abyssal Plain province can simplistically be subdivided into two parts: areas underlain by Louann salt and areas that are salt free. The basinward edges of the original depositional salt (autochthonous Louann) and allochthonous salt (Early Cretaceous emplacement) are present in the northern part of the Abyssal Plain province (Hudec et al., 2013). Structures consist of deformed salt or elevated basement blocks (Post et al., 2001).

Seven fields have been discovered in the province (Table 5). All reservoirs are upper Miocene and were deposited in channel fill or levees. Six fields have four-way closure that developed from compactional drape (Weimer et al., 2017d, this issue). All fields produced by subsea tieback to the Independence Hub in southeastern Mississippi Canyon, until abandoned (Figure 2; Table 5).

What distinguishes this province from the others is the lack of bathymetric expression of the structures. Significantly, fewer wells have been drilled in this area than in the rest of the northern deep-water Gulf of Mexico, so less is known about the details of the stratigraphy.

OTHER PETROLEUM SYSTEMS FACTORS

Source Rocks

The source rocks in the northern deep-water Gulf of Mexico are found at great subsurface depths, commonly

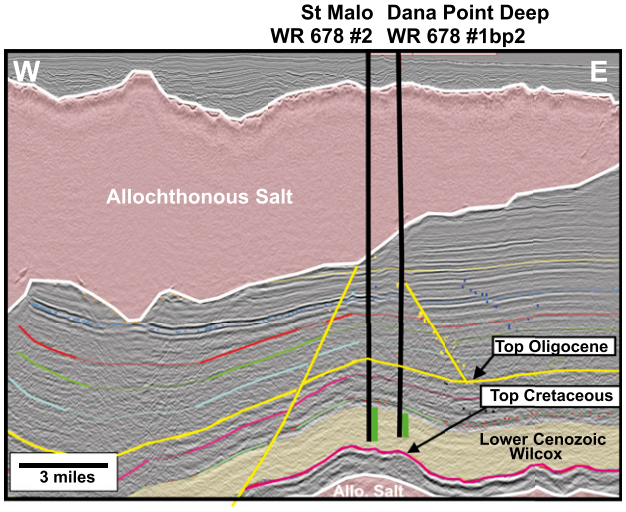

Figure 13. Interpreted seismic profile across St. Malo (Walker Ridge [WR] 678) and Dana Point (WR 678) in WR protraction area. The two wells underlie the shallow allochthonous (Allo.) salt sheet. The field consists of a deep Wilcox Formation reservoir in a four-way closure. This was the first subsalt discovery in the lower Wilcox Formation. Note the thinning of the Wilcox Formation across the crest of the fold, indicating the bathymetric expressions of the folds during the late Paleocene–early Eocene. Green (in online version) bars correspond to reservoir. See Figure 5B for location of profiles. After Lewis et al. (2007). Reproduced with permission of the Gulf Coast Section SEPM Foundation, and any other use requires their permission.

overlain by more than 13,000 m (30,000 ft) of strata. Consequently, only 26 wells have penetrated the source rocks, primarily around the northeastern margin and shallow structural features (Figure 19; Tables 6–8; Weimer et al., 2016a). Thus, the relatively few penetrations mean that the regional distribution of source rocks is interpreted based on primarily the oil composition and biomarker data from reservoirs or by seeps on the slope (Wenger et al., 1994; Cole et al., 2001a, b; Colling et al., 2001; Hood et al., 2002; Jacques and Clegg, 2002).

Two source intervals are interpreted as coeval to upslope shallow-marine–equivalent strata: (1) Oxfordian shallow marine limestones and marls (Smackover equivalent), found primarily to the northeast, and (2) Tithonian shales (Cotton Valley equivalent), which is areally widespread. A third possible source interval, Lower Cretaceous, is interpreted to be present by some authors (Teerman et al., 2010). The areal distribution of these source rocks is shown in Figure 19. Oxfordian source rocks have type I kerogens (Godo, in press), and Tithonian source rocks have type II and type IIS kerogens; they were deposited during the early post-rift history (Cole et al., 2001b). The Lower Cretaceous interval is considered a type II kerogen. One area in the northern slope has oils that are produced from a mixture of these source intervals (Figure 19). Wireline characteristics for these source rocks are shown in Weimer et al. (2016a), and their approximate thicknesses are in Table 6.

Evolution of Exploration Plays and Results

An important part of the continuing exploration success in the northern deep-water Gulf of Mexico is that exploration play concepts have evolved through time, which has resulted in substantial reserve growth. Five major exploration plays (Figure 20), related to the four tectonic provinces (Zarra, 2007a; Figure 5), have been developed during the past 25 yr: the flex trend, minibasins, fold belt, subsalt, and Mesozoic plays. Also shown in Figure 20 are the number of discoveries per year and the timing and transition of the exploration plays. For example, in 1975, Cognac field was the first discovery in greater than 200 m (660 ft) water depth (Figure 20); 2001 was the year for the largest number of discoveries, with no discoveries in 1978, 1979, and 1992. The Macondo incident in April 2010 led to an increase

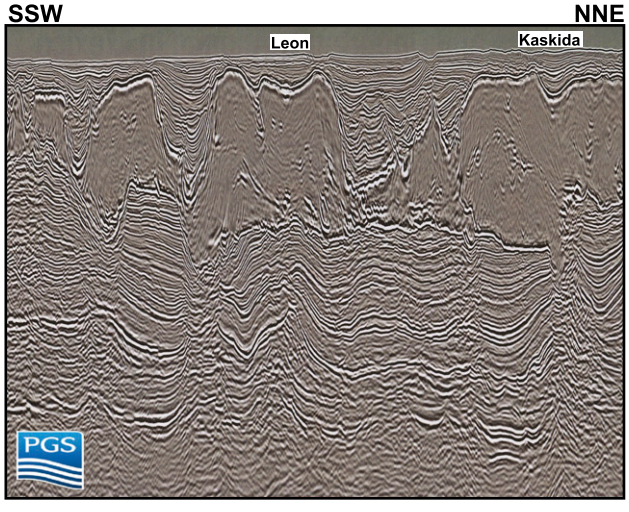

Figure 14. Seismic profile across the Kaskida (Keathley Canyon [KC] 292) and Leon (KC 642) discoveries in KC in the Subsalt province. Kaskida discovery consists of a three-way closure against a salt feeder. Leon discovery consists of a four-way closure below salt. See Figure 5B for location of profile. Reprinted with permission of PGS. Data are proprietary to MKI.

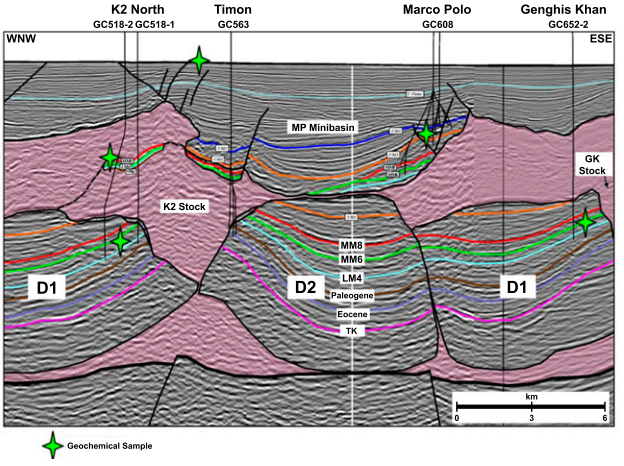

Figure 15. Regional seismic profile across the K2 North, Timon, Marco Polo (MP), and Gengis Khan (GK) fields in the Subsalt province of southern Green Canyon (GC). Note the subsalt truncation traps for the three subsalt fields. See Figure 5B for location of profile. After Mount et al. (2006). Republished by permission of the Gulf Coast Association of Geological Societies, whose permission is required for further publication use. Horizon abbreviations: LM4 = lower Miocene 4; MM6 = middle Miocene 6; MM8 = middle Miocene 8; TK = top Cretaceous.

in regulatory action and a subsequent decrease in discoveries.

The first two deep-water exploration plays—flex trend and minibasins—occurred in the Basins province (Figure 5). In the early to mid–1980s, exploration companies started drilling in greater than 1500 ft (457 m) water depth, focused on drilling in the flex trend, which is the upper slope basinward of the present shelf edge. Discoveries generally had small reserves in reservoirs comprising channel-fill sediments and thin beds in levees. Because of the relatively small reserves and improving drilling technology, exploration activity then moved into the deep water of the middle slope, where larger fields were discovered, such as Mars (800 million BOE), Ursa (500 million BOE), and Mensa (1.2 tcf), all notable fields for their pioneering development.

The third exploration play was in the deep-water fold belts. One exploration well was drilled in this Mississippi Fan fold belt (albeit 8 yr earlier) before the first discovery (Neptune: AT 575; Figures 5; 10B, C; 11) in 1995. In the Perdido fold belt, three wells were drilled before the first commercial discovery (Great White: Alaminos Canyon 857; Figures 5; 10B, C; 11) in 2002.

The fourth exploration play was the subsalt play; subsalt discoveries were initially made on the shelf, and then slowly exploration moved to the middle to lower slope during the 1990s, with more exploration wells drilled since 2000. Initial discoveries were made in areas where the salt partially overhung the prospects. Later discoveries were made where the shallow allochthonous salt extended across the entire prospect field. Finally, the Mesozoic play saw its first exploration success in 2004; since then, there have been three additional discoveries as well as several noncommercial discoveries and dry holes (Tables 6–8). Five exploration wells were drilled before the first commercial discovery was made in 2009 (Rojas, 2015).

The continued evolution in exploration plays has had a major effect on sustained reserve growth by year (Figure 21) and cumulatively (Figure 22). Reserves grew at the highest rates between 1995 and 2001 and have continued to grow more slowly since that time. One challenge in compiling these data is that the sizes of the subsalt fields have not been announced.

The exploration results summarized in Figures 20–22 indicate several important aspects of the deep-water play for the northern deep-water Gulf of Mexico; by analogy, these findings are also important

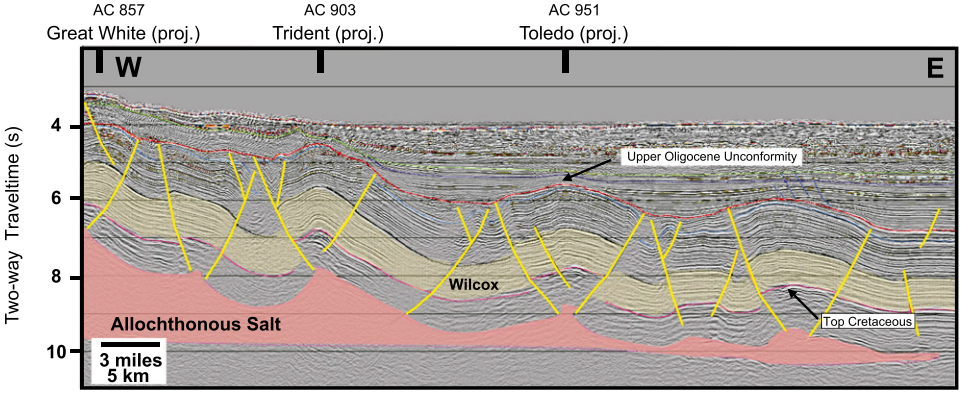

Figure 16. Regional seismic profile across the Perdido fold belt showing the box folds that decrease in height from west to east (left to right). Fold 4 is closest to the Great White and Trident discoveries. See Figure 5B for location of profile. After Zarra (2007a). Reproduced with permission of the Gulf Coast Section SEPM Foundation, and any other use requires their permission. AC = Alaminos Canyon; proj. = projected.

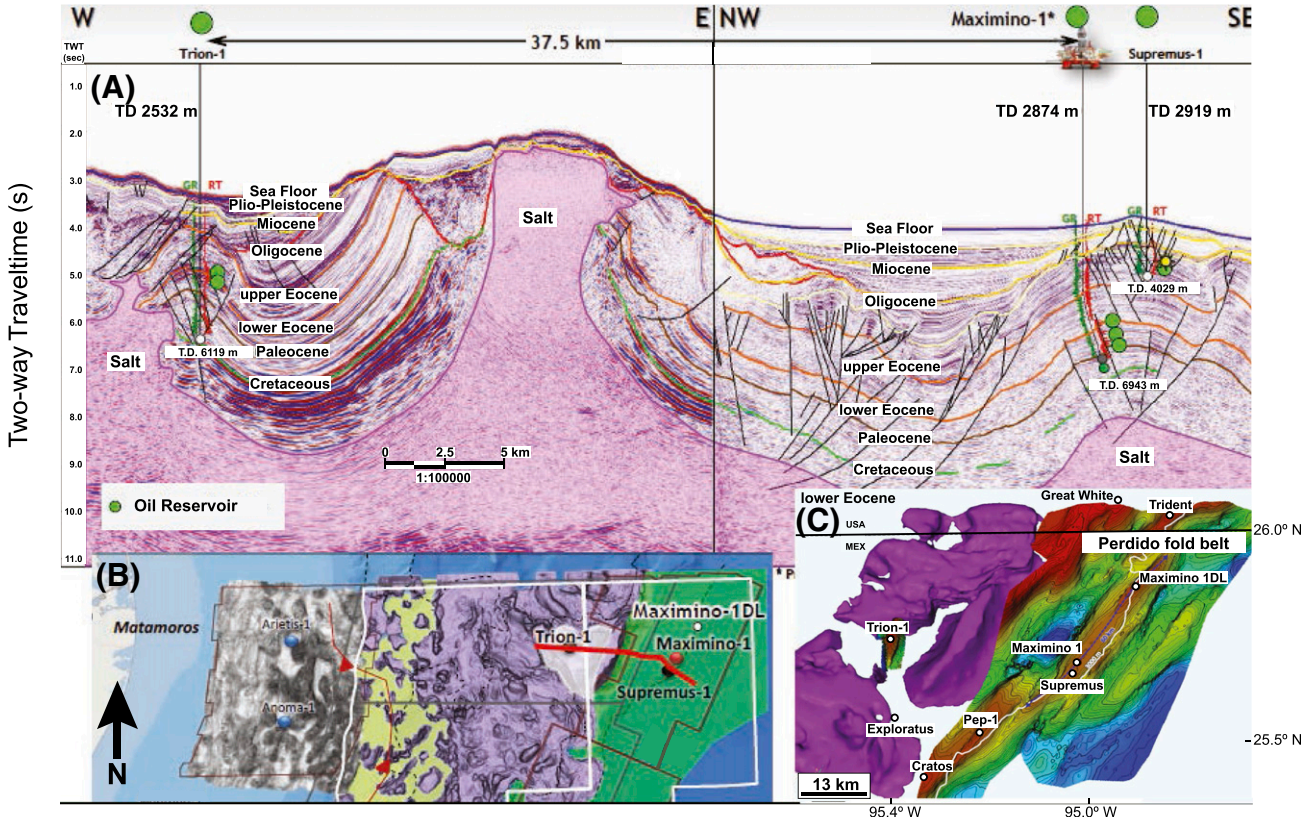

Figure 17. (A) Regional seismic profile across the Trion and Perdido fold belt structures in the northwestern deep-water Gulf of Mexico. Locations of Trion, Maximino, and Supremus wells are shown. (B) Map showing location of the seismic profile in (A). From west to east, light blue = shelf; gray = upper slope; light green = middle slope; purple = lower slope with shallow allochthonous salt; white = Trion structure; green and light blue = undifferentiated abyssal plain. (C) Lower Eocene structure contour map of Perdido fold belt and Trion structure. Depth gradient is red (shallow) to blue (deep). Purple = lower slope with shallow allochthonous salt. After Colmenares (2014). Reprinted with permission of AAPG. 1DL = 1 delineation; GR = gamma ray; MEX = Mexico; Plio = Pliocene; RT = resistivity; TD = total depth. Note: A color version can be seen in the online version.

for many global deep-water basins. First, because drilling technology and seismic imaging have improved, new plays have developed. Second, because new drilling provinces have opened, reserve growth has remained high. Finally, exploration continues today in all of these provinces. The economics of drilling and development discoveries in each province vary considerably. Where development infrastructure exists in a province (middle to upper slope), smaller companies can economically develop fields with smaller reserves (Table 2).

Field Sizes

The sizes of the reserves of the 50 largest fields and discoveries in the northern deep-water Gulf of Mexico are shown in Figure 23. Note that only 24 fields have reserves larger than 300 million BOE, and 38 fields have more than 200 million BOE in reserves; the remaining 186 fields are less than 200 million BOE. The average reserve size for fields in the northern deep-water Gulf of Mexico is 77 million BOE (Beaubouef, 2015). A common theme in many fields is that although there are reservoir-quality sands present in multiple depositional sequences, commonly only some of the sands are charged. Thus, many structures could potentially hold considerably more petroleum if they were fully charged.

Reservoir Quality

When companies decide whether to develop a discovery, one challenge is determining the overall reservoir quality. In many cases, the reservoirs are so

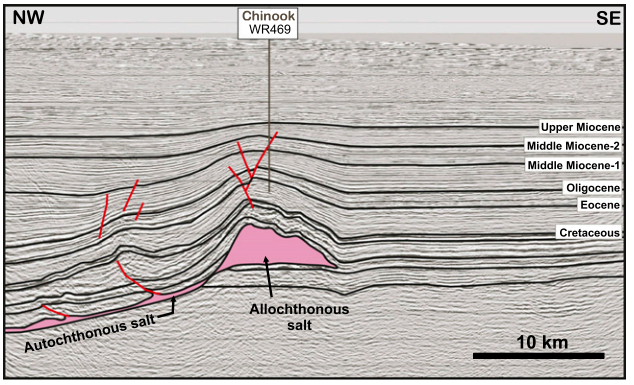

Figure 18. Regional seismic profile across the Chinook field in the Keathley–Walker fold belt. Fold is underlain by Lower Cretaceous allochthonous salt. Note the thinning of the Wilcox Formation across the crest of the fold, indicting the bathymetric expressions of the folds during the late Paleocene–early Eocene. See Figure 5B for location of profile. Modified from Mount et al. (2007). Reproduced with permission of the Gulf Coast Section SEPM Foundation, and any other use requires their permission. WR = Walker Ridge.

deep below the sea floor that predictive models have inaccurate results. For proprietary reasons, companies do not publish the details of reservoir quality until plays have matured and fields have been producing for some time. However, the little publicly available information, reviewed below, indicates that overall reservoir quality is loosely correlated with reservoir age, specifically for fields with reservoirs from the Upper Jurassic (Figure 10A), upper Paleocene–lower Eocene (Figure 10A), or Neogene (Figure 10B–I).

Neogene Reservoirs

The Neogene fields were the first reservoirs discovered and developed in the northern deep-water Gulf of Mexico (Figures 10B–I; 21). In the Basins province, the Miocene and Pliocene sands have relatively high porosity and permeability resulting from less compaction and diagenesis and, locally, lower geothermal gradients. Taylor et al. (2010) noted that the reservoir sands fall within a relatively narrow range in grain size (80–120 μm), are moderately sorted, have variable compositions but similar mechanical properties (within local areas), and are typically overpressured. Overpressure develops in the shallow subsurface, helping to preserve porosity and permeability by decreased rates of compaction. In addition, low geothermal gradients in the region contribute to the decreased rates in diagenesis; today, the reservoir temperatures are less than 80°C (176°F) and thus are not adversely affected by quartz and other kinds of cementation. From the sea floor to 4500-m (14,764-ft) subsurface depth, mechanical compaction, as a function of effective vertical stress, is the main control on sand porosity.

For Miocene reservoir quality in the Subsalt province, Taylor et al. (2010) discussed the effect of allochthonous salt on the subsalt's geothermal gradient and rates of diagenesis. Because the overlying salt is highly conductive, it draws heat away from the sediment below, thus decreasing the sediment's geothermal gradient. To reach this conclusion, Taylor et al. (2010) compared the reservoir quality from two subsalt wells at the same subsurface depth—Tahiti (Green Canyon 640) and Poseidon (Mississippi Canyon 727). Taylor et al. (2010) found that the Tahiti reservoir was approximately 30°C (86°F) cooler than the regional geothermal gradient, whereas the Poseidon reservoir was 40°C (104°F) higher than Tahiti, closer to the measured geothermal gradient. The Tahiti reservoir may also have been affected by its close proximity to the salt feeder that forms the field's trap (Figure 15). Poseidon's higher reservoir temperature enhanced development of quartz overgrowths, effectively causing reservoir quality to degrade significantly. Taylor et al. (2010) concluded that the timing of emplacement, thickness of salt, burial depth of the reservoir, and vertical separation are likely important factors in controlling the magnitude of thermal suppression on quartz cementation.

Upper Paleocene–Lower Eocene Reservoirs

The reservoir quality of the upper Paleocene–lower Eocene deep-water Wilcox reservoirs is, in general, considerably lower than the Neogene sands. To date, six fields are producing from the Wilcox in pairs: Great White–Tobago, Cascade–Chinook, and Jack–St. Malo (Figure 10A; Tables 3, 4). Eikrem et al. (2010) summarized the reservoir quality of the deep-water Wilcox in the Great White field, a suprasalt field, with average porosity values in the shallower producing reservoir sandstones of 25%–30% and permeabilities of 50–250 md. Deeper, nonproducing reservoir sands have lower porosities (<15%) and permeabilities (average of 2 md). In contrast, the subsalt fields have lower porosity and permeability values in the Wilcox reservoirs than those of the Great White field. The following

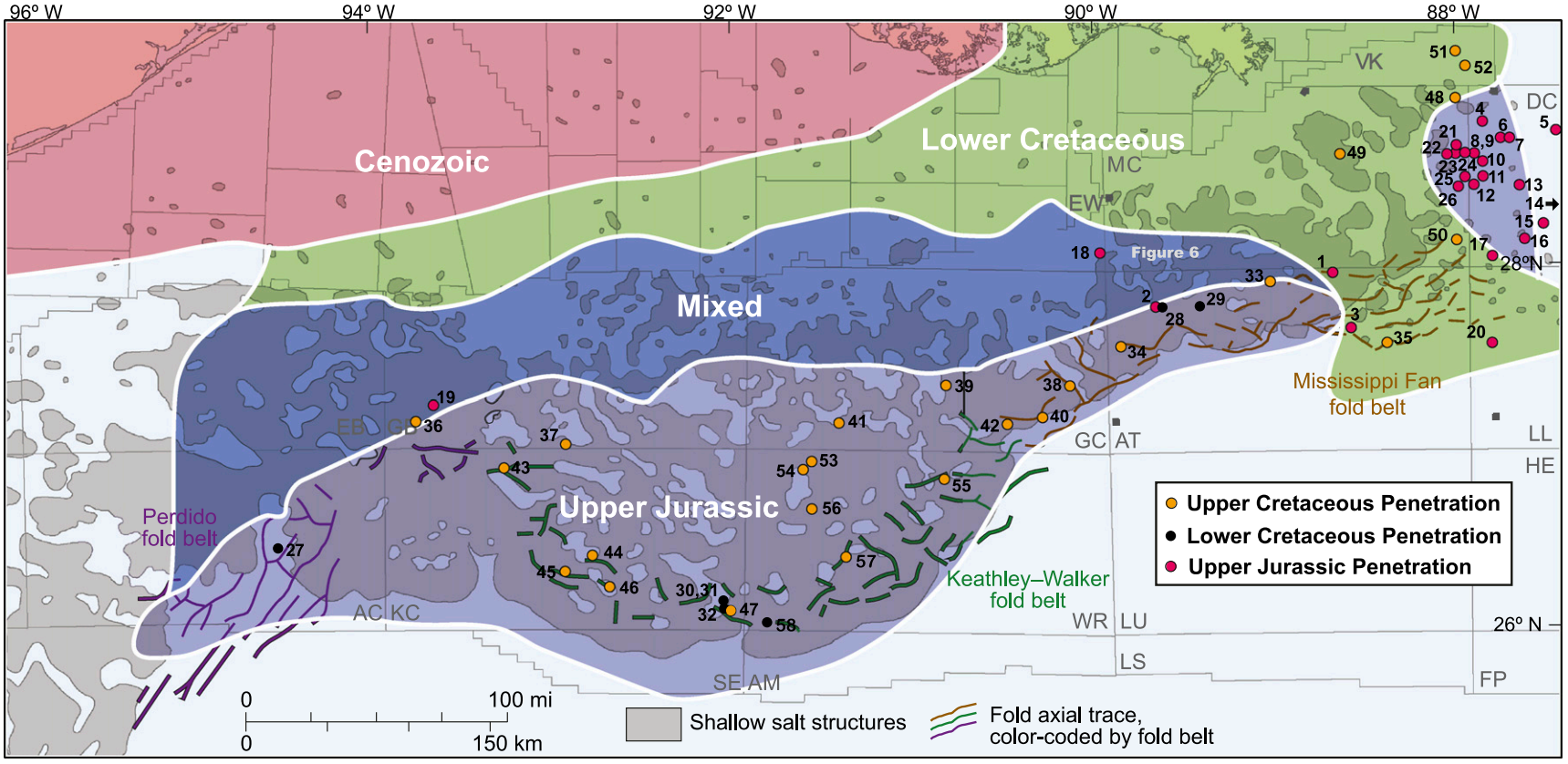

Figure 19. Map showing the distribution of different ages of source rocks and the Upper Cretaceous Chicxulub deposit (after Denne et al., 2013) are shown by numbered circles (see Tables 6–8). Note that well 14 is present east of the figure. Modified and reprinted with permission of John Zumberge and GeoMark Research. Abbreviations for protraction areas: AC = Alaminos Canyon; AM = Amery Terrace; DC = DeSoto Canyon; EB = East Breaks; EW = Ewing Bank; FP = Florida Plain; GB = Garden Banks; GC = Green Canyon; HE = Henderson; KC = Keathley Canyon; LL = Lloyd Ridge; LS = Lund South; LU = Lund; MC = Mississippi Canyon; SE = Sigsbee Escarpment; VK = Viosca Knoll; WR = Walker Ridge.

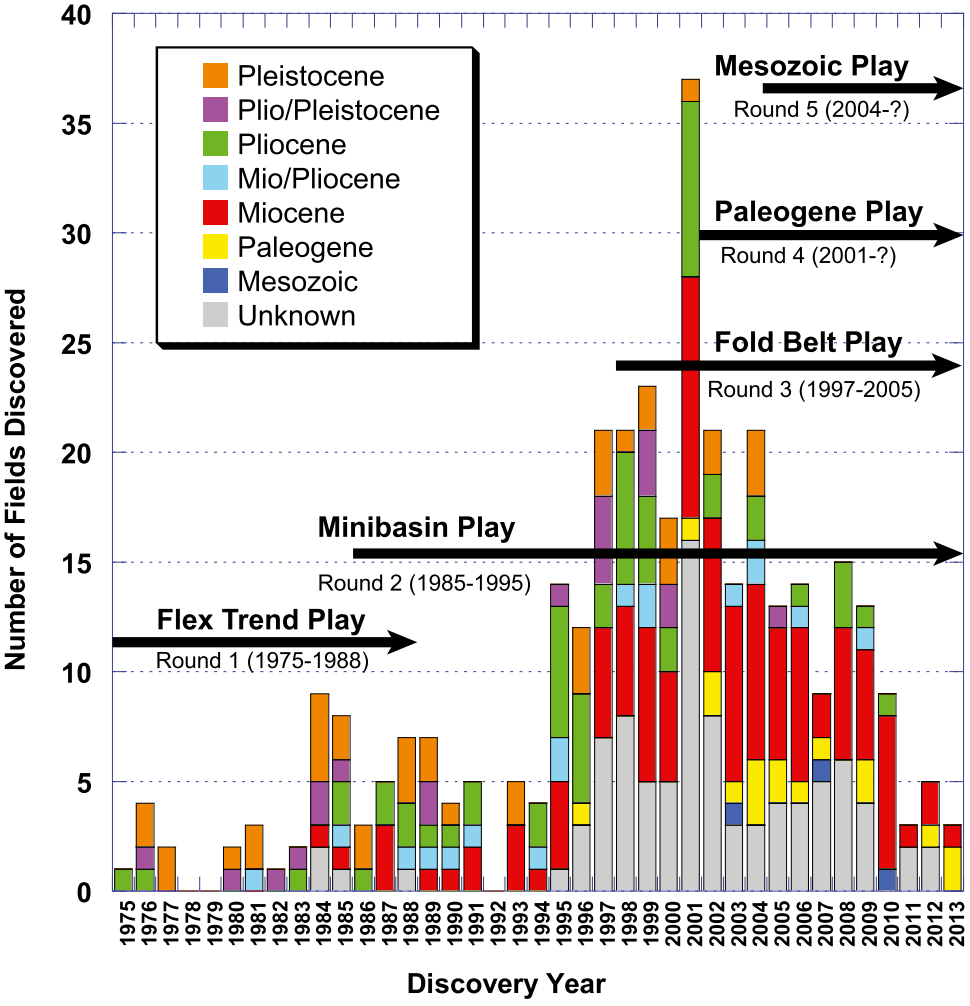

Figure 20. Graph shows the number of discoveries in the northern Gulf of Mexico by year for water depths greater than 200 m (650 ft), the ages of the reservoirs, and the timing of five major exploration plays. Mio = Miocene; Plio = Pliocene.

summary of the subsalt deep-water Wilcox reservoirs is based on several presentations (Zarra, 2007a; Cearley, 2011; Kane and Ponton, 2012; Sullivan et al., 2014; Marchand et al., 2015).

The main factors in controlling the porosity and permeability are the depositional elements, composition and mineralogy of the sandstones, basic sedimentology of the units, and depth of burial. Channel-fill strata have the highest permeability values, with average values of 40 and up to 400 md for maximum values. Channel-lobe transition sands average 17 md, and permeability values decrease to the lobes' fringes. Silt content is higher in the Wilcox than in the Neogene reservoirs. Channel-fill reservoir sands have 20% silt content, increasing to 55% in the lobe fringe. The presence of silt affects permeability much more than porosity; a decrease of 2% to 3% in porosity has a more significant effect in permeability reduction. In addition, the Paleogene sands have greater amounts of ductile grains (20%) than most Miocene sands (5%). Finally, trunk channels have fewer ductile grains, and the amounts tend to increase in the lobe deposits.

As the depths of the reservoirs increase, the amount of quartz cementation is also an important factor. In general, deeper wells have higher bottomhole temperatures, and they may have more cementation. In some cases, the effects of higher temperature can be mitigated by proximity to adjacent or overlying salt bodies, which tend to draw off some excess heat.

Sullivan et al. (2014) noted that porosity and permeability values are dependent on reservoir elements and depth, and they identified three groupings. First, the channel-fill reservoirs of the Wilcox 1A unit, the youngest sandstone unit of Zarra (2007a), have the best porosity and permeability, up to 400 md. Second, the slightly deeper Wilcox 2 channel-fill reservoirs have porosity values that are lower than the channel fill of Unit 1A and slightly lower

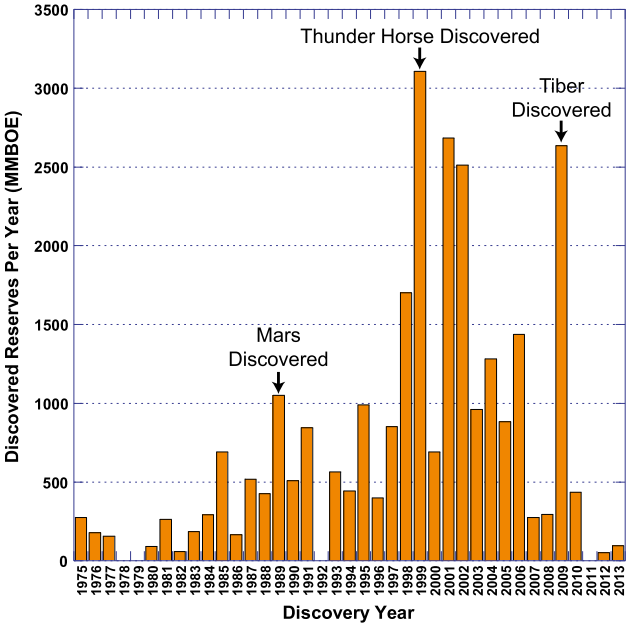

Figure 21. Graph shows the volume of reserves in the northern Gulf of Mexico discovered by year for water depths greater than 200 m (650 ft). Largest discoveries include Mars (1989, Basins province), Thunder Horse (1999, Miocene Subsalt province), and Tiber (2009, Eocene Subsalt province).

permeability. Third, Wilcox 1A lobes have lower permeability and porosity values because of the increased presence of turbidites with linked debrites (transitional flow deposits) throughout the section, especially in the middle to outer lobes. Kane and Ponton (2012) noted that an individual transitional flow deposit is typically 1 to 10 cm thick, with some thicker amalgamated bedsets up to 3 m (10 ft); however, only the turbidite part of the sand has effective porosity and permeability. As a consequence, the potential reservoir is possibly 50%–70% of the deposit.

Cearley (2011) compared the reservoir quality of representative suprasalt Miocene and subsalt Wilcox wells, noting five significant differences. (1) Net reservoir thicknesses range from 150 ft net pay for Miocene to 700 ft net pay for Wilcox. (2) Average permeability values range from 500 (Miocene) to 15 md (Wilcox). (3) The permeability × thickness values are 75,000 and 10,500 md ft, respectively. (4) Initial subsurface pressure may be the same for both at 20,000 psi; however, once production begins, drawdown pressures are less than 1000 psi for Miocene versus greater than 3000 psi for Wilcox. (5) Finally, initial production rates for the Miocene are greater than 20,000 versus 10,000 BOPD for the Wilcox.

Upper Jurassic Reservoirs

Reservoir quality in the Upper Jurassic (Oxfordian) Norphlet eolian reservoirs in the northeastern deep-water Gulf of Mexico (Figure 10A) is also of concern for field development. Based on core analyses from three wells, Douglas (2010) identified seven lithofacies in the Norphlet, two of which form the reservoir facies—grain-flow deposits and wind ripples. Based on the depth and age of the reservoirs, diagenetic models would have suggested low effective porosity and permeability. However, the Norphlet reservoirs in the deep-water Gulf of Mexico have a unique diagenetic history where chlorite grain coats have developed authigenically around the individual sandstone grains (Douglas, 2010; Godo, in press). The presence of the chlorite inhibited the development of authigenic quartz and microquartz, both of which occlude porosity and permeability, keeping pore throats open by preventing quartz from nucleating onto sand-grain surfaces. Similar petrographic relationships have been described in the Norphlet fields both onshore and in the shallow shelf of the northern Gulf of Mexico (Ajdukiewicz et al., 2010; Taylor et al., 2010), although more chlorite is present

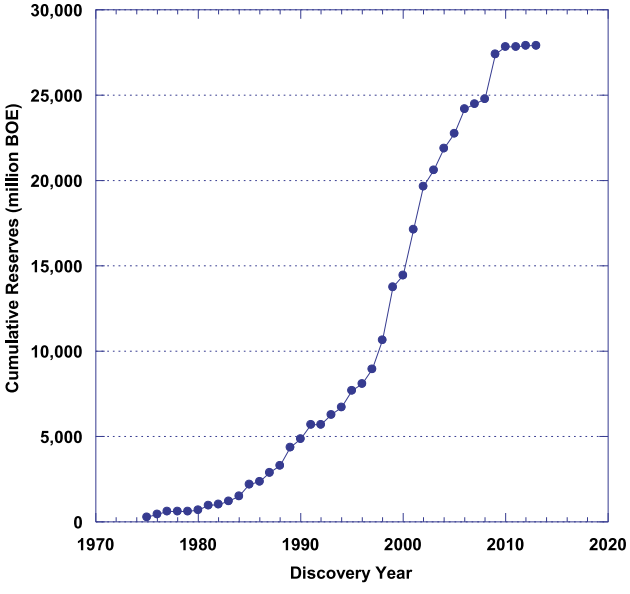

Figure 22. Graph shows the cumulative addition of reserves by year for water depths greater than 600 ft (183 ft) in the northern Gulf of Mexico.

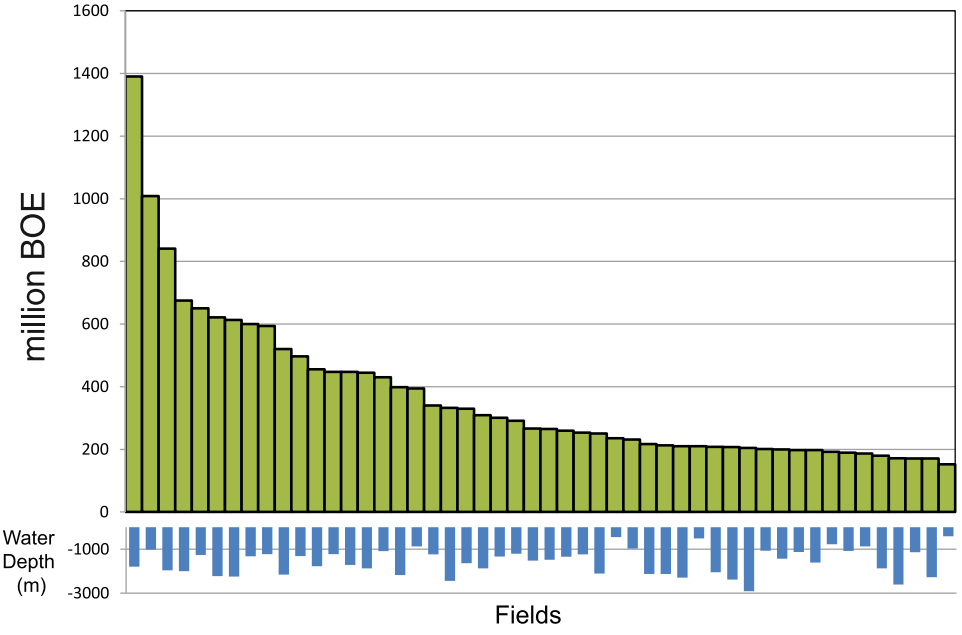

Figure 23. Graph showing the distribution of the largest 50 fields by reserves in the northern deep-water Gulf of Mexico. Lower graph shows the water depth of each discovery. Note that only 16 fields are 300 million BOE or larger. Figure is provided by IHS.

in the shallow water fields, and they consequently have lower porosity values.

STUDY AREA—THIS ISSUE

The study area for this theme issue is located in the northeastern, central, and southern Mississippi Canyon; the northern Atwater Valley; and the easternmost parts of the DeSoto Canyon and Lloyd Ridge protraction areas (Figures 1, 24). Historically, a significant part of the early petroleum exploration in the northern deep-water Gulf of Mexico occurred in this area. This area contains 86 fields and discoveries (Weimer et al., 2017d, this issue), including several of the larger fields in the northern deep-water Gulf of Mexico (Mars, Thunder Horse, Ursa, Appomattox, Thunder Horse North, Tubular Bells, Princess, Sturgis, Vicksburg).

The study area includes parts of all four of the discrete geologic-exploration provinces summarized above—Basins, Subsalt, Fold Belt (Mississippi Fan fold belt), and Abyssal Plain (Figures 5, 24). Water depths range from 437 to 2745 m (1500 to 9000 ft) (Figure 1). In the southern Mississippi Canyon and northernmost Atwater Valley protraction areas, the continental slope has a highly irregular bathymetry, caused by extensive shallow-salt deformation. Bathymetric highs are caused by shallow allochthonous salt, and the intervening low areas form the intraslope basins.

DATABASE

The database for this issue consists of a regional seismic data set, more-detailed seismic data sets, wire-line logs, and biostratigraphy. For the regional study, approximately 12,165 mi (19,550 km) of two-dimensional regional seismic data were interpreted (see figure 3 in Bouroullec and Weimer, 2017, this issue). These data are 24- and 48-fold and were collected in the 1980s. Using newer seismic data with better acquisition and processing parameters would certainly lead to a more robust interpretation, especially for the subsalt structures and Mesozoic stratigraphy. Nonetheless, we believe that the older seismic data still provide valuable insights in the evolution of the geology of the area.

Of the more than 600 wells in the area, we studied 120 exploration wells that were all straight holes. Synthetic seismograms and time-based logs were generated for all 120 wells. We also studied the biostratigraphy from 115 wells, combining data from private sources and the Minerals Management Service (now Bureau of Ocean Energy Management). The biostratigraphic data include foraminifera, calcareous nannoplankton, and high-resolution foraminifera studies. These data allowed us to establish the age dates for the sequence stratigraphic framework.

Finally, for the detailed study of the Mensa and Thunder Horse minibasins (Figure 24), we interpreted three-dimensional (3-D) seismic data, wire-line logs, and biostratigraphic data from six wells. The 3-D

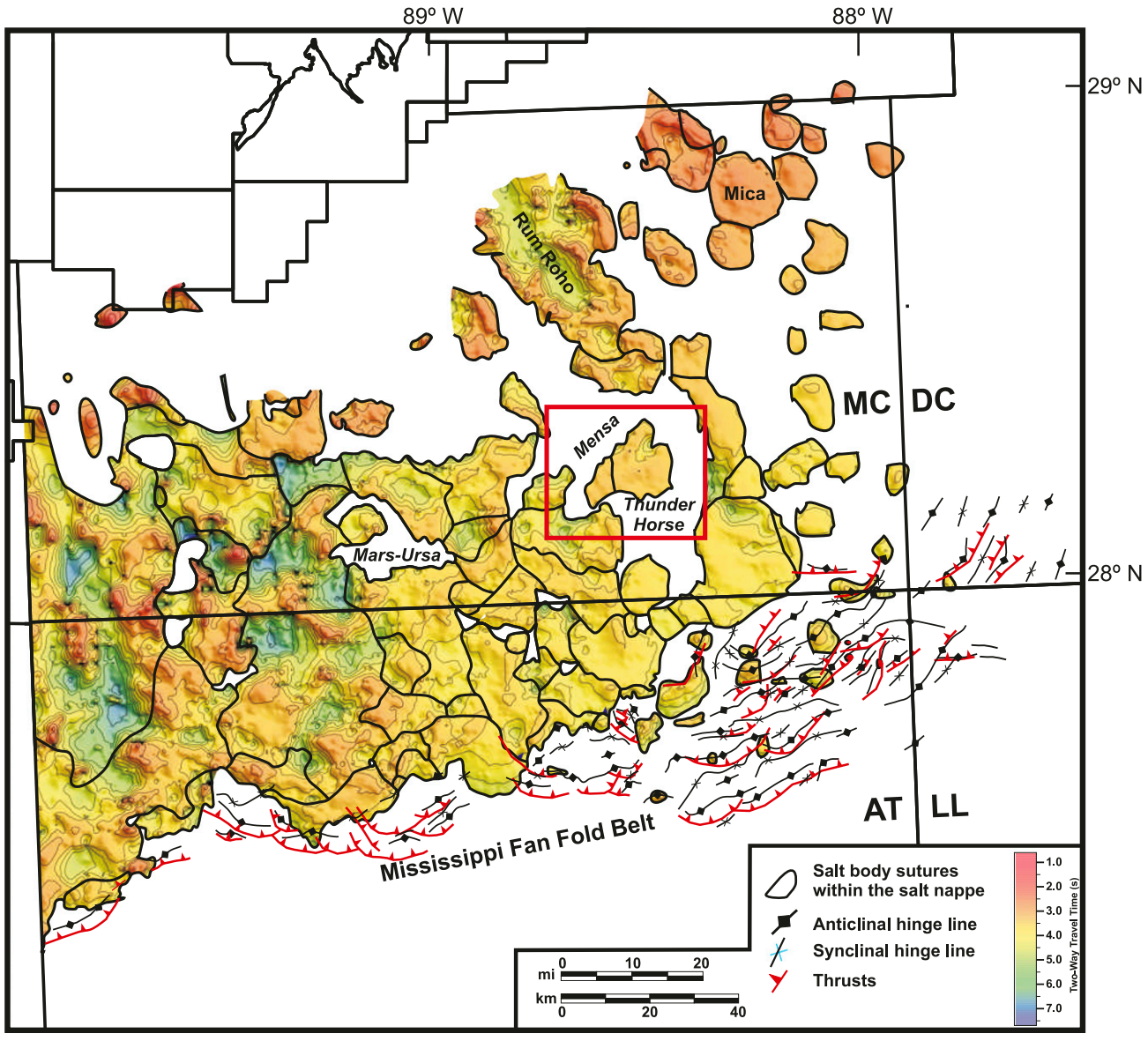

Figure 24. Map showing the outline of the study area in Mississippi Canyon (MC), northern Atwater Valley (AT), westernmost DeSoto Canyon (DC), and western Lloyd Ridge (LL) protraction areas, northern deep-water Gulf of Mexico. Top of Neogene allochthonous salt is shown in two-way traveltime. The Neogene salt consists of a large nappe (Sigsbee Escarpment) in the central and western parts of the area and isolated salt bodies or complexes in the northern, eastern, and four-corners areas. Salt sutures within the salt nappe are shown by the heavy solid line. Red (in online version) box shows the outline of the three-dimensional study area.

seismic data set consists of post-stack time-migrated, minimum-phase, 32-bit seismic data. The data set is 378 mi^2 (979 km^2) in area: 21 mi (34 km) in the east–west direction and 18 mi (29 km) in the north–south direction.

OBJECTIVES OF THESE PAPERS

The following seven papers in this *AAPG Bulletin* theme issue summarize the petroleum systems of the Mississippi Canyon and Atwater Valley protraction areas, northern deep-water Gulf of Mexico (Figures 1, 5, 24). The papers illustrate how we used integrated stratigraphic and structural studies to analyze the petroleum systems and timing of petroleum generation in the area. The latter analyses can only be evaluated once a considerable amount of regional and local geologic interpretation has been done.

Two groups of papers describe different aspects of the area. The first four papers address the

subregional setting in terms of its structural geology, linked tectonics and stratigraphic evolution, and petroleum systems.

1. Weimer et al. (2017d) document the general setting of 86 fields and discoveries, including seismic reflection expression, wire-line logs, and a brief summary of the reservoir. Fields produce from structural (four kinds of traps), combined structural-stratigraphic (three kinds of traps), and stratigraphic traps. A total of 86 fields and discoveries are evaluated: 19 comprise structures with four-way closures, 50 have three-way closures, and 17 are stratigraphic traps. Four of these discoveries are in Upper Jurassic eolian reservoirs; the remainder are in Neogene deep-water reservoirs. Importantly, the purpose of this field atlas is to provide the basis for the following three papers, such that the origins of the fields can be described in terms of the timing of development of their traps, reservoirs, seals, and charging.
2. Bouroullec and Weimer (2017) document the complexity of the regional structural setting. A complex, multilayer allochthonous salt system is present with three periods of shallow-salt emplacement (Barremian, late Cretaceous, and middle Miocene to present). Four kinds of salt systems are present: basement controlled, stepped counterregional, roho, and fold-belt related. A detailed study of the Neogene allochthonous salt systems is used to build conceptual kinematic models.
3. Bouroullec et al. (2017b) describe the structural evolution of the study area, which consists of a complex geological history influenced by basement structures, multiple stages of salt movement, gravitational gliding, and strike-slip movements. Basement structures were the primary control on early salt kinematics, affecting gravity-driven slope deformation and resulting in a wide variety of structural styles. Salt from the autochthonous and two Cretaceous allochthonous salt layers was expelled vertically and basinward during the Neogene, feeding the younger allochthonous salt systems. The autochthonous and early allochthonous salt layers were used as detachments for many of the large Neogene extensional structures (growth faults and turtles) and contractional structures (anticlines and thrust faults), whereas the Neogene allochthonous salt system accommodated suprasalt minibasins associated with counterregional and roho salt systems. These three allochthonous salt layers were successively loaded by gravity-flow sediments, resulting in the formation of deep (above autochthonous or early allochthonous salt layers) and shallow (supra-Neogene allochthonous salt) minibasins and local development of extensive salt welds. Northwest–southeast-oriented strike-slip structures, active during the Neogene, are present in the salt province within the study area. They are related to basin-wide heterogeneities in the original and subsequent salt distribution and are controlled by differential basinward movements of adjacent suprasalt minibasins.
4. Bouroullec et al. (2017a) analyze the tectono-stratigraphic evolution of the area at 11 discrete intervals between 24 Ma and present. Four external stratigraphic forms—troughs, bowls, wedges, and sheets—are identified and integrated with the results of the structural study to understand the changing shape of suprasalt basins during the Neogene. The analyses show how the allochthonous salt systems evolved over time and how they affected sedimentation patterns and the evolution of the individual basins.

   Most of the fields in the study area are contained within sheetlike or wedge-shaped stratigraphic intervals and have four-way or three-way trapping configurations. These findings indicate the profound effect of mobile salt on the petroleum geology of the region.

The final three papers describe the geology and evolution of the Mensa and Thunder Horse fields in adjacent minibasins. The fields are significant because Thunder Horse and Mensa are two of the largest oil and gas fields, respectively, in the northern deep-water Gulf of Mexico.

First, Weimer et al. (2017a) summarize the stratigraphic evolution of the middle to late Miocene in the two basins. The Thunder Horse reservoir sands were deposited in amalgamated sheet and amalgamated channel-fill units within a major paleobathymetric low. Later turtle formation created the trap for the field and a paleobathymetric high. Channelized sands were diverted around and deposited on the flanks of the turtle. At 9.0 Ma, Mensa's sheet-sand reservoir represents a different setting; sands were deposited near the

crest of the Mensa turtle, which had subtle bathymetric expression.

Second, Weimer et al. (2017b) document the linked structural evolution of the two basins from the Early Cretaceous through the late Miocene. Structural features and associated minibasins evolved during several discrete intervals. From 99 to 24 Ma (latest Early Cretaceous through latest Oligocene), an extensive allochthonous salt canopy was present within the Mensa and Thunder Horse minibasins. During this interval, sediments loaded the salt, forming thin wedge- and sheet-form deposits in the Mensa area and a thick, northwest-trending trough in the Thunder Horse area. A secondary allochthonous salt system extruded at the Top Cretaceous level, as evinced by remnant salt bodies. Salt withdrawal from these allochthonous salt systems provided accommodation for bowl- and trough-shaped external stratigraphic forms during the Miocene. High sedimentation rates produced salt evacuation from these allochthonous salt systems and initiated diapirism that formed the Neogene allochthonous salt level. The prominent turtle structures in the two minibasins, critical to the formation of traps to the two major fields, developed at slightly different times: Thunder Horse at 14.35 and Mensa at 11.4 Ma.

Finally, Weimer et al. (2017c) analyze the petroleum systems to explain the distribution of fluids in the Mensa (gas) and Thunder Horse (oil) fields. They conclude that the original allochthonous salt underlying the Mensa minibasin was thicker than in the Thunder Horse area, providing more accommodation for sediments to accumulate. Consequently, the Thunder Horse turtle structure formed 1–2 m.y. before the Mensa structure, and source rocks matured earlier. Today, the source rocks below Mensa are in the dry-gas window, whereas the source rocks underlying Thunder Horse are in the wet-gas generation window.

In summary, these eight papers allow the reader the opportunity to view and analyze different aspects of the petroleum systems of one important part of a deep-water basin in the northern deep-water Gulf of Mexico. Although each paper can be read separately, we suggest that they be read in the order of presentation to follow the petroleum systems logic. Our hope is that these papers can be used as an analog for many other deep-water basins in the world.

REFERENCES CITED

Ajdukiewicz, J. M., P. H. Nicholson, and W. L. Esch, 2010, Prediction of deep reservoir quality using early diagenetic process models in the Jurassic Norphlet Formation, Gulf of Mexico: AAPG Bulletin, v. 94, no. 8, p. 1189–1227, doi:10.1306/04211009152.

Beaubouef, B., 2015, Gulf E&P remains active despite falling oil prices: Offshore Magazine, accessed October 26, 2016, http://www.offshore-mag.com/1/volume-75/issue-1/gom/gulf-e-p/gulf-e-p-remains-active-despite-falling-oil-prices-full.html.

Bouroullec, R., and P. Weimer, 2017, Geometry and kinematics of Neogene allochthonous salt systems in the Mississippi Canyon, Atwater Valley, western Lloyd Ridge, and western DeSoto Canyon protraction areas, northern deep-water Gulf of Mexico: AAPG Bulletin, v. 101, no. 7, p. 1003–1034, doi:10.1306/09011609186.

Bouroullec, R., P. Weimer, and O. Serrano, 2004, Salt tectonic history of the northeastern deep Gulf of Mexico: Gulf Coast Association of Geological Societies Transactions, v. 54, p. 63–80.

Bouroullec, R., P. Weimer, and O. Serrano, 2017a, Petroleum geology of the Mississippi Canyon, Atwater Valley, western DeSoto Canyon, and western Lloyd Ridge protraction areas, northern deep-water Gulf of Mexico: Traps, reservoirs, and tectono-stratigraphic evolution: AAPG Bulletin, v. 101, no. 7, p. 1073–1108, doi:10.1306/09011610093.

Bouroullec, R., P. Weimer, and O. Serrano, 2017b, Regional structural setting and evolution of the Mississippi Canyon, Atwater Valley, western Lloyd Ridge, and western DeSoto Canyon protraction areas, northern deep-water Gulf of Mexico: AAPG Bulletin, v. 101, no. 7, p. 1035–1071, doi:10.1306/09011609187.

Camerlo, R. H., and E. F. Benson, 2006, Geometric and seismic interpretation of the Perdido fold belt: Northwestern deep-water Gulf of Mexico: AAPG Bulletin, v. 90, no. 3, p. 363–386, doi:10.1306/10120505003.

Cearley, J., 2011, The discovery of the lower Tertiary trend in the deepwater Gulf of Mexico: Discovery thinking talk, AAPG Annual Convention and Exhibition, accessed May 2, 2017, http://www.aapg.org/videos/discovery-thinking/articleid/37031/james-cearley-the-discovery-of-the-lower-tertiary-trend-in-the-deepwater-gulf-of-mexico.

Cole, G. A., A. Yu, F. Peel, J. DeVay, B. Bernard, J. Zumberge, and S. Brown, 2001a, Constraining source and charge risk in deepwater areas: World Oil, v. 2001, no. 10, p. 69–77.

Cole, G. A., A. Yu, F. Peel, C. H. Taylor, R. Requejo, J. DeVay, J. Brooks, B. Bernard, J. Zumberge, and S. Brown, 2001b, The deep water Gulf of Mexico petroleum system: Insights from piston coring, defining seepage, anomalies, and background, *in* R. H. Fillon, N. C. Rosen, P. Weimer, A. Lowrie, H. Pettingill, R. L. Phair, H. H. Roberts, and B. van Hoorn, eds., Petroleum systems of deep-water basins: Global and Gulf of Mexico experience: Gulf Coast Section SEPM Foundation 21st Annual Bob F.

Perkins Research Conference, Houston, Texas, December 2–5, 2001, p. 315–342, doi:10.5724/gcs.01.21.0315.

Colling, E. L., R. J. Alexander, and R. L. Phair, 2001, Regional mapping and maturity modeling for the northern deep water Gulf of Mexico, *in* R. H. Fillon, N. C. Rosen, P. Weimer, A. Lowrie, H. Pettingill, R. L. Phair, H. H. Roberts, and B. van Hoorn, eds., Petroleum systems of deep-water basins: Global and Gulf of Mexico experience: Gulf Coast Section SEPM Foundation 21st Annual Bob F. Perkins Research Conference, Houston, Texas, December 2–5, 2001, p. 87–110, doi:10.5724/gcs.01.21.0087.

Colmenares, M., 2014, The Perdido and the southwestern Gulf of Mexico: AAPG Search and Discovery article 30331, accessed October 26, 2016, http://www.searchanddiscovery.com/documents/2014/30331colmenares/ndx_colmenares.pdf.

Day-Stirrat, R. J., P. B. Flemings, Y. You, A. C. Aplin, and B. A. van der Pluijm, 2012, The fabric of consolidation in Gulf of Mexico mudstones: Marine Geology, v. 295–298, p. 77–85, doi:10.1016/j.margeo.2011.12.003.

Denne, R. A., E. Scott, D. Eickhoff, J. Kaiser, R. J. Hill, and J. M. Spaw, 2013, Massive Cretaceous-Paleogene boundary deposit, deep-water Gulf of Mexico: New evidence for widespread Chicxulub-induced slope failure: Geology, v. 41, p. 983–986, doi:10.1130/G34503.1.

Douglas, S. W., 2010, The Jurassic Norphlet Formation of the deepwater eastern Gulf of Mexico: A sedimentologic investigation of eolian facies, their reservoir characteristics, and their depositional history, master's thesis, Baylor University, Waco, Texas, 59 p.

Eikrem, V., R. Li, M. Medeiros, B. J. McKee, E. E. Shumilak, B. L. Boswell, and R. Mohan, 2010, Perdido development project: Great White WM12 Reservoir and Silvertip M. Frio Field, development plans and comparison of recent well results with pre-drill models: Offshore Technology Conference, Houston, Texas, May 3–6, 2010, 10 p.

Galloway, W. E., 2008, Depositional evolution of the Gulf of Mexico sedimentary basin, *in* A. D. Miall, ed., The sedimentary basins of the United States and Canada: Sedimentary Basins of the World 5, p. 505–549.

Galloway, W. E., P. E. Ganey-Curry, X. Li, and R. T. Buffler, 2000, Cenozoic depositional history of the Gulf of Mexico basin: AAPG Bulletin, v. 84, no. 11, p. 1743–1774.

Galloway, W. E., T. L. Whiteaker, and P. E. Ganey-Curry, 2011, History of Cenozoic North American drainage basin evolution, sediment yield, and accumulation in the Gulf of Mexico basin: Geosphere, v. 7, p. 938–973, doi:10.1130/GES00647.1.

Gibson, R., 2012, A methodology to incorporate salt evolution in three-dimensional basin models: Application to regional modeling of the Gulf of Mexico, *in* K. E. Peters, D. J. Curry, and M. Kacewicz, eds., Basin modeling: New horizons in research and applications: AAPG Hedberg Series 4, p. 103–118.

Godo, T., in press, The Appomattox Field Norphlet eolian sand dune reservoirs in the deep water Gulf of Mexico, *in* R. Merrill and C. Sternbach, eds., Giant oil fields of the decade 2000–2010: AAPG Memoir 113, doi:10.1306/13572000M1133680.

Godo, T. J., E. Chuparova, and D. E. McKinney, 2011, Norphlet eolian sand fairway established in the deep water Gulf of Mexico (abs.): AAPG Annual Convention and Exhibition, Houston, Texas, April 10–13, 2011, accessed October 26, 2016, http://www.searchanddiscovery.com/abstracts/html/2011/annual/abstracts/Godo.html.

Hood, K. C., L. M. Wenger, O. P. Gross, and S. C. Harrison, 2002, Hydrocarbon systems analysis of the northern Gulf of Mexico: Delineation of hydrocarbon migration pathways using seeps and seismic imaging, *in* D. Schumacher and L. A. LeSchack, eds., Application of geochemistry, magnetics and remoter sensing: AAPG Studies in Geology 48, p. 25–40.

Horn, B., 2011, Identifying new exploration fairways in the Gulf of Mexico: Deepwater Tuscaloosa/Woodbine play: Gulf Coast Association of Geological Societies Transactions, v. 61, p. 245–256.

Hudec, M. R., M. P. A. Jackson, and F. J. Peel, 2013, Influence of deep Louann structure on the evolution of the northern Gulf of Mexico: AAPG Bulletin, v. 97, no. 10, p. 1711–1735, doi:10.1306/04011312074.

Jacques, J. M., and H. Clegg, 2002, Late Jurassic source rock distribution and quality in the Gulf of Mexico: Inferences from plate tectonic modeling: Gulf Coast Association of Geological Societies Transactions, v. 52, p. 429–440.

Kane, I. A., and A. S. M. Ponton, 2012, Submarine and transitional flow deposits in the Paleogene Gulf of Mexico: Geology, v. 40, p. 1119–1122, doi:10.1130/G33410.1.

Lewis, J., S. Clinch, D. Meyer, M. Richards, C. Skirius, R. Stokes, and L. Zarra, 2007, Exploration and appraisal challenges in the Gulf of Mexico deep-water Wilcox: Part I—Exploration overview, reservoir quality, and seismic imaging, *in* L. Kennan, J. Pindell, and N. C. Rosen, eds., The Paleogene of the Gulf of Mexico and Caribbean Basins: Processes, events, and petroleum systems: Gulf Coast Section SEPM Foundation Bob F. Perkins 27th Annual Research Conference, Houston, Texas, December 2–5, 2007, p. 398–414, doi:10.5724/gcs.07.27.0398.

Magoon, L. B., T. L. Huston, and H. E. Cook, 2001, Pimenta-Tamabra(!)—A giant supercharged petroleum system in the southern Gulf of Mexico, onshore and offshore Mexico, *in* C. Bartolini, R. T. Buffler, and A. Cantu-Chapa, eds., The western Gulf of Mexico basin: Tectonics, sedimentary basins, and petroleum systems: AAPG Memoir 75, p. 83–125.

Mander, J., J. d'Ablaing, J. Howie, K. Wells, R. Ramazanova, D. Shepherd, and C. Lee, 2012, 21st century Atlantis—Incremental knowledge from a staged-approach to development, illustrated by a complex deep-water field, *in* N. Rosen, P. Weimer, S. M. Coutes dos Anjos, S. Henrickson, E. Marques, M. Mayall, R. Fillon, et al., eds., New understanding of the petroleum systems of continental margins of the world: 32nd Annual Gulf Coast Section SEPM Foundation Bob F. Perkins Research Conference, Houston, Texas, December 2–5, 2012, p. 65–95, doi:10.5724/gcs.12.32.0065.

Marchand, A. M. E., G. Apps, W. Li, and J. R. Rozien, 2015, Depositional processes and impact on reservoir quality in

deepwater Paleogene reservoirs, US Gulf of Mexico: AAPG Bulletin, v. 99, no. 9, p. 1635–1648, doi:10.1306/04091514189.

McBride, B. C., M. G. Rowan, and P. Weimer, 1998a, The evolution of allochthonous salt systems, northern Green Canyon and Ewing Bank (offshore Louisiana), northern Gulf of Mexico: AAPG Bulletin, v. 82, no. 5B, p. 1013–1036.

McBride, B. C., P. Weimer, and M. G. Rowan, 1998b, The effect of allochthonous salt on the petroleum systems of northern Green Canyon and Ewing Bank (offshore Louisiana), northern Gulf of Mexico: AAPG Bulletin, v. 82, no. 5B, p. 1083–1121.

Meckel, L. D. III, G. A. Ugueto, D. H. Lynch, B. M. Hewett, E. J. Bocage, C. D. Winker, and B. J. O'Neill, 2002, Genetic stratigraphy, stratigraphic architecture, and reservoir stacking patterns of the upper Miocene–lower Pliocene Greater Mars-Ursa intraslope basins, Mississippi Canyon, Gulf of Mexico, *in* J. M. Armentrout, ed., Sequence stratigraphic models for exploration and production: Gulf Coast Section SEPM Foundation Bob F. Perkins 22nd Annual Research Conference, Houston, Texas, December 8–11, 2002, p. 113–147, doi:10.5724/gcs.02.22.0113.

Mitra, S., J. A. Duran Gonzalez, J. G. Hernandez, S. H. Garcia, and S. Banerjeee, 2006, Structural geometry and evolution of the Ku, Zaap, and Maloob structures, Campeche Bay, Mexico: AAPG Bulletin, v. 90, no. 10, p. 1565–1584, doi:10.1306/04240605101.

Moore, M. G., G. M. Apps, and F. J. Peel, 2001, The petroleum systems of the western Atwater Foldbelt in the ultra deep water Gulf of Mexico, *in* R. H. Fillon, N. C. Rosen, P. Weimer, A. Lowrie, H. W. Pettingill, R. L. Phair, H. H. Roberts, and B. van Hoorn, eds., Petroleum systems of deep-water basins: Global and Gulf of Mexico experience: Gulf Coast Section SEPM Foundation 21st Annual Bob F. Perkins Research Conference, Houston, Texas, December 2–5, 2001, p. 369–380, doi:10.5724/gcs.01.21.0369.

Morris, P. L., and P. Weimer, 2004a, Structural geology of the Mississippi Fan Foldbelt, northern deep-water Gulf of Mexico, Part 1: Geometry and restorations: Gulf Coast Association of Geological Societies Transactions, v. 54, p. 461–481.

Morris, P. L., and P. Weimer, 2004b, Structural geology of the Mississippi Fan Foldbelt, northern deep-water Gulf of Mexico, Part 2: Growth history and evolution: Gulf Coast Association of Geological Societies Transactions, v. 54, p. 483–501.

Mount, V., K. Dull, and S. Mentemeier, 2007, Structural style and evolution in the Paleogene play, deepwater Gulf of Mexico, *in* L. Kennan, J. Pindell, and N. C. Rosen, eds., The Paleogene of the Gulf of Mexico and Caribbean Basins: Processes, events, and petroleum systems: Gulf Coast Section SEPM Foundation Bob F. Perkins 27th Annual Research Conference, Houston, Texas, December 2–5, 2007, p. 54–80, doi:10.5724/gcs.07.27.0054.

Mount, V. S., A. Rodriguez, A. Chauoche, S. G. Crews, P. Gamwell, and P. Montoya, 2006, Petroleum system observations and interpretation in the vicinity of the K2/K2North, Genghis Khan, and Marco Polo fields, Green Canyon, Gulf of Mexico: Gulf Coast Association of Geological Societies Transactions, v. 56, p. 613–625.

Offshore Technology, 2015, Cascade and Chinook subsea development, Gulf of Mexico, United States of America, accessed October 26, 2016, http://www.offshore-technology.com/projects/cascadechinook/.

Pilcher, R. S., B. Kilsdonk, and J. Trude, 2011, Primary basins and their boundaries in the deep-water Gulf of Mexico: Origin, trap type, and petroleum system implications: AAPG Bulletin, v. 95, no. 2, p. 219–240, doi:10.1306/06301010004.

Pilcher, R. S., R. T. Murphy, and J. M. Ciosek, 2014, Jurassic raft tectonics in the northeastern Gulf of Mexico: Interpretation, v. 2, p. SM39–SM55.

Post, P., P. F. Harrison, G. H. Whittle, and J. D. Hunt, 2001, Mesozoic ultra-deep water potential of the U.S. Gulf of Mexico—Conceptual play development and analysis, *in* R. H. Fillon, N. C. Rosen, P. Weimer, A. Lowrie, H. W. Pettingill, R. L. Phair, H. H. Roberts, and B. van Hoorn, eds., Petroleum systems of deep-water basins: Global and Gulf of Mexico experience: Gulf Coast Section SEPM Foundation 21st Annual Bob F. Perkins Research Conference, Houston, Texas, December 2–5, 2001, p. 35–68, doi:10.5724/gcs.01.21.0035.

Radovich, B. J., C. D. Connors, and J. Moon, 2007, Deep imaging of the Paleogene, Miocene structure and stratigraphy of the western Gulf of Mexico using 2D prestack depth migration of mega-regional onshore to deep water, long-offset seismic data, *in* L. Kennan, J. Pindell, and N. C. Rosen, eds., The Paleogene of the Gulf of Mexico and Caribbean Basins: Processes, events, and petroleum systems: Gulf Coast Section SEPM Foundation Bob F. Perkins 27th Annual Research Conference, Houston, Texas, December 2–5, 2007, p. 307–322, doi:10.5724/gcs.07.27.0307.

Ricoy, V., 2005, 3D seismic characterization of the Cantarell Field, Campeche Basin, Mexico, Ph.D. dissertation, Cardiff University, Cardiff, United Kingdom, 418 p.

Rojas, P., 2015, The road to Shell's Appomattox discovery (abs.): Gulf Coast Association of Geological Societies and Gulf Coast Section of SEPM 65th Annual Convention, Houston, Texas, September 20–22, 2015, accessed October 26, 2016, http://www.searchanddiscovery.com/abstracts/html/2015/90219gcags/abstracts/139.html.

Sanford, J. C., 2015, The Cretaceous-Paleogene boundary deposit in the Gulf of Mexico: Oceanic response to the Chicxulub impact, master's thesis, The University of Texas at Austin, Austin, Texas, 130 p.

Scott, E., R. Denne, J. Kaiser, and D. Eickhoff, 2012, Immediate and postevent effects of the K/Pg boundary, Chicxulub impact on the northern Gulf of Mexico, *in* N. Rosen, P. Weimer, S. M. Coutes dos Anjos, S. Henrickson, E. Marques, M. Mayall and R. Fillon, et al., eds., New understanding of the petroleum systems of continental margins of the world: 32nd Annual Gulf Coast Section SEPM Foundation Bob F. Perkins

Research Conference, Houston, Texas, December 2–5, 2012, p. 96–109, doi:10.5724/gcs.12.32.0096.

Scott, E., R. Denne, J. Kaiser, and D. Eickhoff, 2014, Impact on sedimentation into the north-central deepwater Gulf of Mexico as a result of the Chicxulub event: Gulf Coast Association of Geological Societies Journal, v. 3, p. 41–50.

Story, C., 1998, Norphlet geology and 3-D geophysics of Fairway Field Mobile Bay, Alabama, *in* J. L. Allen, T. S. Brown, C. J. John, and C. F. Lobo, eds., 3-D seismic case histories from the Gulf Coast Basin: Gulf Coast Association of Geological Societies Special Publication, p. 123–129.

Stover, S. C., S. Ge, P. Weimer, and B. C. McBride, 2001, The effects of salt evolution, structural development, and fault propagation on Cenozoic oil migration: A two-dimensional fluid flow study along a mega-regional transect in the northern Gulf of Mexico: AAPG Bulletin, v. 85, no. 11, p. 1945–1966.

Sullivan, M., J. Clark, B. Power, T. Dunn, A. Fildani, J. Couvault, L. Zarra, and B. Carson, 2014, Relationship between reservoir quality, facies, and depositional environment: Working towards predictive model for the deepwater Wilcox (abs.): AAPG Annual Convention and Exhibition, Houston, Texas, April 6–9, 2014, accessed October 26, 2016, http://www.searchanddiscovery.com/abstracts/html/2014/90189ace/abstracts/1837768.html.

Taylor, T. R., M. R. Giles, L. A. Haton, T. N. Diggs, N. R. Braunsdorf, G. V. Birbiglia, M. Kittridge, C. I. Macaulay, and I. S. Espejo, 2010, Sandstone diagenesis and reservoir quality prediction: Models, myth, and reality: AAPG Bulletin, v. 94, no. 8, p. 1093–1132, doi:10.1306/04211009123.

Teerman, S. C., R. W. Howe, R. Hwang, and R. Lytton, 2010, A deepwater Gulf of Mexico source rock penetration: Applications to Mesozoic source rocks an depositional systems (abs.): AAPG Annual Convention and Exhibition, New Orleans, Louisiana, April 11–14, 2010, accessed October 26, 2016, http://www.searchanddiscovery.com/pdfz/abstracts/pdf/2010/annual/abstracts/ndx_teerman.pdf.html.

Trudgill, B. D., M. G. Rowan, J. C. Fiduk, P. Weimer, P. E. Gale, B. E. Korn, R. L. Phair et al., 1999, The Perdido Foldbelt: Northwestern deep-water Gulf of Mexico: Part 1: Structural geology, evolution, and regional implications: AAPG Bulletin, v. 83, no. 1, p. 88–113.

Walker, C., P. Belvedere, J. Petersen, S. Warrior, and A. Cunningham, 2012, Straining at the leash: Understanding the full potential of the deep water, sub-salt Mad Dog field from appraisal through early production, *in* N. Rosen, P. Weimer, S. M. Coutes dos Anjos, S. Henrickson, E. Marques, M. Mayall and R. Fillon, et al., eds., New understanding of the petroleum systems of continental margins of the world: 32nd Annual Gulf Coast Section SEPM Foundation Bob F. Perkins Research Conference, Houston, Texas, December 2–5, 2012, p. 25–64, doi:10.5724/gcs.12.32.0025.

Weimer, P., R. Bouroullec, T. G. Lapinski, A. A. van den Berg, R. Cepeda, J. G. Roesink, and M. Leibovitz, 2017a, Sequence stratigraphic evolution of the Mensa and Thunder Horse intraslope basins, northern deep-water Gulf of Mexico—Lower Cretaceous through upper Miocene (8.2 Ma): A case study: AAPG Bulletin, v. 101, no. 7, p. 1109–1143, doi:10.1306/09011608160.

Weimer, P., R. Bouroullec, and G. Tari, 2006, Petroleum traps in deepwater settings, *in* P. Weimer, R. Slatt, R. Bouroullec, R. Fillon, H. Pettingill, M. Pranter, and G. Tari, eds., Introduction to the petroleum geology of deepwater settings: AAPG Studies in Geology 57, p. 15-1–15-90.

Weimer, P., R. Bouroullec, A. A. van den Berg, T. G. Lapinski, J. G. Roesink, and J. Adson, 2017b, Structural setting and evolution of the Mensa and Thunder Horse intraslope basins, northern deep-water Gulf of Mexico: A case study: AAPG Bulletin, v. 101, no. 7, p. 1145–1172, doi:10.1306/09011609112.

Weimer, P., R. Denne, E. Zimmerman, S. Cumella, W. Gutterman, T. Payeur, B. Snyder, H. Hirsh, and D. Bettinger, 2016a, Variations in borehole log expression of the KPg boundary Chicxulub deposit, northern deep-water Gulf of Mexico: Preliminary results: Gulf Coast Association of Geological Societies Transactions, v. 66, p. 583–600.

Weimer, P., R. Denne, E. Zimmerman, S. Cumella, B. Snyder, H. Hirsh, D. Bettinger, W. Gutterman, and T. Payeur, 2016b, Litho- and biostratigraphic evolution of the Upper Jurassic through top Cretaceous section, northern deep-water Gulf of Mexico: Preliminary results: Gulf Coast Association of Geological Societies Transactions, v. 66, p. 569–582.

Weimer, P., V. Matt, R. Bouroullec, A. A. van den Berg, T. G. Lapinski, J. G. Roesink, and J. Adson, 2017c, Three-dimensional petroleum systems modeling of the Mensa and Thunder Horse intraslope basins, northern deep-water Gulf of Mexico: A case study: AAPG Bulletin, v. 101, no. 7, p. 1173–1201, doi:10.1306/09011608153.

Weimer, P., and H. W. Pettingill, 2007, Deep-water exploration and production: A global overview, *in* T. Nilsen, R. D. Shew, G. S. Steffens, and J. Studlick, eds., Atlas of deep-water outcrops of the world: AAPG Studies in Geology 56, 29 p.

Weimer, P., E. Zimmerman, H. Hersh, B. Snyder, M. Leibovitz, K. Schwendeman, B. Hankins et al., 2017d, Atlas of fields and discoveries, central Mississippi Canyon, Atwater Valley, northwestern Lloyd Ridge, and western DeSoto Canyon protraction areas, northern deep-water Gulf of Mexico: AAPG Bulletin, v. 101, no. 7, p. 995–1002, doi:10.1306/bltnfieldatlas070815.

Wenger, L. M., L. R. Goodoff, O. P. Gross, S. C. Harrison, and K. C. Hood, 1994, Northern Gulf of Mexico: An integrated approach to source, maturation, and migration, *in* N. Scheidermann, P. Cruz, and R. Sanchez, eds., Geologic aspects of petroleum systems: First Joint AAPG/Asociación Mexicana de Geólogos Petroleros Hedberg Research Conference, Mexico City, Mexico, October 2–6, 1994, 5 p.

Worrall, D. M., M. W. Bourque, and D. R. Steele, 2001, Exploration in deep water basins…where next? *in* R. H. Fillon, N. C. Rosen, P. Weimer, A. Lowrie, H. W. Pettingill, R. L. Phair, H. H. Roberts, and B. van Hoorn, eds., Petroleum systems of deep-water basins: Global and Gulf of Mexico experience: Gulf Coast Section SEPM Foundation Bob F. Perkins 21st Annual Research Conference, Houston, Texas, December 2–5, 2001, p. 273, doi:10.5724/gcs.01.21.0273.

Yen, T., 2016, Oil production in federal Gulf of Mexico projected to reach record high in 2017, accessed October 25, 2016, http://www.eia.gov/todayinenergy/detail.php?id=25012.

Zarra, L., 2007a, Chronostratigraphic framework for the Wilcox Formation (upper Paleocene–lower Eocene) in the deep-water Gulf of Mexico: Biostratigraphy, sequences, and depositional systems, *in* L. Kennan, J. Pindell, and N. C. Rosen, eds., The Paleogene of the Gulf of Mexico and Caribbean Basins: Processes, events, and petroleum systems: Gulf Coast Section SEPM Foundation Bob F. Perkins 27th Annual Research Conference, Houston, Texas, December 2–5, 2007, p. 81–141, doi:10.5724/gcs.07.27.0081.

Zarra, L., 2007b, Oligocene stratigraphy and depositional systems on the deepwater Gulf of Mexico (abs.): AAPG Annual Convention and Exhibition, Long Beach, California, April 1–4, 2007, accessed October 26, 2016, http://www.searchanddiscovery.com/abstracts/html/2007/annual/abstracts/lbZarra.htm.

Deeper Waters: How Science and Technology Pushed Exploration to Greater Depths*

Paul Weimer[1]

Search and Discovery Article #70315 (2018)**
Posted January 22, 2018

*Adapted from article, by the same author with the same title, in THE AAPG EXPLORER, Historical Highlights, January 2017.
**AAPG © 2018. This adaptation is with permission of *THE AAPG EXPLORER*, Brian Ervin, Managing Editor.

[1]University of Colorado, Boulder (paul.weimer@colorado.edu)

Introduction

Today, there are 31 sedimentary basins worldwide that produce or have economic discoveries in deepwater, in terms of both modern water depths and reservoir type (Figure 1). Exploration wells have now been drilled in water depths up to 11,155 feet (Pelotas Basin, Uruguay) (Figures 2 and 3), and the deepest offshore production at present is 9656 feet (northern Gulf of Mexico).

We all know successful deepwater production has profound economic impact. Sometimes, however, it is difficult to grasp how profound the economic impacts are. To get an idea, consider that the total gross income collected by the U.S. federal government from offshore oil and gas resources averaged $8 billion per year from 2005 to 2014, according to the Congressional Budget Office. That is compared to $3 billion from onshore resources for the same period.

How did our industry move into deepwater provinces in the past seven decades? What were the drivers behind this multibillion-dollar investment of resources?

The global story of deepwater petroleum exploration is not one that has a great deal of intrigue, like the Teapot Dome scandal or other early (mis)adventures in petroleum geology. Likewise, our story never had a master plan. Rather, this is a tale of gradual evolution – one in which the role of technology and science are inextricably linked to the economic need to discover new resources for an expanding global population.

New Technology and Science

The desire to explore in greater water depths required new seismic technology to accurately image the subsurface, new scientific disciplines to analyze the geology and geophysics, and new technology to drill and develop resources.

For example, with the development of common-depth-point seismic and digital recording in the mid-1960s, vast amounts of 2-D marine seismic information began to be collected. The continued improvement in acquisition, in terms of streamer design, allowed for improved

subsurface imaging. This new information, in turn, presented new kinds of geology that had not been imaged before. The fields of seismic and sequence stratigraphy evolved from evaluation of these data, heavily influenced by early exploration of the North Sea and other basins. Meanwhile, the recognition of geophysical "bright spots" on seismic reflection data was critical to exploration success in deepwater, and it became one of the technical drivers in moving into progressively deeper-water frontier provinces for drilling.

Finally, the development of innovative drilling technology and production techniques were also essential to making deepwater economical.

Defining Terms

Like many geologic disciplines, there is a tremendous amount of jargon for deepwater. So let's define two terms. First, let's use the term "turbidite" to refer informally to any sedimentary gravity flow deposit regardless of water depth for deposition. Second, "deepwater" has two definitions. The geologic definition refers to water depths where sediment gravity flows tend to dominate, which generally means greater than 300 meters (although lakes are the exception). The engineering definition considers deepwater to be where fixed platforms can no longer be used for development. Instead, some sort of floating development structure is required; typically this is greater than 1500-feet water depth. I will use the second definition throughout this article.

Pioneers in Sedimentology

The important first step in deepwater exploration was the recognition that turbidite reservoirs exist. Ironically, some of the first oil fields discovered in the world were in turbidite reservoirs. Some of the reservoirs discovered in western Pennsylvania were likely in Devonian turbidities. Many of the giant fields in California discovered in the late 1890s and early 20th century had turbidite reservoirs. Examples include the southern San Joaquin, Los Angeles and Ventura basins. In 1930, Royal Dutch Shell discovered the supergiant Poza Rica field in onshore Mexico. The field produces from primarily Lower Cretaceous base-of-slope carbonate debrites and some turbidites. The Poza Rica field has the largest stratigraphic trap in conventional deepwater deposits.

However, in all of these examples, it was not until the late 1940s and '50s that the correct depositional setting of the reservoirs was recognized. Select companies began to realize that many of their fields in fact had deepwater turbidite reservoirs.

Manley Natland (Figure 4) did pioneering work in the early 1930s in several southern California basins. From modern marine studies, he recognized that the deepwater benthic foraminifers living in offshore basins in the Los Angeles area were also found in the shales encasing the coarser-grained sands and conglomerates in the nearby Plio-Pleistocene reservoirs and outcrops of the Ventura basin. Natland was so intrigued by these processes that he altered the bottom of his swimming pool to create ridges to simulate the effects of irregular bathymetry of the Neogene Los Angeles Basin, and then poured sand and mud into the pool to generate turbidity currents. (His son Martin confirmed this story in July, 2016.)

European sedimentologists Phillip Kuenen, Carlo Migliorini and their students also did pioneering deepwater research at the same general time. Their seminal work in outcrops and flume tanks began to gain acceptance in the late 1940s and '50s. By the 1960s, critical outcrop studies by

Arnold Bouma, Emiliano Mutti and Franco Ricci-Lucci (Figure 5) led to the development of facies classifications that were essential for the correct depositional interpretation of deepwater reservoirs. Later work in the 1970s by several workers continued to advance the understanding of depositional processes and facies association.

Three Key Basins

Initially, three areas were key to the successful transition of exploration into deepwater: the North Sea, the northern Gulf of Mexico and Brazil. The reservoirs discovered in these basins were essential for the recognition that deepwater reservoirs could produce at high and sustained rates, which were critical to making these plays economic.

The exploration story for deepwater sandstones began in earnest with the early oil discoveries in the North Sea basin. Although the modern water depths do not exceed 400 meters, the discovery of turbidite reservoirs in a number of fields was an essential step in the understanding of deepwater reservoir systems, impacting future deepwater exploration. After the 1958 United Nations treaty divided the North Sea into economic zones by country, exploration gradually moved from onshore into the shelf region. Marine seismic acquisition grew throughout the 1960s.

Ironically, two of the first fields discovered in the Central Graben of the North Sea were in turbidite reservoirs. First, Ekofisk was discovered in 1969, where the main reservoirs are lower Paleocene resedimented chalk turbidites. Then, the following year, the Forties field was discovered in upper Paleocene sandstones.

There was considerable internal discussion at BP, the operator, about the depositional origin of the Forties reservoir sandstones – were they shallow marine or deep marine? After a few years, the data collected for the field began to point toward a major delta-fed, base-of- slope deposit. Specifically, the reservoir was encased between deeper water microfaunal and palynological assemblages, distinct clinoforms prograded across the top of the deeper water reservoir systems, and associated sedimentologic studies were pointing toward sedimentary gravity flows. With the discovery of Forties, a number of other deepwater reservoirs were quickly discovered associated with the Paleocene systems as step-out from Forties; these included such fields as Maureen, Andrew, Montrose, Frigg, and Nelson.

Additional turbidite discoveries were made in the syn- and post-rift Jurassic and Lower Cretaceous strata: Magnus, the Brae complex, Britannia and Claymore fields. About 25 percent of the historical production in the U.K. North Sea has come from turbidite reservoirs.

GOM and Bright-spot Technology

In the northern Gulf of Mexico, exploration after World War II continued to move into deeper water depths across the shelf. Offshore Louisiana in 1947, Kerr McGee drilled the first well that could not be seen from land. The progressive movement of exploration into deeper water depths on the shelf continued for the next 30 years. The first significant discovery off the shelf was the 1975 Cognac Field in 1030 feet of water; the reservoirs were primarily upper slope and deltaic sands.

The major technical driver in moving exploration into the upper slope and deeper water was the use of bright-spot technology, initially developed by Mike Forrest and colleagues at Shell, and independently developed at Mobil. This approach was especially effective in discovering fields both on the shelf, as well as in deeper water. The larger fields were discovered beginning in the mid-1980s to early ‘90s and include Auger, Mensa, Mars, Ram Powell, and Ursa. Today, the northern deepwater Gulf of Mexico has 226 fields and discoveries; all but four of them are in turbidite reservoirs. Yearly production in 2014 was 416 million barrels of oil and 688 billion cubic feet of gas.

The movement into deepwater was gradual at first, limited by drilling technology. Drill ships became necessary to drill in much greater water depths. Specialized ships were initially developed for the Deep Sea Drilling Project Scientific Drilling Program in the 1960s. By the mid-1970s, several drill ships were built and used by industry.

Initial record water depths for drilling were in eight basins globally between 1970 to 1984. However, from 1987-2011, all record water depths were in the northern Gulf of Mexico (Figures 2 and 3).

An important trend has been the abrupt increases in the water depths for drilling during short time periods: 2,000 to 5,000 feet (1975-79), 5,000 to 7,000 (1981-84), 7,600 to 9,000 (1998-99), and 9,000 to 10,000 (2000-03) (Figures 2 and 3).

In addition to drilling, new development technology was necessary to develop these large fields. Subsea tiebacks, now a common production technology, got their start in the North Sea. Likewise, underwater pipelines, tension leg platforms, floating platforms and floating production storage offloading units have been essential technologies.

Brazil and Petrobas

Brazil is also a very important part of this deepwater story. Petrobras drilled its first onshore discovery in 1954; by 1968, the first offshore well was drilled in 10 meters of water in the Espirito Santo Basin, testing a structure that had alternative interpretations of a salt diapir or an igneous intrusion. The well was unsuccessful but proved the presence of evaporites in the continental platform, creating expectations of a new frontier with structures and plays similar to the Gulf of Mexico. In 1968, the Guaricema Field in the Sergipe-Alagoas Basin was discovered in a water depth of 20 meters; similar to some of the North Sea discoveries, there was considerable internal discussion as to the environment of deposition of the reservoir. Bill Fisher, working as a consultant, suggested that the reservoirs were, in fact, deepwater sands; this observation led to a change in exploration paradigm for potential reservoirs.

In 1974, Petrobras discovered the first oil field in the Campos Basin in Albian carbonates, and in less than a year the exploration focus moved to siliciclastic reservoirs in shallow waters, which were interpreted as turbidite sands deposited from Late Cretaceous to Mid-Tertiary. By 1982, Petrobras had drilled successfully in the upper slope in the Campos Basin in about 400 meters of water.

The next big jump happened in 1984 when drill ships were brought to the Campos Basin and the Albacora (1400 feet) and Marlim fields (2800 feet) were discovered. These two major discoveries opened an entirely new deepwater frontier in the South Atlantic.

More than 40 fields in the deepwater of offshore Brazil are in Lower Cretaceous to lower Miocene turbidite-related reservoirs. In 2015, the daily production in the Campos Basin from these deepwater sand reservoirs was nearly 1 million BOE/day.

Continued Evolution in Seismic Data

Another major jump for deepwater exploration happened during the early to mid-1990s, when marine 3-D seismic became routinely available for regional evaluations, and countries began to allow deepwater exploration in areas previously inaccessible.

For example, the 3-D seismic data collected along the West African margin led to major discoveries in Angola, Congo, Gabon, Equatorial Guinea, and Nigeria. These new seismic data also stimulated companies to reassess their concepts of how deepwater sedimentary systems operate. The depositional models that had been developed with 2-D seismic data needed modification where the 3-D data could very accurately image the depositional elements. Meanwhile, the need for 3-D seismic to image the geology below thick allochthonous salt led to cost-effective development of pre-stack depth migrated data. In addition, companies began to reassess deepwater outcrops to help construct accurate reservoir models. Flume studies also began to increase in complexity as companies tried to replicate the interpreted processes of the gravity flows. 4-D seismic (repeat 3-D) also became an essential tool for imaging the movement of fluids during field development in many productive basins.

Continental and Shallow Marine Reservoirs

Although most deepwater fields and discoveries have turbidite sand reservoirs, a number of reservoirs deposited in shallow marine to continental environments have been discovered in modern deepwater (greater than 1500 feet). All of these reservoirs represent deposition in the earliest portion of these margins' tectonic development. The most notable are the pre-salt Lower Cretaceous reservoirs in the Santos and Campos basins in Brazil and their mirror image basins in offshore Angola (Kwanza and Namibe). Reservoirs are mainly microbial carbonates, coquinas and cherts deposited in rift lakes. Those fields already produce more than 1 million BOPD in the Santos and Campos basins. Other discoveries include: Upper Jurassic eolian reservoirs in the northern deep Gulf of Mexico; Upper Jurassic fluvial-estuarine reservoirs in the Bay du Nord, offshore eastern Canada; Lower Cretaceous lacustrine deposits in the northern Falkland- Malvinas Basin; Lower Cretaceous shallow to marginal marine reservoirs in offshore Senegal; middle Miocene carbonate buildups in offshore Egypt; and upper Miocene carbonate reservoirs west of the Philippines.

The Future?

At this point we must ask: what is next for deepwater exploration and development? The recent price downturn has had a significant global impact on the economics of deepwater. Many deepwater plays are not profitable in the current low-cost environment due to high capital and operating costs. Clearly, an increase in oil price and/or a decrease in operating expenses are essential for deepwater exploration and production to remain profitable in the future.

Acknowledgments

To insure historical accuracy, I have consulted recently with several colleagues for reconfirmation of facts and more details: Greg Blake, Mike Bowman, Don Clarke, BillFisher, Joan Flinch, Mike Forrest, Bob Frykland, Stephen Graham, Paulo Guimaraes, Will Gutterman, Alfredo Guzman, Andrew Hurst, Laurie Lamar, Todd Lapinski, Dorie McGuinness, Bud McGuire, Bob Mitchum, Webster Mohriak, Martin Natland, Henry Pettingill, David St. Hubbins, Art Saller, Craig Shipp, Matthew Silverman, Derek Smalls, Pete Stark, Mike Sweet, Mario Suarez, Gabor Tari, Clint Tippett, Nigel Tufnel and M. S. Wacker. To all of them, I extend my sincerest thanks.

Author

Paul Weimer (Figure 6) is an AAPG past president and holds the Bruce D. Benson Endowed Chair in the Department of Geological Sciences at the University of Colorado, and serves as the Director of the Energy and Minerals Applied Research Center. He began research on deepwater deposits in 1978 and has continued to prod the broad topic for many years since then. He was also the co-chair of the 100th AAPG Anniversary Committee.

About Historical Highlights

A history-based series, Historical Highlights is an ongoing EXPLORER series that celebrates the “eureka” moments of petroleum geology, the rise of key concepts, the discoveries that made a difference, the perseverance and ingenuity of our colleagues – and/or their luck! – through stories that emphasize the anecdotes, the good yarns and the human interest side of our E&P profession. If you have such a story – and who doesn’t? – and you’d like to share it with your fellow AAPG Members, contact the editor, Hans Krause at historical.highlights@yahoo.com.

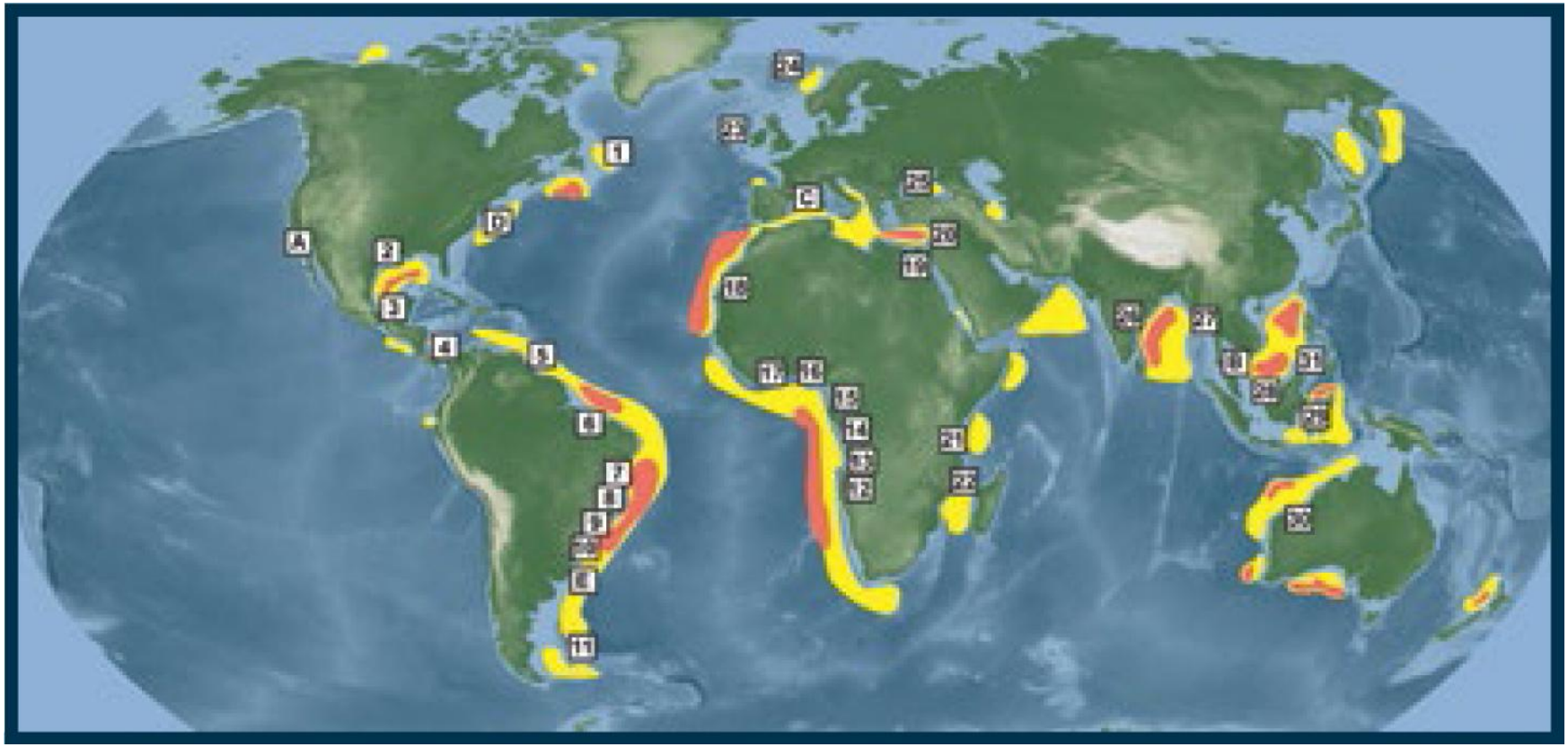

Figure 1. Global map of all basins in greater than 1500 feet water depth with fields or economic discoveries. 1. Eastern Canada. 2. Northern Gulf of Mexico. 3. Southern Gulf of Mexico. 4. Colombia. 5. Guyana. 6. Potiguar. 7. Sergipe Alagoas. 8. Espírito Santo. 9. Campos. 10. Santos. 11. North Falklands. 12. Angola. 13. Cabinda. 14. Gabon. 15. Equatorial Guinea. 16. Nigeria. 17. Ghana-Core D'Ivoire/ 18. Senegal-Mauritania. 19. Nile. 20. Levant. 21. Tanzania 22. Rovuma. 23. Shetlands. 24. Central Norwegian shelf. 25. Black Sea (Romania). 26. Krishna-Godavari. 27. Myanmar. 28. Brunei-Sabah. 29. Mahakam. 30. NW shelf- OZ (three sub-basins). 31. West Philippine Sea. Additional sites for drilling records (Figure 3) are shown: A=Santa Barbara (1970); B=Andaman Sea (1976); C=Gulf of Lion (1982); D=Baltimore Canyon (1983- 1984); E=Pelotas Basin Uruguay (2016). Areas with good exploration potential are shown in yellow (deepwater 1500-6000 feet) and orange (ultra-deepwater greater than 6000 feet).

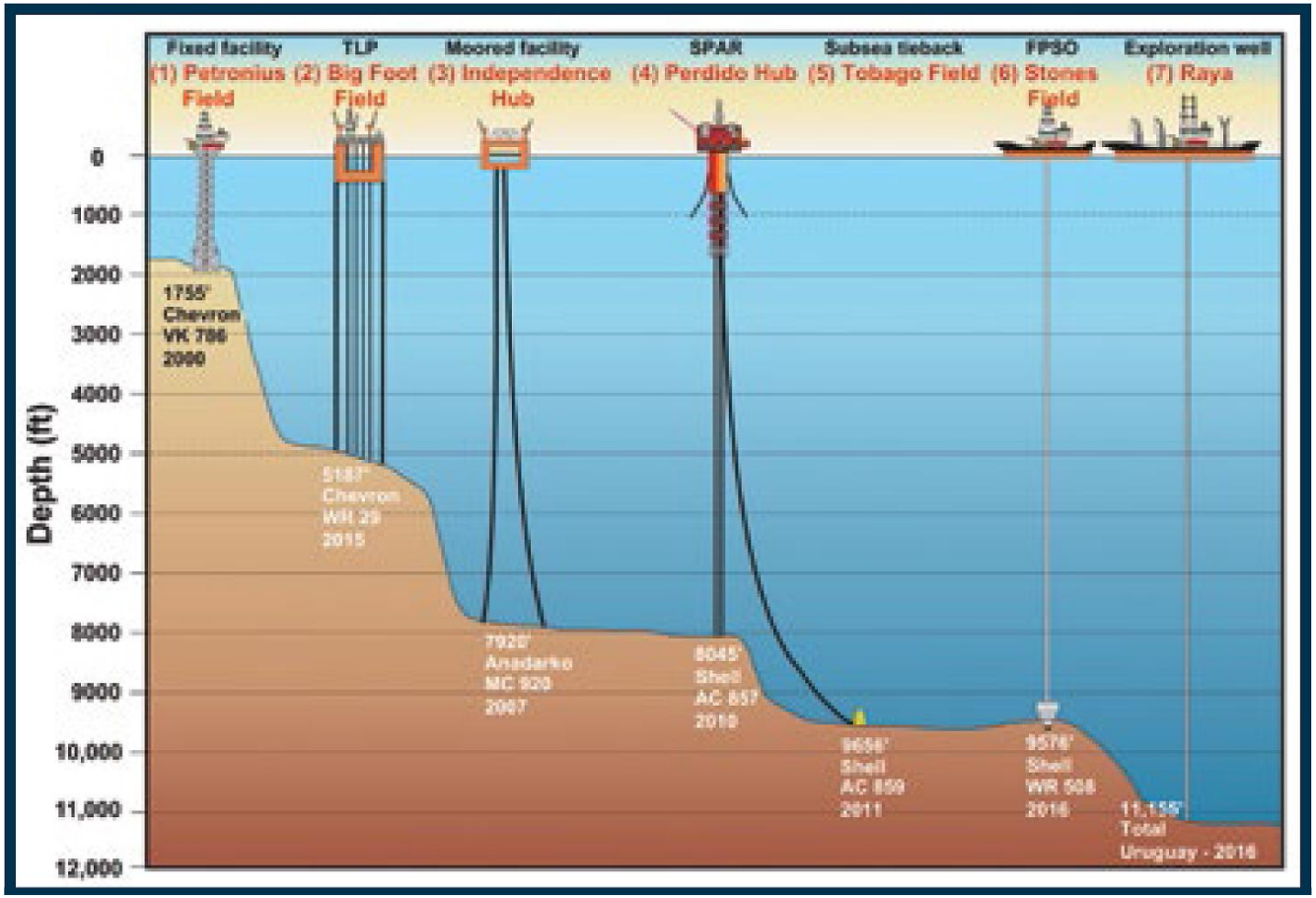

Figure 2. Schematic diagram showing the world-record water depths for exploration and development facilities, and years of first usage. TLP=Tension Leg Platform; FPSO= Floating Production Storage Offloading.

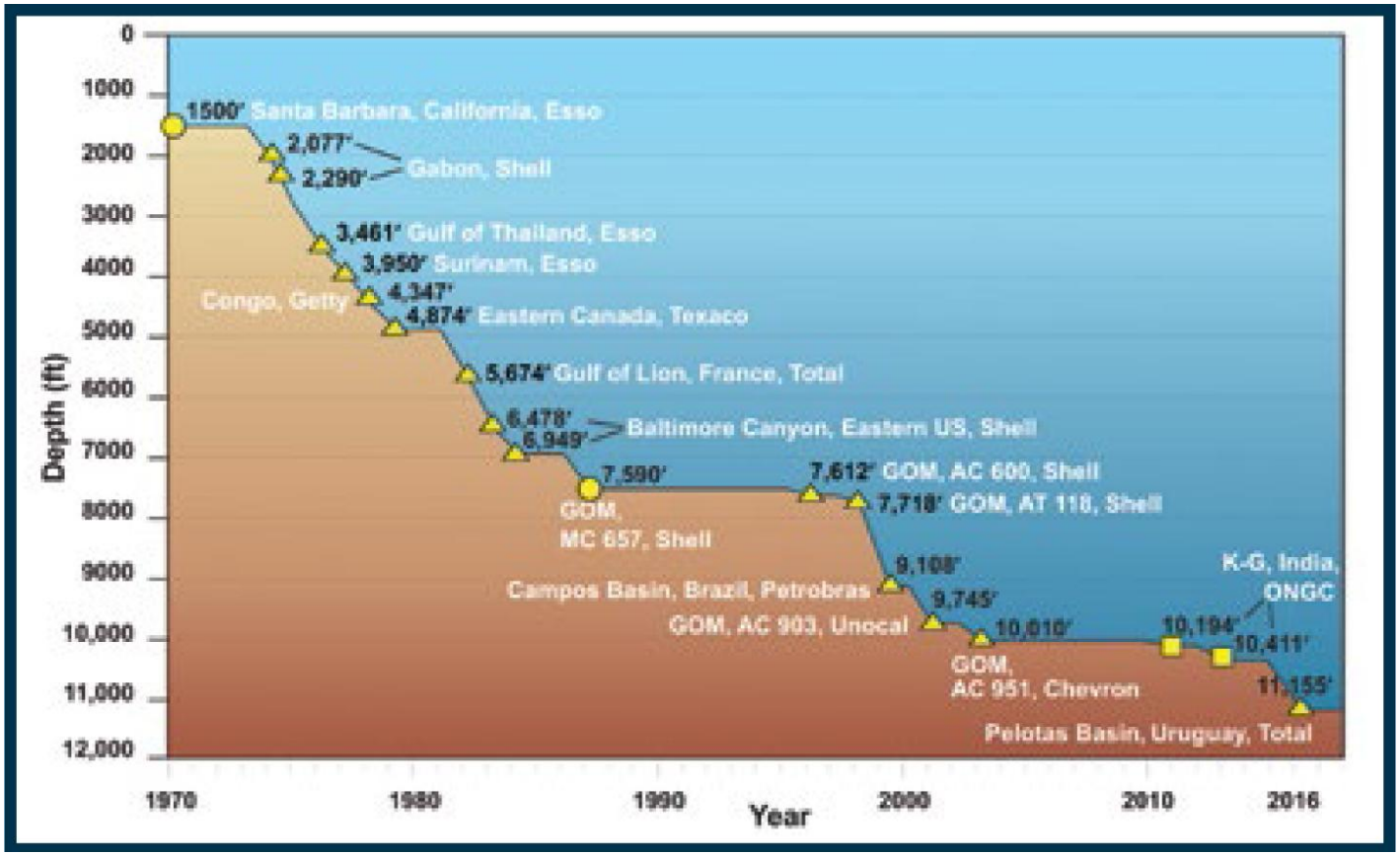

Figure 3. Record water depths for drilling by the end of each year. Location of wells and operator are indicated. GOM=Gulf of Mexico, AC=Alaminos Canyon, AT=Atwater Valley, MC=Mississippi Canyon, K-G=Krishna-Godivari. Triangles=dry holes, circles=producing fields, squares=discoveries. Locations of basins shown in Figure 1.



Figure 4. Manley Natland (with camera) filming the generation of turbidites in a flume at Union Oil Research Laboratory, Brea, Calif., January 1965. Photo courtesy of Martin Natland.

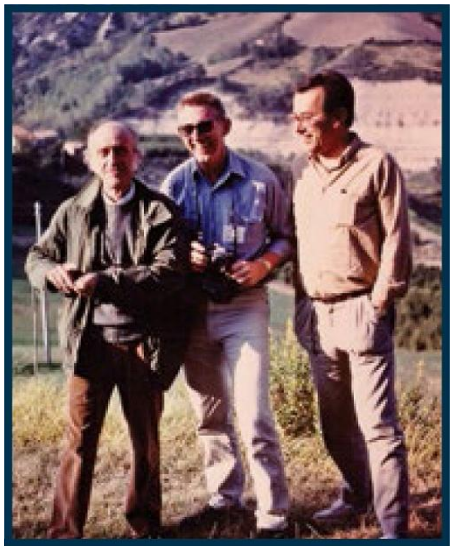

Figure 5. (From left) Emiliano Mutti, Arnold Bouma, and Franco Ricci-Lucchi in the Apennine Mountains, Italy, September 1988. Photo by Martin Link.



Figure 6. Paul Weimer.

5

Paim, P. S. G., E. L. C. Lavina, U. F. Faccini, A. S. da Silveira, H. Leanza, and R. S. F. d'Avila, 2011, Fluvial-derived turbidites in the Los Molles Formation (Jurassic of the Neuquén Basin): Initiation, transport, and deposition, *in* R. M. Slatt and C. Zavala, eds., Sediment transfer from shelf to deep water—Revisiting the delivery system: AAPG Studies in Geology 61, p. 95–116.

Fluvial-derived Turbidites in the Los Molles Formation (Jurassic of the Neuquén Basin): Initiation, Transport, and Deposition

Paulo Sergio Gomes Paim, Ernesto Luiz Correa Lavina, and Ubiratan Ferrucio Faccini

Universidade do Vale do Rio dos Sinos (UNISINOS)-Programa de Pós-Graduação em Geologia (Brazil), São Leopoldo, Brazil

Ariane Santos da Silveira

Universidade do Vale do Rio dos Sinos (UNISINOS), São Leopoldo, Brazil

Héctor Leanza

Servicio Geológico Minero Argentino-Consejo Nacional de Investigaciones Científicas y Técnicas (SEGEMAR-CONICET) and Universidad Nacional de La Plata, Argentina

Roberto Salvador Francisco d'Avila

Petróleo Brasileiro S. A. (Petrobras), Rio de Janeiro, Brazil

ABSTRACT

This chapter is about an almost uninterrupted exposure of the Jurassic Los Molles Formation in the Arroyo La Jardinera region in the southern Neuquén Basin (western Argentina). It is based on the analysis of high-resolution satellite images linked with extensive field data. Its main goal is to present a conceptual model for the studied turbidite system capable of explaining how sand and gravel were brought onto and removed from the shelf margin and how these coarse-grained sediments were transported along and deposited on the slope and basin plain. The facies tract ascribed to this turbidite system represents high-frequency lowstand system tracts. From proximal to distal, it includes the record of fluvial channels incised into mid- to outer-shelf deposits, turbidite channels scoured on slope strata, turbidite lobes resting on slope rise facies, and poorly developed turbidite lobe fringes enclosed within basin-plain strata. These

Copyright ©2011 by The American Association of Petroleum Geologists.
DOI:10.1306/13271352St613437

gravity flow strata were assigned to short-lived (surges) moderately efficient turbidity currents derived from the almost continuous failure of delta-front deposits (sand and gravel) during ordinary fluvial floods.

INTRODUCTION

Based on the interpretation of high-resolution satellite images and extensive fieldwork, Paim et al. (2008) connected the gravity flow strata exposed in the Arroyo La Jardinera area (southern Neuquén Basin, Argentina) to submarine ramps (''sensu''; Heller and Dickinson, 1985), including multiple point sources and no major conduit or canyon, related to high-frequency lowstand (shelf-margin) deltas. Similarly, Mutti et al. (2003) had ascribed the succession exposed in the area to turbidite systems closely related to lowstand deltas (their type-A mixed systems). The main difference between both ideas is the ultimate depositional setting of the turbidite strata, whether a slope-to-basinal setting (Paim et al., 2008) or a distal delta-front–prodelta context (Mutti el al., 2003). A regional description of the Jurassic turbidites in the Neuquén Basin is presented by Burguess et al. (2000), but unfortunately the Arroyo La Jardinera area is only briefly mentioned.

Paim et al. (2008) associated the gravity flow deposits of the area with three independent systems: the first type of gravity flow system (GF1) was ascribed to gravel- and sand-rich density flows. Its facies tract encompasses fluvial channels incised into mid- to outer-shelf deposits, turbidite channels scoured on slope strata, turbidite lobes resting on slope rise facies, and poorly developed lobe fringe facies enclosed within the basin-plain strata. The second type corresponds to a sand-rich system with abundant stratification, including an oscillatory component, which was ascribed to low-concentration combined density flows (GF2). The third system is related to mass gravity flows (slumps and slides) and derived debris flows (GF3). A full description of the entire set of gravity flow deposits and enclosing facies within the Los Molles Formation exposed in the Arroyo La Jardinera area can be found in Paim et al. (2008).

This chapter focuses on the previously mentioned type-1 gravity flow system (GF1), by far the most important in terms of sand and gravel deposition in the study area. It presents many features that reveal several important issues related to the removal of coarse-grained sediments from the shelf margin (triggering processes) and their subsequent transport to the deep sea through sediment gravity flows. In terms of gravity flow initiation, some pieces of evidence suggest that type-1 gravity flows derive from long-lived hyperpycnal currents, whereas other data evoke short-lived depletive surges. In addition, some features indicate that fluid turbulence and other supporting mechanisms are major, but diverse, factors on suspended-load transport. Last but not least, some data indicate a strong connection of the GF1 deposits with high-frequency accommodation cycles and paleophysiography.

Therefore, our main goal is to discuss and present a conceptual model for the GF1 system capable of explaining how sand and gravel were brought into and removed from the shelf margin and how these coarse-grained sediments were transported along and deposited on the slope and basin plain.

GEOLOGICAL SETTING

The Neuquén Basin, located in central western Argentina and eastern Chile, extends northward along the axis of the Andean Cordillera up to 31°S. Between 34°S and 37°S, the basin is restricted by the cordilleran belt as a narrow north-south elongated strip, whereas southward, it broadens eastward into the extra-Andean domain, where it is known as the Neuquén Embayment. The Neuquén Basin features a triangular shape, covers more than 160,000 km^2 (61,700 mi^2), and extends up to 700 km (434 mi) in a north–south direction (Zavala, 1993). Besides the Andean chain to the west, this basin is bounded by the Pampeano-Sierra Pintada and North Patagonian massifs (Figure 1). The infill of the Neuquén Basin (Figure 2) ranges from late Triassic to Paleocene in age (Ramos, 1998) and exceeds 7000 m (22,900 ft) of marine and continental strata (epiclastics, carbonates, evaporites, and pyroclastics).

During the late Triassic, central western Argentina and eastern Chile underwent extensional stresses related to an arc/trench system developed along the western margin of the South American plate (Legarreta and Uliana, 1991; Gulisano and Gutierrez Pleimling, 1995). At that time, sedimentation was confined to isolated fault-bounded depressions controlled by structural features of the underlying sialic substrate. These depressions were filled with nonmarine facies, strongly influenced by pyroclastic and volcanic rocks, presenting abrupt thickness changes (Gulisano and Gutierrez Pleimling, 1995) and known as the Precuyo Group

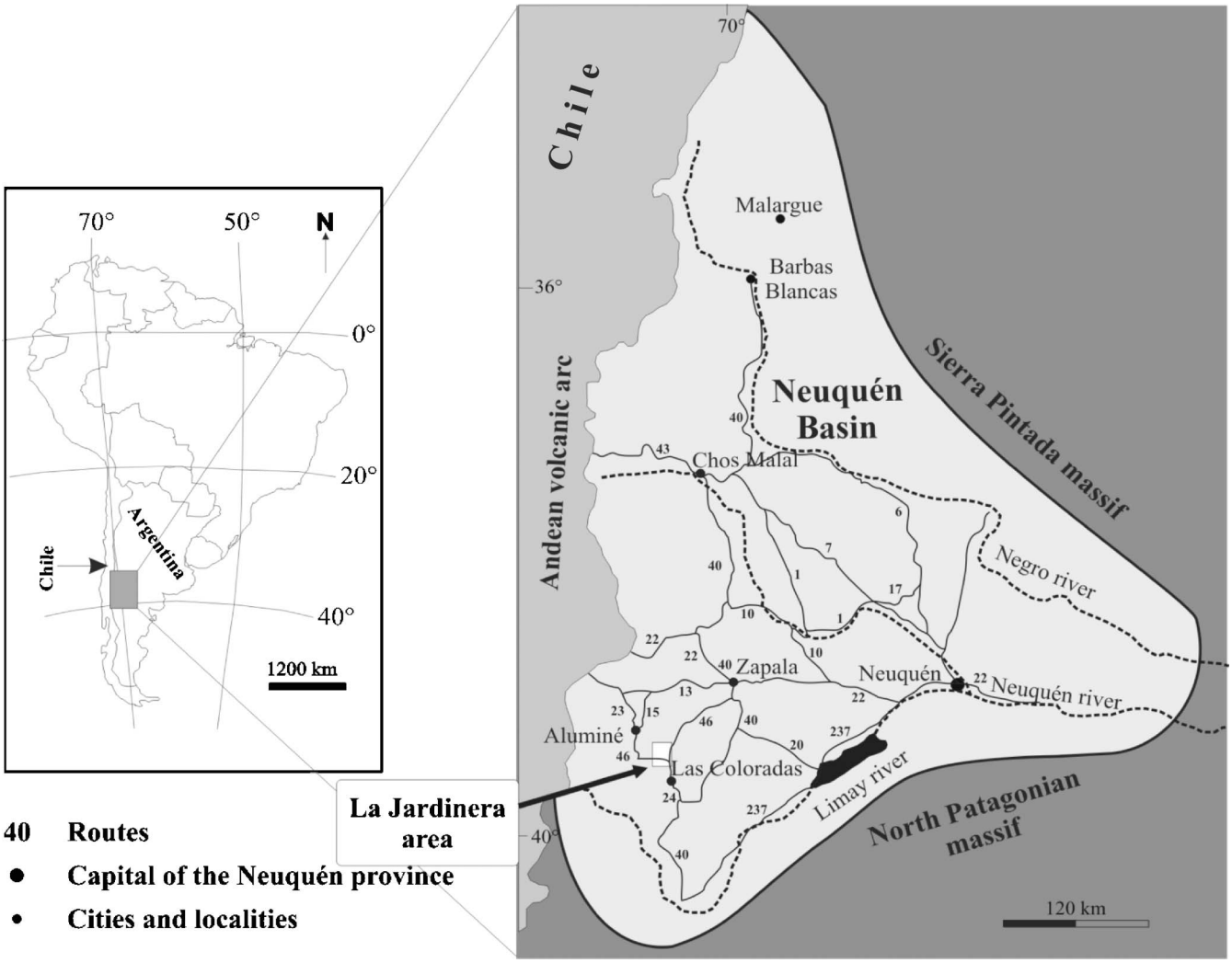

FIGURE 1. The Neuquén Embayment in South America and the location of the study area (Arroyo La Jardinera).

(Lapa Formation in southern Neuquén). These depocenters, sited on the east of the arc/trench system, became ever more unified to ultimately (Pliensbachian) merge into an extensive area of marine sedimentation placed between the volcanic arc to the west and the South American foreland to the east (Vicente, 2005).

From the early Jurassic to part of the middle Jurassic, deposition was chiefly driven by tectonics, a phenomenon that steadily reduced, giving way to a regional subsidence stage from the middle Jurassic to the early Paleogene (Ramos, 1998). Although most of the Neuquén Basin has maintained a nearly steady subsidence rate, records of local episodes of uplift, folding, erosion, and synsedimentary tectonics (Vergani, 2005) exist. Accordingly, sedimentation style and stratigraphic succession are records of those episodes of structural inversion and allied unconformities. The most important of such events produced the Huincul arch, a large east–west transcurrent fault zone in the southern Neuquén Basin associated with extensional stresses caused by the Gondwana fragmentation and ensuing Atlantic Ocean opening (Vergani et al., 1995). Several transgressions and regressions, mainly driven by eustatic sea level changes, occurred before the progressive growth of the Andean chain and cut off any oceanic influence into the basin (Legarreta and Gulisano, 1989). A rise in Andean tectonic activity as from the Miocene made the basin evolution even more complex.

The database used herein comes from the analysis of seismic-scale ($10 \times 10 \times 1.6$ km [$6.2 \times 6.2 \times 0.99$ mi]) high-resolution satellite images and the examination and logging (sedimentologic and gamma ray) of large natural exposures and road cuts. Bedsets and key stratigraphic surfaces can be followed for distances more than 10 km (6.2 mi). The adopted sequence-stratigraphic approach is similar to the approaches proposed by Van Wagoner et al. (1988, 1990), as sequence

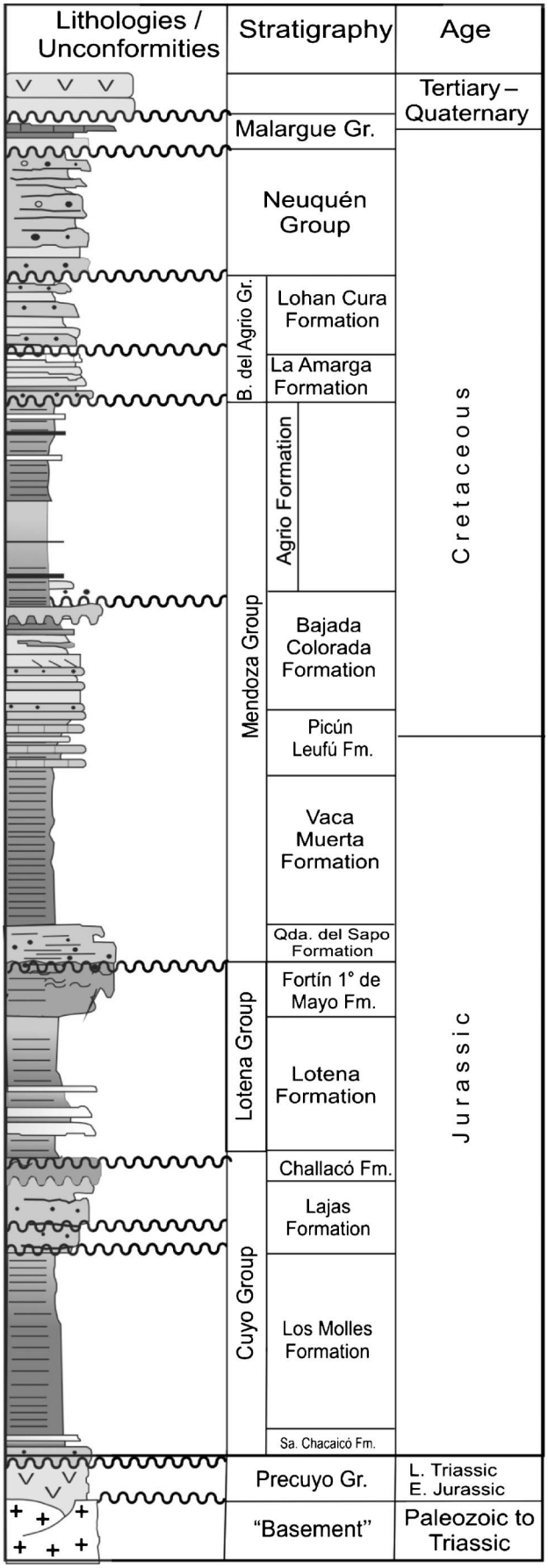

boundaries are tied to the end of base-level fall, and by Hunt and Tucker (1992) and Helland-Hansen and Gjelberg (1994), as four system tracts are discriminated (lowstand, transgressive, highstand, and falling stage).

In the study area, a main unconformity (sequence boundary 1 [SB1]) outlines the base of the Cuyo Group and corresponds to the boundary between the Los Molles and Sierra Chacaico formations (Figure 3). The Cuyo Group comprises 1100 m (3600 ft) of deep-marine strata (Los Molles Formation), 550 m (1800 ft) of shelfal to coastal facies of the Lajas Formation (between SB5 and SB8) and, at the top, the red beds of the Challacó Formation (Figure 4). The studied section is bounded by SB2 and SB6 and includes the middle and upper parts of the Los Molles Formation as well as its transition to the Lajas Formation (Figures 3, 4). It was subdivided into four 3d-order depositional sequences (J21–J24) that encompass nearly 6 m.y. (Figure 4).

In the ensuing sections, the database is presented to highlight the main themes used to understand the turbidity currents in terms of initiation, transport, and deposition, and therefore to support the conceptual model proposed to explain the GF1 system.

MAIN FEATURES

Physiography

Based on the analysis of the facies, facies associations, and architectural elements, the Los Molles and Lajas formations have been ascribed to four paleophysiographic elements, that is, genetic units larger than architectural elements and analogous to present-day physiographic units from several marine basins (Paim et al., 2008). They include the slope rise or basin plain and the slope in the Los Molles Formation, the mid or outer shelf, including the shelf margin, at the transition between the Los Molles and the Lajas formations, and the inner shelf or nearshore in the Lajas Formation (Figures 3, 4). These 10- to 100-m (33- to 330-ft)-thick paleophysiographic units include smaller, few to several meters thick, architectural elements with distinct geometries and facies associations (Figure 4).

FIGURE 2. Regional stratigraphic column for the southern and central parts of the Neuquén Basin (modified after Leanza and Hugo, 1997). The studied interval comprises part of the Los Molles and Lajas formations. Gr. = Group; B. = Bajada; Fm. = Formation; Qda. = Quebrada; Sa. = Sierra, L. = Late; E. = Early.

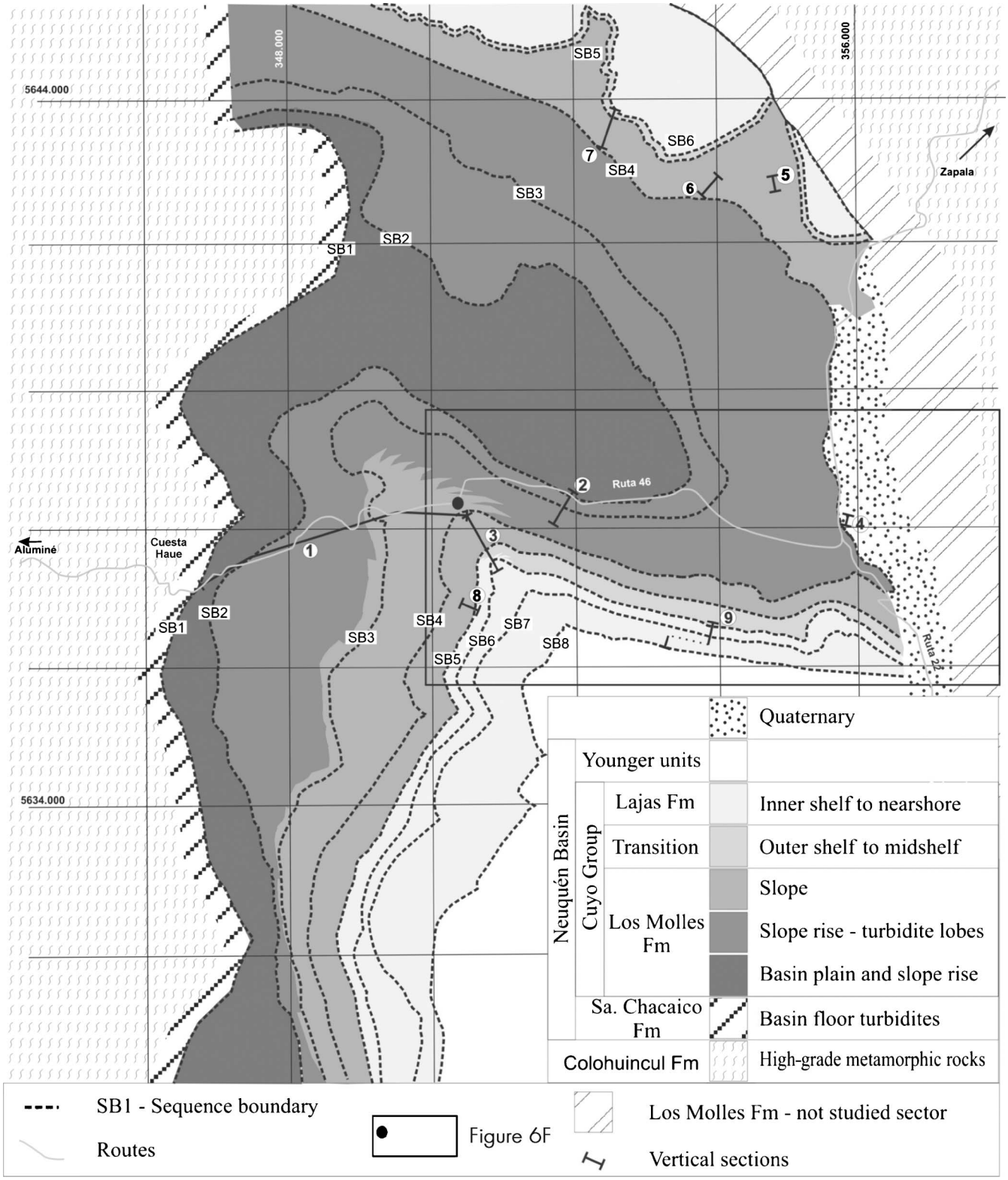

FIGURE 3. **Geological units in the study area (Arroyo La Jardinera Region) and paleophysiographic elements and sequence boundaries in the Los Molles and Lajas formations from the interpretation of a high-resolution satellite image (by IKONOS). The acquisition scale of the vertical sections ranges between 1:100 and 1:500. Fm = Formation; Sa. = Sierra.**

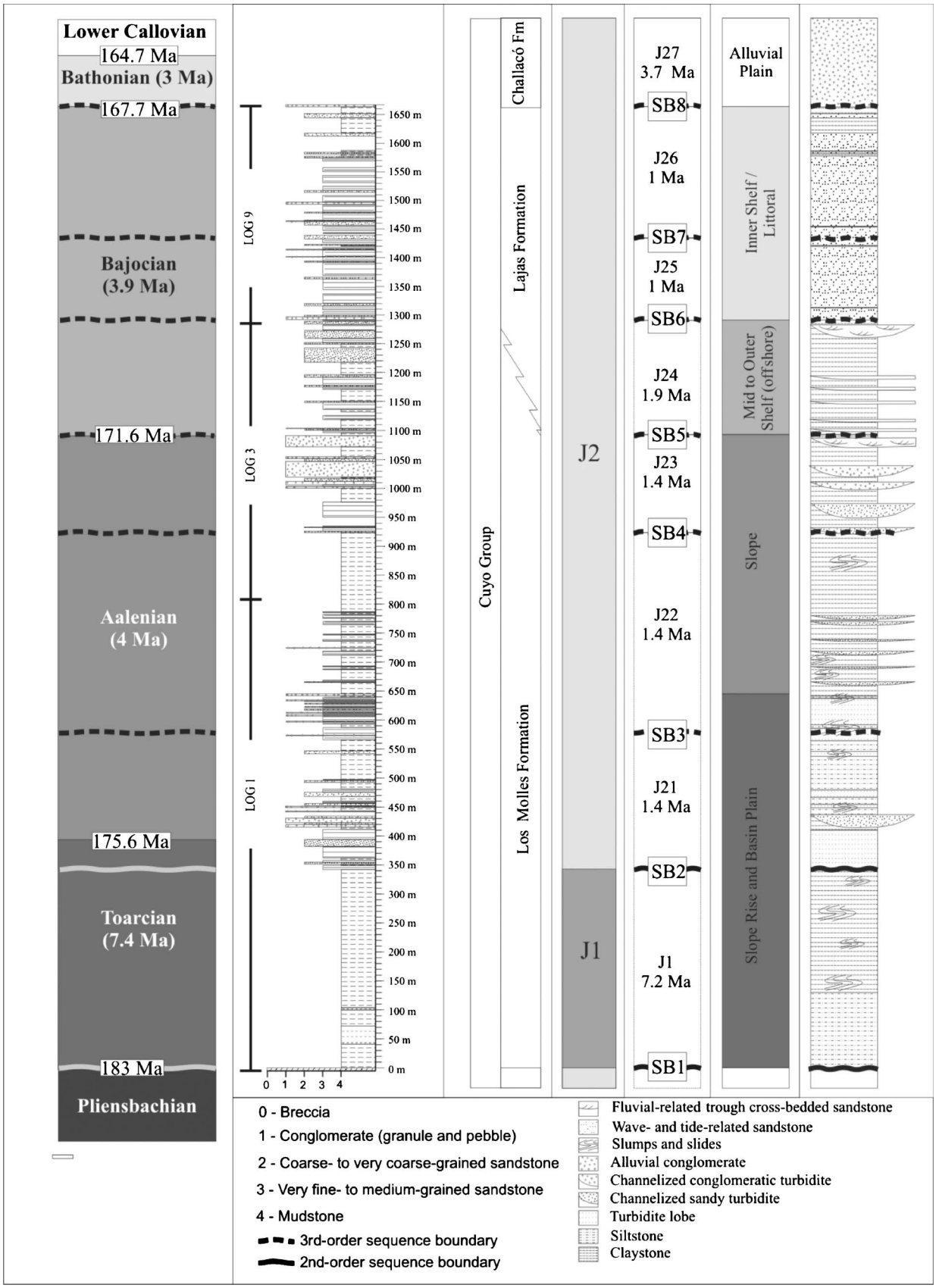

FIGURE 4. Simplified composite vertical section of the study area. Stages obtained from correlation to Gulisano and Gutierrez Pleimling (1995) chart and absolute ages from Gradstein et al. (2004) chart. SB = sequence boundary; Fm = Formation; J21– J27 = 3rd-order depositional sequences; J1, J2 = 2nd-order depositional sequences.

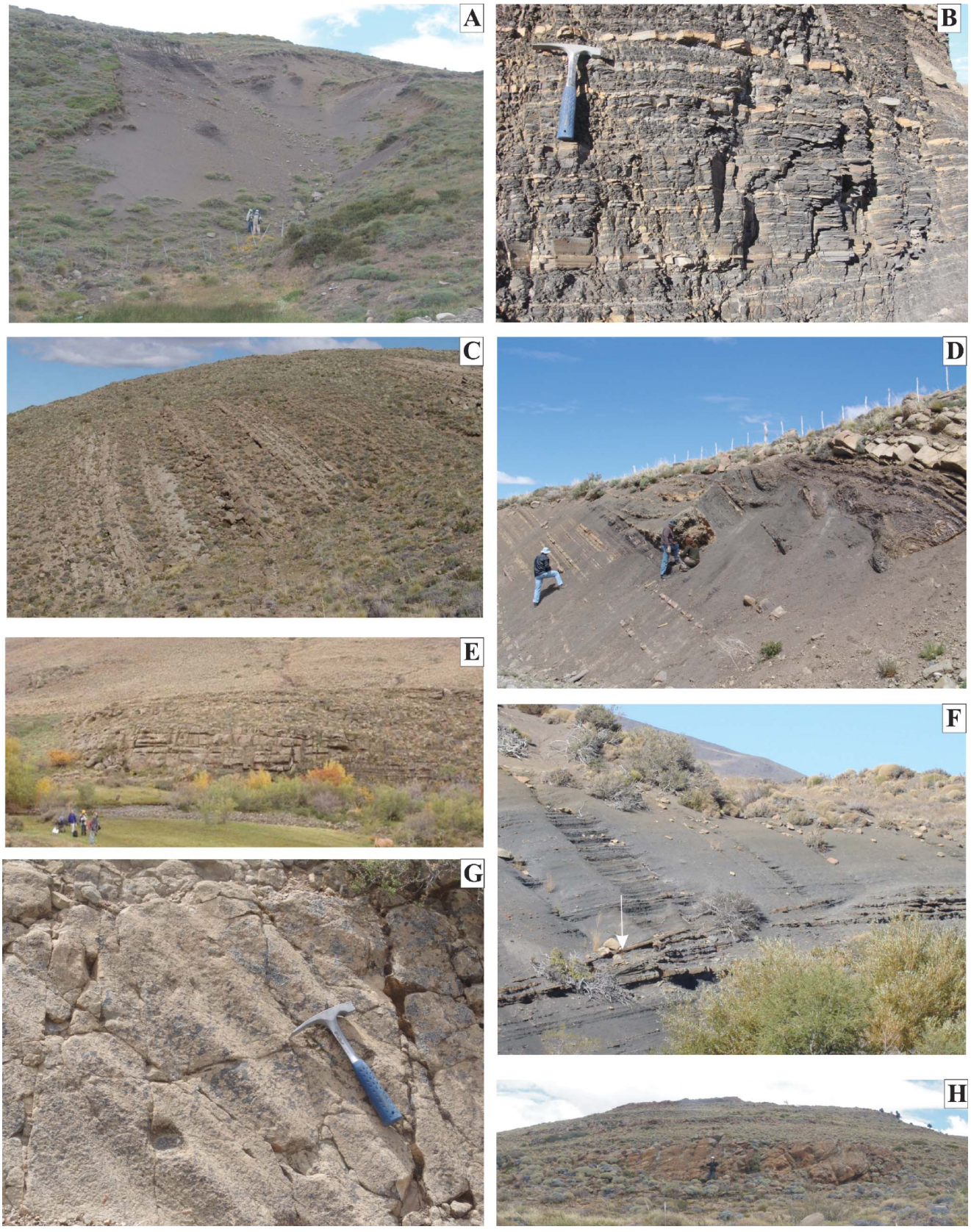

FIGURE 5. Physiography: (A) Fine-grained and (B) heterolithic lobe fringe deposits related to basin plain; (C) lobe sandy (sandstone bedset ranges from 5–15 m [16.4–49.2 ft] in thickness) and (D) slumped beds ascribed to the slope rise; (E) turbidite channel and (F) slide (white arrow) associated with slope strata; and (G) falling-stage wave-rippled sandstone resting on outer-shelf mudstone and scoured by (H) incised channel-fill facies.

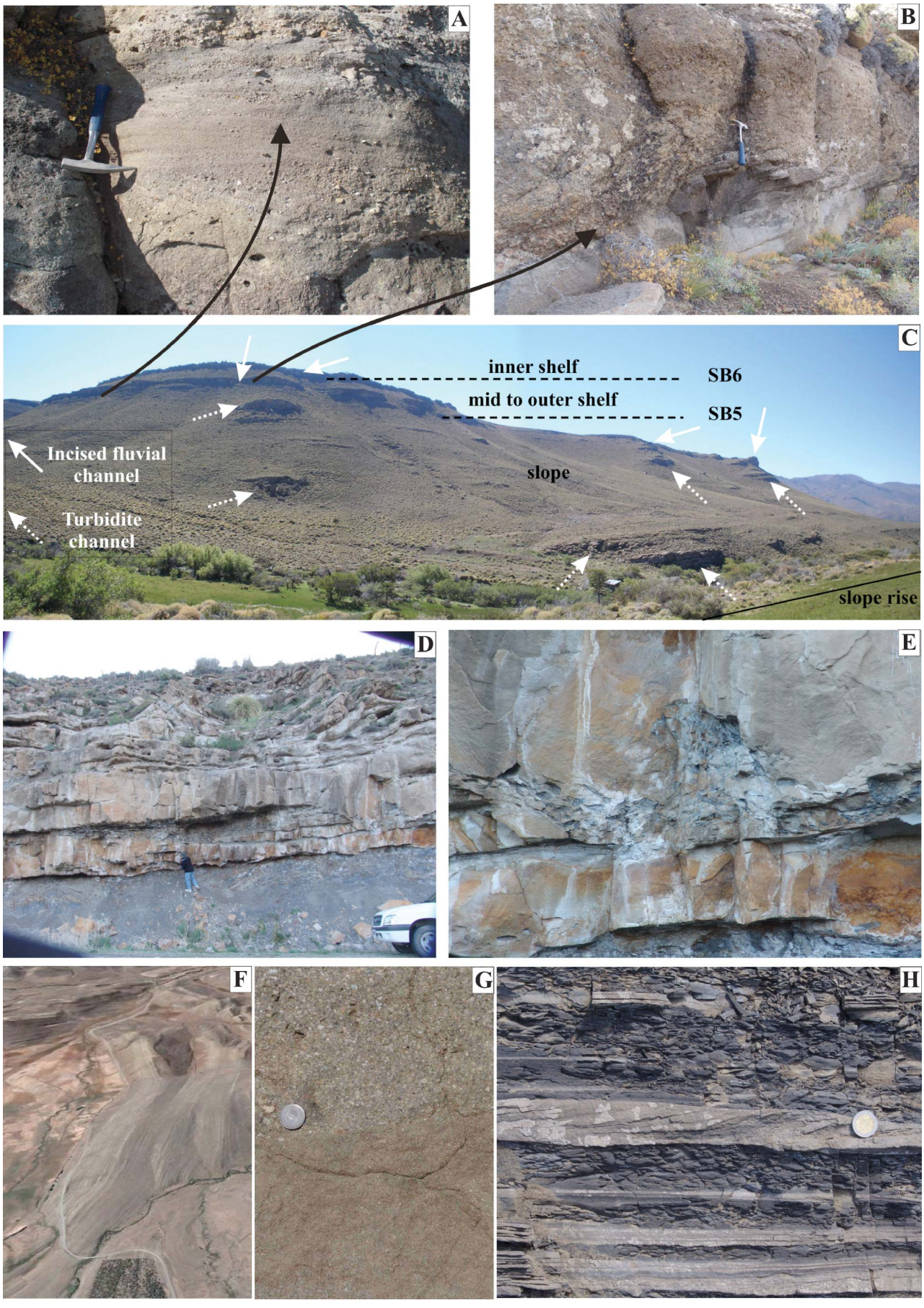
A
B
C
inner shelf
SB6
mid to outer shelf
SB5
Incised fluvial channel
Turbidite channel
slope
slope rise
D
E
F
G
H

In the Los Molles Formation, profuse fine-grained deposits (Figure 5A, B), tabular beds of sandstone sets ascribed to turbidite lobes (Figure 5C), fossil-rich (ammonites and small bivalves) layers, and dominantly planktonic radiolarian specimens among the microfauna (Kochhann et al., 2009) characterize the slope rise to basin plain. The distinction between slope rise and basin-plain strata is based on the exclusive occurrence of slumped beds in the former (Figure 5D). Similar faunal content, slumped beds, commonly coupled with slide deposits (Figure 5F), and turbidite channel fills encased by muddy interchannel facies (Figure 5E) define the slope realm. The transition between the Los Molles and Lajas formations consists of mid- to outer-shelf siltstone, sporadically enclosing sharp-based nearshore facies (Figure 5G) scoured by fluvial channels (Figure 5H). Lastly, a sandy interval (Lajas Formation), which includes wave-, storm- and tidal-related structures and some muddy intervals a few meters thick, defines the inner-shelf–nearshore paleophysiographic element.

Basin-plain shale and lobe–lobe fringe turbidites of the lower and mid–Los Molles Formation, respectively, followed by turbidite and incised fluvial channels encased in extensive fine-grained facies of the slope (upper Los Molles Formation) and mid to outer shelf (transition from Los Molles to Lajas formations), in that order, make up a succession that is very similar to that presented by Gulisano and Gutierrez Pleimling (1995) for the same area. This succession is supposed to be an outcrop analog of the tripartite subdivision of the Los Molles Formation defined by Gómez Omil et al. (2002) and Verzi et al. (2005) from seismic data.

In short, the GF1 system is linked to a paleophysiography composed of two gently dipping surfaces (shelf and basin plain) separated from each other by a steeper unstable slope. The thickness of the slope succession (about 400 m [1300 ft] thick; Figure 4) suggests a fairly deep-water setting (hundreds of meters of water depth) for the basin-plain facies. Similar physiography and water depth of the basin-floor turbidites were described by Steel et al. (2000).

Architectural Elements

The basinward tract of architectural elements of the GF1 system encompasses incised fluvial channels (shelf and shelf margin), turbidite channels (slope), and widespread turbidite lobes and lobe fringes (slope rise and basin plain).

The downdip and vertical changes of the GF1 architectural elements (Figures 3, 4) illustrate the basinward transition from incised fluvial channels through turbidite channels to turbidite lobes and lobe fringes (Figure 6). Incised fluvial channels are encased within shelf to shelf-margin strata; turbidite channels are scoured into and surrounded by slope, commonly remobilized fine-grained deposits; and turbidite lobes and lobe fringes are enveloped by fine-grained slope rise and basin-plain facies.

Facies Tract

Plane- and cross-bedded sandstone and both massive and stratified clast-supported conglomerates with sparse wood pieces represent the main fluvial channel-fill facies (Figure 7A–C). A minor tidal influence is suggested by the rare presence of rippled fine-grained sandstone with flaser and mud drapes near the base of the channel fills. Together, these pieces of evidence, in addition to the lack of sedimentary features associated with hyperconcentrated flows (sensu; Pierson and Costa, 1987), point to prevailing usual conditions of fluvial transport and deposition within incised braided fluvial channels, even during flood events (i.e., ordinary floods).

In contrast, the turbidite channel fills display a clear basinward reduction in mean grain size from clast-supported through matrix (sandy)-supported conglomerates to sandstones (Figure 7D–G). This down-dip segregation strongly suggests that fluid turbulence was a major factor in the long-distance transport of gravel and sand. This inference is reinforced by profuse flute casts at the base of the turbidite channels (Figure 8E) and rip-up clasts near their bases (Figures 7G, 8C). However, nonturbulent granular flows are indicated by the massive (Figure 7D–G) nongraded nature of most of the turbidite channel-fill beds. Their simple (in opposition to complex) and relatively thin character (0.1–0.5 m [0.33–1.6 ft]; Figure 8A, C) suggests short-lived currents. Jointly, both sets of data point to turbulent surges that developed downcurrent, with ever finer grained basal granular layers as a result of gravity transformation (sensu; Fisher, 1983).

FIGURE 6. **Architectural elements and facies associations: (A, B) Incised stratified fluvial deposits (see arrows for location); (C) turbidite and fluvial channels scoured on slope and shelf-margin facies, respectively; (D, E) massive turbidite channel strata; (F, G) tabular bedsets of massive sandstone related to the turbidite lobe; and (H) thin-bedded turbidites of the lobe fringe. SB = sequence boundary.**

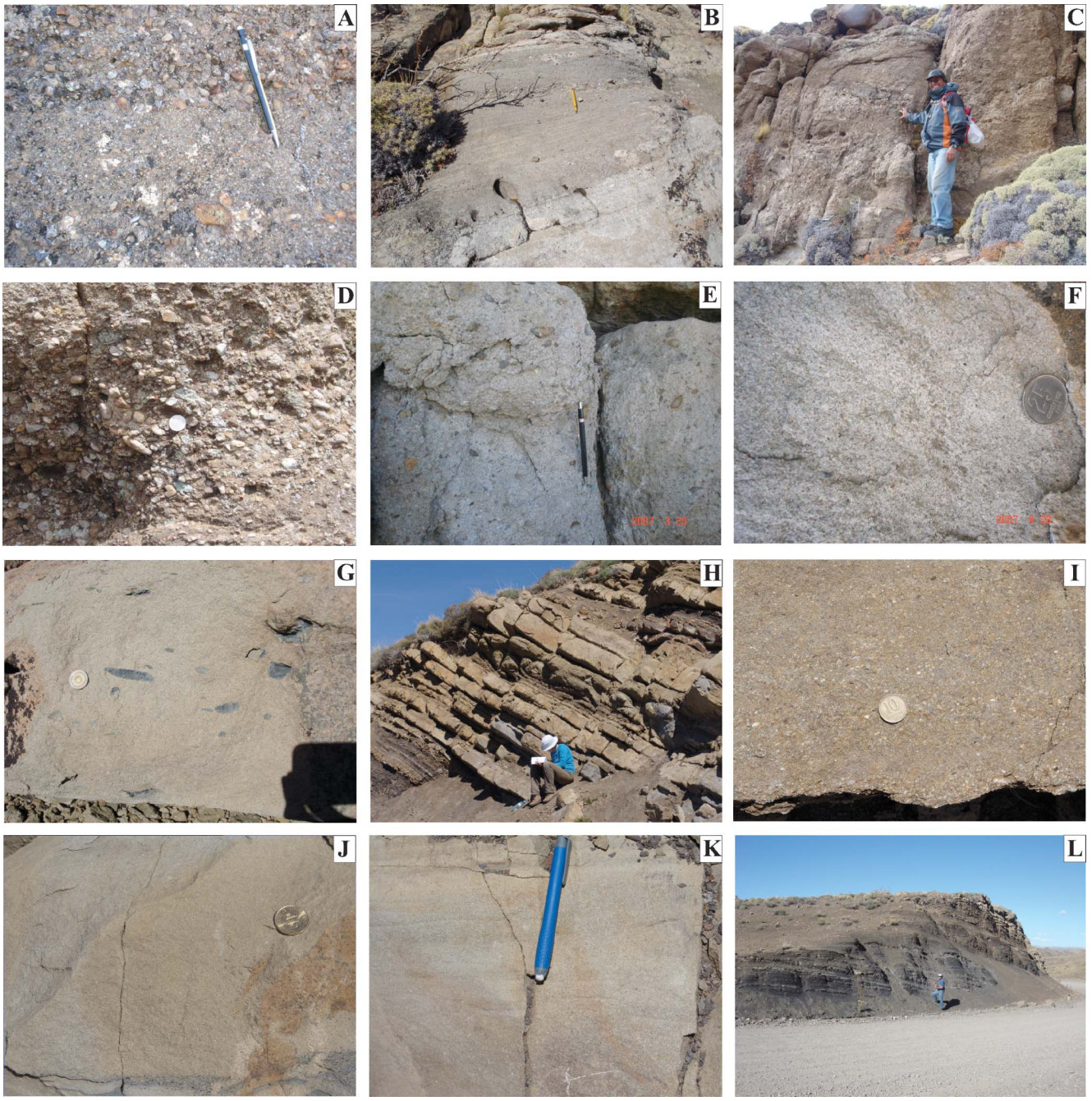

FIGURE 7. Facies tract: Clast-supported conglomerate (A) and plane and trough cross-bedded sandstone (B), sometimes with large pieces of trunks (C), associated with incised fluvial channel fill; clast (D)- and matrix (E)-supported conglomerate and massive sandstone (F), usually with rip-up clasts (G), related to turbidite channel fill; laterally extensive turbidite lobe strata (H) comprising massive coarse (I)- to fine (J)-grained sandstone, occasionally with incipient lamination (K); and heterolithic deposits (L) of the lobe fringe.

Downcurrent turbidite lobe and lobe fringe facies display similar features to those of the turbidite channel fills, except for their extensive geometry (Figures 5C, 6F, 7H, 8B), finer grained nature (Figure 7I–K), less abundant flute casts and rip-up clasts (Figure 8D, E), and more frequent normal grading (Figure 8F) and plane bedding (Figures 7K, 8G). Relative to turbidite channel fill, lobe strata are supposed to represent similar bipartite turbidity currents, but moving a finer grained suspended load in poorly constrained to wholly unconfined flows.

In short, GF1 deposits have been related to short-lived bipartite turbidity currents. Fluid turbulence has acted as the main supporting mechanism in



FIGURE 8. Surgelike density flow suggested by discrete medium-scale sedimentary bodies within turbidite channels (A) and lobes (B); pieces of evidence pointing to the turbulent nature of the long-distance transport, including rip-up clasts in both turbidite channel (C) and lobe strata (D), common to abundant flute casts at the turbidite channel base (E) and normal grading (F) and plane bedding (G) in turbidite lobe strata; and nearby continental sources indicated by common plant debris within both turbidite channel (H) and lobe (I) deposits.

long-distance transport of the coarse-grained suspended load from the shelf margin to the deep sea. However, the massive nongraded nature of most of the turbidites indicates that nonturbulent flow conditions would have left the ultimate mark on the deposits themselves. This non-Newtonian (pseudoplastic) rheology is supposed to represent transient conditions confined to the basal layer of the bipartite density flows and produced just before deposition could occur through frictional freezing.

Paleocurrents

Paleocurrent readings of trough cross-bedding within fluvial beds (incised channels) point to east–northeastward effluents (mean value, 83°; n = 24). Flute casts on turbidite beds show a similar trend (mean value, 67°; n = 60). All together, GF1 paleocurrent data point to northeastward currents (mean value, 72°; number of readings (n) = 84) that are similar to the inferred sediment transport path proposed for the area by Burguess et al. (2000) This mean value is roughly orthogonal (angle of 87°) to that presented by wave-induced cross-bedding (mean value, 159°; n = 126) ascribed to alongshore currents (Figure 9). It is also worth noticing that the sediment dispersal trends of both GF1 and nearshore systems have not changed with time (Figure 10).

The aforementioned paleocurrent data strengthen the idea of some genetic linkage between fluvial effluents and turbidity currents. Both dispersal systems comprise multiple small-scale source points (Figure 6C),

(A)

Depositional systems	Morphological element - sedimentary structure - mean paleocurrent vector	General mean vector
Nearshore, wave and tidal current.	Upper shoreface (trough cross-bedding - 122 readings - mean vector: 159) Flood tidal delta (trough cross-bedding - 4 readings - mean vector: 154) 159	GF1 n = 84 n = 126
GF1 system tract	Muddy slope rise and plain and lobe fringe (current ripples - 22 readings - mean vector: 63) Turbidite lobe (flutes, current ripples, and rare trough cross-bedding - 9 readings - mean vector: 105) Turbidite channel (flutes and a few trough cross-bedding - 29 readings - mean vector: 59) Incised fluvial channel (trough cross-bedding - 24 readings - mean vector: 83) 72	

(B)

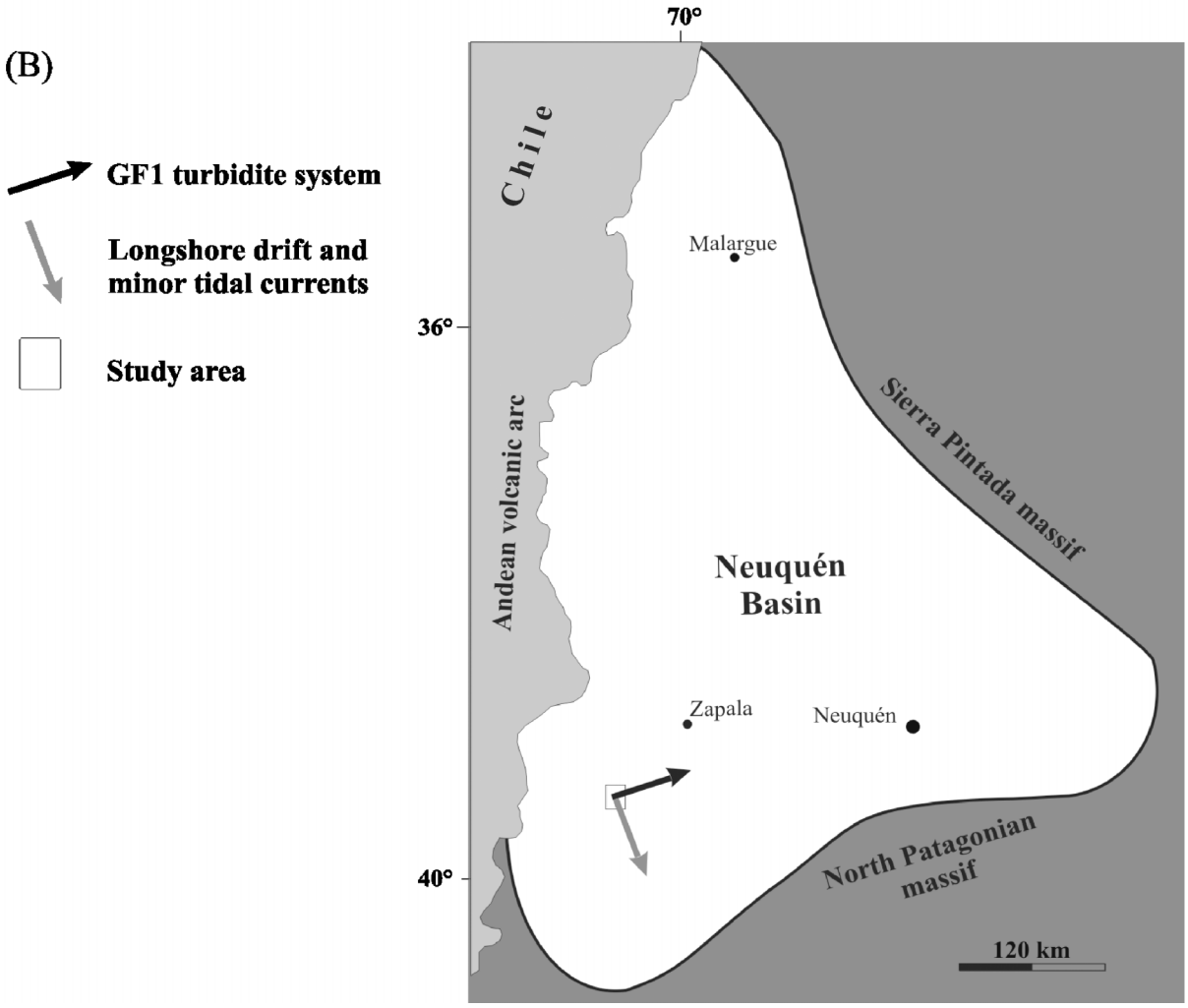

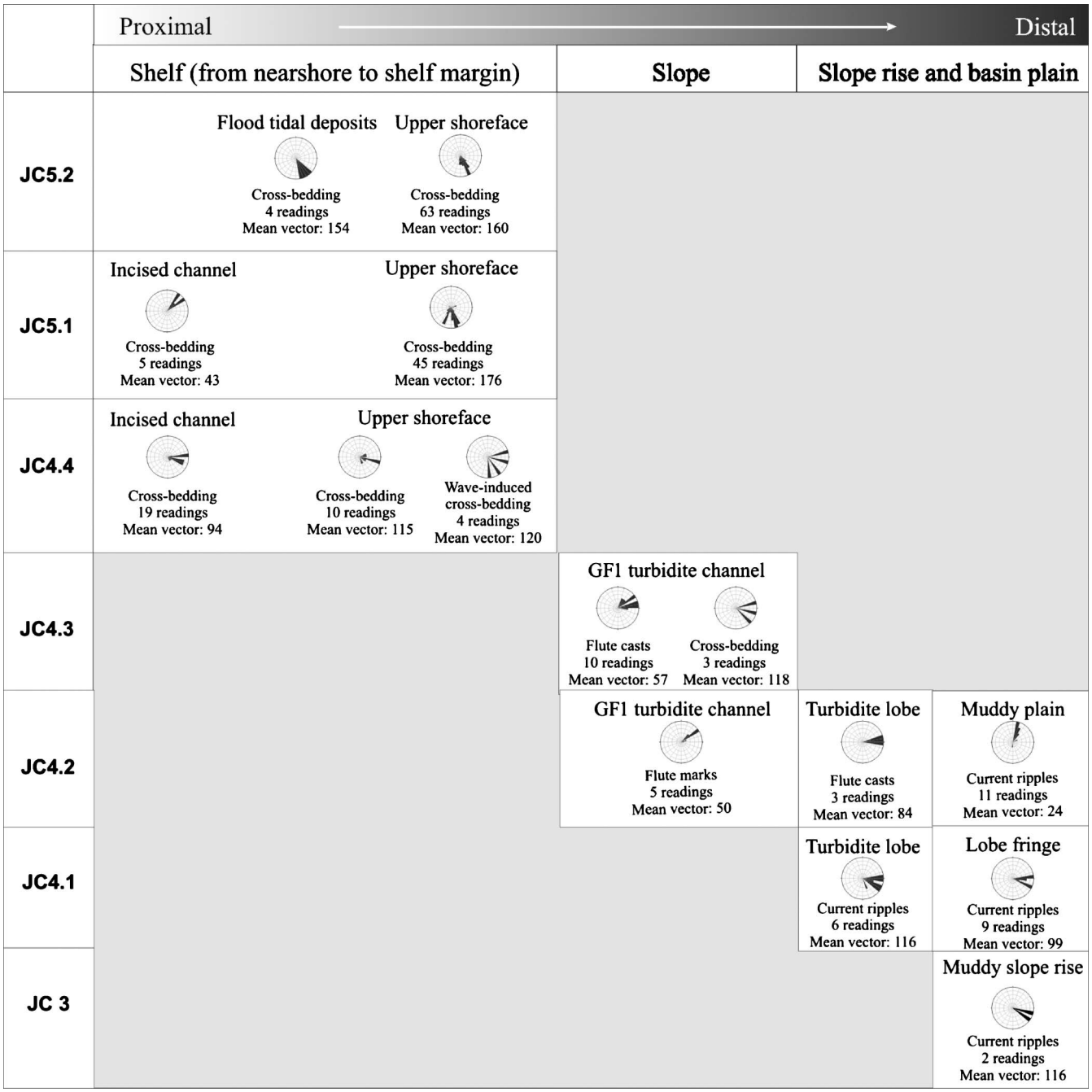

FIGURE 10. Paleocurrents of the first type of gravity flow system (GF1) through time and space. Nearshore, and wave- and tide-induced paleocurrents are also shown for comparison. Notice the steady transport trend of the GF1 strata within distinct paleophysiographic elements, from shelf to basin plain, as well as along time through different 3d-order depositional sequences.

FIGURE 9. The first type of gravity flow system ([GF1] fluvial and turbidity currents) and nearshore, mostly alongshore currents in the study area displaying mean vectors at right angles (A). In the map (B), notice alongshore currents parallel to the presumed local basin margin (north-northwest–south-southeast) and northeasternward toward the basin depocenter GF1 fluvial and turbidity currents. n = number of readings.

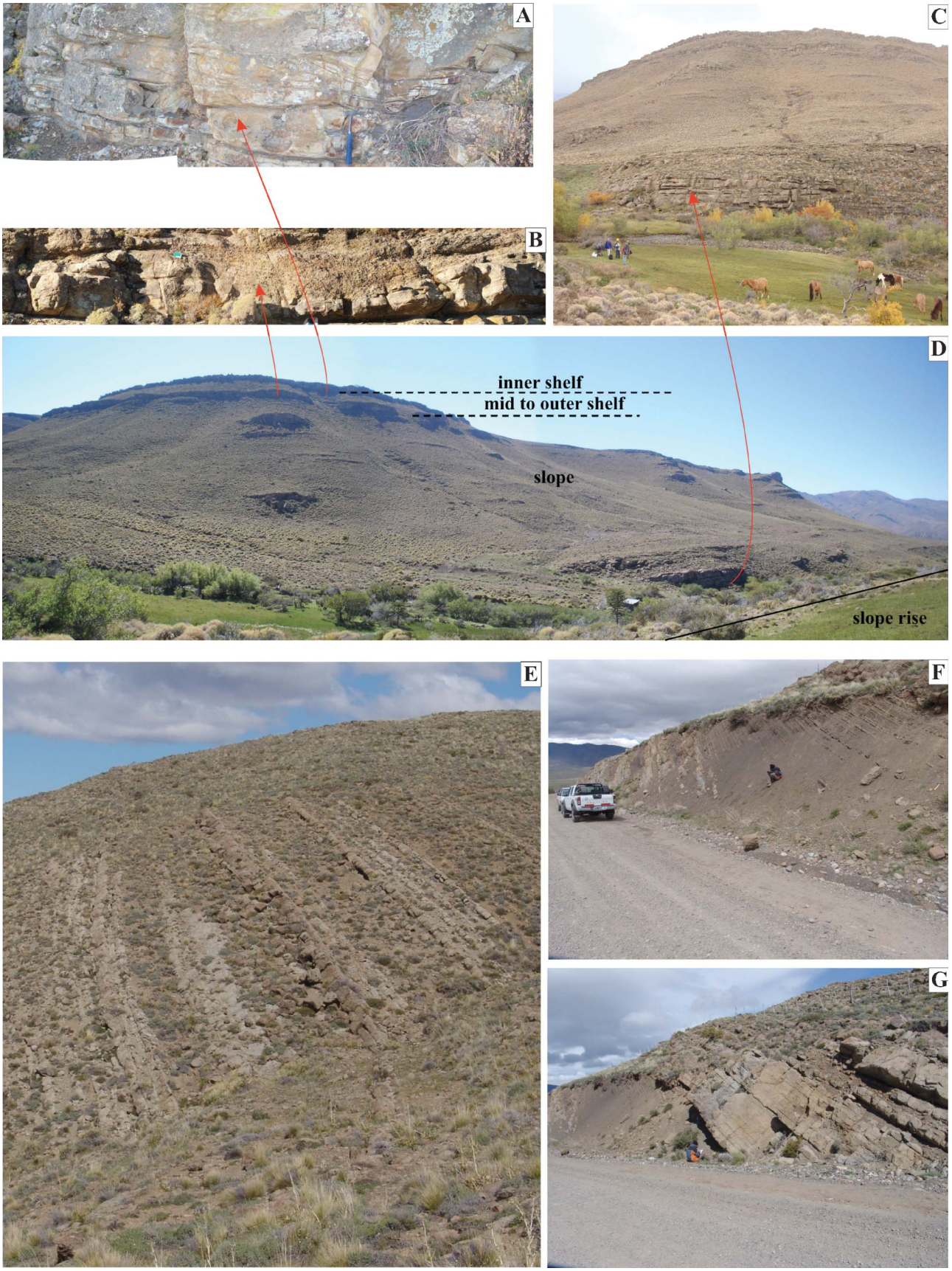
A
B
C
D
inner shelf
mid to outer shelf
slope
slope rise
E
F
G

and they have always flowed toward the basin depocenter, whereas alongshore transport is parallel to the orientation of the local basin border (Figures 9, 10).

High-frequency Sequences

The Cuyo Group is subdivided into two 2d-order depositional sequences, named J1 and J2, which record around 7 and 12 m.y., respectively (Figure 4). A key surface (SB2) delineates their boundary and the onset of a thick package of sandy turbidites that abruptly rests upon a thick package mostly composed of deep marine shale (Figures 3, 4). The J1 depositional sequence comprises the base of the Los Molles Formation, and it records a transgressive-regressive succession. The upper depositional sequence (J2) consists of the Los Molles (mid and upper sections), Lajas, and Challacó formations, and records a regressive unit (Figure 4). The latter sequence is subdivided into seven 3d-order depositional sequences (J21–J27), each one recording 1 to 3 m.y. (Figures 3, 4) and comprising up to two paleophysiographic elements (Figure 3). Besides, the analysis of the facies successions within all paleophysiographic elements and sequences indicates a high-frequency (4th- to 5th-order) modulation of the geological record, which is the theme of the next paragraphs (see also Figures 11, 12). The stacking pattern presented by the turbidite strata exposed in the study area has been used by Mutti (1992) as an example of high-frequency cyclicity on the scale of facies sequences.

In the outer- to midshelf strata, transgressive and highstand mudstones are sharply overlain (regressive surfaces of marine erosion) by wave- and tide-related nearshore deposits of the falling-stage system tract (Figures 5G; 11A, D). In turn, these nearshore facies are then scoured by small fluvial channels (Figure 6B, C) related to the later development of the falling-stage system tract and ensuing expansion of the subaerial unconformity. At the start of relative sea level rise, incised channels were then filled by fluvial (Figures 5H; 6A, B; 7A–C; 11B, D) locally tide-influenced facies. The subsequent increase in the rate of relative sea level rise once more drives the onset of the transgressive system tract over the shelf and consequent extensive silt deposition. In short, high-frequency relative sea level oscillations are recorded in outer- to midshelf strata by the falling-stage (regressive surface of marine erosion and succeeding fluvial incision), lowstand (channel-fill), and transgressive (shelfal siltstone above the surfaces of maximum regression) system tracts.

In the slope, by the end of the falling stage, widespread mudstone connected to the previous system tracts (transgressive, highstand, and falling-stage) was scoured by point-sourced turbidity currents (Figures 6D, E; 11D). Through the lowstand stage, the resultant channels were then filled by amalgamated lenses of gravel- to sand-rich upward and downdip fining turbidites (Figures 6C; 7D–F; 11C). Channel abandonment and resuming widespread mud deposition define the beginning of a new transgressive episode. Thus, 4th- to 5th-order relative sea level fluctuations are recorded in the slope by turbidite scour (early lowstand), turbidite channel fill (late lowstand), and widespread mud deposition (transgressive, highstand, and falling-stage system tracts).

On the slope rise and proximal basin plain, mudstone credited to a preceding high-frequency cycle (late lowstand, transgressive, highstand, and falling-stage system tracts) are regularly overlain (Figure 11G) by tabular bedsets (Figures 5C; 6F; 11E) composed of sand-rich (Figures 6G; 7I–K) few decimeters thick (Figures 7H; 8B) turbidites that supposedly represent the early lowstand system tract. A new increase in the rate of relative sea level rise leads to the deposition of a mud blanket over the sandy turbidites (Figure 11E, F). This package, which is between few to few tens of meters thick, of fine-grained deposits includes the subsequent late lowstand, transgressive, highstand, and falling-stage system tracts.

DISCUSSION

Short- Versus Long-lived Sediment Gravity Flows

Some features suggest a close link between fluvial discharge and sediment gravity flows. The tripartite basin physiography and high-frequency lowstand context promote appropriate conditions for the initiation of turbidity currents from hyperpycnal flows (e.g., Steel et al., 2000; Plink-Björklund and Steel,

FIGURE 11. **High-frequency depositional sequences: (A) sharply based tidal bar deposits (falling stage) and (B) incised fluvial strata (lowstand), both within dominantly muddy shelfal strata; (C) sandy turbidite channel (lowstand) surrounded by muddy slope facies (sandstone bedset ranges from 5–15 m [16.4–49.2 ft] in thickness); (D) relative location of (A), (B), and (C); (E) general view of the high-frequency depositional sequences on the slope rise to basin-plain realm (active and abandonment phases of the turbidite lobes); and detailed view of the upper (F) and lower (G) abrupt limits of the lobe bedsets (sandy facies related to the lowstand active phase) with the dominantly muddy deposits (abandonment phases) ascribed to the transgressive and highstand systems tracts.**

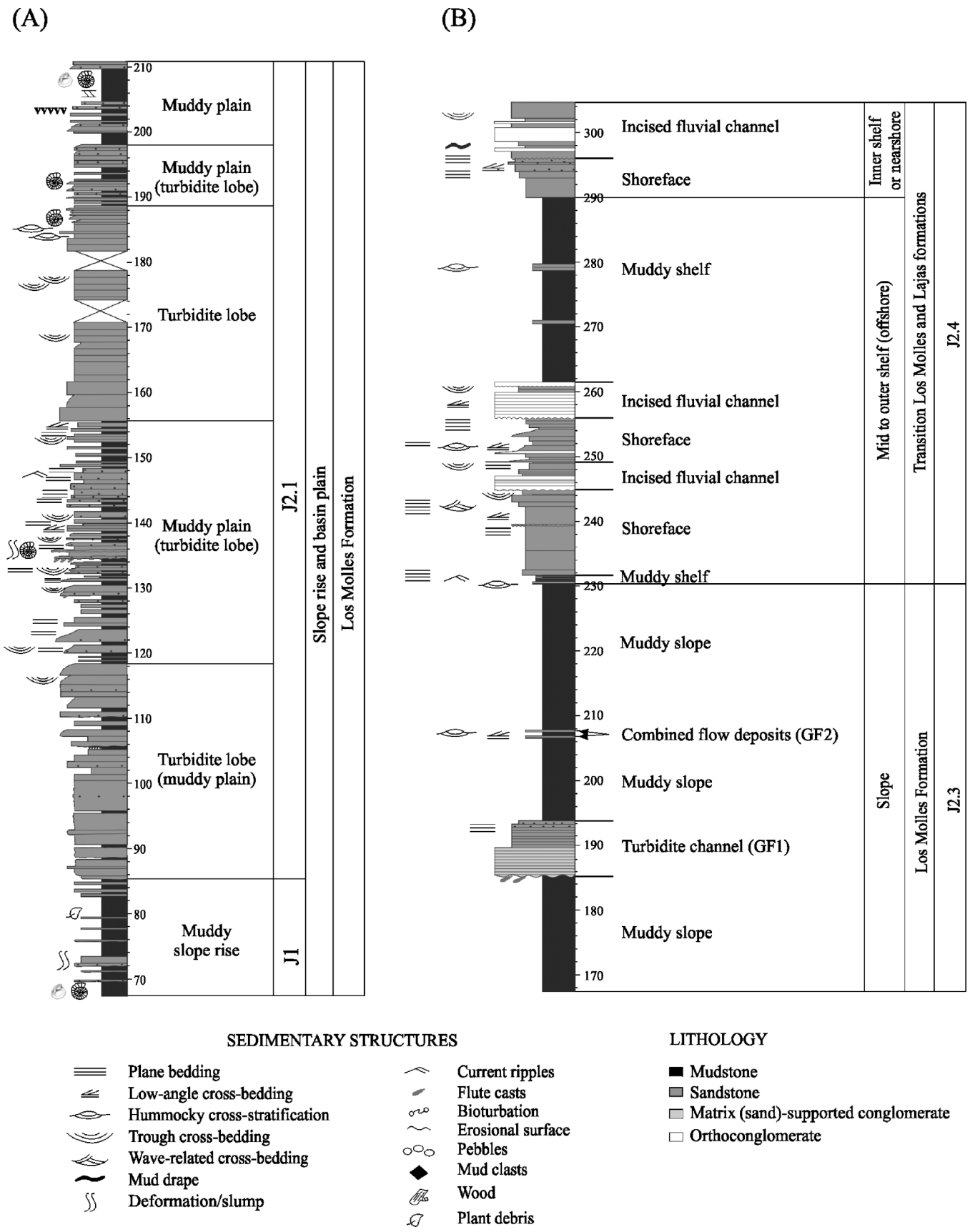

FIGURE 12. Segment of logs 2 (A) and 7 (B). Notice the high-frequency signal modulating the stratigraphic architecture. See log location in Figure 3. Log depths in m. J1 = 2d depositional sequence; J2.1–J2.4 = 3d order depositional sequences.

2004). It is worth noticing that the GF1 facies tract records a downdip change from fluvial facies through gravel- to sand-rich sediment gravity flows. In addition, the fluvial and GF1 systems show parallel paleocurrent trends, a wide range of available grain size (gravel to very fine-grained sand) and prolific plant debris (Figure 8H, I). These data reveal some sort of connection between the fluvial effluents, which delivered sand and gravel to the shelf margin and the GF1 system. However, no support exists in the fluvial deposits to indicate high-density effluents being directly delivered to the slope. On the contrary, the fluvial facies point to braided streams with ordinary gravel and sand bars. The nontorrential character of the fluvial facies associated with the massive and simple (in opposition to complex) nature of the relatively thin gravity flow beds, which lack any internal erosional surface, are evocative of short-lived depletive surges instead of long-lived waxing to waning hyperpycnal currents (Mulder et al., 2003). A brief review of some criteria used elsewhere to recognize hyperpycnal flow deposits in the geological record and their correlation with the GF1 facies is presented in Table 1.

Although these two interpretations (sustained- versus surge-type) seem incompatible at first glance, the specific features that support each one are herein assembled in terms of an indirect fluvial control, that is, surgelike turbidity currents derived from the recurring failure of mouth-bar and delta-front sediments. It is also worth noticing that the clean nature of the sand- and gravel-rich GF1 strata, which display a very fine-grained (or coarser) sandy matrix, indicates that a large part of the fluvial suspended load (silt and clay) was not present in the turbidity currents.

Based on the concepts of Bates (1953) and Wright (1977), and on aforementioned pieces of evidence, it is assumed herein the existence of stratified fluvial effluents with well-defined bed and suspended load that did not enter the sea as inertia flows (truly hyperpycnal flows). Instead, friction-dominated fluvial effluents dumped their bed load (gravel and sand) in the delta front, whereas their suspended load was transported much farther as a hypopycnal plume. This case is similar, but not equal, to the subaerial inflow with an intermediate average density simulated by McLeod et al. (1999). This kind of inflow is strongly influenced by its internal stratification as its sediment-depleted upper layer (richer in finer grained suspended load) becomes a buoyant plume in the receiving basin, whereas its particulate-enriched lower section penetrates the tank as a dense flow. In the case presented herein, this lower sediment-enriched part of the flow could be responsible for the high rate of sediment fallout occurring in the delta front in conjunction with the tractive accumulation of the bed load.

Turbidity Currents Versus Sandy Debris Flows

Massive sandstones are dominant along the entire GF1 system. This fact stresses that other supporting mechanisms instead of fluid turbulence (e.g., fluid escape, hindered settling, and buoyancy) were important factors in the transport of the sediments, as in noncohesive sandy debris flows (Shanmugam, 2000). However, the quite distinct downcurrent grain-size segregation underlines the importance of the fluid turbulence in the long-distance transport of sand and gravel, that is, turbidity currents.

To accommodate such apparently conflicting ideas, bipartite turbidity currents, similar to the density-stratified flows envisaged by many authors (e.g., Kuenen, 1951; Bagnold, 1956; Sanders, 1965; Postma et al., 1988; Mutti et al., 1999), are proposed to equally explain the long (grain-size segregation caused by fluid turbulence)- and the short (ephemeral prefreezing basal inertia flows)-distance transport. The option for using the term ''turbidity currents'' instead of ''noncohesive debris flows'' emphasizes the long-distance mechanism of transport and its resultant facies tract instead of short-distance fluid rheology in the density flow basal layer and its associated massive fabric.

Autogenic and Allogenic Control

Autogenic and allogenic processes control the initiation of turbidity currents. As previously mentioned, turbidity current initiation has been related to high rates of sand and gravel deposition at distributary mouth bars during fluvial floods. This condition has induced the recurrent failure of the delta front and the resulting turbidity currents. However, as already presented, age (Gulisano and Gutierrez Pleimling, 1995) and sedimentologic (facies successions and associations) data about the shelf margin, slope, and basin-plain deposits indicate that GF1 surges were associated with high-frequency (4th to 5th order) lowstand stages and closely related short-lived shelf-margin deltas. This idea implies that an allogenic control, that is, relative sea level fall, is a major factor in promoting the right conditions for turbidity current triggering, that is, high rates of coarse-grained sediments (gravel and sand) being rapidly delivered over a relatively steep slope (lowstand shelf-margin deltas).

Table 1. Positive (yes) and negative (no) correlation between features found in the GF1 deposit and some criteria used elsewhere in terms of hyperpycnal flow identification (from Paim et al., 2008).

Criteria of Hyperpycnal Flow Recognition	*Reference*	*Correlation*
Physical connection between fluvial and turbidite channels at the shelf margin	Plink-Björklund and Steel (2004)	Yes, through small incised channels
Alternating massive and stratified intervals within a single bed	Plink-Björklund and Steel (2004); Bhattacharya and MacEachern (2008); Arcuri and Zavala (2008); Bourget et al. (2008); Vesely (2008)	No. Massive, stratified, or massive with stratified top discrete beds
Coarsening- and thickening-upward trend near the bed base and the reverse above		No. Thin, discrete, and uniform or graded beds
Abundant cut-and-fill features in a single bed		No. Absent
Laterally irregular grain-size changes		No. Absent
Sandy nature and abundant meter-scale beds	Piper and Savoye (1993); Mulder et al. (1998); Kneller and Buckee (2000); Mulder and Alexander (2001); Plink-Björklund and Steel (2004); Arcuri and Zavala (2008); Vesely (2008)	No. Gravel and sand as discrete decimeter-scale-thick beds
Systematically accreted shelf margin with associated turbidites	Plink-Björklund and Steel (2004)	Yes
Abundant continental plant material (leaves, phytodetritus, and coal fragments) in the turbidite beds	Mulder and Alexander (2001); Johnson et al. (2001); Plink-Björklund and Steel (2004)	Yes
Turbidite beds with lamination outlined by phytodetritus	Zavala (2008)	Yes, but more common in GF2 beds
Small amount of slump, slide, and debris-flow deposits	Plink-Björklund and Steel (2004)	No. High proportion of mass and debris-flow facies (GF3 facies)
Downcurrent pinch-out of thick beds of sandy turbidite	Plink-Björklund and Steel (2004)	No (only in GF2 strata)
Rounded and aligned mud clasts		Yes (usually aligned)
Siltstone and claystone-graded couplets with syneresis cracks	Bhattacharya and MacEachern (2008)	No, absent
Low to moderate trace fossil diversity, low bioturbation intensity, normal size ichnotaxa, lack of complex behavior strategies, suspension-feeding organisms	Bhattacharya and MacEachern (2008); Carmona et al. (2008)	Yes, usually low trace fossil diversity and bioturbation intensity and lack of complex behavior strategy

GF1 = first type of gravity flow system.

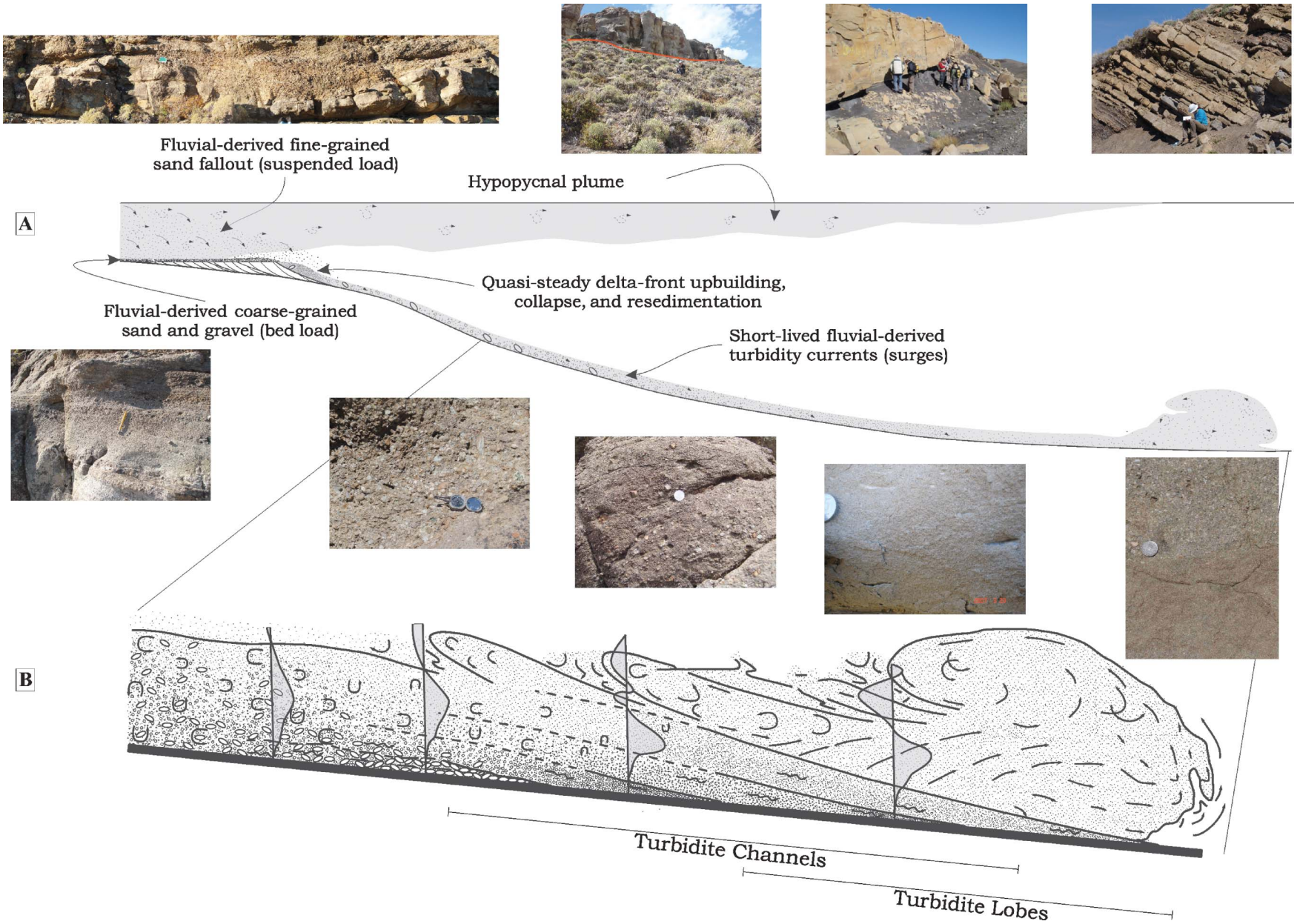

FIGURE 13. Conceptual model of triggering (A), transport with grain segregation (A, B) and deposition (B) of fluvial-derived turbidite surges. The top photographs exemplify the main architectural elements (incised fluvial channels, conglomeratic and sandy turbidite channels, and turbidite lobes), and photographs in the midportion represent the facies tract. Draft shown in panel B was adapted from Postma et al. (1988).

CONCLUDING REMARKS

Fluvial channels at the shelf margin, turbidite channels in the slope, and turbidite lobes and lobe fringes in the slope rise and basin plain represent the GF1 system in terms of architectural elements and physiographic settings. The increase of the gradient at the transition from the outer shelf to the slope enhances gravity flow buildup and entrenchment (turbidite channels in the slope), whereas the opposite alteration at the transition from the slope to the slope rise and basin plain favors large-scale sand deposition through poorly confined channels to widespread turbidite lobes. Multiple point sources related to high-frequency lowstand deltas gave origin to areas of high rates of sedimentation along the shelf margin.

The conceptual model (Figure 13) assumes average fluvial floods producing a quasi-steady delivery of sand and gravel onto continuously aggrading unstable delta-front ramps prograding into ever deeper water. Concurrently, the fluvial suspended load (silt and clay) was dispersed in the basin as hypopycnal plumes. After a brief storage period, debris flows were initiated through episodes of remobilization of the sediments deposited in the distributary mouth bars formed in such unstable areas. Because of flow acceleration along the slope, the gravity flow then builds up, becoming fully turbulent (turbidity current surges) and causing slope erosion. Subsequent deceleration produced a downcurrent grading through consecutive waves of sedimentation. These accumulation pulses were the result of gravity flow transformations driving flow bipartition and ensuing frictional freezing of the lower granular layers composed of ever finer grained sediments (massive strata). The lack of fine-grained particles in the turbidity currents, which results from flow separation at the mouth of the distributary channels, is indicated as the cause of the poor development of the truly tabular lobe beds and extensive lobe fringe facies as flow efficiency is likely to have diminished because of the small amount of clay in the fluid.

ACKNOWLEDGMENTS

This research was supported by Petróleo Brasileiro S. A. (Petrobras) and conducted within the terms of the Agreement for Cooperation and Technical Assistance signed by the Universidade do Vale do Rio dos Sinos (UNISINOS-Brazil) and the Secretaría de Estado de Energía y Minería de la Provincia del Neuquén (Argentina). Special thanks to M. Carminatti, J. E. Faccion, A. J. Andrade Ramos, O. C. Carbone (Petrobras), H. M. Palacios, C. E. Portilla, A. C. Garrido, J. C. Danieli, and Sergio Cocca (Secretaría de Estado de Energía y Minería de la Provincia del Neuquén).

REFERENCES CITED

Arcuri, M., and C. Zavala, 2008, Hyperpycnal shelfal lobes: Some examples from the Lotena and Lajas formations, Neuquén Basin, Argentina (abs.), *in* J. J. Ponce and E. B. Olivero, conveners, Sediment transfer from shelf to deepwater—Revisiting the delivery mechanisms: Conference Proceedings, AAPG Hedberg Research Conference, Ushuaia-Patagonia, Argentina, 4 p.

Bagnold, R. A., 1956, The flow of cohesionless grains in fluids: Philosophical Transactions of the Royal Society of London, Series A: Mathematical and Physical Sciences, v. 249, p. 235–297, doi:10.1098/rsta.1956.0020.

Bates, C. C., 1953, Rational theory of delta formation: AAPG Bulletin, v. 37, p. 2119–2162.

Bhattacharya, J. P., and J. A. MacEachern, 2008, Hyperpycnal rivers and prodeltaic shelves in the Cretaceous seaway of North America (abs.), *in* J. J. Ponce and E. B. Olivero, conveners, Sediment transfer from shelf to deepwater—Revisiting the delivery mechanisms: Conference Proceedings, AAPG Hedberg Research Conference, Ushuaia-Patagonia, Argentina, 4 p.

Bourget, J., S. Zaragosi, T. Mulder, T. Garlan, N. Ellouz-Zimmermann, A. Vantoer, and J.-L. Schneider, 2008, Monsoon-induced hyperpycnal flows recorded in the Gulf of Oman (NW Indian Ocean) (abs.), *in* J. J. Ponce and E. B. Olivero, conveners, Sediment transfer from shelf to deepwater—Revisiting the delivery mechanisms: Conference Proceedings, AAPG Hedberg Research Conference, Ushuaia-Patagonia, Argentina, 2 p.

Burguess, P. M., S. Flint, and S. Johnson, 2000, Sequence stratigraphic interpretation of the turbidítica strata: An example from Jurassic strata of the Neuquén Basin, Argentina: Geological Society of America Bulletin, v. 112, no. 11, p. 1650–1666, doi:10.1130/0016-7606(2000)112<1650:SSIOTS>2.0.CO;2.

Carmona, N., J. J. Ponce, M. I. Lopez-Cabrera, and E. Olivero, 2008, Trace fossil diversity in hyperpycnites: Ethologic implications and comparison to trace fossil in episodic gravity flows (abs.), *in* J. J. Ponce and E. B. Olivero, conveners, Sediment transfer from shelf to deepwater—Revisiting the delivery mechanisms: Conference Proceedings, AAPG Hedberg Research Conference, Ushuaia-Patagonia, Argentina, 2 p.

Fisher, R. V., 1983, Flow transformations in sediment gravity flows: Geology, v. 11, p. 273–274, doi:10.1130/0091-7613(1983)11<273:FTISGF>2.0.CO;2.

Gómez Omil, R. G., J. Schmithalter, A. Cangini, L. Albariño, and A. Corsi, 2002, El Grupo Cuyo en la Dorsal de Huincul: Consideraciones estratigráficas, tectónicas y petroleras, Cuenca Neuquina. Actas 5° Congreso de

Exploración y Desarrollo de Hidrocarburos, Mar del Plata Actas (CD-ROM).

Gradstein, F. M., J. G. Ogg, and A. G. Smith, 2004, A geologic time scale: Cambridge, Cambridge University Press, 589 p.

Gulisano, C. A., and A. R. Gutierrez Pleimling, 1995, Field guide: The Jurassic of the Neuquén Basin, Neuquén Province, Secretaria de Minería de la Nación (Publicación no. 158) y Asociación Geológica Argentina, Serie E (2), 111 p.

Helland-Hansen, W., and J. G. Gjelberg, 1994, Conceptual basis and variability in sequence stratigraphy: A different perspective: Sedimentary Geology, v. 92, p. 31–52, doi:10.1016/0037-0738(94)90053-1.

Heller, P. L., and W. R. Dickinson, 1985, Submarine ramp facies model for delta-fed, sand-rich turbidite systems: AAPG Bulletin, v. 69, no. 6, p. 960–976.

Hunt, D., and M. E. Tucker, 1992, Stranded parasequences and the forced regressive wedge systems tract: Deposition during base-level fall: Sedimentary Geology, v. 81, p. 1–9, doi:10.1016/0037-0738(92)90052-S.

Johnson, K., C. K. Paull, J. P. Barry, and F. P. Chavez, 2001, A decal record of underflows from a coastal river into the deep sea: Geology, v. 29, p. 1019–1022, doi:10.1130/0091-7613(2001)029<1019:ADROUF>2.0.CO;2.

Kneller, B., and C. Buckee, 2000, The structure and fluid mechanics of turbidity currents: A review of some recent studies and their geological implications: Sedimentology, v. 47, no. 1, p. 62–94, doi:10.1046/j.1365-3091.2000.047s1062.x.

Kochhann, K. G. D., S. Baecker-Fauth, G. Fauth, A. S. Silveira, 2009, Aalenian (middle Jurassic) radiolarian fauna from Los Molles Formation, Argentina, and its paleobiogeographic affinities, *in* Congresso Brasileiro de Paleontologia, 2009, Livro de Resumos, v. 1, p. 39.

Kuenen, Ph. H., 1951, Properties of turbidity currents of high density, *in* J. L. Hough, ed., Turbidity currents and the transportation of coarse sediments to deepwater: A symposium: SEPM Special Publication 2, p. 14–33.

Leanza, H. A., and C. A. Hugo, 1997, Hoja Geológica 3969-III, Picún Leufú, provincias del Neuquén y Río Negro, Programa Nacional de Cartas Geológicas de la República Argentina, escala 1: 250.000: Boletín Instituto de Geología y Recursos Naturales, v. 218, p. 1–135.

Legarreta, L., and C. A. Gulisano, 1989, Análisis estratigráfico secuencial de la Cuenca Neuquina (Triásico superior-Terciario inferior, Argentina), *in* G. Chebli and L. Spalletti, eds., Cuencas sedimentarias Argentinas, Instituto Miguel Lillo, Universidad Nacional de Tucumán, San Miguel de Tucumán, Serie Correlación Geológica 6, p. 221–243.

Legarreta, L., and M. A. Uliana, 1991, Jurassic/Cretaceous marine oscillations and geometry of a back-arc basin fill, central Argentine Andes, *in* D. I. M. Mc Donald, ed., Sedimentation, tectonics and eustasy: Oxford, International Association of Sedimentologists Special Publication 12, p. 429–450.

McLeod, P., S. Carey, and R. S. J. Sparks, 1999, Behavior of particle-laden flows into the ocean: Experimental simulation and geological implications: Sedimentology, v. 46, p. 523–536, doi:10.1046/j.1365-3091.1999.00229.x.

Mulder, T., and J. Alexander, 2001, The physical character of subaqueous sedimentary density flows and their deposits: Sedimentology, v. 48, p. 269–299, doi:10.1046/j.1365-3091.2001.00360.x.

Mulder, T., J. P. M. Syvitski, and K. I. Skene, 1998, Modeling of erosion and deposition of turbidity currents generated at river mouths: Journal of Sedimentary Research, v. 68, p. 124–137.

Mulder, T., J. P. M. Syvitski, S. Nigeon, J. C. Faugeres, and B. Savoye, 2003, Marine hyperpycnal flows: Initiation, behavior and related deposits—A review: Marine and Petroleum Geology, v. 20, p. 861–882, doi:10.1016/j.marpetgeo.2003.01.003.

Mutti, E., 1992, Turbidite sandstones San Donato Milanese: Parma, Italy, Azienda Generale Italiana Petroli-Instituto di Geologia, Università di Parma, p. 275.

Mutti, E., R. Tinterri, E. Remacha, N. Mavilla, S. Angela, and L. Fava, 1999, An introduction to the analysis of ancient turbidite basins from an outcrop perspective, AAPG Continuing Education Course Note Series 39, p. 61.

Mutti, E., R. Tinterri, G. Benevelli, D. Di Biase, and G. Cavanna, 2003, Detaic, mixed and turbidite sedimentation of ancient foreland basins: Marine and Petroleum Geology, v. 20, p. 733–755, doi:10.1016/j.marpetgeo.2003.09.001.

Paim, P. S. G., A. S. Silveira, E. L. C. Lavina, U. F. Faccini, H. A. Leanza, J. M. M. Teixeira de Oliveira, and R. S. F. d'Ávila, 2008, High resolution stratigraphy and gravity flow deposits in the Los Molles Formation (Cuyo Group-Jurassic) at La Jardinera region, Neuquén Basin, Argentina: Revista de la Asociación Geológica Argentina, v. 63, no. 4, p. 728–753.

Pierson, T. C., and J. E. Costa, 1987, A rheologic classification of subaerial sediment-water flows, *in* J. E. Costa and G. F. Wieczorek, eds., Debris flows/avalanches: Process, recognition, and mitigation: Geological Society of America Reviews in Engineering Geology, v. VII, p. 1–12.

Piper, D. J. W., and B. Savoye, 1993, Processes of Late Quaternary turbidity current flow and deposition on the Var fan, north-west Mediterranean Sea: Sedimentology, v. 40, p. 557–582, doi:10.1111/j.1365-3091.1993.tb01350.x.

Plink-Björklund, P., and R. J. Steel, 2004, Initiation of turbidity currents: Outcrop evidence for Eocene hyperpycnal flow turbidites: Sedimentary Geology, v. 165, p. 29–52, doi:10.1016/j.sedgeo.2003.10.013.

Postma, G., W. Nemec, and K. L. Kleinspehn, 1988, Large floating clasts in turbidites: A mechanism for their emplacement: Sedimentary Geology, v. 58, p. 47–61, doi:10.1016/0037-0738(88)90005-X.

Ramos, V. A., 1998, Estructura del sector occidental de la Faja Plegada y Corrida del Agrio, Cuenca Neuquina, Argentina, Actas 10° Congreso Latinoamericano Geología y 6° Congreso Nacional Geología Económica 2, Buenos Aires, Argentina, p. 105–110.

Sanders, J. E., 1965, Primary sedimentary structures formed by turbidity currents and related sedimentation mechanisms, *in* G. V. Middleton, ed., Primary sedimentary structures and their hydrodynamic interpretations: SEPM Special Publication 12, p. 192–219.

Shanmugam, G., 2000, 50 Years of the turbidite paradigm (1950s–1990s): Deep-water processes and facies models—A critical perspective: Marine and Petroleum Geology, v. 17, p. 285–342, doi:10.1016/S0264-8172(99)00011-2.

Steel, R. J., J. Crabaugh, M. Schellpeper, D. Mellere, P. Plink-Björklund, J. Deibert, and T. Loeseth, 2000, Deltas vs. river on the shelf edge: Their relative contributions to the growth of the shelf-margin and basin-floor fans (Barreminan to Eocene, Spitsbergen), *in* P. Weimer, ed., Deep-water reservoirs of the world: Gulf Coast Section-Society of Sedimentary Geology (GC-SEPM) Research Conference (CD-ROM), p. 981–1009.

Van Wagoner, J. C., H. W. Posamentier, R. M. Mitchum Jr., P. R. Vail, J. F. Sarg, T. S. Loutit, and J. Hardenbol, 1988, An overview of the fundamentals of sequence stratigraphy and key definitions, *in* C. K. Wilgus, B. S. Hastings, C. G. St. C. Kendall, H. W. Posamentier, C. A. Ross, and J. C. Van Wagoner, eds., Sea level changes: An integrated approach: SEPM Special Publication 42, p. 40–45.

Van Wagoner, J. C., R. M. Mitchum Jr., K. M. Campion, and V. D. Rahmanian, 1990, Siliciclastic sequence stratigraphy in well logs, cores, and outcrops: Concepts for high-resolution correlation of time and facies: AAPG Methods in Exploration Series 50, 10, p. 2150–2175.

Vergani, G. D., 2005, Control estructural de la sedimentación jurásica (Grupo Cuyo) en la Dorsal de Huincul, Cuenca Neuquina, Argentina, Modelo de falla lístrica rampa-plano, invertida: Boletín de Informaciones Petroleras, v. 1, no. 1, p. 32–42.

Vergani, G. D., A. J. Tankard, H. J. Belotti, and H. J. Welsink, 1995, Tectonic evolution and paleogeography of the Neuquén Basin, Argentina, *in* A. J. Tankard, R. Suárez Soruco, and H. J. Welsink, eds., Memoir petroleum basins of South America: AAPG Bulletin, v. 62, p. 383–402.

Verzi, H., M. F. Raggio, and M. Suarez, 2005, Volume interpretation of a turbidite system, Los Molles Formation, Neuquén Basin, Argentina, *in* D. Soubies, M. Arteaga, and F. Fantín, eds., La Sísmica de Reflexión, más allá de la Imagen Estructural, Buenos Aires, Instituto Argentino del Petroleo y del Gas, 2005, p. 219–226.

Vesely, F. F., 2008, Subaqueous sandstones deposited by melt water-fed density flows in a late Paleozoic glaciomarine succession, eastern Paraná Basin, Brazil (abs.), *in* J. J. Ponce and E. B. Olivero, conveners, Sediment transfer from shelf to deepwater—Revisiting the delivery mechanisms: Conference Proceedings, AAPG Hedberg Research Conference, Ushuaia-Patagonia, Argentina, 1 p.

Vicente, J. C., 2005, Dynamic paleogeography of the Jurassic Andean Basin: Pattern of regression and general considerations of the main features: Revista de la Asociación Geológica Argentina, v. 61, no. 3, p. 408–437.

Wright, L. D., 1977, Sediment transport and deposition at river mouths: A synthesis: Geological Society of America Bulletin, v. 88, p. 857–868, doi:10.1130/0016-7606(1977)88<857:STADAR>2.0.CO;2.

Zavala, C., 1993, Estratigrafía y análisis de facies de la Formación Lajas (Jurásico medio) en el sector sur occidental de la Cuenca Neuquina. Provincia del Neuquén, República Argentina, Tesis Doctoral Departamento de Geología, Universidad Nacional del Sur, Bahía Blanca, Buenos Aires, Argentina, 260 p.

Zavala, C., 2008, Toward a genetic facies tract for the analysis of hyperpycnal deposits (abs.), *in* J. J. Ponce and E. B. Olivero, conveners, Sediment transfer from shelf to deepwater—Revisiting the delivery mechanisms: Conference Proceedings, AAPG Hedberg Research Conference, Ushuaia-Patagonia, Argentina, 3 p.

The Vaca Muerta–Quintuco system (Tithonian–Valanginian) in the Neuquén Basin, Argentina: A view from the outcrops in the Chos Malal fold and thrust belt

Diego A. Kietzmann, Alfredo L. Ambrosio, Julieta Suriano, María Susana Alonso, Federico González Tomassini, Gabriela Depine, and David Repol

ABSTRACT

The Vaca Muerta–Quintuco system (uppermost lower Tithonian–lower Valanginian) is a thick shallowing-upward sedimentary cycle consisting of dark bituminous shales, marlstones, limestones, and sandstones, cropping out in the Neuquén Basin, west–central Argentina. This paper analyzes three outcrop sections in Chos Malal area, northem Neuquén province. Detailed facies analysis allows us to differentiate six facies associations, representing basinal to proximal outer ramp facies of a homoclinal carbonate ramp system (Vaca Muerta Formation) and basinal to shoreface facies of a mixed carbonate–siliciclastic shelf system (Quintuco Formation), prograding westward from the eastern margin of the basin. Two sequence hierarchies were recognized: 5 composite depositional sequences (third order) and 15 high-frequency sequences (fourth order). Fluctuations in organic matter content within the Vaca Muerta Formation suggest a relationship with depositional sequences, finding the highest values associated with transgressive systems tract, whereas the transition to the Quintuco Formation shows a strong decrease in total organic carbon. The x-ray diffraction studies show an increase of clay minerals and quartz in the transgressive systems tract of the Vaca Muerta Formation and an increase in the content of calcite in highstand systems tracts. This pattern is reversed in the Quintuco Formation. Our sequence stratigraphic approach contributes to the understanding of the

Copyright ©2016. The American Association of Petroleum Geologists. All rights reserved.

Manuscript received June 12, 2015; provisional acceptance November 18, 2015; revised manuscript received November 21, 2015; final acceptance February 10, 2016.
DOI:10.1306/02101615121

AUTHORS

DIEGO A. KIETZMANN ~ *Instituto de Estudios Andinos Don Pablo Groeber, Departamento de Ciencias Geológicas, Facultad de Ciencias Exactas y Naturales, Universidad de Buenos Aires, Consejo Nacional de Investigaciones Científicas y Técnicas, Ciudad Universitaria, Pabellón II, Intendente Güiraldes 2160, C1428EHA Ciudad Autónoma de Buenos Aires, Argentina; diegokietzmann@gl.fcen.uba.ar*

Diego A. Kietzmann received his B.S. degree and Ph.D. in geological sciences from the University of Buenos Aires, where he is a teacher assistant. His research focuses on sedimentology, cyclostratigraphy, and sequence stratigraphy of the Jurassic–Cretaceous boundary in the Neuquén Basin. He has authored different papers on sedimentology, stratigraphy, paleontology, and taphonomy. He works as an assistant researcher at the National Council of Scientific and Technical Research of Argentina.

ALFREDO L. AMBROSIO ~ *Geoandina SRL, Ciudad de la Paz 3257, Piso 6° D, (C1429ACG) Ciudad Autónoma de Buenos Aires, Argentina; alfredo.ambrosio@geo-andina.com*

Alfredo L. Ambrosio received his B.S. degree in geological sciences from the University of Buenos Aires. He has worked as a consultant since 2006 and currently leads the geosciences consulting firm Geoandina SRL, and has conducted several works on unconventional plays of Argentina. His main topics of interest are sedimentology, sedimentary environments, and stratigraphy.

JULIETA SURIANO ~ *Instituto de Geociencias Básicas, Ambientales y Aplicadas, Departamento de Ciencias Geológicas, Facultad de Ciencias Exactas y Naturales, Universidad de Buenos Aires, Ciudad Universitaria, Pabellón II, Intendente Güiraldes 2160, C1428EHA Ciudad Autónoma de Buenos Aires, Argentina; julietasuriano@yahoo.com.ar*

Julieta Suriano received her B.S. degree and Ph.D. in geological sciences from the University of Buenos Aires, where she is a teacher assistant of sedimentology and paleoenvironment

courses. She works as a researcher for the University of Buenos Aires, focused on depositional systems of Tertiary foreland basins of Argentina.

María Susana Alonso ~ *Instituto de Geociencias Básicas, Ambientales y Aplicadas, Departamento de Ciencias Geológicas, Facultad de Ciencias Exactas y Naturales, Universidad de Buenos Aires, Consejo Nacional de Investigaciones Científicas y Técnicas, Ciudad Universitaria, Pabellón II, Intendente Güiraldes 2160, C1428EHA Ciudad Autónoma de Buenos Aires, Argentina; sualonso@gl.fcen.uba.ar*

Susana Alonso received her B.S. degree and Ph.D. in geological sciences from the University of Buenos Aires, where she is a teacher assistant. She works as a research assistant at the National Council of Science and Technology, focused on depositional systems of Tertiary foreland basins of Argentina. She is devoted to studies on mineralogy, sedimentary petrology, x-ray diffraction, and scanning electron microscopy techniques applied to clay mineralogy.

Federico González Tomassini ~ *Departamento de Ciencias Geológicas, Facultad de Ciencias Exactas y Naturales, Universidad de Buenos Aires, Ciudad Universitaria, Pabellón II, Intendente Güiraldes 2160, C1428EHA Ciudad Autónoma de Buenos Aires, Argentina; federicogonzalez@live.com.ar*

Federico González Tomassini received a B.S. degree in geological sciences from the University of Buenos Aires. He works as a geologist on unconventional resources for an oil company. His main areas of study and interest are sedimentology, stratigraphy, and sedimentary environments with emphasis on unconventional plays.

Gabriela Depine ~ *Shell Exploration and Production Company, 200 N Dairy Ashford Rd, Houston, Texas 77079; gabriela.depine@shell.com*

Gabriela Depine received a B.S. degree in geological sciences from the University of Buenos Aires and a Ph.D. from Cornell University. She worked on the new ventures team evaluating unconventional plays in the Appalachian Basin, northeastern United States

relationship between organic matter, clay minerals, facies, stacking pattern, and relative sea level changes in this exceptional shale oil and shale gas unconventional reservoir. This study may be helpful for a better postulate of petrophysical and geomechanical models for unconventional exploration.

INTRODUCTION

The Vaca Muerta–Quintuco system (uppermost lower Tithonian–lower Valanginian) is a thick shallowing-upward sedimentary cycle, known as the lower Mendoza mesosequence, consisting of dark bituminous shales (Fl), marlstones (Mrh), limestones, and bioclastic sandstones, cropping out in the Neuquén Basin, west–central Argentina (Mitchum and Uliana, 1985; Legarreta and Gulisano, 1989; Legarreta and Uliana, 1991, 1996). This cycle began with a rapid marine transgression from the Panthalassic Ocean during early Tithonian times, probably related to an increase in seafloor spreading rates, and a relatively high eustatic sea level stand, which gave rise to a global Late Jurassic ocean anoxic event (OAE) (Moore et al., 1992; Herbin et al., 1995; Nozaki et al., 2013).

During this OAE the organic-rich deposits of the Vaca Muerta Formation were deposited. This unit is well known as a world-class source rock, as well as for its unconventional resource potential, with high average total organic carbon (TOC) levels, moderate depth, and overpressured conditions. This formation is considered the most effective source rock interval in the Neuquén Basin, containing from 2% up to 12% TOC (Uliana and Legarreta, 1993; Cruz et al., 2002; Legarreta et al., 2005). Conversely, the Quintuco Formation is relatively depleted in organic matter and represents the shallower facies of the system, which progrades from the eastern margin of the basin (Carozzi et al., 1993; Uliana and Legarreta, 1993).

Early regional lithostratigraphical reviews were conducted by Leanza (1973) and Leanza et al. (1977). A modern stratigraphic analysis was published later by Gulisano et al. (1984), Mitchum and Uliana (1985), and Legarreta and Gulisano (1989), who established the sequence stratigraphic framework and interpreted the Vaca Muerta Formation as basinal and slope facies.

Sedimentological studies were carried out in the southernmost part of the basin by Spalletti et al. (2000) and Scasso et al. (2005). In the central part of the basin, only isolated studies were published, including those of Spalletti et al. (1999), who describe the Tithonian herpetofauna in Yesera del Tromen area, and Leanza et al. (2003), Spalletti et al. (2008), and Kietzmann and Vennari (2013), who described slope facies coming from the western margin. In the northern part of the basin (Mendoza sector), detailed sedimentological studies were carried out by

Kietzmann et al. (2008, 2011), Kietzmann and Palma (2009, 2011), and Kietzmann et al. (2014c), who conducted an exhaustive sedimentologic and sequence stratigraphic analysis integrating nine sedimentary sections of the lower Mendoza mesosequence.

The aim of this study is to improve the understanding of the paleoenvironmental evolution of the Vaca Muerta and Quintuco Formations in the Chos Malal fold and thrust belt integrating sedimentological and geochemical outcrop information of three localities (Yesera del Tromen, Puerta Curaco, and Cerro Caicayén sections; Figure 1). This area is of special relevance for this unconventional reservoir because of the proximity of oil–gas fields to the east (e.g., El Trapial block; González Tomassini et al., 2014).

GEOLOGICAL SETTING

The Neuquén Basin was a retroarc basin developed in Mesozoic times in the Pacific margin of South America. Different tectonic regimes exerted a first-order control in basin development and sedimentary evolution: An extensional regime was established during the Late Triassic–Early Jurassic and was characterized by a series of narrow, isolated depocenters controlled by large transcurrent fault systems filled mainly with continental deposits of the Precuyo mesosequence (Legarreta and Uliana, 1991, 1996) (Figure 2).

Thermal subsidence with localized tectonic events characterized the Early Jurassic to Late Cretaceous interval (Vergani et al., 1995). Depocenters were filled by continental and marine siliciclastic, carbonate, and evaporitic sediments (Cuyo, Lotena, and Mendoza Groups).

Marine sequences developed throughout the basin during the Late Jurassic–Early Cretaceous are included in the Mendoza Group or Mendoza mesosequence (Figure 2). Legarreta and Gulisano (1989) divided the Mendoza mesosequence into three main shallowing-upward sedimentary cycles: the lower Mendoza mesosequence (early Tithonian–early Valanginian), the middle Mendoza mesosequence (late Valanginian–early Hauterivian), and the upper Mendoza mesosequence (late Hauterivian–early Barremian).

The lower Mendoza mesosequence includes a Tithonian–Valanginian broad shallowing-upward sedimentary cycle (Figure 2). In the central part of the Neuquén Basin the lower Mendoza mesosequence shows a general progradational sigmoidal geometry, reaching 2000 m (6561 ft) in thickness (Legarreta and Gulisano, 1989) (Figure 3). It starts with the continental deposits of the Tordillo Formation (Kimmeridgian–lowermost lower Tithonian?), which underlay the marine basinal deposits of the Vaca Muerta Formation (uppermost lower Tithonian–upper

and Canada, as well as on the Latin America onshore exploration team at the Shell Oil Company.

DAVID REPOL ~ *Shell Exploration and Production Company, 200 N Dairy Ashford Rd, Houston, Texas 77079; david.repol@shell.com*

David Repol received a B.S. degree in geological sciences from the University of La Plata and a Ph.D. from the University of Calgary in structural geology and tectonics in the southern extent of the Agrio Fold and Thrust Belt, Neuquén Basin, Argentina. He works as senior geologist for the Shell Oil Company.

ACKNOWLEDGMENTS

We thank Shell Exploration and Production Company and Geoandina SRL for authorizing the publication of this study, as well as Sebastian Paulin (Universidad de Buenos Aires) for his assistance in field work. We were honored to have the reviews of Hector Leanza, Roberto Scasso, and Hernan Reijenstein, whose comments and suggestions have substantially improved the original manuscript.

Berriasian to lower Valanginian). To the east the basinal facies change to shoreface deposits of the Quintuco Formation (upper Tithonian–lower Valanginian), to the sabkha deposits of the Loma Montosa Formation (lower Valanginian) and to the continental deposits of the Puesto Gonzalez Formation (lower Valanginian), forming a mixed carbonate–siliciclastic depositional system (Mitchum and Uliana, 1985; Carozzi et al., 1993) (Figure 3). Westward, the Vaca Muerta Formation includes upper Tithonian–lower Berriasian slope facies known as Huncal Member (Leanza et al., 2003; Spalletti et al., 2008) and shifts to shallow marine volcanic deposits in the Chilean territory (Charrier, 1985).

The Upper Jurassic–Lower Cretaceous sequence stratigraphic framework has been based on low-resolution seismic data (Mitchum and Uliana, 1985). These authors defined, in their enormous work, nine depositional sequences (A to I) for the lower Tithonian–lower Valanginian interval and correlated them to third-order depositional sequences defined by Haq et al. (1987, 1988) (see Figure 2). Legarreta and Gulisano (1989) included this set of depositional sequences (Mi_1 to Mi_9) within the lower Mendoza mesosequence. The main difference between these authors is that sequence Mi_1 of Legarreta and Gulisano (1989) includes the Tordillo Formation and the basal part of the Vaca Muerta Formation, whereas the last depositional sequence from the Vaca Muerta–Quintuco system is separated from the Mulichinco Formation by the Intra-Valanginian unconformity or its correlative conformity (Gulisano et al., 1984; Leanza, 2009; Schwarz and Buatois, 2012).

A compressive deformational regime was established during the Late Cretaceous and continued throughout the Cenozoic, although alternating with extensional events (Ramos, 2010). This Andean deformation resulted in the development of a series of north–south-oriented fold and thrust belts, where excellent outcrops of the Mesozoic successions are exposed.

AGE AND TEMPORAL FRAMEWORK

Upper Jurassic–Lower Cretaceous biostratigraphy in the Neuquén Basin is well defined on the basis of ammonite biozones (cf. Leanza and Hugo, 1977; Riccardi et al., 2011) (Figure 2D). Ammonite data from the studied sedimentary sections point out that the Vaca Muerta Formation has an early Tithonian–early Valanginian age (*Virgatosphinctes mendozanus* to lowermost part of the *Neocomites wichmanni* zones), whereas the Quintuco Formation age is early Valanginian (uppermost part of the *Neocomites wichmanni* and *Lissonia riveroi* zones) (Leanza and Hugo, 1977; Mitchum and Uliana, 1985; Aguirre-Urreta et al., 1999). Cyclostratigraphic data published by Kietzmann et al. (2015) allowed them to apply a floating orbital scale and obtain a minimum duration for ammonite biozones. This orbital calibration is consistent with biostratigraphic scheme of Riccardi et al. (2011), which places the Jurassic–Cretaceous boundary within the *Substeueroceras koeneni* ammonite zone.

METHODOLOGY

Detailed sedimentological sections of the Vaca Muerta and Quintuco Formations were measured and described in three localities of the central Neuquén Basin, along the Chos Malal fold and thrust belts. They include the Yesera del Tromen, Puerta Curaco, and Cerro Caicayén sections (Figure 1). Carbonate and siliciclastic facies were analyzed considering bed geometry, lithology, sedimentary structures, fossil content, and taphonomic features. Facies were supplemented by petrographic observations based on 150 thin sections. We used the facies code proposed by Kietzmann et al. (2014c) for carbonate lithologies, consisting of three letters. The first letter refers to texture and lithology (using italic for carbonates), the second letter refers to main grain components (in subscript), and the third letter refers to sedimentary structures (Tables 1, 2). Divisions of sedimentary environments within the carbonate ramp (Vaca Muerta Formation) are based on Burchette and Wright (1992). Divisions of sedimentary environments within the mixed siliciclastic–carbonate shelf (Quintuco Formation) are based on Walker and Plint (1992).

Mineralogical analyses of Fl and Mrh were performed using x-ray diffraction in 21 representative samples from the Puerta Curaco section and 20 samples from the Yesera Tromen section. The analysis was performed on the whole rock sample and in the less than 2 μm fraction, using standard methods

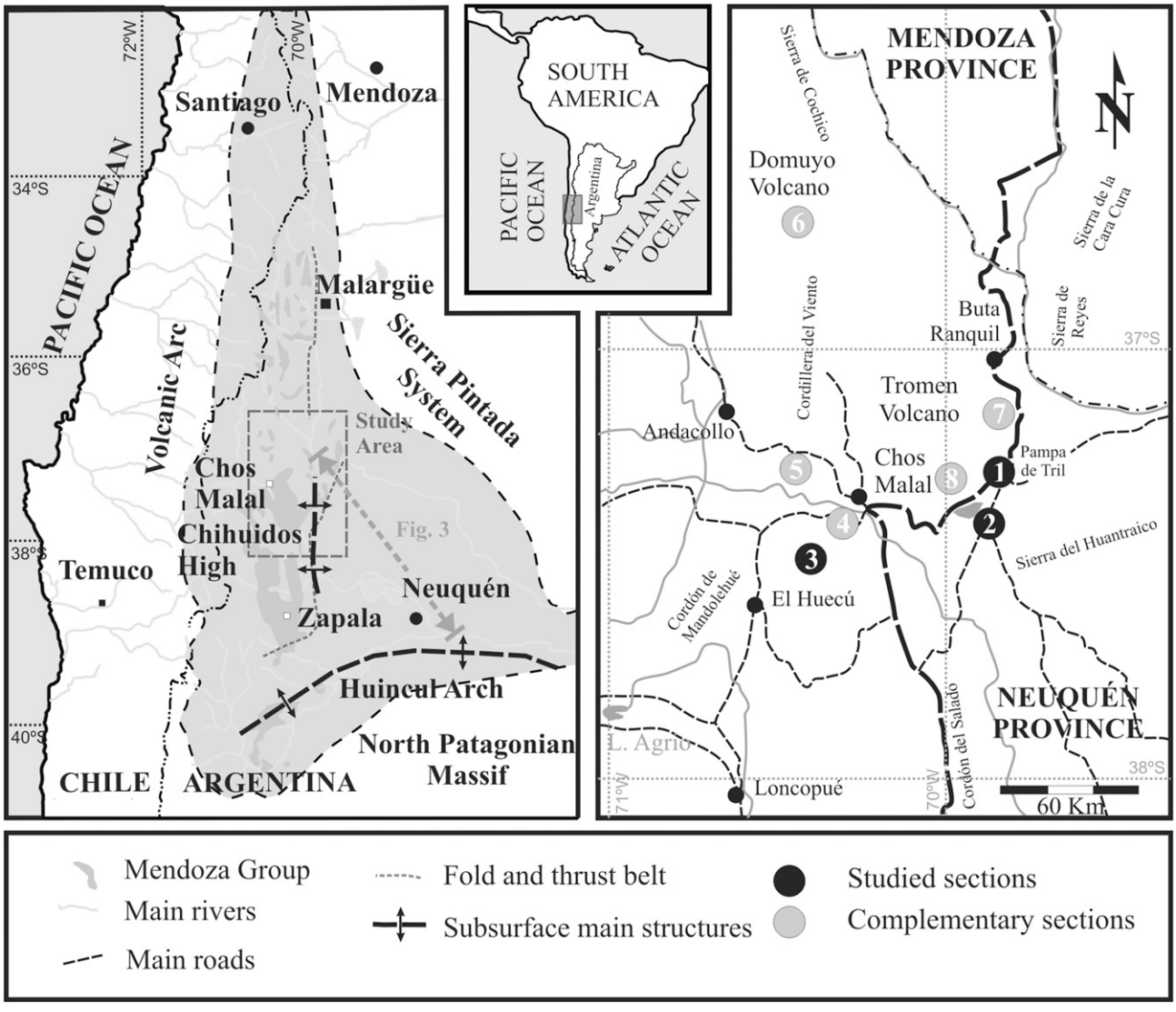

Figure 1. Location map of the Neuquén Basin showing main geological features and studied localities: (1) Yesera del Tromen, (2) Puerta Curaco, (3) Cerro Caicayén, (4) Rahueco, (5) Chacay Melehue, (6) Domuyo, (7) Mina La Carrascosa, and (8) Barranca de los Loros.

of clay mineral analysis for a semiqualitative overview of whole-rock and clay mineralogy (Biscaye, 1965). Rock-Eval pyrolysis methods were used to estimate TOC and the source and thermal maturity of organic matter. These procedures were performed at GeoLab Sur (Geochemical Laboratory, Buenos Aires).

Sequence stratigraphic framework is based on the identification of flooding surfaces. In fact, the position of the Vaca Muerta Formation in the sedimentary system does not allow the recognition of sequence boundaries as subaerial exposure surfaces. Nonetheless, stacking pattern and facies tendencies are used to recognize sequence stratigraphic trends, where flooding surfaces can be interpreted as correlative conformities of subaerial exposure surfaces, forming coplanar or composite surfaces (e.g., Embry and Johannessen, 1992).

FACIES ANALYSIS

The Vaca Muerta and Quintuco Formations consist of different facies, which were combined into five facies associations representing two different systems: a carbonate ramp depositional system (facies associations 1–3) and a mixed siliciclastic–carbonate shelf setting (facies associations 4–6).

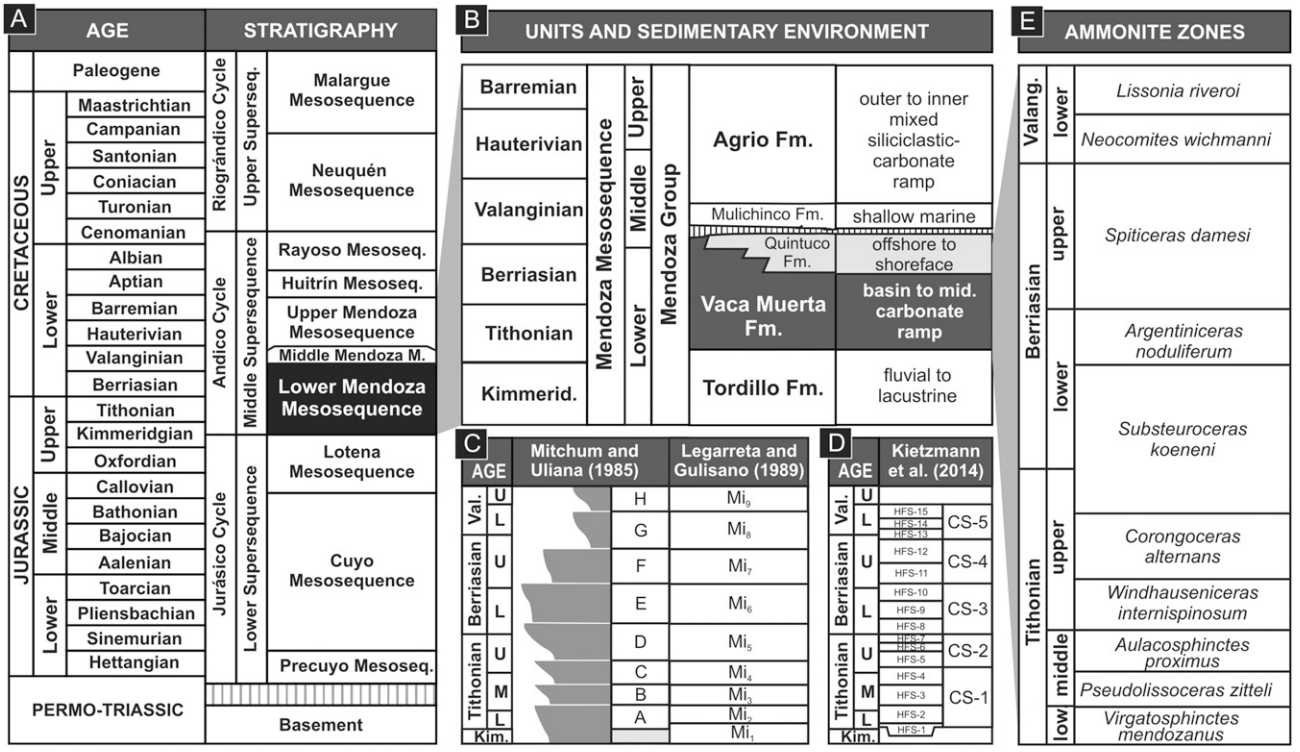

Figure 2. (A) Stratigraphic chart for the Neuquén Basin (after Legarreta and Gulisano, 1989). (B) Lithostratigraphic subdivision and environmental interpretations of the Mendoza mesosequence in Neuquén Province. (C) Depositional sequences identified by Mitchum and Uliana (1985) and Legarreta and Gulisano (1989) through seismic stratigraphy studies. (D) Depositional sequences identified by Kietzmann et al. (2014c) in outcrops from the southern Mendoza area of the Neuquén Basin. (E) Tithonian–Valanginian biostratigraphic subdivision in Neuquén Basin. Ammonite biozones after Riccardi et al. (2011). CS = composite depositional sequences; Fm. = Formation; HFS = high-frequency depositional sequences; Kim. = Kimmeridgian; Kimmerid. = Kimmeridgian; L = lower; M = middle; M. = mesosequence; Mesoseq. = mesosequence; Superseq. = supersequence; U = upper; Val. = Valanginian; Valang. = Valanginian.

Facies Association 1: Basin to Distal Outer Ramp

Description

Facies association 1 (FA-1) is dominated by dark gray to black, well-laminated Fl, and Mrh. Laminated packstones (P_ih), radiolaritic wackestones (W_rh), planar microbialites (B_ml), and tuffs (Tm and Tg) are subordinated (Figures 4, 5). The shale/limestone ratio is approximately 9:1. This facies association is characteristic in the basal part of the Vaca Muerta Formation (lower–middle Tithonian), as well as in the upper Tithonian, in the Yesera del Tromen and Puerta Curaco sections. These intervals are the richest in organic matter content, and are therefore the main Vaca Muerta Formation hydrocarbon source levels (TOC ~4%–5%).

Marlstones are dark gray to black, well laminated, and range in thickness from 10 to 30 cm (3.94–11.81 in.). They contain some disarticulated infaunal bivalves and fish scales. Thin sections of concretions contained therein show the same textural characteristics of packstone or wackestone facies. Some samples show irregular and discontinuous microbial-induced laminae.

Laminated packstones (P_ih) are dark gray to black in color, ranging in thickness from 10 to 20 cm (3.94–7.87 in.). Bases are sharp and planar. They are composed of well-sorted, subangular to angular, fine to medium sand-sized micritic clasts, which correspond to W_rh or microbialites intraclasts. Bioclasts in P_ih are mainly represented by thin-shelled oysters, fish scales, reworked infaunal bivalves, ammonites, radiolarian, epistominid foraminifera, *Saccocoma* microcrinoids, calpionellids, and calcispheres. Fossils contained in the beds are filled by pellets and distributed chaotically or parallel to the lamination. These beds are particularly rich in

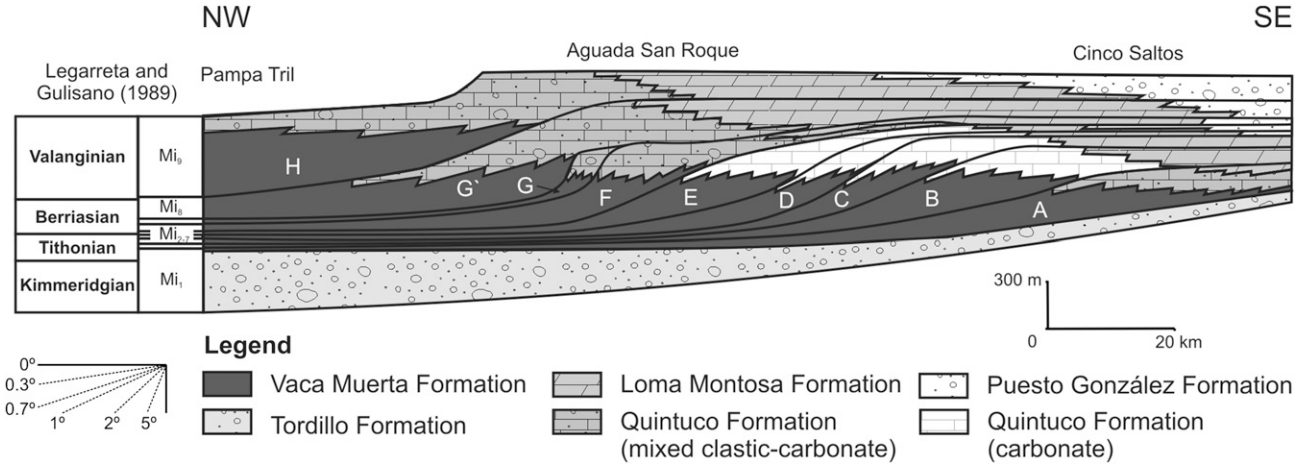

Figure 3. Schematic sections of the lower Mendoza mesosequence in a southeast–northwest (SE–NW) transect in central Neuquén Basin, showing a general sigmoidal or progradational geometry (modified from Mitchum and Uliana, 1985). It is important to note that the Tithoniana–Berriasian carbonate Quintuco facies are not present in the study area, where appears only the Berriasian–Valanginian mixed siliciclastic/carbonate Quintuco Formation (Quintuco sensu stricto of Leanza et al., 2011).

vertebrate remains, including turtles, ichthyosaurs, and crocodiles.

Radiolaritic wackestones are well laminated. They contain abundant radiolarians, including spumellarians and nassellarians with a ratio of 0.5:1. Other bioclasts include ammonites, aptychi, and reworked infaunal bivalves.

Tuff deposits (Tm and Tg) are replaced by carbonate, shown as tabular carbonates beds of crystalline appearance, are gray to greenish in color, with sharp and planar contacts, and have a thickness of 2–15 cm (0.78–5.9 in.). At macroscopic scale, they consist of a crystalline calcite mosaic, with crystals of several millimeters to 2 cm (0.78 in.). They are composed of abundant glass shards and pumiceous fragments in layers 2 to 5 mm (0.08–0.2 in.) thick, commonly with intralaminar inverse gradation. They also contain load cast structures and flute marks.

Interpretation

Sedimentation occurred mainly from suspension. However, presence of reworked bioclastic remains in P_ih and Mrh, such as infaunal bivalves, ammonites, and microcrinoids, suggests shallow-water sediment input, probably associated with storm-generated turbidity flows (Monaco, 1992; Molina et al., 1997; Kietzmann and Palma, 2009). Inverse grading, as well as load cast and flute marks, suggests that tuffs were probably deposited from noncohesive low-density turbidity currents (Whitham, 1993).

Microbialite beds indicate periods of low sedimentation rate, allowing proliferation of microbial mats in a relative low-energy setting. The dark color, probably related to high organic matter content and absence of bottom-dwelling organisms, suggests elevated organic productivity or good preservation and sedimentation in a steady restricted marine environment with poorly oxygenated bottom waters (e.g., Savrda and Bottjer, 1986). The Spumellaria/Nassellaria ratio suggests distal open marine waters, but ratio values near 0.5 also suggest an oxygen-depleted environment (Kiessling, 1996). Similar interpretation arises from the abundance of ammonites, microfossils, and vertebrate remains, indicating an anoxic to dysoxic environment. Facies association 1 is interpreted as deposited below the storm wave base in a poorly oxygenated basinal to distal outer ramp setting.

Facies Association 2: Outer Ramp

Description

Facies association 2 (FA-2) is similar to FA-1 but contains a higher proportion of carbonate beds (marl/limestone ratio ~3:1). Low-energy facies are represented by laminated W_rh and laminated Mrh, interbedded with peloidal or intraclastic P_ih (P_{pi}h), which represent higher-energy facies (Figure 4). Inverse graded lapillite (Lg) and tuff (Tg) deposits are also common. Subordinately appear thin graded bioclastic

Table 1. Facies Distribution in the Vaca Muerta Formation/Quintuco Formation

		Facies Association					
Facies	Facies Code	1: Basin to Outer Ramp	2: Outer Ramp	3: Proximal Outer Ramp	4: Basin to Slope	5: Offshore to Lower Transition Zone	6: Upper Transition Zone to Lower Shoreface
High energy							
Laminated packstones	P_ih	R	MR	R			
Laminated grainstones	G_ih		S	R			
Bioclastic rudstones/grainstones	RG_bm		S				
Low angle stratified grainstones	G_il			MR			
HCS grainstones	$G_i$hcs			MR			
Horizontal laminated sandstones	Sh				S	MR	
Current ripple laminated sandstones	Sr				S		MR
Wave ripple laminated sandstones	Srw						MR
HCS sanstones	Shcs					MR	MR
Low energy							
Microbial bindstones	B_ml	R	S	S			
Laminated wackestones	W_rh-W_eh		R				
Dolomitized wackestones	W_D					S	
Bioclastic marlstones	Mr_bh	MR	MR	MR			
Laminated marlstones	Mrh	MR	MR	MR			
Laminated shales	Fl	MR			MR	MR	MR
Volcaniclastic							
Lapillites	Lm/g			S			
Laminated tuffs	Tm/g	S	R				
HCS tuffs	Thcs			MR			

Abbreviations: HCS = hummocky cross-stratification; MR = most representative facies; R = representative facies; S = subordinate facies.

rudstones–floatstones (RF_bg) and B_ml. This facies association is well represented in the Tithonian and Berriasian of the Yesera del Tromen and Puerta Curaco sections (Vaca Muerta Formation).

The Mrh and W_rh are similar to those described for FA-1. Marlstones have high organic matter content, reaching values of 2%–3%. Concretions in Mrh show the same textural characteristics of packstone facies in thin sections.

Laminated packstones are composed of well-sorted pellets or of rounded to angular medium sand-sized micritic clasts. Bioclasts include reworked infaunal bivalves, serpulids, gastropods, echinoderms, and ammonites. Some globose ammonites (e.g., *Aspidoceras* sp.) are placed with a subvertical arrangement. Bioturbation is rare, although at certain levels, some *Planolites*, *Paleophycus*, and *Thalassinoides* tubes have been identified.

Lapillite deposits (Lg) are 5–10 cm (1.97–3.94 in.) in thickness, massive or graded, with sharp and planar bases. They are composed of coarse sand to granule-size pumiceous fragments. Replaced tuff deposits occur as tabular carbonate beds of crystalline appearance, with sharp and planar contacts. The tops commonly present load deformation structures, whereas the bases preserve locally concentric microfaulting structures (*gleitreppen*; see Schwarz, 1975) and molds of ripple structures. Thickness ranges from 5 to 25 cm (1.97–9.84 in.).

The RF_bm are single-event or multievent concentrations of bivalves, gastropods, ammonites, and foraminifers. Beds have sharp erosive bases, ranging in thickness from 2 to 10 cm (0.79–3.94 in.). The bivalves are disarticulated and highly fragmented; distribution of bioclasts is random or arranged relatively concordant to the bedding plane or stacked.

Table 2. Facies Terminology and Codes for the Vaca Muerta Formation/Quintuco Formation

Facies Type	Facies Name	Facies Code
Low-energy facies		
Volcaniclastic	Laminated or massive argillaceous replaced tuffs	T_ah/m
	Laminated or massive carbonate replaced tuffs	T_ch/m
	Massive or inverse graded lapillites	Lm/g
Carbonate	Planar microbial binstones	B_ml
	Bioturbated bioclastic wackestones	W_bb
	Laminated bioclastic wackestones	W_bh
	Laminated radiolaritic wackestones	W_rh
	Laminates radiolaritic mudstones	M_rh
	Dolomitized wackestones	W_D
Epiclastic–mixed	Laminated marlstones (matrix-supported)	Mrh(m)
	Laminated shales (matrix-supported)	Fl(m)
High-energy facies		
Epiclastic–mixed	Laminated shales (grain-supported)	Fl(g)
	Laminated marlstones (grain-supported)	Mrh(g)
	Horizontal laminated sandstones	Sh
	Current ripple laminated sandstones	Sr
	Wave ripple laminated sandstones	Srw
	Hummocky cross-stratified sandstones	Shcs
Carbonate	Laminated intraclastic packstones	P_ih
	Laminated intraclastic or peloidal packstones	P_{ip}h
	Laminated intraclastic or peloidal grainstones	G_{ip}h
	Ripple laminated intraclastic or peloidal grainstones	G_{ip}r
	Low-angle stratified intraclastic grainstones	G_il
	Hummocky cross-stratified intraclastic or peloidal grainstones	G_{ip}hcs
	Massive or graded bioclastic rudstones-grainstones	RG_bm/g
Volcaniclastic	Inverse graded carbonate replaced tuffs	T_cg
	Hummocky cross-stratified carbonate replaced tuffs	$T_c$hcs

Facies codes for carbonate and volcaniclastic lithologies according to Kietzmann et al. (2014c), consisting of three letters: first letter refers to texture and lithology (using italic for carbonates), second letter refers to main grain components (in subscript), and third letter refers to sedimentary structures.

Interpretation

Fair weather sedimentation is represented by Mrh and laminated W_rh, originated mostly from deposition by settling of fine-grained suspended material, including planktonic microorganisms and carbonate mud. The Spumellaria/Nassellaria ratio suggests distal open marine waters (Kiessling, 1996). On the contrary, higher-energy facies suggest deposition linked to storms. The abundance of micritic intraclasts, as well as disarticulated and fragmented fossils, indicates that these sediments come from reworking of the seafloor during strong storms or storm-induced rip currents. In fact, intraclastic packstones show similar textures to the lenticular F1 fabric described by Schieber et al. (2010), which is associated with intermittent erosion processes and transport by bottom currents. Likewise, vertical arrangement of aspidoceratid ammonites suggests maintenance of the vertical position by fragmocons floating until burial and could have paleobathymetric implications, indicating a maximum depth of 50 m (164 ft) (Raup, 1973). However, this arrangement may be also caused by reorientation and displacement by currents before the final burial, when they had negative buoyancy (Kietzmann and Palma, 2009). Trace fossils are related to the *Cruziana* ichnofacies, characterizing low-energy environments, colonized by deposit- and suspension-feeders and also by mobile carnivores (MacEachern et al., 2008).

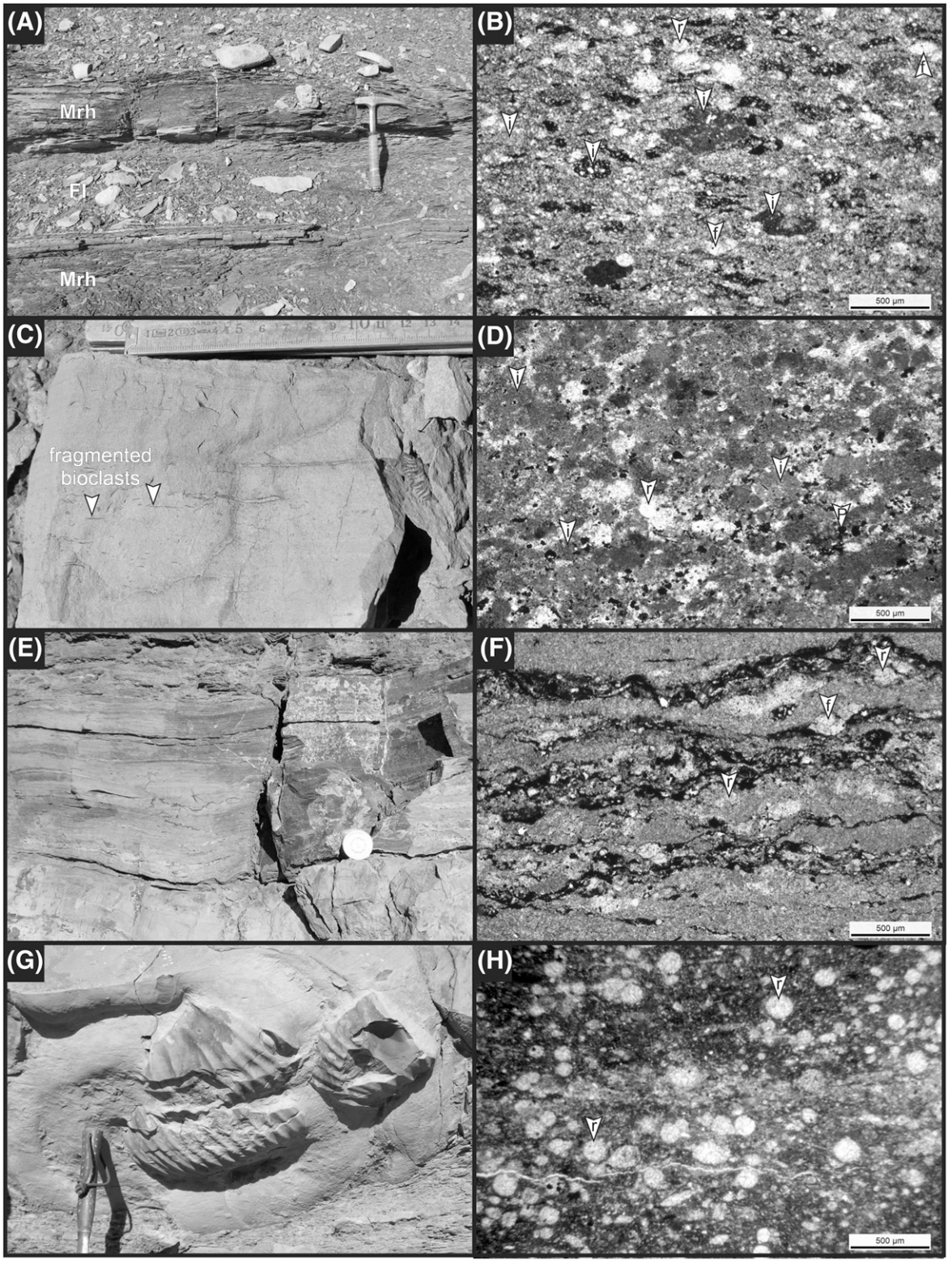

Figure 4. Most typical facies and microfacies of the Vaca Muerta Formation. (A, B) Laminated marlstones (Mrh) and shale (Fl) alternation and intraclastic grain-suported fabric observed in thin section of concretions contained in this facies. (C, D) Laminated intraclastic packstone/grainstone. (E, F) Laminated planar microbialites. (G, H) Laminated radiolaritic wackestone, showing an ammonite fragment of *Himalayites andinus* of late Tithonian age (H. A. Leanza, 2015, personal communication). f = epistominid forams; i = intraclast; P = pyrite; r = radiolarians.

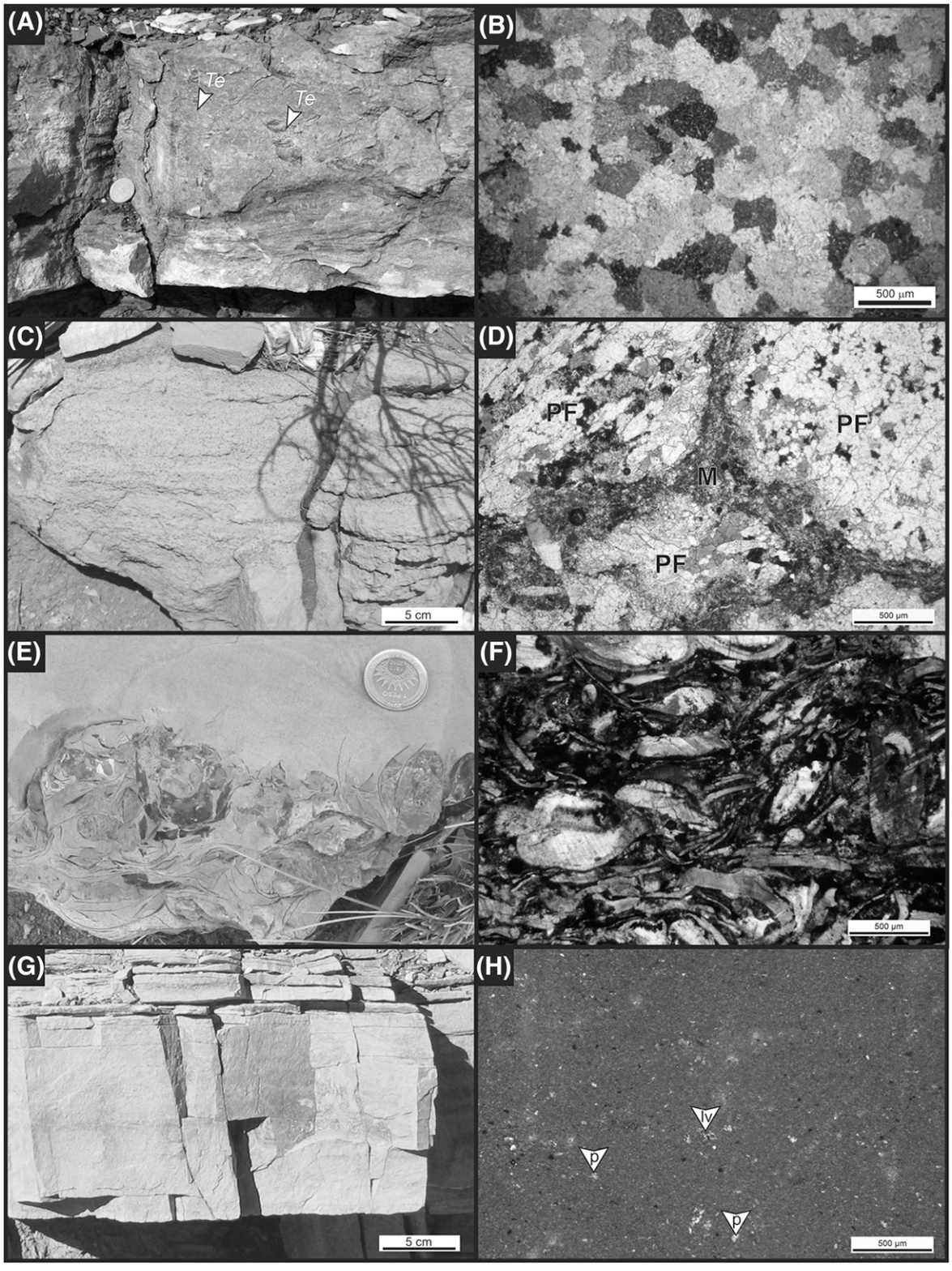

Figure 5. Most typical facies and microfacies of the Vaca Muerta Formation. (A, B) Hummocky cross-stratified tuffs, replaced and cemented by calcite. In thin section this facies is characterized by abundant shards in a mosaic of poikilotopic calcite. (C, D) Laminated and graded lapillite, replaced and cemented by calcite. (E, F) Massive to graded bioclastic rudstones/floatstone, composed of bivalve fragments, ammonites, gastropods, and echinoderms. (G, H) Laminated wackestone. lv = volcanic lithic clasts; M = peloidal micritic matrix; p = plagioclase clasts; PF = pumice fragments; *Te* = *Teichichnus* sp.

Presence of disarticulated and highly fragmented bivalves in thin graded bioclastic rudstones suggests an origin such as storm-generated turbidity-like flows (e.g., Monaco, 1992). Inverse graded lapillite deposits are probably deposited from floating rafts of fallout pumice from the Andean volcanic arc, whereas tuffs were probably deposited from noncohesive low-density turbidity flows (Kietzmann et al., 2014b, c). The preservation of load structures on bed tops responds to the basic mechanism of load cast formation, where gravity acts on beds with different density. In fact, tuffs were probably less dense than Mrh because of their high porosity and low compaction and coherence. Facies association 2 is interpreted as deposited below the storm wave base in a poorly oxygenated bioclastic outer ramp setting.

Facies Association 3: Proximal Outer Ramp

Description

Facies association 3 (FA-3) is represented by an alternation of low-energy facies, comprising laminated Mrh, and high-energy facies, including hummocky cross-stratified grainstones (G_{pi}hcs), hummocky cross-stratified tuffs (Thcs), Tg, laminated grainstone–packstones (GP_ih), and RF_bg (Figures 4, 5). Occasional B_ml and Lg beds (Figure 4) also occur. The Mrh/limestone ratio is approximately 3:1. This facies association is present in Yesera del Tromen and Puerta Curaco sections (Vaca Muerta Formation).

Marlstones, Tg, and Lg are similar to those of previous facies associations. Marlstones are rich in organic matter (2%–3%).

The GP_ih are brown to gray and occur in beds with thickness ranging from approximately 10 to 40 cm (3.94–15.75 in.). Bases are sharp and sometimes irregular. Fossil content include ammonites, articulated and disarticulated bivalves, and gastropods, which are chaotically distributed. Intraclasts are micritic, well sorted, and subangular to angular and range from fine to medium sand size. In places, this facies contains reworked concretions.

The G_{pi}hcs form tabular beds 30–60 cm (11.81–23.6 in.) thick with erosive bases. They consists of peloids or micritic intraclasts and form slightly discordant sets of undulating layers with inclinations less than 15° and laterally can result in horizontal lamination. Wavelengths range from 25 to 150 cm (9.84–59 in.). The Thcs are replaced by carbonates. They are similar to those described in previous facies associations but with a wavelength of 20–30 cm (7.87–11.81 in.). Bioturbation is rare and is represented by *Planolites* and *Teichichnus*.

The RF_bg consist of simple concentrations rich in oysters and other bivalves, gastropods, ammonites, and epistominid foraminifera. Bioclasts are chaotically distributed.

The B_ml form laterally continuous beds of 10–15 cm (3.94–5.9 in.) in thickness but also appear as discrete laminae (1–3 cm [0.39–1.18 in.]) between GP_ih. They show a conspicuous horizontal to subhorizontal lamination of submillimeter- to millimeter-scale micritic laminae rich in organic matter and fine-grained micritic wackestones or packstones with foraminifers, radiolarians, and calcispheres. Some laminae are also rich in microbialite intraclasts and storm wave–induced structures.

The Lg deposits are centimeter-thick, with sharp and planar bases. They are composed of coarse sand to granule-size pumiceous fragments and crustacean microcoprolites.

Interpretation

The G_{pi}hcs and Thcs are interpreted as deposits of accretionary hummock deposits generated from storm-related oscillatory flows with an insignificant unidirectional component. Dimensions and geometries of these structures suggest deposition near the storm wave base (e.g., Dumas and Arnott, 2006). The RF_bg represent distal tempestites originated by turbidity-like gravity flows (Monaco, 1992; Molina et al., 1997).

Intraclastic grain-supported textures in GP_ih and laminated Mrh suggest intermittent erosion processes and transport from bottom currents (e.g., Schieber et al., 2010), probably related to storm-induced currents and/or suspension plumes (e.g., Wright et al., 2001).

Microbialite beds indicate periods of low sedimentation rate, allowing proliferation of microbial mats in a relative low-energy setting, episodically affected by storm-related high-energy events (Schieber, 1998).

The Tg deposits were probably deposited from noncohesive low-density turbidities, whereas massive

and inverse Lg facies deposited probably from floating rafts of air fall pumice (Whitham, 1993).

Low-diversity trace fossil associations of *Teichichnus* and *Planolites* suggests colonization of storm beds by a community of opportunistic organisms in a post-event, high-stress, physically controlled environment (MacEachern et al., 2008). Facies association 3 is interpreted as deposited close to the storm wave base (but probably below because of the presence of deposits with rare hummocky cross-stratification [HCS]) in a moderately oxygenated proximal outer ramp.

Facies Association 4: Basin to Slope

Description

Facies association 4 (FA-4) is represented by black Fl, with intercalations of very fine horizontal laminated sandstones (Sh) and ripple laminated sandstones (Sr) (Figure 6). The shale/sandstone ratio is approximately 6:1 to approximately 9:1. This facies association was recognized in the upper part of the Cerro Caicayén section (Quintuco Formation) and in the upper part of the Chacay Melehue section.

Shales are black to gray and occur in 0.4–15 m (1.32–49.2 ft) thick beds. Fossils are almost absent, with the exception of some ammonite impressions and scarce fragmented bivalve shells. Thin sections of this facies show abundant spumellarian radiolaria and abundant glass shards.

The Sh and Sr are volcanic litharenites. They are tabular in geometry and show thickness of 2–10 cm (0.78–3.94 in.). Litharenites and Fl form coarsening packages of 2 m (6.6 ft), with a Fl/sandstone ratio close to 2:1 on the top of the cycle. These commonly show scars and slumps with westward vergence (Figure 6).

Interpretation

The prevalence of thick intervals of black Fl and the absence of oscillatory structures suggest that sedimentation in FA-4 occurred below the normal storm wave base level. The intercalations of very fine Sh and Sr are interpreted as low-concentration turbidity current deposits. Likewise, the presence of synsedimentary scars and slumps suggests the existence of a slope (Stow and Piper, 1974). Low participation of skeletal particles and trace fossils suggests a distal environment, low-energy, poorly oxygenated setting. This interpretation is consistent with the abundance of Spumellaria over Nassellaria radiolarians, indicating a distal marine depositional environment (Kiessling, 1996). The FA-4 is interpreted as a fine-grained prograding basin slope setting.

Facies Association 5: Ofshore to Lower Transition Zone

Description

Facies association 5 (FA-5) is represented by thick intervals of laminated Fl with intercalations of very fine Sh and thin bedded Shcs organized into coarsening-upward successions up to 10 m (32.8 ft) thick, with subordinate massive bioclastic rudstones, laminated mudstones (*M*h), and dolomitized wackestones (Figure 6) as subordinate lithofacies. The shale/sandstone ratio is approximately 6:1. This facies association (Quintuco Formation) was recognized in the upper part of the Yesera del Tromen, Puerta Curaco, Barranca de Los Loros, and Mina La Carrascosa sections.

Shales are black to gray and occur in beds with thickness ranging from approximately 0.4 to 5 m (1.31–16.4 ft). They contain some ammonite shells, reworked but articulated bivalves (*Eriphyla* and *Cucullaea*), and fish scales. Thin sections show that these facies consists of fine to middle sand-sized intraclasts with abundant radiolaria or *M*h with microbial laminae. Organic matter content ranges between 0.1% and 1.4%, with a mean value of 0.3%.

The Sh and thin bedded Shcs are feldarenites and volcanic litharenites. They are tabular in geometry and show thickness of 2–10 cm (0.79–3.94 in.). The Shcs occur as thin beds with slightly erosive bases, forming anisotropic undulated layers with inclinations less than 15° and wavelengths ranging from 15 to 25 cm (5.9–9.84 in.), which laterally can result in horizontal lamination. Bioturbation in these facies is represented by scarce *Planolites* and *Paleophycus* tubes.

Dolomitized beds are horizontally laminated and laterally continuous. In some cases they develop as layers with brecciated dolomite septarian concretions. In thin section this facies is characterized by an equigranular mosaic of anhedral crystals, containing isolated terrigenous clasts and calcispheres.

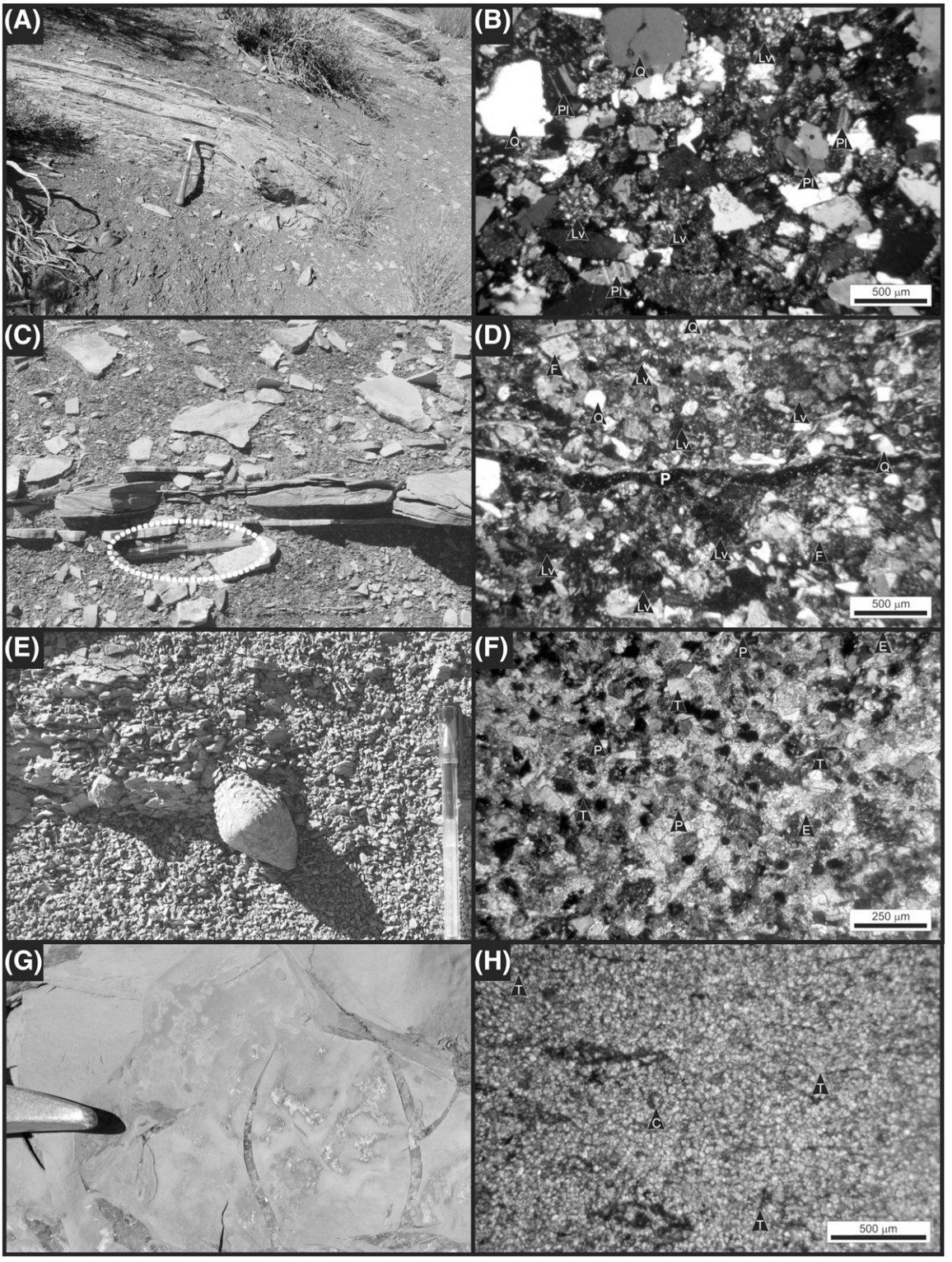

Figure 6. Most typical facies and microfacies of the Quintuco Formation. (A, B) Slumped horizontal and ripple laminated sandstones in facies association 4 (basin to slope), composed of quartz (Q), plagioclase (Pl), and volcanic lithic clasts (Lv). (C, D) Horizontal and ripple laminated sandstones in facies association 3 (offshore to transition zone), composed of Q, Pl, feldespars (F), and Lv. (E, F) Horizontal laminated bioclastic sandstones in facies association 6 (upper transition zone to lower shoreface), with bivalves in life position, composed of terrigenous (T), peloids (P), and echinoderm fragments (E). (G, H) Dolomitized wackestones in facies association 4 (basin to slope), with T clasts and calcispheres (C).

Interpretation

The *M*h with microbially induced laminae observed in laminated Fl are interpreted as fallout of suspended fine material accumulated below fair weather wave base during fair weather periods. Mud intraclasts originated from the erosion of semiconsolidated mud substrate and were transported as bedload of silt- to sand-sized grains, suggesting intermittent erosion processes and transport from bottom currents probably related to storms (Schieber et al., 2010). Similar deposits have been described recently by Plint et al. (2012) for the Cenomanian–Turonian Kaskapau Formation in the Western Interior Basin of North America.

The Sh and thin bedded Shcs reflect the waning flow deposits of storm-generated currents (Cheel and Leckie, 1993). The presence of articulated bivalves suggests reworking from storm episodes.

Dolomitized beds should be studied in detail to understand their origin, as well as their correlation in time with facies of the Loma Montosa Formation. The presence of septarian concretions could indicate an early diagenetic origin (Pratt, 2001). Dolomitization could be formed by replacement of original carbonates caused by the oxidation of organic matter in the sulfate reduction zone (Garrison and Graham, 1984; Meister et al., 2007).

The dark color of Fl and the absence of bioturbation suggest oxygen-deficient conditions; nonetheless, the low TOC indicates that preservation was reduced, probably related to storm activity. The FA-5 is interpreted as deposited close to the storm wave base, in an offshore to transition zone setting.

Facies Association 6: Upper Transition Zone to Lower Shoreface

Description

Facies association 6 (FA-6) consists of laminated Fl interstratified with bioclastic Sh, Shcs, and wave and current ripple laminated sandstones (Srw and Src) organized into coarsening-upward successions up to 7 m (23 ft) thick (Figure 6). The shale/sandstone ratio is approximately 3:1. This facies association was only recognized in the upper part of the Yesera del Tromen and Puerta Curaco sections (Quintuco Formation). This facies association is characterized by low organic matter content (0.1% to 0.5%).

Shales are gray and occur in beds with thickness ranging from approximately 0.15 to 1 m (0.49–3.3 ft). They contain some ammonite shells, reworked articulated bivalves (*Eriphyla* sp., *Cucullaea* sp., *Panopaea* sp., *Steinmanella* sp., and oysters), and fish scales. Thin section observations show that these facies consists of fine to middle sand-sized intraclasts with abundant radiolaria.

The Sh, Shcs, and Src and Srw are feldarenites and volcanic litharenites. They are tabular in geometry and show thickness of 5–40 cm (1.97–15.75 in.), forming coarsening-upward cycles. Trace fossils in these facies are represented by *Planolites*, *Thalassinoides*, *Teichichnus*, and *Gyrochorte*.

Interpretation

As in previous facies associations, grain-supported mud intraclasts, in laminated Fl, are interpreted to be the result of erosion of semiconsolidated mud substrate and transported as silt- to sand-sized grains in bedload (Schieber et al., 2010). The HCS can be interpreted as deposited by waning combined oscillatory and unidirectional flows created by periodic storm events (Dott and Bourgeois, 1982; Dumas and Arnott, 2006), whereas Sh and Src and Srw represent deposition during fair weather stages, above the fair weather wave base.

The association of *Planolites*, *Thalassinoides*, *Teichichnus*, and *Gyrochorte* is indicative of the *Cruziana* ichnofacies, which suggests colonization of storm beds by a community of opportunistic organisms in a postevent, high-stress physically controlled environment (MacEachern et al., 2008). The FA-6 is interpreted as deposited in a well-oxygenated low-energy shoreface to upper transition zone setting.

Sedimentary Environment

According to our facies analysis the Vaca Muerta and Quintuco Formations in Chos Malal area represent two different systems: a Tithonian–Berriasian carbonate ramp depositional system and a Valanginian mixed siliciclastic–carbonate shelf setting (Figures 7, 8). The carbonate ramp depositional system in the study area is primarily related to deposits of the Vaca Muerta Formation and is composed of facies interpreted as basin to distal outer ramp (FA-1), outer ramp (FA-2), and proximal outer ramp (FA-3). The Cerro Caicayén section, as well as the complementary

section in Chacay Melehue, is in a basinal to outer ramp setting throughout the Tithonian–Berriasian interval. It is also important to keep in mind that slope deposits with slump deposits and gravity flows with east–northeast paleodirections intercalate laterally in the Rahueco and Domuyo sections (see Spalletti et al., 2008; Kietzmann and Vennari, 2008, 2013; Kietzmann et al., 2014c), suggesting that this area represents the deepest axis of the basin. In subsurface the carbonate ramp system is represented by shallow-water carbonates of the Quintuco Formation (e.g., Mitchum and Uliana, 1985; Carozzi et al., 1993).

The Yesera del Tromen and Puerta Curaco sections show shallowing sequences from basin to distal middle ramp facies, which pass laterally to outer ramp facies in the Barranca de los Loros and Mina La Carrascosa complementary sections. The high content of volcaniclastic material indicates that the activity of the volcanic arc was intense. The tuffs replaced by carbonate are interpreted as turbidity flows in FA-1 and FA-2 and as tempestites in FA-3, as well as lapillite fallout deposits, suggesting that the pyroclastic material was deposited associated to hydrodynamic processes within the depositional system.

The storm wave base level interface, even if it marks a change in facies, does not produce a substantial change in the stacking pattern or lithofacial proportions with respect to outer ramp deposits. This suggests a low-energy environment with development of moderate-intensity storms, probably related to reduced fetch of the Neuquén Basin. In fact, the storm wave base has been estimated as relatively shallow, approximately 50- to 70-m depth (164–229 ft) (Kietzmann and Palma, 2011).

Carbonate ramp geometry of the Vaca Muerta Formation was probably related to strong offshore transport, as well as the lack of frame-building organisms capable of building steep platform margins, suggesting the dominance of physical accommodation and hydrodynamic processes on a low-gradient ramp or eventually distally steepened ramp setting with a high amount of carbonate exported from the inner ramp (Bádenas et al., 2003; Pomar and Kendall, 2008; Kietzmann et al., 2014c).

The mixed siliciclastic–carbonate shelf depositional system is related to deposits of the Quintuco Formation, which is composed of deposits interpreted as basin to slope (FA-4), offshore to lower transition

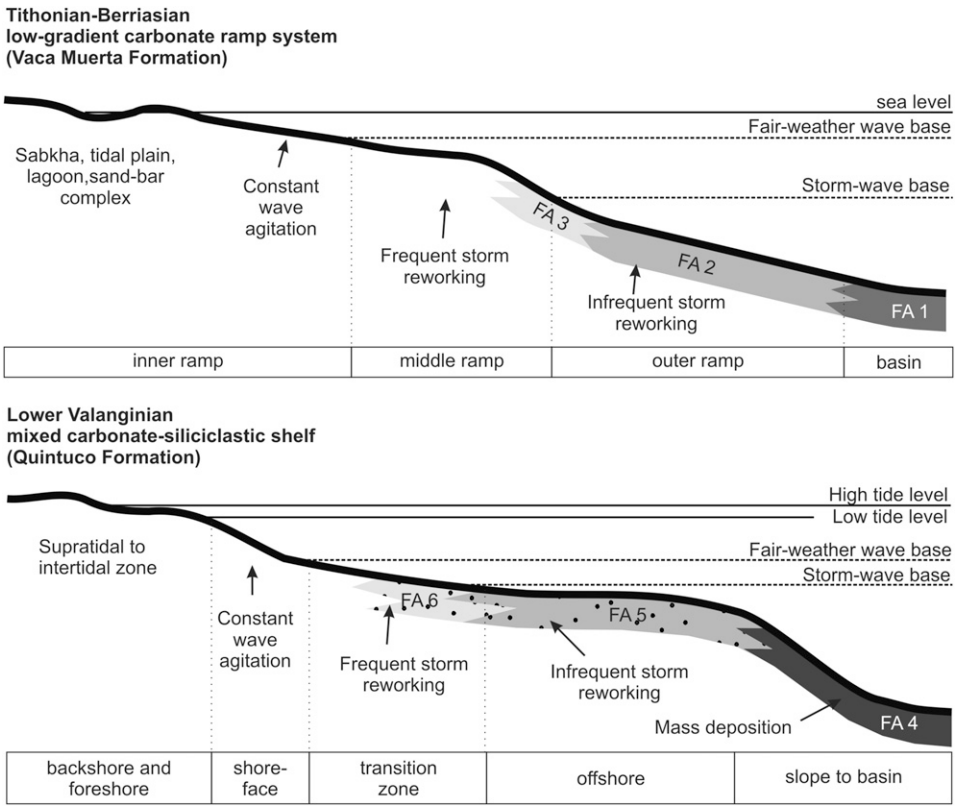

Figure 7. Facies association (FA) distribution within depositional models interpreted for the Vaca Muerta and Quintuco Formations.

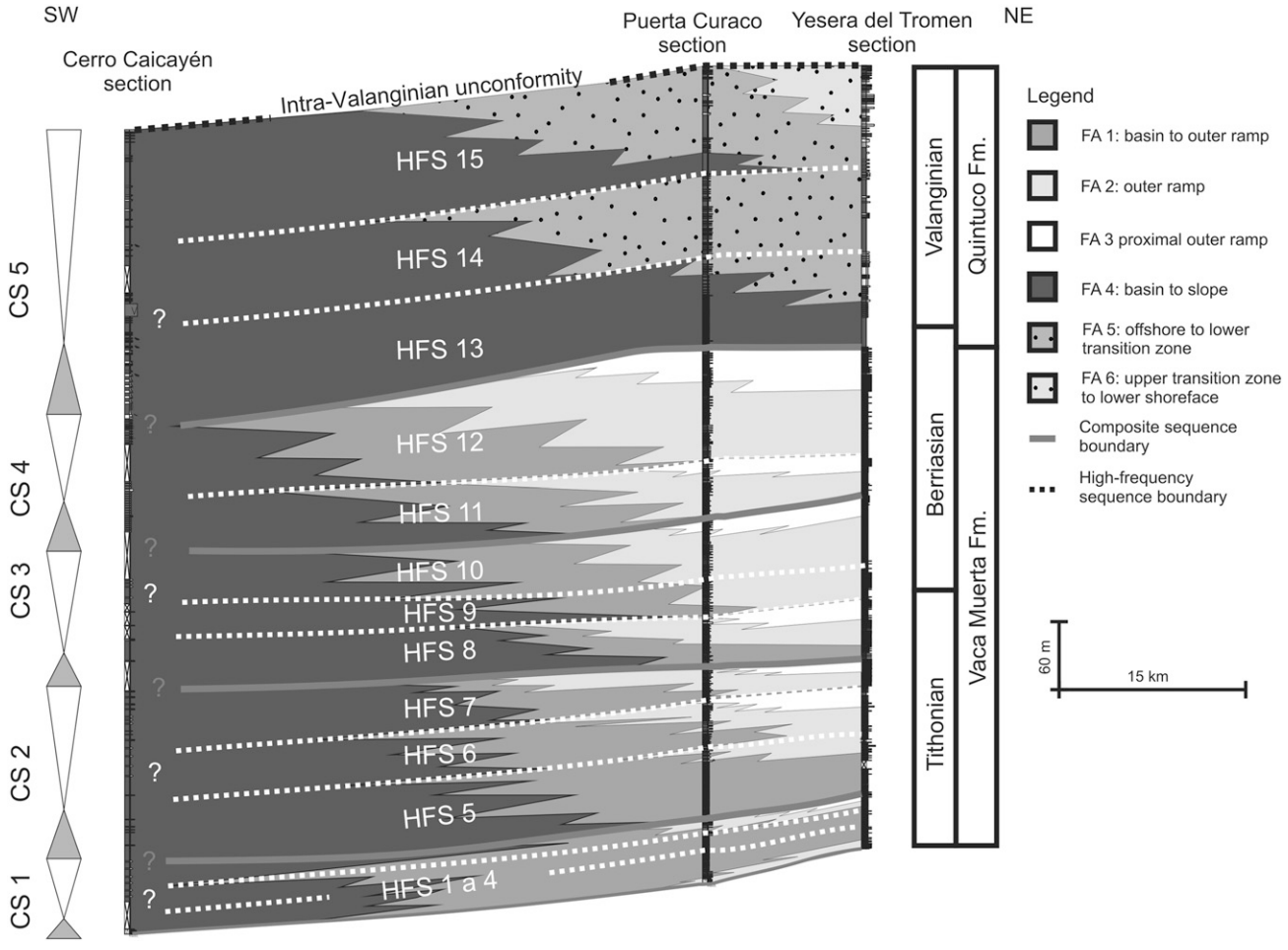

Figure 8. Studied sections of the Vaca Muerta and Quintuco Formations (Fm.) in the Chos Malal fold and thrust belt, northern Neuquén province, showing correlation of facies associations (FA), transgressive surfaces, high-frequency depositional sequences (HFS), composite depositional sequences (CS), and their transgressive systems tracts (gray triangle) and regressive systems tracts (white triangle). NE = northeast; SW = southwest.

zone (FA-5), and upper transition zone to lower shoreface (FA-6).

In the deepest axis of the basin (Cerro Caicayén and Chacay Melehue sections) the uppermost Berriasian and lowermost Valanginian contain basinal to slope deposits, showing westward paleocurrents. In contrast, the Yesera del Tromen and Puerta Curaco sections show shallowing sequences from offshore to lower shoreface facies, which pass laterally from offshore to lower transition zone facies in the Barranca de los Loros and Mina La Carrascosa complementary sections.

The Quintuco depositional system is characterized by a significantly higher input of siliciclastic material, marking a significant change in paleoenvironment. In contrast to distal positions, such as the study area, subsurface seismic sections (Mitchum and Uliana, 1985; Leanza et al., 2011; Reijenstein et al., 2014, 2015) show a general progradational pattern, with an initial strong progradational low clinoform angle (<1°) system, which changes to an aggradational–progradational system with highest clinoform angles (2°–3°) around the Jurassic–Cretaceous boundary. Toward the Valanginian the system becomes clastic and reduces again the clinoform angle (~1°).

As in the Vaca Muerta Formation, the transition from offshore to lower shoreface is almost undetectable, suggesting a relatively shallow and low-energy environment. The lack of a strong development of lower shoreface facies suggests that the environment was influenced by storm waves, but fair weather conditions dominated (e.g., Myrow, 1992).

SEQUENCE STRATIGRAPHY

In this paper we present a new sequence stratigraphic framework for the Vaca Muerta–Quintuco Formations in the Chos Malal fold and thrust belt, based on the intensive stratigraphic work performed by the authors in northern Neuquén during the last years. Two hierarchies of depositional sequences were recognized: 5 composite depositional sequences (CSs) and 15 high-frequency depositional sequences (HFSs) (sensu Kerans and Tinker, 1997) (Figures 8, 9). Because of its average duration, CSs are interpreted to be equivalent to third-order sequences, whereas HFSs are considered as fourth-order sequences.

First Composite Depositional Sequence

The first composite depositional sequence (CS-1) starts with a regional surface where the upper Kimmeridgian–lower Tithonian fluvial and lacustrine deposits of the Tordillo Formation are overlapped by microbialite-dominated outer ramp deposits of the Vaca Muerta Formation (Figure 9). This surface coincides with the basal microbialite level of the Vaca Muerta Formation, which contains ammonites from the lower Tithonian *Virgatosphinctes mendozanus* biozone. The upper limit is determined by another regional marker recognized throughout the basin and is located within the lowermost upper Tithonian *Windhauseniceras internispinosum* biozone (Zeiss and Leanza, 2008).

In the eastern margin of the basin the transgressive systems tract 1 (TST-1) is retrogradational, beginning in almost all stratigraphic sections with basin to outer ramp deposits (FA-1), grading into outer ramp deposits (FA-2), and then to the proximal outer ramp deposits (FA-3), representing a maximum flooding zone located within the lowermost middle Tithonian *Pseudolissoceras zitteli* biozone.

The highstand systems tract HST-1 is defined by a net progradational strata arrangement characterized in distal positions of the carbonate ramp by the progradation of outer ramp deposits (FA-2) and proximal outer ramp facies (FA-3) (Figures 8, 9). In the western margin, facies remain homogeneous, recognizing the progradational pattern by an increase in carbonate content (Kietzmann and Vennari, 2013; Kietzmann et al. 2014c).The first CS contains four HFSs (HFS-1 to HFS-4; Figures 8, 9).

Second Composite Depositional Sequence

The second composite depositional sequence (CS-2) begins with the transgressive surface at the lower part of the upper Tithonian *Windhauseniceras internispinosum* biozone. The upper limit is determined by a regional transgressive surface located within the lower part of the *Substeueroceras koeneni* biozone (uppermost upper Tithonian).

The transgressive systems tract TST-2 is recognized in the eastern margin of the basin by a facies deepening, from proximal outer ramp deposits (FA-3) to basinal deposits (FA-1) (Figure 7). In the western margin the TST-2 is represented by the progradation of carbonate slope deposits related to the generation of a steep slope caused by the increase in accommodation (Kietzmann and Vennari, 2013; Kietzmann et al., 2014c). The highstand systems tract HST-2 in the eastern margin consists of a net progradational strata arrangement from proximal outer ramp deposits (FA-2) to distal middle ramp deposits (FA-3). In the western margin, HST-2 is represented by carbonate slope deposits (Kietzmann and Vennari, 2013; Kietzmann et al. 2014c). Composite depositional sequence (CS-2) contains three HFSs (HFS-5 to HFS-7; Figures 8, 9).

Third Composite Depositional Sequence

The third composite depositional sequence (CS-3) begins with a transgressive surface in the upper Tithonian (*Substeueroceras koeneni* biozone) and ends with another regional transgressive surface in the lowermost upper Berriasian (lower part of the *Spiticeras damesi* biozone) with the progradation of proximal outer ramp facies (Figures 8, 9).

The transgressive systems tract TST-3 is recognized in the eastern margin by a facies deepening, from middle ramp deposits (FA-3) in Yesera del Tromen and Puerta Curaco to outer ramp deposits (FA-2) or basinal deposits (FA-1) in Cerro Caicayén. The highstand systems tract HST-3 in the eastern margin consists of a progradational strata arrangement from proximal outer ramp deposits

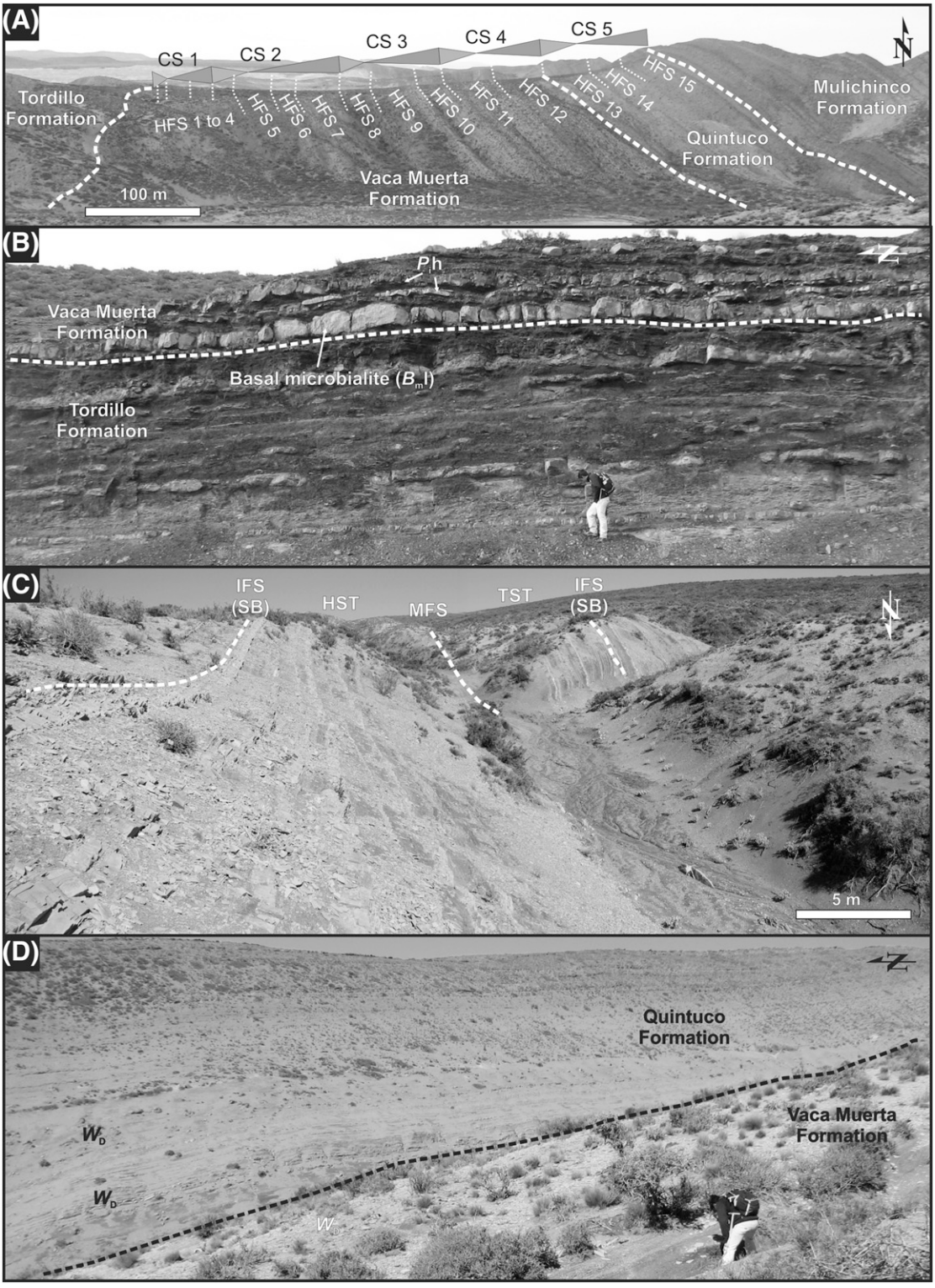

Figure 9. (A) Lower Mendoza mesosequence outcrops at Puerta Curaco section, showing lithostratigraphic divisions and depositional sequences proposed in this study. (B) Contact between the Vaca Muerta and Tordillo Formation at Yesera del Tromen section, showing the passage of lacustrine facies to microbialite marine facies. (C) Example of a high-frequency sequence in the upper part of the Vaca Muerta Formation. (D) Transition to the Quintuco Formation at Yesera del Tromen section, showing abundant dolomitized beds (W_D). B_ml = microbial bindstones; CS = composite sequences; HFS = high-frequency sequences; HST = highstand systems tract; IFS = initial flooding surface; MFS = maximum flooding surface; P_lh = laminated packstones; SB = sequence boundary; TST = transgressive systems tract.

(FA-2) to proximal outer ramp deposits (FA-3) in Yesera del Tromen and Puerta Curaco (Figure 9). Facies in Cerro Caicayén section remains homogeneous between basinal deposits (FA-1 and FA-4).

In the western margin, CS-3 is represented by carbonate slope deposits, which coincide with the Huncal Member (Kietzmann and Vennari, 2013). Composite sequence CS-3 contains three HFSs (HFS-8 to HFS-10; Figures 8, 9).

Fourth Composite Depositional Sequence

The fourth composite depositional sequence (CS-4) lies between two regional transgressive surfaces in the upper Berriasian (*Spiticeras damesi* biozone). The transgressive systems tract TST-4 is recognized in the eastern margin by a facies deepening, from proximal outer ramp deposits (FA- 3) in Yesera del Tromen and Puerta Curaco to outer ramp deposits (FA-2) or basinal deposits (FA-1) in Puerta Curaco. The highstand systems tract HST-4 in the eastern margin consists of a progradational strata arrangement from outer ramp deposits (FA-2) to proximal outer ramp deposits (FA-3) in Yesera del Tromen and Puerta Curaco. Facies in the Cerro Caicayén section remain homogeneous between basinal deposits (FA-1 and FA-4). In the western margin, CS-4 is represented by basinal deposits (Kietzmann and Vennari, 2013). Composite sequence CS-4 contains two HFSs (HFS-11 and HFS-12; Figures 8, 9).

Fifth Composite Depositional Sequence

The fifth composite depositional sequence (CS-5) begins with a regional transgressive surface in the uppermost part of the upper Berriasian (*Spiticeras damesi* biozone) and ends in the lower Valanginian (*Lissonia riveroi* biozone) with the correlative conformity of the Intra-Valanginian unconformity, which generates a dislocation of facies and the progradation of shallow marine facies of the Mulichinco Formation.

The transgressive systems tract TST-5 is recognized in the eastern margin by a facies deepening, from proximal outer ramp deposits (FA-3) to basinal deposits and offshore to lower transition zone (FA-4 and FA-5) in the Yesera del Tromen and Puerta Curaco sections. The highstand systems tract HST-5 consists of a progradational strata arrangement from offshore to lower transition zone (FA-5), to upper transition zone, and to lower shoreface deposits (FA-6). Facies in the Cerro Caicayén section remain homogeneous between basinal to slope deposits (FA-4). In the western margin, CS-5 is not represented because of erosion. Composite sequence CS-5 contains three HFSs (HFS-13 to HFS-15; Figures 8, 9).

MINERALOGY AND PERCENT TOTAL ORGANIC CARBON IN MARLSTONES AND SHALES

X-Ray Mineralogy

Mineral associations found in the studied Fl and marl samples are very similar. In general, quartz is the most abundant component (16%–63%, mean of 34%), followed by plagioclase (1%–28%, mean of 20%; Figure 10). Calcite shows an inverse ratio with respect to quartz content and is highly variable from 0% to 51%. In the lower and middle levels of the Vaca Muerta Formation, diagenetic gypsum appears subordinately (5%–25%).

Clay content ranges between 3% and 20% in the Vaca Muerta Formation and between 22% and 40% in the Quintuco Formation. The associations are dominated by illite, interstratified of illite–smectite and chlorite, with possible presence of kaolinite in few samples (Figure 10). The base of the Vaca Muerta Formation shows a discrete content of chlorite associated with illite and low participation of illite–smectite, whereas at higher levels this ratio is reversed, with illite–smectite becoming the dominant species. The observed behavior in illite–smectite coincides with increase of pyroclastic deposits in the upper part of the Vaca Muerta Formation.

The Quintuco Formation shows a continuous enrichment in illite with respect to illite–smectite. Illite has sharper peaks, indicating higher crystallinity than those from the Vaca Muerta Formation. This trend could be caused by increased detrital muscovite, consistent with the abundance of this mineral in associated sandstones.

Total Organic Content and Maturity

Total organic content values derived from the Yesera del Tromen and Puerta Curaco sections range between 0% and 8%, showing a curve that begins with high TOC levels in the Vaca Muerta Formation and progressively decreases to very low values in the Quintuco Formation. The organic matter–rich interval is about 400 m (1312 ft) thick. In a preliminary way, because of the low number of samples, three main peaks of nearly 8%, 6%, and 4% can be noted (Figure 10).

Pyrolysis data indicate mainly type IV and III kerogens. The low hydrogen index and high Rock-eval pyrolysis T_{max} values (432°C–514°C) obtained suggest poor kerogen convertibility and mature to overmature stages in the Chos Malal fold and thrust belt. Nonetheless, to the east, subsurface data show the dominance of type I and II kerogens associated with algal contribution and a very low level of terrestrial elements, and vitrinite reflectance (R_o) values range from 0.3% to 1.6% (Legarreta et al., 2005, Giusiano et al., 2011). Oil saturation index has an average of 160 to 170 mg HC/g TOC and oil in situ estimates of 0.01679 and 0.01837 m^3/m^3 (0.05508 and 0.06027 ft^3/ft^3), higher than those of the Marcellus, Bakken, Utica, Barnett, and Eagle Ford plays of North America (e.g., Giusiano et al., 2011).

Although organic matter data obtained from the fold and thrust belt are in overmature state, our data contribute to the understanding of organic matter distribution in relation to the sedimentary environment and depositional sequences (see Discussion section) and, therefore, are important to establish potential targets to operate.

DISCUSSION

In this paper we have analyzed the sedimentary facies and sequence stacking pattern, as well as mineralogical and TOC content in marl and Fl, in distal settings of the Vaca Muerta–Quintuco system. In the fold and thrust belt as well as in the east–central part of the Neuquén Basin (subsurface), the Vaca Muerta Formation was traditionally interpreted as basinal to lower slope deposits, whereas the Quintuco Formation was interpreted as upper slope to outer shelf deposits because of the geometry of clinoforms and their lithologies (Mitchum and Uliana, 1985; Legarreta and Gulisano, 1989; Legarreta and Uliana, 1991). Albeit, in central and southern Neuquén embayment the Quintuco–Loma Montosa Formation comprises inner shelf carbonate to sabkha environments, intercalated with lowstand fan deltas (Carozzi et al., 1993; Hurley et al., 1995). However, Mitchum and Uliana (1985) interpreted one lowstand wedge in central areas of the basin.

Although some authors (e.g., Pose et al., 2014) mention the presence of slope facies in the central and southern Neuquén Basin (Añelo trough), in our study we found no sedimentary evidence to interpret slope facies within the Vaca Muerta Formation. In fact, Gangui and Grausem (2014) and Kietzmann et al., (2014b) suggest that these mass transport deposits could be controlled by localized tectonic activity or previous paleostructures. However, the presence of hummocky cross-bedded deposits suggests the interaction of the substrate with combined flows probably caused by storms within a proximal outer ramp setting (e.g., Burchette and Wright, 1992). An alternative interpretation for the formation of HCS is related to the development of internal waves (Pomar et al., 2012; Bádenas et al., 2012), which are caused by the disruption of hydrostatic equilibrium in the pycnocline, for example, by exceptional input of river discharges (Nittrouer and Wright, 1994; Nittrouer et al., 2007).

The last hypothesis has important implications for the study of marine sequences because tempestites indicated the position of storm wave base, whereas internalites indicated the position of the pycnocline. Although we do not rule out that some of these deposits can be related to internal waves, the coarsening-upward arrangement and the gradual increase of bioclasts in HFSs induce us to interpret the action of surface waves related to storms instead of internal waves related to disturbances of pycnocline.

However, fossil content from the Vaca Muerta–Quintuco system suggests a heterozoan association sensu James (1997), and dominant lithofacies are related to accumulation of sand-sized mud intraclasts, so that the shelf equilibrium profile must be considered within a physical accommodation system dominated by sand-sized particles (Pomar and Kendall, 2008). This kind of system forms low-gradient ramps, has a high capacity to fill the accommodation at

shallow-water shelf, and can be affected by storm waves even below the inflection point of clinoforms. Indeed, slope angles in seismic observations doenot exceed 1° during most of the Tithonian and Berriasian interval, reaching maximum inclination of clinoform slopes of approximately 2° around the Jurassic–Cretaceous boundary and in the lower Valanginian (Mitchum and Uliana, 1985; Reijenstein et al., 2015) (see Figure 3). This basin architecture change is reflected in the lower Valanginian part of the Cerro Caicayén section, where small scars and slumps are present, and coincides with the change of depositional system from a low-gradient carbonate ramp to a mixed siliciclastic shelf at the Yesera del Tromen and Puerta Curaco sections.

During early Tithonian–early Valanginian times the Neuquén Basin behaved as a partially closed basin, bounded on the west by a volcanic island arc and connected with the Panthalassic Ocean by narrow marine passages (e.g., Legarreta and Uliana, 1991). This configuration can explain the existence of low-energy and relatively shallow marine ramps with development of carbonate and mixed carbonate–siliciclastic depositional systems.

Early sequence stratigraphic studies recognized nine depositional sequences within the Vaca Muerta–Quintuco system (Gulisano et al., 1984; Mitchum and Uliana, 1985; Legarreta and Gulisano, 1989). Mitchum and Uliana's terminology (A to I) derived from the work by Leanza and Hugo (1977) and corresponds to nine ammonite zones established in this work based on the survey field sections and analysis of their amonitiferous content (H. A. Leanza, 2015, personal communication). These data were employed by Gulisano et al. (1984) and Mitchum and Uliana (1985) to justify and fix the age of the clinoforms that appeared on seismograms, but this was only a first approximation. In fact, we recognize 5 composite depositional sequences and 15 high-frequency depositional sequences, which are consistent with sequence stratigraphic analysis carried out by Kietzmann et al. (2014c) in the southern Mendoza sector of the basin. Also, these five major progradations are outlined in the work of Legarreta et al. (1981) and Legarreta and Gulisano (1989), and recent subsurface studies in the central Neuquén embayment have recognized a similar number of sequences (González Tomassini et al., 2014; Dominguez et al., 2014).

Because no field evidence of subaerial exposure is available for the Vaca Muerta Formation that could help to recognize sequence boundaries, flooding surfaces have proven to be useful as stratigraphic markers. Thus, recognizing the composite depositional sequences, as done in the present work, can be an important subsurface tool for correlation because flooding surfaces can be detected by gamma ray logs, and HFSs probably could be detected with modern seismic resolution. The present outcrop data are extremely difficult to correlate with the nine sequences of Mitchum and Uliana (1985), and more work is needed from well studies to establish this correlation. However, fluctuations in mineralogy and total organic content in Mrh and Fl show a recurring pattern that was related to depositional sequences and can be recognized from well logs and cores (e.g., González Tomassini et al., 2014).

Based on x-ray mineralogy observations and our sequence stratigraphic analysis, in the Vaca Muerta Formation we conclude that there is an enrichment in quartz and plagioclase show in the transgressive systems tract of composite sequences, whereas calcite increases in highstand systems tracts (Figures 10, 11). In the Quintuco Formation these relationships are inverted, showing an increase in quartz and plagioclase in highstand systems tract, together with a decrease in the content of calcite.

The TOC curves in the Yesera del Tromen and Puerta Curaco sections show a declining trend, but at least four peaks can be recognized, which correlate with maximum flooding surfaces of composite depositional sequences CS-1, CS-2, and CS-3 (Figure 10). In fact, transgressive systems tracts are TOC-rich intervals (2%–4%) within sedimentary succession, whereas highstand systems tract are TOC-depleted intervals of 1%–0% total organic content. This behavior was also noted by Kietzmann et al. (2014c) in the southern Mendoza sector of the Neuquén Basin, where percent TOC remains at high values up to the lower Valanginian. Some smaller-scale fluctuations appear to be also present, which could be correlated with high-frequency depositional sequences.

Although organic matter distribution could be controlled by many factors (e.g., Stow et al., 2001), in the Vaca Muerta Formation, TOC-rich intervals are related to transgressive systems tract. The low topographic gradient of the depositional system allowed rapid flooding of the ramp resulting in a landward

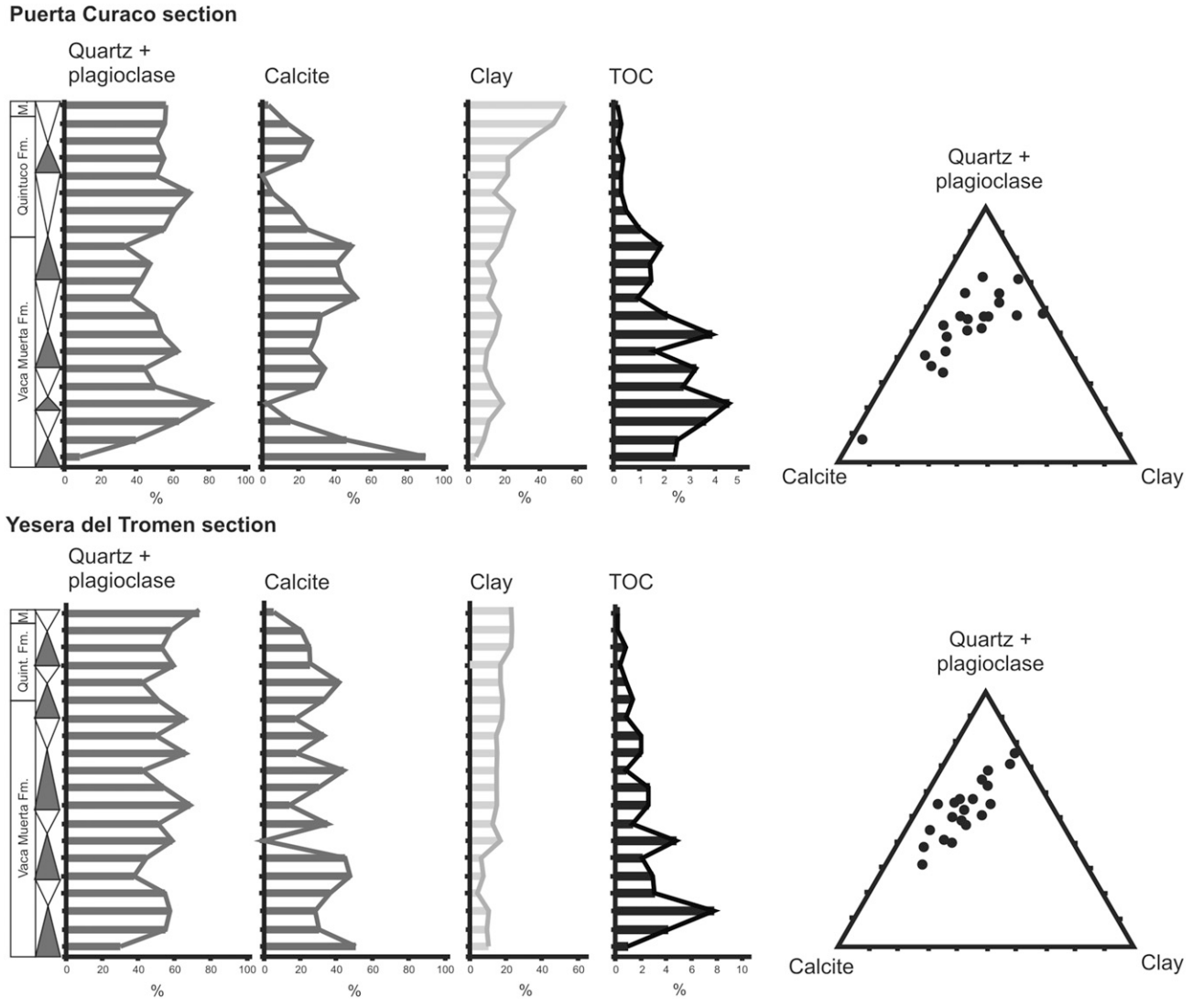

Figure 10. Relationship between the x-ray mineralogical content (quartz, plagioclase, and clay minerals), total organic content (TOC), and composite depositional sequences at Puerta Curaco and Yesera del Tromen sections (samples are not spaced at vertical scale). Fm. = Formation; Quint. = Quintuco.

migration of the carbonate production area. As a result, the sedimentation rate is significantly reduced in the outer ramp, and the environment stays under reduced oxygenation conditions, allowing a significant accumulation and preservation of organic matter (Arthur et al., 1984). However, it is important to note that the sedimentation rate in the Vaca Muerta Formation during transgressive systems tracts is relatively high, with an average value of 25 cm/k.y. (9.84 in./k.y.), favoring the preservation of organic matter without causing a significant dilution. During regressive stage, carbonate ramps prograde increasing erosion and sediment exportation to distal parts of the environment, diluting and oxidizing organic matter (e.g., Burchette and Wright, 1992). Sedimentation rates increase in highstand systems tracts to 50–60 cm/k.y. (17.7–23.6 in./k.y.). In contrast, Quintuco Formation is characterized by the deposition in a more oxygenated environment with high sedimentation rates (~100–120 cm/k.y. [39.4–47.2 ft/k.y.]), so that organic matter contents are greatly reduced.

Besides the distribution patterns of TOC and mineralogy, a recurring pattern of facies with high sequence stratigraphic significance can be recognized from outcrops that can be applied to the study of cores, particularly given the immature state of knowledge of the Vaca Muerta Formation. In distal

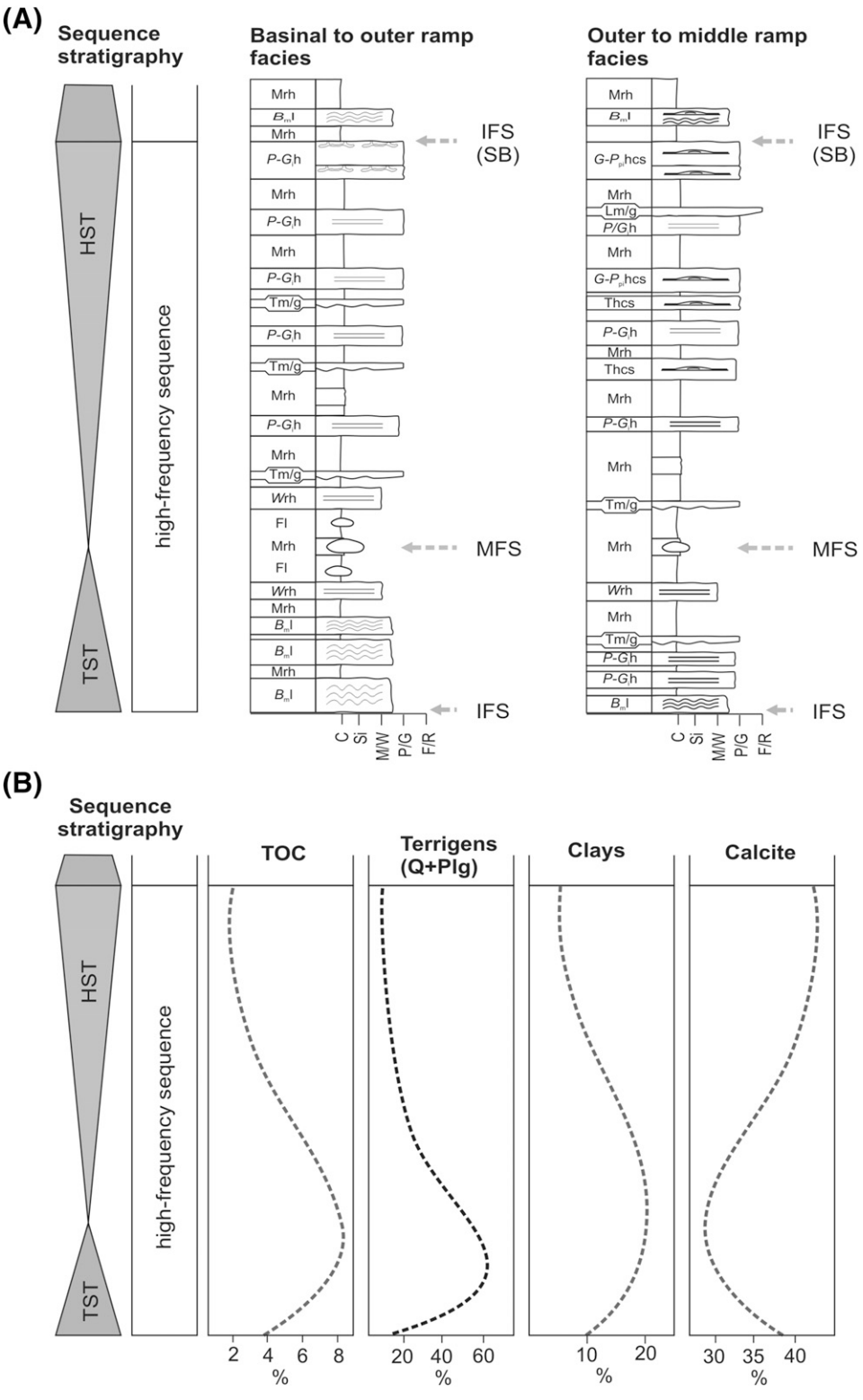

Figure 11. Simplification of lithologic variations related to depositional sequences within the Vaca Muerta Formation. (A) Distribution of facies within the depositional sequences in distal and proximal settings (facies codes in Table 1). (B) Variations in total organic matter, terrigens, clays, and calcite content in marlstones and shales within depositional sequences. B_ml = planar microbial binstones; C = claystone; F/R = floatstone/rudstones; Fl = laminated shales; HST = highstand systems tract; IFS = initial flooding surface; M/W = mudstone/wackestone; MFS = maximum flooding surface; Mrh = marlstone; *P-G*h = laminated intraclastic packstone-grainstone; P/G = packstone/grainstone; Plg = plagioclase; Q = quartz; SB = sequence boundary; Si = siltstone; TOC = total organic carbon; Tm/g = massive to graded tuffs; TST = transgressive systems tract; W_rh: laminated radiolaritic wackestones.

facies, transgressive systems tracts are marked by the presence of microbial deposits (B_ml) that gradually disappear toward the maximum flooding surface. These microbialites were probably built by chemosymbiotic bacteria under suboxic conditions, with high organic matter and low sediment input (e.g., Williams, 1984). Maximum flooding zones are commonly represented by Fl intervals, sometimes with early diagenetic concretions formed because of low sedimentation rate conditions, whereas highstand systems tract is characterized by the progressive enrichment in carbonates facies: laminated W_rh to laminated P_ih (Figure 11A).

In more proximal settings, the initial flooding surface in transgressive systems tracts can be marked eventually by microbial deposits (B_ml) or by outer ramp facies, which gradually are enriched in marl and Fl toward the maximum flooding surface. Highstand systems tracts are characterized by the progressive enrichment in carbonates facies with evidence of storm wave interaction with the seafloor (Figure 11A).

The observed relationship between TOC, mineralogy, and facies in relation to depositional sequences has been described in other Fl systems. However, among United States Fl unconventional reservoirs, there is no comparable analog for the Vaca Muerta Formation, perhaps with the exception of Eagle Ford, which has similar sedimentary facies, mineralogical compositions, and thermal maturity. The Vaca Muerta Formation has thick organic matter–rich intervals but also a much more heterogeneous facies organization than traditionally accepted, so understanding its facies distribution and sequence architecture is essential to delimit intervals of interest within this exceptional stratigraphic unit.

CONCLUSIONS

The data presented in this work show that the deposition of the Vaca Muerta Formation at the Chos Malal fold and thrust belt occurred in shallower conditions than previously accepted, within a distal low-gradient, organic matter–rich carbonate ramp instead of in a slope environment. This interpretation coincides with the idea that rich organic matter systems occurred commonly in shallow environments.

The Quintuco Formation is interpreted as a mixed siliciclastic–carbonate shelf depositional system, marking a significant change in paleoenvironment. This change caused the progressive decrease in total organic contents.

Based on the identification of flooding surfaces, two hierarchies of transgressive–regressive cycles were recognized: 5 composite depositional sequences and 15 high-frequency depositional sequences, which together show a regressive trend.

The first composite depositional sequence starts in the uppermost lower Tithonian (*Virgatosphinctes mendozanus* biozone) with a regional transgressive surface, which overlaps upper Kimmeridgian continental deposits with a microbialite bed and ends in the lowermost upper Tithonian (*Windhauseniceras internispinosum* biozone).

The second composite depositional sequence develops between the lowermost upper Tithonian and the uppermost upper Tithonian (*Windhauseniceras internispinosum* to *Substeueroceras koeneni* biozones), whereas the third composite depositional sequence includes upper Tithonian to upper Berriasian deposits (*Substeueroceras koeneni* to *Spiticeras damesi* biozone).

The fourth composite depositional sequence includes the upper Berriasian (*Spiticeras damesi* biozone), whereas the fifth composite depositional sequence includes upper Berriasian to lower Valanginian deposits (*Spiticeras damesi* to *Lissonia riveroi* biozones) and culminates at the Intra-Valingian unconformity, which is the result of the progradation of the shallower water deposits of the Mulichinco Formation.

Fluctuations in organic matter content within the Vaca Muerta Formation point to their relationship with composite depositional sequences, with the highest values being associated with transgressive systems tract. Furthermore, transgressive systems tracts in the Vaca Muerta Formation are rich in quartz, plagioclase, and clays but poor in calcite, whereas highstand systems tracts show a progressive enrichment in calcite and a decrease in terrigenous clasts. In the Quintuco Formation, the relation between quartz, plagioclase, and clay content with respect to calcite content is reversed. Transgressive systems tracts are rich in calcite, and highstand systems tracts show a progressive enrichment in quartz, plagioclase, and clays, reflecting an increment of terrigenous input and mixing processes during highstand of sea level. This genetic distribution of organic matter and mineral components is important to predict the best targets for hydraulic fracturing and can be used analogously in subsurface.

REFERENCES CITED

Aguirre-Urreta, M. B., A. Concheyro, M. Lorenzo, E. G. Ottone, and P. F. Rawson, 1999, Advances in the biostratigraphy of the Agrio Formation (Lower Cretaceous) of the Neuquén Basin, Argentina: Ammonites, palynomorphs, and calcareous nannofossils: Palaeogeography, Palaeoclimatology, Palaeoecology, v. 150, p. 33–47, doi:10.1016/S0031-0182(99)00006-1.

Arthur, M. A., W. E. Dean, and D. A. V. Stow, 1984, Model for the deposition of Mesozoic-Cenozoic fine-grained organic-carbon-rich sediment in deep-sea, *in* D. A. V. Stow and D. J. W. Piper, eds., Fine-grained sediment: Deep water processes and facies: Geological Society, London, Special Publications 1984, v. 14, p. 527–560, doi:10.1144/GSL.SP.1984.015.01.34.

Bádenas, B., M. Aurell, F. J. Rodríguez-Tovar, and E. Pardo-Igúzquiza, 2003, Sequences stratigraphy and bedding rhythms of an outer ramp limestones succession (Late Kimmeridgian, Northeast Spain): Sedimentary Geology, v. 161, p. 153–174, doi:10.1016/S0037-0738(03)00099-X.

Bádenas, B., L. Pomar, M. Aurell, and M. Morsilli, 2012, A facies model for internalites (internal wave deposits) on a gently sloping carbonate ramp (Upper Jurassic, Ricla, NE Spain): Sedimentary Geology, v. 271–272, p. 44–57, doi:10.1016/j.sedgeo.2012.05.020.

Biscaye, P., 1965, Mineralogy and sedimentation of recent deep-sea clay in the Atlantic Ocean and adjacent seas and oceans: Geological Society of America Bulletin, v. 76, p. 803–832, doi:10.1130/0016-7606(1965)76[803:MASORD]2.0.CO;2.

Burchette, T. P., and V. P. Wright, 1992, Carbonate ramp depositional systems: Sedimentary Geology, v. 79, p. 3–57, doi:10.1016/0037-0738(92)90003-A.

Carozzi, A. V., I. A. Orchuela, and M. L. Rodriguez Schelotto, 1993, Depositional models of the Lower Cretaceous Quintuco-Loma Montosa Formation, Neuquén Basin, Argentina: Journal of Petroleum Geology, v. 16, p. 421–450, doi:10.1111/j.1747-5457.1993.tb00351.x.

Charrier, R., 1985, Estratigrafía, evolución tectónica y significado de las discordancias de los Andes chilenos entre 32°S y 36°S durante el Mesozoico y Cenozoico, *in* J. Frutos, R. Oyarzún, and M. Pincheira, eds., Geologia y Recursos Minerales de Chile: Concepción, Chile, Universidad de Concepción, p. 101–133.

Cheel, R. J., and D. A. Leckie, 1993, Hummocky cross-stratification, *in* V. P. Wright, ed., Sedimentology review, p. 103–122, doi:10.1002/9781444304534.ch7.

Cruz, C., A. Boll, R. Gómez Omil, E. Martínez, C. Arregui, C. Gulisano, G. Laffitte, and H. J. Villar, 2002, Hábitat de hidrocarburos y sistemas de carga Los Molles y Vaca Muerta en el sector central de la Cuenca Neuquina, Argentina (abs.): IAPG V Congreso de Exploración y Desarrollo de Hidrocarburos CD-ROM, Mar del Plata, Argentina, October 29–November 2, 2002, 20 p.

Dominguez, R. F., S. Paulin, M. J. Continanzia, A. D. Askenazi, and F. N. Senoane, 2014, Estratigrafía del interval Vaca Muerta – Quintuco en el sector central de la Cuenca Neuquina (abs.): IAPG IX Congreso de Exploración de Desarrollo de Hidrocarburos, Mendoza, Argentina, November 3–7, 2014, p. 217–232.

Dott, R. J., and J. Bourgeois, 1982, Hummocky stratification: Significance of its variable bedding sequences: Geological Society of America Bulletin, v. 93, p. 663–680, doi:10.1130/0016-7606(1982)93<663:HSSOIV>2.0.CO;2.

Dumas, S., and R. W. C. Arnott, 2006, Origin of hummocky and swaley cross-stratification - The controlling influence of unidirectional current strength and aggradation rate: Geology, v. 34, p. 1073–1076, doi:10.1130/G22930A.1.

Embry, A. F., and E. P. Johannessen, 1992, T–R sequence stratigraphy, facies analysis and reservoir distribution in the uppermost Triassic-Lower Jurassic succession, western Sverdrup Basin, Arctic Canada, *in* T. O. Vorren, E. Bergsager, O. A. Dahl-Stamnes, E. Holter, B. Johansen, E. Lie, and T. B. Lund, eds., Arctic geology and petroleum potential: Norwegian Petroleum Society Special Publication 2, p. 121–146.

Gangui, A., and M. Grausem, 2014, Tectonismo y estilos estructurales en el Engolfamiento Neuquino: Implicancias en la interpretación de las fracturas monitoreadas por microsísmica en la Formación Vaca Muerta (abs.): IAPG IX Congreso de Exploración de Desarrollo de Hidrocarburos, Mendoza, Argentina, November 3–7, 2014, p. 362–279.

Garrison, R. E., and S. A. Graham, 1984, Early diagenetic dolomites and the origin of dolomite-bearing breccias, lower Monterey Formation, Arroyo Seco, Monterey County, California, *in* R. E. Garrison, M. Kastner, and D. H. Zenger, eds., Dolomites of the Monterey Formation and other organic-rich units: Tulsa, Oklahoma, SEPM Pacific Section 41, p. 87–101.

Giusiano, A., J. Alonso, G. Chebli, and G. Ibáñez, 2011, Gas no convencional en la cuenca Neuquina. El shale gas en la provincia del Neuquén: Informe de la Subsecretaría de Hidrocarburos: Energía y Minería, Gobierno de la Provincia del Neuquén, 54 p.

González Tomassini, F., D. A. Kietzmann, M. A. Fantín, L. C. Crousse, and H. M. Reijenstein, 2014, Estratigrafía y análisis de facies de la Formación Vaca Muerta en el área de El Trapial, cuenca Neuquina, Argentina (abs.): IAPG IX Congreso de Exploración y Desarrollo de Hidrocarburos, Mendoza, Argentina, November 3–7, 2014, p. 587–611.

Gulisano, C. A., A. R. Gutiérrez Pleimling, and R. E. Digregorio, 1984, Análisis estratigráfico del intervalo Tithoniano-Valanginiano (Formaciones Vaca Muerta, Quintuco y Mulichinco) en el suroeste de la provincia de Neuquén: 9 Congreso Geológico Argentino, v. 1, p. 221–235.

Haq, B. U., J. Hardenbol, and P. R. Vail, 1987, Chronology of fluctuating sea level since the Triassic: Science, v. 235, p. 1156–1167, doi:10.1126/science.235.4793.1156.

Haq, B. U., J. Hardenbol, and P. R. Vail, 1988, Mesozoic and Cenozoic chronostratigraphy and cycles of sea-level change, *in* C. K. Wilgus, B. S. Hastings, C. A. Ross, H. Posamentier, J. Van Wagoner, and C. G. S. C. Kendall, eds., Sea level changes—An integrated approach: Tulsa, Oklahoma, SEPM Special Publication 42, p. 71–108, doi:10.2110/pec.88.01.0071.

Herbin, J. P., J. L. Fernandez-Martinez, J. R. Geyssant, A. E. Albani, J. F. Deconinck, J. N. Proust, J. P. Colbeaux, and J. P. Vidier, 1995, Sequence stratigraphy of source rocks applied to the study of the Kimmeridgian/Tithonian in the north-west European shelf (Dorset/UK, Yorkshire/UK and Boulonnais/France): Marine and Petroleum Geology, v. 12, p. 177–194, doi:10.1016/0264-8172(95)92838-N.

Hurley, N. H., H. C. Tanner, and C. Barcat, 1995, Unconformity-Related Porosity Development in the Quintuco Formation (Lower Cretaceous), Neuquén Basin, Argentina, *in* D. A. Budd, A. H. Saller, and P. M. Harris, eds., Unconformities and porosity in carbonate strata: AAPG Memoir 63, p. 159–175.

James, N. P., 1997, The cool-water carbonate depositional realm, *in* N. P. James and J. A. D. Clarke, eds., Cool-water carbonates: Tulsa, Oklahoma, SEPM Special Publication 56, p. 1–20, doi:10.2110/pec.97.56.0001.

Kerans, C., and S. Tinker, 1997, Sequence stratigraphy and characterization of carbonate reservoirs: Tulsa, Oklahoma, SEPM Short Course Note 40, p. 1–128.

Kiessling, W., 1996, Facies characterization of Mid-Mesozoic deep-water sediments by quantitative analysis of siliceous microfaunas: Facies, v. 35, p. 237–274, doi:10.1007/BF02536964.

Kietzmann, D. A., and R. M. Palma, 2009, Tafofacies y biofacies de Formación Vaca Muerta en el sector surmendocino de la Cuenca Neuquina: Implicancias paleoecológicas, sedimentológicas y estratigráficas: Ameghiniana, v. 46, p. 321–343.

Kietzmann, D. A., and R. M. Palma, 2011, Las tempestitas peloidales de la Formación Vaca Muerta (Tithoniano-Valanginiano) en el sector surmendocino de la Cuenca Neuquina, Argentina: Latin American Journal of Sedimentology and Basin Analysis, v. 18, p. 121–149.

Kietzmann, D. A., A. Ambrosio, J. Suriano, S. Alonso, V. V. Vennari, M. B. Aguirre-Urreta, G. Depine, and D. Repol, 2014a, Análisis sedimentológico y estratigráfico secuencial de las Formaciones Vaca Muerta y Quintuco en el área de Chos Malal, Cuenca Neuquina: IAPG IX Congreso de Exploración y Desarrollo de Hidrocarburos TT2, Mendoza, Argentina, November 3–7, 2014, p. 269–288.

Kietzmann, D. A., A. Ambrosio, J. Suriano, S. Alonso, V. V. Vennari, M. B. Aguirre-Urreta, G. Depine, and D. Repol, 2014b, Variaciones de facies en las secuencias basales de la Formación Vaca Muerta en su localidad tipo (Sierra de la Vaca Muerta), Cuenca Neuquina: IAPG IX Congreso de Exploración y Desarrollo de Hidrocarburos TT2, Mendoza, Argentina, November 3–7, 2014, p. 299–317.

Kietzmann, D. A., J. Martín-Chivelet, R. M. Palma, J. López-Gómez, M. Lescano, and A. Concheyro, 2011, Evidence of precessional and eccentricity orbital cycles in a Tithonian source rock: The mid-outer carbonate ramp of the Vaca Muerta Formation, Northern Neuquén Basin, Argentina: AAPG Bulletin, v. 95, no. 9, p. 1459–1474, doi:10.1306/01271110084.

Kietzmann, D. A., R. M. Palma, and G. S. Bressan, 2008, Facies y microfacies de la rampa tithoniana-berriasiana de la Cuenca Neuquina (Formación Vaca Muerta) en la sección del arroyo Loncoche – Malargüe, provincia de Mendoza: Revista de la Asociación Geológica Argentina, v. 63, p. 696–713.

Kietzmann, D. A., R. M. Palma, and M. P. Iglesia Llanos, 2015, Cyclostratigraphy of an orbitally-driven Tithonian-Valanginian carbonate ramp succession, Southern Mendoza, Argentina: Implications for the Jurassic-Cretaceous boundary in the Neuquén Basin.: Sedimentary Geology, v. 315, p. 29–46, doi:10.1016/j.sedgeo.2014.10.002.

Kietzmann, D. A., R. M. Palma, A. C. Riccardi, J. Martín-Chiveler, and J. López-Gómez, 2014c, Sedimentology and sequence stratigraphy of a Tithonian–Valanginian carbonate ramp (Vaca Muerta Formation): A misunderstood exceptional source rock in the Southern Mendoza area of the Neuquén Basin, Argentina: Sedimentary Geology, v. 302, p. 64–86, doi:10.1016/j.sedgeo.2014.01.002.

Kietzmann, D. A., and V. V. Vennari, 2008, Facies, ambiente depositacional y estratigrafía de la Formación Vaca Muerta (Tithoniano inferior – Berriasiano superior) en el área del cerro Domuyo, Neuquén: XVII Congreso Geológico Argentino, San Salvador de Jujuy, Argentina, October 7–10, 2008, p. 773.

Kietzmann, D. A., and V. V. Vennari, 2013, Sedimentología y estratigrafía de la Formación Vaca Muerta (Tithoniano-Berriasiano) en el área del cerro Domuyo, norte de Neuquén, Argentina: Andean Geology, v. 40, p. 41–65, doi:10.5027/andgeoV40n1-a02.

Leanza, H. A., 1973, Estudio sobre los cambios faciales de los estratos limítrofes Jurásico-Cretácicos entre Loncopué y Picun Leufú, Provincia del Neuquén, República Argentina: Revista de la Asociación Geológica Argentina, v. 28, p. 97–132.

Leanza, H. A., 2009, Las principales discordancias del Mesozoico de la Cuenca Neuquina según observaciones de superficie: Revista del Museo Argentino de Ciencias Naturales, v. 11, p. 145–184.

Leanza, H. A., and C. A. Hugo, 1977, Sucesión de amonites y edad de la Formación Vaca Muerta y sincrónicas entre los Paralelos 35° y 40° l.s. Cuenca Neuquina-Mendocina: Revista de la Asociación Geológica Argentina, v. 32, p. 248–264.

Leanza, H. A., C. A. Hugo, D. Repol, and M. Salvarredy Aranguren, 2003, El Miembro Huncal (Berriasiano inferior): Un episodio turbidítico en la Formación Vaca Muerta, Cuenca Neuquina, Argentina: Revista de la Asociación Geológica Argentina, v. 58, p. 248–254.

Leanza, H. A., H. G. Marchese, and J. C. Riggi, 1977, Estratigrafía del Grupo Mendoza con especial referencia a la Formación Vaca Muerta entre los Paralelos 35° y 40° l.s. Cuenca Neuquina-Mendocina: Revista de la Asociación Geológica Argentina, v. 32, p. 190–208.

Leanza, H. A., F. Sattler, R. Martinez, and O. Carbone, 2011, La Formación Vaca Muerta y Equivalentes (Jurásico Tardío – Cretácico Temprano) en la Cuenca. Neuquina, *in* H. A. Leanza, C. Arregui, O. Carbone, J. C. Daniela, and J. M. Vallés, eds., Geología y Recursos Naturales de la Provincia del Neuquén: Buenos Aires, Argentina, Asociación Geológica Argentina, p. 113–129.

Legarreta, L., and C. A. Gulisano, 1989, Análisis estratigráfico secuencial de la Cuenca Neuquina (Triásico superior-Terciario inferior, *in* G. Chebli and L. A. Spalletti, eds., Cuencas Sedimentarias Argentinas: Universidad Nacional de Tucumán Serie Correlación Geológica 6, p. 221–243.

Legarreta, L., E. Kozlowski, and A. Boll, 1981, Esquema estratigráfico y distribución de facies del Grupo Mendoza en el ámbito surmendocino de la cuenca Neuquina: 8 Congreso Geológico Argentino Actas, v. 3, p. 389–409.

Legarreta, L., and M. A. Uliana, 1991, Jurassic-Cretaceous marine oscillations and geometry of back-arc basin, Central Argentina Andes, *in* D. I. M. McDonald, ed., Sea level changes at active plate margins: Process and product: Oxford, United Kingdom, IAS Special Publication 12, p. 429–450.

Legarreta, L., and M. A. Uliana, 1996, The Jurassic succession in west central Argentina: Stratal patterns, sequences, and paleogeographic evolution: Palaeogeography, Palaeoclimatology, Palaeoecology, v. 120, p. 303–330, doi:10.1016/0031-0182(95)00042-9.

Legarreta, L., H. J. Villar, G. A. Laffitte, C. E. Cruz, and G. Vergani, 2005, Cuenca Neuquina: Balance de masa enfocado a la evaluación del potencial exploratorio de los distritos productivos y de las zonas no productivas (abs.): IAPG VI Congreso de Exploración y Desarrollo de Hidrocarburos, Mar del Plata, Argentina, November 15–19, 2005, p. 233–250.

MacEachern, J. A., L. B. Kerrie, S. G. Pemberton, and M. K. Gingras, 2008, The ichnofacies paradigm: High-resolution paleoenvironmental interpretation of the rock record, *in* J. A. MacEachern, K. L. Bann, M. K. Gingras, and S. G. Pemberton, eds., Applied ichnology: Tulsa, Oklahoma, SEPM Short Course 52, p. 27–64.

Meister, P., J. A. Mckenzie, C. Vasconcelos, S. Bernasconi, M. Frank, M. Gutjahr, and D. P. Schrag, 2007, Dolomite formation in the dynamic deep biosphere: Results from the Peru Margin: Sedimentology, v. 54, p. 1007–1032, doi:10.1111/j.1365-3091.2007.00870.x.

Mitchum, R. M., and M. A. Uliana, 1985, Seismic stratigraphy of carbonate depositional sequences, Upper Jurassic-Lower Cretaceous. Neuquén Basin, Argentina, *in* R. B. Berg and D. G. Woolverton, eds., Seismic stratigraphy: An integrated approach to hydrocarbon exploration: AAPG Memoir 39, p. 255–274.

Molina, J. M., P. A. Ruiz-Ortiz, and J. A. Vera, 1997, Calcareous tempestites in pelagic facies (Jurassic, Betic Cordilleras, Southern Spain): Sedimentary Geology, v. 109, p. 95–109, doi:10.1016/S0037-0738(96)00057-7.

Monaco, P., 1992, Hummocky cross-stratified deposits and turbidites in some sequences of the Umbria-Marche area (central Italy) during the Toarcian: Sedimentary Geology, v. 77, p. 123–142, doi:10.1016/0037-0738(92)90107-3.

Moore, G. T., D. E. Hayashida, C. A. Ross, and S. R. Jacobson, 1992, Paleoclimate of the Kimmeridgian/Tithonian (Late Jurassic) world: I. Results using a general circulation model: Palaeogeography, Palaeoclimatology, Palaeoecology, v. 93, p. 113–150, doi:10.1016/0031-0182(92)90186-9.

Myrow, P. M., 1992, Bypass-zone tempestite facies model and proximality trends for an ancient muddy shoreline and shelf: Journal of Sedimentary Petrology, v. 62, p. 99–115, doi:10.1306/D426789D-2B26-11D7-8648000102C1865D.

Nittrouer, C. A., J. A. Austin, M. E. Field, J. H. Kravitz, J. P. M. Syvitski, and P. L. Wiberg, 2007, Continental margin sedimentation: From sediment transport to sequence stratigraphy: Oxford, United Kingdom, IAS Special Publication 37, 549 p.

Nittrouer, C. A., and L. D. Wright, 1994, Transport of particles across continental shelves: Reviews of Geophysics, v. 32, p. 85–113, doi:10.1029/93RG02603.

Nozaki, T., Y. Kato, and K. Suzuki, 2013, Late Jurassic ocean anoxic event: Evidence from voluminous sulphide deposition and preservation in the Panthalassa: Scientific Reports, v. 3, 1889, doi:10.1038/srep01889.

Plint, A. G., J. H. S. MacQuaker, and B. L. Varban, 2012, Bedload transport of mud across a wide, storm-influenced ramp: Cenomanian-Turonian Kaskapau Formation, Western Canada Foreland Basin: Journal of Sedimentary Research, v. 82, p. 801–822, doi:10.2110/jsr.2012.64.

Pomar, L., and C. G. St. C. Kendall, 2008, Architecture of carbonate platforms: A response to hydrodynamics and evolving ecology, *in* J. Lukasik and T. J. A. Simo, eds., Controls on carbonate platform and reef development: Tulsa, Oklahoma, SEPM Special Publication 89, p. 187–216, doi:10.2110/pec.08.89.0187.

Pomar, L., M. Morsilli, P. Hallock, and B. Bádenas, 2012, Internal waves, an under-explored source of turbulence events in the sedimentary record: Earth-Science Reviews, v. 111, p. 56–81, doi:10.1016/j.earscirev.2011.12.005.

Pose, F., A. Gangui, and S. Galeazzi, 2014, Estratigrafía secuencial del intervalo Quintuco-Vaca Muerta en el Engolfamiento Neuquino, Cuenca Neuquina, Argentina: IAPG IX Congreso de Exploración y Desarrollo de Hidrocarburos, Mendoza, Argentina, November 3–7, 2014, p. 612–632.

Pratt, B. R., 2001, Septarian concretions: Internal cracking caused by synsedimentary earthquakes: Sedimentology, v. 48, p. 189–213, doi:10.1046/j.1365-3091.2001.00366.x.

Ramos, V. A., 2010, The tectonic regime along the Andes: Present-day and Mesozoic regimes: Geological Journal, v. 45, p. 2–25, doi:10.1002/gj.1193.

Raup, D. M., 1973, Depth inferences from vertically imbedded cephalopods: Lethaia, v. 6, p. 217–225, doi:10.1111/j.1502-3931.1973.tb01195.x.

Reijenstein, H. M., H. W. Posamentier, M. Fantin, F. González Tomassini, and C. Lipinski, 2014, Vaca Muerta seismic stratigraphy and geomorphology: Regional architectural trends for unconventional exploration: IAPG IX Congreso de Exploración y Desarrollo de Hidrocarburos, Mendoza, Argentina, November 3–7, 2014, 8 p.

Reijenstein, H. M., M. A. Fantin, S. Cuervo, F. González Tomassini, D. A. Kietzmann, L. C. Crousse, and D. Vallejo, 2015, Where is the Vaca Muerta sweet spot? The importance of regional facies trends, thickness variations, and thermal maturity in generating play concepts: Unconventional Resources Technology Conference, San

Antonio, Texas, July, 20–22, SPE-178702-MS, 8 p., doi: 10.2118/178702-MS.

Riccardi, A. C., S. E. Damborenea, M. O. Manceñido, and H. A. Leanza, 2011, Megainvertebrados jurásicos y su importancia geobiológica, *in* H. A. Leanza, C. Arregui, O. Carbone, J. C. Daniela, and J. M. Vallés, eds., Geología y Recursos Naturales de la Provincia del Neuquén, Buenos Aires, Argentina, Asociación Geológica Argentina, p. 441–464.

Savrda, C. E., and D. J. Bottjer, 1986, Trace fossil model for reconstruction of paleo-oxygenation in bottom waters: Geology, v. 14, p. 3–6, doi:10.1130/0091-7613(1986)14<3:TMFROP>2.0.CO;2.

Scasso, R. A., S. M. Alonso, S. Lanés, H. J. Villar, and H. Lippai, 2005, Geochemistry and petrology of a Middle Tithonian limestone-marl rhythmite in the Neuquén Basin, Argentina: Depositional and burial history, *in* G. D. Veiga, L. A. Spalletti, J. A. Howell, and E. Schwarz, eds., The Neuquén Basin, Argentina: A case study in sequence stratigraphy and basin dynamics: Geological Society, London, Special Publications 2005, v. 252, p. 207–229.

Schieber, J., 1998, Possible indicators of microbial mat deposits in shales and sandstones. Examples from the Mid-Proterozoic Belt Supergroup, Montana, USA: Sedimentary Geology, v. 120, p. 105–124, doi:10.1016/S0037-0738(98)00029-3.

Schieber, J., J. B. Southard, and A. Schimmelmann, 2010, Lenticular shale fabrics resulting from intermittent erosion of water-rich muds—Interpreting the rock record in the light of recent flume experiments: Journal of Sedimentary Research, v. 80, p. 119–128, doi:10.2110/jsr.2010.005.

Schwarz, E., and L. A. Buatois, 2012, Substrate-controlled ichnofacies along a marine sequence boundary: The Intra-Valanginian Discontinuity in central Neuquén Basin (Argentina): Sedimentary Geology, v. 277–278, p. 72–87, doi:10.1016/j.sedgeo.2012.07.014.

Schwarz, H. U., 1975, Sedimentary structures and facies analysis of shallow marine carbonates (Lower Muschelkalk, Middle Triassic, Southwestern, Germany): Contributions to Sedimentology, v. 3, p. 1–100.

Spalletti, L. A., J. R. Franzese, S. D. Matheos, and E. Schwarz, 2000, Sequence stratigraphy of a tidally dominated carbonate-siliciclastic ramp; the Tithonian-Early Berriasian of the Southern Neuquén Basin, Argentina: Geological Society, London, Special Publications 2000, v. 157, p. 433–446.

Spalletti, L. A., Z. Gasparini, G. Veiga, E. Schwarz, M. Fernández, and S. Matheos, 1999, Facies anóxicas, procesos deposicionales y herpetofauna de la rampa marina titoniano-berriasiana en la Cuenca Neuquina (Yesera del Tromen), Neuquén, Argentina: Revista Geológica de Chile, v. 26, p. 109–123.

Spalletti, L. A., G. D. Veiga, E. Schwarz, and J. Franzese, 2008, Depósitos de flujos gravitacionales subácueos de sedimentos en el flanco activo de la Cuenca Neuquina durante el Cretácico Temprano: Revista de la Asociación Geológica Argentina, v. 63, p. 442–453.

Stow, D. A. V., A. Y. Huc, and P. Bertrand, 2001, Depositional processes of black shales in deep water: Marine and Petroleum Geology, v. 18, p. 491–498, doi:10.1016/S0264-8172(01)00012-5.

Stow, D. A. V., and D. J. W. Piper, 1974, Deep-water fine-grained sediments: facies models: Geological Society, London, Special Publications 1974, v. 15, p. 611–646.

Uliana, M. A., and L. Legarreta, 1993, Hydrocarbons habitat in a Triassic-to-Cretaceous Sub-Andean setting: Neuquén Basin, Argentina: Journal of Petroleum Geology, v. 16, p. 397–420, doi:10.1111/j.1747-5457.1993.tb00350.x.

Vergani, G. D., A. J. Tankard, H. J. Belotti, and H. J. Welkink, 1995, Tectonic evolution and paleogeography of the Neuquén Basin, Argentina, *in* A. J. Tankard, R. Suarez Soruco, and H. J. Welsink, eds., Petroleum basins of South America: AAPG Memoir 62, p. 383–402.

Walker, R. G., and A. G. Plint, 1992, Wave- and storm-dominated shallow marine systems, *in* R. G. Walker and N. P. James, eds., Facies models: Response to sea-level change: Calgary, Alberta, Geological Association of Canada, p. 219–238.

Whitham, A. G., 1993, Facies and depositional processes in an Upper to Lower Cretaceous pelagic sedimentary sequence, Antarctica: Sedimentology, v. 40, p. 331–349, doi:10.1111/j.1365-3091.1993.tb01767.x.

Williams, L. A., 1984, Subtidal stromatolites in Monterey Formation and other organic-rich rocks as suggested source contributors to petroleum formation: AAPG Bulletin, v. 68, no. 12, p. 1879–1893.

Wright, L. D., C. T. Friedrichs, S. C. Kim, and M. E. Scully, 2001, Effects of ambient currents and waves on gravity-driven sediment transport on continental shelves: Marine Geology, v. 175, p. 25–45, doi:10.1016/S0025-3227(01)00140-2.

Zeiss, A., and H. A. Leanza, 2008, Interesting new ammonites from the Upper Jurassic of Argentina and their correlation potential: New possibilities for global correlations at the base of the Upper Tithonian by ammonites, calpionellids and other fossil groups: Newsletters on Stratigraphy, v. 42, p. 223–247, doi: 10.1127/0078-0421/2008/0042-0223.

Click to view video of presentation

[AV]The Evolution of the American Shale Plays: Where We Are and How We Got There*

Richard Kelty Stoneburner[1]

Search and Discovery Article #110228 (2017)**
Posted October 2, 2017

*Adapted from oral presentation given at AAPG 2017 Division of Professional Affairs, Mid-Continent Playmakers Forum, Oklahoma City, Oklahoma, May 11, 2017
**Datapages © 2017 Serial rights given by author. For all other rights contact author directly.

[1]Pine Brook Partners, Managing Director (dstoneburner2@gmail.com)

Abstract

Since around 2006 the exploration, appraisal, and development of shale reservoirs in the Lower 48 has seen a dramatic escalation, first starting with the gas productive shale reservoirs then followed by those that are liquid productive. The result has been a total renaissance for the domestic E & P industry. Each of the plays, which total approximately 14 that have seen substantial development, underwent an evolutionary cycle that was driven by the roles of the various functions that contribute to the success of any given play: land, geologic, drilling, completion, and production. As each play progresses through the evolutionary cycle, the role of each function changes accordingly. Even though all of the plays have certain common characteristics, Richard will attempt to point out something uniquely different about each of the 14 plays that might aid in a better understanding of plays yet to be discovered.

Selected References

Bowker, K.A., 2003, Recent Developments of the Barnett Shale Play, Fort Worth Basin: West Texas Geological Society Bulletin, v. 42/6, p. 4-11.

EIA, U.S. Energy Information Administration. https://www.eia.gov/. Website accessed September 2017.

ITG, Investment Technology Group. https://www.itg.com/. Website accessed September 21017.

Jefferies. http://www.jefferies.com/. Website accessed September 2017.

RSEG, RS Energy Group. https://www.rseg.com/. Website accessed September 2017.

The Evolution of the American Shale Plays: Where We Are and How We Got Here

AAPG DPA Mid-Con Playmakers Forum
May 11, 2017

Richard Stoneburner
Managing Director
Pine Brook

PINE BROOK

Overview

- I first generated this presentation in August 2014 to present at a conference in Australia
- It was meant to be a “primer” on shale oil and gas development in America at the time
- The approach was to create a categorization of the of American shale plays based on level of maturity
- However, MUCH HAS CHANGED in the almost 3 years since this was presentation was created

The Shale Gas Revolution: A Graphical Depiction

The advent of isolated, multi-stage hydraulic fracturing in ~2006 was the game changer

U.S. Natural Gas Production

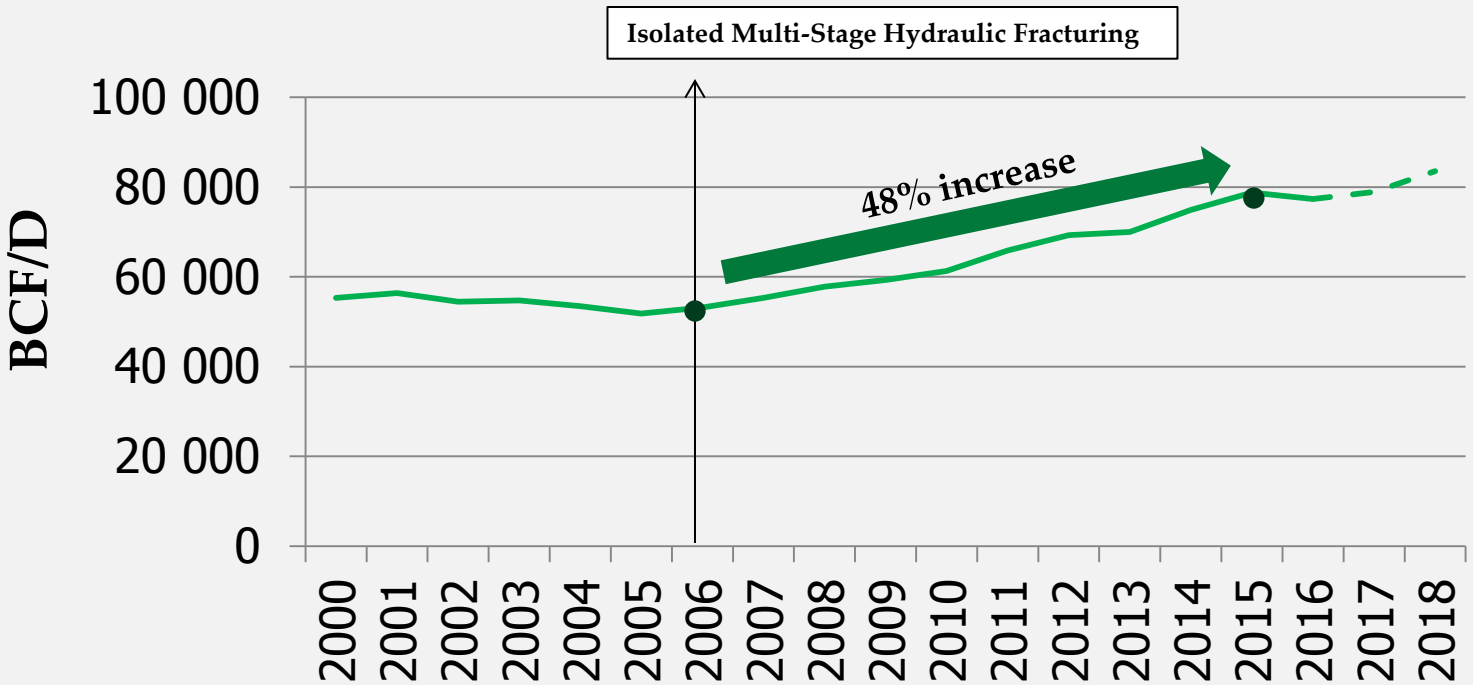

Source: EIA

The Shale Oil Revolution: A Graphical Depiction

The discovery of the Eagle Ford Shale, development in the Bakken Shale and onset of the Permian shale exploration have driven this growth

U.S. Crude Oil Production

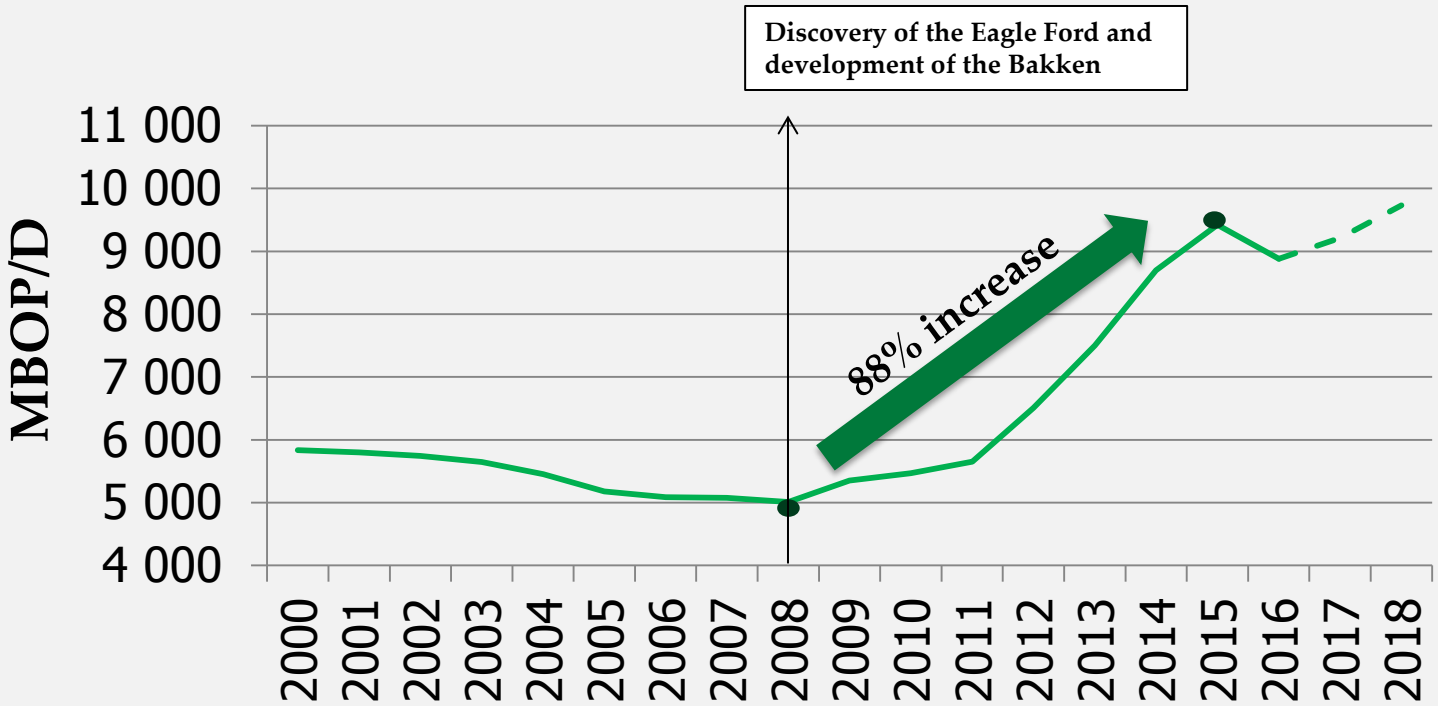

Source: EIA

The Maturity Index for American Shales (Circa August 2014)

Emerging	Evolving	Mature
Utica	Niobrara DJ Basin	Barnett
Tuscaloosa Marine Shale	Wolfcamp Delaware Basin	Fayetteville
Eagle Ford East Texas Basin	Wolfcamp Midland Basin	Haynesville
STACK	Woodford Anadarko Basin	Marcellus
		Bakken
		Eagle Ford Gulf Coast Basin

The Maturity Index for American Shales (Circa April 2017)

Emerging	Evolving	Mature
Mancos Shale	Utica	Barnett
Utica	Niobrara DJ Basin	Fayetteville
Tuscaloosa Marine Shale	Wolfcamp Delaware Basin	Haynesville
Eagle Ford East Texas Basin	Wolfcamp Midland Basin	Marcellus
STACK	SCOOP	Bakken
	STACK	Eagle Ford Gulf Coast Basin

The Maturity Index for American Shales (Circa April 2017)

Emerging	Evolving	Mature
Mancos Shale	Utica	Barnett
	Niobrara DJ Basin	Fayetteville
	Wolfcamp Delaware Basin	Haynesville
	Wolfcamp Midland Basin	Marcellus
	SCOOP/STACK / MERGE	Bakken
		Eagle Ford Gulf Coast Basin

Emerging

The Maturity Index for American Shales

Emerging	Evolving	Mature
Mancos Shale	Utica Niobrara **Wolfcamp Delaware Basin** **Wolfcamp Midland Basin** SCOOP/STACK/Merge	Barnett Fayetteville Haynesville Marcellus Bakken **Eagle Ford** **Gulf Coast Basin**

Emerging

The Functional Processes Associated with Emerging Plays

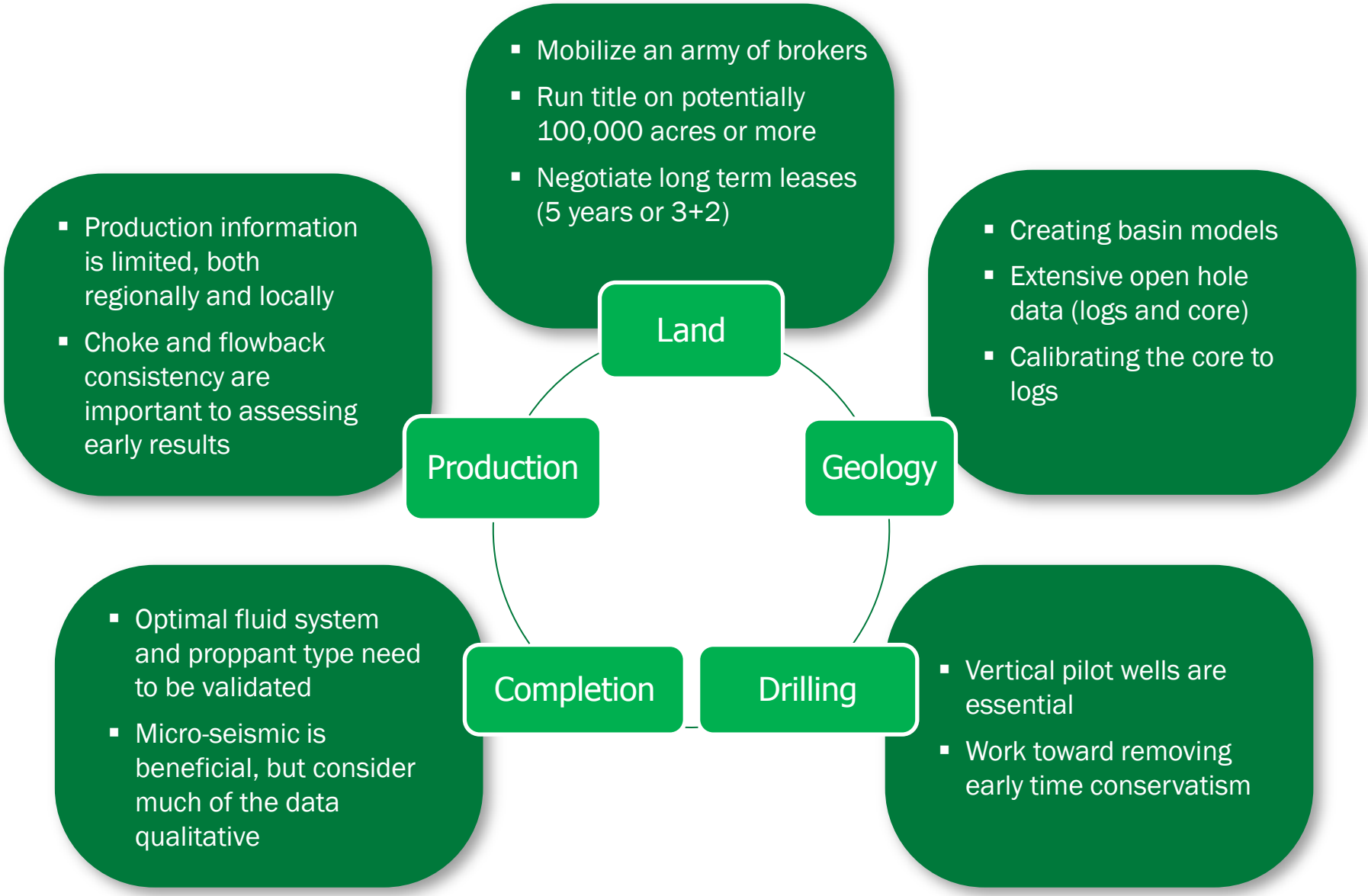

Emerging

Mancos Shale San Juan Basin: Early Results are Encouraging

- WPX Public Comments on oil window (12-7-16 Capital One Conference):
  - 650 MBOE EUR
  - 65% increase since 2015
  - 7250' lateral length
  - >70% ROR @ strip
  - $4.1 MM D & C
- Gas Window
  - ??????

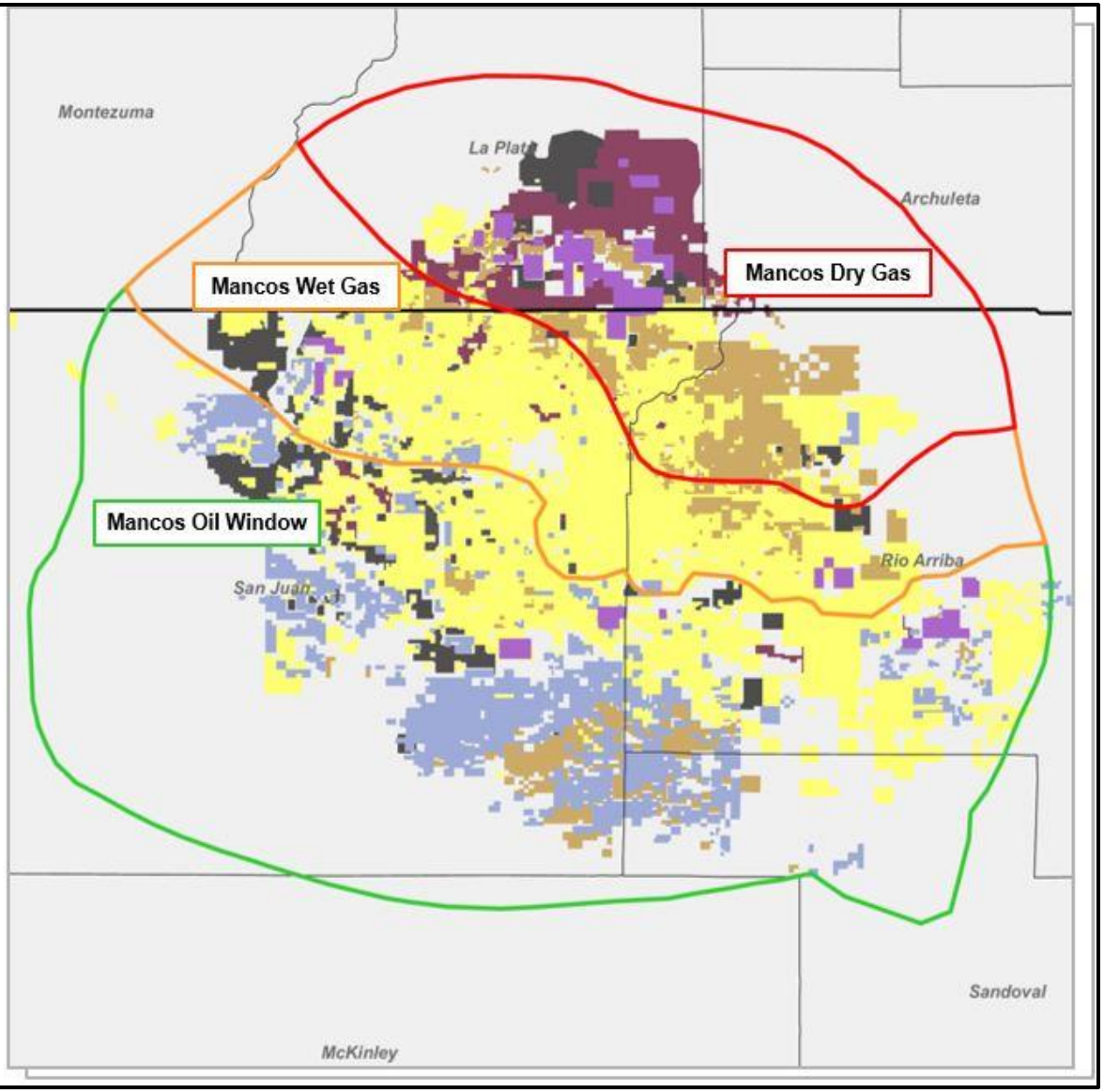

Source: Jefferies

Evolving

The Maturity Index for American Shales

Emerging	Evolving	Mature
Mancos Shale	Utica Niobrara DJ Basin Wolfcamp Delaware Basin Wolfcamp Midland Basin SCOOP/STACK/Merge	Barnett Fayetteville Haynesville Marcellus Bakken Eagle Ford Gulf Coast Basin

Evolving

The Functional Processes Associated with Evolving Plays

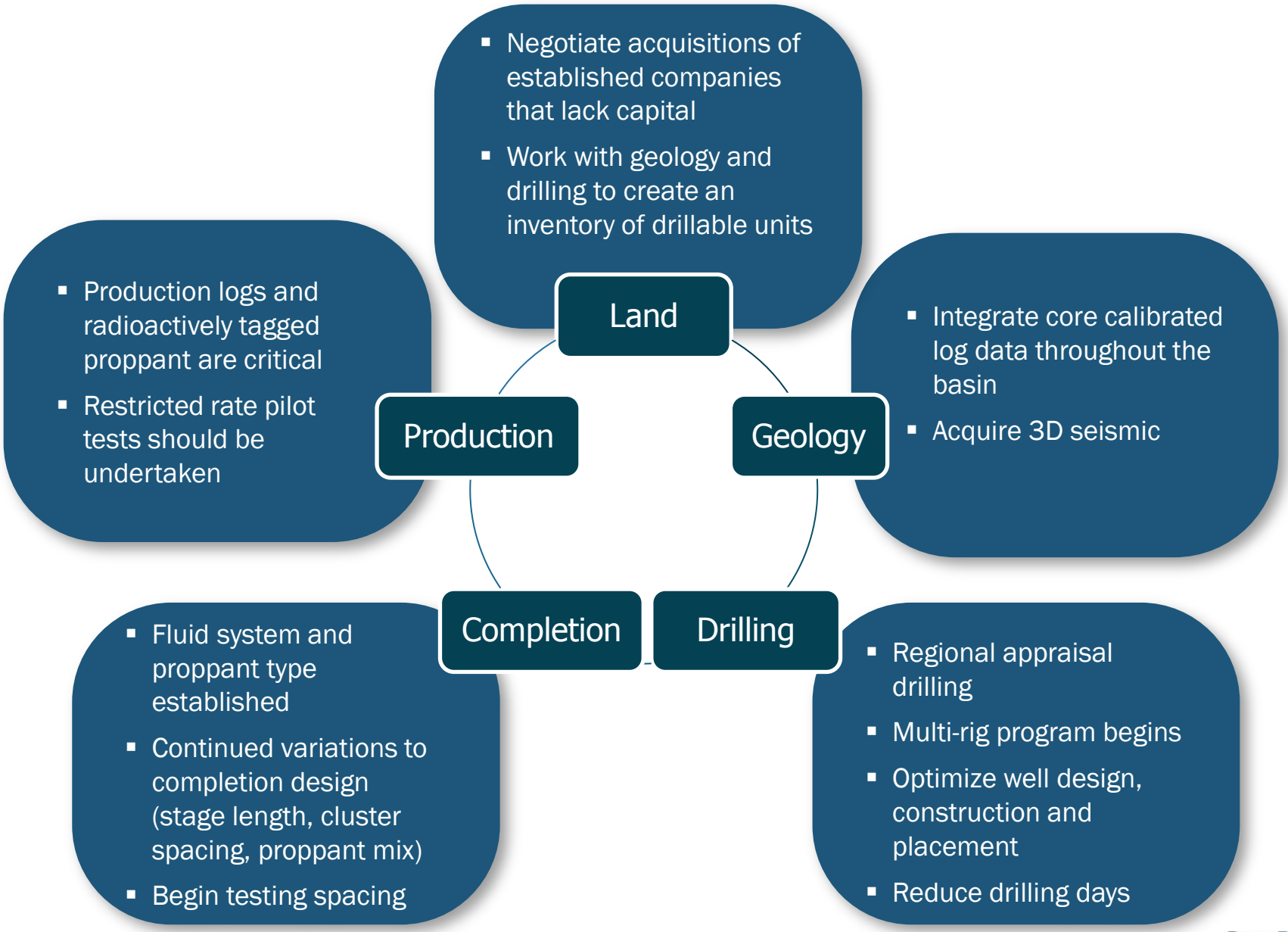

Utica: A Small, but Outstanding, Core of Gas that Could/Should Get a lot Bigger

Evolving

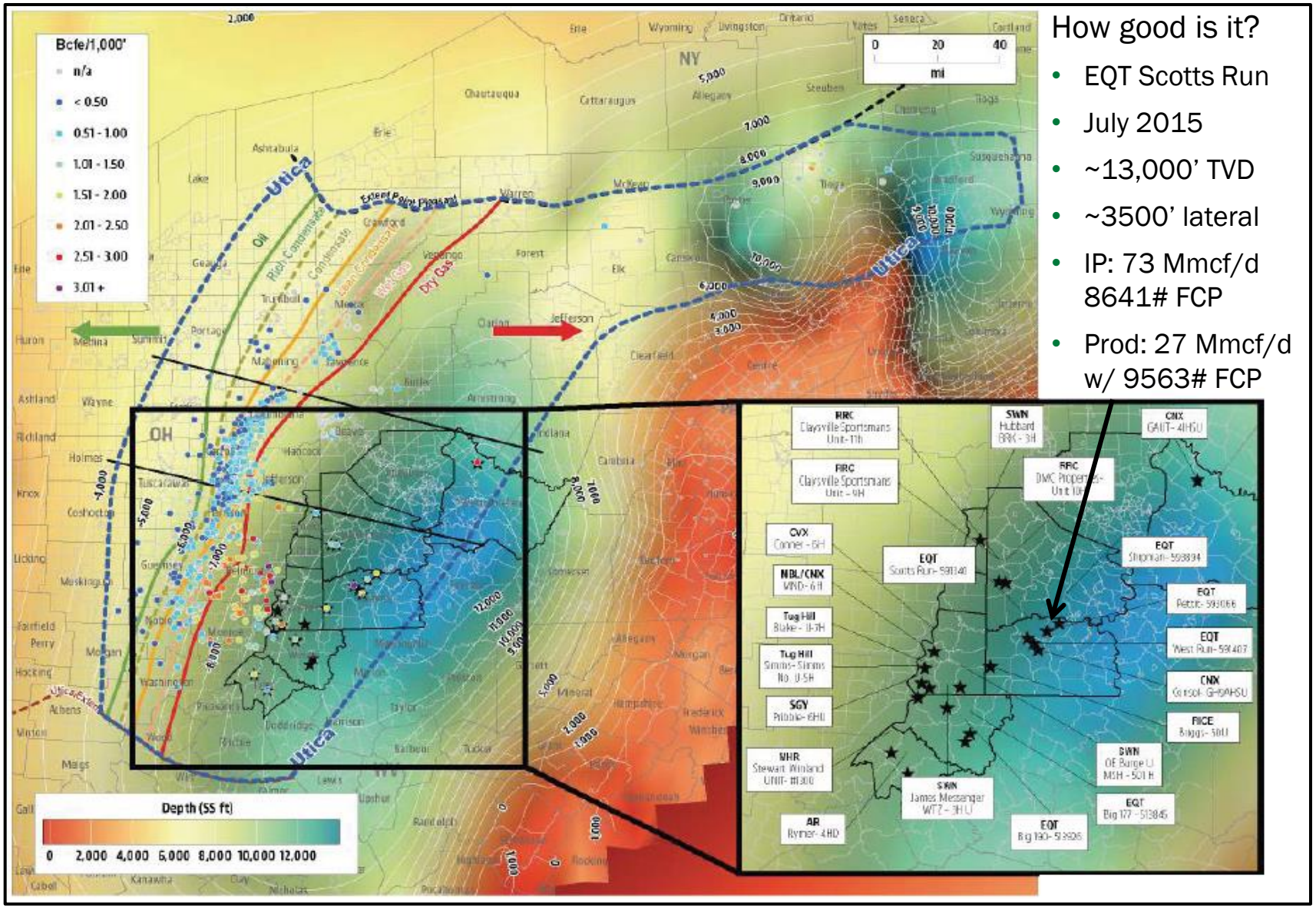

How good is it?

- EQT Scotts Run
- July 2015
- ~13,000' TVD
- ~3500' lateral
- IP: 73 Mmcf/d 8641# FCP
- Prod: 27 Mmcf/d w/ 9563# FCP

Source: RSEG.

Evolving

Niobrara: Anomalous Heat Flow is the Driver, Not Depth

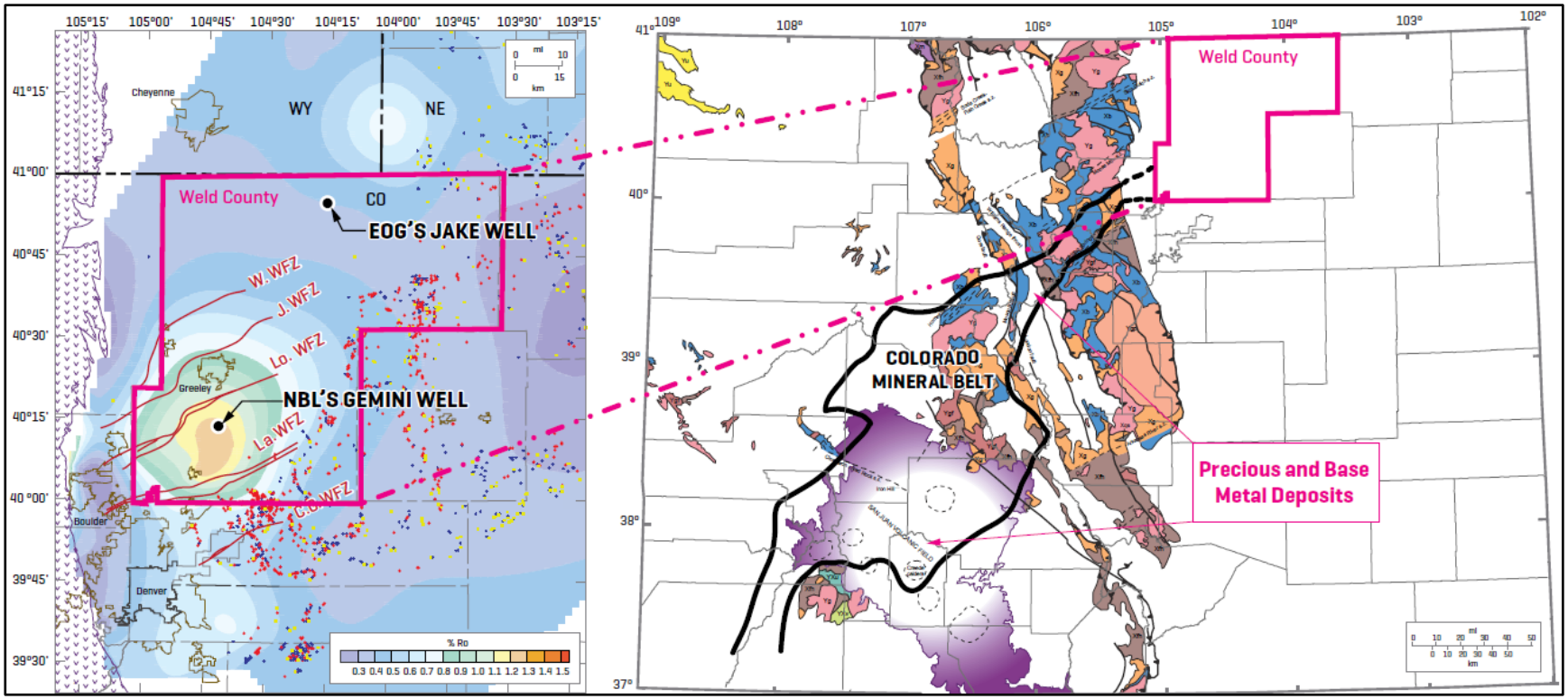

- EOG opened the play with the Jake well in 2009
- It set off a huge land play that focused on not only the entire DJ Basin, but the other Rocky Mountains basins with Niobrara potential
- However, the play failed to prove commercial anywhere other than in the Colorado Mineral Belt as shown above

Source: ITG/RSEG.

Midland vs. Delaware Basin: EUR Comparison (Mboe/1000' Lateral)

Evolving

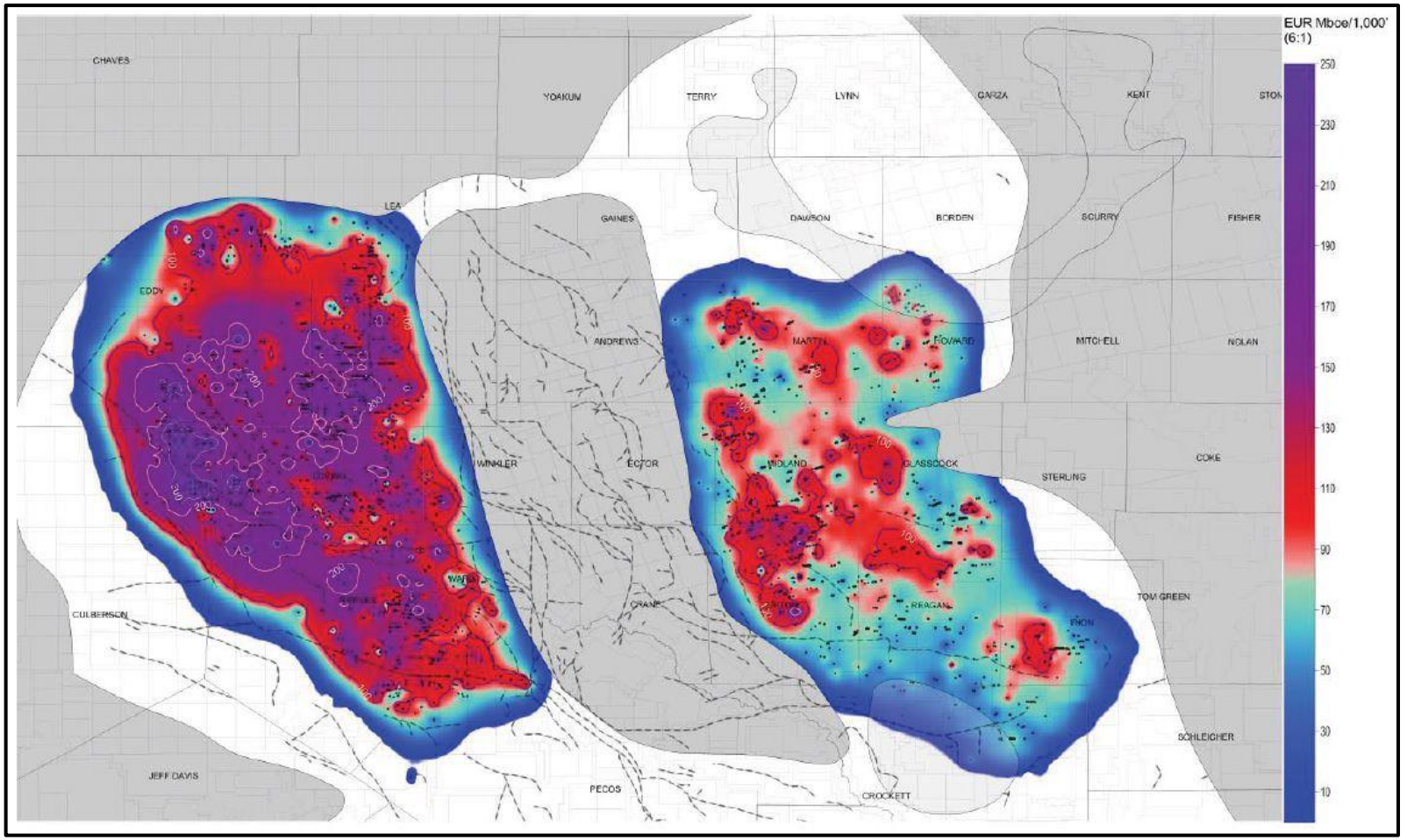

- Midland Basin core ranges from ~70-130 MBOE/1000' (525-975 MBOE normalized to 7500')
- Delaware Basin core ranges from ~100-200 MBOE/1000' (750 MBOE-1500MBOE normalized to 7500')

Source: RSEG

Midland vs. Delaware Basin: Recoverable Stacked Reserves (MMBoe/Section)

Evolving

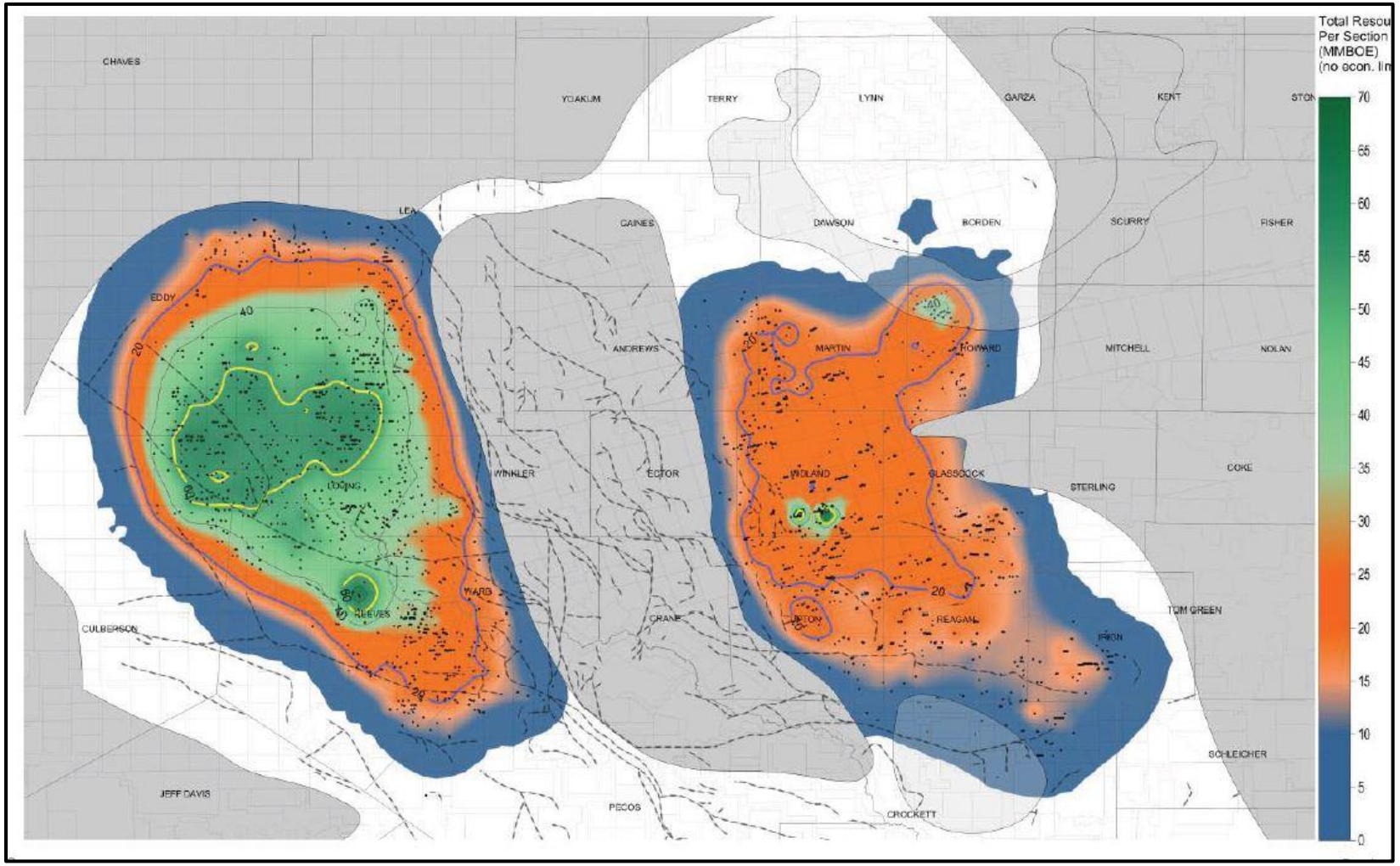

- Midland Basin ranges from ~20-40 MMBOE recoverable per section
- Delaware Basin ranges from 40-60 MMBOE recoverable per section

Source: RSEG

Midland vs. Delaware Basin: Stacked Developed Acreage Value ($/acre)

Evolving

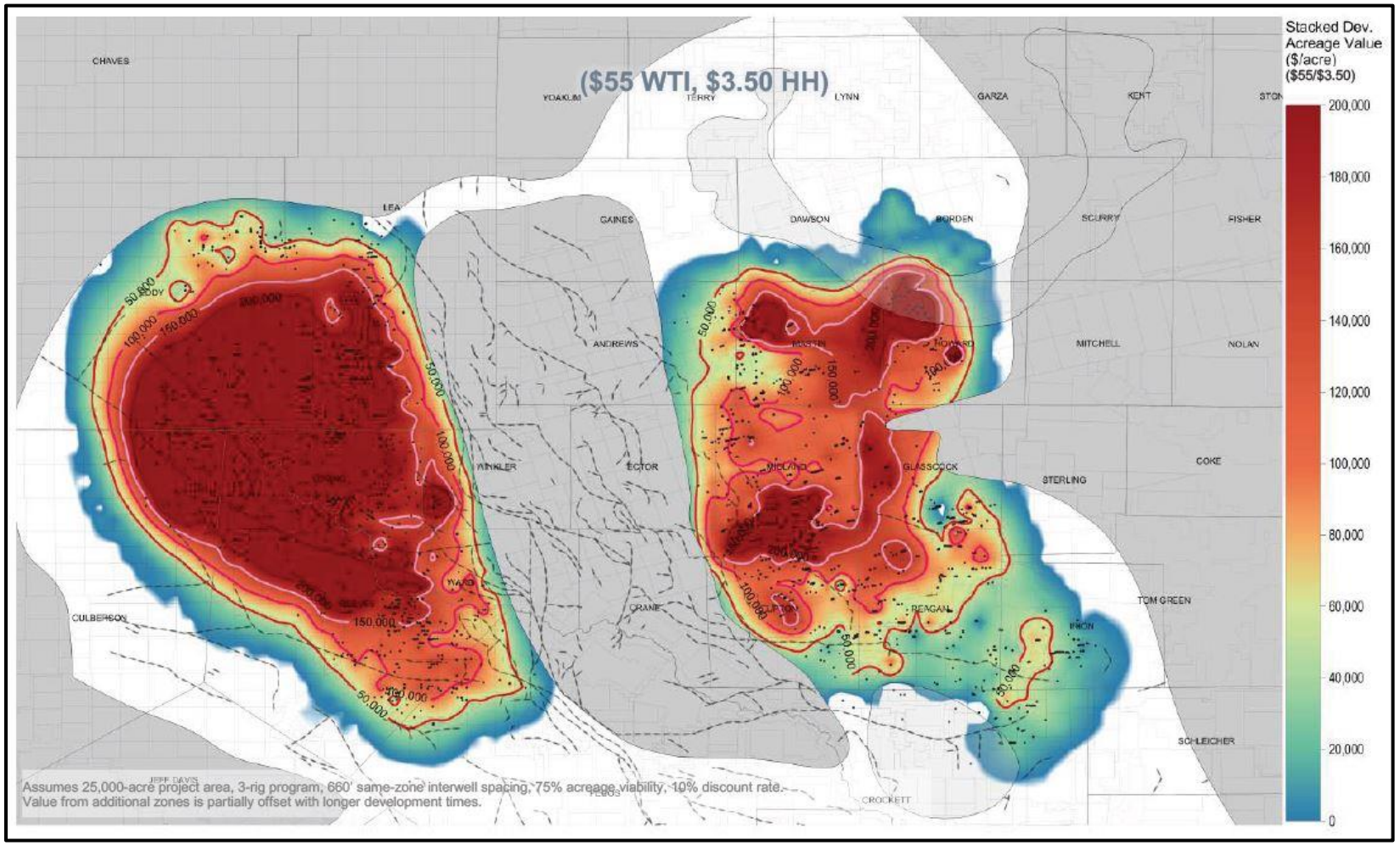

- Midland Basin core ranges from $60,000-$150,000/acre NAV at $55 barrel/$3.50 gas
- Delaware Basin core ranges from $150,000+/acre NAV at $55/barrel/$3.50 gas

Source: RSEG.

Evolving

SCOOP, then STACK, then MERGE, then…..?

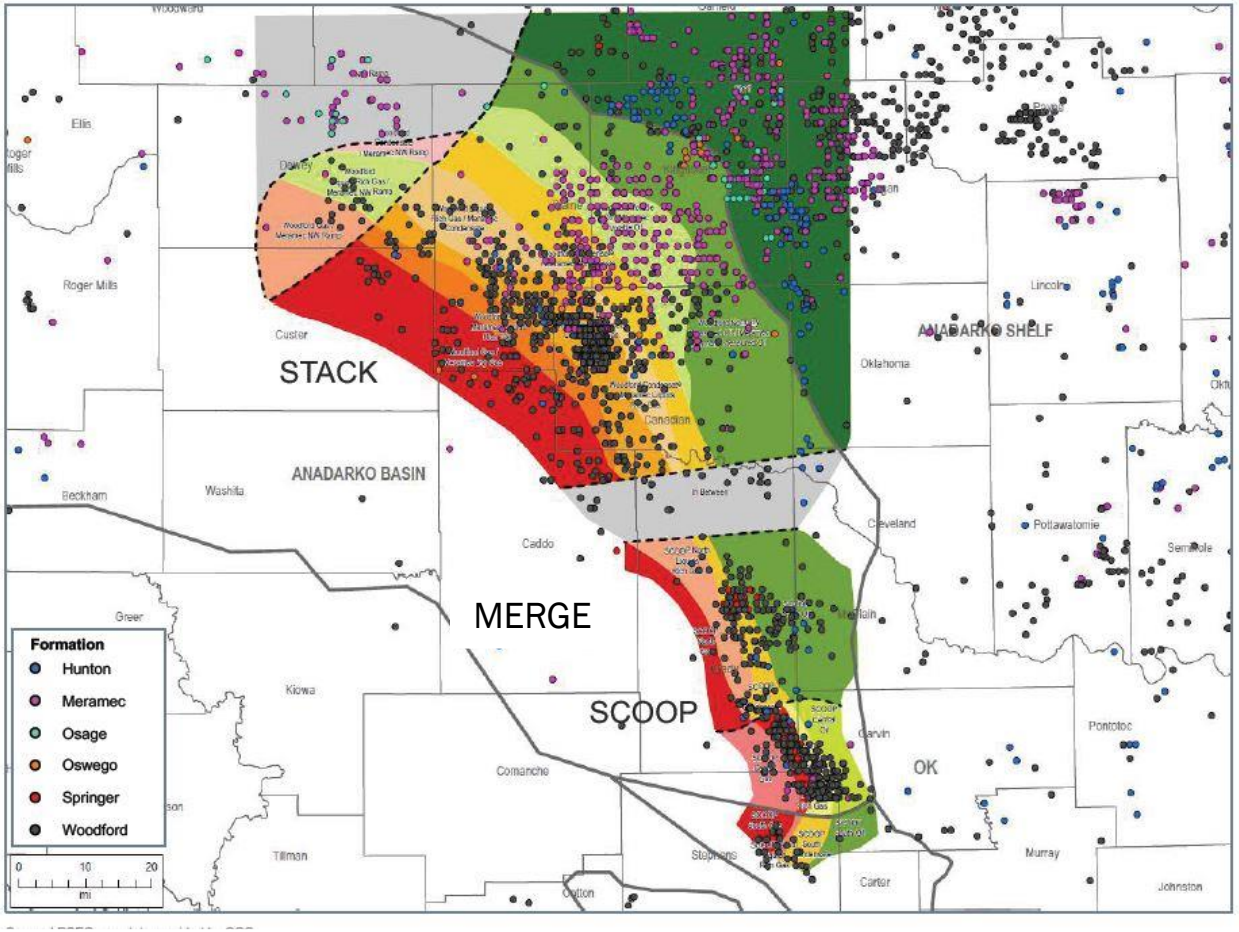

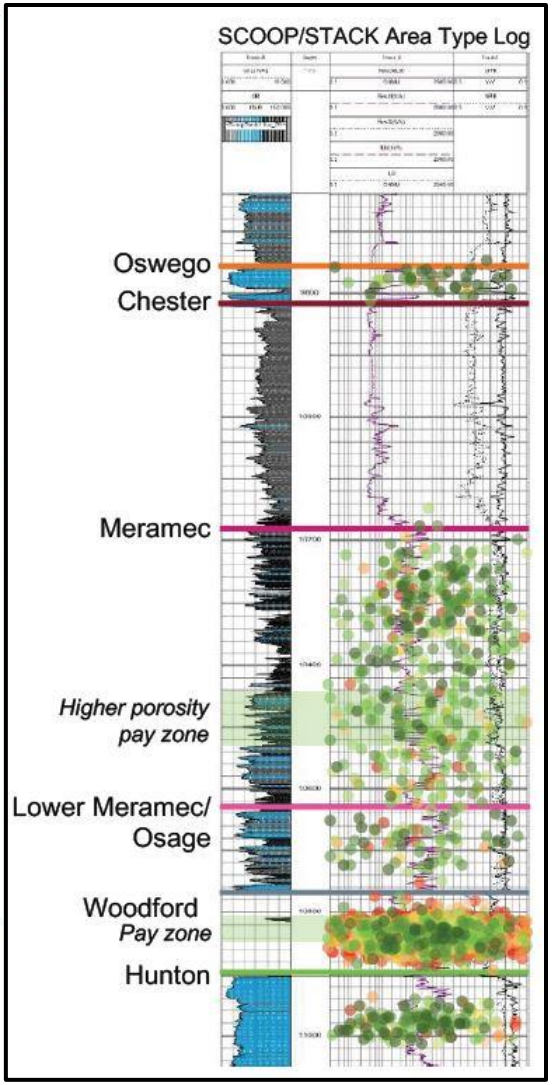

- SCOOP (2012) led to the STACK (2013) which led to the MERGE (2016)
- Where does it go from here? Way too early to say

Source: RSEG

A World Class Petroleum System Drives the Opportunity

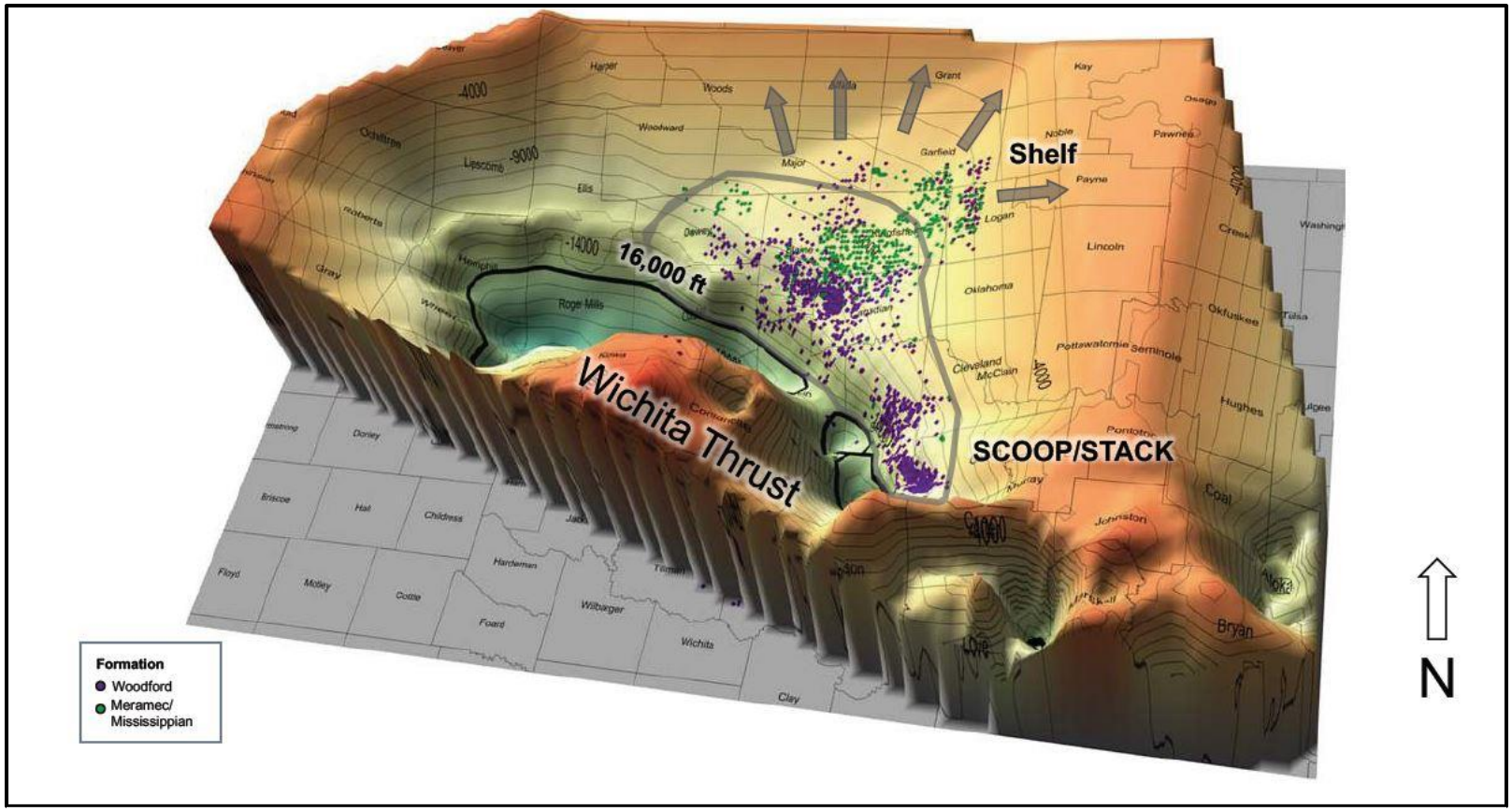

- The Devonian/Mississippian aged rocks on the shelf of the Anadarko Basin comprise a classic petroleum system
- As the plays have progressed from the SCOOP to the STACK to the MERGE, new plays continue to evolve as a result of the number of facies that are contained in these formations

Source: ITG/RSEG

The Maturity Index for American Shales

Emerging	Evolving	Mature
Mancos Shale	Utica Niobrara Wolfcamp Delaware Basin Wolfcamp Midland Basin SCOOP/STACK/Merge	Barnett Fayetteville Haynesville Marcellus Bakken Eagle Ford Gulf Coast Basin

Mature

The Functional Processes Associated with Mature Plays

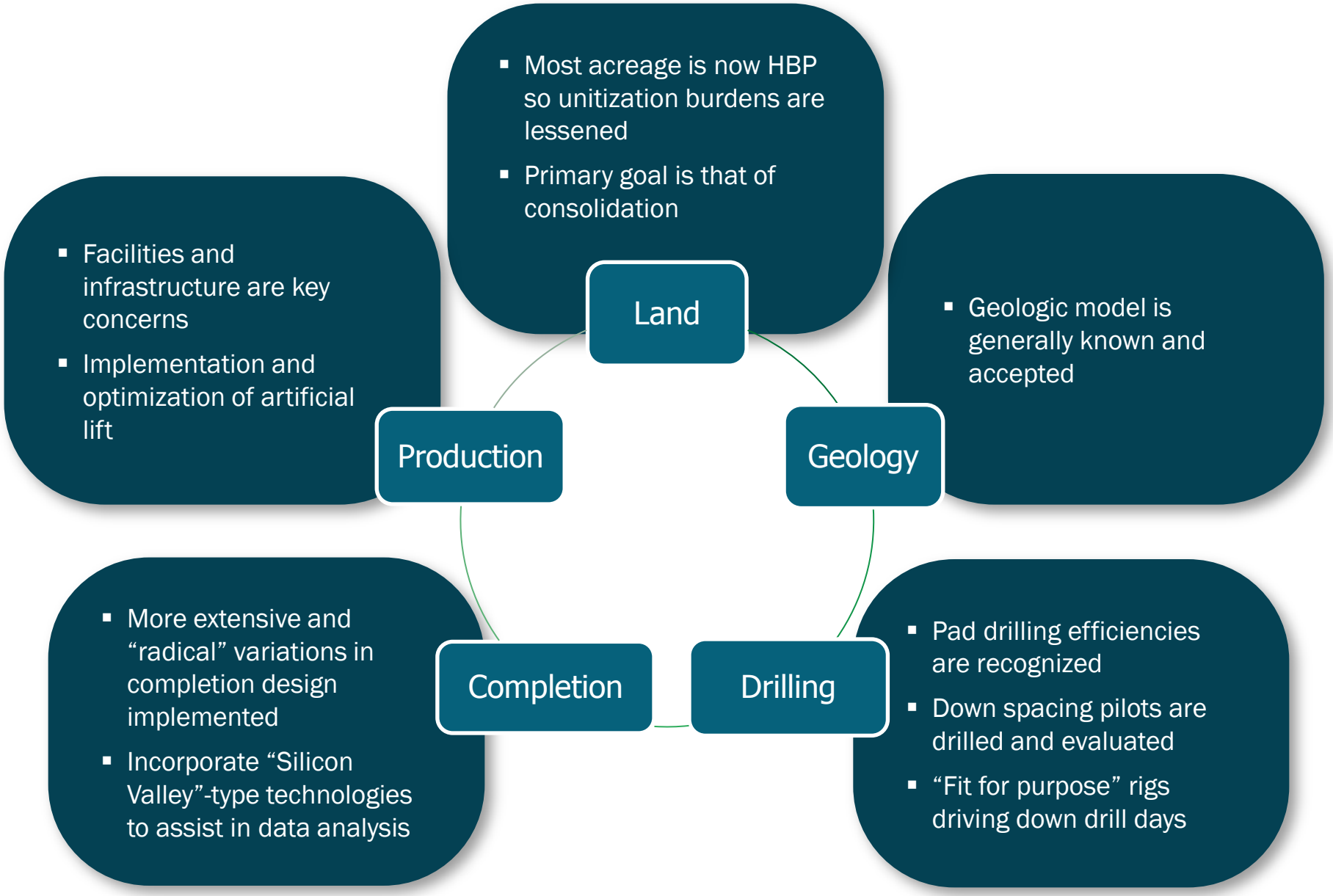

Mature

Barnett: Fracture Containment Matters

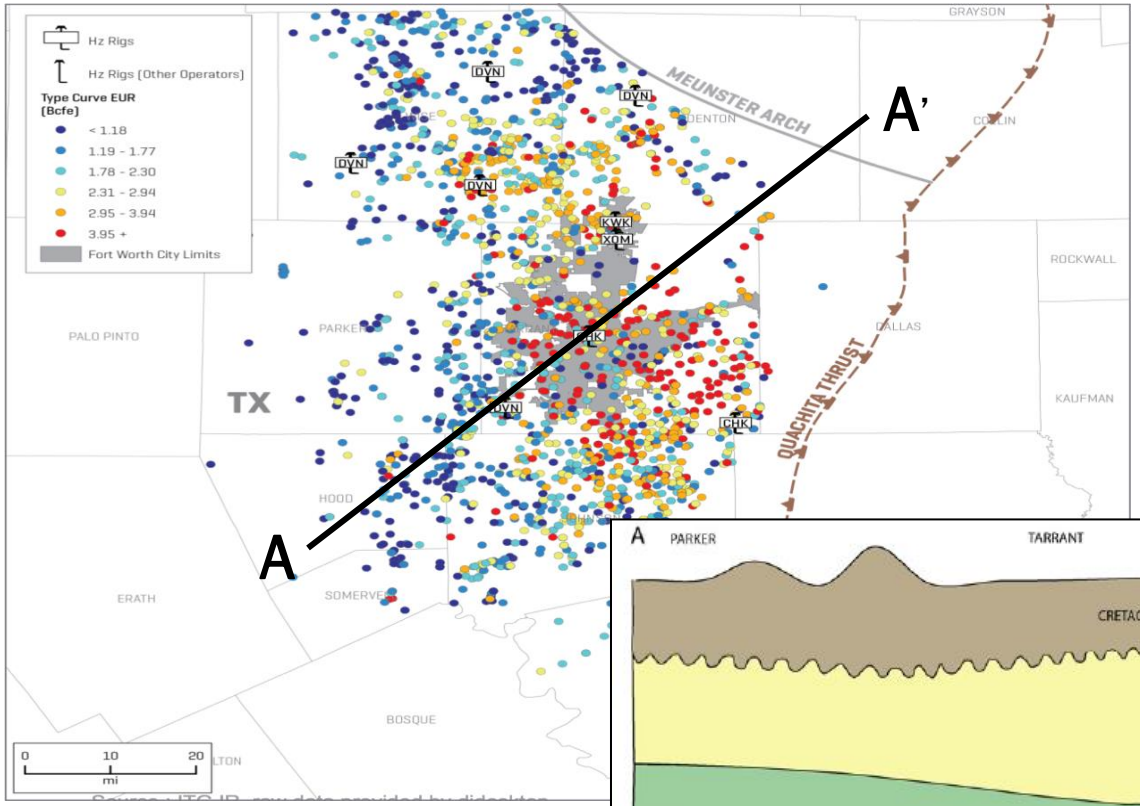

- Current: ~4 BCF/d
- Cum.: ~18 TCF
- EUR: ~44 TCF

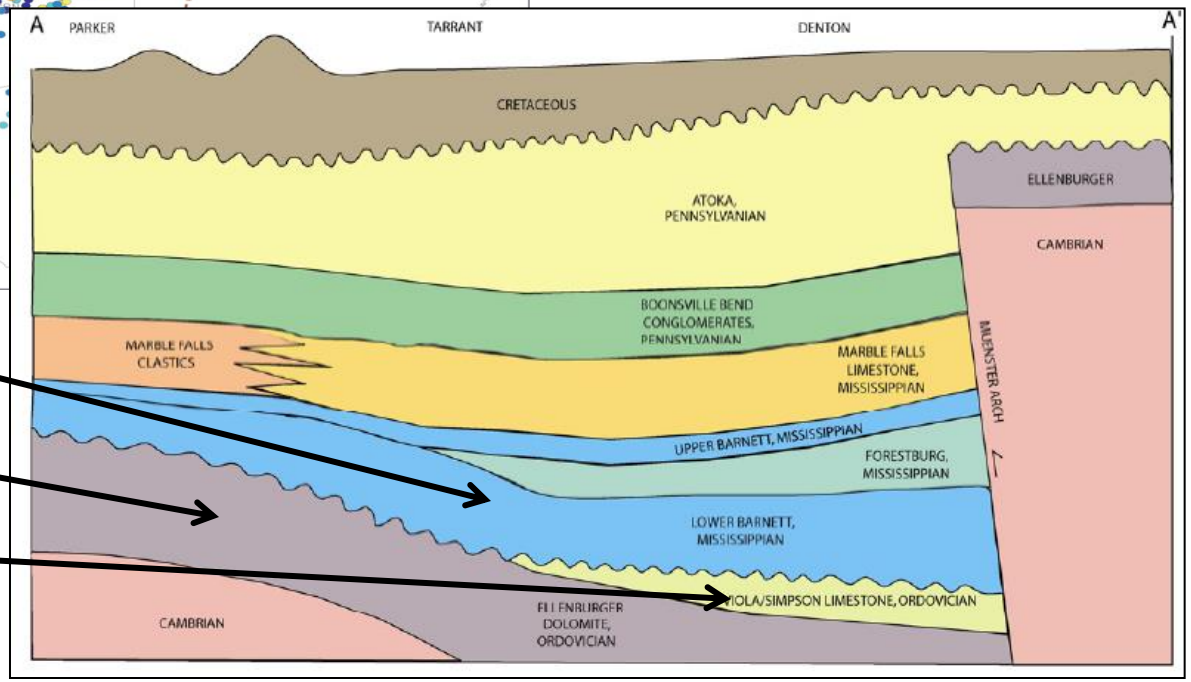

Barnett: Gas Reservoir

Ellenberger: Water Reservoir

Viola: Frac Barrier

Source: ITG/RSEG and University of Texas, Bowker, 2003.

Fayetteville: It Appears to be Structurally Simple, Yet it is Actually Quite Complex

Mature

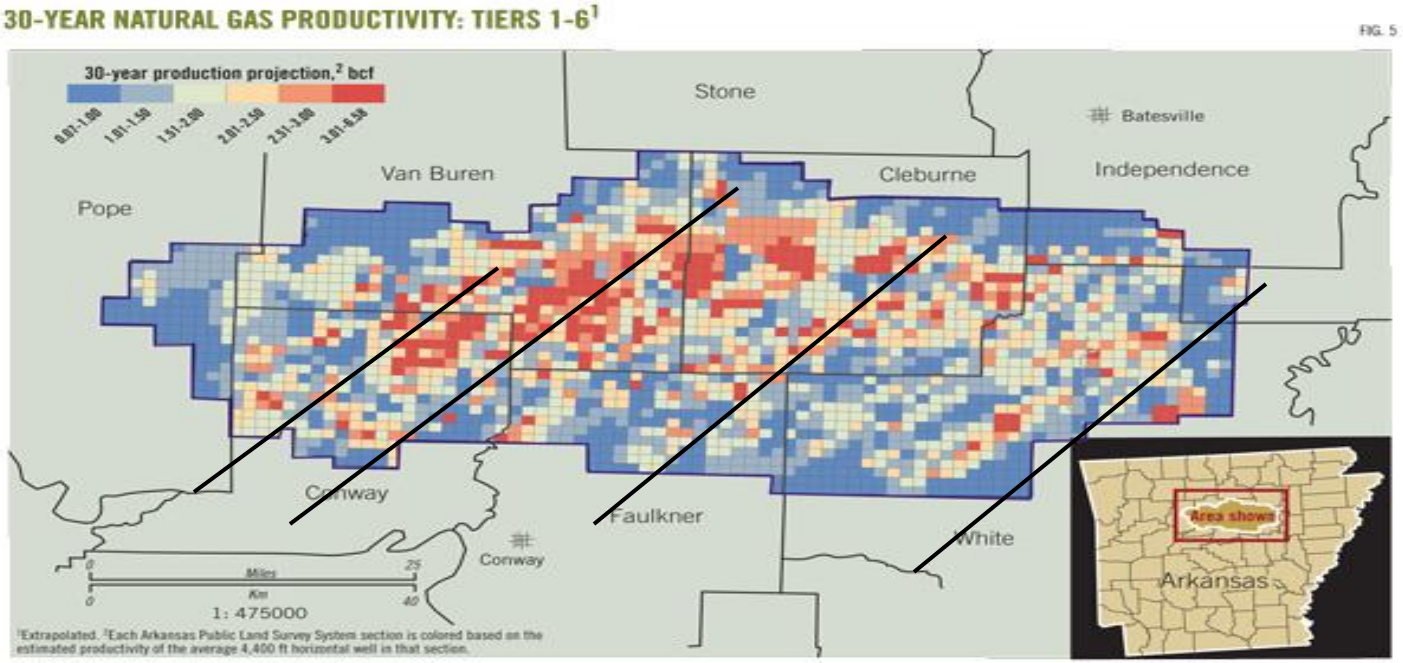

- Current: ~2.5 BCF/d Cum: ~5 TCF EUR: ~18 TCF
- Geologic Overview:
  - The area is dominated by monoclinal dip from north to south with production ranging from as shallow as 1500' to as deep as 8000'+
  - However, there are large regional faults that bisect the play from southwest to northeast
  - In addition to the large regional faults there are a multitude of smaller localized faults that made development highly sensitive to these structural elements

Source: ITG/RSEG and University of Texas Bowker 2003.

Mature

Haynesville: Which Core is Really "The Core"?

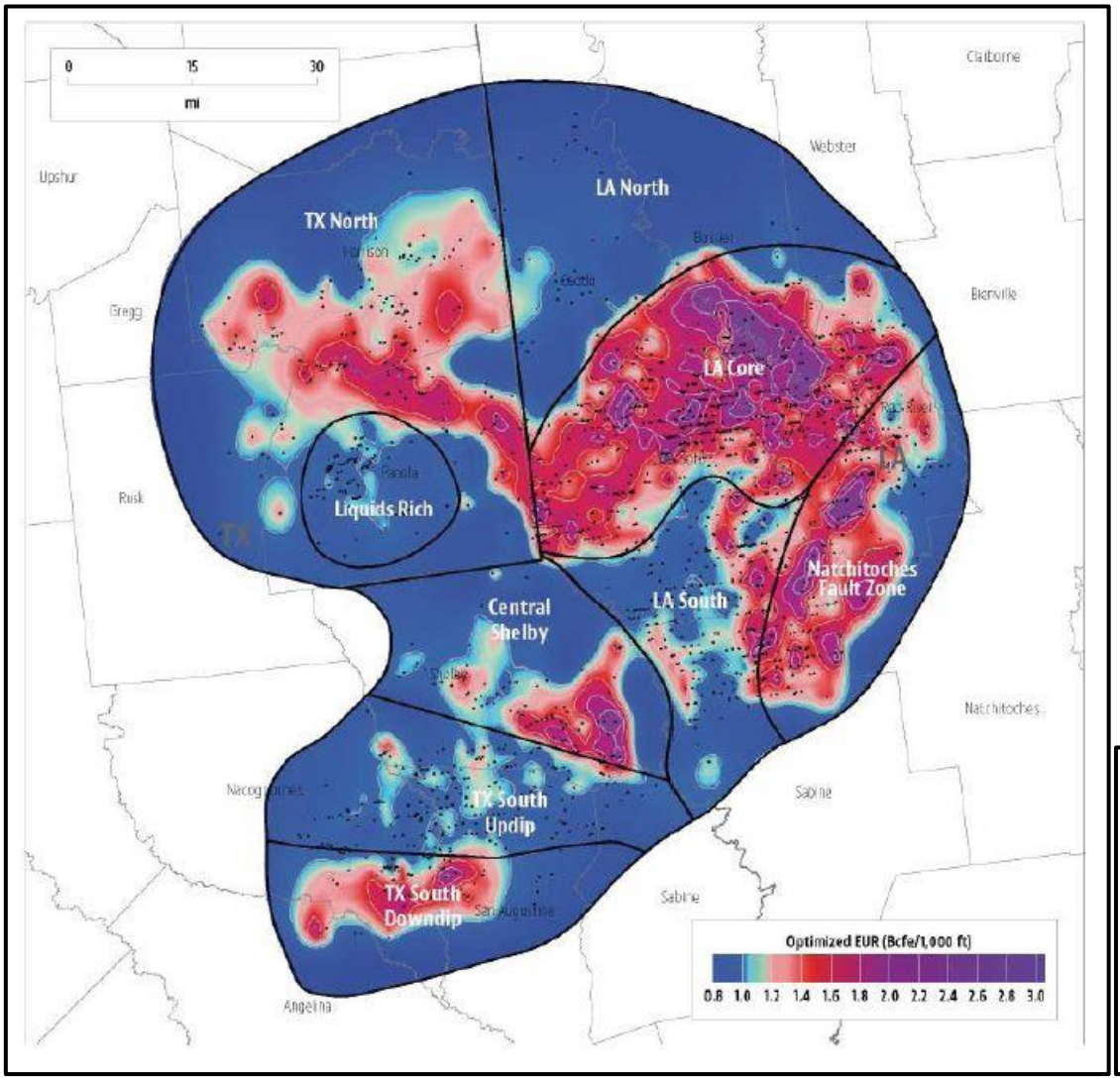

- Current: 6.2 BCF/D
- Three fairly discreet geographical areas of the play
- Each has certain positive attributes
- But only one is the winner and that is the Louisiana Core
- Why? Higher TOC, lower clay content and high pressure gradient (~.9 psi/ft)

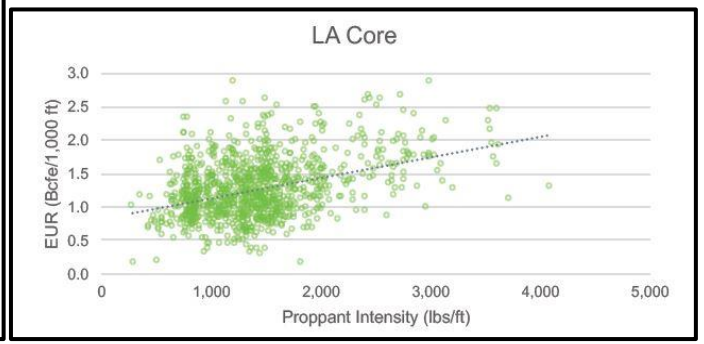

Source: RSEG

Mature

Marcellus: Heads or Tails, but Nowhere Else

- Current: 19.2 BCF/D

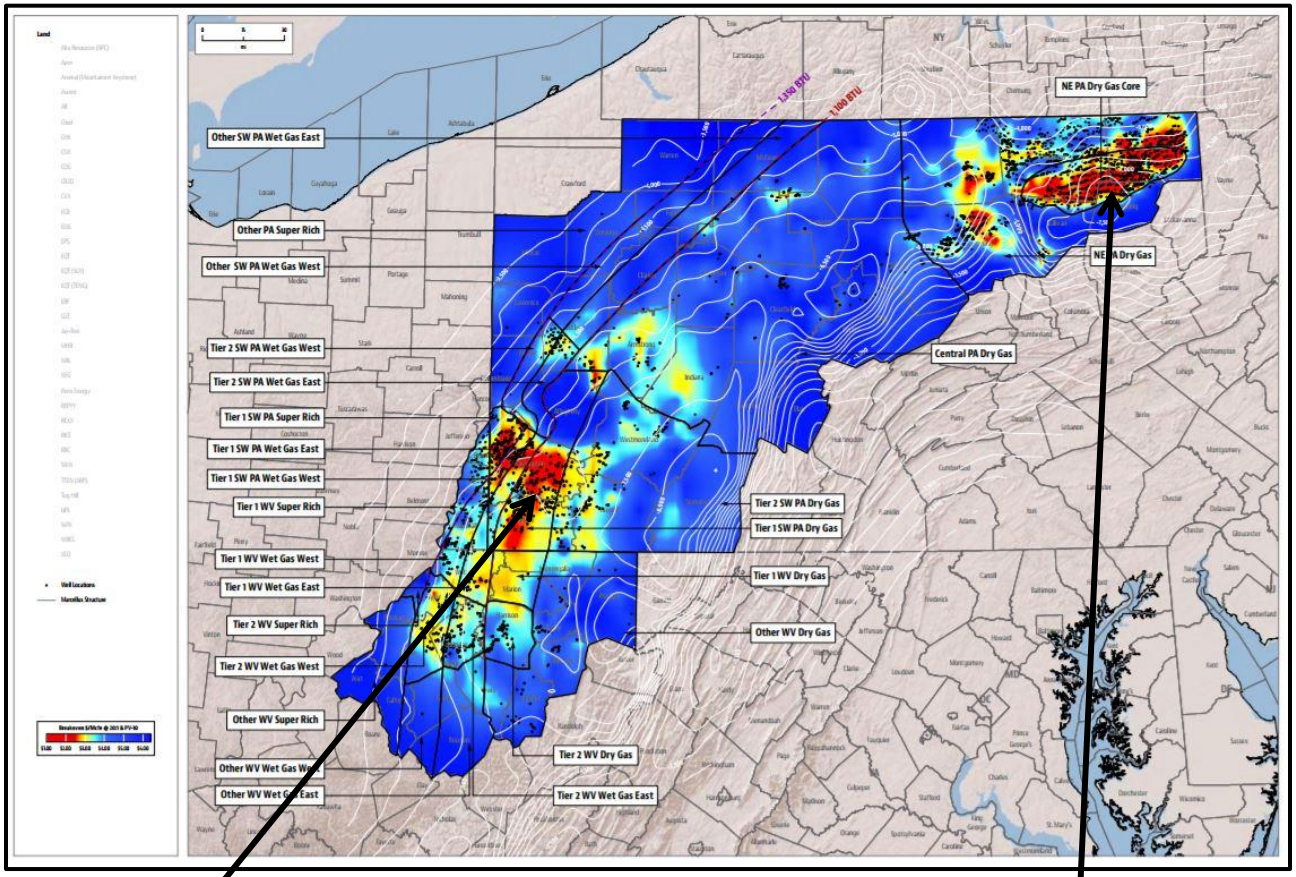

- Ranges Resources (Enercom 3-1-2107):
  - EUR/1000': 2.4-3.0 Bcfe
  - D & C Cost: $6.1-$7.3MM for 8500' lateral
  - Presumed EUR: ~20-25 Bcfe

- Cabot Oil and Gas (Simmons & Co. 3-2-2017)
  - EUR/1000': 4.4 Bcf
  - D & C Cost: $7.2MM for 8000' lateral
  - Presumed EUR: ~35 Bcf

Source: RSEG

Mature

Bakken: A Big Drop from 2014 to 2016

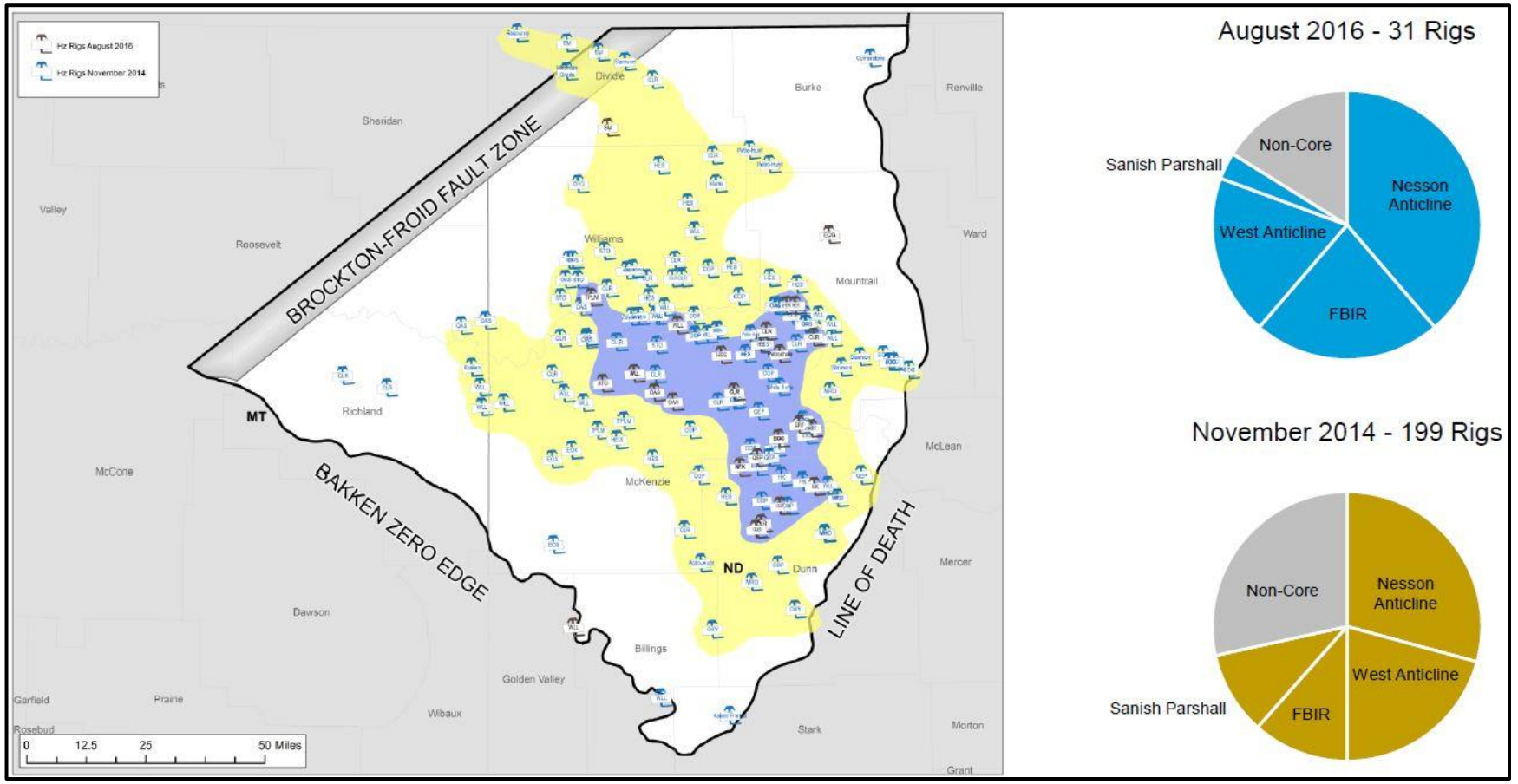

- Current.: 960 MBO/d + 1.6 BCF/d (down from 1.2 MMBO/d + 1.8 BCF/d)
- The blue and yellow shaded areas, and to a lesser extent the white area, all saw rig activity in 2014 (199 total rigs)
- Only the blue shaded area saw the vast majority of the rig activity in 2016 (31 total rigs)

Source: RSEG.

Eagle Ford Gulf Coast Basin: It's All Good (or at Least Most of it)!

Mature

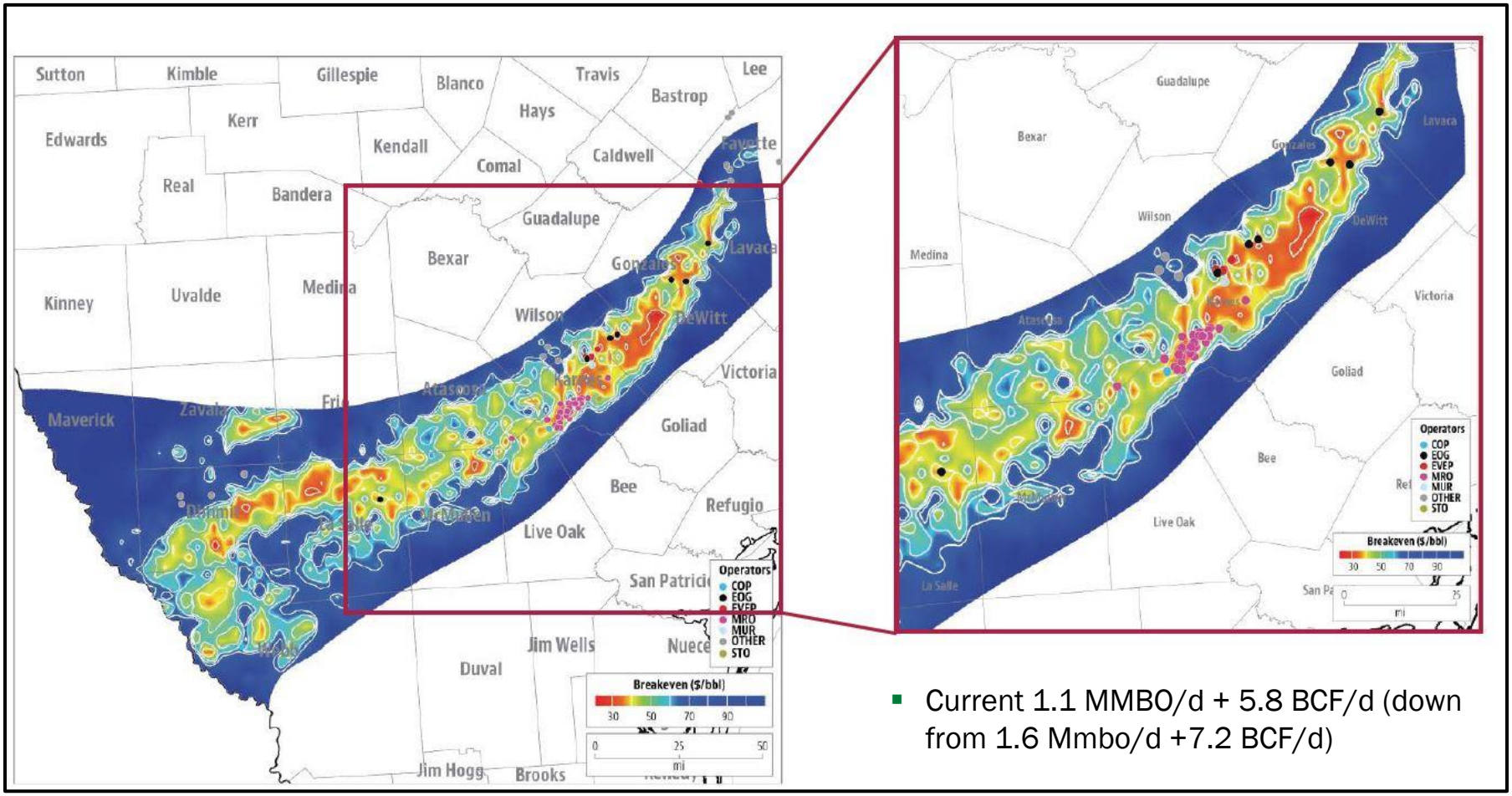

- Current 1.1 MMBO/d + 5.8 BCF/d (down from 1.6 Mmbo/d +7.2 BCF/d)

- The area represented on the map above is approximately 7 million acres
- The areas other than dark blue represent breakeven PV10 <$60/barrel and green/yellow/orange/red represent breakeven PV10 between $60-20 barrel
- This represents an area of over 200 continuous miles that breakeven less than $50 barrel

Source: RSEG.

We Just Keep Getting Better at This!

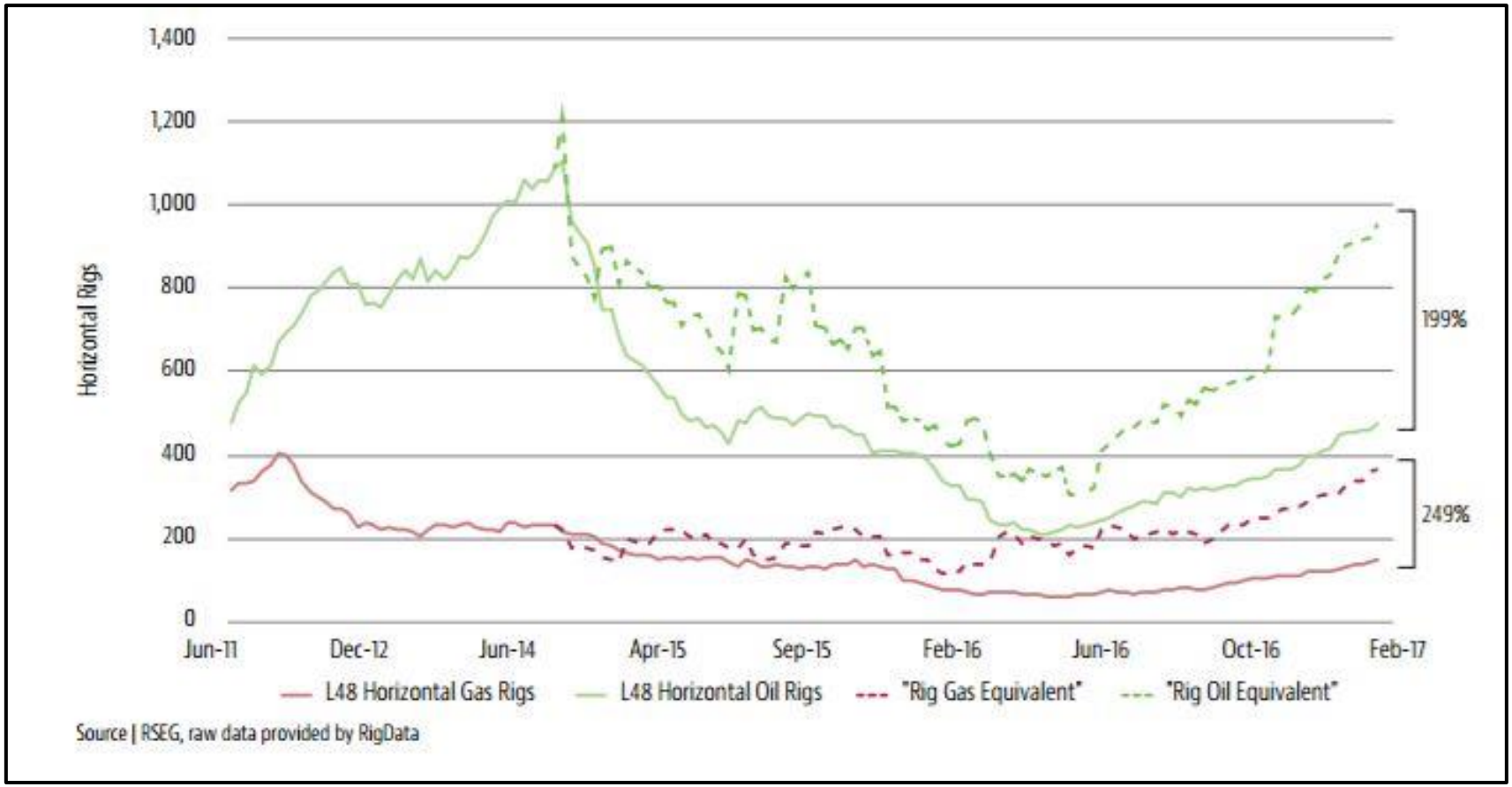

- Since the onset of the decline in the price of oil in late 2014, the industry is 2X more efficient/oil rig and 2.5X more efficient/gas rig
- How? Primarily by faster drill times and more effective completions (geometry and intensity)

Conclusions

- I bet everyone in this room will agree that what has transpired over the past decade is nothing short of amazing
- Our industry in general, and our profession specifically, should be incredibly proud of what we have accomplished
- We have changed the balance of power in one of the most powerful worldwide industries that exists by virtue of our discovery of shale source rocks as commercially productive reservoirs
- In just the last two years, we have proven to the world and to OPEC that they are no longer in control of the commodity
- For the foreseeable future, the United States will play the lead role in the supply of crude oil and natural gas and will need to be cognizant of the importance of that role

2

Davison, Ian, and John R. Underhill, 2012, Tectonics and sedimentation in extensional rifts: Implications for petroleum systems, *in* D. Gao, ed., Tectonics and sedimentation: Implications for petroleum systems: AAPG Memoir 100, p. 15–42.

Tectonics and Sedimentation in Extensional Rifts: Implications for Petroleum Systems

Ian Davison

Earthmoves Ltd., 38-42 Upper Park Rd., Camberley, Surrey, GU15 2EF, United Kingdom (e-mail: i.davison@earthmoves.co.uk)

John R. Underhill

Grant Institute of Earth Science, School of Geosciences, University of Edinburgh, The King's Buildings, West Mains Rd., EH9 3JW, Scotland (e-mail: jru@staffmail.ed.ac.uk)

ABSTRACT

Extensional rifts and their overlying sag basins host prolific hydrocarbon provinces in many parts of the world. This chapter reviews the development of rifts and the controls of tectonics on sedimentation patterns and hydrocarbon prospectivity. Rift tectonics exert the most important control on sedimentation and trap formation, and subsidence rate controls the geometry and facies of the rift fill. Rifting also controls the heat flow and burial history that determine the source rock maturation. Many rifts commence with evenly distributed small extensional faults when they are commonly characterized by closed drainage and continental sedimentation with localized lacustrine facies. As continental rifts develop, source rocks commonly accumulate in deep lakes, especially when the rifting is rapid, and organic shales are commonly located in the bottom third of the rift. Fault displacements increase and faults grow laterally to produce linked normal fault arrays. Marine deposits commonly replace the early rift continental deposition (e.g., North Sea) as the rift propagates to reach the world ocean system. Extremely prolific source rocks may be produced during rapid rifting in the marine phase, especially if half-graben depocenters are starved and oceanographic circulation is poor (e.g., Kimmeridge Clay Formation of northwestern Europe). As rifting wanes the rift fills, and fluvial sedimentation predominates, or in a passive margin, the basins enter into an extensional sag and/or postrift thermal sag phases when shallow-marine to deep-marine sediments infill and bury the former half grabens as sedimentation catches up and exceeds basin subsidence.

Recent studies in western Australia, Brazil, and west Africa indicate that thick (unfaulted) sag basins can develop very rapidly above rifted continental crust. The subsidence is too rapid to be produced by normal thermal conductive cooling and is believed to be caused by stretching of the lower/middle crust with no observable faulting (depth-dependent stretching; Driscoll and Karner, 1998). The stretching process can produce a broad passive margin (100–500 km [62–311 mi]) where the continental crust is only 5 km (3.1 mi) thick ($\beta = 7$). The sag basin

Copyright ©2012 by The American Association of Petroleum Geologists.
DOI:10.1306/13351547M1001556

in southern Brazil reaches about 1 to 2 km (0.6–1.2 mi) in thickness and drapes over the earlier rifted blocks to produce some of the largest oil fields discovered in the last 30 yr (e.g., Lula with 20 to 30 billion bbl of oil in place). These fields are trapped in lacustrine algal-bacterial carbonates that pinch out onto the fault block crests. Many rift basins remain unexplored in remote or inaccessible areas, and new future hydrocarbon provinces are anticipated in the African, Southeast Asian, Arctic, and Atlantic margin rift basins.

INTRODUCTION

Extensional rift systems have proven to be highly prospective petroleum provinces, especially in sedimentary basins where migration from a mature source rock occurred during the postrift phase of thermal subsidence following trap formation (e.g., Harding, 1984). It is now thought that rift basins on old passive continental margins (e.g., west Africa and Brazil) and intracontinental rift systems like the North Sea rift, host hundreds of billions of barrels of recoverable oil, and some estimates suggest that more than two thirds of the world's petroleum reserves lie in rift settings (Mann et al., 2003), making extensional systems the most significant of all tectonic regimes. In recent years, additional oil reserves have been discovered in young (Miocene–Holocene) intracontinental rifts such as the Albertine Graben in the East African rift, and more discoveries are expected to be realized in new opportunities like the previously inaccessible rifted margins adjacent to the Labrador Sea, West Greenland, the Beaufort Sea of northern Alaska and Canada, the Russian Arctic Ocean, and the Atlantic Ocean margins. Other rift exploration opportunities exist in areas that were previously off limits and lie on trend with known extensional petroleum provinces such as the offshore Sirte Basin, Libya.

Despite the evident prospectivity associated with rift systems, the study of extensional basins was a rather neglected subject in earth sciences (e.g., Gregory, 1896, 1921; McConnell, 1972) until the oil crisis in the early 1970s provoked an upsurge in hydrocarbon exploration, and seismic reflection surveys became a routine exploration tool. One of the reasons that extensional systems were neglected for so long was that most are buried and, hence, difficult to study. Furthermore, many of the ancient examples are only exposed because they have been inverted and uplifted in response to basin compression (e.g., Palymira fold and thrust belt; Wessex Basin) or now form parts of mountain belts (e.g., Tethyan continental margin of the Alpine-Himalayan Chain), and therefore it is difficult to observe the original rift geometry and facies relationships. However, important insights can be gained using seismic stratigraphy in shallowly buried rifts (e.g., the Inner Moray fifth in the North Sea; Underhill, 1991a), or by the study of well-exposed relatively undeformed rifts (e.g., Gulf of Suez, Aegean domain of Greece, and East Africa).

The amount of extension the crust has undergone is commonly expressed as the β factor (McKenzie, 1978). Continental rifts commonly develop to approximately 20% extension (β = 1.2), then strain hardening of the lithosphere occurs because of replacement of crust by cold continental mantle, and rifting ceases. However, rifts can continue to extend and develop into a passive margin with the formation of new oceanic crust. Complete opening commonly happens where thermal weakening of the lithosphere occurs because of the either focused heat source (e.g., the Parana-Etendeka plume in the South Atlantic; Turner et al., 1994) or a more diffuse thermal weakening (e.g., Central Atlantic Magmatic Province; McHone, 2000). On passive margins, the largest hydrocarbon accumulations are commonly trapped in the postrift thermal sag phase where high-quality reservoirs exist (e.g., South Atlantic margins of Brazil and west Africa). The initial sag basin in the South Atlantic developed in something like 5 m.y. and reaches up to 5 to 6 km (3.1–3.7 mi) thick on the west African margin in the vicinity of the Congo Fan (Henry et al., 2004) (Figure 1). This sag phase is located above the rifted zone and does not overlap onto the basin margins, as is expected with a thermal sag phase (Figure 1) (McKenzie, 1978). The very rapid development of this sag phase also precludes the conductive cooling model of McKenzie (1978), and the rapid subsidence is attributed to lower crustal stretching, where the upper crust remains unaffected, so that no large extensional faults or bed rotations are observed in this presalt sag phase (e.g., Karner and Gamboa, 2007).

This chapter will cover the deposition of the syn-rift fill and the rapid sag phase attributed to depth-dependent stretching but will not cover the later thermal subsidence phase of sedimentation. We aim to summarize a variety of basins in different locations, but will not cover the longer (postrift) thermal subsidence through time. Most of the examples we will discuss are basins that we have actually worked on ourselves. A plethora of reviews on rift tectonics and sedimentation exists, and here we recommend the following to gain an overview of the main factors to consider when addressing

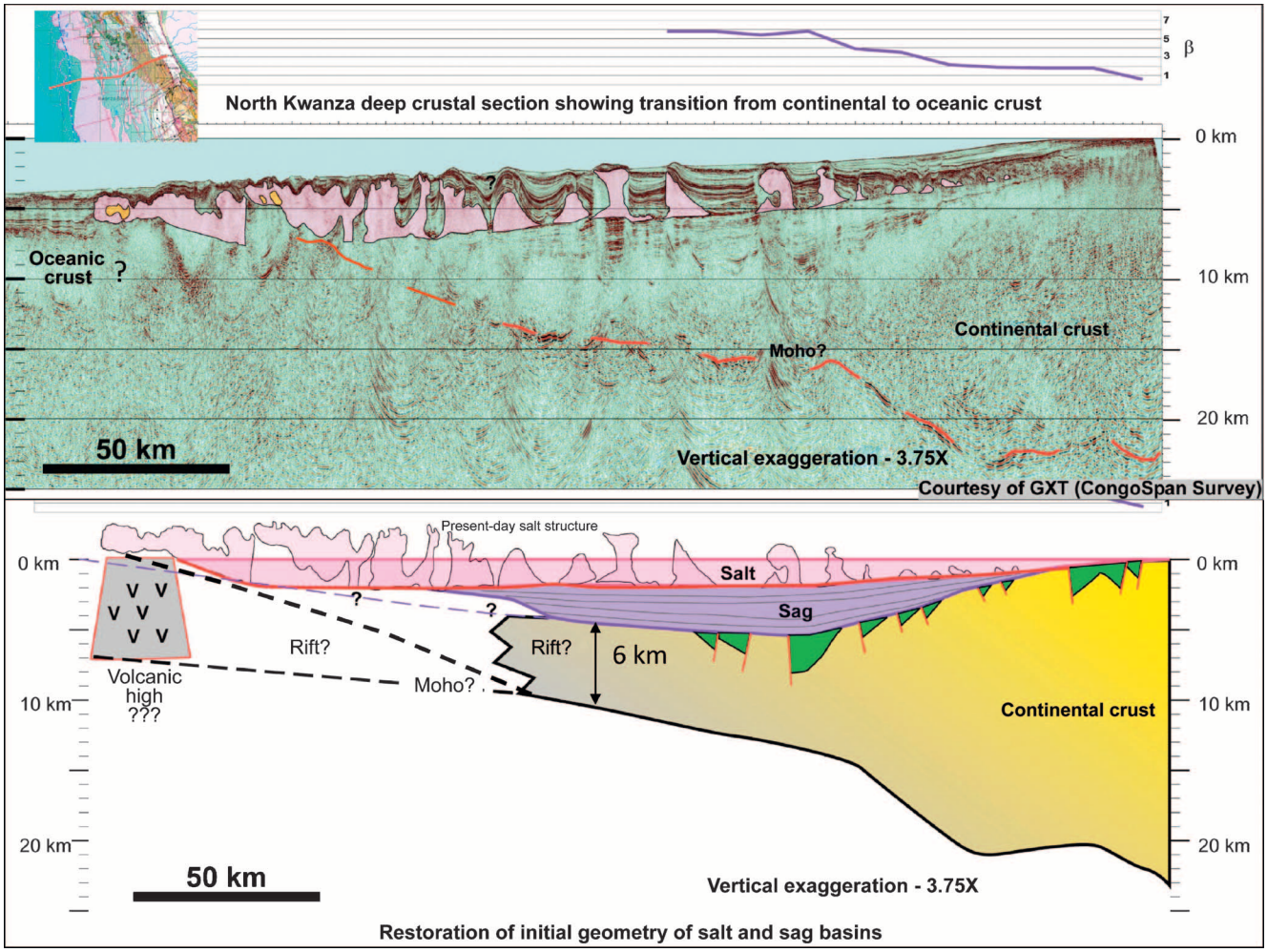

Figure 1. Seismic section and cross section flattened at the top salt level (to remove the tilt effect of thermal subsidence) through a rifted continental margin of west Africa showing a rifted series of relatively small half graben (3–4 km [1.9–2.5 mi] deep), an extensional sag basin approximately 5 km (~3.1 mi) thick, and a thermal sag phase of sedimentation (4 km [2.5 mi] deep). The β curve above the diagram indicates the calculated stretching profile across the eastern half of the section where the moho is imaged clearly. Seismic data courtesy of ION's Basin SPAN programs. 50 km (31 mi).

synsedimentary controls on petroleum play fairways: Frostick and Reid (1989), Schlische (1993), Roberts and Yielding (1994), Lambiase and Bosworth (1995), Morley (1995), Ravnas and Steel (1998), Lambiase and Morley (1999), Gawthorpe and Leeder (2000), Morley (2002b), Leeder (2007), and their impact in seismic stratigraphy (Underhill, 1991b).

RIFT TECTONICS

Rifting can be caused by lithospheric stretching and thinning without volcanic involvement, in such cases, narrow rifts are developed. In hotter heat flow regimes, broad rifted zones (e.g., Afar Triangle and Basin and Range province) develop that have complex fault patterns produced by multiple-phased extension on planar domino and/or listric faults (Morton and Black, 1975; Proffett, 1977) (Figure 2). The very large extensions produced in the Basin and Range province create steeply dipping early rift strata developed on low-angle normal faults with broad shallow basins. These hotter highly extended ($\beta > 2$) shallow basins are generally less prospective than colder rift basins because the fault spacings are relatively small, and the increased heat input maintains the rift elevation so that deep lakes are generally not developed.

Other workers, most notably Wernicke (1985, 2009), argued that rift processes were inherently asymmetric and cited cases like the Basin and Range province in the

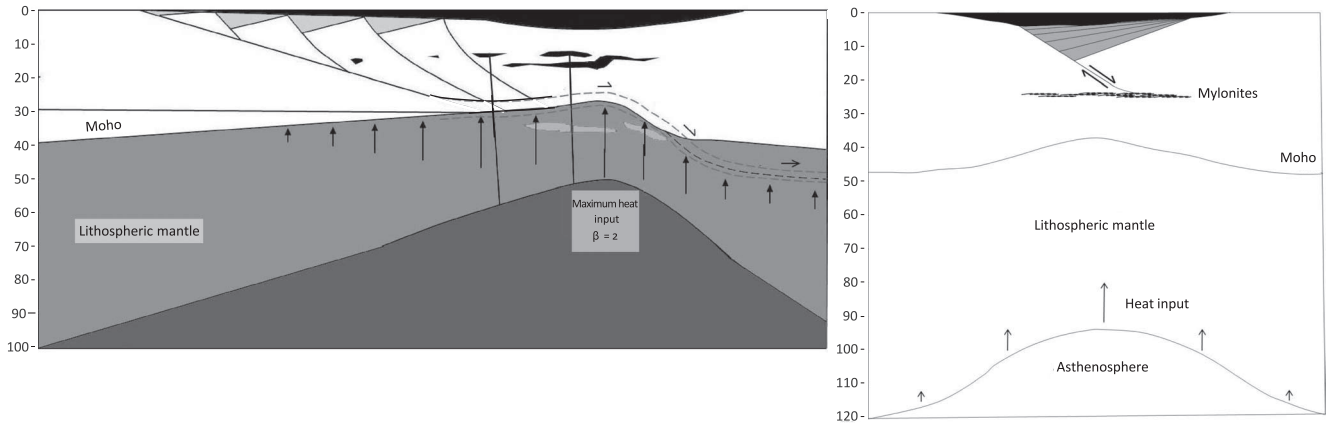

Figure 2. Different rift styles. (A) Basin and range style wide shallow rift with simple shear (Wernicke) model. (B) Deep simple rift with pure shear (McKenzie) stretching model.

western United States, where the locus of main volcanism and uplift appeared to lie outside the zone of extensional deformation. This model is referred to as the simple-shear model and is dominated by the formation of low-angle detachment faults and predicts that the axis of volcanism (and uplift) lies outside the main zone of rifting (Figure 2). A simple shear rift basin may have similar rift geometry and sedimentary fill to an asymmetric half graben produced by pure shear, but the thermal history should be different with less thermal subsidence sag phase developed directly above the central rift axis in the simple shear case (Figure 2). Continental rifting commonly occurs during a 5- to 20-m.y. period, with subsidence of up to 12 km (7.5 mi) recorded in some basins (e.g., Central Tucano Basin, northeastern Brazil; Magnavita et al., 1994; Colorado Basin, Argentina, authors' own observations). This represents a subsidence rate of 0.5 mm to 2 mma^{-1}, with the most rapid rifts reaching 5 mm^{-1} (Ravnas and Steel, 1998). Sedimentation rates can keep pace with even the most rapid subsidence rate where major river input points exist, but commonly, sedimentation rate is less than the maximum tectonic subsidence rate, so that deep lakes form, where the exposed basin floor may dip as much as 10° (Ravnas and Steel, 1998).

RIFT ARCHITECTURE

The main feature of extensional rifts is tilted half grabens where the deepest part of the half graben is adjacent to the fault (Figure 3). Rift fault blocks generally range from 5 to 25 km (3.1–15.5 mi) in width but occasionally reach up to 50 km (31 mi) (Ravnas and Steel, 1998). The deepest rifts (~10 km [~6.2 mi]) appear to develop where the crust is thickest and strongest (and the seismogenic layer thickest) such that local deep basin depocenters develop (e.g., Colorado Basin in Argentina has 10 km [6.2 mi] thickness and is located in the thickest surrounding crust (~40 km [~25 mi]) on the Argentine margin, authors' own observations). The rift is commonly a single half graben (e.g., North American Triassic rifts; Schlische, 1993; Olsen, 1997). In such cases, no structural closures exist within the basin, and any hydrocarbons generated can migrate out to the surface on the flexed rift margin. Stratigraphic traps with ponded lacustrine turbidites or fluvial and shoreline progrades off the hanging wall would be required for the petroleum system to work.

The various aspects of the fault and basin geometry are described below, and the implications for sedimentation and hydrocarbon potential are discussed at the end of this chapter.

Fault Geometry

The recognition of low-angle normal faulting in Wernicke's (1985) model, together with the apparent listricity displayed by seismic time sections, led many interpreters to produce structural interpretations that were consistent with the listric fault model (e.g., Gibbs, 1984). There appeared to be an inconsistency with neotectonic observations, however, because coseismic activity on neotectonic faults (e.g., linking surface or bathymetric rupture with earthquake epicenters) demonstrated that most normal faults in continental rifts are almost planar (straight in cross section) within the upper crust dipping at angles between 30 and 60° (Stein and Barrientos, 1985; Jackson and White, 1989) down to midcrustal levels. The increasing appreciation that the curvature and progressively shallow dip of the faults seen on seismic sections was removed when velocity

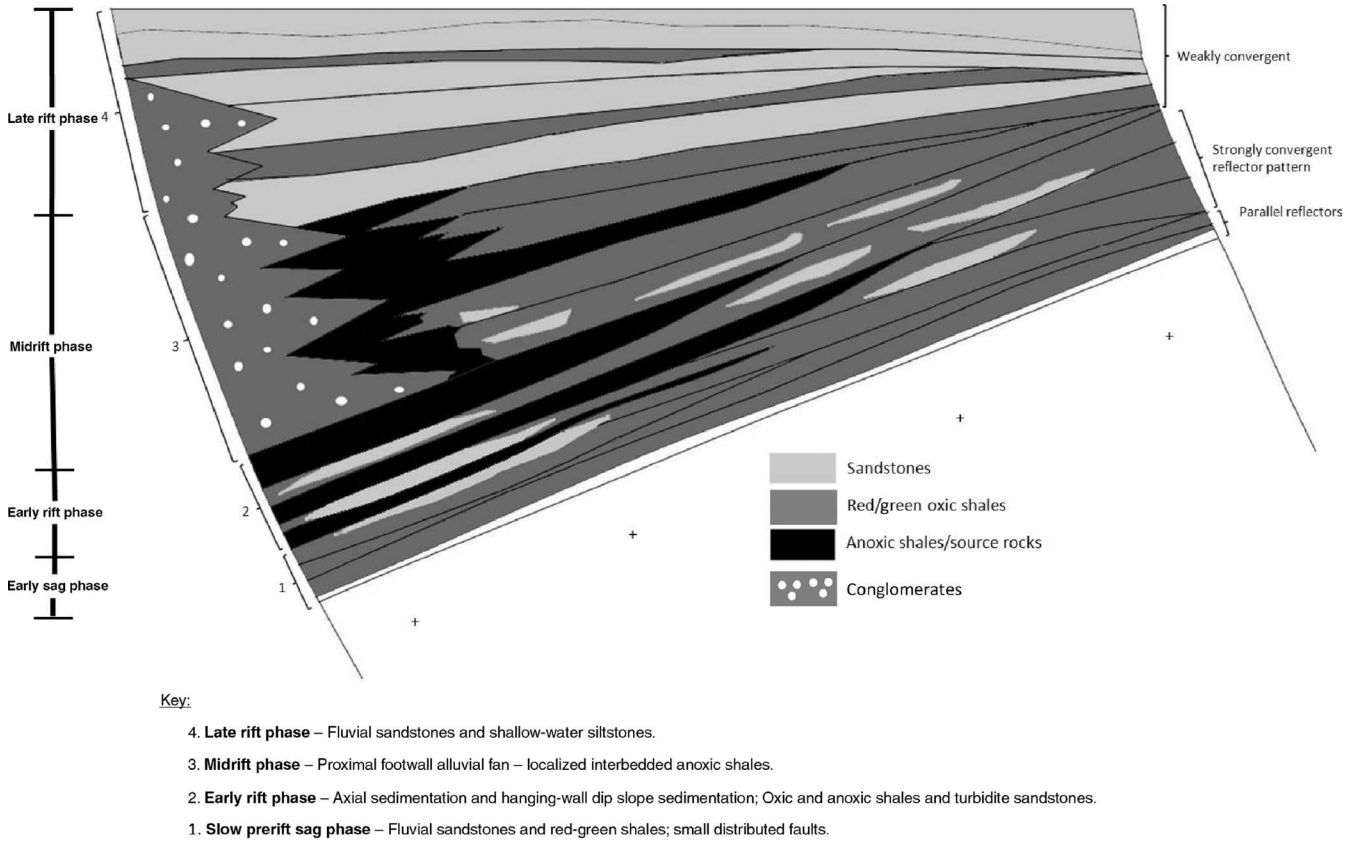

Figure 3. Half graben showing a typical continental rift fill with an early fluvial phase, a middle rift lacustrine phase, and a late fluvial alluvial fill.

models were applied and they were depth converted led to consistency between neotectonic observation and the interpretation of ancient subsurface examples (Badley et al., 1990; Yielding et al., 1991; Roberts and Yielding, 1994).

It is now generally accepted that planar faults develop at dip angles of 50° (softer rocks with lower angles of friction) to 70° (in subhorizontal lithified sedimentary rock, Walsh and Watterson, 1988b) to depths where they may flatten into a ductile middle/lower crust. The planar faults will rotate to lower angles as the intervening blocks rotate to accommodate increasing extension (the domino model, Morton and Black, 1975). However, sometimes faults can develop at much lower angles and act as superdetachments where they accommodate most of the deformation and very few smaller faults exist in the basin (e.g., Hørnelen Graben in Norway, Seranne and Seguret, 1987; or the Sevier Desert Detachment in Utah, Armstrong, 1972). These faults are thought to have been initiated along preexisting shallow-dipping faults and basement shear zones, some of which in the case of the Rockies, may have been precursor thrust faults (a process known as negative structural inversion).

The low-angle detachments were first mapped in the Basin and Range province (Hunt and Mabey, 1966; Armstrong, 1972) and became generally accepted after the May 1977 Penrose Conference where metamorphic core complexes were described for the first time. The existence and slip mechanics on low-angle detachments are still the subjects of considerable debate (Wernicke, 2009) because no large earthquakes are generated along low-angle detachments (Jackson and White, 1989). Hence, low-angle fault slips may be aseismic, which can be explained by the low strength of the fault zone. The initial dip of faults is important as high-angle faults produce faster subsidence rates than low-angle faults for a given strain rate; and hence, deep rift-lake development is favored by faults initiated at a high angle.

Fault Growth

Although structure maps like the (top synrift) Base Cretaceous Unconformity surface generated in the North Sea (Figure 4) are effective in locating the main normal faults and their structural closures, they do not

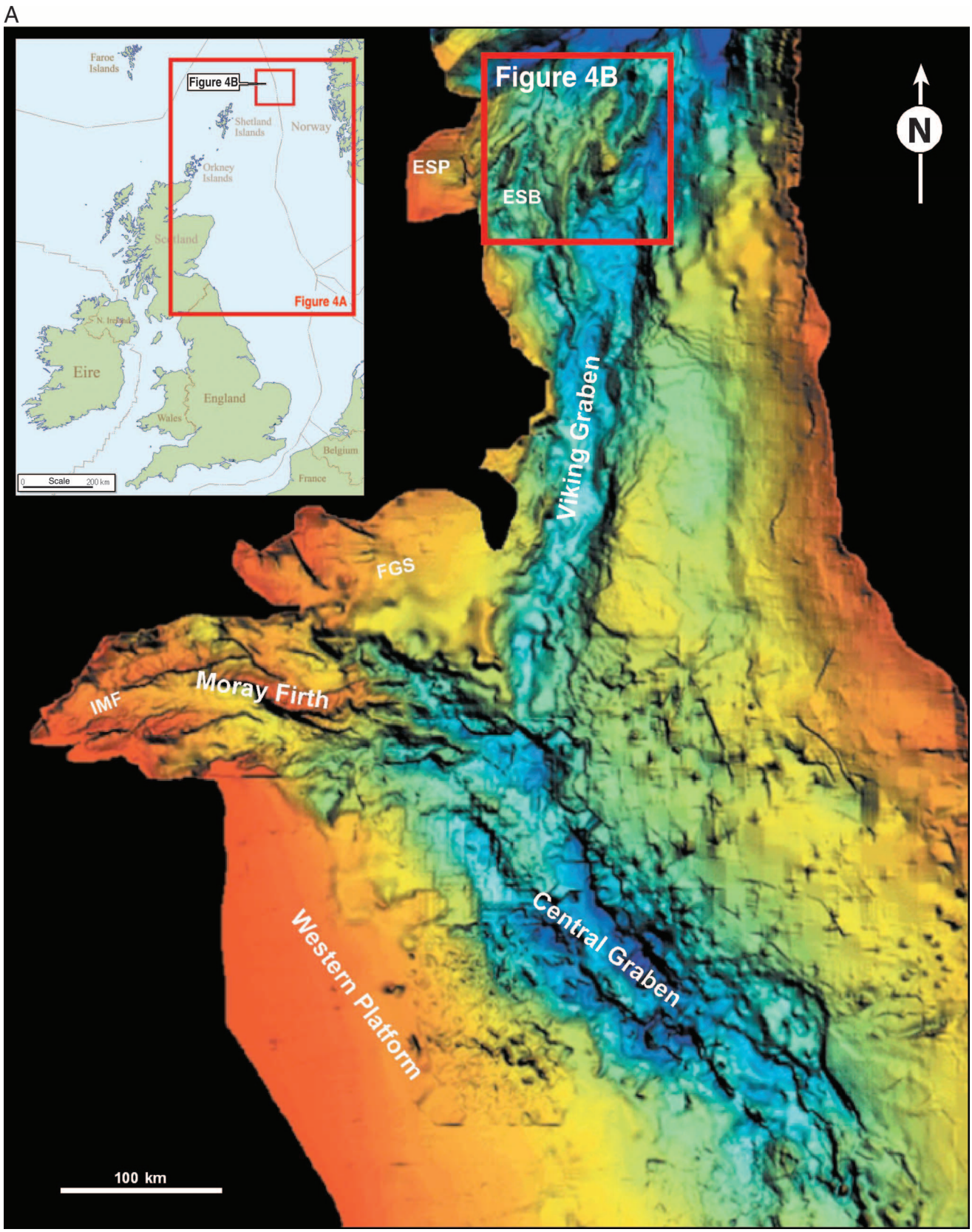

Figure 4. (A) Shaded relief map of the Base Cretaceous Unconformity in the North Sea. (B) Detailed Base Cretaceous Unconformity shaded relief map. Courtesy of Petroleum Geo-Services (PGS). ESP = East Shetland Platform; ESB = East Shetland Basin; FGS = Fladen Ground Spur; IMF = Inner Moray Firth. 100 km (62 mi), 30 km (18.6 mi).

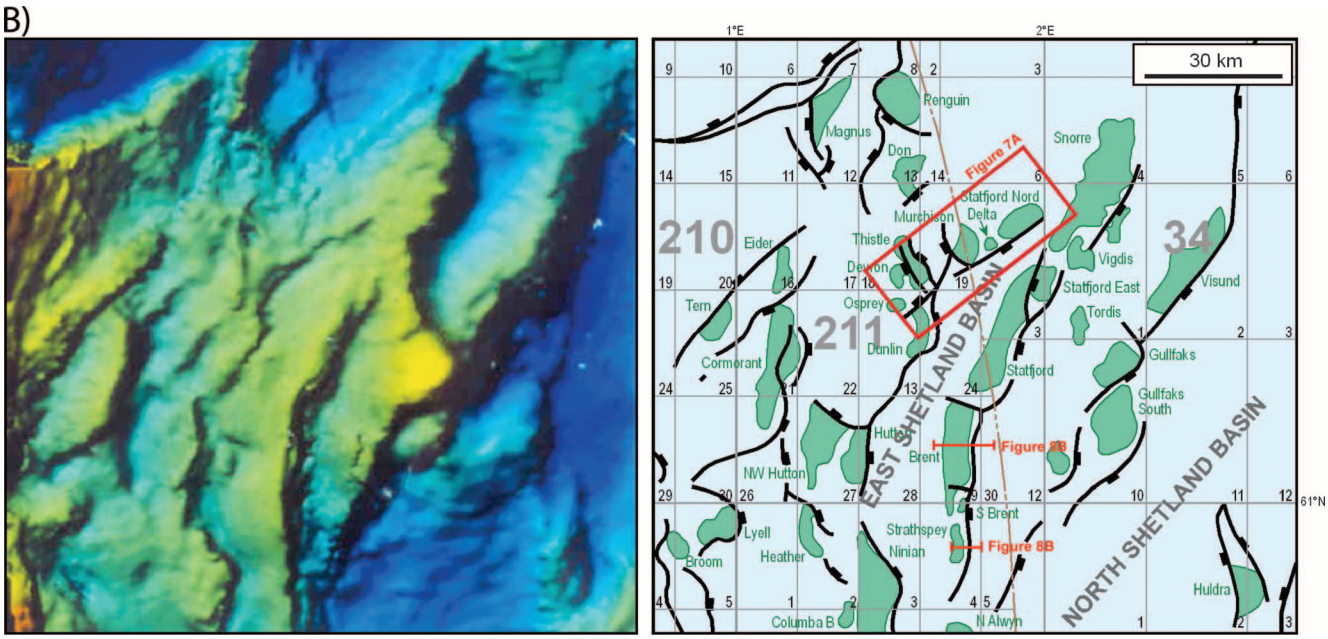

Figure 4. (cont.).

provide insights into how the normal faults nucleated, grew, and evolved to form their final patterns as they represent the end point of the rift process. Instead, insights have had to be gained from physical analog and numerical modeling (e.g., McClay, 1995), from neotectonic studies of active rifts (Cowie and Scholz, 1992a, b; Scholz et al., 1993), and from ancient examples where sufficient stratigraphic control exists to produce structural restorations through time (e.g., the Late Jurassic rift system of the northern North Sea; Dawers and Underhill, 2000; McLeod et al., 2000, 2002).

The growth of normal faults have been studied extensively (e.g., Walsh and Watterson, 1988a; Cowie and Scholz, 1992a, b; Scholz et al., 1993) and is believed to be a self-similar process that leads to fractal geometry (Scholz and Aviles, 1986). These models have predicted growth of the fault displacement to be greatest at the central fault nucleus and decrease outward following a power law decrease (Walsh and Watterson, 1988a) or simple linear displacement gradient to the fault tip (Cowie and Scholz, 1992a). However, the growth of individual faults becomes much more complex as the faults become larger, interact, and link to produce multisegmented major normal faults (Machette et al., 1991; Dawers et al., 1993; Cartwright et al., 1996; Morley, 2002a). Hence, individual depocenters are small and shallow when faulting commences, then depocenters grow and merge through time, and finally, only the largest faults remain active and localized major depocenters develop in their hanging walls. These will be the preferred sites of lake development in continental rifts (Figure 5).

The fault displacement to fault length relationship changes when the fault extends across the whole brittle crust and can no longer grow upward or downward so the fault plane is constrained to grow only laterally. Large faults are also most likely to link up with smaller faults, hence, large faults tend to have larger length/displacement ratios. Most large normal faults have horizontal lengths of 100 to 200 km (62–124 mi) and average maximum displacements approximately 5 km (~3.1 mi); however, the longest active part of a fault that breaks in a single seismic event is approximately 25 km (~15.5 mi) (Jackson and White, 1989) with coseismic slips as great as 6 m (20 ft) and earthquake recurrence intervals ranging from 500 to 7600 yr (Ravnas and Steel, 1998). One of the main controls on ultimate fault length appears to be the thickness of the seismogenic layer. East African examples demonstrate that the thicker the seismogenic layer is, the longer the faults are; and the thinner it is, the shorter the segment lengths (e.g., Jackson and Blenkinsop, 1993; Bilila-Mtakataka fault in Malawi, East Africa; Ebinger et al., 1999). Consequently, a thicker, brittle layer favors large faults and deeper half graben and source rock development. In general, the locus of extension migrates toward the center of a rift province (e.g., Goldsworthy and Jackson, 2001), leading to many faults becoming dormant as rifting proceeds (Gupta et al., 1998) whereas those that lie closest to the rift axis had the longest activity and greatest throw (Cowie et al., 2005). The process also accentuates rift flank uplift and exposure of early synrift sediments in basin margin positions.

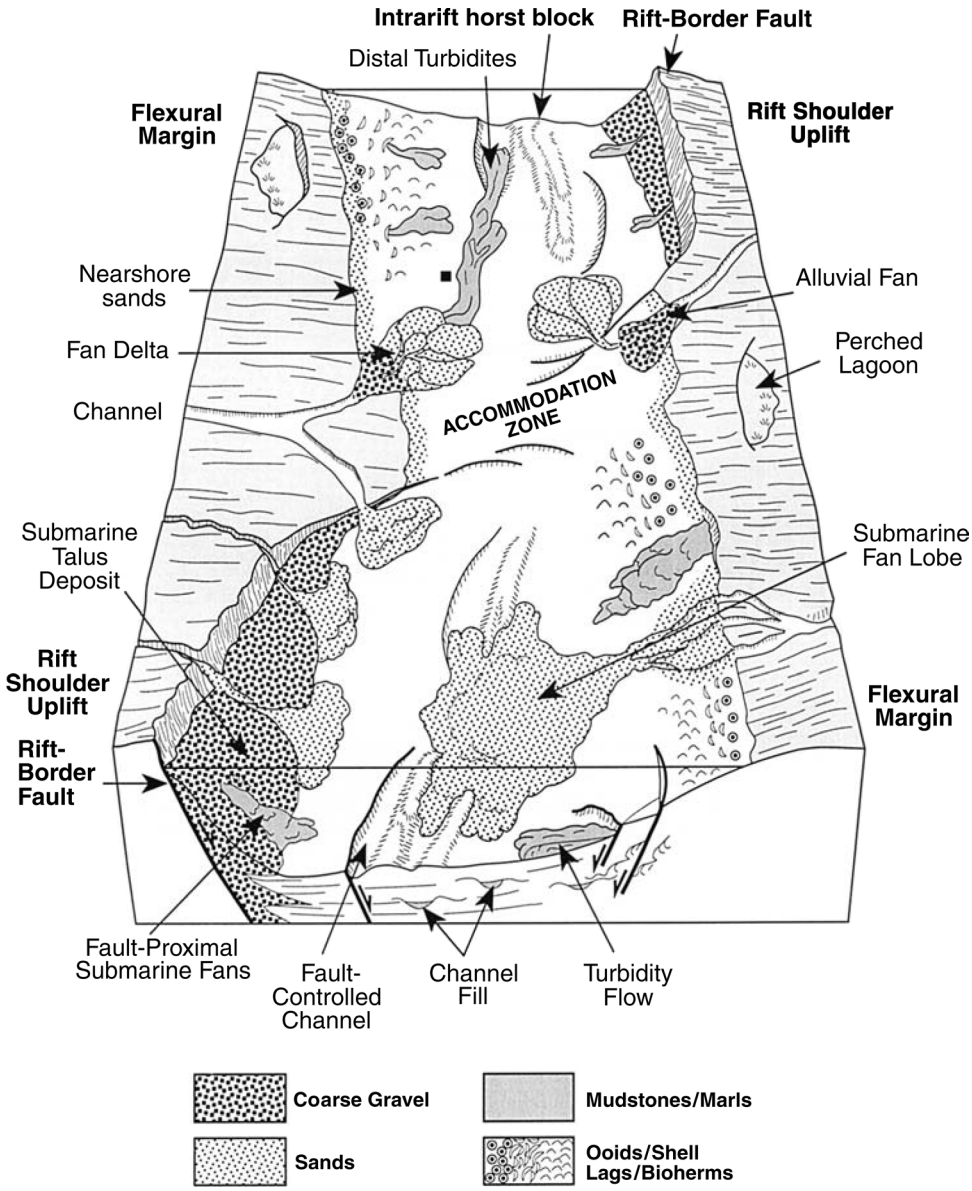

Figure 5. Block diagram of rift showing the footwall uplift zones and accommodation zone produced by the overlapping faults. Modified from Younes and McClay (2002).

Footwall Uplift

Footwall uplift and plume dynamics under a rift commonly produces surrounding rift shoulders up to 1–4 km (0.6–2.5 mi) high. These can trap large isolated lakes, 1–3 km (0.6–1.9 mi) deep, where very large fluctuations in lake level occur because of rapid evaporation and precipitation. For example, the water level of Lake Tanganyika has risen by more than 600 m (>1970 ft) in the last 25 k.y. (Scholz and Rosendahl, 1988). The zone of footwall uplift adjacent to a normal fault reaches a maximum in the center of the fault where the fault displacement reaches a maximum (Jackson and McKenzie, 1983; Yielding, 1990) and the width of the zone affected by footwall uplift can reach up to approximately 20 km (~12.4 mi) distance away from the surface fault trace (Stein and Barrientos, 1985; Stein et al., 1988). The amount of footwall uplift ranges from about 5 up to 20% of the fault throw (Roberts and Yielding, 1994), where uplift is related to the elastic properties of the lithosphere, the throw and dip on the fault, and the fault spacing (Jackson and McKenzie, 1983; Barr, 1987a, b). The amount of footwall uplift also depends on the density of the rift valley fill. Air-filled empty graben footwalls are uplifted more than water-filled or sediment-filled rifts, where the sediment loads in the hanging wall is loading the footwall of the major normal faults. Conversely, when the uplifted footwall block is eroded and the material is removed and is not deposited in the adjacent hanging-wall basin, then the basin itself will be uplifted across a

zone up to 50 km (31 mi) wide away from the fault (Magnavita et al., 1994). This effect is most marked in rift shoulders of passive margins. Eventually, the footwall fault scarp will be eroded back to create a drainage catchment area so that sediment will be transported toward the rift instead of away from it. This change in sediment flow direction from the uplifted footwall blocks may take several million years.

If the footwall is uplifted above sea or lake level, subaerial erosion is important and sediment is redeposited into the surrounding hanging-wall graben. However, if the footwall blocks are submerged, subaqueous erosion is limited and the basin will be relatively more starved (e.g., Upper Jurassic of the Central Graben, North Sea).

Unconformities and surprising thickness trends are commonly produced in extensional provinces as new fault sets develop and transect older footwall uplifts (e.g., in Grand Banks, offshore Morocco, northwestern Australia) such that restoration of the later rift system is the only way to accurately assess the disposition of older plays. In the North Sea, restoration for the Late Jurassic extension has revealed prospectivity in the underlying precursor Triassic rift (Tomasso et al., 2008) with discovery of new fields (e.g., Alwyn North). This has extended the production life of the basin and allowed for a better understanding of the footwall and hanging-wall positions, the synsedimentary control on sedimentation and, hence, highlighted new exploration opportunities at that stratigraphic level.

Cross-Faults, Relay Ramps, and Accommodation Zones

Faults that form at high angles to the rift axis were termed transfer faults by Gibbs (1984) and transverse faults by Colletta et al. (1988). These faults do not form in isotropic scaled models of extension (McClay, 1995), nor are they observed in many rifts even where dip polarity changes occur along strike (e.g., Gulf of Suez and the North Sea). Instead, these areas are flexed and only lightly deformed. Where two major bounding faults of opposing polarity propagate toward each other, this produces a zone of arching between the two faults known as an accommodation zone (Bosworth, 1985; Rosendahl, 1987; Moustafa, 1997) (Figures 5, 6), and the interference of two hanging-wall flexures can produce a structural arch between the two interacting faults (Magnavita et al., 1994).

Most hard-linked transfer faults in rifts are believed to be controlled by inherited structures from the basement (e.g., Milani and Davison, 1988; McClay and Khalil, 1998) (Figures 5, 6) or reactivated precursor normal fault systems that underlie the later rift, which are activated during rifting because they are preferred zones of weakness.

Shorter cross-fault elements that branch from the master extensional fault are increasingly being recognized along normal fault arrays. They tend to be perpendicular to their controlling faults, show rapid decrease in displacement away from the master fault, and appear unrelated to preexisting faults. They have been interpreted as release faults (Destro, 1995; Destro et al., 2003) and accommodate the strain resulting from alongstrike differential line stretch (Figure 7A). Although published examples have been confined to the hanging wall, where the stretch is greatest, several North Sea fields lying in the footwalls to major normal faults are believed to be either defined by such structures or compartmentalized by them (e.g., along the Brent-Statfjord and Murchison-Statfjord Nord fault arrays in the northern North Sea; McLeod et al., 2002) (Figure 7B). However, larger cross faults (>1 km [>0.6 mi] throw) could not be generated by this mechanism because the predicted differential strains along a fault are relatively small.

Relay ramps and transfer faults are preferred entry points for clastic sediments to enter the rift, and they also produce a highly structured zone with multiple structural closures along the transfer fault. They are a natural focus for oil fields to develop. In the Gulf of Suez, 4 of the 6 billion bbl of oil reserves are hosted by transfer zones (Morley, 1995), and a concentration of oil fields is apparent along the Matu-Catu Fault in the Recôncavo Basin of Brazil, where several major fields are located (Figure 6A) (Figueiredo et al., 1995).

Scarp Degradation and Failure

One major consequence of fault propagation and ever-increased displacement on the master normal fault is that a progressive increase in bathymetric or topographic relief exists in the center of fault segments as the fault arrays propagate and accumulate strain. This leads to the footwall block being exposed to subaerial weathering and erosion, or to it forming a major submarine scarp. In cases, where the footwall lithology is strong, such as with metamorphosed Mesozoic limestones in the Aegean domain, or the Mazagan Plateau in northwestern Morocco, large topographic fault scarps up to 4 km (2.5 mi) high can result (Ruellan and Auzende, 1985). However, where weaker and unconsolidated sediments make up the exposed footwall, landslides or submarine slumping commonly result. The progressive degradation of footwalls can lead to complete erosion of the scarp and subsequent stratal onlap characterizing the leading edge of many extensional fault blocks (Figure 8). In some cases, the more resistant

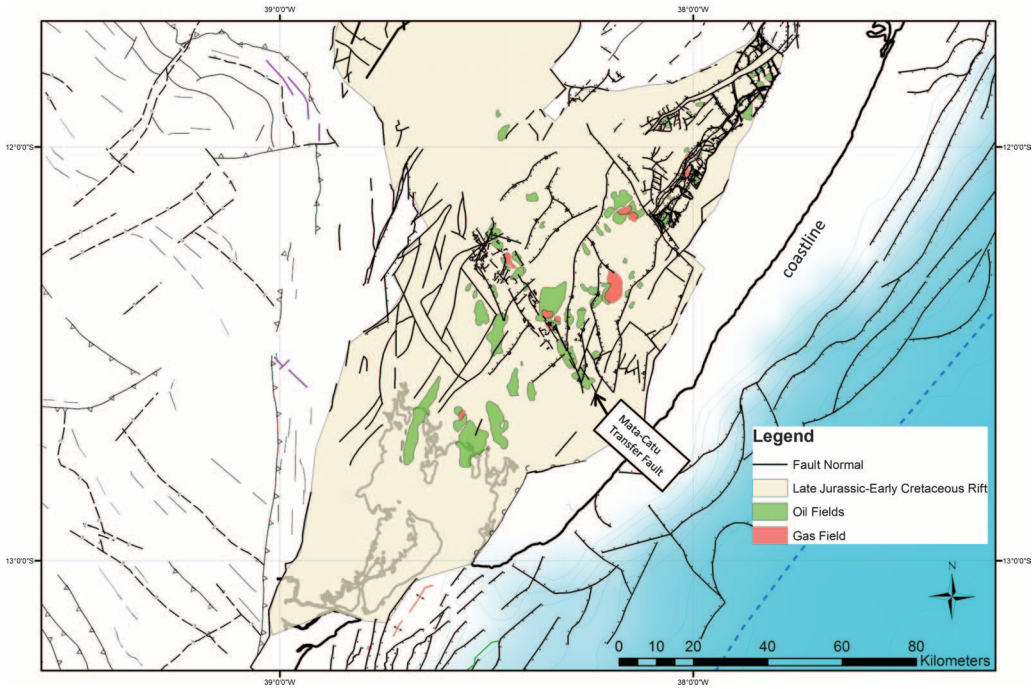

Figure 6. Maps of normal and transfer fault surface or subsurface traces. (A) Recôncavo. (B) Gulf of Suez. Modified from Younes and McClay (2002). 10 km (6.2 mi).

lithologies lead to the erosional unconformity having a distinctive stepped (ramp-flat) topographic profile; whereas in others, the footwall domain can be dominated by footwall-mounted fault-scarp degradation complexes with intense collapse faulting (Figure 8) (Underhill et al., 1997). These features are inherently difficult to image seismically and to produce oil from, being so structurally complex. However, as examples from the Brent Province in the northern North Sea demonstrate (e.g., Brent, Statfjord, Ninian, and Strathspey fields), a significant oil prize is commonly contained within them. Consequently, new methods of seismic processing are being used in an attempt to exploit these features in large North Sea oil fields affected by fault scarp degradation (e.g., Underhill et al., 1997; McLeod and Underhill, 1999).

SEDIMENTATION IN RIFTS

Tectonic subsidence is the main control on the geometry and facies of the synrift fill (Ravnas and Steel, 1998). However, in the early stages of a shallow-marine rift, glacioeustatic sea level changes can be very important. The initial subsidence can be very slow in some basins, for example, Viking Graben when the Middle Jurassic Brent Group was deposited or the Upper Jurassic Sergi and Alliance formations were deposited in the Recôncavo Basin of Brazil. Both of these occurrences represent approximately 500 m (~1640 ft) of subsidence through 10 m.y. These sediments appear as parallel-bedded units that spread evenly across the rift. When the extension rate increases, several main extensional faults dominate the system, and large asymmetric half grabens are developed. It is rare for symmetric graben to develop where the boundary faults are of equal magnitude and opposite polarity, except in zones of overlapping fault tips with opposing polarity.

Many continental rifts have a similar overall stratigraphy that commences with a basal fluvial unit dominated by coarse clastic sediment, followed by a transition to deep lacustrine sediments. When the lake fills up, the sedimentation produces a deltaic and lake shoreline and deep-water lacustrine facies and, finally, fluvial and alluvial facies (Figure 3). The thickness of the early-stage fluvial deposits will depend on the subsidence rate, and this phase may even be absent with very fast subsidence rates. This sequence development is produced by a slow initial extension with distributed faulting, followed by the accelerated subsidence and deep lake development during the main rifting phase, terminating with a waning of rift subsidence when the basin fills in.

When subsidence is more rapid than sedimentation rates, strong onlap of stratigraphic units is observed onto the flexed margin of the rift (underfilled model Figure 9A). If subsidence is equal to sedimentation rates (balanced model), stratigraphic units thicken into the hanging wall of the main graben boundary fault and the stratigraphic bounding surfaces converge to the edge of

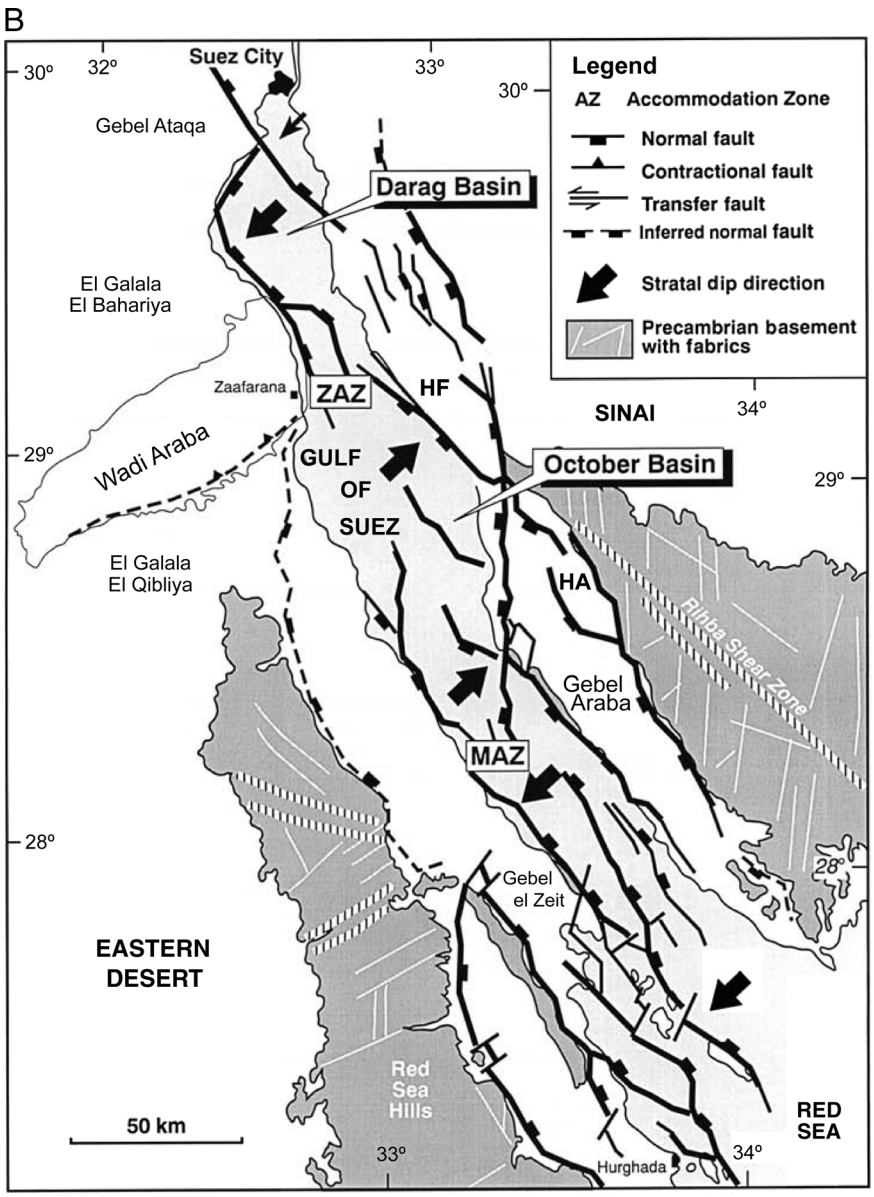

Figure 6. (cont.).

the flexed margin (Figure 9B). In rifts where sedimentation outpaces subsidence, prograding wedges of sediment will be observed that can either prograde along the rift or perpendicular to the rift axis (e.g., overfilled model). The reader is referred to an excellent discussion of facies variation and marine rift fill architecture based on North Sea examples by Ravnas and Steel (1998).

Footwall uplift produced during rifting causes sediments to initially flow away from rifts (Frostick and Reid, 1989). However, once fault scarps begin to erode these, source coarse-grained alluvial fans and deltas are distributed along the basin margins. The fans are generally limited to a zone of approximately 5 km (~3.1 mi) in width away from the border fault and reach up to 4 km (2.5 mi) in thickness (Steel, 1976; Magnavita and Da Silva, 1995). A lag of several million years commonly exists before marginal alluvial fans begin to develop as the footwall scarp has to degrade before a drainage catchment area develops that is large enough to source significant volumes of coarse conglomeratic material. Hence, early axial-derived turbidites, with good reservoir properties, can sometimes be found below the alluvial fan. These deep reservoirs are not imaged on the seismic data as the overlying alluvial fan top reflects all the energy and the top of the fan is commonly mistaken as top basement (e.g., Figure 10).

In some cases, these marginal alluvial fans do not develop because little or no erosion of the footwall exists. This can occur in areas where the rift is marine

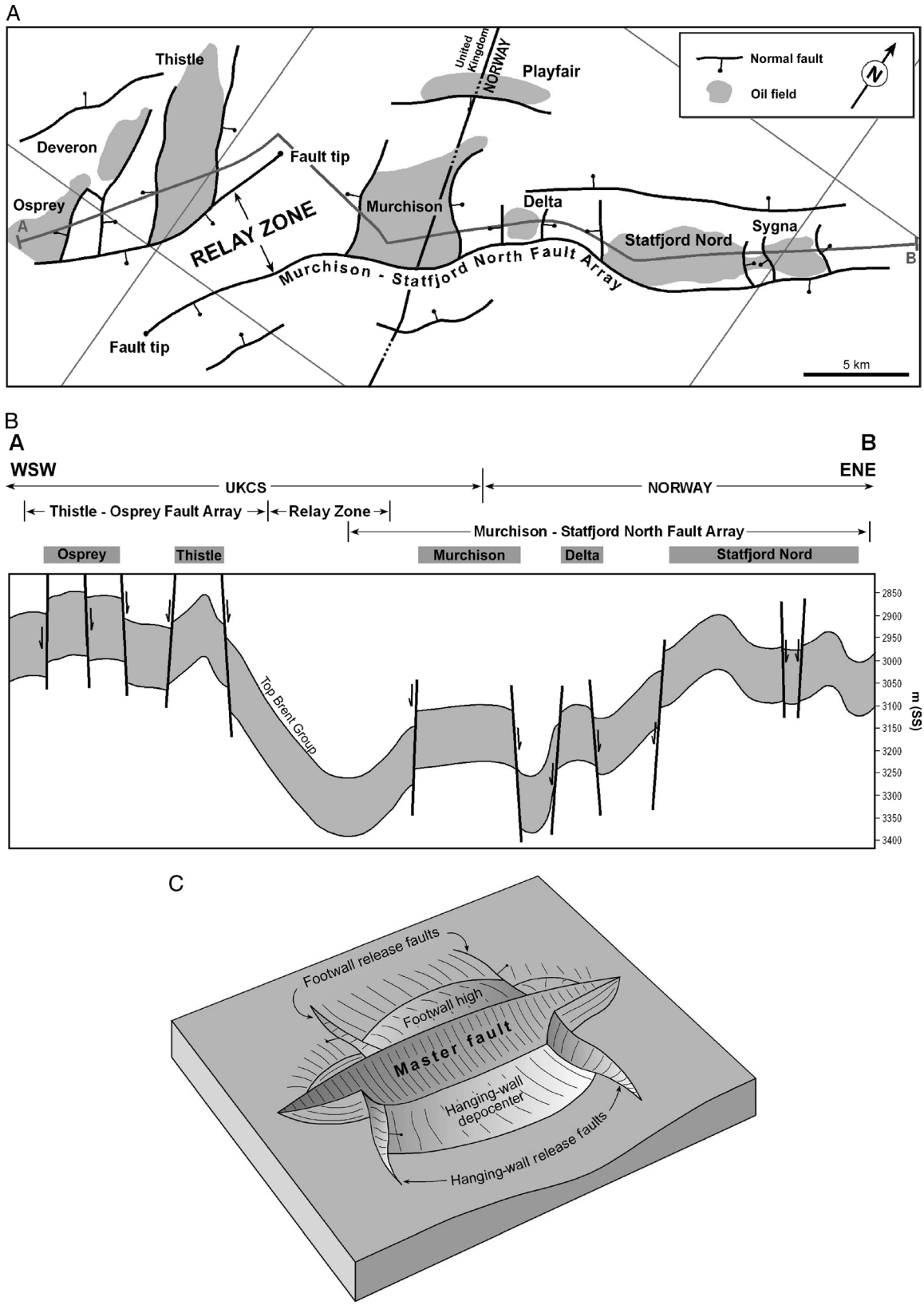

Figure 7. (A) Block diagram showing the major normal fault and release faults. (B) Map of northern North Sea oil fields located in Figure 4. (C) Longitudinal section along the major North Sea fault showing the interpreted release faults. UKCS = UK continental shelf; ss = subsea. 5 km (3 mi).

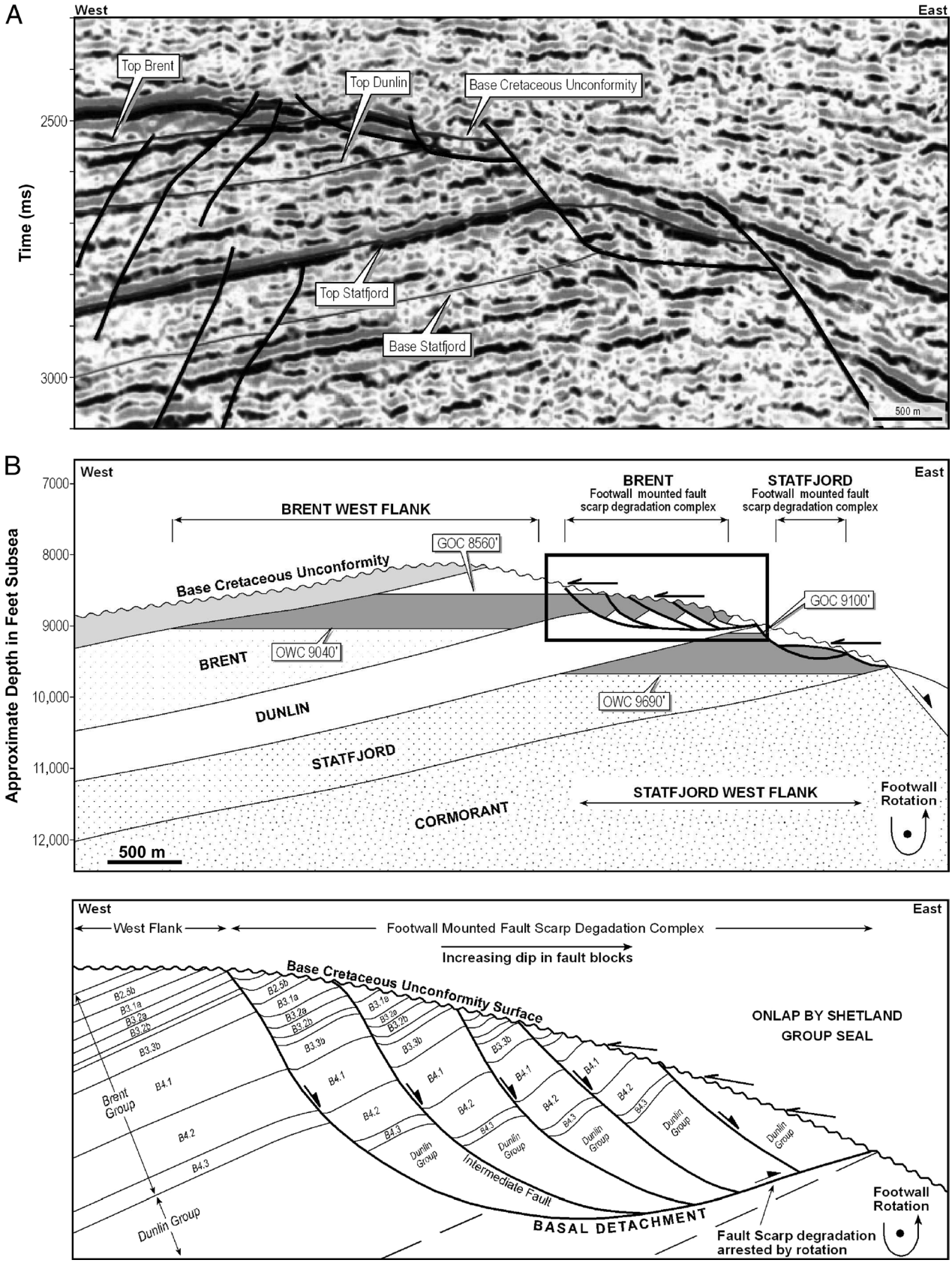

Figure 8. Fault scarp degradation complex on Statfjord field. (A) Seismic section. (B) Detailed cross section of the degradation complex. Location of the section shown in Figure 4B. Modified after Taylor et al. (2003). 500 m (1640 ft), 1000 ft (305 m).

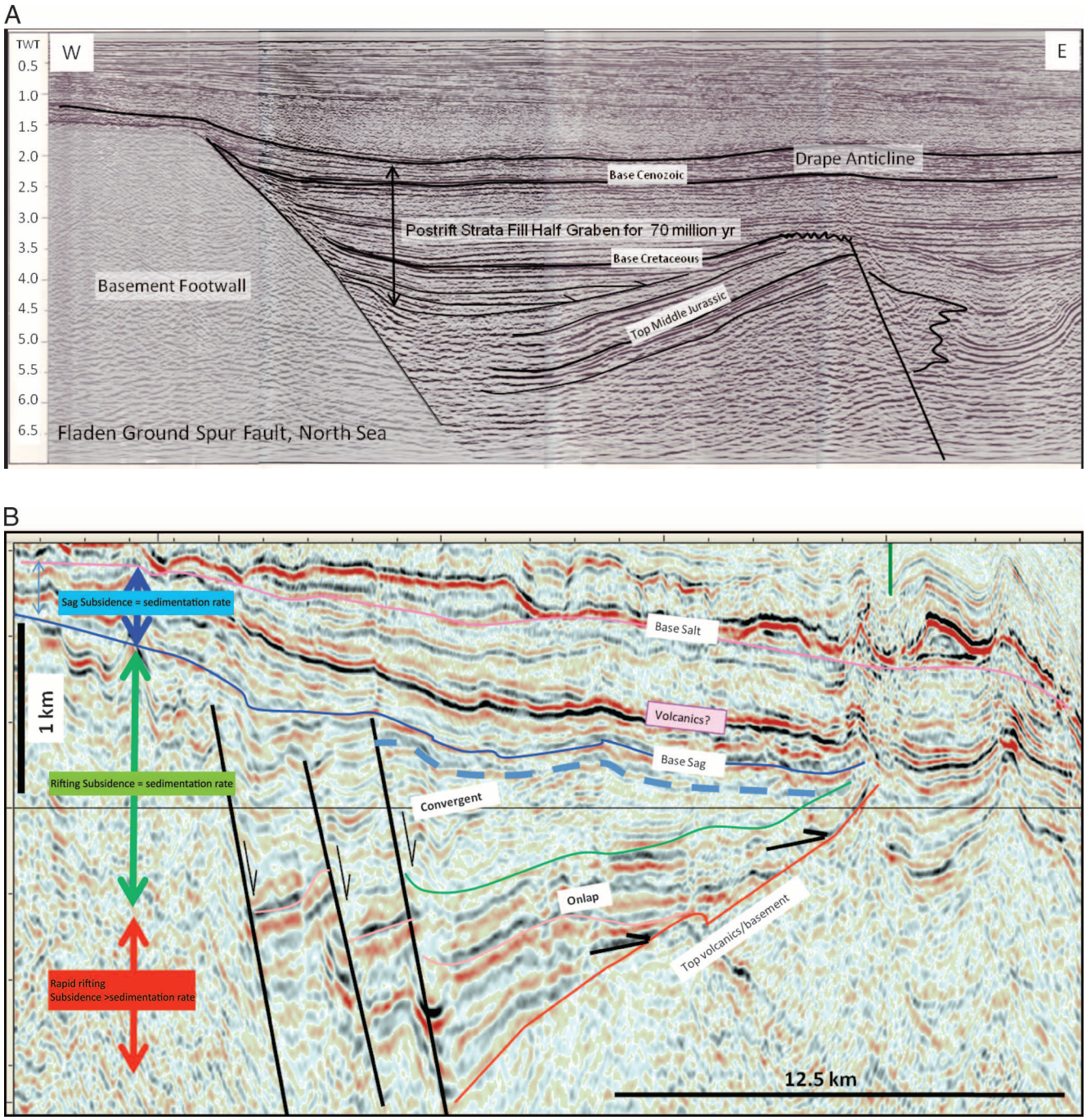

Figure 9. Stratal geometries in (A) underfilled starved half-graben basin geometry from the Fladen Ground Spur North Sea. (B) Balanced basin in mid rift phase where subsidence = sedimentation rate from the Santos Basin in Brazil. Data courtesy of ION's basin SPAN programs. 1 km (0.6 mi), 12.5 km (7.8 mi).

and the footwall is submerged, as is the case in the Central Graben of the North Sea during Late Jurassic rifting, so only deep-water shales are developed adjacent to the Coffee Soil Fault scarp (Cartwright, 1991).

In many rift systems, the main fault scarp and associated footwall uplift act as a topographic barrier for drainage, and dispersal patterns are either directed away from the adjacent half graben or are routed and focused into it through relay ramps between individual fault segments (Peacock and Sanderson, 1991). During the main rift phase in the Recôncavo and East African rift systems, the main coarse clastic sediment input to

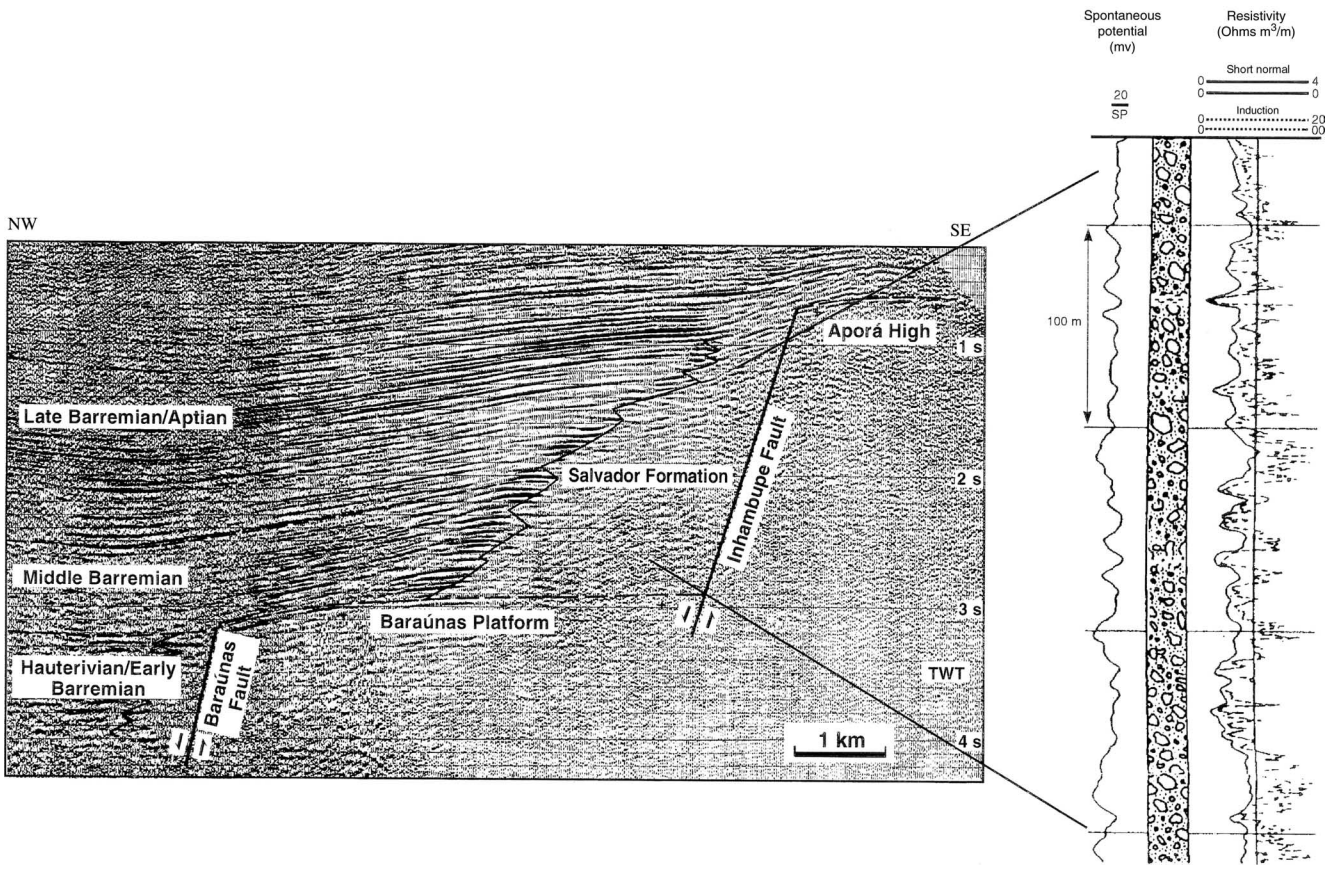

Figure 10. Section of marginal fanglomerates that developed along the rift border fault. The top of the conglomerate fan is commonly confused with the top basement seismic pick, so basin size is underestimated. High-quality turbidite sandstone reservoirs have been found below the marginal fan in the Recôncavo Basin of Brazil. TWT = two-way traveltime (Magnavita, 1992). 1 km (0.6 mi).

the basin was from the flexed margin of the half graben (Figures 11, 12) and the deep hanging-wall graben is sediment starved, with lakes forming there (Frostick and Reid, 1989) (e.g., Lake Tanganyika). As recent exploration success on the eastern shore of Lake Albert has demonstrated, the flexed margin (otherwise known as the hanging-wall dip slope) can be the site for significant sandstones and produce major stratigraphic traps for updip oil accumulations charged from more deeply buried interdigitating lacustrine source rocks (Figure 11B). A similar system characterized the Triassic rifts of the eastern parts of the United States (Schlische, 1992, 1993) and beneath the North Sea (Tomasso et al., 2008).

Carbonates in Rifts

The Toca and Lagoa Feia synrift carbonates in Brazil and Angola are developed along lake shorelines on footwall highs. These Barremian–early Aptian carbonates are composed mainly of pelecypods (called coquinas in Brazil). The shelly banks are reworked along the highs in a high-energy environment, but slumped blocks and reworked turbidites are shed off into the deeper parts of the basin. Moderate-size oil fields 50 to 200 million bbl in place have been discovered in these shelly limestones, but the presence of the reservoirs is very difficult to see on the seismic data sets.

Carbonate banks are developed along footwall highs in the Gulf of Suez where rifting occurred in a shallow-marine setting (Bosence, 2005; Cross and Bosence, 2008) (Figure 13A). Prograding carbonate wedges are observed over the fault blocks and the geometry of these prograding sequences is similar to a clastic delta, but there is no obvious source region for the clastic material in a delta developed along linear fault block crests, which are not undergoing erosion, so the presence of a prograding wedge initiating from an uneroded shallow-water fault block crest is a characteristic of in-situ carbonate growth and reworking (Figure 13B).

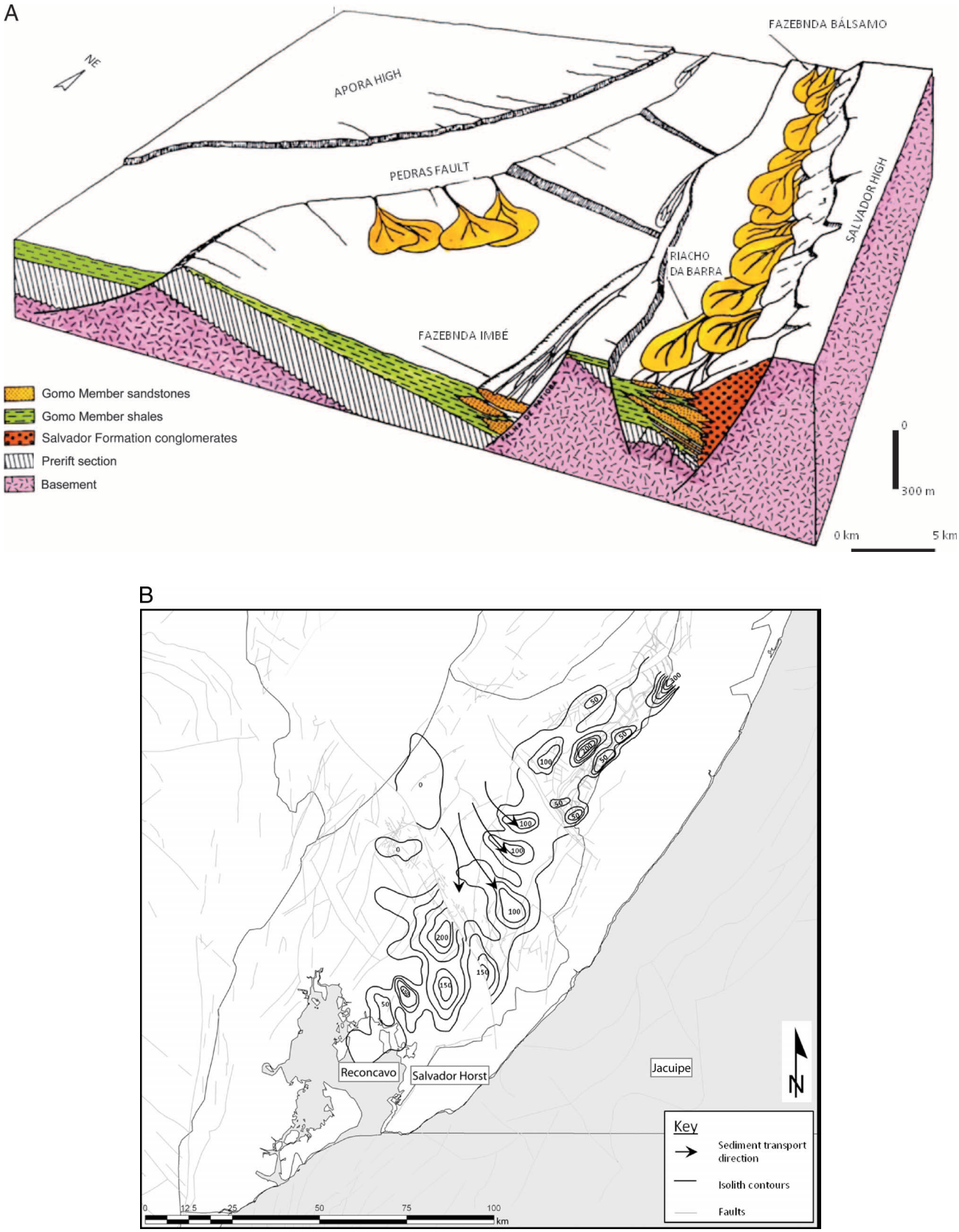

Figure 11. Block diagram (A) and map (B) showing hanging-wall reservoir sandstone deposition during the active rifting phase. Thickness of Gomo sandstones in meters. Note the possibility of turbidite sandstones below the marginal alluvial fan in (A). Modified from Bruhn (1985). 5 km (3 mi), 300 m (984 ft).

INTERACTION BETWEEN CLIMATE AND TECTONIC CONTROL ON RIFT SEDIMENTATION

Tectonics exerts the most important control on sedimentation in rifts (Ravnas and Steel, 1998; Caroll and Bohacs, 1999; Lambiase and Morley 1999), with climate being a second-order control (Olsen, 1990, 1997; Scholz et al., 1997). Milankovitch cycles produce climate variations with a cyclicity of 10 to 100 k.y. and produce high-frequency variations in the stratigraphic record generally on a scale of 1 to 10 m (see Olsen, 1997, for an excellent review of sediment cyclicity in Triassic rifts of North America). In the early stages of rifting, drainage pathways are commonly short, and closed internal drainage basins dominate. In arid regions, this commonly leads to evaporation exceeding sediment supply and runoff to produce evaporite basins (e.g., the modern lakes of East Africa).

Climate will have a control on whether lacustrine, fluvial, or eolian sedimentation dominates a rift. High rainfall in a hot climate may produce lakes with carbonates, in contrast to clastics in a cooler rift. A dry climate may also produce evaporite-filled basins such as the South Atlantic or the Gulf of Suez, where a restricted seawater entry point is present. Most evaporite deposition is very rapid (1 cm a^{-1}) and 2-km (1.2-mi)-thick evaporite sequences can develop in 200 k.y. Most large evaporite sequences are produced from seawater, but occasionally, saline lakes can locally develop with hydrothermal activity and leaching of volcanic rocks, leading to evaporite units several hundred meters thick (a possible example is the Macalungo-1 well in the Kwanza Basin, Angola).

Wind Direction

The prevailing wind direction can affect the local climate within a basin. Where the wind blows from the footwall to hanging wall of a half graben, the main runoff is away from the basin. However, if the wind blows toward the footwall, the main runoff is toward the basin, down the hanging-wall dip slope (Figure 14). Hence, wind blowing toward the footwall will favor deeper lakes and source rock development.

IMPLICATIONS FOR PETROLEUM SYSTEMS

Controls on Source Rock Deposition in Rifts

Source rocks in most hydrocarbon-producing rifts can be type I (algal) to type III (higher land plant) kerogens or, more commonly, a mixture of the two (type II) (Katz, 1995). Source rocks in tropical rifts are presently forming in the East African rift lakes today (Talbot, 1988). Demaison and Moore (1980) observed the Tanganyika Lake and suggested that organic-rich sediments will deposit in a deep anoxic lake in a warm humid climate regime with minimal seasonal contrasts, which is typical of low-latitude climate. Talbot (1988) also concluded from a study of several African rift lakes that the favorable climate conditions for source rock development are a humid climate with reduced wind conditions. In such conditions, lakes will be deep, fresh to slightly alkaline, with stable stratification (Talbot, 1988). Humid conditions will also promote dense vegetation growth, and large amounts of organic material will be washed into the basin. The dense vegetation inhibits surface erosion and clastic sediment runoff, which further enhances the source rock potential. Intense chemical weathering in a hot humid climate enhances the nutrient content of the water to promote organic productivity, especially of phytoplankton, which are common in present-day African lakes. Dry climate conditions produce shallow saline lakes, which are less favorable for major source rock development, although localized highly productive source rocks may develop, as in the Green River shales (Eugster and Hardie, 1975).

In marine rifts, oil-prone source rocks accumulate in half-graben depocenters especially those that experience poor circulation and anoxia. The main prolific source rock for the North Sea petroleum system, the Upper Jurassic Kimmeridge Clay Formation, formed in such a setting in water depths of several hundred meters to 1 km or more ($\geq$0.6 mi).

A deep narrow rift will enhance the source rock potential as the water is deeper, and this enhances the preservation potential of the organic matter. The deepest rifts form in cold stable lithosphere, where the crustal deformation localizes into a narrow rift zone. If one master fault develops along an initial weakness, the rift will be deep and narrow. If several faults of equal magnitude develop, the rift will be broader and shallower. Hence, rifts cutting through old cratons should be the deepest (e.g., the Tucano Rift cutting the Sao Francisco Craton in northeastern Brazil, which has 12 km (7.5 mi) of synrift sediment fill. Rapid rifting will also increase the depth of the rift lake where subsidence outpaces sedimentation.

Reservoirs in Rifts

In general, sandstones are the primary reservoir in rifts and carbonates are fairly rare (Bruhn et al., 1988; Morley, 2002b). The main clastic reservoir types are prerift or

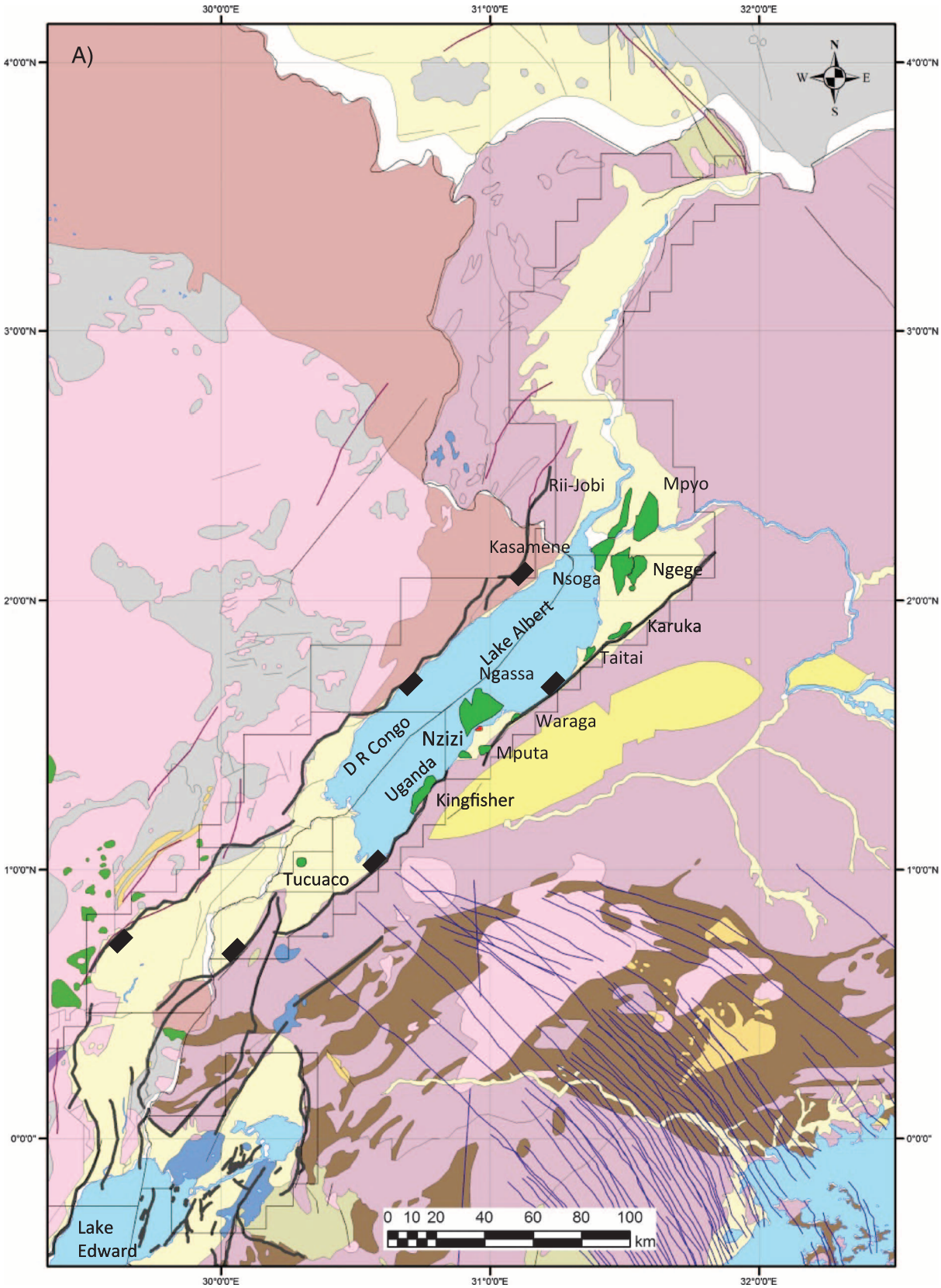

Figure 12. (A) Map of the Albertine Rift in East Africa showing the newly discovered hydrocarbon fields. (B) Block diagram showing the Albertine Rift and sediment input along the accommodation zone at the northern end of the rift. Pale yellow areas indicate Cenozoic sedimentary basin. Green areas indicate oil fields. Blue areas indicate lakes. DRC = Democratic Republic of Congo. 10 km (6.2 mi).

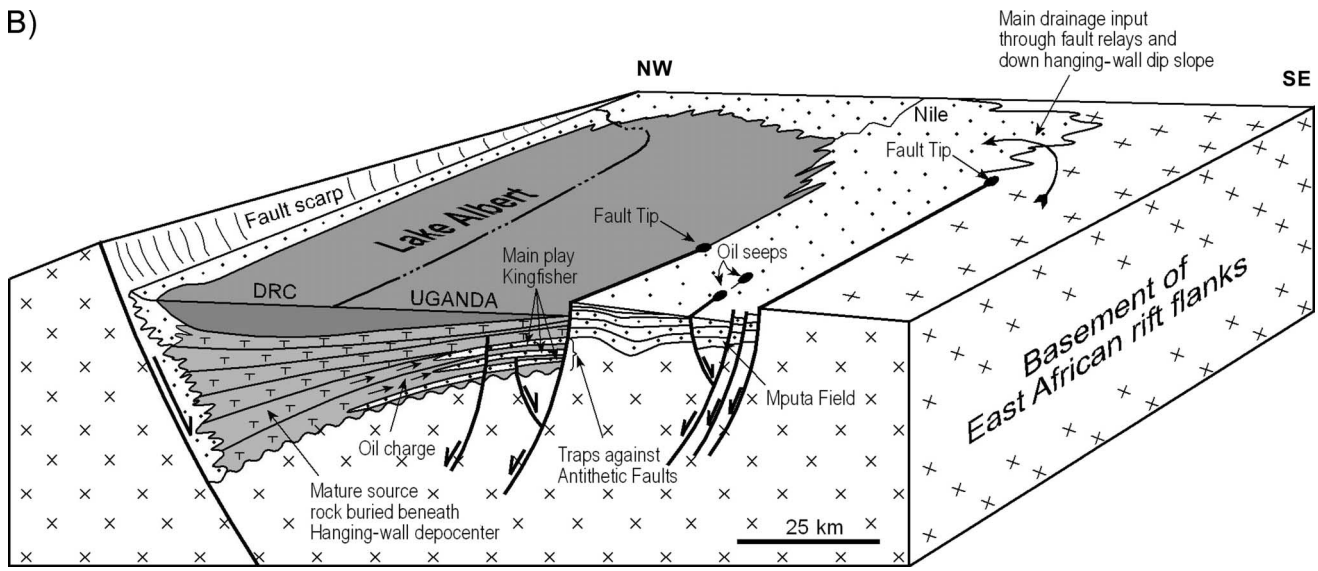

Figure 12. (cont.).

early-phase fluvial sandstones, synrift deeper water turbidite sandstones, and lacustrine deltas and late-stage fluvial or shallow-marine sandstones (Figure 3). Early-phase fluvial sandstones can be widespread and occur across the tops of rotated fault blocks except where later erosion has removed them (e.g., Lucula sandstones in west Africa). Synrift turbidite sandstones can be deposited along axially flowing canyon systems in the deep half graben or be deposited down the shallow flexural margin, but will be rarely found on fault block crests (Figure 11). Poor-quality conglomerates will occur along the hanging walls of major normal faults and may even act as seals to adjacent better quality reservoirs. Care should be taken that the border conglomerate fan is not mistakenly identified as the true basement, especially where only drill cuttings and logs are used.

Good-quality sandstones will develop where sediment provenance sources are also good quality. Examples include where high-grade granitic basement rocks or preexisting sandstones are exposed in the drainage catchment area; poor-quality reservoirs often derive from volcaniclastic or exotic terranes where mineral assemblages are such that primary depositional textures, sorting, or diagenetic effects may be detrimental to reservoir quality. Porosity, permeability and, hence, sandstone reservoir quality often deteriorate rapidly with burial as a consequence of diagenetic reactions and greater compaction. Sandstones in rifts are generally moderately sorted basement-derived arkoses, which undergo drastic reduction in porosity and permeability when feldspars break down. The porosity reduces most rapidly in the first 2 km (1.2 mi) of burial but can increase again because of secondary porosity development, where organic acids are generated as a precursor to oil expulsion from source rock shales. Hence, reservoir rocks with 20 to 25% porosity may be preserved at 4 km (2.5 mi) burial depth (Bruhn et al., 1988).

Occasionally, carbonates are important in the right climatic conditions either regionally or as fringing reef facies within what is otherwise a clastic system, such as the Gulf of Suez (Bosence, 2005) or the Santos and Campos basins in Brazil. A shallow-marine setting in a tropical climate will favor carbonate growth, and this should most likely be in the late phase of rifting when the basin is beginning to fill up, but regional subsidence and lateral rift propagation increase the likelihood of marine incursion.

Hydrocarbon Seals in Rifts

In the early stages of rift formation, closed drainage systems are commonly created. This leads to the formation of lakes that are a prerequisite for development of organic-rich shale source rocks and regional seals. The shales in a continental rift section are best developed in deep-lacustrine or -marine waters. The reason for exploration failure in many continental rift basins is commonly the lack of a good regional source rock and seal horizon, where the seal and source rocks can be the same formation.

If arid climatic conditions prevail, seawater or saline lake evaporation may lead to the formation of extensive evaporites during the extension. These act as seals for the underlying prerift and synrift reservoirs (e.g.,

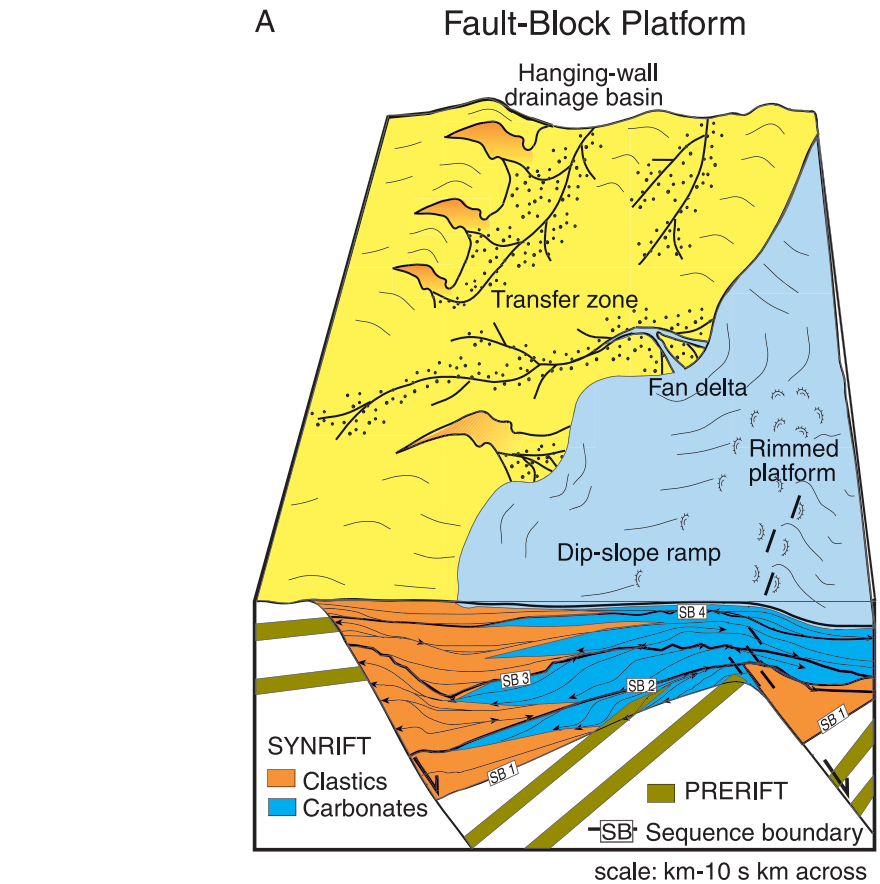

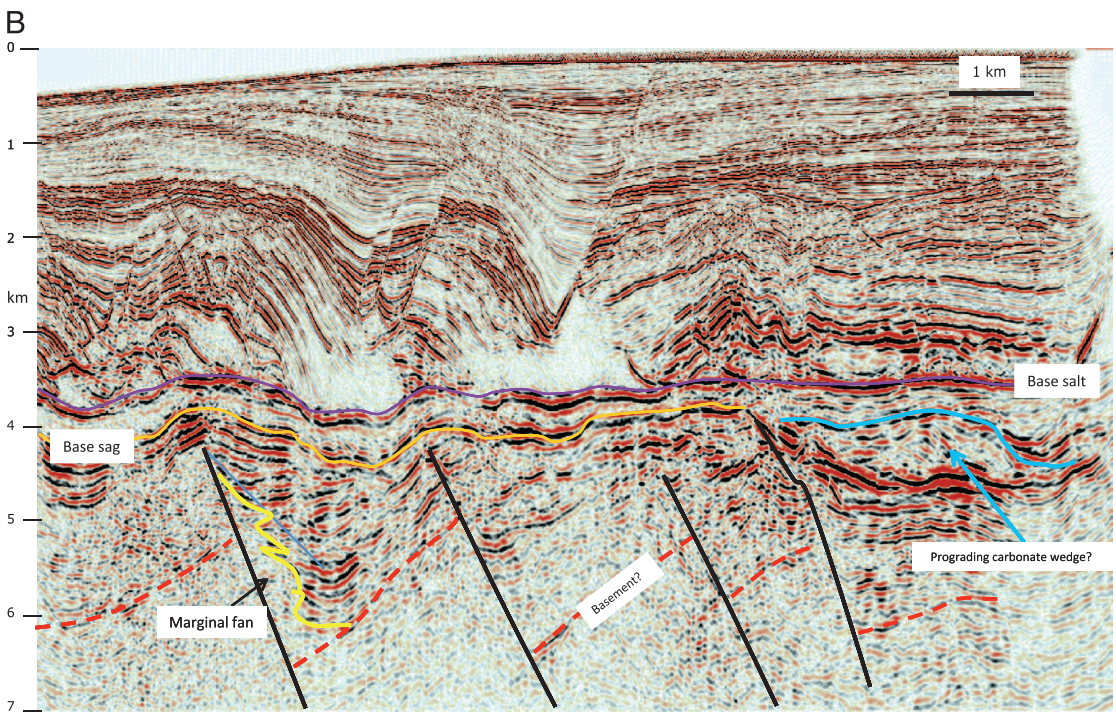

Figure 13. Examples of carbonate reservoir targets in emerging subsalt synrift plays. (A) Carbonate platform development on the footwall block crest based on Gulf of Suez examples. Modified from Bosence (2005); reproduced with the permission of Elsevier. (B) Seismic section through a west African rifted margin showing a prograding wedge (in blue) that has prograded eastward toward the continent from a narrow fault block that does not show any large erosion features on the fault block crest. This is characteristic of in-situ carbonate growth (courtesy of Maersk Oil and Sonangol). 1 km (0.6 mi).

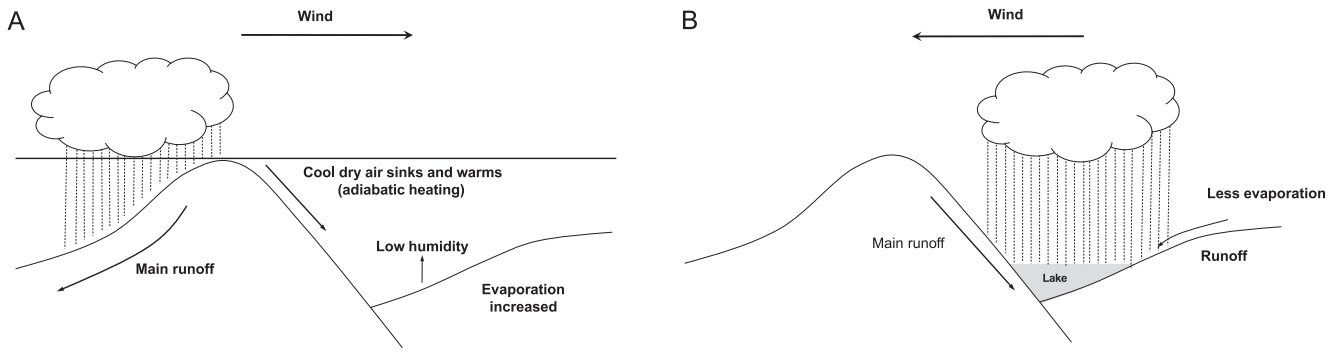

Figure 14. Cartoon sketch showing how wind direction and rift polarity control the microclimate in a half graben and the likelihood of lake formation and organic-rich source material.

existing and emerging deep-water plays of the west African and Brazilian continental margins, such as the Lula Field, and in the Gulf of Suez and northern Red Sea in Egypt).

CONCLUSIONS

Extensional rifts and their overlying sag basins contain large volumes of hydrocarbons in many part of the

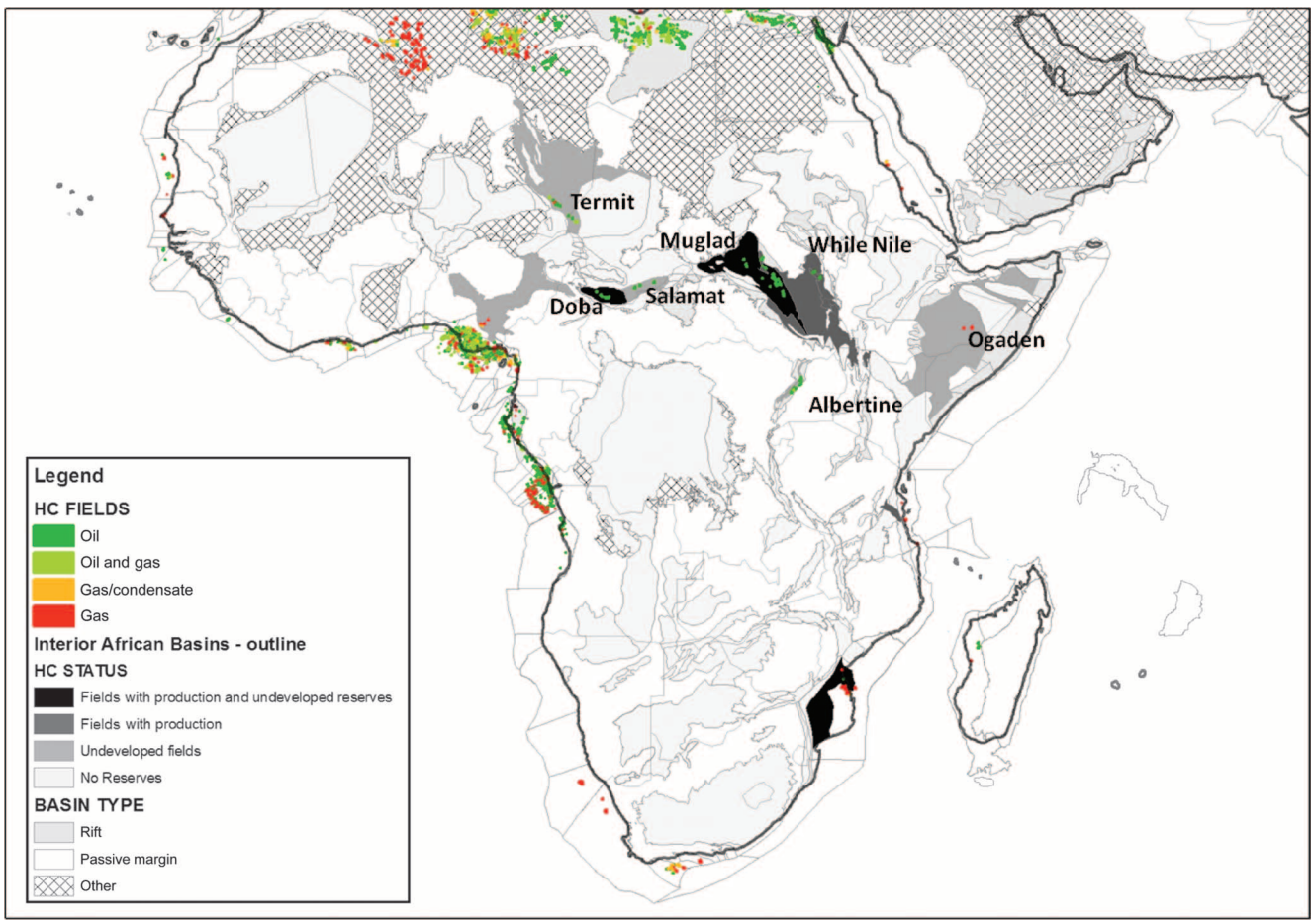

Figure 15. Map of the African rifts showing the rifts with proven potential for commercial production. Pipelines are marked as thin green lines.

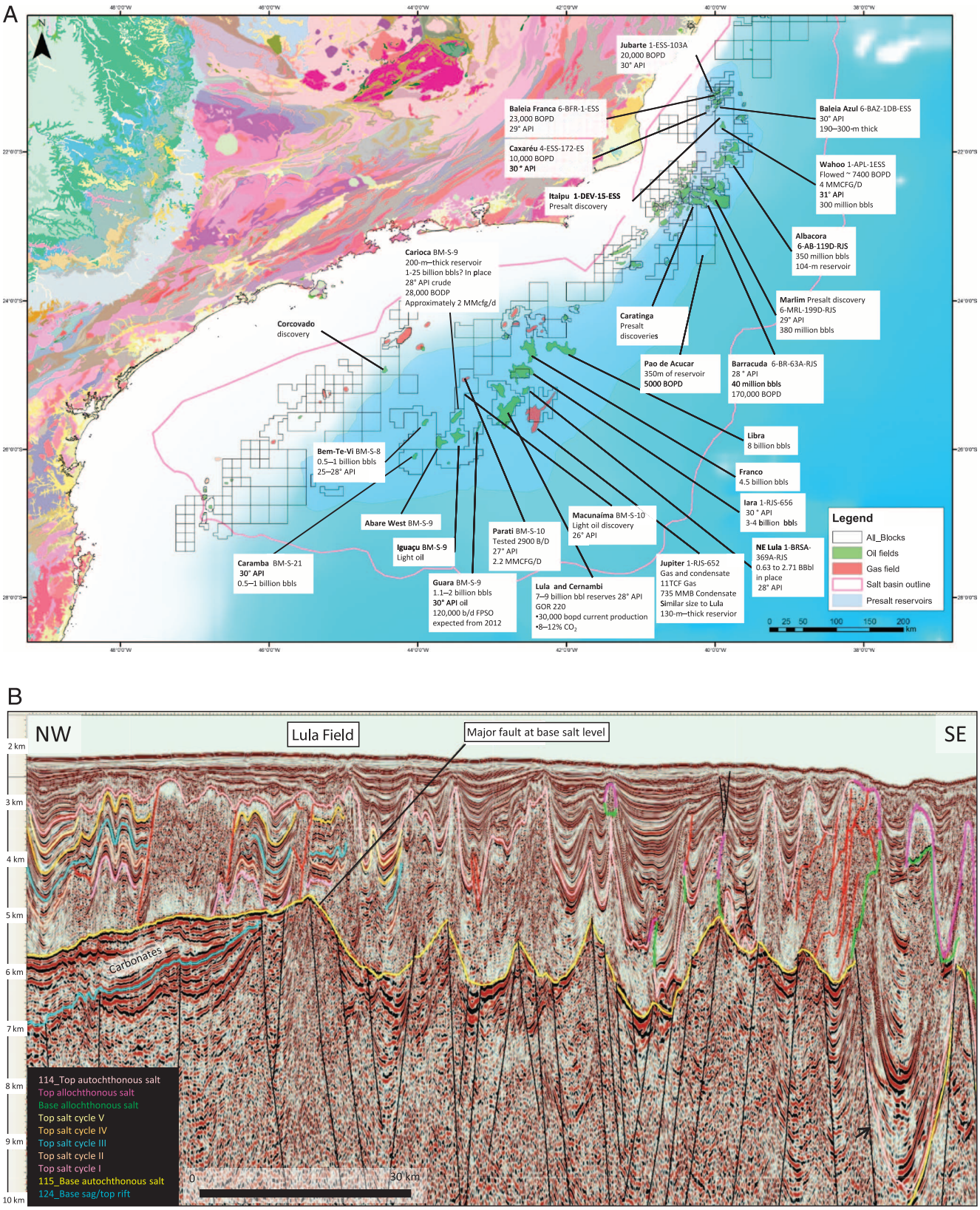

Figure 16. (A) Map of Santos and Campos basin major oil fields in presalt synextensional sag. (B) Seismic section through the Lula Field in the Santos Basin, Brazil. Seismic data courtesy of ION's Basin SPAN programs. 30 km (18.6 mi).

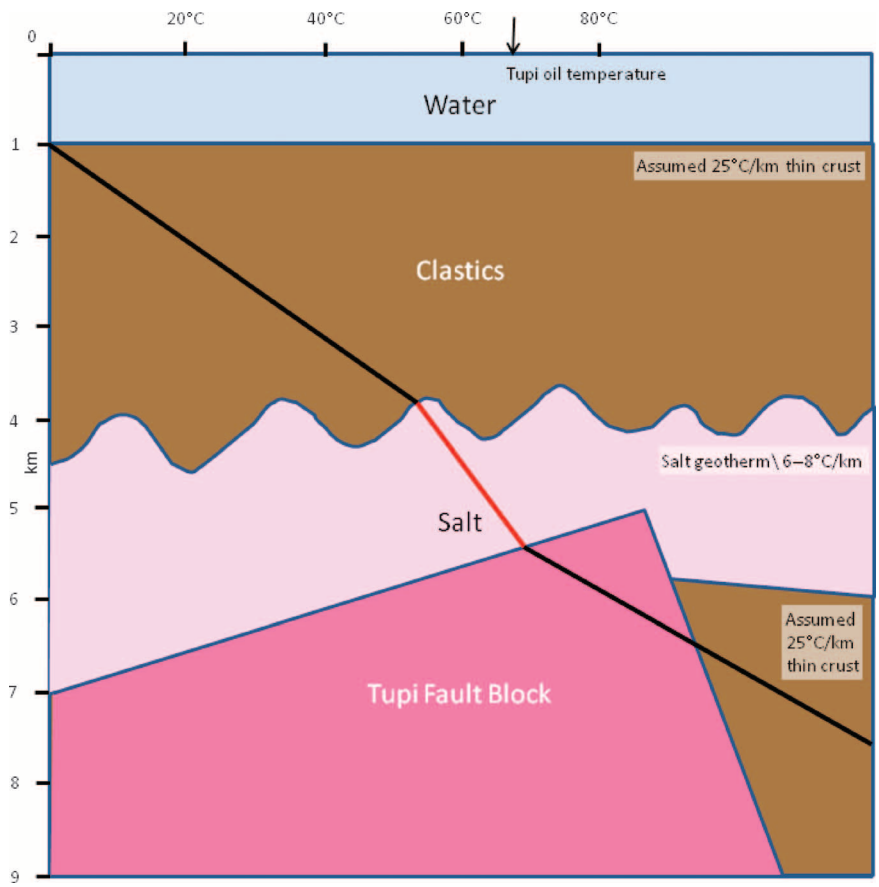

Figure 17. Cross section showing the cooling effect of the continuous salt layer. The presalt layer cools down by approximately 20°C/km of salt. Oil in the Lula Field is only 68°C. 1 km (0.6 mi).

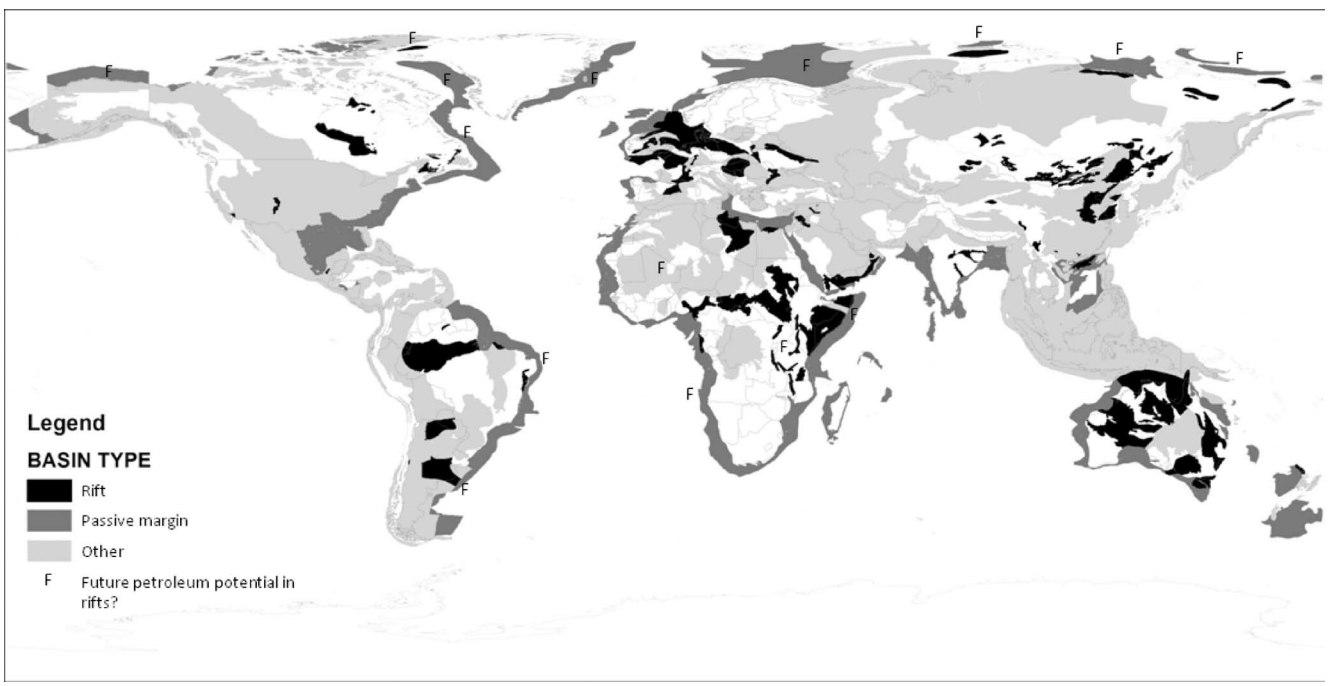

Figure 18. Map of the world showing some areas with potential for future hydrocarbon discoveries in extensional rifts, marked F (courtesy of M. K. Taylor and P. V. Baptista, 2010).

world and remain the focus for global exploration efforts. Asymmetric half grabens characterize most rifts, with rivers and turbidites flowing along the deep axis of the graben transporting sediment along the rift, and also rivers and tubidites flowing down the hanging-wall flexural margin will be important. Footwall-derived alluvial fans develop through time as the footwall is eroded back to create a drainage catchment area. Otherwise, sediment entering from the footwall side of a half graben commonly enters along accommodation or transfer zones, where a topographic low occurs along the footwall.

Source rock development in rifts is favored by development of large steeply dipping normal faults, where deep sediment-starved lakes or marine incursions occur in the hanging walls of the faults. A humid hot climate with light winds blowing toward the footwall of an isolated half graben favor source rock development (Figure 14). The source rocks are commonly developed in the bottom one third of the rift fill during the early to the main phase of rifting, when the most rapid subsidence phase occurs, and sediment infill is slower as sediment is directed away from the graben along the footwall margin.

The African rifts have produced several important hydrocarbon provinces (Albertine Graben Uganda; White Nile Rift, Sudan; Termit-Tenere Graben, Chad; Figure 15). However, exploration is still in its infancy in many rifts where no wells or seismic data exist. Gravity anomalies and surface seeps indicate that many of these undrilled African basins have hydrocarbon potential. The remote locations of many onshore rifts mean that the basins have to host large volumes of hydrocarbons in place before pipelines can be installed to tap these resources, unless they are close to an existing oil refinery. The total volume of hydrocarbons in place in the Albertine Graben now appears to be great enough to warrant building a 2000 km (1243 mi) pipeline to the East African seaboard (Figure 15).

Aptian carbonates deposited along the Brazilian margin host the largest hydrocarbon fields discovered in the last 20 yr (Figure 16A). The reservoir is a lacustrine carbonate composed of thrombolites and stromatolites, with local tufa development, dolomitization, and leaching that created porous reservoirs capable of producing 20,000 bbl of oil per day per well. These limestones are distributed over a very large area of the Santos, Campos, and Espírito Santo basins and are trapped in draped closures over large rotated fault blocks top sealed with Aptian salt (Figure 16B). The reservoirs were actually deposited after the main faulting phase but are interpreted to be part of the synextensional presalt sag caused by lower crustal stretching. The equivalent sag interval occurs along the west African margin, but the only well that appears to have drilled into this sag in deep water (>1000 m [>3280 ft]) is Falcao-1, which encountered good-quality source rock shales and carbonates but did not flow oil. Less prospective structures are present in the upper part of the sag phase, along the African margin, as the rifted fault block topography was buried by up to 6 km (3.7 mi) of synextension sag strata. These preliminary indications suggest that the presalt sag on the African margin may not be as prolific as the Brazilian margin, but we await further drilling to confirm whether this is the case.

The synrift source rocks in the Santos Basin are generating light oils, although they may be buried to 8- to 12-km (5- to 7.5-mi) depth. At this depth, gas generation would normally be predicted, but the high thermal conductivity of a 2 km (1.2 mi) thickness of salt reduces the presalt temperature by approximately 40°C compared with a shale-filled basin (Mello et al., 1995). Subsalt cooling is supported by the temperature of the oil produced in Lula, which is measured at only 68°C at a depth of 3.5 km (2.2 mi) below the seabed (Figure 17). Cooling of presalt synrift sections can be expected in many other rifts, where salt has developed late in the rift section (e.g., eastern Canada and United States, northwestern Africa, Gulf of Suez), and superdeep wells are required to test these presalt oil targets. Many passive margins have only been tested in the upper thermal sag phase of sedimentation, and the underlying deep rifts remain to be tested in deep water (Figure 18).

ACKNOWLEDGMENTS

We thank ION/GXT, PGS, and Maersk Oil and Sonangol for permission to publish seismic sections used in this chapter. Matthew Taylor and Pedro Baptista kindly provided maps for Figures 17 and 18. We thank Dengliang Gao and Scott Fraser for their reviews of this chapter. We also thank Dan Harris who kindly provided a review of our rifts chapter for this volume.

REFERENCES CITED

Armstrong, R. L., 1972, Low-angle (denudation) faults, hinterland of Sevier orogenic belt, eastern Nevada and western Utah: Geological Society of America Bulletin, v. 83, p. 1729–1754, doi:10.1130/0016-7606(1972)83[1729:LDFHOT]2.0.CO;2.

Badley, M. E., B. Freeman, A. M. Roberts, J. S. Thatcher, J. Walsh, J. Watterson, and G. Yielding, 1990, Fault interpretation during seismic interpretation and reservoir evaluation:

The integration of geology, geophysics and petroleum engineering in reservoir delineation, description and management: 1st Archie Conference, AAPG, p. 224–241.

Barr, D., 1987a, Lithospheric stretching, detached normal faulting and footwall uplift, *in* M. P. Coward, J. F. Dewey, and P. L. Hancock, eds., Continental extensional tectonics: Geological Society (London) Special Publication 28, p. 75–94, doi:10.1144/GSL.SP.1987.028.01.07.

Barr, D., 1987b, Structural/stratigraphic models for extensional basins of half-graben type: Journal of Structural Geology, v. 9, p. 491–500, doi:10.1016/0191-8141(87)90124-6.

Bosence, D. W. J., 2005, Toward a genetic classification of carbonate platforms: A proposal based on the basinal and tectonic settings of Cenozoic platforms: Sedimentary Geology, v. 175, p. 49–72, doi:10.1016/j.sedgeo.2004.12.030.

Bosworth, W., 1985, Geometry of propagating continental rifts: Nature, v. 316, p. 625–627, doi:10.1038/316625a0.

Bruhn, C. H. L., 1985, Sedimentação e evolução diagenética dos turbiditos eocretácicos do membro Gomo, Formação Candeias, no compartimento nordeste da Bacia do Recôncavo, Bahia: Master's thesis, Universidade Federal de Ouro Preto, Minas Gerais, Brazil, 203 p.

Bruhn, C. H. L., C. Cainelli, and R. M. D. Matos, 1988, Habitat do Petroleo e fronteiras exploratorias nos rifts brasileiros: Boletim de Geociencias da Petrobras, v. 2, p. 217–253.

Caroll, A. R., and K. M. Bohacs, 1999, Stratigraphic classification of ancient lakes: Balancing tectonic and climatic controls: Geology, v. 27, p. 99–102, doi:10.1130/0091-7613(1999)027<0099:SCOALB>2.3.CO;2.

Cartwright, J., 1991, The kinematic evolution of the Coffee Soil Fault, *in* A. M. Roberts, G. Yielding, and B. Freeman, eds., The geometry of normal faults: Geological Society (London) Special Publication 56, p. 29–40, doi:10.1144/GSL.SP.1991.056.01.03.

Cartwright, J. A., B. D. Trudgill, and C. M. Mansfield, 1996, Fault growth by segment linkage: An explanation for scatter in maximum displacement and trace length data for the Canyonlands Grabens of SE Utah: Journal of Structural Geology, v. 17, p. 1319–1326, doi:10.1016/0191-8141(95)00033-A.

Colletta, B., P. Le Quellec, J. Letouzey, and I. Moretti, 1988, Longitudinal evolution of the Suez rift structure (Egypt): Tectonophysics, v. 153, p. 221–233, doi:10.1016/0040-1951(88)90017-0.

Cowie, P. A., and C. H. Scholz, 1992a, Physical explanation for the displacement-length relationship of faults using a post-yield fracture mechanics model: Journal of Structural Geology, v. 14, p. 1133–1148, doi:10.1016/0191-8141(92)90065-5.

Cowie, P. A., and C. H. Scholz, 1992b, Displacement-length scaling relationship for faults: Data synthesis and discussion: Journal of Structural Geology, v. 14, p. 1149–1156, doi:10.1016/0191-8141(92)90066-6.

Cowie, P., J. R. Underhill, M. Behn, J. Lin, and C. M. Gill, 2005, Spatiotemporal evolution of strain accumulation derived from multiscale observations of Late Jurassic rifting in the northern North Sea: A critical test of models for lithospheric extension: Earth and Planetary Science Letters, v. 234, p. 401–419.

Cross, N., and D. W. J. Bosence, 2008, 3-D tectonosedimentary models for marine, rift-margin, systems, *in* J. Lakasik and T. Simo, eds., Controls on carbonate platform and reef development: SEPM Special Publication 89, p. 83–106, doi:10.2110/pec.08.89.0083.

Dawers, N. H., and J. R. Underhill, 2000, The role of fault interaction and linkage in controlling synrift stratigraphic sequences: Late Jurassic, Statfjord East area, northern North Sea: AAPG Bulletin, v. 84, p. 45–64, doi:10.1306/C9EBCD5B-1735-11D7-8645000102C1865D.

Dawers, N. H., M. H. Anders, and C. H. Scholz, 1993, Growth of normal faults: Displacement-length scaling: Geology, v. 21, p. 1107–1110, doi:10.1130/0091-7613(1993)021<1107:GONFDL>2.3.CO;2.

Demaison, G. J., and G. T. Moore, 1980, Anoxic environments and oil source bed genesis: Organic Geochemistry, v. 2, p. 9–31, doi:10.1016/0146-6380(80)90017-0.

Destro, N., 1995, Release fault: A variety of cross fault in linked extensional fault systems, in the Sergipe-Alagoas Basin, NE Brazil: Journal of Structural Geology, v. 17, p. 615–629, doi:10.1016/0191-8141(94)00088-H.

Destro, N., P. Szatmari, F. F. Alkmim, and L. P. Magnavita, 2003, Release faults, associated structures, and their control on petroleum trends in the Recôncavo rift, northeast Brazil: AAPG Bulletin, v. 87, p. 1123–1144, doi:10.1306/02200300156.

Driscoll, N., and G. Karner, 1998, Lower crustal extension across the Northern Carnarvon Basin, Australia: Evidence for an eastward-dipping detachment: Journal Geophysical Research, v. 103, p. 4975–4991, doi:10.1029/97JB03295.

Ebinger, C. J., J. A. Jackson, A. N. Foster, and N. J. Hayward, 1999, Extensional basin geometry and the elastic lithosphere: Philosophical Transactions Royal Society London A, v. 357, p. 741–765, doi:10.1098/rsta.1999.0351.

Eugster, H. P., and L. A. Hardie, 1975, Sedimentation in an ancient playa-lake complex: The Wilkins Peak Member of the Green River Formation of Wyoming: Geological Society of America Bulletin, v. 86, p. 319–334, doi:10.1130/0016-7606(1975)862.0.CO;2.

Figueiredo, A. M. F., J. A. E. Braga, J. C. Zabalaga, J. J. Oliveira, G. A. Aguiar, O. B. Silva, and L. F. Mato, 1995, Recôncavo Basin, Brazil: A prolific intracontinental rift basin, *in* S. M. Landon, ed., Interior rift basins: AAPG Memoir 59, p. 157–203.

Frostick, L., and I. Reid, 1989, Is structure the main control of river drainage and sedimentation in rifts?: Journal of African Earth Science, v. 8, p. 165–182, doi:10.1016/S0899-5362(89)80022-3.

Gawthorpe, R. L., and M. R. Leeder, 2000, Tectonosedimentary evolution of active extensional basins: Basin Research, v. 12, p. 195–218, doi:10.1046/j.1365-2117.2000.00121.x.

Gibbs, A. D., 1984, Structural evolution of extensional basin margins: Journal of the Geological Society (London), v. 141, p. 609–620, doi:10.1144/gsjgs.141.4.0609.

Goldsworthy, M., and J. Jackson, 2001, Migration of activity within normal fault systems: Examples from the

Quaternary of mainland Greece: Journal of Structural Geology, v. 23, p. 489–506.
Gregory, J. W., 1896, The Great Rift Valley: London, John Murray, 405 p.
Gregory, J. W., 1921, The rift valleys and geology of East Africa: London, Seeley Service, 479 p.
Gupta, S., P. A. Cowie, N. H. Dawers, and J. R. Underhill, 1998, A mechanism to explain rift-basin subsidence and stratigraphic patterns through fault-array evolution: Geology, v. 26, p. 595–598.
Harding, T. P., 1984, Graben hydrocarbon occurrences and structural styles: AAPG Bulletin, v. 68, p. 333–362.
Henry, S., A. Danforth, S. Ventrakaman, and C. Willacy, 2004, PSDM subsalt imaging reveals new insights into petroleum systems and plays in Angola-Congo-Gabon (abs.): Petroleum Exploration Society of Great Britain-Houston Geological Society Africa Symposium, September 7–8, 2004.
Hunt, C. B., and D. R. Mabey, 1966, Stratigraphy and structure of Death Valley, California: U.S. Geological Survey Professional Paper 494-A, 162 p.
Jackson, J. A., and T. Blenkinsop, 1993, The Bilila-Mtakataka fault in Malawi: An active, 100-km long, normal fault segment in thick seismogenic crust: Tectonics, v. 16, p. 137–150, doi:10.1029/96TC02494.
Jackson, J. A., and D. McKenzie, 1983, The geometrical evolution of normal fault systems: Journal of Structural Geology, v. 5, p. 471–482, doi:10.1016/0191-8141(83)90053-6.
Jackson, J. A., and N. J. White, 1989, Normal faulting in the upper continental crust: Observations from regions of active extension: Journal of Structural Geology, v. 11, p. 15–36, doi:10.1016/0191-8141(89)90033-3.
Karner, G. D., and L. A. P. Gamboa, 2007, Timing and origin of the South Atlantic pre-salt sag basins and their capping evaporites *in* B. C. Schreiber, S. Lugli, and M. Babel, eds., Evaporites through space and time: Geological Society (London) Special Publication 285, p. 15–35, doi:10.1144/SP285.2.
Katz, B., 1995, A survey of rift basin source rocks, *in* J. J. Lambiase, ed., Hydrocarbon habitat in rift basins: Geological Society (London) Special Publication 80, p. 213–240, doi:10.1144/GSL.SP.1995.080.01.11.
Lambiase, J. J., and W. Bosworth, 1995, Structural controls on sedimentation in continental rifts, *in* J. J. Lambiase, ed., Hydrocarbon habitat in rift basins: Geological Society (London) Special Publication 80, p. 117–144, doi:10.1144/GSL.SP.1995.080.01.0.
Lambiase, J. L., and C. K. Morley, 1999, Hydrocarbons in rift basins: The role of stratigraphy: Philosophical Transactions of the Royal Society, v. 357, p. 877–900, doi:10.1098/rsta.1999.0356.
Leeder, M. R., 2007, Cybertectonic Earth and Gais's weak hand: Sedimentary geology, sediment cycling and the earth system: Journal of the Geological Society (London), v. 164, p. 277–296.
Machette, M. N., S. F. Personius, A. R. Nelson, D. P. Schwartz, and W. R. Lund, 1991, The Wasatch fault zone, Utah: Segmentation and history of earthquakes: Journal of Structural Geology, v. 13, p. 137–149, doi:10.1016/0191-8141(91)90062-N.
Magnavita, L. P., 1992, Geometry and kinematics of the Recôncavo-Tucano-Jatobá rift, northeast Brazil: Ph.D. thesis, University of Oxford, Oxford, England, 493 p.
Magnavita, L. P., I. Davison, and N. J. Kusznir, 1994, Rifting, erosion and uplift in Recôncavo-Tucano-Jatobá Rift, NE Brazil: Tectonics, v. 13, p. 367–388, doi:10.1029/93TC02941.
Magnavita, L. P., and H. T. F. Da Silva, 1995, Rift border system: The interplay between tectonics and sedimentation in the Recôncavo Basin: AAPG Bulletin, v. 79, p. 1590–1607.
Mann, P., L. Gahagan, and M. B. Gordon, 2003, Tectonic setting of the world's oil and gas fields, *in* M. T. Halbouty, ed., Giant oil and gas fields of the decade 1990–1999: AAPG Memoir 78, p. 15–105.
McClay, K. R., 1995, 2-D and 3-D analog modeling of extensional structures: Templates for seismic interpretation: Petroleum Geoscience, v. 1, p. 163–178.
McClay, K., and S. Khalil, 1998, Extensional hard-linkages, eastern Gulf of Suez, Egypt: Geology, v. 26, p. 563–566, doi:10.1130/0091-7613(1998)0262.3.CO;2.
McConnell, R. B., 1972, Geological development of the rift system of eastern Africa: Geological Society of America Bulletin, v. 83, p. 2549–2572, doi:10.1130/0016-7606(1972)83[2549:GDOTRS]2.0.CO;2.
McHone, J. G., 2000, Nonplume magmatism and rifting during the opening of the central Atlantic Ocean: Tectonophysics, v. 316, p. 287–296, doi:10.1016/S0040-1951(99)00260-7.
McKenzie, D., 1978, Some remarks on the development of sedimentary basins: Earth and Planetary Sciences, v. 40, p. 25–32, doi:10.1016/0012-821X(78)90071-7.
McLeod, A. E., and J. R. Underhill, 1999, Footwall scarp instability and the processes and products of degradation, northern Brent Field, northern North Sea, *in* A. J. Fleet and S. A. R. Boldy, eds., Petroleum geology of northwest Europe: 5th Conference of the Geological Society of London, p. 91–106, doi:10.1144/0050091.
McLeod, A. E., N. H. Dawers, and J. R. Underhill, 2000, The propagation and linkage of normal faults: Insights from the Strathspey-Brent-Statfjord fault array, northern North Sea: Basin Research, v. 12, p. 263–284, doi:10.1111/j.1365-2117.2000.00124.x.
McLeod, A. E., J. R. Underhill, S. J. Davies, and N. H. Dawers, 2002, The influence of fault array evolution on synrift sedimentation patterns: Controls on deposition in the Strathspey-Brent-Statfjord half graben, northern North Sea: AAPG Bulletin, v. 86, p. 1061–1093, doi:10.1306/61EEDC24-173E-11D7-8645000102C1865D.
Mello, U. T., G. Karner, and R. N. Anderson, 1995, Role of salt in restraining the maturation of subsalt source rocks: Marine and Petroleum Geology, v. 12, p. 697–716.
Milani, E. J., and I. Davison, 1988, Basement control, and transfer tectonics in the Recôncavo-Tucano-Jatoba rift, northeast Brazil: Tectonophysics, v. 18, p. 41–70, doi:10.1016/0040-1951(88)90227-2.
Morley, C. K., 1995, Developments in the structural geology of rifts over the last decade and their impact on

hydrocarbon exploration, *in* J. J. Lambiase, ed., Hydrocarbon habitat in rift basins: Geological Society (London) Special Publication 80, p. 1–32, doi:10.1144/GSL.SP.1995.080.01.01.

Morley, C. K., 2002a, Evolution of large normal faults: Evidence from seismic reflection data: AAPG Bulletin, v. 86, p. 961–978, doi:10.1306/61EEDBFC-173E-11D7-8645000102C1865D.

Morley, C. K., 2002b, Tectonic settings of continental extensional provinces and their impact on sedimentation and hydrocarbon prospectivity: Sedimentation in continental rifts: SEPM Special Publication 73, p. 25–55.

Morton, W. H., and R. Black, 1975, Crustal attenuation in Afar, *in* A. Pilger and A., Rosier, eds., Afar depression of Ethiopia: Inter-Union Commission on Geodynamics Scientific Report 14, p. 55–65.

Moustafa, A. R., 1997, Controls on the development and evolution of transfer zones: The influence of basement structure and sedimentary thickness in the Suez rift and Red Sea: Journal of Structural Geology, v. 19, p. 755–768, doi:10.1016/S0191-8141(97)00007-2.

Olsen, P. E., 1990, Tectonic, climatic and biotic modulation of lacustrine ecosystems: Examples from Newark Supergroup of eastern North America, *in* B. J. Katz, ed., Lacustrine basin exploration-case studies and modern analogs: AAPG Memoir 50, p. 209–224.

Olsen, P. E., 1997, Stratigraphic record of the early Mesozoic breakup of Pangea in the Laurasia-Gondwana rift system: Annual Review of Earth Planetary Science, v. 25, p. 337–401, doi:10.1146/annurev.earth.25.1.337.

Peacock, D. C. P., and D. J. Sanderson, 1991, Displacements, segment linkage and relay ramps in normal fault zones: Journal of Structural Geology, v. 13, p. 721–733, doi:10.1016/0191-8141(91)90033-F.

Proffett, J. M., 1977, Cenozoic geology of the Yerington district, Nevada, and implications for the nature of basin and range faulting: Geological Society America Bulletin, v. 88, p. 247–266, doi:10.1130/0016-7606(1977)882.0.CO;2.

Ravnas, R., and R. J. Steel, 1998, Architecture of marine rift-basin successions: AAPG Bulletin, v. 82, p. 110–146.

Roberts, A. M., and G. Yielding, 1994, Continental extensional tectonics, *in* P. Hancock ed., Continental deformation: Oxford, England, Pergamon Press, p. 223–250.

Rosendahl, B. R., 1987, Architecture of continental rifts with special reference to the eastern Africa: Annual Review of Earth and Planetary Sciences, v. 15, p. 445–503, doi:10.1146/annurev.ea.15.050187.002305.

Ruellan, E., and J.-M. Auzende, 1985, Structure and evolution of El Jadida submarine plateau (Mazagan, West Morocco): Bulletin de la Societé Géologique de France, v. 11, p. 103–114.

Schlische, R. W., 1992, Structural and stratigraphic development of the Newark extensional basin, eastern North America: Evidence for the growth of the basin and its bounding structures: Geological Society America Bulletin, v. 104, p. 1246–1263, doi:10.1130/0016-7606(1992)104<1246:SASDOT>2.3.CO;2.

Schlische, R. W., 1993, Anatomy and evolution of the Triassic–Jurassic continental rift system, eastern North America: Tectonics, v. 12, p. 1026–1042, doi:10.1029/93TC01062.

Scholz, C. A., and B. R. Rosendahl, 1988, Low lake stands in lakes Malawi and Tanganyika, East Africa, delineated with multifold seismic data: Science, v. 240, p. 1645–1648, doi:10.1126/science.240.4859.1645.

Scholz, C. H., and C. Aviles, 1986, The fractal geometry of faults and faulting, *in* S. Das, J. Boatwright, and C. Scholz, eds., Earthquake source mechanics: American Geophysical Union Monograph 37, p. 147–155.

Scholz, C. H., N. H. Dawers, J.-J. Yu, M. H. Anders, and P. Cowie, 1993, Fault growth and fault scaling laws: Preliminary results: Journal Geophysical Research, v. 98, p. 21,951–21,161, doi:10.1029/93JB01008.

Scholz, C. A., T. C. Moore, D. R. Hutchinson, A. J. Golmshtok, K. D. Klitgord, and A. G. Kurotchkin, 1997, Comparative sequence stratigraphy of low-latitude versus high-latitude lacustrine rift basins: Seismic data examples from the East African and Baikal rifts: Paleoecology, Palaeoclimatolology, Palaeoecology, v. 140, p. 401–420.

Seranne, M., and M. Seguret, 1987, The Devonian basins of western Norway: Tectonics and kinematics of an extending crust, *in* M. P. Coward, J. F. Dewey, and P. L. Hancock, eds., Continental extensional tectonics: Geological Society (London) Special Publication 28, p. 537–548, doi:10.1144/GSL.SP.1987.028.01.35.

Steel, R., 1976, Devonian basins of western Norway: Sedimentary response to tectonism and to varying tectonic context: Tectonophysics, v. 36, p. 207–224, doi:10.1016/0040-1951(76)90017-2.

Stein, J. B., G. C. P. King, and R. S. Rundle, 1988, The growth of geological structures by repeated earthquakes: 2. Field examples of continental dip-slip faults: Journal of Geophysical Research, v. 93, p. 13,307–13,318, doi:10.1029/JB093iB11p13319.

Stein, R. S., and S. E. Barrientos, 1985, Planar high angle faulting in the basin and range: Geodetic analysis of the 1983 Borah Peak, Idaho, earthquake: Journal of Geophysical Research, v. 90, p. 11,355–11,366, doi:10.1029/JB090iB13p11355.

Talbot, M. R., 1988, The origins of lacustrine oil source rocks: Evidence from lakes of tropical Africa, *in* A. J. Fleet, K. Kelts, and M. R. Talbot, eds., Lacustrine petroleum source rocks: Geological Society (London) Special Publication 40, p. 29–43, doi:10.1144/GSL.SP.1988.040.01.04.

Taylor, S. R., J. Almond, S. Arnott, D. Kemshell, and D. Taylor, 2003, The Brent field, Block 211/29, U.K. North Sea: Geological Society Memoirs 20, p. 233–250.

Tomasso, M., J. R. Underhill, R. A. Hodgkinson, and M. J. Young, 2008, Structural styles and depositional architecture in the Triassic of the Ninian and Alwyn North fields: Implications for basin development and prospectivity in the northern North Sea: Marine and Petroleum Geology, v. 25, p. 588–605.

Turner, S., M. Regelous, C. J., Hawkesworth, and M. Mantovani, 1994, Magmatism and continental break up in the South Atlantic: High-precision ^{40}Ar-^{39}Ar geochronology: Earth

Planetary Science Letters, v. 121, p. 333–348, doi:10.1016/0012-821X(94)90076-0.

Underhill, J. R., 1991a, Implications of Mesozoic–Recent basin development in the Inner Moray Firth, UK: Marine and Petroleum Geology, v. 8, p. 359–369, doi:10.1016/0264-8172(91)90089-J.

Underhill, J. R., 1991b, Controls on Late Jurassic seismic sequences, Inner Moray Firth: A critical test of Exxon's original sea level chart: Basin Research, v. 3, p. 79–98, doi:10.1111/j.1365-2117.1991.tb00141.x.

Underhill, J. R., M. J. Sawyer, P. Hodgson, M. D. Shallcross, and R. L. Gawthorpe, 1997, Implications of fault scarp degradation for Brent Group prospectivity, Ninian Field, northern North Sea: AAPG Bulletin, v. 81, p. 999–1022.

Walsh, J. J., and J. Watterson, 1988a, Analysis of the relationship between displacements and dimensions of faults: Journal of Structural Geology, v. 10, p. 239–247, doi:10.1016/0191-8141(88)90057-0.

Walsh, J. J., and J. Watterson, 1988b, Dips of normal faults in coal measures and other sedimentary sequences: Journal of the Geological Society (London), v. 145, p. 859–873, doi:10.1144/gsjgs.145.5.0859.

Wernicke, Â., 1985, Uniform-sense normal simple shear of the continental lithosphere: Canadian Journal of Earth Sciences, v. 22, p. 108–125.

Wernicke, B., 2009, The detachment era (1977-1982) and its role in revolutionizing continental tectonics, *in* U. Ring and B. Wernicke, eds., Extending a continent: Architecture, rheology and heat budget: Geological Society (London) Special Publication 321, p. 1–8, doi:10.1144/SP321.1.

Yielding, G., 1990, Footwall uplift associated with Late Jurassic normal faulting in the northern North Sea: Journal of the Geological Society (London), v. 147, p. 219–222, doi:10.1144/gsjgs.147.2.0219.

Yielding, G., M. E. Badley, and B. Freeman, 1991, Seismic reflections from normal faults in the northern North Sea, *in* A. M. Roberts, G. Yielding, and B. Freeman, eds., The geometry of normal faults: Geological Society (London) Special Publication 56, p. 79–89, doi:10.1144/GSL.SP.1991.056.01.06.

Younes, A. I., and K. R. McClay, 2002, Development of accommodation zones in the Gulf of Suez-Red Sea rift, Egypt: AAPG Bulletin, v. 86, p. 1003–1026, doi:10.1306/61EEDC10-173E-11D7-8645000102C1865D.

Geomechanical restoration as a tool for fractured reservoir characterization: Application to the Permian Basin, west Texas

Joseph M. Stockmeyer, John H. Shaw, Lee T. Billingsley, Andreas Plesch, Michael Wales, Leore C. Lavin, Ray Knox, and Luke Finger

ABSTRACT

We present a three-dimensional (3-D) geomechanical-restoration method as a reservoir characterization tool in the Permian Basin, west Texas. The Oates SW field produces gas from the Lower Devonian Thirtyone Formation within structural traps. The Thirtyone is a brittle chert with characteristics of a fractured reservoir: field development has experienced variable production trends for decades. To assess the impact of deformation on reservoir properties, we employ 3-D geomechanical restorations to model strain patterns associated with fault displacement and fold growth. We correlate these model strains with independent measures of natural rock strain to assess the viability of the restoration results. A semblance volume generated from 3-D seismic reflection data illuminates secondary faults and fracture zones that are not incorporated in the geomechanical restorations. Our analysis yields strong correlations between low semblance and elevated strain throughout the Thirtyone reservoir. These correlations indicate that restoration strains may be used to describe the distribution of secondary faults and fractures that are not represented in our models, providing predictive capabilities for defining fractured reservoir properties. We integrate strain and semblance with production data to evaluate these correlations at the borehole scale in the study area. We describe how tectonic strain likely enhanced permeability, directly impacting observed production trends. Our characterization of the Thirtyone reservoir demonstrates the ability to accurately predict strain distributions with geomechanical restorations where structure has been a significant factor in the development of reservoir permeability. We suggest that these methods show promise as

Copyright ©2018. The American Association of Petroleum Geologists. All rights reserved.

Manuscript received May 3, 2016; provisional acceptance August 22, 2016; revised manuscript received November 12, 2016; final acceptance March 23, 2017.
DOI:10.1306/03231716076

AUTHORS

JOSEPH M. STOCKMEYER ~ *Department of Earth and Planetary Sciences, Harvard University, 20 Oxford Street, Cambridge, Massachusetts 02138; present address: Chevron North America Exploration and Production Company, 1500 Louisiana, Houston, Texas 77002; stockmeyer@chevron.com*

Joseph M. Stockmeyer is an exploration geologist at Chevron Corporation in its Deepwater Gulf of Mexico business unit. He holds degrees in geology from Washington and Lee University and Harvard University.

JOHN H. SHAW ~ *Department of Earth and Planetary Sciences, Harvard University, 20 Oxford Street, Cambridge, Massachusetts 02138; shaw@eps.harvard.edu*

John H. Shaw is the Harry C. Dudley Professor of Structural and Economic Geology at Harvard University and leads the Structural Geology and Earth Resources Group at Harvard, an industry–academic partnership that supports research on petroleum exploration and production methods. Shaw's research interests include complex trap and reservoir characterization in fold-thrust belts and deep-water passive margins.

LEE T. BILLINGSLEY ~ *Abraxas Petroleum Corporation, 18803 Meisner Drive, San Antonio, Texas 78258; present address: Windridge Oil & Gas, LP, 518 North Main Street, Boerne, Texas 78006; lee@windridgeoil.com*

Lee T. Billingsley has almost 40 years of experience in the petroleum industry and recently started a new company with his son, Matthew, and another partner. Prior to starting Windridge, Billingsley served for 18 years as vice president–exploration at Abraxas Petroleum Corporation, which provided the data set for this research.

ANDREAS PLESCH ~ *Department of Earth and Planetary Sciences, Harvard University, 20 Oxford Street, Cambridge, Massachusetts 02138; andreas_plesch@harvard.edu*

Andreas Plesch is a research associate in the Structural Geology and Earth Resources Group at Harvard University. His research interests involve three-dimensional modeling and analysis of contractional structures on the reservoir to mountain-belt scale using a variety of methods, focusing on quantitative aspects and interpretations of seismic reflection data. He has worked on structures worldwide, commonly with industry partners.

MICHAEL WALES ~ *Department of Earth and Planetary Sciences, Harvard University, 20 Oxford Street, Cambridge, Massachusetts 02138; michaelkwales@gmail.com*

Michael Wales holds a Bachelor of Arts degree from Harvard University, where he studied history, economics, and geology. Wales currently works at Warwick Energy Group in Oklahoma City, where he evaluates and invests in unconventional onshore exploration and production assets.

LEORE C. LAVIN ~ *Department of Earth and Planetary Sciences, Harvard University, 20 Oxford Street, Cambridge, Massachusetts 02138; leorelavin@college.harvard.edu*

Leore C. Lavin is a Bachelor of Arts candidate at Harvard University (2017 graduation), where she studies earth and planetary sciences. Lavin currently conducts research related to geophysics, earthquake hazards, and emergency management.

RAY KNOX ~ *Abraxas Petroleum Corporation, 18803 Meisner Drive, San Antonio, Texas 78258; rknox@abraxaspetroleum.com*

H. Ray Knox has 37 years of experience in the petroleum industry and is currently a senior geologist at Abraxas Petroleum Corporation in San Antonio, Texas. Knox obtained his master's degree from The University of Texas at San Antonio in applied geology.

LUKE FINGER ~ *Abraxas Petroleum Corporation, 18803 Meisner Drive, San Antonio, Texas 78258; lfinger@abraxaspetroleum.com*

Luke Finger is a petroleum geologist at Abraxas Petroleum Corporation in San Antonio, Texas. Finger specializes in

a reservoir characterization tool for conventional and unconventional development operations.

INTRODUCTION

Effective tools for fractured reservoir characterization are in great demand for development operations in conventional and unconventional petroleum basins around the world. In deformed basins, understanding the influence of tectonic strain on reservoir properties is particularly important. Indeed, structural elements may aid hydrocarbon production by generating or enhancing secondary permeability within the target reservoir (e.g., Lorenz and Finley, 1989; Engelder et al., 2009; Ghosh and Mitra, 2009; Gale et al., 2014). Similarly, tectonic strain may enable vertical or lateral communication with adjacent facies or formations. In the presence of stacked reservoirs, this may reduce completion costs or perhaps increase ultimate recoveries during field development. However, elevated permeability may also divert hydrocarbons to less economic zones (e.g., Aydin, 2000; Bowker, 2007), thus reducing development recovery rates. In addition, faults or fracture networks may facilitate water incursion, leading to higher water cuts and, ultimately, increasing development costs. Clearly, an appropriate characterization of natural structures impacting reservoir properties is critically important during appraisal and field development (e.g., Hennings et al., 2000). Indeed, accurate predictions of strain patterns in fractured reservoirs may prove to be quite valuable during development operations, informing such decisions as well placement, borehole orientation, perforation intervals, and choke management. However, fault and fracture patterns at the reservoir scale are often complex and difficult to characterize properly because of the resolution limits of conventional seismic reflection data.

In this study, we seek to evaluate if a new suite of three-dimensional (3-D) geomechanical-restoration methods can be an effective tool to model fault and fracture patterns in hydrocarbon reservoirs. Kinematic restoration methods have been developed over the past few decades in attempts to model structural growth and the associated strain patterns (e.g., Allmendinger, 1998; Egan et al., 1999; Rouby et al., 2000; Griffiths et al., 2002; Benesh et al., 2014). However, kinematic techniques are inherently limited because they do not explicitly consider stress or variable rock strengths. A new generation of geomechanical methods may address some of these concerns (e.g., Muron, 2005; Maerten and Maerten, 2006; Moretti et al., 2006; Durand-Riard et al., 2011; Chauvin et al., 2015). Specifically, geomechanical restorations incorporate mechanical rock properties, including stratigraphic variations in rock strength, and are able to address the inherent 3-D nature of deformation (e.g., Plesch et al., 2007; Guzofski et al., 2009; Durand-Riard et al., 2013). Moreover, these

restorations can employ geologically reasonable boundary conditions, such as a restoration datum and fault displacements.

The current generation of 3-D geomechanical-restoration tools uses linear- or nonlinear-elastic constitutive laws to model large, permanent rock strains. Geomechanical forward models that employ elastic stress–strain laws have demonstrated their ability to capture the inherent 3-D nature of fold development in addition to accurately modeling 3-D stress and strain patterns of fault-related fold growth (e.g., Cooke and Pollard, 1997; Bellahsen et al., 2006; Shackleton and Cooke, 2007). However, there are important physical limitations to the elastic constitutive relationships used in current geomechanical-restoration methods that must be considered. Geomechanical-restoration methods seek to address this limitation by incorporating faults, detachments, and bedding-plane slip surfaces that separate the models into many small elastic regions. Moreover, these methods can recover small increments of deformation with stress relaxation to model large strains. Despite these approaches, however, it seems reasonable to conclude that geomechanical-restoration methods may be limited in their abilities to precisely define stress and strain associated with structural growth. Thus, in this study, we employ an objective, empirical approach to assess the viability of these strain predictions by comparing them with independent geophysical attributes and dynamic well production data.

In this study, we use a 3-D geomechanical-restoration method (Muron, 2005) to assess the impact of tectonic strain on reservoir performance within a natural-gas reservoir—the Lower Devonian Thirtyone Formation—in the Oates SW field, Delaware Basin, west Texas. Using well logs and a 3-D seismic reflection survey, we build a 3-D structural model of the Paleozoic Atoka–Ellenburger stratigraphic section, including prominent fault-related folds that serve as structural traps in the Oates SW field. We restore our 3-D structural model using horizon and fault-displacement boundary conditions and calculate rock strain from the resulting displacement fields. In conjunction with these restorations, we generate a 3-D semblance volume from our seismic volume to serve as a proxy for natural rock strain. We seek to validate the restoration method as a predictor of natural rock strain by quantifying the correlation between modeled strain distributions and semblance throughout the Thirtyone reservoir in the study area. We further explore the viability of the method by addressing the impact of reservoir-scale strains on the production histories of vertical and deviated natural-gas wells in the Oates SW field.

GEOMECHANICAL RESTORATIONS

Structural restoration is the process of retrodeforming tectonic-induced strains accumulated over geologic timescales (e.g.,

exploration of the Texas Gulf Coast with an emphasis on Eagle Ford and Austin Chalk reservoir characterization. He holds a bachelor's degree in geology from Texas A&M University and a master's degree in geology from The University of Texas at San Antonio.

ACKNOWLEDGMENTS

We thank Abraxas Petroleum Corporation for supporting this industry–academic collaboration, including the publication of this paper. Subsurface interpretations, structural modeling, and geomechanical restorations were performed in Gocad software provided by Paradigm, and we thank them for their support. Structural modeling and restoration plug-ins developed within the Research for Integrative Numerical Geology Consortium (formerly the Gocad Consortium) were used throughout this study. Benjamin Chauvin provided helpful insight into mesh generation and boundary conditions. We also thank Guillaume Caumon, John Cole, Pauline Durand-Riard, Chris Guzofski, Pete Lovely, Don Medwedeff, and Carlos Rivero for their contributions to related geomechanical-restoration research efforts. Kevin Smart, Richard Groshong, and AAPG Editor Barry Katz provided comments that improved the quality of this paper.

DATASHARE 87

Figure S1 is available in an electronic version on the AAPG website (www.aapg.org/datashare) as Datashare 87.

Dahlstrom, 1969). Standard restoration methods remove fault offsets while simultaneously unfolding geologic structures. Most traditional methods follow line-length or area balancing constraints or are governed by kinematic rules to recover deformation. In contrast, new 3-D geomechanical-restoration methods use finite-element methods governed by constitutive relationships that define rock strength and strength contrasts, providing a more physics-based approach to structural restoration. These developments have provided the ability to model the inherent 3-D nature of deformation for complex geologic structures. In addition, these methods have provided important insight into the effects of rock properties and mechanical stratigraphy on strain distributions associated with structural growth (e.g., Guzofski et al., 2009). In the following sections, we provide a concise description of the general restoration approach and workflow. For a complete description of the methodology, we refer the reader to Muron (2005) or Chauvin et al. (2015).

General Methodology

The geomechanical-restoration tool used in this study applies the finite-element method coupled with a dampening algorithm to restore 3-D geologic structures while minimizing changes in volume and global energy state of the model (Muron and Mallet, 2004; Muron, 2005; Chauvin et al., 2015). This method restores a stratigraphic surface within the volume to a defined datum while simultaneously honoring additional boundary conditions, which commonly include (1) fixed nodes, pin lines, or boundary walls within the model; (2) displacement of boundary walls or fault-slip constraints; and (3) fault-compliance constraints, requiring adjacent fault blocks to remain in contact across the fault surface. A linear- or nonlinear-elastic constitutive relationship governs the strength of model elements within fault-bounded blocks during the restoration. This geomechanical approach incorporates isotropic rock properties—such as Young's modulus and Poisson's ratio—that can vary between subvolumes of the model (e.g., stratigraphic intervals; fault blocks). Moreover, the method prescribes neither a kinematic theory nor a complete velocity field to direct a structural restoration. Instead, the restoration seeks the absolute minimum strain-energy state (Muron and Mallet, 2004), which is primarily controlled by the defined boundary conditions and material properties. Our extensive testing of geomechanical restorations, in addition to previous studies (e.g., Lovely et al., 2012), indicates the importance of defining geologically constrained boundary conditions. Nonphysical boundary conditions will yield inaccurate structural restorations, ultimately leading to inaccurate interpretations of structural growth or strain distributions.

As structural restoration seeks to remove permanent rock strain over geologic timescales, we recognize that there are inherent limitations to the linear-elastic constitutive relationship in our restoration tool. In theory, this approach should restore infinitesimally small increments of folding and faulting. In practice, this is typically not possible because of limits on our knowledge of deformation path over these small increments. We attempt to overcome these limitations by restoring modest stages of deformation. With growth (i.e., syntectonic) strata, sequential restoration is possible by incrementally restoring each growth section in succession (e.g., Guzofski et al., 2009; Vidal-Royo et al., 2012). In a similar vein, restorations of modest structures that lack growth strata have been able to accurately model strain distributions using a single-step restoration (e.g., Plesch et al., 2007; Durand-Riard et al., 2013). The restoration tool used in this study has been able to overcome some limitations of the linear-elastic simplification by dividing a structural model into subvolumes bounded by stratigraphic horizons, fault ramps, and detachments. Thus, although each subregion retrodeforms elastically, the full model endures large-scale, permanent strain influenced by fault displacements. Indeed, several studies have found this method of geomechanical structural restoration to be well suited for modeling strain orientations and their relative magnitudes distributed through 3-D geologic structures and stratigraphic formations (e.g., Maerten and Maerten, 2006; Moretti et al., 2006; Plesch et al., 2007; Guzofski et al., 2009; Shokair et al., 2009; Vidal-Royo et al., 2012; Durand-Riard et al., 2013). In this study, we seek to extend this geomechanical-restoration method to characterize reservoir-scale structures that impact observed production trends from a naturally fractured reservoir in the Delaware Basin, west Texas.

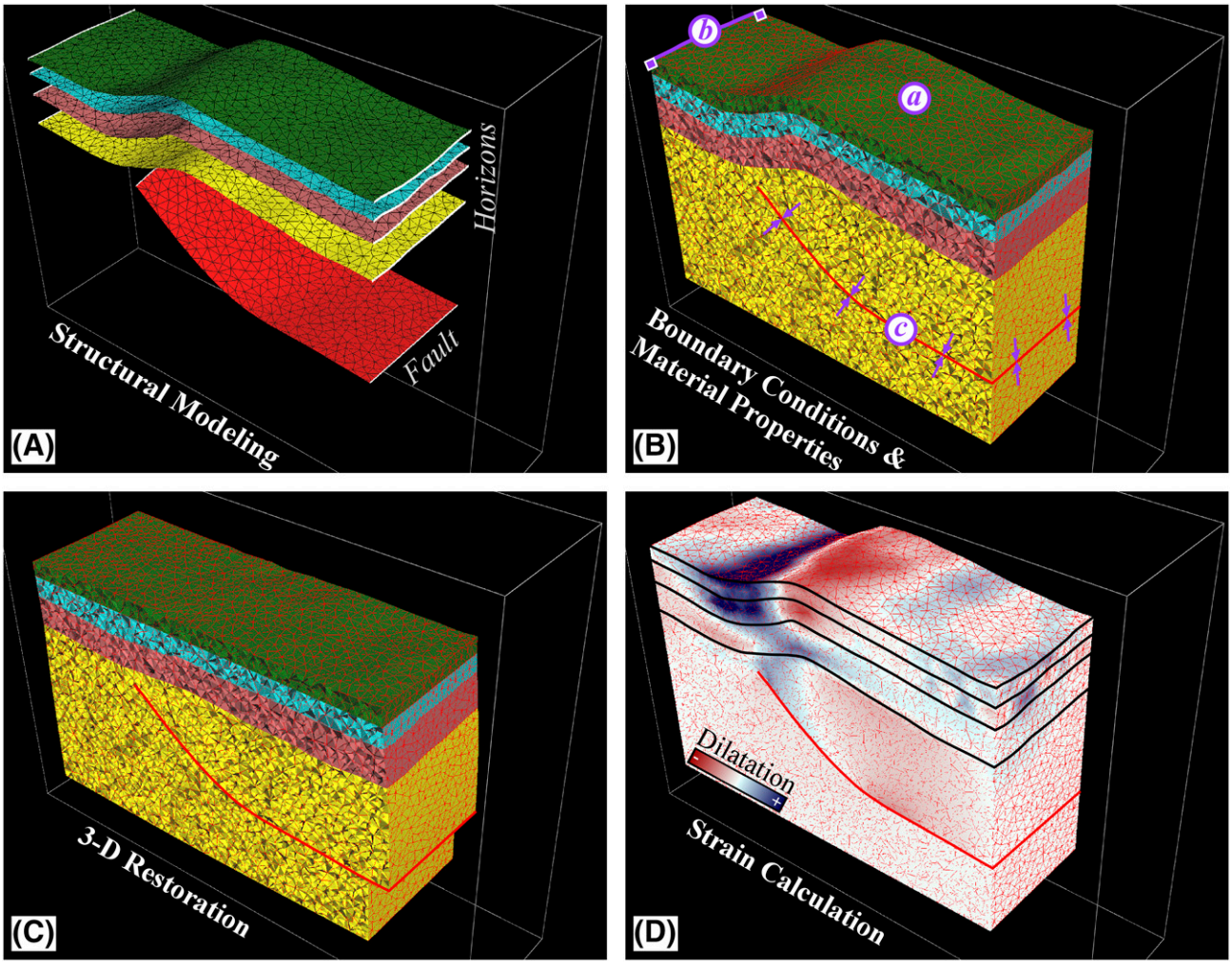

Figure 1. General workflow for geomechanical restoration illustrated by a restoration of the Elsinore anticline model used in this study. (A) Three-dimensional (3-D) geologic surfaces derived from interpretations of 3-D seismic reflection data and well logs. (B) Generation of the volumetric mesh. Material properties are applied to each 3-D region. Boundary conditions are required for the restoration problem: (a) datum of a deformed horizon, (b) fixed boundary wall(s), and (c) fault compliance. (C) Restored model after solving the defined restoration problem. (D) Strain visualization for detailed analysis of the restoration result.

Workflow

The 3-D geomechanical-restoration workflow used in our study first requires a topologically consistent 3-D structural model of surfaces representing the faults and stratigraphic horizons of interest (Figure 1A). These surfaces are often generated from interpretations of well logs and depth-converted 3-D seismic reflection data. Ensuring topologic consistency of all surface contacts produces several volumetric regions of varying spatial dimension that are stored within the structural model: 3-D region volumes bounded by stratigraphic and/or fault surfaces, two-dimensional region surfaces (e.g., geologic and boundary surfaces), one-dimensional (1-D) region line contacts of intersecting surfaces (e.g., hanging-wall and footwall fault contacts), and zero-dimensional region node contacts (e.g., end points of 1-D regions). The structural model and contact data are used to generate a volumetric mesh composed of tetrahedral elements (Figure 1B). Isotropic material properties are defined in each 3-D region of the mesh by Young's modulus (E) and Poisson's ratio (ν) or Lamé's first (λ) and second (μ) parameters. The last step of model setup requires defining geologically and physically reasonable boundary conditions (Figure 1B). Typical boundary conditions include flattening a deformed datum surface; holding a node, line, and/or surface fixed in one or more directions; defining fault compliance; and restoring fault offsets. With material properties and

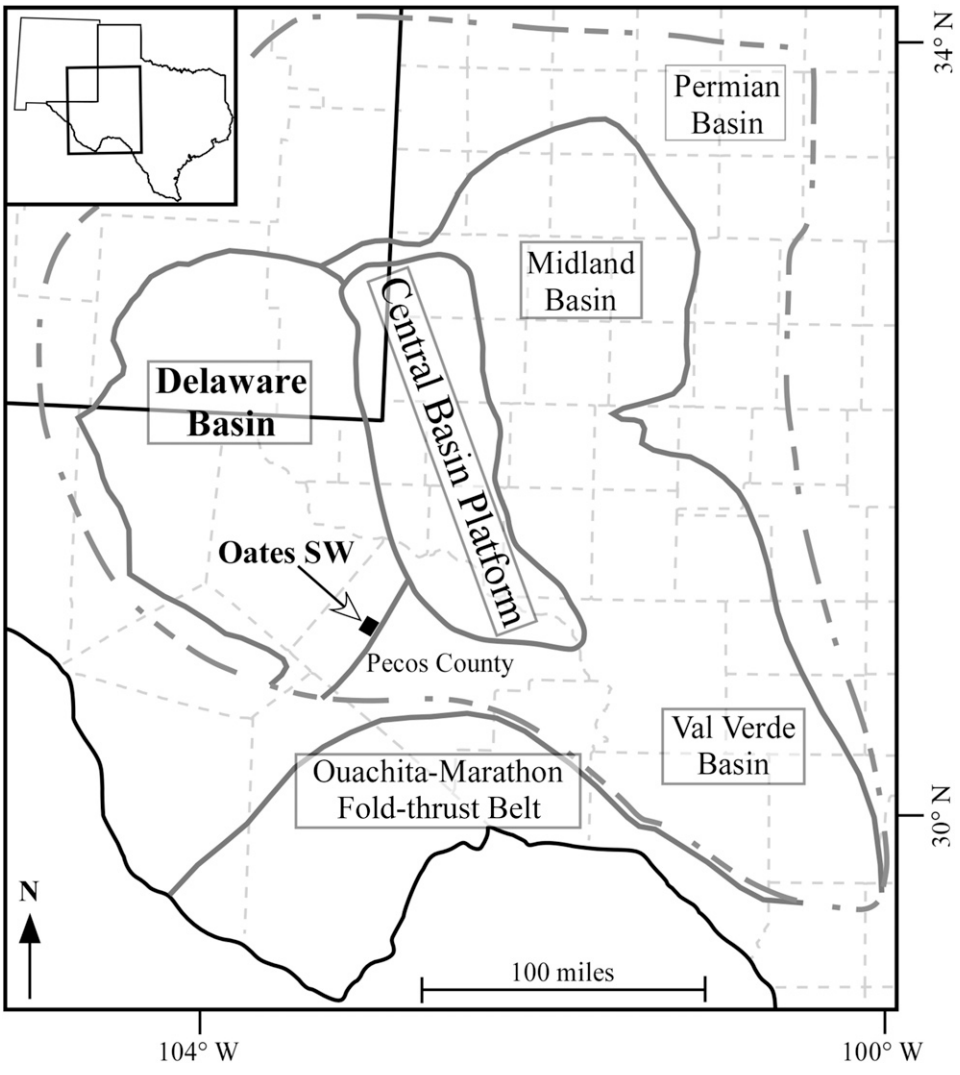

Figure 2. The Permian Basin (dashed outline) of West Texas and New Mexico is composed of the Midland Basin, the Central Basin Platform, and the Delaware Basin. To the south is the Ouachita–Marathon fold-thrust belt that formed in the Early Pennsylvanian. The study area is the Oates SW gas field in the Delaware Basin, Pecos County, Texas.

boundary conditions applied to the model, the restoration tool can solve the assigned restoration problem. After numerical convergence to a minimum strain-energy state (Muron and Mallet, 2004), a restoration vector and strain tensor are calculated at each node of the model. Using these outputs, the 3-D model can be displayed in the restored state (Figure 1C) and individual components of strain—such as strain invariants—can be calculated for a detailed analysis of strain distributions (Figure 1D).

GEOLOGIC SETTING OF OATES SW FIELD

We use the geomechanical-restoration tool described above to assess the impact of tectonic strain on production trends from the Lower Devonian Thirtyone Formation in the Oates SW field, Delaware Basin, west Texas (Figures 2, 3). The Thirtyone reservoir is a cherty dolomite that exhibits characteristics of a naturally fractured reservoir (Ruppel and Hovorka, 1995; Montgomery, 1998; Saller et al., 2001; Billingsley, 2006). In the Central Basin platform, the Thirtyone reservoir is thought to have spatially heterogeneous primary porosity and permeability, often controlled by the original depositional attributes such as chert abundance and facies geometry (Ruppel and Hovorka, 1995; Montgomery, 1998). However, fracturing and faulting have complicated reservoir property variations by developing compartmentalization, preferred flow paths, and potentially flow barriers (Ruppel and Hovorka, 1995; Montgomery, 1998).

Production from the Lower Devonian Thirtyone in the Oates SW field (Figures 2, 3) has exhibited similar production-trend heterogeneities. Some wells have been shut in soon after initial production

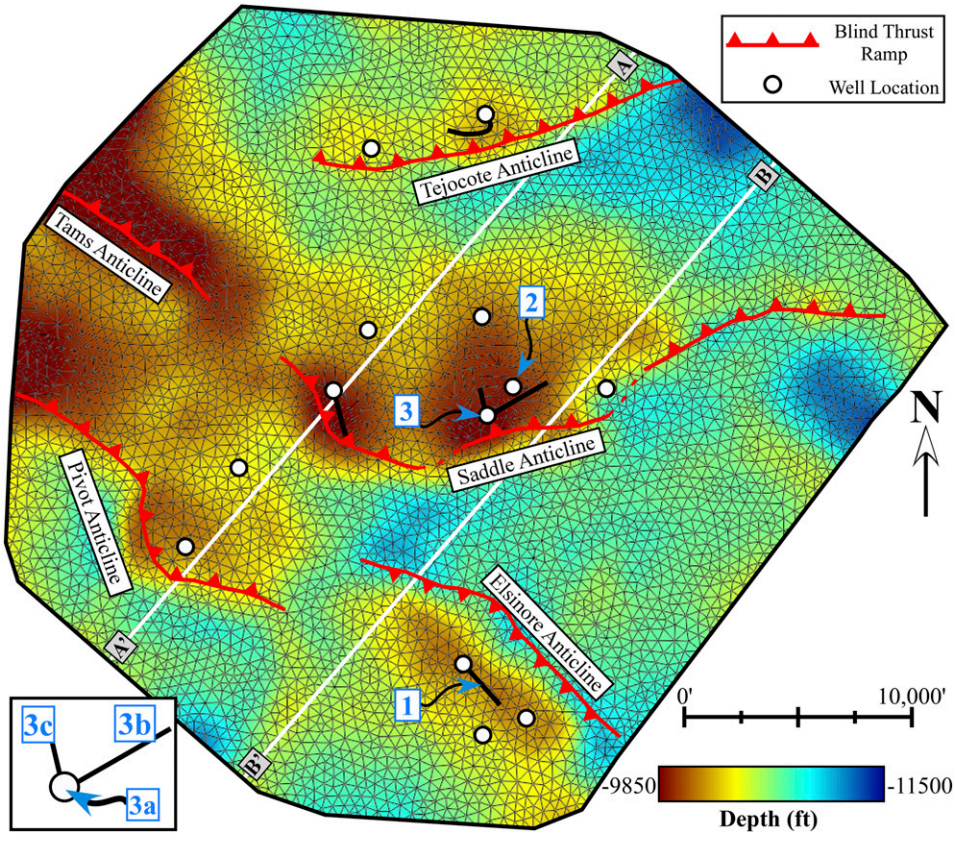

Figure 3. Structure map of the Lower Devonian Thirtyone Formation, the primary reservoir target in the Oates SW field (Figure 2). Structural traps have been the primary targets during field development. Vertical and horizontal wells have produced natural gas with varying degrees of success to date. Water cuts are also variable across the field. Well 1 is a horizontal well drilled by Abraxas within the Thirtyone reservoir. Well 2 is a legacy vertical borehole that produced from the both the Thirtyone and the Montoya reservoirs. Well 3a is a vertical well that produced from the uppermost section of the Devonian Thirtyone reservoir. Abraxas drilled well 3b by reentering well 3a and drilling horizontally at an east–northeast azimuth, targeting the Montoya reservoir, directly below the Devonian Thirtyone. After well 3b was shut in, Abraxas drilled well 3c with a west–northwest-directed horizontal leg through the Thirtyone reservoir. Sections AA′ and BB′ are shown in Figure 5. 1 = well 1; 2 = well 2; 3 = well 3.

resulting from low flow rates, whereas cumulative production in several wells has exceeded 1 BCF gas (~28.3 MMCM; Billingsley, 2006). Water cuts have been similarly inconsistent, with no clear pattern between or even within individual structures. Indeed, water incursion is a significant concern in places, with cumulative water production exceeding 8 million bbl (~1.3 MMCM) in the most water-rich well of the field (Billingsley, 2006). Thus, the Lower Devonian Thirtyone reservoir in the Oates SW field is an ideal test case for applying our geomechanical-restoration tool for fractured reservoir characterization.

Paleozoic Stratigraphy

This study focuses on the Lower Ordovician–Lower Pennsylvanian rock units in the Oates SW field (Figure 4). The deepest unit clearly imaged in the seismic data is the Ellenburger Group, a Lower Ordovician carbonate (Figure 4). Regionally, the Ellenburger Group has undergone significant diagenesis, including extensive dolomitization, tectonic fracturing, and karstification. As a result, the Ellenburger can be quite permeable and source undesirable levels of water to shallower reservoirs in the presence of vertical flow networks (e.g., Loucks, 2008). Above the Ellenburger sits the Middle Ordovician Simpson Group (e.g., Suhm and Ethington, 1975; Frenzel et al., 1988). The Simpson is a thick group of interbedded limestone, shale, and sandstone (Figure 4). The Upper Ordovician is marked by the Montoya dolostone. The Montoya is a carbonate deposit that has been almost entirely dolomitized (Pope, 2014). In addition, abundant chert within the Montoya is present throughout west Texas, including our study area (Figure 4), interpreted to indicate a period of strong marine upwelling (Pope, 2014). The Early Devonian marks the deposition of the primary reservoir in the study area, the Thirtyone Formation. The Thirtyone is another cherty dolomite (Figure 4). In Oates SW, the abundance of chert within the Thirtyone is likely to be laterally heterogeneous and perhaps even discontinuous, akin to

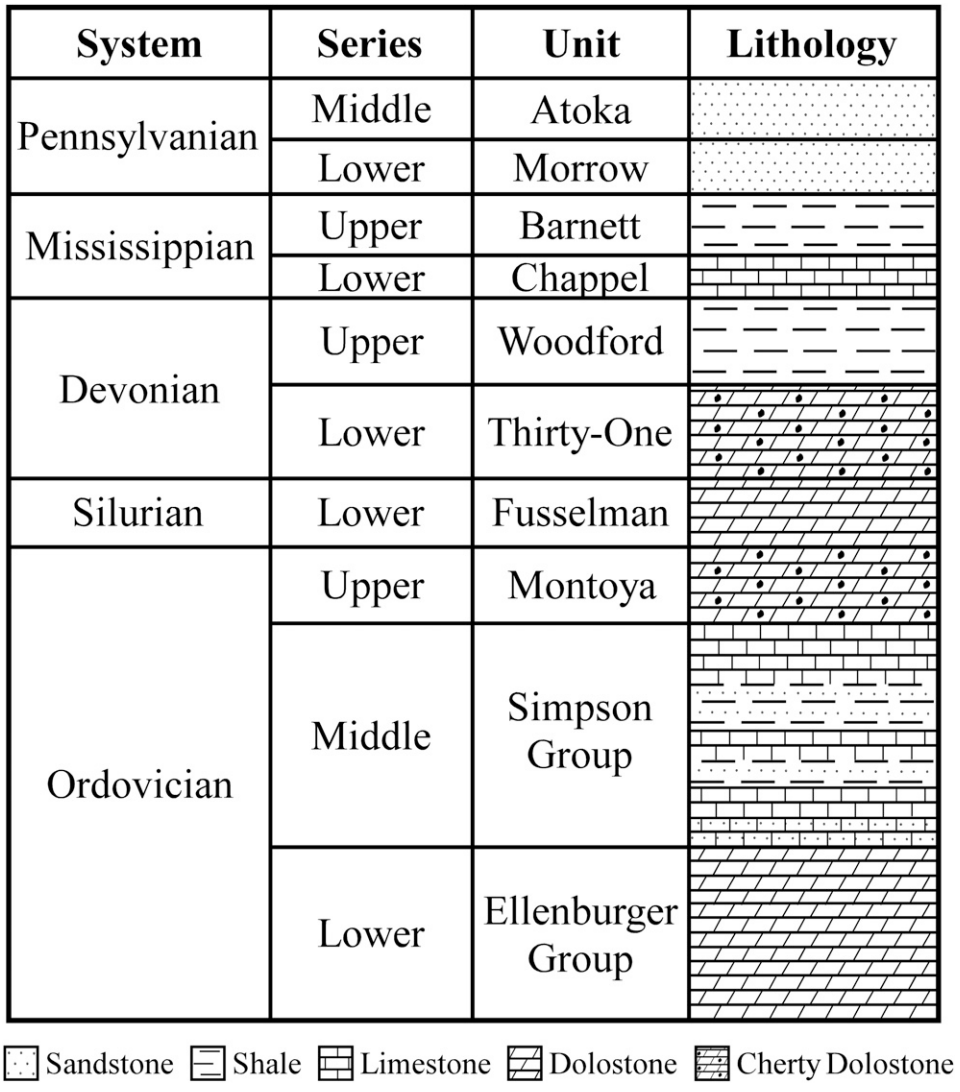

Figure 4. Simplified description of mapped units in the Oates SW field. The Devonian Thirtyone is the primary reservoir target for development. The Ellenburger Group is known to be a significant water source regionally.

the distal chert depositional environment of Ruppel and Barnaby (2001). The Thirtyone is overlain by the Upper Devonian Woodford Shale. Through much of the study area, the Woodford is followed in stratigraphic succession by the Lower Mississippian Chappel limestone, the Upper Mississippian Barnett Shale, and Lower Pennsylvanian Morrow and Atoka sandstones (Figure 4).

Structural Characterization

The primary tectonic activity deforming the Paleozoic Ellenburger–Atoka units in west Texas occurred during the late Paleozoic Ouachita–Marathon orogeny, marking the closure of the proto-Atlantic Ocean (e.g., Hills, 1985; Shumaker, 1992), immediately south of our study region (Figure 2). Using a depth-converted 3-D seismic reflection survey and industry well logs, we interpreted the major stratigraphic units deformed by the Ouachita–Marathon collisional event and characterized the prominent structures defining the major structural traps in the field. Our structural interpretations of the major traps are presented in Figure 5. The Paleozoic section of interest is well imaged and allows for straightforward mapping of the fold structure within this unit. We generally observe structures to be characterized by wide, gentle backlimbs with steeper, narrow forelimbs (Figure 5A). The geometries of the folds in section AA′ (Figure 5A) are consistent with an anticlinal fault-bend–fold structural style (Suppe, 1983). We do not observe the continuation of axial surfaces or folded reflectors below our top

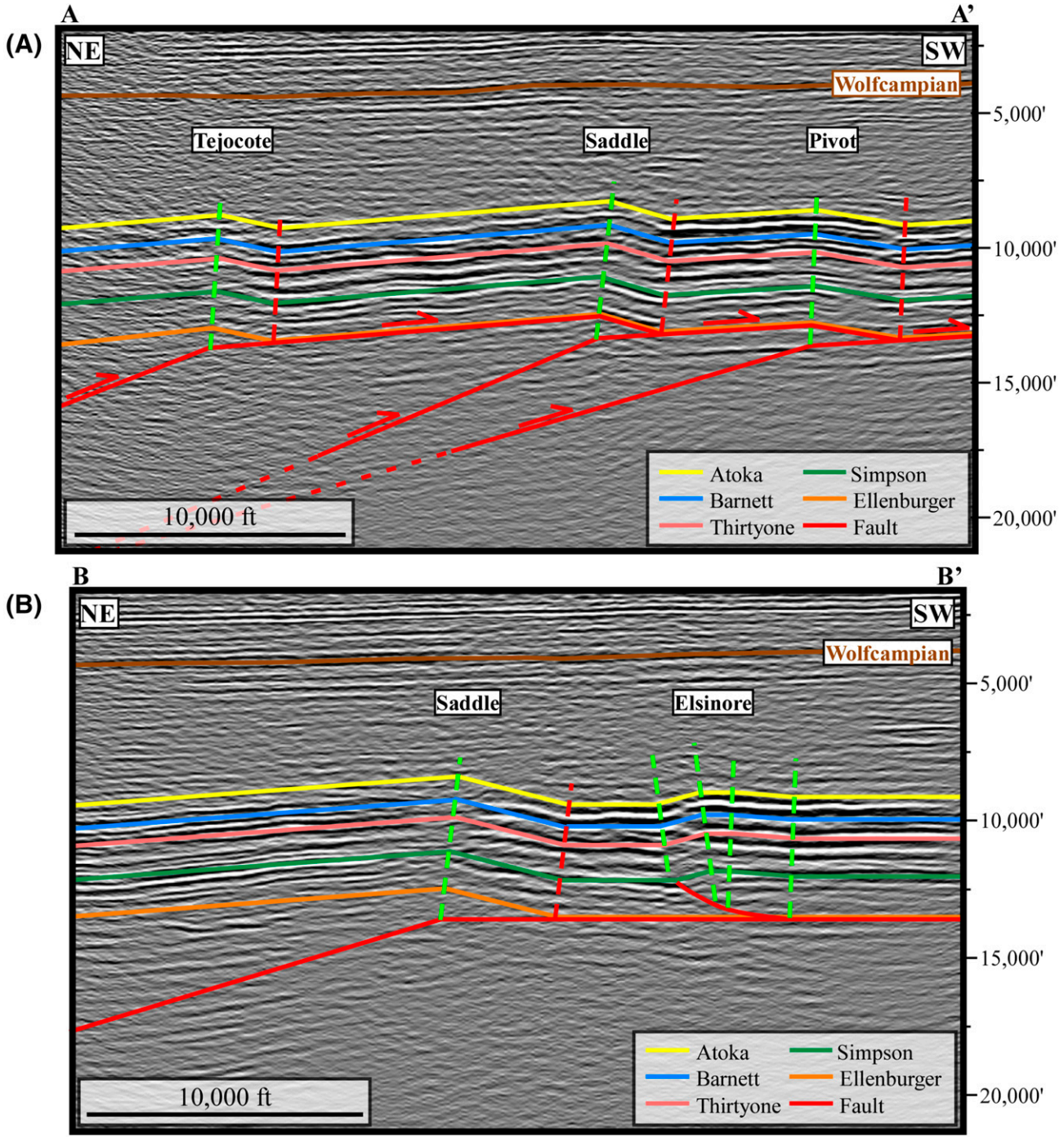

Figure 5. Structural interpretation of the Atoka–Ellenburger interval across the study area. (A) Section AA′, interpretation of basement-involved anticlinal fault-bend folds. A regional upper detachment lies along the top Ellenburger. These structures developed in a break-forward sequence of thrusting (e.g., Shaw et al., 1999). (B) Section BB′, interpretation of the Saddle and Elsinore structures. The Elsinore is a fault-propagation fold, in contrast to the other prominent traps in Oates SW field. Top Ellenburger serves as the basal detachment for the Elsinore Thrust, shielding the Ellenburger from hanging-wall deformation in this prospect. Green and red dashes are active and inactive axial surfaces, respectively. Line locations shown in Figure 3. Vertical exaggeration is 1:1. Sections are extracted from the available three-dimensional seismic volume. Uninterpreted versions of both sections are shown in Figure S1, supplementary material available as AAPG Datashare 87 at www.aapg.org/datashare.

Ellenburger interpretation. Thus, we interpret the upper detachment of the fault-bend folds to be at or near the top Ellenburger (Figure 5A). The deeper units are not well imaged, making it difficult to directly interpret the fault-ramp geometry beneath the anticlinal folds from offset reflectors or direct fault-plane reflections. Thus, we use the observed fold shape to interpret the geometry of the thrust ramps at depth (e.g., Suppe, 1983; Shaw et al., 2005). These thrust ramps generally dip in the northwest, north, and northeast directions. The seismic data do not suggest the presence of a prominent syncline in the backlimbs of the structures indicating a shallowing of thrust ramps to a basal detachment level (Suppe, 1983). Thus, we interpret these structures to be basement-involved anticlinal fault-bend folds (Figure 5A). This structural style describes the Pivot, Tams, Saddle, and Tejocote structures (Figures 3, 4A).

Our interpretation of the top Ellenburger marker in section AA′ (Figure 5A) suggests that it is folded in the hanging wall of some structures, despite serving as an upper detachment surface. Our observation of a folded upper detachment is consistent with a break-forward sequence of thrusting (e.g., Shaw et al., 1999). It is a mechanically inefficient process to thrust downward, such as along the forelimb of a folded detachment (Dahlen and Barr, 1989), further supporting our interpretation of break-forward sequence of thrusting. In this interpretation, the Tejocote structure formed initially, with the top Ellenburger only folded in the immediate hanging wall of the structure. This was followed in sequence by the Saddle and Pivot folds, respectively, folding the part of the top Ellenburger detachment in the hanging wall of the active structure (Figure 5A). We do not observe any significant stratigraphic thickness changes across these structures that would indicate the presence of growth stratigraphy constraining the timing of fold development. However, most of the reflectors between the interpreted Wolfcampian horizon and the Atoka Formation are relatively undeformed (Figure 5). Thus, faulting and associated uplift of the fault-related folds in Oates SW likely occurred shortly after the Middle Pennsylvanian. Moreover, the lack of significant deformation in strata above top Atoka indicates the lack of, or perhaps limited, deformation associated with the Late Cretaceous–early Cenozoic Laramide orogeny in the western continental United States (e.g., Dickinson and Snyder, 1978).

The Elsinore fold in section BB′ (Figure 5B) is distinct from the structural style of the other major traps. The Elsinore structure exhibits a northeastern vergence, whereas the other structures have vergence directions generally in the range of south-southeast–south-southwest (Figure 3). This suggests that the underlying Elsinore fault dips to the southwest, approximately opposite to the other major fault dip directions (Figure 5). Moreover, we observe offset reflectors between our interpreted Simpson and Ellenburger levels, indicating the presence of a thrust ramp above the top Ellenburger detachment. Lastly, we interpret a synclinal axial surface pinned to the tip of this observed thrust (Figure 5B). These observations indicate that the Elsinore anticline is best described as a fault-propagation fold (Suppe and Medwedeff, 1990; Shaw et al., 2005). Notably, the top Ellenburger serves as a basal detachment for the Elsinore thrust, whereas it serves as an upper detachment for the other fault-related folds. This basal detachment for the Elsinore structure shields the Ellenburger Group—and its potential water source—from hanging-wall deformation in the vicinity of the Elsinore structure.

THREE-DIMENSIONAL GEOMECHANICAL RESTORATIONS

Structural Modeling

We used our fault and horizon interpretations of the seismic and well log data to build 3-D geologic surfaces in the Gocad modeling environment (Mallet, 1992). We used these surfaces to construct our volumetric mesh for restoration. Given the size and complexity of the structures, it was most efficient from both a modeling and computational standpoint to divide our regional model into four subdomains: (1) Pivot anticline, (2) Elsinore anticline, (3) Saddle and Tams anticlines, and (4) Tejocote anticline (Figure 6A). This choice is appropriate in our study area because the hanging-wall deformation associated with each structure is isolated to an individual fold due to the modest size of each anticline (Figure 5). We restored each of these 3-D geologic models separately to characterize the Lower Devonian Thirtyone reservoir throughout the Oates SW field.

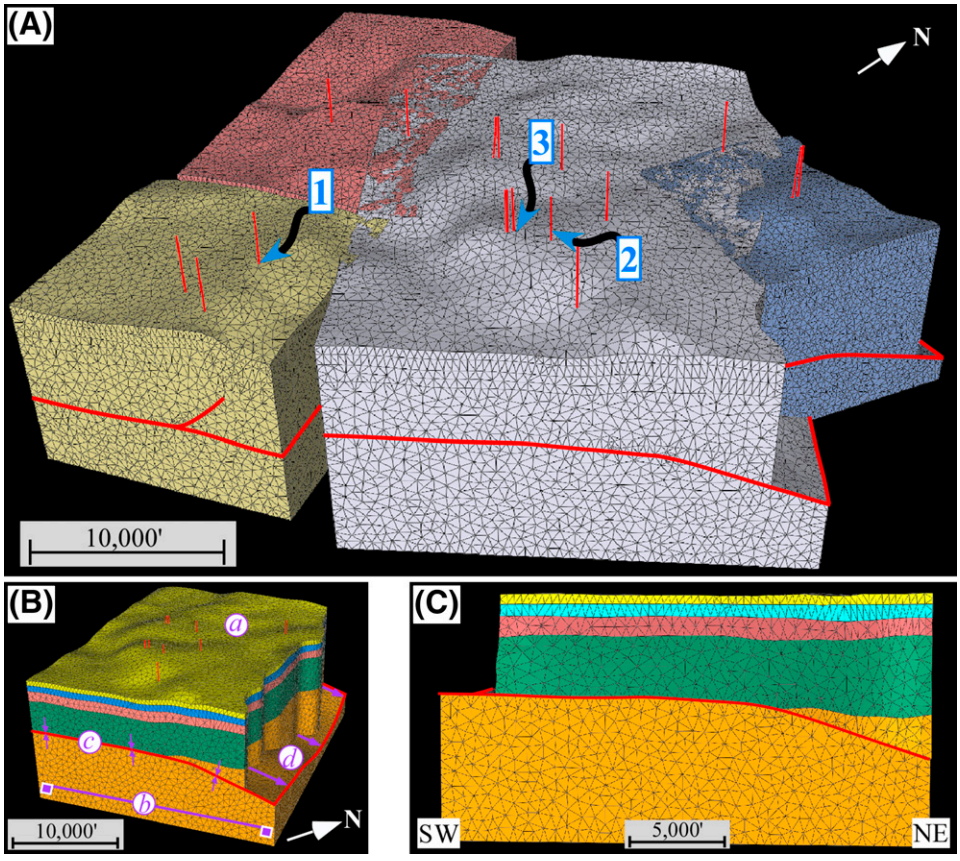

Figure 6. Three-dimensional models of the Oates SW field. (A) The regional model was broken into separate structural subdomains, requiring four volumetric meshes to restore all of the structures in the study area. (B) Material properties are applied to each structural model. Boundary conditions are also required for the restoration problem. Boundary conditions for the fault-bend–fold models include (a) a datum horizon, (b) a boundary wall fixed in one direction, (c) fault compliance, and (d) a fault-slip constraint (Appendix 1). See Figure 1B for boundary conditions applied to the Elsinore anticline model. (C) Restored state of the Elsinore and Tams model. 1 = well 1; 2 = well 2; 3 = well 3.

We included the following surfaces as stratigraphic layers in each model: top Atoka, top Barnett, top Thirtyone, top Simpson, and top Ellenburger. Fault surfaces and detachments were included in each structural model as well (e.g., Figure 1). Moreover, we removed any observed regional dip of the top Ellenburger detachment surface from each structural model, allowing us to restore horizons to a horizontal datum. After restoration, the regional dip was restored to each model for subsequent analysis. We note that restoring any regional dip to a 3-D model after restoration does not rotate the output restoration vectors nor the strain tensors, because these outputs are defined within a local coordinate system of the 3-D volume. Separate rotations must be applied to the restoration vectors and strain tensors to ensure that all components of the restoration result are in a consistent frame of reference.

Boundary Conditions

Fault-Bend–Fold Models

For each fault-bend–fold model—the Pivot, Tams and Saddle, and Tejocote anticlines—we restore the top Atoka surface to a horizontal reference elevation. Our structural interpretation (Figure 5) indicates that both the Atoka and Thirtyone intervals are pregrowth strata; thus, a datum applied to the Atoka should fully restore the Thirtyone. An additional boundary condition is applied to one side of the model such that it can only move in the dip-slip and vertical directions. Fixed-wall boundary conditions have been shown to aid the restoration problem by providing a frame of reference (e.g., Guzofski et al., 2009; Durand-Riard et al., 2013). Fault-compliance boundary conditions are also defined (e.g., Figure 6B); we force all displacement along faults during restoration to occur in the hanging wall of the model. Although this assumption is not necessarily an accurate description of near-fault deformation observed in nature, we deem it to be a reasonable first-order approximation of fault-related folding over geologic timescales. We note that alternative styles of structural growth (e.g., trishear, salt tectonics) may produce sufficient footwall strains that could require consideration.

Because our restoration tool does not adhere to a specific kinematic model or geometric theory, it is generally difficult to produce a geologically reasonable

restoration of fault-bend folds without providing footwall cutoffs, which are not present in our 3-D models, to govern the direction of motion. This challenge arises because the restoration of a datum horizon can simply flatten the folded intervals by imposing translation in many different directions along the upper detachment. In effect, this amounts to a near-vertical flattening of the fold. To overcome this challenge, geomechanical restorations generally rely on hanging-wall and footwall cutoffs (e.g., Guzofski et al., 2009) or a boundary-wall displacement that reflects fault slip (e.g., Durand-Riard et al., 2013). In this study, we developed a workflow (Appendix 1) that defines a fault-slip estimate from the anticlinal fold width (Suppe, 1983) and implements this as a boundary-wall displacement in the hanging wall of the fault (Figure 6B). This offset boundary wall serves as the fault-slip constraint on the thrust ramp, acting to drive hanging-wall motion across the underlying thrust fault in the appropriate, downdip direction during restoration (e.g., Figure 6C). This boundary condition guides the restoration tool to produce a geologically reasonable restoration path and avoids some other pitfalls associated with restorations that lack sidewall boundary conditions (Lovely et al., 2012).

Fault-Propagation–Fold Model

As described above, the Elsinore structure stands out from the other prominent folds in the Oates SW field (Figure 5B). Relative to the anticlinal fault-bend folds, the Elsinore anticline is characterized by (1) an opposite vergence and fault dip direction, (2) a different structural style, and (3) the presence of a basal detachment, not an upper detachment. Therefore, the boundary conditions for the Elsinore restoration (Figure 1B) are slightly modified relative to the fault-bend–fold models (Figure 6B). Similar to the other structural models, we restore the top Atoka unit to a planar surface and limit movement of one sidewall to the dip-slip and vertical directions (Figure 1B). In addition, we define fault compliance and restrict all motion to the hanging-wall fault block. Because the Elsinore structure is a fault-propagation fold, all of the fault slip is consumed at the fault tip (e.g., Suppe and Medwedeff, 1990), precluding any large-scale motion beyond the anticlinal forelimb. Therefore, we fix the north–northeastern boundary wall of the Elsinore anticline (in the foreland of the fault tip) in the dip-slip direction (Figure 1B). Another difference compared with the fault-bend–fold models is that we do not define a fault-slip boundary condition for the Elsinore anticline model (Figure 1B). The absence of an upper detachment surface and the pinned foreland boundary wall were sufficient to generate geologically reasonable restoration slip directions and magnitudes (Figure 1C).

Material Properties

Material properties, particularly property contrasts, can impart a strong influence on the strain distributions of thrust sheets (e.g., Erickson, 1996; Hughes et al., 2014; Morgan, 2015). For each volumetric mesh, we defined a Young's modulus (E) and Poisson's ratio (ν) to govern the strengths of each stratigraphic layer. Although mechanical properties can be estimated using well logs, these values are not necessarily representative at the scale of an entire field because of, at least in part, unknown heterogeneities in lithology, fracture density, porosity, and permeability. Therefore, we used synthetic values for E and ν to define our model strengths. To assess the effect of mechanical stratigraphy on our restoration results, we tested a suite of restorations using deformable and rigid definitions for rock strengths. Deformable regions are assigned material properties of $E = 3.5 \times 10^9$ Pa and $\nu = 0.325$. In contrast, rigid regions are defined by $E = 3.5 \times 10^{10}$ Pa and $\nu = 0.225$. We provide a brief description of our tests of various material-property contrasts using our deformable and rigid properties in Appendix 2. Following these results, we continue our analysis using a model defined with deformable material properties in the Ellenburger and Simpson intervals and the rigid properties in the Atoka, Barnett, and Devonian sections.

STRAIN DISTRIBUTIONS

Restoration Strains

Because the deformation associated with structural growth was likely modest—and limited to the immediate hanging wall of each fold—we merge the strain results from each of the four restorations and extract these strains onto a single top Thirtyone 3-D surface for subsequent analysis. To avoid nonphysical strain predictions associated with the fault-slip boundary conditions (Appendix 1) and other edge

effects, we omitted near-edge regions of each model from our strain analysis. This led to a slightly reduced surface-area extent of modeled strain for analysis compared with the total mapped coverage of top Thirtyone (Figure 3). However, the limits of our semblance calculations controlled our final extent for analysis (discussed below).

We extract I_1 and I_2 components of strain (Appendix 3) onto the top Thirtyone surface to isolate volume changes and shear strains, respectively, across the Thirtyone reservoir. The restoration results across the Oates SW field indicate dilatation is concentrated in the prominent anticlinal forelimbs (Figure 7A), which are steeper and more narrow than the corresponding back limbs (Figure 5). Relatively modest magnitudes of dilatation exist in the back limbs of the structural traps. Figure 7B illustrates similar distributions of distortional strain across the top Thirtyone. Interestingly, along-strike variations in I_2 within the anticlinal forelimbs (Figure 7B) correspond to along-strike variations in structural relief (Figure 3), which is a function of fault slip for fault-bend and fault-propagation folds (Suppe, 1983; Suppe and Medwedeff, 1990). In addition, the restorations predict lower-magnitude distortional strain in the back limbs of the prominent structures, similar to the patterns observed for dilatation in Figure 7A. Together, these first-order strain patterns defined by the restorations are consistent with observations of natural structures and forward mechanical models of similar structural styles (e.g., Gregg Erickson and Jamison, 1995; Strayer et al., 2004; Hughes et al., 2014). However, the local distributions and patterns of each strain type have noticeable differences, which may indicate variations in how strain associated with secondary structures is manifest within the Thirtyone reservoir. These variations have the potential to impart heterogeneities in reservoir character across the Oates SW field that can impact hydrocarbon development, such as secondary porosity and changes in permeability.

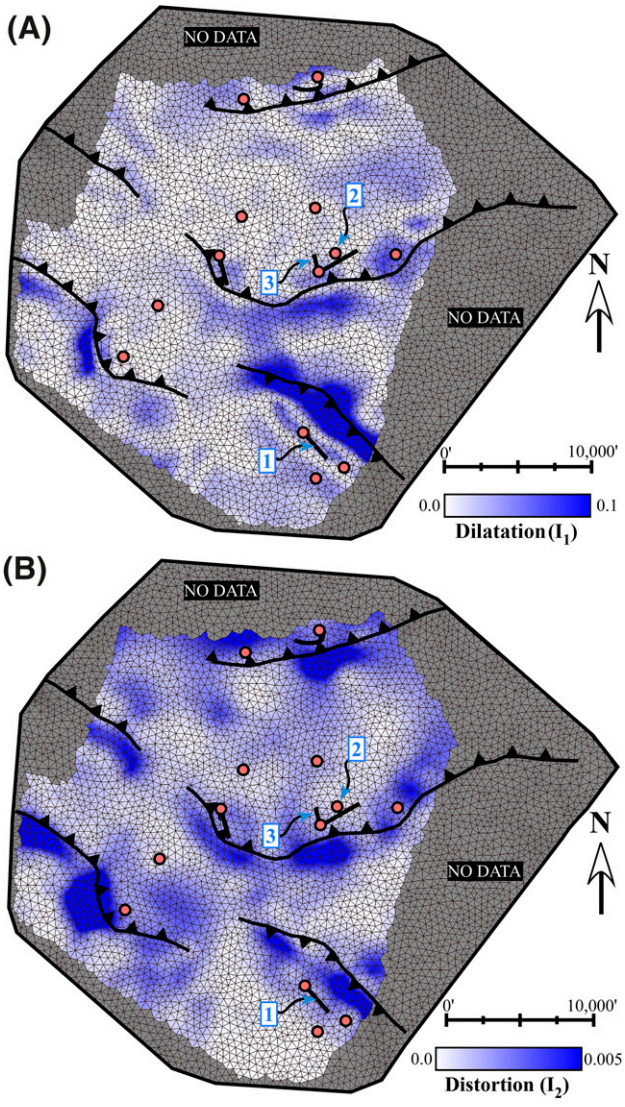

Figure 7. Calculated strain distributions across the top Devonian Thirtyone horizon. (A) Magnitude of dilatational (I_1) strain. (B) Distortional (I_2) strain magnitudes. The geomechanical restorations indicate that the majority of strain across the top Thirtyone surface is localized in anticlinal forelimbs. Subtle strain signatures are predicted in the back limbs of each structure as well. 1 = well 1; 2 = well 2; 3 = well 3.

Semblance

To assess whether the restoration strains effectively represent deformation in the Oates SW structures, we compare the modeled strain patterns with an independent measure of natural rock strain. For this purpose, we rely on semblance, a coherency-based seismic attribute, to serve as a proxy for natural strain (Marfurt et al., 1998). Semblance is measured as the similarity of a stacked seismic trace relative to adjacent traces within a defined depth range (Bahorich and Farmer, 1995; Marfurt et al., 1998). This geophysical attribute is measured from zero to unity; a semblance value of zero represents total dissimilarity between two adjacent stacks, whereas a semblance of unity indicates total similarity. Accordingly, semblance is a measure of the lateral continuity of acoustic

impedance and has been shown to be quite effective in the identification of macroscale, secondary, and subseismic faults and fracture zones (e.g., Bahorich and Farmer, 1995; Marfurt et al., 1998; Shokair et al., 2009; Chopra and Marfurt, 2010; Frankowicz and McClay, 2010).

We extract semblance data onto the top Thirtyone surface (Figure 8). The region of the well-imaged 3-D seismic data used to calculate our semblance volume limits the extent of analysis. We use an approximately 1066-ft (325-m) vertical window for the semblance calculation to discriminate between large-scale discontinuities caused by the faults and folds likely represented in our starting model and smaller-scale features that were not explicitly meshed in our structural models. This large vertical window for the semblance calculation mutes local discontinuities associated with the local stratigraphy and minor processing artifacts (Bahorich and Farmer, 1995; Marfurt et al., 1998). Thus, we interpret low-semblance features to indicate the presence of secondary structures, potentially imaged in the 3-D seismic data. The extracted semblance data (Figure 8) reveal wide, continuous, low-semblance zones within the forelimbs of the major fault-related folds. These are interpreted to represent one or more faults that disrupt the seismic continuity. The locations of these secondary faults suggest that they are associated with fold growth (Figures 3, 7). In addition, we identified several tight, linear bands of low semblance that illuminate observable faults in the seismic data. Subsequent mapping of these secondary faults in the 3-D seismic volume indicates that they are present in both the forelimbs and back limbs of structures (Figure 8). The spatial coincidence of these secondary structures with discrete bands of moderate-low semblance (Figure 8) strengthens our interpretation that low-semblance zones likely indicate faulted regions. We emphasize that these secondary faults are not explicitly represented in our structural models.

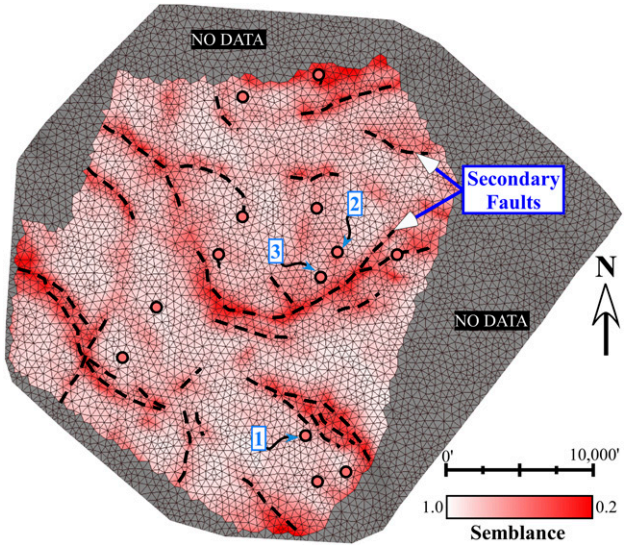

Figure 8. Semblance–used as a proxy for natural rock strain–extracted onto the top Thirtyone Formation surface. Semblance values are low where seismic reflectors are laterally discontinuous and high where they are more continuous (Bahorich and Farmer, 1995; Marfurt et al., 1998). Low-semblance values are concentrated in the anticlinal forelimbs of the Oates SW structures. Linear semblance features in the forelimbs and backlimbs often illuminate secondary faults imaged in the seismic data that deform the Thirtyone reservoir. These secondary faults are not represented in the structural models. 1 = well 1; 2 = well 2; 3 = well 3.

Strain–Semblance Correlations

We compare the strain distributions (Figure 7) with the spatial patterns of semblance (Figure 8) across the Devonian Thirtyone reservoir and identify a strong correlation between low semblance and elevated magnitudes of strain predicted by the geomechanical restorations. The increased dilatation and distortion in anticlinal forelimbs (Figure 7) correlate particularly well with the low-semblance values in the same areas across the structures in the Oates SW field (Figure 8). To quantitatively assess these correlations, we generated Model II (i.e., reduced major axis; geometric mean) regressions between strain and semblance within the Devonian reservoir across individual structures. A Model II regression is a linear-regression approach that treats both variables as independent with an unknown error variance (Rayner, 1985). The results of our I_1-semblance and I_2-semblance regressions are presented in Figure 9. For both structures, there is a clear trend of decreasing semblance with increasing strain, indicated by the negative slopes of the best-fit regression line and negative values of each regression coefficient (r). The negative correlation between dilatation and semblance across the Elsinore anticline (Figure 9A) is particularly strong ($r = -0.81$). In addition, the central Saddle structure exhibits a moderately strong negative I_2-semblance correlation coefficient ($r = -0.54$). The leftward tilt of the outer data density contours of all four correlations (Figure 9) further suggests this correlation between low

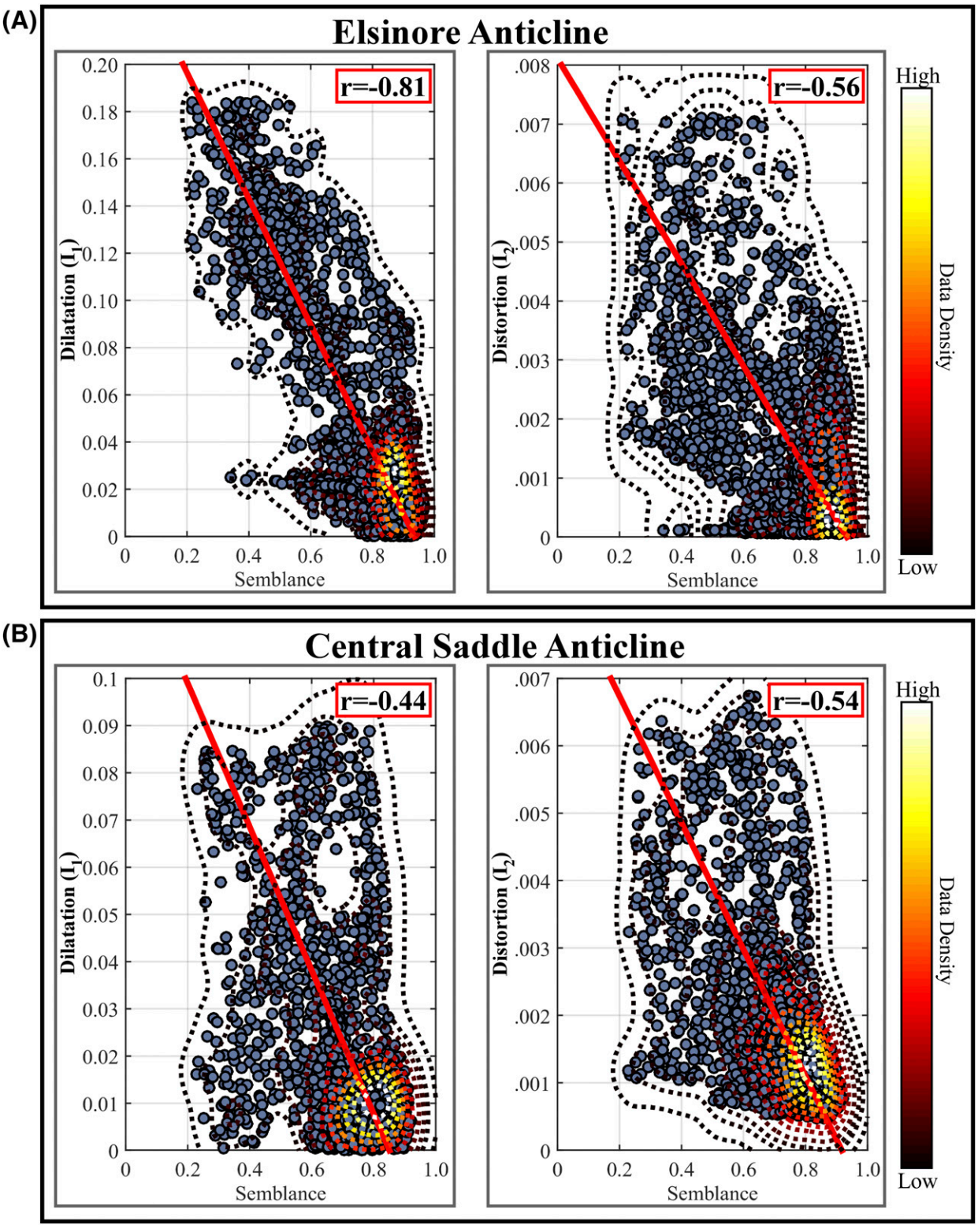

Figure 9. Strain–semblance Model II regressions (Rayner, 1985) across two of the structural traps in the study area. (A) Elsinore anticline, which includes well 1 (Figure 3). (B) Central Saddle anticline, which includes well 2 and well 3 (Figure 3). The negative strain–semblance correlations for both dilatation and distortion suggest that the geomechanical restorations accurately modeled strain associated with primary and secondary structural growth. r = Model II regression coefficient (i.e., goodness of fit).

semblance and elevated strain is a robust result. These correlations, combined with our ability to explicitly map secondary faults that correlate with highly and moderately strained regions (Figures 7, 8), support our finding that the geomechanical-restoration method used here can accurately model strain distributions without explicitly including secondary structures in the volumetric mesh. Thus, we conclude that geomechanical restoration can serve as a viable tool for accurately modeling secondary fault and fracture distributions in deformed reservoirs. In the following section, we continue our characterization of the Lower Devonian Thirtyone reservoir in the Oates SW field by incorporating dynamic well data.

FRACTURED RESERVOIR CHARACTERIZATION USING GEOMECHANICAL RESTORATIONS

The Oates SW field (Figure 3) began producing gas in the 1950s. The majority of field development has been by vertical wells completed in the Thirtyone reservoir. Currently, Abraxas Petroleum Corporation operates the field and produces gas from open-hole horizontal wells drilled by Abraxas in the mid-2000s (Billingsley, 2006). Legacy and recent production across the field have encountered heterogeneities in reservoir performance. Vertical wells within the Pivot anticline (Figure 3) produced negligible amounts of hydrocarbons, whereas the most productive structure—the Elsinore anticline—has produced approximately 10 BCF (~283 MMCM) to date, including 8 BCF (~227 MMCM) from one horizontal well. Moreover, water cuts across the field have ranged from modest to substantial (Billingsley, 2006). Figure 10 presents cumulative production curves of three wells—two horizontal and one vertical—in the study area, highlighting some of the production variability in the Oates SW field. In this final section, we investigate the impact of tectonic strain and structural growth on reservoir properties and production trends for these three wells in the Oates SW field.

Well 1

Well 1 (Figure 3) is a horizontal well drilled by Abraxas Petroleum in the mid-2000s within the Elsinore anticline, a fault-propagation fold (Figure 5B). Well 1 produces from an interval approximately 175 ft (~50 m) below the top of the Devonian Thirtyone. The lateral azimuth is southeast, parallel to the trend of the structural crest (Figure 3). Open-hole production from this lateral segment has exceeded 8 BCF (~227 MMCM) natural gas—the most of any well in the field—and 1 million bbl (~159 MCM) water to date, with water cut increasing through the life of the well (Figure 10A). Figure 11 presents the strain and semblance trends along the lateral section of well 1. Beginning at the heel of the lateral, dilatation (Figure 11A) is a maximum magnitude (>3.0%) and quickly decreases away from the heel to a minimum (<1.5%) in the first third of the total lateral length. The middle third remains at very low dilatational strain, ranging between less than 1.5% and approximately 2.0%. Continuing across the outer third of the lateral segment, dilatation then increases to approximately 2.5% (Figure 11A). The trend of distortional strain is quite similar; strains are a minimum in the middle third of the lateral section and increase in both directions toward the toe and heel of the well (Figure 11C). Figure 11B depicts the semblance variations along well 1. We observe relatively low-semblance magnitudes near the heel of the lateral and across most of the first third of the lateral section. Semblance then increases to a maximum magnitude across the middle third of the lateral segment. Continuing toward the toe, semblance decreases to a local minimum before increasing again at the toe (Figure 11B).

In summary, there is elevated strain and lower semblance along the outer sections (i.e., the heel and toe) of the well 1 horizontal section. In contrast, the middle section of the lateral is characterized by greater semblance and minimal amounts of strain. These findings indicate a strong, negative correlation between both strain properties, dilatation and distortion, and semblance along much of the lateral section of well 1, consistent with the negative strain–semblance correlations at larger scales (e.g., Figure 9). Thus, we conclude that there is a structural control on the strain and semblance values along the well 1 lateral track.

Figure 12A visualizes distortional strain along the outer third—near the toe—of the well 1 lateral with the nearby seismic imaging. In this perspective view, we observe a distinct, narrow kink band within the top Barnett–base Devonian interval around the wellbore. This subtle fold limb is coincident with the increase in

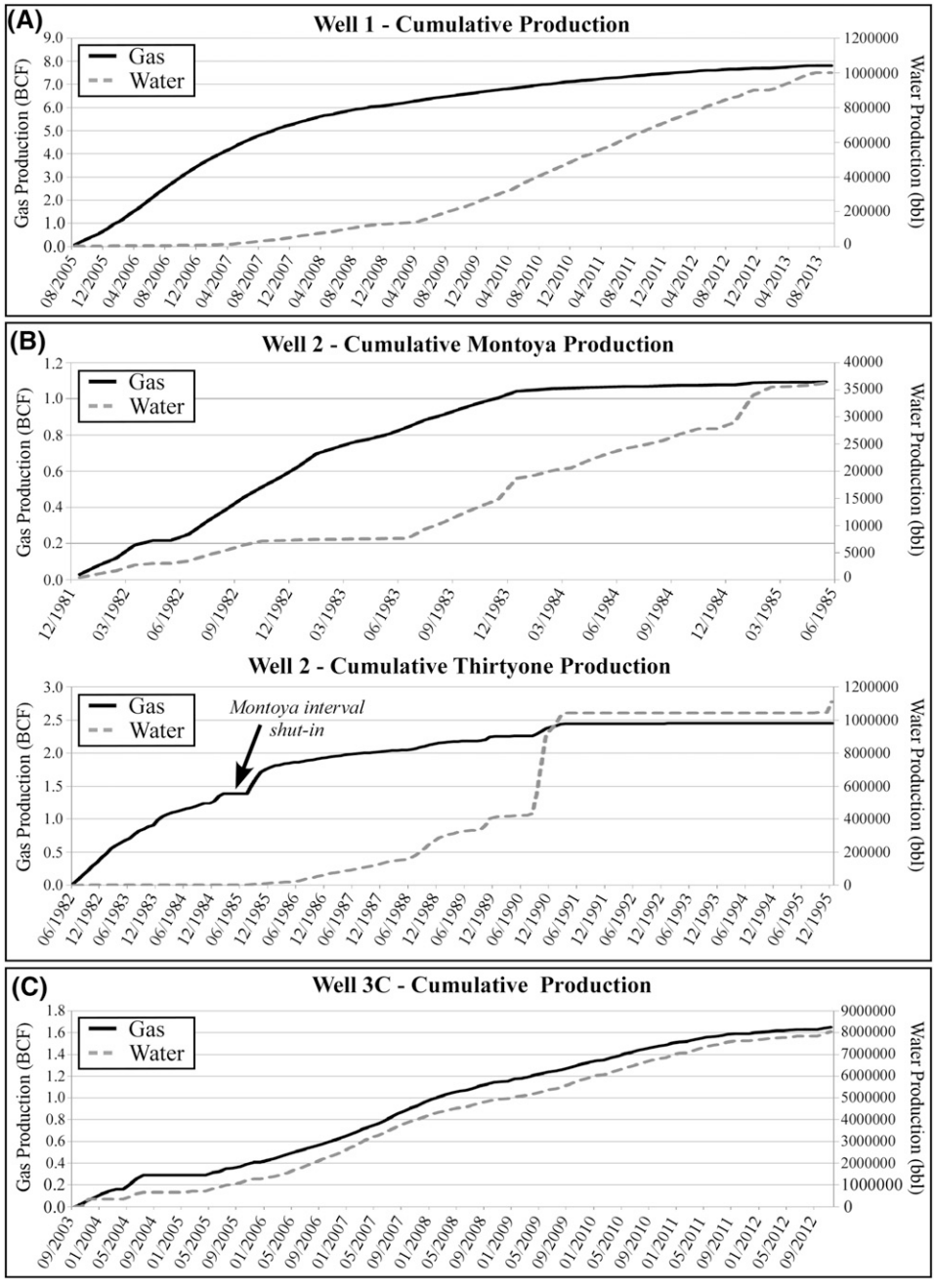

Figure 10. Production data of three different wells across Oates SW field. (A) Well 1 was drilled along the crest of the Elsinore anticline (Figure 3). Cumulative production has approached 8 BCF (~227 MMCM) gas. Water cut had increased through the life of the well. (B) Well 2 is a vertical well in the backlimb of the Saddle anticline that produced approximately 1 BCF (~28.3 MMCM) gas from the Montoya reservoir and greater than 2.5 BCF (~70.8 MMCM) from the Thirtyone reservoir. The spike in Thirtyone production immediately following shut in of the Montoya interval suggests the two reservoirs are in pressure communication. (C) Well 3c is a horizontal well in the backlimb of the Saddle anticline. Production has exceeded 1 BCF (~28.3 MMCM) to date but with a very high water cut throughout the life of the well.

distortional and dilatational strain along the well path (Figure 12A). We suggest that this kink band reflects elevated amounts of strain in this region of the borehole, consistent with the elevated strain predictions from our restorations and the lower semblance in this section of the lateral (Figure 12). This folding may have led to enhanced natural fracturing yielding a pocket of enhanced permeability, likely improving the productivity of the well 1 reservoir, consistent with the 8 BCF (~227 MMCM) of gas production to date (Figure 10).

Figure 12B is the same perspective as Figure 12A but now viewing the well 1 path in the middle third of the lateral, where semblance is relatively higher and both strain measures are near minima. Indeed, neither the Barnett nor Devonian section are folded, indicating that the kink band observed in the outer third of the wellbore is a local feature and does not extend into this region of the lateral. This further supports our interpretation of a structural origin to the strain and semblance trends along the lateral section of well 1. Specifically, we suggest that the kink band in

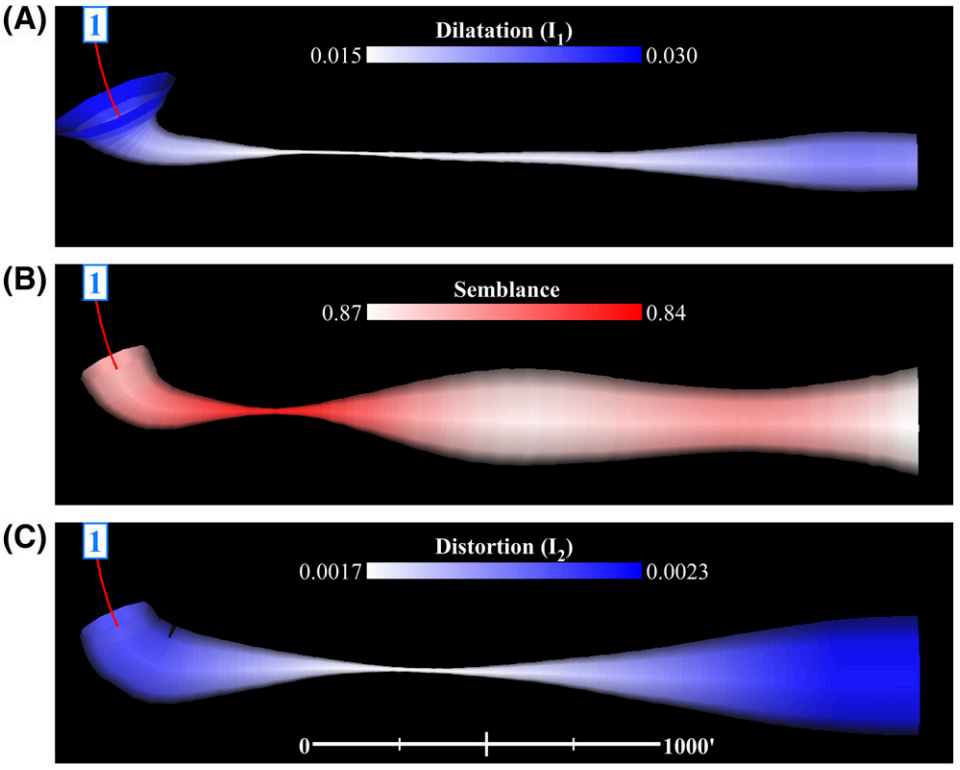

Figure 11. Strain and semblance values along the lateral part of well 1. (A) Dilatation (I_1); (B) semblance; (C) distortion (I_2). The radius of each plot scales with the magnitude of each attribute. To estimate these values along the wellbore, we sample the strain and semblance data at approximately 165-ft (50-m) intervals along the wellbore. At each interval step, the mean values of strain and semblance are calculated within an approximately 325-ft (100-m) spherical radius of the wellbore. 1 = well 1.

Figure 12A is the cause for the increased strain and decreased semblance observed near the toe of the well 1 lateral segment. This result supports the viability of geomechanical restorations to predict subtle strain patterns in fractured reservoirs that may influence reservoir properties.

The vertical extent of the kink band penetrated by well 1 may also shed light on its water production history. Notably, the kink band is limited to the Barnett–base Devonian section and, thus, does not extend far above or below the reservoir. This restricted interval of folding—and corresponding high strain—would presumably limit the vertical extent of any enhanced permeability. Thus, increased water charge from adjacent aquifers would not be expected, which is consistent with the observed water production trends for well 1 (Figure 10). Moreover, structural style is likely a first-order barrier to water incursion. We interpret the Elsinore structure as a fault-propagation fold that soles into the top Ellenburger detachment (Figure 5B). The stratigraphic level of this detachment may effectively shield the underlying water-rich Ellenburger (Loucks, 2008) from the overlying hanging-wall deformation and reservoir. This would limit the vertical flow pathways from the Ellenburger, preventing significant water charge into the Thirtyone reservoir. Together, these three structural interpretations—(1) local fold limbs generating enhanced fracture permeability along the wellbore, (2) folding and enhanced permeability confined to the Barnett–Devonian stratigraphic sections, and (3) the Thirtyone reservoir shielded by the basal detachment from the underlying Ellenberger Formation—provide a viable explanation for the significant gas production and typical water cuts in well 1 of the Oates SW field.

Well 2

Well 2 (Figure 3) is a legacy vertical well drilled in the early 1980s. This well originally produced from the Montoya dolostone, immediately below the Devonian Thirtyone. Shortly after initial production, the operator began production from a second interval in the uppermost Thirtyone using a separate line of production tubing (Figure 10B). Twenty-two months after production commenced from the Thirtyone interval, the Montoya production line was shut in. Immediately following shut in of the Montoya section, there was a temporary surge in production from the Thirtyone production line (Figure 10B), implying vertical

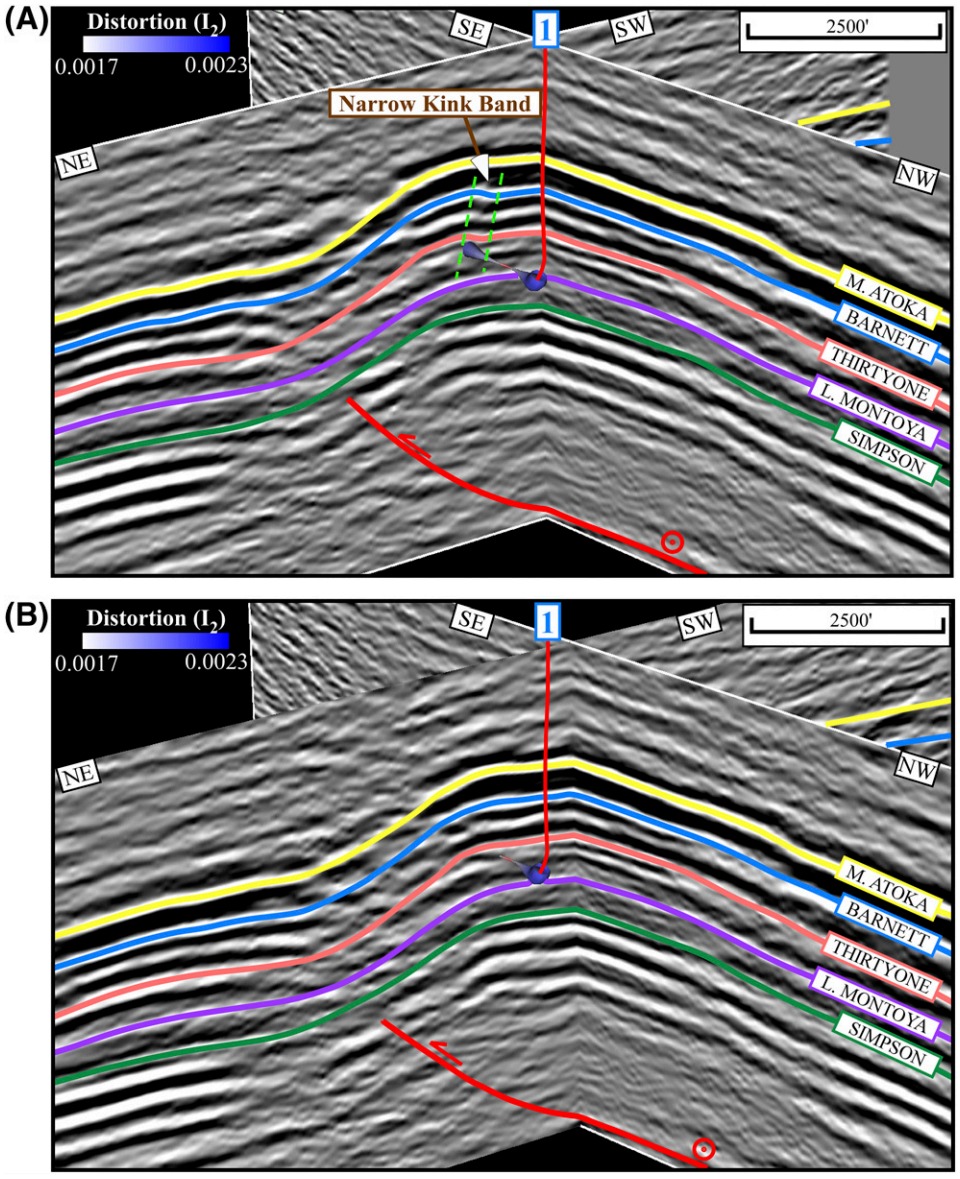

Figure 12. (A) A region of increased strain and decreased semblance in the outer third of well 1 lateral (Figure 11) corresponds to a narrow kink band–imaged in the three-dimensional seismic data–localized within the Barnett–Devonian interval of the Elsinore anticline. (B) In the middle third of the well path–where modeled strain and semblance are relatively lower and higher, respectively (Figure 11)–the narrow kink band in (A) is not present. These observations suggest strains caused by very subtle fold limbs can be resolved by our geomechanical-restoration tool. Vertical exaggeration is 1:1. 1 = well 1; L. = Lower; M. = Middle.

pressure communication between these two reservoirs. In total, well 2 produced in excess of 3.5 BCF (~99.1 MMCM), with a fairly modest water cut.

In Figure 13, we visualize the seismic imaging at the location of well 2, overlain by the calculated semblance. In addition, we display the distortional strain (I_2) predicted by our geomechanical restoration along the vertical wellbore within the Devonian–Montoya interval. Well 2 is drilled in a section of relatively low semblance, likely indicating the presence of secondary structures leading to seismic reflector discontinuities. Indeed, our interpretations of possible secondary faults in the seismic data suggest two or more secondary faults adjacent to well 2 (Figure 13). These faults cause small-scale folding and/or reflector offset observed in the seismic reflection data. We interpret the downward increase in dilatational strain along the well 2 borehole to be consistent with the presence of these secondary faults. We suggest that this interpretation can also explain the observed production history for well 2. In this interpretation, the secondary fault structures increased vertical permeability within the Devonian–Montoya interval around well 2. This facilitated pressure communication between the Montoya and Thirtyone reservoirs, thus explaining the observed Thirtyone production trends. After initial Thirtyone production, this interval began to experience the initial stages of transient-state decline, while production from the Montoya continued (Figure 10B). However, immediately following

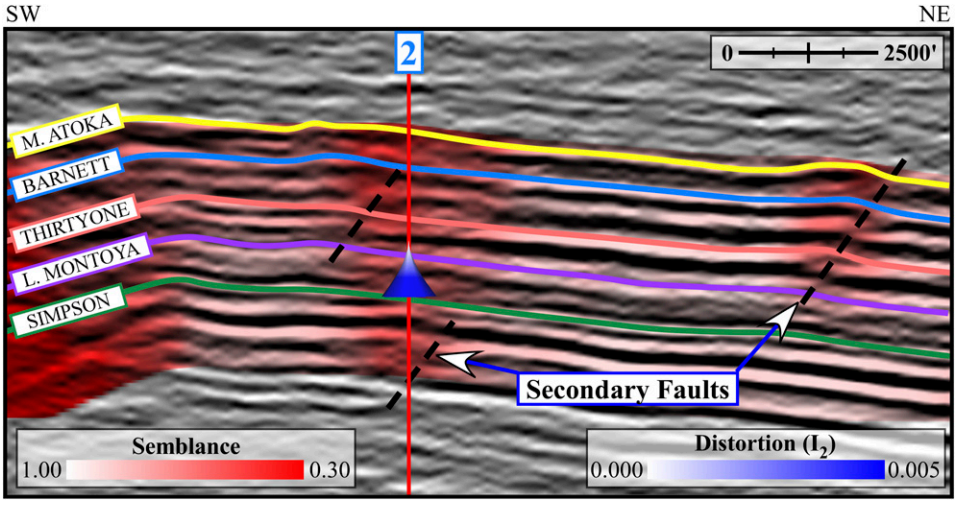

Figure 13. Seismic section through the location of well 2 in the backlimb of the Saddle anticline. Semblance is overlain on the seismic reflector amplitudes. Distortional strain (I_2) is displayed along the well 2 borehole within the Devonian–Montoya section. Well 2 was drilled in a region of decreased semblance, potentially resulting from the presence of secondary faulting. We suggest that these small structures allow Montoya and Thirtyone to be in pressure communication, as indicated by the production spike after Montoya was shut in (Figure 10). Vertical exaggeration is 1:1. 2 = well 2; L. = Lower; M. = Middle.

shut in of the Montoya interval, there was an abrupt spike in Thirtyone production, followed by typical production decline.

Well 3

Well 3 constitutes a suite of three wells drilled in the backlimb of the central Saddle anticline (Figure 3). Well 3a is a legacy vertical borehole that produced from a perforated zone in the uppermost section of the Thirtyone reservoir. Total production included 1.8 BCF (~51.0 MMCM) gas and 160,000 bbl (~25.4 MCM) water. Water cut was initially low and increased during transient-state decline of gas production. Abraxas re-entered this vertical and drilled well 3b, a horizontal well drilled with an east–northeast azimuth (Figure 3). This lateral targeted the Montoya reservoir, immediately below the Thirtyone (Figure 4). An image log of the lateral indicates that the lateral encountered a prominent fracture set in the reservoir. These fractures had a dominant strike of approximately N25°W. Despite this seemingly ideal penetration of a natural fracture set perpendicular to the horizontal section, well 3b experienced extremely low flow rates, totaling 9.0 MMCF (~255 MCM) gas and 32,000 bbl (~5.1 MCM) water during the 10 months of production (Billingsley, 2006). The lack of economic flow rates suggests that the penetrated fracture set did not produce sufficient secondary permeability to aid production. There are several mechanisms by which fractures will not enhance permeability and aid production. For example, under the appropriate stress conditions or in the presence of mechanical heterogeneities, natural fractures may not maintain dilatancy (e.g., Fischer and Jackson, 1999; Laubach et al., 2009). Similarly, open-mode fractures can be cemented soon after rupture depending on the structural fabric of the fracture set or when the rate of crystal growth exceeds the fracture propagation rate (e.g., Gale et al., 2010). It is worth noting that two or more dominant fracture orientations are common in contractional structures (e.g., Bellahsen et al., 2006), which can occur when two principal stresses have similar magnitudes or if stresses of unequal magnitude rotate. If economic flow rates require vertical charge from an adjacent region in this prospect, then perhaps the fracture set encountered by well 3b is confined to the producing reservoir interval, preventing charge and economic recovery (e.g., Odling et al., 1999). Alternatively, one or more additional fracture sets may dominate reservoir permeability and divert fluid flow away from the Montoya reservoir here. An additional fracture set oriented approximately orthogonal to that imaged in well 3b would likely go undetected by the image log.

After shut in of the first lateral, Abraxas drilled well 3c, a horizontal well with a north–northwest azimuth, approximately perpendicular to the azimuth of well 3b. Well 3c produces from the Lower Devonian Thirtyone reservoir, approximately 1650 ft (~500 m) southwest from well 2 but in the same structure (Figure 3). To date, well 3c has produced 1.6 BCF

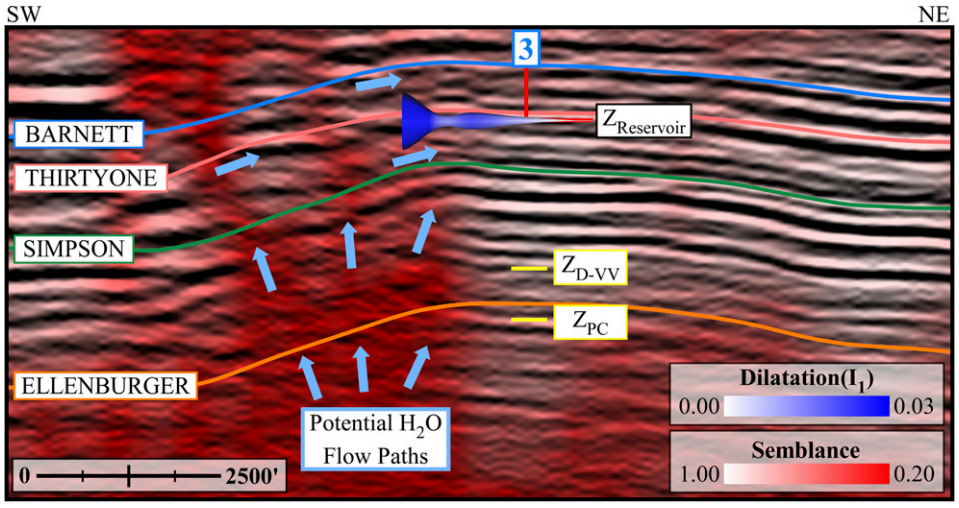

Figure 14. Seismic section through the central Saddle anticline in the vicinity of well 3c. Semblance is overlain on the seismic reflector amplitudes. Dilatation (I_1) is displayed along the well 3c borehole. We extend the display of I_1 from the heel of the lateral section to the anticlinal crest. Measured water temperatures at the wellhead suggest water produced from this location of the Thirtyone reservoir originates from the Ellenburger Group. We suggest that high strains developed during anticlinal fault-bend folding of the central Saddle anticline formed vertical fault or fracture networks, which facilitate water incursion from the Ellenburger Group water up the anticlinal crest of the central Saddle structure into the Thirtyone reservoir (e.g., Figures 7, 8). Z_{D-VV} and Z_{PC} are calculated depths from temperature–depth data from wells located in Delaware–Val Verde Basin and Pecos County, respectively. Vertical exaggeration is 1:1. 3 = well 3.

(45.3 MMCM) gas, approximately 64% of the production from the Thirtyone production line of well 2 (Figure 10C). However, well 3c has produced 640% more water than the Thirtyone production line of well 2 (Figure 10C).

Figure 14 presents the extracted dilatation along the well 3c lateral section and a cross section across the central Saddle fold. Strain is quite low along the entire borehole and around the region of the lateral away from the fold crest (Figure 7). However, the strain and semblance patterns indicate a distinct zone of elevated strain and low semblance that is concentrated just beyond the heel of the lateral, within the forelimb of the central Saddle anticlinal fault-bend fold (Figures 7, 8, 14). This zone of high strain is vertically continuous within the forelimb fold, extending through the Devonian reservoir into the underlying formations, including the Ellenberger (Figure 14). We speculate that the presence of vertical permeability associated with this highly strained zone near well 3c may have facilitated water incursion from the Ellenburger Group, an abundant water source in the Permian Basin (Loucks, 2008). In this interpretation, vertical flow paths from the Ellenburger to shallower sections are responsible for the elevated water cut in well 3c relative to other wells in the field (Figure 10).

To evaluate this prospect of water incursion from the Ellenburger, we examine the water temperature encountered in well 3c to infer its origin depth. The depth of the well 3c lateral is approximately 13,390 ft (~4080 m). Initial production from well 3c recorded water temperature at the wellhead to be 198°F (92.2°C). The geothermal gradient has been modeled using temperature data from thousands of industry wells for the Delaware–Val Verde Basin region as

$$Z_{D-VV} = 3200.9 \times \ln(T) - 10,461 \qquad (1)$$

where Z is depth in meters, and T is temperature in degrees Celsius (Erdlac, 2006). Using wells only in Pecos County (Figure 2), the modeled geothermal gradient is

$$Z_{PC} = 3399.9 \times \ln(T) - 11,198 \qquad (2)$$

(Erdlac, 2006). These temperature gradients suggest that the initial water production corresponds to depths of 13,200 ft (~4025 m) and 13,725 ft (~4185 m), respectively, consistent with the depth of well 3c (Figure 14). Thus, we conclude that the initial coproduced water originated from the Thirtyone reservoir. However, coproduced water temperature started to exceed this initial temperature soon after initial production, with a maximum measured temperature of 238°F (114°C) at the wellhead. From the regional and county-specific geothermal gradients, this maximum temperature corresponds to aquifer depths of 15,450 ft (~4710 m) and 16,130 ft (4920 m), respectively. These depths correspond to the lower

Simpson or uppermost Ellenburger (Figure 14). However, this water was likely sourced deeper than suggested by our basic temperature analysis, as we have not corrected for cooling effects associated with decompression and diffusion during open-hole production from the well 3c lateral to the wellhead. This would place the water source fully within the Ellenberger Formation. Our temperature analysis—in addition to the intense water production observed throughout the history of well 3c (Figure 10)—suggests that there is an effective charge pathway between the Devonian and Ellenburger sections. Our geomechanical restorations define a vertically continuous zone of high strain adjacent to the well that we interpret to correspond to potential charge pathways for water incursion (Figures 8, 13). The thrust ramp below the central Saddle anticline and within the Ellenberger Formation may also contribute to water-charge pathways. In contrast, faulting and related folding within the Elsinore anticline do not extend into the Ellenberger section. Thus, wells within the Elsinore structure—including well 1—generally have lower water cuts.

CONCLUSIONS

1. The prominent structural traps in the Oates SW field, Pecos County, Texas, are characterized as basement-involved anticlinal fault-bend folds and fault-propagation folds. The top Ellenburger serves as a regional detachment surface for these structures. Timing of structural growth appears to be soon after the Middle Pennsylvanian, and the fault-bend folds appear to have developed in a break-forward thrusting sequence.
2. The 3-D geomechanical-restoration tool used in this study accurately predicts strain patterns across the Lower Devonian Thirtyone reservoir in the Oates SW field. These geomechanical restorations accurately describe strain patterns over a range of scales, including trap-scale features as well as smaller, secondary faults and kink bands. It is especially encouraging that such subtle strains are predicted without explicitly representing these secondary structures in the structural models.
3. Model II regressions validate strain–semblance correlations and suggest that geophysical attributes and restoration strains can be used effectively to describe reservoir properties.
4. We document how strain predictions from our restoration tool accurately describe several production trends in the Oates SW field, including variations in gas production, water cut, and reservoir fluid temperatures. This illustrates the ability of geomechanical restorations to accurately predict tectonic strains in deformed reservoirs, which can be used to drive development decisions and potentially inform operators of reservoir properties in advance of field development.

Care should be taken in the application of these methods to reservoir characterization studies, given the current limitations of the constitutive relations used by the restoration tool and the uncertainties associated with defining the appropriate reservoir properties and boundary conditions. Nevertheless, this case study illustrates that by testing a range of material properties and geologically constrained boundary conditions, in addition to objective comparisons of restoration strains with independent strain attributes (e.g., geophysical attributes; well data), robust correlations between restoration strains and reservoir properties can be established. Such relationships provide a valuable tool that can help forecast reservoir properties in ways that help explain well performance and can be used in reservoir simulations to optimize field development.

APPENDIX 1

The 3-D seismic volume across Oates SW does not resolve any reflectors within the Ellenburger or older section that can be mapped across the field. Thus, we are unable to incorporate direct hanging-wall and footwall cutoffs to serve as boundary conditions for the restorations. Without these fault-displacement constraints, the datum boundary condition and strain minimization technique of the geomechanical-restoration tool generally produce a restored hanging wall that flattens in all directions. Clearly, such results are not physically reasonable.

To resolve this issue, we offset the downdip boundary wall by the amount of slip that likely occurred along the thrust ramp to produce the observed anticlinal fault-bend fold. To do this, we first measure total slip on the upper detachment (S_1) from the width of the anticlinal forelimb fold (Suppe, 1983). We calculate this at all points along strike from our 3-D structural model to obtain $S_1(x,y)$. Fault-bend–folding theory predicts fault slip along the thrust ramp (S_0) to be consumed during anticlinal fold development when the angle between hanging-wall strata and

the thrust ramp (i.e., θ) is nonzero (Suppe, 1983). Thus, we infer that $R(x,y) < 1$, where $R = S_1/S_0$ (Suppe, 1983), for the interpreted fault-bend folds (Figure 5A). Following fault-bend–fold theory, we use measures of fault and anticlinal fold geometries with measures of $S_1(x,y)$ to calculate $R(x,y)$ and, in turn, $S_0(x,y)$ for each fault-bend fold. To implement this constraint in the restorations, we offset the downdip boundary wall by $S_0(x,y)$ (e.g., Figure 6B). This allows us to prescribe a fault offset boundary condition, even in the absence of cutoffs, and obtain a geologically reasonable restoration result.

APPENDIX 2

Our extensive testing with the restoration tool used in this study has found that—all other variables being equal (e.g., boundary conditions)—material-property contrasts can significantly affect restoration results, but the absolute magnitudes of these properties within reasonable limits have little effect on the restoration outcomes. To determine what material properties to use in the strain analysis of our restorations, we tested the 32 unique combinations (2^5) of material-property definitions on each of the 4 structural models, yielding 128 geomechanical restorations (e.g., Figures 1, 6). For each restored model, we assessed the residual structural relief and modeled strain distributions along the top Devonian to determine whether the defined material-property contrasts generated a geologically reasonable restoration. If a combination of material properties yielded a reasonable result for all four structural domains, we treated that combination of material properties as viable for our modeling purposes. Our analysis found that models with rigid Barnett and Devonian layers yielded the least amount of residual structural relief across the top Thirtyone surface. We suggest that this occurs because the layers are sufficiently rigid to transmit the applied forces on the top Atoka to the top Thirtyone surface. Thus, these models were able to most effectively restore the structural relief across the Thirtyone reservoir. Of these seven models, we assessed the modeled strain distributions across the Devonian layer at approximately 164-ft (50-m) vertical intervals. We anticipated strains to be localized in the anticlinal forelimbs, with lower-magnitude strains in the broad, gentle back limbs. Moreover, we sought models that produced negative restoration dilatation in the fold crest and positive restoration dilatation in the fold limbs (e.g., Figure 1D). This strain distribution is consistent with numerous mechanical forward models of fault-related folds (e.g., Gregg Erickson and Jamison, 1995; Cooke and Pollard, 1997; Strayer and Hudleston, 1997; Strayer et al., 2004; Bellahsen et al., 2006; Benesh, 2010; Hughes et al., 2014). Two of the remaining material-property definitions passed this strain assessment in all four structural models. These two models differ only by the strength of Atoka. We continued our analysis with rigid Atoka models, because the strain distributions of the two remaining material-property combinations were nearly identical, and the difference in residual structural relief across the top Thirtyone surface was, at most, 2.7 ft (0.8 m) for each of the four models.

APPENDIX 3

Gradients in the restoration velocity field of each restoration yield the full strain tensor at all nodes of each volumetric mesh:

$$\begin{bmatrix} \varepsilon_{11} & \varepsilon_{12} & \varepsilon_{13} \\ \varepsilon_{12} & \varepsilon_{22} & \varepsilon_{23} \\ \varepsilon_{13} & \varepsilon_{23} & \varepsilon_{33} \end{bmatrix}$$

We express each tensor solely as a function of its eigenvalues (ε_i), avoiding off-diagonal components of the strain tensor:

$$\begin{bmatrix} \varepsilon_1 & 0 & 0 \\ 0 & \varepsilon_2 & 0 \\ 0 & 0 & \varepsilon_3 \end{bmatrix}$$

From this, we calculate the first invariant of the strain tensor (I_1)—dilatation—at all nodes of a volumetric mesh:

$$I_1 = \varepsilon_1 + \varepsilon_2 + \varepsilon_3$$

To calculate the second invariant of the strain tensor (I_2)—distortion—we first generate the deviatoric strain tensor by subtracting the mean strain (ε_m) from the diagonal components of the strain tensor:

$$\begin{bmatrix} \varepsilon_1 - \varepsilon_m & 0 & 0 \\ 0 & \varepsilon_2 - \varepsilon_m & 0 \\ 0 & 0 & \varepsilon_3 - \varepsilon_m \end{bmatrix}$$

where

$$\varepsilon_m = (\varepsilon_1 + \varepsilon_2 + \varepsilon_3)/3$$

From this expression, we calculate I_2 at every node of a volumetric mesh:

$$I_2 = (\varepsilon_1 - \varepsilon_m)(\varepsilon_2 - \varepsilon_m) + (\varepsilon_1 - \varepsilon_m)(\varepsilon_3 - \varepsilon_m) + (\varepsilon_2 - \varepsilon_m)(\varepsilon_3 - \varepsilon_m)$$

We are able to discriminate between volume increases or decreases (e.g., Figure 1D) and, similarly, the relative orientations of distortion using the signs of calculated strain invariants. The signs of strain are particularly helpful where we attempt to validate a restoration result (see Appendix 2). However, as we generate linear regressions between strain, a signed attribute, and semblance, a parameter defined between zero and one, we use the absolute values of strain for our correlation analysis in the Strain Distributions section (Figure 9).

REFERENCES CITED

Allmendinger, R. W., 1998, Inverse and forward numerical modeling of trishear fault-propagation folds: Tectonics, v. 17, p. 640–656,doi:10.1029/98TC01907.

Aydin, A., 2000, Fractures, faults, and hydrocarbon entrapment, migration and flow: Marine and Petroleum Geology, v. 17, no. 7, p. 797–814,doi:10.1016/S0264-8172(00)00020-9.

Bahorich, M., and S. Farmer, 1995, 3-D seismic discontinuity for faults and stratigraphic features: The coherence cube:

Leading Edge, v. 14, no. 10, p. 1053–1058, doi:10.1190/1.1437077.
Bellahsen, N., P. E. Fiore, and D. D. Pollard, 2006, From spatial variation of fracture patterns to fold kinematics: A geomechanical approach: Geophysical Research Letters, v. 33, no. 2, p. L02301, doi:10.1029/2005GL024189.
Benesh, N. P., 2010, The mechanics of fault-bend folding and tear-fault systems in the Niger Delta, Ph.D. thesis, Harvard University, Cambridge, Massachusetts, 109 p.
Benesh, N. P., A. Plesch, and J. H. Shaw, 2014, Geometry, kinematics, and displacement characteristics of tear-fault systems: An example from the deep-water Niger Delta: AAPG Bulletin, v. 98, no. 3, p. 465–482,doi:10.1306/06251311013.
Billingsley, L., 2006, Exploiting the Devonian reservoir in Oates SW area, Western Delaware Basin, Texas (abs.): Houston Geological Society Bulletin, v. 49, no. 4, p. 41.
Bowker, K. A., 2007, Barnett shale gas production, Fort Worth Basin: Issues and discussion: AAPG Bulletin, v. 91, no. 4, p. 523–533,doi:10.1306/06190606018.
Chauvin, B., A. Mazuyer, and G. Caumon, 2015, Mechanics-based restoration: A physical and mathematical review, *in* Proceedings of the 35th Gocad Meeting–Research for Integrative Numerical Geology Meeting: Nancy, France, Association Scientifique pour la Geologie et ses Applications, 34 p.
Chopra, S., and K. J. Marfurt, 2010, Integration of coherence and volumetric curvature images: Leading Edge, v. 29, no. 9, p. 1092–1107, doi:10.1190/1.3485770.
Cooke, M. L., and D. D. Pollard, 1997, Bedding-plane slip in initial stages of fault-related folding: Journal of Structural Geology, v. 19, no. 3–4, p. 567–581, doi:10.1016/S0191-8141(96)00097-1.
Dahlen, F. A., and T. D. Barr, 1989, Brittle frictional mountain building: 1. Deformation and mechanical energy budget: Journal of Geophysical Research Solid Earth, v. 94, no. B4, p. 3906–3922, doi:10.1029/JB094iB04p03906.
Dahlstrom, C. D. A., 1969, Balanced cross sections: Canadian Journal of Earth Sciences, v. 6, p. 743–757, doi:10.1139/e69-069.
Dickinson, W. R., and W. S. Snyder, 1978, Plate tectonics of the Laramide orogeny, *in* V. Matthews III, ed., Laramide folding associated with basement block faulting in the Western United States: Boulder, Colorado, Geological Society of America Memoir 151, p. 355–366.
Durand-Riard, P., L. Salles, M. Ford, G. Caumon, and J. Pellerin, 2011, Understanding the evolution of syn-depositional folds: Coupling decompaction and 3D sequential restoration: Marine and Petroleum Geology, v. 28, no. 8, p. 1530–1539, doi:10.1016/j.marpetgeo.2011.04.001.
Durand-Riard, P., J. H. Shaw, A. Plesch, and G. Lufadeju, 2013, Enabling 3D geomechanical restoration of strike- and oblique-slip faults using geological constraints, with applications to the deep-water Niger Delta: Journal of Structural Geology, v. 48, p. 33–44, doi:10.1016/j.jsg.2012.12.009.
Egan, S. S., S. Kane, T. S. Buddin, G. D. Williams, and D. Hodgetts, 1999, Computer modelling and visualisation of the structural deformation caused by movement along geological faults: Computers & Geosciences, v. 25, no. 3, p. 283–297, doi:10.1016/S0098-3004(98)00125-3.
Engelder, T., G. G. Lash, and R. S. Uzcátegui, 2009, Joint sets that enhance production from Middle and Upper Devonian gas shales of the Appalachian Basin: AAPG Bulletin, v. 93, no. 7, p. 857–889,doi:10.1306/03230908032.
Erdlac, R. J. Jr., 2006, A resource assessment of geothermal energy resources for converting deep gas wells in carbonate strata into geothermal extraction wells: A Permian Basin evaluation (year 1 progress report): US Department of Energy Report DE-FG36-05GO85023, 113 p.
Erickson, S. G., 1996, Influence of mechanical stratigraphy on folding versus faulting: Journal of Structural Geology, v. 18, no. 4, p. 443–450, doi:10.1016/0191-8141(95)00064-K.
Fischer, M. P., and J. B. Jackson, 1999, Stratigraphic controls on deformation patterns in fault-related folds: A detachment fold example from the Sierra Madre Oriental, northeast Mexico: Journal of Structural Geology, v. 21, no. 6, p. 613–633, doi:10.1016/S0191-8141(99)00044-9.
Frankowicz, E., and K. R. McClay, 2010, Extensional fault segmentation and linkages, Bonaparte Basin, outer North west shelf, Australia: AAPG Bulletin, v. 94, no. 7, p. 977–1010, doi:10.1306/01051009120.
Frenzel, H. N., R. R. Bloomer, R. B. Cline, J. M. Cys, J. E. Galley, W. R. Gibson, J. M. Hills, et al., 1988, The Permian basin region, *in* L. L. Sloss, ed., The geology of North America, v. D-2: Sedimentary cover—North American craton: U.S.: Boulder, Colorado, Geological Society of America, p. 261–306.
Gale, J. F., R. H. Lander, R. M. Reed, and S. E. Laubach, 2010, Modeling fracture porosity evolution in dolostone: Journal of Structural Geology, v. 32, no. 9, p. 1201–1211, doi:10.1016/j.jsg.2009.04.018.
Gale, J. F. W., S. E. Laubach, J. E. Olson, P. Eichhubl, and A. Fall, 2014, Natural fractures in shale: A review and new observations: AAPG Bulletin, v. 98, no. 11, p. 2165–2216, doi:10.1306/08121413151.
Ghosh, K., and S. Mitra, 2009, Two-dimensional simulation of controls of fracture parameters on fracture connectivity: AAPG Bulletin, v. 93, no. 11, p. 1517–1533,doi:10.1306/07270909041.
Gregg Erickson, S., and W. R. Jamison, 1995, Viscous-plastic finite-element models of fault-bend folds: Journal of Structural Geology, v. 17, no. 4, p. 561–573, doi:10.1016/0191-8141(94)00082-B.
Griffiths, P., S. Jones, N. Salter, F. Schaefer, R. Osfield, and H. Reiser, 2002, A new technique for 3-D flexural-slip restoration: Journal of Structural Geology, v. 24, no. 4, p. 773–782, doi:10.1016/S0191-8141(01)00124-9.
Guzofski, C., J. Mueller, J. H. Shaw, P. Muron, D. Medwedeff, F. Bilotti, and C. Rivero, 2009, Insights into the mechanisms of fault-related folding provided by volumetric structural restorations using spatially varying mechanical constraints: AAPG Bulletin, v. 93, no. 4, p. 479–502, doi:10.1306/11250807130.
Hennings, P. H., J. E. Olson, and L. B. Thompson, 2000, Combining outcrop data and three-dimensional structural models to characterize fractured reservoirs: An example from Wyoming: AAPG Bulletin, v. 84, no. 6, p. 830–849.

Hills, J. M., 1985, Structural evolution of the Permian basin of west Texas and New Mexico, in P. W. Dickerson and W. R. Muehlberger, eds., Structure and tectonics of trans-pecos Texas: Midland, Texas, West Texas Geological Society Publication 85-81, p. 89–99.

Hughes, A. N., N. P. Benesh, and J. H. Shaw, 2014, Factors that control the development of fault-bend versus fault-propagation folds: Insights from mechanical models based on the discrete element method (DEM): Journal of Structural Geology, v. 68, p. 121–141, doi:10.1016/j.jsg.2014.09.009.

Laubach, S. E., J. E. Olson, and M. R. Gross, 2009, Mechanical and fracture stratigraphy: AAPG Bulletin, v. 93, no. 11, p. 1413–1426,doi:10.1306/07270909094.

Lorenz, J. C., and S. J. Finley, 1989, Differences in fracture characteristics and related production: Mesaverde Formation, Northwestern Colorado: SPE Formation Evaluation, v. 4, no. 1, p. 11–16, doi:10.2118/16809-PA.

Loucks, R. G., 2008, Review of the lower Ordovician Ellenburger group of the Permian basin, West Texas, accessed January 3, 2016, http://www.beg.utexas.edu/resprog/permianbasin/PBGSP_members/writ_synth/Ellenburger%20report.pdf.

Lovely, P., E. Flodin, C. Guzofski, F. Maerten, and D. D. Pollard, 2012, Pitfalls among the promises of mechanics-based restoration: Addressing implications of unphysical boundary conditions: Journal of Structural Geology, v. 41, p. 47–63, doi:10.1016/j.jsg.2012.02.020.

Maerten, L., and F. Maerten, 2006, Chronologic modeling of faulted and fractured reservoirs using geomechanically based restoration: Technique and industry applications: AAPG Bulletin, v. 90, no. 8, p. 1201–1226, doi:10.1306/02240605116.

Mallet, J. L., 1992, GOCAD: A computer aided design program for geological applications, *in* T. A. Keith, ed., Three-dimensional modeling with geoscientific information systems: Dordrecht, The Netherlands, Springer, p. 123–141, doi:10.1007/978-94-011-2556-7_11.

Marfurt, K. J., R. L. Kirlin, S. L. Farmer, and M. S. Bahorich, 1998, 3-D seismic attributes using a semblance-based coherency algorithm: Geophysics, v. 63, no. 4, p. 1150–1165, doi:10.1190/1.1444415.

Montgomery, S. L., 1998, Thirtyone formation, permian basin, Texas: Structural and lithologic heterogeneity in a Lower Devonian chert reservoir: AAPG Bulletin, v. 82, no. 1, p. 1–24.

Moretti, I., F. Lepage, and M. Guiton, 2006, Kine3D: A new 3D restoration method based on a mixed approach linking geometry and geomechanics: Oil & Gas Science and Technology, v. 61, no. 2, p. 277–289, doi:10.2516/ogst:2006021.

Morgan, J. K., 2015, Effects of cohesion on the structural and mechanical evolution of fold and thrust belts and contractional wedges: Discrete element simulations: Journal of Geophysical Research. Solid Earth, v. 120, p. 3870–3896, doi:10.1002/2014JB011455.

Muron, P., 2005, Méthodes numériques 3D de restauration des structures géologiques faillées, Ph.D. dissertation, Institut Polytechnique National de Lorraine, Nancy, France, 145 p.

Muron, P., and J.-L. Mallet, 2004, 3-D balanced unfolding and rock properties, *in* Proceedings of the 24th Gocad Meeting: Nancy, France, Association Scientifique pour la Geologie et ses Applications, 16 p.

Odling, N. E., P. Gillespie, B. Bourgine, C. Castaing, J. P. Chiles, N. P. Christensen, E. Fillion, et al., 1999, Variations in fracture system geometry and their implications for fluid flow in fractured hydrocarbon reservoirs: Petroleum Geoscience, v. 5, no. 4, p. 373–384, doi:10.1144/petgeo.5.4.373.

Plesch, A., J. H. Shaw, and D. Kronman, 2007, Mechanics of low-relief detachment folding in the Bajiaochang field, Sichuan basin, China: AAPG Bulletin, v. 91, no. 11, p. 1559–1575, doi:10.1306/06200706072.

Pope, M. C., 2014, High-resolution sequence stratigraphy of the Upper Ordovician Montoya Group, southern New Mexico and western Texas: Outcrop analog of an unconventional chert and carbonate reservoir: AAPG Bulletin, v. 98, no. 8, p. 1577–1597, doi:10.1306/10151312177.

Rayner, J. M., 1985, Linear relations in biomechanics: The statistics of scaling functions: Journal of Zoology, v. 206, no. 3, p. 415–439, doi:10.1111/j.1469-7998.1985.tb05668.x.

Rouby, D., H. Xiao, and J. Suppe, 2000, 3-D restoration of complexly folded and faulted surfaces using multiple unfolding mechanisms: AAPG Bulletin, v. 84, no. 6, p. 805–829.

Ruppel, S. C., and R. J. Barnaby, 2001, Contrasting styles of reservoir development in proximal and distal chert facies: Devonian Thirtyone Formation, Texas: AAPG Bulletin, v. 85, no. 1, p. 7–33.

Ruppel, S. C., and S. D. Hovorka, 1995, Controls on reservoir development in Devonian chert, Permian Basin, Texas: AAPG Bulletin, v. 79, no. 12, p. 1757–1785.

Saller, A., B. Ball, S. Robertson, B. McPherson, C. Wene, R. Nims, and J. Gogas, 2001, Reservoir characteristics of Devonian cherts and their control on oil recovery: Dollarhide field, west Texas: AAPG Bulletin, v. 85, no. 1, p. 35–50.

Shackleton, J. R., and M. L. Cooke, 2007, Is plane strain a valid assumption in non-cylindrical fault-cored folds?: Journal of Structural Geology, v. 29, no. 7, p. 1229–1240, doi:10.1016/j.jsg.2007.03.011.

Shaw, J. H., F. Bilotti, and P. A. Brennan, 1999, Patterns of imbricate thrusting: Geological Society of America Bulletin, v. 111, no. 8, p. 1140–1154, doi:10.1130/0016-7606(1999)111<1140:POIT>2.3.CO;2.

Shaw, J. H., C. Connors, and J. Suppe, 2005, Seismic interpretation of contractional fault-related folds: An AAPG seismic atlas: AAPG Studies in Geology 53, 156 p.

Shokair, K. M., A. Plesch, and J. H. Shaw, 2009, 3D structural restoration approach for fracture prediction—A case study from Kingdom of Saudi Arabia (abs.): AAPG International Conference and Exhibition, Rio de Janeiro, Brazil, November 15–18, 2009, accessed July 24, 2014, http://www.searchanddiscovery.com/abstracts/html/2009/intl/abstracts/shokair.htm.

Shumaker, R. C., 1992, Paleozoic structure of the central basin uplift and adjacent Delaware Basin, West Texas: AAPG Bulletin, v. 76, no. 11, p. 1804–1824.

Strayer, L. M., S. G. Erickson, and J. Suppe, 2004, Influence of growth strata on the evolution of fault-related folds—Distinct-element models, *in* K. R. McClay, ed., Thrust tectonics and hydrocarbon systems: AAPG Memoir 82, p. 413–437.

Strayer, L., and P. Hudleston, 1997, Numerical modeling of fold initiation at thrust ramps: Journal of Structural Geology, v. 19, p. 551–566,doi:10.1016/S0191-8141(96)00109-5.

Suhm, R. W., and R. L. Ethington, 1975, Stratigraphy and conodonts of Simpson Group (Middle Ordovician), Beach and Baylor Mountains, West Texas: AAPG Bulletin, v. 59, no. 7, p. 1126–1135.

Suppe, J., 1983, Geometry and kinematics of fault-bend folding: American Journal of Science, v. 283, p. 684–721, doi:10.2475/ajs.283.7.684.

Suppe, J., and D. A. Medwedeff, 1990, Geometry and kinematics of fault-propagation folding: Eclogae Geologicae Helvetiae, v. 83, no. 3, p. 409–454.

Vidal-Royo, O., N. Cardozo, J. A. Muñoz, S. Hardy, and L. Maerten, 2012, Multiple mechanisms driving detachment folding as deduced from 3d reconstruction and geomechanical restoration: The Pico del Águila anticline (External Sierras, Southern Pyrenees): Basin Research, v. 23, p. 1–19.

E&P NOTES

Play analysis and leading-edge oil-reservoir development methods in the Permian basin: Increased recovery through advanced technologies

Shirley P. Dutton, Eugene M. Kim, Ronald F. Broadhead, William D. Raatz, Caroline L. Breton, Stephen C. Ruppel, and Charles Kerans

ABSTRACT

The Permian basin of west Texas and southeast New Mexico remains an important oil-producing province, accounting for 17% of United States production (327 million bbl) in 2002. With a resource base of such size, increased understanding of reservoir geology and improved use of enhanced-recovery practices in the basin can have a substantial impact on United States oil production. Thirty-two oil plays covering both the Texas and New Mexico portions of the Permian basin were defined on the basis of reservoir stratigraphy, lithology, depositional environment, and structural and tectonic setting. One thousand three hundred and thirty-nine significant-sized reservoirs (cumulative production of >1 million bbl [1.59×10^5 m^3] of oil through 2000) were assigned to a geologic play. Cumulative production from these reservoirs was 28.9 billion bbl (4.59×10^9 m^3), or 95% of the basin's total. Examples of successful reservoir-development practices are listed by play because methods demonstrated to work well in one reservoir should be applicable to other reservoirs in the play.

The Permian basin is dominantly a carbonate province. Carbonate reservoirs account for 75% of total oil production; clastics, 14%; mixed clastics and carbonates, 8%; and chert, 3%. The plays having the largest cumulative production are the Northwest shelf San Andres platform carbonate play (4.0 billion bbl; 6.31×10^8 m^3), the Leonard restricted platform carbonate play (3.3 billion bbl; 5.25×10^8 m^3), the Pennsylvanian and Lower Permian Horseshoe atoll carbonate play

Copyright ©2005. The American Association of Petroleum Geologists. All rights reserved.

Manuscript received September 10, 2004; provisional acceptance November 3, 2004; revised manuscript received December 3, 2004; final acceptance December 7, 2004.
DOI:10.1306/12070404093

AUTHORS

SHIRLEY P. DUTTON ~ *Bureau of Economic Geology, Jackson School of Geosciences, University of Texas at Austin, Austin, Texas 78713-8924; shirley.dutton@beg.utexas.edu*

Shirley Dutton is a senior research scientist at the Bureau of Economic Geology with research interests in sedimentology, reservoir characterization, sedimentary petrology, and clastic diagenesis. She received a B.A. degree from the University of Rochester and an M.A. degree and a Ph.D. from the University of Texas at Austin, all in geology. She has been an AAPG Distinguished Lecturer.

EUGENE M. KIM ~ *Bureau of Economic Geology, Jackson School of Geosciences, University of Texas at Austin, Austin, Texas 78713-8924; present address: Wood Mackenzie, 5847 San Felipe, Suite 100, Houston, 77057; eugene.kim@woodmac.com*

Eugene Kim is a specialist on North America gas supply. Prior to joining Wood Mackenzie, he was a research associate at the Bureau of Economic Geology, involved in play analysis, resource assessment, and reserve evaluation. He holds a B.S.E. degree in mineral and petroleum engineering from Seoul National University and an M.A. degree in energy and mineral resources and a Ph.D. in geological sciences, both from the University of Texas at Austin.

RONALD F. BROADHEAD ~ *New Mexico Bureau of Geology and Mineral Resources, New Mexico Institute of Mining and Technology, Socorro, New Mexico 87801-4681; ron@gis.nmt.edu*

Ron Broadhead received his B.S. degree in geology from the New Mexico Institute of Mining and Technology and his M.S. degree in geology from the University of Cincinnati. He worked for Cities Service Company in Oklahoma and has been with the New Mexico Bureau of Geology and Mineral Resources at the New Mexico Institute of Mining and Technology since 1981, where he is currently a principal petroleum geologist and adjunct faculty.

WILLIAM D. RAATZ ~ *New Mexico Bureau of Geology and Mineral Resources, New Mexico Institute of Mining and Technology, Socorro, New Mexico 87801-4681; present address: Oxy Permian, 5 Greenway Plaza, Houston, Texas 77046; bill_raatz@oxy.com*

Bill Raatz is a Permian basin sequence stratigrapher. Formerly, he worked on international exploration and Alaska development with Arco and Phillips and worked as a researcher and adjunct faculty with the New Mexico Bureau of Geology and Mineral Resources and the New Mexico Institute of Mining and Technology. He received his Ph.D. from the University of Wisconsin and his M.S. and B.S. degrees from the University of Iowa, and he now serves on the AAPG Grants-in-Aid Committee.

CAROLINE L. BRETON ~ *Bureau of Economic Geology, Jackson School of Geosciences, University of Texas at Austin, Austin, Texas 78713-8924; cari.breton@beg.utexas.edu*

Caroline Breton is currently working as a research associate at the Bureau of Economic Geology, University of Texas at Austin. She graduated with a B.A. degree in geography from the University of Texas at Austin in 2000. Her research interests include Geographic Information Systems and cartography.

STEPHEN C. RUPPEL ~ *Bureau of Economic Geology, Jackson School of Geosciences, University of Texas at Austin, Austin, Texas 78713-8924; stephen.ruppel@beg.utexas.edu*

Steve Ruppel is a senior research scientist at the Bureau of Economic Geology at the University of Texas at Austin, where he specializes in the characterization of Paleozoic carbonate-reservoir successions. His current research is focused on identifying the stratigraphic and diagenetic controls of reservoir development in outcropping and subsurface Permian carbonates in the Permian basin.

CHARLES KERANS ~ *Bureau of Economic Geology, Jackson School of Geosciences, University of Texas at Austin, Austin, Texas 78713-8924*

Charles Kerans has been a senior research scientist at the Bureau of Economic Geology, the University of Texas at Austin, since 1985. His research emphasis is on the construction of sequence-stratigraphic frameworks for carbonate-reservoir characterization. He has been an AAPG Distinguished Lecturer and has won seven awards for best paper, including those from the Permian Basin Section–SEPM and the West Texas Geological Society, and the Pratt Memorial Award from AAPG.

ACKNOWLEDGEMENTS

This research was funded by the U.S. Department of Energy under contract number DE-FC26-02NT15131 under Daniel F. Ferguson, project manager. Support was also provided by the Bureau of Economic Geology's University Lands Project and the Characterization of San Andres and Grayburg Reservoirs Project, as well as by the New Mexico Bureau of Geology and Mineral Resources. Mark H. Holtz and F. Jerry Lucia generously provided to the project their expertise on Permian basin geology and hydrocarbon production. Jianhua Zhou performed the Geographic Information System mapping of New Mexico oil fields. We gratefully acknowledge the constructive comments of peer reviewers Wayne M. Ahr, Salvatore J. Mazzullo, and Emily L. Stoudt and AAPG Editor Ernest A. Mancini. Lana Dieterich edited the manuscript. Published by permission of the director, Bureau of Economic Geology, John A. and Katherine G. Jackson School of Geosciences, University of Texas at Austin.

(2.7 billion bbl; 4.29×10^8 m^3), and the San Andres platform carbonate play (2.2 billion bbl; 3.42×10^8 m^3). The Permian system dominates production, accounting for 73% of cumulative production, followed by the Pennsylvanian (13%) and the Ordovician (6%). The estimated remaining reserves from that component of the resource base that is already discovered and producing is 3.25 billion bbl (5.17×10^8 m^3).

INTRODUCTION

The Permian basin of west Texas and southeast New Mexico (Figure 1) has produced oil for more than 80 yr, and it is still the third largest petroleum-producing area in the United States after the offshore Gulf of Mexico and Alaska. In 2002, it accounted for 17% of the total United States oil production (327 million bbl; 5.20×10^7 m^3), and it contains an estimated 22% of the United States proved oil reserves (5 billion bbl; 7.95×10^8 m^3) (Energy Information Administration, 2003). Moreover, this region has the greatest potential for production growth in the country, containing 29% (17.6 billion bbl; 2.80×10^9 m^3) of estimated future oil reserve growth (Root et al., 1995). Original oil in place (OOIP) in the Permian basin was estimated to be 106 billion bbl (1.69×10^{10} m^3) (Tyler and Banta, 1989); the 30.4 billion bbl (4.61×10^9 m^3) of oil produced through 2000 represents only 29% of the OOIP. An estimated 30 billion bbl of unrecovered mobile oil remains (Tyler and Banta, 1989).

Because of the substantial amount of oil remaining in the basin, a new oil play portfolio of the Permian basin was developed as part of the U.S. Department of Energy Preferred Upstream Management Practices Program (Dutton et al., 2004). The portfolio geologically defines 32 oil plays in the Permian basin and assigns all reservoirs that had cumulative production of greater than 1 million bbl (1.59×10^5 m^3) through the year 2000 to a play. This new, comprehensive characterization of oil plays includes the entire Permian basin in Texas and New Mexico. Successful reservoir-development practices used in the Permian basin are summarized because in this mature area, much of the future production will result from improved recovery from existing fields.

A simple but effective method of increasing recovery in a reservoir is to apply methods that have been successful in similar reservoirs. To do so, however, it is necessary to understand how reservoirs group naturally into larger families or plays. A play is an assemblage of geologically similar reservoirs exhibiting the same source, reservoir, and trap characteristics (White, 1980). Reservoirs in a play are related geologically and commonly have similar production characteristics (Galloway et al., 1983), thus allowing characteristics of better known reservoirs to be extrapolated with relative confidence to other reservoirs in the same play. Reservoir-development methods that have been demonstrated to work well in one reservoir should therefore be applicable to other reservoirs in the play.

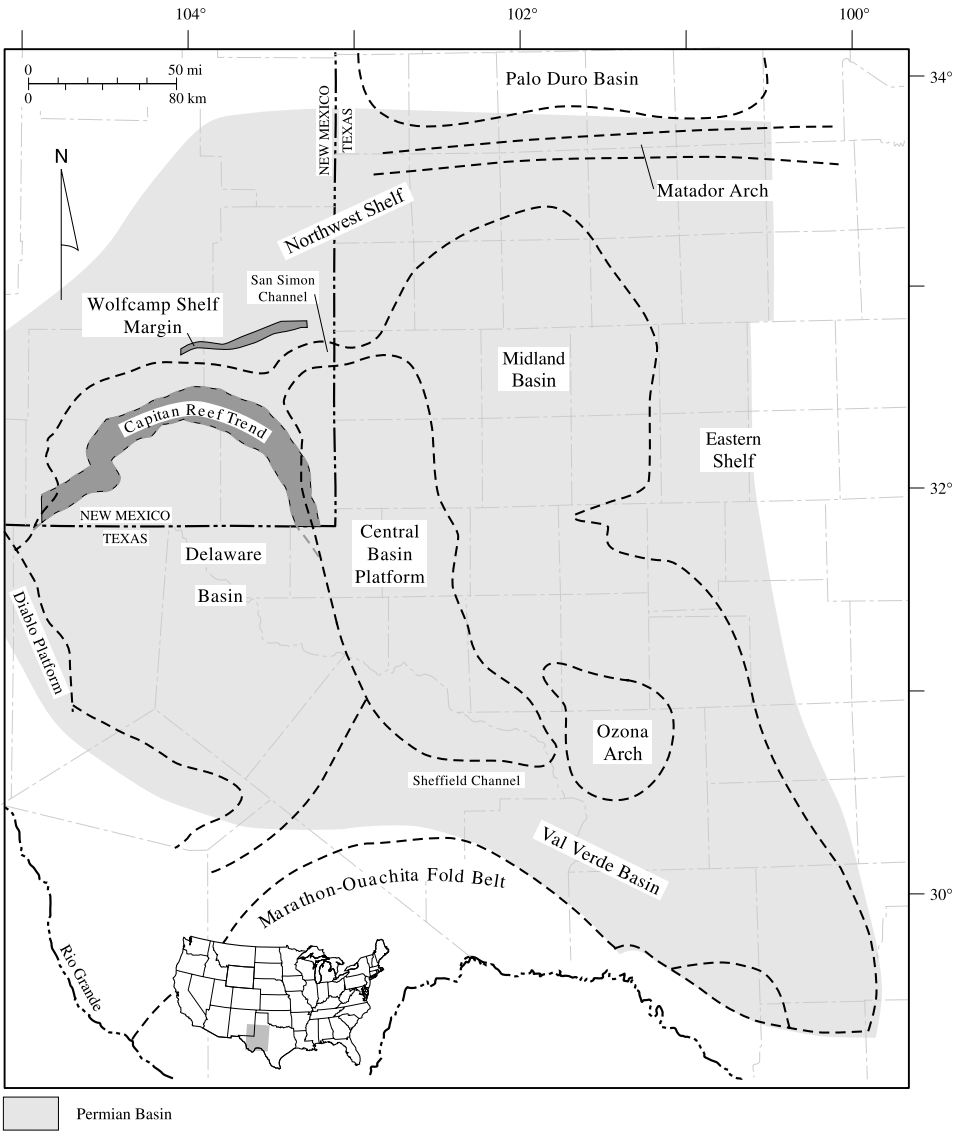

Figure 1. Major subdivisions and boundaries of the Permian basin (shaded area) in west Texas and southeast New Mexico (modified from Silver and Todd, 1969; Hills, 1984; Frenzel et al., 1988; Kosters et al., 1989; Ewing, 1990; Tyler et al., 1991; Kerans and Fitchen, 1995).

This paper geologically defines and describes 32 oil plays of the Permian basin, lists reservoir-development practices that have been used in various plays, and provides an overview of the basin-production history. It is intended as a summary reference to Permian basin oil plays and a guide to published examples of best practices. More extensive details and data from the study can be found in Dutton et al. (2004). Although this study is specific to the Permian basin, its insights into mature basin development may help guide development of other maturing basins worldwide.

Geologic Setting

The Permian basin is a foredeep basin that developed during the late Mississippian and early Pennsylvanian (Hills, 1984; Frenzel et al., 1988) at the south margin of the North American plate, north of the present-day Marathon–Ouachita thrust belt (Figure 1). Prior to development of the Permian basin, a shallow, intracratonic, downwarped area named the Tobosa basin (Galley, 1958) was present in west Texas and southeast New Mexico. Oil production in the Permian basin has come predominantly from reservoirs of Ordovician to Permian age (Figure 2).

Methods

We defined 32 Permian basin oil plays (Table 1) on the basis of reservoir stratigraphy, lithology, depositional environment, and structural and tectonic setting. This new play analysis builds on and revises earlier play assessments of the Permian basin by Galloway et al. (1983), Kosters et al. (1989), Tyler et al. (1991), Holtz and

Figure 2. Stratigraphic nomenclature for the Paleozoic section in the Permian basin. Ages are based on Harland et al. (1989), Tucker and McKerrow (1994), and Bowring et al. (1998). Source rock identification is from J. A. Williams (1977, personal communication) and Hill et al. (2004).

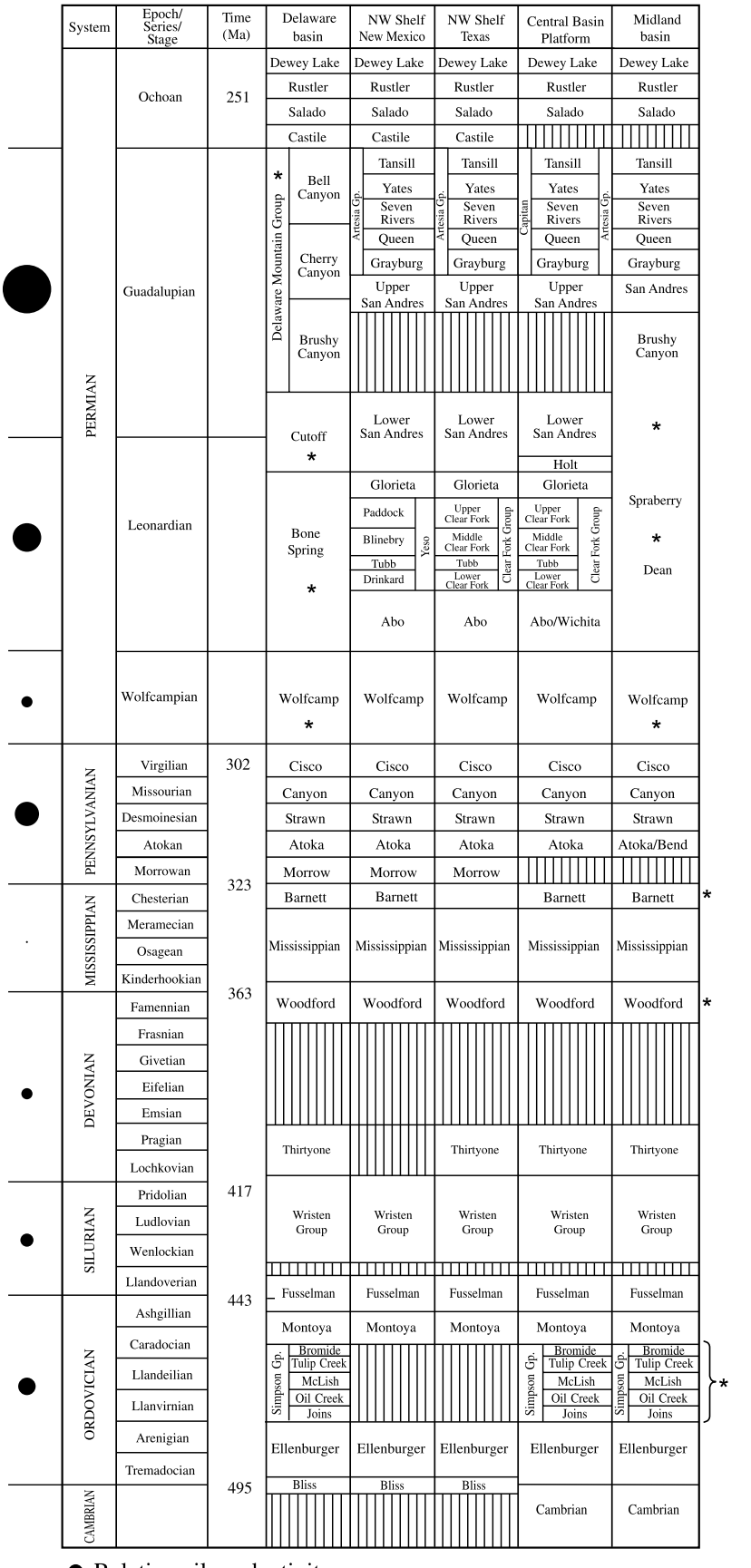

Kerans (1992), Holtz (1993), New Mexico Bureau of Mines and Mineral Resources (1993), Ruppel and Holtz (1994), Holtz and Garrett (1997), and Dutton et al. (2000), as well as unpublished studies by the authors.

We identified 1339 significant-sized oil reservoirs in the Permian basin, defined as reservoirs having cumulative production of greater than 1 million bbl (1.59×10^5 m^3) through the year 2000, and assigned each of them to a play. Cumulative production information for reservoirs in Texas was taken from production records of the Railroad Commission of Texas (RRC, 2001). Cumulative production for reservoirs in New Mexico was calculated by taking the annual production from 1994 to 2000 and adding it to the cumulative production data obtained from the 1993 annual report (New Mexico Oil and Gas Engineering Committee, 1993). We calculated cumulative production for each play by summing production from the significant-sized reservoirs. We drew play boundaries for each play to include areas where oil reservoirs in that play occur but are smaller than 1 million bbl (1.59×10^5 m^3) of cumulative production. We used decline-curve analysis to estimate remaining reserves of each play in the Permian basin.

PLAY SUMMARIES

A brief definition of each oil play in the Permian basin is given in this section. More extensive information and references about each play are included in Dutton et al. (2004).

Ordovician Plays

Three oil plays in the Permian basin produce from Ordovician reservoirs (Table 1; Figure 3). The Lower Ordovician Ellenburger Group (Figure 2) consists of thick (up to 1700 ft [520 m]), areally extensive sequences of mud-dominated carbonates, with localized grainstones deposited on a restricted carbonate ramp (Kerans, 1990). Sea level fall at the end of the Early Ordovician resulted in the exposure of the ramp and the development of widespread karst terrain (Kerans, 1990). Subsequent multiple karst events, erosion, and compressive tectonism from the Ordovician to the Pennsylvanian also affected Ordovician rock characteristics (Holtz and Kerans, 1992).

The carbonates of the Ellenburger selectively dolomitized ramp carbonate play reflect a range of environments from inner to outer ramp (Figure 3). Reservoirs include both dolomitized and undolomitized (limestone) intervals. Subtidal carbonates are locally common, reflecting the more basinward setting (Holtz and Kerans, 1992). Ellenburger rocks in this play experienced several episodes of exposure, karstification, and fracturing (Combs et al., 2003). Main influences on reservoir character are variable dolomitization and karstification.

Pervasively dolomitized reservoirs of the Ellenburger karst-modified restricted ramp carbonate play (Figure 3) were deposited in an inner-ramp setting (Kerans, 1990). The main controls on porosity distribution are extensive erosion and karstification that occurred during the early Middle Ordovician lowstand (Kerans, 1988). Reservoir heterogeneity results from extensive dissolution, cave formation, and subsequent cave infilling (Kerans, 1988; Loucks, 1999), which formed a pervasive breccia-fracture system (Holtz and Kerans, 1992).

Middle Ordovician transgression of the area resulted in the deposition of shales, carbonates, and sandstones of the Simpson Group (Figure 3). These deposits accumulated in a broad depocenter commonly referred to as the Tobosa basin (Galley, 1958). Reservoirs in the Simpson cratonic sandstone play are found in three regionally extensive sandstones, the Connell, Waddell, and McKee (Galley, 1958). The Connell sandstone is interpreted as having been deposited in a range of environments, from high-energy shoreface and nearshore environments to more distal and lower energy marine environments (Suhm and Ethington, 1975).

Silurian Plays

Reservoirs productive from Silurian rocks can be subdivided into two distinct lithologic successions: the Fusselman Formation (Upper Ordovician to middle Silurian) and the Wristen Group (middle to Upper Silurian) (Figure 2). The reservoirs of the Fusselman shallow-platform carbonate play (Figure 4) are composed of limestones, dolostones, and cherty dolostones that were deposited on an open-marine, shallow-water carbonate platform that extended over much of the mid-continent region (Ruppel and Holtz, 1994; Mazzullo, 1997). Reservoir facies are pelmatozoan packstones and grainstones and ooid grainstones. Also included in this play are reservoirs that produce from shallow-water limestones and dolostones of the Upper Ordovician Montoya Formation (Behnken, 2003).

Rocks of the Wristen Group (Figure 2) reflect deposition in a spectrum of platform-to-basin settings

Table 1. Production in 2000 and Cumulative Production Through December 31, 2000, of Oil Plays in the Permian Basin, Listed by Reservoir Age

Play	State	2000 Production (bbl)	Cumulative Production (bbl)
Permian			
Guadalupian			
Artesia platform sandstone	Texas and New Mexico	6,526,676	1,855,409,025
Queen tidal-flat sandstone	Texas	1,517,501	179,600,166
Delaware Mountain Group basinal sandstone	Texas and New Mexico	9,208,247	351,912,395
Grayburg high-energy platform carbonate–Ozona arch	Texas	1,968,685	298,378,769
Grayburg platform carbonate	Texas	10,104,204	1,271,232,325
Grayburg platform mixed clastic-carbonate	Texas	7,806,840	669,727,337
San Andres–Grayburg lowstand carbonate	Texas	9,357,241	681,131,877
Upper San Andres and Grayburg platform mixed–Artesia Vacuum trend	New Mexico	11,392,997	796,416,386
Upper San Andres and Grayburg platform mixed–Central Basin platform trend	New Mexico	5,790,360	808,957,693
San Andres platform carbonate	Texas	26,420,818	2,151,296,650
San Andres karst-modified platform carbonate	Texas	11,460,129	1,567,103,814
Eastern shelf San Andres platform carbonate	Texas	6,613,837	706,897,011
Northwest shelf San Andres platform carbonate	Texas and New Mexico	50,666,870	3,969,256,500
		158,834,405	**15,307,319,948**
Leonardian			
Spraberry–Dean submarine-fan sandstone	Texas	27,576,283	1,287,098,237
Bone Spring basinal sandstone and carbonate	New Mexico	2,455,154	70,703,460
Leonard restricted platform carbonate	Texas and New Mexico	49,928,957	3,297,197,998
Abo platform carbonate	Texas and New Mexico	6,105,583	541,459,683
		86,065,977	**5,196,459,378**
Wolfcampian			
Wolfcamp–Leonard slope and basinal carbonate	Texas and New Mexico	9,093,948	195,077,551
Wolfcamp platform carbonate	Texas and New Mexico	4,012,646	457,405,339
		13,106,594	**652,482,890**
Pennsylvanian			
Upper Pennsylvanian and Lower Permian slope and basinal sandstone*	Texas	1,802,373	271,448,389
Pennsylvanian and Lower Permian Horseshoe atoll carbonate	Texas	13,686,639	2,699,242,936
Pennsylvanian platform carbonate	Texas	2,076,281	340,469,274
Northwest shelf upper Pennsylvanian carbonate	New Mexico	4,883,971	353,848,173
Northwest shelf Strawn patch reef	New Mexico	1,539,376	70,337,831
Pennsylvanian and Lower Permian reef and bank**	Texas	315,183	92,104,283
Upper Pennsylvanian shelf sandstone#	Texas	426,556	7,264,141
		24,730,379	**3,834,715,027**
Mississippian			
Mississippian platform carbonate	Texas	91,765	15,110,822
		91,765	**15,110,822**
Devonian			
Devonian Thirtyone ramp carbonate	Texas	1,747,319	110,249,504

Table 1. Continued

Play	State	2000 Production (bbl)	Cumulative Production (bbl)
Devonian Thirtyone deepwater chert	Texas and New Mexico	6,786,521	785,929,988
		8,533,840	**896,179,492**
Silurian			
Wristen buildups and platform carbonate	Texas and New Mexico	4,773,912	888,757,885
Fusselman shallow-platform carbonate	Texas and New Mexico	2,046,889	356,268,389
		6,820,801	**1,245,026,274**
Ordovician			
Simpson cratonic sandstone	Texas and New Mexico	420,651	103,228,356
Ellenburger karst-modified restricted ramp carbonate	Texas and New Mexico	2,802,096	1,487,309,287
Ellenburger selectively dolomitized ramp carbonate*	Texas	537,120	163,734,910
		3,759,867	**1,754,272,553**
Total		**301,943,628**	**28,901,566,384**

*Includes all reservoirs in this play, including ones in north-central Texas geologic province.
**Production listed here represents only the 10 reservoirs in the Permian basin portion of the play.
#Production listed here represents only the five reservoirs in the Permian basin portion of the play.

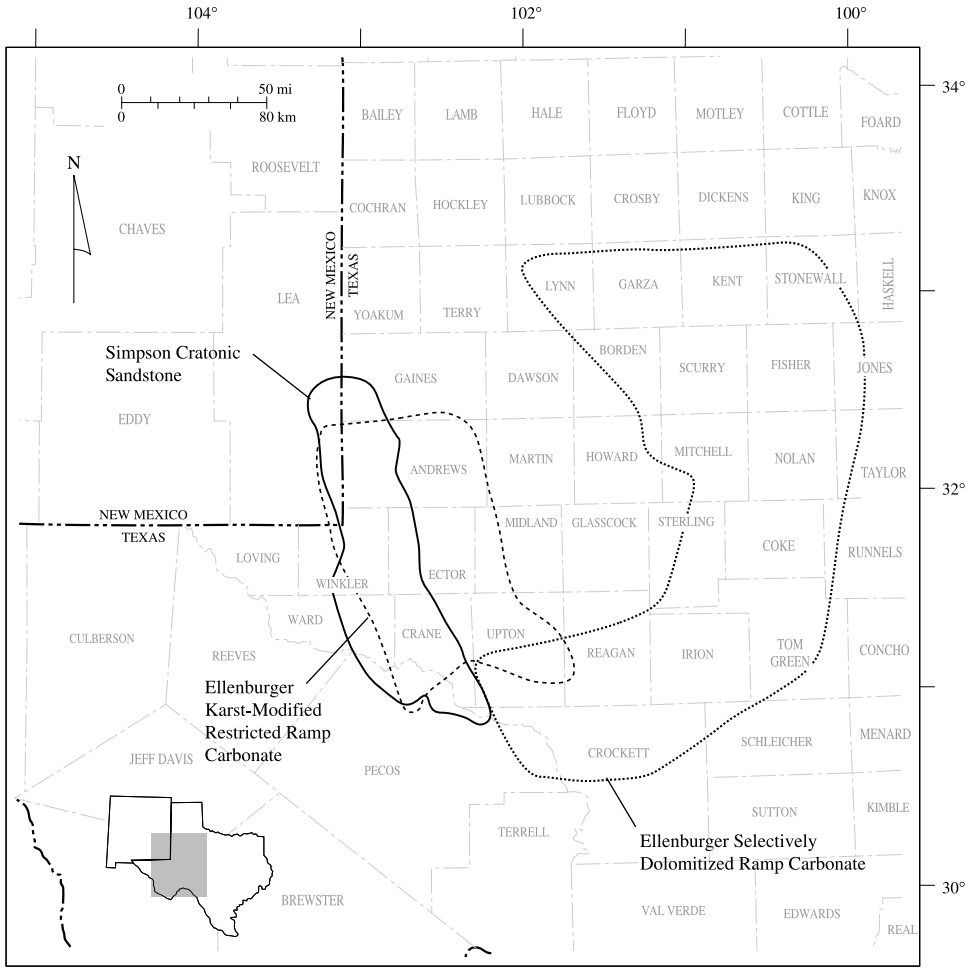

Figure 3. Play boundaries of Ordovician oil plays in the Permian basin. Play outlines are, in part, derived from outlines previously published by Holtz and Kerans (1992) and Holtz and Garrett (1997).

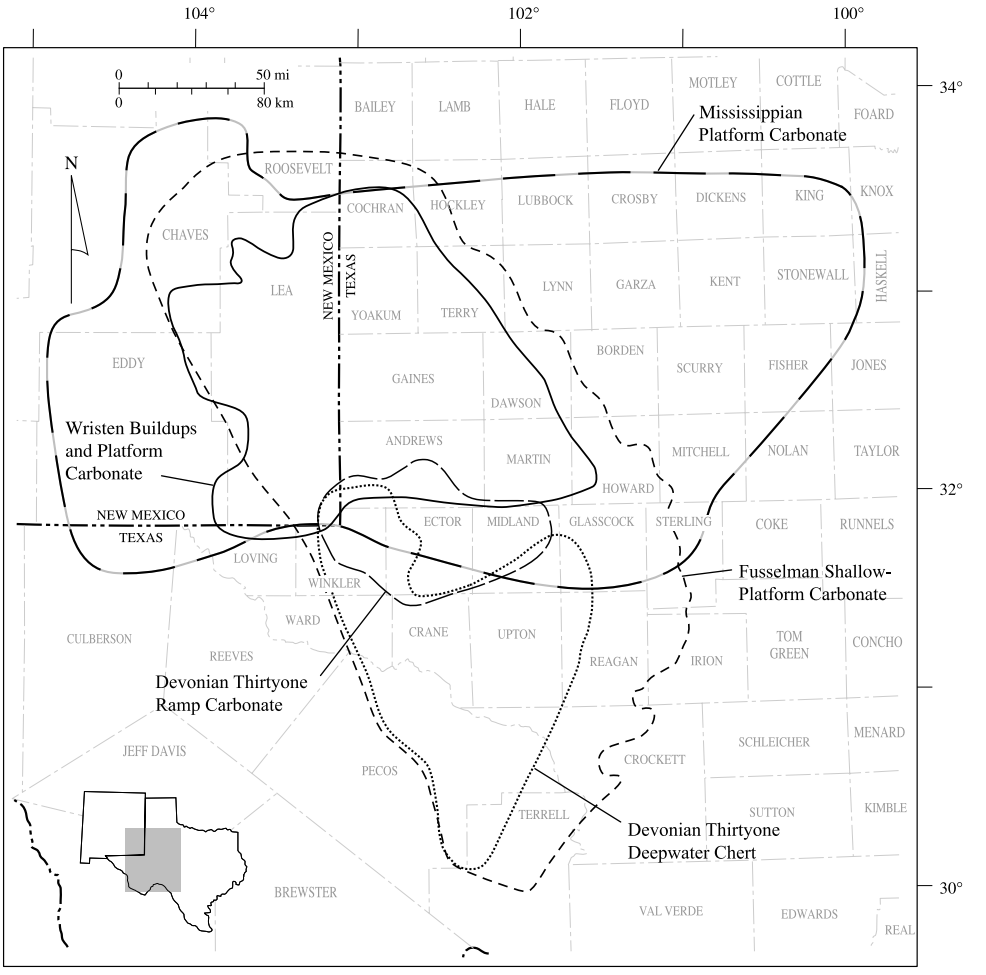

Figure 4. Play boundaries of Silurian, Devonian, and Mississippian oil plays in the Permian basin. Silurian and Devonian play outlines are, in part, derived from outlines previously published by Ruppel and Holtz (1994).

following the downwarping and drowning of the preexisting Fusselman shallow-water platform during the middle Silurian (Ruppel and Holtz 1994). The middle Silurian (Wristen) platform margin trended east-west across southern Andrews and northern Midland counties and marks the southern limit of the Wristen buildups and platform carbonate play (Figure 4). Wristen production is derived almost entirely from carbonates deposited either in platform-margin buildups or in shallow-water facies of the platform interior (Ruppel and Holtz 1994).

Devonian and Mississippian Plays

A major rise in relative sea level occurred in the Early Devonian in west Texas and southeast New Mexico. The Lower Devonian Thirtyone Formation (Figure 2) records infilling of the Silurian (Wristen Group) basin (Ruppel and Holtz 1994). Reflecting this fact, the northern boundary of the Thirtyone closely approximates the position of the Wristen platform margin. The Thirtyone Formation contains two end-member facies, (1) carbonate packstones and grainstones and (2) spiculitic chert (Ruppel and Holtz 1994). Carbonates deposited as in-place accumulations on the Early Devonian shallow-water platform and as resedimented skeletal sands on the outer ramp to slope form the Devonian Thirtyone ramp carbonate play (Figure 4). Reservoir rocks in this play are skeletal packstones and grainstones composed primarily of pelmatozoan debris (Ruppel and Holtz 1994; Weiner and Heyer, 1999). Reservoir quality is a function of diagenesis; both silicification and local leaching of carbonate mud are important in reservoir development.

Cherts that accumulated in deeper water in areas of reduced carbonate deposition form the Devonian Thirtyone deepwater chert play (Figure 4). Thick-bedded laminated chert, commonly called ''tripolitic chert,'' is the most important reservoir facies in the Thirtyone Formation (Ruppel and Holtz 1994; Saller et al., 2001). The chert is highly porous and contains varying amounts of carbonate. Thirtyone Formation chert

strata accumulated in deepwater slope and basin settings by submarine gravity flow and hemipelagic sedimentation (Ruppel and Holtz 1994; Ruppel and Barnaby, 2001).

The Mississippian platform carbonate play extends across much of the Permian basin (Figure 4). Upper Mississippian platform carbonates are shelf equivalents of the Barnett Shale, which was deposited in the deeper water to the south and east (Hamilton and Asquith, 2000). Mississippian fields in eastern Gaines and western Dawson counties are interpreted as occurring in Chesterian ooid grainstones that developed landward of the platform margin (Hamilton and Asquith, 2000).

Pennsylvanian Plays

Present structural features of the Permian basin, including the Central Basin platform and Midland and Delaware basins (Figure 1), began forming in the early Pennsylvanian (Frenzel et al., 1988). Most of the anticlines that form the traps for oil-producing reservoirs in the area formed during Pennsylvanian faulting. The thickness and distribution of Pennsylvanian rocks in the Permian basin are quite variable because of nondeposition and erosion over positive areas such as the Central Basin platform.

Five Pennsylvanian oil plays occur in the Permian basin (Figure 5). Most Pennsylvanian reservoirs produce from ramp and platform carbonates, but sandstones deposited in slope and basin environments on the east side of the Midland basin are also productive. Two additional plays, the Pennsylvanian and Lower Permian reef and bank play and upper Pennsylvanian shelf sandstone play, are located mostly in north-central Texas but extend into the eastern Midland basin. Production from only those reservoirs that are in Permian basin has been included for these plays in the total Permian basin oil production shown in Table 1.

Patch reefs in the Northwest shelf Strawn patch reef play (Figure 5) grew on a south-dipping carbonate ramp in the western Permian basin before it segmented into the Northwest shelf and the Delaware

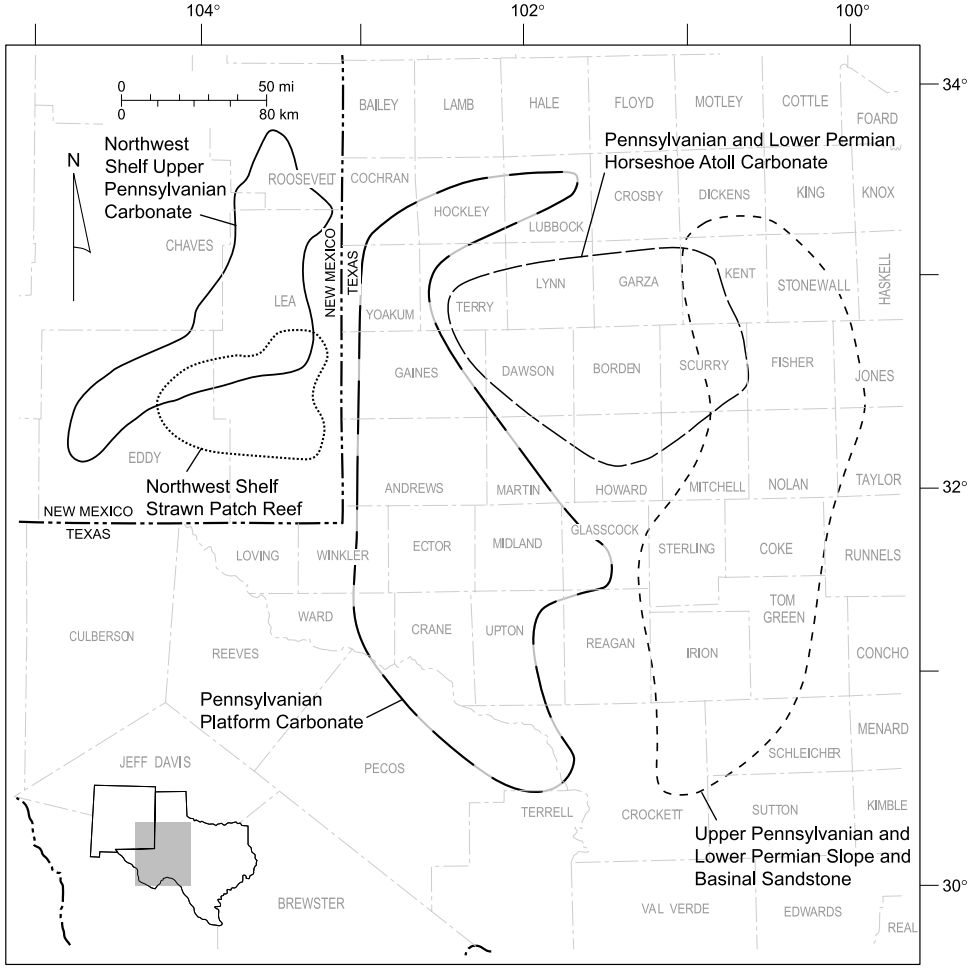

Figure 5. Play boundaries of Pennsylvanian oil plays in the Permian basin. Some play outlines are, in part, derived from outlines previously published by Holtz and Garrett (1997) and Dutton et al. (2000) and from the work of Mazzullo (1997).

basin. Reservoirs are principally bioherms composed of phylloid algal, coralgal, and foraminiferal wackestones and packstones (Harris, 1990). Bioherm growth was localized on preexisting structures having bathymetric expression.

Later in that area, upper Pennsylvanian and earliest Wolfcampian reservoir rocks of the Northwest shelf upper Pennsylvanian carbonate play (Figure 5) were deposited on a shallow-water carbonate shelf and at the shelf margin. Traps in the play are primarily stratigraphic, with reservoirs formed by phylloid-algal mounds and associated grainstones and packstones (Cys, 1986). Massive, dolomitized, phylloid-algal mound reservoirs grew at bathymetric breaks at or near the shelf edge (Wahlman, 2001).

Pennsylvanian carbonates deposited on the Central Basin platform and in the Midland basin (Figure 5) compose the Pennsylvanian platform carbonate play. Atokan and Desmoinesian carbonates were deposited on low-relief ramps at a time of relatively low regional subsidence, whereas Missourian and Virgilian carbonates were deposited on higher relief carbonate platforms at a time of higher rates of regional subsidence (Hanson et al., 1991; Mazzullo, 1997). High-frequency glacioeustatic sea level fluctuations during the Pennsylvanian resulted in highly cyclic successions of shallow-water carbonate-platform facies (Heckel, 1986; Reid and Reid, 1999; Wahlman, 2001). Porosity in these rocks is developed primarily in thick grainstones and phylloid-algal boundstones (Saller et al., 1999).

The Pennsylvanian and Lower Permian Horseshoe atoll carbonate play produces from reservoirs on the Horseshoe atoll, a nonreefal isolated carbonate platform system in the northern Midland basin (Figure 5). Production is from stacked Strawn through Wolfcamp limestones and dolomitic limestones that aggraded from the floor of the basin in a northward-opening arc (Galloway et al., 1983). Deposition of the Horseshoe atoll began on a broad Strawn carbonate platform (Vest, 1970), with later development of isolated carbonate knolls and pinnacles. Exposure and erosion at sequence boundaries during the late Missourian through Virgilian produced a series of truncation surfaces and local development of erosionally generated slope wedges associated with major eustatic sea level falls (Reid and Reid, 1991, 1999; Kerans, 2001).

The Cisco to Wolfcamp clastic rocks of the upper Pennsylvanian and Lower Permian slope and basinal sandstone play (Figure 5) were deposited as submarine fans that accumulated basinward of the Eastern shelf as it prograded westward (Galloway and Brown, 1972). Reservoir-quality sand bodies were deposited in the lower portions of slope wedges along a broad north-south–trending belt during sea level lowstands (Brown et al., 1990). Production is from turbidite sandstones deposited in submarine-fan channel, lobe, and overbank and levee environments (Neuberger, 1987).

Lower Permian Plays

During the Early Permian (Wolfcampian and Leonardian), carbonate deposition occurred on the shelves around the Midland and Delaware basins; carbonate debris and siliciclastics were deposited in the basins. Some portions of the western Central Basin platform remained emergent throughout the Wolfcampian, but by the Leonardian, this area was a stable, shallow-water carbonate platform (Frenzel et al., 1988).

The Wolfcamp platform carbonate play (Figure 6) lies along the east side of the Central Basin platform and north of the east-west–trending Wolfcampian shelf margin in New Mexico (Figure 1). The reservoirs in this play are composed of cyclic, shallow-water carbonate facies that are overprinted by diagenesis at and below cycle tops formed during sea level fall (Saller et al., 1994, 1999).

During the Wolfcampian and into the Leonardian, carbonate debris was shed off the carbonate shelf margins rimming the Central Basin platform and Eastern shelf and deposited in the Midland and Delaware basins. Reservoirs of the Wolfcamp–Leonard slope and basinal carbonate play (Figure 6) are resedimented carbonates deposited by debris flows and turbidity currents on the lower slope and basin floor (Hobson et al., 1985; Loucks et al., 1985; Mazzullo and Reid, 1987; Mazzullo, 1997). These rocks contain clasts of shallow-water facies identical to those observed on the platform, indicating that they were derived by downslope transport from the platform margin. Reservoirs in this play also contain a high proportion of oolitic and skeletal grainstone deposited as massive sediment-gravity flows, producing a superficial resemblance to shallow-water reservoirs (Ahr, 2000).

Abo deposition at the beginning of the Leonardian (Figure 2) marks the transition from paleogeographically complex late Pennsylvanian–Wolfcampian isolated build-ups to more organized shelf-margin platforms (Kerans, 2000). Reservoirs in the Abo platform carbonate play (Figure 7) are developed in shelf and shelf-margin facies along the south margin of the Northwest shelf.

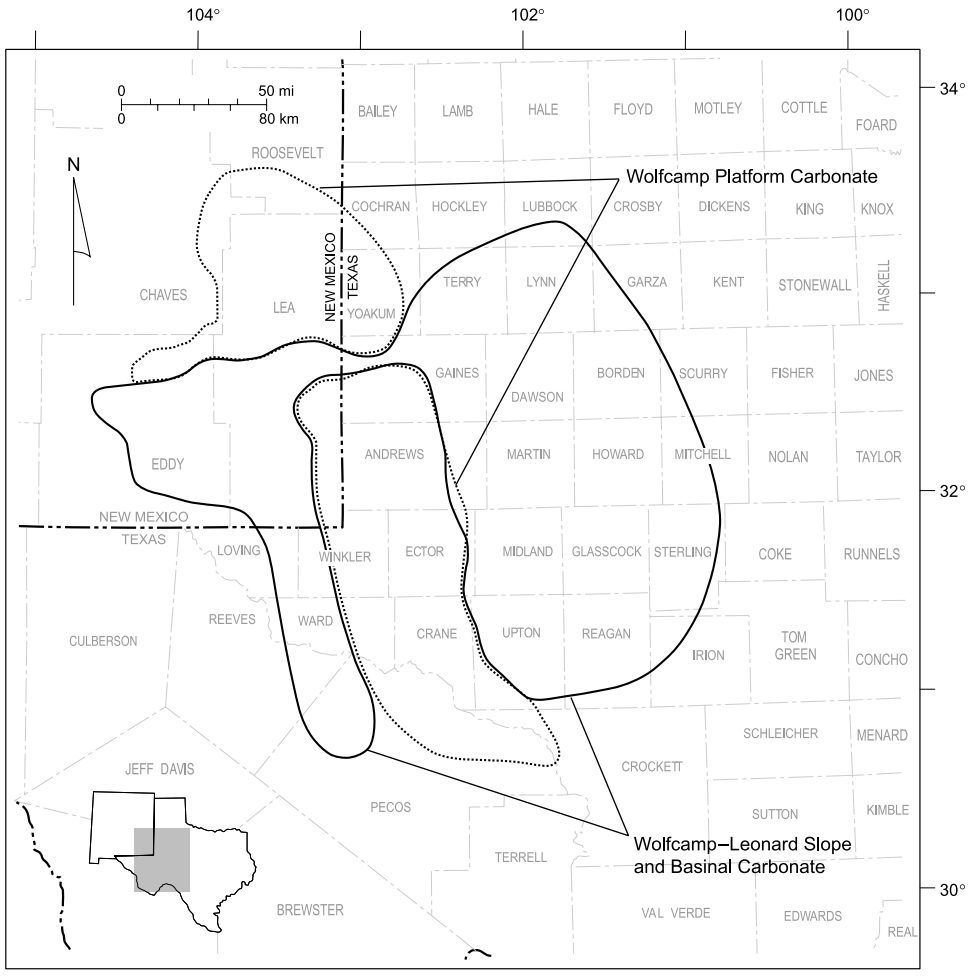

Figure 6. Play boundaries of Wolfcampian oil plays in the Permian basin. Some play outlines are, in part, derived from outlines previously published by New Mexico Bureau of Mines and Mineral Resources (1993), Holtz and Garrett (1997), and Dutton et al. (2000) and from the work of Mazzullo (1997).

Platform-margin Abo successions are dominated by grain-rich packstones and grainstones that underwent significant karst-related diagenesis (Kerans, 2000; Kerans et al., 2000) and are extensively dolomitized in the New Mexico portion of the play.

Reservoirs of Leonardian age on the Central Basin platform, Northwest shelf, and Eastern shelf are included in the Leonard restricted platform carbonate play (Figure 7). Leonardian rocks in this play were deposited in restricted, low-energy depositional conditions on a shallow-water, flat-topped carbonate platform. The best reservoir quality is commonly associated with grain-dominated, dolomitized, subtidal rocks (Ruppel, 2002).

Reservoirs in the Bone Spring basinal sandstone and carbonate play were deposited in a basinal setting seaward of the Abo shelf edge in the Delaware basin (Figure 7). Production is from deepwater carbonate debris flows and fine-grained turbidite sandstones (Wiggins and Harris, 1985; Saller et al., 1989; Montgomery, 1997).

Reservoirs of the Spraberry–Dean submarine-fan sandstone play (Figure 7) were deposited as large basin-floor submarine-fan systems in the Midland basin that were fed by turbidity currents and debris flows (Handford, 1981; Tyler et al., 1997). Most of the production is from very fine-grained sandstone and coarse siltstone units in the Spraberry. Natural fractures cause high rates of initial production, but the matrix contains most of the oil and controls long-term recovery (Montgomery et al., 2000).

Upper Permian (Guadalupian) Plays

Guadalupian reservoirs in the Permian basin (Table 1) are developed primarily in San Andres and Grayburg carbonates deposited on shallow-water shelves that surrounded the Midland and Delaware basins and on the Central Basin platform and Ozona arch. Deepwater sandstones deposited in the Delaware basin and shelf sandstones associated with sabkha carbonates and evaporites are also productive.

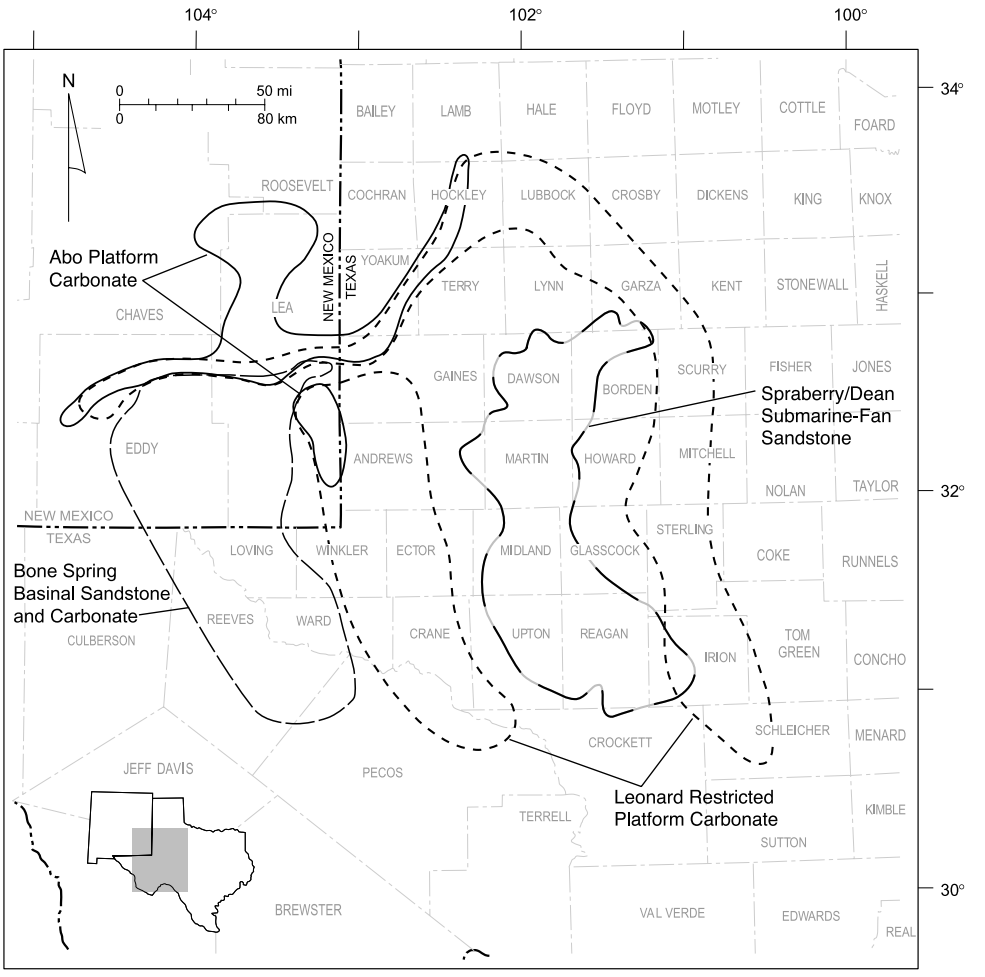

Figure 7. Play boundaries of Leonardian oil plays in the Permian basin. Some play outlines are, in part, derived from outlines previously published by New Mexico Bureau of Mines and Mineral Resources (1993), Holtz and Garrett (1997), and Dutton et al. (2000) and the work of Ruppel (2002).

The Northwest shelf San Andres platform carbonate play (Figure 8a) represents a regressive series of cyclic deposits that prograded southward across the broad, low-relief, shallow-water Northwest shelf. Restricted-marine, subtidal dolostones in the lower and middle San Andres form the main reservoir facies (Cowan and Harris, 1986). Porous zones are offset basinward and occur in increasingly younger strata southward (Ramondetta, 1982; Cowan and Harris, 1986; Ward et al., 1986).

The Eastern shelf San Andres platform carbonate play (Figure 8a) produces mainly from dolostones in the San Andres and Grayburg formations, as well as sandstones in the Queen, Seven Rivers, and Yates formations (Figure 2) (Mooney, 1982). The Eastern shelf prograded westward into the Midland basin during the Permian. Carbonate deposition ended on the Eastern shelf during the middle Guadalupian, and upper Guadalupian rocks are composed of cyclic deposits of sandstone, anhydrite, and halite (Silver and Todd, 1969; Ward et al., 1986).

Reservoirs of the San Andres karst-modified platform carbonate play produce from the structurally high south end of the Central Basin platform (Figure 8a); most production has come from Yates field. The main reservoirs are dolostones characterized by thick accumulations of grainstones at the top of a shallowing-upward sequence (Tinker, 1996). Permeability was greatly increased by open caves and solution-enlarged joints that developed by karstification during multiple subaerial exposure events during and following San Andres deposition (Craig, 1988; Tinker et al., 1995).

Carbonates of the San Andres platform carbonate play were deposited on the shallow-water Central Basin platform during the early Guadalupian (Figure 8a). Reservoirs in this play are developed primarily in thick, dolomitized, subtidal portions of shoaling-upward cycles (Ruppel and Cander, 1988; Garber and Harris, 1990). Early, pervasive dolomitization preserved much of the primary porosity in these San Andres reservoirs (Ruppel and Cander, 1988).

Production is commingled from both dolostone and clastic reservoirs in the upper San Andres and Grayburg formations on the northwest portion of the Central

Basin platform and on the Northwest shelf. In the upper San Andres and Grayburg platform mixed–Central Basin platform trend play (Figure 8a), reservoirs consist of high-energy dolograinstones formed in shoal environments and shallow-marine dolomitic sandstones (Garber and Harris, 1990; Lindsay, 1991). Similar reservoirs in the upper San Andres and Grayburg platform mixed–Artesia Vacuum trend play (Figure 8a) occur along the Artesia-Vacuum arch, a shallow east-west–trending structure that overlies the Abo shelf-edge trend. In both plays, some karst development has occurred in the San Andres (Pranter et al., 2004). Grayburg reservoir sandstones were deposited in coastal, sabkha, sand-flat, and eolian environments (Handford et al., 1996).

Reservoirs in the San Andres–Grayburg lowstand carbonate play (Figure 8a) lie structurally and topographically below the San Andres and Grayburg shelf-margin reservoirs on the Central Basin platform and the Northwest shelf. The shallow-water facies in these reservoirs are interpreted as having been deposited in the Midland basin during periods of sea level lowstand. In contrast to San Andres and Grayburg reservoirs on the Central Basin platform, oolite grainstones are common reservoir facies in this play (Dull, 1994). The oolite grainstones probably formed by focused tidal energy when the Midland basin was restricted to the center of the basin and shoreline was lowered.

Reservoirs in the Grayburg platform carbonate play occupy the southeast side of the Central Basin platform in Texas (Figure 8b). Depositional style and petrophysical properties of Grayburg platform carbonate reservoirs are similar to those of the San Andres, being thick, dolomitized, subtidal portions of shoaling-upward cycles (Bebout et al., 1987; Tyler et al., 1991). Reservoir quality has been influenced strongly by diagenesis, particularly dolomite alteration and anhydrite alteration and removal (Ruppel and Lucia, 1996).

The Grayburg platform mixed clastic-carbonate play is located northwest of the Grayburg platform carbonate play on the Central Basin platform in Texas (Figure 8b). It has been designated a separate play because production comes from porous and permeable lower Grayburg fine-grained sandstones and coarse siltstones, as well as from San Andres and Grayburg carbonates. Grayburg siliciclastics are interpreted to be eolian facies deposited during sea level falls and reworked during subsequent sea level rises (Ruppel, 2001).

By the time of Grayburg deposition, the Midland basin was areally restricted and shallow, and the Ozona arch was a shallow-water platform across which water was exchanged between the open ocean to the south and west (Sheffield Channel, Figure 1) and the restricted basin to the north (Tyler et al., 1991). The Grayburg high-energy platform carbonate–Ozona arch play produces from upper San Andres and Grayburg carbonate reservoirs (Figure 8b). The reservoir section in these fields is composed of numerous shoaling-upward cycles of fusulinid grain-dominated packstones and ooid grainstones (Zahm and Tinker, 2000).

Reservoirs in the Delaware Mountain Group basinal sandstone play produce from deepwater sandstones of the Bell Canyon, Cherry Canyon, and Brushy Canyon formations (Delaware Mountain Group) (Figures 2, 8b). Delaware sandstones are interpreted as having been deposited by turbidity currents, possibly derived from dunes that prograded to the shelf break during sea level lowstands; eolian sands were then carried into the slope and basin by turbidity currents (Fischer and Sarnthein, 1988; Gardner, 1992). Bell Canyon sandstones, the most productive unit, were deposited in a basin-floor setting by a system of leveed channels having attached lobes and overbank splays (Barton and Dutton, 1999; Dutton et al., 2003).

The Queen tidal-flat sandstone play on the east and south margins of the Central Basin platform (Figure 8b) produces from the middle Guadalupian Queen Formation. The reservoir sandstones, which form the bases of progradational, shoaling-upward cycles, were deposited in intertidal-flat, tidal-channel, and shoreface environments (Holtz, 1994; Price et al., 2000). They are overlain by supratidal dolomudstones and massive anhydrite at the top.

Siliciclastics, carbonates, and evaporites of the Artesia Group were deposited on a broad, shallow shelf in a back-reef lagoonal setting located updip of the shelf-margin reef carbonates that rimmed the Delaware basin (Silver and Todd, 1969; Ward et al., 1986). Sandstones in the Queen, Seven Rivers, and Yates formations of the Artesia Group (Figure 2) make up the Artesia platform sandstone play, located along the west edge of the Central Basin platform and on the Northwest shelf (Figure 8b). Dolostones of the Queen, Seven Rivers, Yates, and Tansill formations form secondary reservoirs.

RESERVOIR-DEVELOPMENT METHODS

A variety of new reservoir-development techniques have been applied to Permian basin reservoirs recently because of the large remaining resource target. Tyler and Banta (1989) estimated that conventional recovery in the Permian basin using then-current technology

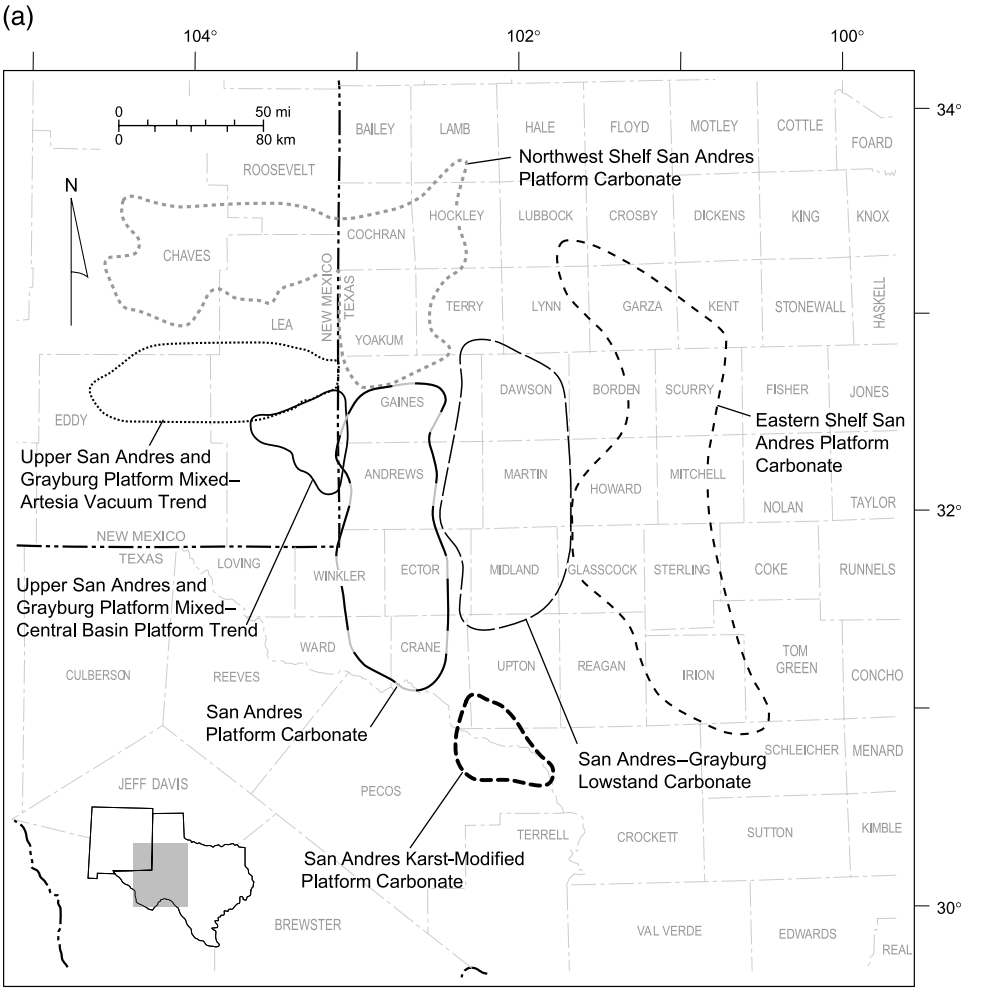

Figure 8. Play boundaries of Upper Permian (Guadalupian) oil plays in the Permian basin: (a) part 1, (b) part 2. Some play outlines are, in part, derived from outlines previously published by New Mexico Bureau of Mines and Mineral Resources (1993), Holtz and Garrett (1997), and Dutton et al. (2000).

would be only 30% of OOIP. Advanced secondary and tertiary production techniques can improve the recovery ratio by targeting remaining mobile oil and residual oil in mature fields. The Permian basin is estimated as having the greatest potential for additional oil production in the United States, containing 29% (17.6 billion bbl [2.80×10^9 m^3]) of estimated future oil reserve growth (Root et al., 1995). Most reserve growth from the basin will result from application of improved reservoir-development practices to existing fields. Newly implemented reservoir-development methods being used in the Permian basin are listed by play in Table 2. Enhanced-recovery methods that have been demonstrated to work well in one reservoir in a play should be applicable to other reservoirs in that play because they share production characteristics.

Because many reservoirs in the Permian basin produce by solution-gas drive (Galloway et al., 1983), primary recovery efficiencies are typically low. Average primary recovery in selected Permian basin reservoirs characterized by solution-gas-drive mechanisms was 14.8% (Tyler et al., 1991). Secondary waterflooding is the most common reservoir-development method used in the basin. Typical waterfloods have evolved from peripheral floods to line-drive floods to pattern floods, such as five-spot or inverted nine-spot patterns. In plays in which solution-gas drives have been supplemented by waterfloods, recovery efficiencies have increased to an average of 26% (primary and secondary) (Tyler et al., 1991). Waterflooding is used so commonly throughout the basin that it has not been included in Table 2 unless a particular pattern realignment or other modification enhanced recovery.

Recent reservoir-development approaches in the Permian basin include CO_2 injection, horizontal drilling, and drilling targeted by seismic-attribute analysis (Table 2). Carbon dioxide flooding has worked well in plays such as the Pennsylvanian and Lower Permian Horseshoe atoll carbonate, San Andres platform carbonate, Grayburg platform carbonate, Devonian Thirtyone

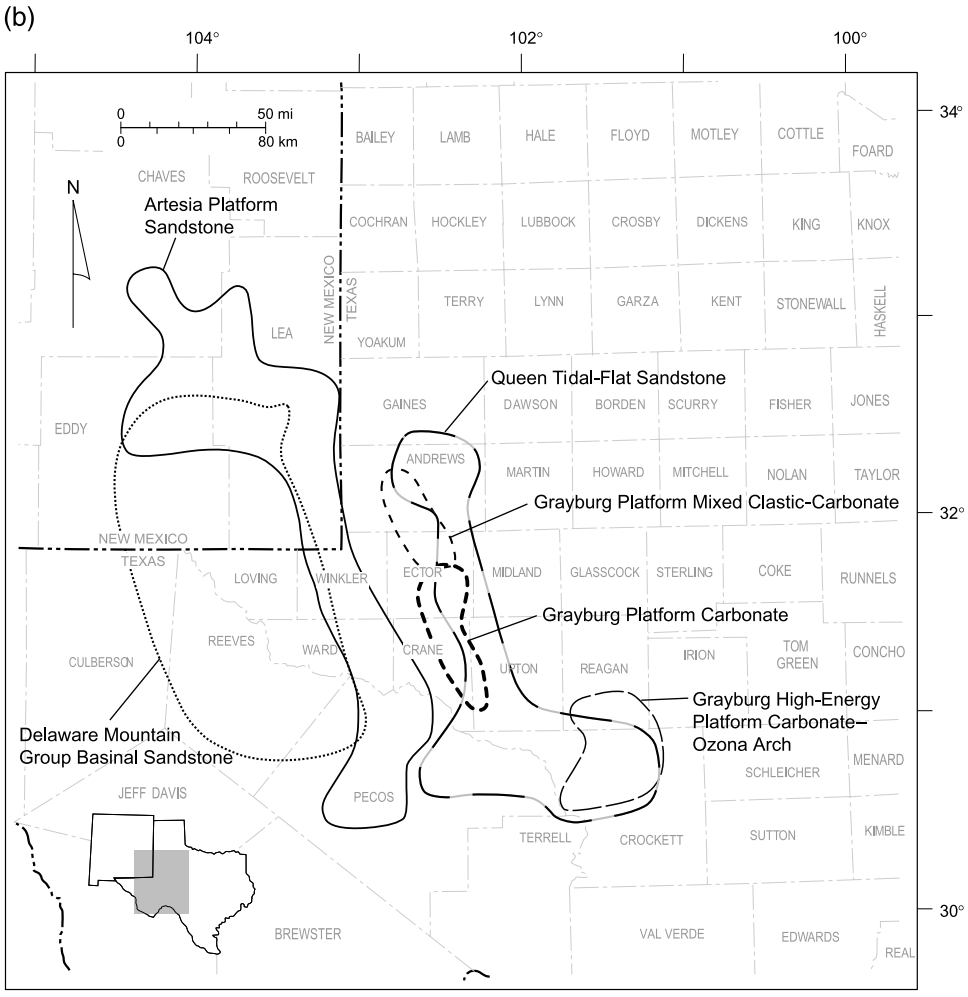

Figure 8. Continued.

deepwater chert, and Delaware Mountain Group basinal sandstone. The reservoirs in these plays have clear target intervals, such as stacked grainstone-rich carbonate cycles or sandstones, and good top and lateral seals. Carbon dioxide flooding is less likely to be successful in plays having strongly fractured, bottom-water-drive reservoirs, such as the San Andres karst-modified platform carbonate and the Ellenburger plays.

A variety of techniques have been applied at Yates field (San Andres karst-modified platform carbonate play), including gravity drainage assisted by nitrogen and CO_2 injection, water coproduction, and steam injection (Table 2) (Snell and Close, 1999; Campanella et al., 2000). High-pressure air injection, a tertiary oil-recovery technology used in low-permeability reservoirs (Kumar et al., 1995), was tested for the first time in the Permian basin in a pilot project in Barnhart field (Ellenburger selectively dolomitized ramp carbonate play) (Loucks et al., 2003). Artificially created, downhole high-energy, low-frequency shockwaves designed to coalesce and allow bypassed oil to be swept to producers are being tested in the Wasson South Clearfork unit (Wasson 72 field, Leonard restricted platform carbonate play).

PERMIAN BASIN PRODUCTION ANALYSIS

Production analysis of this mature basin was conducted to better understand production trends through time, by reservoir age and by lithology. Production data compiled for the 1339 significant-sized reservoirs in the 32 oil plays in the Permian basin were used as the main data source (Table 1). The remaining reserves in the Permian basin were estimated by play.

Production History and Attributes

The first large oil field (Westbrook) was discovered in the Permian basin in 1921, and other major discoveries followed in the 1920s and 1930s, including Yates

Table 2. Newly Implemented Recovery Techniques Used in Permian Basin Oil Plays*

Play Name	Reservoir-Development Techniques	References
Artesia platform sandstone	Improved waterflooding by drilling infill wells, realigning patterns, and increasing water injection	Ring and Smith (1995)
	CO_2 flooding	Ring and Smith (1995)
Queen tidal-flat sandstone	Drilling bypassed pay identified by 3-D seismic-attribute analysis	Lufholm et al. (1996)
Delaware Mountain Group basinal sandstone	CO_2 flooding	Pittaway and Rosato (1991); Flanders and DePauw (1993); Dutton et al. (2003)
	Horizontal and vertical wells drilled in areas identified by 3-D seismic-attribute analysis	Hardage et al. (1998a, b)
Grayburg high-energy platform carbonate–Ozona arch	Infill drilling guided by a 3-D reservoir model	Zahm and Tinker (2000)
Grayburg platform carbonate	CO_2 flooding	Tucker et al. (1998)
	Horizontal CO_2 injection wells	Phillips Petroleum Company (2002)
	Drilling bypassed pay identified by 3-D seismic-attribute analysis	Weinbrandt et al. (1998); Ferdinand et al. (2002)
Grayburg platform mixed clastic-carbonate	Strategic plugbacks, infill drilling, and horizontal drilling	Entzminger et al. (2000); Petersen and Jacobs (2003)
San Andres–Grayburg lowstand carbonate	CO_2 flooding	Dull (1994); Watts et al. (1998)
Upper San Andres and Grayburg platform mixed–Artesia Vacuum trend	CO_2 flooding; multilateral serpentine horizontal wells	Pranter et al. (2004)
Upper San Andres and Grayburg platform mixed–Central Basin platform trend	No information	
San Andres platform carbonate	CO_2 flooding	Magruder et al. (1990)
San Andres karst-modified platform carbonate	Gravity drainage assisted by nitrogen injection, water coproduction, and steam injection	Snell and Close (1999); Campanella et al. (2000)
Eastern shelf San Andres platform carbonate	Tiltmeter fracture mapping to establish waterflood pattern orientation, spacing, and injection rates	Griffin et al. (2000)
Northwest shelf San Andres platform carbonate	CO_2 flooding	Drozd and Gould (1991)

Table 2. Continued

Play Name	Reservoir-Development Techniques	References
Spraberry–Dean submarine-fan sandstone	Waterflooding using low-rate water injection	Schechter et al. (2001)
Bone Spring basinal sandstone and carbonate	Limited entry, two-stage stimulation	Montgomery (1997)
Leonard restricted platform carbonate	Targeted 10-ac (4-ha) infill development using a line-drive waterflood pattern	Montgomery et al. (1998); Nevans et al. (1999)
	Drilling lateral waterflood wells in unfractured intervals	Martin and Hickey (2002)
	Sinusoidal horizontal drilling	Johnson et al. (1997)
	High-energy, low-frequency shockwaves	
Abo platform carbonate	Selective perforation to prevent coning of gas cap into oil rim	Hueni and Schuessler (1993)
Wolfcamp–Leonard slope and basinal carbonate	Drilling channel facies on the basis of 3-D seismic data	Montgomery (1996)
Wolfcamp platform carbonate	Horizontal drilling	Martin et al. (2002)
Upper Pennsylvanian and Lower Permian slope and basinal sandstone	No information	
Pennsylvanian and Lower Permian Horseshoe atoll carbonate	CO_2 flooding	Raines et al. (2001); Genetti et al. (2003)
Pennsylvanian platform carbonate	No information	
Northwest shelf upper Pennsylvanian carbonate	No information	
Northwest shelf Strawn patch reef	No information	
Mississippian platform carbonate	No information	
Devonian Thirtyone ramp carbonate	Horizontal drilling	Weiner and Heyer (1999); Burkett (2002)
Devonian Thirtyone deepwater chert	CO_2 flooding	Kinder Morgan (2004)
	Tertiary infill drilling and CO_2 injection	Saller et al. (2001)
	High-pressure, lean-gas injection and infill drilling	Galloway et al. (1983); Ebanks (1988)

Table 2. Continued

Play Name	Reservoir-Development Techniques	References
Wristen buildups and platform carbonate	No information	
Fusselman shallow-platform carbonate	Recompletions and infill drilling	Ball (2003)
Simpson cratonic sandstone	No information	
Ellenburger karst-modified restricted ramp carbonate	Selective recompletions	Kerans (1988)
Ellenburger selectively dolomitized ramp carbonate	High-pressure air injection	Loucks et al. (2003)

*Waterflooding is used so commonly throughout the basin that it has not been included unless a particular pattern realignment or other modification enhanced recovery.

field in 1926 and Wasson and Slaughter fields in 1937 (Figure 9). The late 1940s and early 1950s saw additional major discoveries, including Kelly-Snyder field in 1948. Fewer major oil reservoirs were discovered after the late 1950s, when cumulative reserves discovered in the Permian basin began to level off (Figure 9).

The Permian basin produced 30.4 billion bbl (4.83×10^9 m^3) of oil through 2000. Oil production from all reservoirs in the Texas portion of the Permian basin (RRC districts 7C, 8, and 8A) was 25.6 billion bbl (4.07×10^9 m^3) (Railroad Commission of Texas, 2001). Production from all reservoirs in the New Mexico portion of the basin was 4.8 billion bbl (7.63×10^8 m^3) (Dutton et al., 2004).

A total of 1339 reservoirs in the Permian basin had individual cumulative production of greater than

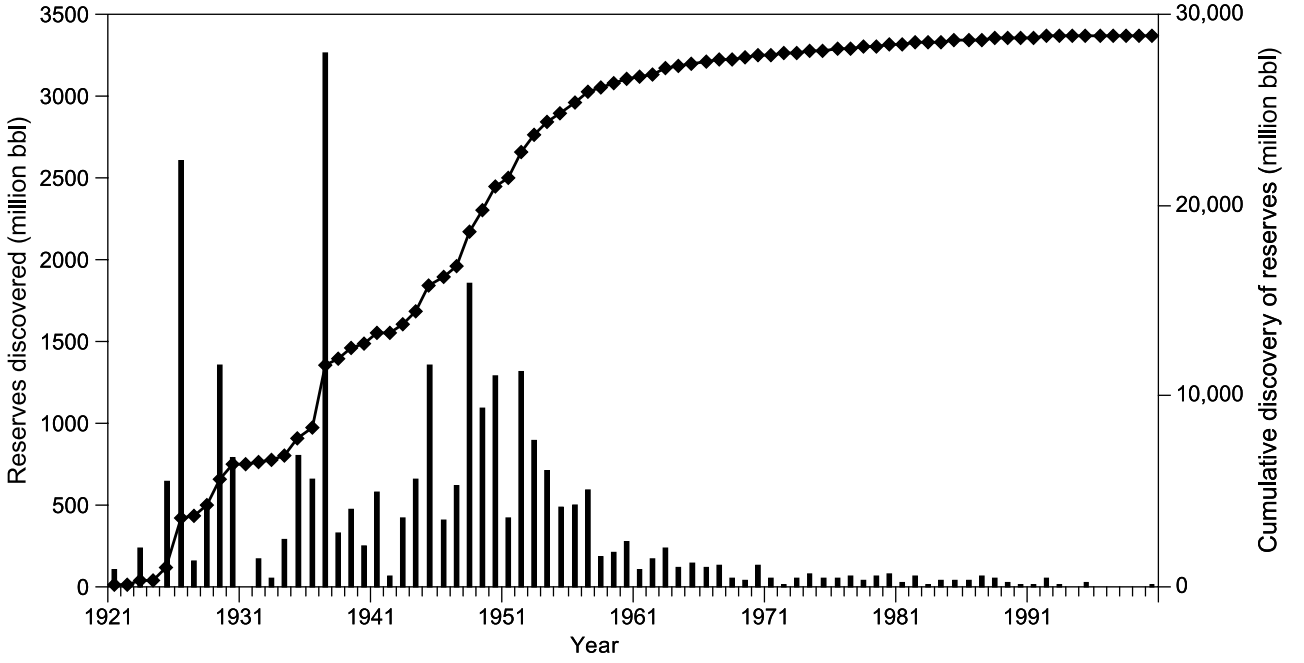

Figure 9. Permian basin cumulative oil production discovered by year. Bars show years in which reservoirs were discovered, with the height of bar indicating volume of oil produced by those reservoirs through 2000. Data are for the significant-sized reservoirs having cumulative production of greater than 1 million bbl (1.59×10^5 m^3) through 2000.

1 million bbl (1.59×10^5 m^3) through 2000. These significant-sized reservoirs produced 28.9 billion bbl (4.59×10^9 m^3) of oil through 2000 (Table 1): 24.4 billion bbl (3.88×10^9 m^3) from 1040 reservoirs in Texas and 4.5 billion bbl (7.15×10^8 m^3) from 299 reservoirs in New Mexico. Analysis of the characteristics of these significant-sized reservoirs provides valuable insight into Permian basin oil production because they account for 95% of the total production of 30.4 billion bbl (4.83×10^9 m^3) through 2000.

Production data for the significant-sized oil reservoirs in the Permian basin compiled from 1970 to 2000 show that oil production has steadily decreased. Peak production of more than 665 million bbl/yr (1.06×10^8 m^3/yr) was reached in the early 1970s. By 2000, annual oil production from significant-sized reservoirs was 301.9 million bbl (4.80×10^8 m^3) (Table 1) or less than half the peak production. Some of the largest plays in the Permian basin, the Northwest shelf San Andres platform carbonate and the Pennsylvanian and Lower Permian Horseshoe atoll carbonate plays, have experienced significant decline. By contrast, the Leonard restricted platform carbonate play has exhibited a relatively stable to slightly declining production history, and the Spraberry–Dean submarine-fan sandstone play has recorded a stable to slightly increasing production history.

Guadalupian-age reservoirs dominate cumulative oil production in the Permian basin (54%), followed by Leonardian (18%) and Pennsylvanian-age reservoirs (13%) (Figure 10a). In 2000, the proportion of oil produced from Leonardian reservoirs was 29% (Figure 10b). The increased proportion of production from Leonardian plays occurs because production from Guadalupian and Pennsylvanian plays has declined since the early 1970s, whereas Leonardian plays have a stable production trend. Carbonates are, by far, the most productive reservoirs in the Permian basin, accounting for 75% of the cumulative production. Sandstone reservoirs have produced 14%, mixed sandstone and carbonate reservoirs have produced 8%, and chert reservoirs have produced 3%. Approximately 80% of significant-sized oil reservoirs in the Permian basin produce from depths of less than 10,000 ft (<3050 m).

Remaining Reserves

The remaining reserves of significant-sized oil reservoirs in the Permian basin were estimated by play using decline-curve analysis. Because most significant-sized oil reservoirs in the Permian basin are in mature stages of production and reaching depletion, exponential decline curves were used. Historical production

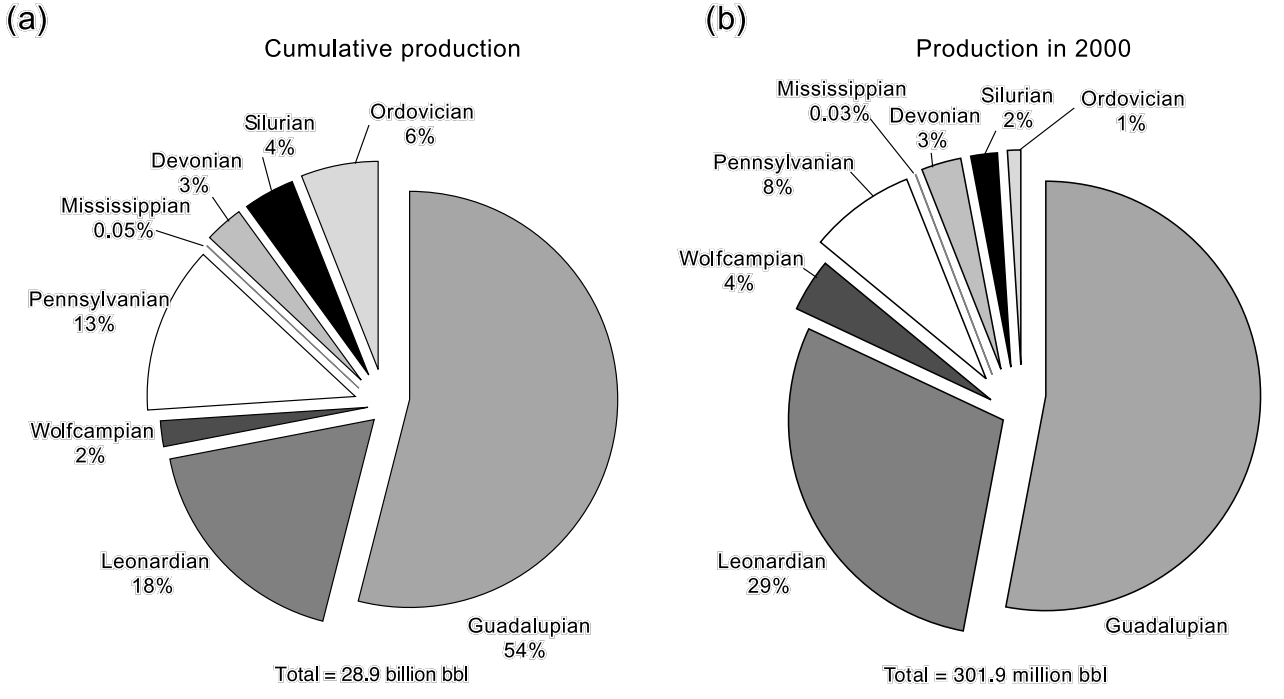

Figure 10. Permian basin production by geologic age: (a) cumulative production through 2000; (b) production in 2000.

Table 3. Permian Basin Remaining Reserves to 2015 By Play

Play	Million Barrels
Northwest shelf San Andres platform carbonate	679.8
Leonard restricted platform carbonate	665.7
San Andres platform carbonate	331.9
Spraberry–Dean submarine-fan sandstone	277.3
Pennsylvanian and Lower Permian Horseshoe atoll carbonate	139.5
Upper San Andres and Grayburg platform mixed–Artesia Vacuum trend	128.0
San Andres–Grayburg lowstand carbonate	106.9
Grayburg platform carbonate	89.8
Devonian Thirtyone deepwater chert	89.2
Grayburg platform mixed clastic-carbonate	72.7
Wolfcamp–Leonard slope and basinal carbonate	72.4
Delaware Mountain Group basinal sandstone	69.0
Eastern shelf San Andres platform carbonate	66.9
Artesia platform sandstone	61.0
Upper San Andres and Grayburg platform mixed–Central Basin platform trend	52.8
San Andres karst-modified platform carbonate	48.3
Wristen buildups and platform carbonate	44.7
Abo platform carbonate	43.4
Wolfcamp platform carbonate	41.3
Ellenburger karst-modified restricted ramp carbonate	25.2
Devonian Thirtyone ramp carbonate	19.0
Fusselman shallow-platform carbonate	17.5
Pennsylvanian platform carbonate	17.3
Grayburg high-energy platform carbonate–Ozona arch	17.2
Northwest shelf upper Pennsylvanian carbonate	17.2
Bone Spring basinal sandstone and carbonate	16.9
Upper Pennsylvanian and Lower Permian slope and basinal sandstone	11.0
Queen tidal-flat sandstone	8.0
Northwest shelf Strawn patch reef	7.9
Ellenburger selectively dolomitized ramp carbonate	3.8
Upper Pennsylvanian shelf sandstone (Permian basin portion only)	3.4
Simpson cratonic sandstone	3.2
Pennsylvanian and Lower Permian reef and bank (Permian basin portion only)	1.8
Mississippian platform carbonate	0.8
Total	**3250.9**

profiles of the 32 oil plays in the Permian basin were plotted using production data from 1970 to 2000.

The remaining reserves to be produced from the 32 oil plays in the Permian basin were calculated to year-end 2015 (Table 3). The total remaining oil reserves from significant-sized oil reservoirs are calculated at 3.25 billion bbl (5.17×10^8 m^3). The Northwest shelf San Andres platform carbonate and Leonard restricted platform carbonate plays compose more than 41% (1.34 billion bbl [2.13×10^8 m^3)]) of this total. It should be noted that the remaining reserves to be produced to year-end 2015 are that component of the resource base that has already been discovered and is currently being produced using the technologies presently in place. Most additional future production from the Permian basin will be attributable to reserve growth in existing fields.

CONCLUSIONS

The Permian basin of west Texas and southeast New Mexico remains a significant oil-producing basin. Thirty-two geologically distinct oil plays covering both the Texas and New Mexico portions of the Permian basin have been defined, and significant-sized reservoirs in the Permian basin having cumulative production of greater than 1 million bbl (1.59×10^5 m^3) of oil through 2000 were assigned to plays. The remaining oil reserves that will be produced through 2015 from the currently producing component of the resource were calculated to be 3.25 billion bbl (5.17×10^8 m^3). Application of successful reservoir-development practices to analogous reservoirs will aid in future production in this mature basin, most of which will come from improved recovery from existing fields.

REFERENCES CITED

Ahr, W. M., 2000, Carbonate pore properties as indices of reservoir quality (abs.): AAPG Annual Meeting Program, v. 13, p. A3–A4.

Ball, B. C., 2003, Identifying bypassed pay in the Fusselman and Montoya reservoirs of the Dollarhide field, Andrews County, Texas, *in* T. J. Hunt and P. H. Lufholm, eds., The Permian basin: Back to basics: West Texas Geological Society Publication 03-112, p. 1–12.

Barton, M. D., and S. P. Dutton, 1999, Outcrop analysis of a sand-rich, basin-floor turbidite system, Permian Bell Canyon Formation, west Texas: Transactions, Gulf Coast Section SEPM 19th Annual Bob F. Perkins Research Conference, December 5–8, Houston, p. 53–64.

Bebout, D. G., F. J. Lucia, C. R. Hocott, G. E. Fogg, and G. W. Vander Stoep, 1987, Characterization of the Grayburg reservoir,

University Lands Dune field, Crane County, Texas: University of Texas at Austin, Bureau of Economic Geology Report of Investigations 168, 98 p.

Behnken, F. H., 2003, Montoya conventional core description, depositional lithofacies, diagenesis and thin section petrography from the Pure Resources, Inc., Dollarhide Unit 25-2-S, Andrews County, Texas, *in* T. J. Hunt and P. H. Lufholm, eds., The Permian basin: Back to basics: West Texas Geological Society Publication 03-112, p. 13–35.

Bowring, S. A., D. H. Erwin, Y. G. Jin, M. W. Martin, K. Davidek, and W. Wang, 1998, U/Pb zircon geochronology and tempo of the end-Permian mass extinction: Science, v. 280, p. 1039–1045.

Brown, L. F. Jr., R. F. Solís-Iriarte, and D. A. Johns, 1990, Regional depositional systems tracts, paleogeography, and sequence stratigraphy, upper Pennsylvanian and Lower Permian strata, north- and west-central Texas: University of Texas at Austin, Bureau of Economic Geology Report of Investigations 197, 116 p.

Burkett, M. A., 2002, Application of horizontal drilling in low-permeability reservoirs: Transactions, Southwest Section, AAPG, Ruidoso, New Mexico, p. 139–146.

Campanella, J. D., E. E. Wadleigh, and J. R. Gilman, 2000, Flow characterization—Critical for efficiency of field operations and IOR: Society of Petroleum Engineers International Petroleum Conference, Villahermosa, Mexico, SPE Paper 58996, 14 p.

Combs, D. M., R. G., Loucks, and S. C. Ruppel, 2003, Lower Ordovician Ellenburger Group collapsed paleocave facies and associated pore network in the Barnhart field, Texas, *in* T. J. Hunt and P. H. Lufholm, eds., The Permian basin: Back to basics: West Texas Geological Society Publication 03-112, p. 397–418.

Cowan, P. E., and P. M. Harris, 1986, Porosity distribution in San Andres Formation (Permian), Cochran and Hockley counties, Texas: AAPG Bulletin, v. 70, p. 888–897.

Craig, D. H., 1988, Caves and other features of Permian karst in San Andres dolomite, Yates field reservoir, west Texas, *in* N. P. James and P. W. Choquette, eds., Paleokarst: New York, Springer-Verlag, p. 342–363.

Cys, J. M., 1986, Lower Permian grainstone reservoirs, southern Tatum basin, southeastern New Mexico, *in* J. L. Ahlen and M. E. Hanson, eds., Southwest Section of AAPG Transactions and Guidebook of 1986 Convention, Ruidoso, New Mexico: New Mexico Bureau of Mines and Mineral Resources, p. 115–120.

Drozd, J. W., and J. Gould, 1991, East Mallet unit CO_2 flood log monitoring program, Slaughter field, Hockley County, Texas, *in* M. Candelaria, ed., Permian basin plays, tomorrow's technology today: West Texas Geological Society Publication 91-89, p. 31–33.

Dull, D. W., 1994, Geostatistical method to improve permeability estimates—application to the Mabee field, Andrews and Martin Counties, Texas, *in* J. F. Gibbs, ed., Synergy equals energy-teams, tools, and techniques: West Texas Geological Society Publication 94-94, p. 23–33.

Dutton, S. P., H. H., Zirczy, T. A. Tremblay, and A. R. Scott, 2000, Update of oil and gas reservoir data base, Permian and Fort Worth basins, Texas: University of Texas at Austin, Bureau of Economic Geology, final report prepared for the U.S. Geological Survey under order no. 99CRSA1102, 31 p.

Dutton, S. P., W. A. Flanders, and M. D. Barton, 2003, Reservoir characterization of a Permian deep-water sandstone, East Ford field, Delaware basin, Texas: AAPG Bulletin, v. 87, p. 609–627.

Dutton, S. P., E. M. Kim, R. F. Broadhead, C. L. Breton, W. D. Raatz, S. C. Ruppel, and C. Kerans, 2004, Play analysis and digital portfolio of major oil reservoirs in the Permian basin: Application and transfer of advanced geological and engineering technologies for incremental production opportunities: University of Texas at Austin, Bureau of Economic Geology, final report prepared for the U.S. Department of Energy, under contract no. DE-FC26-02NT15131, 408 p.

Ebanks, W. J. Jr., 1988, Geologic description of Middle Devonian chert reservoir, Block 31 field, Crane County, Texas (abs.): AAPG Bulletin, v. 72, p. 181.

Energy Information Administration, 2003, U.S. crude oil, natural gas, and natural gas liquids reserves: 2002 annual report, DOE/EIA-0216 (2002), 48 p.

Entzminger, D. J., K. Ferdinand, D. Lawson, B. Loucks, P. Mescher, and K. Patty, 2000, Corrigan-Cowden—Breathing new life into an old waterflood, *in* W. D. DeMis, M. K. Nelis, and R. C. Trentham, eds., The Permian basin: Proving ground for tomorrow's technologies: West Texas Geological Society Publication 00-109, p. 75.

Ewing, T. E., 1990, Tectonic map of Texas: University of Texas at Austin, Bureau of Economic Geology, scale 1:750,000, 4 sheets.

Ferdinand, K. J., D. J. Entzminger, and D. Lawson, 2002, The integration of seismic attributes and rock properties for mapping porosity thickness in the heterogeneous Grayburg carbonate reservoir, Corrigan Cowden unit, west Texas, *in* T. J. Hunt and P. H. Lufholm, eds., Permian basin: Preserving our past—Securing our future: West Texas Geological Society Publication 02-111, p. 209–210.

Fischer, A. G., and M. Sarnthein, 1988, Airborne silts and dune-derived sands in the Permian of the Delaware basin: Journal of Sedimentary Petrology, v. 58, p. 637–643.

Flanders, W. A., and R. M. DePauw, 1993, Update case history: Performance of the Twofreds Tertiary CO_2 project: Proceedings, 1993 Society of Petroleum Engineers Annual Technical Conference, SPE Paper 26614, 10 p.

Frenzel, H. N., et al., 1988, The Permian basin region, *in* L. L. Sloss, ed., Sedimentary cover—North American craton; U.S.: Boulder, Colorado, Geological Society of America, The Geology of North America, v. D-2, p. 261–306.

Galley, J. D., 1958, Oil and gas geology in the Permian basin in Texas and New Mexico, *in* L. G. Weeks, ed., Habitat of oil: AAPG Symposium, p. 395–446.

Galloway, W. E., and L. F. Brown Jr., 1972, Depositional systems and shelf-slope relationships in upper Pennsylvanian rocks, north-central Texas: University of Texas at Austin, Bureau of Economic Geology Report of Investigations 75, 62 p.

Galloway, W. E., T. E. Ewing, C. M. Garrett Jr., N. Tyler, and D. G. Bebout, 1983, Atlas of major Texas oil reservoirs: University of Texas at Austin, Bureau of Economic Geology Special Publication, 139 p.

Garber, R. A., and P. M. Harris, 1990, Depositional facies of Grayburg/San Andres dolostone reservoirs, Central Basin platform, Permian basin, *in* D. G. Bebout and P. M. Harris, eds., Geologic and engineering approaches in evaluation of San Andres/Grayburg hydrocarbon reservoirs—Permian basin: University of Texas at Austin, Bureau of Economic Geology, p. 1–19.

Gardner, M. H., 1992, Sequence stratigraphy of eolian-derived turbidites: Patterns of deep water sedimentation along an arid carbonate platform, Permian (Guadalupian) Delaware Mountain Group, west Texas, *in* D. H. Mruk and B. C. Curran, eds., Permian basin exploration and production strategies: Applications of sequence stratigraphic and reservoir characterization concepts: West Texas Geological Society Publication 92-91, p. 7–12.

Genetti, D. B., C. A. Whitaker, D. P. Smith, and L. M. Price, 2003, Applying improved recovery processes and effective reservoir management to maximize oil recovery at Salt Creek: Society of Petroleum Engineers, SPE 13th Middle East Oil Show and Conference, Bahrain, April, SPE Paper 81458, 11 p.

Griffin, L. G., C. A. Wright, S. L. Demetrius, B. D. Blackburn, and D. G. Price, 2000, Identification and implications of induced hydraulic fractures in waterflood: Case history Howard Glasscock East Unit: Society of Petroleum Engineers, Permian Basin Oil and Gas Recovery Conference, Midland, Texas, SPE Paper 59525, 8 p.

Hamilton, D. C., and G. B. Asquith, 2000, Depositional, diagenetic, and production histories of Chester ooid grainstones in the Austin (upper Mississippian) field: Lea County, New Mexico, *in* W. D. DeMis, M. K. Nelis, and R. C. Trentham, eds., The Permian basin: Proving ground for tomorrow's technologies: West Texas Geological Society Publication 00-109, p. 95–106.

Handford, C. R., 1981, Sedimentology and genetic stratigraphy of Dean and Spraberry formations (Permian), Midland basin, Texas: AAPG Bulletin, v. 65, p. 1602–1616.

Handford, C. R., M. P. Candelaria, and S. Lafollette, 1996, Accommodation cycles in peritidal carbonate and continental to shoreface siliciclastic facies, San Andres–Grayburg formations, Eddy County, New Mexico, *in* R. L. Martin, ed., Permian basin oil and gas fields: Keys to success that unlock future reserves: West Texas Geological Society Publication 96-101, p. 65–80.

Hanson, B. M., et al., 1991, The Permian basin, *in* H. J. Gluskoter, D. D. Rice, and R. B. Taylor, eds., Economic Geology, U.S.: Geological Society of America, The Geology of North America, v. P-2, p. 339–356.

Hardage, B. A., V. M. Pendleton, J. L. Simmons Jr., B. A. Stubbs, and B. J. Uszynski, 1998a, 3-D instantaneous frequency used as a coherency/continuity parameter to interpret reservoir compartment boundaries across an area of complex turbidite deposition: Geophysics, v. 63, p. 1520–1531.

Hardage, B. A., J. L. Simmons Jr., V. M. Pendleton, B. A. Stubbs, and B. J. Uszynski, 1998b, 3-D seismic imaging and interpretation of Brushy Canyon slope and basin thin-bed reservoirs, northwest Delaware basin: Geophysics, v. 63, p. 1507–1519.

Harland, W. B., R. L. Armstrong, A. V. Cox, L. E. Craig, A. G. Smith, and D. G. Smith, 1989, A geologic time scale: Cambridge, Cambridge University Press, 263 p.

Harris, D. C., 1990, Ramp buildups in the lower Strawn limestone (Penn.): Controls on stratigraphic reservoir variability, *in* J. E. Flis and R. C. Price, eds., Permian basin oil and gas fields: Innovative ideas in exploration and development: West Texas Geological Society Publication 90-87, p. 91–101.

Heckel, P. H., 1986, Sea-level curve for Pennsylvanian eustatic marine transgressive-regressive depositional cycles along the midcontinent outcrop belt, North America: Geology, v. 14, p. 330–334.

Hill, R. J., D. M. Jarvie, B. L. Claxton, J. D. Burgess, M. H. Tobey, and J. A. Williams, 2004, Petroleum systems of the Permian basin (abs.): AAPG Annual Meeting Program, v. 13, p. A63.

Hills, J. M., 1984, Sedimentation, tectonism, and hydrocarbon generation in Delaware basin, west Texas and southeastern New Mexico: AAPG Bulletin, v. 68, p. 250–267.

Hobson, J. P., C. D. Caldwell, and D. F. Toomey, 1985, Early Permian deep-water allochthonous limestone facies and reservoir, west Texas: AAPG Bulletin, v. 69, p. 2130–2147.

Holtz, M. H., 1993, Estimating oil reserve variability by combining geologic and engineering parameters: Society of Petroleum Engineers Hydrocarbon Economics and Evaluation Symposium, Dallas, Texas, SPE Paper 25827, p. 85–95.

Holtz, M. H., 1994, McFarland (Queen) reservoir, *in* Selected oil and gas fields in west Texas, part VI: West Texas Geological Society Publication 94-96, p. 171–176.

Holtz, M. H., and C. M. Garrett Jr., 1997, Play analysis and resource assessment of Texas state lands, *in* R. P. Major, ed., Oil and gas on Texas state lands: An assessment of the resource and characterization of type reservoirs: University of Texas at Austin, Bureau of Economic Geology Report of Investigations 241, p. 1–30.

Holtz, M. H., and C. Kerans, 1992, Characterization and categorization of west Texas Ellenburger reservoirs, *in* M. P. Candelaria and C. L. Reed, eds., Paleokarst, karst-related diagenesis, and reservoir development: Examples from Ordovician–Devonian age strata of west Texas and the mid-continent: Permian Basin Section SEPM, Field Trip Guidebook, v. 92-33, p. 45–54.

Hueni, G. B., and K. L. Schuessler, 1993, Associated gas reservoirs, *in* Atlas of major Rocky Mountain gas reservoirs: New Mexico Bureau of Mines and Mineral Resources, p. 190.

Johnson, I. G., J. L. Brown, and G. B. Asquith, 1997, Using sinusoidal drilling techniques in a diagenetically complex carbonate reservoir: West Dollarhide Drinkard unit (mid-Leonardian), Lea County, southeast New Mexico, *in* W. D. DeMis, ed., Permian basin oil and gas fields: Turning ideas into production: West Texas Geological Society Publication 97-102, p. 93–95.

Kerans, C., 1988, Karst-controlled reservoir heterogeneity in Ellenburger Group carbonates of west Texas: AAPG Bulletin, v. 72, p. 1160–1183.

Kerans, C., 1990, Depositional systems and karst geology of the Ellenburger Group (Lower Ordovician), subsurface west Texas: University of Texas at Austin, Bureau of Economic Geology Report of Investigations 193, 37 p.

Kerans, C., 2000, Stratigraphic architecture and paleokarst development within the Abo (Leonardian 1) composite sequence, Apache Canyon and Kingdom Abo field, Permian basin, *in* S. T. Reid, Southwest Section AAPG 2000 Convention Transactions: West Texas Geological Society Publication SWS 2000-107, p. 250.

Kerans, C., 2001, Stratigraphic and diagenetic controls on reservoir architecture of a non-reefal icehouse isolated platform—Sacroc unit, Horseshoe atoll, Texas (abs.): AAPG Bulletin, v. 85, p. 386–387.

Kerans, C., and W. M. Fitchen, 1995, Sequence hierarchy and facies architecture of a carbonate-ramp system: San Andres Formation of Algerita escarpment and western Guadalupe Mountains, west Texas and New Mexico: University of Texas at Austin, Bureau of Economic Geology Report of Investigations 235, 86 p.

Kerans, C., K. Kempter, and J. Rush, 2000, Facies and stratigraphic controls on a coastal paleokarst, Lower Permian, Apache Canyon, west Texas, *in* R. Lindsay, R. Trentham, R. F. Ward, and A. H. Smith, eds., Classic Permian geology of west Texas and southeastern New Mexico, 75 years of Permian basin oil and gas exploration and development: West Texas Geological Society Publication 00-108, p. 55–81.

Kinder Morgan, 2004, North Cross Devonian unit http://www.kindermorgan.com/business/co2/success_north_cross.cfm (accessed December 7, 2004).

Kosters, E. C., D. G. Bebout, S. J. Seni, C. M. Garrett Jr., L. F. Brown Jr., H. S. Hamlin, S. P. Dutton, S. C. Ruppel, R. J. Finley, and N. Tyler, 1989, Atlas of major Texas gas reservoirs: University of Texas at Austin, Bureau of Economic Geology Special Publication, 161 p.

Kumar, V. K., M. R. Fassihi, and D. V. Yannimaras, 1995, Case history and appraisal of the Medicine Pole Hills unit air-injection project: Society of Petroleum Engineers Reservoir Engineering, v. 10, no. 3, p. 198–202.

Lindsay, R. F., 1991, Grayburg Formation (Permian–Guadalupian): Comparison of reservoir characteristics and sequence stratigraphy in the northwest Central Basin platform with outcrops in the Guadalupe Mountains, New Mexico, *in* S. Meader-Roberts, M. P. Candelaria, and G. E. Moore, eds., Sequence stratigraphy, facies, and reservoir geometries of the San Andres, Grayburg, and Queen formations, Guadalupe Mountains, New

Mexico and Texas: Permian Basin Section SEPM Publication 91-32, p. 111–118.

Loucks, R. G., 1999, Paleocave carbonate reservoirs: Origins, burial-depth modifications, spatial complexity, and reservoir implications: AAPG Bulletin, v. 83, p. 1795–1834.

Loucks, R. G., A. A. Brown, C. W. Achauer, and D. A. Budd, 1985, Carbonate gravity flow sedimentation on low angle slopes off the Wolfcampian Northwest shelf of the Delaware basin, *in* P. D. Crevello and P. M. Harris, eds., Deep-water carbonates—A core workshop: SEPM Core Workshop 6, p. 56–92.

Loucks, R. G., S. Ruppel, J. F. W. Stowell, J. Holder, J. Olsen, D. Combs, D. Dembla, and L. Gomez, 2003, High-pressure air injection: Application in a fractured and karsted dolomite reservoir: University of Texas at Austin, Bureau of Economic Geology, and Goldrus Producing Company, semi-annual report prepared for the U.S. Department of Energy under DOE Award Number DE-FC26-02NT15442, 20 p. + 32 figures.

Lufholm, P., G. Watts, and L. Lofton, 1996, Improved reservoir modeling using gridded seismic attributes: North Concho Bluff field, west Texas, *in* R. L. Martin, ed., Permian basin oil and gas fields: Keys to success that unlock future reserves: West Texas Geological Society Publication 96-101, p. 145–159.

Magruder, J. B., L. H. Stiles, and T. D. Yelverton, 1990, Review of the means San Andres unit full-scale CO_2 tertiary project: Journal of Petroleum Technology, v. 42, no. 5, p. 638–644.

Martin, R. L., and K. F. Hickey, 2002, Horizontal drilling at Vacuum Glorieta West unit, Lea County, New Mexico: A case history, *in* T. J. Hunt and P. H. Lufholm, eds., The Permian basin: Preserving our past—Securing our future: West Texas Geological Society Publication 02-111, p. 117–124.

Martin, R. L., C. L. Welch, G. D. Hinterlong, J. Meyer, and R. Evans, 2002, Using crosswell seismic tomography to provide better resolution in the Wolfcamp Formation in Lea County, New Mexico, *in* T. J. Hunt and P. H. Lufholm, eds., The Permian basin: Preserving our past—Securing our future: West Texas Geological Society Publication 02-111, p. 25–34.

Mazzullo, S. J., 1997, Stratigraphic exploration plays in Ordovician to Lower Permian strata in the Midland basin and on the Eastern shelf, *in* W. D. DeMis, ed., Permian basin oil and gas fields: Turning ideas into production: West Texas Geological Society Publication 97-102, p. 1–37.

Mazzullo, S. J., and A. M. Reid, 1987, Basinal Lower Permian facies, Permian basin: Part II. Depositional setting and reservoir facies of Wolfcampian–lower Leonardian basinal carbonates: West Texas Geological Society Bulletin, v. 26, no. 8, p. 5–10.

Montgomery, S. L., 1996, Permian ''Wolfcamp'' limestone reservoirs: Powell Ranch field, eastern Midland basin: AAPG Bulletin, v. 80, p. 1349–1365.

Montgomery, S. L., 1997, Permian Bone Spring Formation: Sandstone play in the Delaware basin: Part I. Slope: AAPG Bulletin, v. 81, p. 1239–1258.

Montgomery, S. L., D. K. Davies, R. K. Vessell, J. E. Kamis, and W. H. Dixon, 1998, Permian Clear Fork Group, North Robertson unit: Integrated reservoir management and characterization for infill drilling: Part II. Petrophysical and engineering data: AAPG Bulletin, v. 82, p. 1985–2002.

Montgomery, S. L., D. S. Schechter, and J. C. Lorenz, 2000, Advanced reservoir characterization to evaluate carbon dioxide flooding, Spraberry Trend, Midland basin, Texas: AAPG Bulletin, v. 84, p. 1247–1273.

Mooney, T. D., 1982, Howard Glasscock, *in* Selected oil and gas fields in west Texas: West Texas Geological Society Publication 82-75, p. 323–337.

Neuberger, D. J., 1987, Swastika (upper Pennsylvanian) shelf-margin deltas and delta-fed turbidites, Flowers ''Canyon Sand field'' area, Stonewall County, Texas: Master's Thesis, University of Texas at Austin, Austin, Texas, 171 p.

Nevans, J. W., J. E. Kamis, D. K. Davies, R. K. Vessell, L. E. Doublet, and T. A. Blasingame, 1999, An integrated geologic and engineering reservoir characterization of the North Robertson (Clear Fork) unit, Gaines County, Texas, *in* R. A. Schatzinger and J. F. Jordan, eds., Reservoir characterization—Recent advances: AAPG Memoir 71, p. 109–124.

New Mexico Bureau of Mines and Mineral Resources, 1993, Atlas of major Rocky Mountain gas reservoirs: New Mexico Bureau of Mines and Mineral Resources, 206 p.

New Mexico Oil and Gas Engineering Committee, 1993, Annual report of the New Mexico Oil and Gas Engineering Committee, v. 1A, southeast New Mexico: Hobbs, New Mexico, New Mexico Oil and Gas Engineering Committee, Inc., 703 p.

Petersen, L. M., and R. S. Jacobs, 2003, Stratigraphic and lithologic zonation in the East Cowden Grayburg unit, Ector County, Texas: Potential for horizontal redevelopment of a mature waterflood, *in* T. J. Hunt and P. H. Lufholm, eds., The Permian basin: Back to basics: West Texas Geological Society Publication 03-112, p. 119–121.

Phillips Petroleum Company, 2002, Design and implementation of a CO_2 flood utilizing advanced reservoir characterization and horizontal injection wells in a shallow shelf carbonate approaching waterflood depletion: Phillips Petroleum Company, final report prepared for U.S. Department of Energy, Assistant Secretary for Fossil Energy, under contract no. DE-FC22-94BC14991, 450 p.

Pittaway, K. R., and R. J. Rosato, 1991, The Ford Geraldine unit CO_2 flood-update 1990: Society of Petroleum Engineers Reservoir Engineering, v. 6, no. 4, p. 410–414.

Pranter, M. J., N. F. Hurley, T. L. Davis, M. A. Raines, and S. C. Wehner, 2004, Dual-lateral horizontal wells successfully target bypassed pay in the San Andres Formation, Vacuum field, New Mexico: AAPG Bulletin, v. 88, p. 99–113.

Price, C., C. Ryu, and J. Mazzullo, 2000, Lithofacies, depositional environments, and reservoir properties of the Permian (Guadalupian) Grayburg and Queen formations, Means field, Andrews County, Texas, *in* S. T. Reid, ed., Geo-2000: Into the future: Transactions of the Southwest Section AAPG, Publication SWS 2000-107, p. 80–97.

Railroad Commission of Texas, 2001, 2000 Oil and gas annual report, v. I: Austin, Texas, Railroad Commission of Texas Oil and Gas Division, 454 p.

Raines, M. A., J. K. Dobitz, and S. C. Wehner, 2001, A review of the Pennsylvanian SACROC unit, *in* J. J. Viveiros and S. M. Ingram, eds., The Permian basin: Microns to satellites, looking for oil and gas at all scales: West Texas Geological Society Publication 01-110, p. 67–74.

Ramondetta, P. J., 1982, Facies and stratigraphy of the San Andres Formation, northern and northwestern shelves of the Midland basin, Texas and New Mexico: University of Texas at Austin, Bureau of Economic Geology Report of Investigations 128, 56 p.

Reid, A. M., and S. A. T. Reid, 1991, The Cogdell field study, Kent and Scurry counties, Texas: A post-mortem, *in* M. Candelaria, ed., Permian basin plays, tomorrow's technology today: West Texas Geological Society Publication 91-89, p. 39–66.

Reid, A. M., and S. A. T. Reid, 1999, Glacio-eustatic sea level fluctuations and the formation of Pennsylvanian age carbonate reservoirs in the Permian basin of west Texas, *in* D. T. Grace and G. D. Hinterlong, eds., The Permian basin: Providing energy for America: West Texas Geological Society Publication 99-106, p. 71–79.

Ring, J. N., and D. J. Smith, 1995, An overview of the North Ward–Estes CO_2 flood: Society of Petroleum Engineers Annual Technical Conference, SPE Paper 30729, p. 293–300.

Root, D. H., E. D. Attanasi, R. F. Mast, and D. L. Gautier, 1995, Estimates of inferred reserves for the 1995 U.S. Geological Survey national oil and gas resource assessment: U.S. Geological Survey Open-File Report 95-75L, 29 p.

Ruppel, S. C., 2001, Opportunities for recovery of remaining oil in San Andres reservoirs: Example from Fuhrman-Mascho field, University Lands Block 10, Andrews County, Texas, *in* J. J. Viveiros and S. M. Ingram, eds., The Permian basin: Microns to satellites, looking for oil and gas at all scales: West Texas Geological Society Publication 01-110, p. 105–125.

Ruppel, S. C., 2002, Geological controls on reservoir development in a Leonardian (Lower Permian) carbonate platform reservoir, Monahans field, west Texas: University of Texas at Austin, Bureau of Economic Geology Report of Investigations 266, 58 p.

Ruppel, S. C., and R. J. Barnaby, 2001, Contrasting styles of reservoir development in proximal and distal chert facies: Devonian Thirtyone Formation, Texas: AAPG Bulletin, v. 84, p. 7–34.

Ruppel, S. C., and H. S. Cander, 1988, Effects of facies and diagenesis on reservoir heterogeneity: Emma San Andres field, west Texas: University of Texas at Austin, Bureau of Economic Geology Report of Investigations 178, 67 p.

Ruppel, S. C., and M. H. Holtz, 1994, Depositional and diagenetic facies patterns and reservoir development in Silurian and Devonian rocks of the Permian basin: University of Texas at Austin, Bureau of Economic Geology Report of Investigations 216, 89 p.

Ruppel, S. C., and F. J. Lucia, 1996, Diagenetic control of permeability development in a highly cyclic, shallow water carbonate reservoir: South Cowden Grayburg field, Ector County, Texas, *in* R. L. Martin, ed., Permian basin oil and gas fields: Keys to success that unlock future reserves: West Texas Geological Society Publication No. 96-101, p. 7–24.

Saller, A. H., J. W. Barton, and R. E. Barton, 1989, Mescalero Escarpe field, oil from carbonate slope detritus, southeastern New Mexico, *in* J. E. Flis, R. C. Price, and J. F. Sarg, eds., Search for the subtle trap, hydrocarbon exploration in mature basins: West Texas Geological Society Publication 89-85, p. 59–74.

Saller, A. H., J. A. D. Dickson, and S. A. Boyd, 1994, Cycle stratigraphy and porosity in Pennsylvanian and Lower Permian shelf limestones, eastern Central Basin platform, Texas: AAPG Bulletin, v. 78, p. 1820–1842.

Saller, A. H., J. A. D. Dickson, and F. Matsuda, 1999, Evolution and distribution of porosity associated with subaerial exposure in upper Paleozoic platform limestones, west Texas: AAPG Bulletin, v. 83, p. 1835–1854.

Saller, A. H., B. Ball, S. Robertson, B. McPherson, C. Wene, R. Nims, and J. Gogas, 2001, Reservoir characteristics of Devonian cherts and their control on oil recovery: Dollarhide field, west Texas: AAPG Bulletin, v. 85, p. 35–50.

Schechter, D. S., E. Putra, R. O. Baker, W. H. Knight, W. P. McDonald, P. Leonard, and C. Rounding, 2001, CO_2 pilot design and water injection performance in the naturally fractured Spraberry Trend area, west Texas: Society of Petroleum Engineers Paper 71605, 16 p.

Silver, B. A., and R. G. Todd, 1969, Permian cyclic strata, northern Midland and Delaware basins, west Texas and southeastern New Mexico: AAPG Bulletin, v. 53, p. 2223–2251.

Snell, J. S., and A. D. Close, 1999, Yates field steam pilot applies latest seismic and logging monitoring techniques: Society of Petroleum Engineers Annual Technical Conference, Houston, Texas, SPE Paper 56791, 10 p.

Suhm, R. W., and R. L. Ethington, 1975, Stratigraphy and conodonts of Simpson Group (Middle Ordovician), Beach and Baylor Mountains, west Texas: AAPG Bulletin, v. 59, p. 1126–1135.

Tinker, S. W., 1996, Building the 3-D jigsaw puzzle: Applications of sequence stratigraphy to 3-D reservoir characterization, Permian basin: AAPG Bulletin, v. 80, p. 460–485.

Tinker, S. W., J. R. Ehrets, and M. D. Brondos, 1995, Multiple karst events related to stratigraphic cyclicity: San Andres Formation, Yates field, west Texas, *in* D. A. Budd, A. H. Saller, and P. M. Harris, eds., Unconformities and porosity in carbonate strata: AAPG Memoir 63, p. 213–237.

Tucker, K. E., P. M. Harris, and R. C. Nolen-Hoeksema, 1998, Geologic investigation of cross-well seismic response in a carbonate reservoir, McElroy field, west Texas: AAPG Bulletin, v. 82, p. 1463–1503.

Tucker, R. D., and W. S. McKerrow, 1994, Early Paleozoic chronology: A review in light of new U-Pb ages from Newfoundland and Britain: Canadian Journal of Earth Sciences, v. 32, p. 368–379.

Tyler, N., and N. J. Banta, 1989, Oil and gas resources remaining in the Permian basin: Targets for additional hydrocarbon recovery: University of Texas at Austin, Bureau of Economic Geology Geological Circular 89-4, 20 p.

Tyler, N., et al., 1991, Integrated characterization of Permian basin reservoirs, University Lands, west Texas: Targeting the remaining resource for advanced oil recovery: University of Texas at Austin, Bureau of Economic Geology Report of Investigations 203, 136 p.

Tyler, N., J. C. Ghoston, and E. H. Guevara, 1997, Basin morphological controls on submarine-fan depositional trends: Spraberry Sandstone, Permian basin, Texas: University of Texas at Austin, Bureau of Economic Geology Geological Circular 97-6, 43 p.

Vest, E. L., 1970, Oil fields of Pennsylvanian–Permian Horseshoe atoll, west Texas, *in* M. T. Halbouty, ed., Geology of giant petroleum fields: AAPG Memoir 14, p. 185–203.

Wahlman, G. P., 2001, Pennsylvanian–Lower Permian mounds and reefs in the Permian basin (west Texas–New Mexico): Composition, evolution, distribution, and reservoir characteristics, *in* J. J. Viveiros and S. M. Ingram, eds., The Permian basin: Microns to satellites, looking for oil and gas at all scales: West Texas Geological Society Publication 01-110, p. 57–64.

Ward, R. F., C. G. St. C. Kendall, and R. M. Harris, 1986, Upper Permian (Guadalupian) facies and their association with hydrocarbons—Permian basin, west Texas and New Mexico: AAPG Bulletin, v. 70, p. 239–262.

Watts, G. P., G. D. Hinterlong, and A. R. Taylor, 1998, Seismic description of a complex carbonate porosity system; Welch field, Permian basin, Texas, *in* W. D. DeMis and M. K. Nelis, eds., The search continues into the 21st century: West Texas Geological Society Publication 98-105, p. 223–229.

Weinbrandt, R. M., R. C. Trentham, and W. Robinson, 1998, Incorporating seismic attribute porosity into a flow model of the Grayburg reservoir in the Foster-South Cowden field, *in* W. D. DeMis and M. K. Nelis, eds., The search continues into the 21st century: West Texas Geological Society Publication 98-105, p. 231–238.

Weiner, S., and J. Heyer, 1999, Geological model of a highly compartmentalized reservoir: The Devonian Thirtyone Formation, University Block 9 field, *in* D. T. Grace and G. D. Hinterlong, eds., The Permian basin: Providing energy for America: West Texas Geological Society Publication 99-106, p. 1–8.

White, D. A., 1980, Assessing oil and gas plays in facies-cycle wedges: AAPG Bulletin, v. 64, p. 1158–1178.

Wiggins, W. D., and P. M. Harris, 1985, Burial diagenetic sequence in deep-water allochthonous dolomites, Permian Bone Spring Formation, southeast New Mexico, *in* P. D. Crevello and P. M. Harris, eds., Deep-water carbonates: Buildups, turbidites, debris flows and chalks—A core workshop: SEPM Core Workshop 6, p. 140–173.

Zahm, L. C., and S. W. Tinker, 2000, 3-D reservoir characterization in the absence of seismic; Olson field, San Andres/Grayburg, west Texas: AAPG Annual Meeting Program, v. 9, p. A165.

WolfBone Play Evolution, Southern Delaware Basin: Geologic Concept Modifications That Have Enhanced Economic Success*

Bill Fairhurst[1], Mary Lisbeth Hanson[1], Frank Reid[1], and Nick Pieracacos[1]

Search and Discovery Article #10412 (2012)**
Posted June 18, 2012

*Adapted from oral presentation given at AAPG 2012 Southwest Section Meeting, Ft. Worth, Texas, May 19-22, 2012
Please refer to a closely companion article, entitled "Evolution and Development of the WolfBone Play, Southern Delaware Basin, West Texas: An emerging frontier: An oil-rich unconventional resource," Search and Discovery Article #10411 (2012).
**AAPG©2012 Serial rights given by author. For all other rights contact author directly.

[1]Eagle Oil & Gas, Co., Dallas, Texas (Bill.Fairhurst@eagleog.com)

Abstract

The WolfBone play is an emerging unconventional oil resource. Exploration and development have been a systematic evolution from geologic concept to drilling, evaluation, and revision of targets. Originally, Wolfcamp sandstone reservoirs below and Third Bone Spring sandstone reservoirs above the Wolfcampian shale source section were targeted. Current drilling and production are focused on the 1000-ft-thick, oil-rich, unconventional Wolfcamp shale.

The Wolfcamp is an ideal heterogenetic resource consisting of quartz, carbonate, and kerogen. Exploration and field development will be successful over a large area. However, the geologic and economic sweet spot is limited to the basin floor. In this setting quartz and kerogen accumulated in the quiet deep basin interrupted by episodic deposition of shelf to basin-floor carbonate debris flows that settled basinward of the deceleration boundary. These depositional processes resulted in compositional and grain-size heterogeneities and accumulation of the thick organic-rich targets.

During maturation large volumes of oil were sealed in place (108 MMBOIP per section). Expansion from kerogen to oil in a sealed system resulted in overpressure and abundant fracturing that has resulted in enhanced productivity. Individual wells have flowed 45 MBO from 11,000 ft prior to initiating artificial lift, which is atypical of Permian Basin reservoirs. Farther into the basin and upslope these conditions do not exist and are outside the economic sweet spot. Basinward, the unit is consistently thick; however, there is more shale, and the section is starved of siltstones and carbonates. Upslope, the unit thins and is more gas-prone. In these slope environments the mixture of coarser-grained shelf carbonates and sandstones breached the system, providing migration pathways which have limited productivity and lower ultimate economic recoveries.

Since 2009, this play has been developed with vertical wells comingling the oil resource with conventional reservoirs. Interpretation of imaging logs has identified the primary fracture orientation and zones with conjugate fractures systems. Integration with production logs has optimized horizontal target identification, and horizontal drilling has begun. The Leonardian Avalon sweet spots occur at similar depositional setting as the Wolfcampian resource and the same geographic position in this portion of the basin. The Avalon is estimated to have 103 MMBOIP per section.

References

Fitchen, W.M., 1997,Carbonate sequence stratigraphy and its application to hydrocarbon exploration and reservoir development, *in* I. Palaz, and K.J. Marfurt (eds.), Carbonate Seismology: SEG Geophysical Development Series, no. 6, p. 121-178.

Wright, W.F., 1962, Abo reef: prime West Texas target, Parts 1 and 2: Oil and Gas Journal, Part 1, v. 60/31, p. 226-235, Part 2, v. 60/32, p. 188-194.

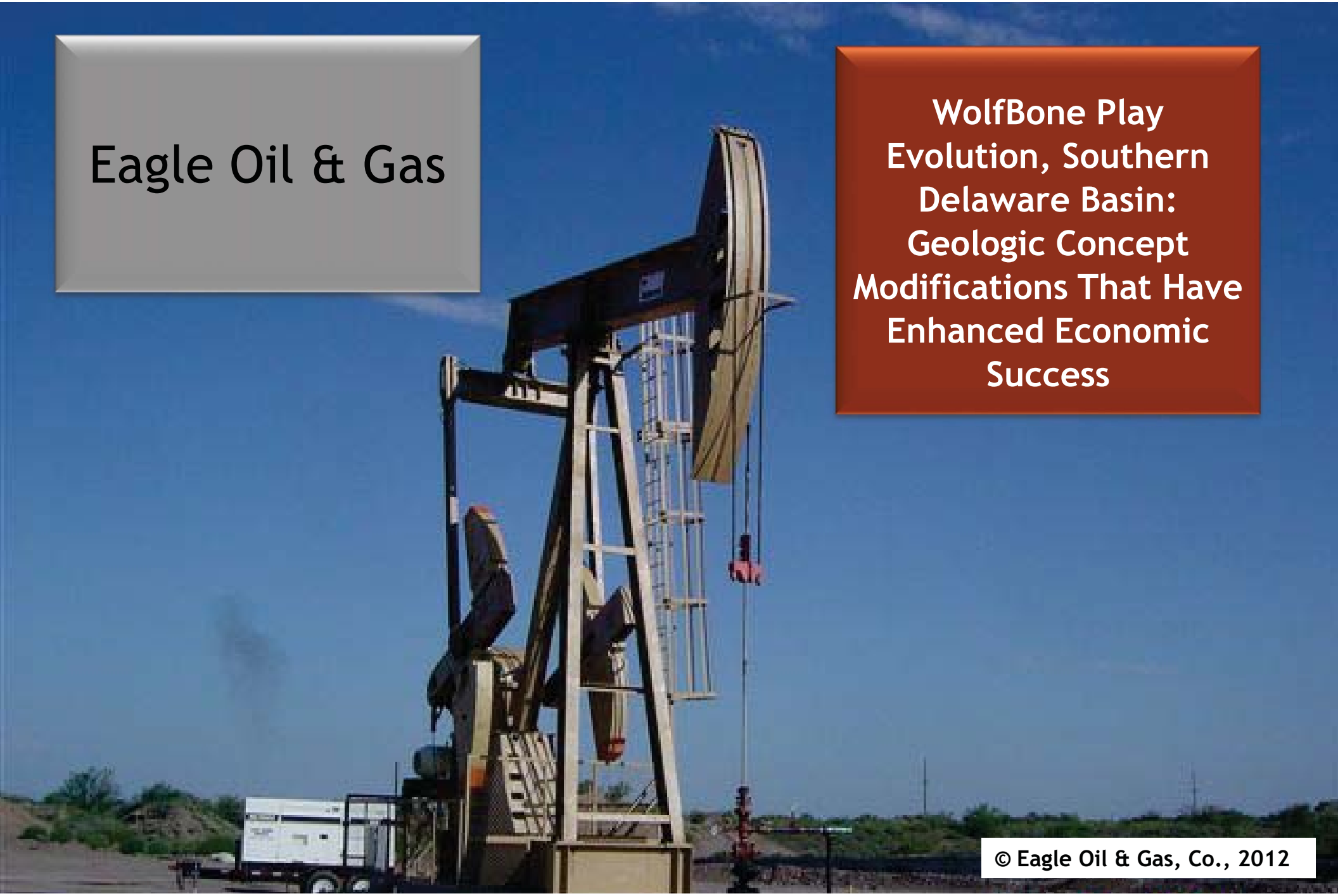

Eagle Oil & Gas

WolfBone Play Evolution, Southern Delaware Basin: Geologic Concept Modifications That Have Enhanced Economic Success

© Eagle Oil & Gas, Co., 2012

Fairhurst, Bill; Hanson, Mary Lisbeth; Reid, Frank; and Pieracacos, Nick

EAGLE OIL & GAS CO.

WolfBone Play Evolution, Southern Delaware Basin: Geologic Concept Modifications That Have Enhanced Economic Success

© Eagle Oil & Gas, Co., 2012

Bill Fairhurst, Mary Lisbeth Hanson, Frank Reid, and Nick Pieracacos
Eagle Oil & Gas, Co., Dallas, Texas
5950 Berkshire Lane, Suite 1100
Dallas, Texas 75225
214/323-4515
832/928-5303

The WolfBone play is an emerging unconventional oil resource. Exploration and development have been a systematic evolution from geologic concept to drilling, evaluation, and revision of targets. Originally, Wolfcamp sandstone reservoirs below and Third Bone Spring sandstone reservoirs above the Wolfcampian shale source section were targeted. Current drilling and production are focused on the 1000-ft-thick, oil-rich, unconventional Wolfcamp shale.

The Wolfcamp is an ideal heterogenetic resource consisting of quartz, carbonate, and kerogen. Exploration and field development will be successful over a large area. However, the geologic and economic sweet spot is limited to the basin floor. In this setting quartz and kerogen accumulated in the quiet deep basin interrupted by episodic deposition of shelf to basin-floor carbonate debris flows that settled basinward of the deceleration boundary. These depositional processes resulted in compositional and grain-size heterogeneities and accumulation of the thick organic-rich targets.

During maturation large volumes of oil were sealed in place (108 MMBOIP per section). Expansion from kerogen to oil in a sealed system resulted in overpressure and abundant fracturing that has resulted in enhanced productivity. Individual wells have flowed 45 MBO from 11,000 ft prior to initiating artificial lift, which is atypical of Permian Basin reservoirs. Farther into the basin and upslope these conditions do not exist and are outside the economic sweet spot. Basinward, the unit is consistently thick; however, there is more shale, and the section is starved of siltstones and carbonates. Upslope, the unit thins and is more gas-prone. In these slope environments the mixture of coarser-grained shelf carbonates and sandstones breached the system, providing migration pathways which have limited productivity and lower ultimate economic recoveries.

Since 2009, this play has been developed with vertical wells comingling the oil resource with conventional reservoirs. Interpretation of imaging logs has identified the primary fracture orientation and zones with conjugate fractures systems. Integration with production logs has optimized horizontal target identification, and horizontal drilling has begun. The Leonardian Avalon sweet spots occur at similar depositional setting as the Wolfcampian resource and the same geographic position in this portion of the basin. The Avalon is estimated to have 103 MMBOIP per section.

Overview - Location

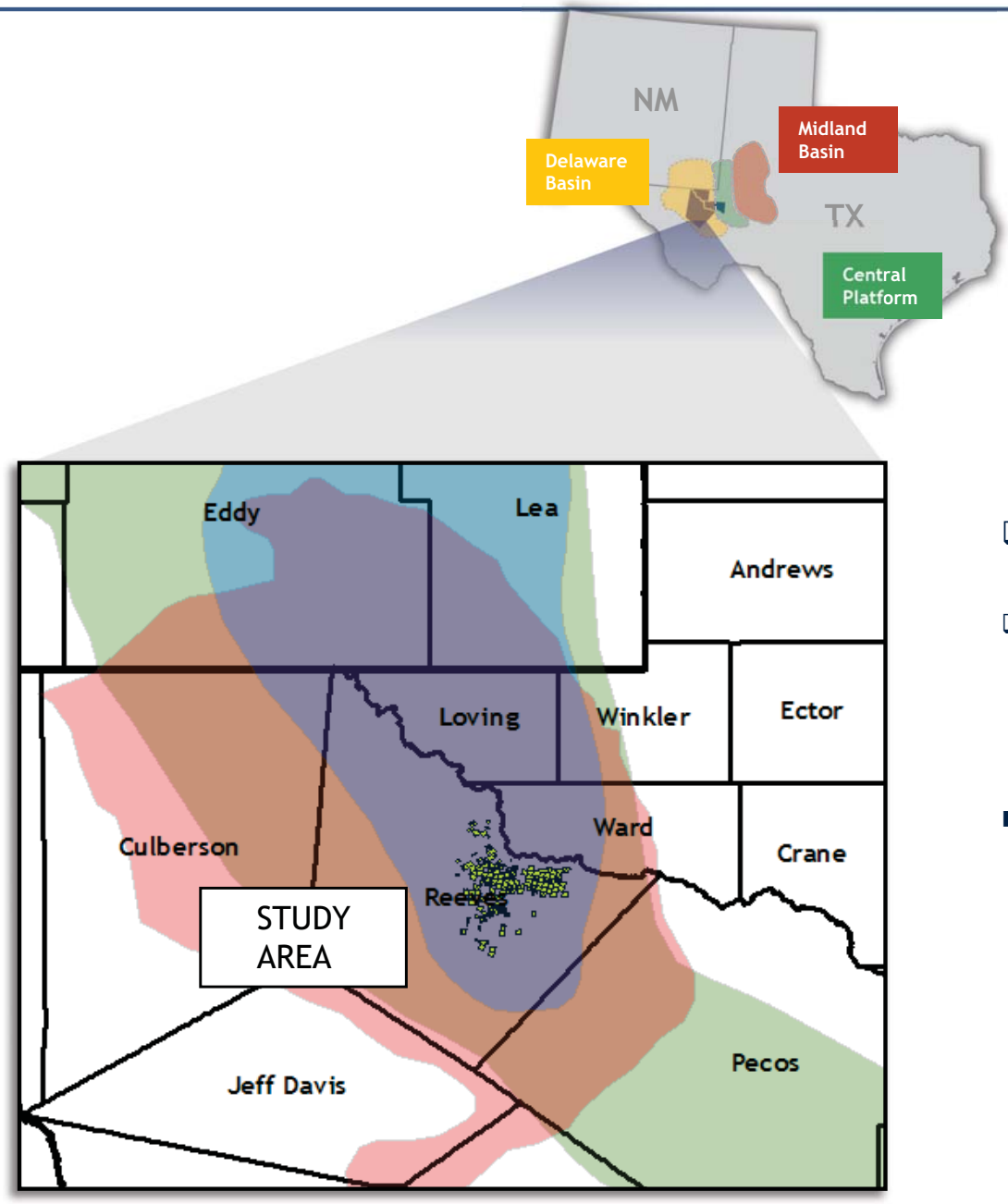

- Most active US basin with 433 rigs (Delaware Basin: 214), Hz Rigs: ~35%(1)
- *Total Resource in place per section: 108 Mmboe*
  - *Horizontal Development:*
    - *Alternative Wolfcamp development strategy modeled*
    - *3rd Bone Spring development*
- ***Upside Potential***
  - Horizontal resource in Avalon Shale
    - Avalon Shale - 105 MMboe in place per section
  - Delaware Sands – ongoing vertical & horizontal exploitation
  - Vertical drilling targeting deeper gas zones

© Eagle Oil & Gas, Co., 2012

(1) Source: RigData, TPH. Hz % includes horizontal and directional rigs. As of September 30, 2011, or most recent data available.

Production from the Permian System

Summary

- Permian system comprised of multiple basins:
  - Delaware Basin
  - Central Basin Platform
  - Midland Basin
- Development progression:
  - Early production from shallow formations on the basin edges
  - *Transition to deeper deposits in the central Delaware (Avalon, Bone Spring, & Wolfcamp)*
- Recent basin revitalization:
  - *Comingled vertical completions*
  - Modern horizontal drilling and completion technologies

Permian Basin Cross Section

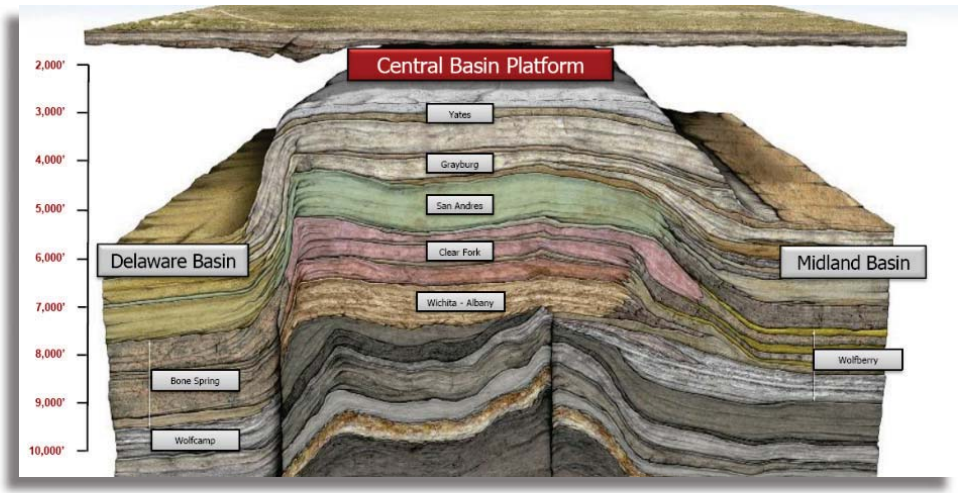

Permian Basin Structure

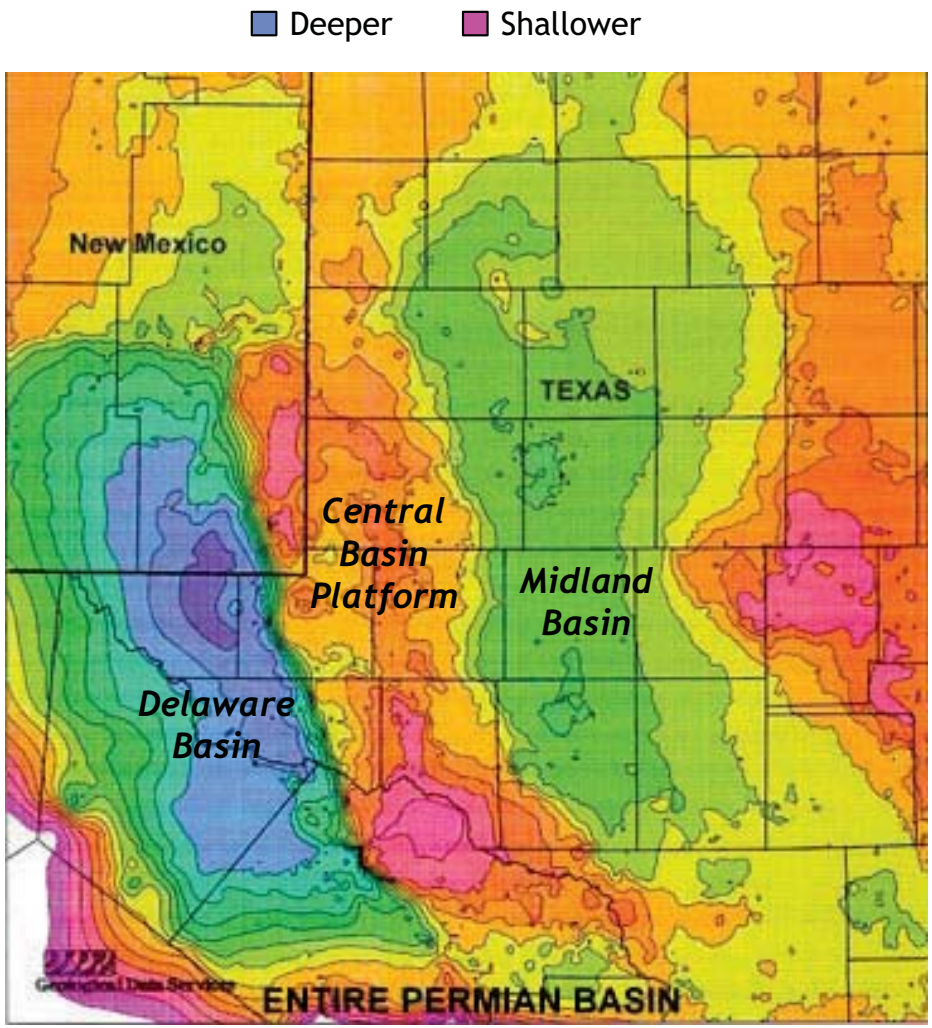

© Eagle Oil & Gas, Co., 2012

Source: Center for Energy & Economic Diversification UTPB, Geology of National Parks, National Park Service US Dept of the Interior, Society for Sedimentary Geology, Sandridge IR presentation.

Delaware Basin Deposition

- 2 depositional systems in place
  - Deep submarine channels running off the NW Shelf and Central Basin Platform
  - Periods of influx of carbonate debris
- 3rd process in generation of organics in the photic zone across the entire basin as debris settled
  - Mostly organics settling in the deep basin; carbonates mainly deposited on the Shelf and on the Slope

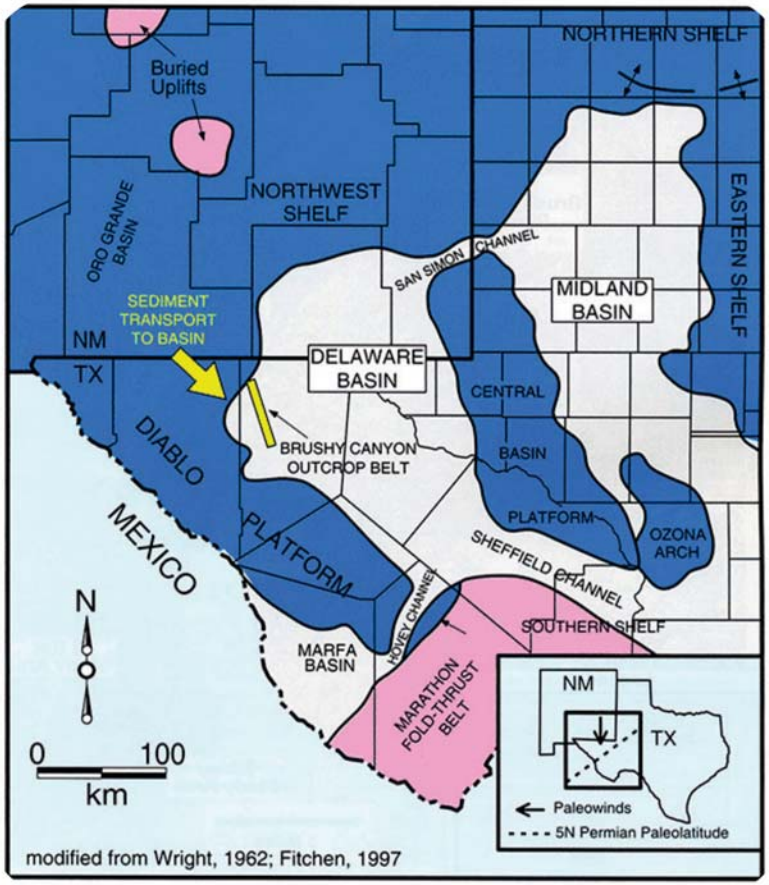

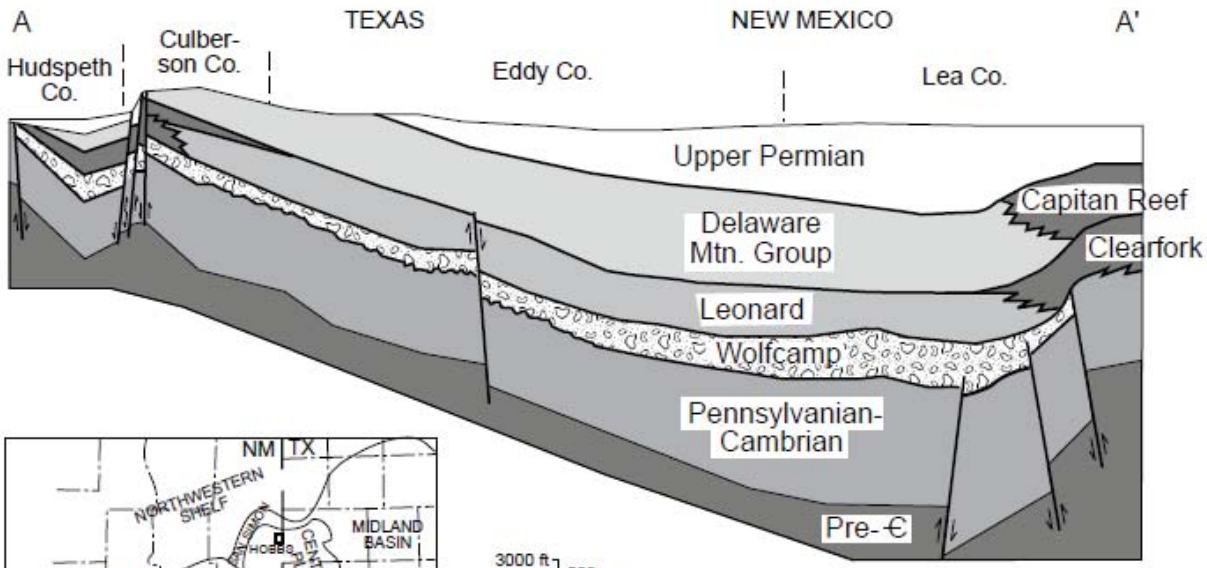

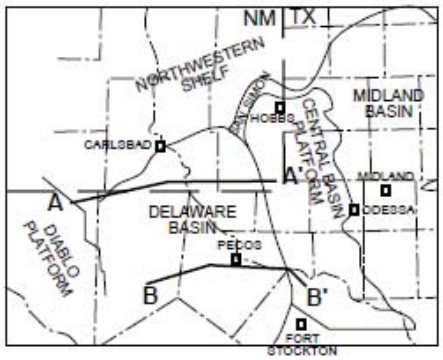

© Eagle Oil & Gas, Co., 2012

Source: Center for Energy & Economic Diversification UTPB, Geology of National Parks, National Park Service US Dept of the Interior, Society for Sedimentary Geology.

Wolfbone Industry Activity

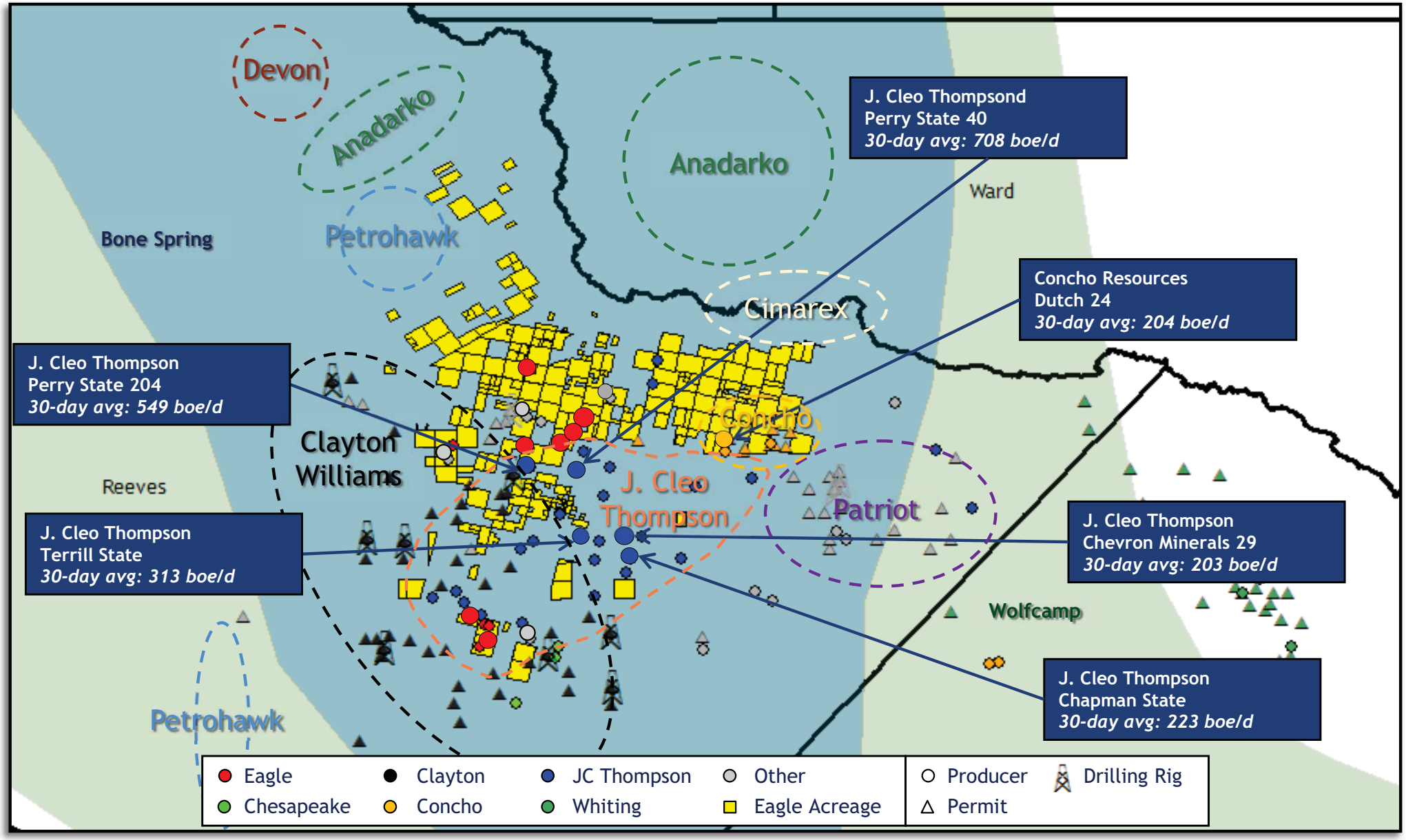

Source: HPDI and Eagle data. Producing wells.

© Eagle Oil & Gas, Co., 2012

DELAWARE BASIN

PERIOD	SERIES	FORMATION
GUADALUPE	DELAWARE GROUP	LAMAR BELL CANYON
		CHERRY CANYON
		BRUSHY CANYON
LEONARD	1ST BONE SPRING	UPPER AVALON SH.
		LOWER AVALON SH.
		1ST BONE SPRING SD
	2ND BONE SPRING	
	3RD BONE SPRING	
WOLF-CAMP	WOLFCAMP	

MIDLAND BASIN

PERIOD	SERIES	FORMATION
GUADALUPE	WHITE-HORSE	TANSILL
		YATES
		7 RIVERS
		QUEEN
		GRAYBURG
	WARD	SAN ANDRES
		SAN ANGELO
LEONARD	CLEAR FORK	UPPER LEONARD
	UPPER SPRABERRY	
	LOWER SPRABERRY	
	DEAN	
WOLF-CAMP	WOLFCAMP	

EAGLE OIL & GAS CO.

© Eagle Oil & Gas, Co., 2012

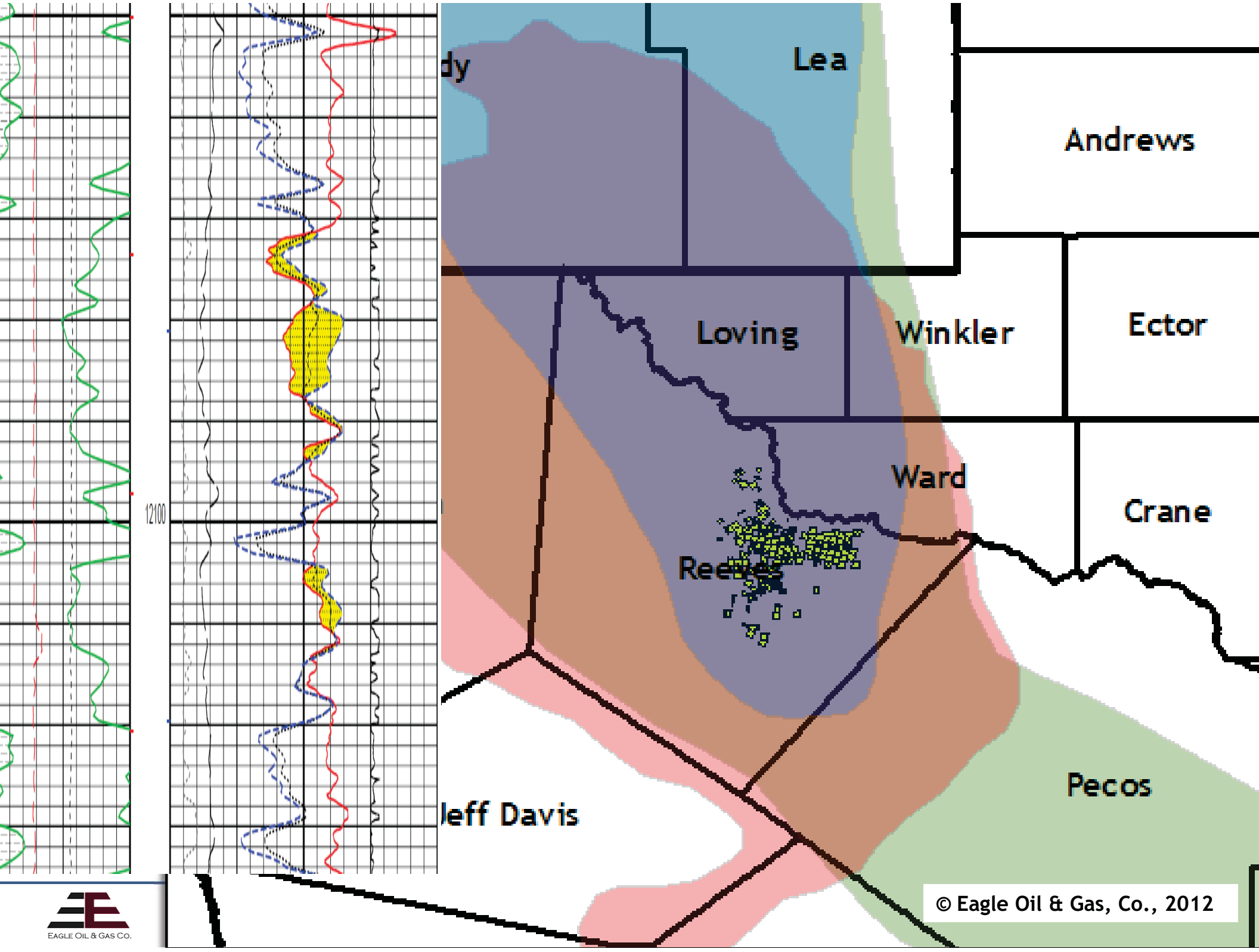
12100
dy
Lea
Andrews
Loving
Winkler
Ector
Ward
Crane
Reeves
Pecos
leff Davis
© Eagle Oil & Gas, Co., 2012
EAGLE OIL & GAS CO.

Bone Spring Type Log Section

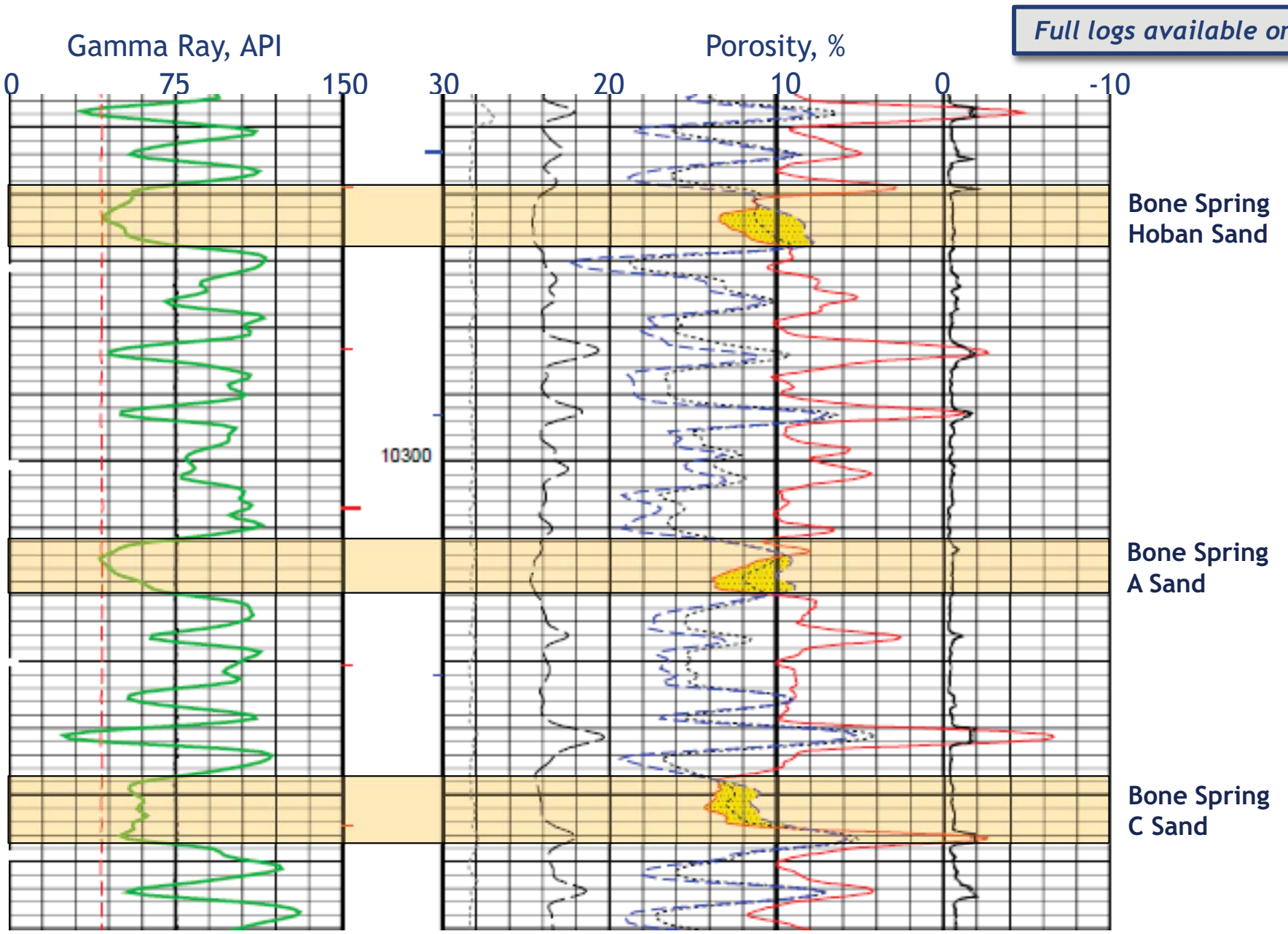

© Eagle Oil & Gas, Co., 2012

Hz Bone Spring IP Bubble Map

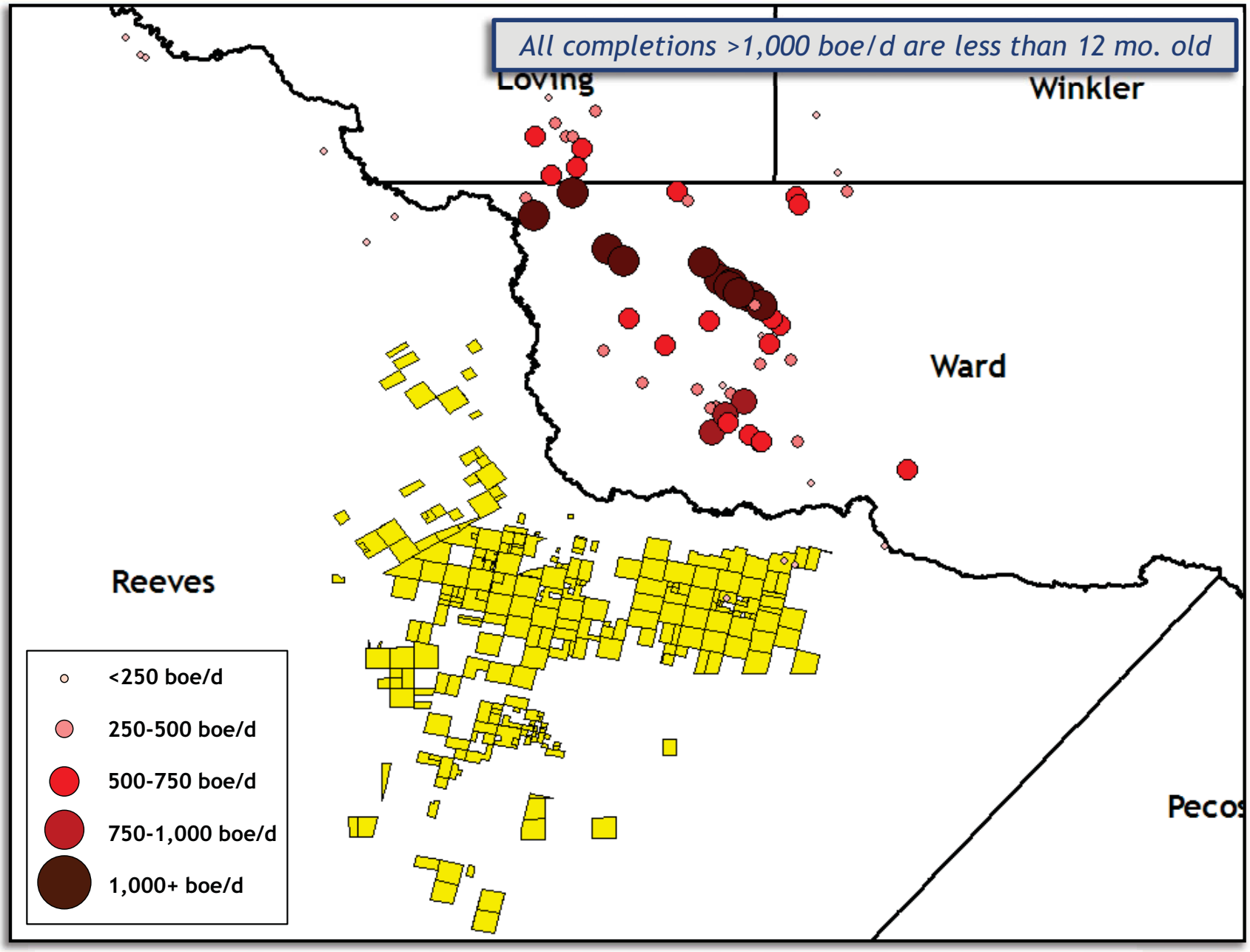

Wells completed as Wolfbone producers after 1/1/2009 – Hoban, Wolfbone fields

© Eagle Oil & Gas, Co., 2012

Eagle Oil & Gas Co.

TUDOR PICKERING HOLT & CO | ENERGY INVESTMENT & MERCHANT BANKING

5/84

GETTY OIL CO.
UNIVERSITY "44-20" #1
1320' FNL & 1320' FWL
SEC 44, BLK 20, UNIVERSITY LANDS SURVEY
WARD COUNTY, TEXAS
ELEV 2801'
TD 20,155'

12/05

BROWNING OIL COMPANY INC.
UNIVERSITY "18-42" #1
1320' FNL & 1320' FEL
SEC 42, BLK 18, UNIVERSITY LANDS SURVEY
WARD COUNTY, TEXAS
ELEV 2614'
TD 11,660'

8/78

C & K PETROLEUM INC.
MEEKER "45" #1
1320' FNL & 1320' FWL
SEC 45, BLK 9, H&GN SURVEY
REEVES COUNTY, TEXAS
ELEV 2562'
TD 20,246'

© Eagle Oil & Gas, Co., 2012

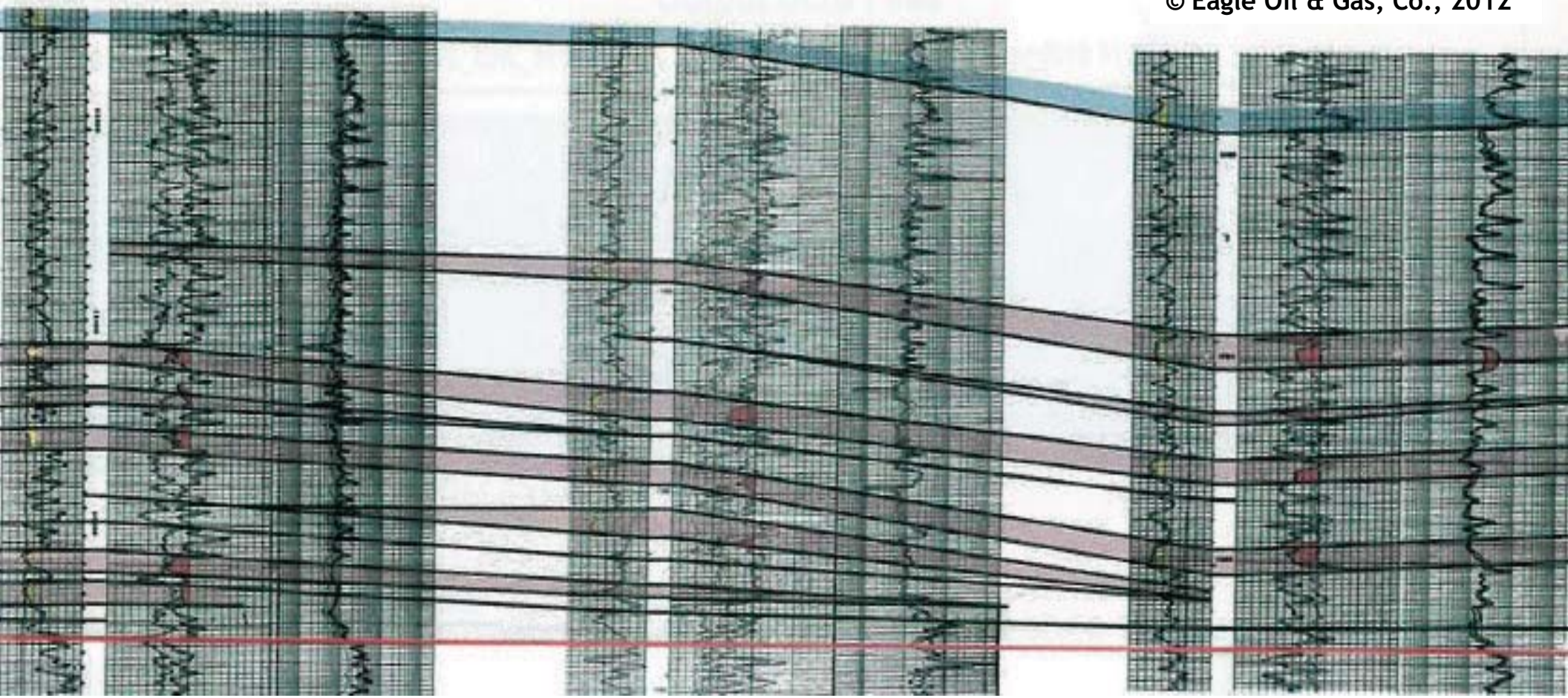

Hz Bone Spring IP Bubble Map

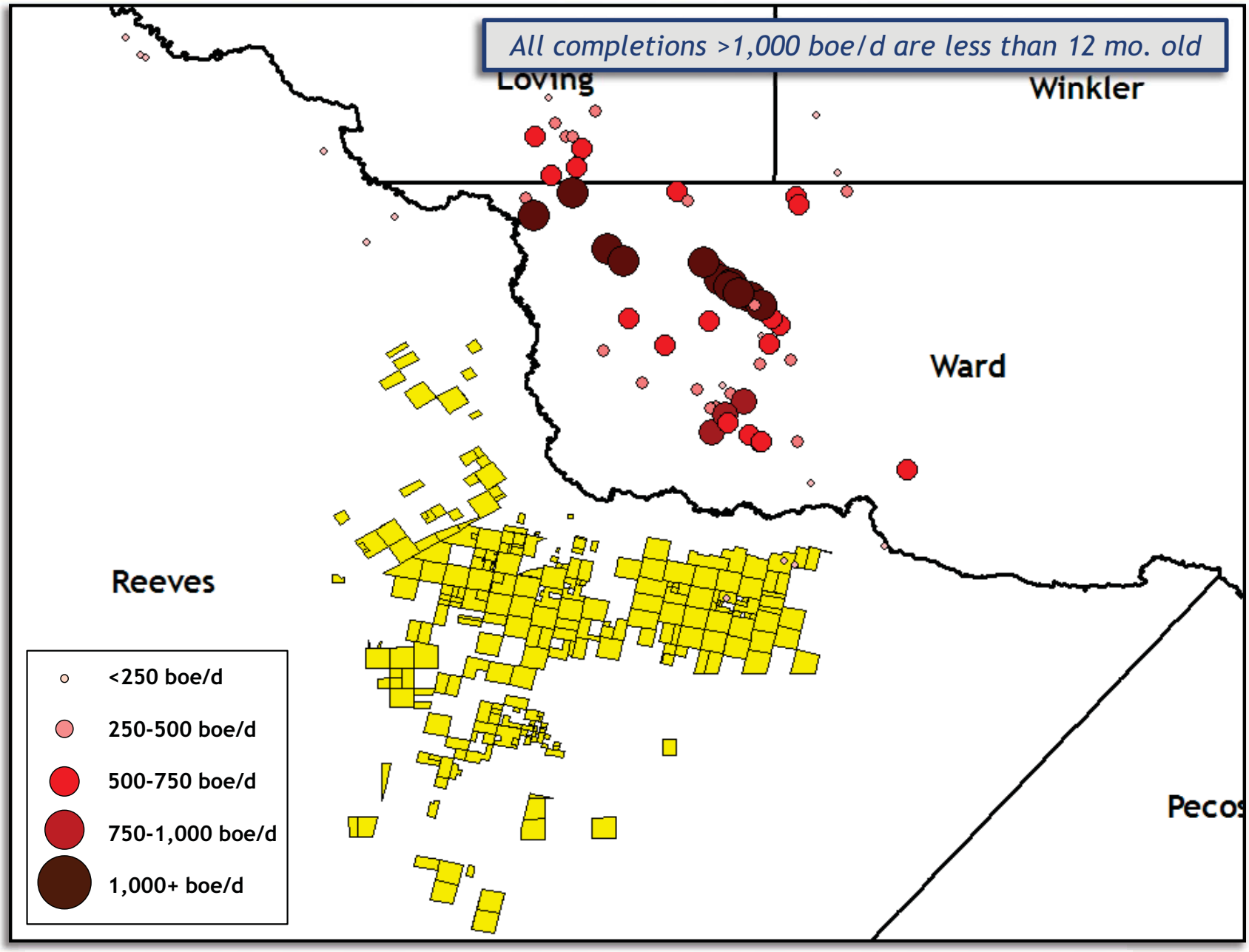

Wells completed as Wolfbone producers after 1/1/2009 – Hoban, Wolfbone fields.

© Eagle Oil & Gas, Co., 2012

EAGLE OIL & GAS CO.

TUDORPICKERING HOLT&CO | ENERGY INVESTMENT & MERCHANT BANKING

Bone Spring Type Log Section

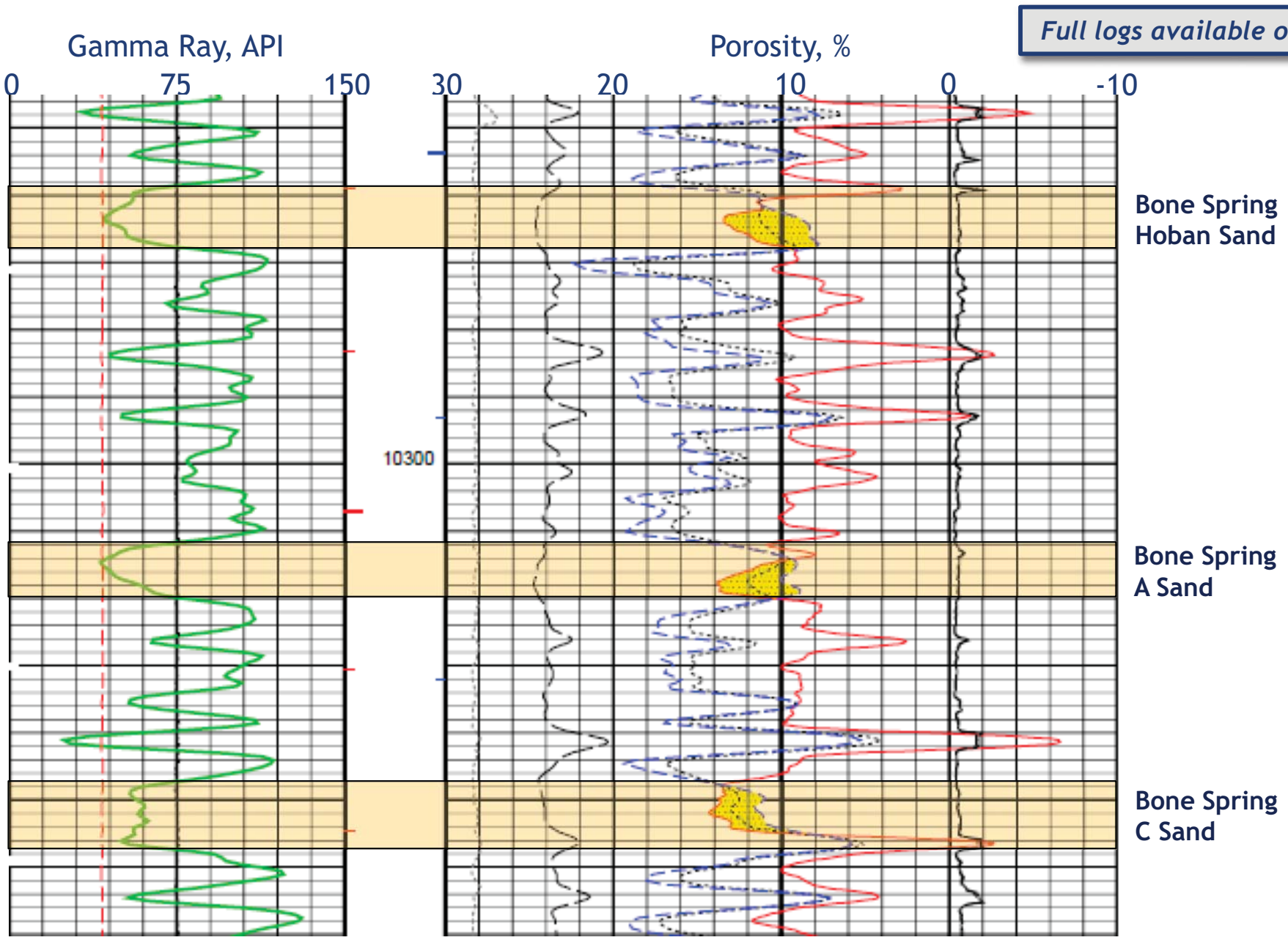

© Eagle Oil & Gas, Co., 2012

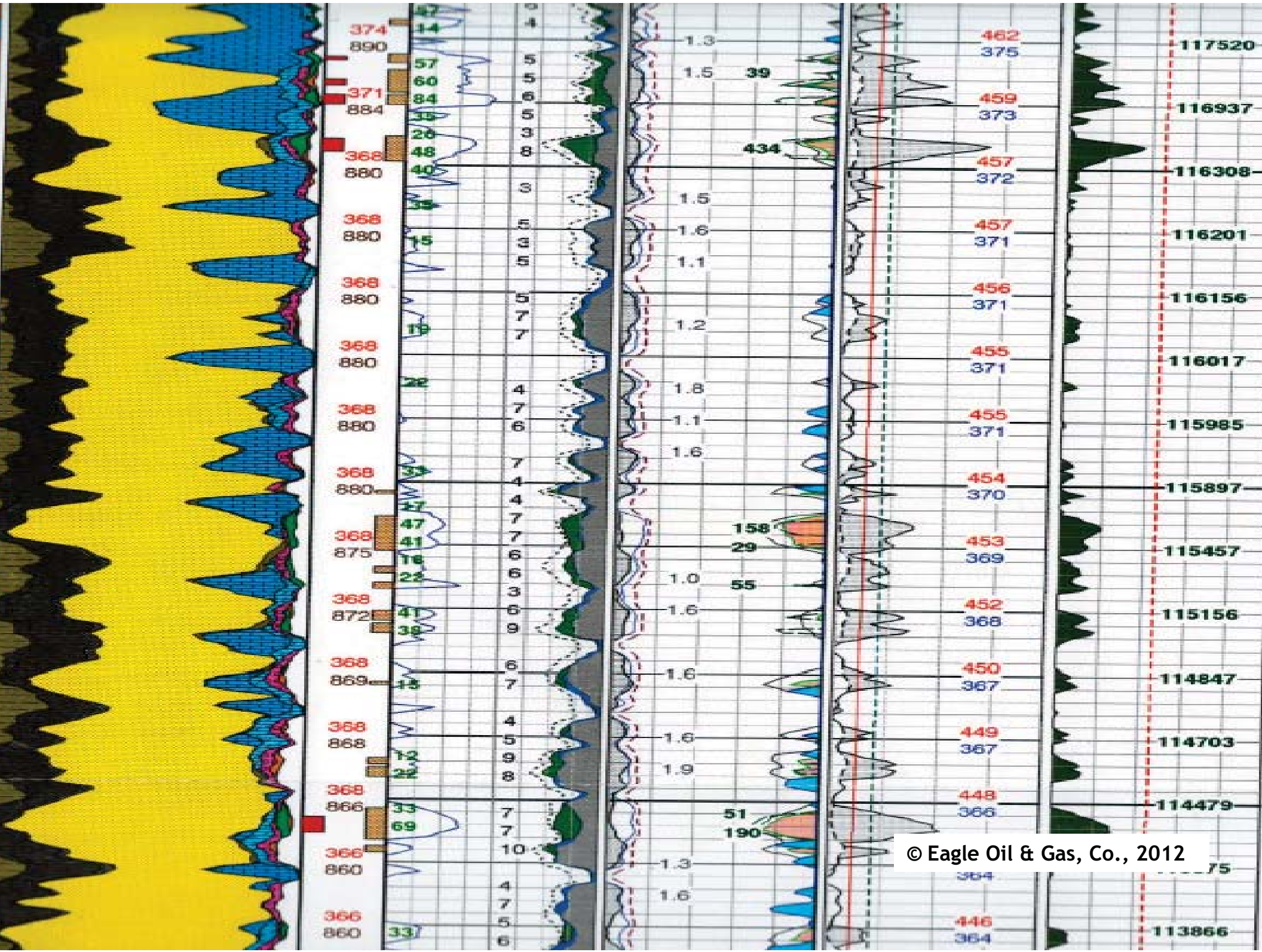
© Eagle Oil & Gas, Co., 2012

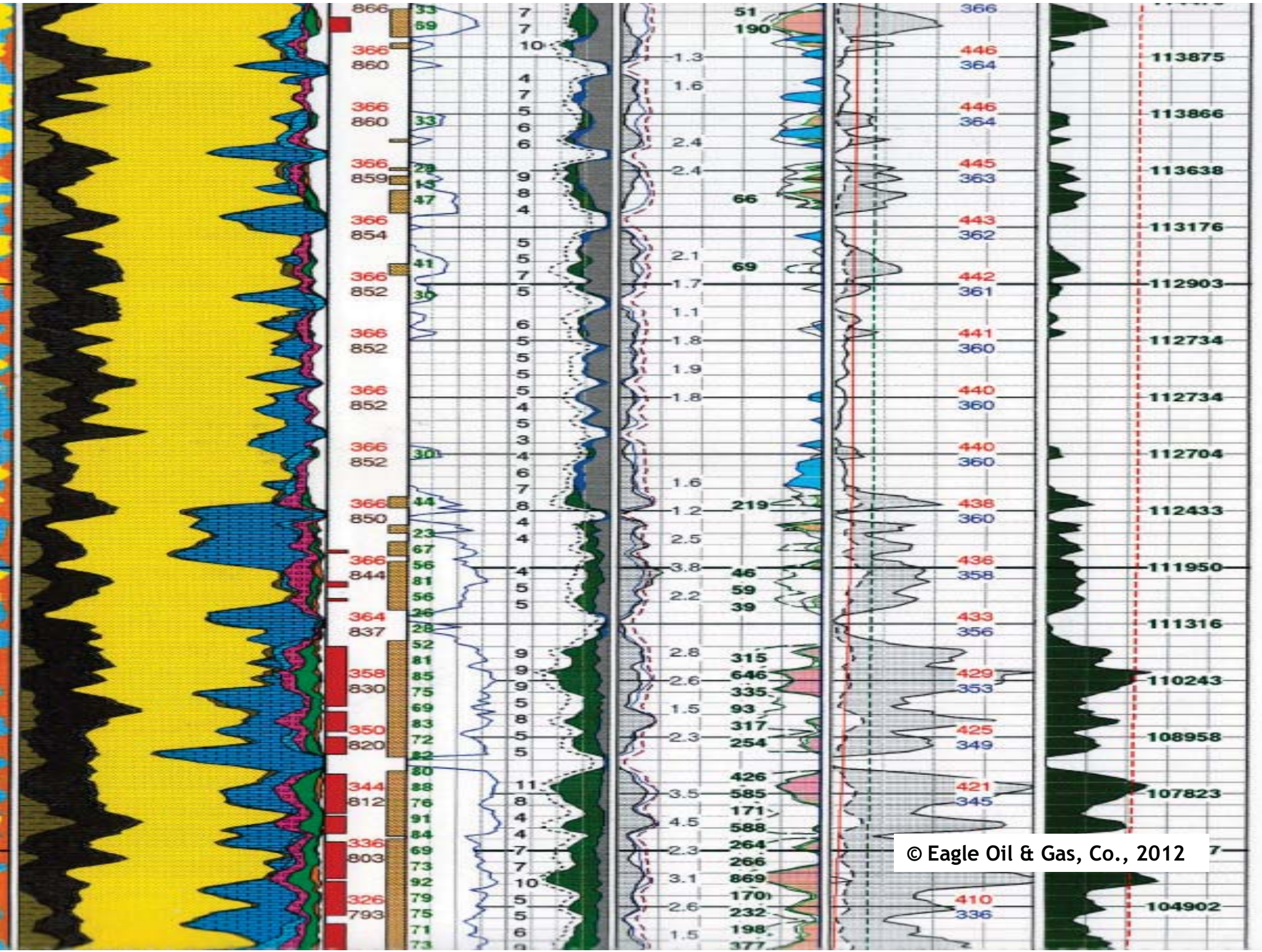
113875
113866
113638
113176
112903
112734
112734
112704
112433
111950
111316
110243
108958
107823
104902
© Eagle Oil & Gas, Co., 2012

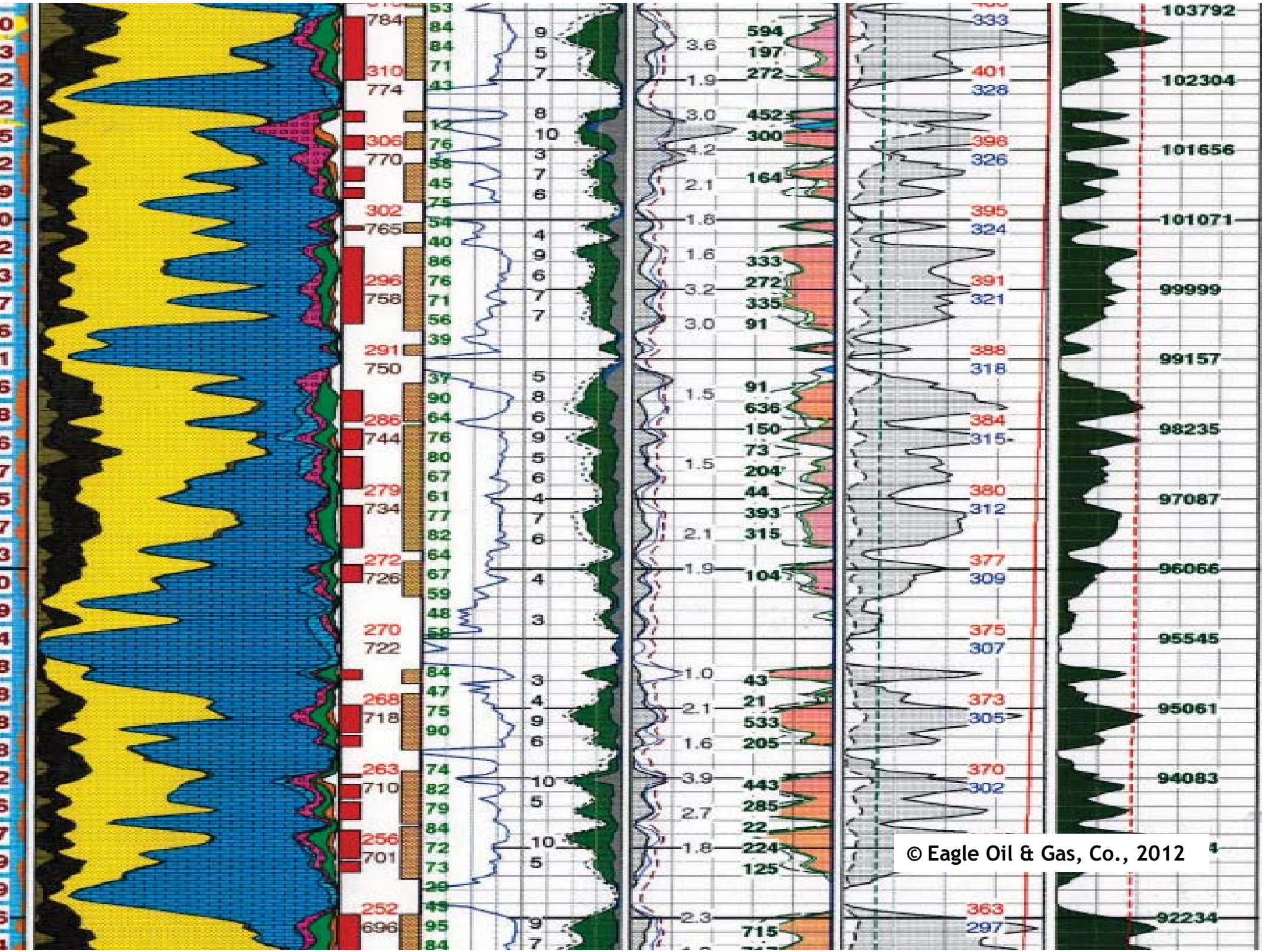

© Eagle Oil & Gas, Co., 2012

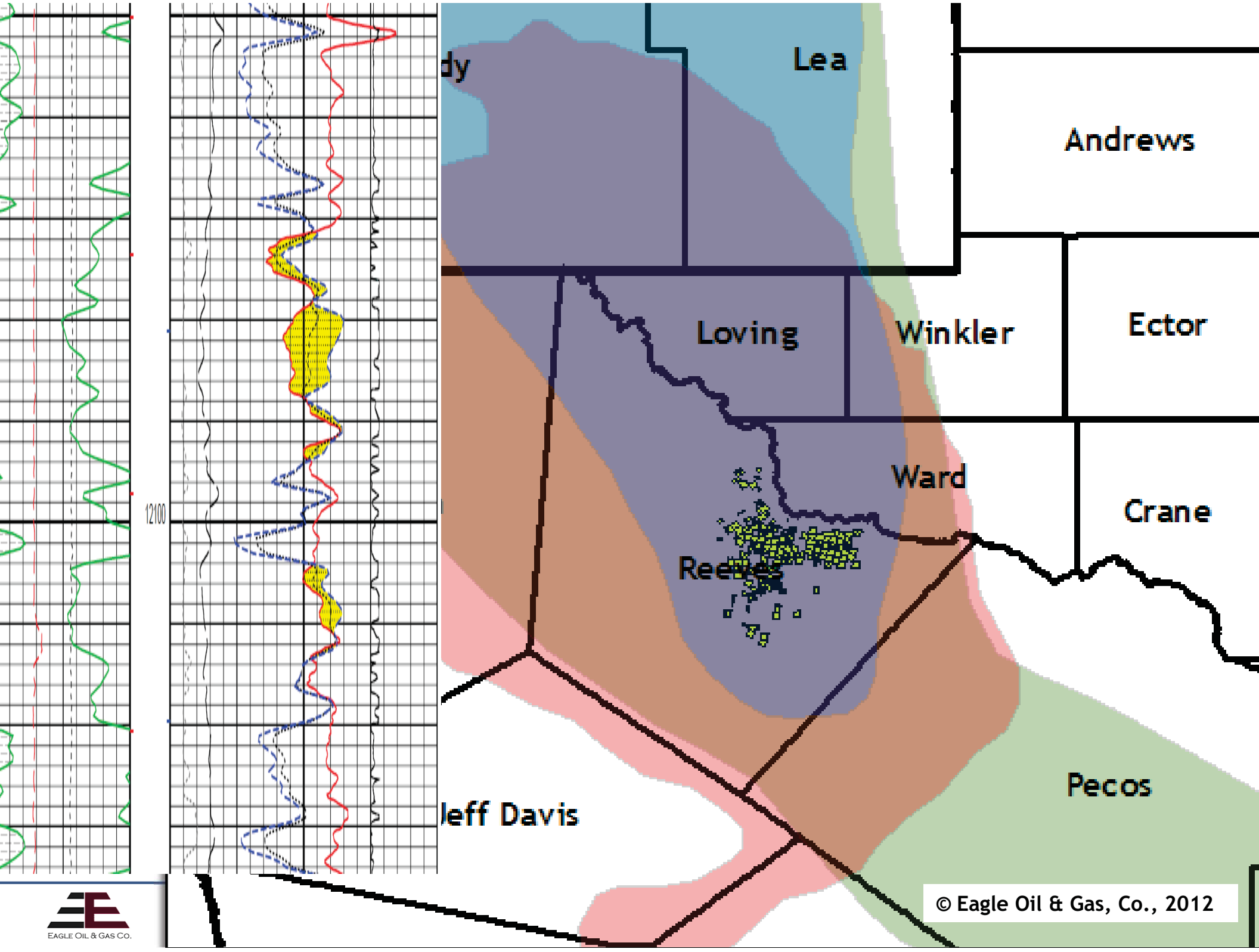
12100
dy
Lea
Andrews
Loving
Winkler
Ector
Ward
Crane
Reeves
Pecos
leff Davis
© Eagle Oil & Gas, Co., 2012
EAGLE OIL & GAS CO.

Plugging Water-Bearing Zones Improves Profits

Pistola #1 Case History

- Eagle's 2nd Wolfbone completion
- Well initially flowed >1,000 bblw/d
- Leveled out ~150 bblw/d
- Re-entered wellbore and cement squeezed Middle Wolfcamp Sands C&D
- Re-completed Middle and Upper Wolfcamp shales and 3rd Bone Spring Sands
- ***Well IP'd > 450 bopd following intervention***

Pistola #1 Production History

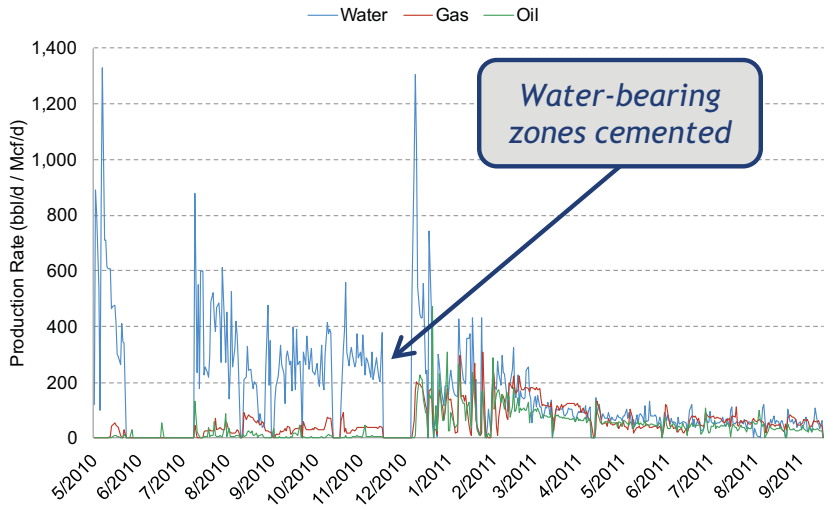

City of Pecos 15 #1 Case History

- Ealge's 6th Wolfbone completion
- Well initially flowed >1,200 bblw/d
- Decreased to ~600 bblw/d over 30 days
- Re-entered wellbore and cement squeezed Middle Wolfcamp Sands C
- Re-completed Middle and Upper Wolfcamp shales and 3rd Bone Spring Sands
- ***WOR cut in half to ~1.5 from 3+ vastly improving economics***

City of Pecos 15 #1 Production History

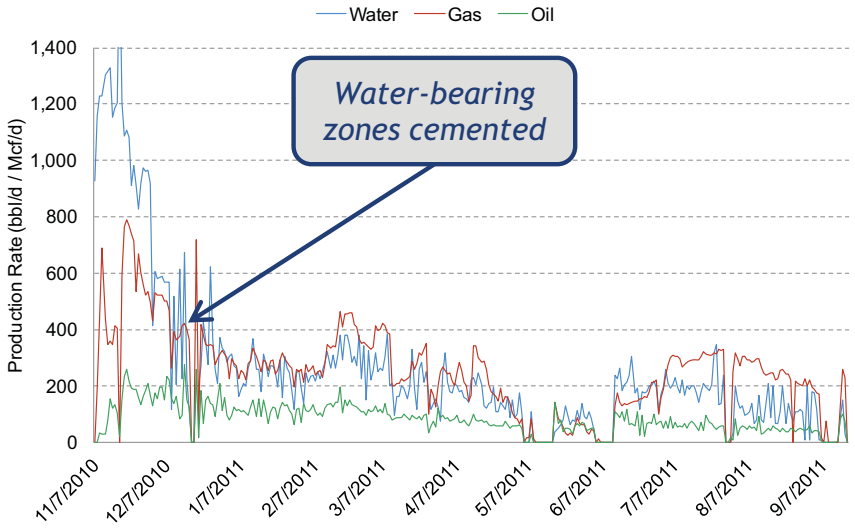

© Eagle Oil & Gas, Co., 2012

Production Logs = Precision Completions

Production Logs Used to Identify Target Intervals

- Eagle has run production logs in 9 Wolfbone wells
- Tool has multiple sensors to identify contributing intervals:
  - Spinner with dual-axis caliper
  - Pressure and temperature sensors
  - Digital Entry Flowview Imaging Tool (DEFT)
    - Water measurement
  - Gas Holdup Optical Sensing Tool (GHOST)
    - Gas measurement

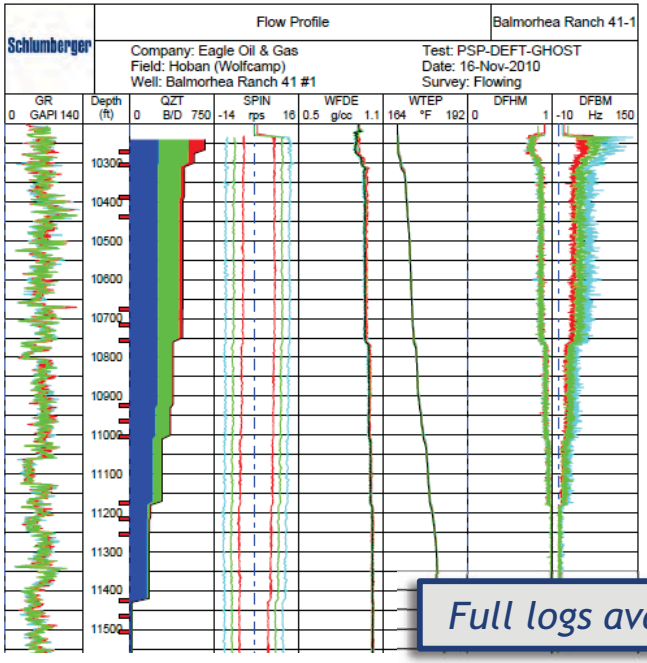

Full logs available in VDR

Previously Drilled Hz Target

Current Hz Target
Monroe 39 #2H

Relative Flow Contribution by Member[1]

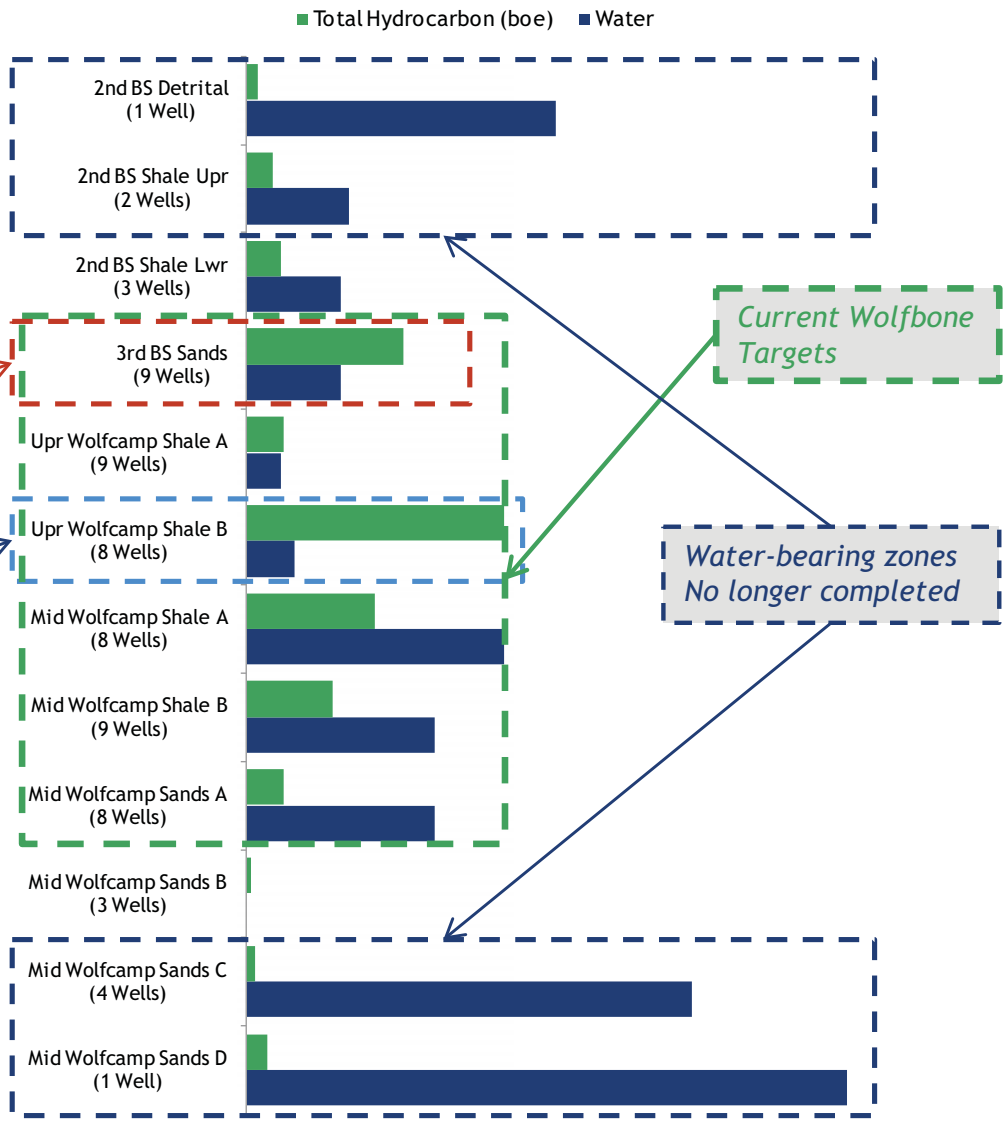

Current Wolfbone Targets

Water-bearing zones No longer completed

© Eagle Oil & Gas, Co., 2012

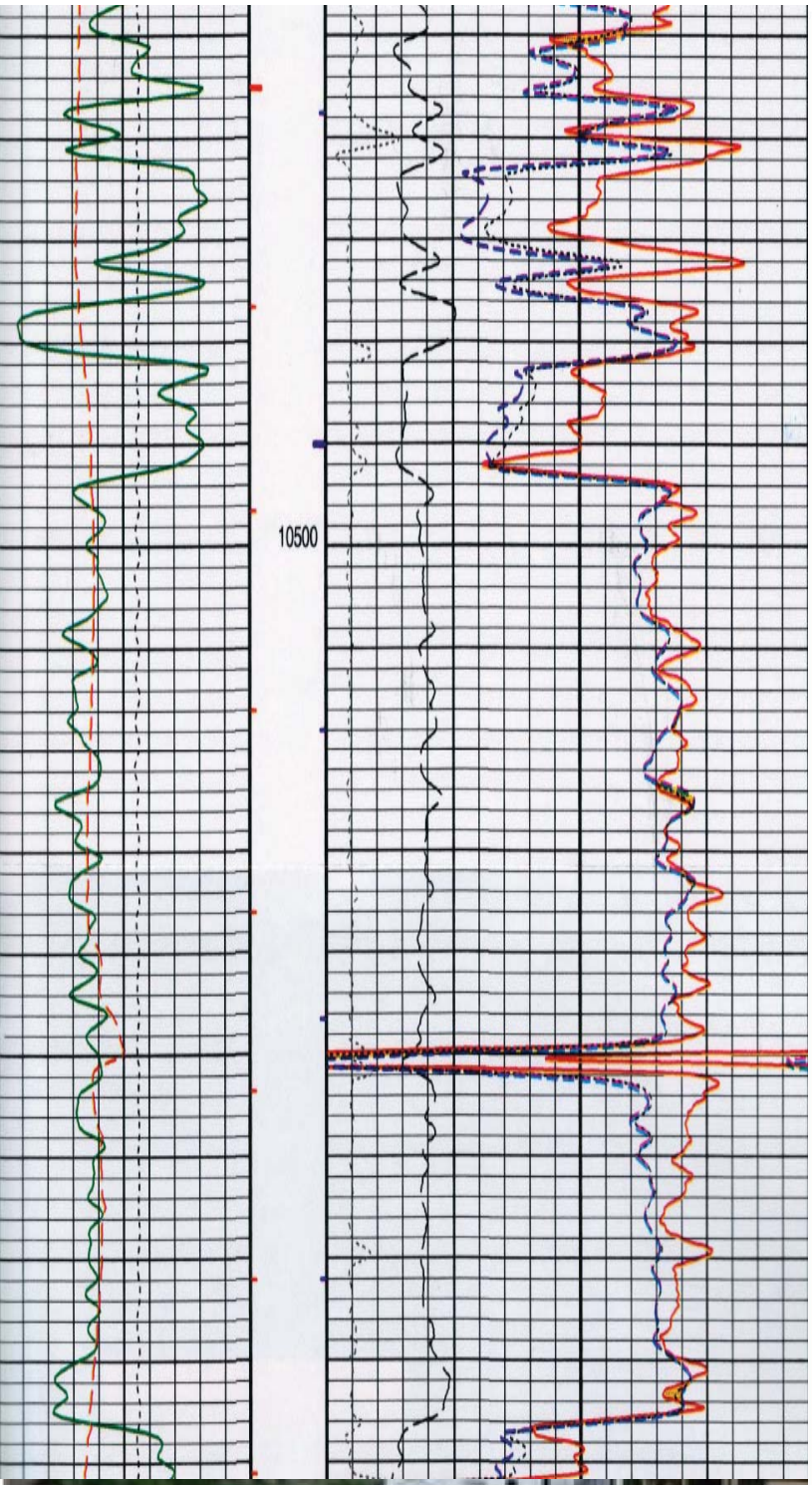
10500


EAGLE OIL & GAS CO.

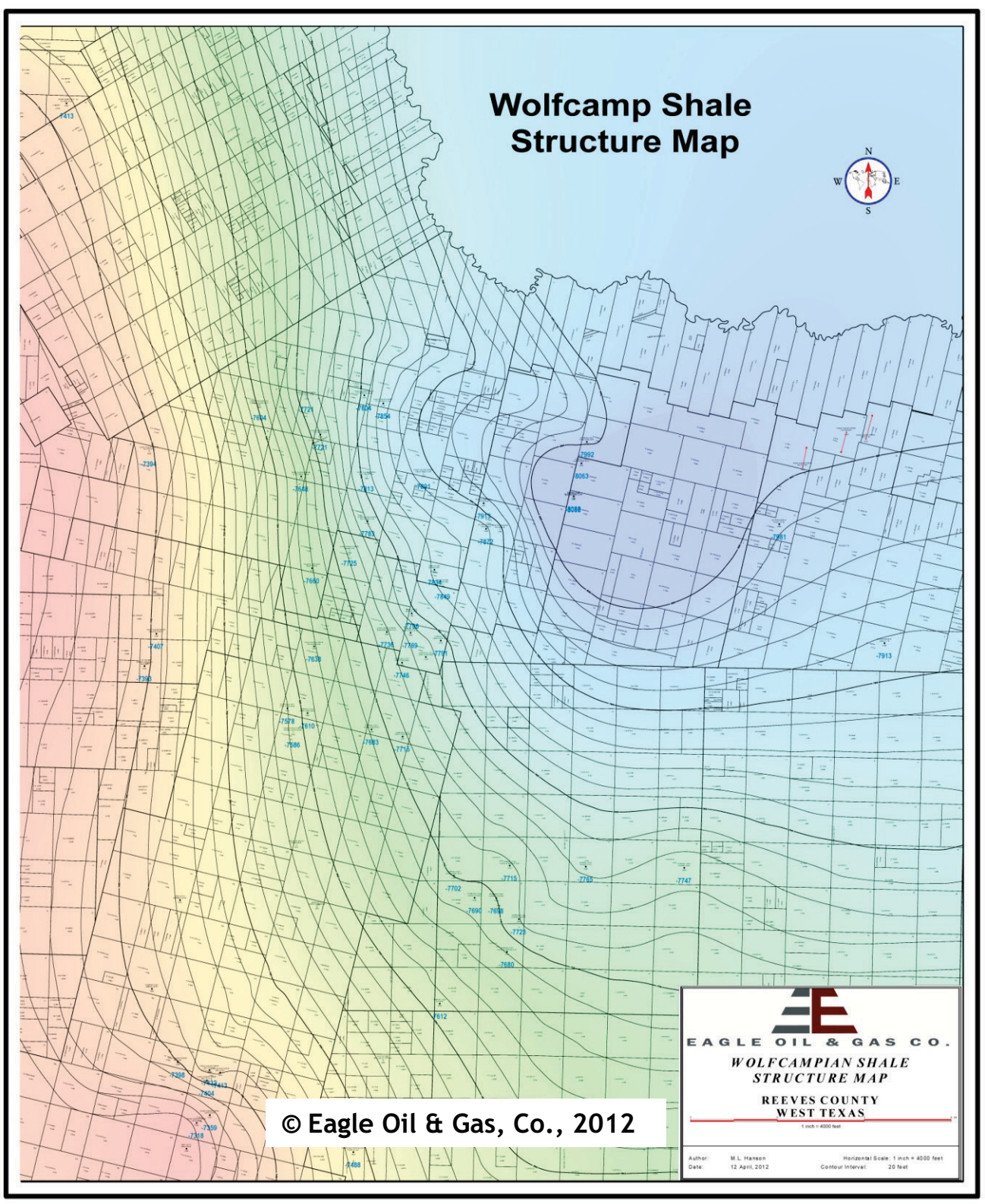
Wolfcamp Shale
Structure Map
N
W
E
S
© Eagle Oil & Gas, Co., 2012
EAGLE OIL & GAS CO.
WOLFCAMPIAN SHALE
STRUCTURE MAP
REEVES COUNTY
WEST TEXAS
Author: M.L. Hanson
Date: 12 April, 2012
Horizontal Scale: 1 inch = 4000 feet
Contour Interval: 20 feet

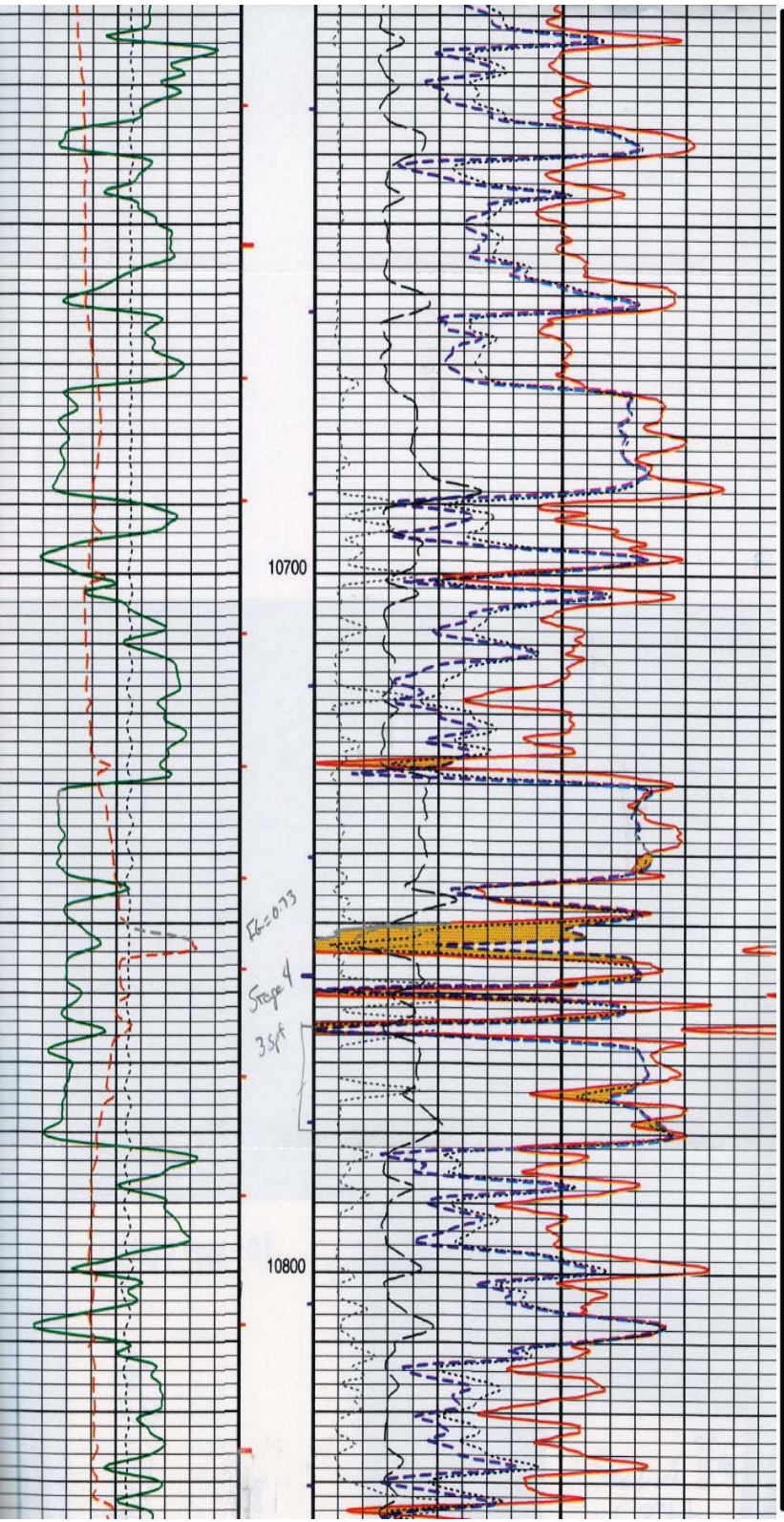
10700
10800
Eb-073
Stage 4
35ft

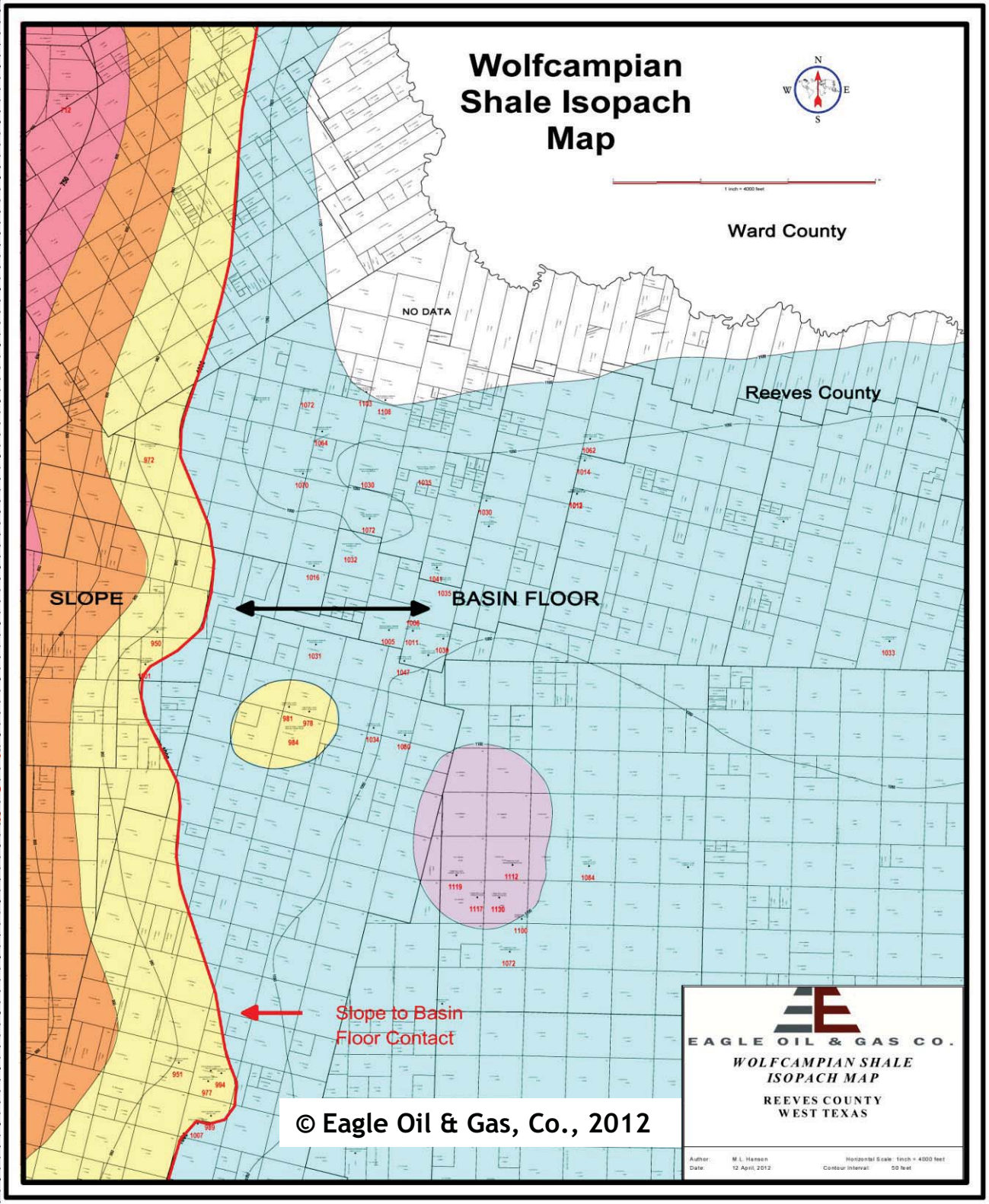
Wolfcampian Shale Isopach Map
N
W
E
S
1 inch = 4000 feet
Ward County
NO DATA
Reeves County
SLOPE
BASIN FLOOR
Slope to Basin Floor Contact
© Eagle Oil & Gas, Co., 2012
EAGLE OIL & GAS CO.
WOLFCAMPIAN SHALE ISOPACH MAP
REEVES COUNTY
WEST TEXAS
Author: M.L. Hanson
Date: 12 April, 2012
Horizontal Scale: 1inch = 4000 feet
Contour Interval: 50 feet

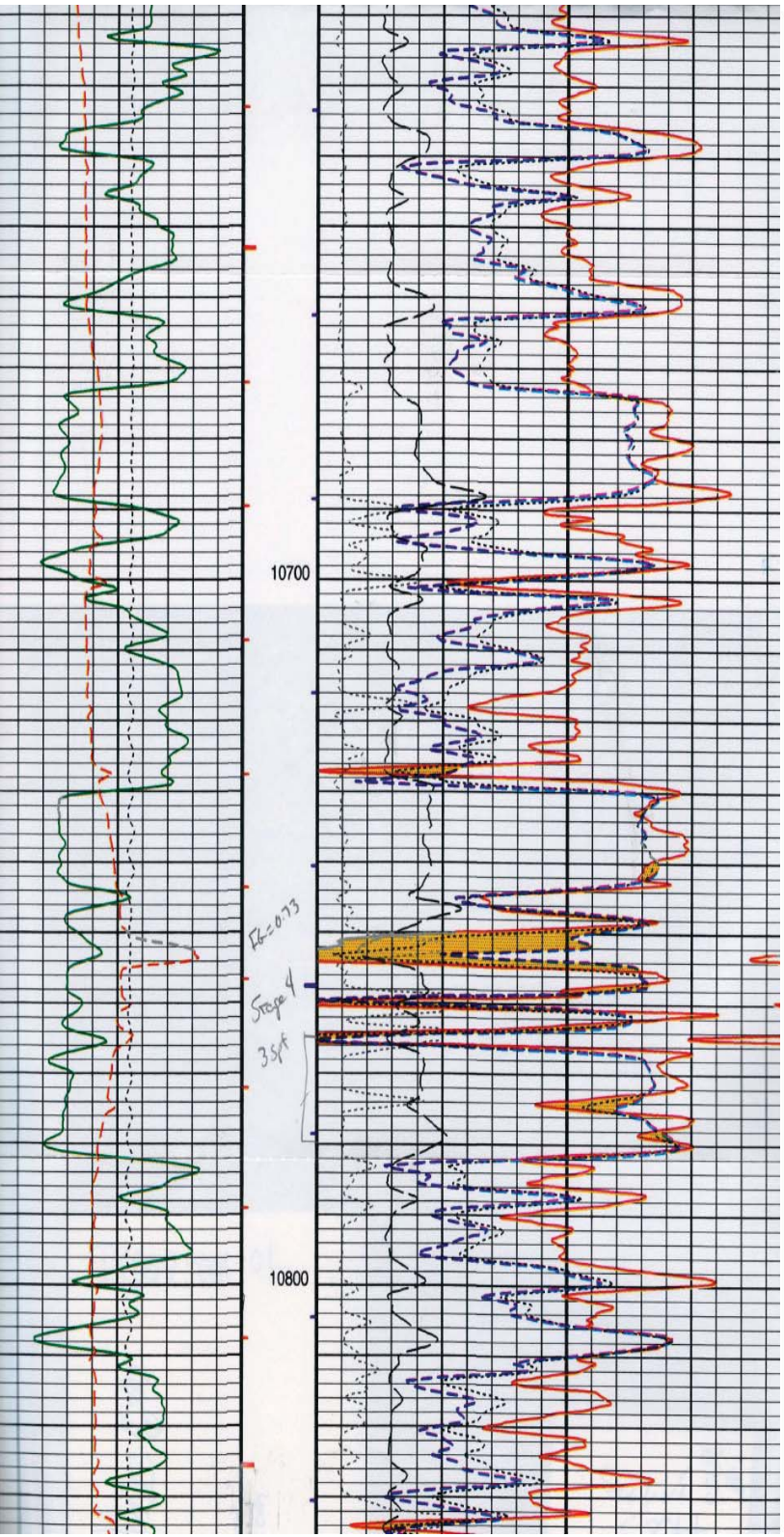
10700
10800
Eb-073
Stage 4
35ft

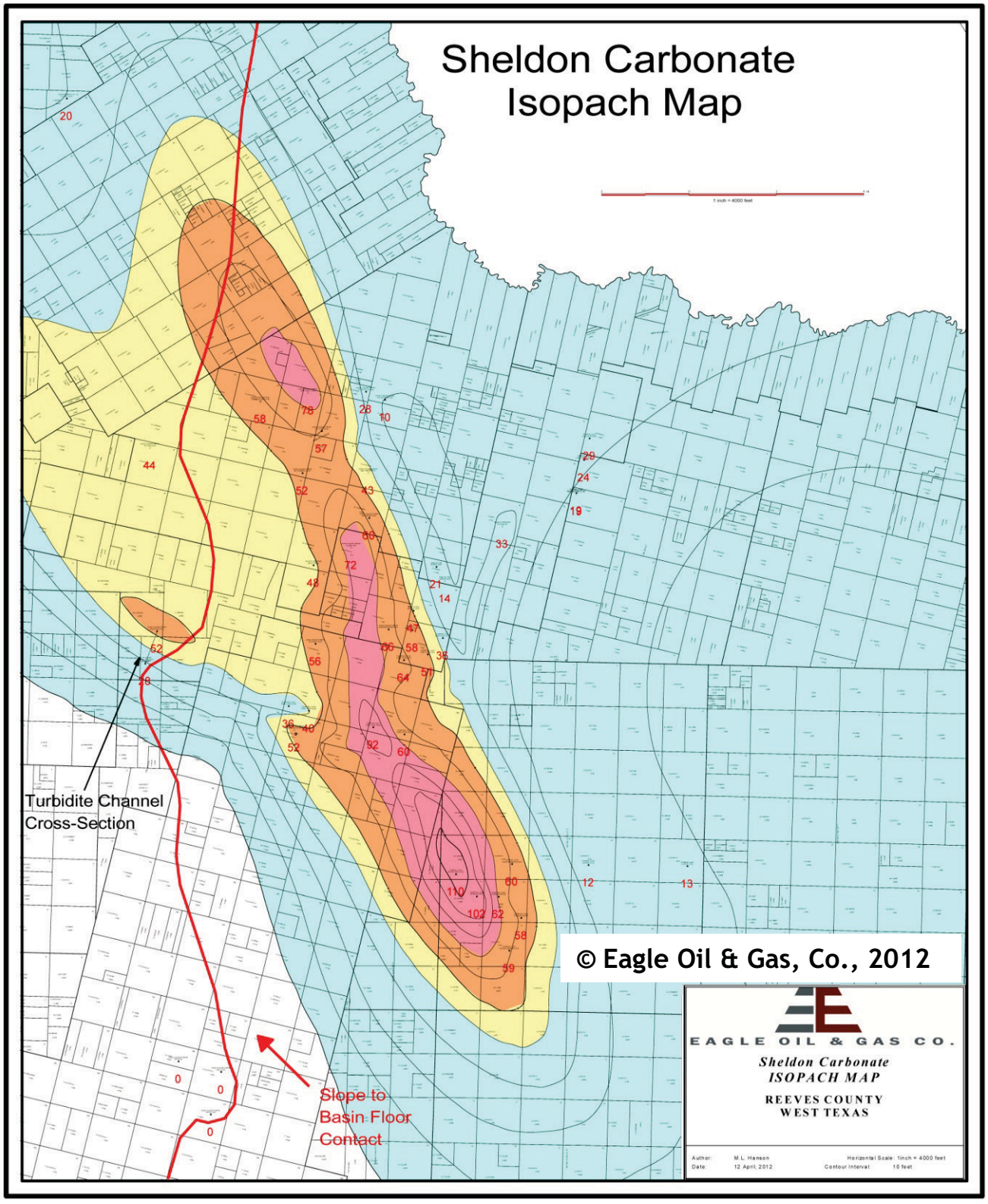
Sheldon Carbonate
Isopach Map
Turbidite Channel
Cross-Section
Slope to
Basin Floor
Contact
© Eagle Oil & Gas, Co., 2012
EAGLE OIL & GAS CO.
Sheldon Carbonate
ISOPACH MAP
REEVES COUNTY
WEST TEXAS
Author: M.L. Hanson
Date: 12 April, 2012
Horizontal Scale: 1inch = 4000 feet
Contour Interval: 10 feet

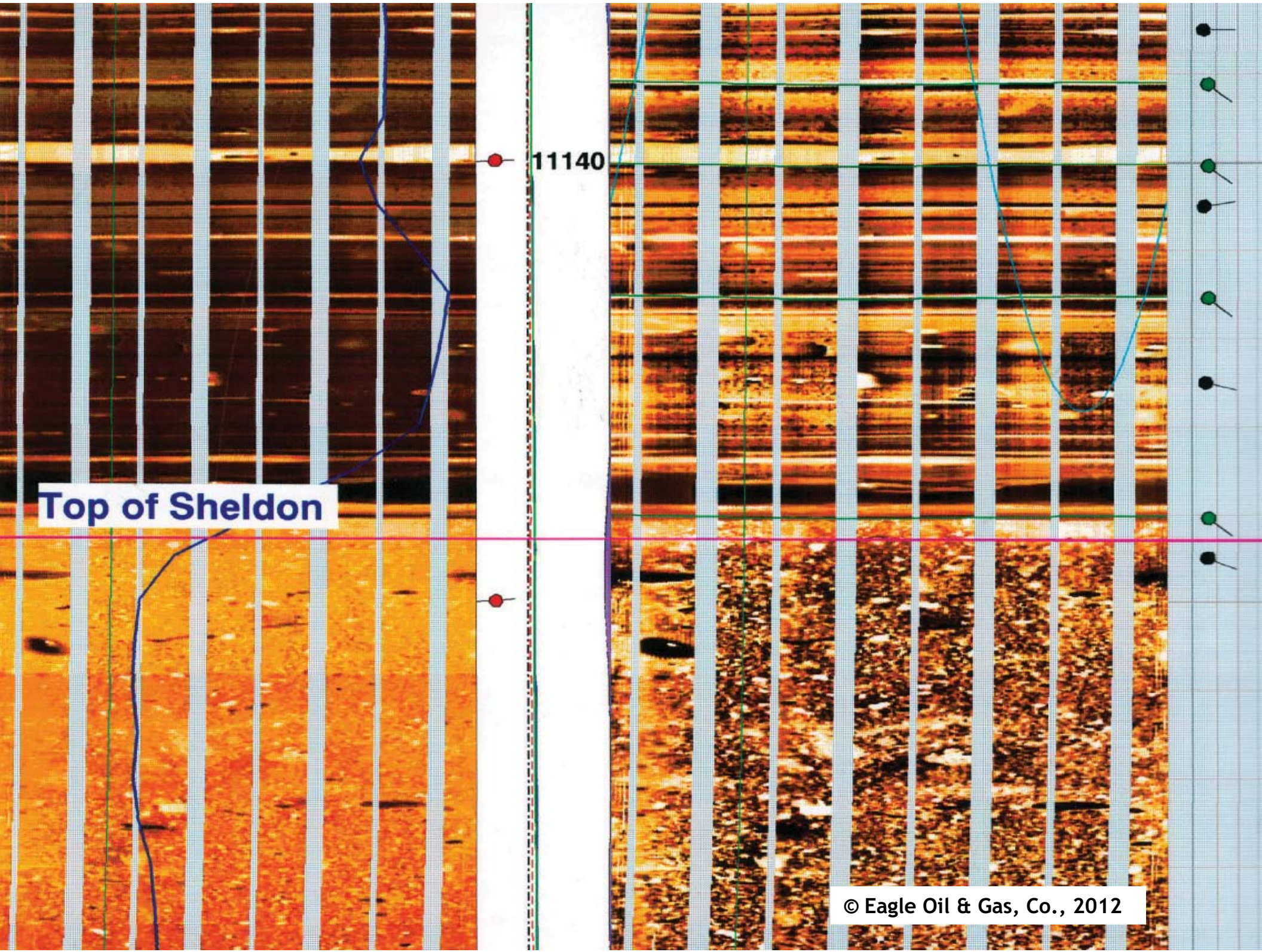

© Eagle Oil & Gas, Co., 2012

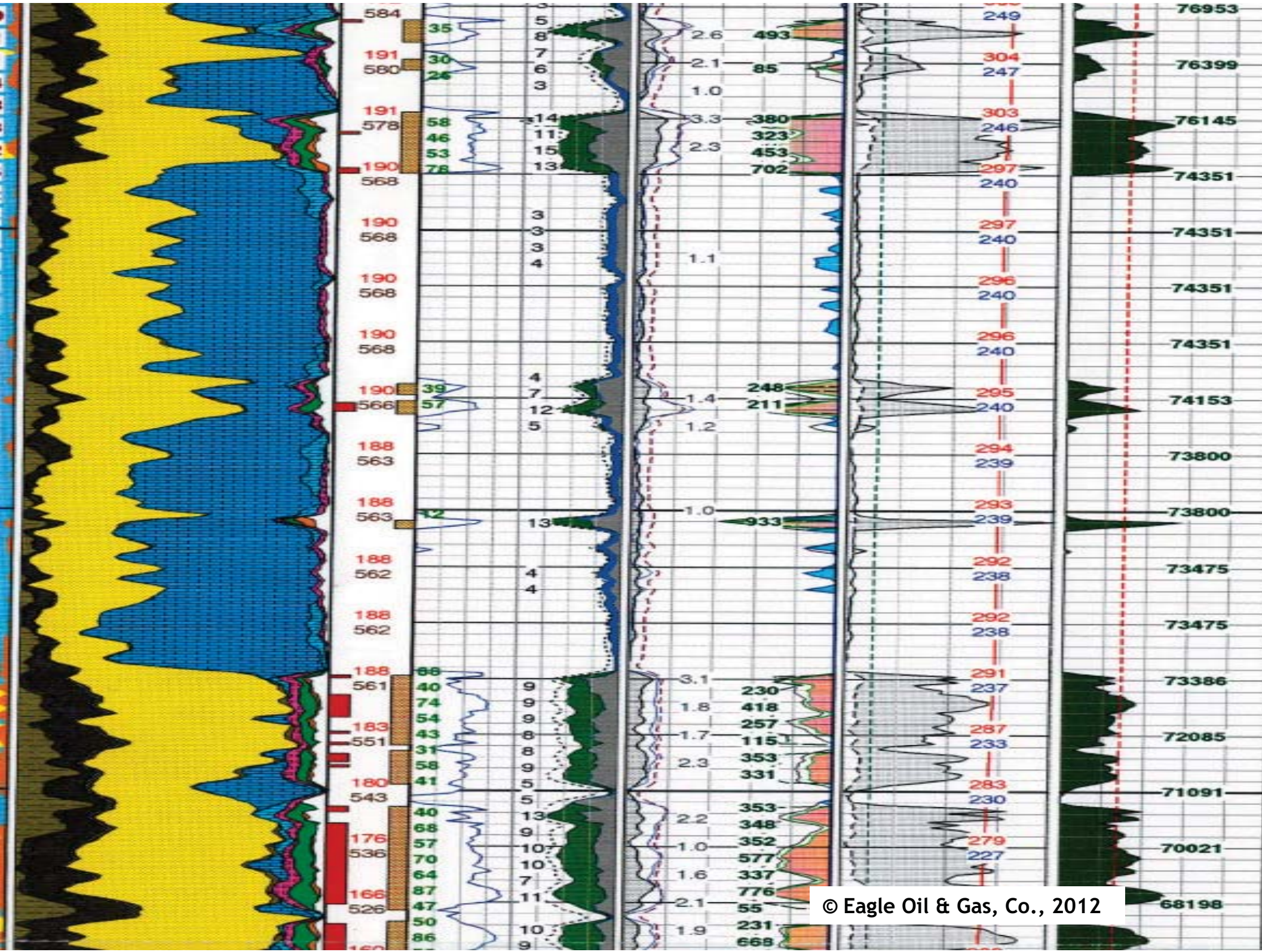
© Eagle Oil & Gas, Co., 2012

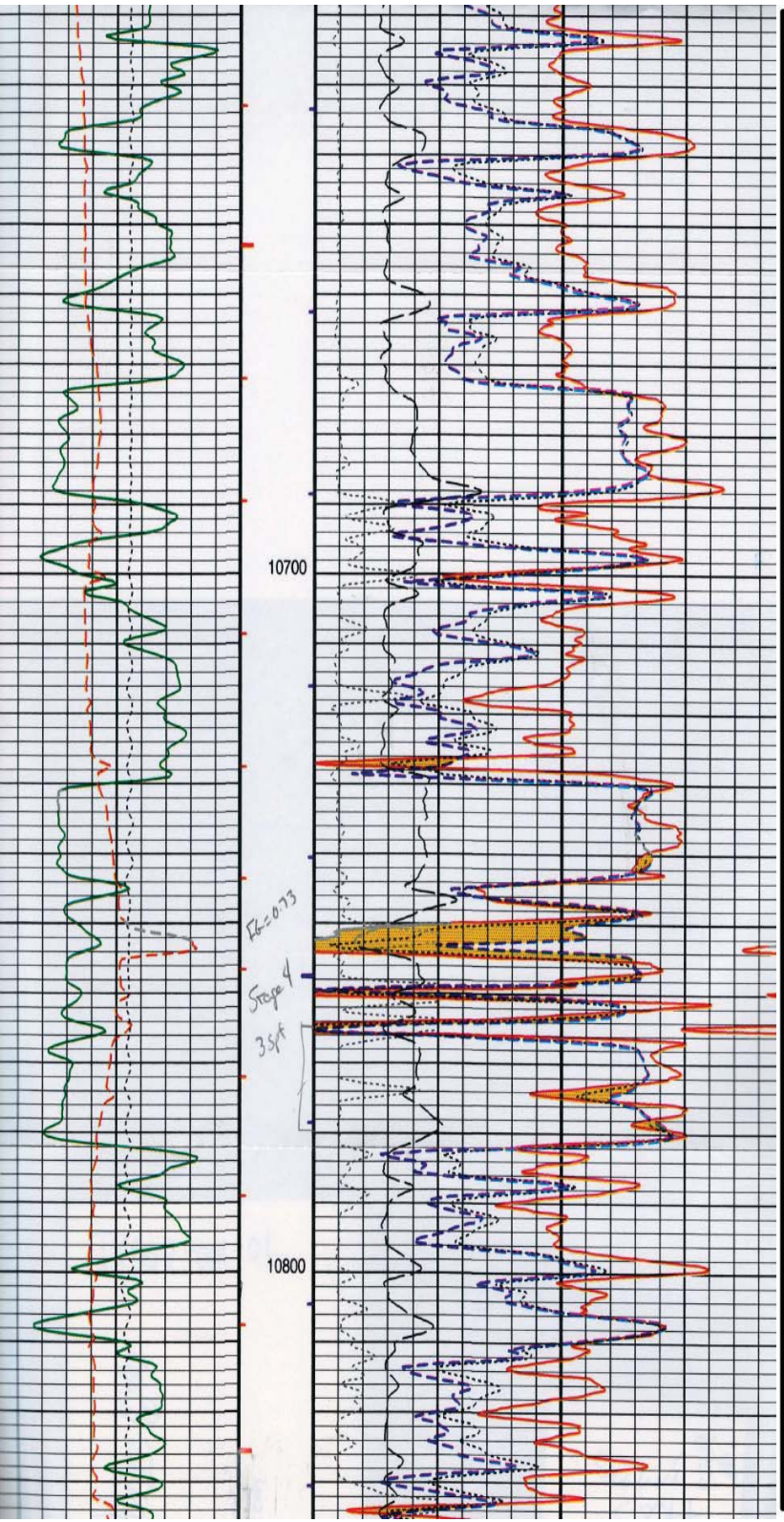

Wolfcampian Shale Isopach Map

N
W
E
S

1 inch = 4000 feet

Ward County

NO DATA

Reeves County

SLOPE

BASIN FLOOR

Slope to Basin Floor Contact

EAGLE OIL & GAS CO.

WOLFCAMPIAN SHALE ISOPACH MAP

REEVES COUNTY
WEST TEXAS

Author: M.L. Hanson
Date: 12 April, 2012
Horizontal Scale: 1inch = 4000 feet
Contour Interval: 50 feet

© Eagle Oil & Gas, Co., 2012

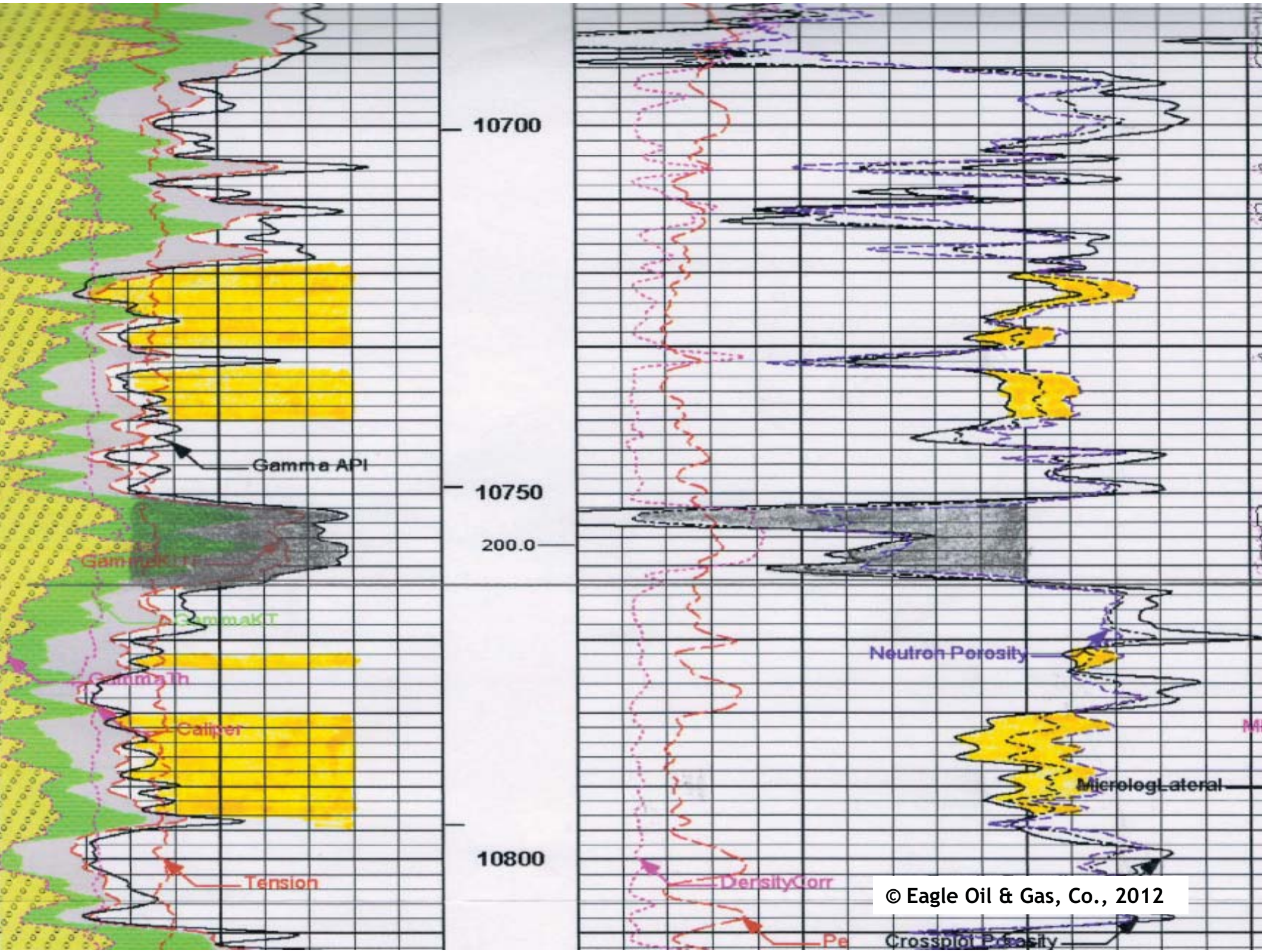

© Eagle Oil & Gas, Co., 2012

Focusing the Effort



Most recent wells completed consistently with excellent results

© Eagle Oil & Gas, Co., 2012

IP's Trending Upward as Completions Improve

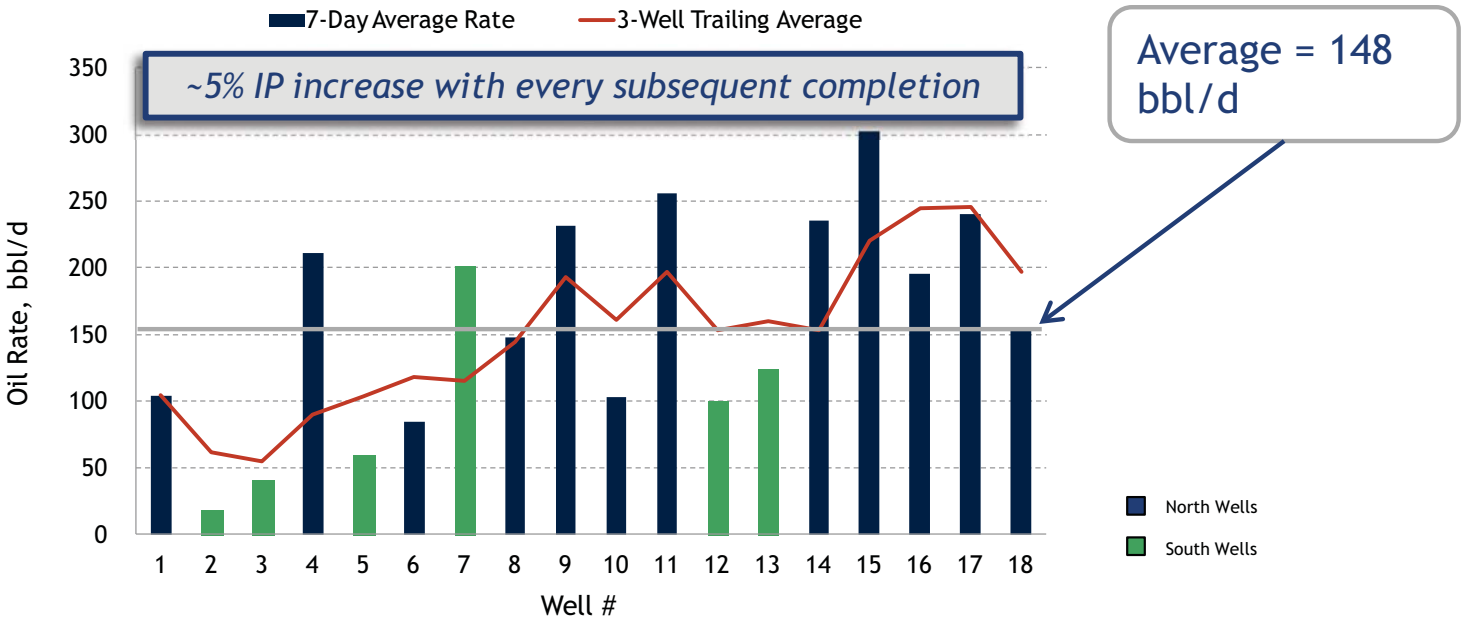

North Wells

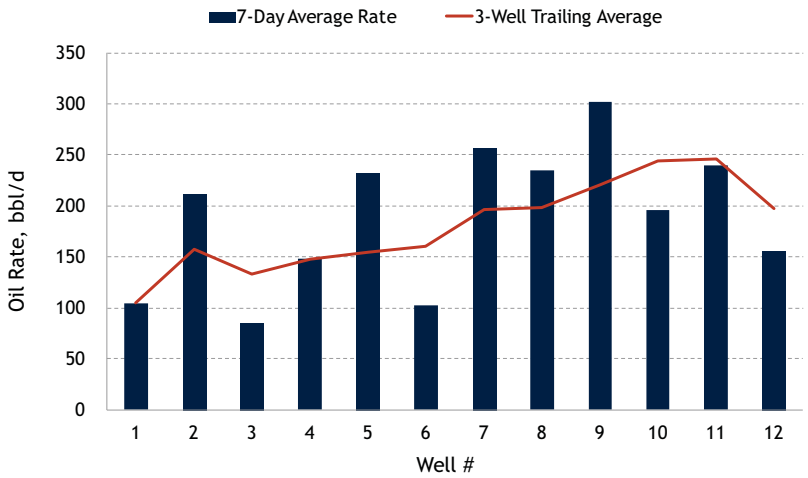

South Wells

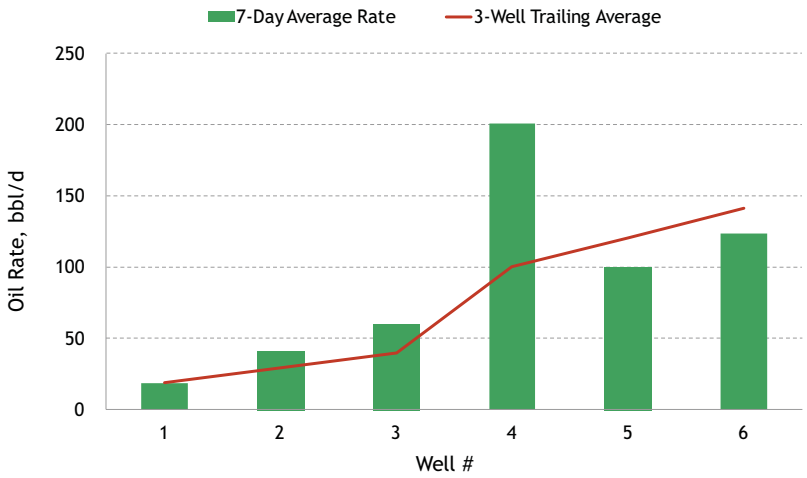

NOTE: Eagle operated Wolfbone completions.

© Eagle Oil & Gas, Co., 2012

Honoring Recent Data

Recent well data; supports type curve IP

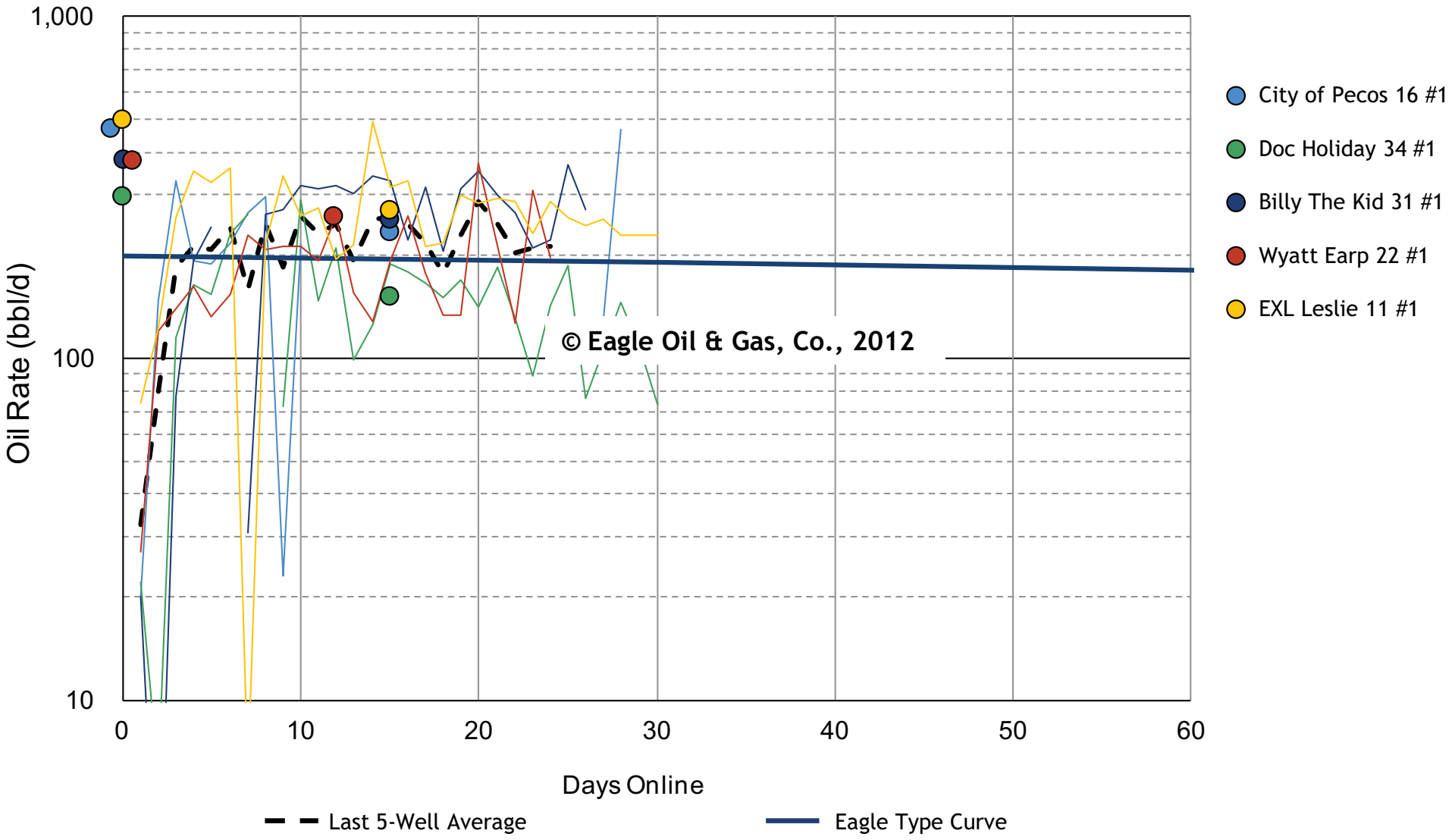

© Eagle Oil & Gas, Co., 2012

* Courtesy of Riverford Exploration, LLC

RIVERFORD EXPLORATION, LLC WOLFBONE WELLS RATE:TIME

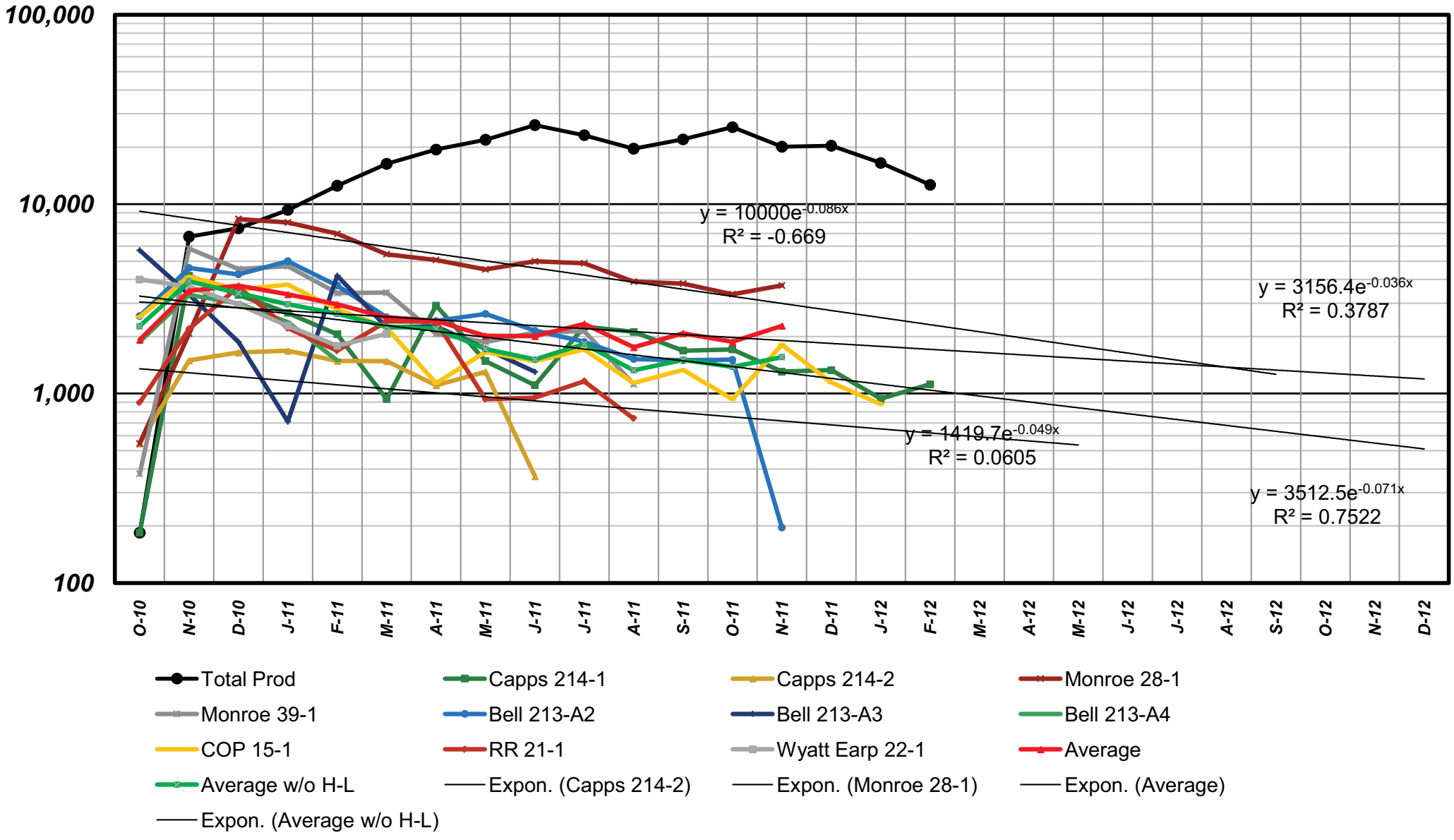

EAGLE OIL & GAS CO.

© Riverford Exploration, LLC, 2012

TUDOR PICKERING HOLT & CO | ENERGY INVESTMENT & MERCHANT BANKING

* Courtesy of Riverford Exploration, LLC

RIVERFORD EXPLORATION, LLC WOLFBONE WELLS
RATE : CUM (BO)

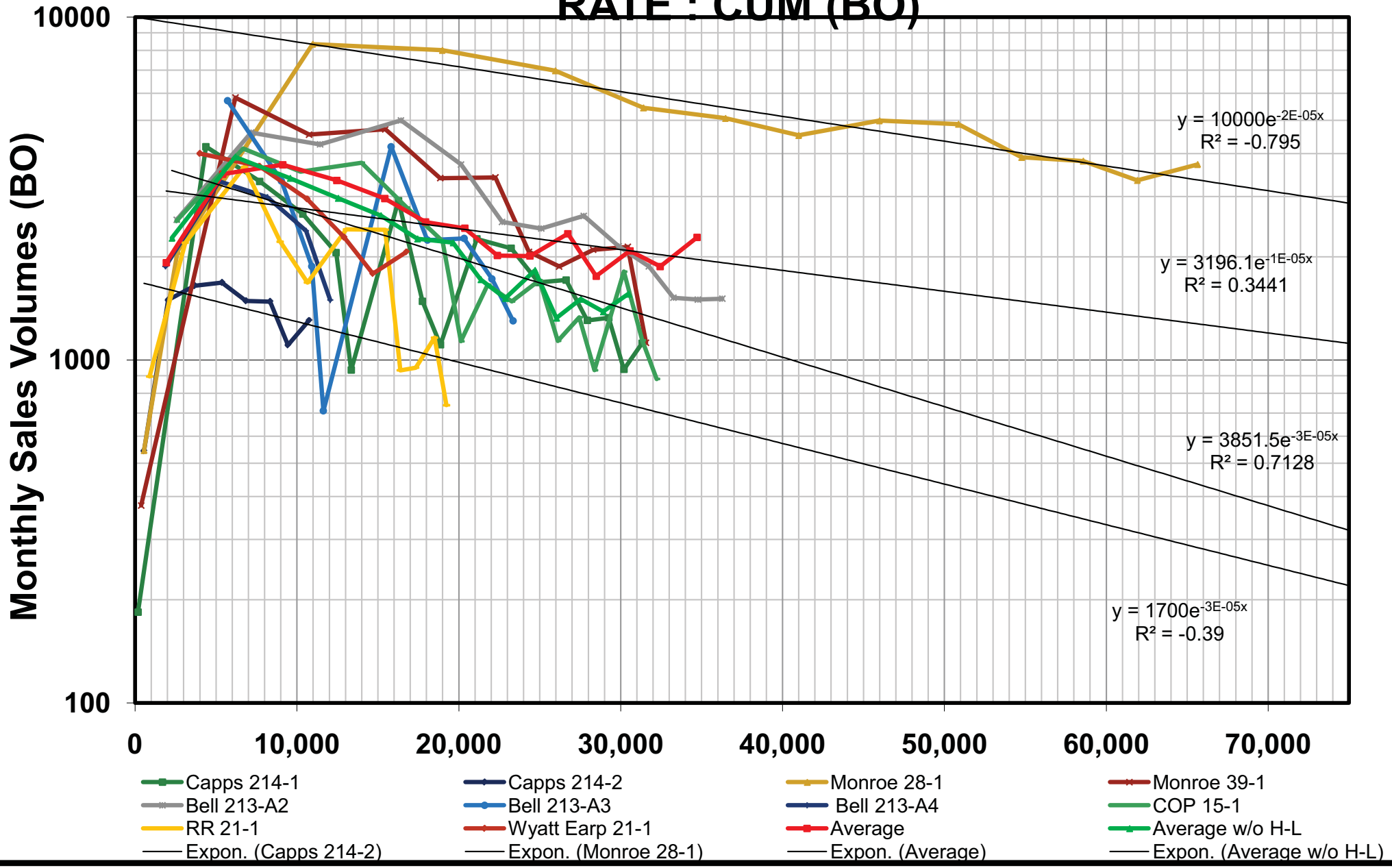

© Riverford Exploration, LLC, 2012

* Courtesy of Riverford Exploration, LLC

RIVERFORD EXPLORATION, LLC WOLFBONE WELLS, RATE : CUM (BO)

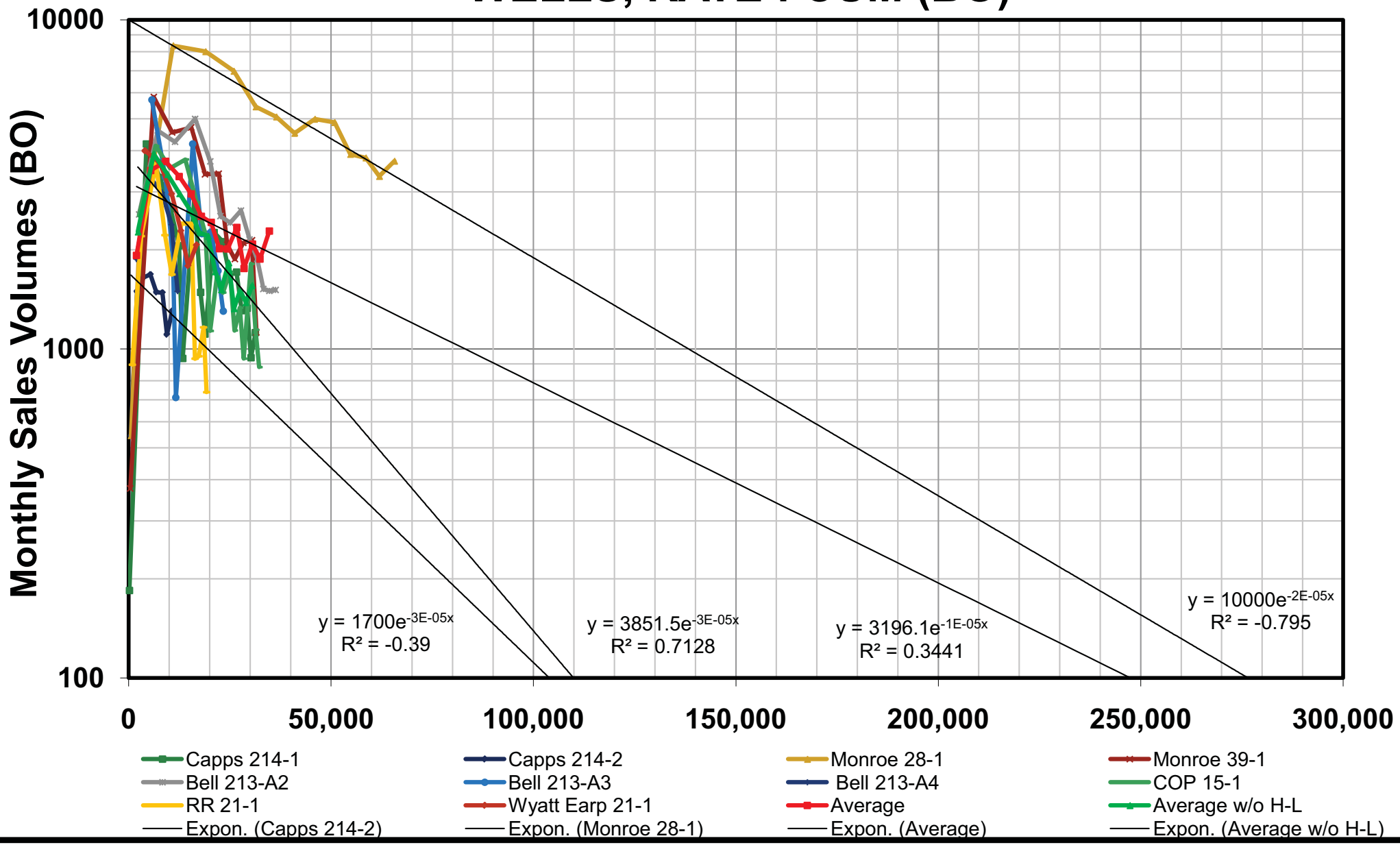

EAGLE OIL & GAS CO.

© Riverford Exploration, LLC, 2012

TUDOR PICKERING HOLT & CO | ENERGY INVESTMENT & MERCHANT BANKING

* Courtesy of Riverford Exploration, LLC

BELL 213-A2 ("TYPE WELL"), RATE : CUM (BO)

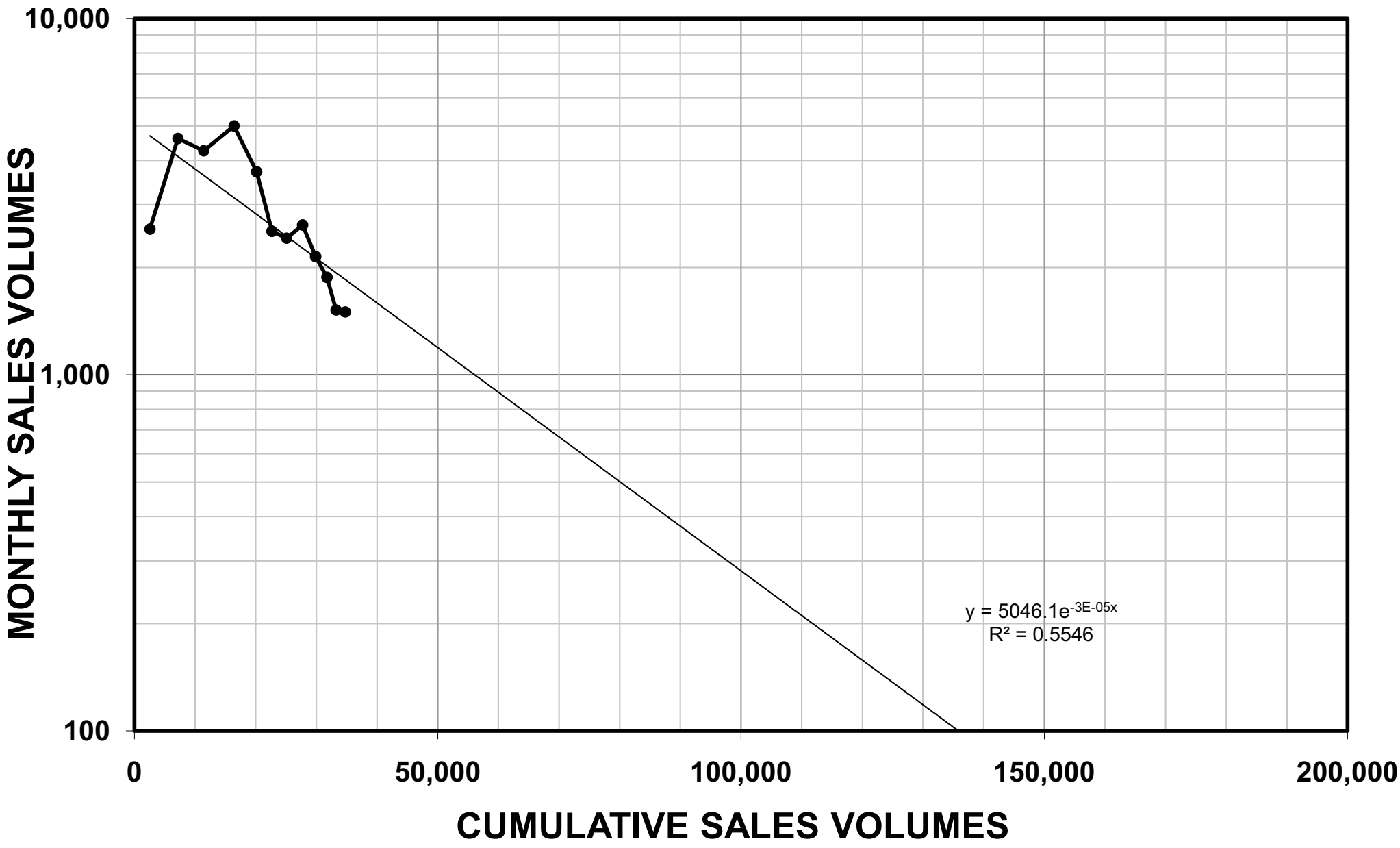

© Riverford Exploration, LLC, 2012

EAGLE OIL & GAS CO.

TUDORPICKERING HOLT&CO | ENERGY INVESTMENT & MERCHANT BANKING

* Courtesy of Riverford Exploration, LLC

MONROE 28 #1 ("HIGH-SIDE WELL)
RATE : CUM (BO)

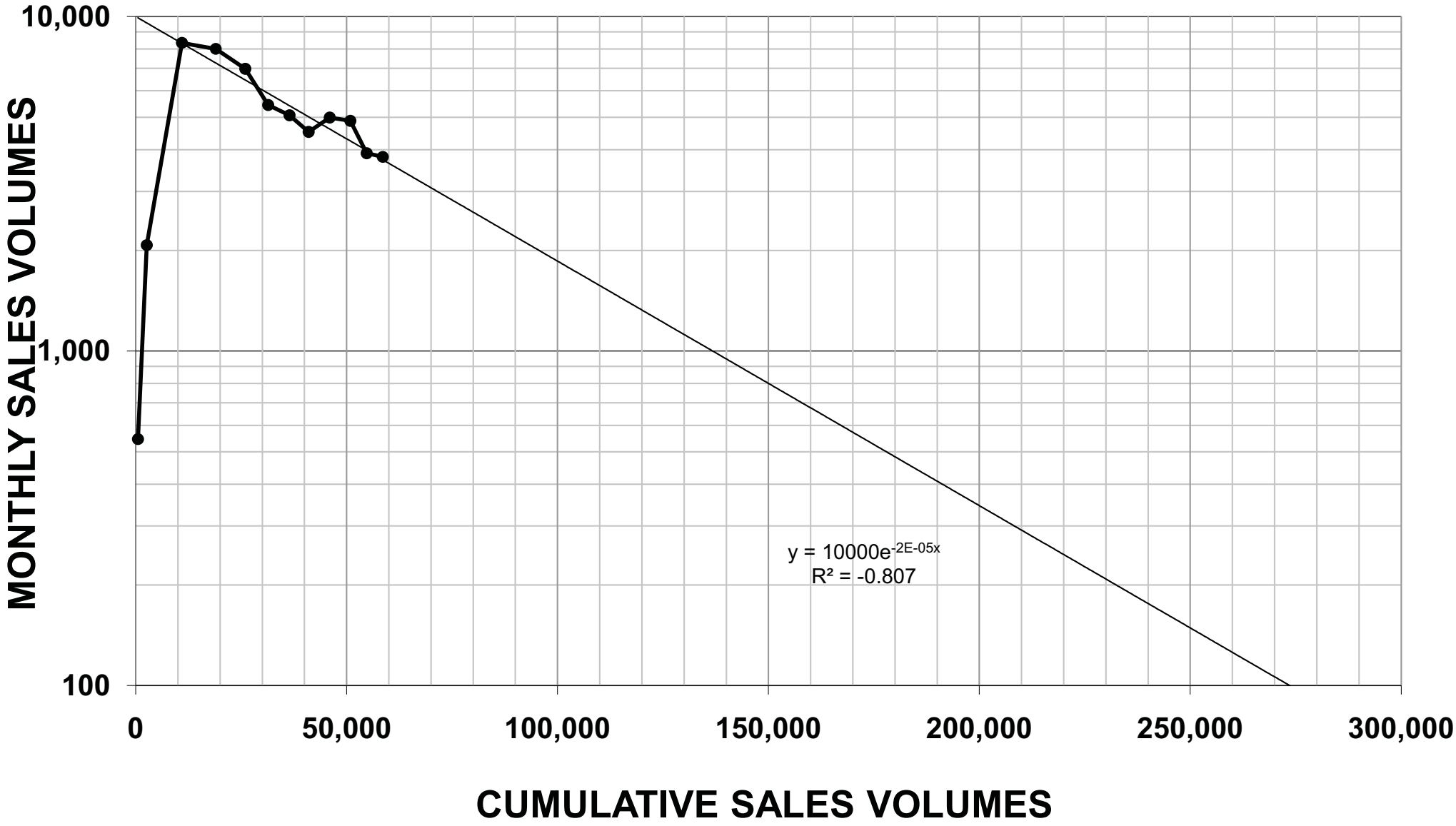

© Riverford Exploration, LLC, 2012

EAGLE OIL & GAS CO.

TUDOR PICKERING HOLT & CO | ENERGY INVESTMENT & MERCHANT BANKING

Wolfcamp – The Source of the Delaware's Success

Wolfcamp Geologic Characterization

- Ideal mineralogy and grain-size distribution to behave as both a source rock and a reservoir
- 108 MMboe in-place per square mile
- Approximately 1,000' thick
  - 2-5% TOC
  - 50-90% quartz & carbonate, 10% clay
- 0.7 psi/ft pressure gradient
  - From in-situ hydrocarbon generation & storage
  - Higher production rates
  - Shallower declines
- Carbonate debris flows were the primary target
  - Conventional Wolfcamp production
- Industry now targeting the source rock
  - Modern D&C techniques

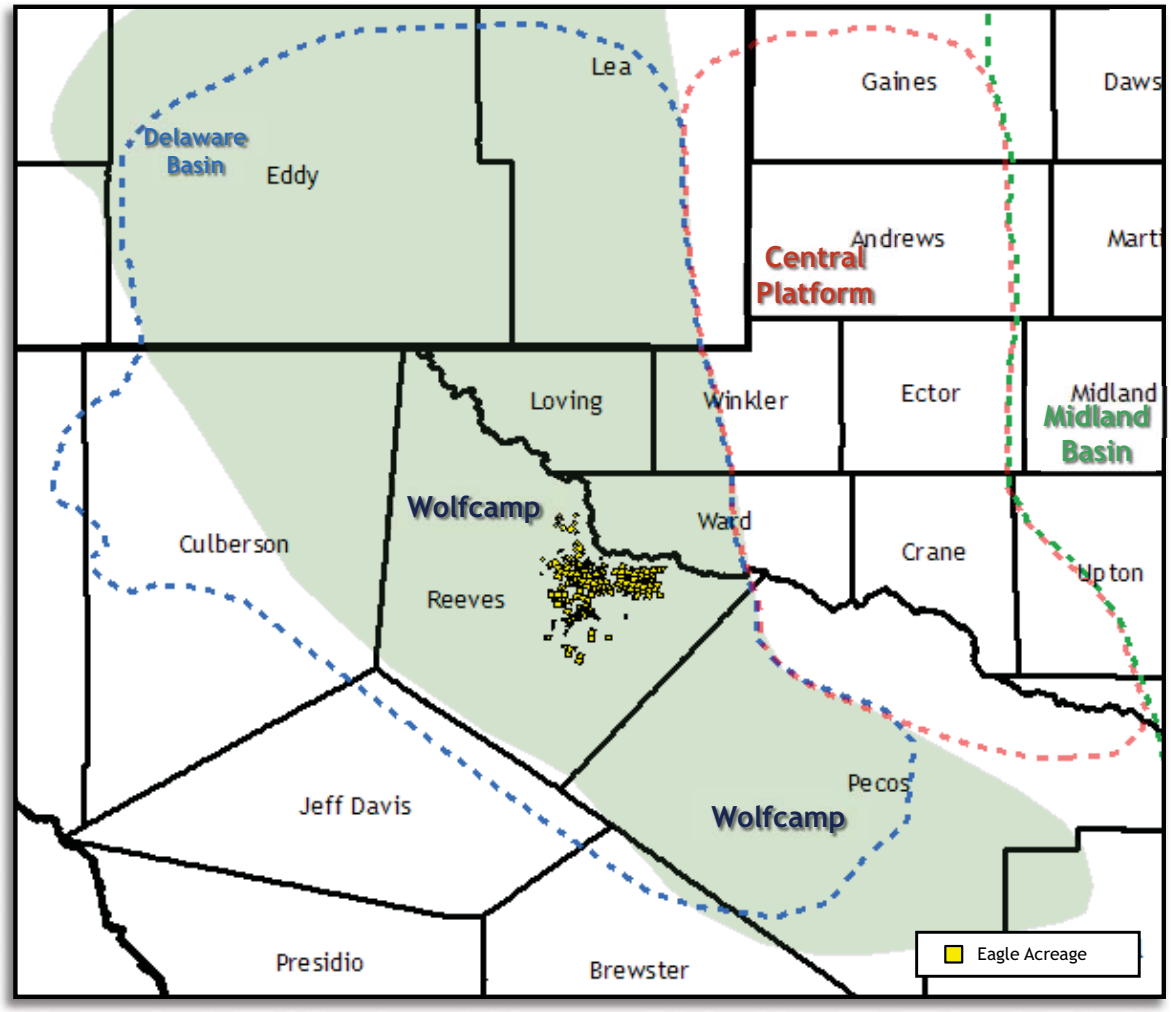

© Eagle Oil & Gas, Co., 2012

© Eagle Oil & Gas, Co., 2012

Wolfberry vs. Wolfbone

Wolfbone has Superior Reservoir Properties

- Depth and Pressure → Greater Reservoir Energy
  - Wolfbone is highly overpressured (~ 0.7 psi/ft)
  - Wolfbone is ~ 2,000' deeper
  - ***Wolfbone up to 2x Wolfberry pressure***
- Thicker vertical section leads to additional upside
  - Both completed over 1,250' interval
  - Wolfbone has 2,000' additional potential
- Substantial upside in the Delaware Basin
  - Uphole potential in Delaware Sands
  - Hz develoment

Wolfbone Well Count is Quickly Growing

STUDY AREA

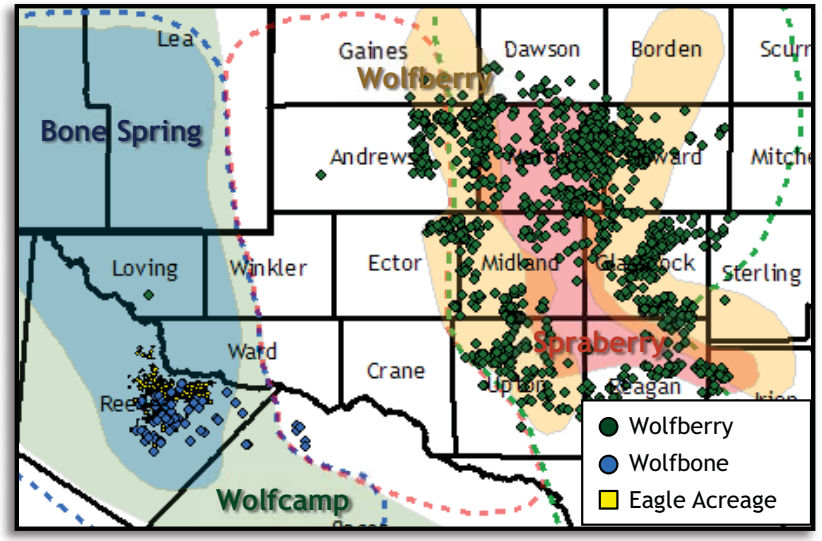

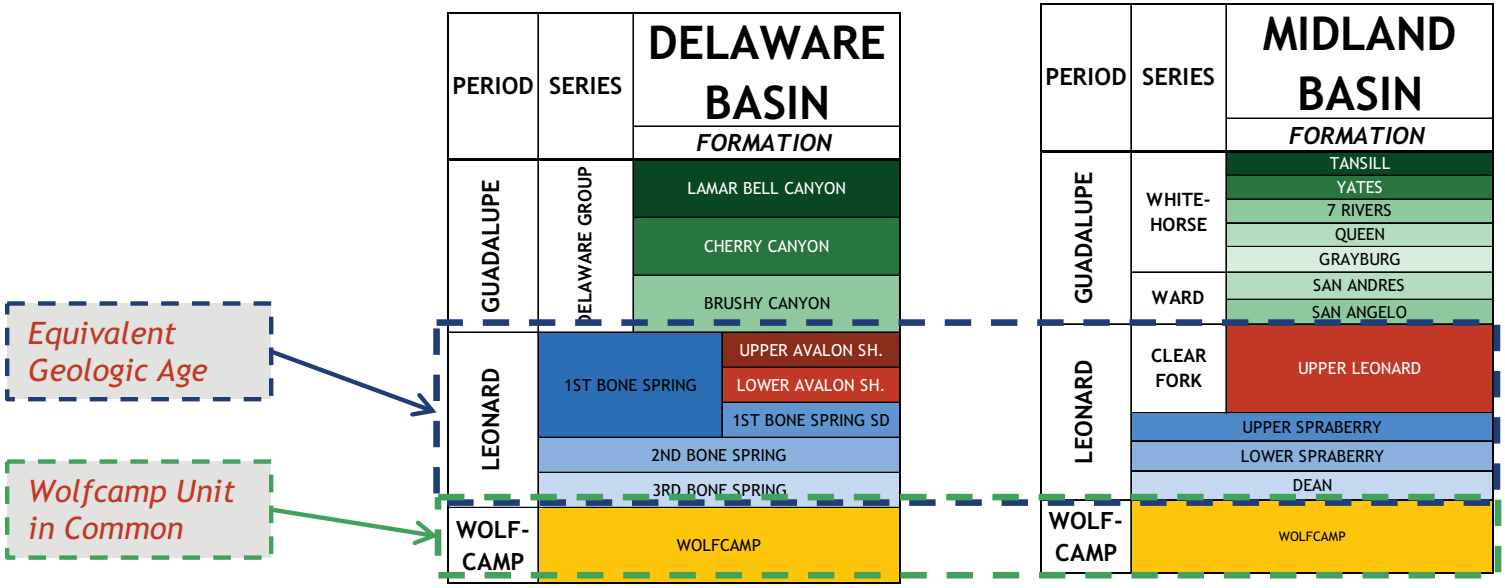

Map source: HPDI. Wolfberry wells drilled since 1/1/2010

© Eagle Oil & Gas, Co., 2012

EAGLE OIL & GAS CO.

TUDOR PICKERING HOLT & CO | ENERGY INVESTMENT & MERCHANT BANKING

Wolfbone… the Delaware's Wolfberry… only Better

Industry Bringing Midland Basin Technology to the Delaware

- Industry has increased Wolfberry EUR over time by comingling more zones
  - Activity significantly increased with improved results (now > 700 wells/year)
- Deeper, overpressured Delaware yielding superior Wolfbone EUR vs. Wolfberry
- Wolfbone wells flow 3-6 months before pump (20+ Mbo)

	Wolfbone (Delaware)	Wolfberry (Midland)
Primary Zones	3rd Bone Spring to Wolfcamp	Upr Spraberry to Wolfcamp
Additional Zones	Delaware Sands, Avalon Shale, Deeper zones	Non-traditional shale/silt zones and Deeper Zones *(Strawn, Atoka, Mississipian)*
EUR (Mboe)	240	165
% Liquids	> 80%	~ 65%
Depth (feet)	11,000 - 12,500	7,500 - 11,000
Spacing (acres)	40 acres 1 well will HBP 160 acres	40 acres (current), testing on 20

Strat Column

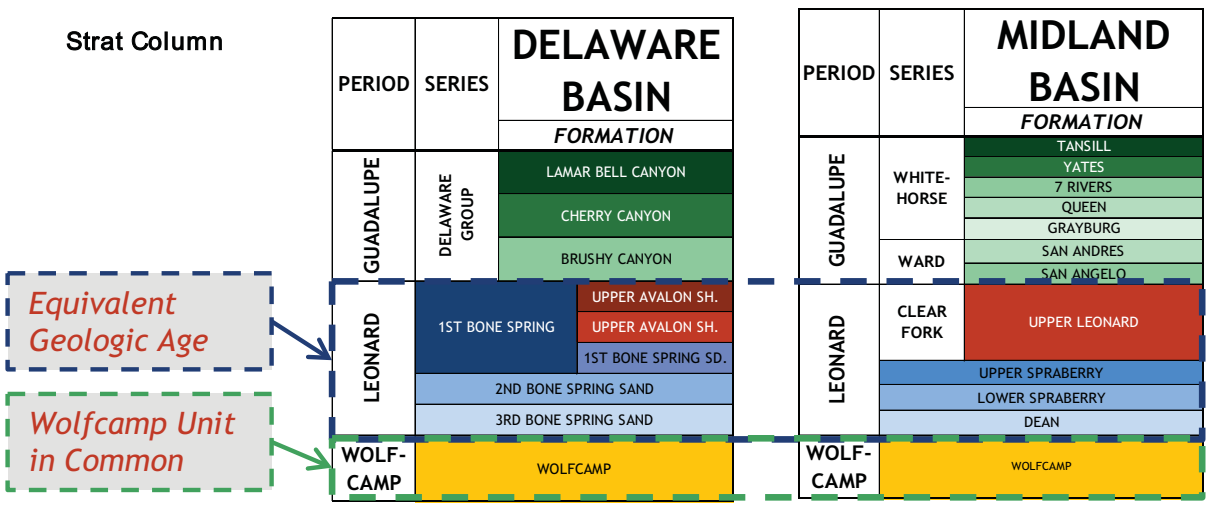

Wolfberry Evolution Through Technology[1]

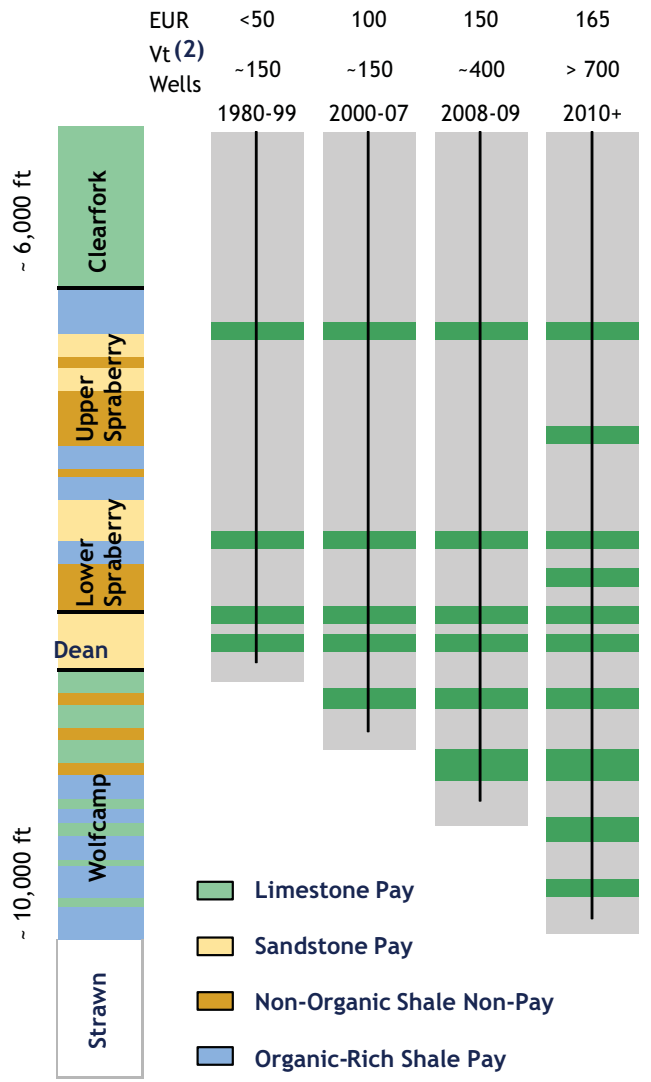

(1) Chart adapted from Pioneer Natural Resources.
(2) Approximate yearly average.

© Eagle Oil & Gas, Co., 2012

EAGLE OIL & GAS CO.

TUDOR PICKERING HOLT & CO | ENERGY INVESTMENT & MERCHANT BANKING

Wolfbone Type Curve (vs. Wolfberry)

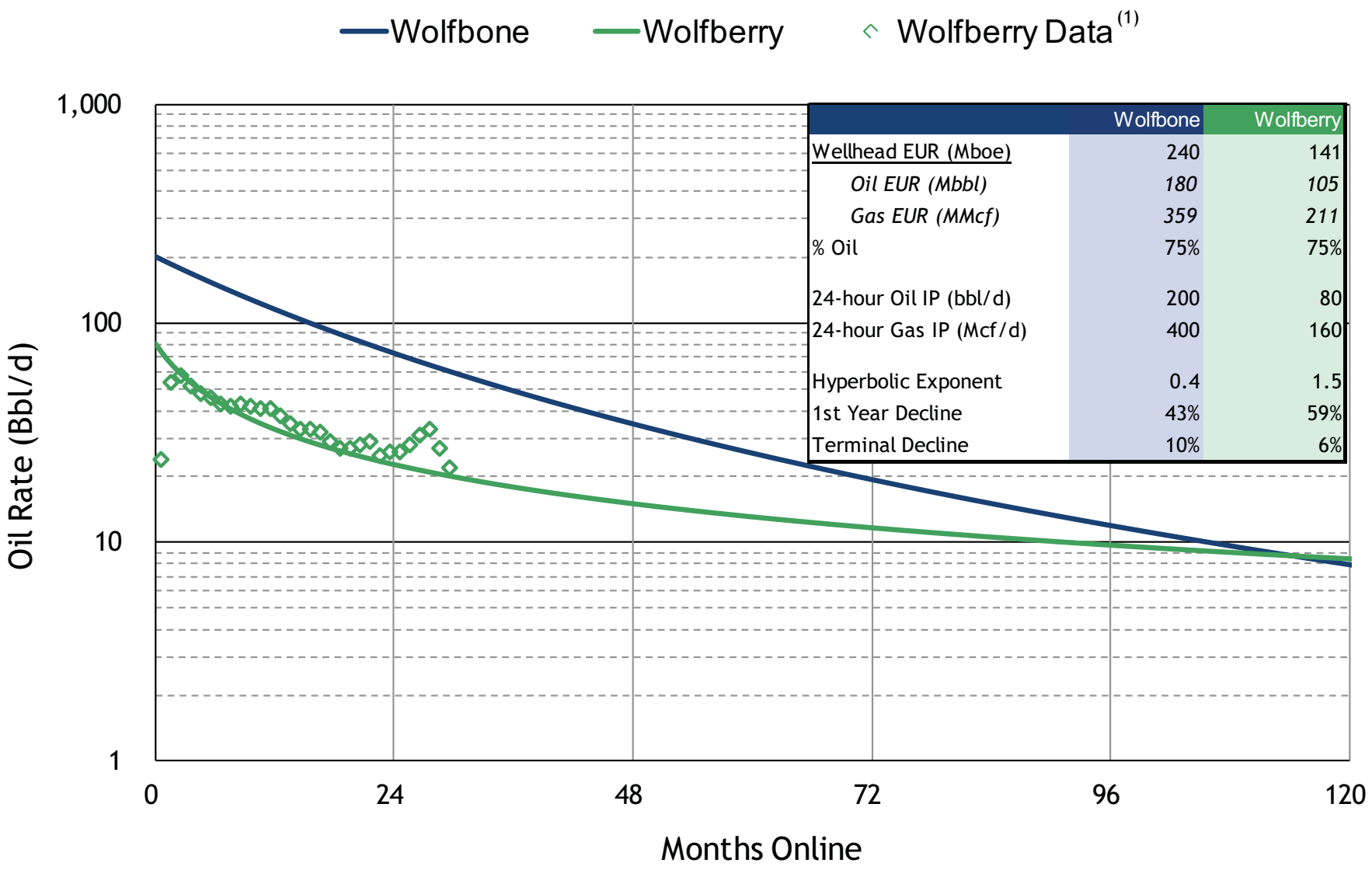

	Wolfbone	Wolfberry
Wellhead EUR (Mboe)	240	141
Oil EUR (Mbbl)	*180*	*105*
Gas EUR (MMcf)	*359*	*211*
% Oil	75%	75%
24-hour Oil IP (bbl/d)	200	80
24-hour Gas IP (Mcf/d)	400	160
Hyperbolic Exponent	0.4	1.5
1st Year Decline	43%	59%
Terminal Decline	10%	6%

GOR (scf/stb): 2,000

(1) 2009+ vintage Wolfberry completions.

© Eagle Oil & Gas, Co., 2012

Wolfbone 30-Day IP Bubble Map

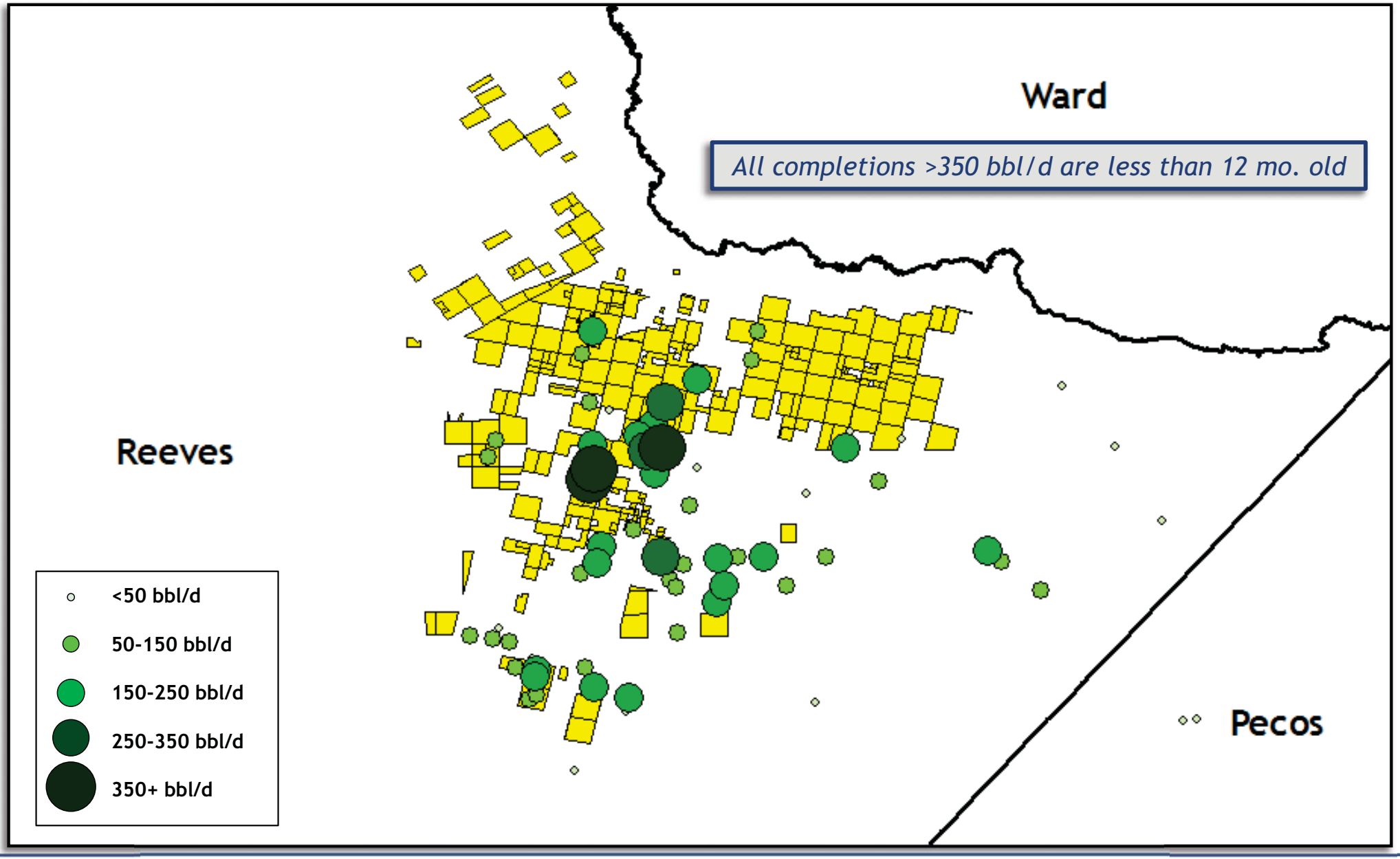

NOTE: Wells completed as Wolfbone producers after 1/1/2009 – Hoban, Hoban South, Wolfbone fields.

© Eagle Oil & Gas, Co., 2012

EAGLE OIL & GAS CO.

TUDOR PICKERING HOLT & CO | ENERGY INVESTMENT & MERCHANT BANKING

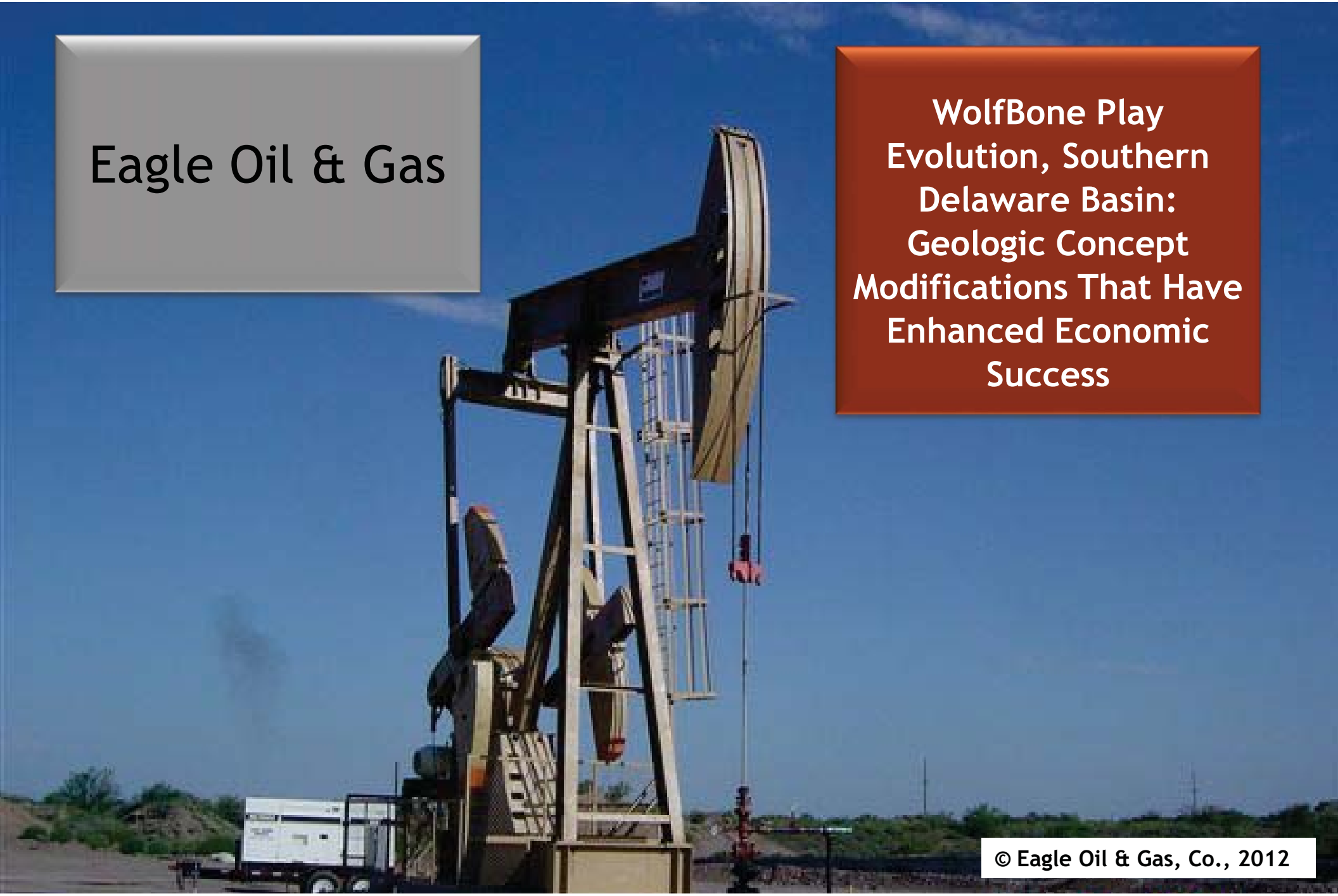

Eagle Oil & Gas

WolfBone Play Evolution, Southern Delaware Basin: Geologic Concept Modifications That Have Enhanced Economic Success

© Eagle Oil & Gas, Co., 2012

Fairhurst, Bill; Hanson, Mary Lisbeth; Reid, Frank; and Pieracacos, Nick

EAGLE OIL & GAS CO.

* Courtesy of Carrollton Minerals Partners

Avalon –
- ~800' thick.
- 105 MMboe in-place per sq. mile

Period		Unit	~ Depth	
Permian	Guadalupian	Bell Canyon		
		Cherry Canyon		
		Brushy Canyon		
	Leonardian	Upper Avalon Shale	8,800	500'-700'
		Lower Avalon Shale		
		1st Bone Spring Sand		
		2nd Bone Spring Shale Upr	9,600	
		2nd Bone Spring Shale Lwr	9,850	
		3rd Bone Spring	10,150	150'
	Wolfcampian	Upr Wolfcamp Shale A	10,440	900'-1200'
		Upr Wolfcamp Shale B	10,700	
		Mid Wolfcamp Shale A	10,900	
		Mid Wolfcamp Shale B	11,100	
		Md Wolfcamp Sand A	11,650	
		Md Wolfcamp Sand B	12,000	
		Md Wolfcamp Sand C	12,250	

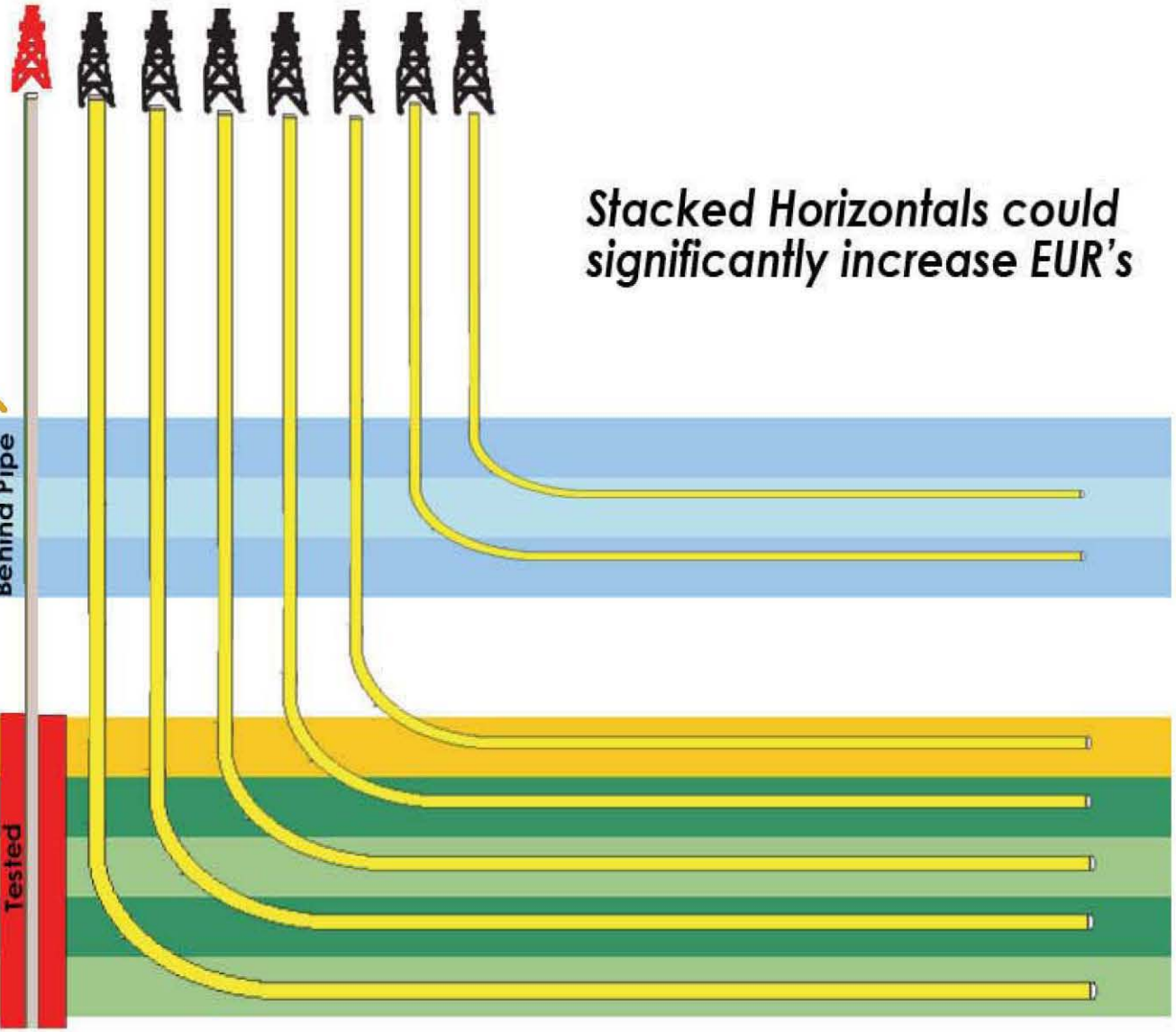

Stacked Horizontals could significantly increase EUR's

Stacked pay Verticals producing in 3rd Bone - Wolfcamp series

Wolfbone Vertical –
- ~1200' thick.
- 108 MMboe in-place per sq. mile

© Carrollton Minerals Partners, 2012

EAGLE OIL & GAS CO.

TUDORPICKERING HOLT&CO | ENERGY INVESTMENT & MERCHANT BANKING

Going Sideways to Get Ahead

Horizontals in the Delaware

- Operators have been developing the 3rd Bone Spring with horizontal wells
  - Capture more acreage than vertical wells
  - More stimulated rock volume leads to higher rates
  - Larger drainage area leads to greater ultimate recovery
- Thick sections perfect for horizontal development
  - 2+ laterals per unit (Bone Spring, Wolfcamp, Avalon)
  - More laterals increase recovery factor per section

Horizontal Wells consistently Outperform Vertical

- Vertical to Horizontal EUR factor:

Play	EUR Multiplier
Bakken	3 - 5x
Eagle Ford	5 - 7x
Granite Wash	4 - 5x
Miss Lime	3 - 4x
Niobrara	6 - 8x
Wolfcamp (Midland)	5 - 6x
Wolfcamp (Delaware)	3x

Average ~ 5x

Vertical vs. Horizontal Drainage Area

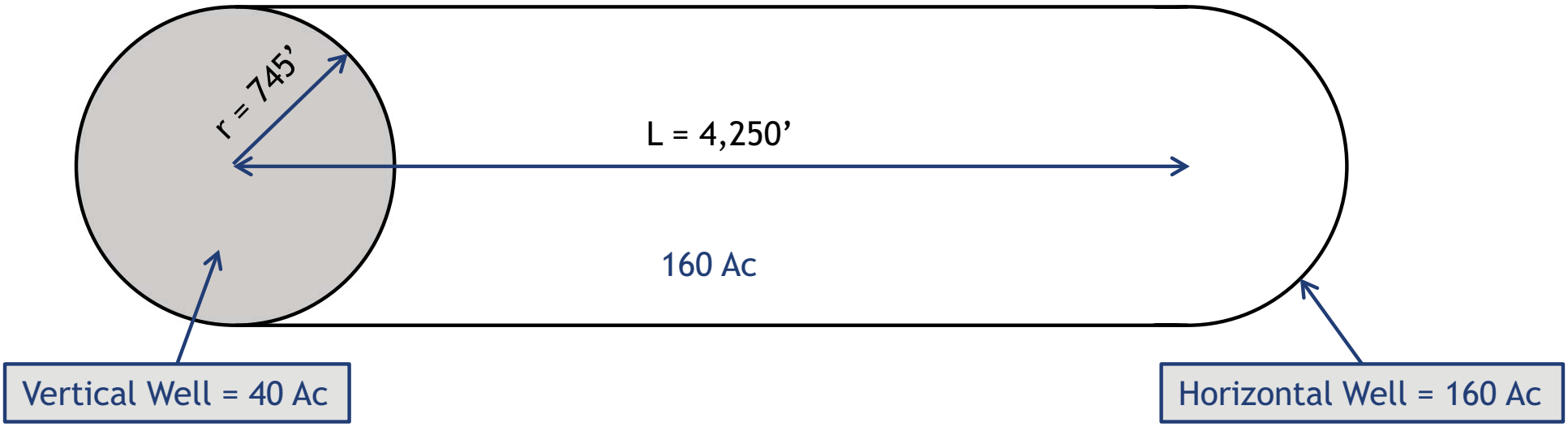

Source: CHK IR presentation. TPH internal research.

© Eagle Oil & Gas, Co., 2012

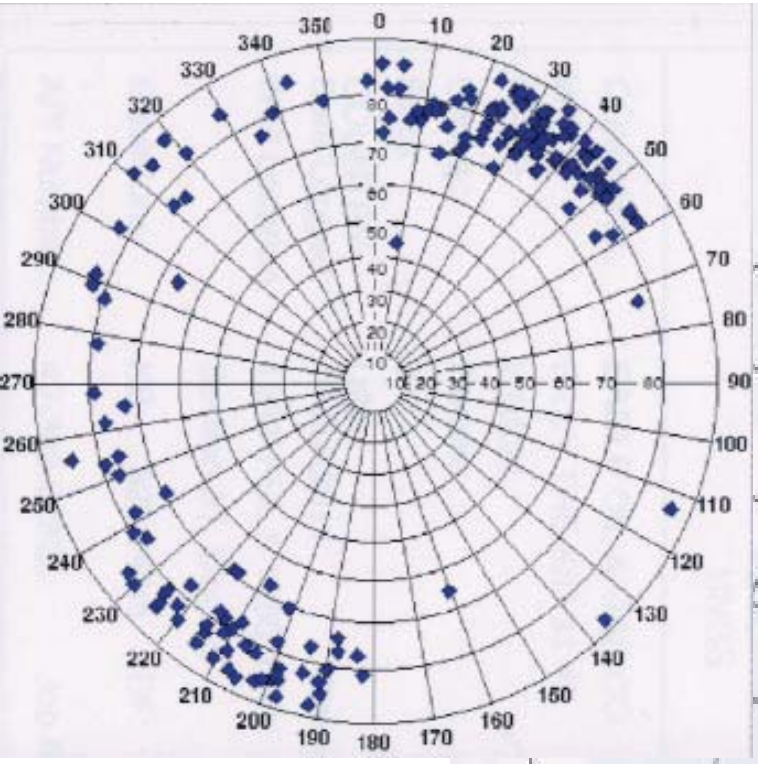

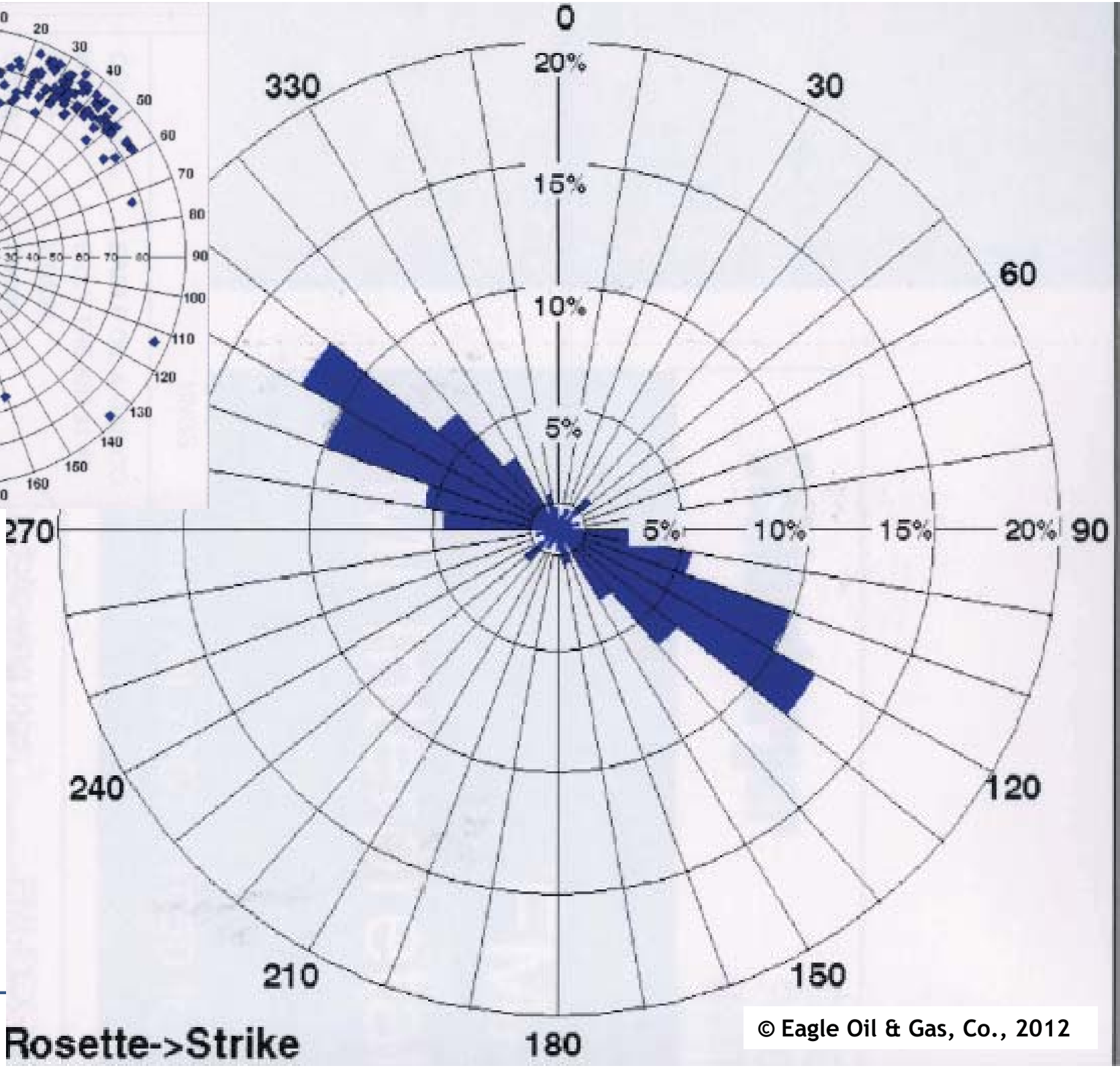

© Eagle Oil & Gas, Co., 2012



© Eagle Oil & Gas, Co., 2012

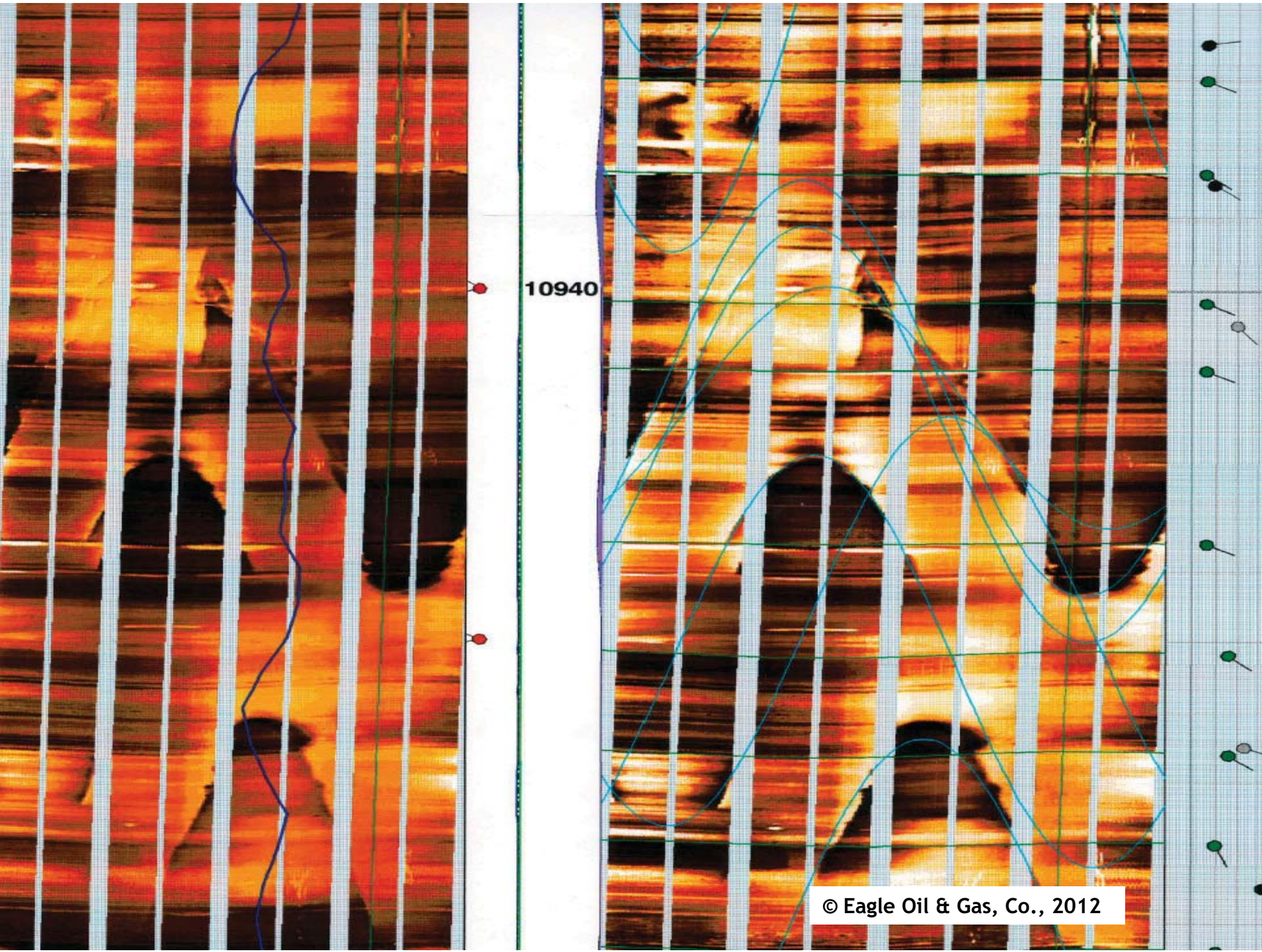

© Eagle Oil & Gas, Co., 2012

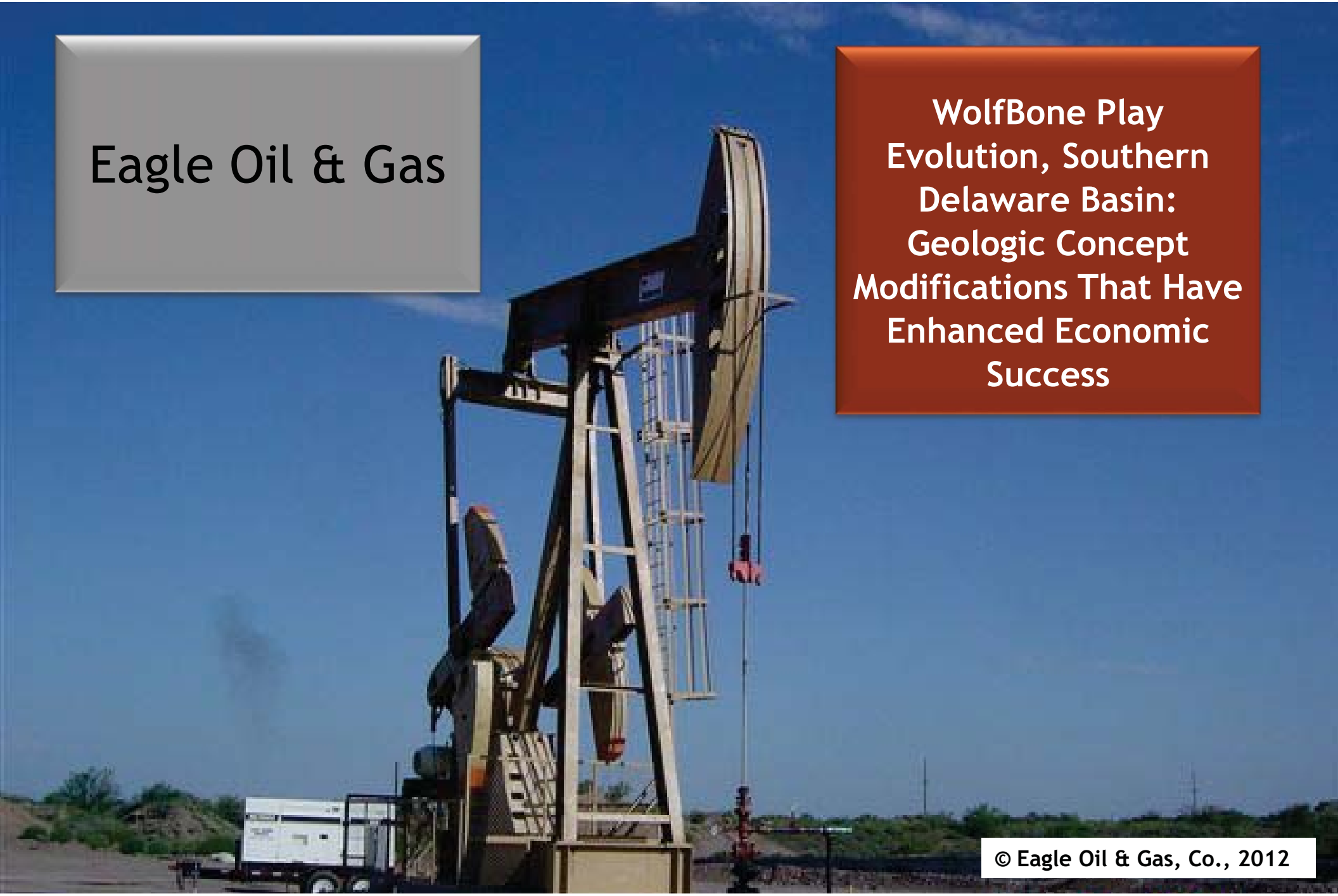

Eagle Oil & Gas

WolfBone Play Evolution, Southern Delaware Basin: Geologic Concept Modifications That Have Enhanced Economic Success

© Eagle Oil & Gas, Co., 2012

Fairhurst, Bill; Hanson, Mary Lisbeth; Reid, Frank; and Pieracacos, Nick

EAGLE OIL & GAS CO.

Bone Spring

Bone Spring Depositional Area

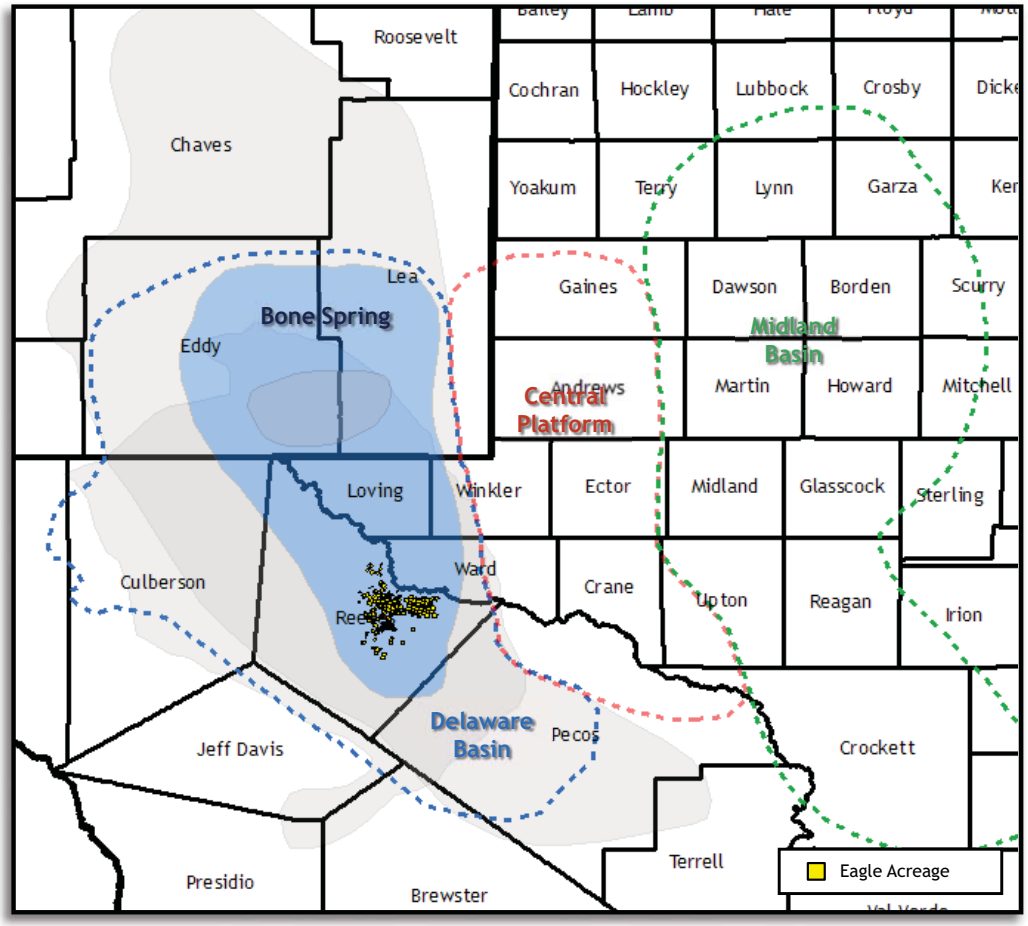

PERIOD	SERIES	DELAWARE BASIN FORMATION		
QUATERNARY / TERTIARY		ALLUVIUM		
CRETACEOUS	GULFIAN			
	COMAN-CHEAN	FREDERICKSBURG		
		TRINITY SD.		
	UPPER			SANTA ROSA
PERMIAN	OCHOAN		DEWEY LAKE	
			RUSTLER	
			SALDO	
			CASTILLE	
	GUADALU-PIAN	DE SANDS	BELL CANYON	
			CHERRY CANYON	
			BRUSHY CANYON	
	LEONARDIAN	1ST BONE SPRING		UPPER AVALON SH.
				LOWER AVALON SH.
				1ST BONE SPRING SD.
		2ND BONE SPRING		
		3RD BONE SPRING		
	WOLFCAMPIAN	WOLFCAMP		
Pennsylvanian	VIRGIL	CISCO		
	MISSOURI	CANYON		
	DES MOINES	STRAWN		
	ATOKA	ATOKA		
	MORROW	MORROW		

The Bone Spring package exists across much of the Delaware Basin though different members are more prevalent in specific areas

© Eagle Oil & Gas, Co., 2012

Avalon Shale

Avalon Shale Depositional Area

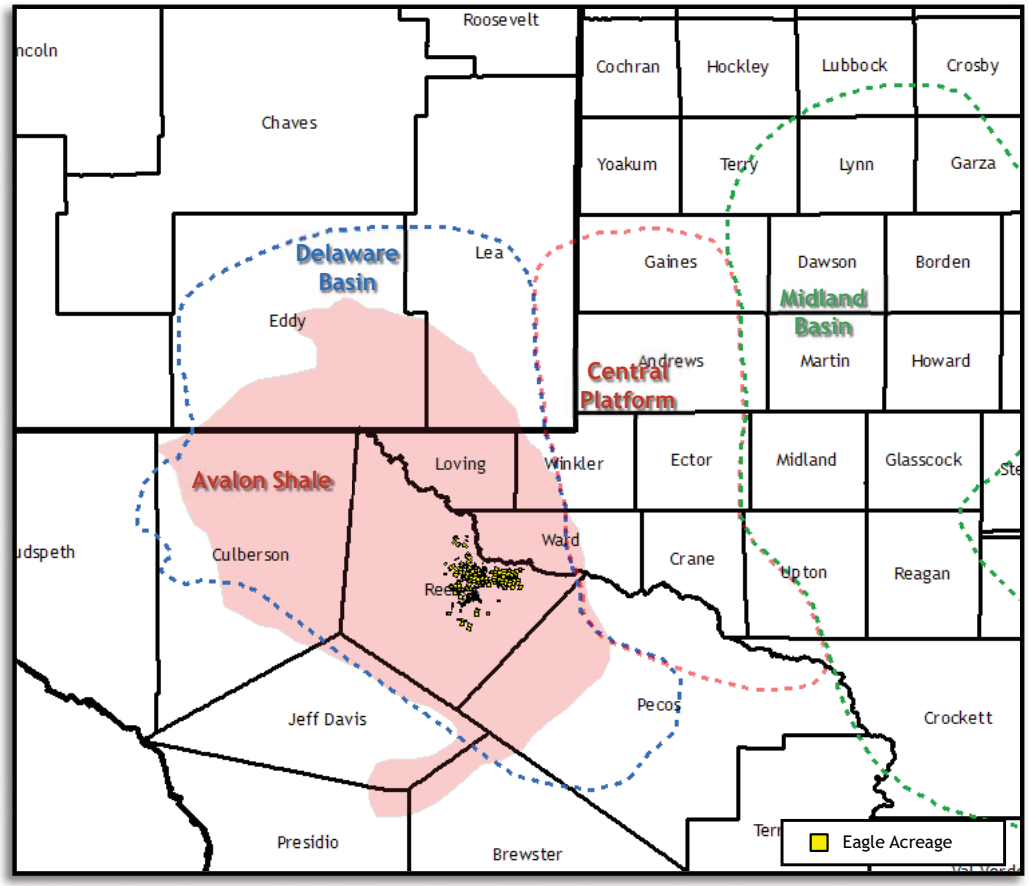

PERIOD	SERIES	DELAWARE BASIN FORMATION		
QUATERNARY / TERTIARY		ALLUVIUM		
CRETACEOUS	GULFIAN			
	COMAN-CHEAN	FREDERICKSBURG		
		TRINITY SD.		
	UPPER			SANTA ROSA
PERMIAN	OCHOAN	DEWEY LAKE		
		RUSTLER		
		SALDO		
		CASTILLE		
	GUADALU-PIAN	DE SANDS	BELL CANYON	
			CHERRY CANYON	
			BRUSHY CANYON	
	LEONARDIAN	1ST BONE SPRING		UPPER AVALON SH.
				LOWER AVALON SH.
				1ST BONE SPRING SD.
		2ND BONE SPRING		
		3RD BONE SPRING		
	WOLFCAMPIAN	WOLFCAMP		
Pennsylvanian	VIRGIL	CISCO		
	MISSOURI	CANYON		
	DES MOINES	STRAWN		
	ATOKA	ATOKA		
	MORROW	MORROW		

The Avalon Shale is present throughout the Delaware basin and is currently being pursued as an unconventional play in the Northern half

EAGLE OIL & GAS CO.

© Eagle Oil & Gas, Co., 2012

TUDOR PICKERING HOLT & CO ENERGY INVESTMENT & MERCHANT BANKING

What is the Avalon Shale?

The Avalon Shale is the stratigraphic interval between the top of the Bone Spring Formation & the 1st Bone Spring Sand

Basin Geology

- Bounded by carbonate shelves & platforms
  - North: Northwest Shelf
  - East: Central Basin Platform
  - South: Marathon Fold Belt
  - West: Diablo Platform
- Bone Spring stratigraphy varies across the Delaware Basin
  - NW Shelf: predominantly carbonate
  - Slope: 1st/2nd/3rd sandstones developing in the lower part of the interval
- Deep Basin → Avalon Shale
  - "Shale" development within the upper 1st Carbonate section
  - Organic-rich siltstone and carbonate debris flow
  - Unconventional, continuous accumulation
  - 900 – 1,000' gross thickness

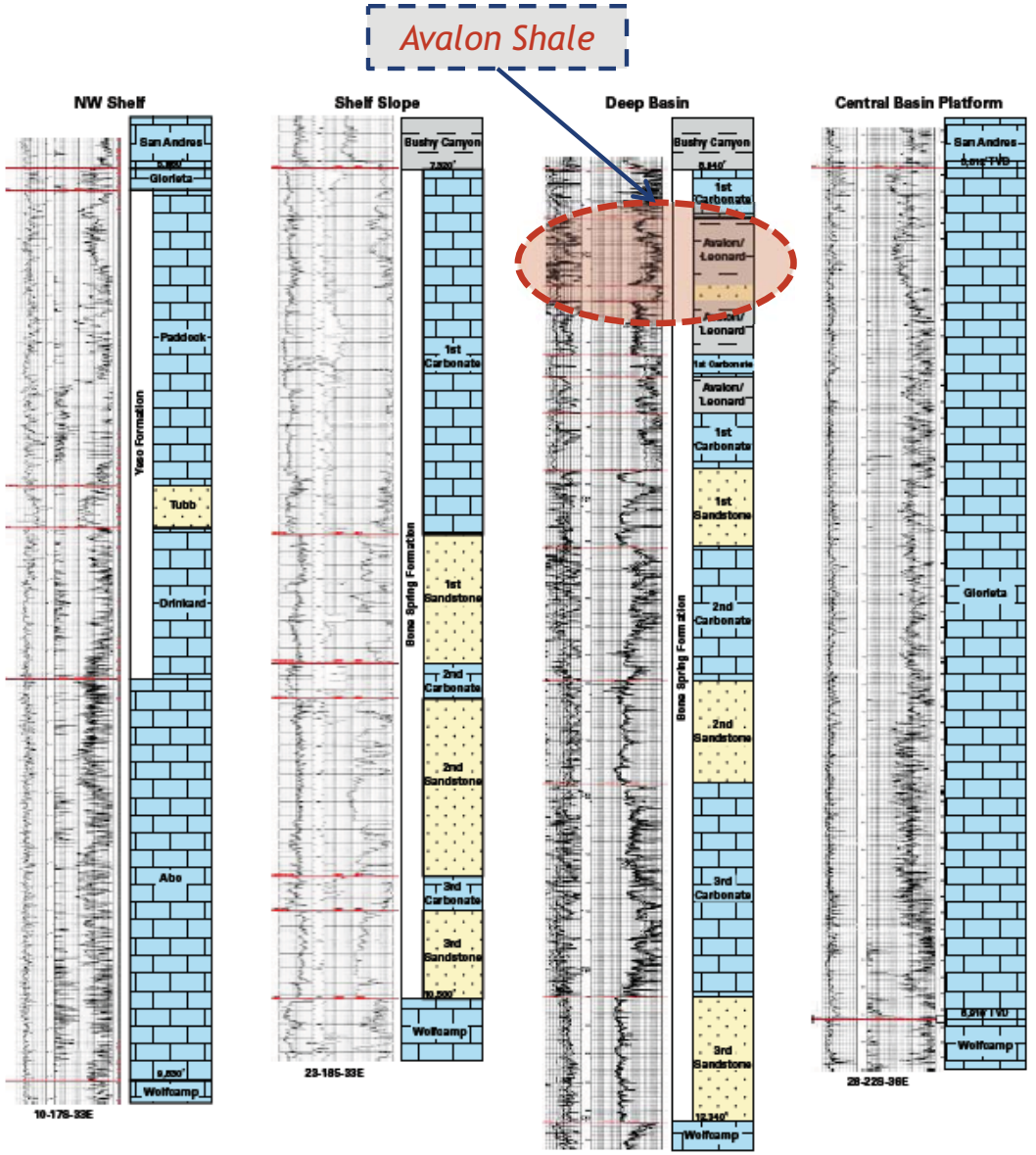

© Eagle Oil & Gas, Co., 2012

EAGLE OIL & GAS CO.

TUDOR PICKERING HOLT & CO | ENERGY INVESTMENT & MERCHANT BANKING

Avalon Shale Net Isopach

Summary

- Map Parameters
  - Ft > 12% Density Porosity
  - GR > 75 Units
  - Resistivity > 20 ohm-m
  - From 600 data points
- Isopach is concentric from basin edges
- Porosity thick coincides with Bone Spring thick above basin low
- Primarily Pelagic deposition

Structure

- Regional Structure dips east at 100’ per mile
- 6,000’ deep in W. Eddy to 10,000’ deep in Lea County
- Lea County has more structural nosing and dip reversals than Eddy
- Axial low of basin trends N-S through Lea and Loving Counties
- GOR varies with depth with oily production in deeper basin

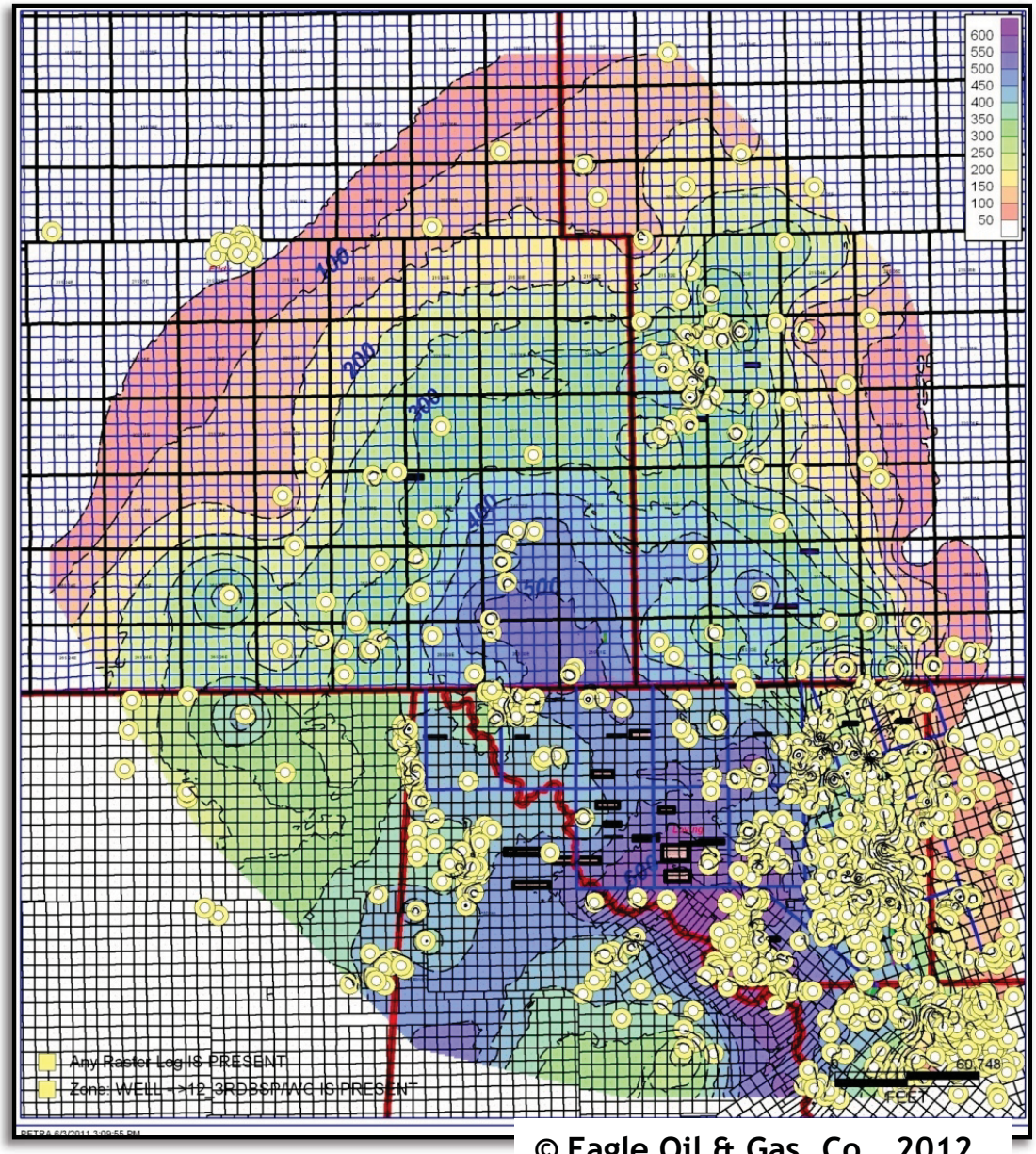

© Eagle Oil & Gas, Co., 2012

Source: Net isopach map and summary bullets from John Worrall (Geologist and Partner, Bold Energy II, LLC and Manzano Energy Partners), and Chad Kronkosky (Reservoir Engineer, Bold Energy II, LLC).

Eagle Avalon Shale Isopach

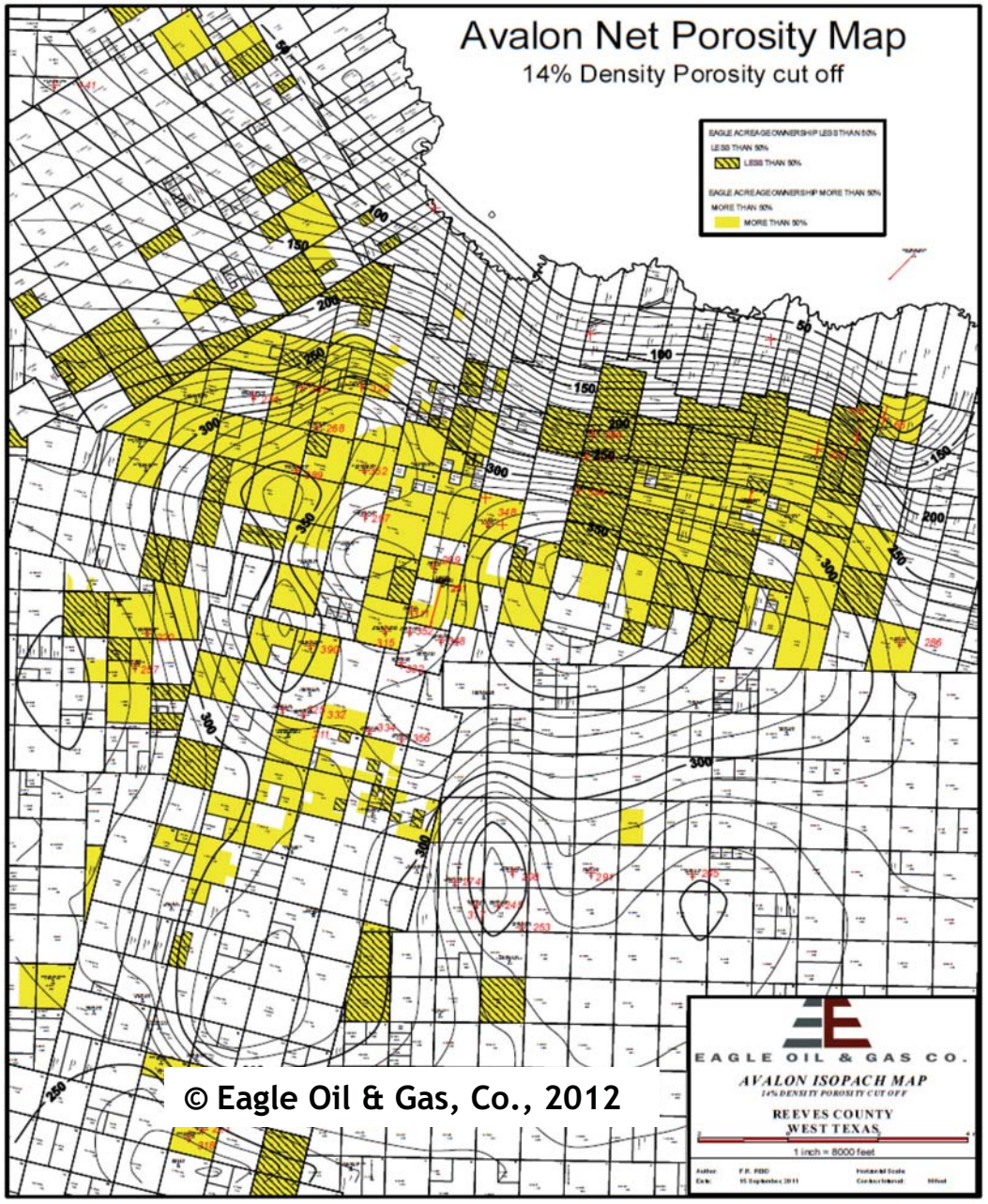

105 MMboe in-place per square mile across Eagle position

Texas Avalon / Bone Spring Production Increasing

Production growth expected to continue recent momentum given industry focus on liquids and public statements from operators

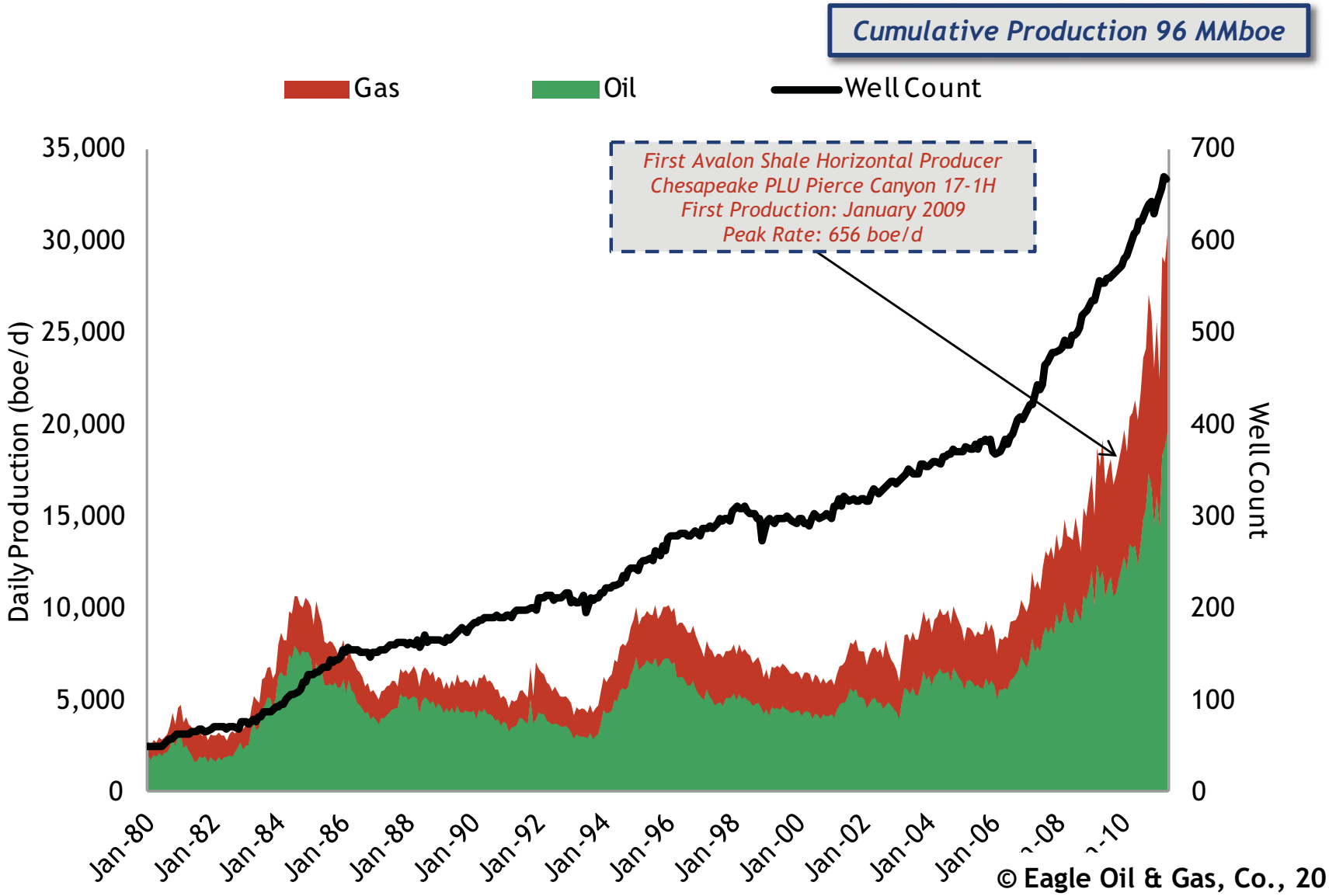

© Eagle Oil & Gas, Co., 2012

Source: HPDI. Includes vertical and horizontal wells with a target reservoir of Bone Spring or Avalon (HPDI does not currently distinguish between the zones) in the following counties: Reeves, Loving, Ward, Pecos, Winkler

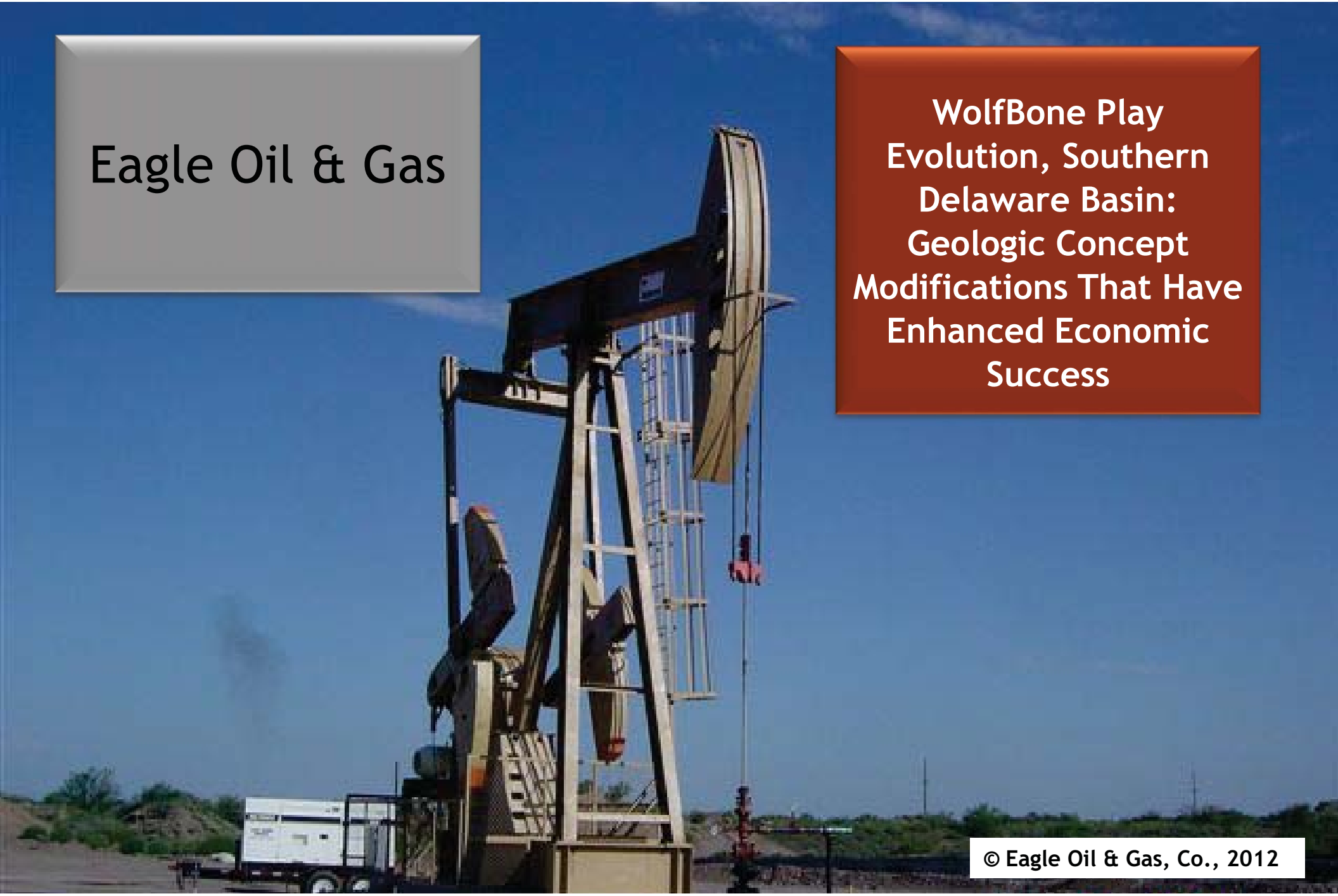

Eagle Oil & Gas

WolfBone Play Evolution, Southern Delaware Basin: Geologic Concept Modifications That Have Enhanced Economic Success

© Eagle Oil & Gas, Co., 2012

Fairhurst, Bill; Hanson, Mary Lisbeth; Reid, Frank; and Pieracacos, Nick

EAGLE OIL & GAS CO.

Turbidite Channel Cross-Section

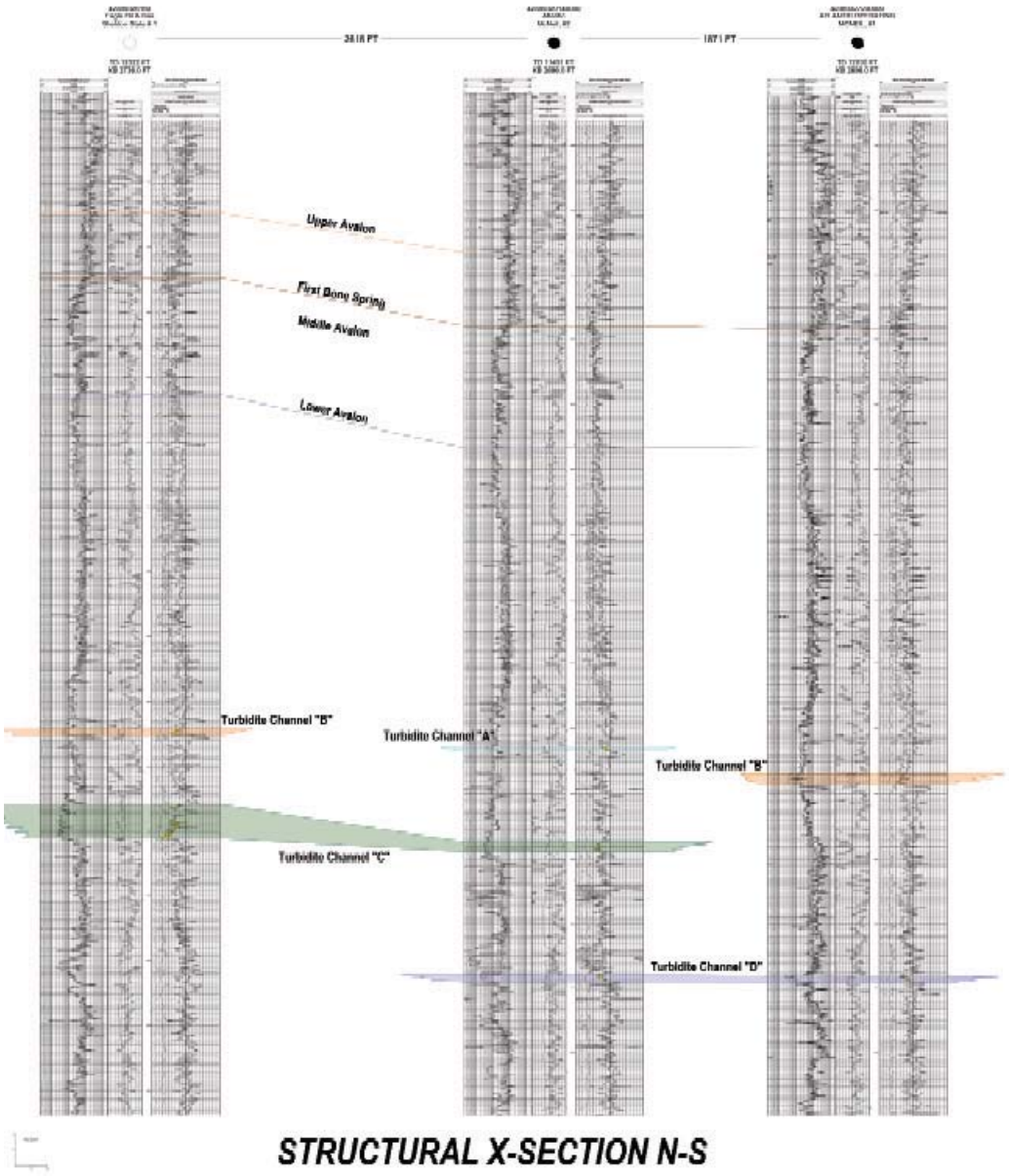

STRUCTURAL X-SECTION N-S



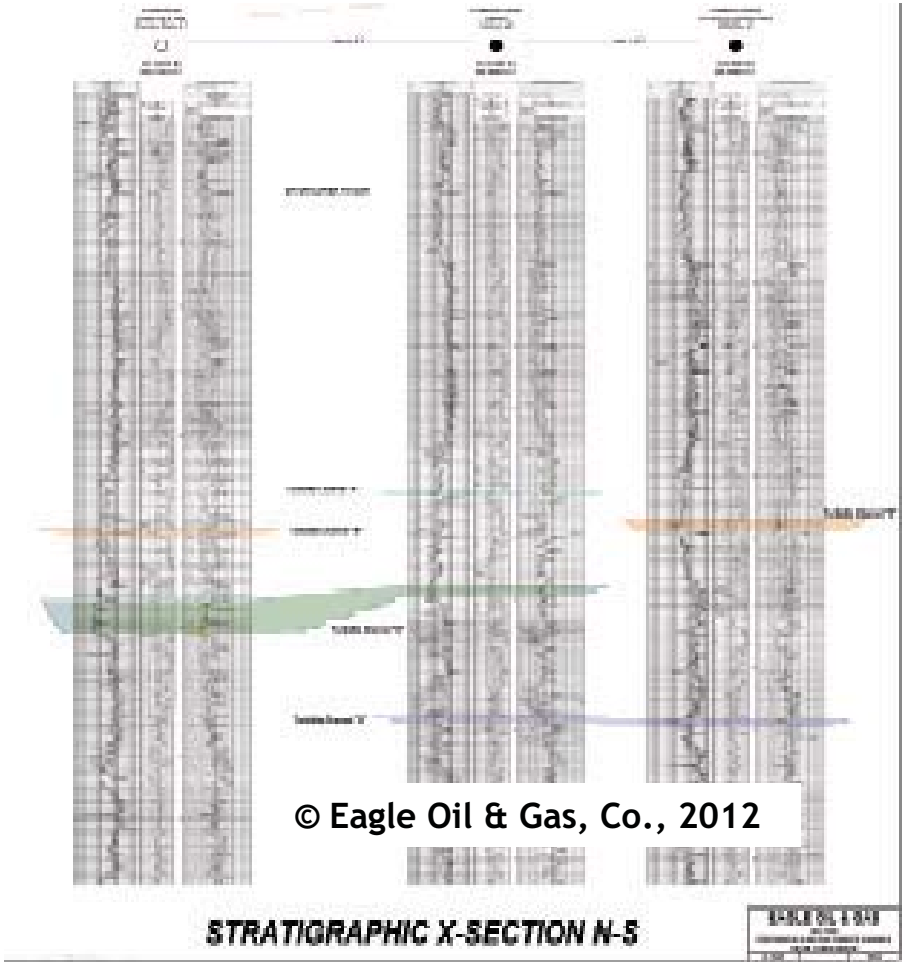

© Eagle Oil & Gas, Co., 2012

STRATIGRAPHIC X-SECTION N-S

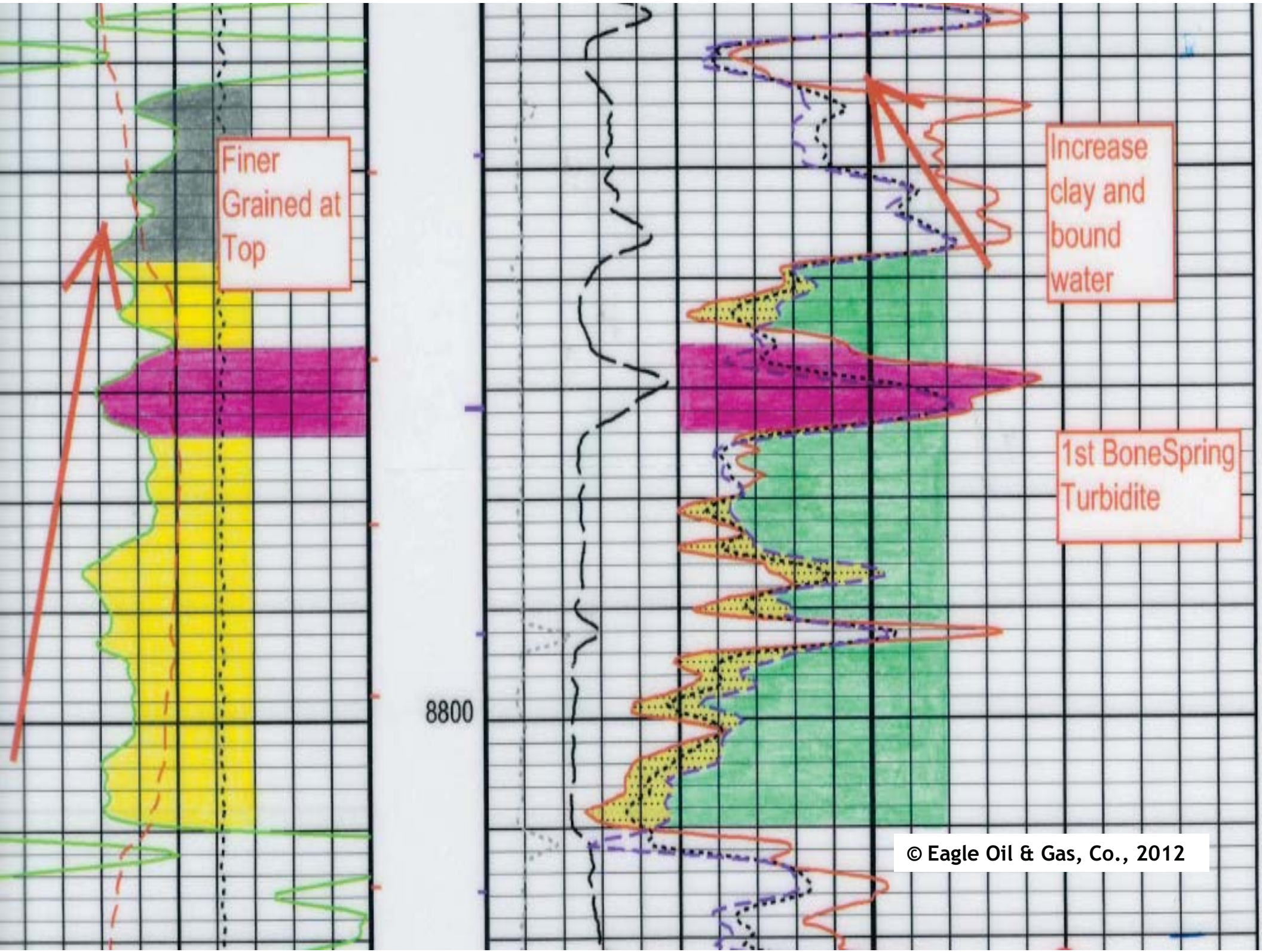

© Eagle Oil & Gas, Co., 2012

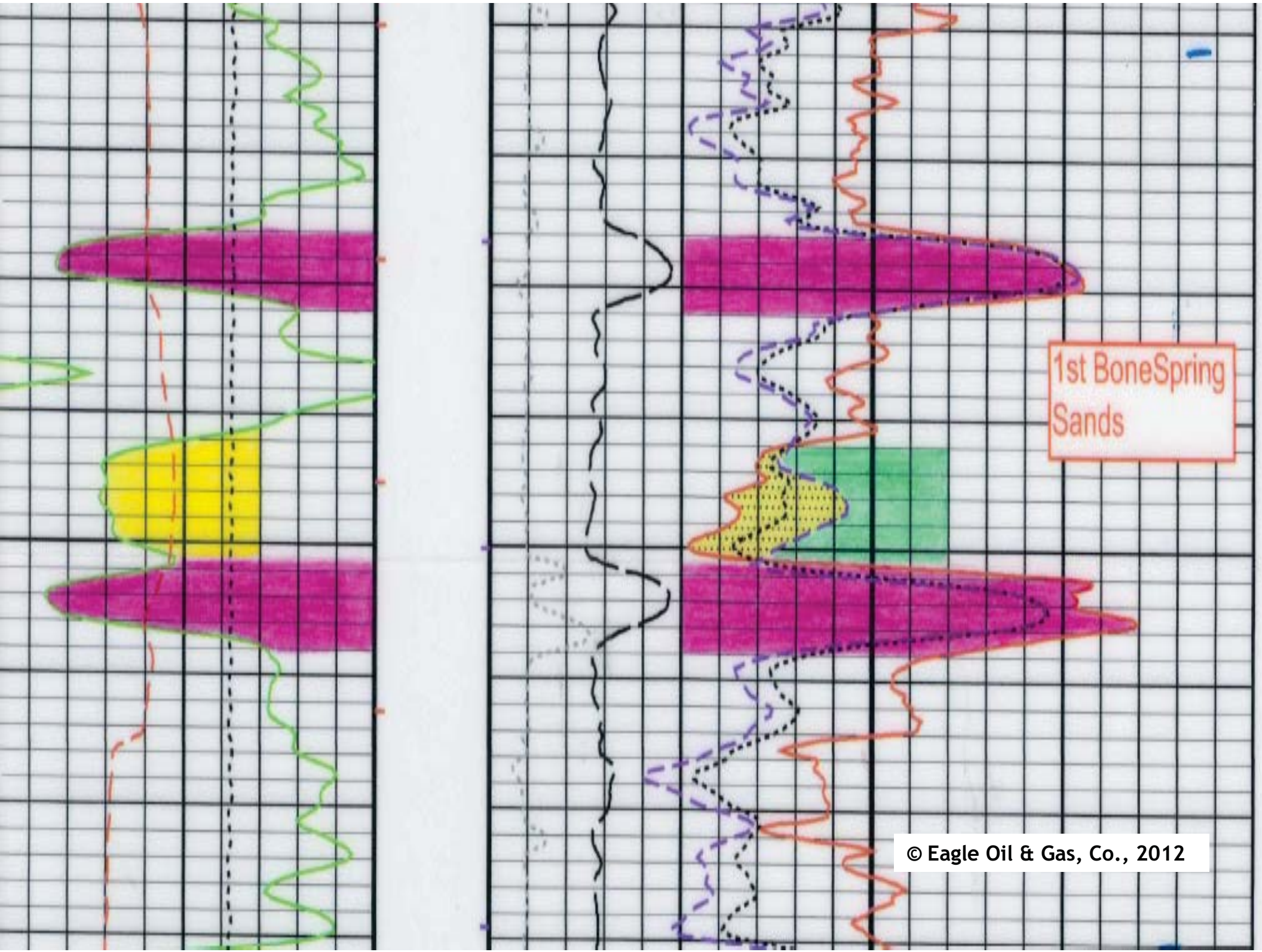

© Eagle Oil & Gas, Co., 2012

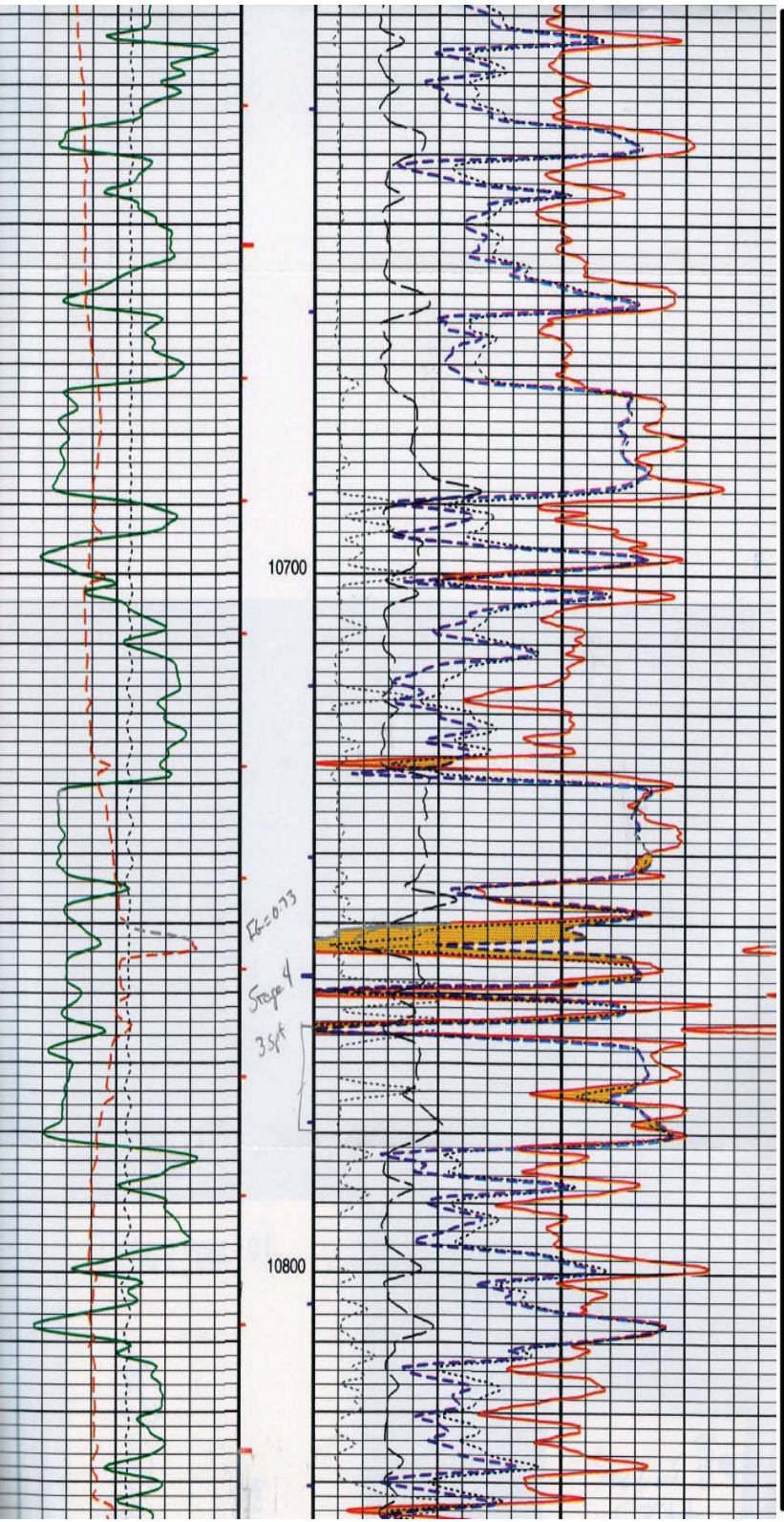

Wolfcampian Shale Isopach Map

N
W
E
S

1 inch = 4000 feet

Ward County

NO DATA

Reeves County

SLOPE

BASIN FLOOR

Slope to Basin Floor Contact

EAGLE OIL & GAS CO.

WOLFCAMPIAN SHALE ISOPACH MAP

REEVES COUNTY
WEST TEXAS

Author: M.L. Hanson
Date: 12 April, 2012
Horizontal Scale: 1inch = 4000 feet
Contour Interval: 50 feet

© Eagle Oil & Gas, Co., 2012

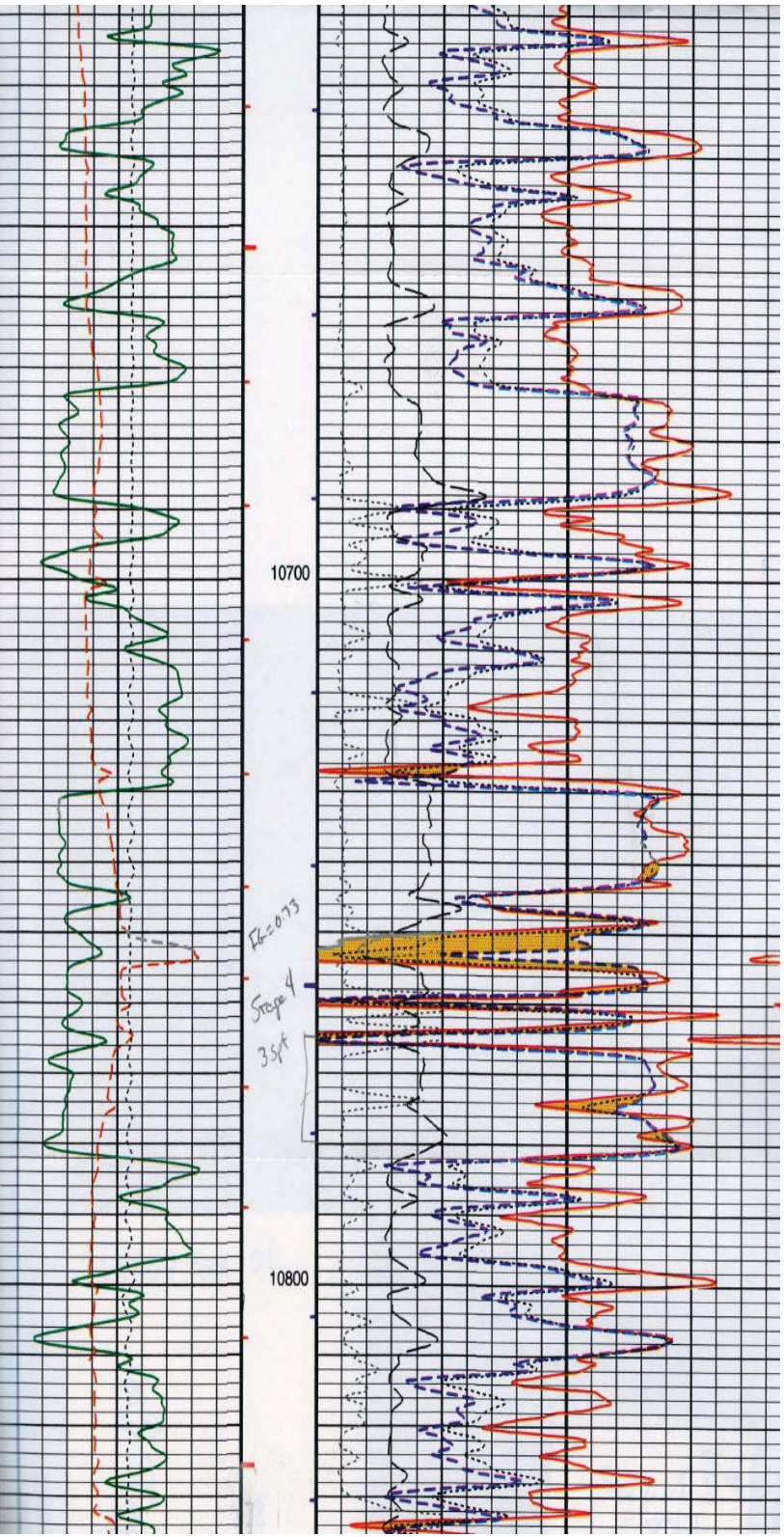
10700
10800
Eb-073
Stage 4
35ft

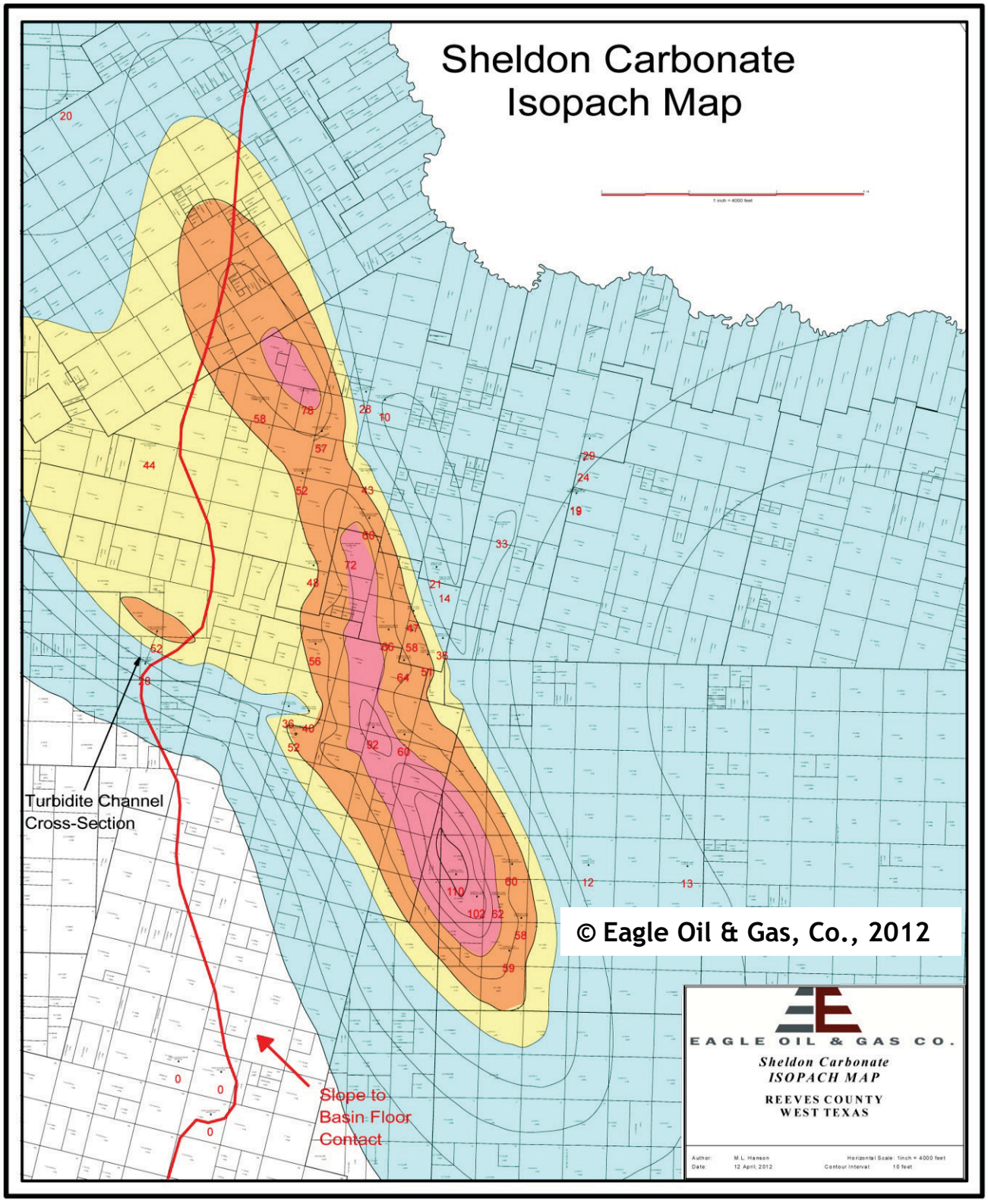
Sheldon Carbonate
Isopach Map
Turbidite Channel
Cross-Section
Slope to
Basin Floor
Contact
© Eagle Oil & Gas, Co., 2012
EAGLE OIL & GAS CO.
Sheldon Carbonate
ISOPACH MAP
REEVES COUNTY
WEST TEXAS

The Permian is the Premier US Oil Basin

Multi-Zone Vertical and Hz Development Potential

- *Wolfbone*
  - *Commingled vertical* wells that capture oil-rich 3rd Bone Spring and Wolfcamp over a *1,250' interval*
  - *Overpressured analog* to Wolfberry in the Midland Basin
  - *High-liquid content* provides superior economics
  - 108 MMboe in-place per square mile
- *Wolfcamp*
  - Horizontal drilling has begun in TX and Eddy, NM
  - Thick interval provides multi-lateral potential
- *3rd Bone Spring*
  - Substantial nearby horizontal drilling
- *Avalon Shale*
  - Up to 1,000' gross thickness across the basin
  - Laterally extensive & continuous across Reeves, Co.
  - 105 MMboe in-place per square mile
- *Delaware Sands (Brushy, Cherry, and Bell Canyon)*
  - Vertical & horizontal exploitation of the 3,000 - 3,500' thick interval with dozens of potential pays

Eagle Development is Proving Many Zones

- Eagle currently produces 1,888 boe/d from 28 wells
  - 24 vertical wells commingling production across 3rd Bone Spring members and Upper Wolfcamp members
  - 4 horizontal wells drilled into the 3rd Bone Spring Sands
- Eagle is currently drilling their first horizontal Wolfcamp well in the Upper Wolfcamp Shale B member
  - Excellent results to date with >100' flares during drilling with 12.6 ppg mud
  - Over 100 bbl oil returned to pit while drilling lateral

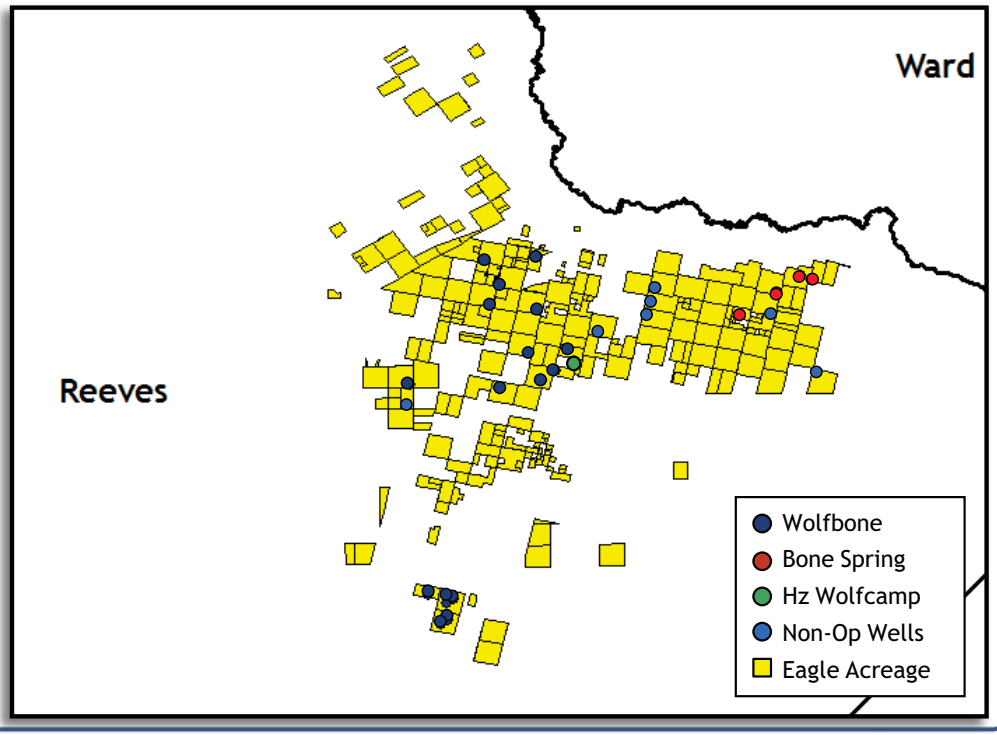

EAGLE OIL & GAS CO.

© Eagle Oil & Gas, Co., 2012

TUDOR PICKERING HOLT & CO | ENERGY INVESTMENT & MERCHANT BANKING

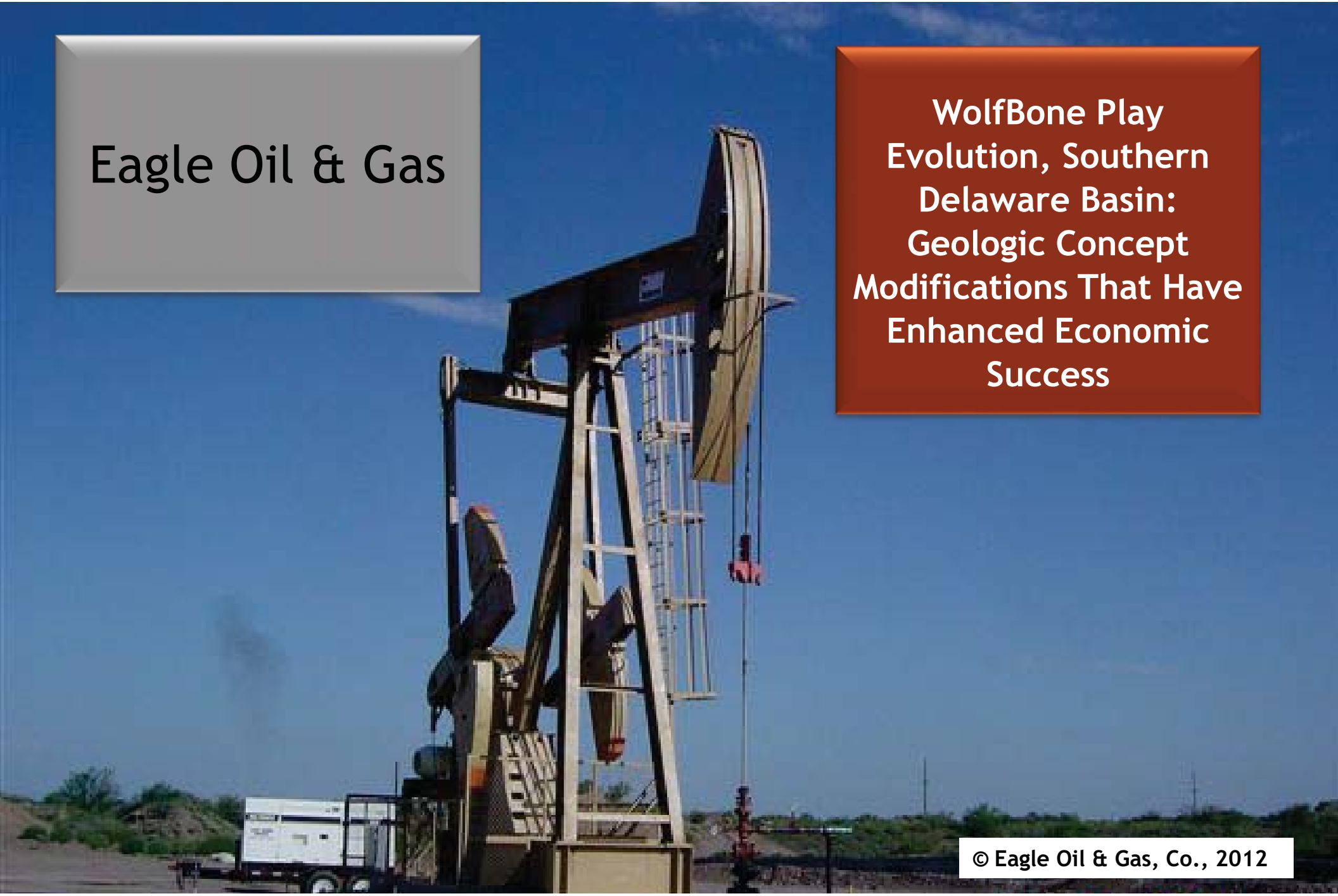

Eagle Oil & Gas

WolfBone Play Evolution, Southern Delaware Basin: Geologic Concept Modifications That Have Enhanced Economic Success

© Eagle Oil & Gas, Co., 2012

EAGLE OIL & GAS CO.

Fairhurst, Bill; Hanson, Mary Lisbeth; Reid, Frank; and Pieracacos, Nick

Eagle Well Locations

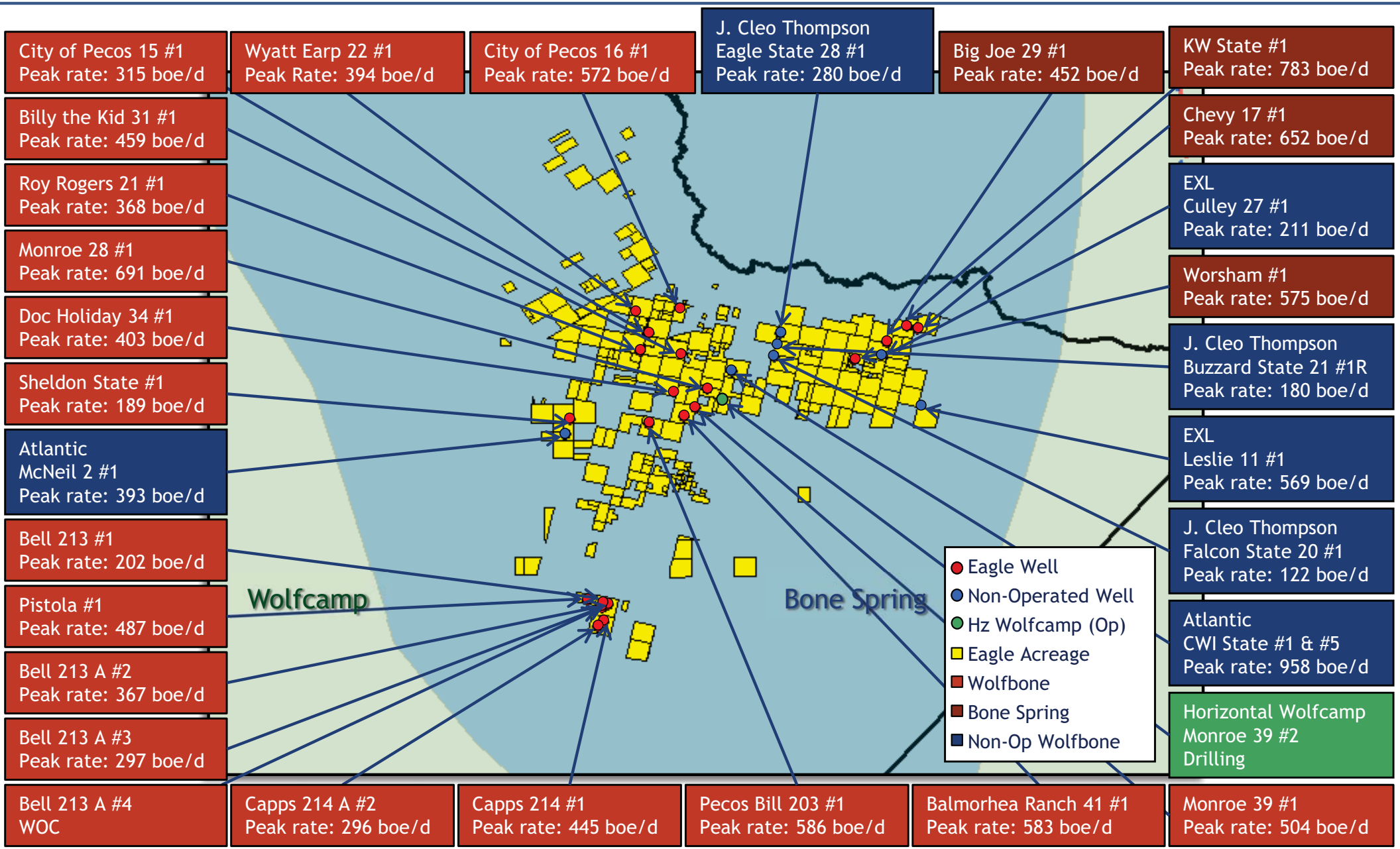

© Eagle Oil & Gas, Co., 2012

Recent Nearby Industry Results

Avalon Shale
Chesapeake
Ross Ranch Federal 6-1H
IP rate: 1,528 boe/d

Avalon Shale
Apache
Bullhead 55-1-41 1H
IP rate: 835 boe/d

Bone Spring
Chesapeake
Johnson 1-86
30-day rate: 920 boe/d

Bone Spring
Devon
Talladega 65 1H
30-day rate: 1,281

Bone Spring
Chesapeake
Monroe 1-17
30-day rate: 1,614 boe/d

Wolfbone
J. Cleo Thompson
Perry State 204
30 day rate: 549 boe/d

Wolfbone
J. Cleo Thompson
Terrill State
30-day rate: 313 boe/d

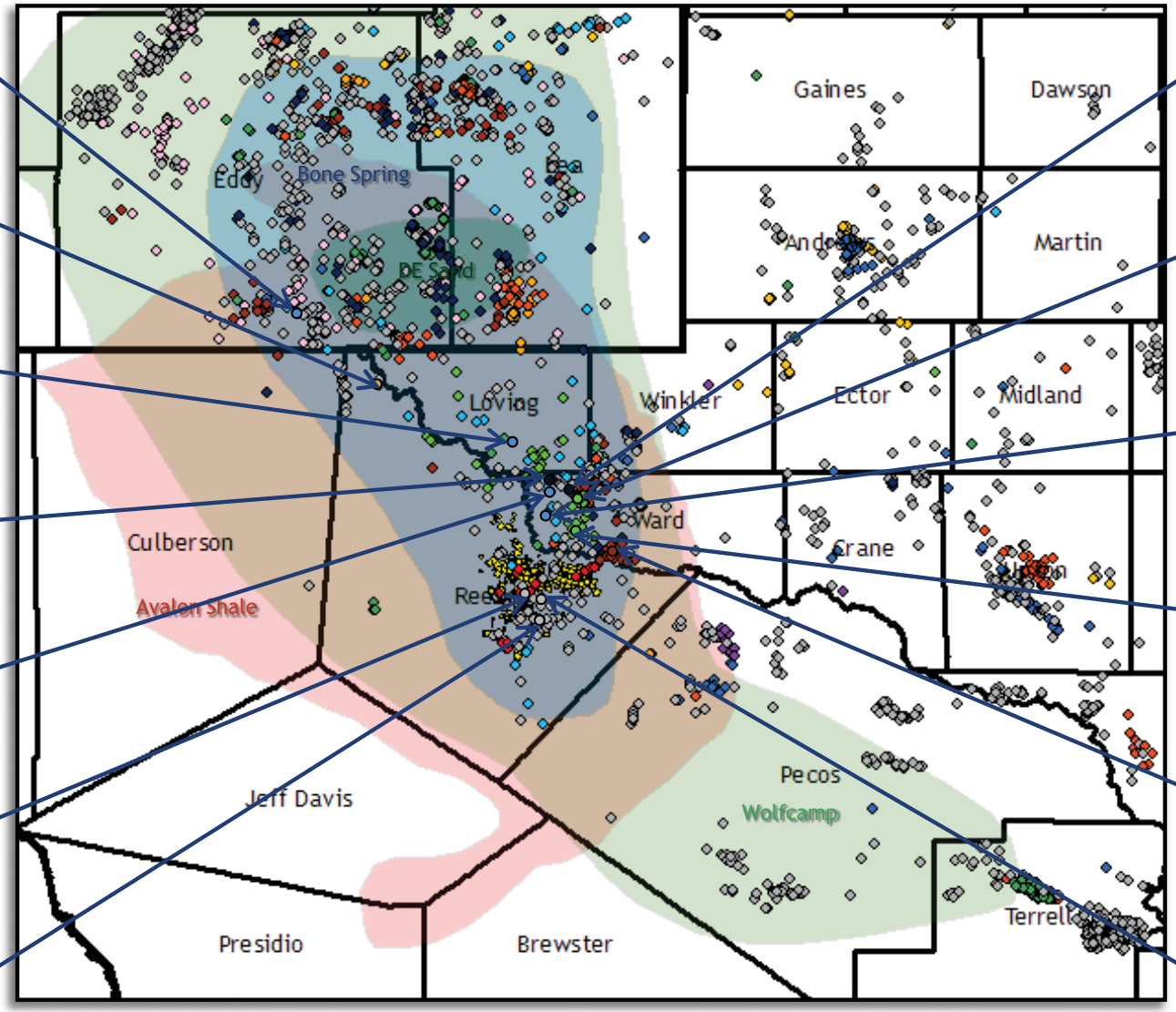

Delaware
Devon
Colonel Drake 24 1H
30-day rate: 518 boe/d

Bone Spring
Anadarko
Monroe 34-220
30-day rate: 1,345 boe/d

Bone Spring
Chesapeake
Crockett 1-26 1H
30-day rate: 1,383 boe/d

Bone Spring
Anadarko
Blacktip Johnson 1-39H
30-day rate: 1,364 boe/d

Bone Spring
Cimarex
KHC '33-26'
30-day rate: 1,226

Wolfbone
J. Cleo Thompson
Perry State 40
30 day rate: 708 boe/d

Source: HPDI, Corporate IR Presentations.

© Eagle Oil & Gas, Co., 2012

EAGLE OIL & GAS CO.

TUDOR PICKERING HOLT & CO | ENERGY INVESTMENT & MERCHANT BANKING

Eagle Wolfbone Activity

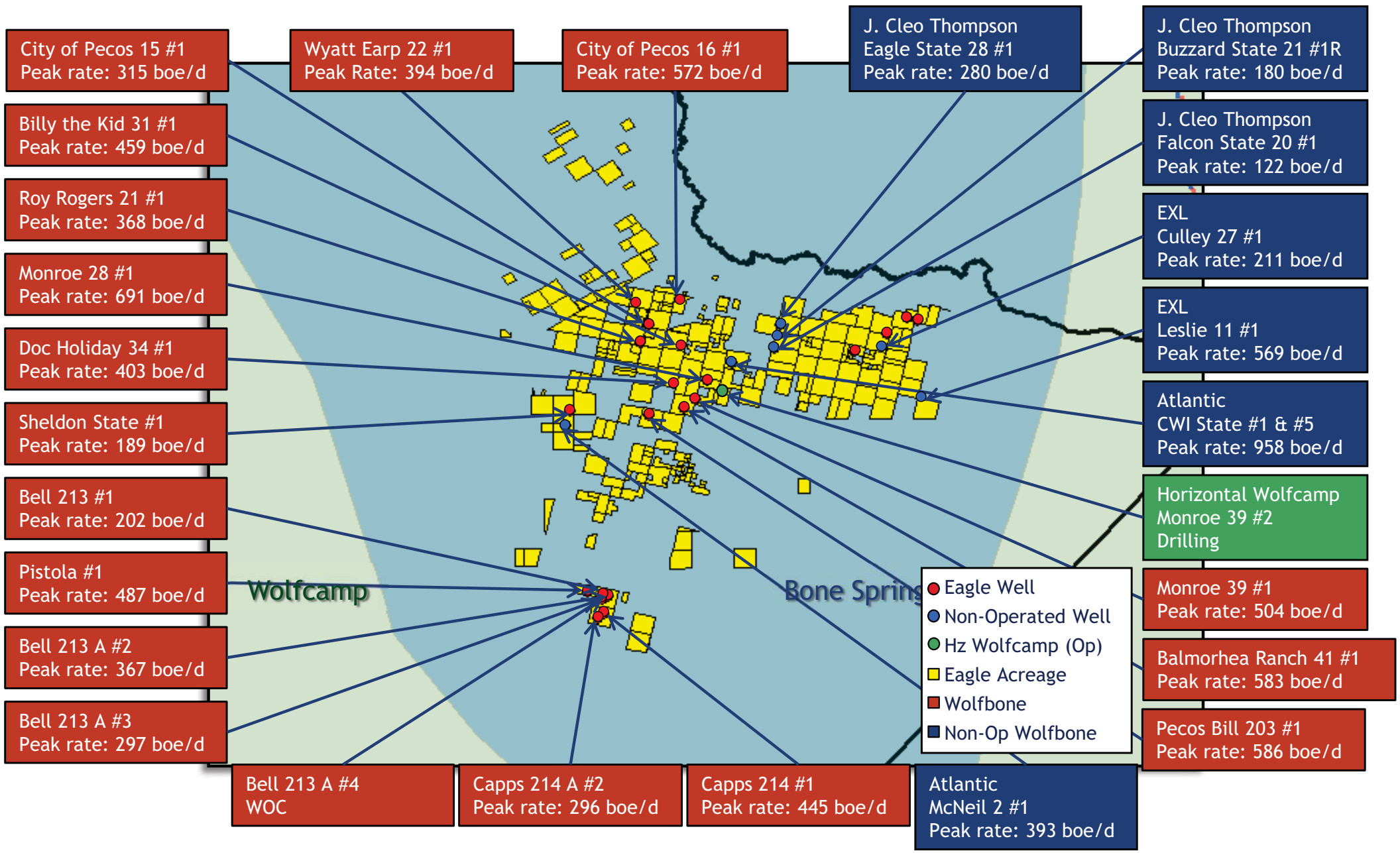

© Eagle Oil & Gas, Co., 2012

Eagle Operated Wolfbone Production

Total Current Net Production: 1,780 boe/d (2,404 boe/d gross) (1)

Includes 17 operated wells

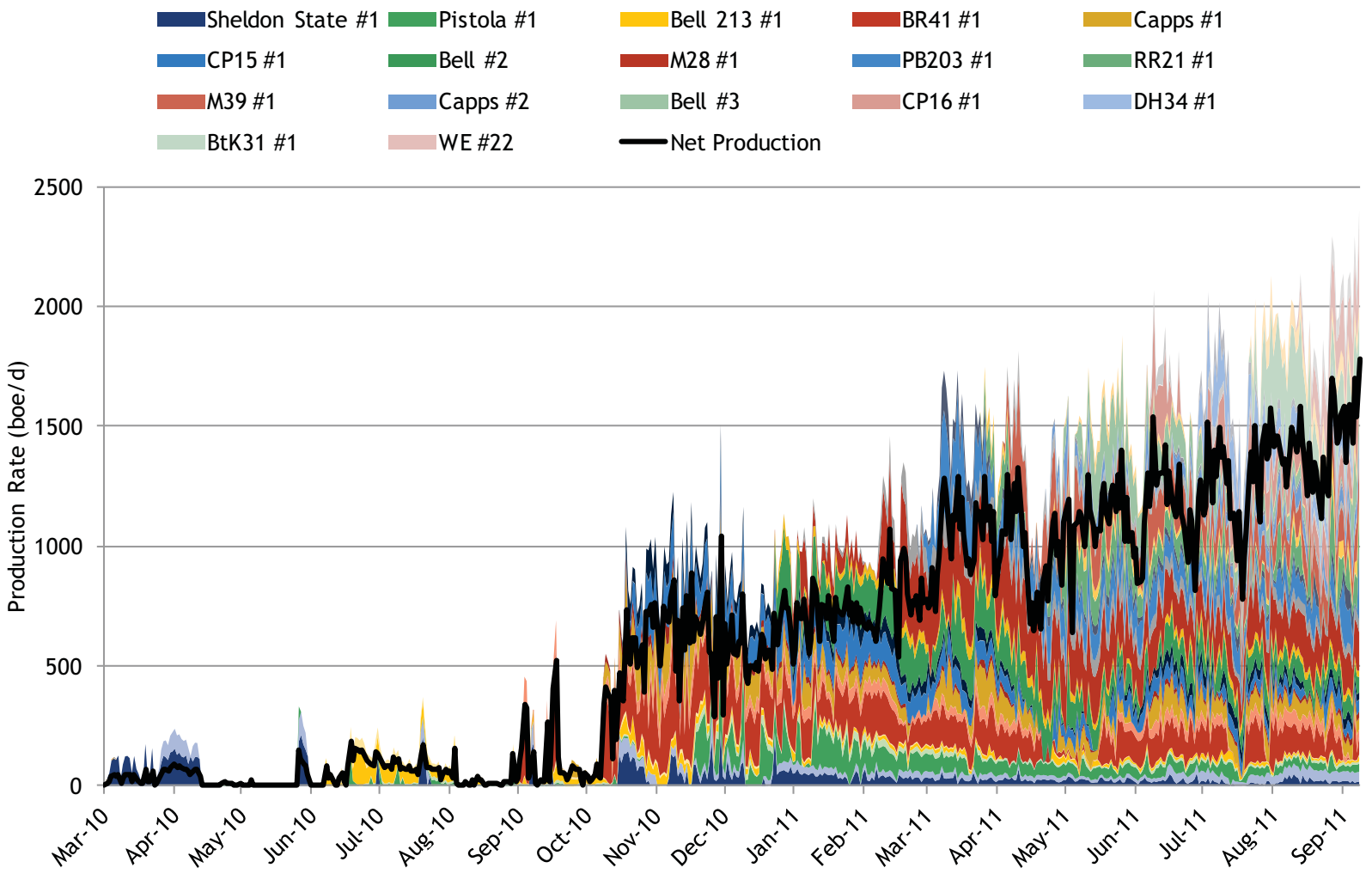

Source: Company Data

(1) Production Data as of 9/30/11.

Wolfbone Drilling Curves

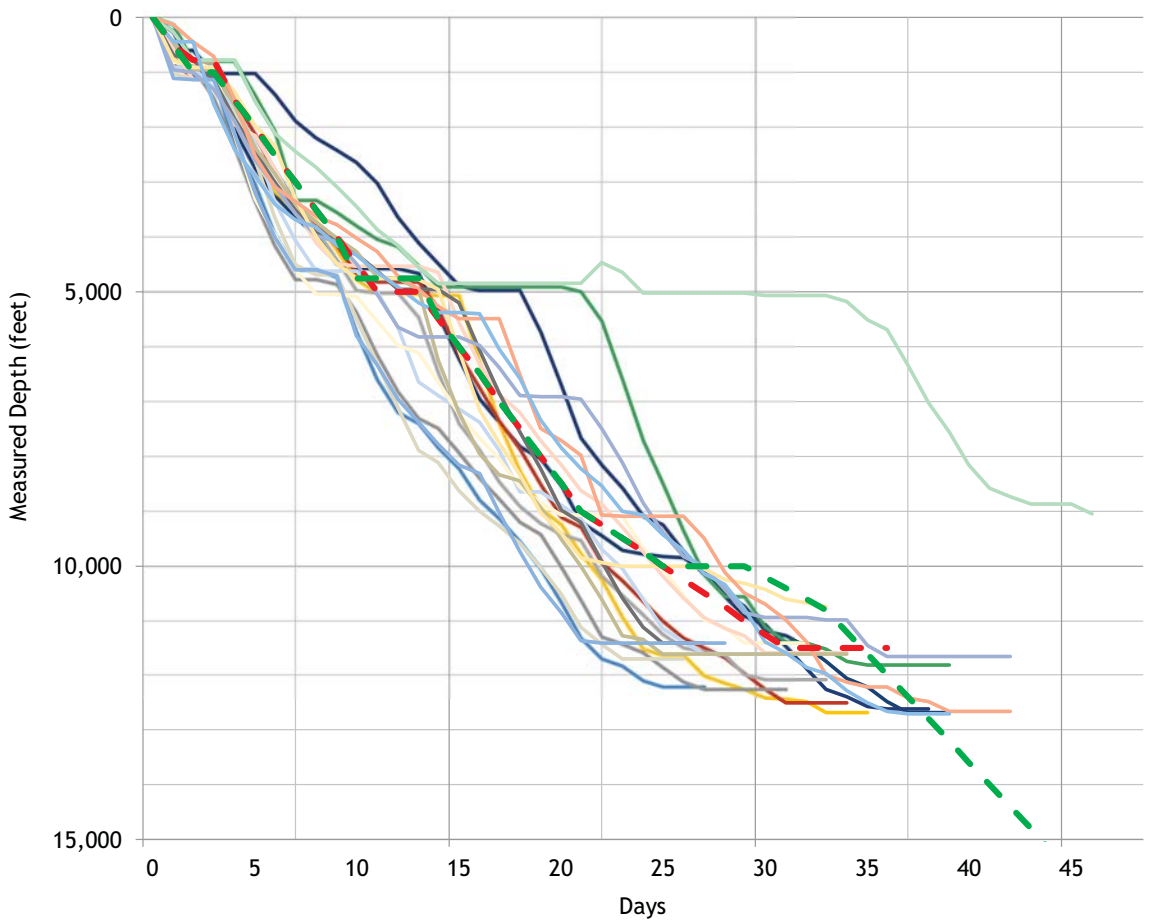

Well	Spud	TVD (ft)	Spud-to-TD	Spud-to-RR
Sheldon #1	12/28/2009	12,685	37	39
Pistola #1	2/15/2010	12,602	36	38
Bell #2	4/10/2010	11,800	35	39
Bell #1	4/12/2010	12,674	33	35
Balamorhea Ranch	6/18/2010	12,500	31	34
Capps #1	8/4/2010	12,084	30	33
City of Pecos 15 #1	9/17/2010	12,206	25	27
Monroe 28 #1	10/21/2010	12,250	27	31
Pecos Bill 203 #1	12/30/2010	11,690	23	26
Monroe 39 #1	1/30/2011	11,601	27	31
Capps #2	3/7/2011	11,405	29	32

Well	Spud	TVD (ft)	Spud-to-TD	Spud-to-RR
Wyatt Earp #1	3/7/2011	11,582	30	34
Culley 27 #1	3/18/2011	12,655	39	42
Bell #3	3/19/2011	11,407	25	27
Doc Holliday 34 #1	4/3/2011	11,600	25	34
Leslie 11 #1	4/30/2011	12,700	37	39
City of Pecos 16 #1	5/4/2011	11,419	22	28
Billy the Kid 31 #1	6/10/2011	11,650	36	42
Bell #4	7/17/2011	9,055	46	46
Monroe 39 #2H	7/30/2011	10,753	33	33
Planned Vt		11,500	31	36
Planned Hz		15,500	45	48

© Eagle Oil & Gas, Co., 2012

Vertical Development Plan Rapidly Proves Acreage

- Drilling a single vertical well allows an operator to book the following:
  - 1 PDP
  - 8 PUD
  - 16 Probable
  - 56 Possible

  80 total 3P locations

- Using a "fence post" development technique allows an operator to quickly prove an entire field

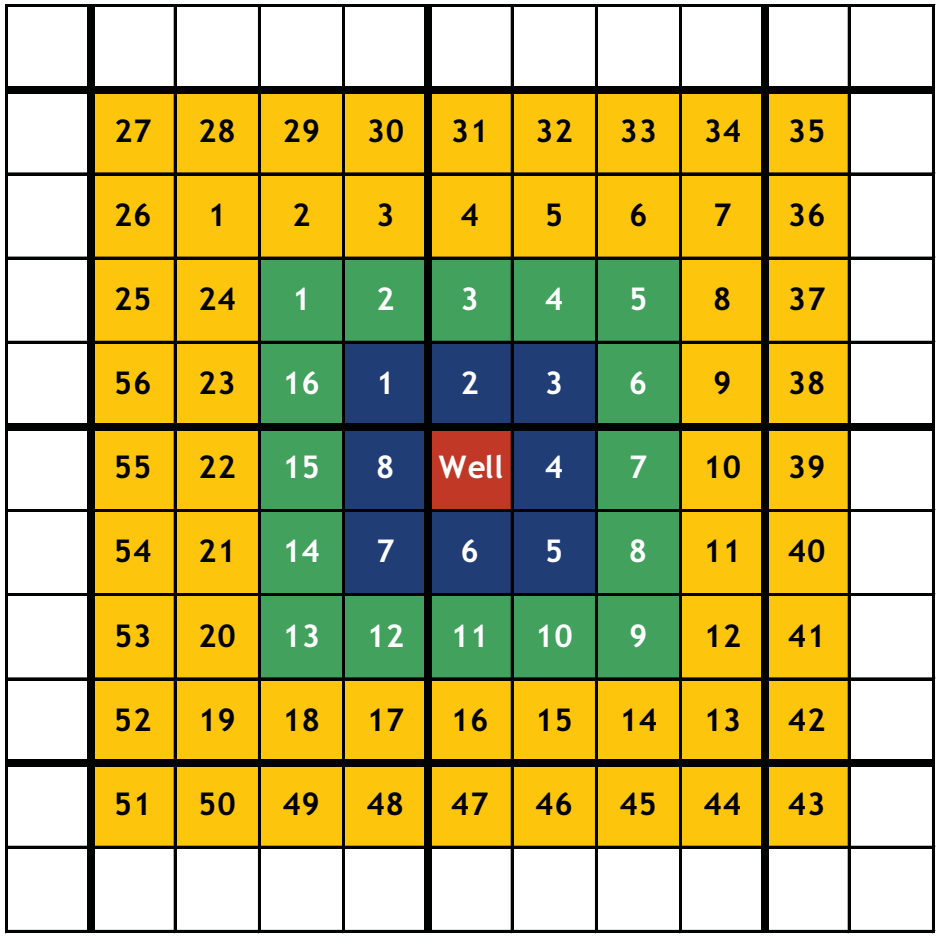

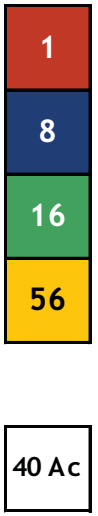

1 Proved Developed Producing

8 Proved Undeveloped

16 Probable

56 Possible

Eagle has already proven a large portion of their acreage → Only 11 wells required to convert 100% of locations to 3P

© Eagle Oil & Gas, Co., 2012

40-Acre Spacing Works in the Wolfbone

Focused Fracture – Capps 214 #1 Case Study

- Bell 213 #1 completed as a "typical" sandstone
  - Unconcentrated frac targeted sand intervals
    - Wolfcamp Upper and Middle A Shales
    - 3rd Bone Spring Sand
    - *Not completed in Wolfcamp Upper B Shale*
  - Wolfcamp C & D Sands produced excessive water and were plugged
- Capps 214 #1 was completed with a more focused "shale frac"
  - Upper and Middle Wolfcamp Shale
  - Wolfcamp A & B Sand
  - 3rd Bone Spring Sand
  - ***>2x Bell 213 #1 peak production rate***

Same Area – Completely Different Results

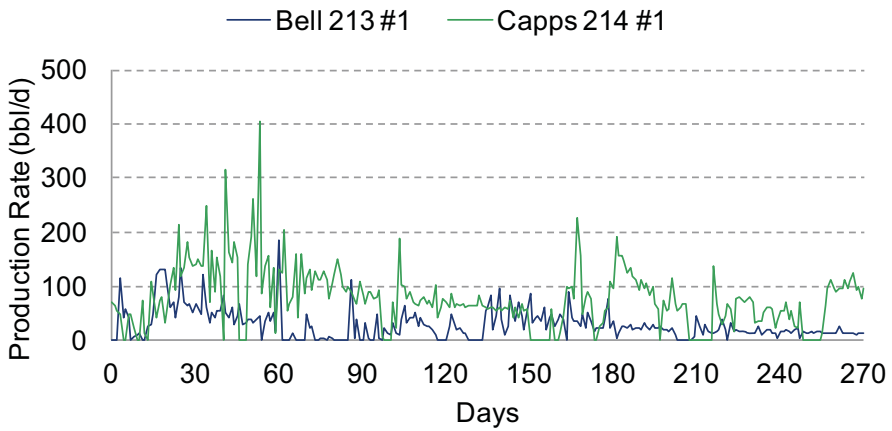

Bell/Capps Lease (Southern Area of Eagle Position)

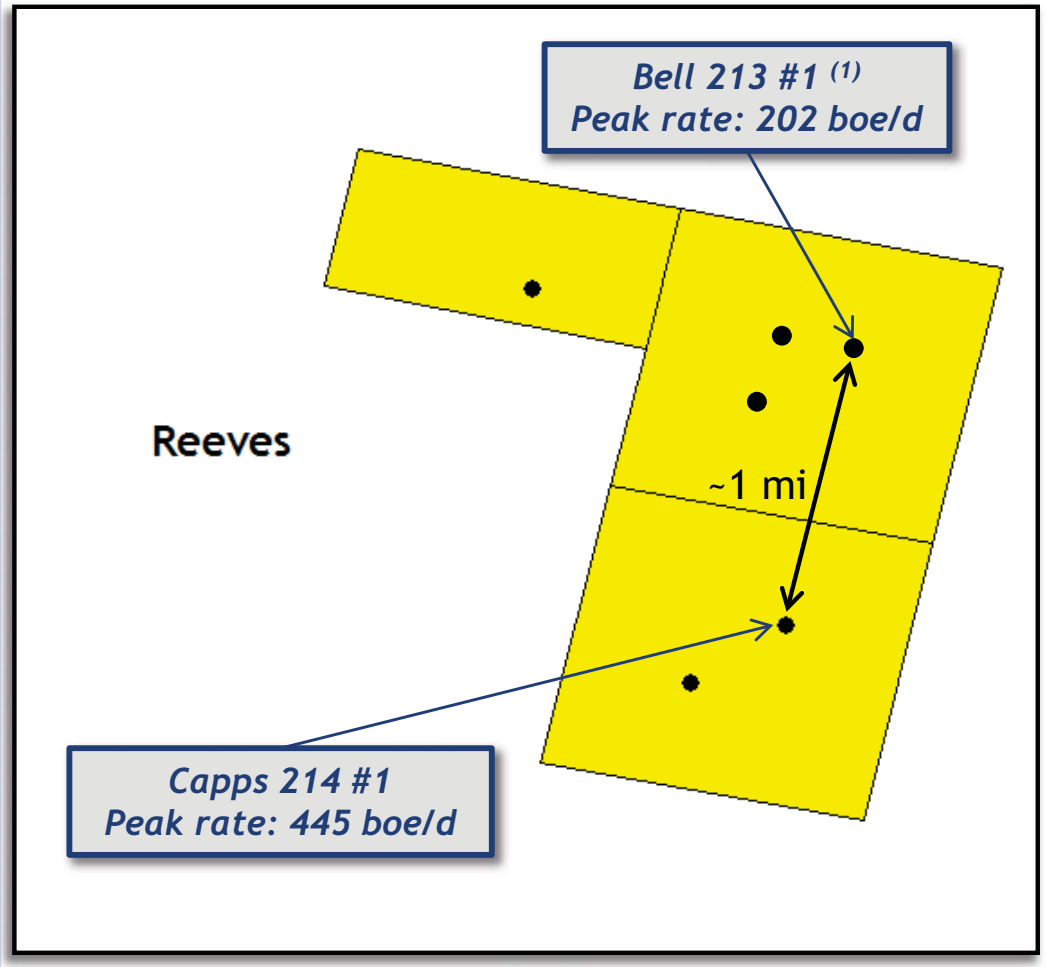

© Eagle Oil & Gas, Co., 2012

NOTE: Bell 213 #1 was completed in the WC Upr and Mid A shales → but not in the best zone, the WC Upr B shale

40-Acre Spacing Works in the Wolfbone

Wolfbone 40-acre Case Study (Bell Lease)

- Bell 213 1, "A" 2, and "A" 3 drilled ~6 months apart
  - 213 1: June 29, 2010
  - 213 "A" 2: Jan 13, 2011
  - 213 "A" 3: May 21, 2011
- No observed interference during completion or production
- Decline rate unaffected by offsetting production
- ***40-acre spacing is norm in the Wolfberry (analog)***
  - ***20-acre development underway in many areas***

Wolfbone Down-Spacing Potential (Recovery Factor)

- Oil-in-Place per sq mile = 108 MMboe

EUR/Well (Mboe)	Well Spacing (acres) 40	20	10
200	3.0%	5.9%	11.9%
225	3.3%	6.7%	13.3%
250	3.7%	7.4%	14.8%

Bell Lease (Southern Area of Eagle Position)

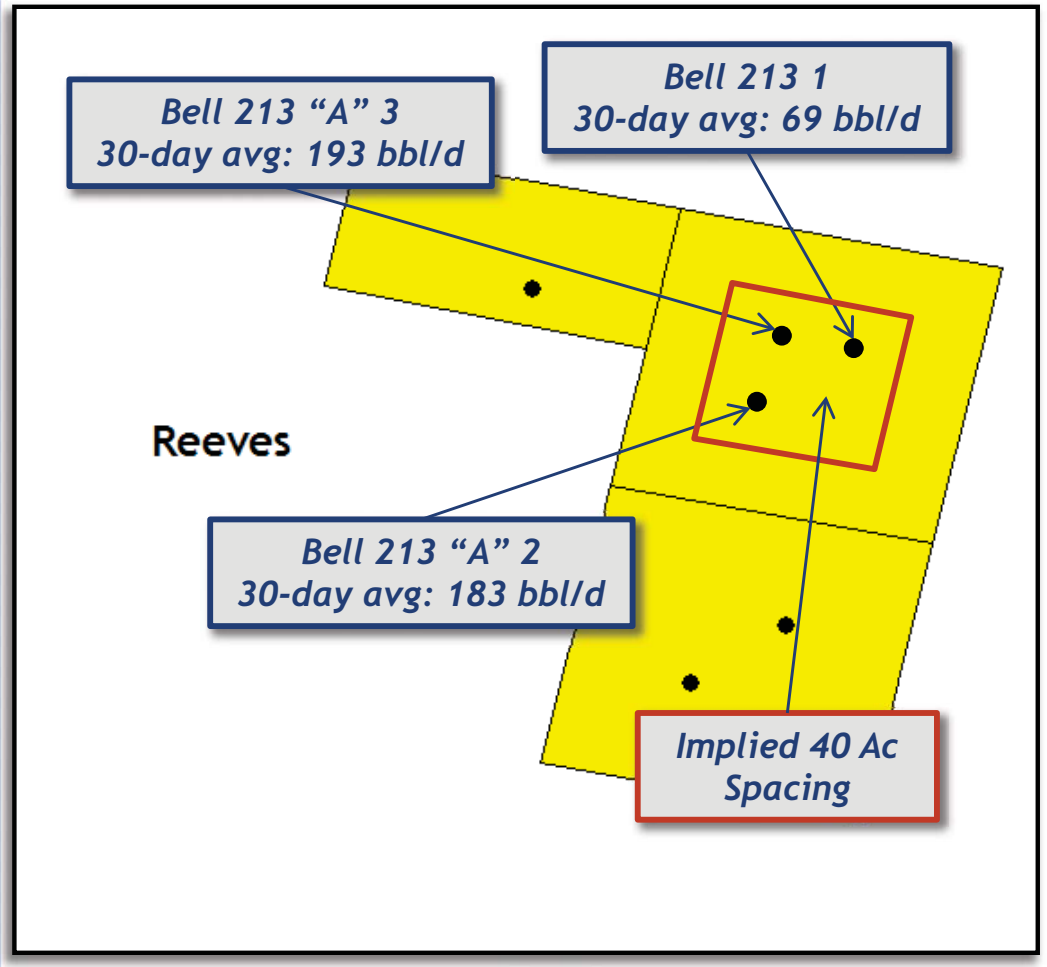

© Eagle Oil & Gas, Co., 2012

SEC Rules Favor Horizontal Well Development

- Drilling a single horizontal well allows an operator to book the following:
  - 1 PDP (4 x 40 Ac)
  - 4 PUD (16 x 40 Ac)
  - 8 Probable (32 x 40 Ac)
  - 28 Possible (112 x 40 Ac)

  40 total Hz 3P locations

- Horizontal wells are being used to prove fields quickly in North Dakota using the "fence post" development plan
- 2009 SEC booking guideline changes made proving reserves with horizontal wells more favorable to operators
- Old method: Only direct lateral offsets
- New method: Includes toe+ heel offsets

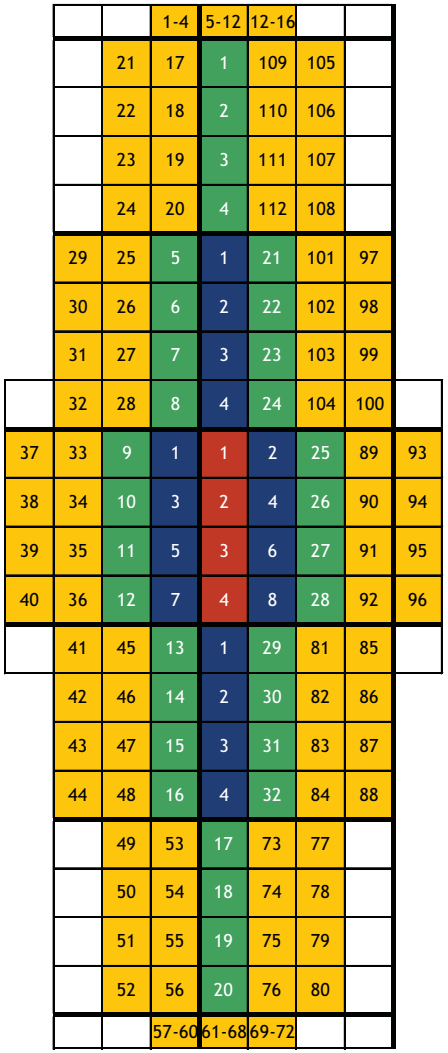

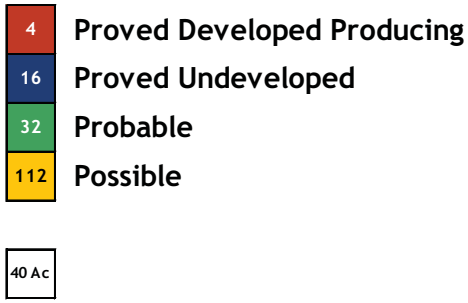

Eagle is currently completing their first Wolfcamp Shale horizontal well

© Eagle Oil & Gas, Co., 2012

Bone Spring Industry Activity

Bone Spring
Concho
Morning Fed. 1H
Test: 700 boe/d

Bone Spring
Chesapeake
Johnson 1-86
30-day: 920 boe/d

Bone Spring
Chesapeake
Crockett 1-26 1H
IP rate: 2,445 boe/d

Bone Spring
Chesapeake
Monroe 1-17 1H
30-day: 1,475 boe/d

Bone Spring
Anadarko
Blacktip Johnson 1-39H
30-day: 920 boe/d

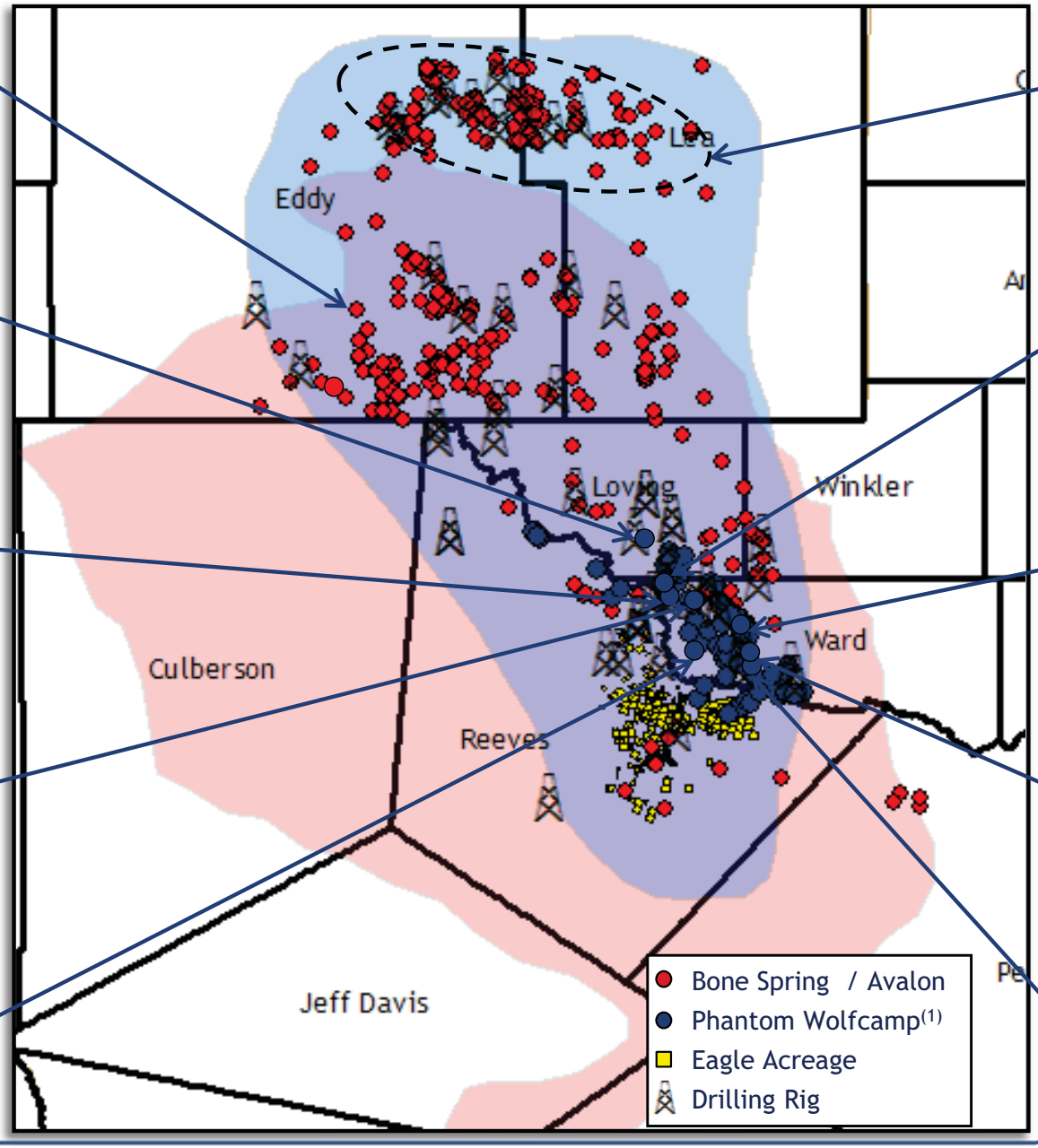

Bone Spring
Cimarex Activity:
7 wells with reported IPs between 560-1,100 boe/d
Avg rate ~856 boe/d

Bone Spring
Devon
Talladega 65 1H
30-day: 1,281 boe/d

Bone Spring
Chesapeake
Monroe 34-220
30-day: 1,345 boe/d

Bone Spring
Cimarex
KHC '33-26'
30-day: 1,226 boe/d

Bone Spring
Cimarex
Davis '33-20'
30-day: 1,293 boe/d

(1) 3rd Bone Spring horizontal wells listed in HPDI as Phantom field, Wolfcamp reservoir.

EAGLE OIL & GAS CO.

© Eagle Oil & Gas, Co., 2012

TUDOR PICKERING HOLT & CO | ENERGY INVESTMENT & MERCHANT BANKING

Hz Bone Spring IP Rate

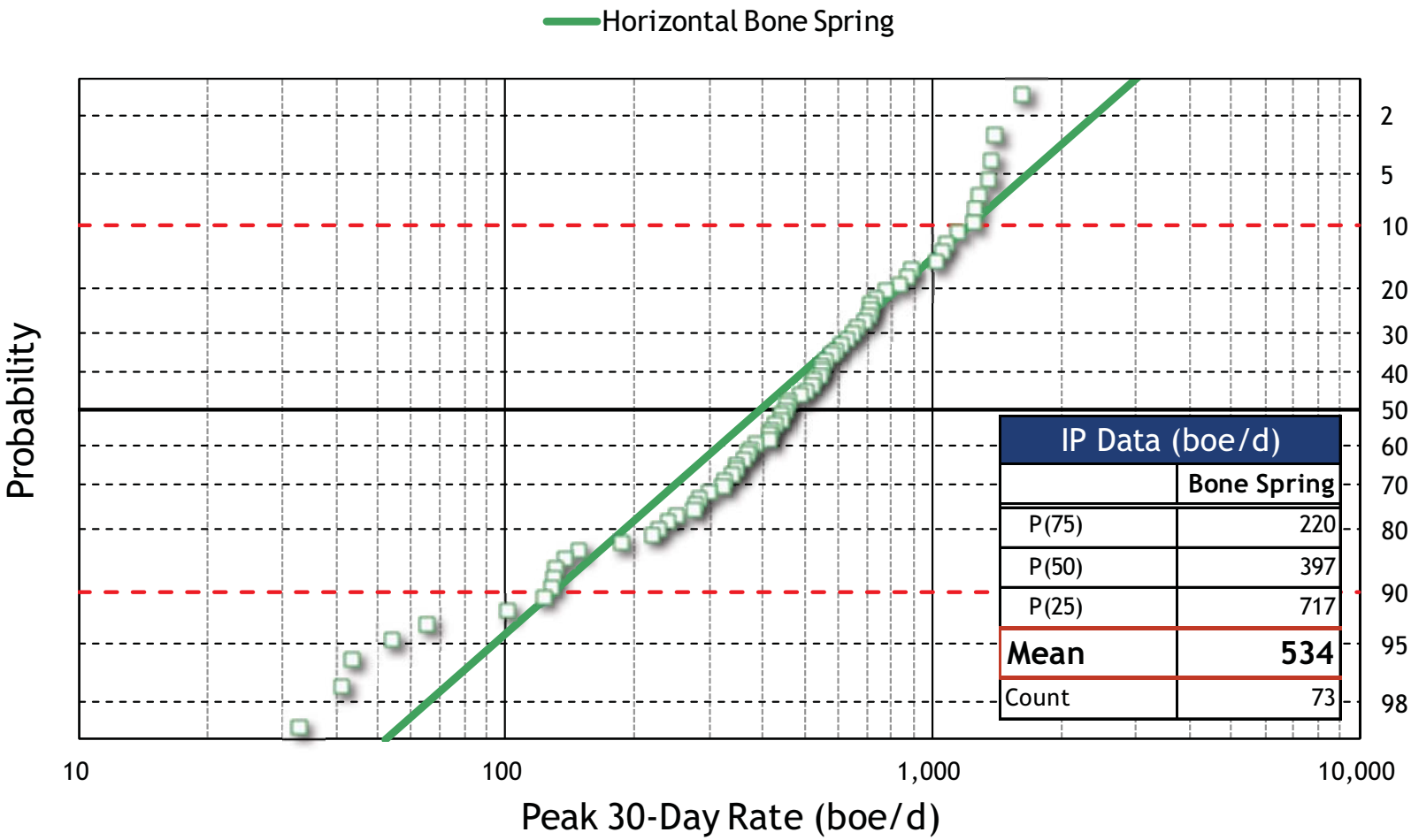

IP Data (boe/d)	
	Bone Spring
P(75)	220
P(50)	397
P(25)	717
Mean	**534**
Count	73

© Eagle Oil & Gas, Co., 2012

15 wells deviating from a standard lognormal distribution were removed from the dataset.

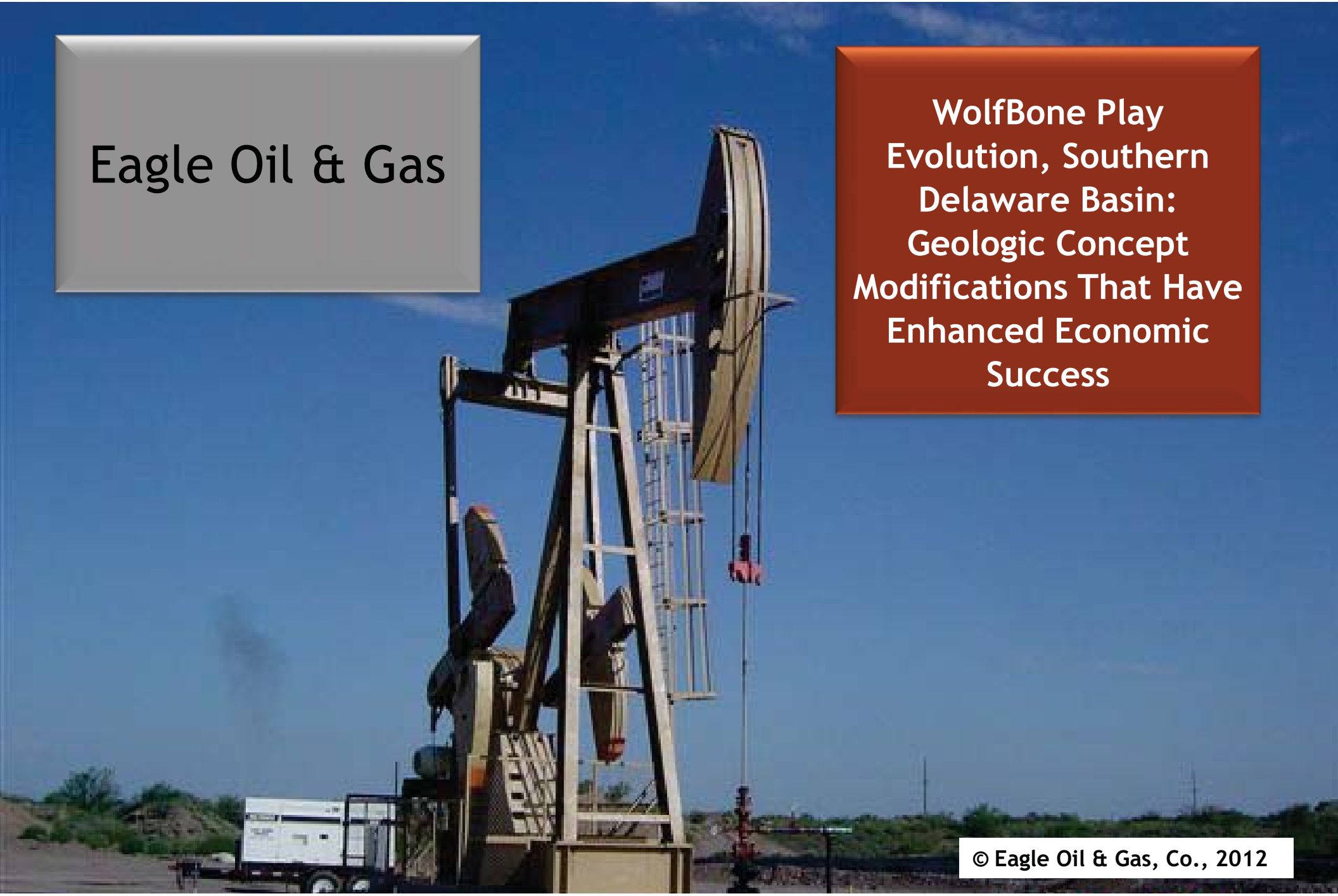

Eagle Oil & Gas

WolfBone Play Evolution, Southern Delaware Basin: Geologic Concept Modifications That Have Enhanced Economic Success

© Eagle Oil & Gas, Co., 2012

EAGLE OIL & GAS CO.

Fairhurst, Bill; Hanson, Mary Lisbeth; Reid, Frank; and Pieracacos, Nick

Are Geologic/Reservoir/Completion Models Properly Constrained (are they working) in the Permian Basin?*

Bill Fairhurst[1]

Search and Discovery Article #41797 (2016)**
Posted May 2, 2016

*Adapted from oral presentation given at AAPG Geosciences Technology Workshop, Revitalizing Reservoirs, San Antonio, Texas, December 1-2, 2015
**Datapages © 2016 Serial rights given by author. For all other rights contact author directly.

[1]Riverford Exploration, LLC, The Woodlands, Texas (bfairhurst@riverford-resources.com)

Abstract

Multiple resource horizons are being targeted in the Permian Basin. These include the Spraberry, Bone Spring (Spraberry time equivalent in the Delaware Basin) and Cline (Upper Pennsylvanian). It also includes re-exploration and development of Upper Permian targets on the Central Basin Platform, northern shelf, deeper basins, Woodford and others. The Wolfberry in the Midland Basin and WolfBone in the Delaware Basin have been the main focus over the last several years, with growing interest and attention focused on the other reservoirs as knowledge, implementation and execution have enhanced economic results and applied to other reservoirs. As an example, the WolfBone development in the southern Delaware Basin is a sample of combining geologic, reservoir and completion results to guide economic development of the play and are reviewed. The Wolfcamp is an ideal heterogenetic resource consisting of quartz, carbonate and kerogen.

Exploration and field development will be successful over a large area. However, the geologic and economic sweet spot is generally found in the deeper basin floors. In this setting quartz and kerogen accumulated in the quiet deep-basin interrupted by episodic deposition of shelf-to-basin-floor carbonate debris flows that settled basin ward of the de-acceleration boundary between the slope and basin floor. These depositional processes resulted in compositional and grainsize heterogeneities and accumulation of the thick organic-rich, technically and economically exploitable targets. During maturation, large volumes of oil were sealed in place (108 MMBOIP per section). Upslope, up dip or in more shaly facies, these conditions do not exist and are outside the economic sweet spot. Units thin, become more shaly retarding geochemical maturation, some units become more gas-prone and the mixture of coarser-grained shelf carbonates and sandstones provided migration pathways breaching the closed system, limiting productivity and ultimate economic recoveries. In those environments, generally deeper stratigraphic units are targeted. This play has been developed initially and continuing today with vertical wells co-mingling the oil-resource with conventional reservoirs. Interpretation of imaging logs has identified the primary fracture orientation and zones with conjugate fractures systems. Integration with production logs, chemical tracers, and micro-seismic has optimized horizontal target identification and horizontal drilling has overtaken vertical well development. Have we maximized and fully integrated drilling, geology, reservoir description, stimulation, production

information and economic results? Are we working on the same scales and communicating observations providing feedback among disciplines? Some observations are provided.

Reference Cited

Creaney, S., and Q.R. Passey, 1993, Recurring patterns of total organic carbon and source rock quality within a sequence stratigraphic framework: AAPG Bulletin, v. 77/3, p. 386-401.

Are Geologic, Reservoir, Completion Models Properly Constrained (are they working) in the Permian Basin?



Bill Fairhurst
Riverford Exploration, LLC
PetroTex Energy Partners, LLC
The Woodlands and Dallas, Texas

AAPG Geosciences Technology Workshop:
Revitalizing Reservoirs – Texas, Gulf Coast and Latin America,
San Antonio, Texas
December 1 - 2, 2015

OUTLINE:

1. Exploration, Synthesis of Early Development Geologic Information and Reservoir Performance to Enhance Economic Performance: Example from the Southern Delaware Basin, West Texas.

2. Are we Integrating our Input with other Disciplines, communicating with Management and other Interest Holders to Maximize Economic Outcomes?

Production from the Permian System

- Permian system comprised of multiple basins:
  - Delaware Basin
  - Central Basin Platform
  - Midland Basin
- Development progression:
  - Early production from shallow formations on the basin edges
  - *Transition to deeper deposits in the central Delaware (Avalon, Bone Spring, & Wolfcam*
- Recent basin revitalization:
  - *Comingled vertical completions*
  - Modern horizontal drilling and completion technologies

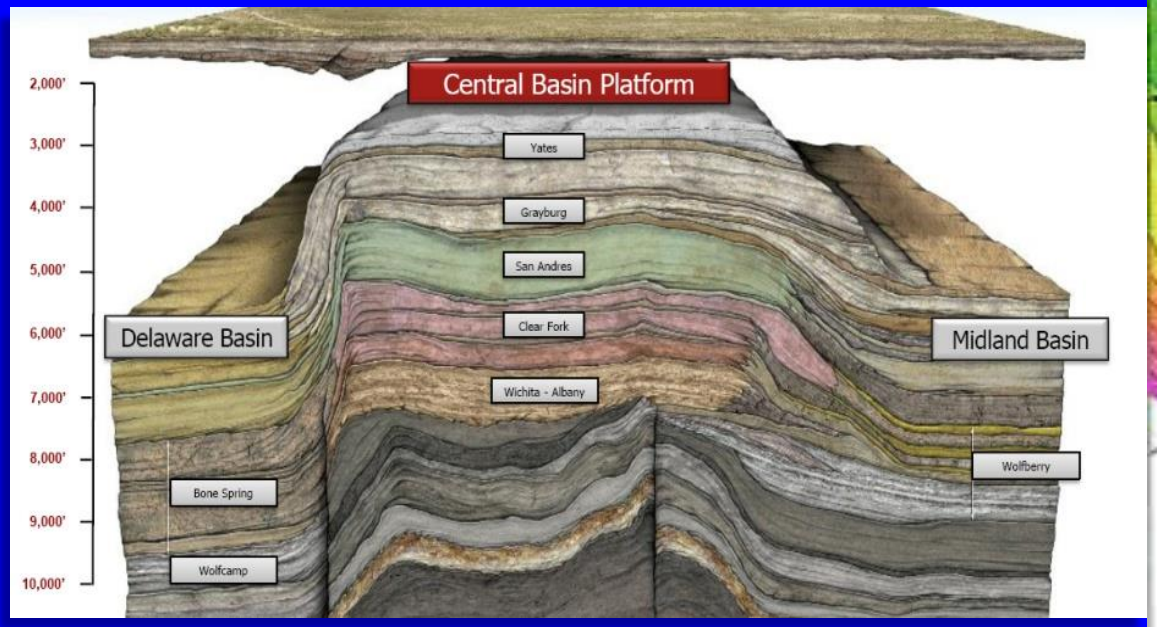

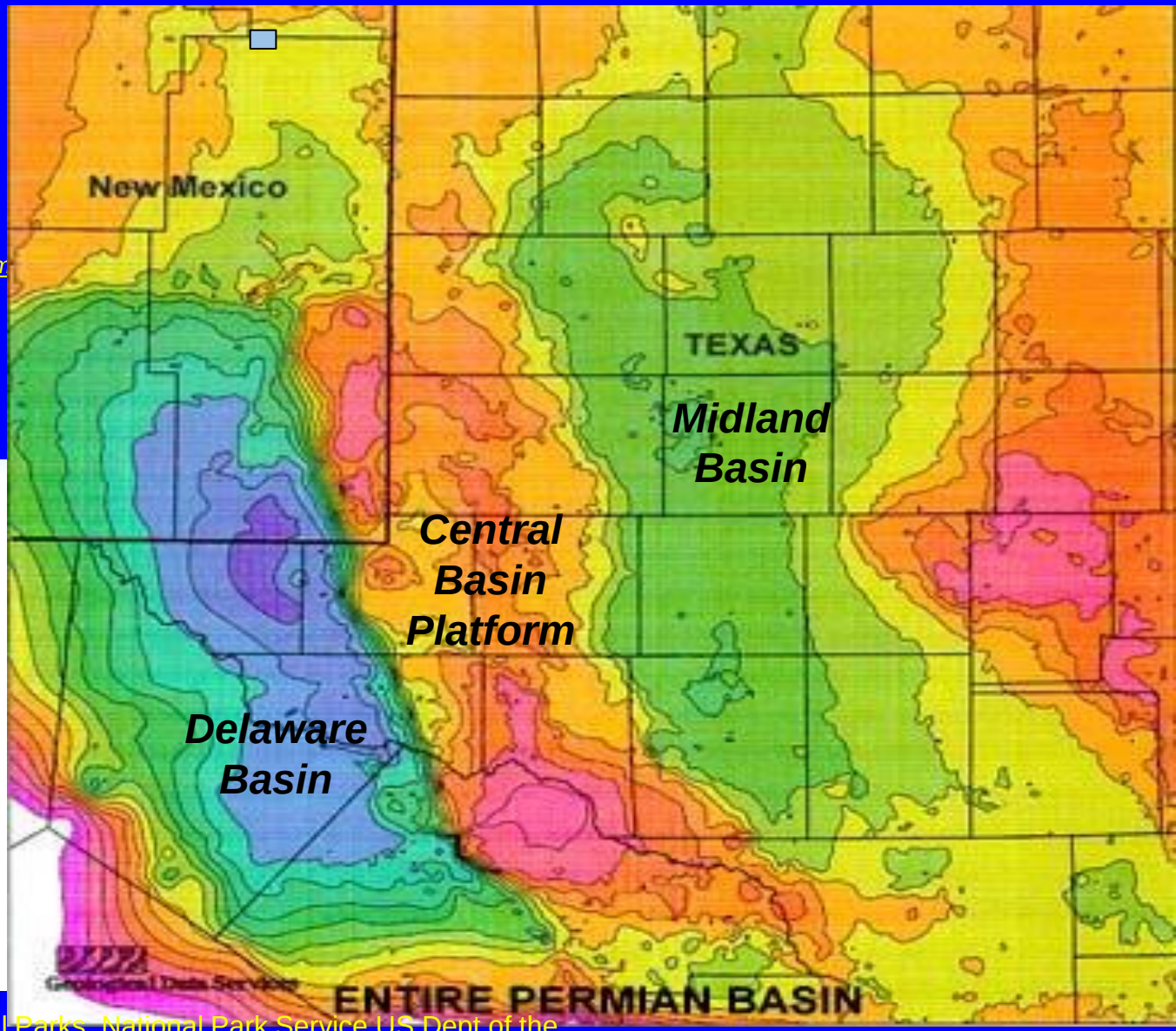

Source: Center for Energy & Economic Diversification UTPB, Geology of National Parks, National Park Service US Dept of the Interior, Society for Sedimentary Geology, Sandridge IR presentation.

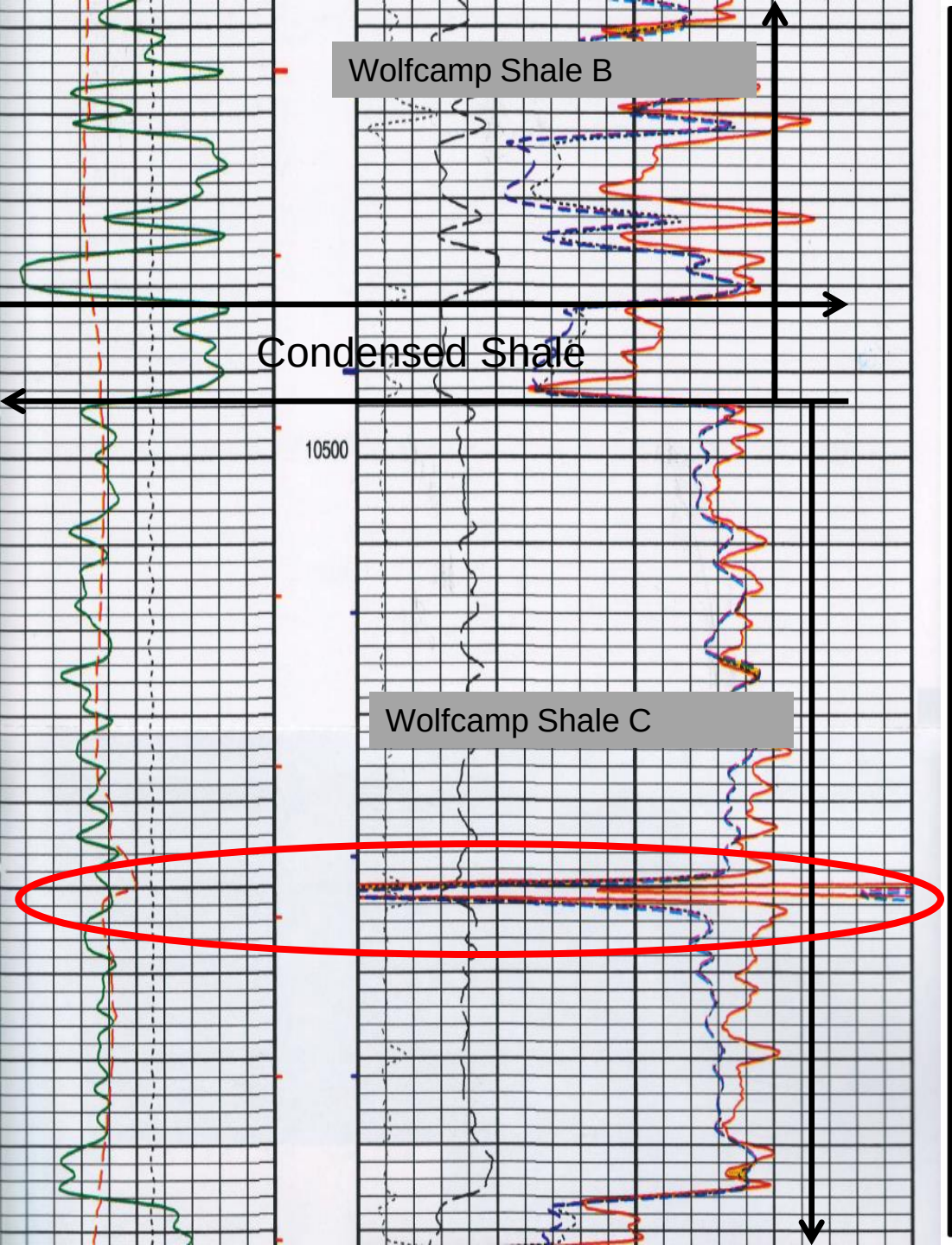
Wolfcamp Shale B
Condensed Shale
10500
Wolfcamp Shale C

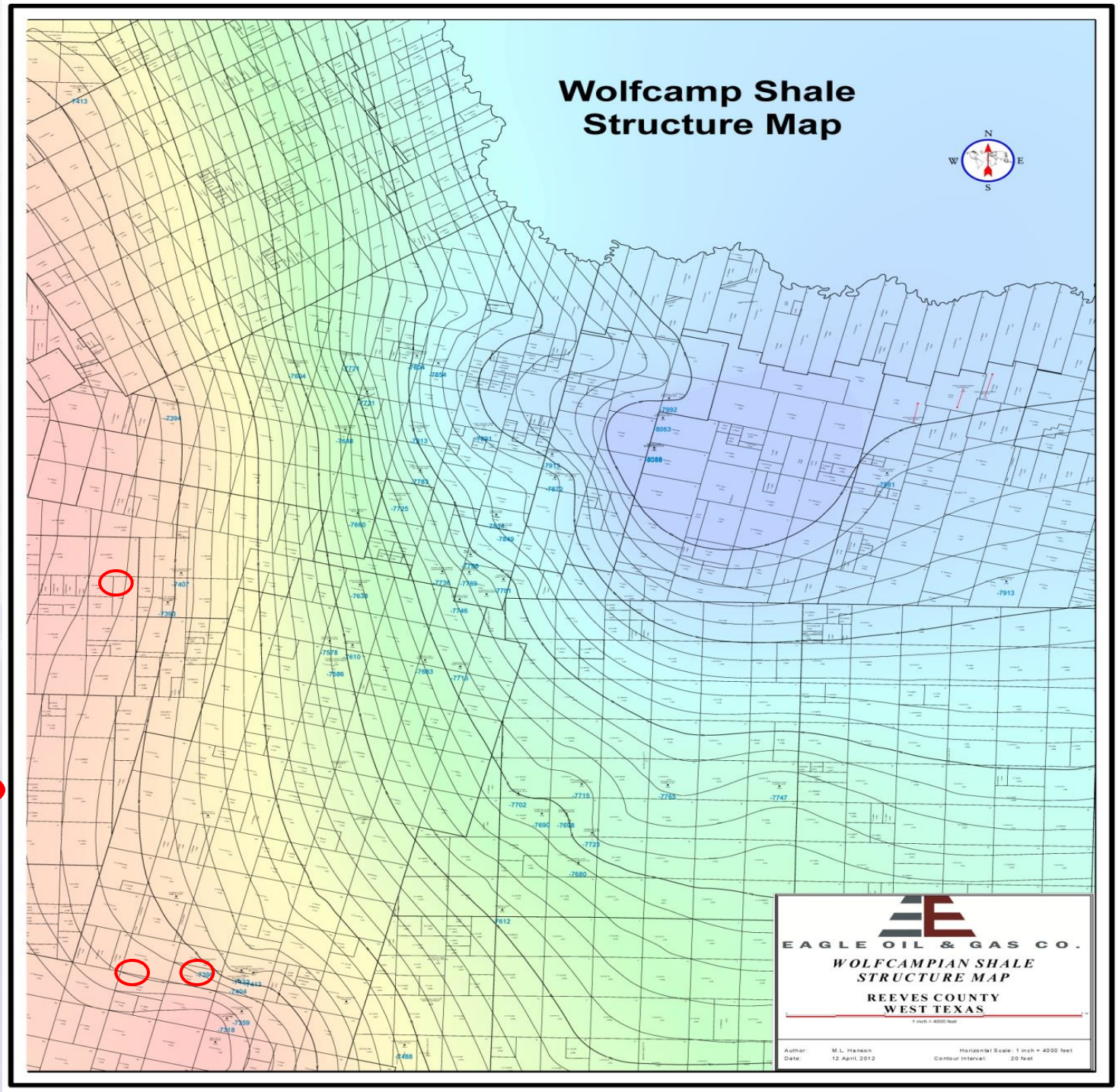
Wolfcamp Shale
Structure Map
N
W
E
S
EAGLE OIL & GAS CO.
WOLFCAMPIAN SHALE
STRUCTURE MAP
REEVES COUNTY
WEST TEXAS
1 inch = 4000 feet
Author: M.L. Hanson
Date: 12 April, 2012
Horizontal Scale: 1 inch = 4000 feet
Contour Interval: 20 feet

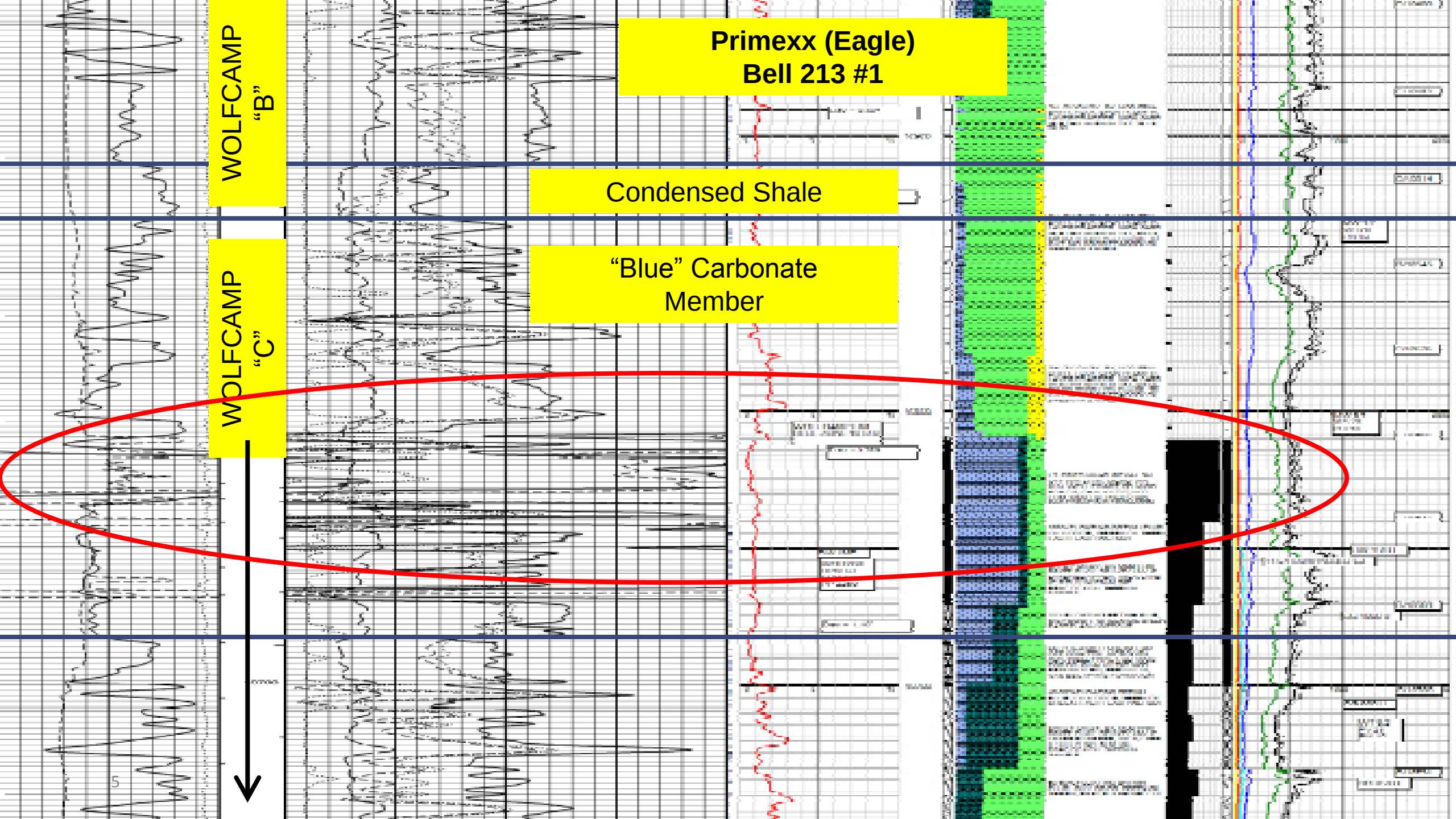
Primexx (Eagle)
Bell 213 #1
WOLFCAMP "B"
Condensed Shale
"Blue" Carbonate Member
WOLFCAMP "C"

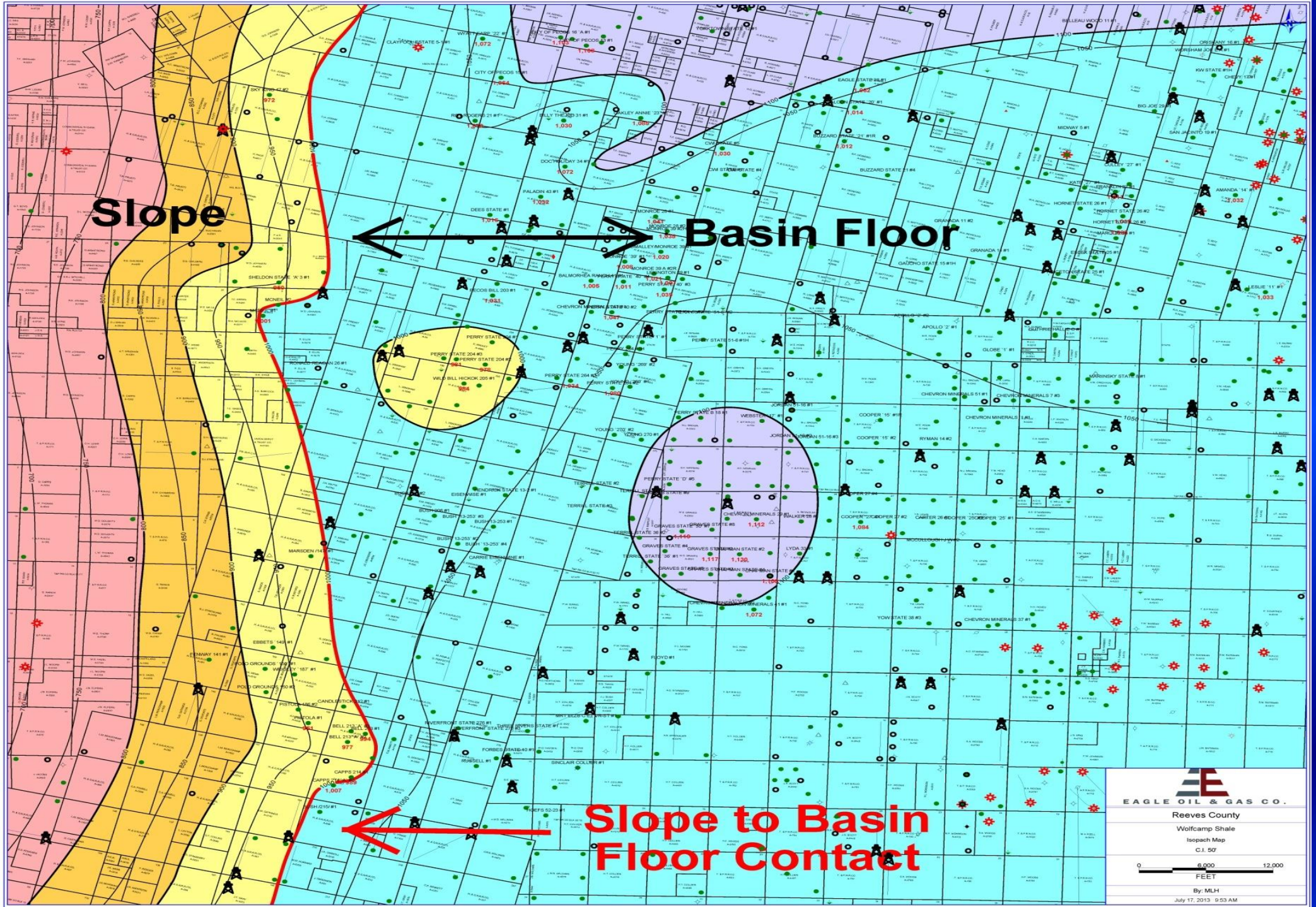
Slope
Basin Floor
Slope to Basin Floor Contact
EAGLE OIL & GAS CO.
Reeves County
Wolfcamp Shale
Isopach Map
C.I. 50'
0
6,000
12,000
FEET
By: MLH
July 17, 2013 9:53 AM

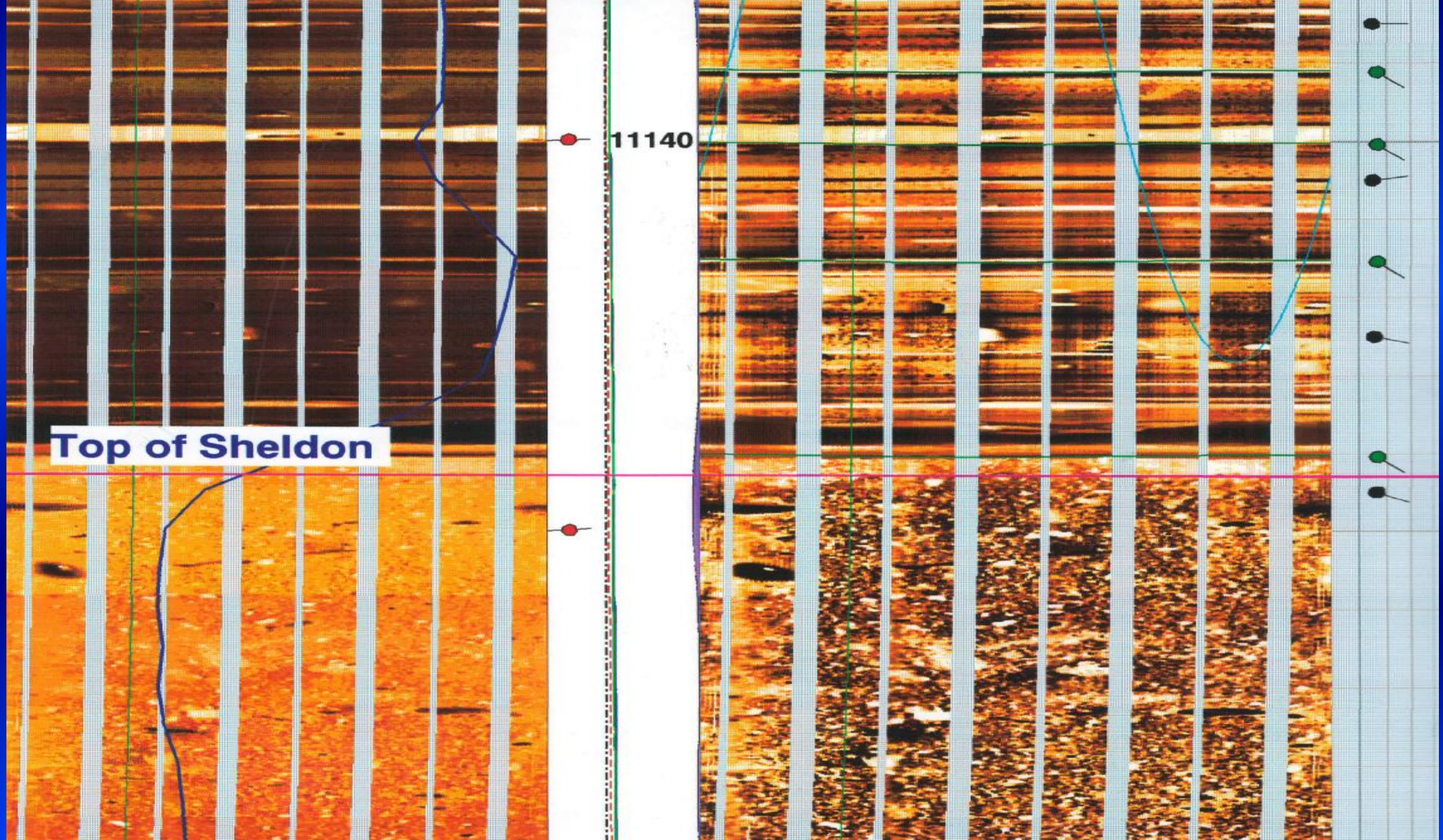
11140
Top of Sheldon

Blessing of Heterogeneities:

- It is the Heterogeneities in mineralogy, grain size, texture, organic material, stage of maturation that define high potential source rock (resource plays) from low potential systems.
- It is the Heterogeneities within each source rock (resource play) that define the economic “Sweet Spots” within each of those systems from lower-potential, generally more basin-wide distribution of lower quality economic objective acreage.
- It is the responsibility of the Geoscientist working within their teams to define these as early as possible, to be the first to the right play, to be first to the “Sweet Spot” and assist in the optimum development of the resource.

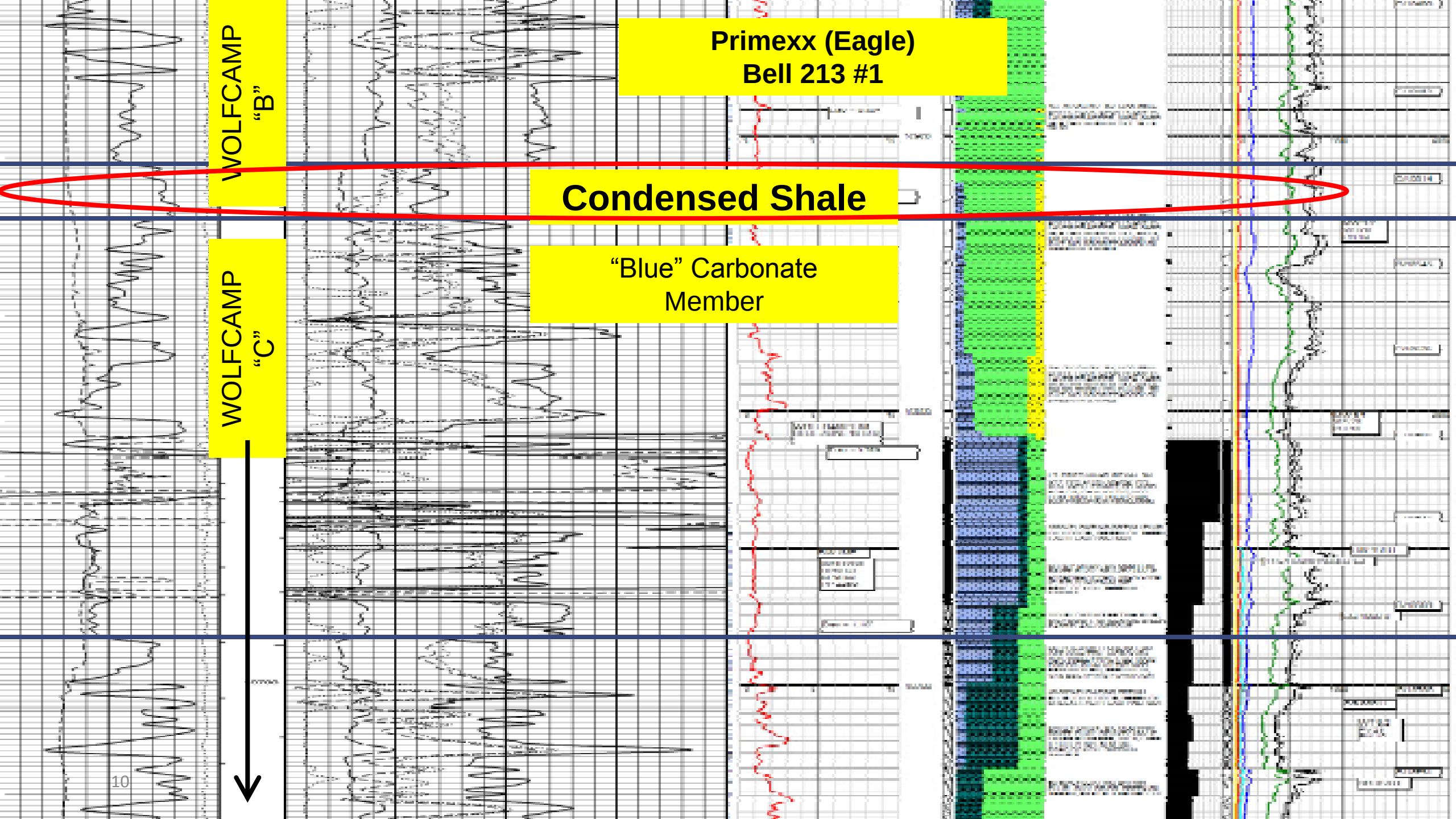
Primexx (Eagle)
Bell 213 #1
WOLFCAMP
"B"
Condensed Shale
"Blue" Carbonate
Member
WOLFCAMP
"C"

Walter Wornardt, 2012

Condensed Section

A thin chronostratigraphic interval of time correlative sediments deposited at extremely slow rates during sediment starvation, in each of the marine environments through a period of maximum relative sea-level rise and maximum transgression of the shoreline. It is characterized by autothonous sedimentation and maximum abundance and diversity peaks of planktonic fossils. The maximum flooding surface within this maximum flooding surface condensed section, provides a chronostratigraphic (time) correlation between shelf and slope sediments.

and is typically "Enriched in Organic Carbon".

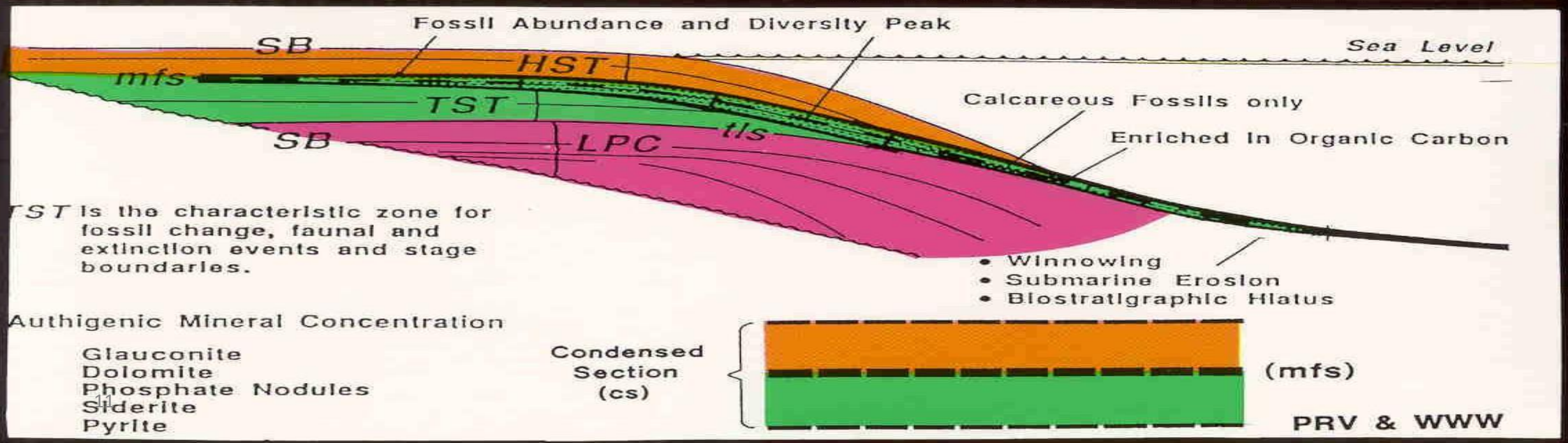

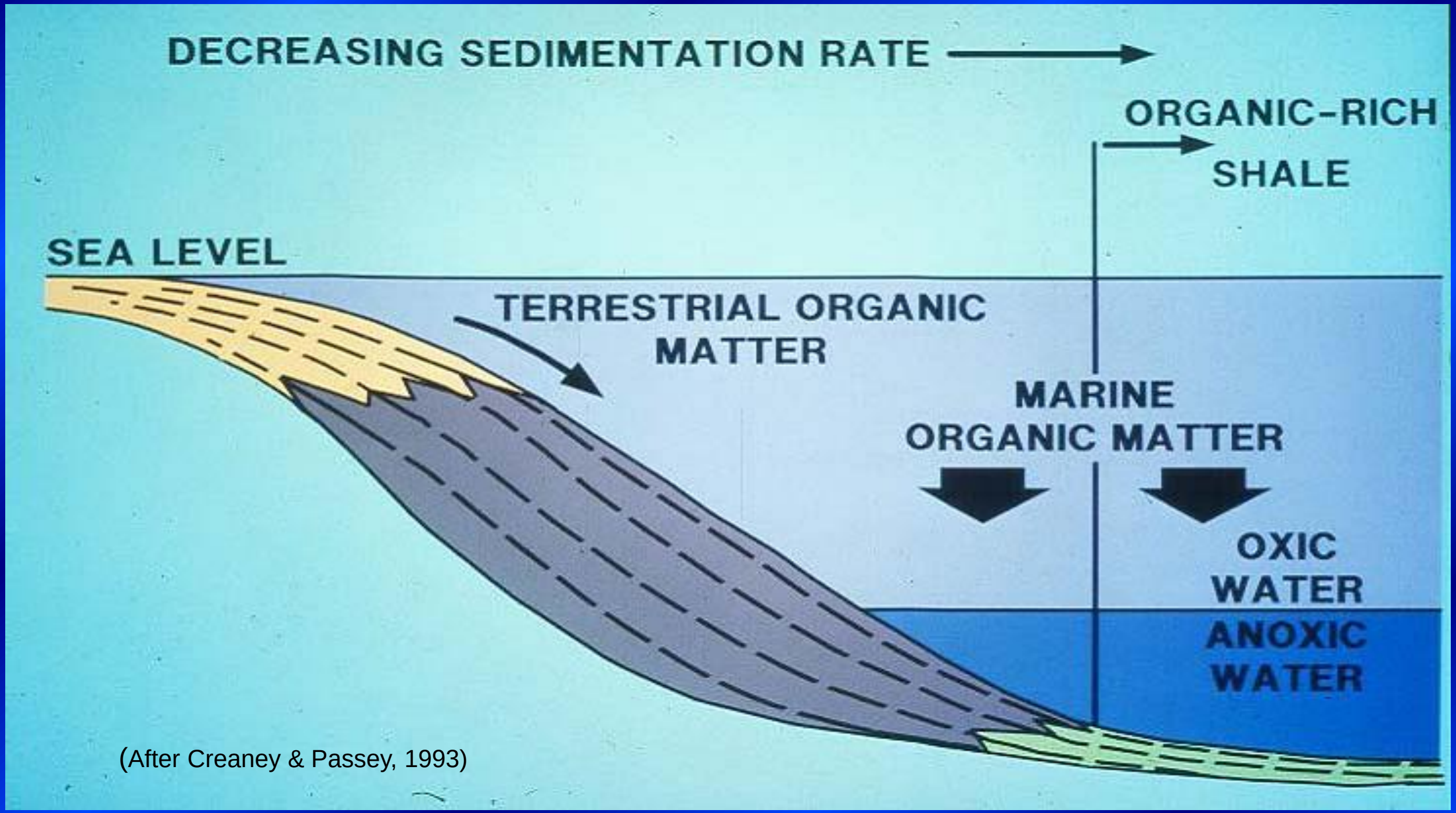

(After Creaney & Passey, 1993)


10990

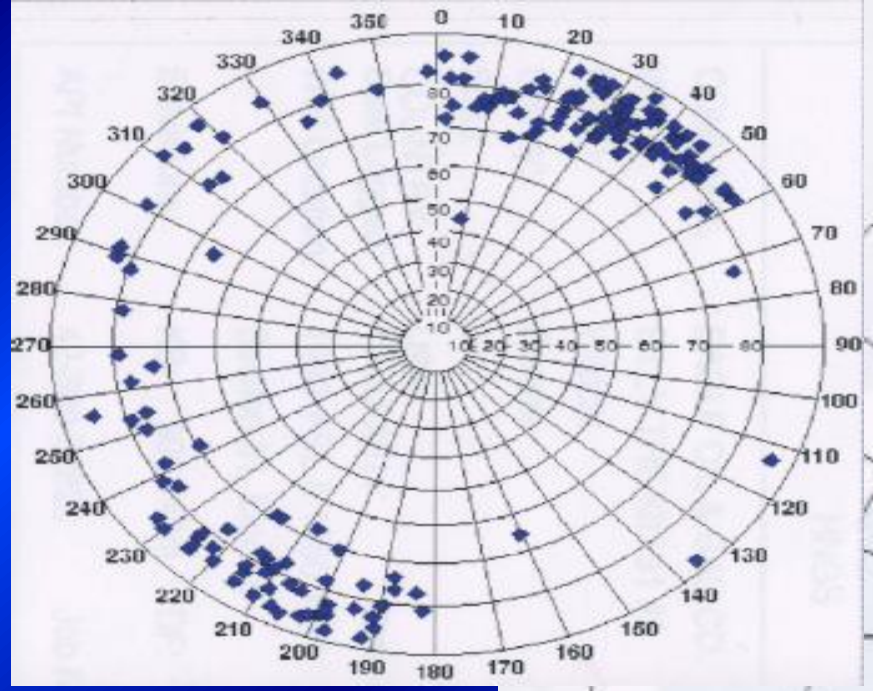

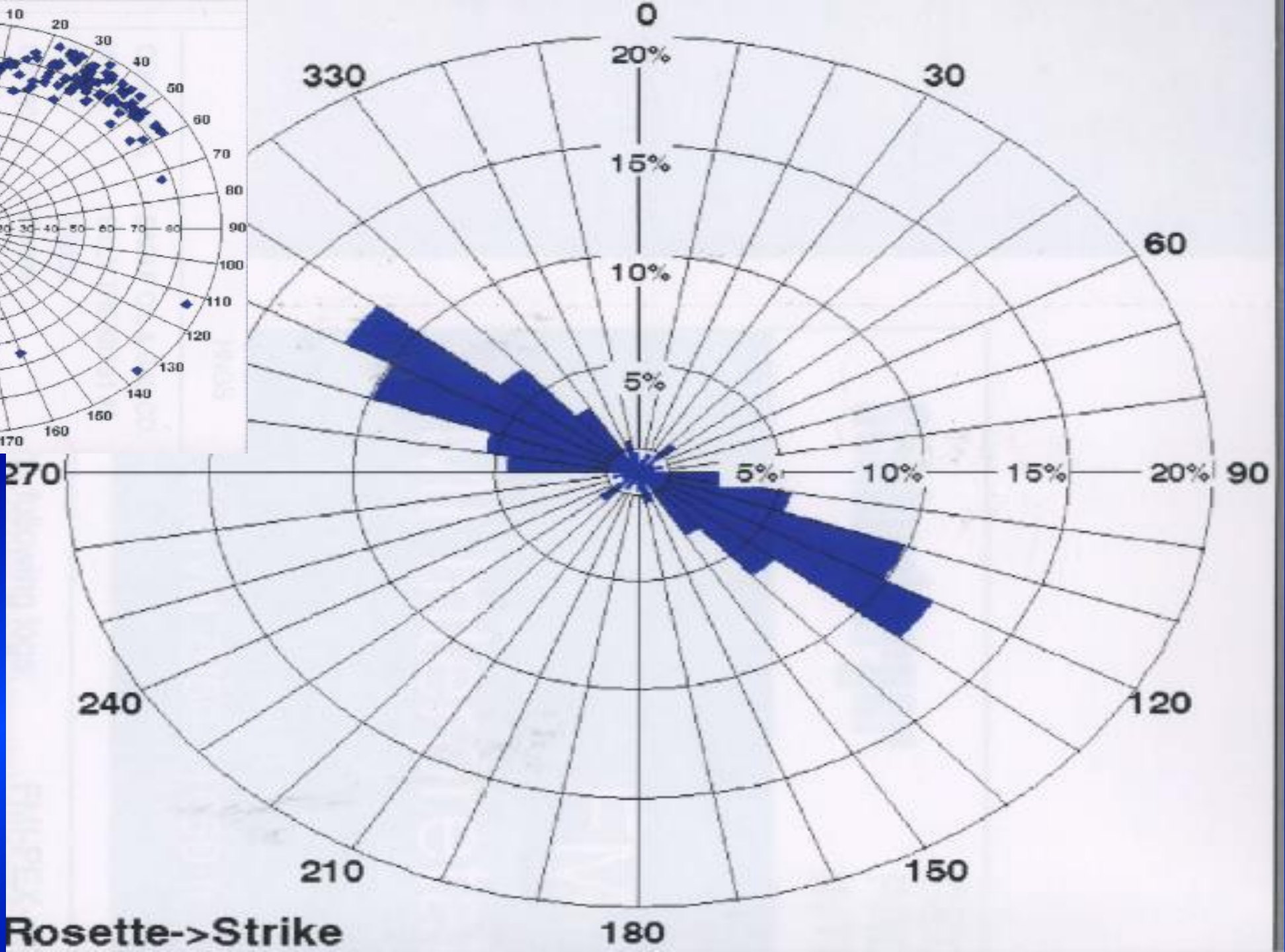

Rosette->Strike

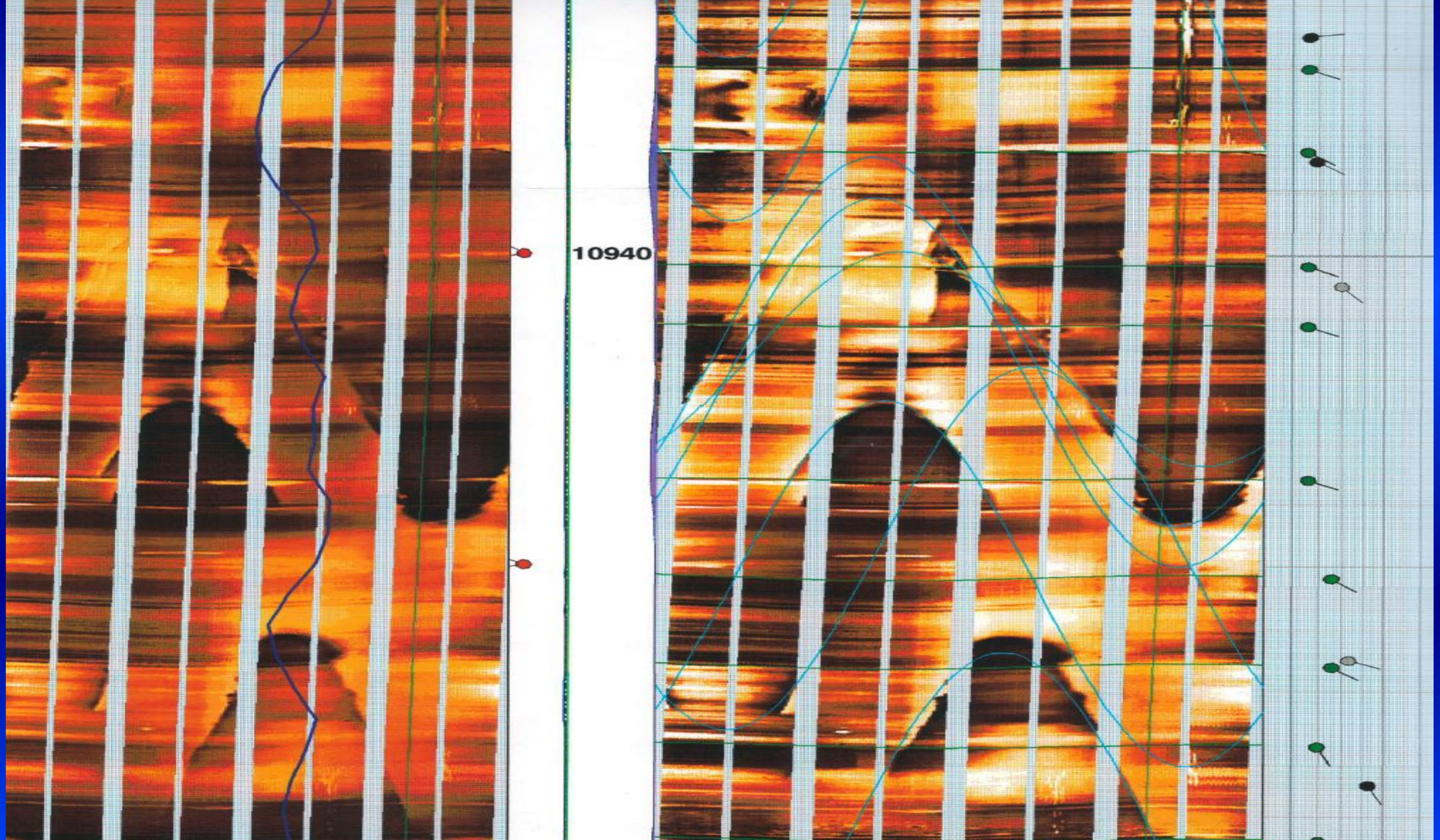
10940

Production Logs = Precision Completions

Production Logs Used to Identify Target Intervals

- Eagle has run production logs in 9 Wolfbone wells
- Tool has multiple sensors to identify contributing intervals:
  - Spinner with dual-axis caliper
  - Pressure and temperature sensors
  - Digital Entry Flowview Imaging Tool (DEFT)
    - Water measurement
  - Gas Holdup Optical Sensing Tool (GHOST)
    - Gas measurement

Previously Drilled Hz Target

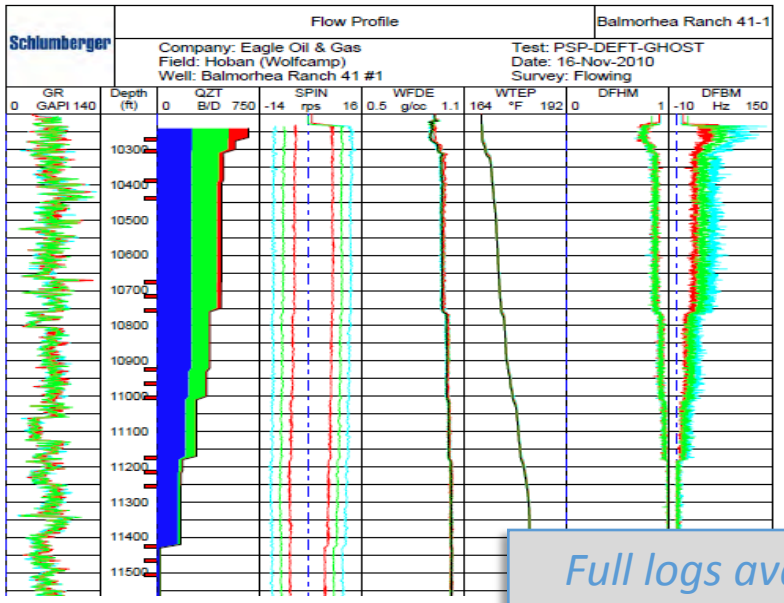

Current Hz Target Monroe 39 #2H

Full logs available in VDR

Relative Flow Contribution by Member(1)

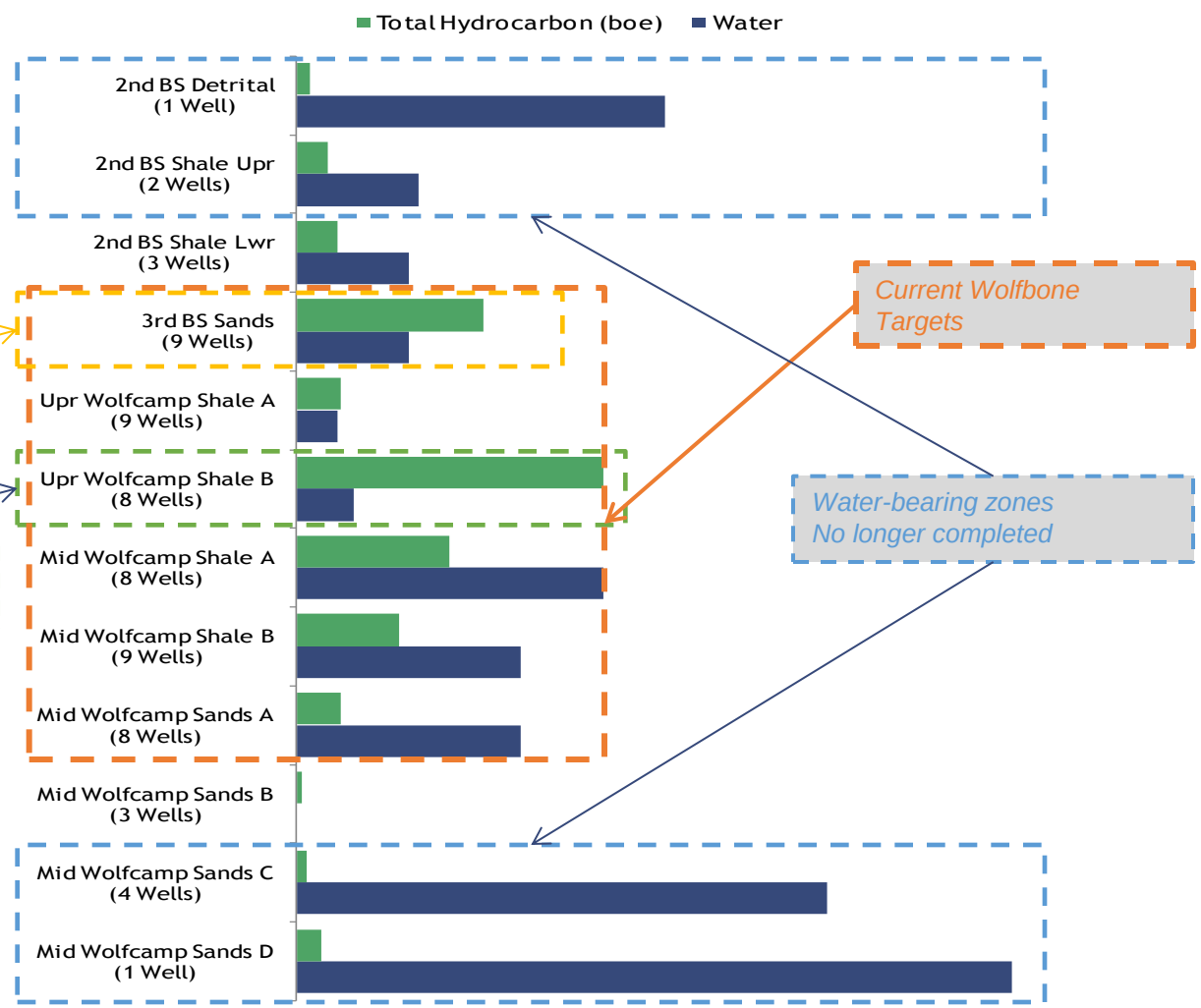

Current Wolfbone Targets

Water-bearing zones No longer completed

First 60-Day Average Production in Sequential Order Completed With 5-Well Moving Average

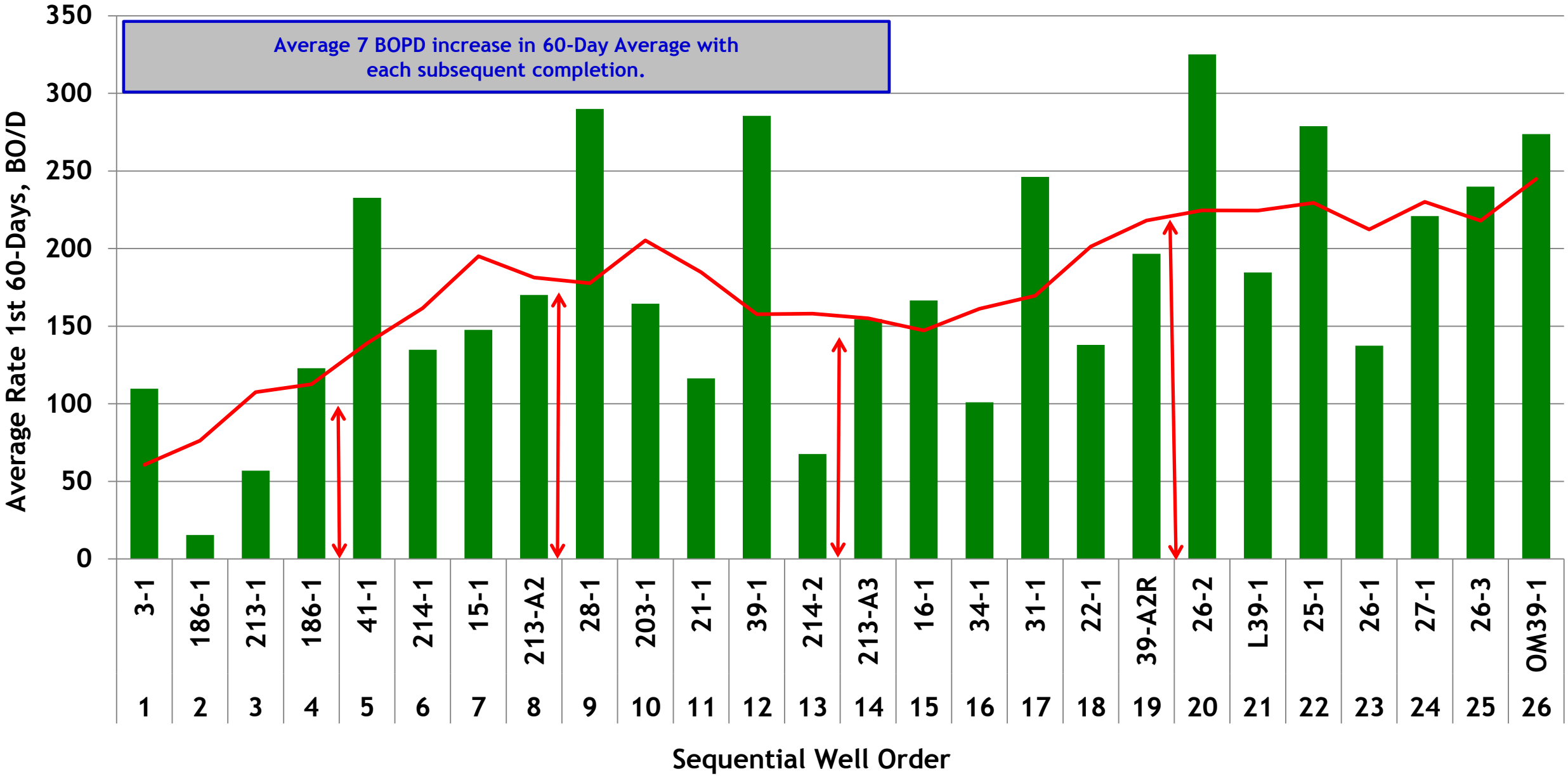

Focusing the Effort

	Approx. Depth	Sheldon #1	Pistola #1 (Sand Zones)	Bell #1	Pistola #1 (Recompletion)	BR41 #1	Capps #1	CP15 #1	Bell #2	M28 #1	PB203 #1	RR21 #1	M39 #1	Capps #2	Bell #3	CP16 #1	DH34 #1	BtK31 #1	Wyatt 22 #1
Peak Rate (boe/d)		315	132	202	487	583	445	394	367	691	586	368	504	296	392	572	403	459	394
1st BS Shale - Avalon																			
2nd BS Detrital	9,250	1																	
2nd BS Shale Upr	9,600							1											
2nd BS Shale Lwr	9,850	1						1											
3rd BS Sands	10,150	1		1	1	1	1	1	1	1	1	1	1	1	1	1	1	1	1
Upr Wolfcamp Shale A	10,440	1		1	1	1	1	1	1	1	1	2	2	1	2	3	2	3	3
Upr Wolfcamp Shale B	10,700				1	1	1	1	1	2	2	2	2	2	1	2	2	2	2
Mid Wolfcamp Shale A	10,900			1	1	1	1	1	1	1	1	2	2	2	2	3	2	2	2
Mid Wolfcamp Shale B	11,100	1			1	1	1	1	1	1	1	2	2	2	2	2	3	3	3
Mid Wolfcamp Sands A	11,400	1	2	1		1	1	1	1	1	1								
Mid Wolfcamp Sands B	11,650					1	1		1	1									
Mid Wolfcamp Sands C	12,000	1	1	1		1	1	1											
Mid Wolfcamp Sands D	12,250	1	1	1															

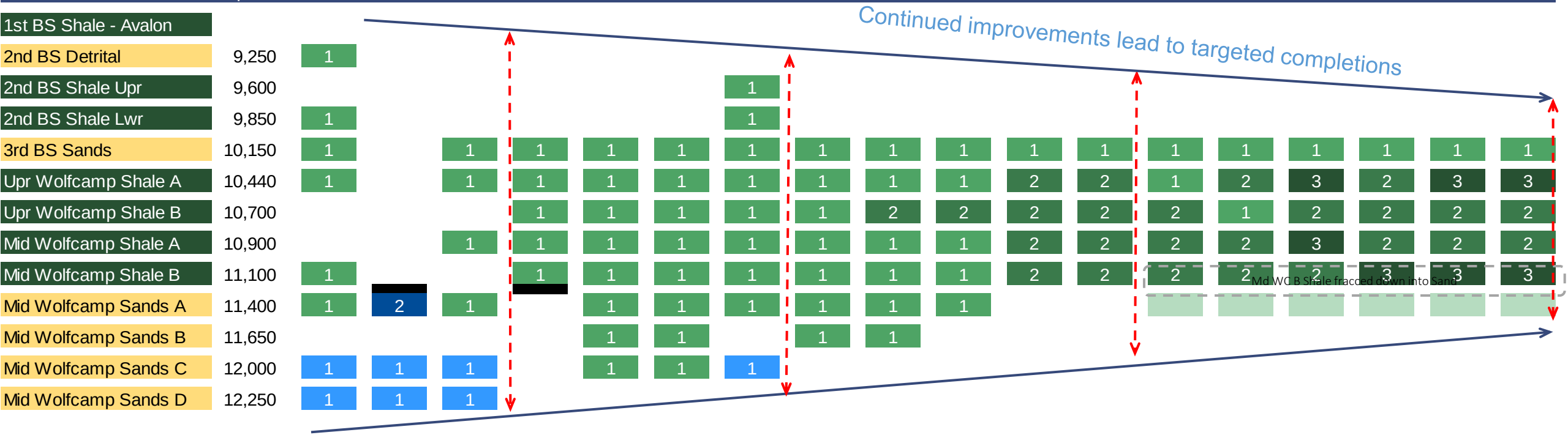

Most recent wells completed consistently with excellent results

First 60-Day Average Production in Sequential Order Completed With 5-Well Moving Average

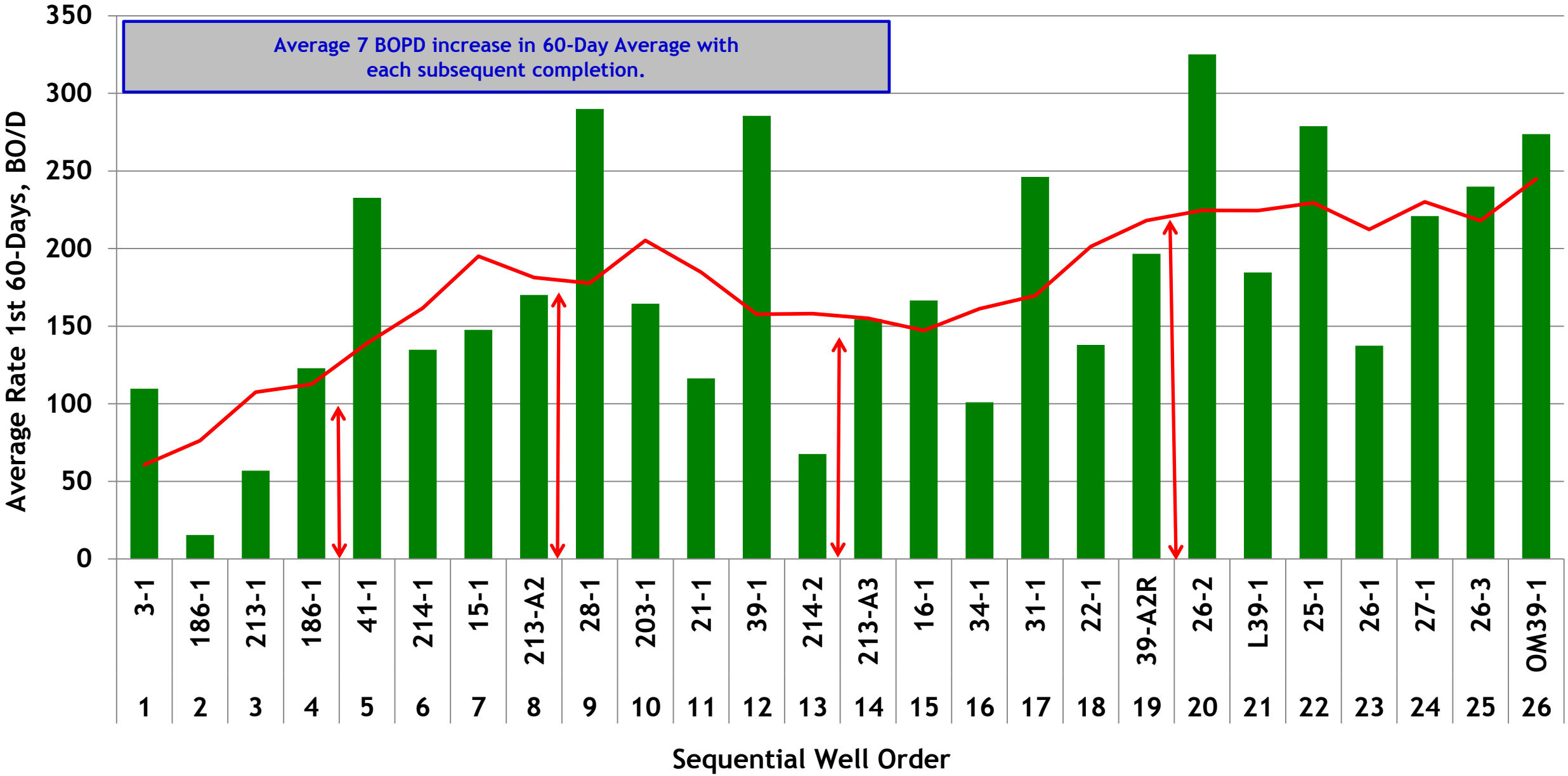

OUTLINE:

1. Exploration, Synthesis of Early Development Geologic Information and Reservoir Performance to Enhance Economic Performance: Example from the Southern Delaware Basin, West Texas.

2. Are we Integrating our Input with other Disciplines, communicating with Management and other Interest Holders to Maximize Economic Outcomes?

Drilling:

- Drilling limitations of approximately 20,000’ have been overcome.
- Drilling time has been reduced in some cases by as much as 85%.
- Walking rigs, vertical / horizontal manufacturing processes have increased efficiencies and reduced costs.




RAG
E 200
RAG

Drilling:

Horizontal technology and interactive, synthesis of Geologic input has reduced horizontal drilling times, increased geologic data collection and maximized horizontal length in the target zone.

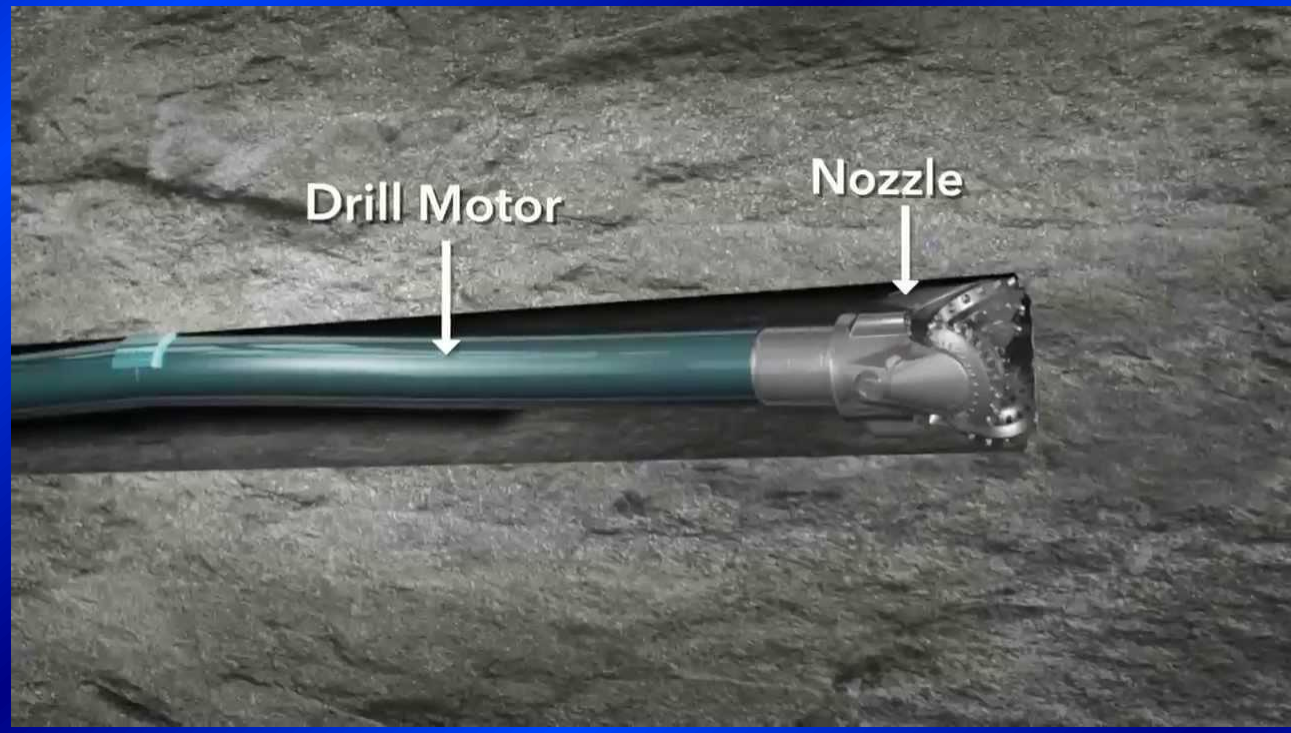

* Courtesy of Carrollton Minerals Partners

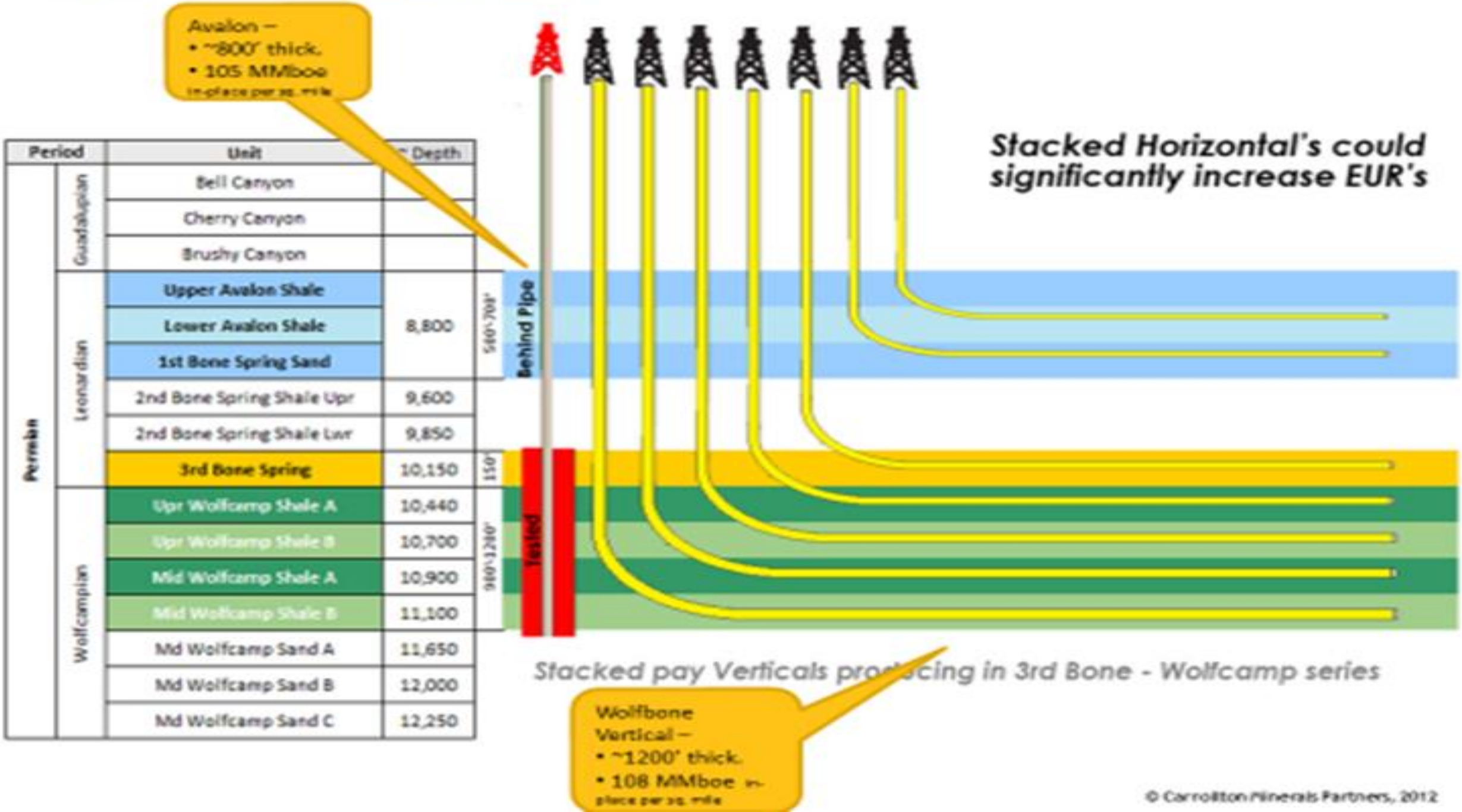

Period		Unit	~ Depth	
Permian	Guadalupian	Bell Canyon		
		Cherry Canyon		
		Brushy Canyon		
	Leonardian	Upper Avalon Shale	8,800	540'-700'
		Lower Avalon Shale		
		1st Bone Spring Sand		
		2nd Bone Spring Shale Upr	9,600	
		2nd Bone Spring Shale Lwr	9,850	
		3rd Bone Spring	10,150	150'
	Wolfcampian	Upr Wolfcamp Shale A	10,440	960'-1200'
		Upr Wolfcamp Shale B	10,700	
		Mid Wolfcamp Shale A	10,900	
		Mid Wolfcamp Shale B	11,100	
		Md Wolfcamp Sand A	11,650	
		Md Wolfcamp Sand B	12,000	
		Md Wolfcamp Sand C	12,250	

AVERAGES OF ALL GRADES OF VERTICAL AND HORIZONTAL WELLS, REEVES COUNTY

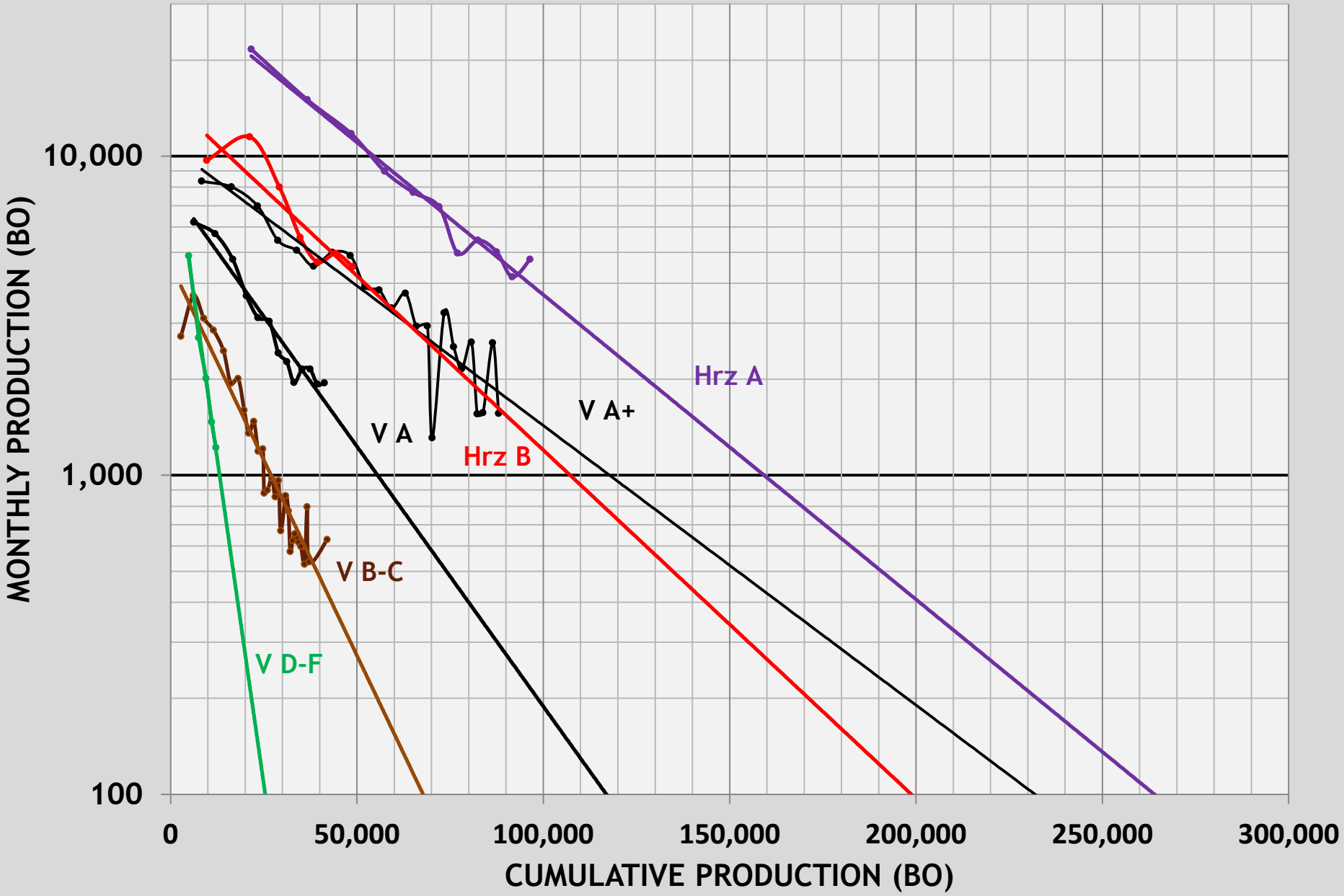

Type	Well $	1st Mo	EUR	NPV9	D(ROI)	ROI	I(ROR)	Payout
Well	($MM)	Prod (BO)	(MBO)	($MM)	I(EFF)	$:$		
Target					2.0	3.0		
V D-F	$3.5	5,000	25	N/A	N/A	N/A	N/A	N/A
V B-C	$3.5	4,000	73	-0.07	0.98	1.16	4.88	6.20
V A	$3.5	6,500	236	5.27	2.50	4.76	37.45	1.86
Hrz B	$7.5	10,000	434	11.08	2.47	4.34	37.32	1.91
Hrz A	$7.5	20,000	722	22.07	3.97	7.97	57.87	1.75
Hrz A "Best To Date"	$7.5	20,000	268	7.5	2.00	2.31	49.72	1.75

© Riverford Exploration, LLC, 2012

Geologic / Reservoir Modeling:

- 10 years ago we could not adequately explain how gas moved through reservoir rocks but knew that oil would never be economically producible from such reservoirs.
- Obviously our explanations have changed.
- What about our measurement tools, techniques, methods output and analyses.

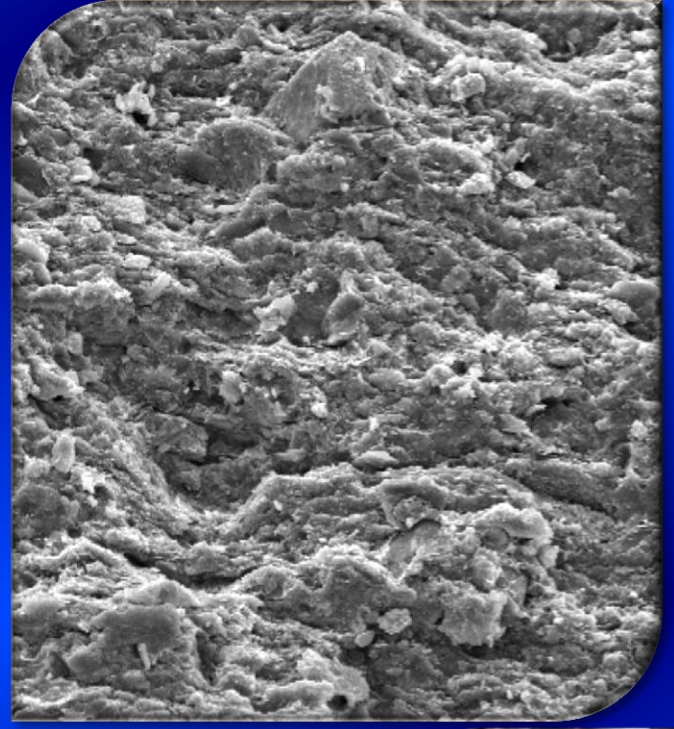

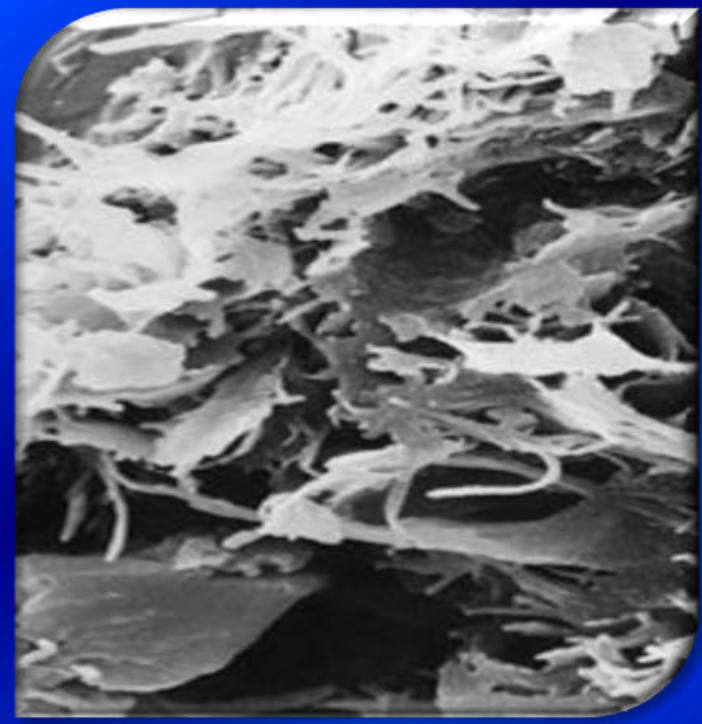

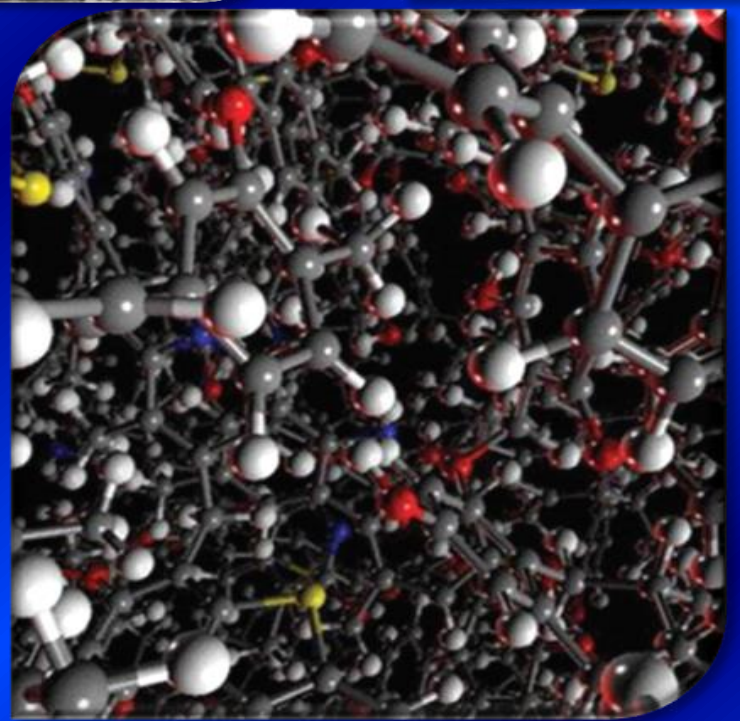

Pictures from Halliburton's website.

Reservoir Modeling Scale?

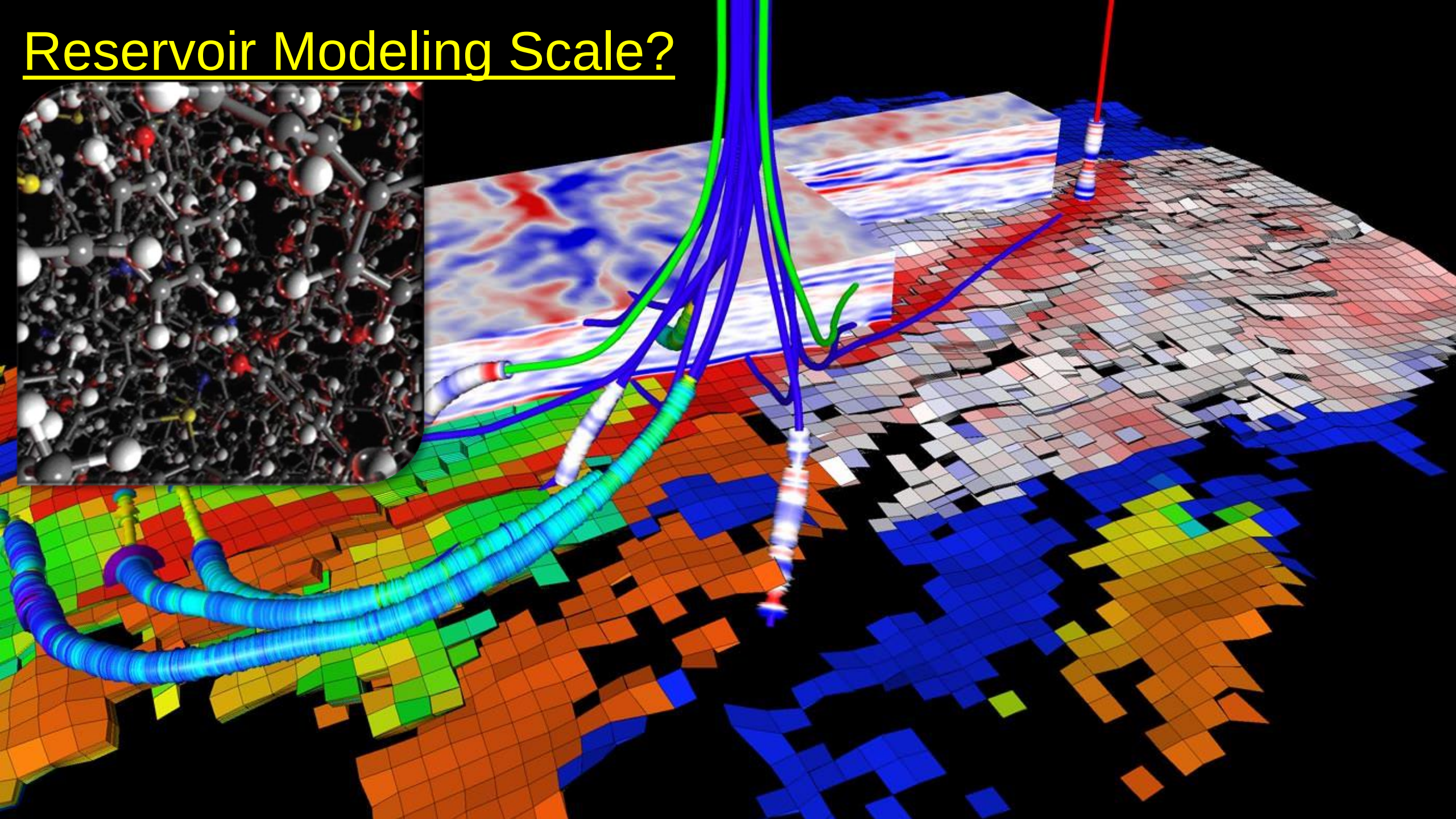

MicroSeismic and Stimulation Modeling Scale

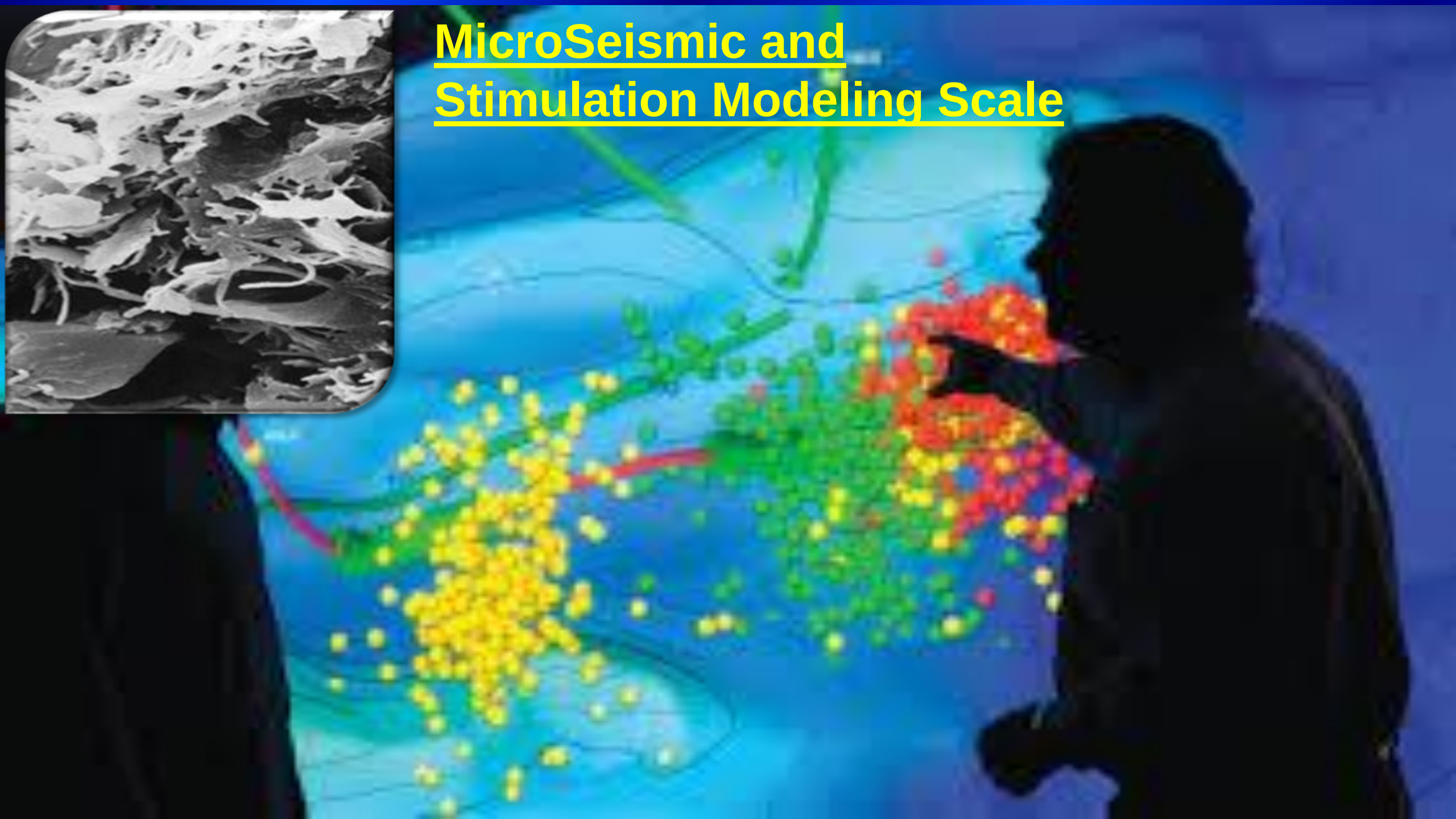

MicroSeismic and Stimulation Modeling Scale

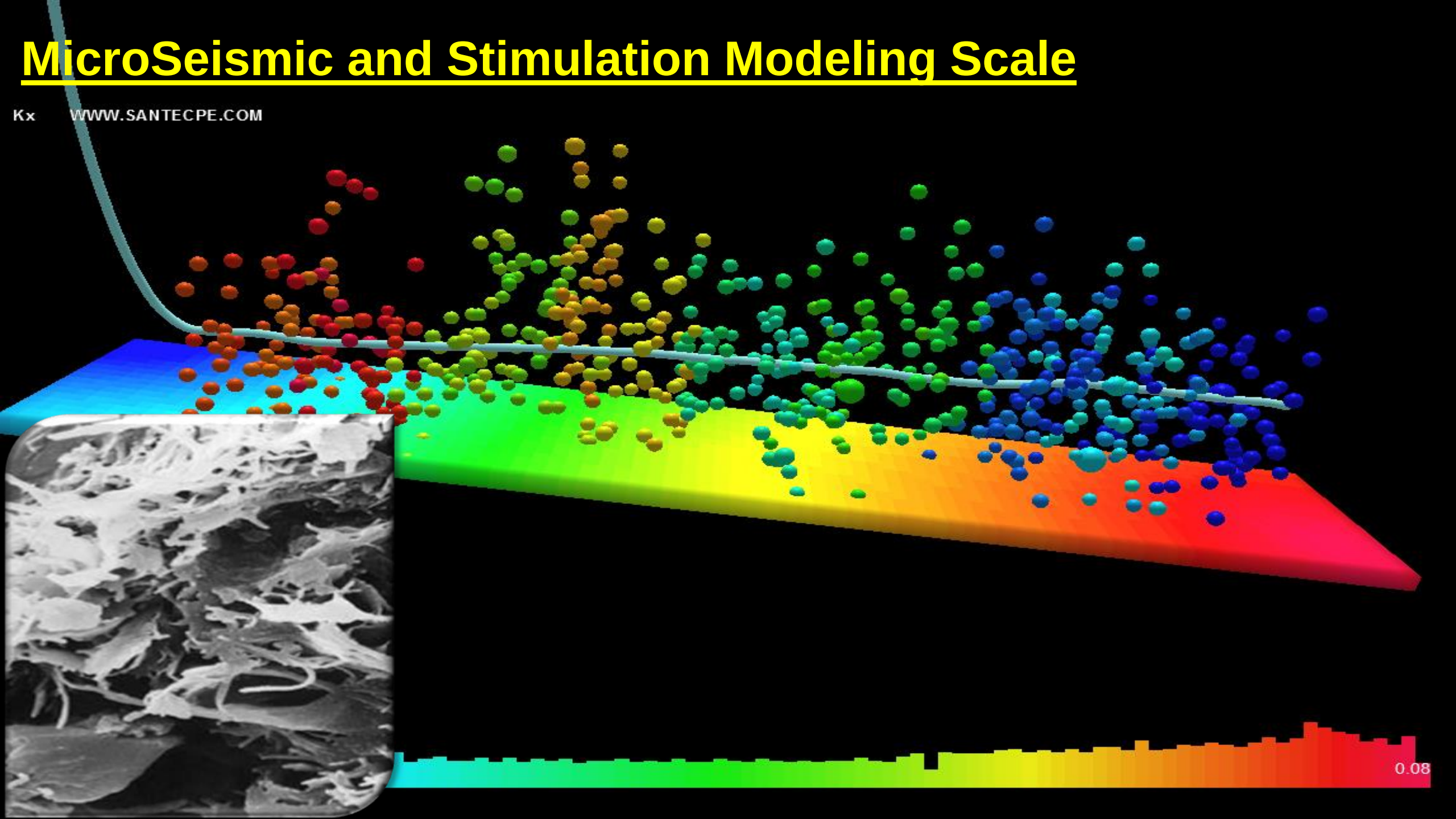

The Permian Basin – Intracratonic Subsidence Triggered by ARM Compression, Making an American "Superbasin"*

Thomas E. Ewing[1]

Search and Discovery Article #10988 (2017)**
Posted August 21, 2017

*Adapted from oral presentation given at AAPG 2017 Southwest Section Annual Convention, Midland, Texas, April 29-May 2, 2017
**Datapages © 2017 Serial rights given by author. For all other rights contact author directly.

[1]Frontera Exploration Consultants, San Antonio, TX (tewing@fronteraexploration.com)

Abstract

One distinctive feature of the West Texas branch of the Ancestral Rocky Mountains is its burial by over 2.5 km of post-deformational Permian strata - the Permian Basin. Subsidence probably began during ARM deformation in Pennsylvanian time, as evidenced by very limited subaerial exposure and erosion related to uplifts in the central basin. Subsidence increased in rate by the early Permian and continued to the end of the Permian. Permian subsidence resulted in the maintenance of isolated deep-water marine basins until Ochoan (late Permian) time, when they were filled with evaporites and nonmarine sediments. The thrusted Marathon orogen probably participated in this subsidence, as little clastic material was shed from this orogenic belt into the basin (and none in the Permian; most Permian deep-water clastics appear to have northerly sources).

The margins of the Permian Basin have been modified during the Mesozoic, but the pattern of post-Wolfcamp Permian isopachs suggests a bowl-shaped subsidence centered on the Central Basin "Platform" or axis of uplift.

References Cited

Ewing, T.E., 2016, Texas Through Time: Lone Star Geology, Landscapes, and Resources: The University of Texas at Austin, Bureau of Economic Geology Udden Series No. 6, 431 p.

Ewing, T.E., 1991, Structural Framework, *in* A. Salvador (ed.), The Gulf of Mexico Basin: The Geology of North America, Geological Society of America, v. J, p. 31-52.

McKee, E.D., and S.S. Oriel, 1967, Paleotectonic Maps of the Permian System: U.S. Geological Survey, Miscellaneous Geological Investigations Map I-450, 164 p.

Muehlberger, W.R., 1996, Tectonic Map of North America: 1:5,000,000: American Association of Petroleum Geologists, 14 p.

Ye, H., L. Royden, C. Burchfiel, and M. Schuepbach, 1996, Late Paleozoic Deformation of Interior North America: The Greater Ancestral Rocky Mountains: American Association of Petroleum Geologists Bulletin, v. 80, p. 1397-1432

THE PERMIAN BASIN – Intracratonic subsidence triggered by ARM compression, making an American "Superbasin"

Thomas E. Ewing
Frontera Exploration Consultants
San Antonio, TX

For Southwest Section AAPG Meeting May, 2017

ABSTRACT

- One distinctive feature of the West Texas branch of the Ancestral Rocky Mountains is it's burial by over 2.5 km of post-deformational Permian strata - the Permian Basin.
- Subsidence probably began during ARM deformation in Pennsylvanian time, as evidenced by very limited subaerial exposure and erosion related to uplifts in the central basin. Subsidence increased in rate by the early Permian and continued to the end of the Permian. Permian subsidence resulted in the maintenance of isolated deep-water marine basins until Ochoan (late Permian) time, when they were filled with evaporites and nonmarine sediments.
- The thrusted Marathon orogen probably participated in this subsidence, as little clastic material was shed from this orogenic belt into the basin (and none in the Permian; Permian deep-water clastics appear to have northerly sources).
- The margins of the Permian Basin have been modified during the Mesozoic, but the pattern of post-Wolfcamp Permian isopachs suggests a bowl-shaped subsidence centered on the Central Basin "Platform" or axis of uplift. The size and shape of the Permian basin are similar to other intracratonic basins (Illinois, Michigan, Williston). One method to form these basins is suggested to be downwarping due to densification of the lower crust or lithosphere.
- The central basin area hosts a Tonian layered mafic complex, which was subjected to compression and thrusting in Pennsylvanian time. Depression of a mafic crust or its subjacent lithosphere may have been the driving force for Permian subsidence, originated by NE-SW compression during the Pennsylvanian and Wolfcampian.
- Over most of the basin, Permian subsidence was responsible for putting source rocks into the oil window. Further maturation to gas happened in the deep Delaware and Val Verde Basins due to foredeep or yoked basin development during ARM deformation and Marathon convergence.

WEST TEXAS (PERMIAN) BASIN

- Defined by thick accumulation of Permian rocks by geologists in 1910s, 1920s; major Permian oil fields found
- Later, complex Ancestral Rocky Mountain (ARM) structures were found in older rocks and more large oil fields found
- Why do we have the thick Permian section?
- What is the nature of this ‘Permian Basin’?

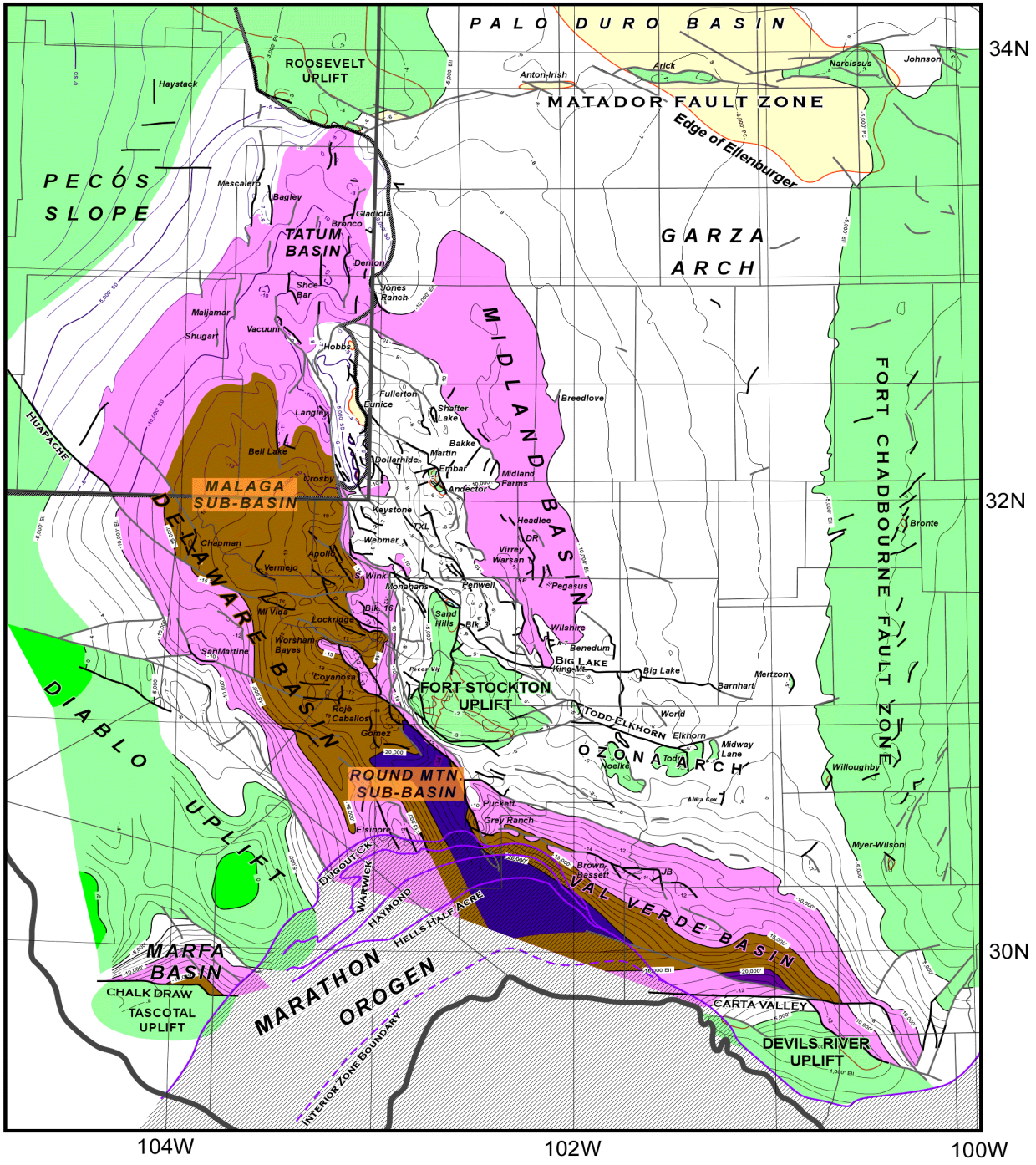

STRUCTURE , TOP ELLEN-BURGER

ANCESTRAL ROCKY MOUNTAINS

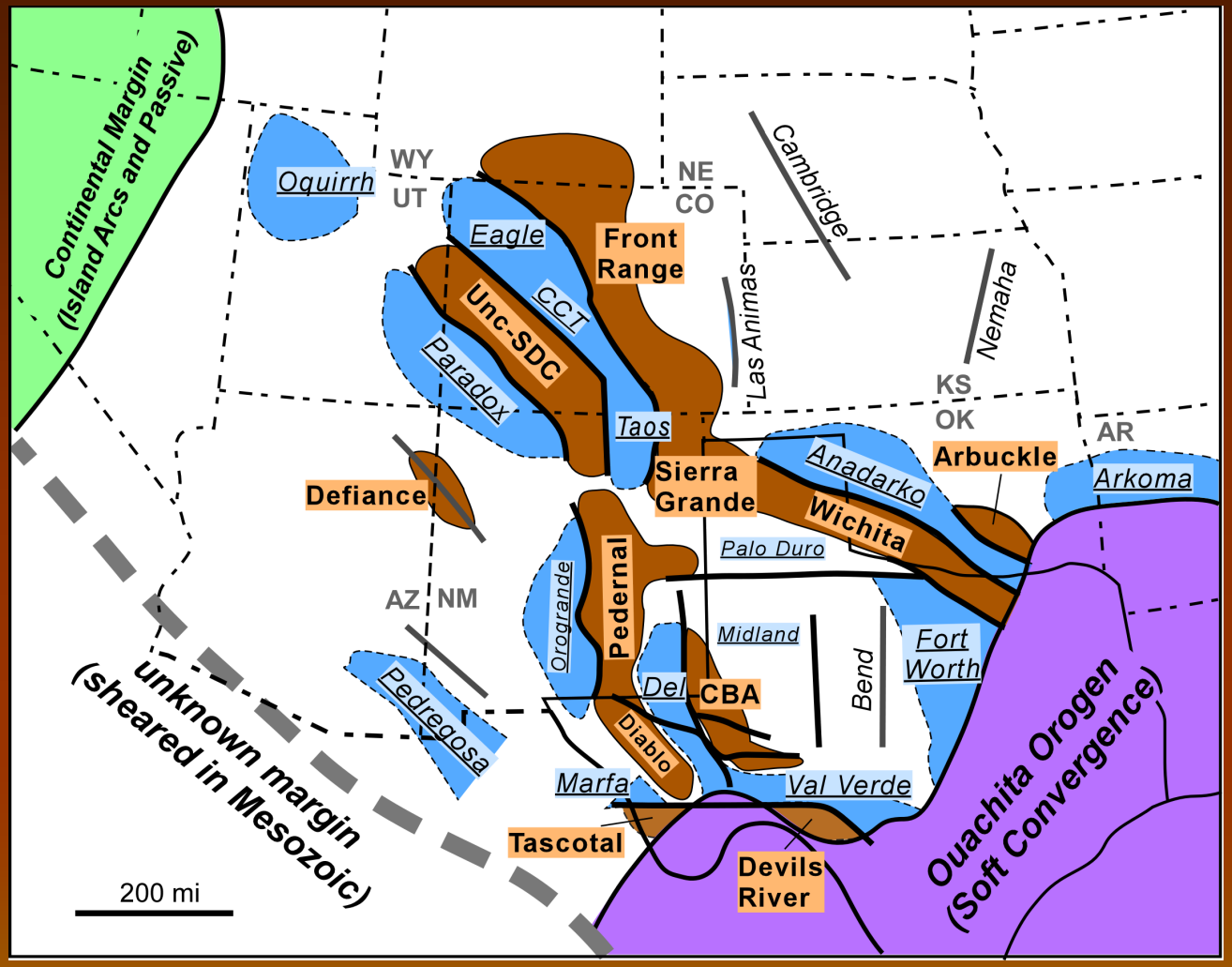

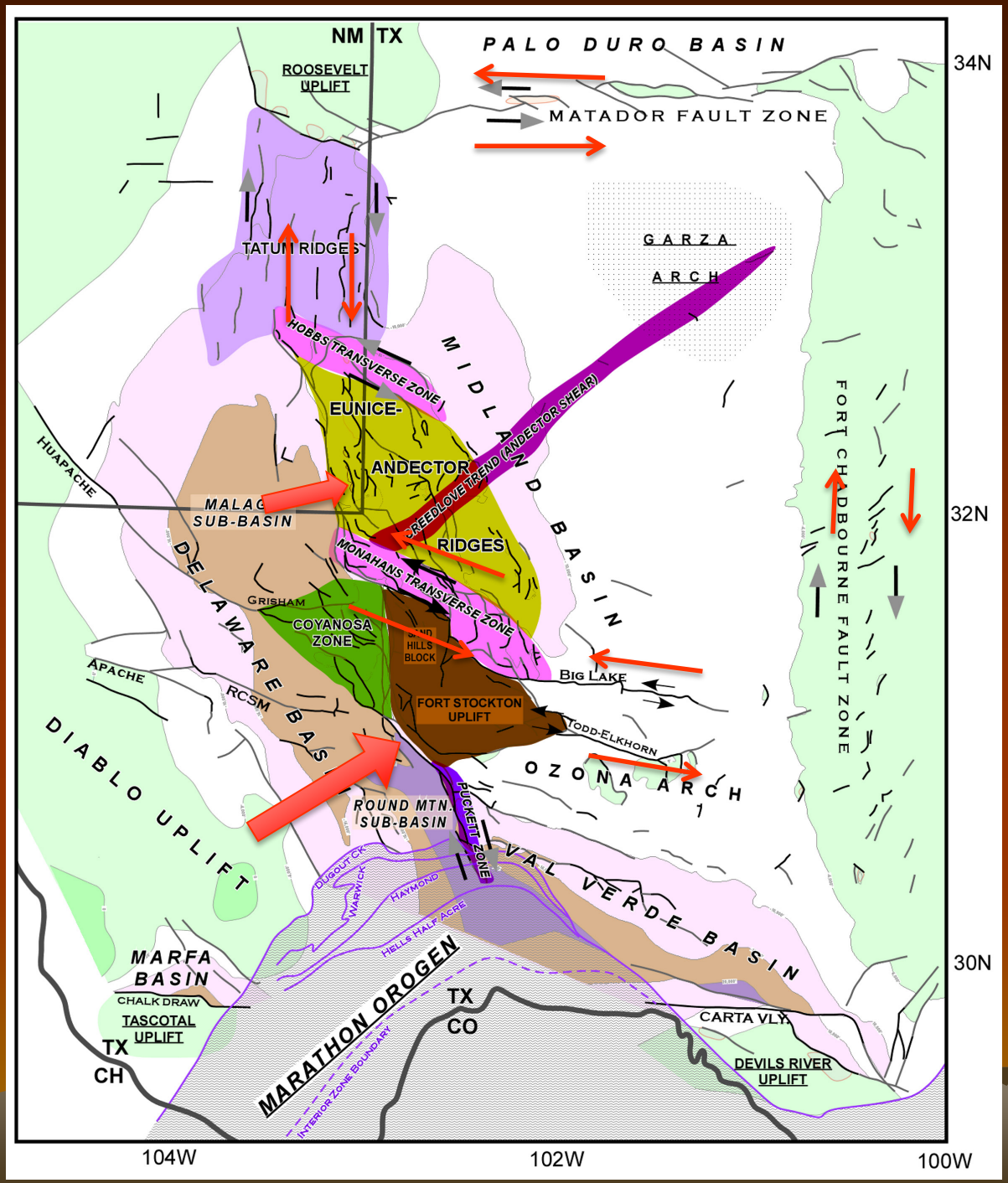

MACRO-SCALE DOMAINS AND KINEMATICS

CENTRAL SECTION (FT. STOCKTON UPLIFT)

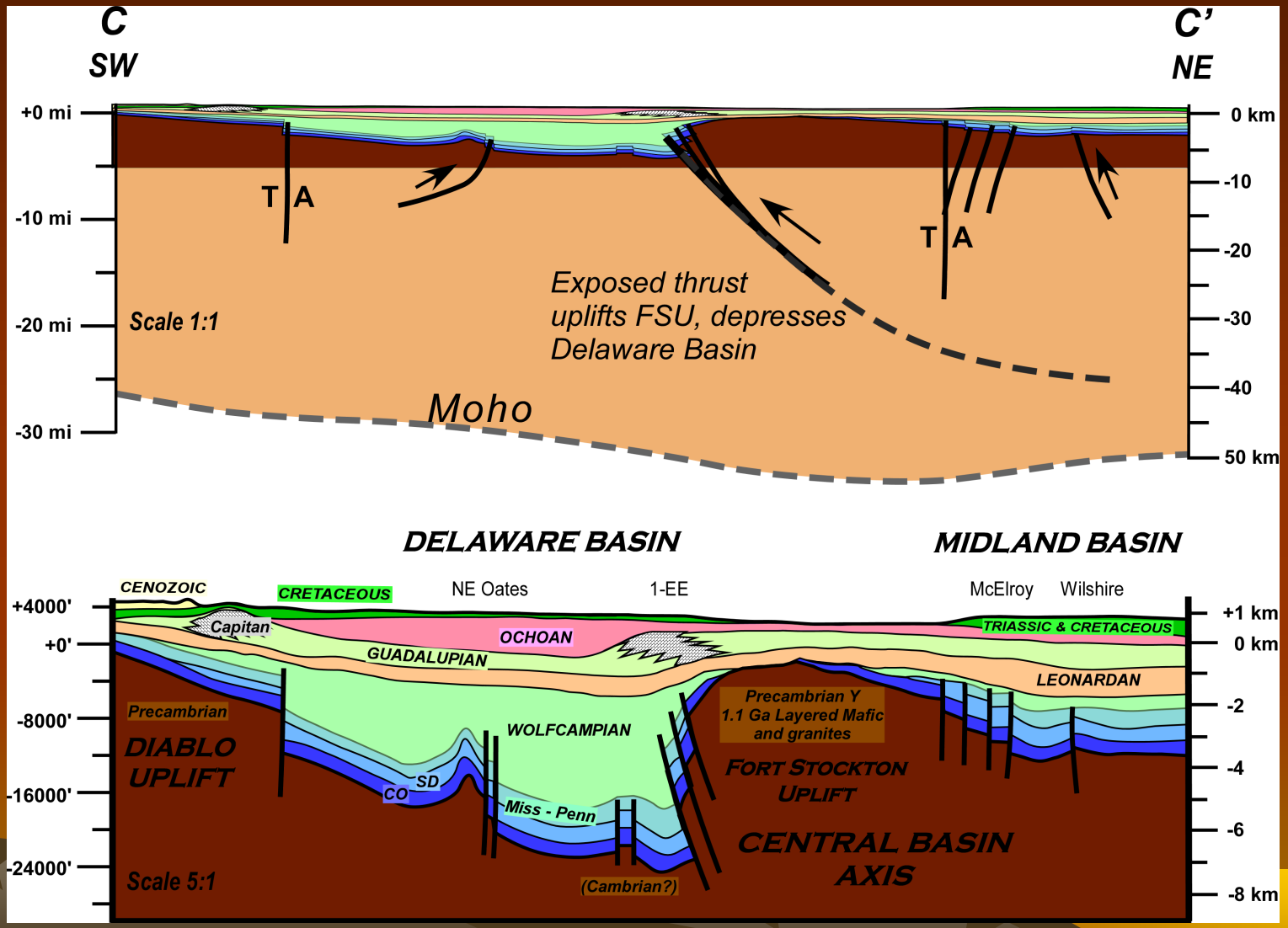

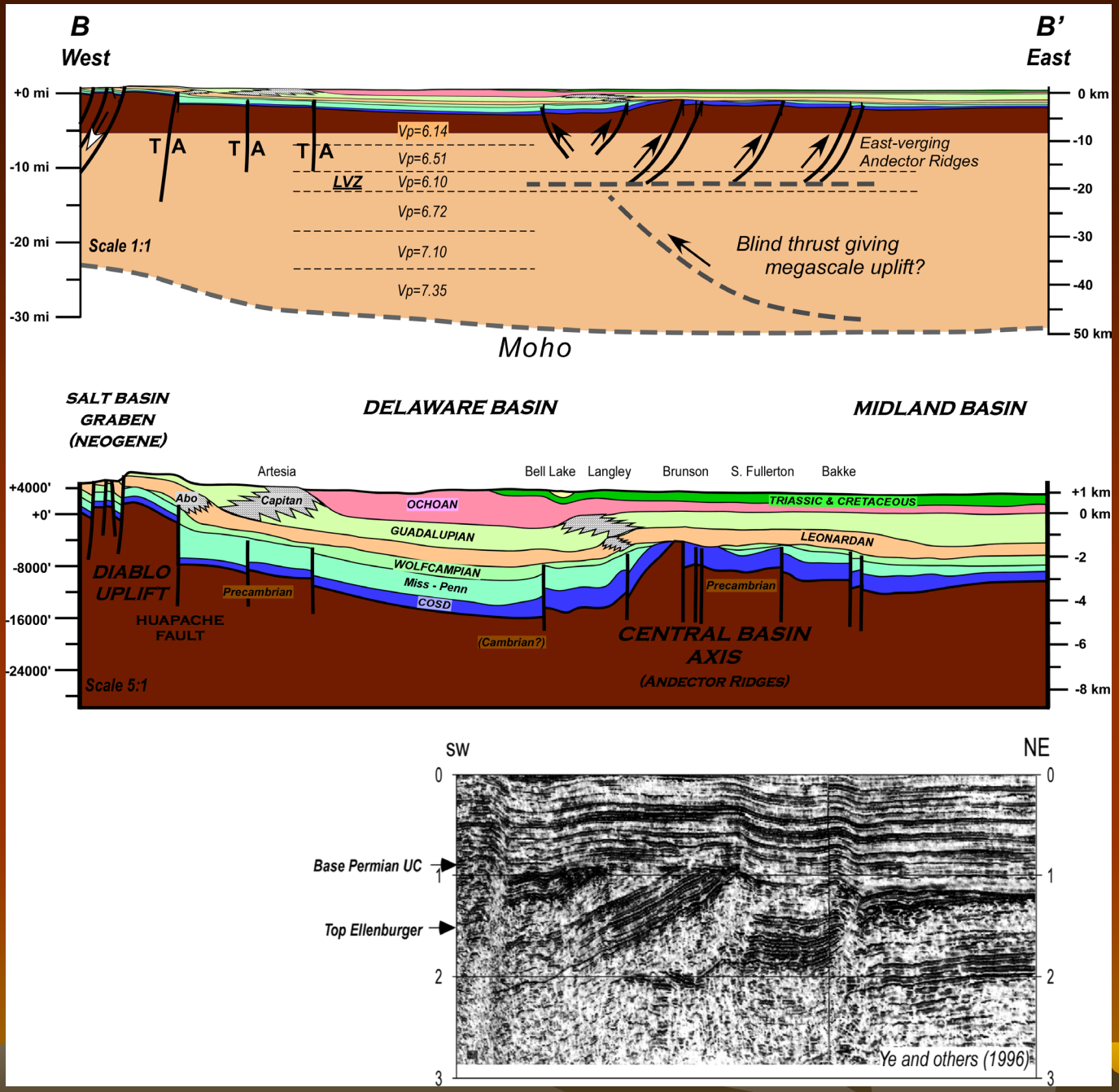

NORTHERN SECTION (GUADALUPE PEAK TO BIG SPRING)

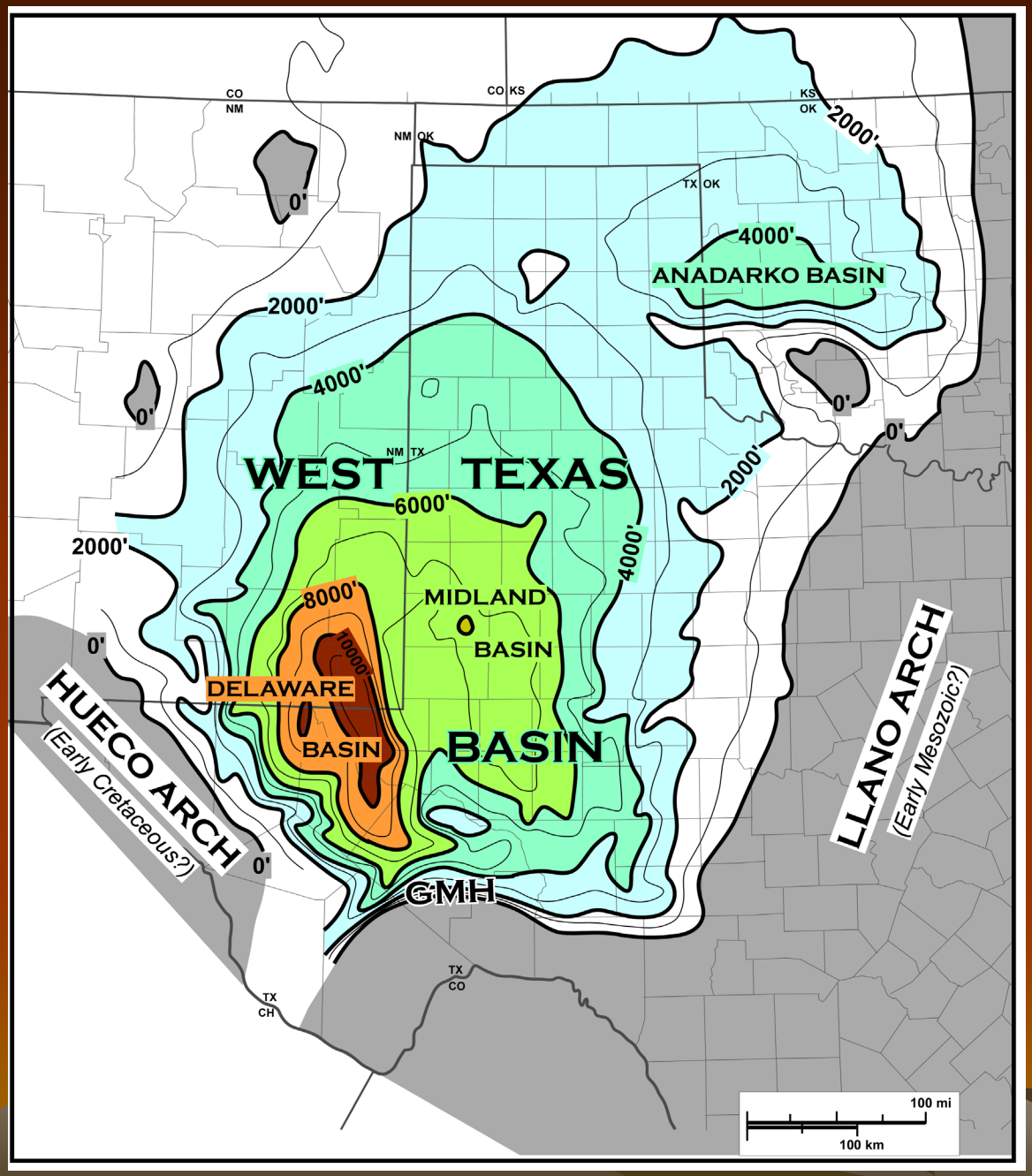

ISOPACH, POST-WOLFCAMP PERMIAN STRATA

Ewing, 1991, after McKee and Oriel (1967)

PRE-CRETACEOUS SUBCROP

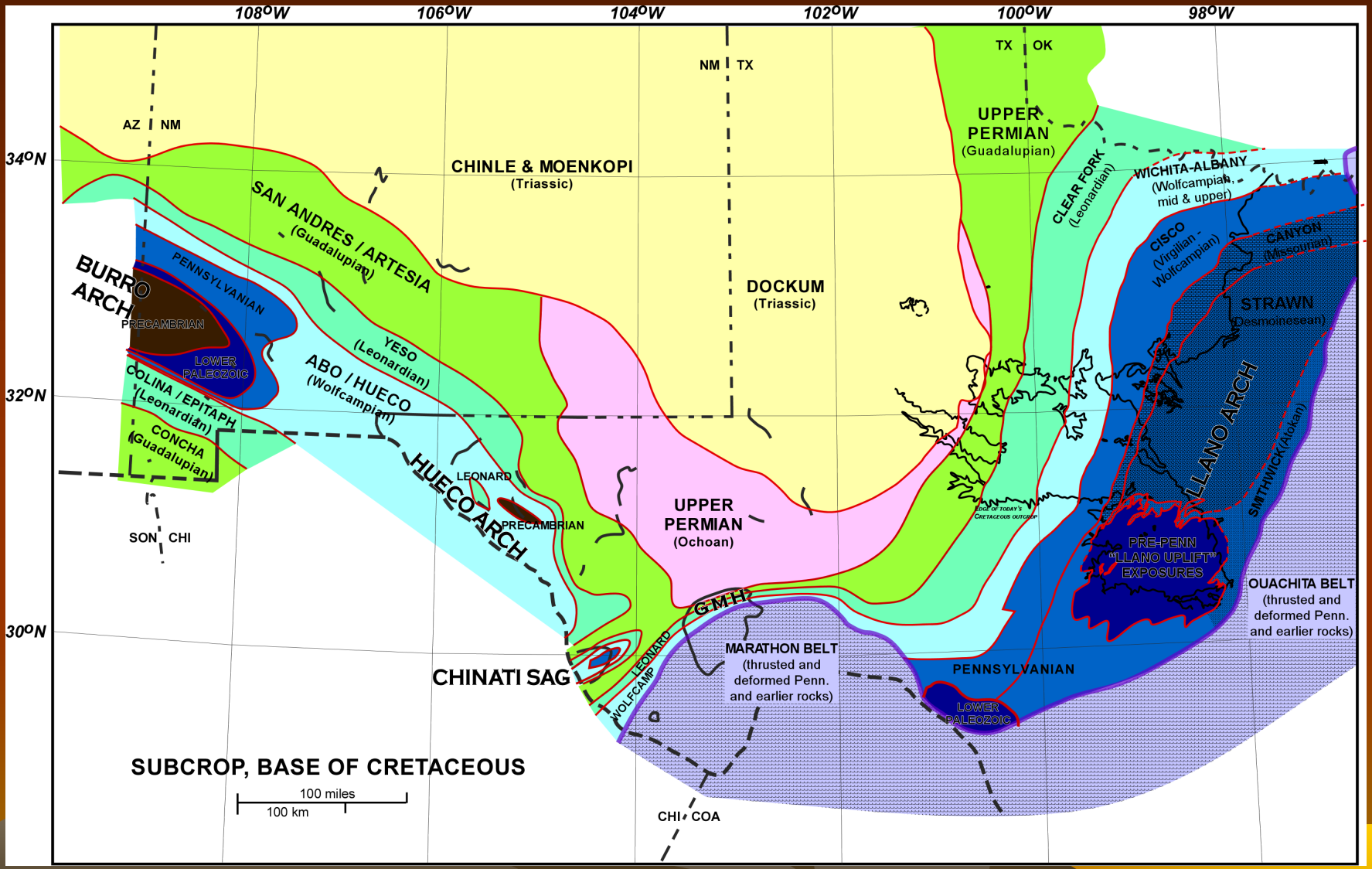

1D SUBSIDENCE – PECOS, TX

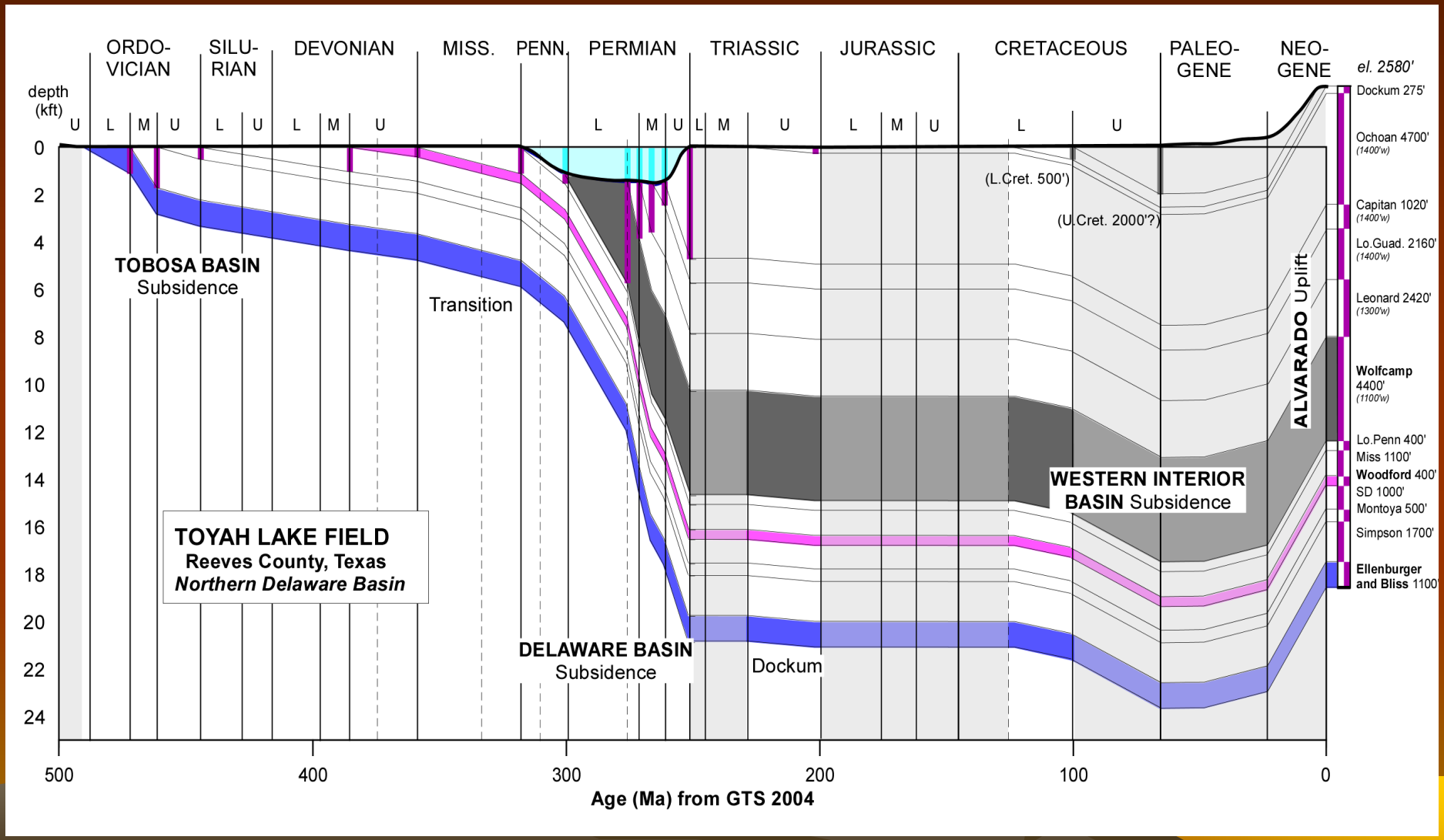

BASINWIDE SUBSIDENCE

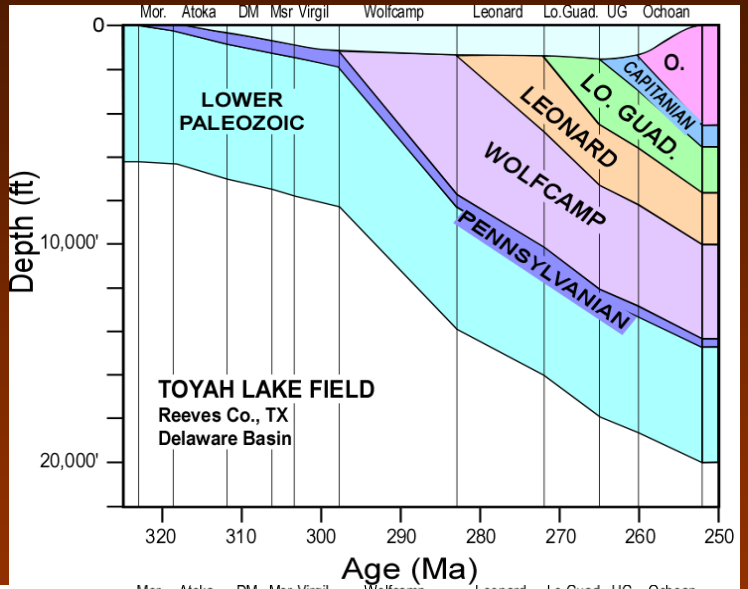

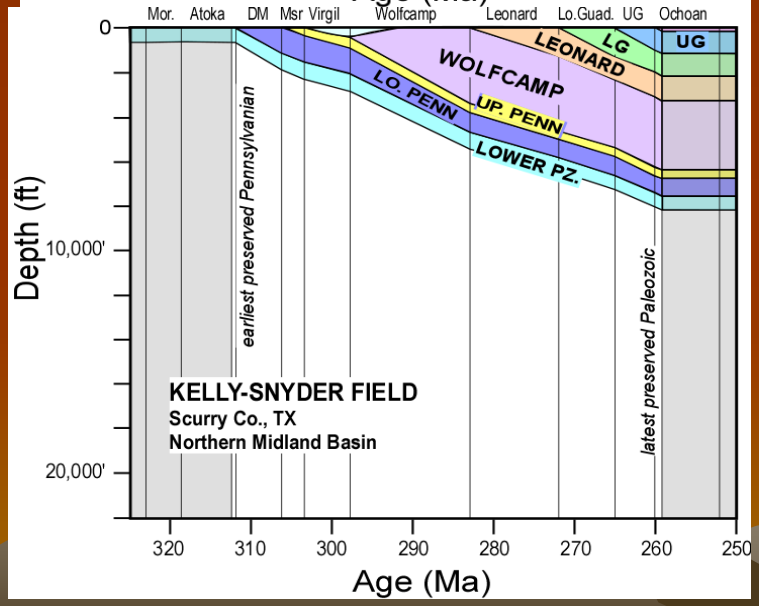

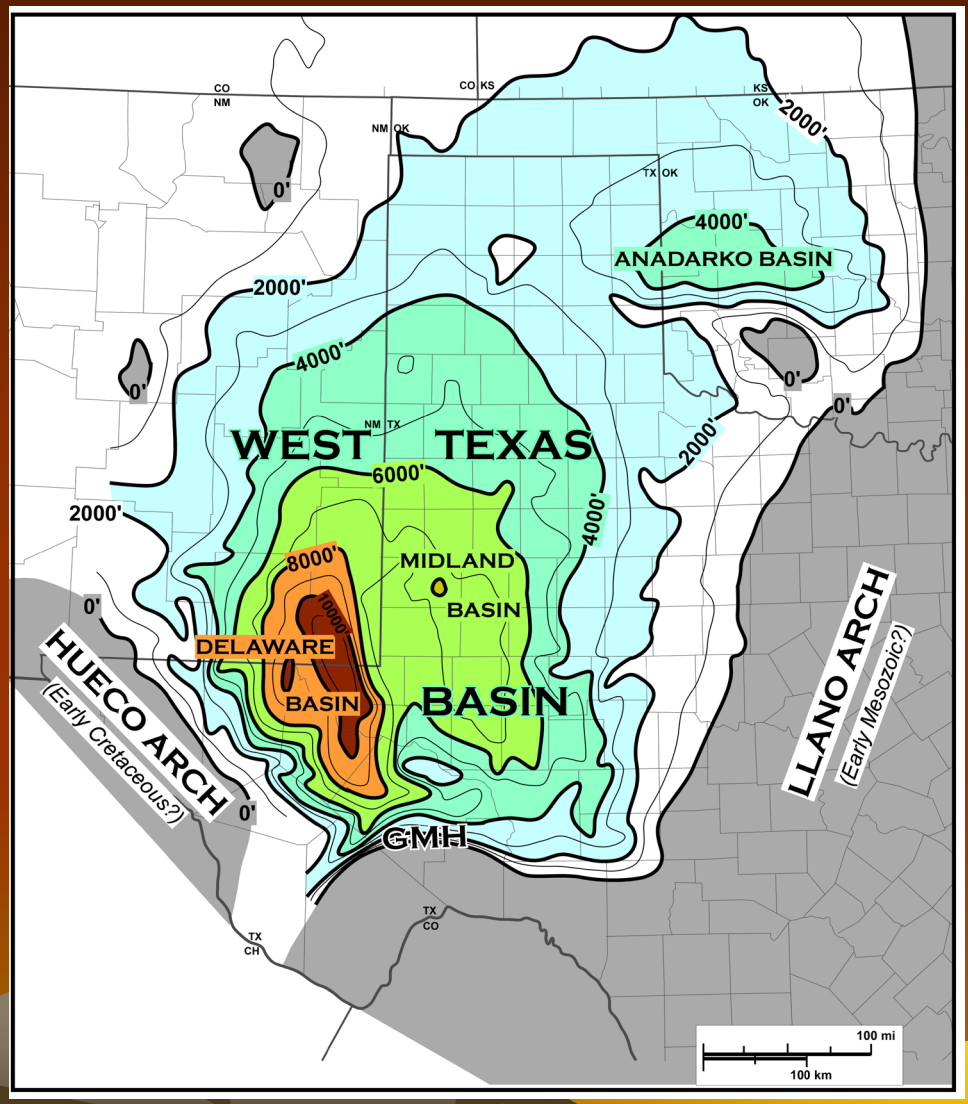

LATE PALEOZOIC SUBSIDENCE

(Sections restored for sediment compaction)

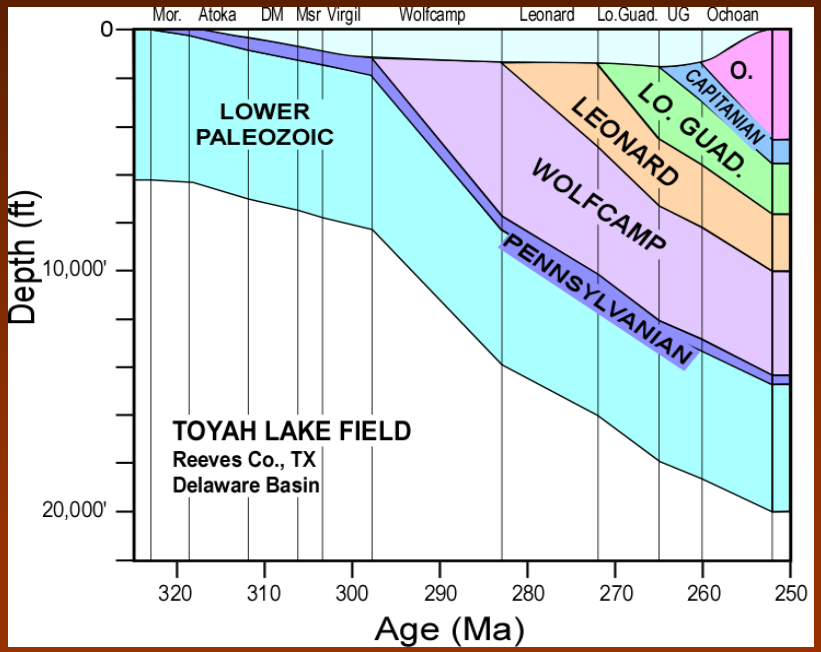

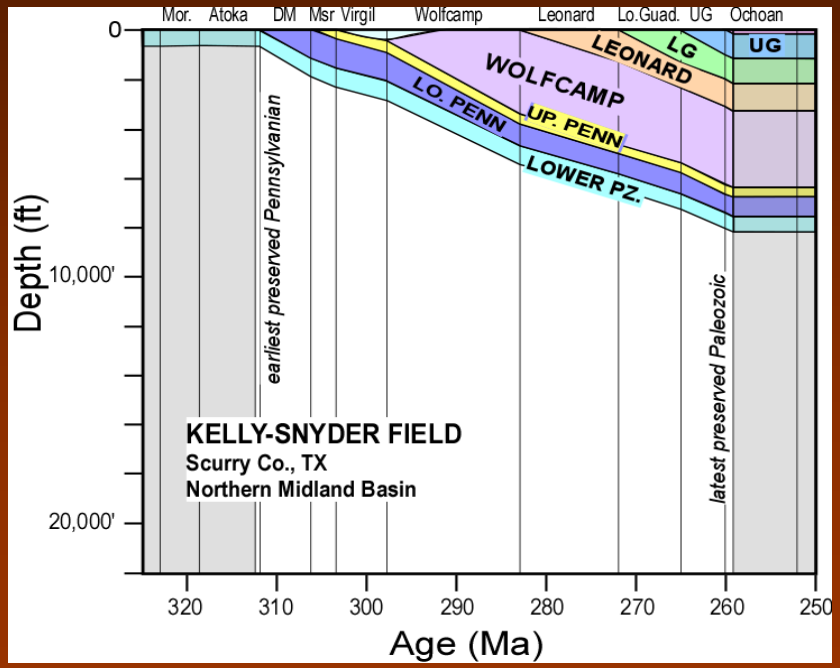

A) Pecos Area – near center of Permian Basin; deep water in Delaware Basin

B) Snyder Area – NE margin of Permian Basin; on Horseshoe Atoll, near sea level most of time

NOTE STEADY SUBSIDENCE IN PERMIAN!

2D VIEW: CALCULATE TECTONIC SUBSIDENCE

TECTONIC SUBSIDENCE – Subsidence from 1D chart, corrected for the isostatic response to sediment loading; attempts to show times and places where active tectonic processes are causing subsidence.

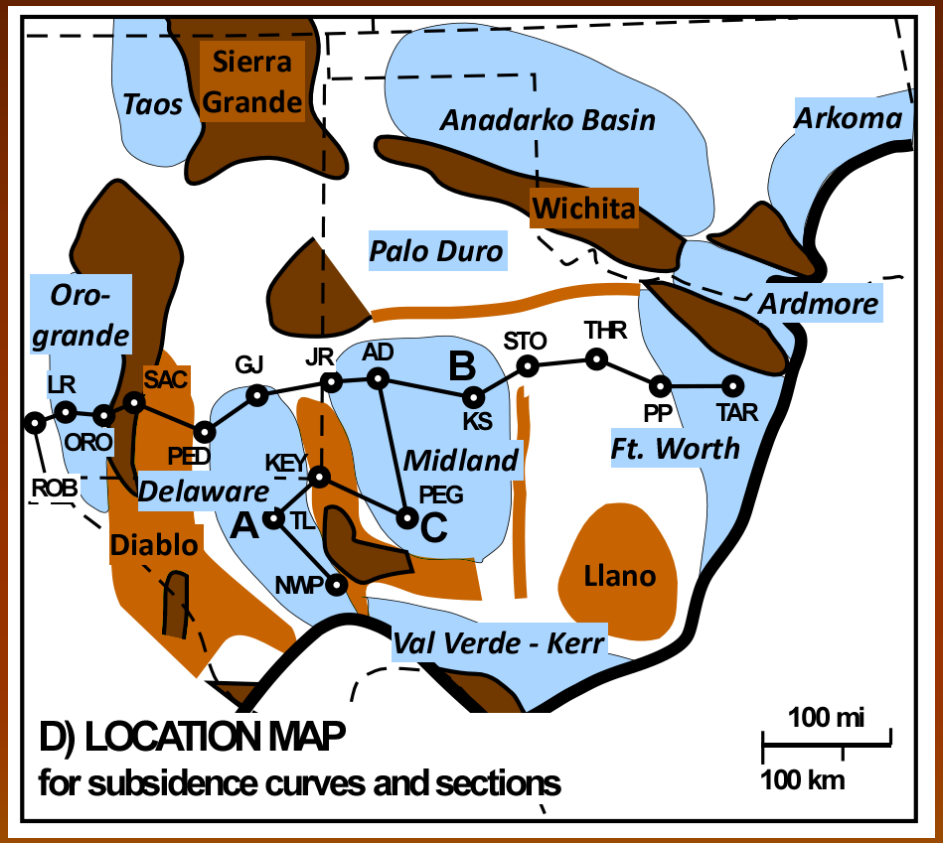

TECTONIC SUBSIDENCE THROUGH TIME

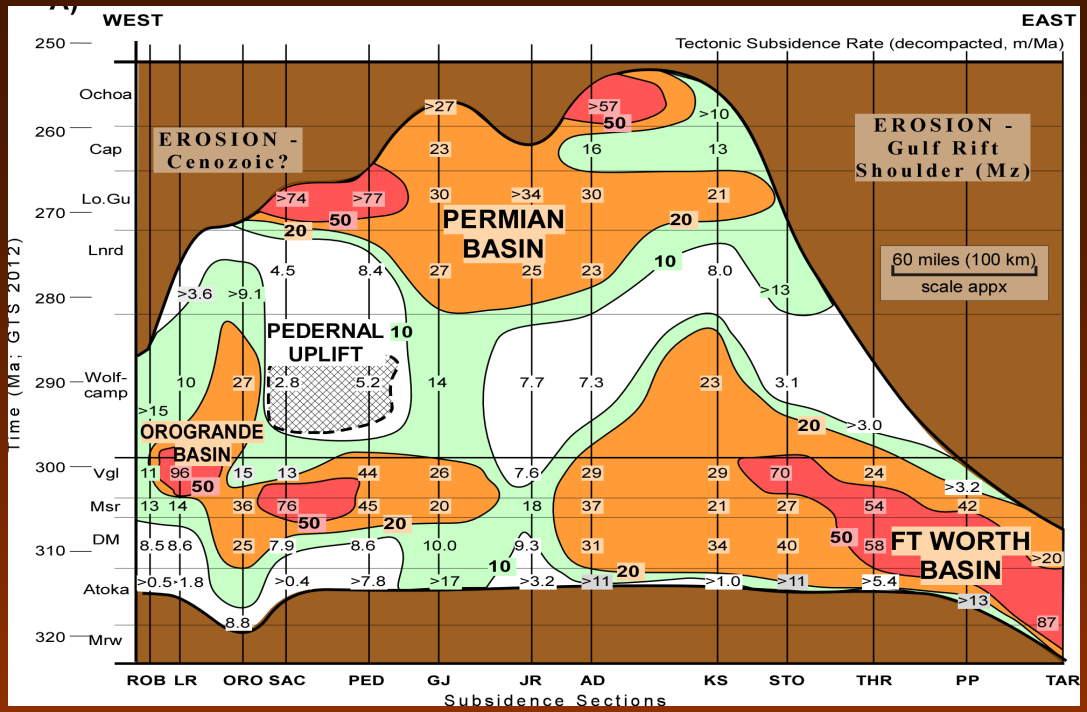

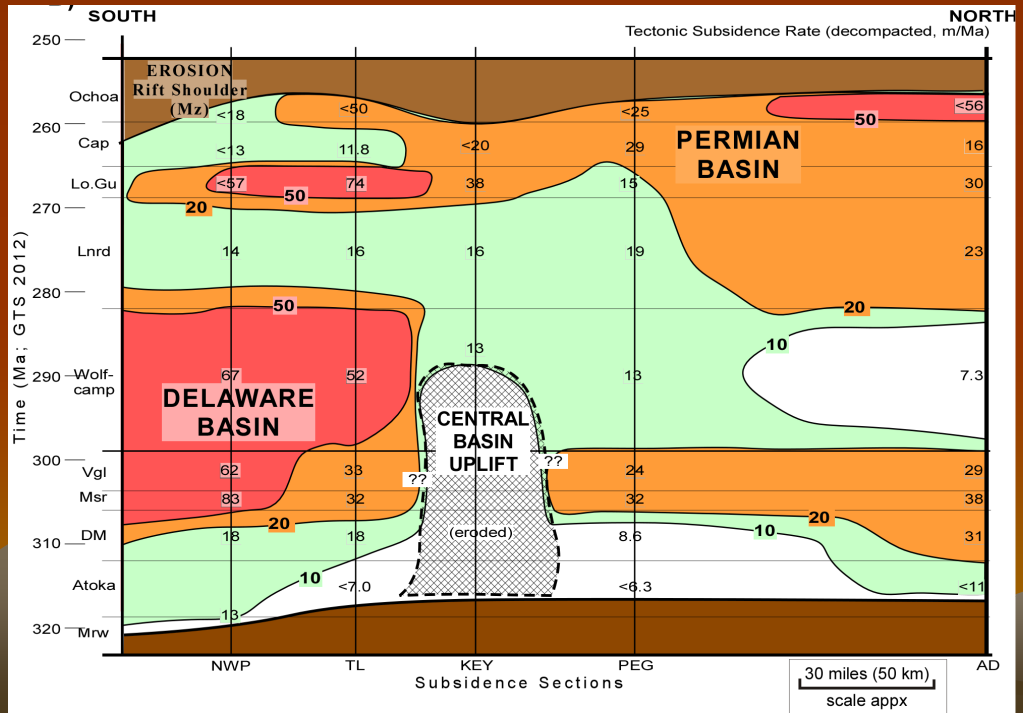

A) W-E section; note strong Ft Worth Basin subsidence due to Ouachita loading; ARM basins; later increase in Permian Basin subsidence.

B) S-N section; note strong Delaware Basin subsidence, later Permian Basin subsidence.

LEONARDAN PALEO-GEOGRAPHY

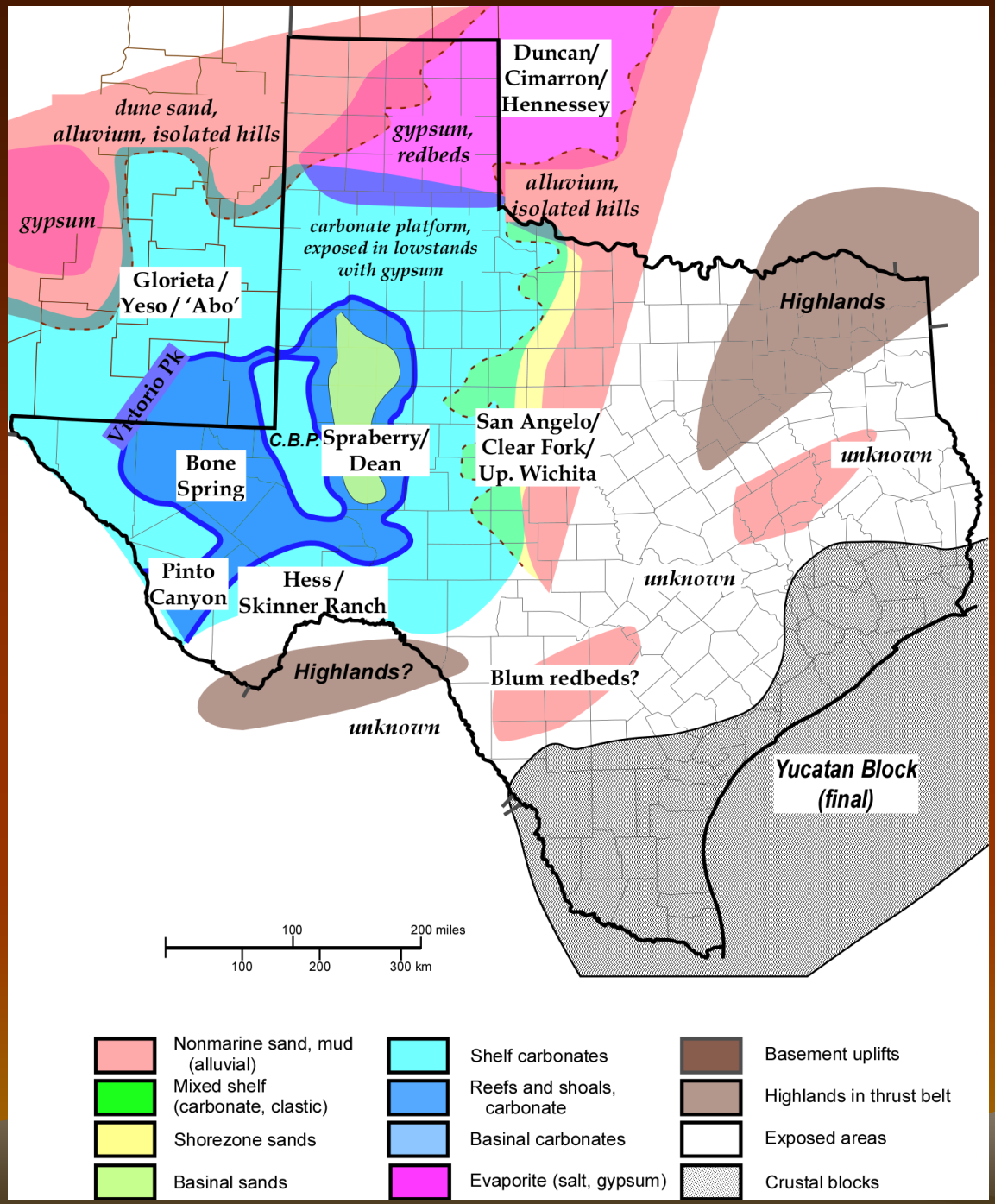

Note clastics from E,
Lack of clastics from S

Suggesting subsidence of Marathon orogen during Permian

(from Ewing 2016, TTT)

WHAT IS THE PERMIAN BASIN?

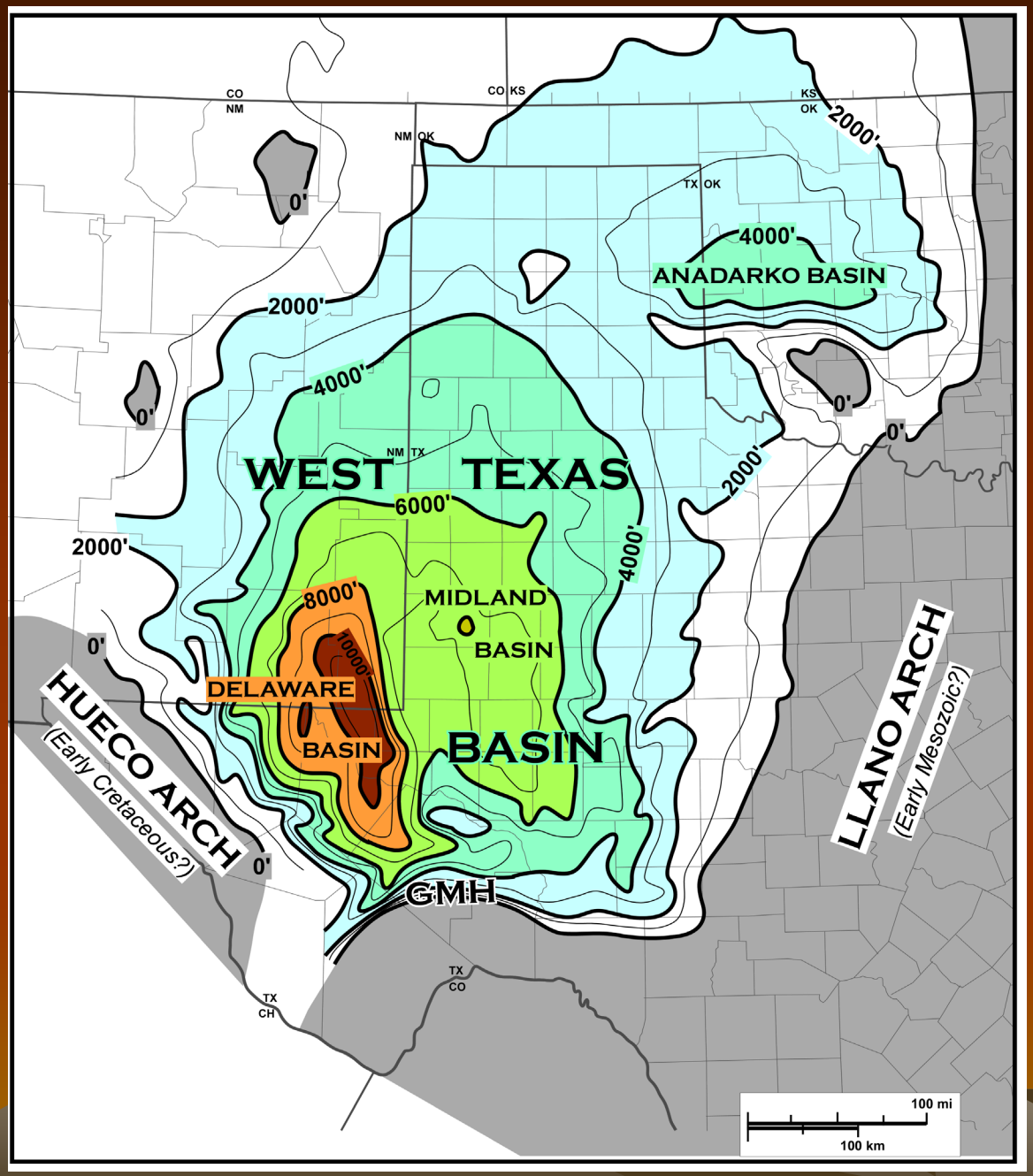

Bowl of subsidence centered on Kermit area

SW, S, E margins modified by Mesozoic, Cenozoic uplift

INTRACRATONIC BASIN centered on Ft Stockton

Uplift (cf Michigan, Williston, Illinois Basins)

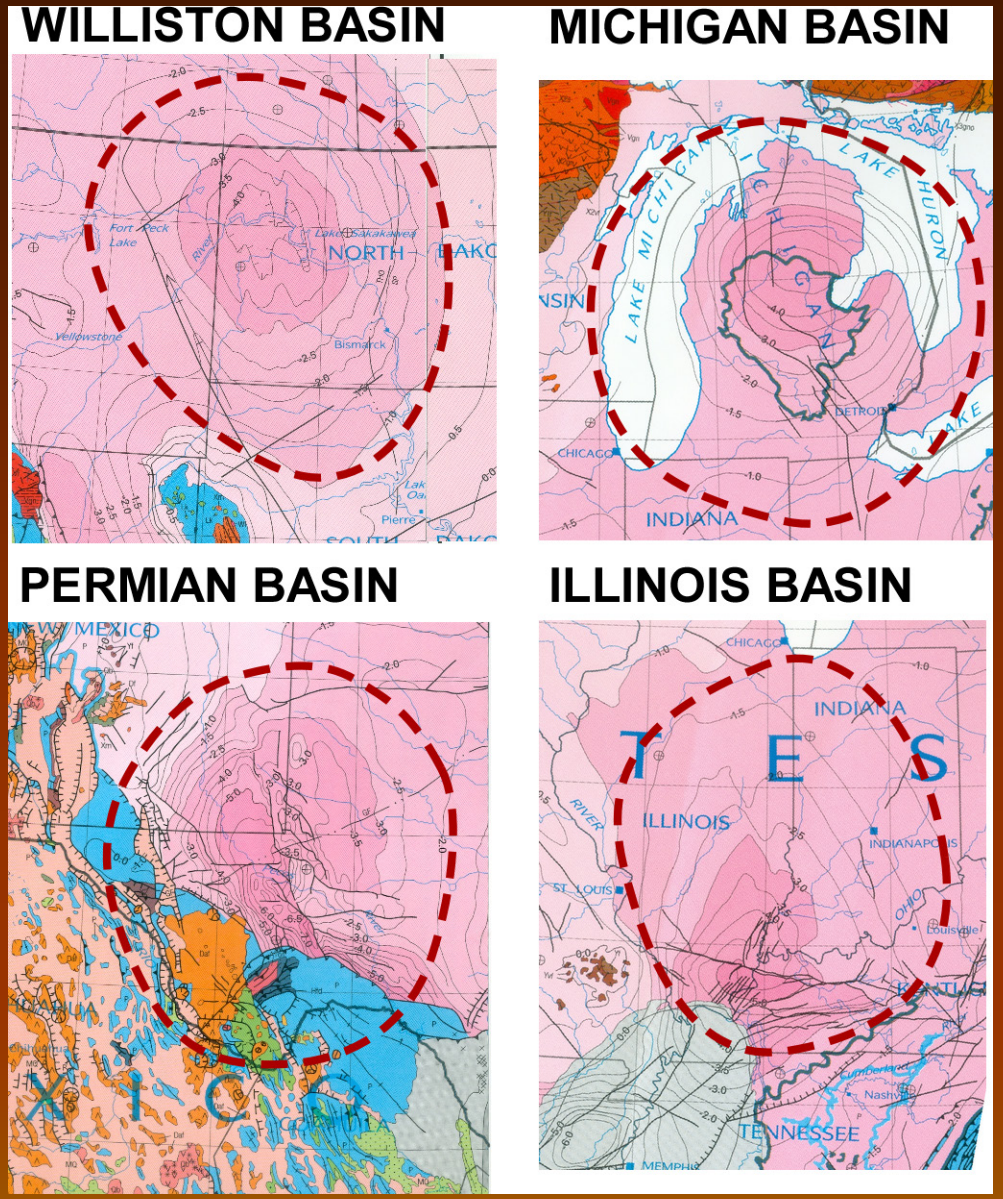

COMPARISON OF BASINS

Muehlberger, 1996, Tectonic Map of North America

FT. STOCKTON UPLIFT AND PECOS INTRUSIVE COMPLEX

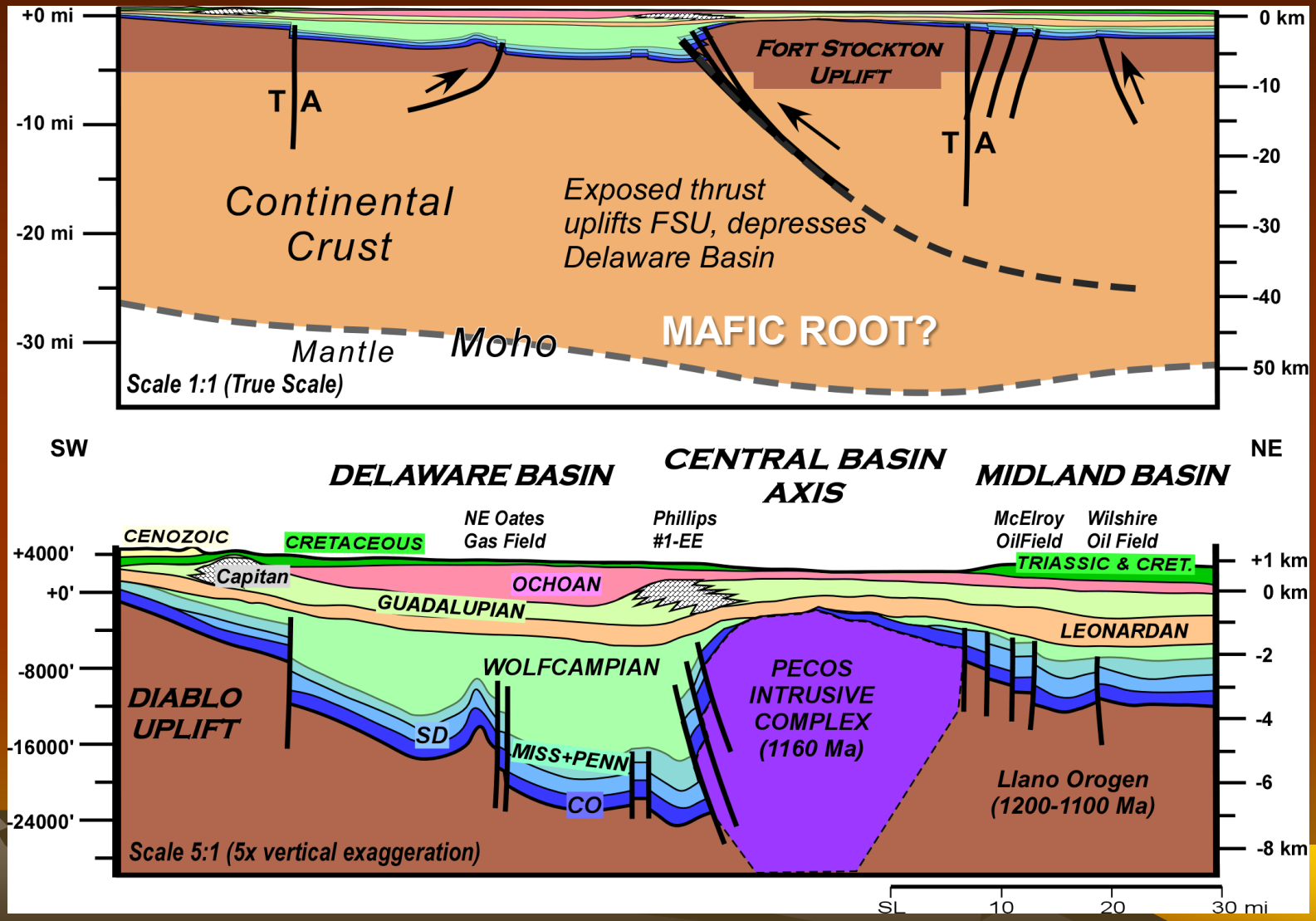

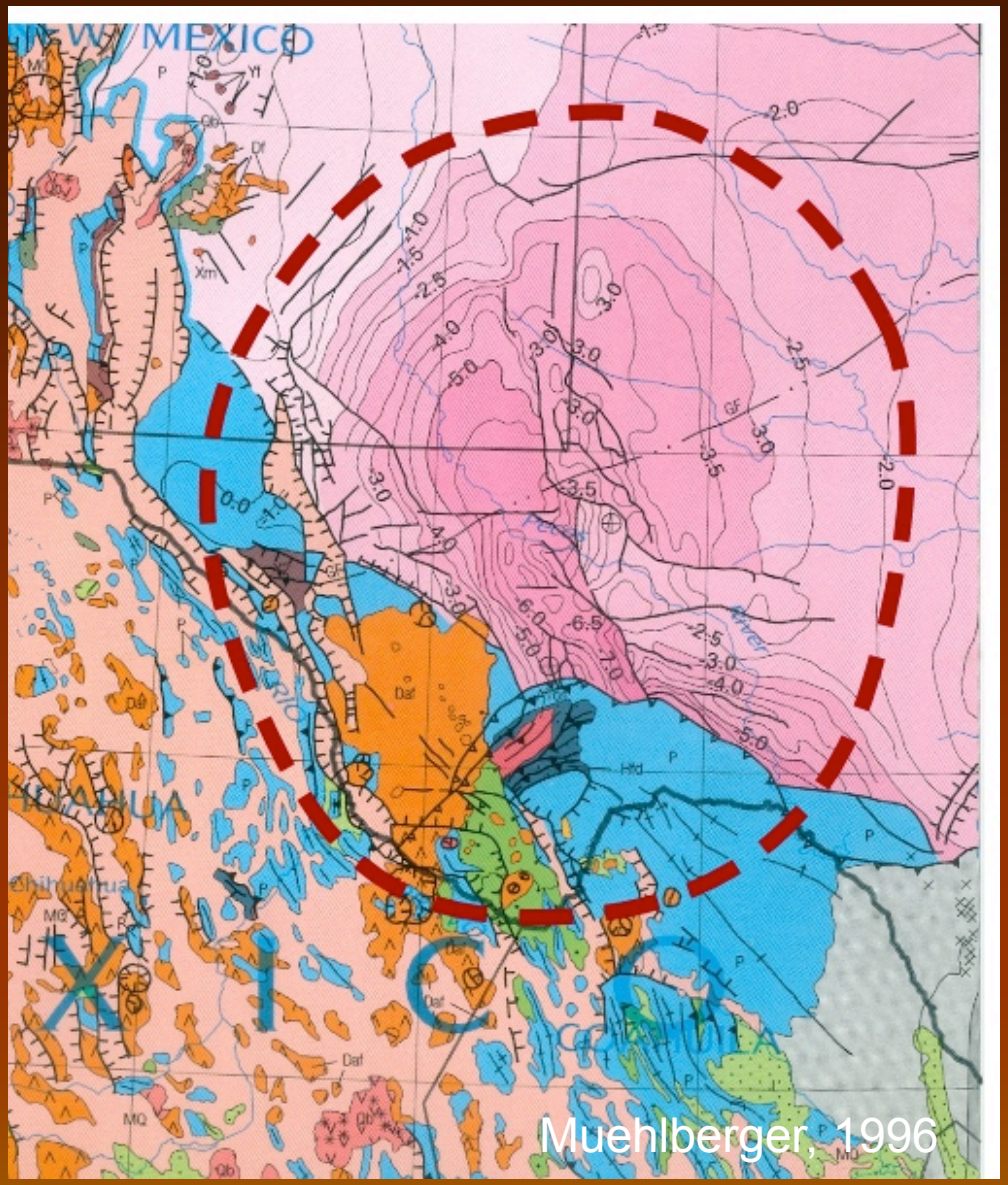

ANOTHER PROCESS MAY CONTRIBUTE!

To SW is Permian volcanic arc related to Pacific-side subduction;

so Permian Basin may include back-arc subsidence. But…

ADD IN HYDROCARBONS…

- Today, most all of Midland Basin and eastern Delaware Basin are in oil window in major source rocks; deep and western Delaware in gas window.
- Without Permian subsidence, probably only deep Delaware would be in oil window!
- Also, Permian subsidence enhanced the deep, silled marine basins that let organics accumulate to form Penn-Perm source rocks.

QUESTIONS?


reef
slope
reef
reef
slope
toe of slope
Cherry Canyon Fm (older basin deposits)

Segmentation of an obliquely rifted margin, Campos and Santos basins, southeastern Brazil

Kristian E. Meisling, Peter R. Cobbold, and Van S. Mount

ABSTRACT

We make the case for Early Cretaceous transfer zones that segment the obliquely rifted Atlantic margin of southeastern Brazil. Our interpretation is based on published literature, Bouguer-corrected gravity, regional reflection seismic profiles, and well data. In the Santos and Campos basins, Neocomian rift architecture was strongly influenced by preexisting fabric and structures of the Late Proterozoic (Brasiliano orogeny). The Atlantic margin inherited an east-northeast–west-southwest orientation so that rifting was oblique to the margin.

On a regional map of Bouguer-corrected gravity, a nearshore belt of positive anomalies correlates with an interpreted broad Moho uplift in the footwall of Neocomian extensional faults. Farther offshore, a second belt of positive anomalies correlates with a presalt ridge of eroded volcanic or basement anticlines covered by thin Aptian evaporites, interpreted as a failed spreading center. Intervening negative anomalies coincide with the main rift basin. All three belts show apparent offsets along linear zones trending west-northwest–east-southeast, which we interpret as transfer zones. The vergence of half rifts tends to change across transfer zones, compartmentalizing the rifted margin into subbasins.

Our results have implications for the risks associated with distribution, maturation, and migration of hydrocarbons within the prolific Early Cretaceous lacustrine petroleum system of the Campos and Santos basins.

INTRODUCTION

In this article we review literature and document evidence for Early Cretaceous transfer zones that segment the obliquely rifted Atlantic margin of southeastern Brazil. Rift segmentation has important implications for risk factors of petroleum systems in deep-water

Copyright ©2001. The American Association of Petroleum Geologists. All rights reserved.

Manuscript received September 28, 1999; revised manuscript received November 16, 2000; final acceptance January 9, 2001.

AUTHORS

KRISTIAN E. MEISLING ~ *ARCO Exploration Technology and Operations, 2300 W. Plano Parkway, Plano, Texas, 75075; current address: BP America, Inc., 200 Westlake Park Blvd., Houston, Texas, 77079; meislik@bp.com*

Kristian Meisling earned his Ph.D. in geology from Caltech and his B.S. degree in engineering geology from UCLA. His 17-year career includes positions in research, applied technology, and exploration at ARCO, Mobil, and BP-Amoco. While at ARCO Kris was director of the Structural Geology Research Group. Kris has broad research interests, including strike- and oblique-slip structures, regional tectonics, syntectonic sedimentation, basin analysis, and paleogeographic reconstructions. He is currently in the Upstream Technology Group at BP America, Inc.

PETER R. COBBOLD ~ *Géosciences-Rennes, 35042 RENNES Cedex, France; peter.cobbold@univ-rennes1.fr*

Peter Cobbold received his B.Sc. degree and Ph.D. in geology from Imperial College, London. After short periods as a lecturer at London and Leeds, he moved to Rennes, France. He now works as a research director for the Centre National de la Recherche Scientifique, France, and consults for the oil and mining industries. His research interests include structural geology, tectonics, and basin development. He has been active in analog modeling, palinspastic restoration, and field work, especially in South America and central Asia.

VAN S. MOUNT ~ *ARCO Latin America, 2300 W. Plano Parkway, Plano, Texas, 75075; current address: Anadarko Petroleum Corporation, 17001 Northchase Drive, P.O. Box 1330, Houston, Texas, 77251; van_mount@anadarko.com*

Van S. Mount received a Ph.D. in structural geology from Princeton University and a B.A. degree in geology from Hamilton College, New York. Van joined the Structural Geology Research Group at ARCO in 1989, where his work focused on quantitative analysis and interpretation of complexly deformed structures and regional structural syntheses. His exploration work at ARCO International concentrated on the Middle East and Latin America. Van is presently in the Basin Studies Group at Anadarko Petroleum Corporation.

ACKNOWLEDGEMENTS

We thank the management of ARCO Latin America and New Exploration Ventures, including Steve Sinclair, Dusty Marshall, and Jamie Robertson, for supporting our work and its release for publication. The gravity data set was provided by Lamont-Doherty Geological Observatory. Bouguer correction and filtering were carried out by Wayne Suyenaga at ARCO. We have benefitted greatly from discussions with colleagues on the Brazil Bid Round team at ARCO, including Chandra Suria, Christopher Legg, Stephen Scott, Stuart Gordon, Mike Crawford, Wayne Suyenaga, Zhiyong He, Ed Elliot, Lih Quo, Randy Roe, Steve Bergman, Mark Ward, and Brad Huizinga. We also thank those who contributed insights in previous years, including Bob Krantz, Lillian Flakes, and Claudio Bartolini. Robert Sprague, Jan-Nel Nye, and James Aston kindly provided graphics support. We are grateful to the reviewers, Ian Davison, Edison J. Milani, and Chris Morley, for their constructive comments. Finally, we thank the management of BP Trinidad Exploration and BP America, Inc. for supporting the publication of this article.

exploration plays. Our new tectonic model will primarily address the risks associated with distribution, maturation, and migration of hydrocarbons within the prolific Early Cretaceous lacustrine petroleum system of the Campos and Santos basins.

We base our conclusions on integration and synthesis of offshore and onshore data that include regional reflection seismic lines, Bouguer-corrected gravity, and well data. The area of study (Figure 1) covers the Santos, Campos, and southern Espírito Santo basins, which extend from the Florianópolis Platform in the south to the Abrolhos Plateau in the north and from the coastal mountains in the west to the outer São Paulo Plateau in the east.

The Campos Basin is the most prolific Brazilian oil-producing basin. Proven and probable reserves of 2160×10^6 m^3 (13,559 million bbl) oil and 266×10^9 m^3 (9.4 tcf) gas account for 78% of Brazil's total proven and probable oil and 43% of its total proven and probable gas (IHS [Petroconsultants] Energy Group, 2001). Commercial production began in the Campos Basin with the discovery of the Garoupa oil field in 1974. By 1989, more than 30 fields had been discovered that had reserve estimates for oil in excess of 223×10^6 m^3 (1400 million bbl) (Guardado et al., 1990). Over the last 10 yr, Petrobrás has shifted exploration to the deep-water Campos Basin (Figure 1), leading to the discovery of the supergiant Marlim (517×10^6 m^3 [3250 million bbl] oil in place; 207×10^6 m^3 [1300 million bbl] oil recoverable; 92×10^9 m^3 [3.25 tcf] gas in place; 31×10^9 m^3 [1.1 tcf] gas recoverable), Albacora (307×10^6 m^3 [1930 million bbl] oil in place; 107×10^6 m^3 [676 million bbl] oil recoverable; 13×10^9 m^3 [0.445 tcf] gas recoverable), and Roncador (1540×10^6 m^3 [9690 million bbl] oil in place; 463×10^6 m^3 [2910 million bbl] oil recoverable; 50×10^9 m^3 [1.75 tcf] gas recoverable) fields (IHS [Petroconsultants] Energy Group, 2001). All commercial accumulations of hydrocarbons in the Campos Basin are believed to be sourced from lacustrine rocks within the Early Cretaceous rift system, below a layer of Aptian salt, and the vast majority are in turbidite reservoirs above the salt (Figure 2).

By comparison, the Santos Basin is relatively underexplored, having proven reserves of 1.00×10^6 m^3 (6.3 million bbl) liquids and 4.8×10^9 m^3 (0.17 tcf) gas (ANP, 2000). For many years, exploratory drilling was confined to the shelf, where success was limited to a few marginally commercial gas and condensate fields (Figure 1). At the southwestern edge of the basin (Tubarão and related fields), the source rocks are believed to be Late Cretaceous marine sedimentary rocks. Our own study leads us to believe that Neocomian rift strata are present over wide areas of the Santos Basin. Indeed, while this article was in review, Petrobrás purportedly discovered oil in deeper waters of the northern Santos Basin, for which the source rocks are presumed to be Neocomian.

The deep-water play trend of the Campos and Santos basins carries significant new exploration risks for turbidite reservoirs above salt that include (1) the presence, distribution, thickness, quality, and maturity of Early Cretaceous lacustrine source rocks;

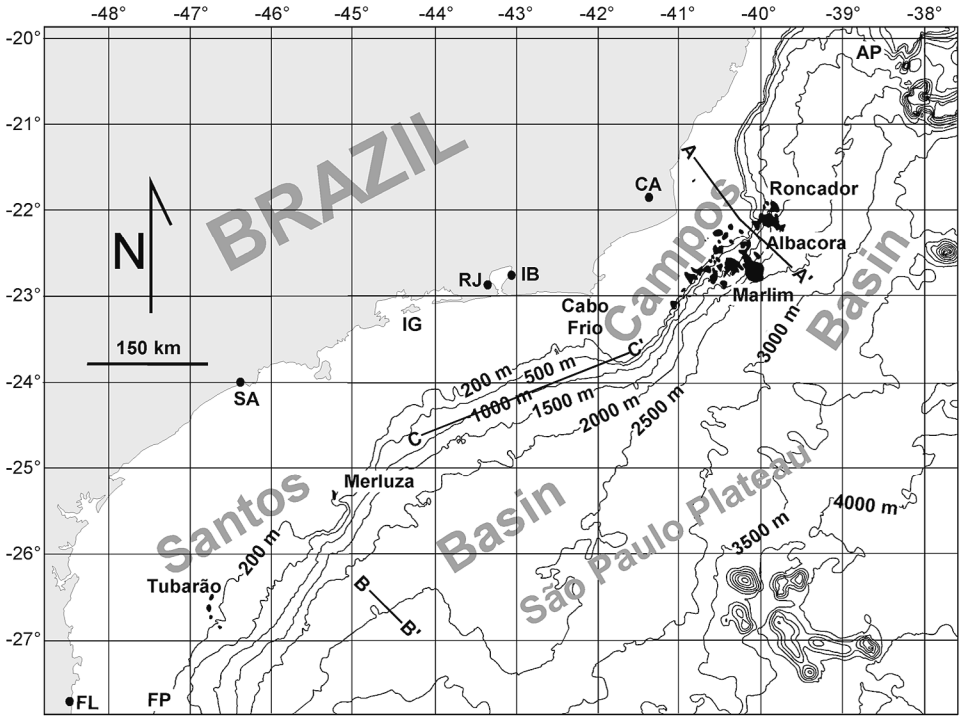

Figure 1. Map showing location of studied area, offshore bathymetry, geoseismic sections (AA′, BB′, and CC′), and main hydrocarbon fields, southeastern Brazil. Onshore localities are (from southwest to northeast) Florianópolis (FL), Santos (SA), Ilha Grande (IG), Rio de Janeiro (RJ), Itaboraí (IB), and Campos (CA). Offshore localities are (from southwest to northeast) the Florianópolis Platform (FP) and the Abrolhos Plateau (AP).

(2) the potential for regional subsalt migration; (3) the viability of migration pathways through thick Aptian evaporites; and (4) the mechanism for hydrocarbon charging of suprasalt turbidite reservoirs in a deep-water mud-prone system. Unlike the shelfal Campos Basin, lacustrine source rocks are considered overmature for oil generation on the shelf of the Santos Basin, but the new discovery shows that potential exists for favorable maturity of Early Cretaceous source rocks in the deep-water areas. The deep-water Santos and Campos basins also have additional risks associated with subsalt and suprasalt volcanics.

To address these new risk factors, it is necessary to understand the regional tectonic framework and evolution of the southeast Brazilian margin. In this article, we first review the geological structure and history of the Campos and Santos basins in the framework of plate tectonics, emphasizing crustal inheritance and hot-spot activity. We then use newly available data to better define the architecture of the rifted margin, including the distribution of rift basins and transfer zones. Finally, we assess the implications for hydrocarbon prospectivity and exploration risk.

In a companion article (Cobbold et al., 2001), we discuss evidence for the reactivation of Early Cretaceous and older structures on the obliquely rifted margin of southeastern Brazil due to far-field plate stresses and hot-spot activity. Late Cretaceous and Tertiary reactivation has resulted in (1) onshore uplift and exhumation, (2) increased sediment supply, (3) offshore subsidence, (4) increased salt tectonics, and (5) probable creation of new migration pathways. These factors have important implications for petroleum system risk factors in deep-water exploration plays.

PLATE TECTONIC EVENTS

Precambrian Orogenesis

The Atlantic continental margin of southeastern Brazilian is underlain by prerift basement that has a long geologic history (Almeida, 1967; Almeida et al., 1981; Asmus and Baisch, 1983). The supercontinent of Gondwana (Figure 3) formed in the Late Proterozoic. Archean and Early Proterozoic cratons were welded by mobile belts during the Brasiliano (Pan-African) orogeny (Almeida and Hasui, 1984; Unrug, 1996). Metamorphic rocks and structures of the Brasiliano (750–480 Ma) are widely exposed in southeastern Brazil (Almeida, 1967; Hasui et al., 1975; Campanha, 1981; N. Machado et al., 1996), where they impart a pervasive tectonic fabric to the continental crust and lithosphere. The Brasiliano mobile belt in southeastern Brazil was formed in dextral transpression, and it is doubly verging, in the form of a crustal flower structure

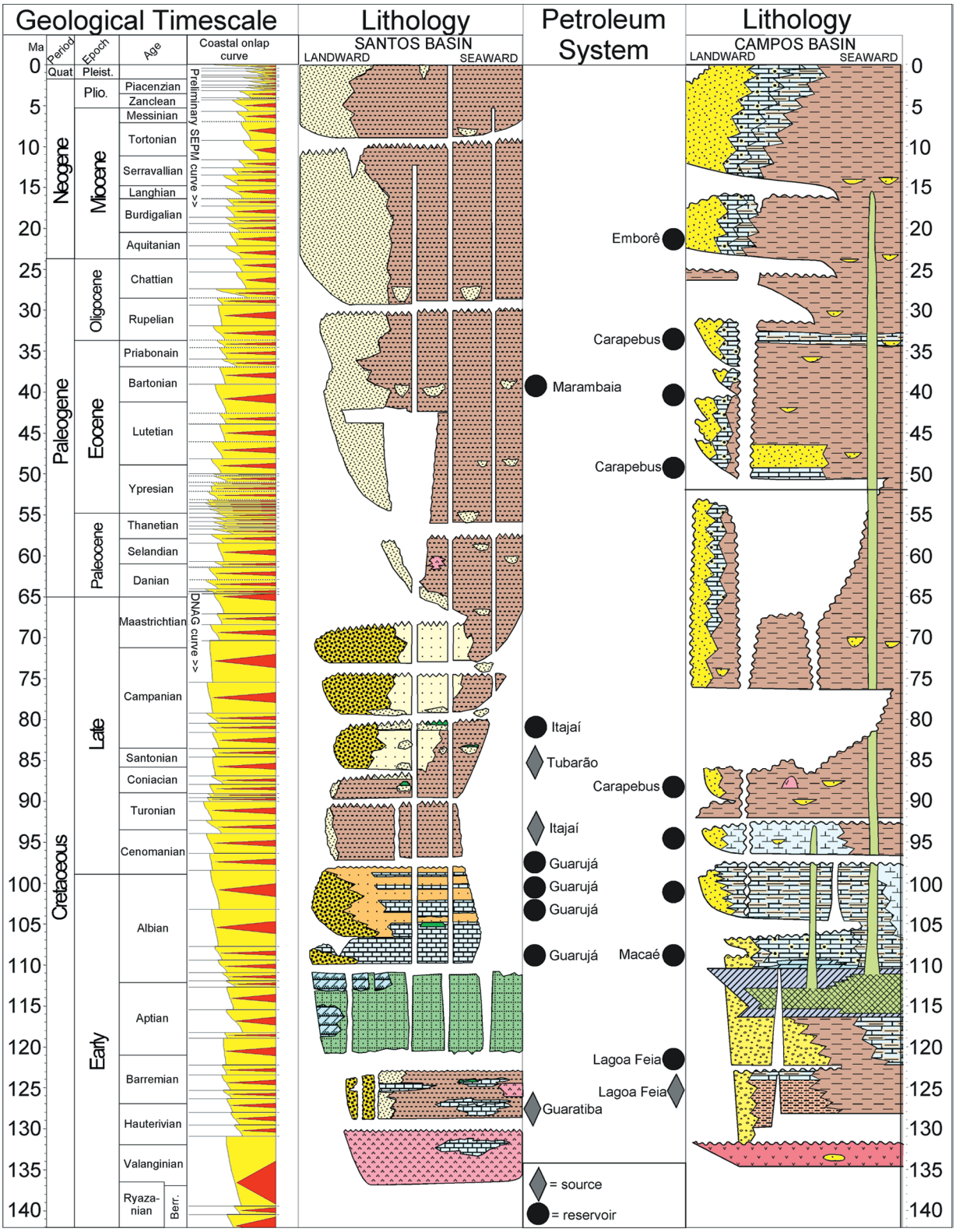

Figure 2. Tectonostratigraphic events chart for the Campos and Santos basins, showing timing of regional lithostratigraphic packages relative to hot-spot, rifting, and structural events. The stratigraphic columns are modified from Rangel et al. (1994) and Pereira and Feijó (1994). (Dark yellow/heavy dots = coarse clastic rocks; light yellow/fine dots = fine-grained clastic rocks; brown/dashes = shale and mud rocks; blue/bricks = carbonate rocks; green/squares and green-blue hatchures = evaporites; mixed colors/mixed symbols = mixed lithology; pink/vees = volcanic rocks.)

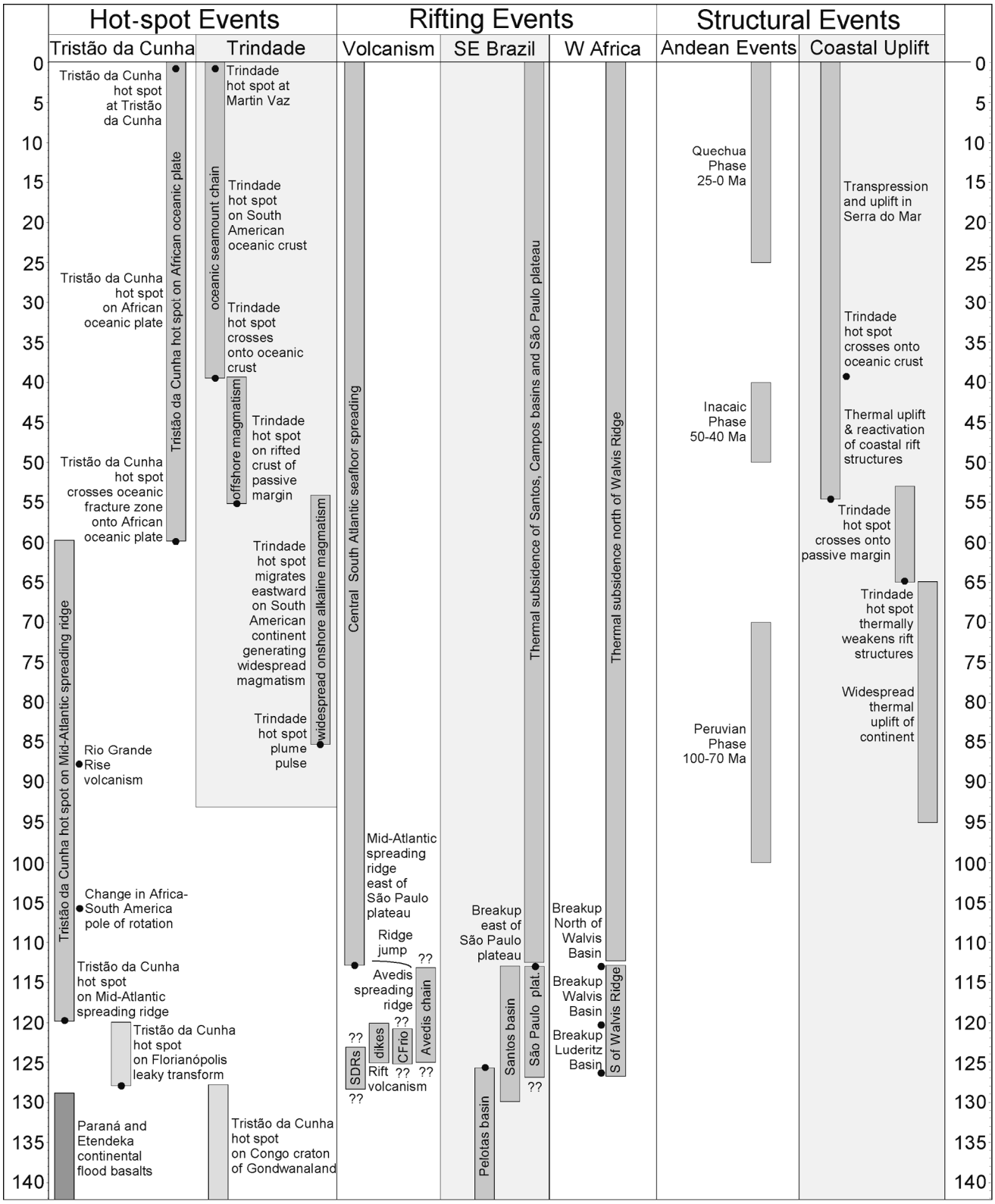

Figure 2. Continued.

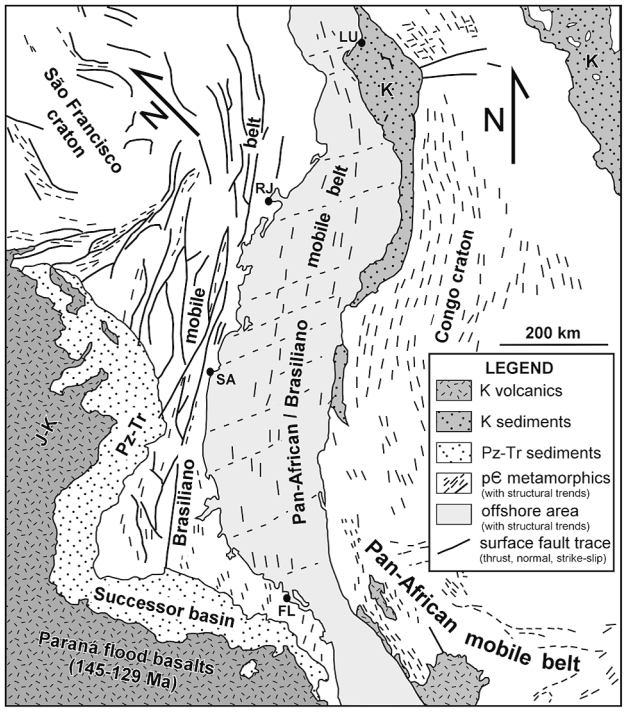

Figure 3. Geological map of southeastern Brazil and southwestern Africa prior to opening of the Atlantic (modified from De Wit et al., 1988). Onshore localities are (from southwest to northeast) Florianópolis (FL), Santos (SA), and Rio de Janeiro (RJ) in Brazil; and Luanda (LU) in Africa.

(R. Machado and Endo, 1993; Campos Neto and Figueiredo, 1995; N. Machado et al., 1996). In the center are northeast-trending right-lateral shear zones, including the Além-Paraíba shear zone (Almeida et al., 1975; Campanha, 1981; Campos Neto and Figueiredo, 1995). Eastward from Rio de Janeiro the shear zones curve into a more north-south trend and become thrusts (Campanha, 1981; DNPM, 1981; Radambrasil, 1981; Schobbenhaus et al., 1981; Campos Neto and Figueiredo, 1995), in keeping with the geometry of a right-lateral restraining bend.

In the early Paleozoic–middle Mesozoic, broad intracratonic successor basins developed across the peneplaned mobile belts of the Gondwana supercontinent (Schobbenhaus et al., 1981; Zalán et al., 1990a) (Figure 3). In the Paraná basin of southeastern Brazil, Ordovician–Cretaceous strata of the Paraná sequence unconformably onlap basement of Brasiliano age and locally preserved orogenic molasse. Paleozoic siliciclastic sequences of the Paraná basin were deposited under shallow-marine conditions within the Gondwana supercontinent during a long period of relative tectonic stability (Zalán et al., 1990a, b, 1991). The nonmarine Mesozoic sequence is made up of lacustrine, fluvial, and eolian deposits of the Triassic, Jurassic, and Cretaceous (Zalán et al., 1990a, b, 1991), which immediately underlie the extensive Paraná continental flood basalts of the Late Jurassic–Cretaceous.

Brasiliano faults and folds project offshore beneath the Santos and Campos basins (Ojeda, 1982), where they are parallel with later rift structural trends (Figure 3). Coastal outcrops along the narrow conjugate margin of Angola, however, are of Archean Congo craton (Unrug, 1996), suggesting that the eastern limit of the mobile belt lies within the offshore rift basins. Reactivation of Brasiliano (Pan-African) mobile belts during rifting has been documented in the Walvis Basin of Namibia (Clemson et al., 1997) and in the numerous coastal and interior rift basins of northeastern Brazil (Castro, 1987; Françolin and Szatmari, 1987; Matos, 1992; Françolin et al., 1994). The South Atlantic margin adopts a more easterly trend in the Santos and Campos basins, where the Brasiliano mobile belt has also been reactivated (G. Baccocoli and L. G. F. Aranha, 1984, unpublished data; Figueiredo, 1985; Szatmari et al., 1985; Dias et al., 1987; Macedo, 1989) to form the wide and highly extended continental margin of southeastern Brazil.

South Atlantic Rifting and Its Timing

The Campos and Santos basins, which are currently on the passive margin of Brazil, were part of the East Brazil rift system (Chang et al., 1988, 1990, 1992). The rift system formed in the Jurassic–Early Cretaceous and led to the opening of the Atlantic (Figure 4). The structure and stratigraphy of the East Brazil rift system (Figure 2) have been well known for many years, mainly as a result of exploration for hydrocarbons (Almeida, 1967; Asmus and Ponte, 1973; Campos et al., 1974; Ojeda, 1982; Figueiredo, 1985). Also well-known is that the main phase of rifting initiated in the south and propagated northward (Sibuet et al., 1984; Figueiredo, 1985; Szatmari et al., 1985; Conceição et al., 1988). Although the precise age of onset and the sequence of rifting are subjects of debate (Davison, 1999), availability of new data for the conjugate margin of southern Africa has made clearer some of the details of this process.

Rifting started at the southern tip of South Africa in the Late Triassic–Early Jurassic (220–200 Ma), propagated along the northern Argentinean margin in the Middle Jurassic (~170 Ma), and expanded into the southeastern Brazil margin up to the Florianópolis

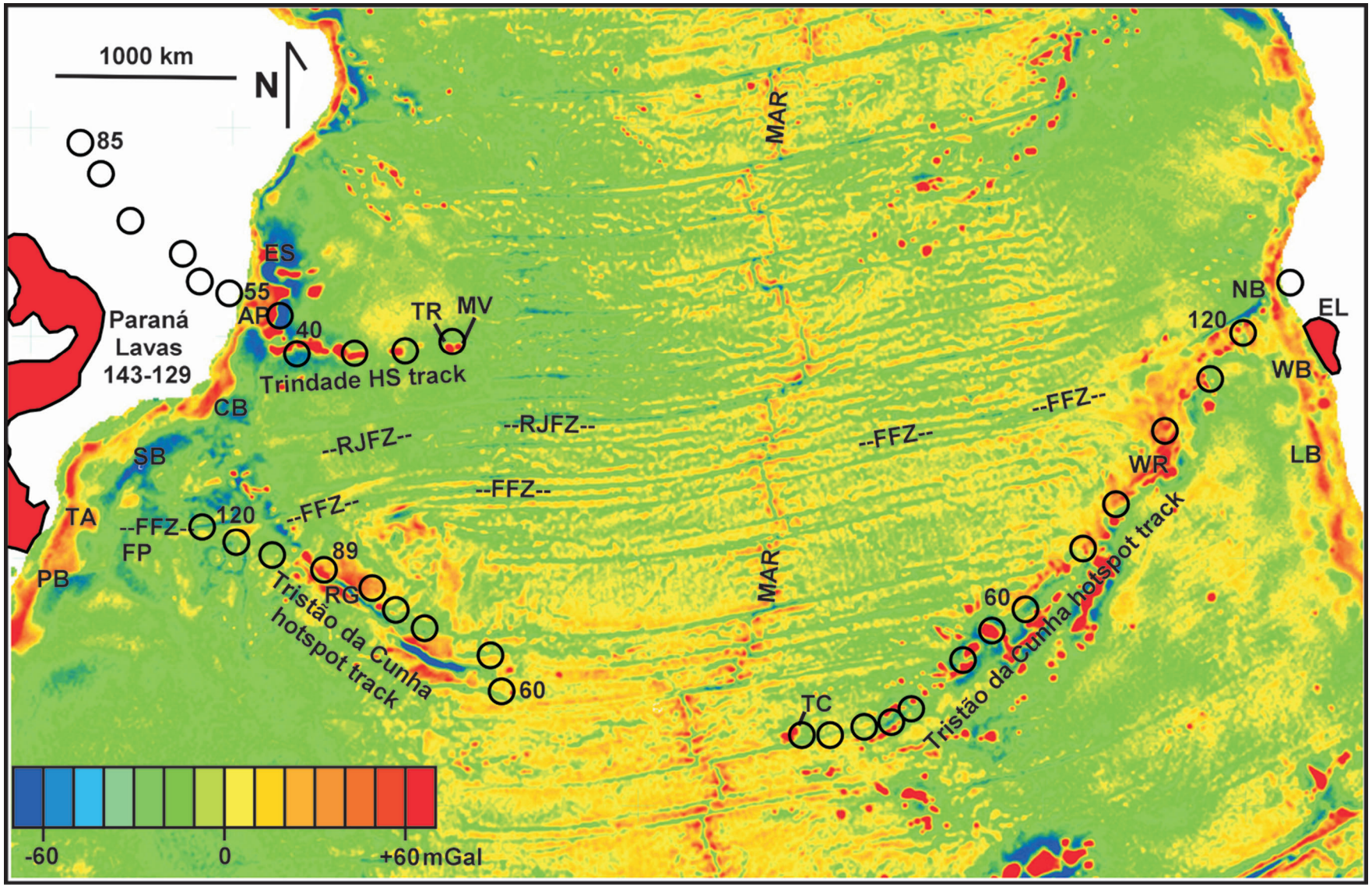

Figure 4. Map of South Atlantic and adjacent continents showing marine gravity anomalies from satellite altimetry (Sandwell and Smith, 1995), outline of onshore Paraná and Etendeka (EL) lavas, Mid-Atlantic Ridge (MAR), major fracture zones (Rio de Janeiro fracture zone = RJFZ; Florianópolis fracture zone = FFZ), tracks of Tristão da Cunha and Trindade hot spots (unfilled circles with ages in Ma), resulting seamounts (TR = Trindade; MV = Martin Vaz; TC = Tristão da Cunha), and other offshore features (PB = Pelotas Basin; TA = Torres Arch; FP = Florianópolis Platform; RG = Rio Grande Rise; SB = Santos Basin; CB = Campos Basin; AP = Abrolhos Plateau; ES = Espírito Santo Basin; NB = Namib Basin; WB = Walvis Basin; LB = Luderitz Basin). The color bar shows anomaly values in mGal.

fracture zone in the Late Jurassic–Early Cretaceous (~140 Ma) (Peate, 1997). According to evidence from the offshore Walvis Basin of Namibia, rifting did not reach the Florianópolis fracture zone (Figure 4) until the Hauterivian (Clemson et al., 1997). In the offshore Campos Basin, basal strata of the synrift lacustrine Lagoa Feia Formation (Aratu local stage, late Barremian, ~123 to ~121 Ma [Guardado et al., 1990]) overlie Early Cretaceous basalts (Figure 2) that may represent an earlier synrift sequence (Chang et al., 1992). In northeastern Brazil, extensive intracratonic rifting along reactivated Brasiliano structural trends began in the Neocomian–early Barremian (128[?]–125 Ma), although an earlier episode of crustal stretching may account for widespread latest Jurassic sedimentation (Matos, 1992) of the Tithonian (~150–144 Ma). Thus, evidence suggests that the main phase of rifting in the Santos and Campos basins began in the Hauterivian–Barremian, possibly following an earlier volcanic phase of rifting.

Onset of sea-floor spreading in the South Atlantic was also time transgressive (Rabinowitz and LaBrecque, 1979; White and McKenzie, 1989; Nürnberg and Müller, 1991; Light et al., 1992; Clemson et al., 1997). On the African side, spreading started in the Cape Basin in the middle Hauterivian (anomaly M9; ~130 Ma); in the Luderitz Basin in the earliest Barremian (anomaly M4; ~127–125 Ma); in the Walvis Basin (conjugate to Pelotas) in the early Aptian (~120 Ma); and in the Namib Basin (conjugate to southern Santos in Figure 4), north of the Walvis Ridge, in the late Aptian (~113 Ma). Similarly, according to data from the Brazilian margin (Chang et al., 1992), breakup and sea-floor spreading did not occur north of the Florianópolis fracture zone until the late Aptian (~113 Ma). This timing model is consistent with extensive hot-spot–related extrusive volcanism evidenced by seaward-dipping reflectors south of the Florianópolis fracture zone and a lack thereof to the north, reflecting a difference in the timing of breakup (Gladczenko et al., 1997). Thus, based on differences in timing of rifting and spreading, the southeast Brazilian Atlantic margin can be divided into southern and central compartments, which are separated by the Florianópolis fracture zone.

Tristão da Cunha Hot Spot

The onset of rifting on the southeast Brazilian Atlantic margin south of the Florianópolis fracture zone was coeval with a huge outpouring of continental flood basalt (Figure 4) from 145 to 129 Ma (Rocha Campos et al., 1988; Hawkesworth et al., 1992; Renne et al., 1992; Gallagher and Hawkesworth, 1994; Turner et al., 1994, 1996; Stewart et al., 1996). The magmatism has been attributed to the Tristão da Cunha (Walvis) mantle plume or hot spot (Morgan, 1981; White and McKenzie, 1989; O'Connor and Duncan, 1990). As much as 1.2 million km^3 of basalt erupted in the Paraná basin of Brazil and the Etendeka province of Namibia (White and McKenzie, 1989; Peate, 1997). Flood basalts also prograded out onto the rift margins of the southern compartment of the South Atlantic, built an emergent volcanic ridge (Torres Arch in Figure 4) along the Florianópolis fracture zone (Peate, 1997; Gladczenko et al., 1997), and covered parts of the Santos and Campos basins around the time of rift onset. Following Early Cretaceous breakup, the Tristão da Cunha hot spot migrated from the southern end of the Santos Basin across the oceanic crust of the South Atlantic to its current location at the island of Tristão da Cunha (White and McKenzie, 1989). En route, it left a trail of basaltic plateaus, including the Rio Grande Rise and Walvis Ridge (White and McKenzie, 1989).

Ebinger and Sleep (1998) suggested that extrusive volcanism may occur at distances of up to 2000 km from an active mantle hot spot because of sublithospheric melting and long-distance migration of melts to the surface along zones of crustal weakness. Large-scale transient basaltic volcanism of the Paraná extrusive event is interpreted to have resulted from an initial thermal plume pulse that accompanied the birth of the Tristão da Cunha (Walvis) hot spot (Wilson, 1992). Hot-spot volcanism may have contributed to rifting and breakup in the southern compartment of the South Atlantic, but it also probably delayed the rift-drift transition in the central compartment because of heating, softening, and stretching of the subcontinental lithosphere of the Brasiliano mobile belt.

According to plate reconstructions for the South Atlantic, the Paraná flood basalts of Brazil were adjacent to the Etendeka lavas of Namibia in the Early Cretaceous (White and McKenzie, 1989). Radiometric dating and basalt geochemistry confirm that the extensive Paraná basalts of Brazil and the Etendeka lavas of Namibia are part of the same flood basalt province (Erlank et al., 1984; Renne et al., 1992, 1996). Paraná basalts have been linked to a swarm of northwest-southeast–trending feeder dikes on the Ponta Grossa arch of Brazil (Hawkesworth et al.,

1992), and dikes of equivalent trend are associated with the Etendeka lavas in west Africa (Peate, 1997). The Paraná-Etendeka lavas were most likely much more extensive at the time of rifting than they are today. Offshore grabens in the Santos and Campos basins are floored with early-rift Paraná basalts (Mizusaki et al., 1988, 1992; Chang et al., 1992).

Paraná hot-spot volcanism ceased by 129 Ma (Hauterivian) as Walvis hot-spot activity moved onto the leaky Florianópolis oceanic transform fault. This transform separates the southern and central compartments of the South Atlantic. In the latest Jurassic, the transform fault may have been the northern terminus of South Atlantic spreading. South of the Florianópolis fracture zone, breakup was largely complete by the Valanginian (~133 Ma). Basalts prograded onto the thermally subsiding continental margins in the late stages of rifting and during breakup (Gladczenko et al., 1997). Seismic data from the margins of Brazil, Uruguay, Argentina, Angola, Namibia, and South Africa indicate that the basalts fill fault-bounded grabens or form massive extrusive wedges (Gladczenko et al., 1997; Hinz et al., 1999), which contain seaward-dipping reflectors.

Trindade Hot Spot

In the Late Cretaceous and Paleogene, the southeast Brazilian Atlantic margin was profoundly affected by a second mantle plume, the Trindade (Martin Vaz) hot spot (Figure 4). Researchers have suggested that this originated at 90–80 Ma as a plume pulse beneath the interior of the South American continent (Gibson et al., 1995; Thompson et al., 1998), where it generated the alkaline magmatism that is widespread in southeastern Brazil (Amaral et al., 1967). Geochemically, this magmatism is indistinguishable from oceanic island basaltic magmatism (Thompson et al., 1998). An eastward-younging age progression of onshore volcanic centers (Woolley, 1987; Thompson et al., 1998) is probably a result of westward motion of the South American plate. The volcanic centers, however, are some 500 km south of the reconstructed hot-spot track (Thompson et al., 1998) derived from plate reconstructions of the South Atlantic (Müller et al., 1993). Thompson et al. (1998) suggested that the magmas were displaced to the south by a deflection at the base of the subcontinental lithosphere. The hot spot crossed the Brazilian passive margin in the Espírito Santo Basin between 55 and 40 Ma, building the Abrolhos volcanic edifice (Figures 1, 4) across the rifted margin. Since about 40 Ma, the Trindade hot spot has built a chain of volcanic seamounts out to its current location at the active volcanic islands of Trindade and Martin Vaz (Figure 4).

The Trindade hot spot had a profound impact on the Late Cretaceous and Tertiary evolution of the Santos and Campos basins. In a companion article (Cobbold et al., 2001), we argue that the Trindade hot spot was a significant factor, in conjunction with the Andean far-field stress regime, in promoting coastal uplift, increased sediment supply, drainage diversion, offshore volcanism, and reactivation of structures on the passive margin.

RIFT ARCHITECTURE

In our study, we integrated seismic data, potential field data, and previously published work to develop a regionally consistent rift framework for the southeast Brazilian margin. The seismic database for the area is very large, but little of it is in the public domain. Data are concentrated in nearshore areas at water depths of 1000 m or less, where hydrocarbon exploration and production have been intensive. At the scale of the Campos and Santos basins, the available seismic database is insufficient to yield a fully three-dimensional view of the rift architecture.

Potential field data have a resolution that is sufficient to constrain horizontal variations in rift architecture. Gravity data are excellent for interpolating between seismic lines. We have interpreted residual gravity anomalies after removal of a fifth-order trend surface from Bouguer-corrected data (Figure 5). To unravel the complex structure of the rift, we first interpreted the main gravity anomalies using regional seismic lines. On this basis, we defined structural provinces and mapped them (Figure 6). Our approach was similar to that of Fichler et al. (1999), who studied part of the North Sea (Norwegian shelf) and adjacent onshore areas.

Nearshore Positive Gravity Anomalies

Near the shore in the Campos and Santos basins is a strip of strong positive gravity anomalies (up to 80 mGal, more commonly up to 60 mGal), about 50 km wide (Figure 5). This strip is mostly continuous but significantly offset in some places. In general, the strip runs northeast-southwest, about 70 km from the shore. At Cabo Frio, however, it runs obliquely into

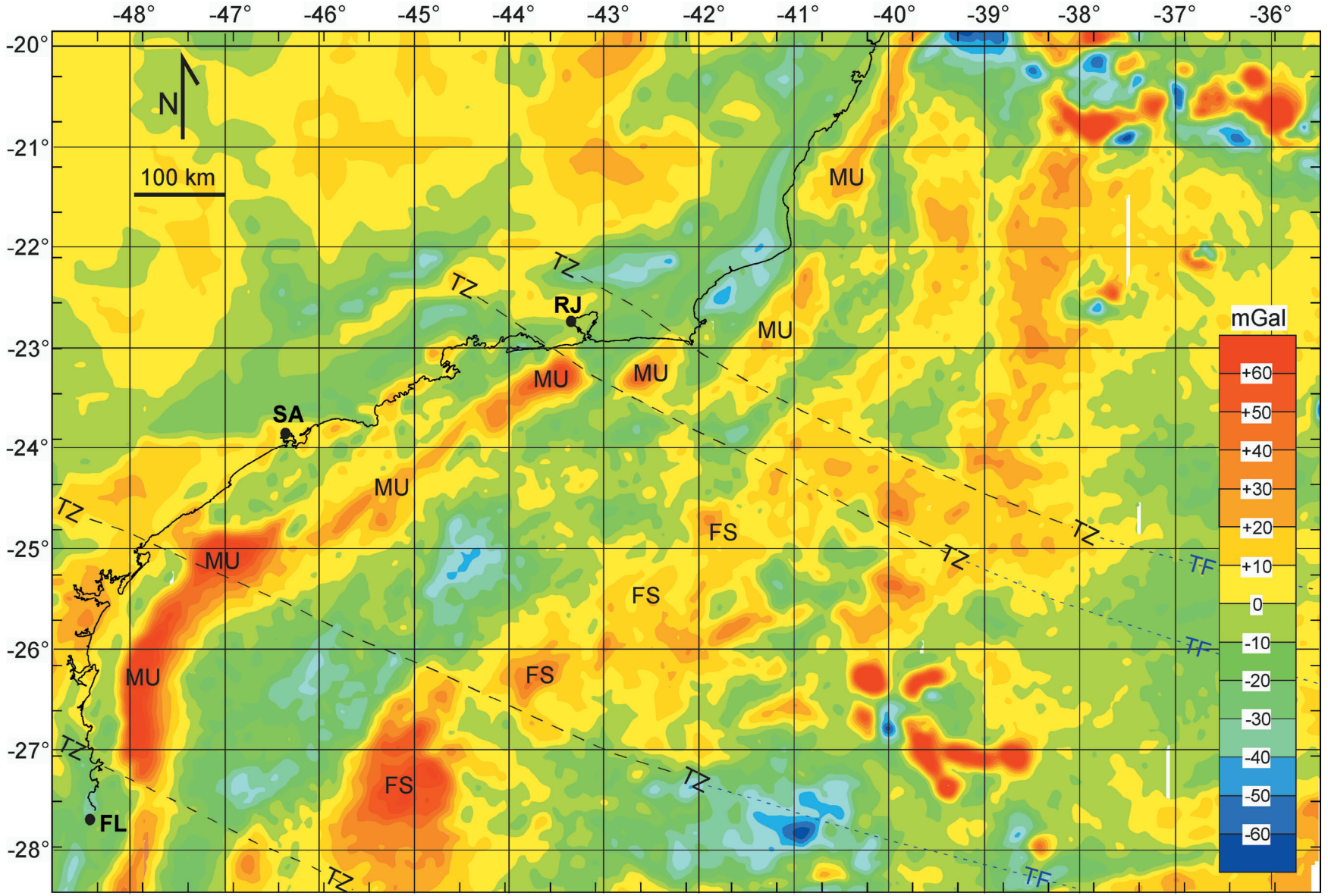

Figure 5. Map of gravity anomalies, Campos and Santos basins. Anomalies are residual, after removal of a fifth-order trend surface from Bouguer-corrected data provided by Lamont-Doherty Geological Observatory. Onshore localities are (from southwest to northeast) Florianópolis (FL), Santos (SA), and Rio de Janeiro (RJ). Main anomalies have been interpreted (MU = nearshore Moho uplift; FS = failed spreading ridge). Dashed lines (TZ) identify some of the more prominent transfer zones; blue dotted lines (TF) are prominent fossil ocean ridge transform faults. The color bar shows residual anomaly values in mGal.

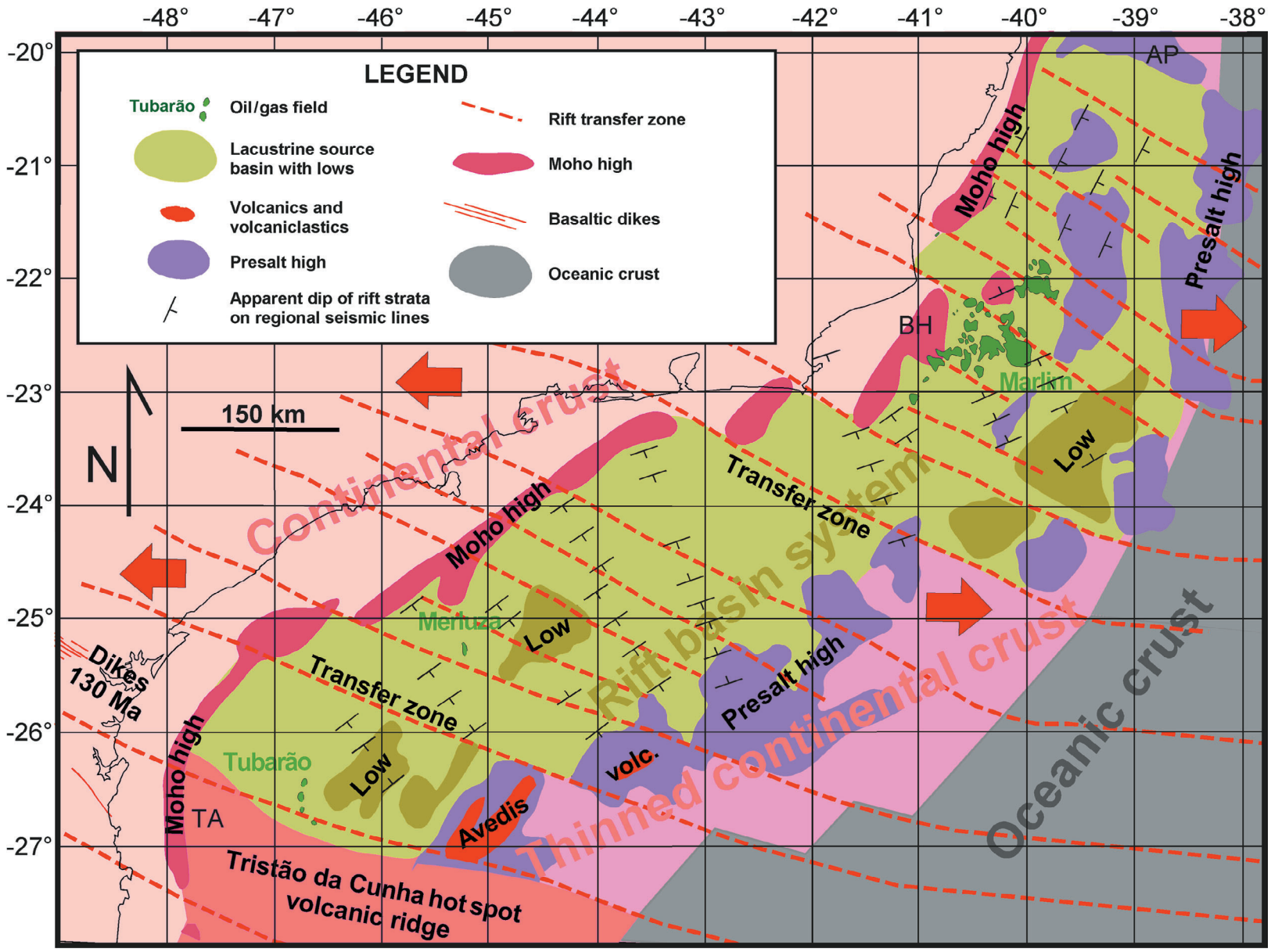

Figure 6. Map of main rift-related structural provinces, Campos and Santos basins. East–west extension direction (large red arrows) is from plate tectonic reconstructions of the early (Hauterivian) stage of Atlantic opening (Nürnberg and Müller, 1991, figure 10). Inferred rift transfer zones are not parallel with this extension direction (see text for possible reasons). TA = Torres Arch; BH = Badejo High; AP = Abrolhos Plateau.

the coastline. In the southern Santos Basin, both the strip and the shoreline trend north-south.

On regional seismic lines, the gravity anomalies may be accounted for by an anomalously shallow Moho. On deep seismic lines across the Campos Basin, such as line 203-RL-76 (Mohriak and Dewey, 1987, figure 7; Mohriak et al., 1990a, figure 15), prominent seismic reflectors appear to mark the lower crust and the Moho. Near the coast, the seismic Moho rises to about 7 s of two-way traveltime (equivalent to a depth of approximately 20 km), forming an antiform approximately 50 km wide (Figure 7). In the Santos Basin, proprietary deep seismic lines reveal a similar antiform coincident with the nearshore positive gravity anomaly, which we interpret as a southward continuation of the Moho uplift by analogy with the Campos Basin. Overlying the Moho high in the Campos Basin are major extensional faults and an associated half rift, which is filled with Neocomian volcanic rocks and sedimentary rocks. Based on this evidence, the Moho became uplifted during Early Cretaceous rifting and crustal extension. Gravity modeling based on the observed reflection Moho has provided a good fit to Bouguer anomalies in this area (Mohriak and Dewey, 1987; Mohriak et al., 1990a). The dominant vergence of the extensional faults is landward, and we infer that the southwest-dipping master fault continues downward into the basement, becoming a low-angle extensional detachment at the Moho (Figure 7). The Moho uplift is in its footwall. We suggest that the low-angle detachment was originally a Brasiliano (Pan-African) thrust fault, which became reactivated during Neocomian rifting. If so, the vergence of the Neocomian half rifts is inherited from the vergence of the Brasiliano fold belt.

Offshore Positive Gravity Anomalies

A second strip of positive gravity anomalies (up to 70 mGal, more commonly up to 40 mGal) lies approximately 300 km offshore (Figures 5, 6). These anomalies are relatively wide (approximately 80–150 km) and not as sharply defined as the nearshore anomalies. Nevertheless, they also tend to form strips trending northeast-southwest. On regional seismic lines, they coincide with areas interpreted to be volcanic rocks. In some instances, the volcanic rocks are unconformably overlain, or progressively onlapped, by thin Aptian evaporites, whose seismic facies are well layered and interpreted to be anhydrite (Figure 8). We infer that these anticlines were ridges of high ground during evaporite deposition. Along some of the ridges, volcanic activity continued during and after the Aptian, mobilizing the evaporites and covering them with volcanoclastic deposits. A good example is the Avedis volcanic chain in the southern Santos Basin, which has been mapped as a presalt high (L. S. Demercian, 1996). The suggestion has been made that this chain was originally in the middle of a symmetric rift basin and that continental rifting became concentrated there, producing a failed spreading center (L. S. Demercian, 1996, p. 108 and figure 20). We concur with this interpretation. More generally, we argue that the entire set of offshore positive gravity anomalies represents a failed spreading ridge (Figure 6).

Intervening Negative Gravity Anomalies

Between the nearshore and offshore strips of positive gravity anomalies is a broader domain (approximately 300 km wide), where anomalies are mainly negative

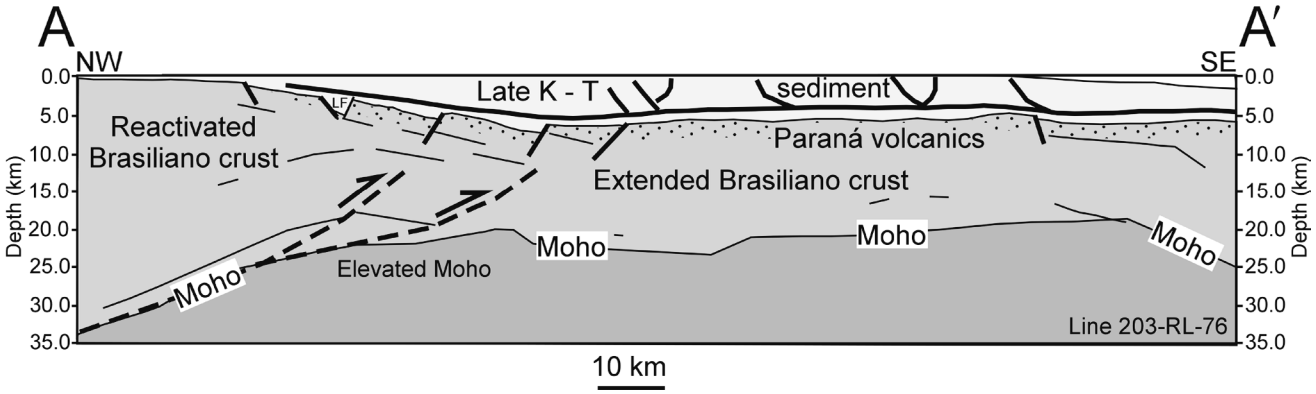

Figure 7. Geoseismic section AA′ across nearshore Moho uplift, Campos Basin (modified from Mohriak and Dewey, 1987; Mohriak et al., 1990a). Brasiliano structures were reactivated in oblique extension during rifting and in later far-field compression (see Cobbold et al., 2001). See Figure 1 for location.

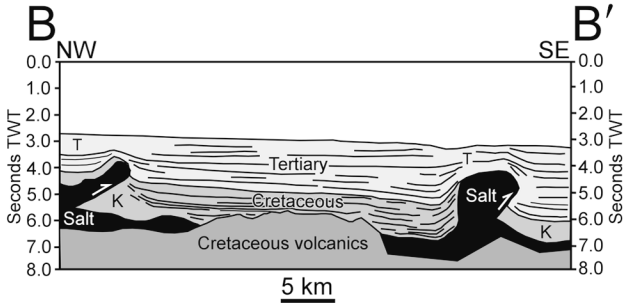

Figure 8. Geoseismic section BB′ across volcanic basement anticline of failed spreading ridge, unconformably onlapped by Aptian evaporites, southern Santos Basin (modified from L. S. Demercian, 1996). See Figure 1 for location.

(down to −50 mGal). They form several parallel strips trending northeast-southwest (Figures 5, 6). Mesozoic and Tertiary sedimentary rocks in this domain are up to 8 km thick in the Santos Basin. The Moho has been imaged on deep seismic sections across this area of the Campos Basin (Mohriak and Dewey, 1987) and on seismic refraction profiles across the Santos Basin (Leyden et al., 1971; Leyden, 1976). For several representative sections, gravity anomalies have been well matched by modeling (Chang et al., 1990, 1992). The strongest negative anomalies correlate with half rifts that are visible on deep seismic lines, for example, in the Campos Basin (Mohriak and Dewey, 1987) and in the area around Cabo Frio (Mohriak et al., 1995). The half rifts typically contain an early-rift sequence and a late-rift sequence separated by a regional unconformity (Abrahão and Warme, 1990; Guardado et al., 1990; Mohriak et al., 1995). In the Campos Basin (Rangel et al., 1994), the late-rift sequence consists of freshwater limestones (Coqueiro Member).

In the central Campos Basin, most of the extensional faults dip seaward (Dias et al., 1990, figure 5). In contrast, over much of the Santos Basin, the extensional faults that bound the half rifts dip landward (Mohriak et al., 1995, figures 10, 14).

Apparent Offsets of Gravity Anomalies

Coast-parallel gravity anomalies show apparent offset across a series of narrow zones that trend west-northwest–east-southeast (Figures 5, 6). Most of these zones can be traced continuously across the rift basin: they appear to offset the trends of nearshore positive anomalies, intervening negative anomalies, and offshore positive anomalies. Most of these apparent offsets are right lateral. The most pronounced are off Cabo Frio and in the Santos Basin. Other apparent offsets are left lateral, notably in the Campos and southernmost Santos basins. Commonly, the amount of apparent offset is not constant along each zone.

Variable apparent offsets are typical of transfer zones (Gibbs, 1984) such as those in the East African rift system, for example, (Rosendahl, 1987; Morley et al., 1990). In general, strike-slip displacements along transfer zones are synchronous with extensional faulting in intervening rifts or half rifts. The sense and amount of strike-slip displacement, however, can be quite variable along any given transfer zone (Gibbs, 1984). An apparent offset may represent a true fault displacement that accumulated during rifting, or it may be inherited from an earlier event.

Researchers generally accept that transfer zones in rifts are parallel, or nearly parallel, with the principal direction of horizontal extension (Gibbs, 1984; Milani and Davison, 1988), as are transform faults in oceanic crust. If so, the direction of the Campos and Santos extension was (1) perpendicular to the main axis of rifting in the Campos and southern Santos basins and (2) oblique to the rift axis over much of the northern Santos Basin and off of Cabo Frio.

Transfer zones can be inferred from the fault map for basalts near the base of the rift sequence in the Campos Basin (Dias et al., 1990, figure 5). The main transfer zones are immediately to the northeast and southwest of the Campos salient. Across them, extensional faults have sigmoidal traces. More generally, the extensional fault vergence tends to switch across the transfer zones.

The subsurface expressions of transfer zones are high-angle faults or flower structures. One of the main transfer zones in the Cabo Frio area, between the Campos and Santos basins, has been illustrated by Mohriak et al. (1995). In cross section, it has a normal sense of separation (Figure 9). In the Campos and Santos basins, most transfer faults display normal separation, although some show reverse separation. They are similar in style and orientation to those described for the onshore Recôncavo basin of northeastern Brazil (Milani and Davison, 1988), which is also part of the East Brazil rift system (Chang et al., 1992). A steep transfer fault at the southern edge of the Marlim field has been illustrated by Carminatti (1987).

The transfer faults had an influence on early-rift sedimentation in the Campos Basin. Their influence can be seen on the total isopach map for the rift fill sequence (Dias et al., 1988, figure 3) and on the facies distributions for each of the depositional sequences

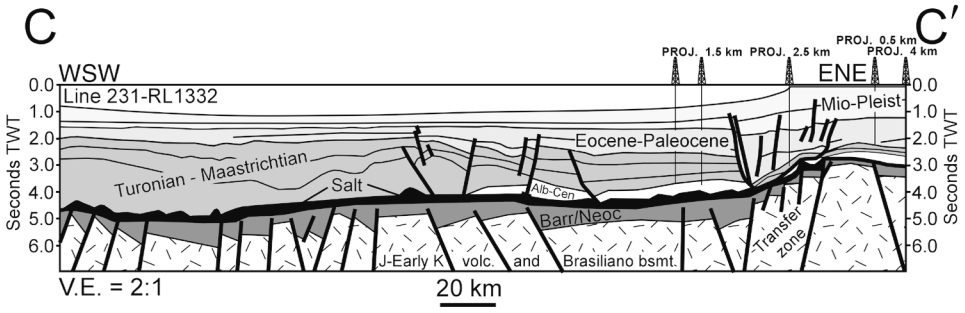

Figure 9. Geoseismic section CC′ across transfer zone, Cabo Frio area (modified from Mohriak et al., 1995). See Figure 1 for location.

from basal clastic rocks to Aptian evaporites (Dias et al., 1988, figure 6). On a smaller scale, the extensional transfer fault that bounds the Badejo High on its northeastern side has an alluvial fan in its hanging wall (Abrahão and Warme, 1990).

Transfer zones divide the main Campos and Santos basins into domains, each spanning several half rifts or rifts. As previously mentioned, the dominant vergence of the extensional faults is landward. In some domains, however, the vergence is seaward. Notable examples can be found in the central Campos Basin (Dias et al., 1990; Mohriak et al., 1995, figure 12) and central Santos Basin.

At the southwestern edge of the Santos Basin, the salt comes to an end along a line trending west-northwest–east-southeast (S. Demercian et al., 1993). This is the interpreted limit of rift basins beneath the salt and the northern boundary of the Torres Arch. The line is in fact a transfer zone, which generally lies on trend with the Florianópolis fracture zone. In fact, many of the transfer zones in the Santos Basin appear to lie on the projected trend of the oceanic fracture zones that are visible on SEASAT gravity data (Figure 4).

Neocomian Igneous Intrusions

Dikes that are synchronous with Early Cretaceous rifting and the Paraná-Etendeka flood basalts are known from two main areas. Along the coast, between Santos and Rio de Janeiro, a major dike swarm is parallel with the southwest-northeast–trending main extensional faults of the rift phase. The dike swarm has been dated at 133–129 Ma by ^{40}Ar-^{39}Ar geochronology (Turner et al., 1994). Another major dike swarm in the Ponta Grossa area is also broadly contemporaneous with the flood basalts (Turner et al., 1994; Renne et al., 1996), but it trends northwest-southeast, almost at right angles to the extensional faults (Figure 6). The origin of this dike swarm is controversial. The angular relationships are reminiscent of a classic triple junction, in which case the Ponta Grossa dike swarm would be the aborted arm. The dikes, however, are not oriented radially above an inferred plume head (Peate, 1997). Perhaps the Ponta Grossa dike swarm, like the Salado and Colorado basins in Argentina, resulted from northeast-southwest extension during counterclockwise rotation of southern South America relative to northern South America (Leyden, 1976; Chang et al., 1992). Alternatively, perhaps the dike swarm is parallel with a major continental strike-slip zone (Nürnberg and Müller, 1991) or a Neocomian transfer zone. Also in the Ponta Grossa area are several intrusions of alkaline igneous rocks (Amaral et al., 1967), which are broadly contemporaneous with the Paraná flood basalts (Amaral et al., 1967) and have been attributed to the Walvis hot spot (White and McKenzie, 1989; Wilson, 1992; Peate, 1997). Two belts of intrusions, one immediately to the southwest of São Paulo and the other close to Curitiba, strike west-northwest–east-southest, parallel to the transfer faults (Amaral et al., 1967; Herz, 1977; Cobbold et al., 2001, figure 2).

Oceanic Crust and Transform Faults

Seaward of the failed spreading ridge (Figure 6), gravity anomalies change in character, becoming typical of oceanic crust (Figure 4). Over large areas, they coincide with magnetic anomalies and show apparent offsets across fossil transform faults or fracture zones (Nürnberg and Müller, 1991).

The main fossil transform faults of the South Atlantic are offshore extensions of the main transfer zones in the Cabo Frio area, where the opening of the Atlantic followed the zone of weakness provided by the Brasiliano Ribeira fold belt (Le Pichon and Hayes, 1971; Asmus, 1978; Szatmari et al., 1985; Macedo, 1989).

Near the Brazilian margin, fossil transform faults trend nearly east-west (Le Pichon and Hayes, 1971;

Nürnberg and Müller, 1991). In contrast, transfer zones in the adjacent thinned continental crust trend west-northwest–east-southeast (Figure 6). Each transform fault, however, can be traced into a discrete transfer fault (Figure 4). This suggests that the former are inherited from the latter.

The abrupt change in trend between transfer faults and transform faults can be explained in terms of (1) a change in the mechanism of faulting, (2) a change in the direction of motion between South America and Africa immediately after opening of the Atlantic, or (3) a clockwise rotation of all transfer faults during postrift tectonics.

IMPLICATIONS FOR PETROLEUM SYSTEMS

All of the six petroleum systems recognized in the Campos Basin involve subsalt Early Cretaceous oil-prone lacustrine source rocks, which charge suprasalt Tertiary turbidite reservoirs (E. M. Meister, 1982, unpublished data; Figueiredo, 1985; Szatmari et al., 1985; Carminatti, 1987; Mello et al., 1988, 1994, 1995; Dias et al., 1990; Guardado et al., 1990; Mohriak et al., 1990b; Trindade et al., 1995). Suprasalt structural traps, especially faulted rollovers, are commonly associated with salt movement and detached deformation. The traps are sealed by marine shelf and slope shales (Figure 10). Traps involving turbidite reservoirs commonly have a significant stratigraphic component and are multiply stacked. Lesser accumulations of lacustrine-sourced oils are found in subsalt coquina shoal facies and suprasalt marine shelf carbonates.

Until recently, reserves in the Santos Basin were limited (1.00×10^6 m^3 [6.3 million bbl] liquids and 4.8×10^9 m^3 [0.17 tcf] gas [ANP, 2000]). Most reserves were attributed to a petroleum system in which suprasalt Turonian shelfal organic-rich shales (Mello et al., 1989, 1995) charge reservoirs in suprasalt Albian shelfal calcarenites and Late Cretaceous–early Tertiary turbiditic sandstones (Pereira and Macedo, 1990). Turonian rocks are limited by erosion landward of the hinge zone and in some shelf areas of the northern Santos and Campos basins. Source potential is restricted to gas-prone marine facies between the paleoshoreline and the shelf edge.

According to regional reflection seismic and gravity data, potentially source-prone subsalt lacustrine rift basins extend well beyond the limits of existing hydrocarbon discoveries into the underexplored deep-water Santos, Campos, and southern Espírito Santo basins. If large additional reserves are to be found in this deep-water play trend, regional variations in rift structure and stratigraphy can be expected to impact petroleum system risk factors such as source rock presence, thickness, facies, preservation, and access to migration pathways.

Distribution and Quality of Lacustrine Source Rocks

Proven source rocks for hydrocarbon accumulations in the Campos Basin are the Early Cretaceous (Barremian) lacustrine black shales and carbonates of the Lagoa Feia Formation (Figure 2). They can be recognized on reflection seismic data, have been encountered in wells, and have been characterized by geochemical analysis of oils (Mello et al., 1988, 1994, 1995; Trindade et al., 1995). On reflection seismic data, lacustrine facies are recognizable by their bright, parallel-continuous reflection character and can be carried into the deep-water Campos, Santos, and southern Espírito Santo basins.

Lacustrine facies observed on seismic data can be subdivided into a rift phase and a drift phase, commonly separated by an angular unconformity. The rift phase is widespread but areally restricted to half rifts. The drift phase is expressed as a distinctive seismic package 100–400 m thick and has greater lateral extent than the rift phase, perhaps because of the existence of a broad lacustrine basin during postrift thermal subsidence. Many normal faults within the half rifts terminate upward into the drift phase.

The limit of potential lacustrine source rocks can be broadly constrained by regional arguments (Figure 11). Except within the nearshore Campos area, half rifts are not observed shoreward of the Moho high. They are seldom observed outboard of the outer high on the São Paulo Plateau and are probably not buried deep enough to be mature. The volcanic edifice of the Torres Arch is the southern limit of the central rift system, and the massive postsalt Abrolhos volcanic plateau of the Trindade hot spot places an effective northern limit in the Espírito Santo Basin.

Based on the parallel-continuous character of seismic facies, lacustrine source rocks can be extrapolated southward from their known occurrence in the Campos Basin across the Cabo Frio High into the Santos Basin (Figure 11). Half rifts and drift phase facies are locally observed below salt windows in the central rift system. According to gravity and regional seismic data, several local deeps exist within the rift system beneath

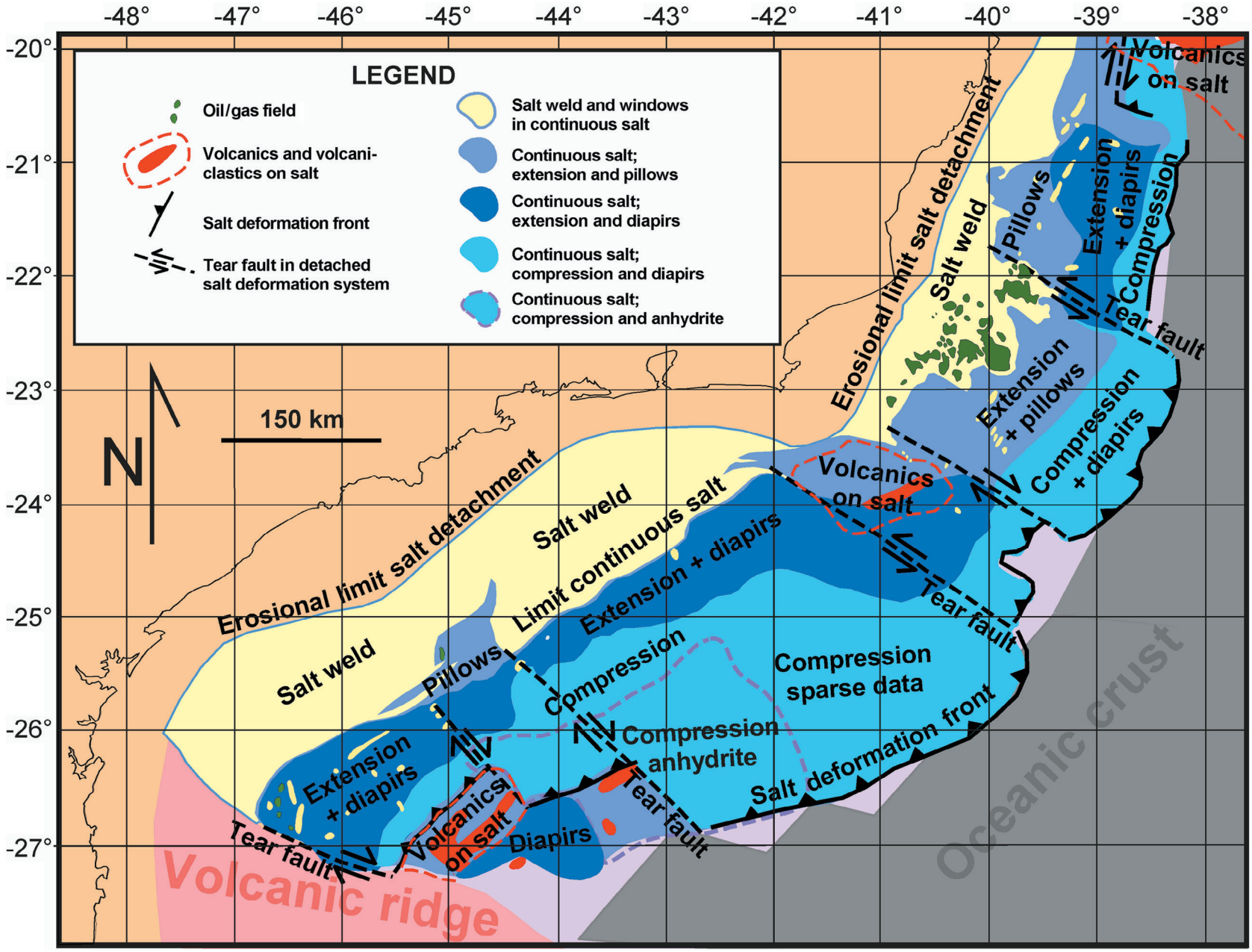

Figure 10. Summary map of salt-detached structural domains, Campos and Santos basins.

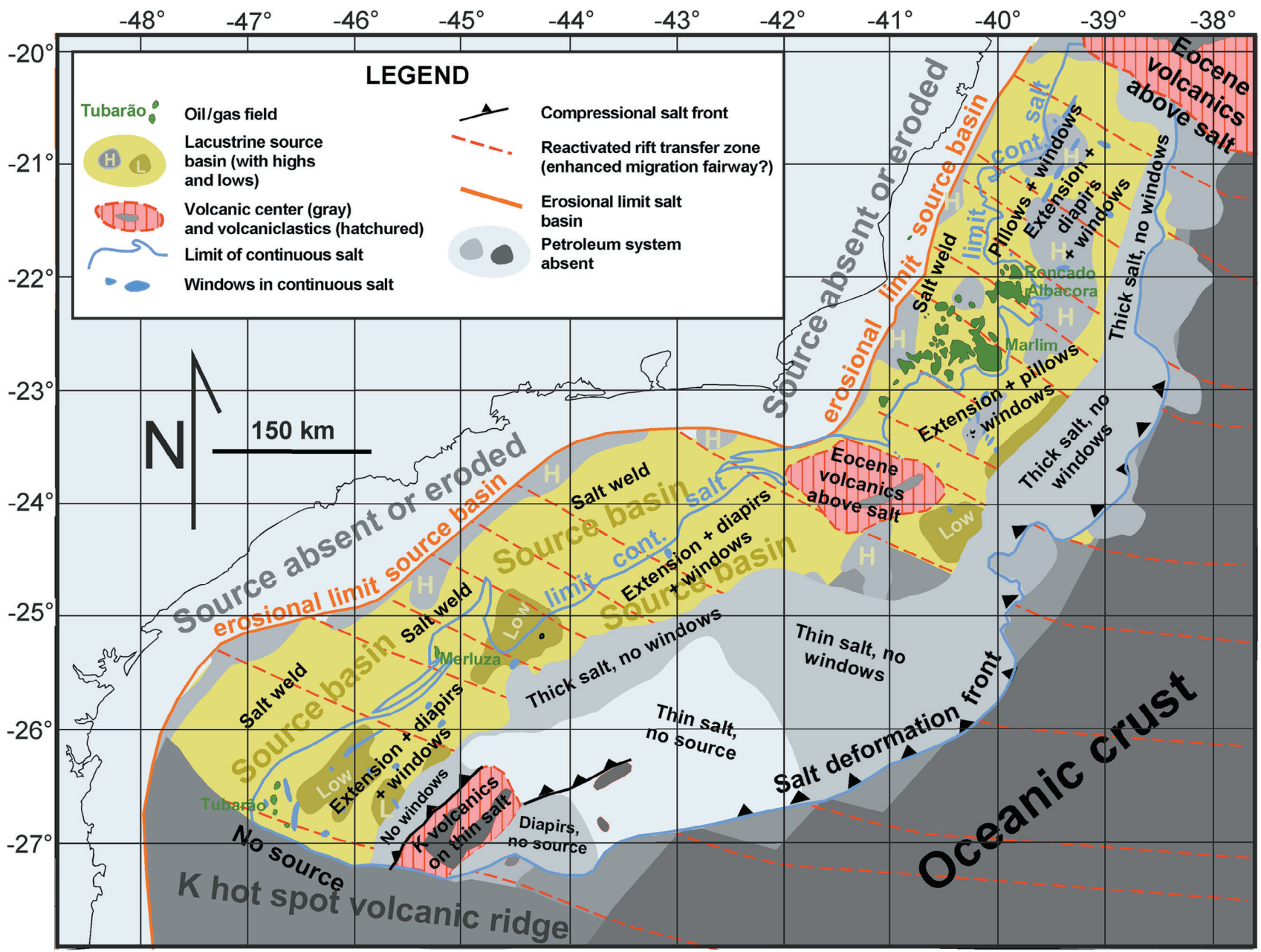

Figure 11. Summary map of main features influencing petroleum systems, Campos and Santos basins.

salt, outboard of the Tubarão, Merluza, and Marlim fields (Figure 11).

The drift phase thins over synrift highs, and lacustrine facies are inferred to undergo facies changes, which might impact local source quality. Evidence for facies variations within the lacustrine drift phase can be found in variability of lithofacies within the Campos Basin encountered in wells (Dias et al., 1988). This inference is supported by facies changes observed in the overlying Aptian evaporite section, in which bright reflections suggest anhydrite deposition on presalt highs.

In the southern Santos Basin, there is a high risk that volcanics will be found in subsalt strata (Williams and Hubbard, 1984), which are near the Tristão da Cunha hot-spot track and Avedis volcanic chain (Figures 6, 11). Near the Avedis volcanic ridge, Early Cretaceous volcanics are observed to overlie and interfinger with Aptian evaporites, and they may interfinger with rift and drift phase strata as well.

Subsalt Migration Pathways

Most of the proven reserves in the Campos Basin are contained in Late Cretaceous–Miocene deep-water turbiditic sandstone reservoirs (Guardado et al., 1990). For hydrocarbons to reach suprasalt reservoirs, they must migrate from rift lacustrine strata across salt (E. M. Meister, 1982, unpublished data). Transfer zones, which are associated with oblique rifting, can provide a mechanism for subsalt focusing and migration of hydrocarbons to windows at base salt (see Cobbold et al., 2001).

Transfer zones compartmentalize the rift basin. They are transverse, structurally complex intrarift highs and may act to focus stratal hydrocarbon migration from intrarift lows. Cross-stratal hydrocarbon migration may be enhanced along transfer zones, where fracturing and structural complexity are associated with distributed shear, allowing hydrocarbons to reach base salt. Early Cretaceous carbonates of the drift phase are local reservoir targets in the Campos Basin (Guardado et al., 1990). Barremian lacustrine coquinas, associated with shoaling on intrarift highs, might be preferentially developed along transfer zones, where fracturing could further enhance reservoir quality. Fractured transfer zones may also offer paths for long-distance subsalt hydrocarbon migration in the absence of a stratigraphic carrier bed at base salt.

Once hydrocarbons have reached base salt, a mechanism must be found for traversing it. Figure 10 shows the general regional distribution of salt tectonic domains. Continuous salt acts as a barrier to hydrocarbon migration, but numerous windows can be recognized through which migration might occur. Windows located above transfer zones in the rift system would be better positioned to receive charge via subsalt focusing and vertical migration pathways. Landward of the limit of continuous salt, salt evacuation produced a weld, enhancing the potential for migration. Note that major fields in the Campos and Santos basins lie at the edge of continuous salt. In a companion article (Cobbold et al., 2001), we suggest that the neotectonic reactivation of transfer zones may be an important factor in facilitating subsalt focusing and migration of hydrocarbons through salt via faulted welds and windows.

Constraints on Petroleum System Risk

Figure 11 summarizes the main features of the lacustrine petroleum system. The Campos, Santos, and Espírito Santo basins can be subdivided into regional domains that have variable risk for presence of lacustrine source rock and potential for migration across salt. A lack of source limits the petroleum system along the shoreward hinge line and volcanic Torres Arch; suprasalt volcanics hinder interpretation beneath the Abrolhos Plateau; and thick salt and questionable source limit potential within the compressional salt domain and São Paulo Plateau. The axis of the central rift system has the greatest potential for presence of lacustrine source rock. Migration risk is greater, however, seaward of the limit of continuous salt than it is within the salt weld domain (Cobbold et al., 2001). To traverse salt, hydrocarbons migrating seaward of the limit of continuous salt must pass through windows at grounded synclines.

SUMMARY AND CONCLUSIONS

1. The passive margin of southeastern Brazil initiated as a rift system in the Neocomian. Rifting propagated northward into the central South Atlantic. Rift architecture was strongly influenced by preexisting fabric and structures of the Late Proterozoic (Brasiliano orogeny). Between the Santos and Campos basins, the Atlantic margin inherited an east-northeast–west-southwest orientation, so rifting was oblique to the margin, assuming east-west extension.

2. On a regional map of Bouguer-corrected gravity, a nearshore belt of positive anomalies correlates with a broad interpreted Moho uplift in the footwall of Neocomian extensional faults.
3. Farther offshore, a second belt of positive gravity anomalies correlates with a presalt ridge of eroded volcanic and basement anticlines, which are covered by thin Aptian evaporites, especially anhydrite. We interpret this ridge as a failed spreading center.
4. An intervening belt of negative gravity anomalies coincides with the main Santos-Campos rift system axis.
5. All three belts of gravity anomalies show apparent offsets along linear zones, trending west-northwest–east-southest. We interpret these as transfer zones that developed during Neocomian rifting.
6. The vergence of half rifts tends to change across transfer zones, compartmentalizing the rifted margin into subbasins. Transfer zones exerted controls on the thicknesses and facies of the Neocomian rift sequence.
7. At the eastern limit of continental crust, transfer zones become aligned with ocean ridge transform faults, which trend east-west across the South Atlantic.
8. The Campos, Santos, and Espírito Santo basins can be subdivided into regional domains that have variable risk for presence of lacustrine source rock.
9. Transfer zones, which are associated with oblique rifting, can provide a mechanism for subsalt focusing and migration of hydrocarbons to windows at base salt.

REFERENCES CITED

Abrahão, D., and J. E. Warme, 1990, Lacustrine and associated deposits in a rifted continental margin—Lower Cretaceous Lagoa Feia Formation, Campos Basin, offshore Brazil, *in* B. J. Katz, ed., Lacustrine basin exploration: case studies and modern analogs: AAPG Memoir 50, p. 287–305.

Almeida, F. F. M., 1967, Origem e evolução da plataforma brasileira: Ministério de Minas e Energia, Departamento Nacional de Produção Mineral (DNPM), Rio de Janeiro, Boletim da Divisão de Geologia e Mineralogia, v. 241, 36 p.

Almeida, F. F. M., and Y. Hasui, 1984, O Pré-Cambriano do Brasil: São Paulo, Edgard Blücher, 378 p.

Almeida, F. F. M., Y. Hasui, and C. D. R. Carneiro, 1975, Lineamento de Além—Paraíba: Anais da Academia Brasileira de Ciências, v. 47, p. 575.

Almeida, F. F. M., Y. Hasui, B. B. de Brito Neves, and R. A. Fuck, 1981, Brazilian structural provinces: an introduction: Earth Science Reviews, v. 17, p. 1–29.

Amaral, G., J. Bushee, U. G. Cordani, K. Kawashita, and J. H. Reynolds, 1967, Potassium-Argon ages of alkaline rocks from southern Brazil: Geochimica et Cosmochimica Acta, v. 31, p. 117–142.

ANP (Agência Nacional do Petróleo), 2000, Anauario Estadistico (ANP 1999 Statistical Review): Rio de Janeiro, Brazil, Agência Nacional do Petróleo (Brazil National Petroleum Agency), 182 p.

Asmus, H. E., 1978, Hipótese sobre a origem dos sistemas de zonas de fraturas oceânicas/alinhamentos continentais que ocorrem nas regiões sudeste e sul do Brasil: Série Projeto Remac, v. 4, p. 39–73.

Asmus, H. E., and P. R. Baisch, 1983, Geological evolution of the Brazilian continental margin: Episodes, v. 4, p. 3–9.

Asmus, H. E., and F. C. Ponte, 1973, The Brazilian marginal basins, *in* A. E. Nairn and F. G. Stehli, eds., The ocean basins and margins: v. 1: the South Atlantic: New York, Plenum Press, p. 87–132.

Campanha, G. A. da C., 1981, O lineamento de Além-Paraíba na área de Três Rios (RJ): Revista Brasileira de Geociências, v. 11, p. 159–171.

Campos, C. W. M., F. C. Ponte, and K. Miura, 1974, Geology of the Brazilian continental margin, *in* C. A. Burk and C. L. Drake, eds., The geology of the continental margins: New York, Springer-Verlag, p. 447–461.

Campos Neto, M. C., and M. C. H. Figueiredo, 1995, The Rio Doce orogeny, southeastern Brazil: Journal of South American Earth Sciences, v. 8, p. 143–162.

Carminatti, M., 1987, Relações entre a evolução estrutural e a ocorência de campos gigantes de hidrocarbonetos na area nordeste da Bacia de Campos: TECTOS (Primeiro Simposio da Tectônica), p. 517–530.

Castro Jr., A. C. M., 1987, The northeastern Brazil and Gabon basins: a double rifting system associated with multiple crustal detachment surfaces: Tectonics, v. 6, p. 727–738.

Chang, H. K., R. O. Kowsmann, and A. M. F. Figueiredo, 1988, New concepts on the development of east Brazilian marginal basins: Episodes, v. 2, p. 194–202.

Chang, H. K., R. O. Kowsmann, and A. M. F. Figueiredo, 1990, Novos conceitos sobre o desenvolvimento das bacias marginais do leste brasileiro, *in* G. P. Raja Gabaglia and E. J. Milani, eds., Origem e evolução de bacias sedimentares: Rio de Janeiro, Petrobrás, p. 269–289.

Chang, H. K., R. O. Kowsmann, A. M. F. Figueiredo, and A. A. Bender, 1992, Tectonics and stratigraphy of the East Brazil rift system: an overview: Tectonophysics, v. 213, p. 97–138.

Clemson, J., J. Cartwright, and J. Booth, 1997, Structural segmentation and the influence of basement structure on the Namibian passive margin: Journal of the Geological Society, v. 154, p. 477–482.

Cobbold, P. R., K. E. Meisling, and V. S. Mount, 2001, Reactivation of an obliquely-rifted margin, Campos and Santos basins, southeastern Brazil: AAPG Bulletin, v. 85, no. 11, p. 1925–1944.

Conceição, J. C. J., P. V. Zalán, and S. Wolff, 1988, Mecanismo, evolução e cronologia do rift sul-atlântico: Boletim de Geociências da Petrobrás, v. 2, p. 255–265.

Davison, I., 1999, Tectonics and hydrocarbon distribution along the Brazilian South Atlantic margin, *in* N. R. Cameron, R. H. Bate and V. S. Clure, eds., The oil and gas habitats of the South Atlantic: Geological Society Special Publication, v. 153, p. 133–151.

Demercian, L. S., 1996, A halocinese na evolução do Sul da Bacia de Santos do Aptiano ao Cretáceo Superior: Master's thesis, Universidade Federal do Rio Grande do Sul, Porto Alegre, Brazil, 201 p.

Demercian, S., P. Szatmari, and P. R. Cobbold, 1993, Style and pattern of salt diapirs due to thin-skinned gravitational gliding, Campos and Santos basins, offshore Brazil: Tectonophysics, v. 228, p. 393–433.

De Wit, M. J., M. Jeffery, H. Bergh, and L. Nicolaysen, eds., 1988, Geological map of sectors of Gondwana reconstructed to their disposition—150 Ma: University of the Witwatersrand and AAPG, oversized map, scale 1:10,000,000, 2 sheets.

Dias, J. L., W. Guazelli, and A. J. Catto, 1987, Integração do arcabouço estrutural da Bacia de Campos com o embasamento pré-Cambriano adjacente: Anais do I Simpósio de Geologia Regional RJ-ES, Rio de Janeiro, p. 189–197.

Dias, J. L., J. Q. de Oliveira, and J. C. Vieira, 1988, Sedimentological and stratigraphic analysis of the Lagoa Feia Formation, rift phase of Campos Basin, offshore Brazil: Revista Brasileira de Geociências, v. 18, p. 252–260.

Dias, J. L., J. C. Scarton, L. R. Guardado, F. R. Esteves, and M. Carminatti, 1990, Aspectos da evolução tectono-sedimentar e a ocorrência de hidrocarbonetos na Bacia de Campos, *in* G. P. Raja Gabaglia and E. J. Milani, eds., Origem e evolução de bacias sedimentares: Rio de Janeiro, Petrobrás p. 333–360.

DNPM (Departamento Nacional de Produção Mineral), 1981, Mapa geológico do Brasil e da área oceânica adjacente incluindo depósitos minerais: Ministério de Minas e Energia, Departamento Nacional de Produção Mineral, Brasília, scale 1:2,500,000, 4 sheets.

Ebinger, C. J., and N. H. Sleep, 1998, Cenozoic magmatism throughout East Africa resulting from impact of a single plume: Nature, v. 395, p. 788–791.

Erlank, A. J., J. S. Marsh, A. R. Duncan, R. M. Miller, C. J. Hawkesworth, P. J. Betton, and D. C. Rex, 1984, Geochemistry and petrogenesis of the Etendeka volcanic rocks from South West Africa/Namibia: Geological Society of South Africa Special Publication, v. 13, p. 195–246.

Fichler, C., E. Rundhovde, O. Olesen, B. M. Sæther, H. Rueslatten, E. Lundin, and A. G. Doré, 1999, Regional tectonic interpretation of image enhanced gravity and magnetic data covering the mid-Norwegian shelf and adjacent mainland: Tectonophysics, v. 306, p. 183–197.

Figueiredo, A. M. F. de, 1985, Geologia das bacias brasileiras, *in* E. J. Viro, ed., Avaliação de Formacões no Brasil: Rio de Janeiro, Schlumberger, p. I-1–I-38.

Françolin, J. B. L., and P. Szatmari, 1987, Mecanismo de rifteamento da porção oriental da margem norte brasileira: Revista Brasileira de Geociências, v. 17, p. 196–207.

Françolin, J. B. L., P. R. Cobbold, and P. Szatmari, 1994, Faulting in the Early Cretaceous Rio do Peixe basin (NE Brazil) and its significance for the opening of the Atlantic: Journal of Structural Geology, v. 16, p. 647–661.

Gallagher, K., and C. J. Hawkesworth, 1994, Mantle plumes, continental magmatism and asymmetry in the South Atlantic: Earth and Planetary Science Letters, v. 123, p. 105–117.

Gibbs, A. D., 1984, Structural evolution of extensional basin margins: Journal of the Geological Society, v. 141, p. 609–620.

Gibson, S. A., R. N. Thompson, O. H. Leonardos, A. P. Dickin, and J. G. Mitchell, 1995, The Late Cretaceous impact of the Trindade mantle plume: evidence from large-volume, mafic, potassic magmatism in SE Brazil: Journal of Petrology, v. 36, p. 189–229.

Gladczenko, T. P., K. Hinz, O. Eldholm, H. Meyer, S. Neben, and J. Skogseid, 1997, South Atlantic volcanic margins: Journal of the Geological Society, v. 154, p. 465–470.

Guardado, L. R., L. A. P. Gamboa, and C. F. Lucchesi, 1990, Petroleum geology of the Campos Basin, a model for a producing Atlantic-type basin, *in* J. D. Edwards and P. A. Santogrossi, eds., Divergent/passive margin basins: AAPG Memoir 48, p. 3–79.

Hasui, Y., C. D. R. Carneiro, and A. M. Coimbra, 1975, The Ribeira folded belt: Revista Brasileira de Geociências, v. 5, p. 257–266.

Hawkesworth, C. J., K. Gallagher, M. Mantovani, D. W. Peate, M. Regelous, and W. Rogers, 1992, Paraná magmatism and the opening of the South Atlantic, *in* B. C. Storey, T. Alabaster, and R. J. Pankhurst, eds., Magmatism and the causes of continental break-up: Geological Society Special Publication, v. 68, p. 221–240.

Herz, N., 1977, Timing of spreading in the South Atlantic: information from Brazilian alkaline rocks: Geological Society of America Bulletin, v. 88, p. 101–112.

Hinz, K., S. Neben, B. Schreckenberger, H. A. Roeser, M. Block, K. Gonçalves de Souza, and H. Meyer, 1999, The Argentine continental margin north of 48°S: sedimentary successions, volcanic activity during breakup: Marine and Petroleum Geology, v. 16, p. 1–25.

IHS [Petroconsultants] Energy Group, 2001, International oil & gas activity database: Geneva, Switzerland, Accessed June 14, 2001.

Le Pichon, X., and D. E. Hayes, 1971, Marginal offsets, fracture zones and the early opening of the South Atlantic: Journal of Geophysical Research, v. 76, p. 6283–6293.

Leyden, R., 1976, Salt distribution and crustal models for the eastern Brazilian margin: Anais da Academia Brasileira de Ciências, v. 48, p. 159–168.

Leyden, R., W. J. Ludwig, and M. Ewing, 1971, Structure of the continental margin of Punta del Este, Uruguay, and Rio de Janeiro, Brazil: AAPG Bulletin, v. 55, p. 2161–2173.

Light, M. P. R., M. P. Maslanyj, and N. L. Banks, 1992, New geophysical evidence for extensional tectonics on the divergent margin offshore Namibia, *in* B. C. Storey, T. Alabaster, and R. J. Pankhurst, eds., Magmatism and the causes of continental break-up: Geological Society Special Publication, v. 68, p. 257–270.

Macedo, J. M., 1989, Evolução tectônica da Bacia de Santos e áreas continentais adjacentes: Boletim de Geociências da Petrobrás, v. 3, p. 159–173.

Machado, R., and I. Endo, 1993, Cinturão de cisalhamênto Atlântico; un exemplo de tectônica transpressional Neoproterozóica: Anais do IV Simpósio Nacional de Estudos Tectônicos, Sociedade Brasileira de Geología, Boletim 12, p. 189–191.

Machado, N., C. Valladares, M. Heilbron, and C. Valeriano, 1996, U-Pb geochronology of the central Ribeira belt (Brazil) and implications for the evolution of the Brazilian orogeny: Precambrian Research, v. 79, p. 347–361.

Matos, R. M. D. de, 1992, The northeast Brazilian rift system: Tectonics, v. 11, p. 766–791.

Mello, M. R., N. Telnaes, P. C. Gaglianone, M. I. Chicarelli, S. C. Brassell, and J. R. Maxwell, 1988, Organic geochemical characterisation of depositional palaeoenvironments of source rocks and oils in Brazilian marginal basins, *in* L. Matavelli and L. Novelli, eds., Advances in organic geochemistry 1987: Organic Geochemistry, v. 13, p. 31–45.

Mello, M. R., E. A. M. Kotsoukos, M. B. Hart, S. C. Brassell, and J. R. Maxwell, 1989, Late Cretaceous anoxic events in the Brazilian continental margin: Organic Geochemistry, v. 14, p. 529–542.

Mello, M. R., E. A. M. Kotsoukos, W. U. Mohriak, and G. Bacoccoli, 1994, Selected petroleum systems in Brazil, *in* L. B. Magoon and W. G. Dow, eds., The petroleum system—from source to trap: AAPG Memoir 60, p. 499–512.

Mello, M. R., N. Telnaes, and J. R. Maxwell, 1995, The hydrocarbon source potential in the Brazilian marginal basins: a geochemical and paleoenvironmental assessment, *in* A. Huc, ed., Paleogeography, paleoclimate, and source rocks: AAPG Studies in Geology 40, p. 233–272.

Milani, E. J., and I. Davison, 1988, Basement control and transfer tectonics in the Recôncavo-Tucano-Jatobá Rift, northeast Brazil: Tectonophysics, v. 154, p. 41–70.

Mizusaki, A. M. P., A. Thomaz Filho, and J. Valença, 1988, Volcano-

sedimentary sequence of Neocomian age in Campos Basin (Brazil): Revista Brasileira de Geociências, v. 18, p. 247–251.
Mizusaki, A. M. P., R. Petrini, G. Bellieni, P. Comin-Chiramonti, J. Dias, A. De Min, and E. M. Piccirillo, 1992, Basalt magmatism along the passive continental margin of SE Brazil (Campos Basin): Contributions to Mineralogy and Petrology, v. 111, p. 143–160.
Mohriak, W. U., and J. F. Dewey, 1987, Deep seismic reflectors in the Campos Basin, offshore Brazil: Geophysical Journal of the Royal Astronomical Society, v. 89, p. 133–140.
Mohriak, W. U., R. Hobbs, and J. F. Dewey, 1990a, Basin-forming processes and the deep structure of the Campos Basin, offshore Brazil: Marine and Petroleum Geology, v. 7, p. 94–112.
Mohriak, W. U., M. R. Mello, J. F. Dewey, and J. R. Maxwell, 1990b, Petroleum geology of the Campos Basin, offshore Brazil, *in* J. Brooks, ed., Classic petroleum provinces: Geological Society Special Publication, v. 50, p. 119–141.
Mohriak, W. U., et al., 1995, Salt tectonics and structural styles in the deep-water province of the Cabo Frio region, Rio de Janeiro, Brazil, *in* M. P. A. Jackson, D. G. Roberts, and S. Snelson, eds., Salt tectonics: a global perspective: AAPG Memoir 65, p. 273–304.
Morgan, W. J., 1981, Hotspot tracks and the opening of the Atlantic and Indian Ocean, *in* C. Emiliani, ed., The sea: v. 7: the oceanic lithosphere: New York, Wiley, p. 443–487.
Morley, C. K., R. A. Nelson, T. L. Patton, and S. G. Munn, 1990, Transfer zones in the East African rift system and their relevance to hydrocarbon exploration in rifts: AAPG Bulletin, v. 74, p. 1234–1253.
Müller, R. D., J.-Y. Royer, and L. A. Lawver, 1993, Revised plate motions relative to hotspots from combined Atlantic and Indian Ocean hotspot tracks. Geology, v. 21, p. 275–278.
Nürnberg, D., and R. D. Müller, 1991, The tectonic evolution of the South Atlantic from Late Jurassic to present: Tectonophysics, v. 191, p. 27–53.
O'Connor, J. M., and R. A. Duncan, 1990, Evolution of the Walvis Ridge—Rio Grande Rise hotspot system: implications for African and South American plate motions over plumes: Journal of Geophysical Research, v. 95, p. 17474–17502.
Ojeda, H. A., 1982, Structural framework, stratigraphy and evolution of Brazilian marginal basins: AAPG Bulletin, v. 66, p. 732–749.
Peate, D. W., 1997, The Paraná-Etendeka province, *in* J. J. Mahoney and M. F. Coffin, eds., Large igneous provinces: American Geophysical Union Geophysical Monograph Series, v. 100, p. 217–245.
Pereira, M. J., and F. J. Feijó, 1994, Bacia de Santos: Boletim de Geociências da Petrobrás, v. 8, p. 219–234.
Pereira, M. J., and J. M. Macedo, 1990, A Bacia de Santos: perspectivas de uma nova província petrolífera na plataforma continental sudeste brasileira: Boletim de Geociências da Petrobrás, v. 4, p. 3–11.
Rabinowitz, P. D., and J. LaBrecque, 1979, The Mesozoic South Atlantic Ocean and evolution of its continental margins: Journal of Geophysical Research, v. 84, p. 5973–6002.
Radambrasil, 1981, Projeto RADAMBRASIL: mapa geológico: Ministerio das Minas e Energia, Brasilia, scale 1:100,000, 1 sheet.
Rangel, H. D., F. A. L. Martins, F. R. Esteves, and F. J. Feijó, 1994, Bacia de Campos: Boletim de Geociências da Petrobrás, v. 8, p. 203–217.
Renne, P. R., M. Ernesto, I. G. Pacca, R. S. Coe, J. M. Glen, M. Prévot, and M. Perrin, 1992, The age of Paraná flood volcanism, rifting of Gondwanaland and the Jurassic–Cretaceous boundary: Science, v. 258, p. 975–979.
Renne, P. R., K. Deckart, M. Ernesto, G. Féraud, and E. M. Piccirillo, 1996, Age of the Ponta Grossa dike swarm (Brazil) and implications to Paraná flood volcanism: Earth and Planetary Science Letters, v. 144, p. 199–212.
Rocha Campos, A. C., U. G. Cordani, K. Kawashita, H. M. Sonohi, and I. K. Sonohi, 1988, Age of the Paraná flood volcanism, *in* The Mesozoic flood volcanism of the Paraná basin: petrogenetic and geophysical aspects: São Paulo, Instituto Astronômico e Geofísico da Universidade de São Paulo, p. 24–45.
Rosendahl, B. R., 1987, Architecture of continental rifts with special reference to East Africa: Annual Reviews of Earth and Planetary Science, v. 15, p. 445–503.
Sandwell, D. T., and W. H. F. Smith, 1995, Marine gravity anomaly from satellite altimetry: La Jolla, California, Geological Data Center, Scripps Institute of Oceanography, oversized plate.
Schobbenhaus, C., D. A. Campos, G. R. Derze, and H. E. Asmus, 1981, Geologic map of Brazil and adjoining ocean floor including mineral deposits: Ministerio de Minas e Energia, Brasilia, Brazil, scale 1:2,500,000, 4 sheets.
Sibuet, J. C., W. W. Hay, A. Prunier, L. Montadert, K. Hinz, and J. Fritsch, 1984, The early evolution of the South Atlantic Ocean: role of the rifting episode, *in* R. Amidei, ed., Initial reports of the Deep Sea Drilling Project covering Leg 75 of the cruises of the drilling vessel *Glomar Challenger*, Walvis Bay, South Africa to Recife, Brazil, July–September 1980, College Station, Texas, Texas A&M University, Ocean Drilling Program, v. 75, p. 469–481.
Stewart, K., S. Turner, S. Kelley, C. J. Hawkesworth, L. Kirstein, and M. S. M. Mantovani, 1996, 3-D ^{40}Ar-^{39}Ar geochronology in the Paraná flood basalt province: Earth and Planetary Science Letters, v. 143, p. 95–110.
Szatmari, P., E. Milani, M. Lana, J. Conceição, and A. Lobo, 1985, How South Atlantic rifting affects Brazilian oil reserves: Oil & Gas Journal, v. 83, no. 2 (January 14), p. 107–113.
Thompson, R. N., S. A. Gibson, J. G. Mitchell, A. P. Dickin, O. H. Leonardos, J. A. Brod, and J. C. Greenwood, 1998, Migrating Cretaceous–Eocene magmatism in the Serra do Mar alkaline province, SE Brazil: melts from the deflected Trindade mantle plume?: Journal of Petrology, v. 39, p. 1493–1526.
Trindade, L. A. F., J. L. Dias, and M. R. Mello, 1995, Sedimentological and geochemical characterization of the Lagoa Feia Formation, rift phase of the Campos Basin, Brazil, *in* B. J. Katz, ed., Petroleum source rocks: New York, Springer-Verlag, p. 149–165.
Turner, S. P., M. Regelous, S. Kelley, C. J. Hawkesworth, and M. S. M. Mantovani, 1994, Magmatism and continental breakup in the South Atlantic: high precision ^{40}Ar-^{39}Ar geochronology: Earth and Planetary Science Letters, v. 121, p. 333–348.
Turner, S. P., C. J. Hawkesworth, K. Gallagher, K. Stewart, D. W. Peate, and M. S. M. Mantovani, 1996, Mantle plumes, flood basalts and thermal models for melt generation beneath continents: assessment of a conductive heating model and application to the Paraná: Journal of Geophysical Research, v. 101, p. 11503–11518.
Unrug, R., ed., 1996, Geodynamic map of Gondwana Supercontinent assembly: Bureau de Recherches Géologiques et Minières, Orléans, France, scale 1 :10,000,000, 1 sheet.
White, R. S., and D. P. McKenzie, 1989, Magmatism at rift zones: the generation of volcanic continental margins and flood basalts: Journal of Geophysical Research, v. 94, p. 7685–7729.
Williams, B. G., and R. J. Hubbard, 1984, Seismic stratigraphic framework and depositional sequences in the Santos Basin, Brazil: Marine and Petroleum Geology, v. 1, p. 90–104.
Wilson, M., 1992, Magmatism and continental rifting during the opening of the South Atlantic Ocean: a consequence of Lower Cretaceous super-plume activity?, *in* B. C. Storey, T. Alabaster,

and R. J. Pankhurst, eds., Magmatism and the causes of continental break-up: Geological Society Special Publication, v. 68, p. 241–255.

Woolley, A. R., 1987, Alkaline rocks and carbonatites of the world: part I: North and South America: London, British Museum (Natural History), 216 p.

Zalán, P. V., S. Wolff, M. A. M. Astolfi, I. S. Vieira, J. C. J. Conceição, V. T. Appi, E. V. S. Neto, J. R. Cerqueira, and A. Marques, 1990a, The Paraná basin, Brazil, *in* M. W. Leighton, D. R. Kolata, D. F. Oltz, and J. J. Eidel, eds., Interior cratonic basins: AAPG Memoir 51, p. 681–708.

Zalán, P. V., S. Wolff, J. C. J. Conceição, M. A. M. Astolfi, I. S. Vieira, V. T. Appi, E. V. S. Neto, and O. A. Zanotto, 1990b, Bacia do Paraná, *in* G. P. Raja Gabaglia and E. J. Milani, eds., Origem e evolução de bacias sedimentares: Rio de Janeiro, Petrobrás, p. 135–168.

Zalán, P. V., S. Wolff, J. C. J. Conceição, A. Marques, M. A. M. Astolfi, I. S. Vieira, V. T. Appi, O. A. Zanotto, and A. Marques, 1991, Tectonics and sedimentation of the Paraná basin: Proceedings, Gondwana VII, Universidade de São Paulo, p. 83–117.

Reservoir Distribution on a Salt-Influenced Deep-Water Slope: Santos Basin, Offshore Brazil*

Clara R. Rodriguez[1], Christopher A-L. Jackson[2], Atle Rotevatn[3], Rebecca E. Bell[2], and Malcolm Francis[4]

Search and Discovery Article #11049 (2018)**
Posted January 29, 2018

*Adapted from oral presentation given at AAPG/SEG 2017 International Conference and Exhibition, London, England, October 15-18, 2017
**Datapages © 2018 Serial rights given by author. For all other rights contact author directly.

[1]Basins Research Group (BRG), Department of Earth Science and Engineering, Imperial College London, United Kingdom (c.rodriguez11@imperial.ac.uk)
[2]Basins Research Group (BRG), Department of Earth Science and Engineering, Imperial College London, United Kingdom
[3]Department of Earth Science, University of Bergen, Bergen, Norway
[4]WesternGeco, Schlumberger, Schlumberger House, Gatwick, United Kingdom

Abstract

Salt tectonics controls reservoir distribution, trapping development, and hydrocarbon migration in salt-influenced basins. It is therefore critical for the oil industry to understand how sediment interacts with salt in such basins. Previous studies in the Santos Basin, offshore Brazil suggest that most clastic sediment was trapped behind the 'Albian Gap', a salt-controlled, intra-slope depocentre. As a result, no significant post-salt deep-water exploration has been conducted on the assumption that little or no clastic sediment was dispersed basinward. In this study we challenge this notion by integrating 3D seismic and borehole data to determine the distribution and types of deep-water reservoirs of the previously underexplored post-salt sequence. We identify six main seismic facies types within the post-salt sequence, which we relate to the following deep-water depositional elements: (i) channels, (ii) levees, (iii) lobes, (iv) mass-transport complexes (MTCs), and (v) background deposits. We recognise three main tectono-stratigraphic phases during deposition of the post-salt sequence. During the first phase (Turonian-to-middle Campanian), channels, lobes, and MTCs were confined within proximal minibasins and to the hanging walls of landward-dipping, salt-detached listric faults. During the second phase (middle Campanian-to-Maastrichtian), channels and lobes eventually filled and bypassed proximal minibasins, with deposition then occurring further downslope in distal minibasins. In these distal minibasins, salt-induced syn-depositional seabed deformation, caused: (i) channel diversion around salt-cored highs; (ii) asymmetric levee deposition, and uplift and rotation of levees on minibasin flanks; (iii) lateral channel migration, expressed in the form of lateral accretion packages (LAPs); and (iv) confinement of lobes. During the final phase (Maastrichtian-to-middle Oligocene), continued rise of proximal salt walls dissected previously deposited deep-water systems. In addition, diapir- and shelf-edge sourced MTCs filled the minibasins, and locally capped and spilled across flanking salt walls. These results have implications for post-salt hydrocarbon prospectivity in the Santos Basin, with a range of reservoir types and trapping styles being developed in this previously underexplored interval. In addition, the results of our study can be applied to other basins, where syndepositional salt-induced seabed deformation controls reservoir deposition and architecture.

Selected References

Booth, J.R., M.C. Dean, A.E. DuVernay, and M.J. Styzen, 2003, Paleobathymetric Controls on the Stratigraphic Architecture and Reservoir Development of Confined Fans in the Auger Basin: Central Gulf of Mexico Slope: Marine and Petroleum Geology, v. 20, p. 563-586.

Clark, I.R., and J.A. Cartwright, 2011, Key Controls on Submarine Channel Development in Structurally Active Settings: Marine and Petroleum Geology, v. 28, p. 1333-1349.

Clark, I.R., and J.A. Cartwright, 2009, Interactions Between Submarine Channel Systems and Deformation in Deep-Water Fold Belts: Examples from the Levant Basin, Eastern Mediterranean Sea: Marine and Petroleum Geology, v. 26, p. 1465-1482.

Gee, M., and R. Gawthorpe, 2007, Early Evolution of Submarine Channels Offshore Angola Revealed by Three-Dimensional Seismic Data: Geological Society, London, Special Publications, v. 277, p. 223-235.

Gee, M., and R. Gawthorpe, 2006, Submarine Channels Controlled by Salt Tectonics: Examples from 3D Seismic Data Offshore Angola: Marine and Petroleum Geology, v. 23, p. 443-458.

Guerra, M.C.M., and J.R. Underhill, 2012, Role of Halokinesis in Controlling Structural Styles and Sediment Dispersal in the Santos Basin, Offshore Brazil: Geological Society, London, Special Publications, v. 363, p. 175-206.

Jackson, C.A-L., 2012, The Initiation of Submarine Slope Failure and the Emplacement of Mass Transport Complexes in Salt-Related Minibasins: A Three-Dimensional Seismic-Reflection Case Study from the Santos Basin, Offshore Brazil: Geological Society of America Bulletin, v. 124, p. 746-761.

Mayall, M., L. Lonergan, A. Bowman, S. James, K. Mills, T. Primmer, D. Pope, L. Rogers, and R. Skeene, 2010, The Response of Turbidite Slope Channels to Growth-Induced Seabed Topography: American Association of Petroleum Geologists Bulletin, v. 94, p. 1011-1030.

Modica, C.J., and E.R. Brush, 2004, Postrift Sequence Stratigraphy, Paleogeography, and Fill History of the Deep-Water Santos Basin, Offshore Southeast Brazil: American Association of Petroleum Geologists Bulletin, v. 88, p. 923-945.

Oluboyo, A., R. Gawthorpe, K. Bakke, and F. Hadler-Jacobsen, 2014, Salt Tectonic Controls on Deep-Water Turbidite Depositional Systems: Miocene, Southwestern Lower Congo Basin, Offshore Angola: Basin Research, v. 26, p. 597-620.

Imperial College London

Basins Research Group

Reservoir distribution on a salt-influenced deep-water slope: Santos Basin, Offshore Brazil

Clara R. Rodriguez[1*], Christopher A-L. Jackson[1], Atle Rotevatn[2], Rebecca E. Bell[1], Malcolm Francis[3]

[1] *Basins Research Group (BRG), Department of Earth Science and Engineering, Imperial College London, SW7 2BP, UK*

[2] *Department of Earth Science, University of Bergen, Allegaten 41, 5007 Bergen, Norway*

[3] *WesternGeco, Schlumberger, Schlumberger House, Gatwick, UK*

email: c.rodriguez11@imperial.ac.uk

Universitas Bergensis

CGG

Statoil

anp Agência Nacional do Petróleo

Schlumberger

Salt-dominated slopes

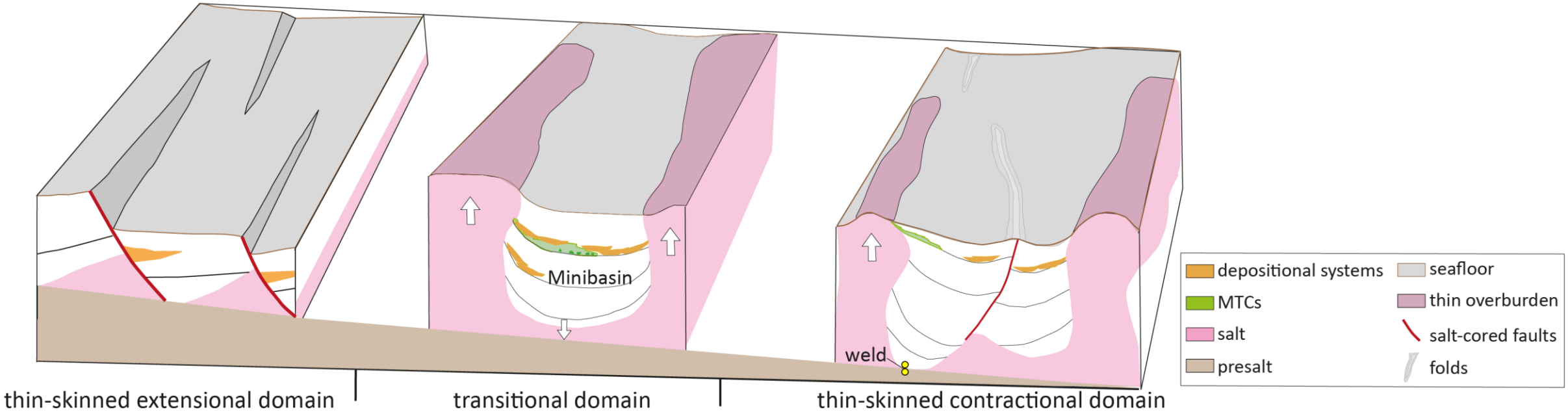

Salt-dominated slopes

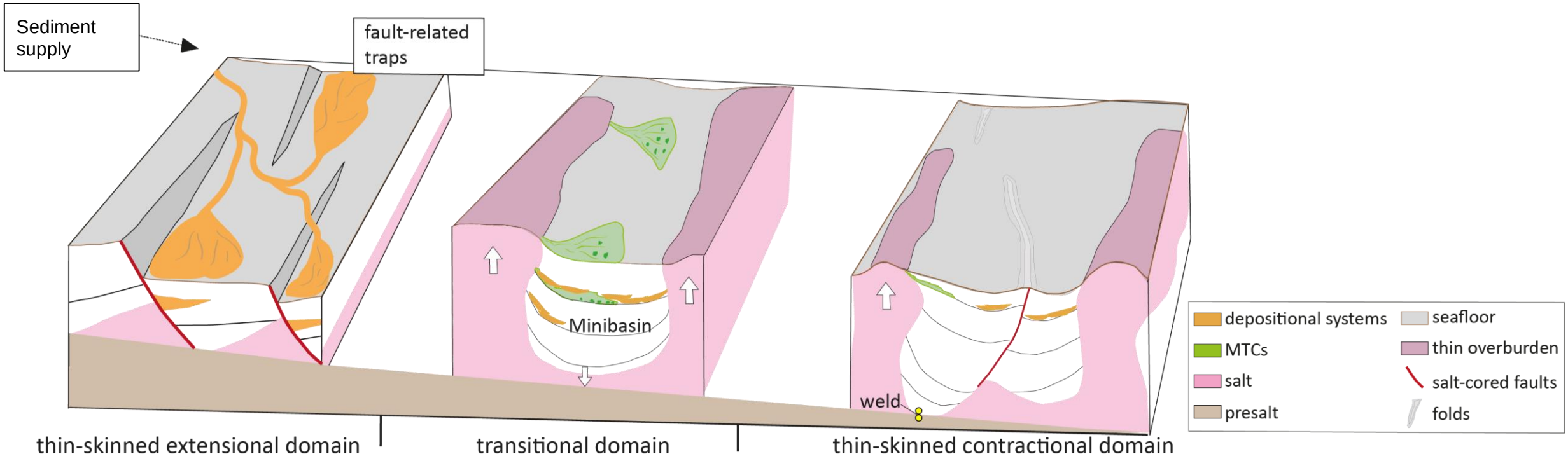

Salt-dominated slopes

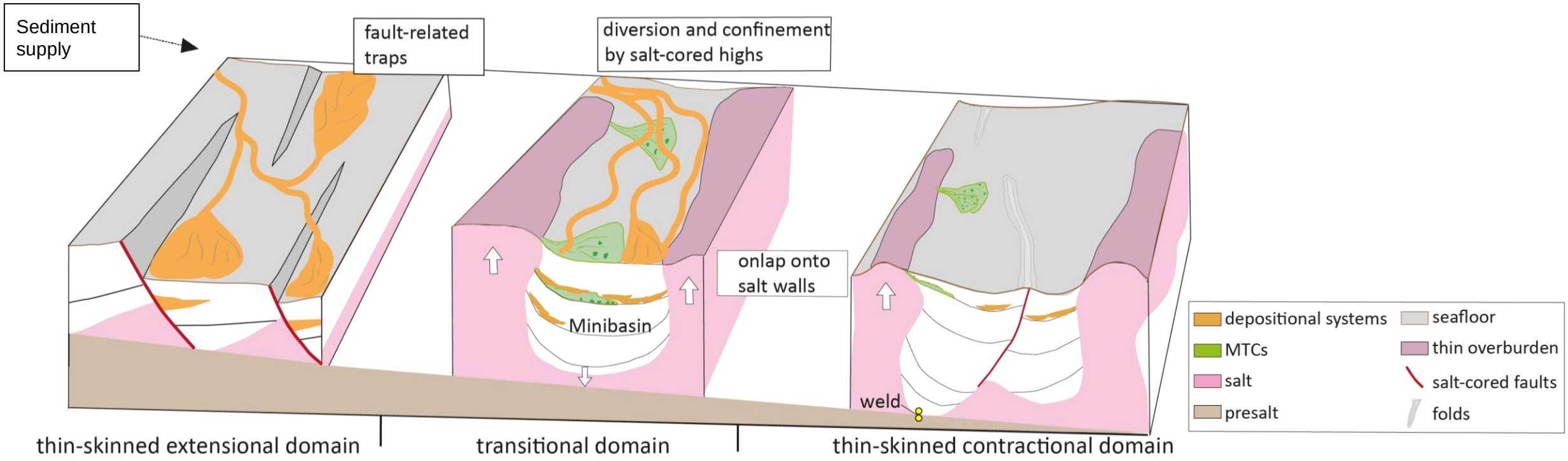

Salt-dominated slopes

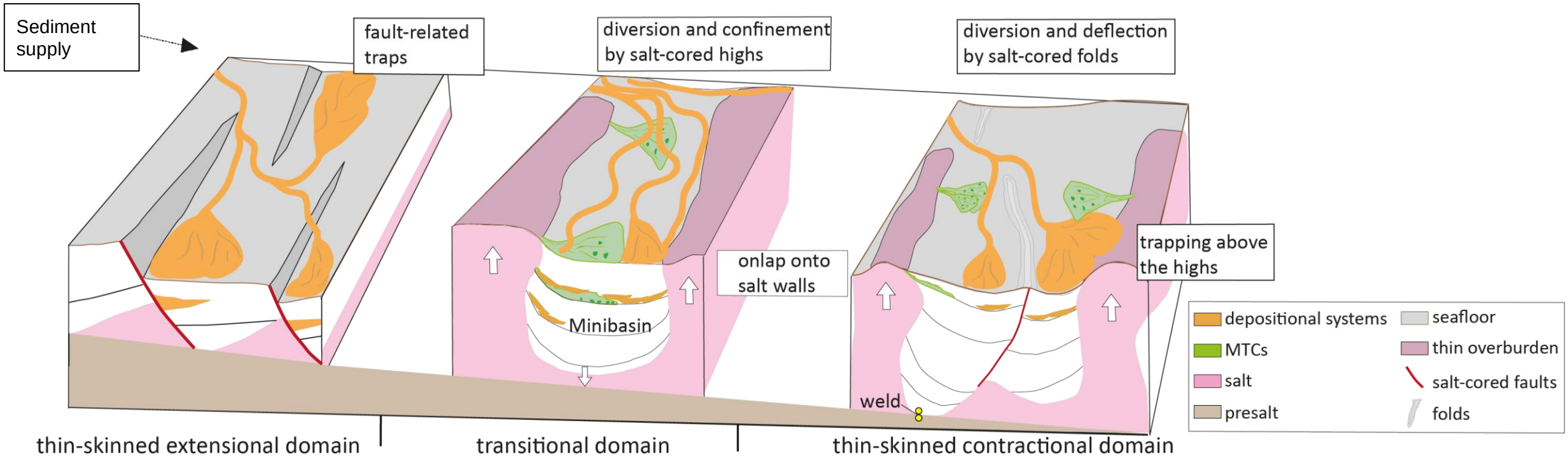

Key controls on reservoir distribution and architecture:

- Nature of deep-water depositional systems
- Salt-related structural styles along the slope
- Timing of deposition relative to salt-induced seafloor deformation

Salt-dominated slopes

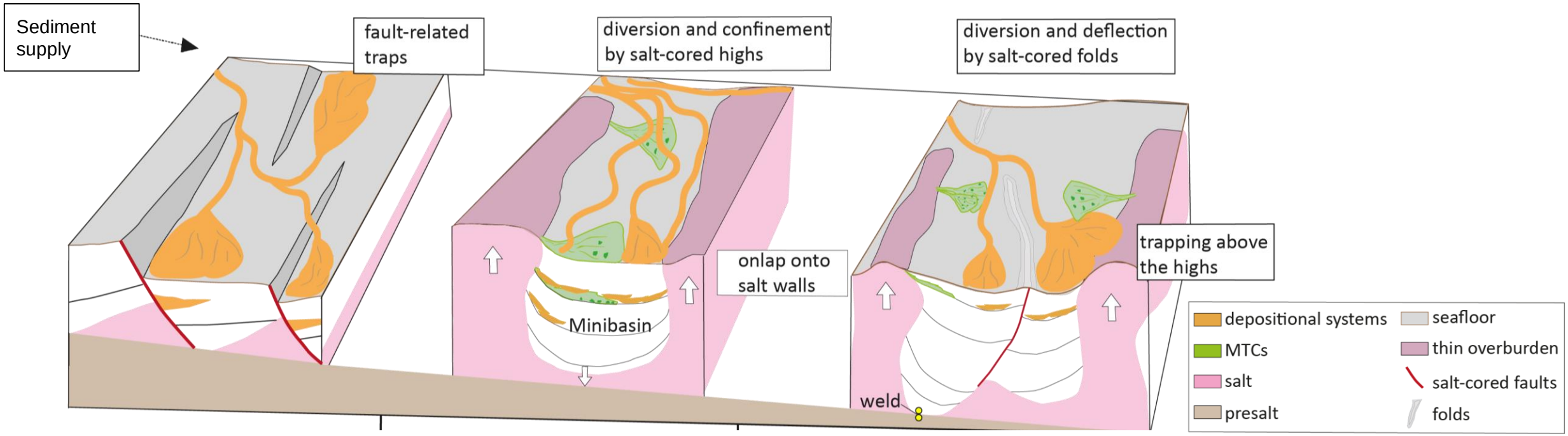

Santos Basin, offshore Brazil

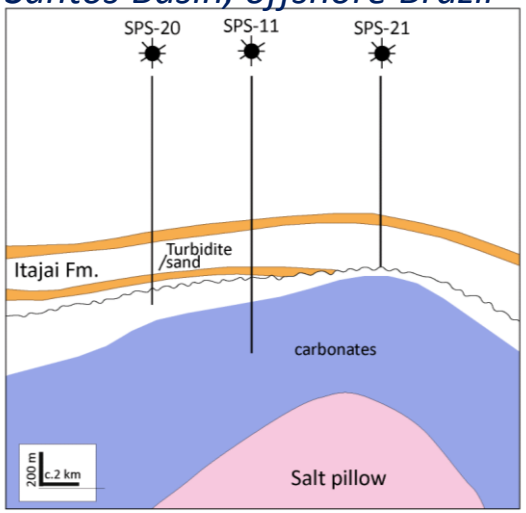

Modified from Riddle et al. (1995)

Auger Basin, Gulf of Mexico

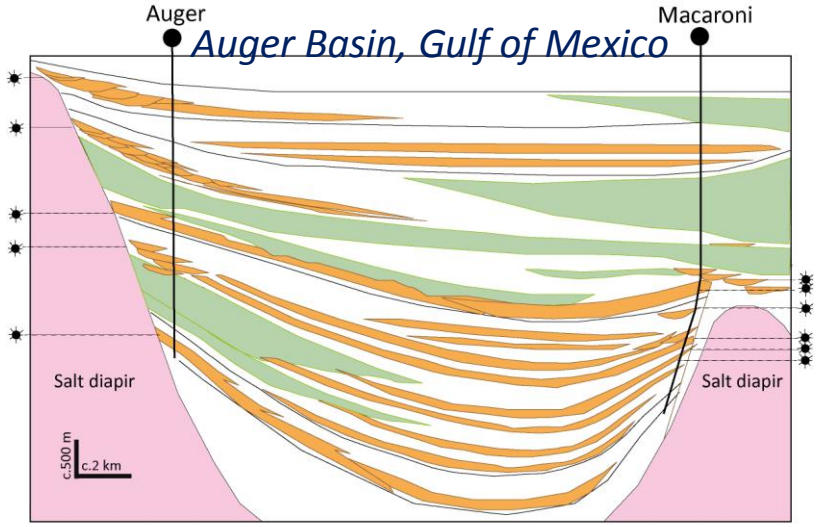

Modified from Booth et al. (2003)

Study area



Present-day topography and bathymetry

BRAZIL

Serra do Mantiqueira

Serra do Mar

Present-day Shelf margin

Campos Basin

3D outline

Santos Basin

(m)
2000
1200
400
0
-400
1200
2000
2800
3600

N

100 km

Dataset: 3D time-migrated seismic volume (20122 km^2)
8 wells (well markers, lithology)

Aim: Investigate evidence of deep-water clastic deposition
Document key controls on reservoir distribution and architecture.

Motivation

No exploration wells have targeted **post-salt**, **deep-water** reservoir in the **Santos Basin, offshore Brazil.**

Why?

Motivation

Post-salt clastic sediment trapped in proximal locations behind the Albian Gap

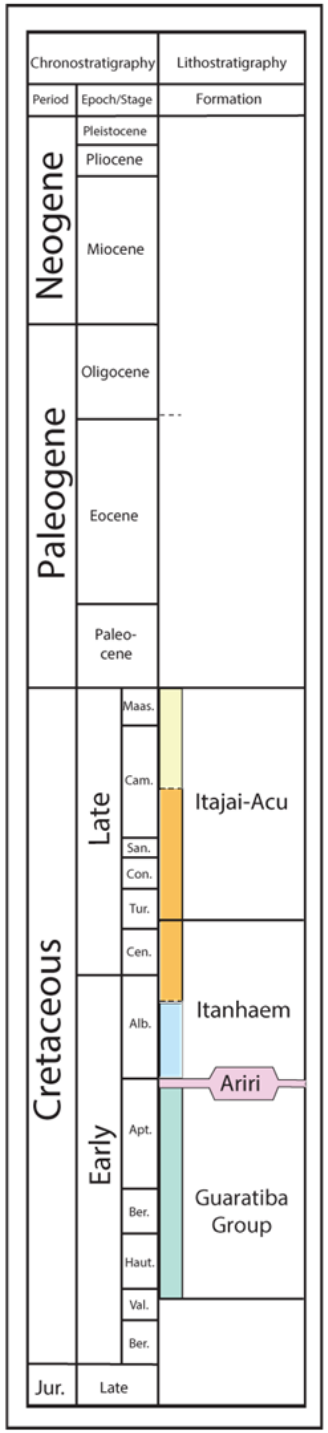

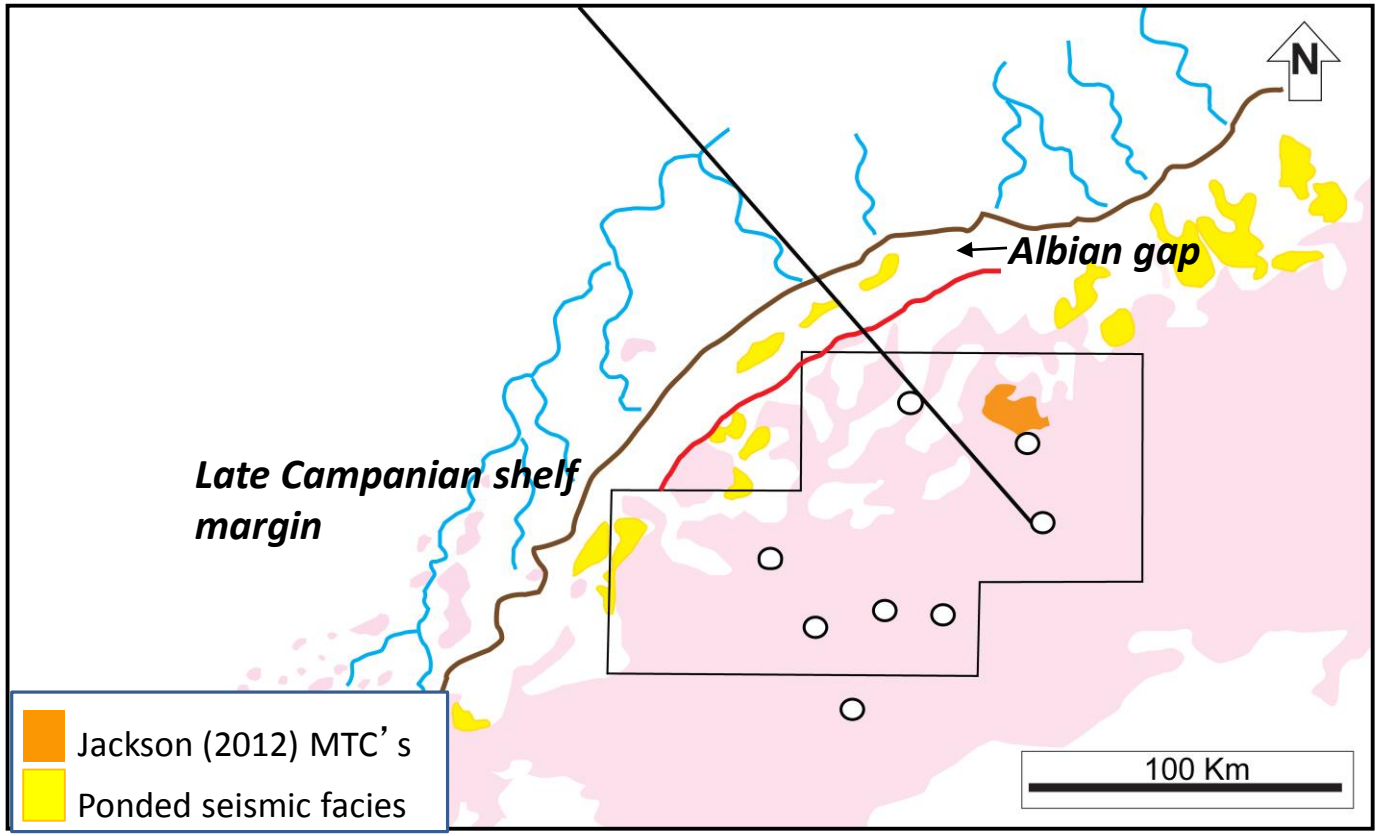

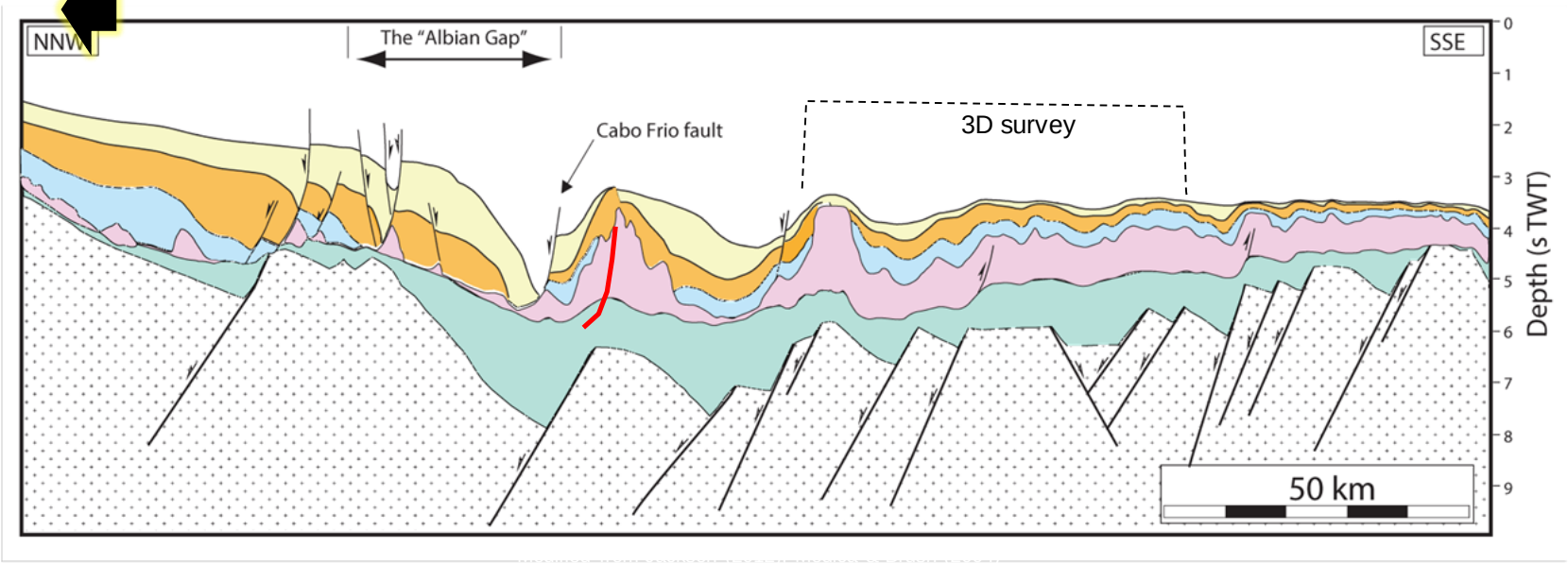

Motivation

Onshore uplift led to change in sediment supply to the North and towards the Campos Basin

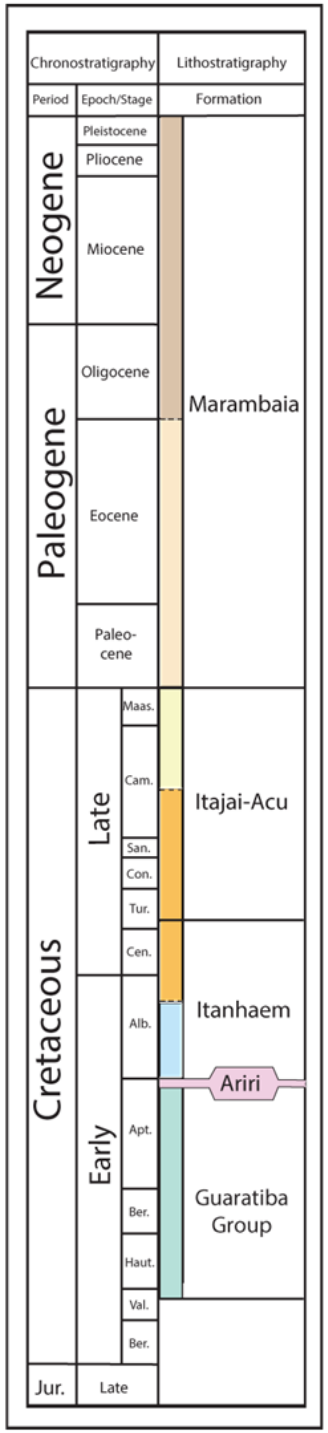

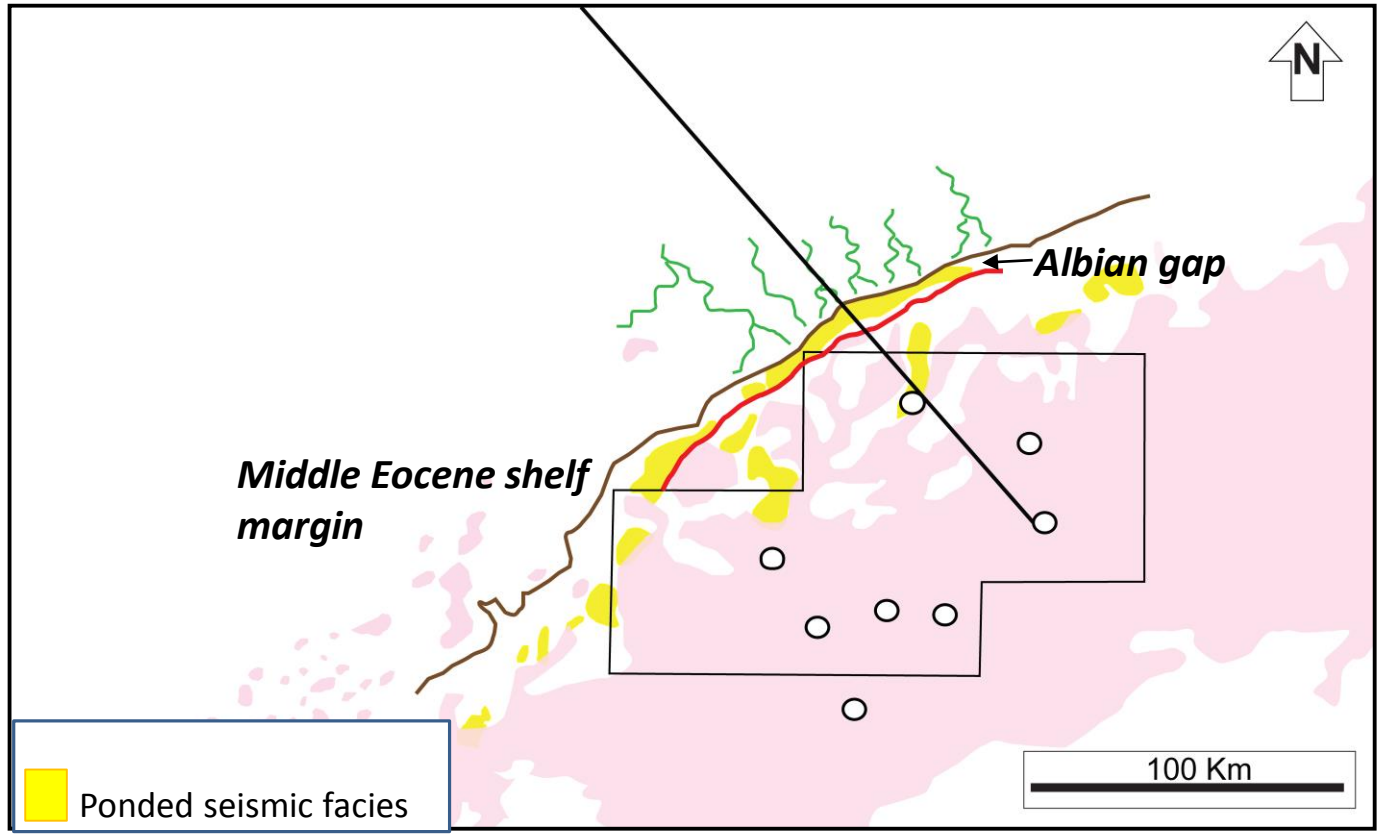

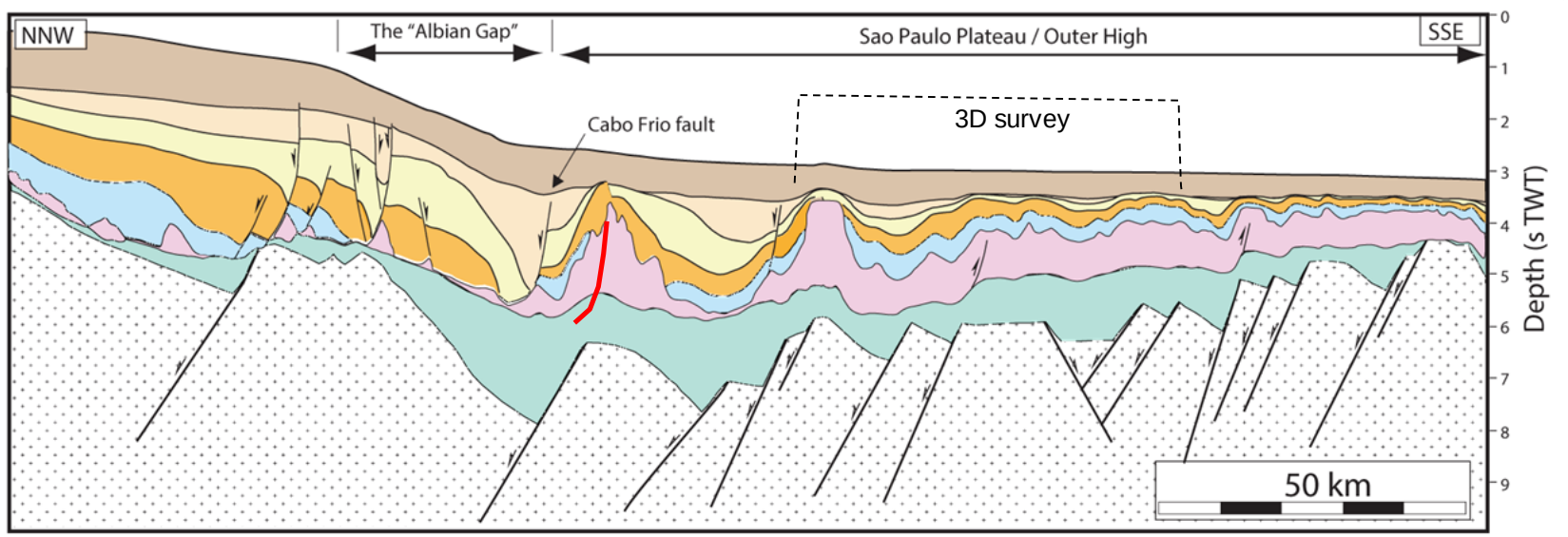

Motivation

Starved shelf. Failure of the shelf margin led to widespread MTCs deposition

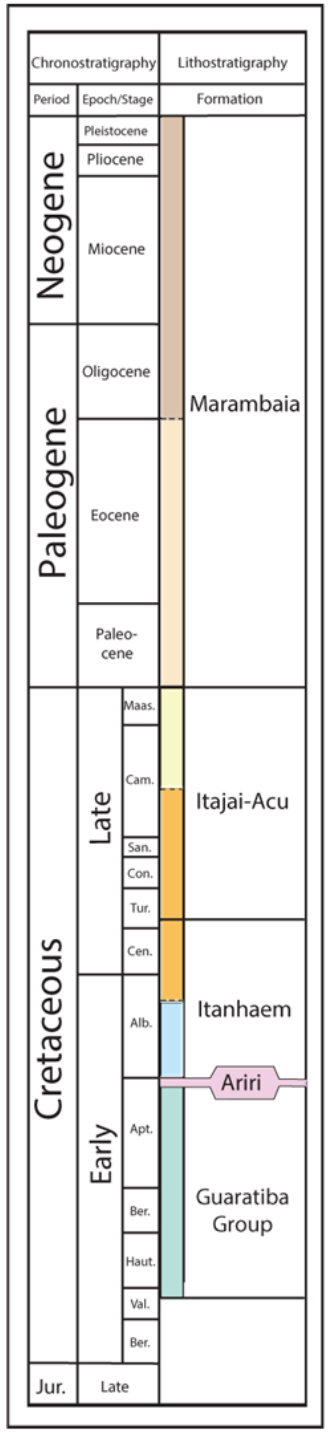

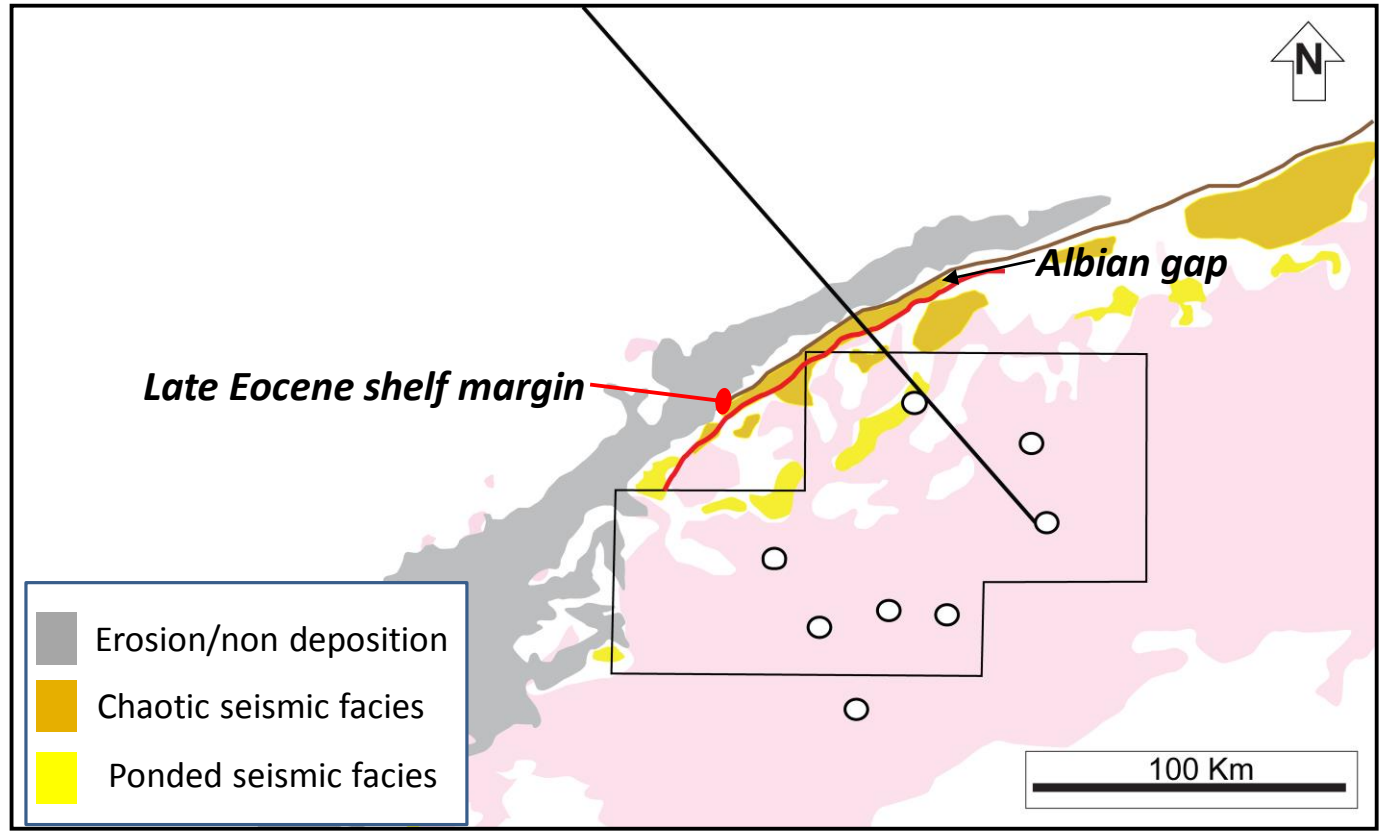

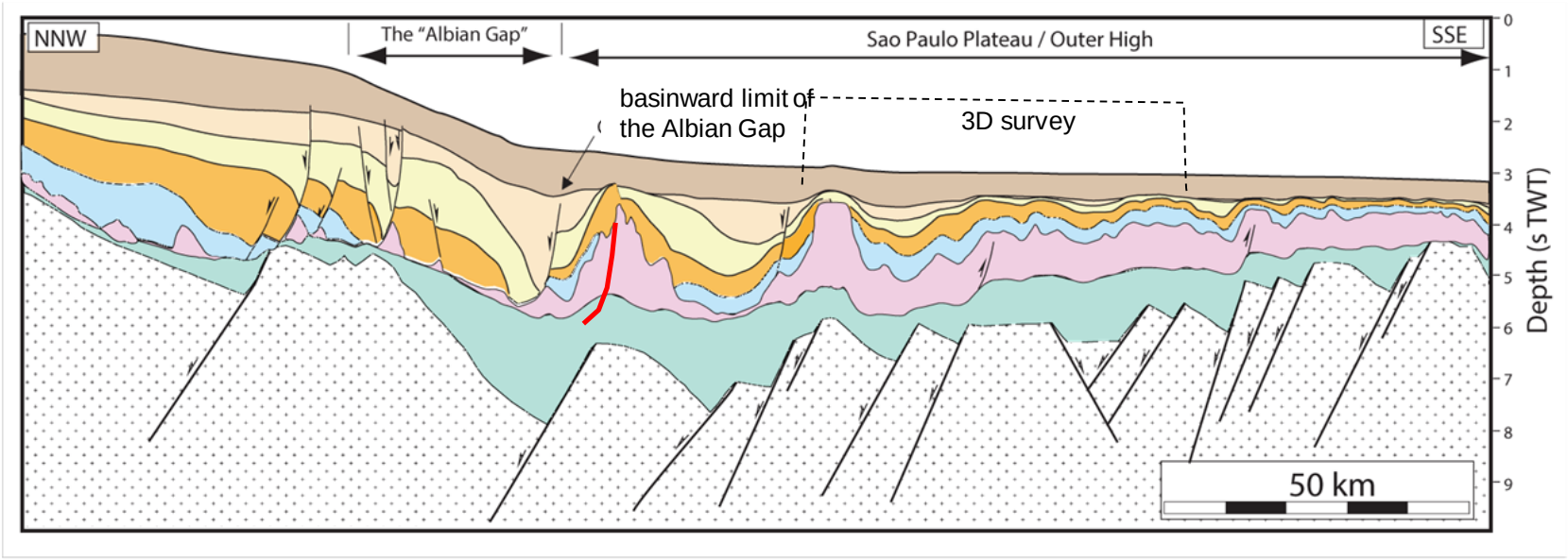

Minibasin structure and stratigraphy

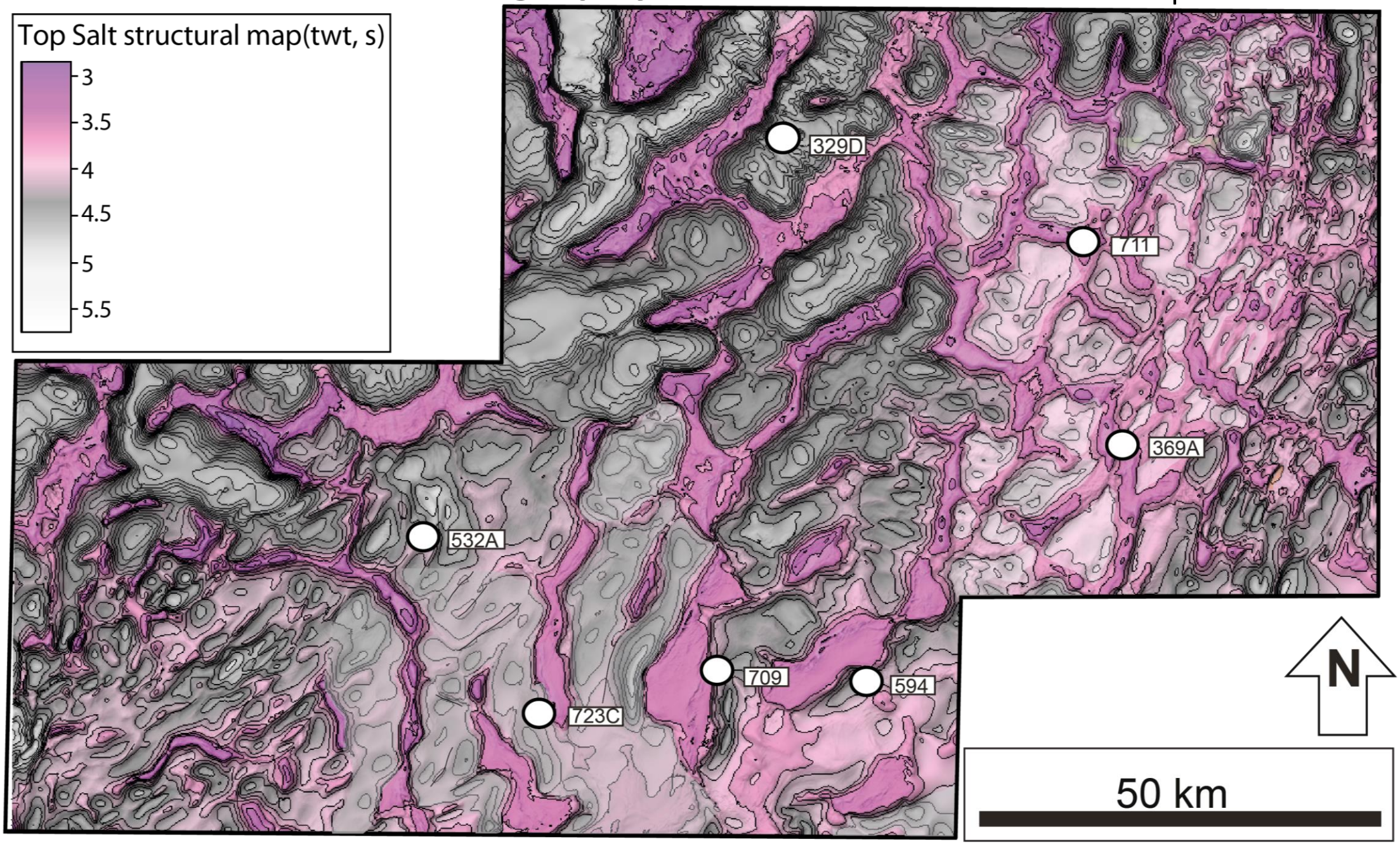

Minibasin structure and stratigraphy

Post-salt thickness distribution

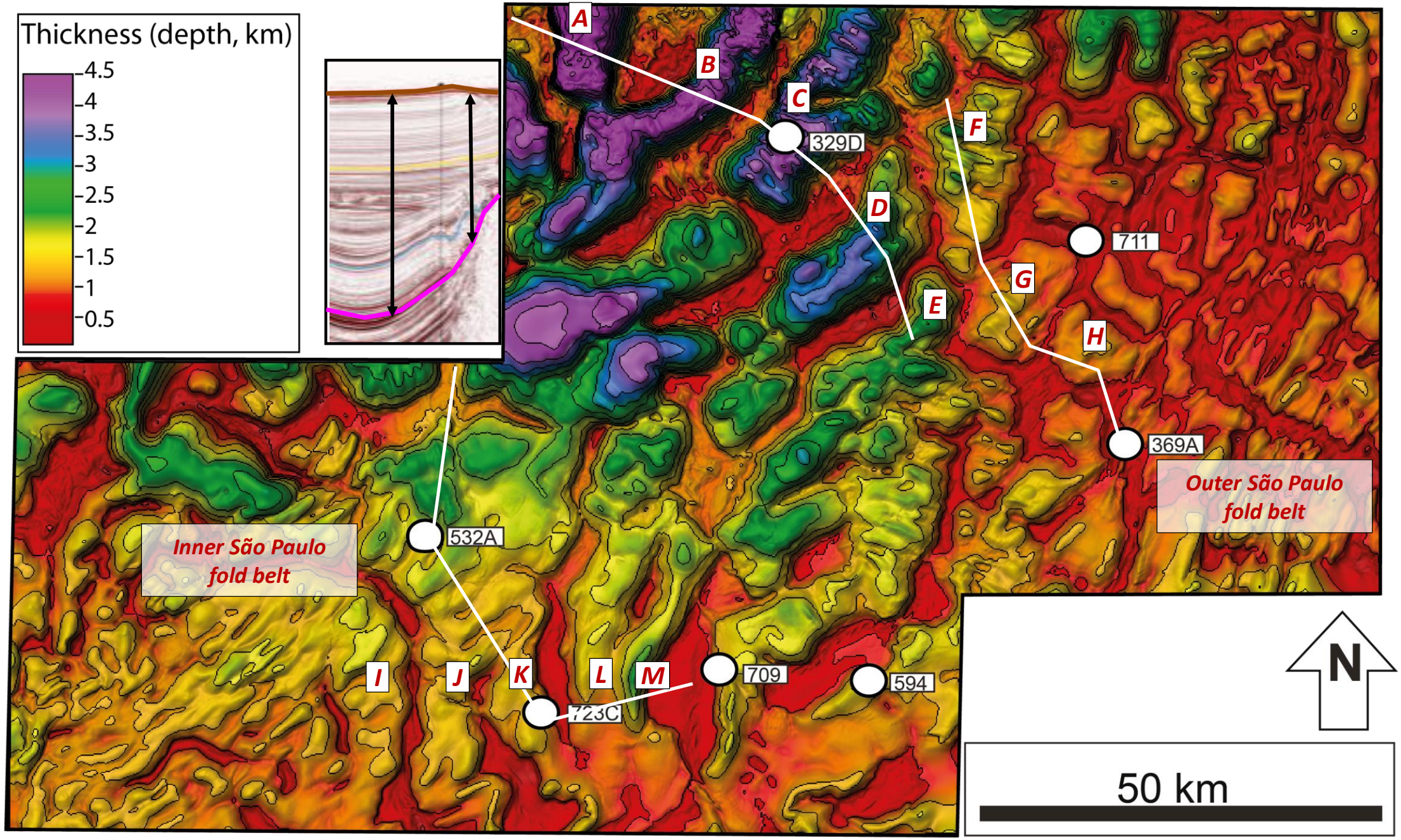

Proximal thick minibasins

> 2.5 km thick

Thin salt (< 500 m) or welded

Upright salt walls

Sandstone-rich units (c.45%)

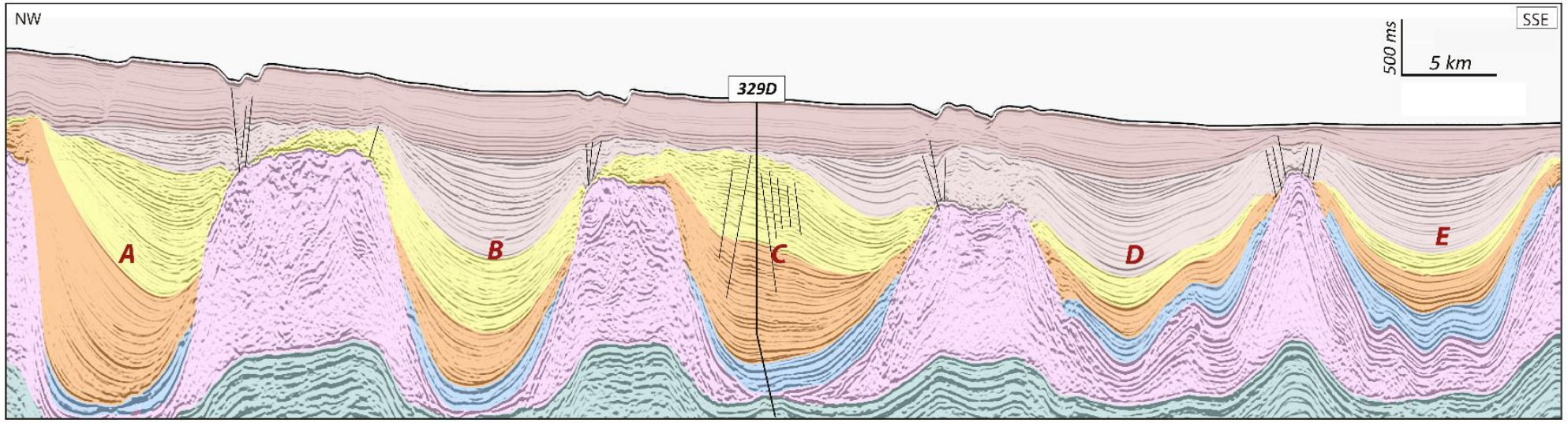

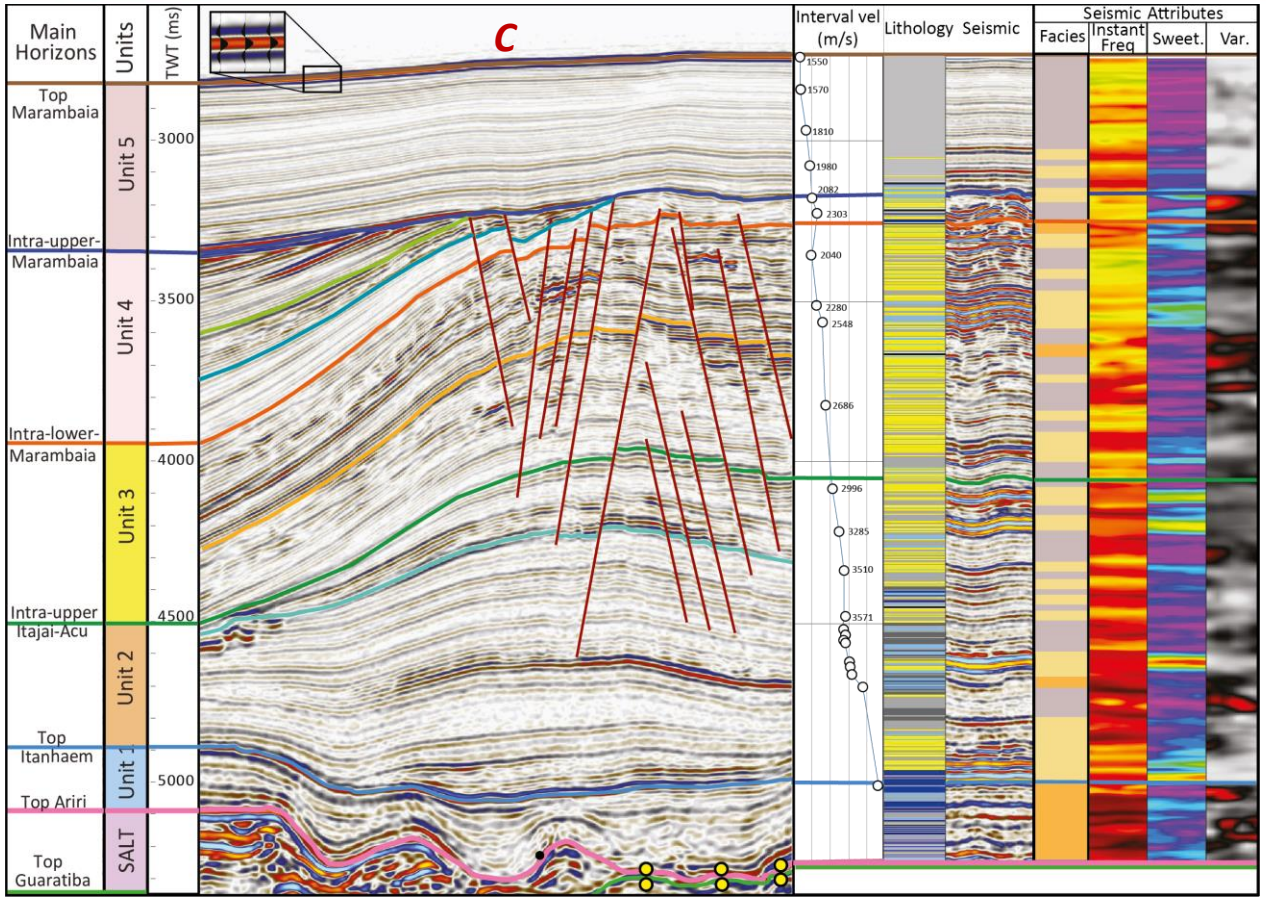

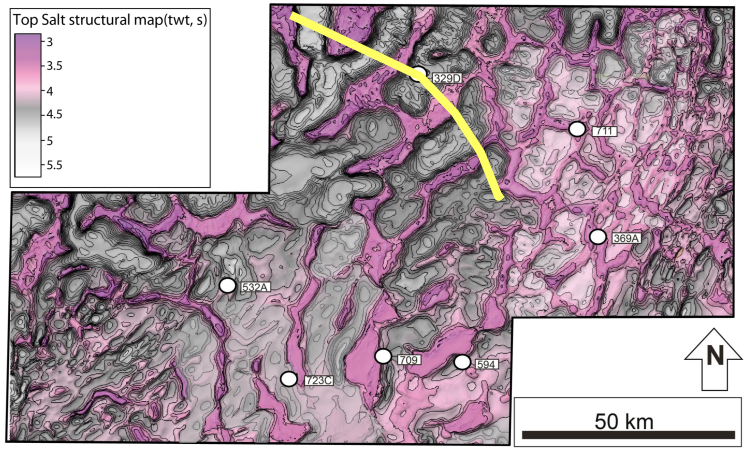

Medial shallow minibasins

< 1.5 km thick

Thick salt (>2 km)

Narrow, nearly-triangular salt diapirs

Mudstone-dominated units

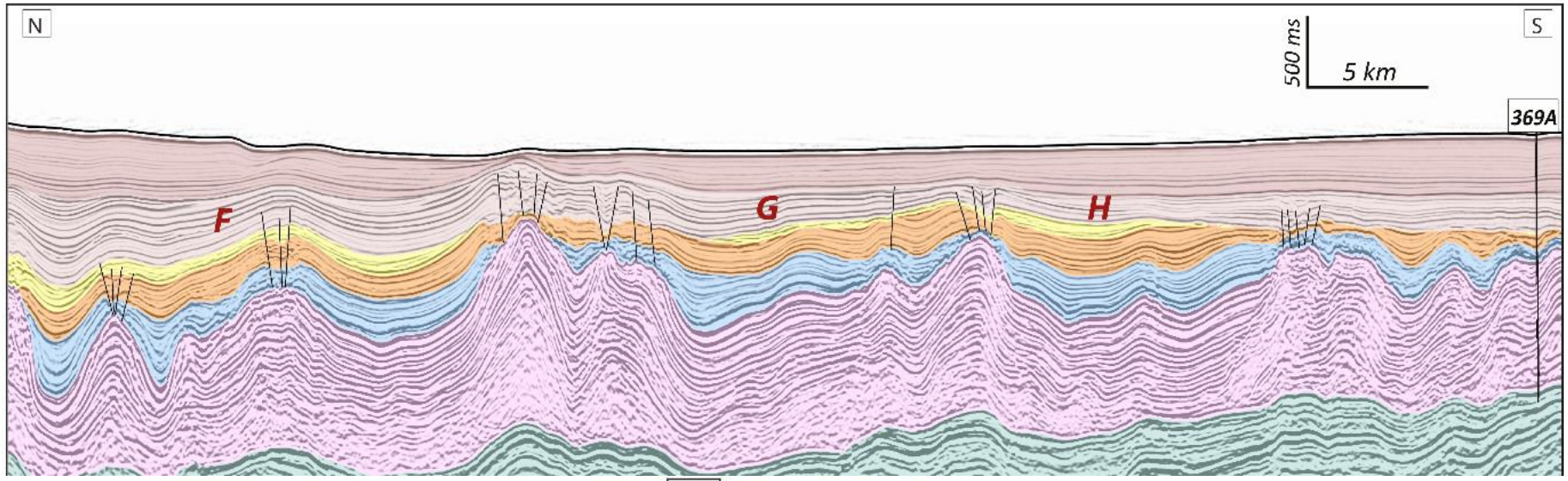

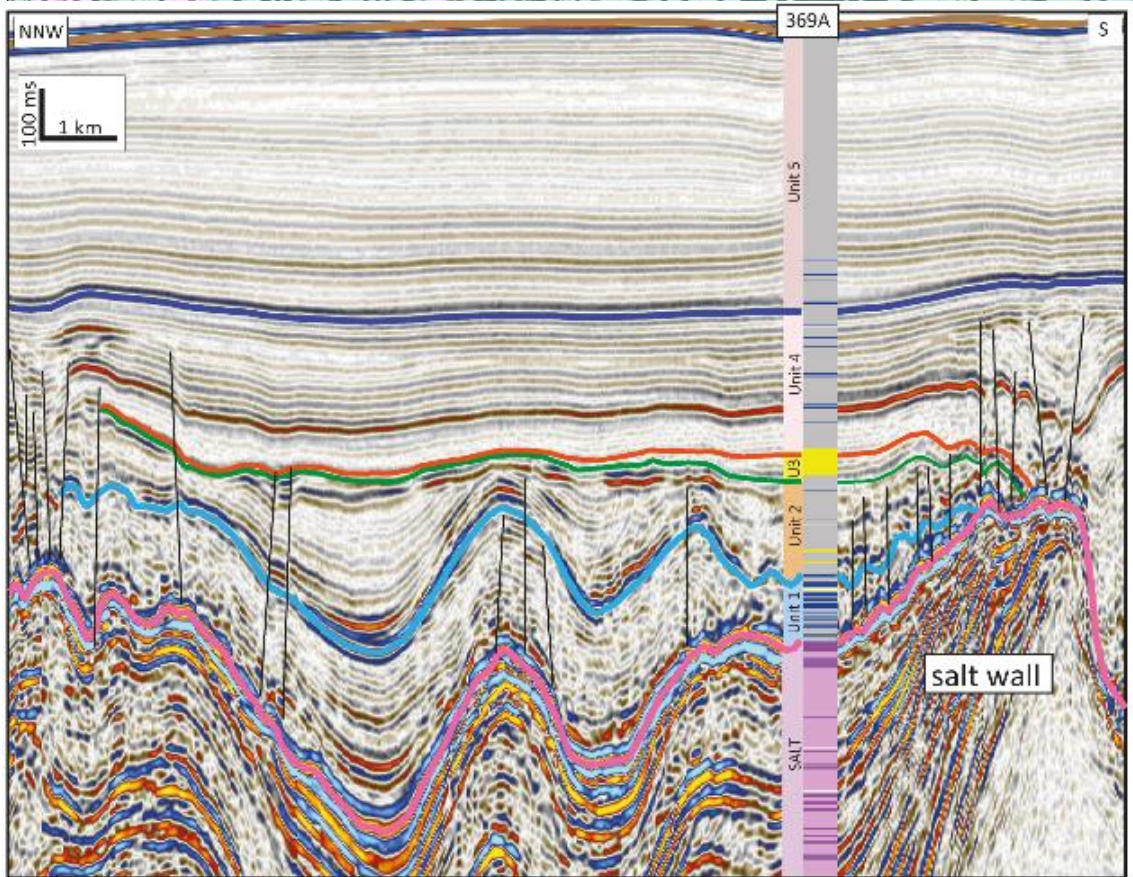

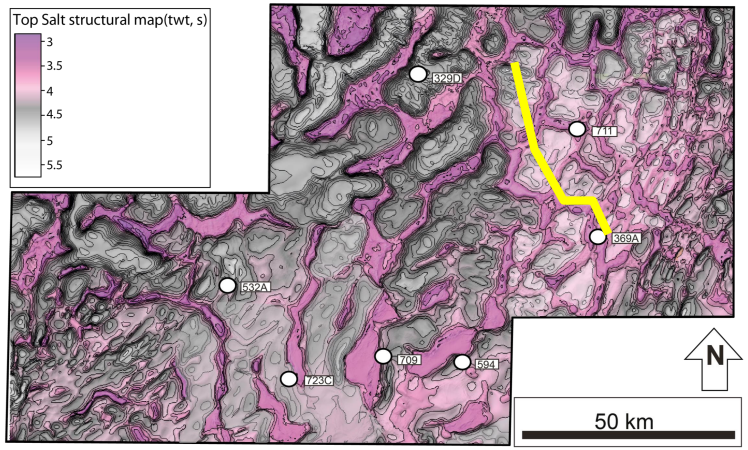

Distal elongated minibasins

< 1.5 km thin

Thick salt (c. 1km)

Highly-rugose or flat-topped salt walls

Mudstone-dominated units

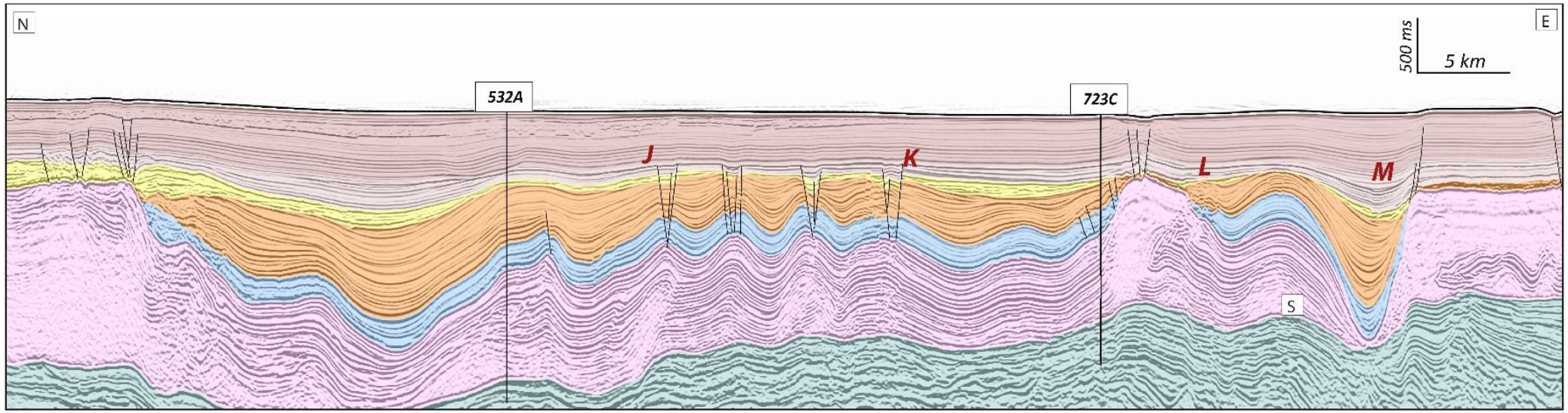

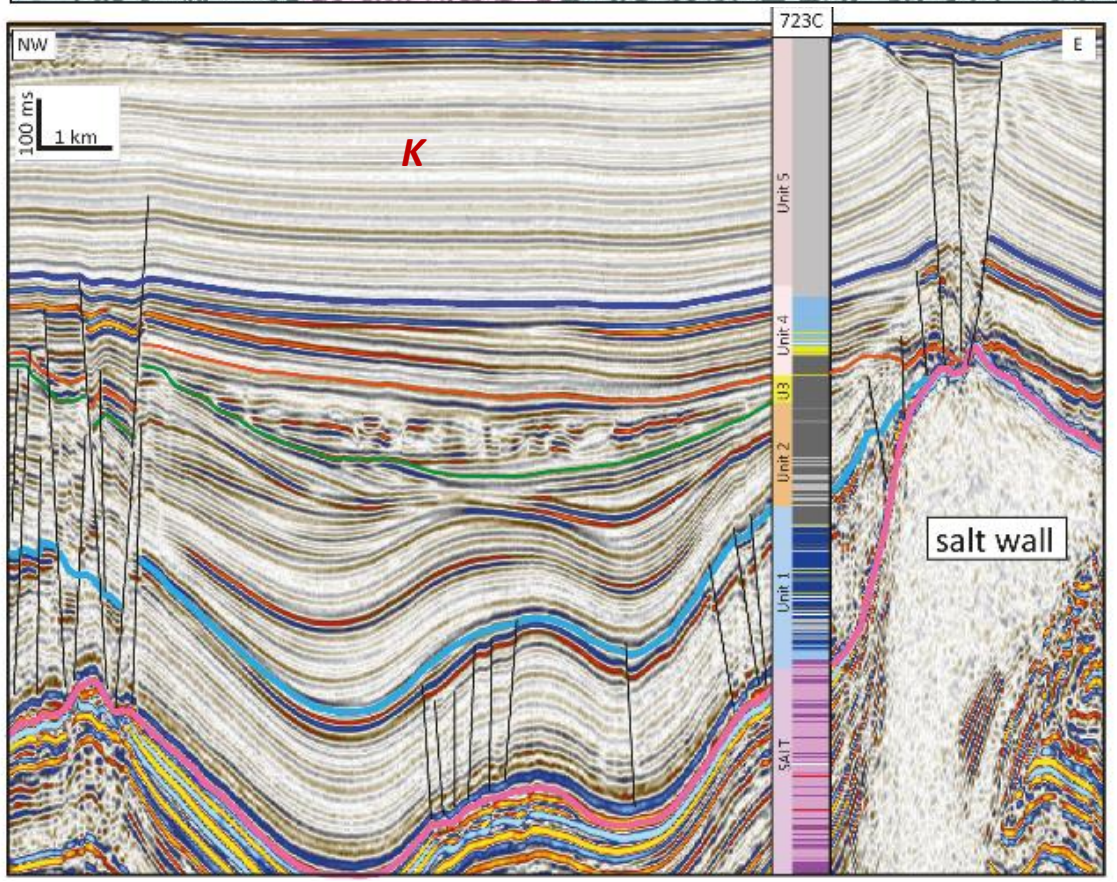

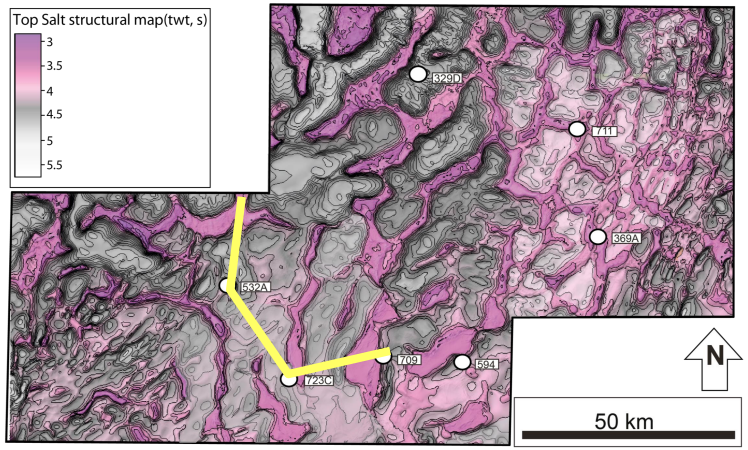

Minibasins seismic facies and depositional elements

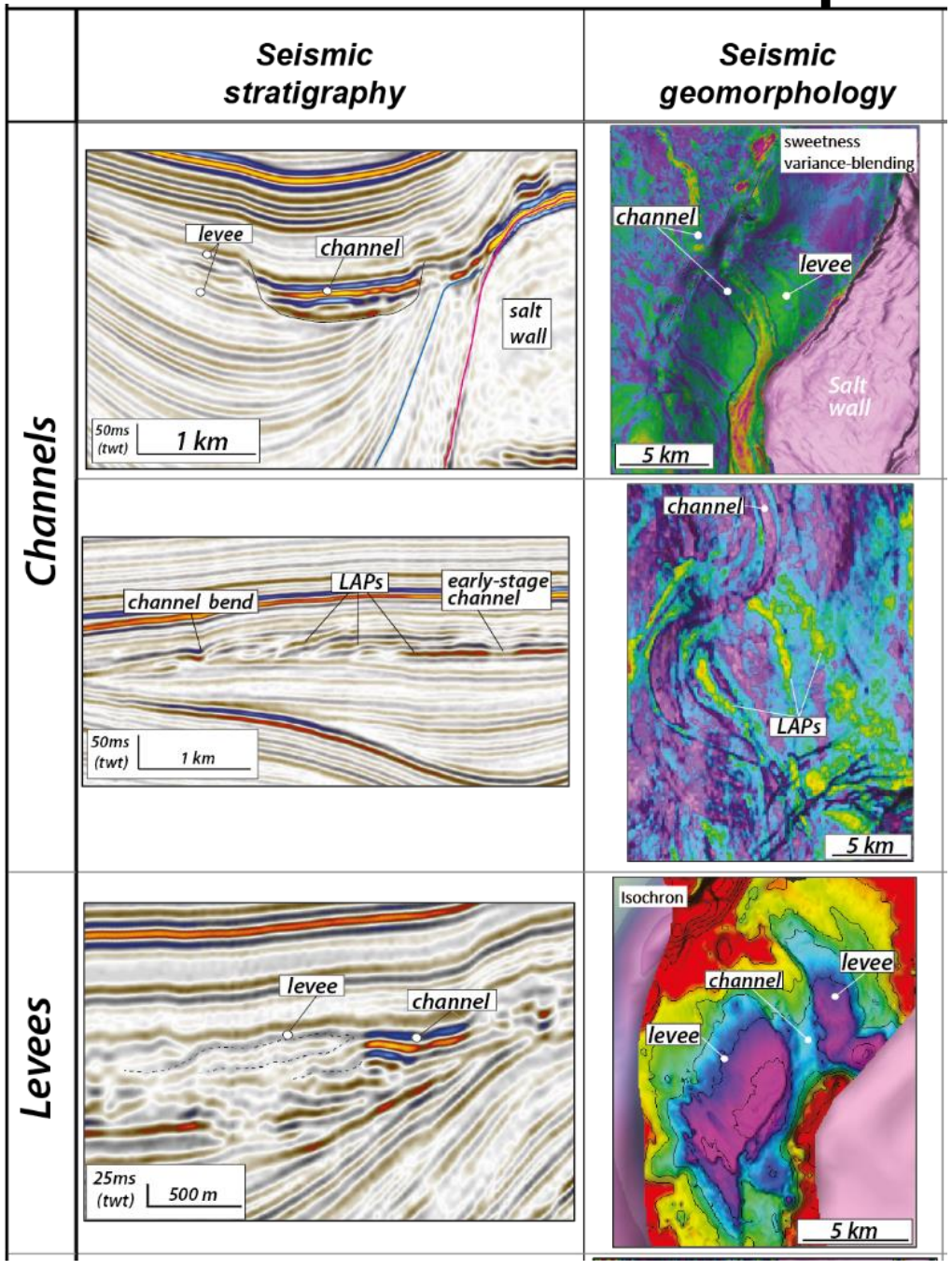

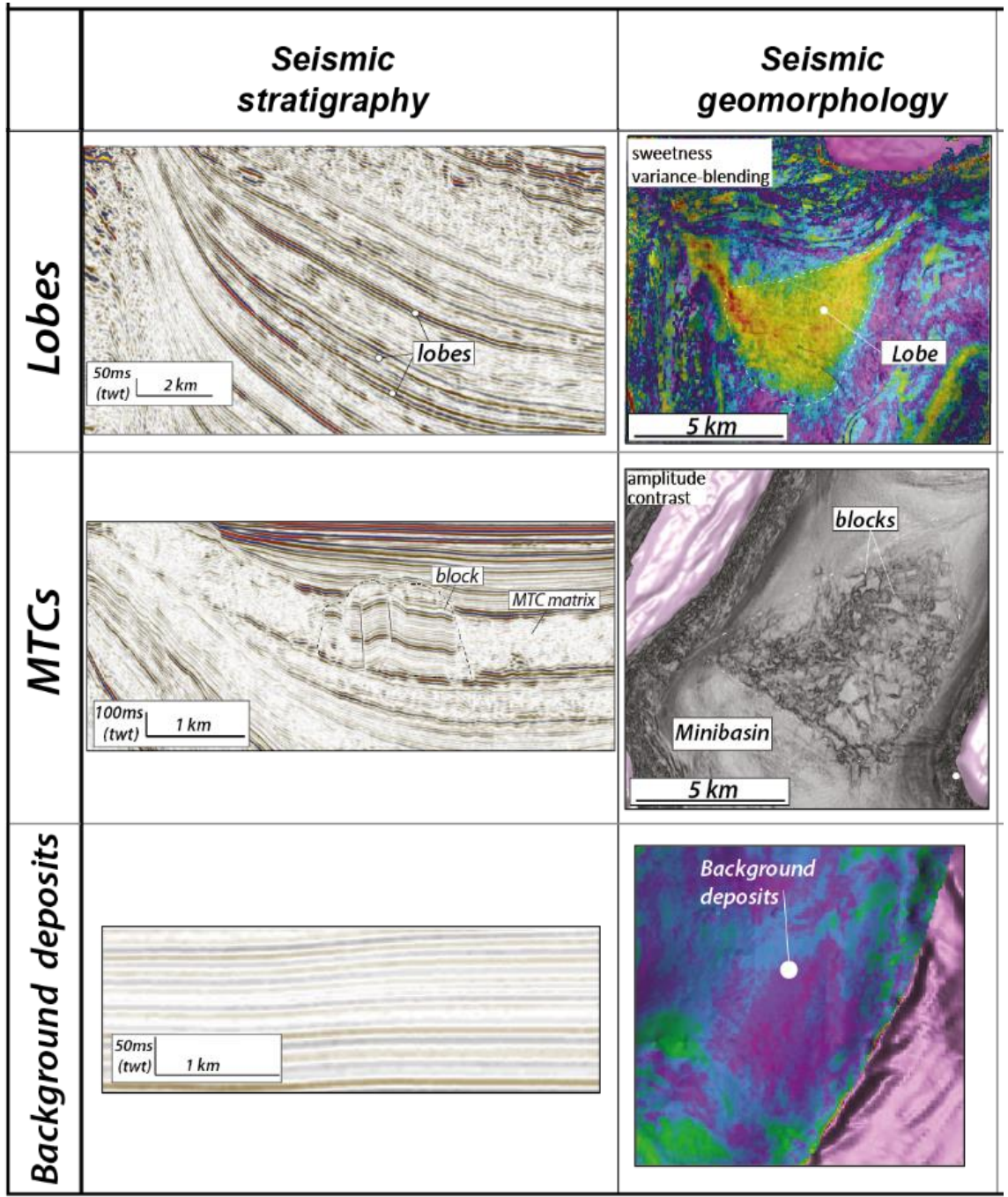

Phase 1

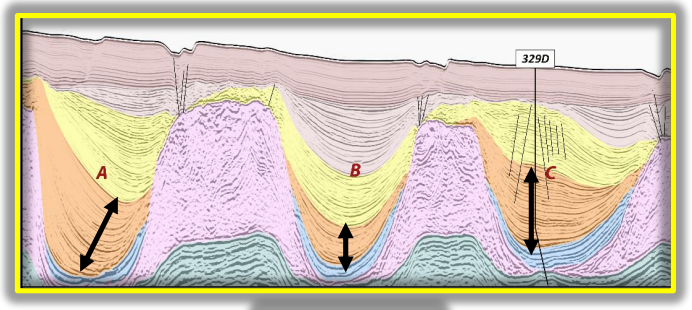
329D
A
B
C

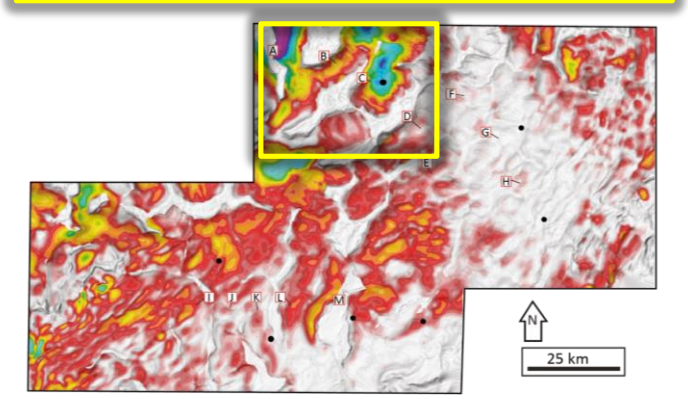
25 km

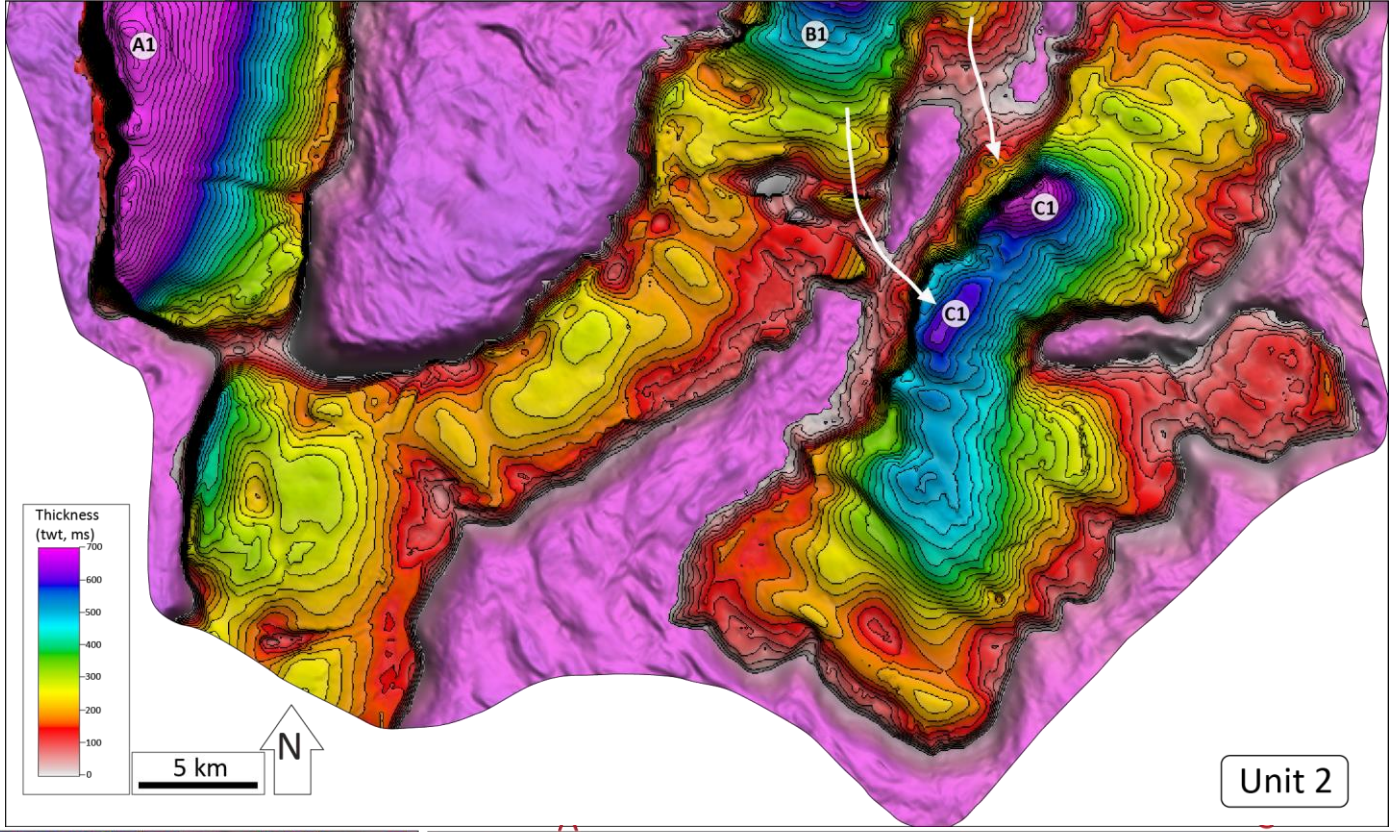
A1
B1
C1
C1
Thickness
(twt, ms)
700
600
500
400
300
200
100
0
5 km
N
Unit 2

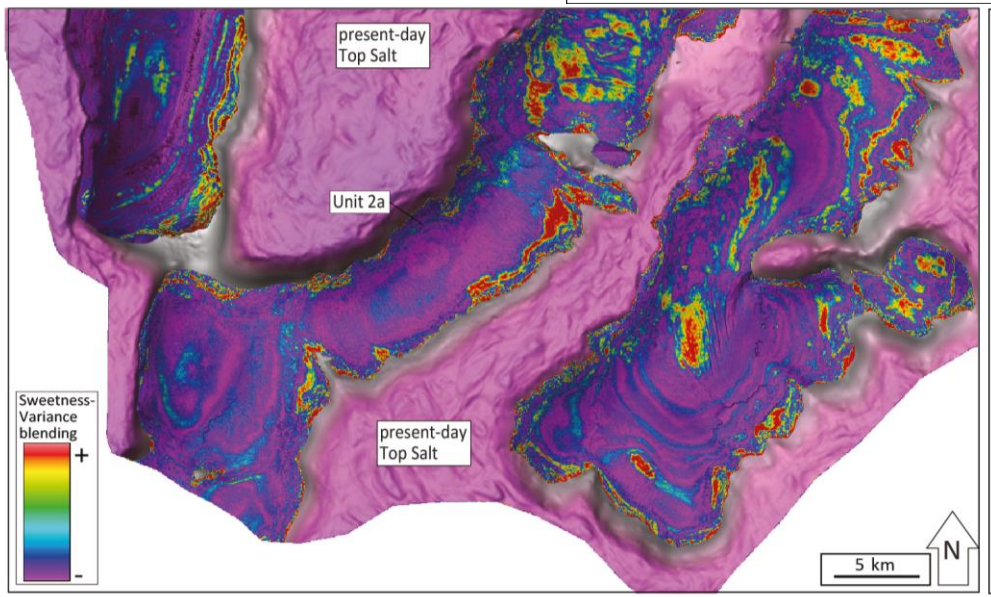
present-day
Top Salt
Unit 2a
present-day
Top Salt
Sweetness-
Variance
blending
+
-
5 km
N

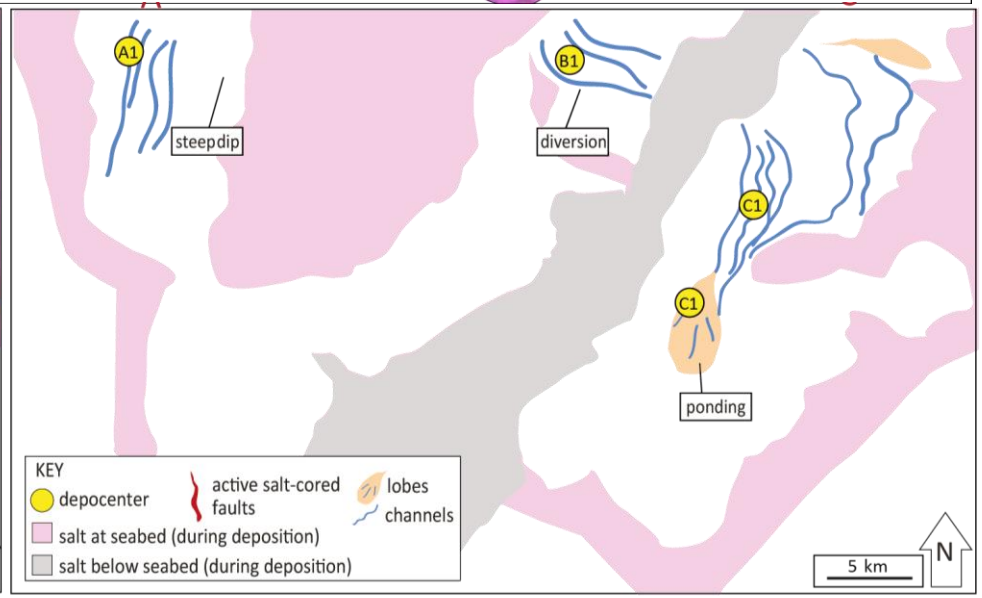
A1
steepdip
B1
diversion
C1
C1
ponding
KEY
depocenter
active salt-cored
faults
lobes
channels
salt at seabed (during deposition)
salt below seabed (during deposition)
5 km
N

Phase 2

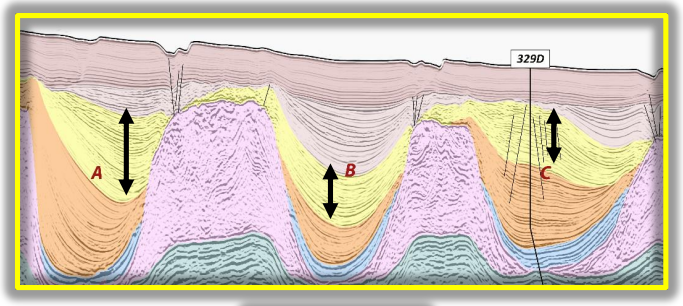
329D
A
B
C

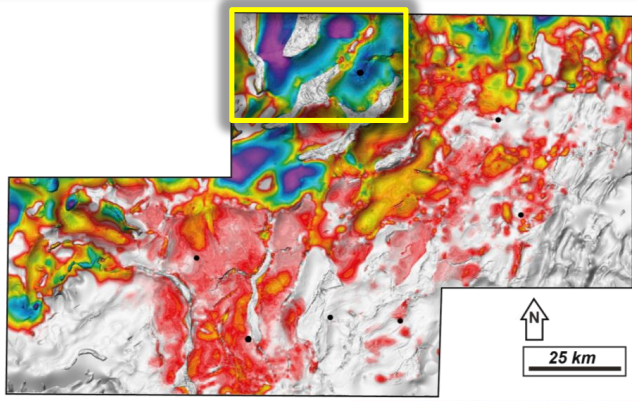
N
25 km

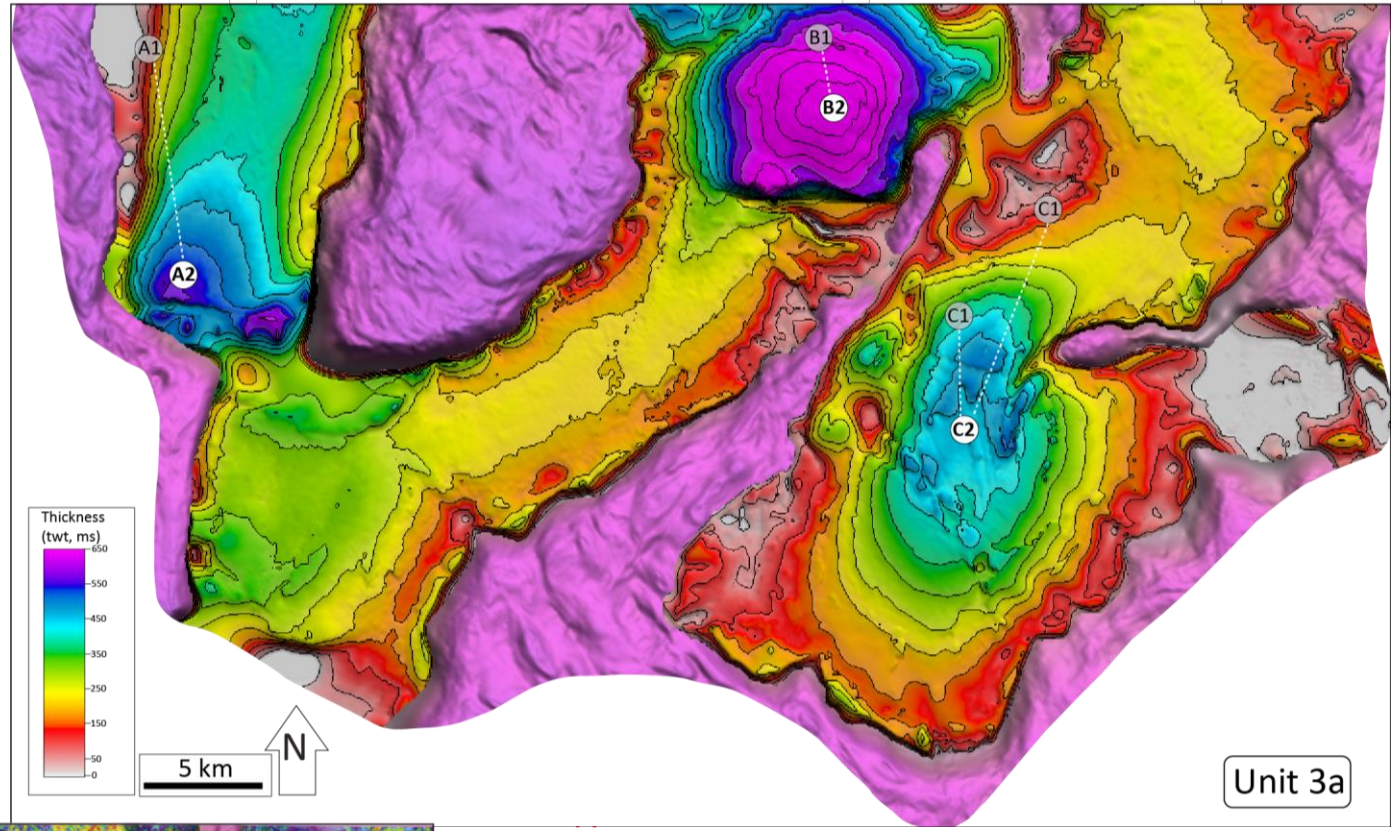
A1
A2
B1
B2
C1
C2
Thickness (twt, ms)
650
550
450
350
250
150
50
0
5 km
N
Unit 3a

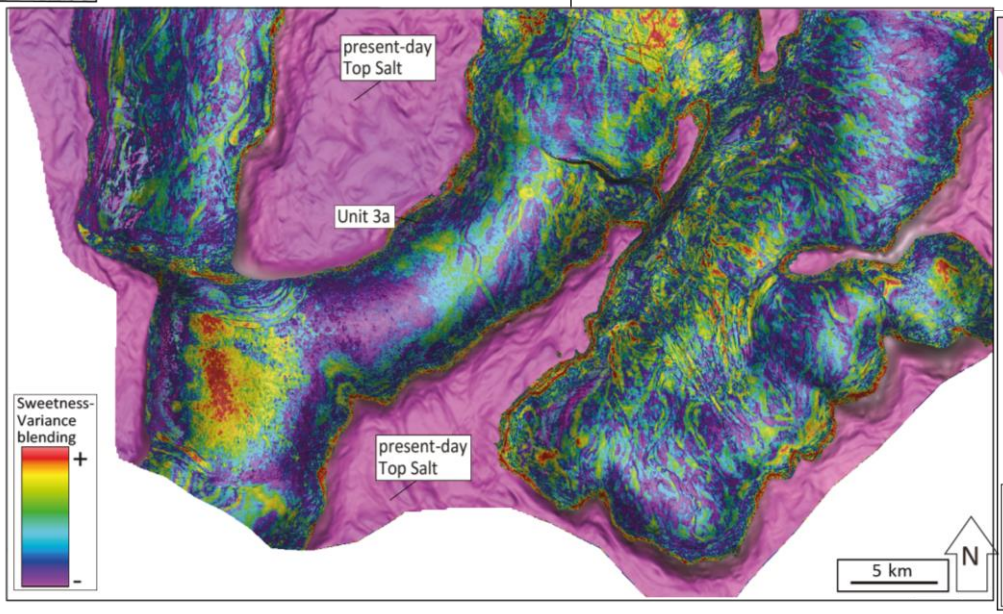
present-day Top Salt
Unit 3a
present-day Top Salt
Sweetness-Variance blending
+
-
5 km
N

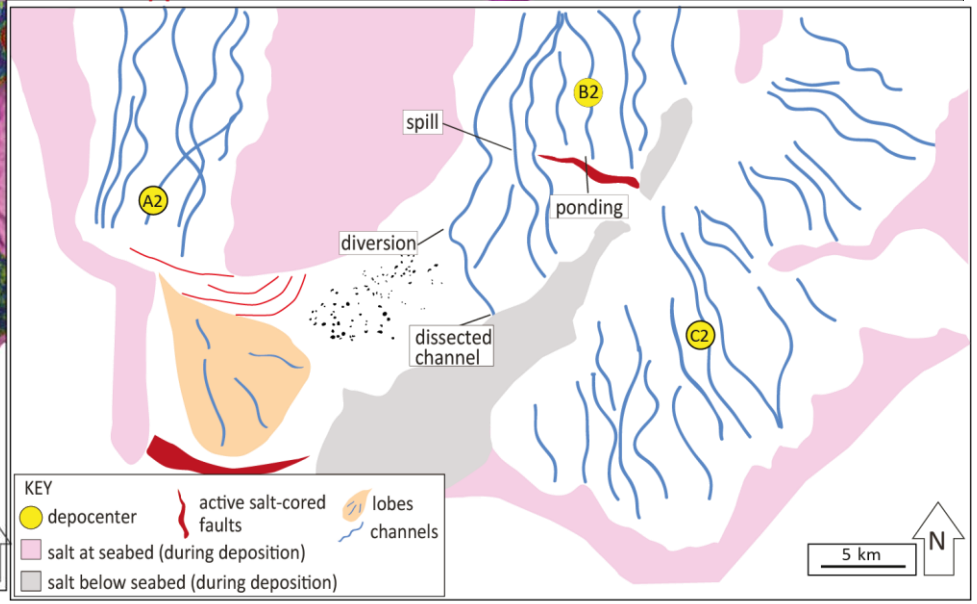
B2
spill
A2
ponding
diversion
dissected channel
C2
KEY
depocenter
active salt-cored faults
lobes
channels
salt at seabed (during deposition)
salt below seabed (during deposition)
5 km
N

Phase 2

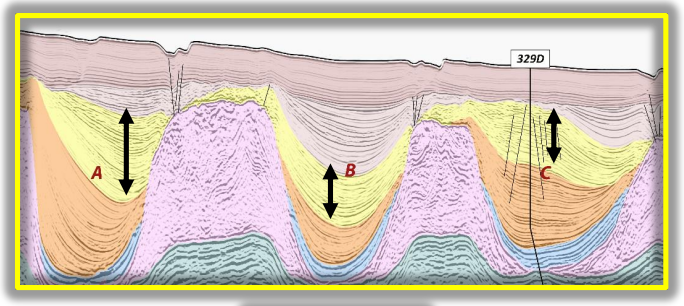
329D
A
B
C

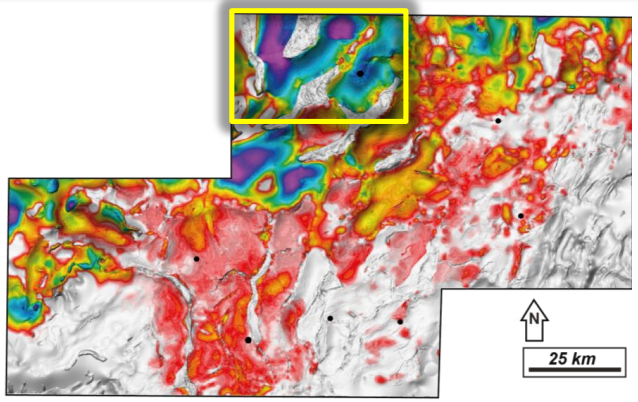
N
25 km

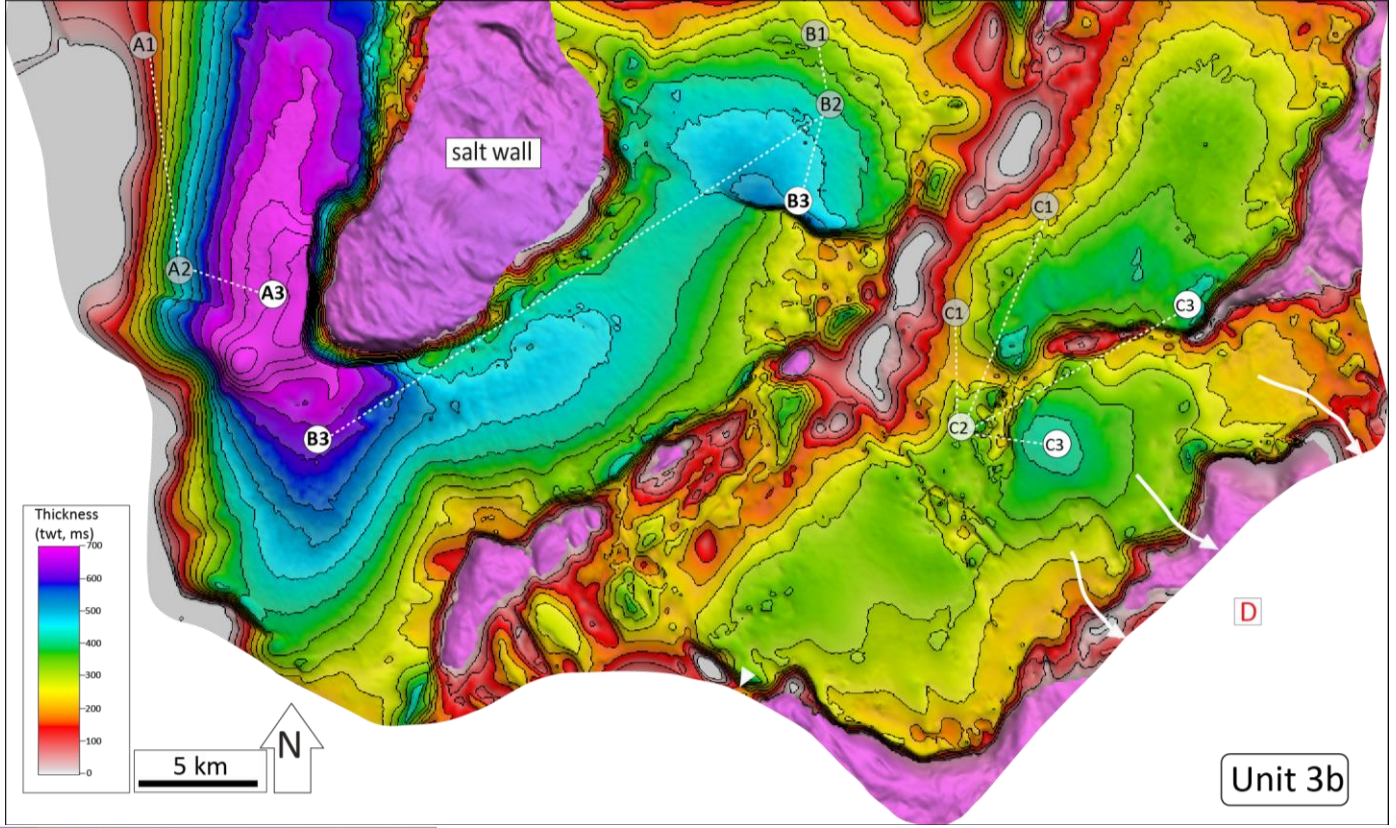
A1
A2
A3
B1
B2
B3
C1
C2
C3
salt wall
Thickness (twt, ms)
700
600
500
400
300
200
100
0
5 km
N
D
Unit 3b

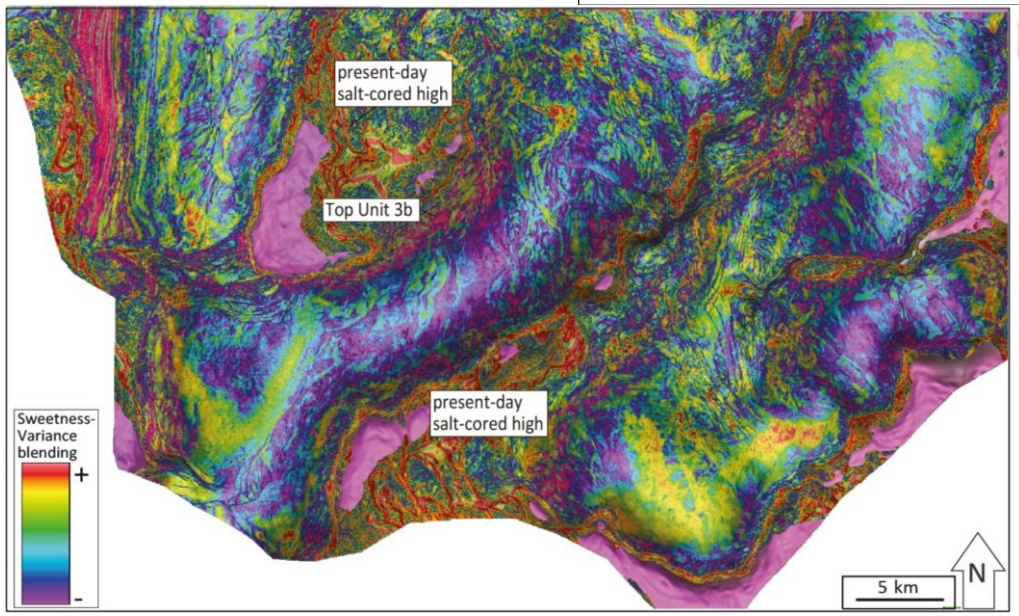
present-day salt-cored high
Top Unit 3b
present-day salt-cored high
Sweetness-Variance blending
+
-
5 km
N

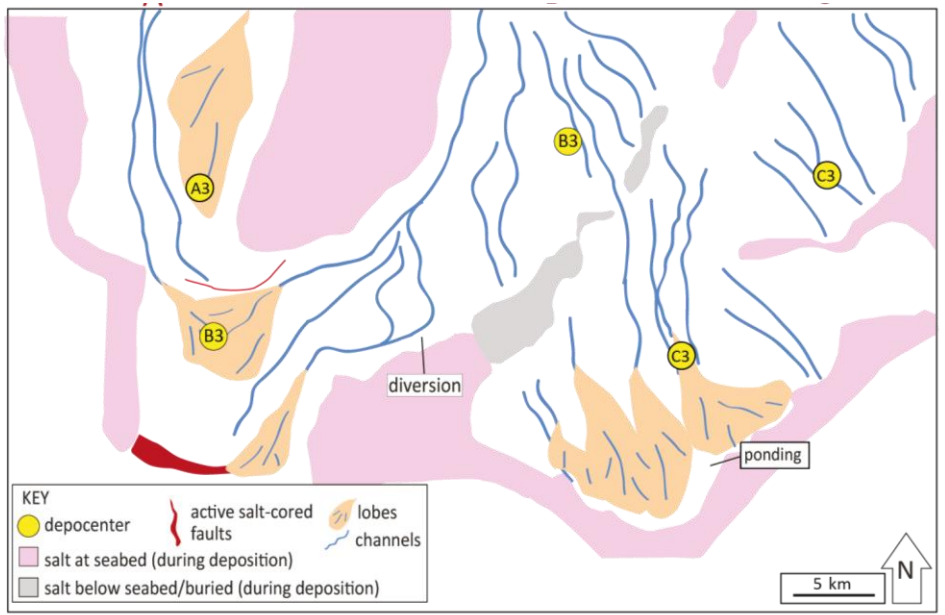
A3
B3
C3
diversion
ponding
KEY
depocenter
active salt-cored faults
lobes
channels
salt at seabed (during deposition)
salt below seabed/buried (during deposition)
5 km
N

Phase 2

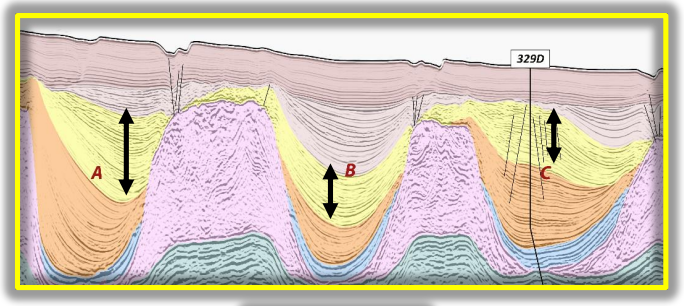
329D
A
B
C

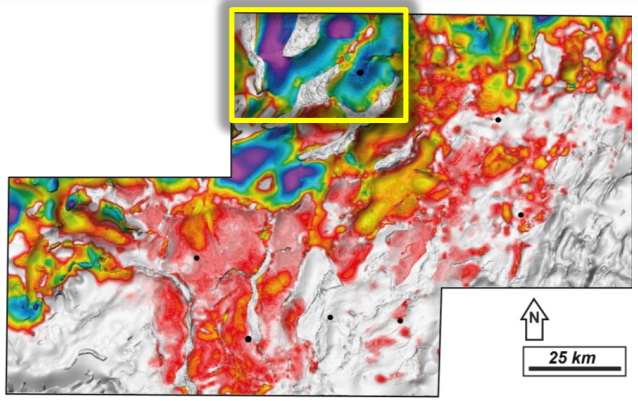
N
25 km

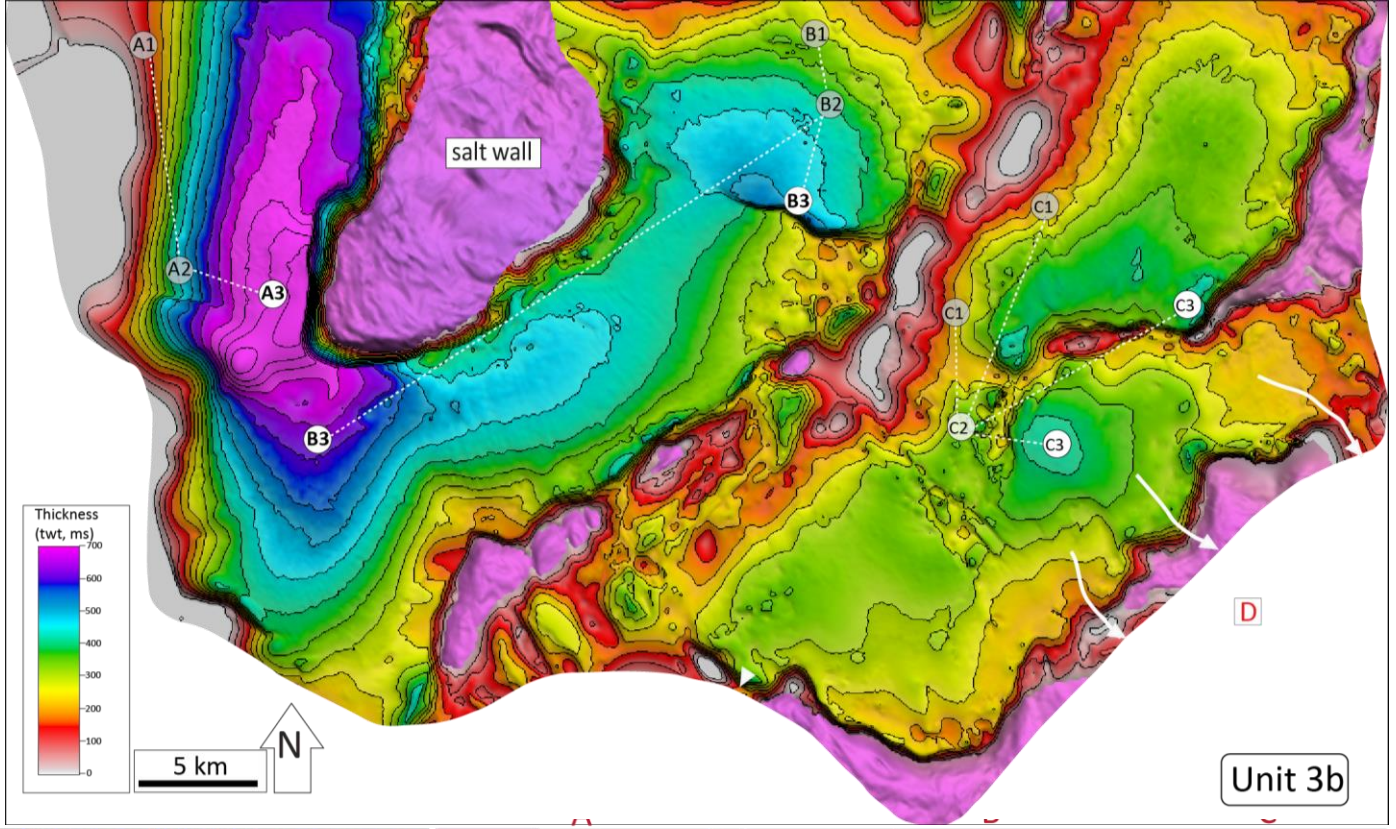
A1
A2
A3
B1
B2
B3
C1
C2
C3
salt wall
Thickness (twt, ms)
700
600
500
400
300
200
100
0
5 km
N
D
Unit 3b

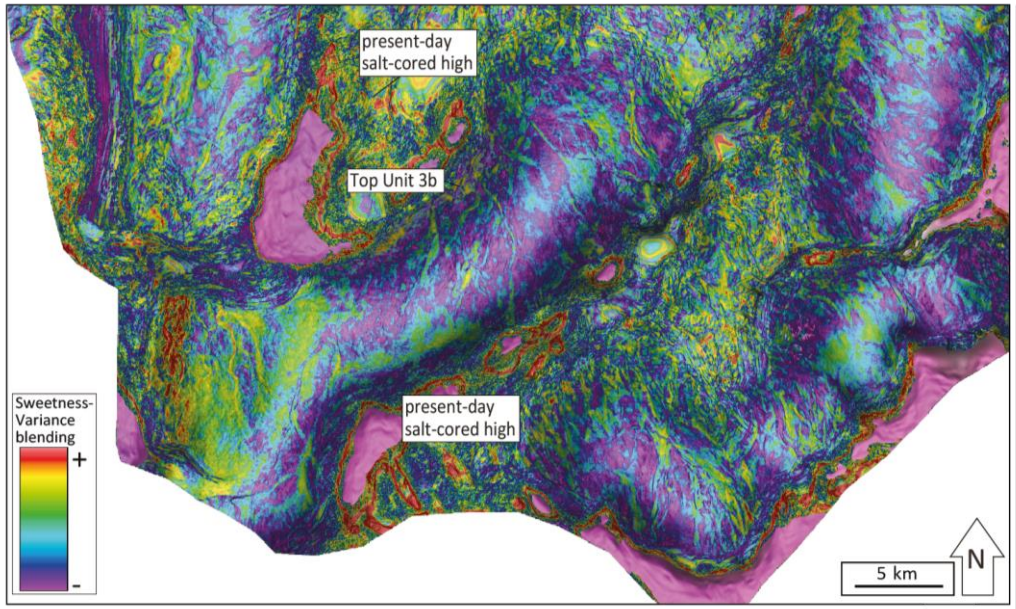
present-day salt-cored high
Top Unit 3b
present-day salt-cored high
Sweetness-Variance blending
+
-
5 km
N

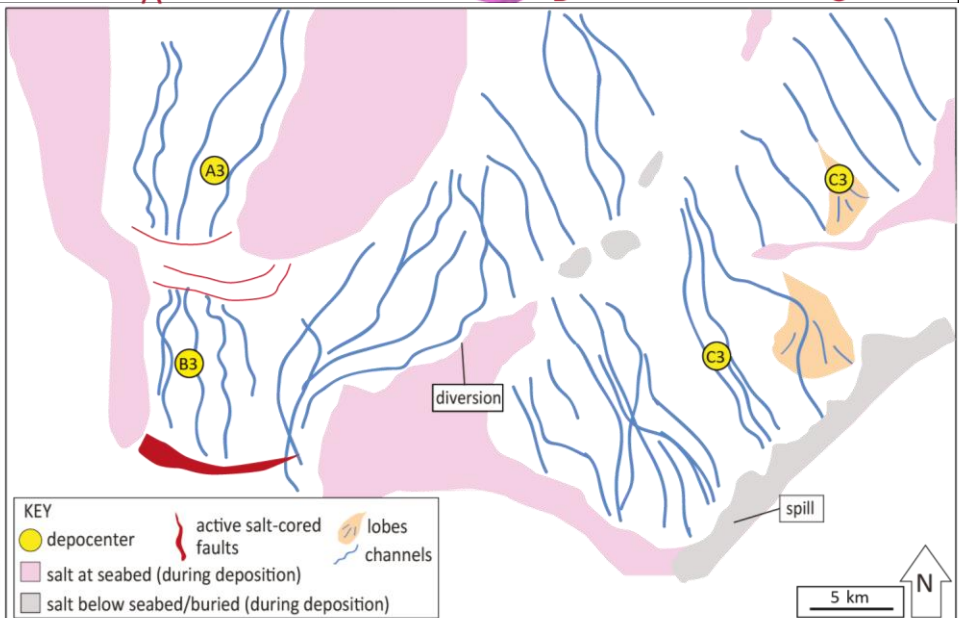
A3
B3
C3
C3
diversion
spill
KEY
depocenter
active salt-cored faults
lobes
channels
salt at seabed (during deposition)
salt below seabed/buried (during deposition)
5 km
N

Phase 2

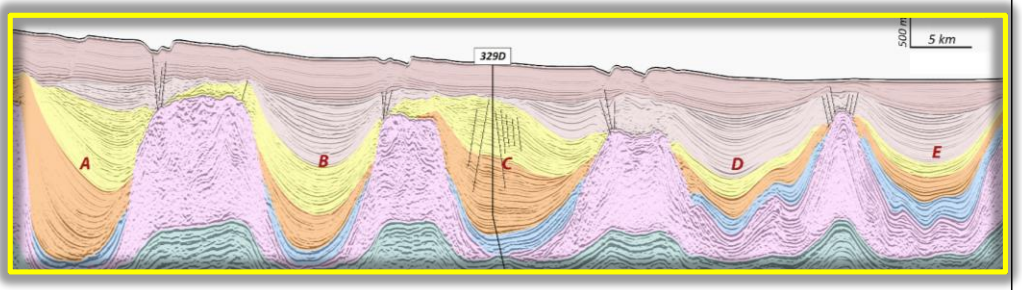
500 m
5 km
329D
A
B
C
D
E

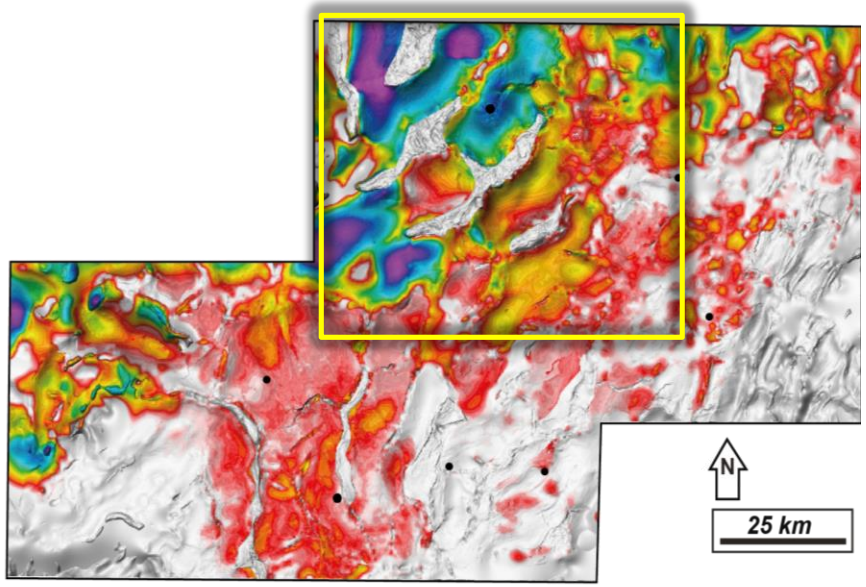
N
25 km

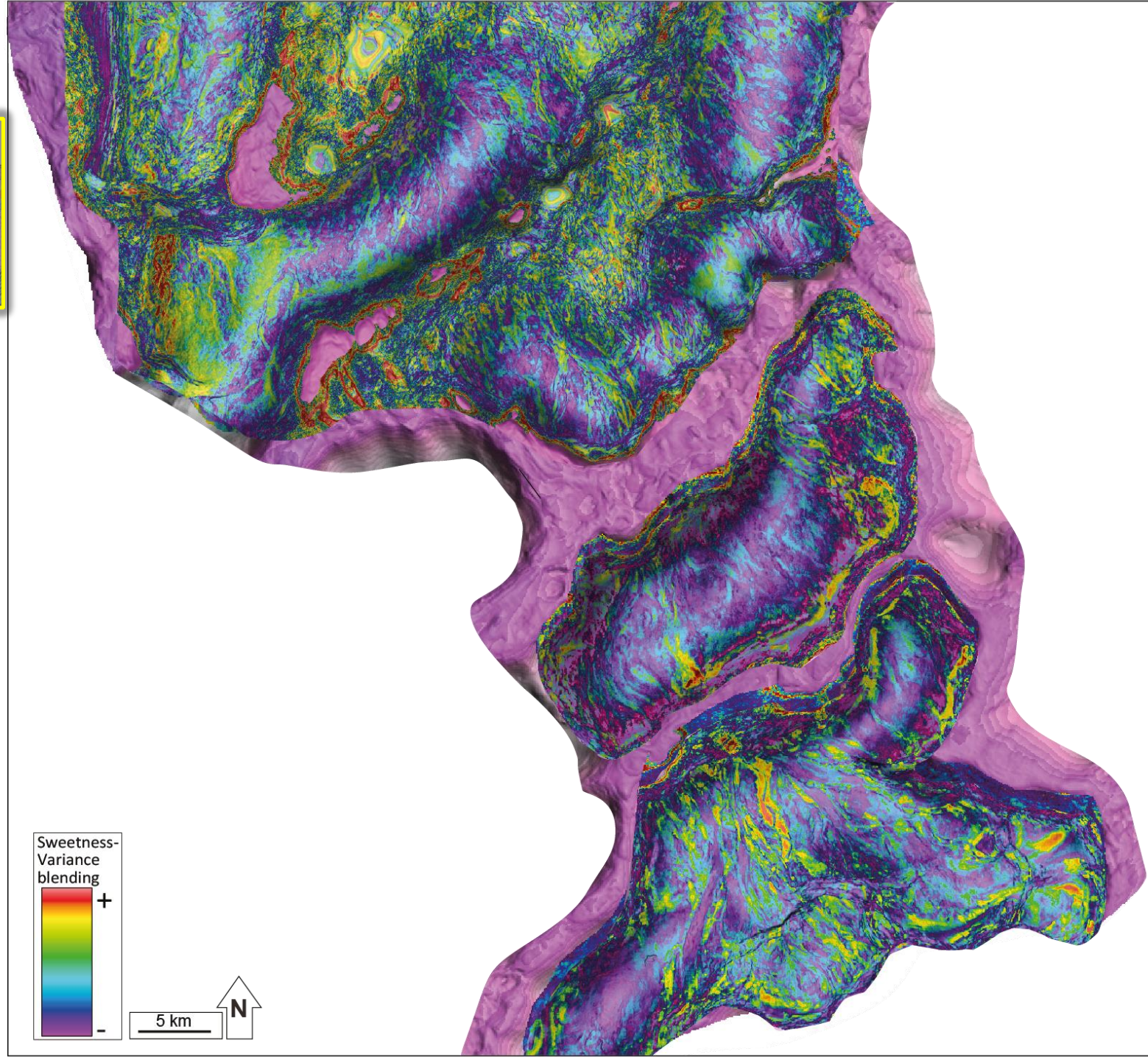
Sweetness-
Variance
blending
+
-
5 km
N

Phase 2

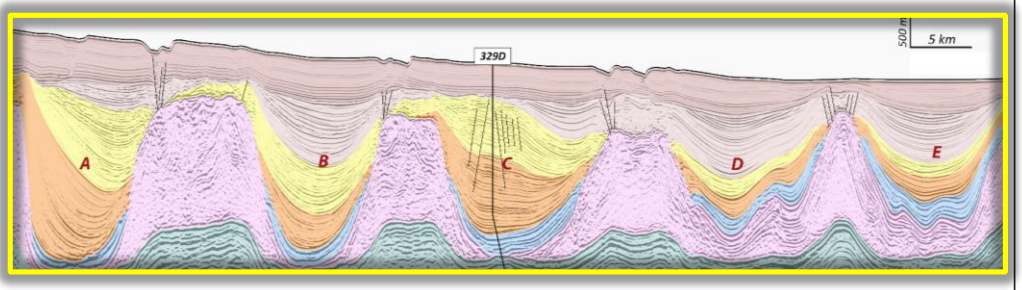
5 km
329D
A
B
C
D
E

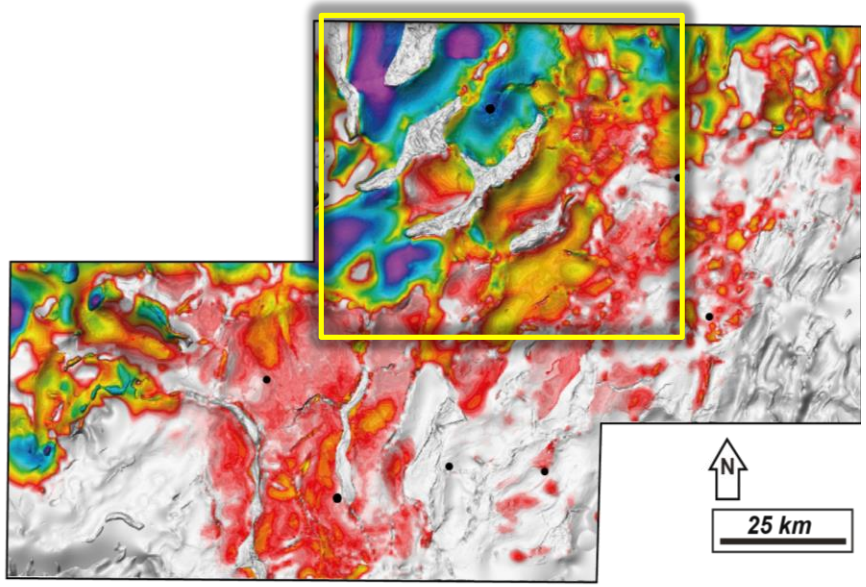
N
25 km

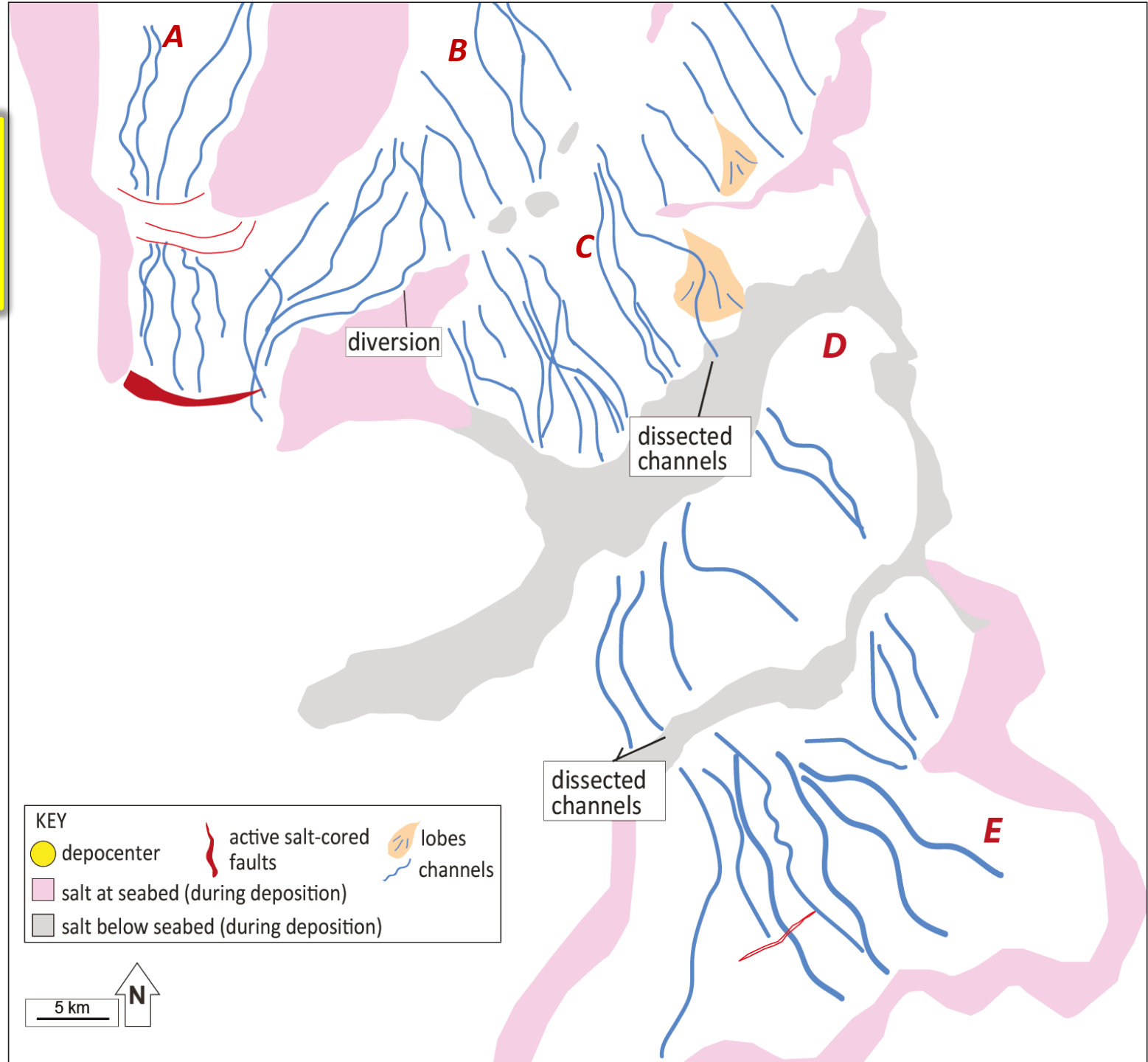
A
B
C
D
E
diversion
dissected channels
dissected channels
KEY
depocenter
active salt-cored faults
lobes
channels
salt at seabed (during deposition)
salt below seabed (during deposition)
5 km
N

Phase 2

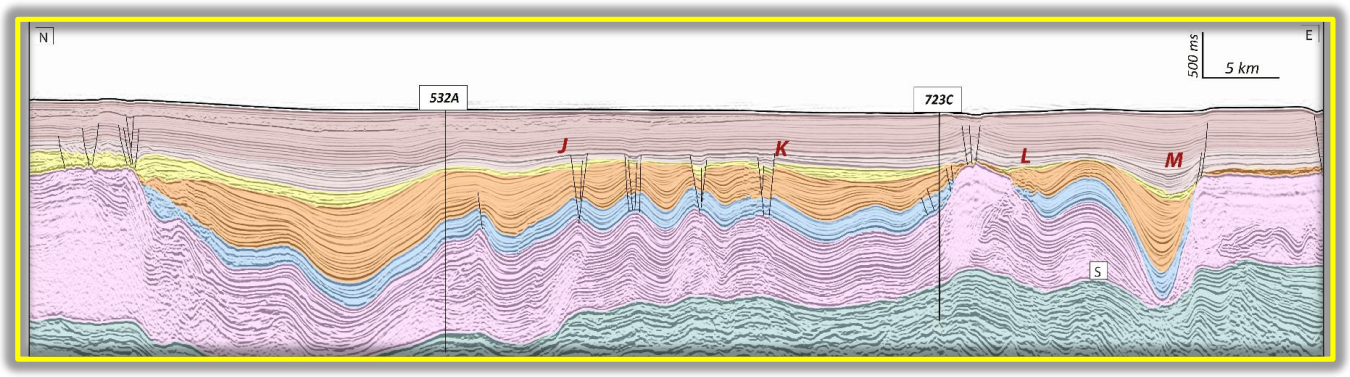

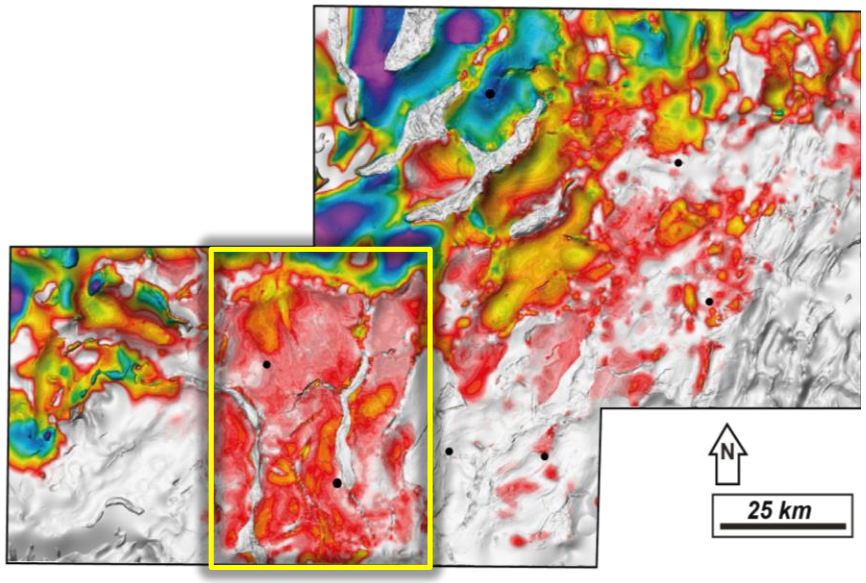

KEY

- present-day salt-cored structures
- submarine channels
- confined depositional lobes
- salt-cored faults
- salt-cored folds and anticlines

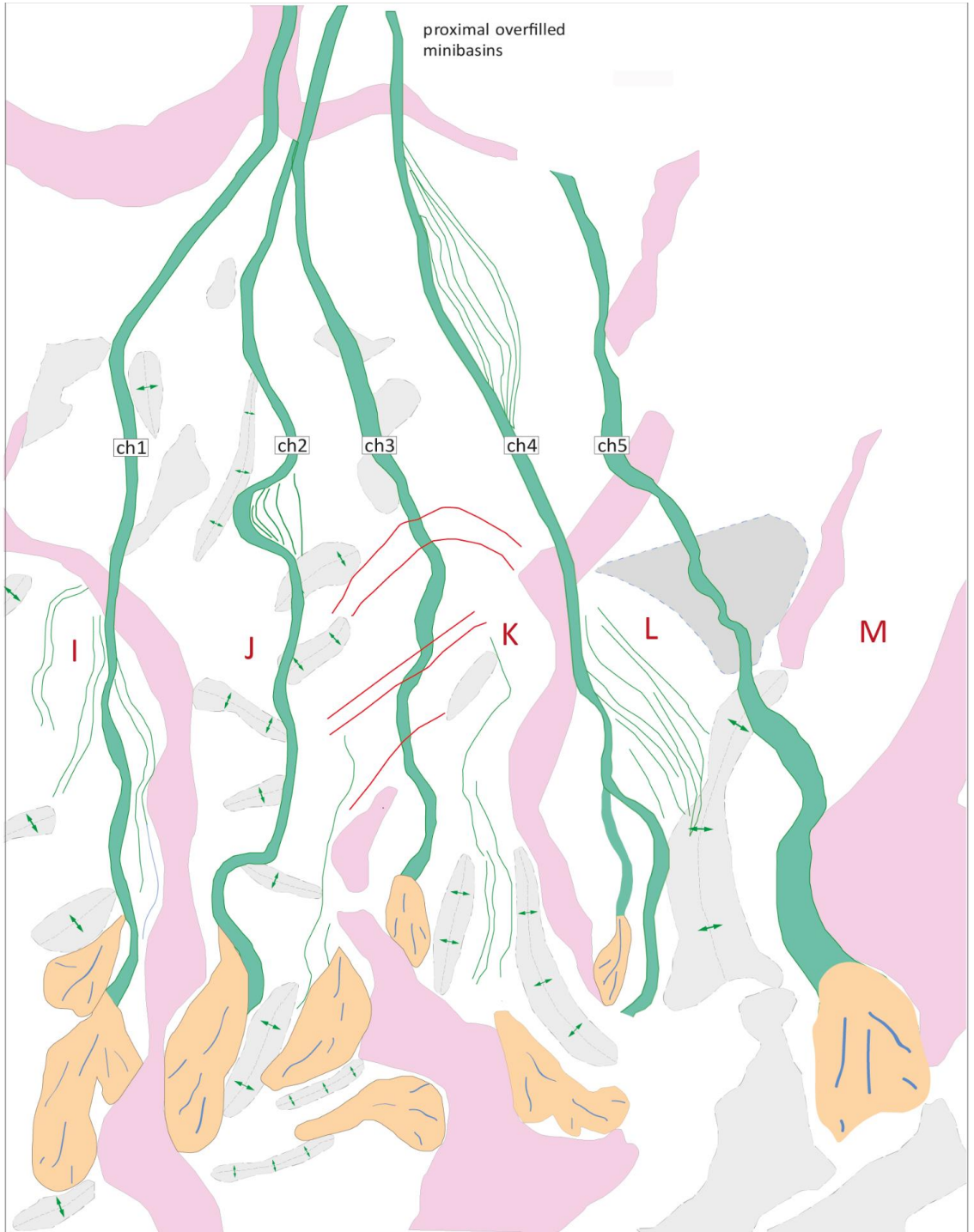

Phase 2

Lateral and frontal confinement of depositional lobes

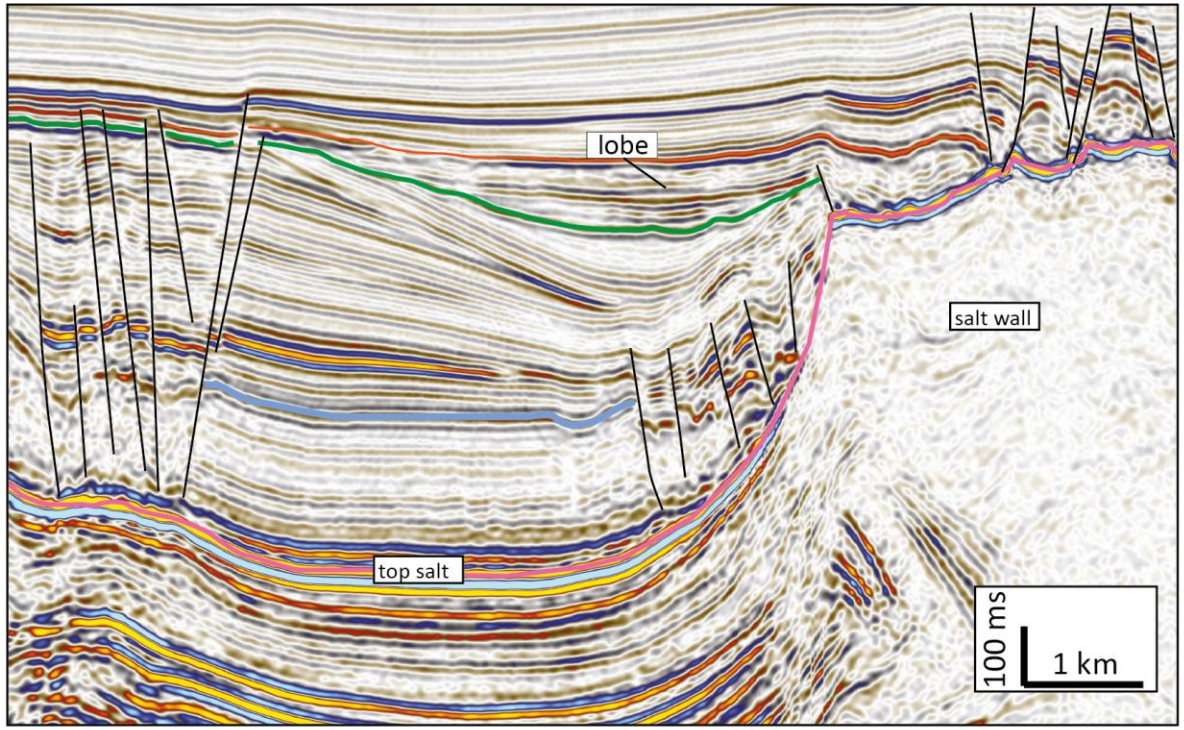

Minibasin I

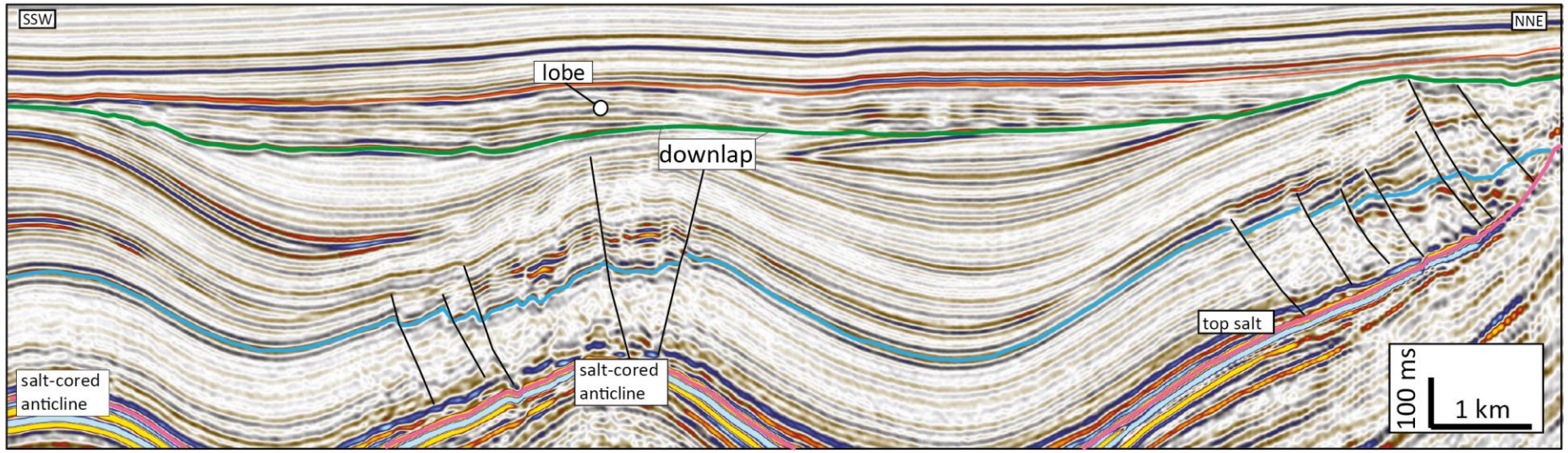

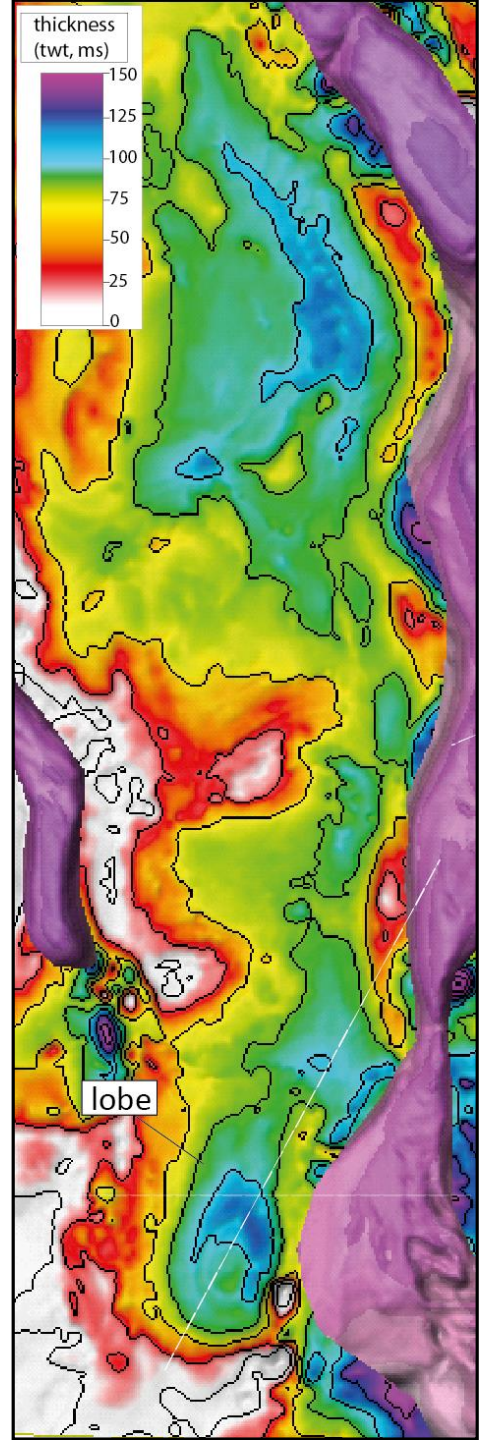

Phase 2

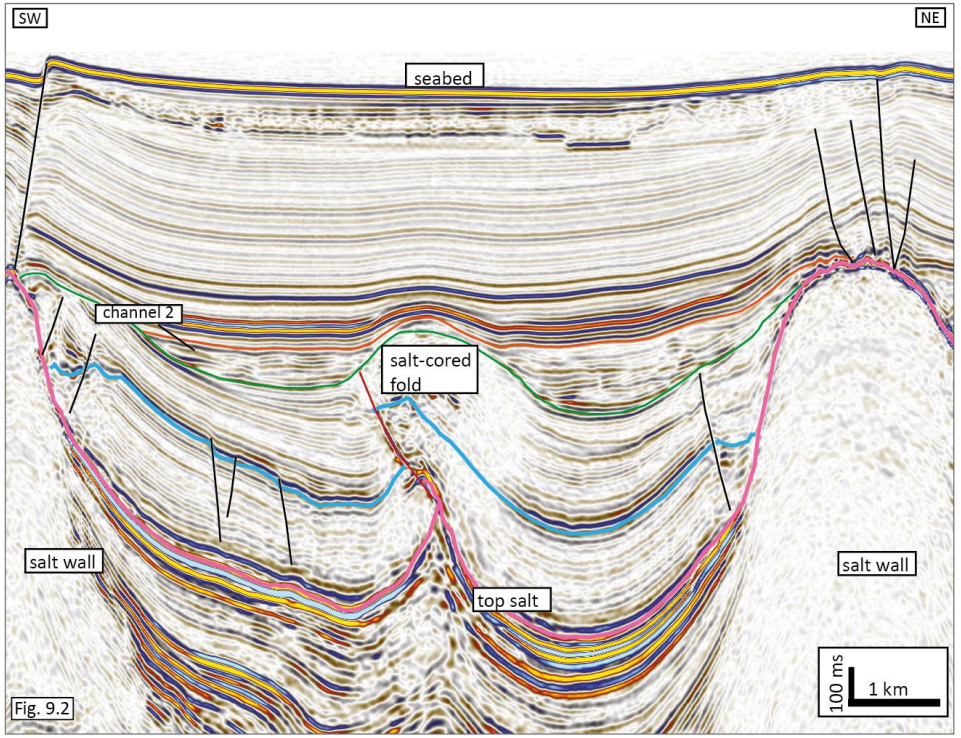
SW
NE
seabed
channel 2
salt-cored fold
salt wall
salt wall
top salt
100 ms
1 km
Fig. 9.2

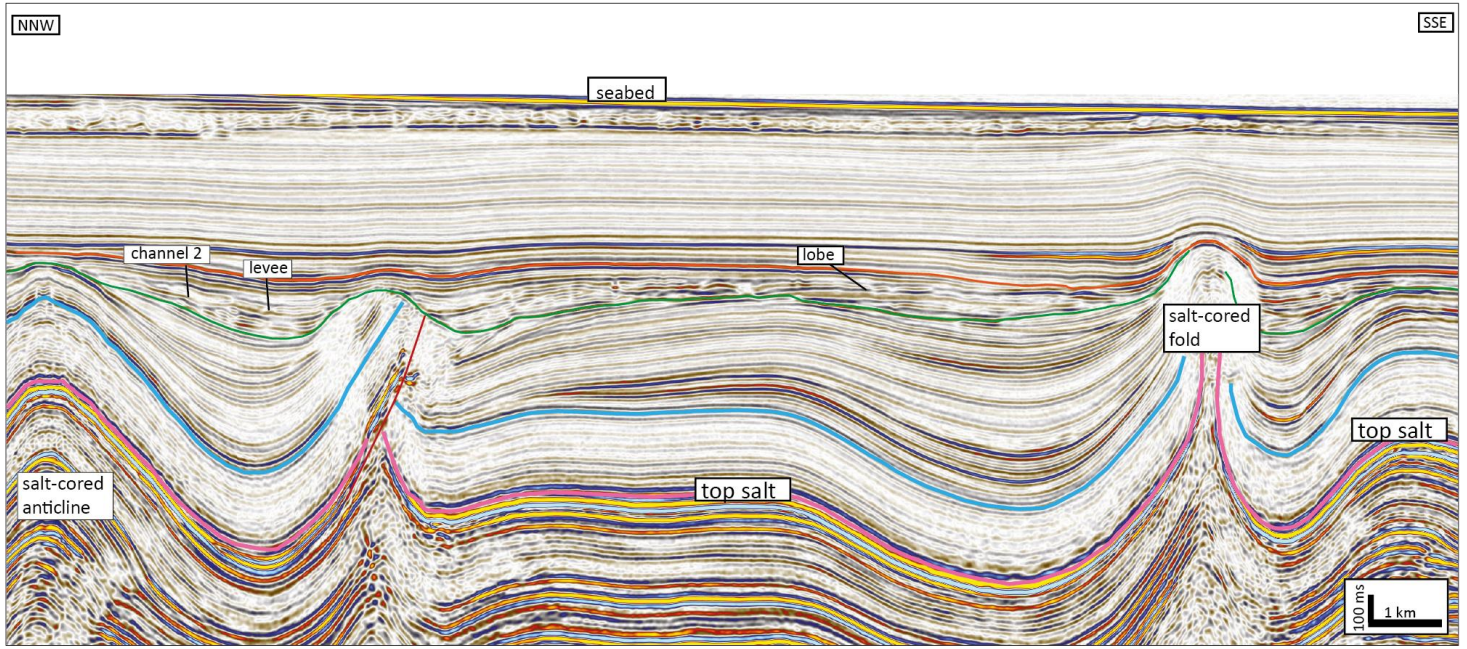
NNW
SSE
seabed
channel 2
levee
lobe
salt-cored fold
top salt
salt-cored anticline
top salt
100 ms
1 km

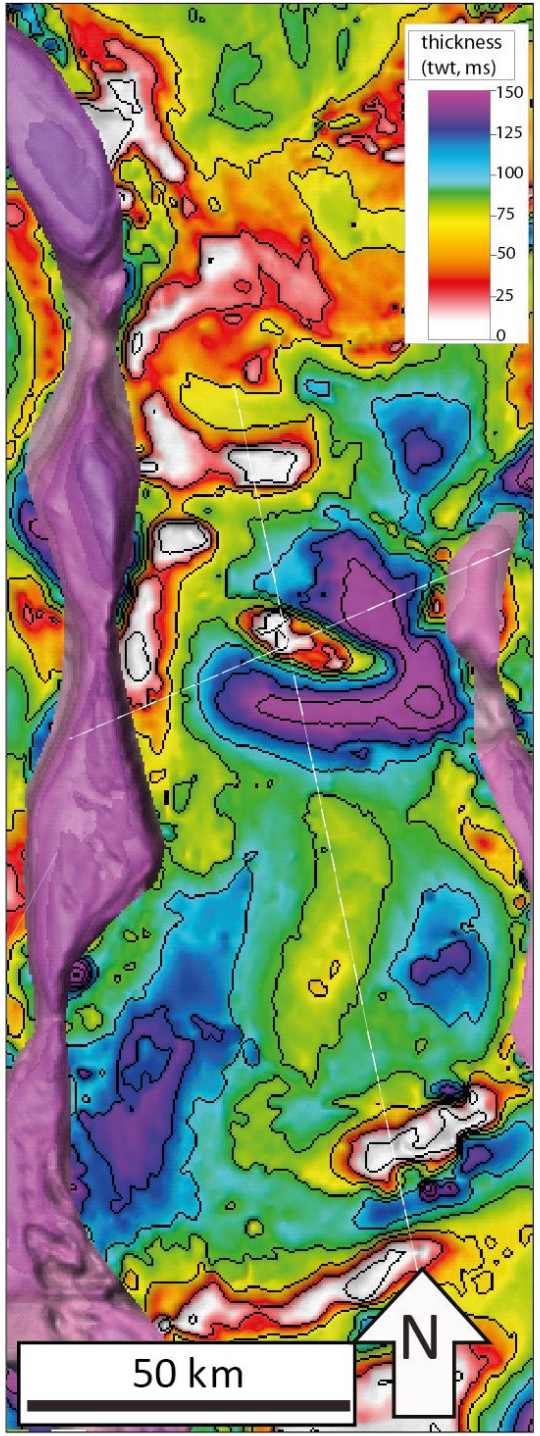
thickness (twt, ms)
150
125
100
75
50
25
0
N
50 km

Phase 2

Local diversion around intra-minibasin folds

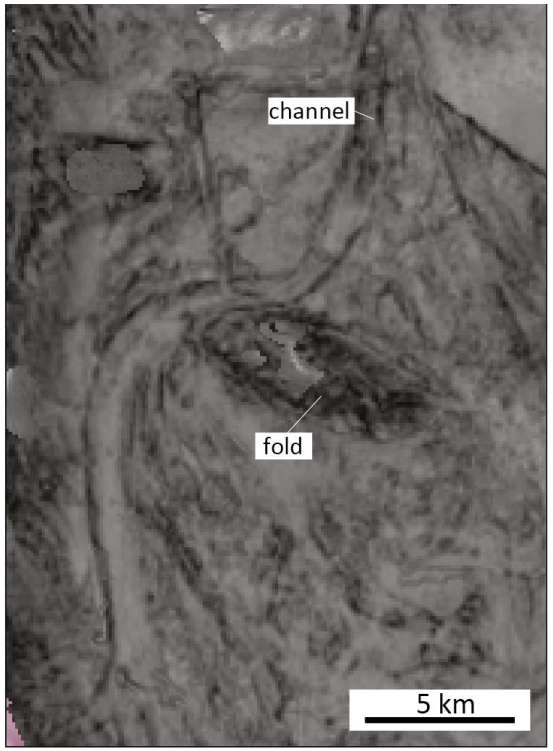

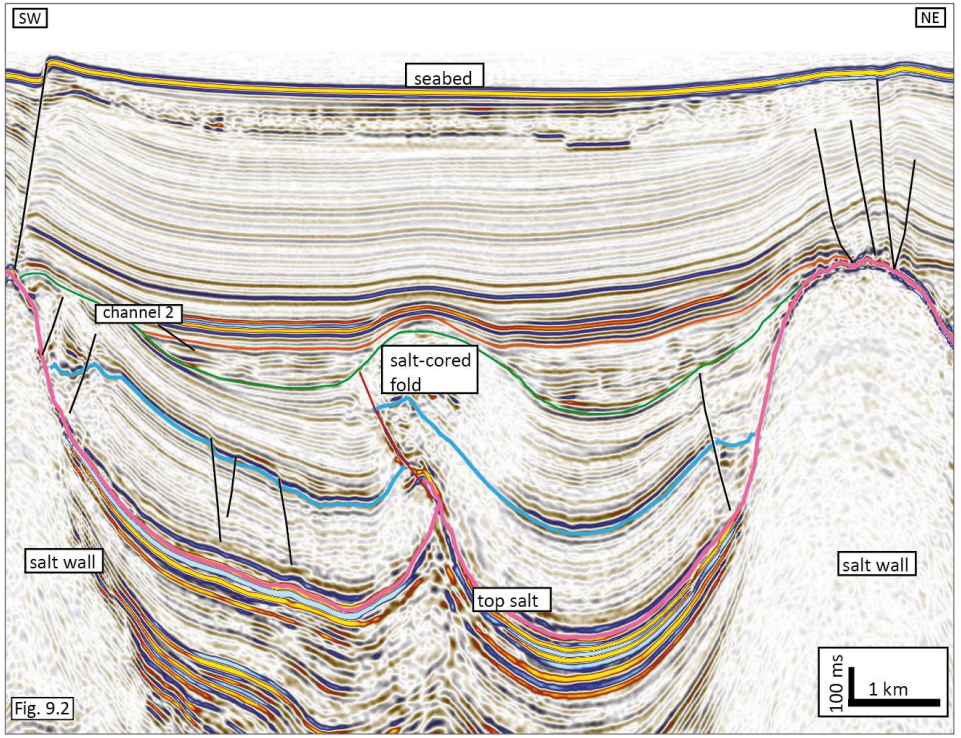

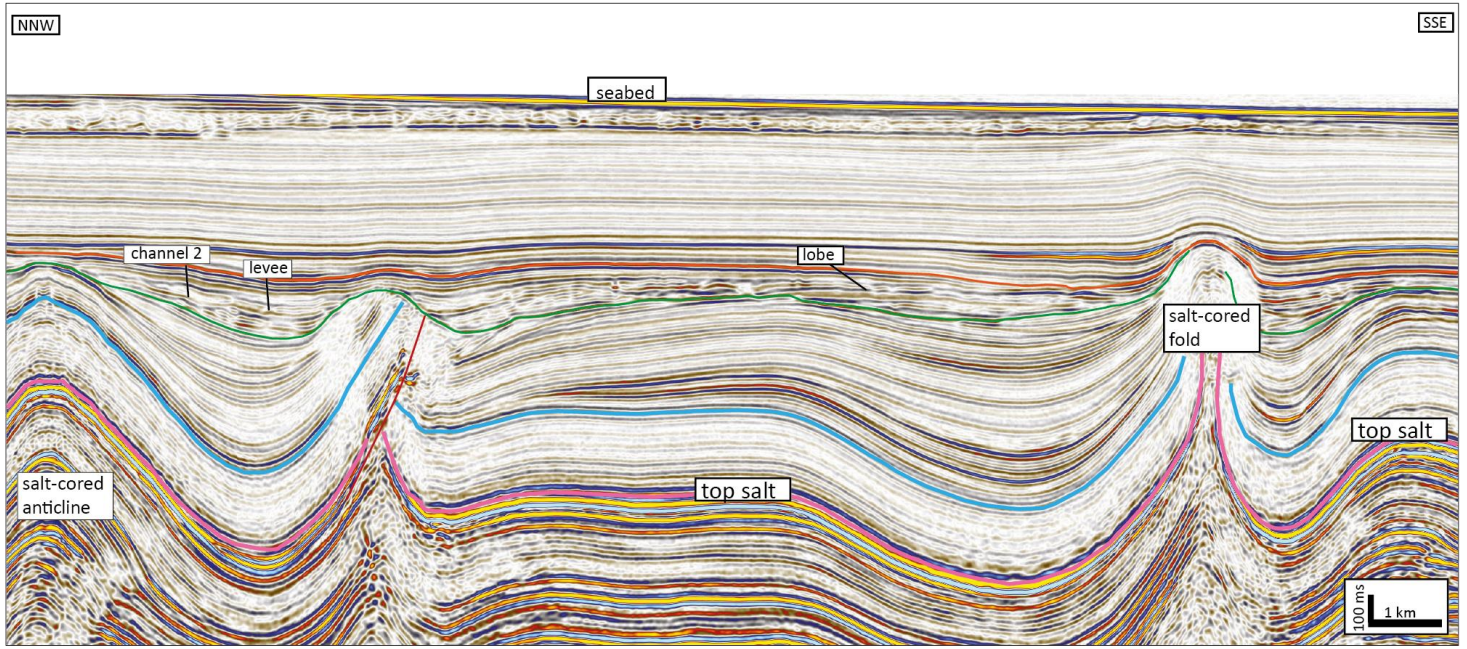

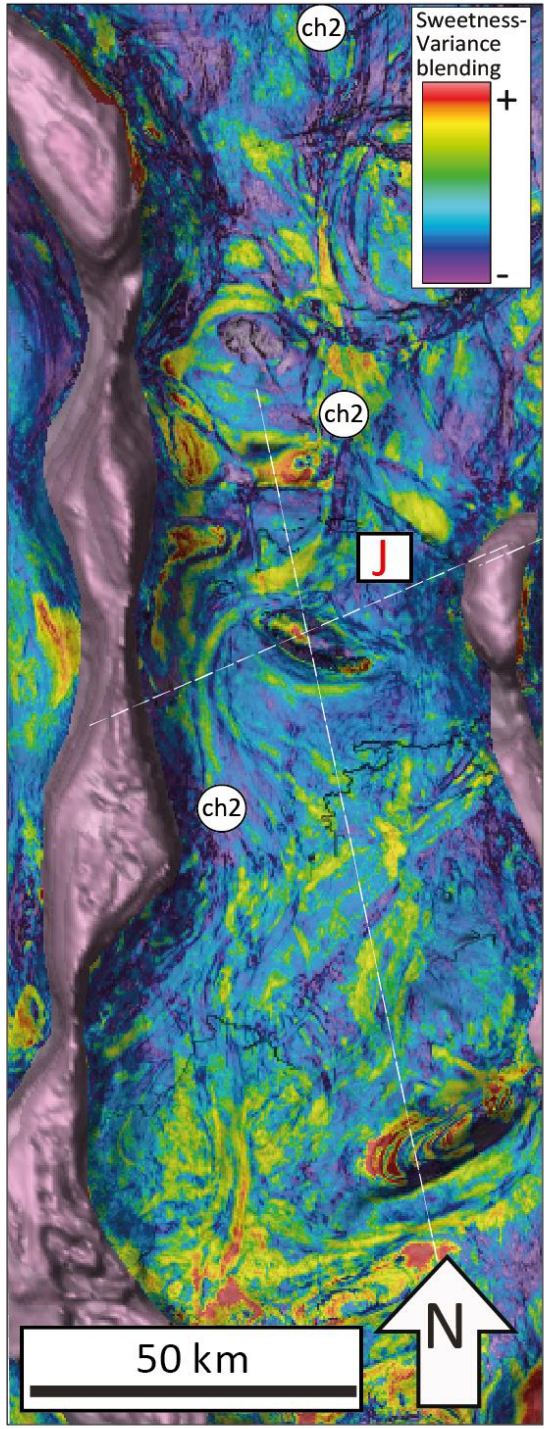

Phase 2

Changes in channel geometry between Minibasins L and M

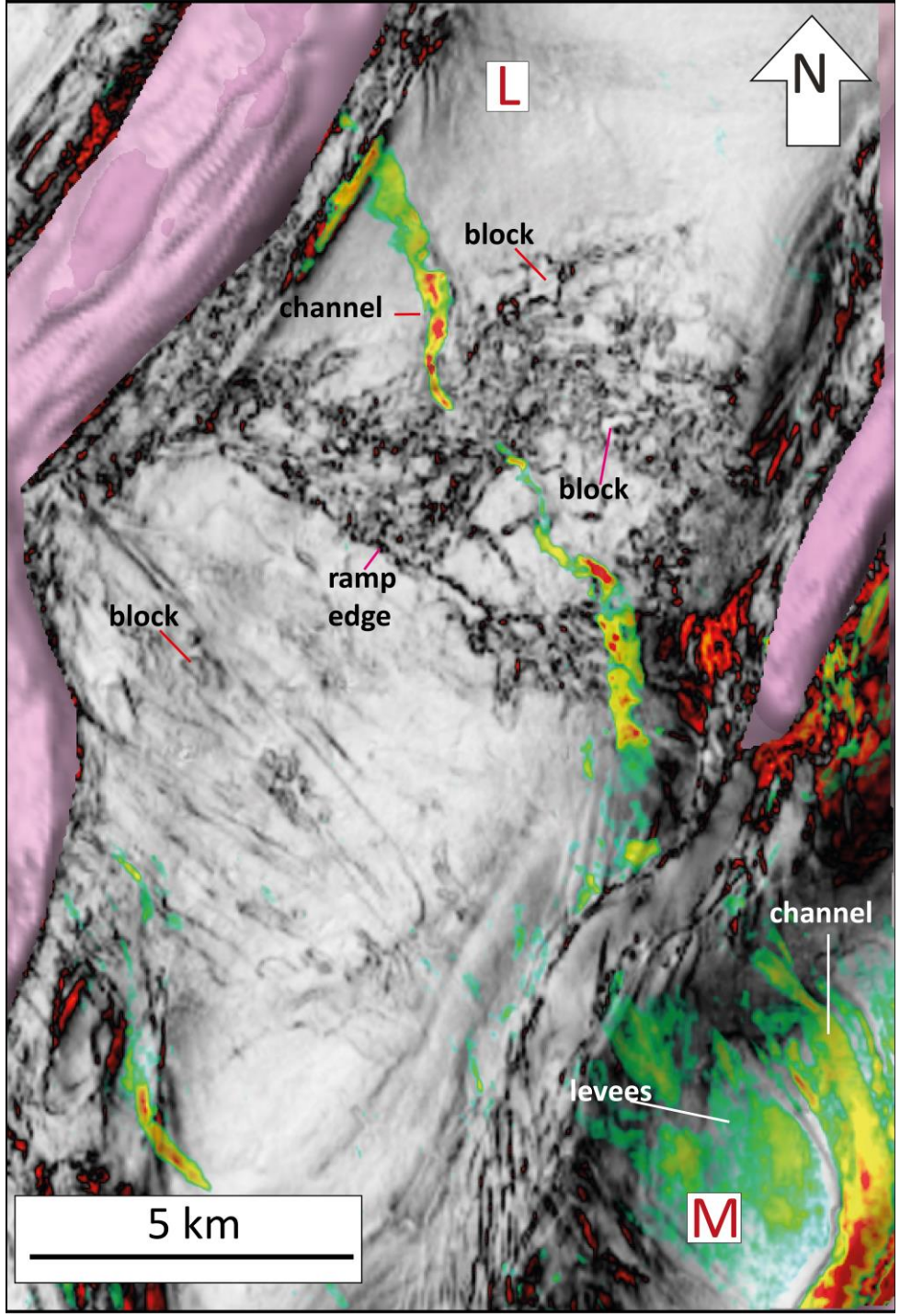

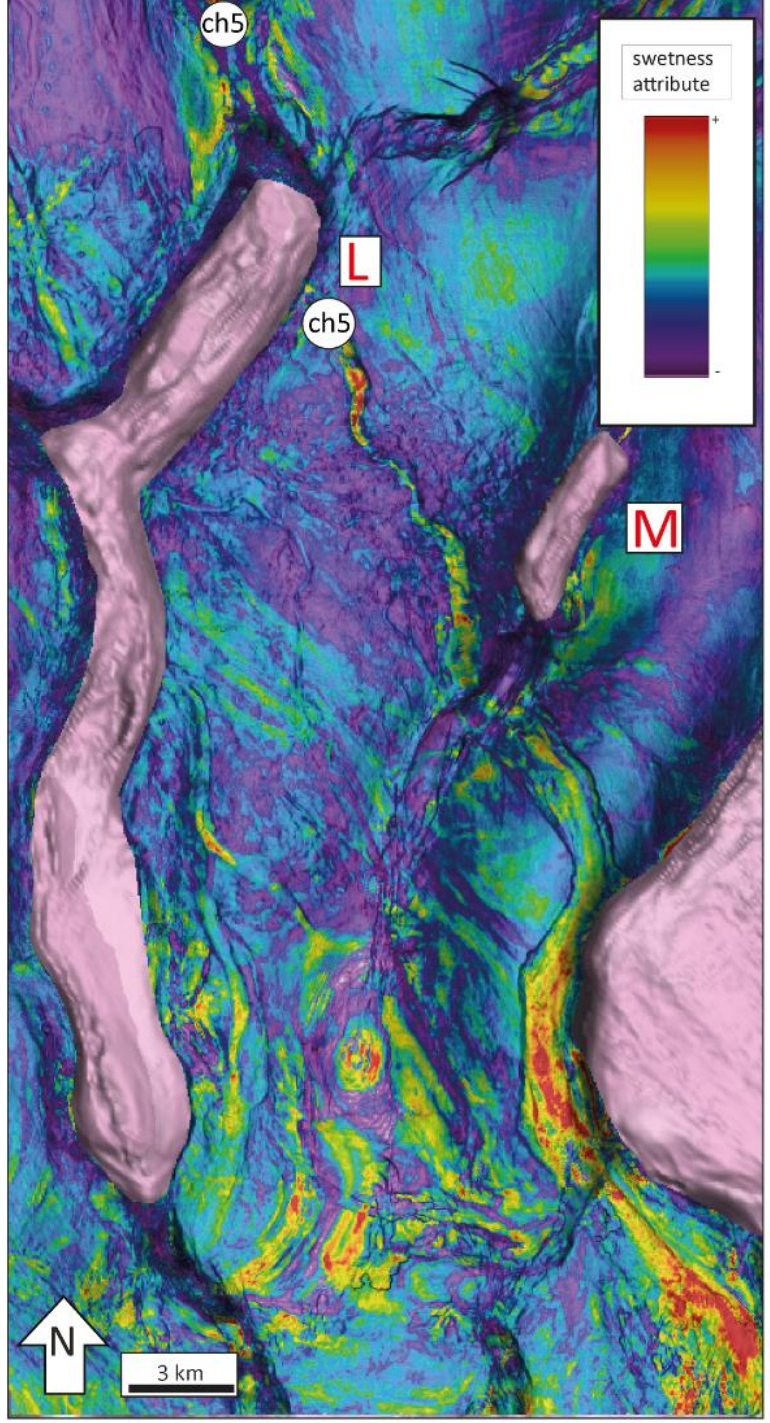

Phase 2

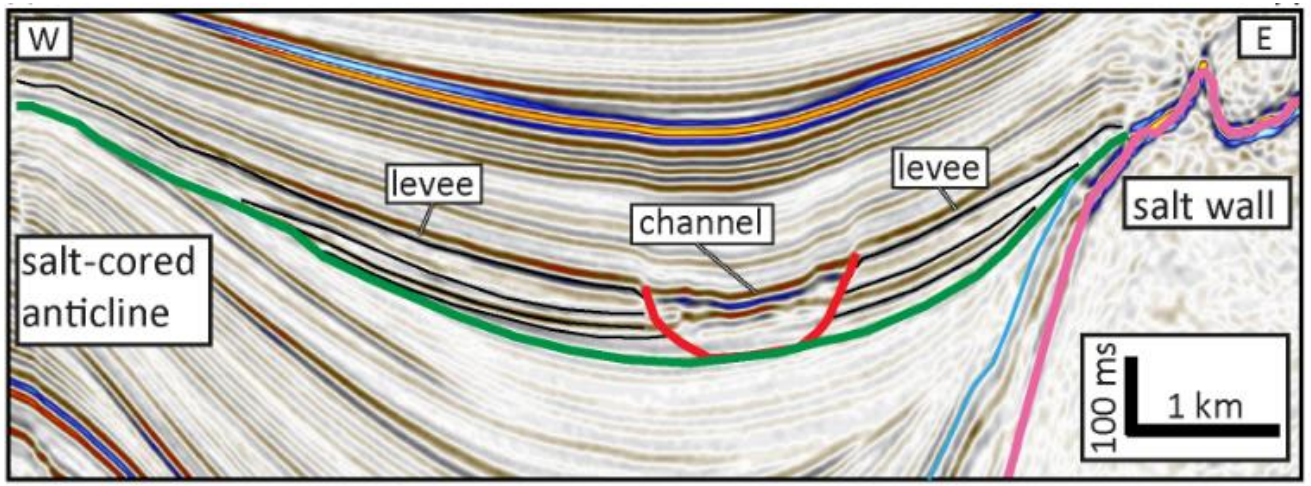

Levees onlap onto and are rotated on the limbs of the salt-cored-anticline

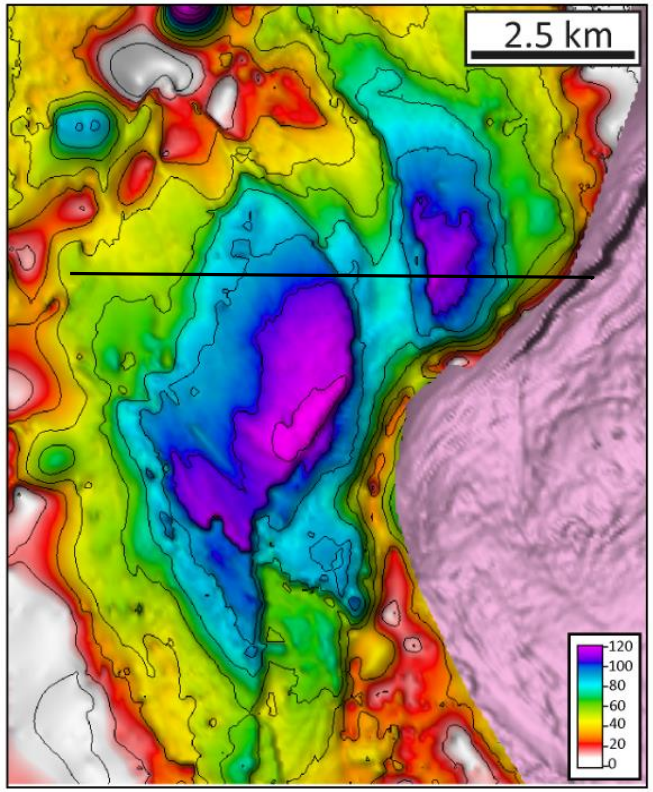

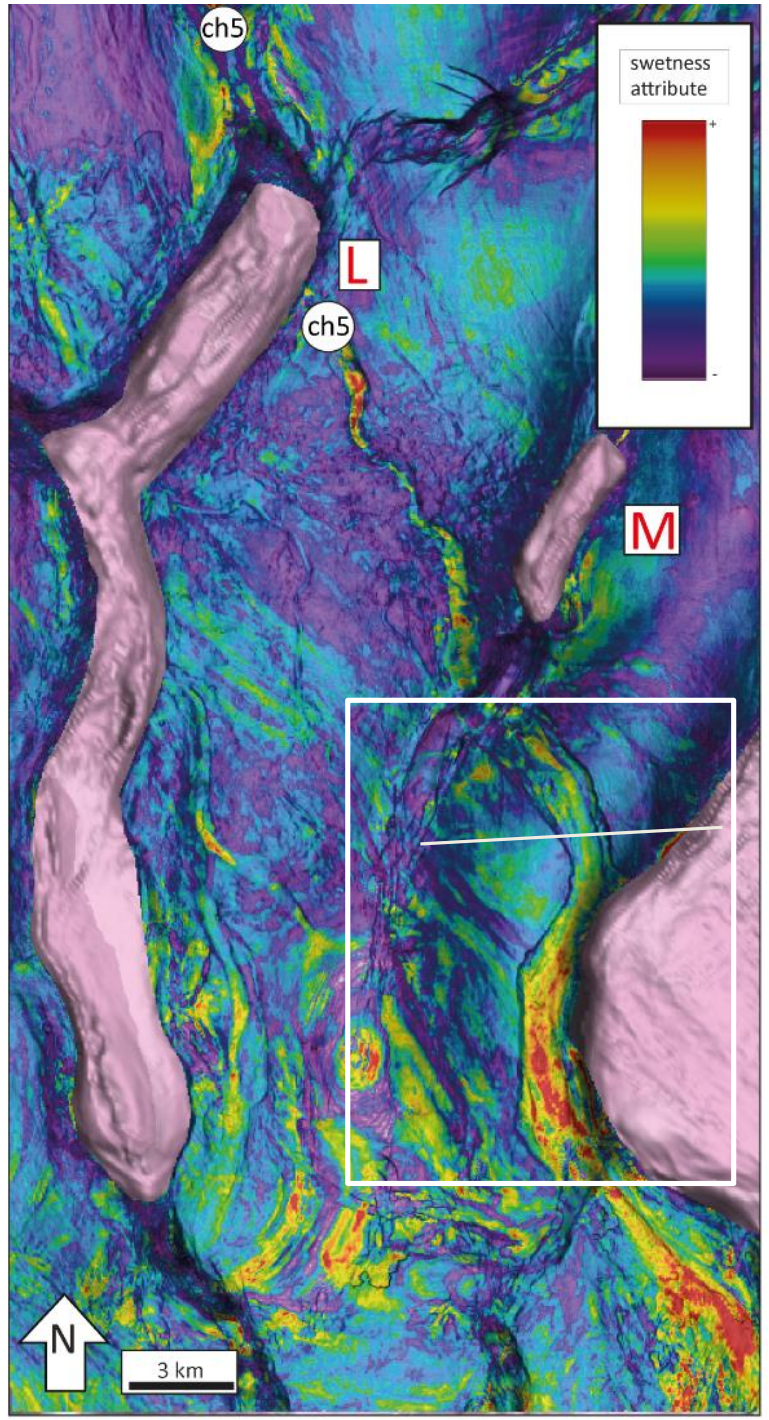

Phase 2

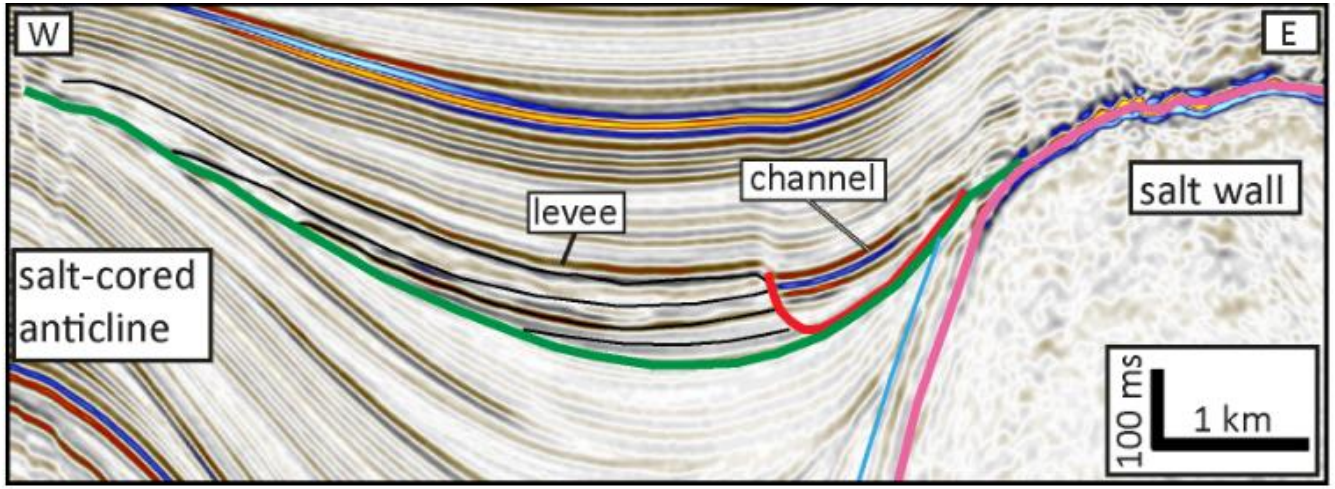

Levees onlap onto and are rotated on the limbs of the salt-cored-anticline

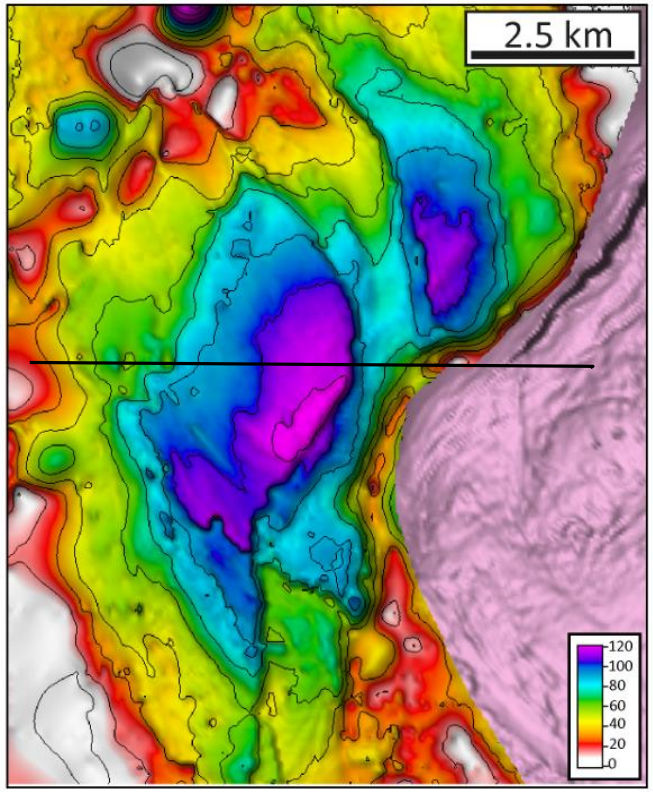

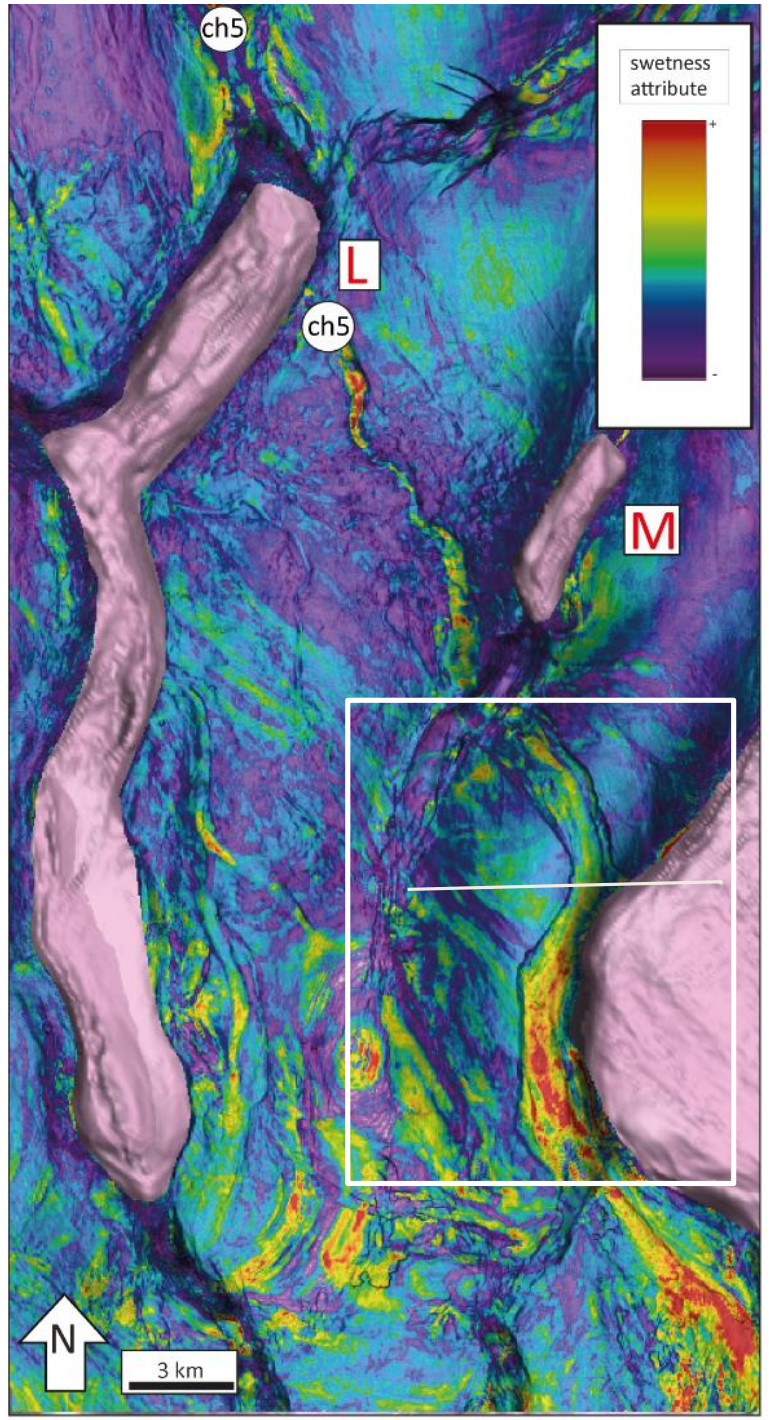

Phase 2

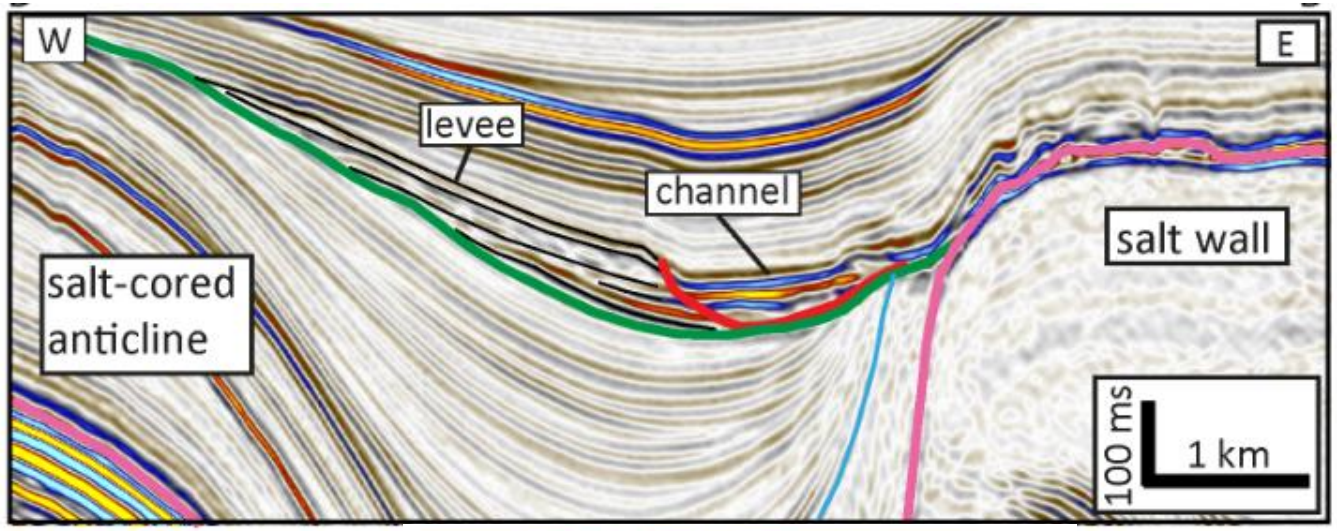

Levees onlap onto and are rotated on the limbs of the salt-cored-anticline

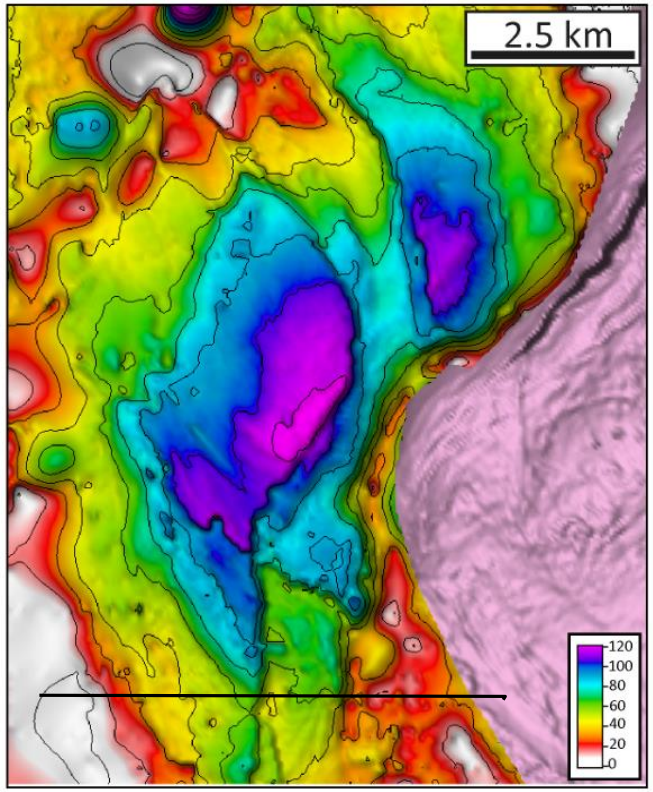

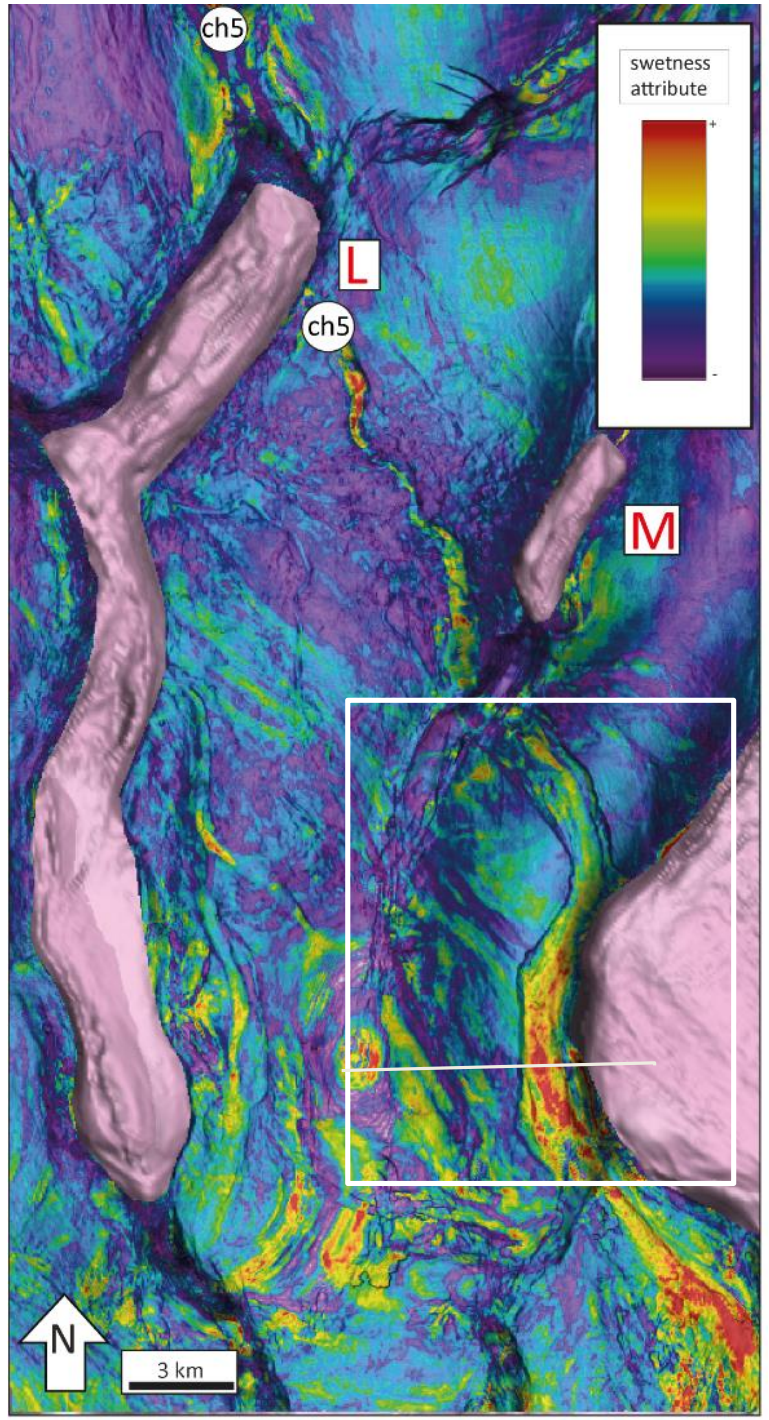

Phase 3

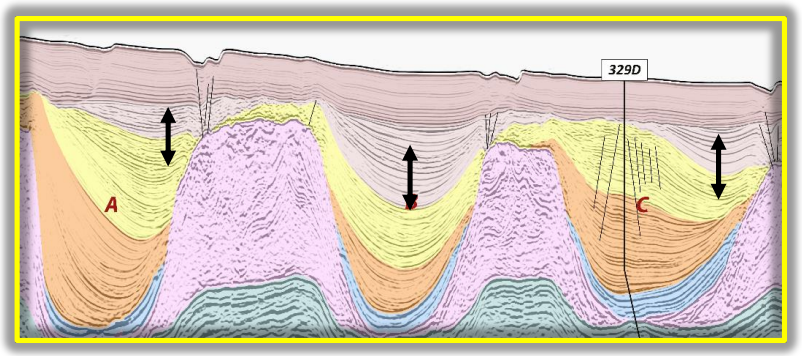

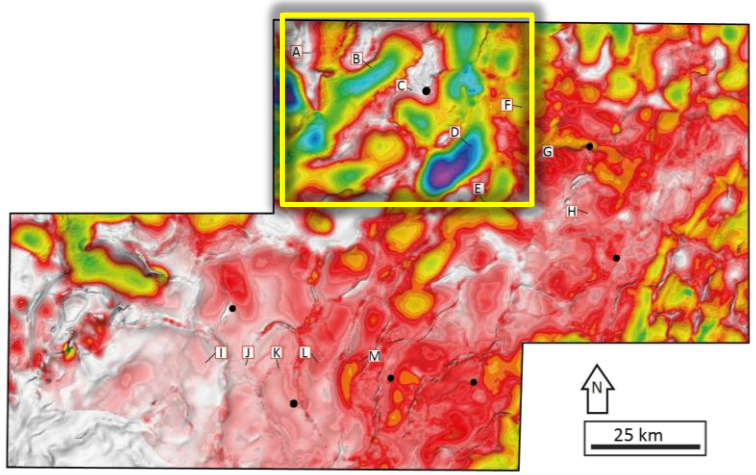

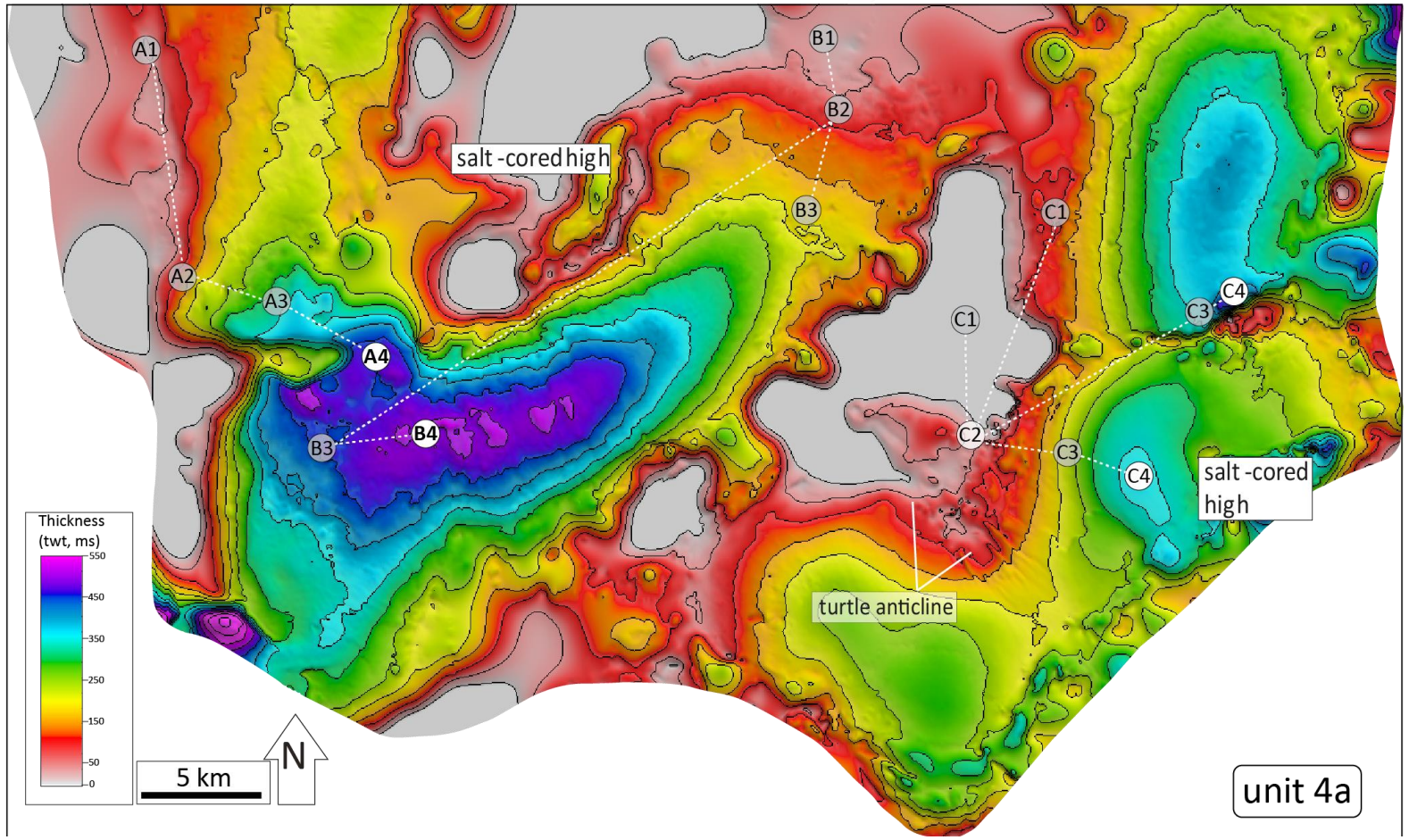

- Proximal minibasin are still actively subsiding
- Cessation of clastic deposition with channels and lobes
- Initiation of widespread MTC emplacement

Phase 3

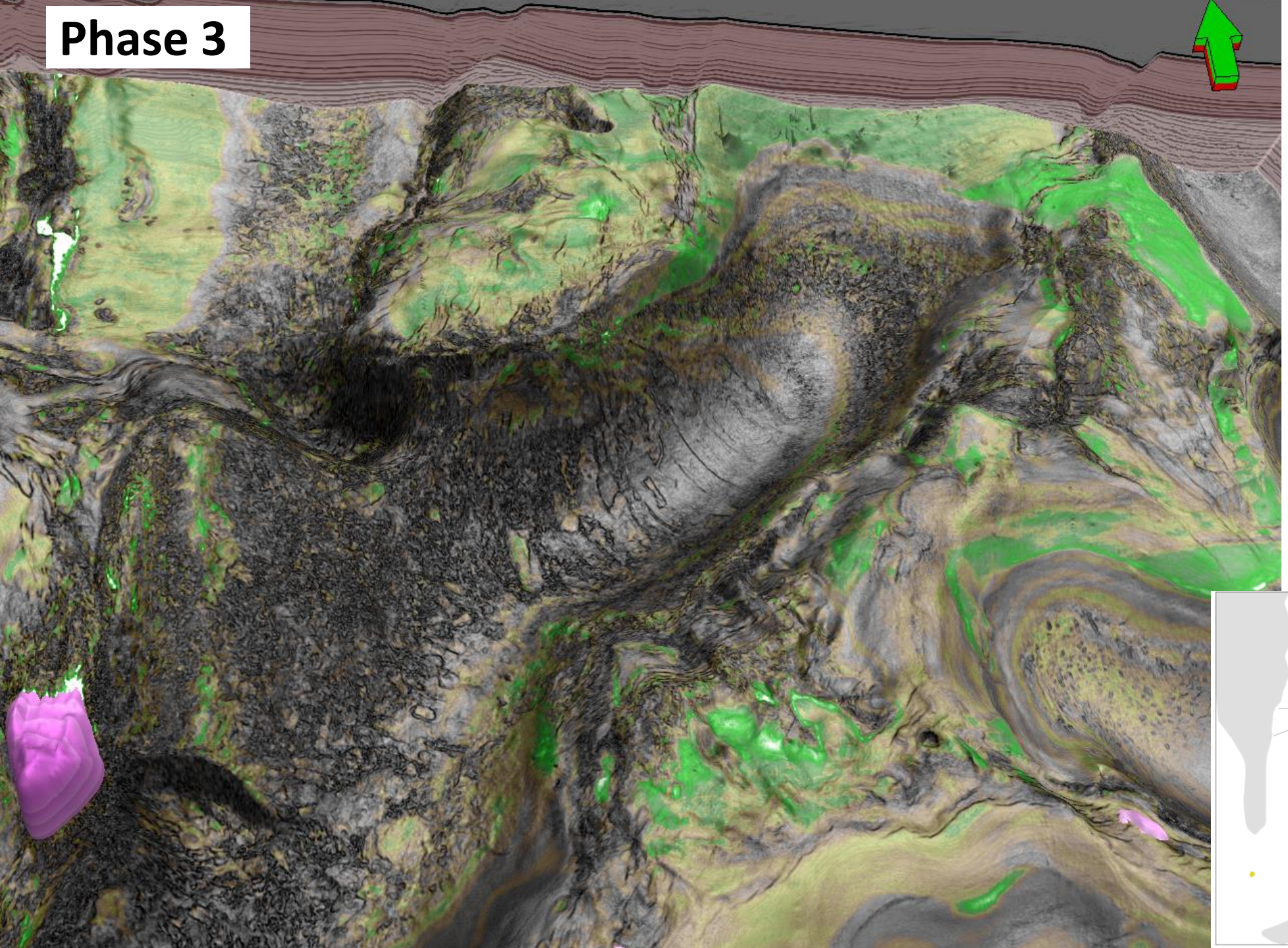

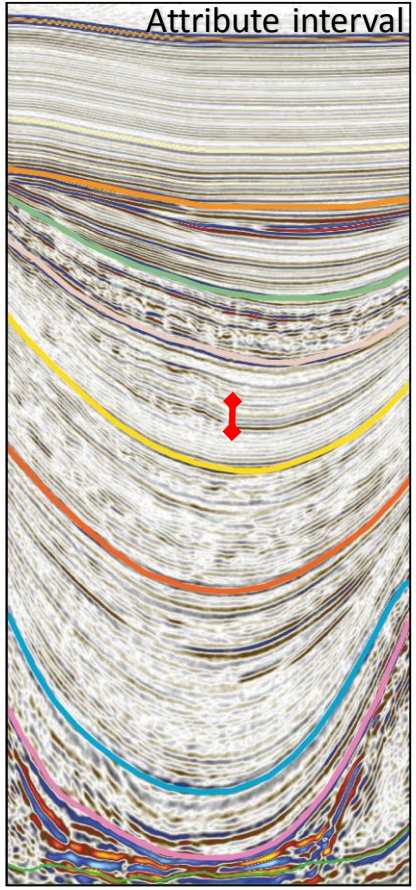
Attribute interval

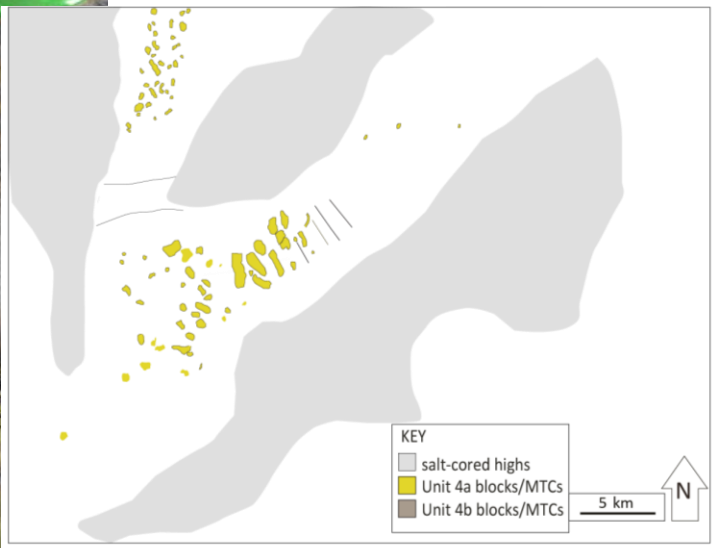
KEY
salt-cored highs
Unit 4a blocks/MTCs
Unit 4b blocks/MTCs
5 km
N

Phase 3

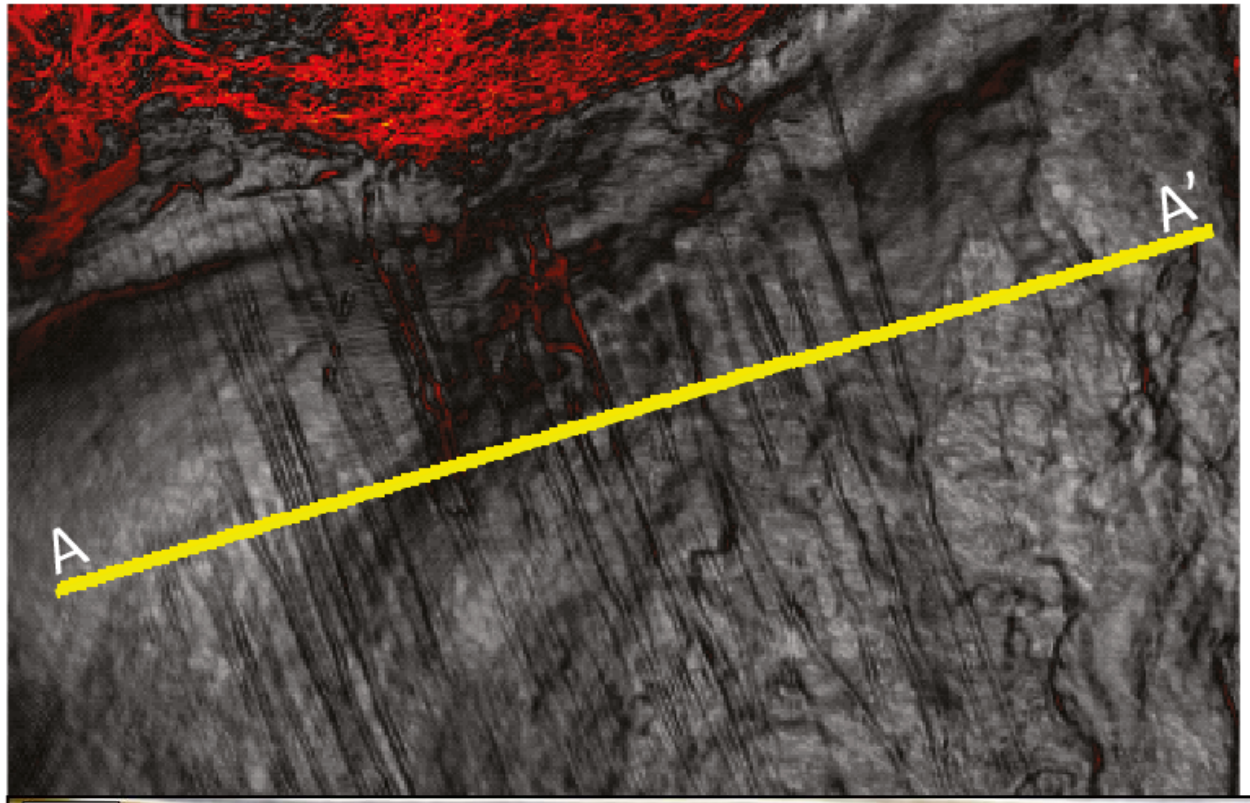

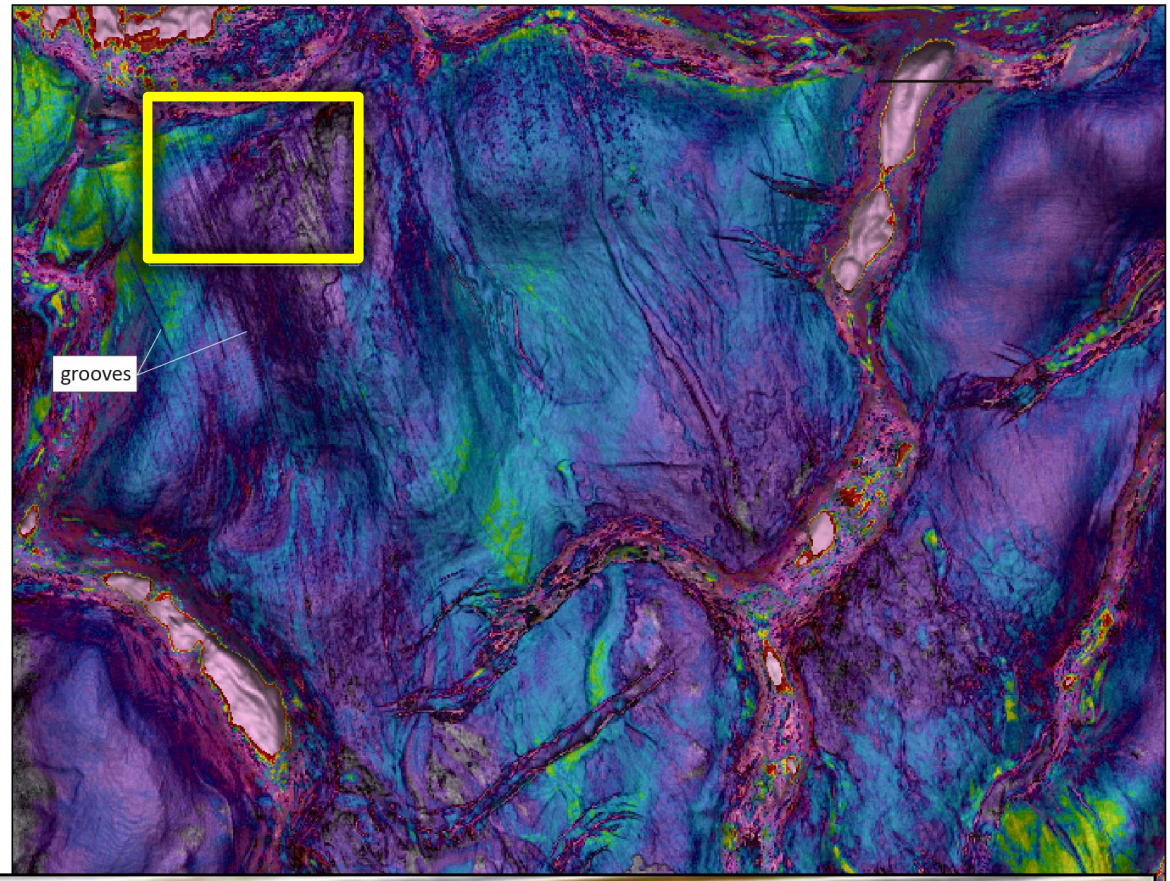

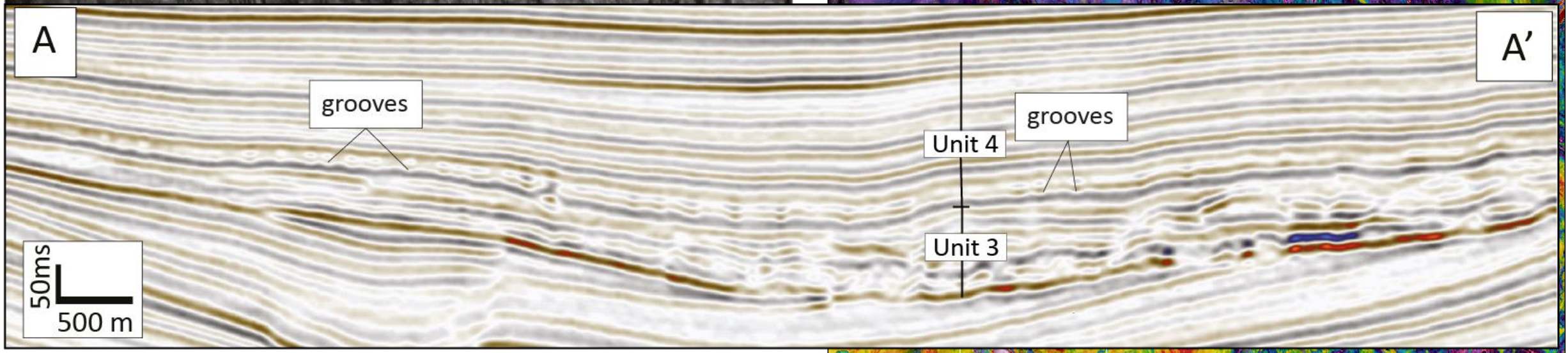

Phase 3

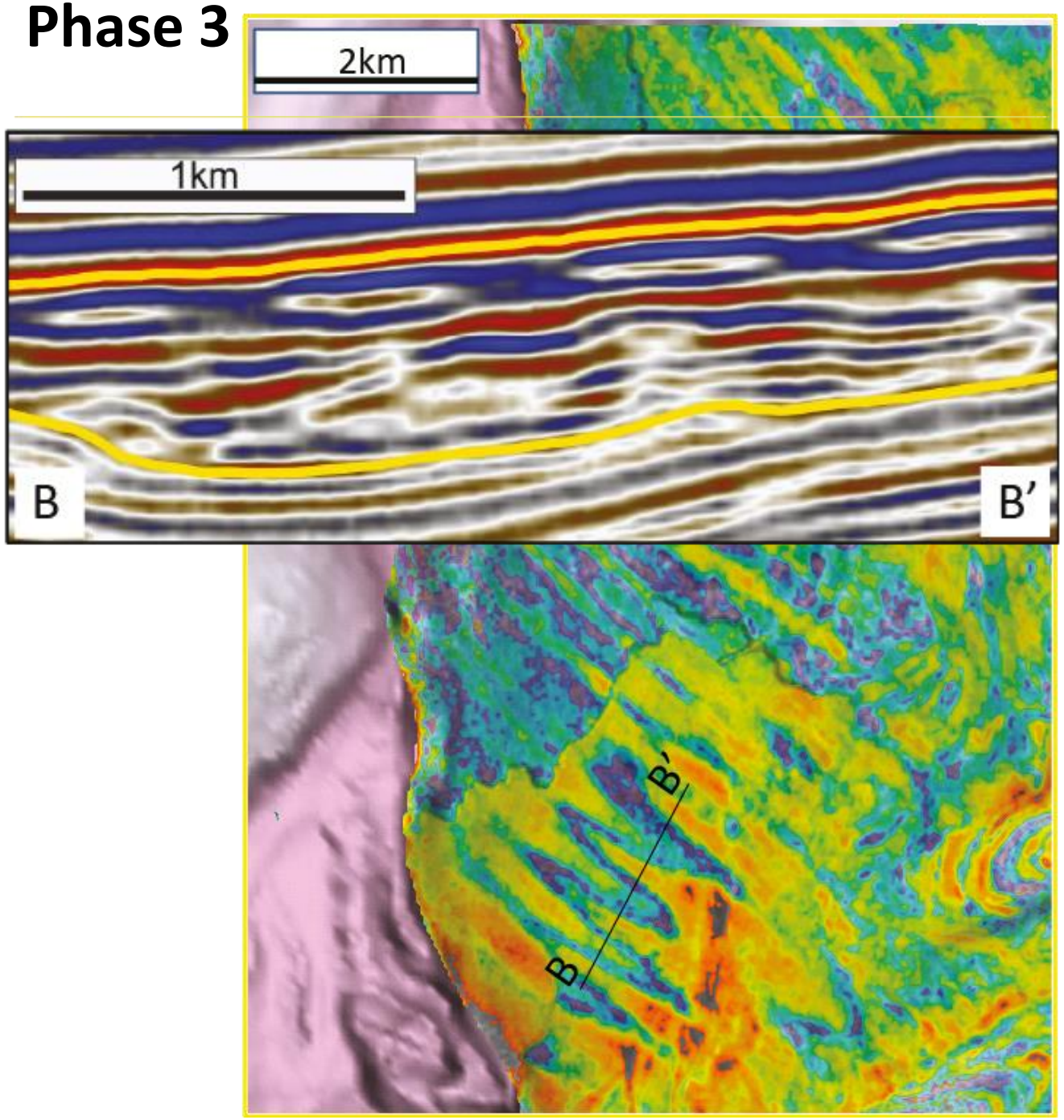
2km
1km
B
B'
B'
B

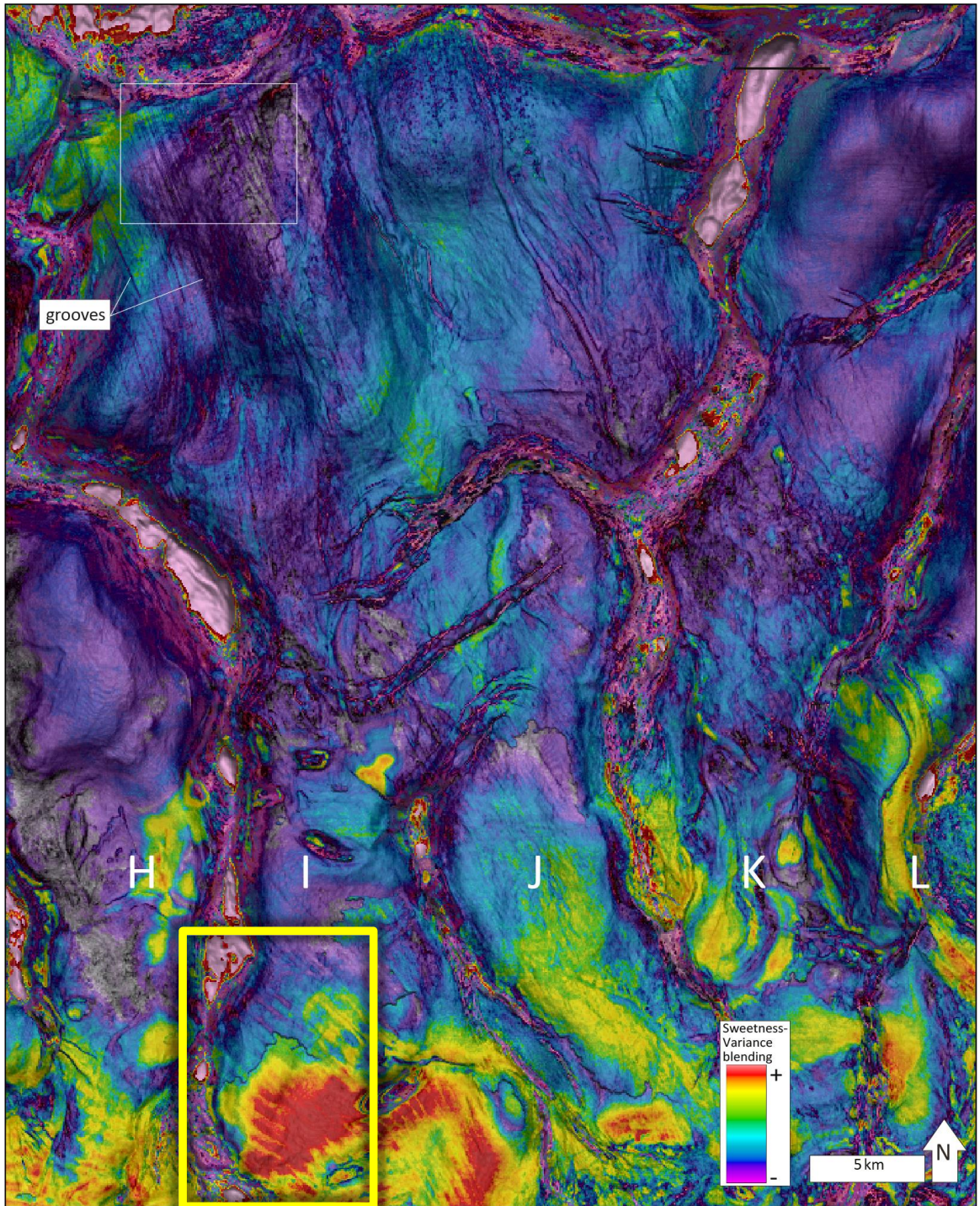
grooves
H
I
J
K
L
Sweetness-Variance blending
+
-
5 km
N

Phase 4

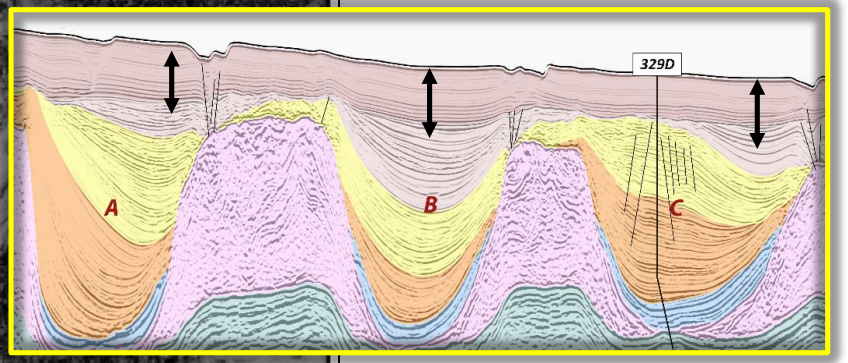

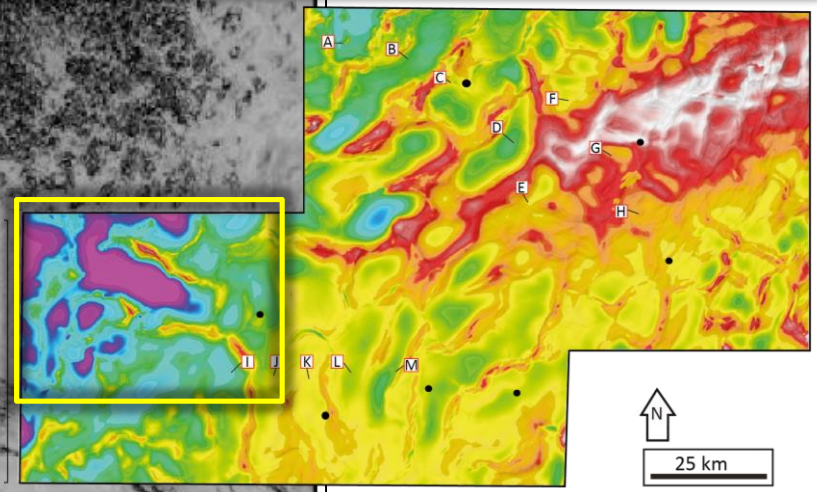

clasts

Amplitude contrast
+
-

N

5 km

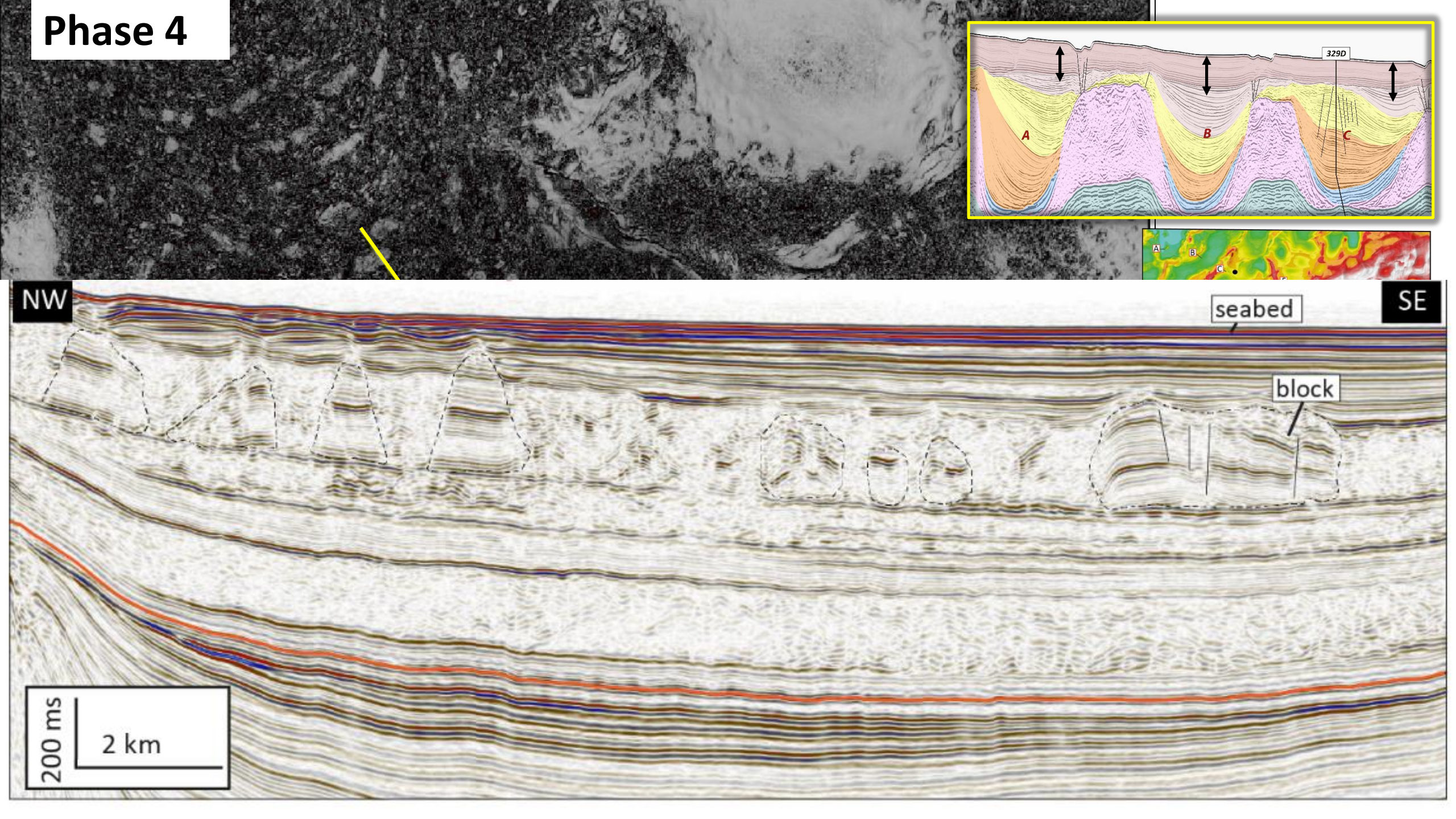
Phase 4
329D
A
B
C
NW
SE
seabed
block
200 ms
2 km

Exploration significance

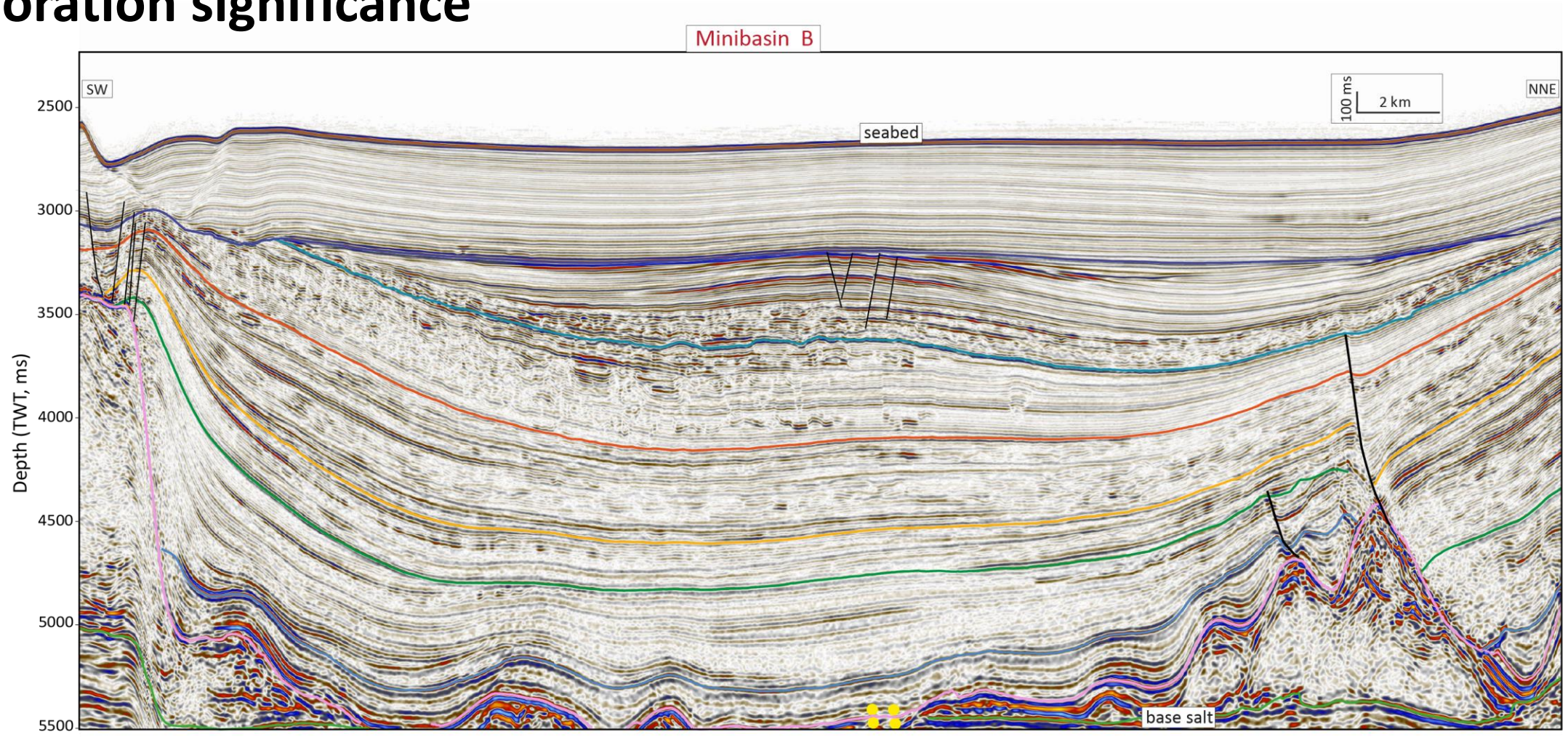

Salt-related controls led to:

- Changes in the geometry and distribution of deep-water depositional elements
- Development of potential structural and stratigraphic trapping (fault-block traps, onlap, turtle anticlines)

Exploration significance

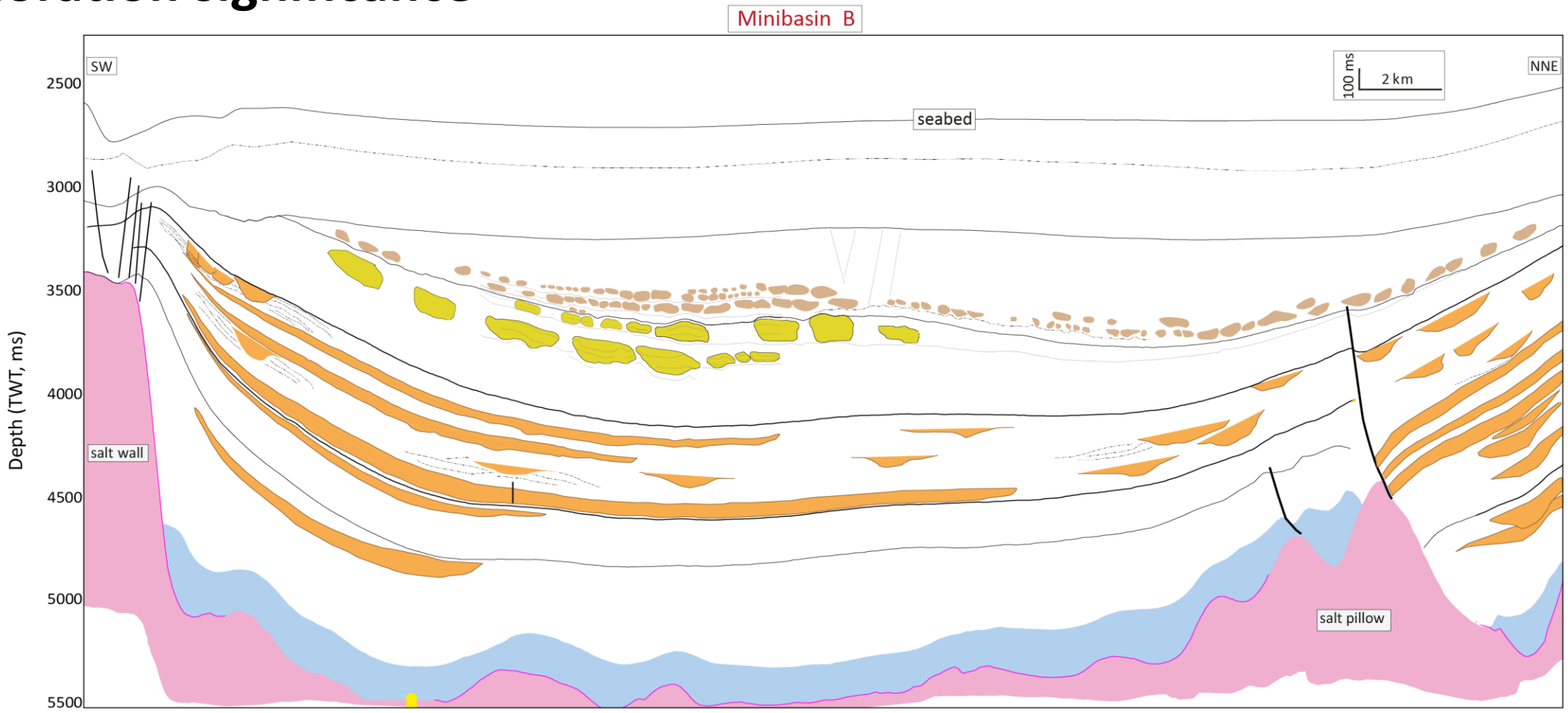

- Reservoir-prone units: channels, lobes and to a lesser-extent levees
- Seals: Background deposits such as slope mudstone, salt and mud-rich MTCs
- Key risks: Migration due to the thick, very low permeability salt. Welding can facilitate migration.
- Risks associated to MTCs.

Exploration significance

Pinch-out towards salt-cored highs

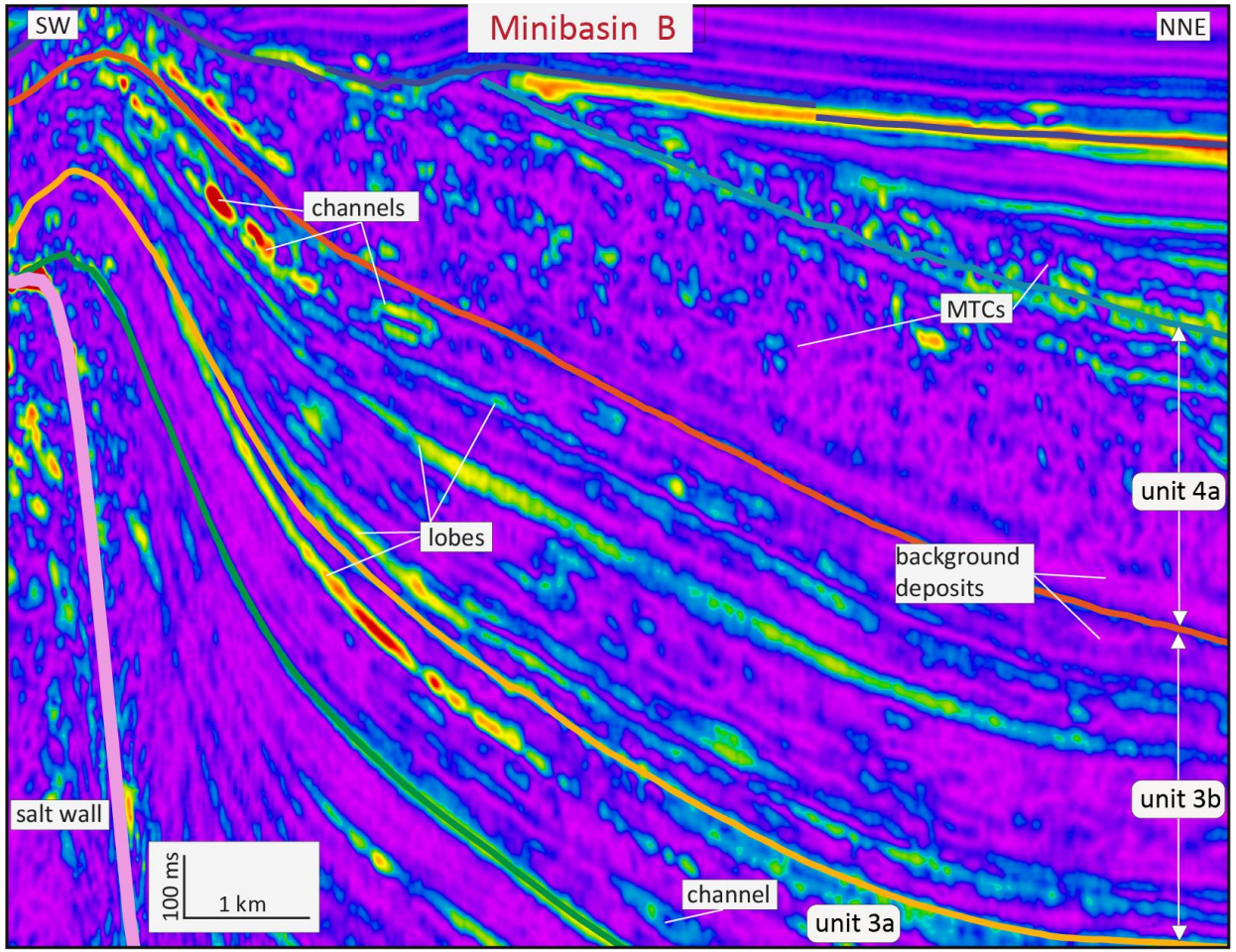

Fault-block trap

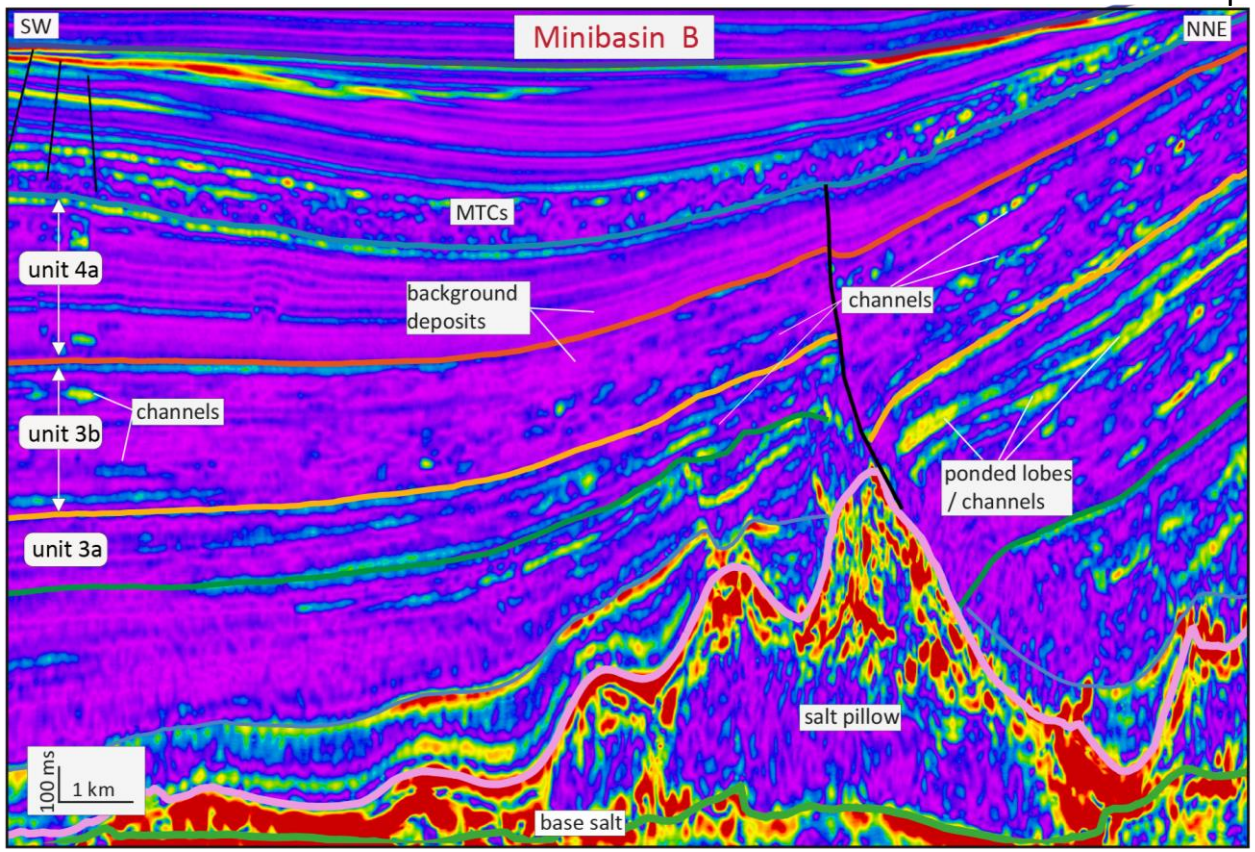

Take-away message:

The post-salt sequence in central deep-water Santos Basin may have exploration potential,

Distal analogues of the Merluza field in the Santos Basin and the Campanian and Maastrichtian deposits in the Roncador field in the Campos Basin.

U.S. Shale-Gas Reserves and Production Forecast: A Bottom-Up Approach*

Scott Tinker[1], John R. Browning[1], Svetlana Ikonnikova[1], Gurcan Gulen[1], Tad Patzek[1], Eric Potter[1], William Fisher[1], Qilong Fu[1], Susan Horvath[1], Frank Male[1], Ken Medlock[1], Forrest Roberts[1], and Katie Smye[1]

Search and Discovery Article #10542 (2013)**
Posted December 9, 2013

*Adapted from oral presentation given at AAPG International Conference and Exhibition, Cartagena, Colombia, September 8-11, 2013
**AAPG © 2013 Serial rights given by author. For all other rights contact author directly.

[1]Bureau of Economic Geology, University of Texas at Austin, Austin, TX (gurcan.gulen@beg.utexas.edu)

Abstract

This presentation develops an estimate for the Barnett and Fayetteville shales of their technically recoverable reserves (TRR) and their estimated ultimate recovery (EUR). The key drivers of both reserve estimates are discussed and the key distinguishing characteristics between the two fields are discussed.

The analysis is based on field-wide geologic mapping and well-by-well production analysis of every producing well in each field. Well-by-well EUR's are determined using an innovative decline analysis technique. The acreage is then into divided 10 production quality tiers per field. Individual drainage areas are then determined for each well. The remaining acreage available for development is then used to determine a drillwell location inventory assuming an average well for each rock quality tier. The location inventory added to the EUR of existing wells creates a theoretical technically recoverable reserve for each field. A production model is then used to predict the pace of development of the drillwell location inventory constrained by well economics. The pace and production impact of expected drilling is then tracked for each year through 2030 to determine a field-wide EUR. The study investigates how EUR will be impacted by many of the underlying drivers.

Several results of the study are new to industry. Our approach to decline analysis assuming linear transient flow better aligns with physical models. Our study generally points to higher recovery across smaller drainage areas than is commonly accepted. These estimates result in a higher estimate of TRR than has been estimated previously by EIA and USGS. However, the development of the TRR will be greatly constrained by the economic thresholds for development in each rock quality tier leading to a smaller EUR as a percent of TRR than previous estimates.

The study will highlight the differences in the Fayetteville and Barnett. The study draws insights that will be helpful as other shale gas fields are developed with each exhibiting their individual characteristics. This study serves to highlight the key issues that control industry's ability to estimate TRR and to fully develop into EUR.

References Cited

Fu, Q., S. Horvath, E.C. Potter, F. Roberts, S.W. Tinker, S. Ikonnikova, W.L. Fisher, and J. Yan, in press, Log-derived thickness and porosity of the Barnett Shale Play, Fort Worth Basin, Texas: A proxy for reservoir-quality assessment: AAPG Bulletin, in press.

Montgomery, S.L., D.M. Jarvie, K.A. Bowker, and R.M. Pollastro, 2005, Mississippian Barnett Shale, Fort Worth Basin, north-central Texas; gas-shale play with multitrillion cubic foot potential: AAPG Bulletion, v. 89/2, p. 155-175.

U.S. Shale-Gas Reserves and Production Forecast: A Bottom-Up Approach

Funded by Alfred P. Sloan Foundation

Scott Tinker, John R. Browning, Svetlana Ikonnikova, Gürcan Gülen, Tad Patzek, Eric Potter, William Fisher, Qilong Fu, Susan Horvath, Frank Male, Ken Medlock, Forrest Roberts, Katie Smye

U.S. Shale Gas Plays

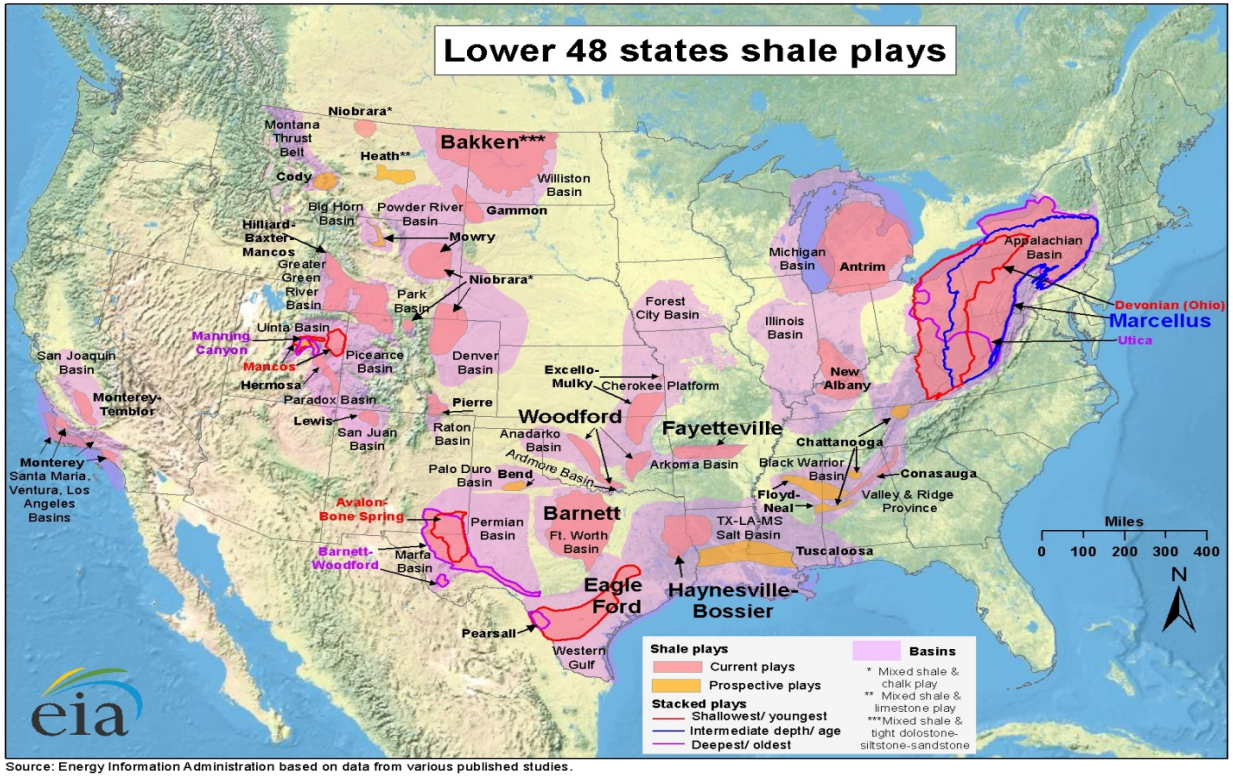

Source: Energy Information Administration based on data from various published studies.
Updated: May 9, 2011

Workflow

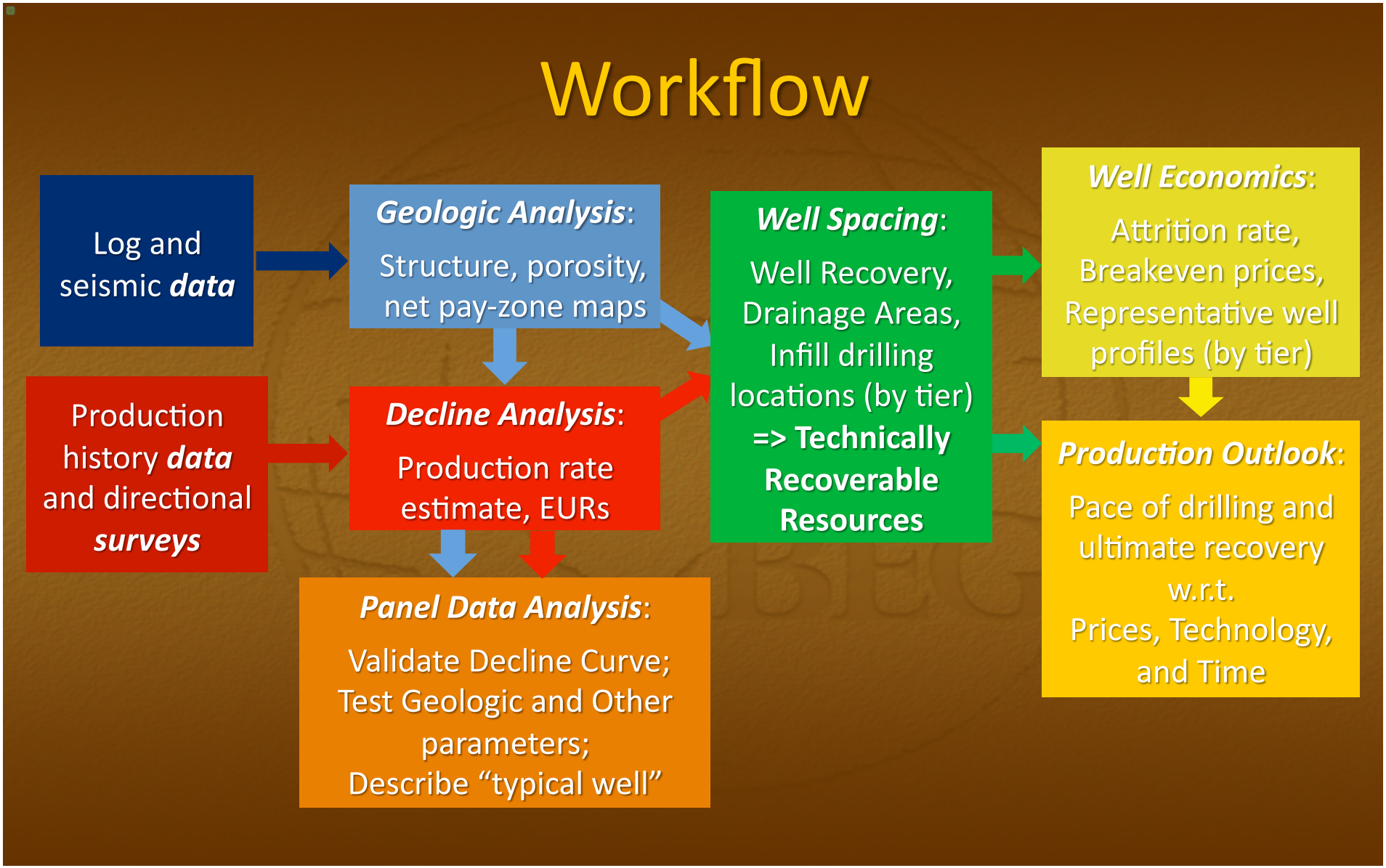
Log and seismic *data*
Production history *data* and directional *surveys*
Geologic Analysis: Structure, porosity, net pay-zone maps
Decline Analysis: Production rate estimate, EURs
Panel Data Analysis: Validate Decline Curve; Test Geologic and Other parameters; Describe "typical well"
Well Spacing: Well Recovery, Drainage Areas, Infill drilling locations (by tier) => Technically Recoverable Resources
Well Economics: Attrition rate, Breakeven prices, Representative well profiles (by tier)
Production Outlook: Pace of drilling and ultimate recovery w.r.t. Prices, Technology, and Time

Geological Approach

- Utilize gamma ray, density, and neutron porosity logs to pick pay-zone
- Calibrate density porosity using core data
- Map pay-zone thickness and porosity (cf. Ver Hoeve et al. 2010), and depth across the field
- Calculate original free gas-in-place and compare to production to determine main drivers
- Look at other geologic drivers/barriers, e.g. natural fractures, swelling clays.

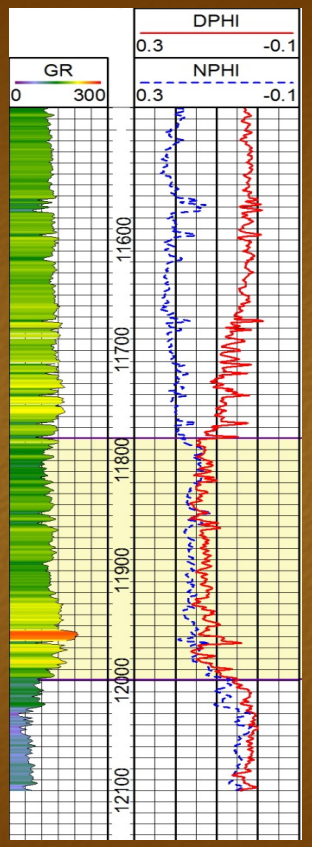

porosity and thickness maps

$$OGIP^{free} = 43560 \cdot 10^{-9} \cdot (1 - S_w) \cdot \phi \cdot H \cdot {}^{640}/_{B_g}$$

assumed 0.25

includes depth-specific reservoir pressure and temperature

Barnett Shale

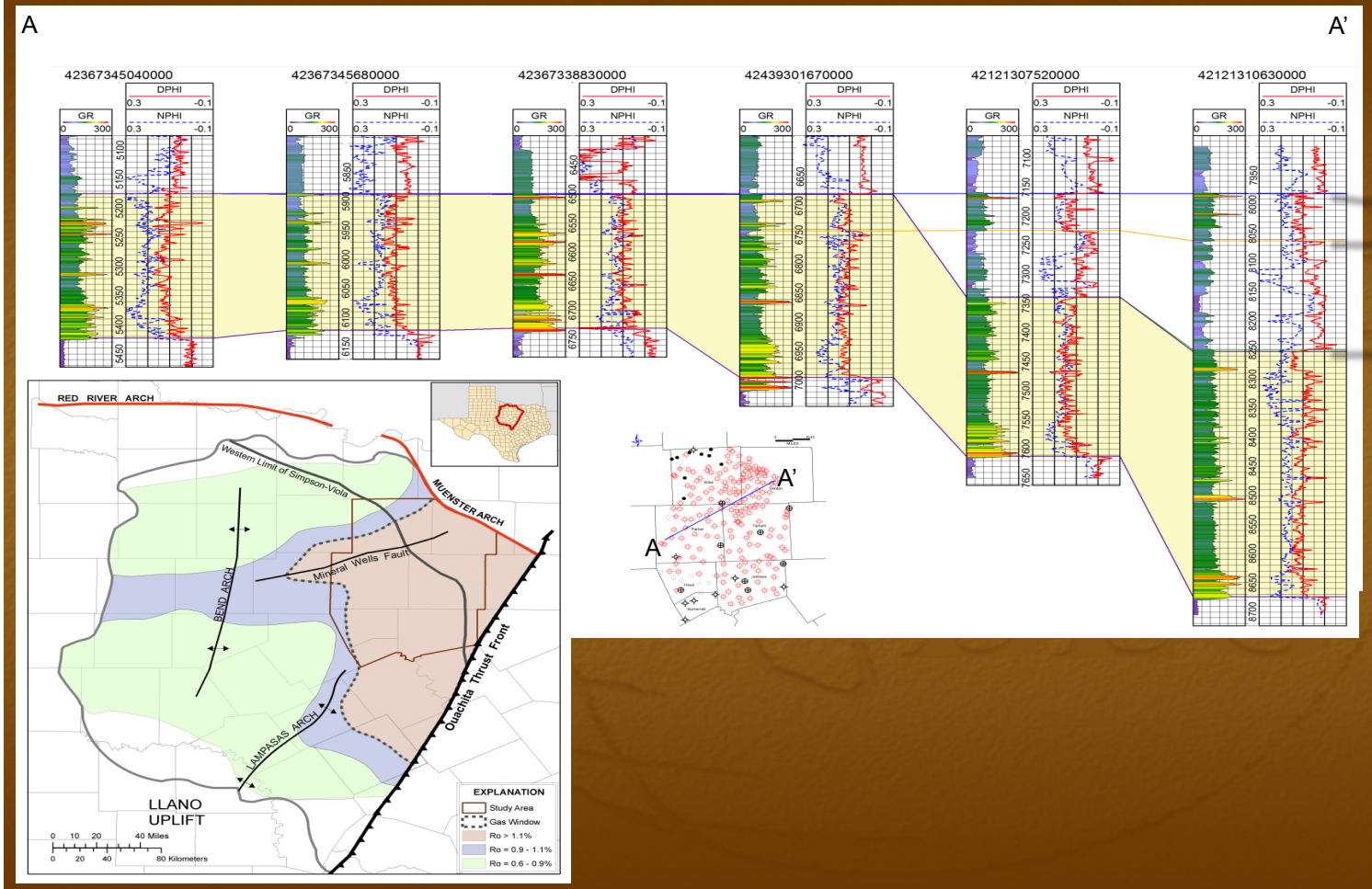

Top of the Barnett
Top of the Forestburg

Top of the pay-zone
(lower Barnett)

Modified from Montgomery et al. (2005)

Barnett Shale

Phi * H

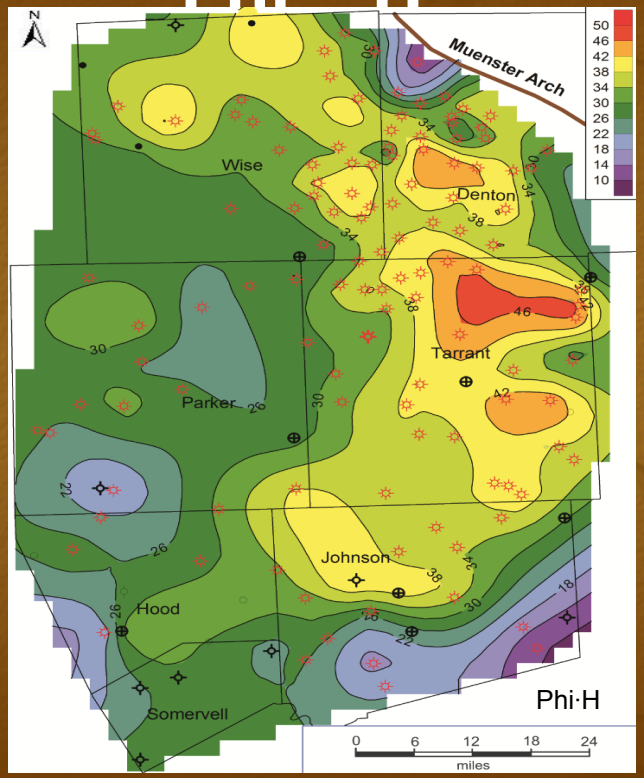

OGIP^{free}

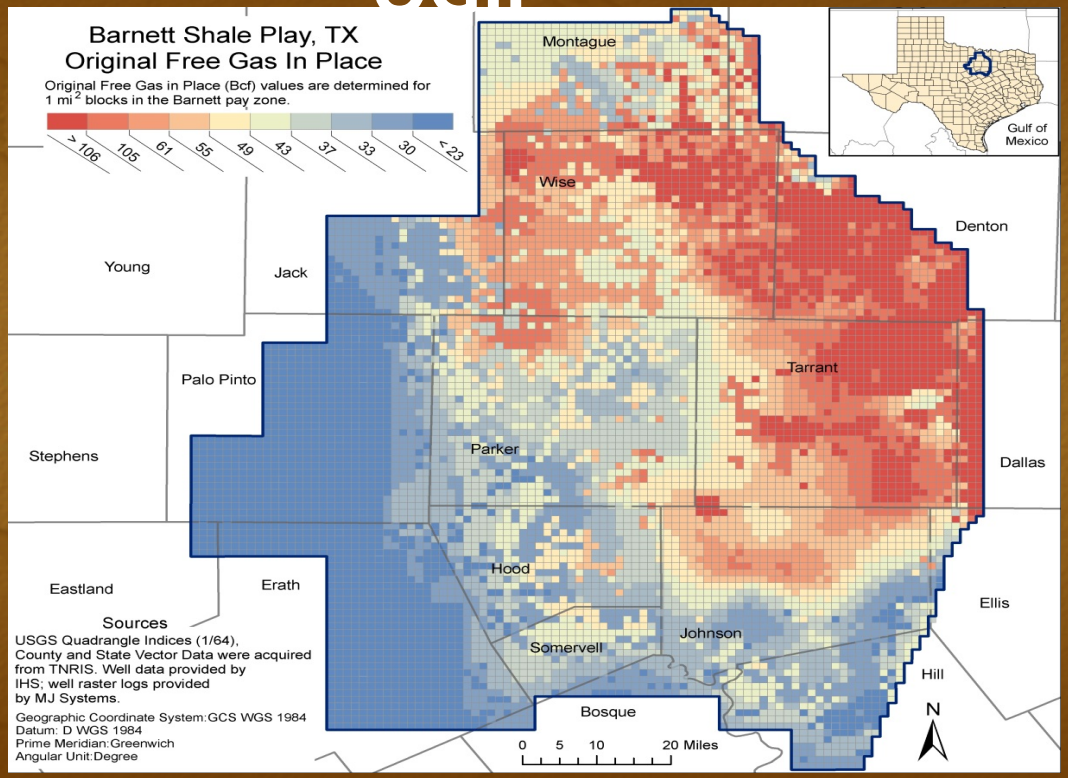

For complete Barnett geologic analysis see Fu et al. (AAPG Bulletin *in press*)

Barnett Productivity Tiers

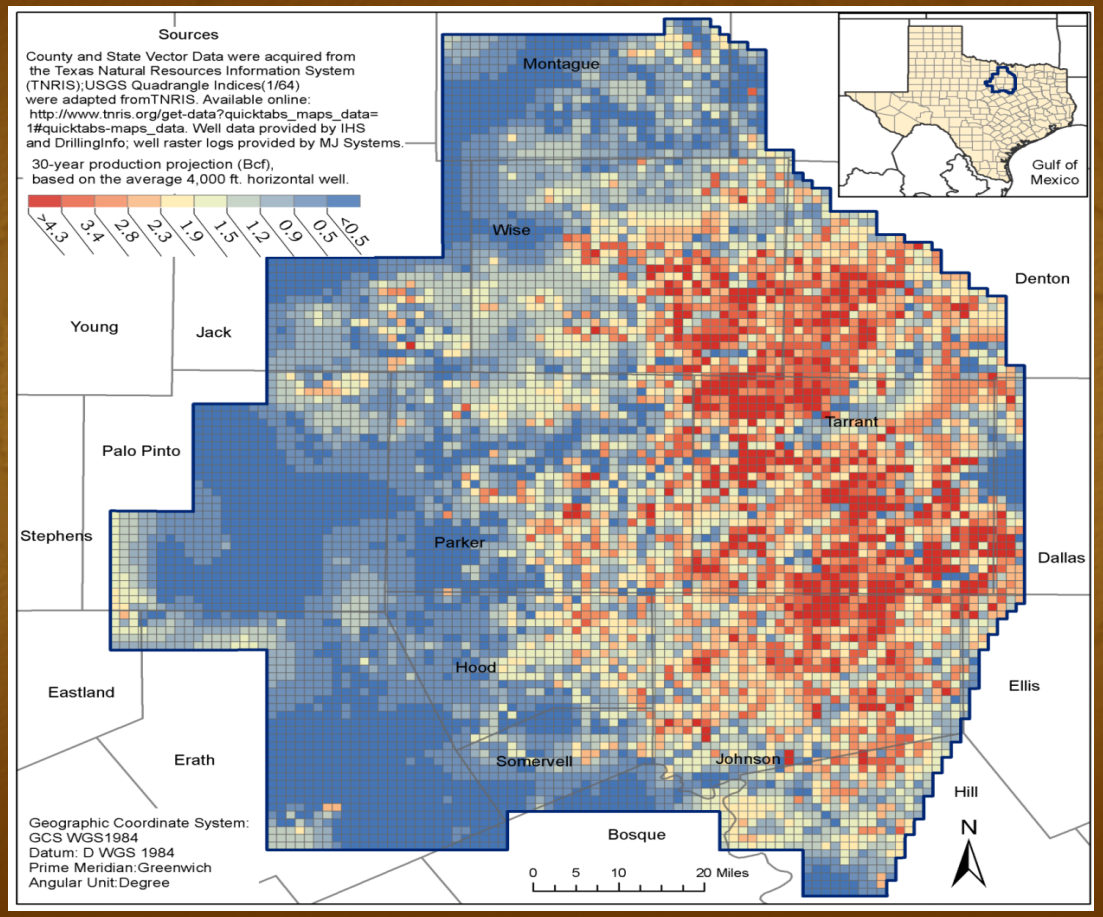

Drainage Areas and Drilling Patterns

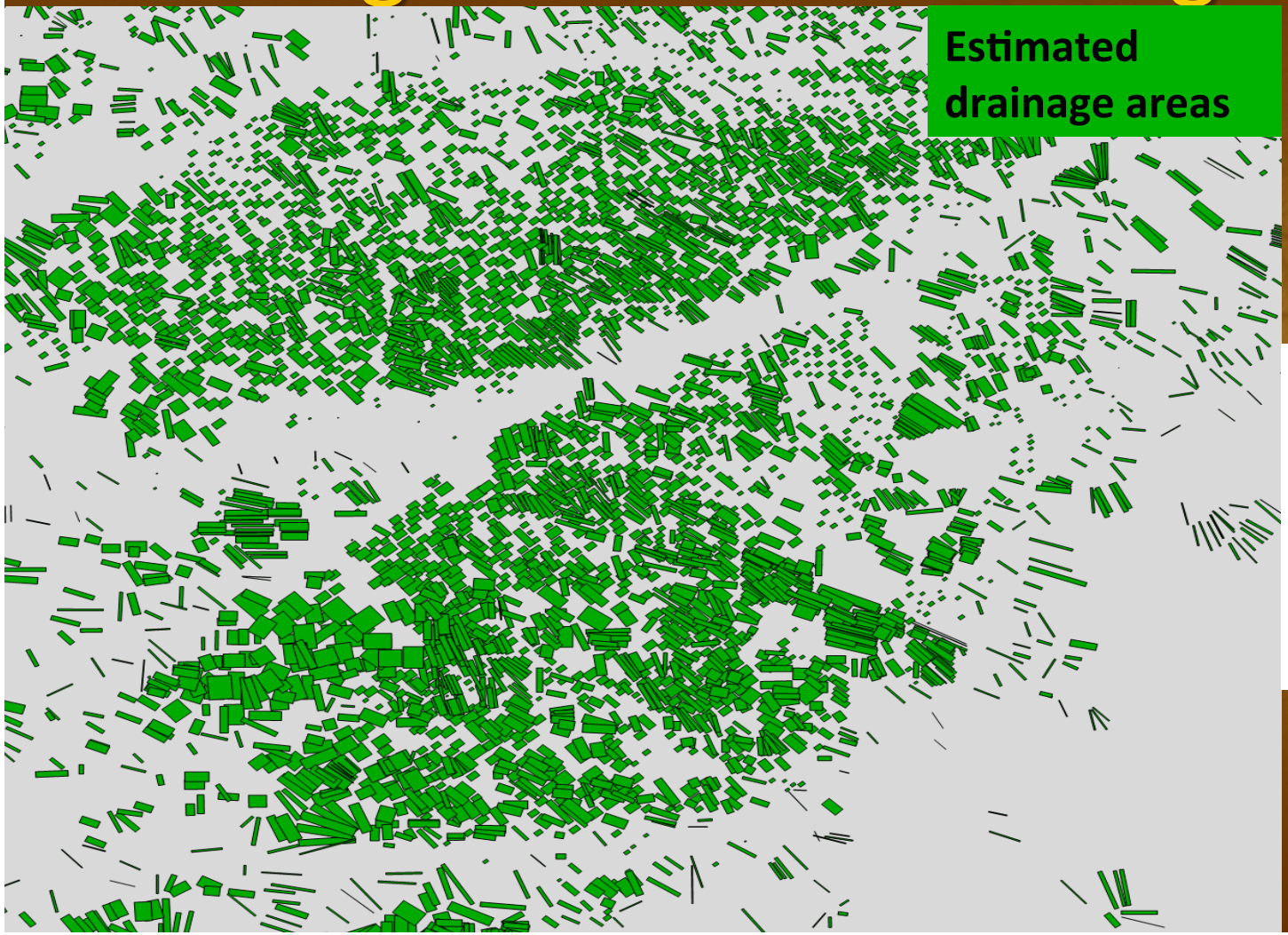

Barnett:

- Smaller leases
- Multiple operators
- Wide range of completion types

Inventory of Future Wells

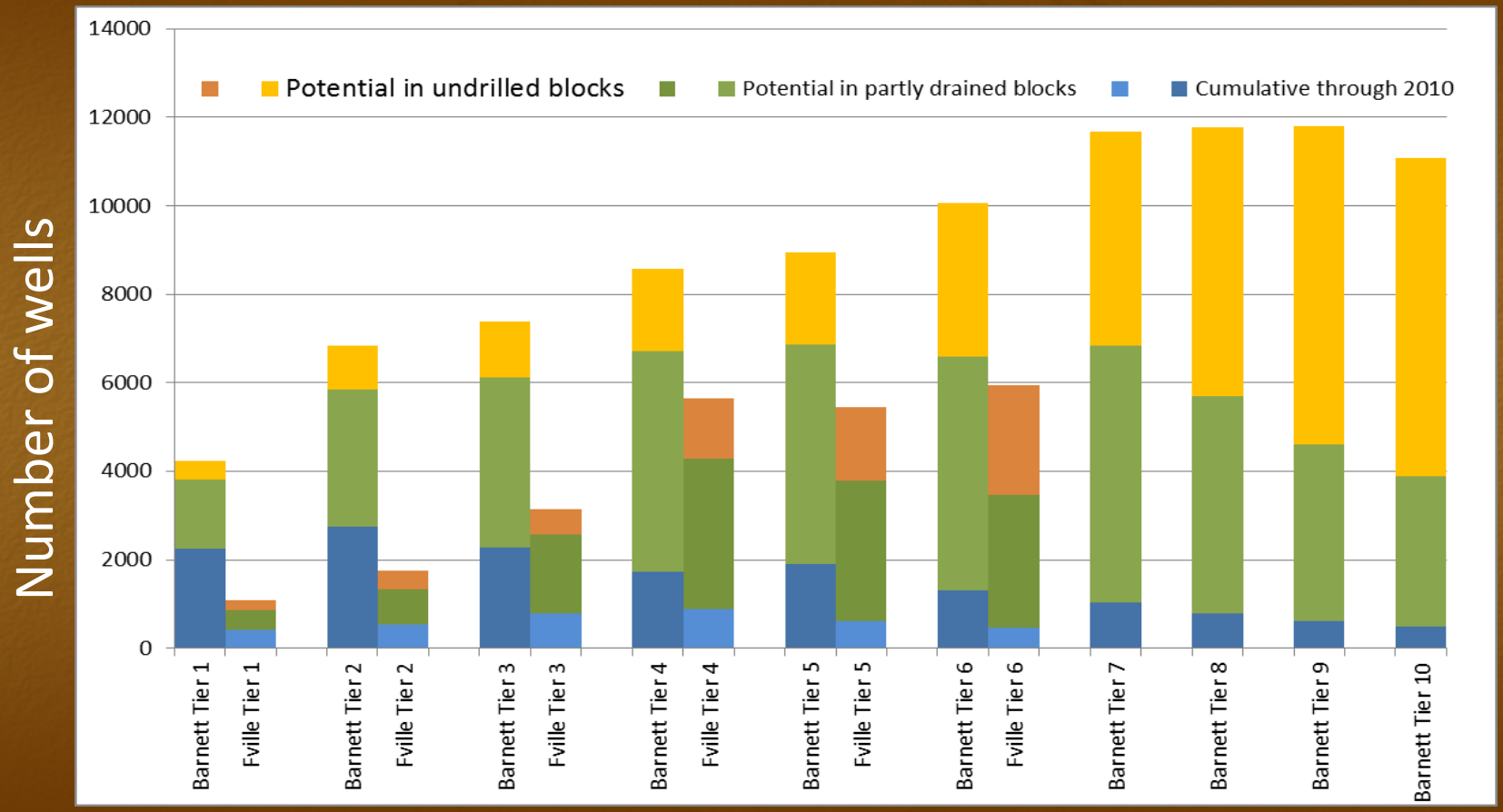

OGIP and Technically Recoverable

	Barnett
$OGIP^{free}$ (Tcf) Total area/**Developed**	444/**280**
TRR^{free} (Tcf)	86

Summary

- Multidisciplinary study by geologists, engineers, and economists, linking geologic mapping, production analysis, well economics, and development forecasting.
- Development of a physics-based decline curve that accounts for interfracture interference later in well life.
- Well-by-well analysis of production and calculation of individual well EUR for all wells.
- Improved granularity for reserve forecasting and economics through productivity tiers.
- Quantification of well-drainage volumes and recovery factors.
- Calculation of OGIPfree and TRR for each square mile.
- Work is basis for field production forecast and EUR estimate

[PS]Upper Bakken Shale Resource Play, Williston Basin*

Stephen A. Sonnenberg[1]

Search and Discovery Article #10625 (2014)**
Posted August 18, 2014

*Adapted from poster presentation given at AAPG Rocky Mountain Section Meeting, Denver, CO, July 20-22, 2014
**AAPG©2014 Serial rights given by author. For all other rights contact author directly.

[1]Colorado School of Mines, Golden, CO (ssonnenb@mines.edu)

Abstract

The Upper and Lower Bakken shales are the source beds for the Bakken Petroleum System of the Williston Basin. Reservoirs for this system include the shales, the lower Lodgepole, Middle Bakken silty dolostones, and Three Forks silty dolostones. The Upper shale was a drilling target in the late 1970s through the early 1990s in southwest part of the basin in North Dakota (termed the depositional limit play or Billings Nose play). The discovery of the giant Elm Coulee Field changed drilling strategies to focus on the Middle Bakken dolostone member. As this play extended into North Dakota, drilling success was also encountered in the upper Three Forks dolostones. The Upper Bakken shale has recently been targeted with horizontal drilling and multistage fracture stimulations along the southwest edge of Elm Coulee Field where the Middle Member pinches out. In this area wells are drilling into the Upper shale and then completed with multistage fracture stimulations. The fracture stimulations extend into the adjacent Lodgepole and Three Forks formations. So in essence, these new wells target multiple pays. Factors thought to be important in this Upper shale play include: orientation of horizontal laterals, bed thickness, natural fractures, shale mineralogy, abnormal pressure, and TOC content. This play is a similar to the previous depositional limit play in North Dakota except the wells are completed with multistage fracture stimulations. Exploration success in the Upper Bakken shales suggests that future drilling should also target the Lower Bakken shales.

Upper Bakken Shale Resource Play, Williston Basin

Stephen A. Sonnenberg
Colorado School of Mines

ABSTRACT

The Upper and Lower Bakken shales are the source beds for the Bakken Petroleum System of the Williston Basin. Reservoirs for this system include the shales, the lower Lodgepole, Middle Bakken silty dolostones, Pronghorn dolostones, and Three Forks silty dolostones. The Upper Shale was a drilling target in the late 1970s through the early 1990s in southwest part of the basin in North Dakota (termed the depositional limit play or Billings Nose play). The discovery of the giant Elm Coulee Field in Montana changed drilling strategies to focus on the Middle Bakken dolostone member. As this play extended into North Dakota, drilling success was also encountered in the upper Three Forks dolostones.

The Upper Bakken Shale has recently been targeted with horizontal drilling and multistage fracture stimulations along the southwest edge of Elm Coulee Field where the Middle Member pinches out. In this area wells are drilling into the Upper Shale and then completed with multistage hydraulic fracture stimulations. The fracture stimulations extend into the adjacent Lodgepole and Three Forks formations. So in essence, these new wells target multiple pays. Factors thought to be important in this Upper Shale play include: orientation of horizontal laterals, bed thickness, natural fractures, shale mineralogy, abnormal pressure, and TOC content. This play is a similar to the previous depositional limit play in North Dakota except the wells are completed with multistage fracture stimulations.

Exploration success in the Upper Bakken shales suggests that future drilling should also target the Lower Bakken Shale.

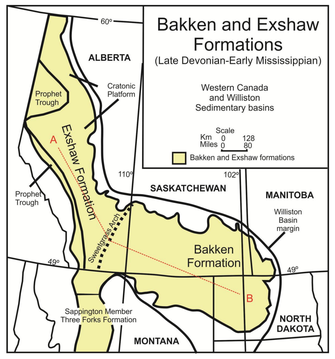

Distribution of Bakken and Exshaw sediments.

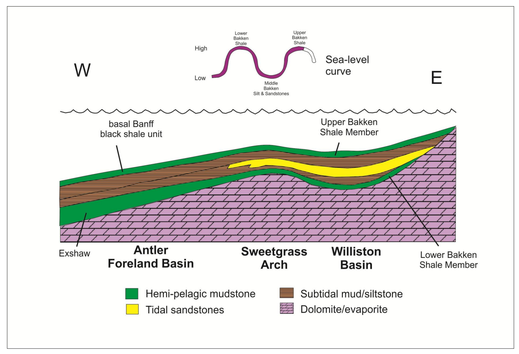

Cross section A-B showing Bakken and Exshaw correlations.

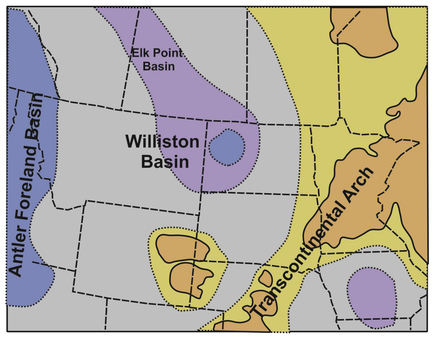

Paleogeography of the Williston Basin, Late Devonian.

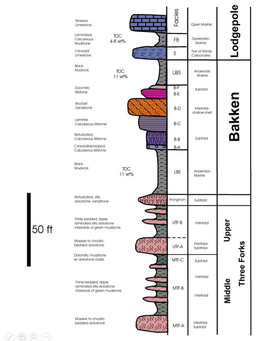

USGS 2013
7.4 BBO
6.7 TCFG

Production
North Dakota only
548 MMBO cumulative
847,000 BOPD

Stratigraphic column for the Bakken Petroleum System.

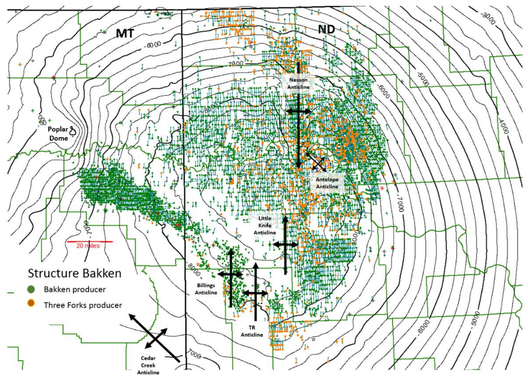

Structure map top Bakken. Three Forks and Bakken producers also indicated. Wells shown are Bakken, Three Forks producers only.

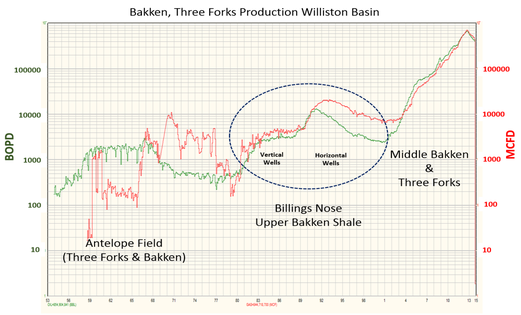

Bakken and Three Forks production, US Williston Basin. The Billings Nose part of the plot illustrates production from the Upper Bakken Shale and adjacent beds.

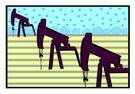

The Bakken Cycles

- **Vertical drilling: Bakken (pre--1987)**
  - **Antelope Structure (1950s--60s)**
  - **Depositional Edge (1970s--80s)**
- **Horizontal Drilling of the Bakken Shale (post-1987)**
- **Horizontal Drilling of the Bakken Middle Member (2001 to present)**
- **Horizontal Drilling of the Three Forks (2008 – P)**

Modified from LeFever, 2004

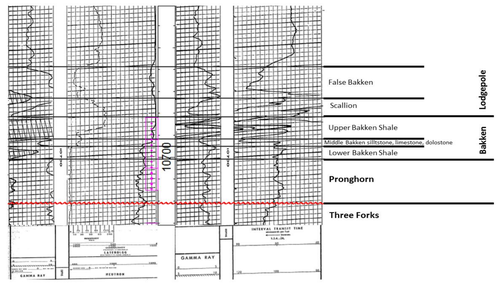

Type log Billings Nose area, Shell Federal 41X-5-1 (Sec. 5, T143N, R101W). Discovery well for the Billings Anticline Bakken play drilled in 1961.

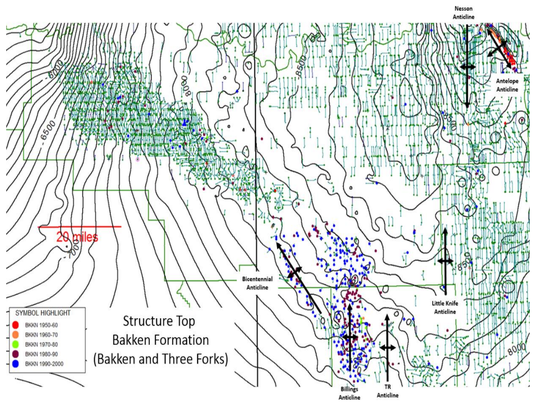

Structure top Bakken, southern Williston Basin showing completion of wells by various decades. Wells shown are Bakken, Three Forks producers only.

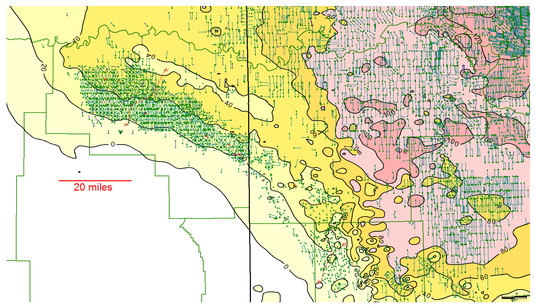

Figure 5. Isopach total Bakken, Billings Nose area. Wells shown are Bakken, Three Forks producers only.

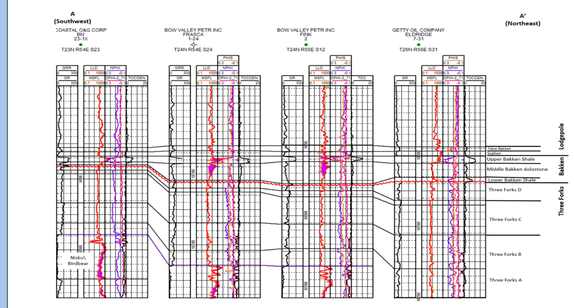

Cross-section Elm Coulee. Shaded area on resistivity track is where MSFL is less than LLD curve resistivity. This is an indication of matrix and/or fracture permeability. Shaded areas on resistivity logs indicate mud filtrate invasion caused by salt based mud and the presence of fracture or matrix permeability.

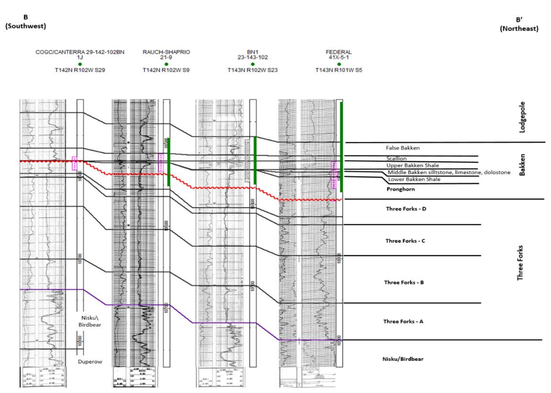

Cross-section Billings Nose area. Note dramatic pinchout of Bakken to the southwest. Note also thickening of False Bakken in this area. The 21-9 and BN 1 wells show resistivity separation in the Upper Bakken Shale suggesting the presence of fractures.

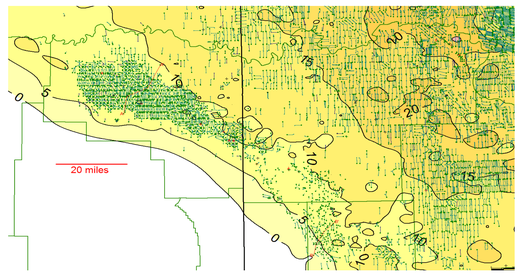

Isopach Upper Bakken Shale. Wells shown are Bakken, Three Forks producers only.

Upper Bakken Shale Resource Play, Williston Basin
2

Bakken Fractures

- Regional
- Tectonic
- Diagenetic (expulsion)

"mineralization on fracture surfaces is absent" Carlisle et al., 1992

Regional Fractures

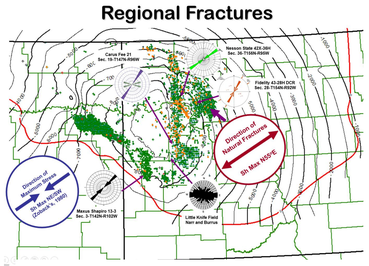

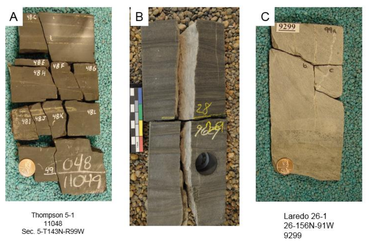

Thompson 5-1
11048
Sec. 5-T143N-R99W

Laredo 26-1
26-156N-91W
9299

Core photographs showing regional fractures. A) Photo illustrates regional fractures in upper Bakken shale from Thompson 5-1 (11048 ft, Sec. 5, T143N, R99W). B) fractures in middle Bakken from Liberty 2-11H (9629 ft, Sec. 11, T151N, R91W); fractures are mineralized partially open; C) fractures in middle Bakken from Laredo 26-1 (9299 ft, Sec. 26, T156N, R91W); fractures are cemented with calcite and partially open.

LOG RESPONSES

MERIDIAN OIL INC
MOI
21-11

T143N R102W S11

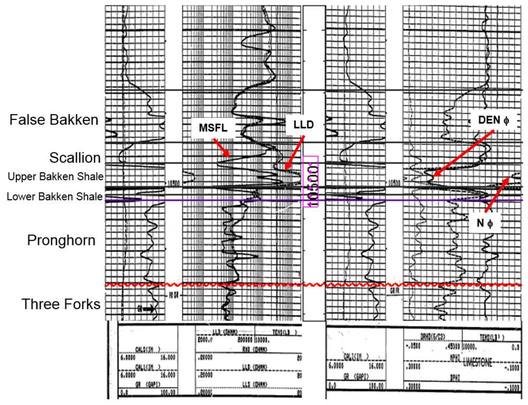

Pfs: 10490-10506
IP: 217 BOPD; 178 MCFD
CUM: 199 MBO
258 MMCF

Separation between MSFL and LLD can indicate fracture permeability (invasion)

"Separation between neutron and density porosity curves can indicate the presence or absence of fractures" Carlisle et al., 1992

Conceptual Burial History of Unit – Volume of Oil - Source

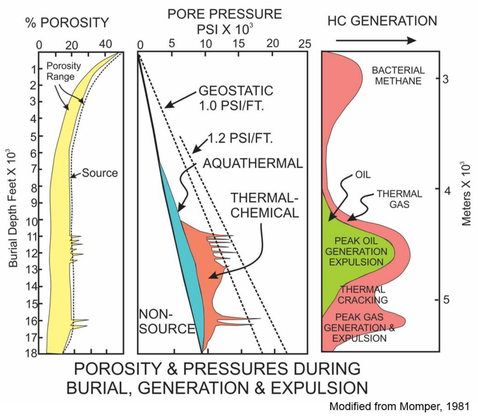

POROSITY & PRESSURES DURING BURIAL, GENERATION & EXPULSION

Modified from Momper, 1981

Overpressures generated by HC generation

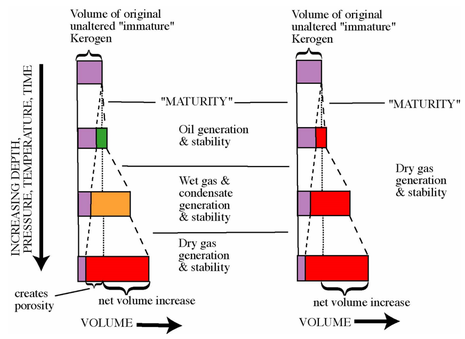

Meissner, 1980

Bakken Maturity

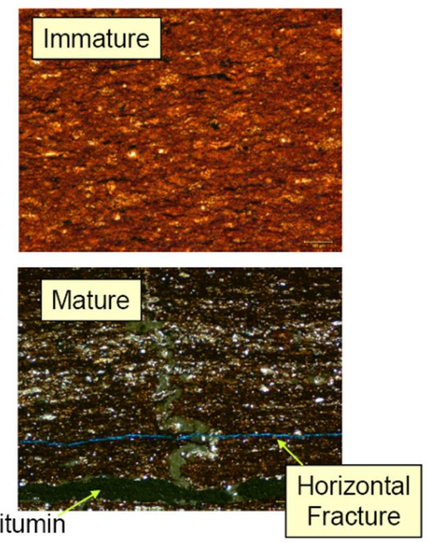

LeFever et al., 2008

Non-Tectonic Fractures

HC Generation - Upper Bakken Shale

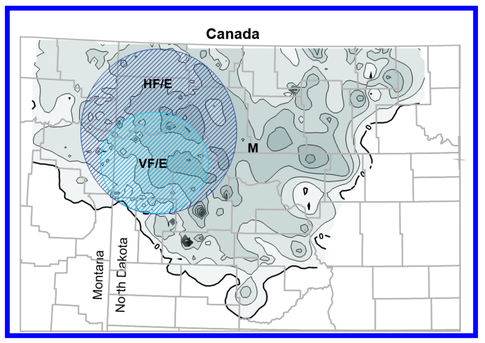

From LeFever

Carus Fee 21
Sec. 19-147N-96W

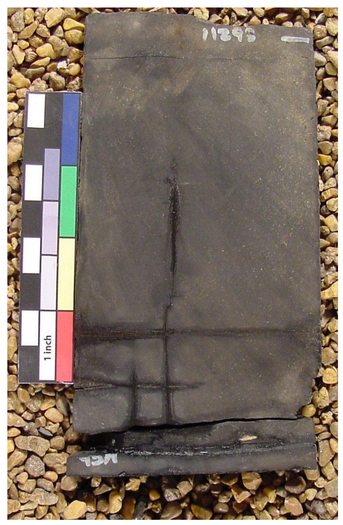

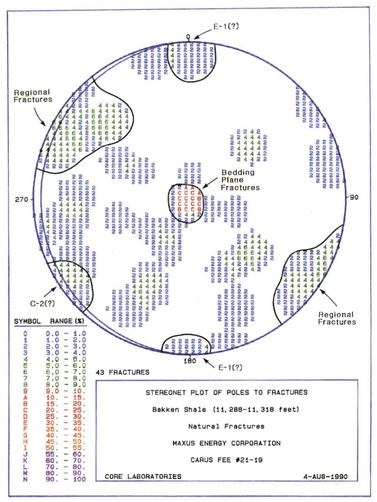

Stereonet plot of poles to fractures, Bakken Shale. Note "bedding plane fractures"

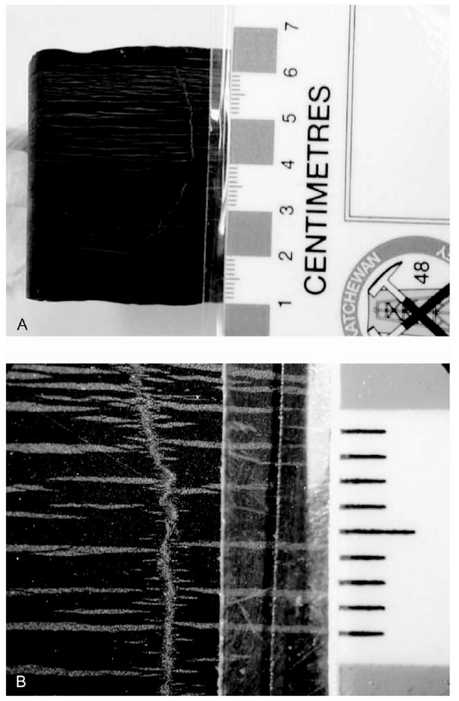

Figure 16 - A) Network of calcite-filled horizontal fractures cross-cut by a vertical calcite-lined fracture which starts and terminates within a 5 cm thick interval (well 12-27-1-6W2, between approximately 2081.0 and 2082.0m. B) Magnified view of a portion of this 5 cm thick interval.

Kreis, Costa, Osadetz, 2006

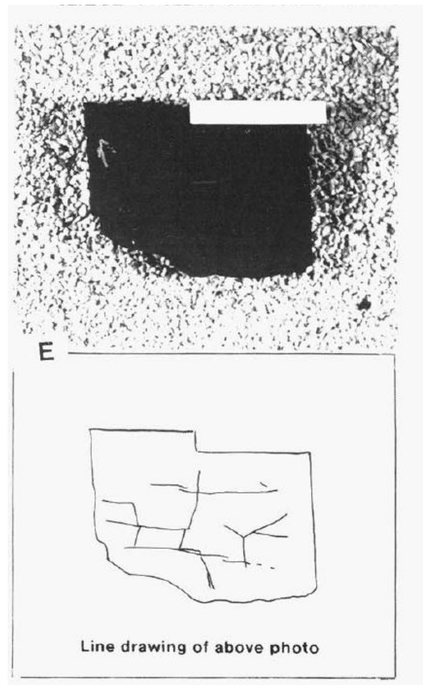

"microfractures occur in all Bakken units"
Carlisle et al., 1992

Upper Bakken Shale Resource Play, Williston Basin



Calcite-lined horizontal fracture networks.

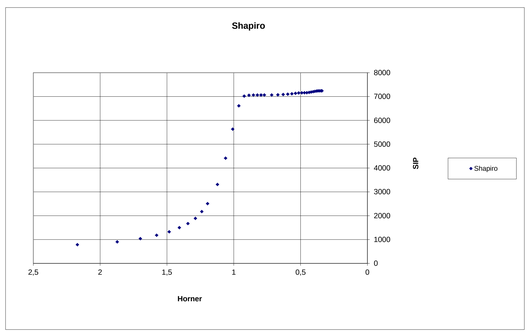

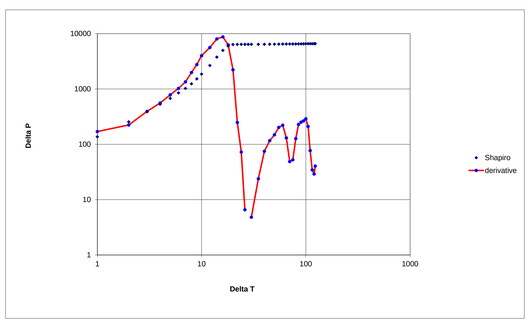

Horner plot for Shapiro 21-9 (Sec. 9, T142N, R102W). B. Delta P and delta T plot with derivative analysis. The derivative plot suggests the presence of fractures. See Figure 7 for Shapiro log.

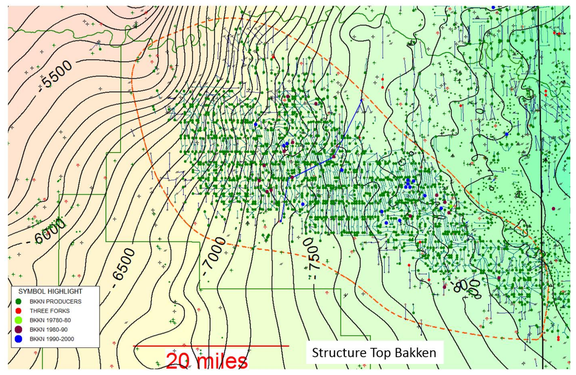

Structure top Bakken.

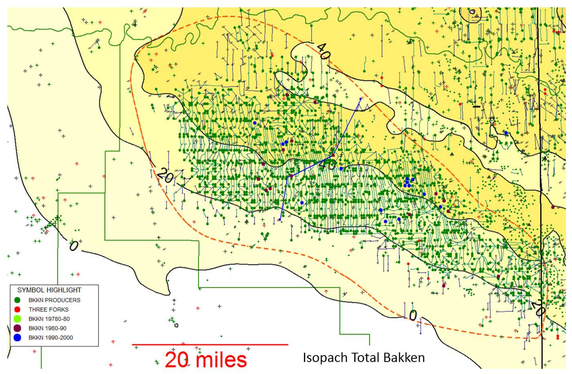

Isopach total Bakken.

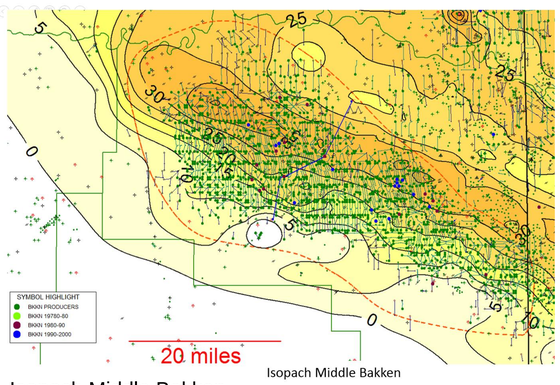

Isopach Middle Bakken.

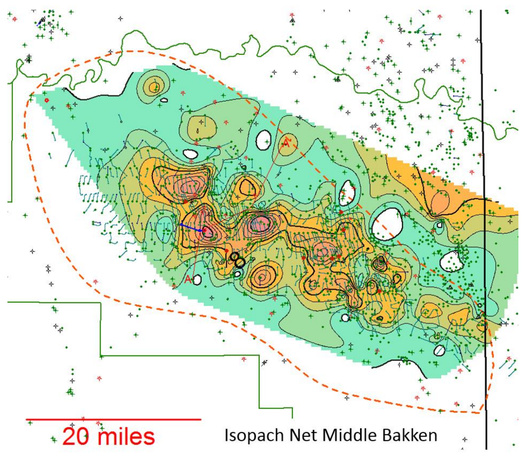

Isopach Net Middle Bakken.

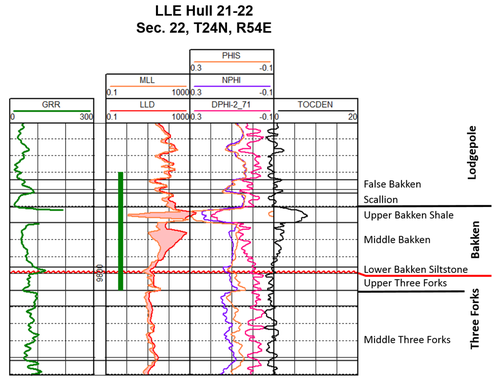

Log response for Bakken and Three Forks intervals from Elm Coulee.

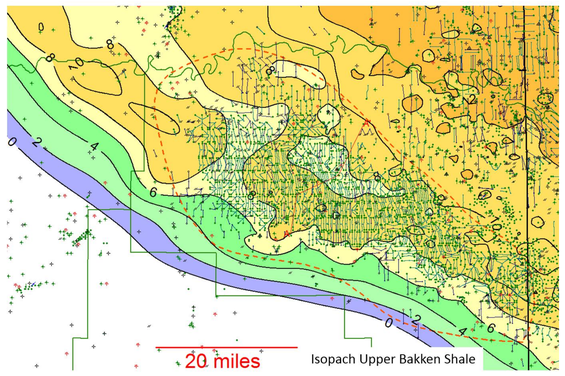

Isopach Total Upper Bakken Shale.

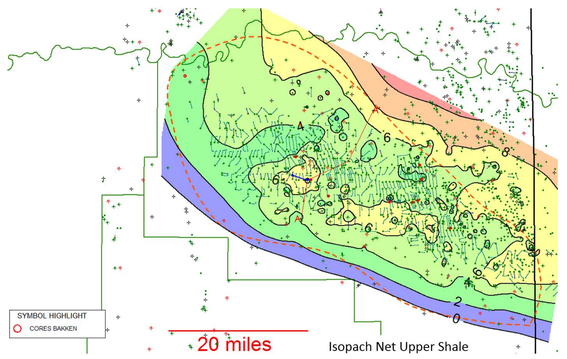

Isopach Net Upper Bakken Shale.

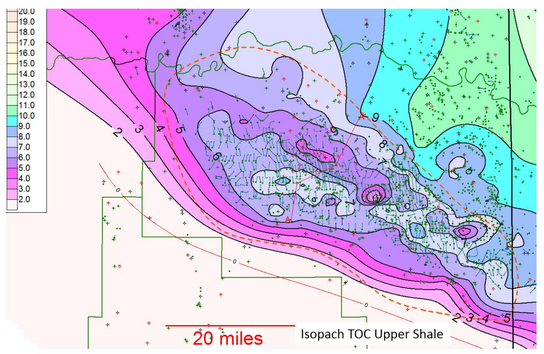

Isopach TOC Upper Bakken Shale.

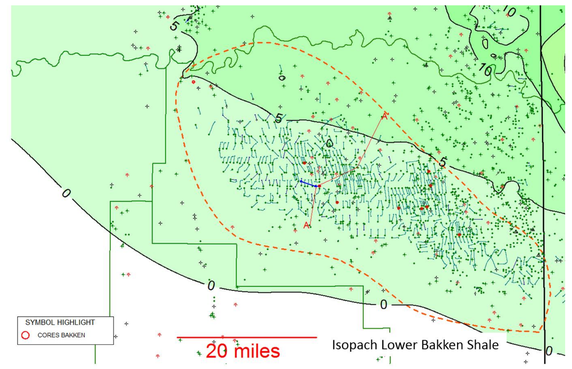

Isopach Lower Bakken Shale.

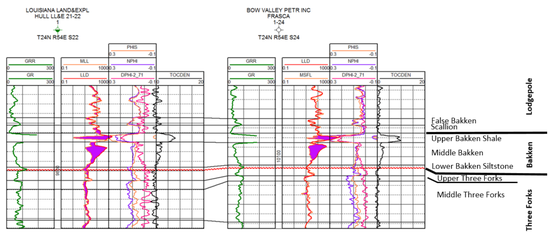

Cross section indicating fractures, Upper Bakken Shale and matrix permeability in Middle Bakken, from Elm Coulee.

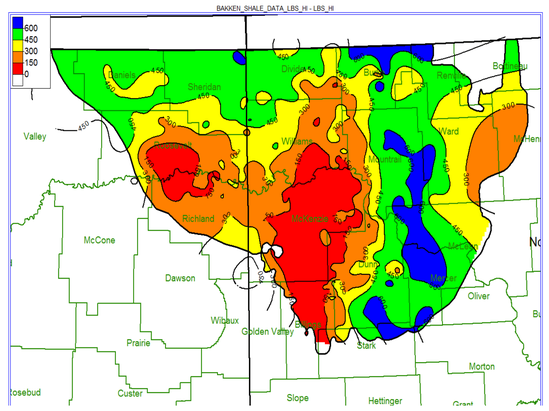

Hydrogen Index map for lower Bakken shales.

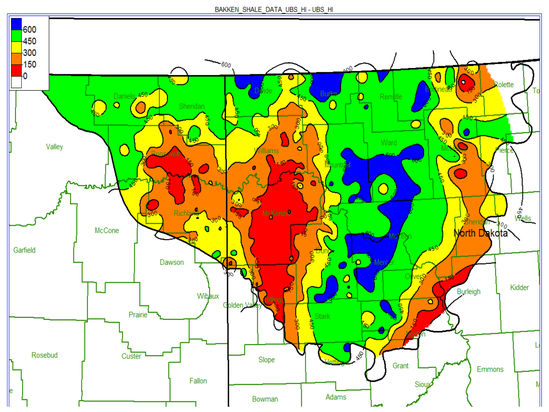

Hydrogen Index map for upper Bakken shales.

Upper Bakken Shale Resource Play, Williston Basin

4

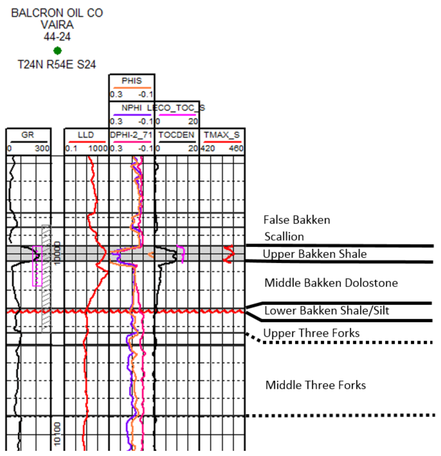

Log for Vaira well, Elm Coulee Field, Bakken Petroleum System.

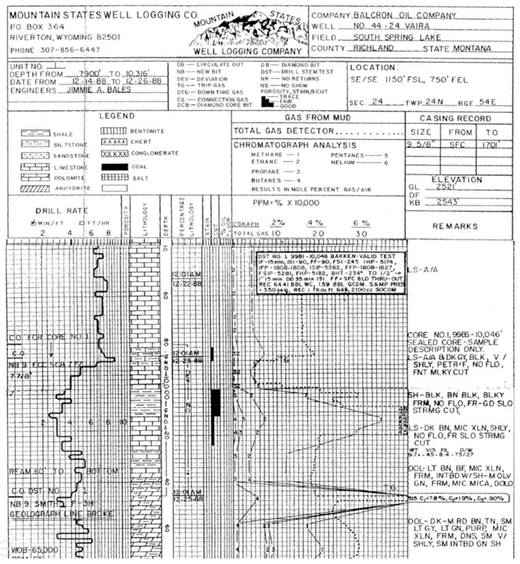

Mud log for Vaira well. Note shows in Upper Bakken Shale.

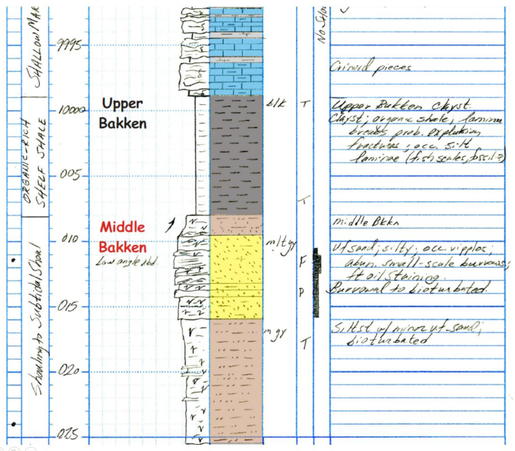

Core description for Vaira well, USGS files (Smith et al.) Expulsion fractures noted in the Upper Bakken Shale.



Core photos for Upper Bakken Shale, Vaira Well.

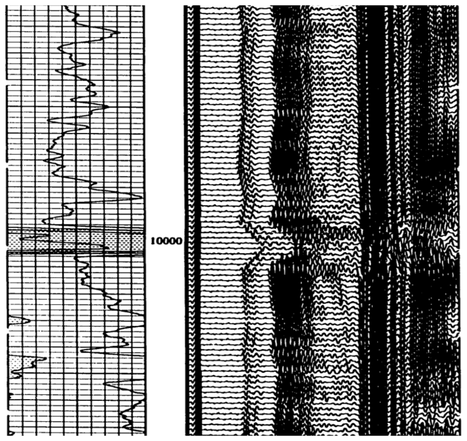

Full sonic waveforms, Vaira well. Note response in Upper Bakken Shale (suggests presence of fractures).

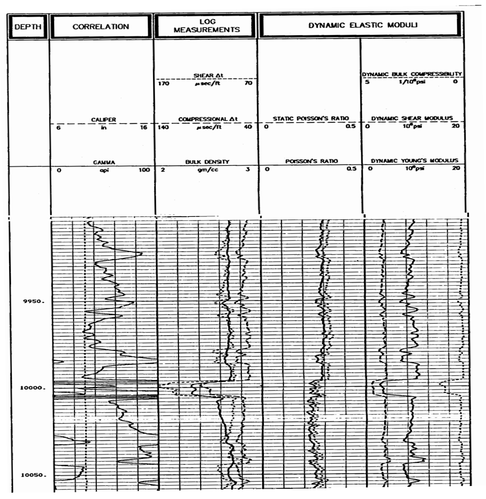

Sonic, gamma ray, and dynamic elastic moduli for Vaira well, Elm Coulee Field.

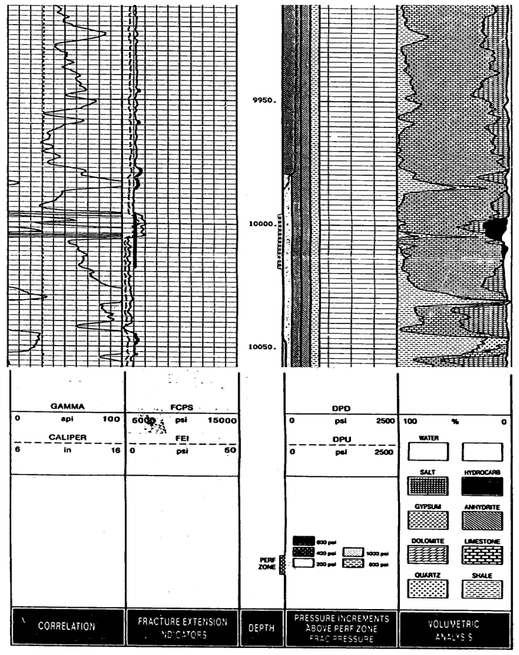

Lithology, gamma ray, fracture extension indicator, frac pressure, and volumetric analysis for Vaira Well.

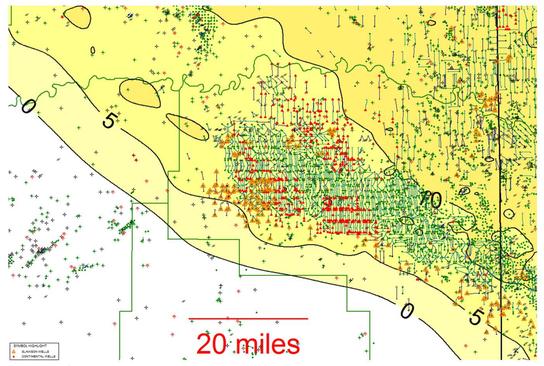

Isopach Upper Bakken Shale

Isopach Upper Bakken Shale, and new activity on southern flank of field targeting Upper Bakken Shale.

CONCLUSIONS

The Upper Bakken Shale is an important part of the Bakken petroleum system. It serves both as a source rock and also contributes as a reservoir to production. The Upper Bakken Shale is fractured and fracturing has been observed in cores, drill stem test data plots, and well logs from the Billings Nose area. The success of the Upper Bakken Shale in the Billings Nose area is in part due to production from the adjacent formations (Lodgepole, Pronghorn, Three Forks). The key to production in the Billings Nose area appears to be due to the following: presence of mature source rocks, natural fractures, presence of reservoirs adjacent to the Upper Shale, along with drilling and completion technologies.

REFERENCES CITED

Carlisle, J., 1991, The Bakken Formation of the Williston Basin: deposition, maturation, and fracturing (abs), *in* B. Hansen, ed., Geology and horizontal drilling of the Bakken Formation: Montana Geological Society, p. 89.

Carlisle, J., L. Dryff, M. Fryt, J. Artindale, and H. Von Der Dick, 1992, The Bakken Formation—An integrated geologic approach to horizontal drilling, *in* J. E. Schmoker, E. Coalson, and C. Brown, eds., Geologic studies relevant to horizontal drilling: Examples from western North America: Rocky Mountain Association of Geologists, p. 215-226

Cramer, D. D., 1986, Reservoir characteristics and stimulation techniques in the Bakken Formation and adjacent beds, Billings Nose area, Williston Basin, *in* S. Goolsby and M. W. Longman, eds., Proceedings from SPE Rocky Mountain Region Technical Meeting, Society of Petroleum Engineers Paper No. 15166, p. 331-344

Cramer, D. D., 1991, Stimulation treatments in the Bakken Formation: Implications for horizontal completions, *in* W. B. Hansen, W, ed., Geology and Horizontal Drilling of the Bakken Formation: Montana Geological Society, p. 117-140

Dow, W. G., 1974, Application of oil-correlation and source-rock data to exploration in Williston Basin: AAPG Bulletin, Vol. 58, No. 7, p. 1253-1262.

Druyff, L., 1991, Reservoir properties of the Bakken shale (abs.), *in* W. B. Hansen, ed., Geology and horizontal drilling of the Bakken Formation: Montana Geological Society, p. 91.

Gerhard, L. C., S. B. Anderson, and D. W. Fischer, 1990, Petroleum geology of the Williston Basin, *in* M. W. Leighton, D. R. Kolata, D. T., Oltz, and J. J., Eidel, eds., Interior Cratonic Basins: AAPG Memoir 51, p. 507-559.

Hansen, W. B., and G. Long, 1991, Criteria for horizontal and vertical prospects in the Bakken Formation, Williston Basin, *in* Hansen, W. B., ed., Geology and Horizontal Drilling of the Bakken Formation: Montana Geological Society, p. 151-163

LeFever, J. A., 1992, Horizontal drilling in the Williston Basin, United States and Canada, *in* J.W. Schmoker, E. B. Coalson, C. A. Brown, eds. Geological Studies Relevant to Horizontal Drilling: Examples from Western North America: Rocky Mountain Association of Geologists Guidebook, p. 177-198

LeFever, J., 2006, Oil production from the Bakken Formation: a short history: North Dakota Geological Survey Newsletter, Vol. 32, No. 1, p. 1-6.

LeFever, J., 2007, Evolution of oil production in the Bakken formation: RMS-AAPG meeting and NDIC Geologic Investigation 49, NDIC website PowerPoint presentation, <https://www.dmr.nd.gov/ndgs/bakken/Papers/Petroleum%20Council%202004.ppt> Accessed December 15, 2008.

LeFever, J. A., 2008, Isopach of the Bakken Formation: North Dakota Geological Survey Geologic Investigations No. 59, Bakken Map Series: Sheet 1-5.

LeFever, J.A., C.D. Martiniuk, E.F.R. Dancsok and P.A. Mahnic, 1991, Petroleum potential of the middle member, Bakken Formation, Williston Basin, *in* J.E. Christopher and F. Haidl, eds., Proceedings of the Sixth International Williston Basin Symposium: Saskatchewan Geological Society, Special Publication 11, p. 76-94

Lempp, C., O. Natau, U. Bayer, D. Welte, 1994, The effect of temperature on rock mechanical properties and fracture mechanisms in source rocks – experimental results: Society of Petroleum Engineers Paper No. 28039, p. 147-154.

Meissner, F. F., 1978, Petroleum geology of the Bakken formation, Williston Basin, North Dakota and Montana, *in* Estelle, D., and Miller, R., eds., The Economic Geology of the Williston Basin, 1978 Williston Basin Symposium, Montana Geological Society, p. 207-230.

Meissner, F. F., J. Woodward, and J. L. Clayton, 1984, Stratigraphic relationships and distribution of source rocks in the Greater Rocky Mountain Region, *in* J. Woodward, F. F. Meissner, and J. L. Clayton, eds., Hydrocarbon Source Rocks of the Greater Rocky Mountain Region: Rocky Mountain Association of Geologists Guidebook, p. 1-34.

Momper, J. A., 1980, Oil expulsion: A consequence of oil generation: American Association of Petroleum Geologists slide/tape series.

Murray, G. H., 1968, Quantitative fracture study – Sanish Pool, McKenzie County, North Dakota: American Association of Petroleum Geologists Bulletin, vol. 52, no. 1, p. 57-65

Narr, W., and R. C. Burruss, 1984, Origin of fractures in Little Knife Field, North Dakota: AAPG Bull., v. 68, no. 9, p. 1087-1100.

Nordeng, S. H., 2009, The Bakken petroleum system: an example of a continuous Petroleum accumulation: North Dakota Department of Mineral Resources Newsletter, vol. 36, no. 1, p. 19-22.

Pitman, J. K., L. C. Price, and J. A. LeFever, 2001, Diagenesis and fracture development in the Bakken Formation, Williston Basin: Implications for reservoir quality in the Middle Member: US Geological Survey Professional Paper 1653, 19 p.

Price, L. C., T. Ging, T. Daws, A. Love, M. Pawlewicz, and D. Anders, 1984 Organic metamorphism in the Mississippian-Devonian Bakken shale North Dakota portion of the Williston Basin: *in* J. Woodward, F. F. Meissner and J. C. Clayton, eds., Hydrocarbon source rocks of the greater Rocky Mountain Region, Rocky Mountain Association of Geologists, Denver, p. 83-134.

Price, L. C., 2000, Origins and Characteristics of the Basin-Centered Continuous Reservoir Unconventional Oil-Resource Base of the Bakken Source System, Williston Basin (unpublished), paper available at: < http://www.undeerc.org/Price/>

Schmoker, J. W., and T. C. Hester, 1983, Organic carbon in Bakken Formation, United States portion of Williston Basin: AAPG Bull. Vol. 67, No. 12, p. 2165-2174.

Smith, M. G., and M. Bustin, 1996, Lithofacies and paleoenvironments of the upper Devonian and lower Mississippian Bakken Formation, Williston Basin: Bulletin of Canadian Petroleum Geology, Vol. 44, No. 3, p. 495-507.

Smith, M.G., and M. Bustin, 2000, Late Devonian and Early Mississippian Bakken and Exshaw Black shale source rocks, Western Canada Sedimentary basin: a sequence stratigraphic interpretation: AAPG Bull., V. 84, No. 7, P. 940-960.

Sonnenberg, S. A., and A. Pramudito, 2009, Petroleum geology of the giant Elm Coulee field, Williston Basin: AAPG Bull., v. 93, no. 9, p. 1127-1153

Webster, R. L., 1984, Petroleum source rocks and stratigraphy of the Bakken Formation in North Dakota, *in* J. Woodward, F. F. Meissner, and J. C. Clayton, eds., Hydrocarbon source rocks of the Greater Rocky Mountain Region: Denver, Rocky Mountain Association of Geologists, p. 57–81.

6

Sonnenberg, Stephen A., Cosima Theloy, and Hui Jin, 2017, The giant continuous oil accumulation in the Bakken petroleum system, U.S. Williston Basin, *in* R. K. Merrill and C. A. Sternbach, eds., Giant fields of the decade 2000–2010: AAPG Memoir 113, p. 91–120.

The Giant Continuous Oil Accumulation in the Bakken Petroleum System, U.S. Williston Basin

Stephen A. Sonnenberg
Department of Geology, Colorado School of Mines, Golden, Colorado, U.S.A. (e-mail: ssonnenb@mines.edu)

Cosima Theloy
Independent Geologist, 1690 S. Deframe Ct., Lakewood, Colorado, U.S.A. 80228 (e-mail: ctheloy@gmail.com)

Hui Jin
BP America, Inc., 501 Westlake Park Blvd., Houston, Texas, U.S.A. 77079 (e-mail: hui.jin4@bp.com)

ABSTRACT

The Williston Basin Bakken petroleum system is a giant continuous accumulation. The petroleum system is characterized by low-porosity and -permeability reservoirs, organic-rich source rocks, and regional hydrocarbon charge. Total Bakken and Three Forks production to December 2014 was 1.289 billion barrels (bbl) of oil and 1.3 trillion cubic feet of gas (TCFG) from 12,051 wells. U. S. Geological Survey (USGS) (Gaswirth et al., 2013) mean technologically recoverable resource estimates for the Bakken petroleum system are 7.375 billion barrels of oil, 6.7 tcf of gas, and 527 million barrels of natural gas liquids.

The Bakken Formation regionally in the Williston Basin consists of four members: upper and lower organic-rich black shale, a middle member (silty dolostone or limestone to sandstone lithology), and a basal member recently named the Pronghorn. The Bakken Formation ranges in thickness from a wedge edge to over 140 ft (43 m) with the thickest area in the Bakken located in northwest North Dakota, east of the Nesson anticline.

The Three Forks is a silty dolostone throughout much of its stratigraphic interval. The Three Forks ranges in thickness from less than 25 ft (8 m) to over 250 ft (76 m) in the mapped area. Thickness patterns are controlled by paleostructural features such as the Poplar Dome, Nesson, Antelope, Cedar Creek, and Bottineau anticlines. Thinning and/or truncation occurs over the crest of the highs, and thickening of strata occurs on the flanks of the highs. The Three Forks can be subdivided into three units (up to six by some authors; e.g., Webster, 1984; Gutierrez, 2014; Gantyno, 2011). Most of the development activity in the Three Forks targets the upper Three Forks.

The upper Three Forks is dominated by silt-sized quartz and dolomite and some very-fine-grained sandstones and has low permeabilities and porosities. The upper Three Forks ranges in thickness from a wedge edge to over 40 ft (12 m) in areas east of the Nesson anticline. The unit thins toward the margins of the depositional basin because of erosional truncation.

Copyright ©2017 by The American Association of Petroleum Geologists.
DOI:10.1306/13572002M113508

The upper and lower shale members are potential source rocks and are lithologically similar throughout much of the basin. The shales are regarded as dominantly type II kerogens. The shales average 11 wt.% total organic carbon.

Measured core porosity and permeability are very low in the Bakken, Sanish, and Three Forks reservoirs (<10% porosity and <0.1 md permeability) in the Williston Basin, so productivity is assumed to be due to natural and artificial fracturing. The reservoirs generally require advanced technology to get them to produce (fracture stimulation and horizontal stimulation). For this reason, they should be considered to be technology reservoirs. Natural fractures in some areas (e.g., Billings Nose area and Antelope field) are sufficient for vertical well production.

Reservoir pressure in the Bakken is regarded as overpressured with pressure gradients exceeding 0.5 psi/ft. A new pressure map for the Bakken petroleum system was generated. The map is based on 92 BHP (bottom-hole pressure) and DFIT (diagnostic fracture injection test) data points, including six additional hydrostatic points at the eastern margin as well as six data points for the Sanish–Parshall area. High overpressures are found in large parts of the central basin and the Parshall area in the east, where gradients exceed 0.7 psi/ft. Elm Coulee has a pressure gradient around 0.55 psi/ft. Parshall is reported to have a gradient of 0.74 psi/ft. The area west of the Nesson anticline has pressure gradients of 0.6 to 0.7 psi/ft. Pressure gradients in Montana are generally in the 0.5+ psi/ft range.

INTRODUCTION

The Mississippian–Devonian Bakken petroleum system of the Williston Basin is characterized by low-porosity and -permeability reservoirs, organic-rich source rocks, and regional hydrocarbon charge. The unconventional play is the current focus of exploration and development activity by many operators.

The structure of the Williston Basin at the top of the Bakken is illustrated by Figure 1. The basin is semicircular in shape, and prominent structural features are the Nesson, Billings, Little Knife, Poplar, and Cedar Creek anticlines. Many of the structural features have a documented ancestral origin and influenced Paleozoic sedimentary patterns (Gerhard et al., 1990). Recurrent movement on Precambrian faults or shear zones is seen elsewhere in the Rocky Mountain region (Weimer, 1980). The Nesson anticline is the location of the first oil discoveries in the 1950s. The first oil production on the Nesson anticline was from the Silurian Interlake Formation in 1951, and subsequent oil production was established from the Mississippian Madison Group (the main producer in the basin). The Williston Basin produces mainly oil from several Paleozoic reservoirs (Figure 2). The probable source rock to reservoir rock petroleum systems is illustrated by Figure 2. Seven different petroleum systems have been identified in the Williston Basin (Lillis, 2013).

The Bakken petroleum system consists of the Bakken Formation, lower Lodgepole, and upper and middle Three Forks (Figures 2 and 3). A petroleum system consists of source beds and all the genetically related hydrocarbon accumulations. The Bakken Formation over most of the Williston Basin consists of four members: (1) upper shale, (2) middle silty dolostone or dolomitic siltstone and sandstone, (3) lower shale, and (4) Pronghorn (LeFever, 2008; LeFever et al., 2011). The source beds for the petroleum system are the upper and lower organic-rich Bakken shales. Source bed potential also exists in the False Bakken interval of the lower Lodgepole (Stroud, 2010). The reservoir rocks for the petroleum system are all the members of the Bakken, the lower Lodgepole, and upper and middle Three Forks.

Previous workers have described significant Bakken source rock potential and estimates of oil generated

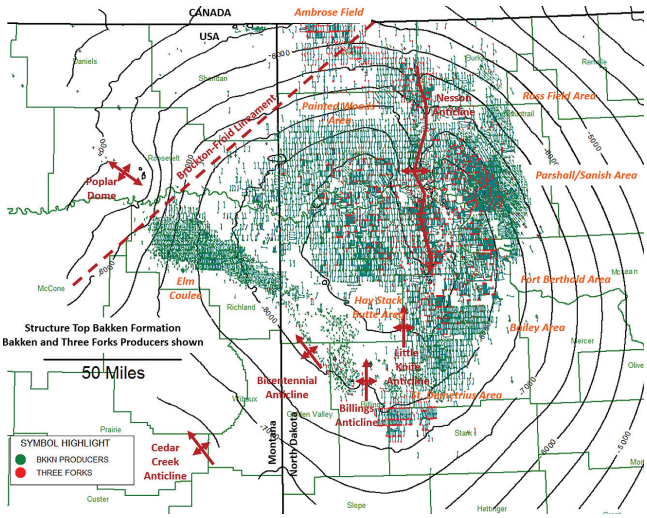

Figure 1. Structure map on top of Bakken. Contour interval is 500 ft (152 m). Prominent structural features in the Williston Basin include the Poplar, Cedar Creek, Billings, Bicentennial, Little Knife, and Nesson anticlines. The Nesson, Billings, and Little Knife anticlines trend north–south which is most likely related to the Precambrian geology. All the major structural features show evidence of recurrent structural movement during the Phanerozoic.

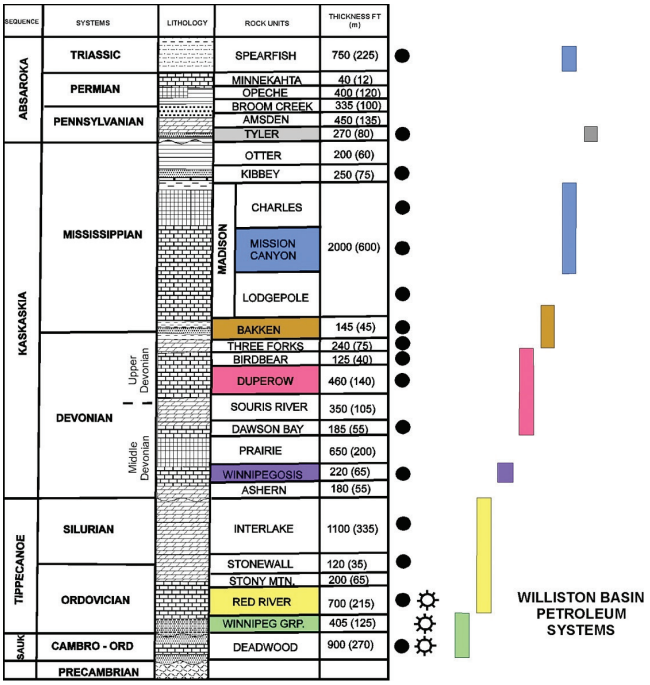

Figure 2. Stratigraphic column for Paleozoic producing units in the Williston Basin. Producing units shown by oil and gas symbols. The Bakken petroleum system consists of source beds in the Bakken and reservoirs in the lower Lodgepole, Bakken, and upper Three Forks. The upper Three Forks is the main producer in the Antelope field. Sedimentary sequences following Sloss (1963) are indicated. Thickness of stratigraphic units indicated in the column to the right (ft/m). Oil and gas symbols indicate producing formations. Modified from LeFever (1992). Petroleum systems are modified from Lillis (2013).

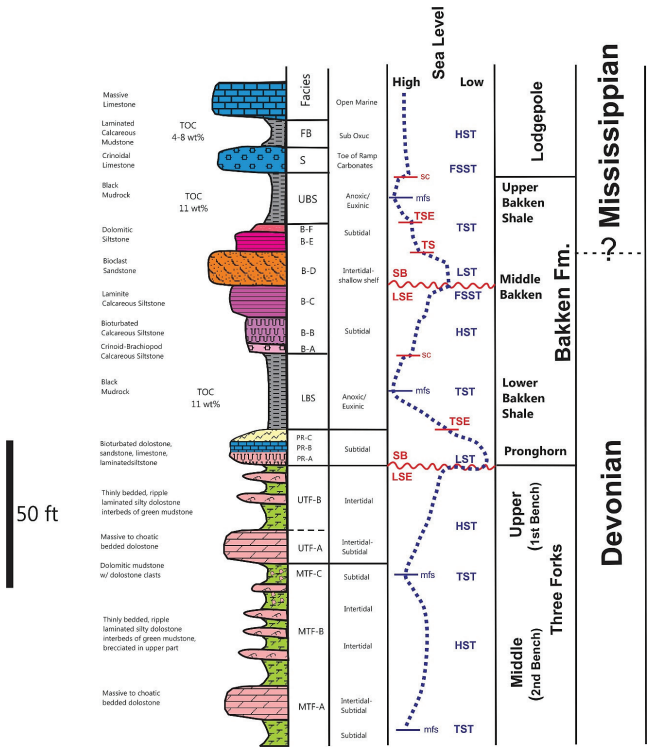

Figure 3. Diagram illustrating members of the Bakken petroleum system. Source beds are the Lower and Upper Bakken shales and the false Bakken member of the Lodgepole. Reservoirs are the middle and upper Three Forks, middle member of the Bakken, and the Scallion member of the Lodgepole.

from the petroleum system range from 10 to 400 billion barrels (Dow, 1974; Williams, 1974; Meissner, 1978; Schmoker and Hester, 1983; Webster, 1984; Price et al., 1984; Meissner and Banks, 2000; Pitman et al., 2001; Flannery and Kraus, 2006; LeFever and Helms, 2006). The USGS (Gaswirth et al., 2013) mean technologically recoverable resource estimates for the Bakken petroleum system is 7.375 billion barrels oil, 6.7 tcf gas, and 527 million barrels of natural gas liquids (Gaswirth et al., 2013). The technologically recoverable resource estimates for the Bakken Formation are 3.644 billion barrels of oil, 3.1 trillion cubic feet of associated/dissolved natural gas, and 246 million barrels of natural gas liquids. The technologically recoverable resource estimate for the Three Forks is 3.731 billion barrels of oil, 3.5 trillion cubic feet of gas, and 281 million barrels of natural gas liquids.

The Bakken petroleum system is thought to have created a continuous type of accumulation in the deeper parts of the Williston Basin (Nordeng, 2009). A continuous accumulation is a hydrocarbon accumulation that has some or all of the following characteristics: pervasive hydrocarbon charge throughout a large area, no well-defined oil– or gas–water contact, diffuse boundaries, commonly abnormally pressured, large in-place resource volume but low recovery factor, little water production, geologically controlled "sweet spots," reservoirs commonly in close proximity to mature source rocks, reservoirs with very low matrix permeabilities, and water that occurs updip from hydrocarbons. The Bakken petroleum system meets all these characteristics.

Many of the reservoirs in the Bakken petroleum system have low permeability. Productive areas or sweet spots are localized areas of improved reservoir permeability through natural fracturing, the development of matrix permeability, or a combination of both. The Bakken petroleum system is a continuous system with no real boundaries between fields (Figure 1). Total Bakken and Three Forks production to December 2014 was 1.289 billion bbl of oil and 1.3 TCFG from 12,051 wells (Figure 4). Thus the petroleum system easily meets the definition of a giant accumulation (500 million barrels of oil). Total Bakken production to December 2014 was 1.022 billion bbl of oil and 1.0 TCFG (Figure 5). Total Three Forks production to December 2014 was 263,448 MBO and 294 billion cubic feet gas (Figure 6). The most notable sweet spot areas are the Elm Coulee, Sanish, and Parshall fields. Field names are abundant through the continuous

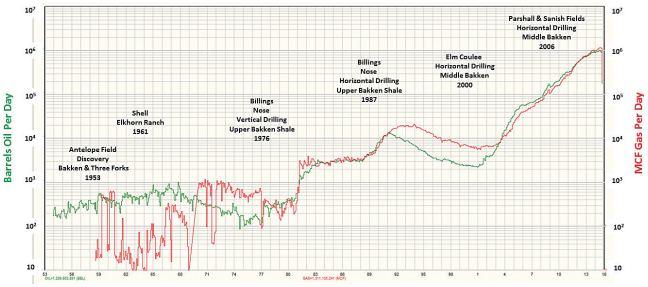

Figure 4. Total U.S.A. Williston Basin Bakken and Three Forks production. Current cumulative total is: 1,289,803,891 bbl of oil and 1,311,105,241 MCFG.



Figure 5. Total U.S.A. Williston Basin Bakken only production. Current cumulative total is: 1,022,855,380 bbl of oil and 1,011,814,857 MCFG.

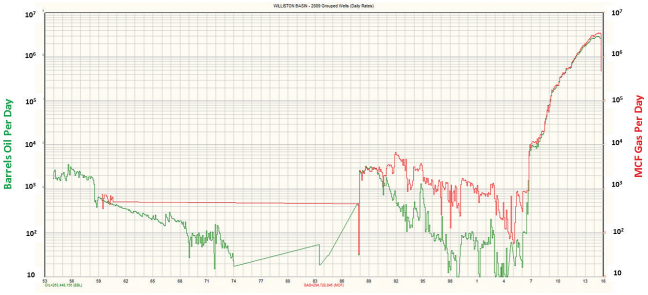

Figure 6. Total U.S.A. Williston Basin Three Forks only production. Current cumulative total is: 263,448,155 bbl of oil and 294,728,845 MCFG.

accumulation, but no barriers exist between the fields. At the end of 2014, the U.S. Williston Basin accounted for approximately 25% of domestic oil production.

This chapter summarizes the regional geology of the Bakken and Three Forks formations in the Williston Basin.

BAKKEN EXPLORATION: HISTORY OF BASIN

The Bakken Formation of the Williston Basin has seen three cycles of exploration and development since the 1950s (Figure 4) (LeFever, 2006, 2007; Sonnenberg, 2010a). The first cycle is the Antelope field discovery and development (Bakken and Three Forks vertical drilling). The next cycle is the upper Bakken shale Billings Nose edge play (vertical and horizontal drilling for the upper Bakken shale). The last cycle is the middle Bakken–Three Forks horizontal play.

The earliest discovery occurred in the Antelope field of North Dakota in 1953, and development continued into the 1960s. Sixty-three wells targeted the Bakken and upper Three Forks (referred to as the Sanish member) on a tightly folded structure. The Bakken and upper Three Forks are low-permeability, fracture-enhanced reservoirs in Antelope with fracturing related to the tight fold (Murray, 1968). The wells were drilled vertically and after a sand-oil fracture stimulation treatment were capable of producing an average of 209 BOPD. Antelope field has produced 11 million barrels of oil and 20 BCF of gas from the Three Forks Bakken interval. Average cumulative production per Three Forks well is 550 million bbl of oil and 1.4 BCF. Following the Antelope discovery, exploration proceeded slowly. All three members of the Bakken and the upper Three Forks were perforated in Antelope, and production established these formations as petroleum reservoirs in the basin.

The next significant discovery in the Bakken was by Shell in the Elkhorn Ranch field in 1961 (Billings Nose area) (Figures 1 and 4). The upper Bakken shale was completed in the well as a secondary objective after the deeper primary objective, the Red River zone (Ordovician), was not successful. The Elkhorn Ranch well was very significant in that it showed significant reserves could be found in the upper Bakken shale. Because of product prices and the remoteness of the area, the next Bakken well was not drilled until 1976. This area then became known as the Bakken fairway area. Wells drilled in the fairway targeted the upper Bakken shale and other Paleozoic horizons (both shallower and deeper). The area occurs along the southwest margin of the Bakken depositional basin in the general area of the Billings Nose (Figure 1). Reservoir characteristics for this area were described by Cramer (1986). Where the Bakken thins, fracture density increases (Sperr, 1991). Sand-oil fracture stimulation treatment was used on these wells.

Horizontal drilling in the upper Bakken shale commenced in 1987 in the Billings anticline (fairway) area (LeFever, 1992, 2006). The first horizontal well, drilled by Meridian, was the #33-11 MOI well (Sec. 11, T143N, R102W, Elkhorn Ranch field), which had a horizontal displacement of 2603 ft (793 m) in the Bakken. The well was completed for 258 BOPD and 299 MCFGD, and production was remarkably stable for the first 2 years. The success of this well set off the horizontal drilling phase of the upper Bakken shale. The play continued into the 1990s with over 20 operators. Product prices

declined significantly in the 1990s, and this—along with the somewhat unpredictable production in the upper Bakken shale—brought this phase to a close. The fairway play met with mixed results. Good-producing wells were often offset with poor-producing wells. In addition, some pressure depletion and cross-well communication was reported (LeFever, 2006).

Because of mixed results in the fairway trend and low product prices, the Bakken again returned to the status of being a secondary objective type of reservoir rather than a primary objective of exploration. This status changed with the discovery of significant reserves in the middle Bakken in the Elm Coulee field. The discovery and development of the middle Bakken has resulted in the most significant exploration cycle to date.

The Elm Coulee field was discovered in 2000 with horizontal completions in the middle Bakken. The field is located in the western part of the Williston Basin in northeast Montana (Figure 1). Prior to the horizontal drilling in 2000, the area had scattered vertical well production (marginal to uneconomic) from the Bakken (the Bakken was a secondary objective for wells targeting deeper horizons). Horizontal drilling began in the field in 2000 and to date, over 1500 wells have been drilled. The estimated ultimate recovery for the field is over 200 million bbl of oil. Cumulative production from the Elm Coulee area from the Bakken to December 2014 was 152 million bbl of oil and 136 BCF. Horizontal drilling and fracture stimulation of the horizontal leg are key technologies that enable a low-permeability reservoir to produce. The original drilling and spacing unit at Elm Coulee was a 640-acre unit. Wells were drilled using bi- or trilaterals in a section and then were fracture stimulated with one hydraulic fracture stimulation stage (which became known as the pump and pray type of fracture stimulation). Stratigraphic trapping plays a key role at Elm Coulee (Sonnenberg and Pramudito, 2009; Alexandre, 2011). Horizontal wells in the Elm Coulee field target mainly the B facies of the middle Bakken (Figure 3). The unit is dominated by dolostone (Alexandre, 2011). The mineral composition in the main pay interval is 50 to 60% dolomite, 30 to 35% quartz, 10% feldspar, and 5% clay.

The Elm Coulee discovery and development prompted operators to also target the middle Bakken in North Dakota. Prior to Elm Coulee, most operators targeted only the upper shale in the Bakken. The expansion of the play into North Dakota is currently underway and has resulted in many new discoveries, including the Parshall and Sanish fields. The new discoveries in North Dakota suggest the existence of an extremely large unconventional resource play. Product prices will probably influence this cycle too.

The Parshall Field located on the east side of the Nesson anticline was discovered in 2006 with horizontal completion in the middle Bakken. EOG drilled and completed the 1-36 Parshall (Sec. 36, T150N, R90W) for 463 BOPD and 128 MCFGD. Through December 2014, the field had produced approximately 94 million bbl of oil and 46 BCF from 346 wells completed in the Bakken. This field illustrates that significant production from the middle Bakken and Three Forks exists in North Dakota. The field connects to the Sanish field to the west and the Ross field to the north. By the time Parshall was discovered, multistage fracture stimulation had been tried and tested in the Barnett shale play of the Fort Worth basin. Therefore, during the development of the Parshall field, multistage hydraulic stimulation in the Williston Basin was developed. Fracture stages were originally around 10 but have evolved up to 40 fracture stages.

The Sanish field was also discovered in 2006. Whiting drilled the discovery well: 44-1 Bartleson (Sec. 1, T152N, R93W). Through December 2014, the field had produced approximately 101 million bbl of oil and 74 BCF from 592 wells completed in the Bakken and Three Forks. The geology of the Parshall and Sanish areas has been described by Kowalski (2010), Kowalski and Sonnenberg (2011), Simenson (2010), and Simenson et al. (2011).

Horizontal wells in the Parshall–Sanish areas target specific facies (C, D, E) of the middle Bakken (Figure 3). Production is related to fracture development and matrix development in the middle Bakken. The original oil in place in the Parshall greater area is estimated by various operators to be 8 to 11 million barrels per section for the Bakken and 4 to 6 million barrels per section for the Three Forks. Wells are drilled on either 1280-acre spacing units or 640 spacing units. Estimated ultimate recoveries for the Bakken are 600,000 to 900,000 barrels of oil per section; estimated ultimate recoveries for the Three Forks are 350,000 to 500,000 barrels of oil per section. The recovery factor for the tight reservoirs is estimated to be approximately 3 to 10% (LeFever and Helms, 2006). Because of high production rates, wells can pay out in 4 to 6 months. Some operators prefer the 1280 spacing units over the 640 spacing units because of cost savings associated with the drilling of one well instead of two. Operators are fracture stimulating wells with 20-plus stages.

Various methods have been proposed to explore the Bakken (Sperr, 1991; Rogers and Mattox, 1985). The methods include exploring along the depositional or erosional edge (more susceptible to fracturing and fracture spacing decreases as bed thickness decreases); exploring structural flexures and lineaments; looking for Prairie dissolution areas, as they may be areas of more intense fracturing (Parker, 1967); looking for geothermal anomalies (intense hydrocarbon generation

may cause more intense fracturing); looking for primary reservoirs (e.g., middle Bakken); and looking for fractured areas identified by well logs. The fracture signature on well logs has been described by Hansen and Long (1991) and Sonnenberg et al. (2011c).

The latest cycle of exploration and development in the Williston Basin is the most significant to date. Production for the U.S. part of the Williston Basin has gone from 2500 BOPD to close to a million BOPD.

REGIONAL GEOLOGY

The Williston Basin is a large intracratonic sedimentary basin that occupies parts of North Dakota, Montana, South Dakota, Saskatchewan, and Manitoba. The basin probably originated as a craton-margin basin and evolved to an intracratonic basin during the Cordilleran orogen (Gerhard et al., 1982, 1987, 1990) (Figure 7). Sedimentation occurred throughout much of the Phanerozoic, and the thickness of the stratigraphic section is approximately 16,000 ft (Figure 8). Many unconformities are described in the stratigraphic section, but rocks of all Phanerozoic time periods are represented by some deposits (Figures 2 and 8). Paleozoic strata consist mainly of cyclic carbonate deposits; the Mesozoic and Cenozoic strata consist mainly of siliciclastics.

During the late Devonian and early Mississippian, the basin was an area of active subsidence in a broad shelf area that existed along the western margin of

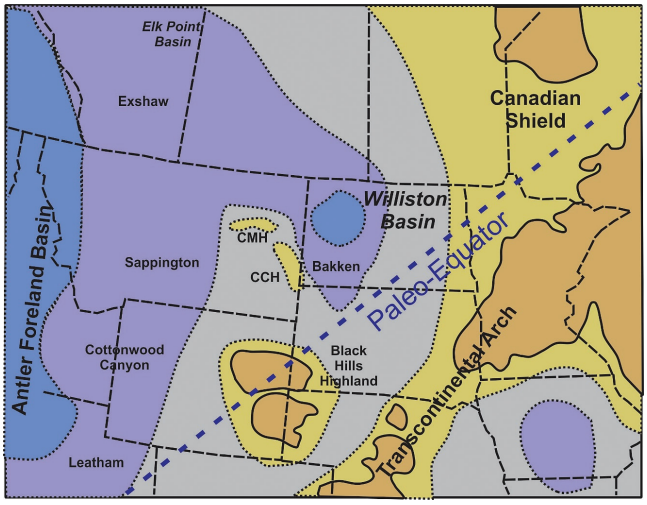

Figure 7. North America paleogeography and black shale deposits for Late Devonian, 360 Ma (modified from Blakey, 2005). Structural features: Canadian Shield, Transcontinental Arch, Black Hills Highland, Cedar Creek High (CCH), Central Montana High (CMH). Position of equator marked by dashed line (Paleo-Equator).

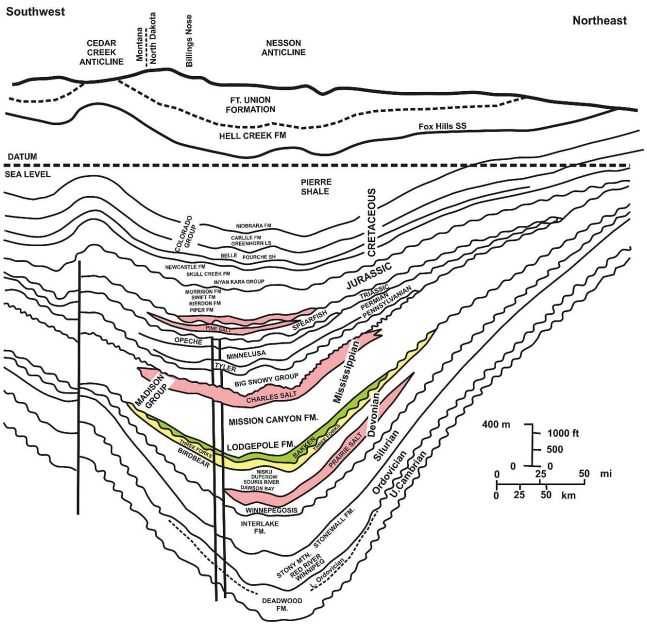

Figure 8. Generalized southwest to northeast cross section across Williston Basin. Modified from Peterson and MacCary (1987). The Cedar Creek anticline is a probably source of sediments for parts of the Bakken, Pronghorn, and Three Forks intervals.

North America. The proto-Williston Basin was an extension of the Devonian Elk Point basin of Canada and was situated in tropical regions near the equator.

Source areas for clastics found in the Bakken and Three Forks include the Cedar Creek High, Central Montana High, Black Hills Highland, Transcontinental Arch, and Canadian Shield.

The depositional and/or erosional limits of the Three Forks Formation and subsequent deposits of the Bakken members are shown in Figure 9 (Theloy, 2014). The

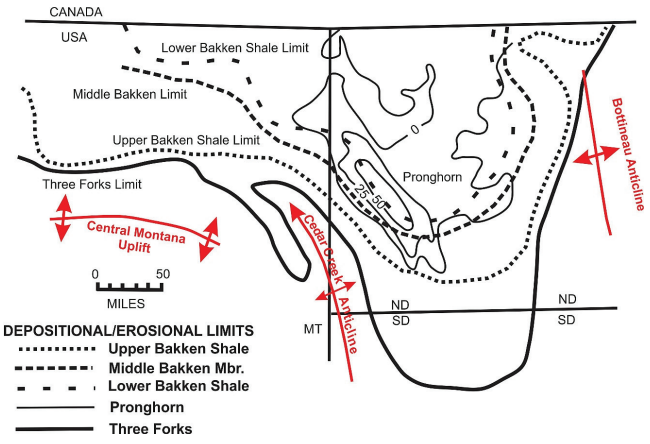

Figure 9. Depositional and erosional limits of the Bakken formation members and the Three Forks formation (modified from Theloy, 2014; after Meissner, 1978; Pronghorn limits from LeFever et al., 2011).

Three Forks has the largest areal extent. After a period of erosion and nondeposition, Pronghorn sediments filled in topographic lows. The Pronghorn has, unlike overlying Bakken strata, a depocenter at the southern margin of the basin with maximum thickness of 54 ft (16 m). The thickest Pronghorn accumulation extends in a linear trough shape, which coincides with both the edge of the Prairie salt and the Heart River fault on the southwestern side (LeFever et al., 2011; Bottjer et al., 2011). The fault may have facilitated movement of fluids into the Prairie salt, which in turn could have triggered dissolution and larger-scale salt collapse features.

After the major drop in sea level at the Three Forks–Bakken boundary, all four members of the Bakken exhibit a successively larger areal extent and onlapping relationships with the Three Forks at the basin margin, reflecting rising sea level conditions.

Three Precambrian provinces underlie the Williston Basin: the Superior craton, Trans-Hudson orogenic belt, and Wyoming craton (LeFever, 1992). These provinces trend north–south, and structures associated with them have strongly influenced later sedimentation and structural features. Notable structural features with a north grain in the Williston Basin include the Nesson, Billings, Little Knife, and Tree Top anticlines. Northwest-trending prominent structural feature include the Cedar Creek, Antelope, and Poplar anticlines. Periodically, these structural features are reactivated (LeFever, 1992; Gerhard et al., 1990).

The Devonian Prairie evaporite occurs about 800 to 1100 ft (244 to 335 m) beneath the Bakken Formation (Figure 8). Regional and local dissolution is known to have occurred in the Prairie (Parker, 1967; Rogers and Mattox, 1985; Gerhard et al., 1990; Martiniuk, 1991; LeFever and LeFever, 2005). Dissolution occurs both as a roughly linear front and also in isolated semicircular areas. Dissolution of the Devonian Prairie evaporite occurred at multiple times during the Paleozoic and Mesozoic (Rogers and Mattox, 1985; Parker, 1967). Isopach thicks in formations above Prairie thins help document the timing of dissolution. Models suggested for salt dissolution include (1) depositional facies control (dissolving fluids move through permeable beds adjacent to the salt horizon), (2) compaction and dewatering of surrounding sediments (supplies the fluid necessary for salt dissolution), (3) surface water recharge at the outcrop (resulting basinward flow dissolves salts), and (4) direct or indirect result from minor tectonic movement related to Precambrian basement features (e.g., faults create pathways for fluids) (Martiniuk, 1991; LeFever and LeFever, 2005). Dissolution of the Prairie occurred during Bakken time and affected Bakken sediments (Martiniuk, 1991; Rogers and Mattox, 1985; Sperr, 1991). Sonnenberg and Pramudito (2009) attributed anomalous thickening in the middle Bakken member at the Elm Coulee field to be due to Prairie salt dissolution coincident with middle Bakken member deposition.

BAKKEN FORMATION: GEOLOGY AND PRODUCTION

The Bakken Formation regionally in the Williston Basin consists of four members: upper and lower organic-rich black shale, a middle member (silty dolostone or limestone to sandstone lithology), and a basal member recently named the Pronghorn (LeFever et al., 1991, 2011; LeFever, 2006) (Figures 3, 8, 9, 10, and 11). The Bakken Formation ranges in thickness from a wedge edge to over 140 ft (43 m) (Figure 12) with the thickest area in the Bakken located in northwest North Dakota, east of the Nesson anticline. The members of the Bakken thin and converge toward the margins of the Williston Basin and have an onlapping relationship with the underlying Three Forks (Figures 8 and 9). The contact between the Bakken and Three Forks is probably unconformable throughout much of the Williston Basin. The Bakken is sharply overlain by the Lodgepole. This sharp contact suggests a period of erosion or nondeposition prior to Lodgepole deposition. The lower, middle, and upper members of the

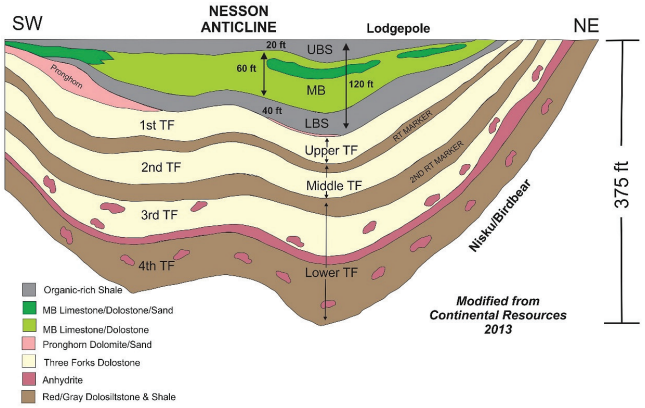

Figure 10. Generalized stratigraphic cross section southwest to northeast across the Williston Basin illustrating Bakken and Three Forks stratigraphy. The Bakken consists of the Pronghorn, Lower Bakken shale (LBS), middle member (MB), and upper Bakken shale (UBS). Industry generally divides the Three Forks into four units or benches (1st TF, 2nd TF, 3rd TF, 4th TF). In this chapter, the Three Forks is divided into three informal units (upper, middle, and lower units). Marker beds or anhydrites separate the units. The targets for horizontal drilling are currently the middle member of the Bakken and the first two units in the Three Forks.

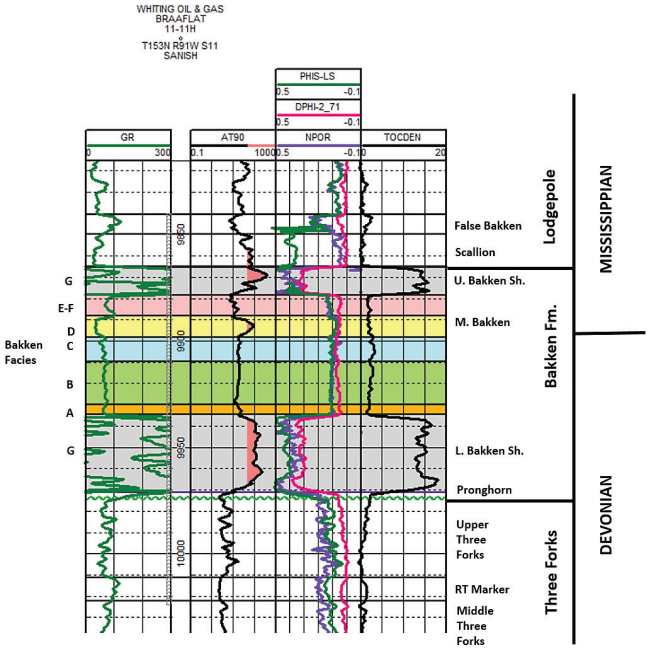

Figure 11. Well log display of the Bakken and upper Three Forks from the Whiting Braaflat 11-11H (Sec. 11, T153N, R91W). Upper and lower Bakken shales have very high GR readings (>200 API). Middle Bakken and Three Forks have low porosities (<10%). Middle Bakken can be subdivided into facies A–F. This well was completed in a horizontal leg for 2669 BOPD. GR = gamma ray; AT20 and AT90 = resistivity curves; PHIS = sonic porosity; DPHZ = density porosity; NPOR = neutron porosity; TOCDEN = calculated TOC from density log.

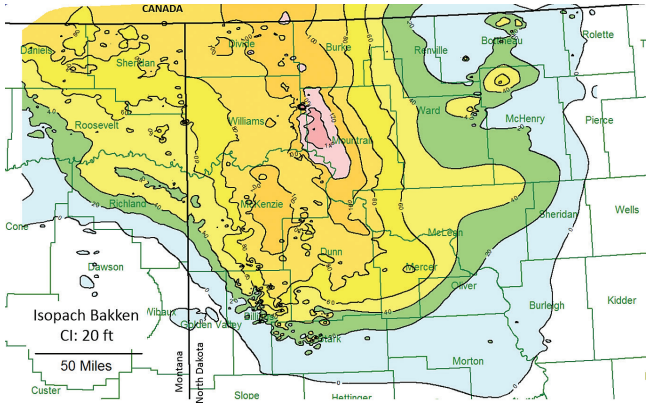

Figure 12. Isopach map of Bakken Formation. The Bakken ranges in thickness from a wedge-edge to over 140 ft (43 m). The thickest area is just east of the Nesson anticline in Mountrail County.

Bakken may represent two regressive–transgressive cycles of sedimentation (Meissner et al., 1984). Following Three Forks deposition, major uplift and erosion occurred along the margins of the Williston Basin (Webster, 1984). This erosion resulted in deposition of the Pronghorn member of the Bakken. With a subsequent relative sea-level rise and low-energy transgression, the lower Bakken shales were deposited. Another regressive event resulted in the middle Bakken being deposited, which was then followed by the next transgressive event, which deposited the upper Bakken shale.

The middle member of the Bakken was deposited in a shallow-water setting following a sea-level drop, resulting in a regressive event (Meissner et al., 1984; Smith and Bustin, 1996, 2000). In the central part of the basin, the middle member consists of argillaceous, greenish-gray, highly fossiliferous, pyritic siltstones that indicate an environment that was moderately well oxygenated but occasionally suboxic. The upper parts of the middle member have cross-stratified sandy intervals that suggest strong current action (LeFever et al., 1991). The mineralogy of the middle Bakken is variable across the basin and consists of 30 to 60% siliciclastic material (quartz and feldspar), 30 to 80% carbonate (calcite and dolomite), and minor matrix material (illite, smectite, chlorite, and kaolinite) (LeFever, 2007). The sources of the detrital fraction in the middle Bakken are thought to be from the north and northwest (Webster, 1984). The middle member ranges in thickness from a wedge edge to over 70 ft (21 m) (Figure 13A and 13B). The thickest middle member occurs east of the Nesson anticline. Figure 13B shows thinning of the middle member east of the Sanish and Parshall fields. A thick also occurs in the general Elm Coulee area. Isolated thicks also occur along the east flank of the Williston, which may be due to Prairie salt dissolution (Cobb, 2013).

The middle Bakken can be subdivided into multiple facies (LeFever et al., 1991; Canter et al., 2009; Sonnenberg et al., 2011c) (Figures 3, 11, 13–19). All the facies are thought to be related to deposition in a shelf setting and appear to represent a shallowing upward sequence followed by a water-deepening event. The facies from bottom to top are facies A, a fossiliferous calcareous siltstone; facies B, bioturbated calcareous clay-rich siltstone to very fine-grained sandstone; facies C is a thinly bedded to laminated calcareous very-fine-grained sandstone; facies D is the highest energy facies and consists of alternating beds of fine-grained sandstone to carbonate grainstones (oolites and bioclastic debris); facies E represents the start of the water deepening and consists of thinly bedded, occasionally microbial laminated, to parallel laminated siltstone; and facies F consists of fossiliferous dolomitic to calcitic siltstone (Figures 14–16). The facies are widespread across the Williston Basin with some exceptions. Laminites in facies C were

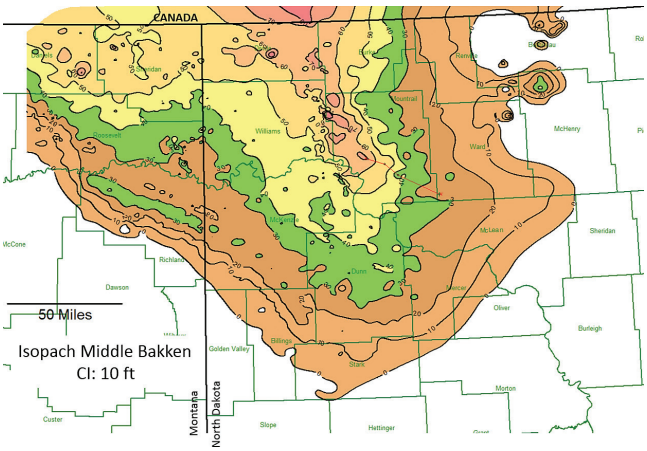

Figure 13A. Isopach map of middle Bakken. Contour interval equals 10 ft (3 m). The middle Bakken ranges in thickness from a wedge-edge to over 70 ft (21 m).

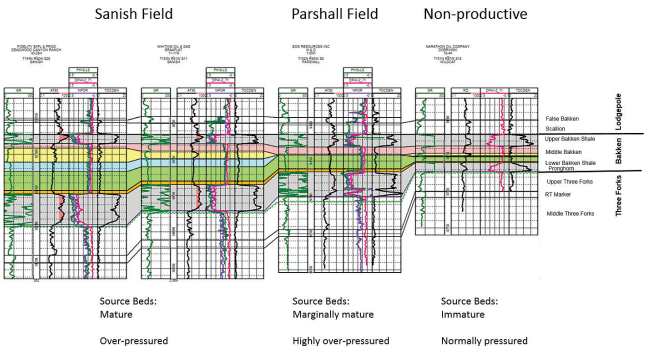

Figure 13B. Four well cross-section Sanish to Parshall fields (W–E). Upper and lower Bakken shales (facies G) have very high GR readings (>200 API). Middle Bakken and Three Forks have low porosities (<10%). Middle Bakken can be subdivided into facies A–F. GR = gamma ray; AT90 = deep resistivity curves; PHIS = sonic porosity; DPHI = density porosity; NPOR = neutron porosity; TOCDEN = calculated TOC from density log. Resistivity greater than 50 ohm-m shaded pink. Note decrease in resistivity to the east (decrease in thermal maturity). Note pinching out of facies C and D to the east. Horizontal wells were drilled from these pilot wells. Deadwood Canyon well completed for 362 BOPD and 364 MCFGD; Braaflat well completed for 2669 BOPD and 1968 MCFGD; N&D well completed for 1285 BOPD and 404 MCFGD.

recently interpreted to be the result of tidal energies (Gent, 2011). Facies D is only locally developed; the amount of dolomite changes from area to area; production is associated with matrix development in facies B, C, D, and E and microfracturing. Facies B and C produce at Elm Coulee (facies D is not present or very thin), whereas facies C, D, and E produce in the Sanish–Parshall areas. Typical facies found in the

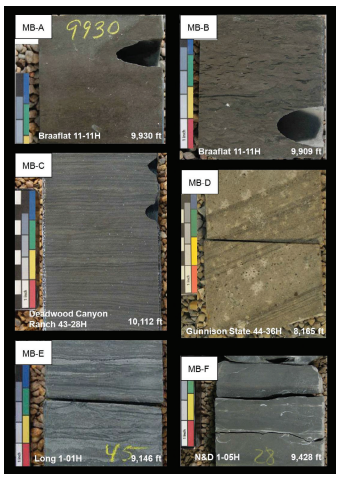

Figure 14. Core photographs of middle Bakken facies: MB-A) skeletal lime wackestone with crinoids, MB-B) characteristic helminthopsis burrows in argillaceous siltstone, MB-C) thinly interbedded silty sandstones and mudstones, MB-D) cross-stratified limy sandstone, MB-E) laminated to wavy, lightly bioturbated dolomitic siltstones and mudstones, and MF-F) massive skeletal dolomitic mudstone with brachiopod fragments. Well locations: Braaflat 11-11H, Sec. 11, T153N, R91W, Mountrail County; Deadwood Canyon Ranch 43-28H, Sec. 28, T154N, R92W, Mountrail County; Gunnison State 44-36H, Sec. 36, T161N, R91W, Burke County; Long 1-01H, Sec. 1, T152N, R90W, Mountrail County; N&D 1-05H, Sec. 5, T152N, R90W, Mountrail County. Core photos are from the North Dakota Industrial Commission (NDIC) and from Kowalski (2010), Simenson (2010), and Theloy (2014).

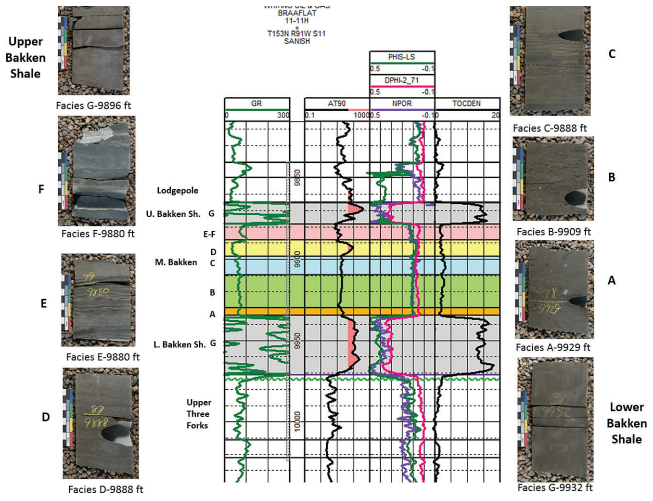

Figure 15. Well log display of the Bakken and upper Three Forks from the Whiting Oil and Gas Braaflat 11-11H (Sec. 11, T153N, R91W). Upper and lower Bakken shales have very high GR readings (>200 API). Middle Bakken and Three Forks have low porosities (<10%). Middle Bakken can be subdivided into facies A–F. GR = gamma ray; AT90 = resistivity curves; PHIS = sonic porosity; DPHI = density porosity; NPOR = neutron porosity; TOCDEN = calculated TOC from density log. Resistivity greater than 50 ohm-m shaded pink.

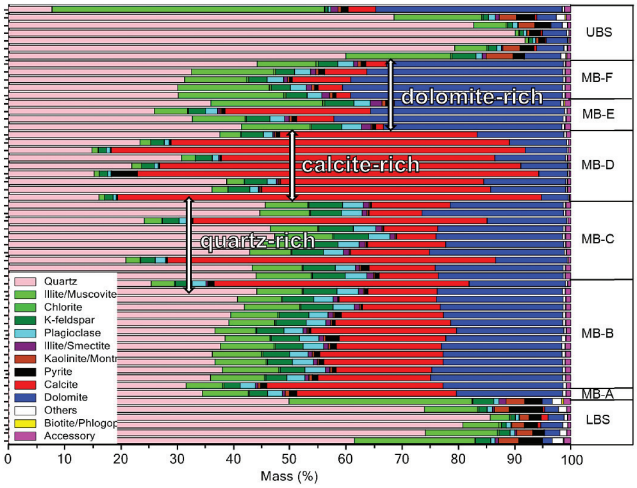

Figure 16. Mineralogical composition of middle Bakken facies and the Bakken shales based on quantitative evaluation of minerals by scanning electron microscope (QEMSCAN) data from the well Braaflat 11-11H, Sec. 11, T153N, R91W, Mountrail County; LBS = Lower Bakken shale; MB-A through MB-F = middle Bakken facies; UBS = upper Bakken shale. From Theloy (2014).

Sanish–Parshall area is shown by Figures 14–16. Mineralogy changes in the middle Bakken across the Williston Basin (Vickery, 2010). Typical mineralogy found in the Sanish–Parshall field areas is shown by Figure 16.

For ease in mapping purposes, the middle Bakken is subdivided into three intervals (facies A–C, facies D, and facies E–F). The thickness of facies A–C is shown in Figure 17. The unit ranges in thickness from a wedge edge (0 ft) to over 50 ft (15 m). The thickest development is east of the Nesson anticline. A thick in the unit develops in the Elm Coulee field area. This thick may be due to two-stage Prairie salt dissolution (Sonnenberg and Pramudito, 2009). Facies B is the main producer at Elm Coulee. Facies D represents the highest energy and shallowest water unit within the middle Bakken (Figures 3, 11, and 18). The unit is typically cross-stratified and consists of alternating beds of bioclast-rich grainstones and fine- to very-fine-grained sandstone. The unit ranges in thickness from 0 to over 20 ft (6 m). The thickest areas are east of the Nesson anticline in what may have been a sag area. A well-developed thick is also present in the northwest part of the mapped area. The reservoir quality of the D unit is variable and depends on the amount of carbonate cement present. Parts of the D represent sag deposits, and isolated shoal deposits are also present. Locally, facies C appears to be eroded by an unconformity at the base of facies D. This unconformity is thought to represent a low-stand surface of erosion. Facies E–F ranges in thickness from a wedge edge to over 20 ft (6 m) (Figure 19). This interval consists of very-fine-grained sandstone

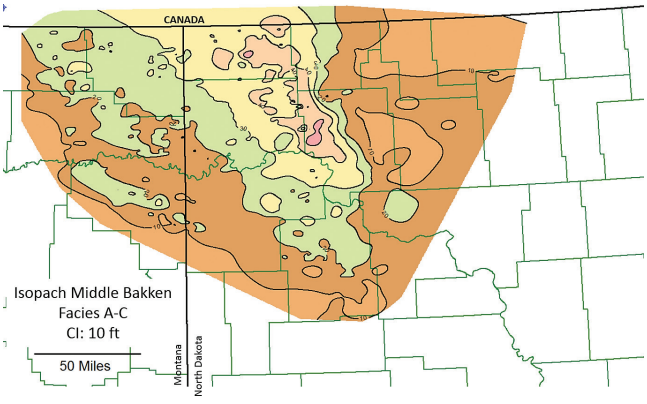

Figure 17. Isopach middle Bakken facies A–C. The unit ranges in thickness from less than 10 to over 50 ft (3 to over 15 m).

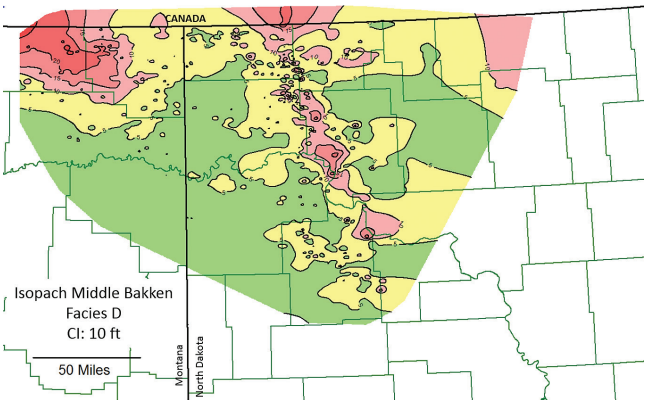

Figure 18. Isopach middle Bakken facies D. The unit ranges in thickness from less than 0 to over 20 ft (0 to over 6 m).

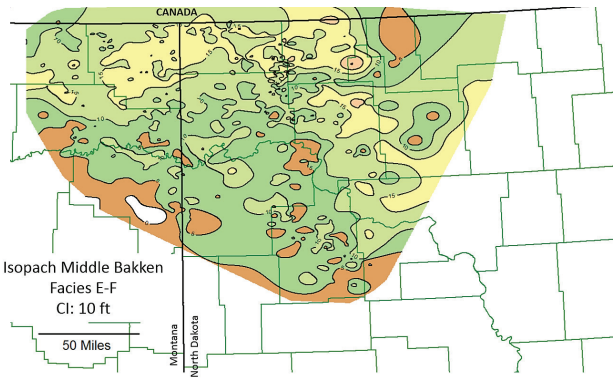

Figure 19. Isopach middle Bakken facies E–F. The unit ranges in thickness from less than 0 to over 20 ft (0 to over 6 m).

to siltstone and is planar to undulose laminated. Some burrowing is present, and fossil-rich beds occur in the F facies. Microbial laminations have been observed in the upper parts of facies C and lower parts of facies E.

A variety of geologic factors and technological factors influence middle Bakken productivity (Theloy, 2014). Technological factors include lateral length, number of hydraulic fracturing stages, proppant volume and type, proppant loading, fluid type used in hydraulic fracturing and volume, fluid–proppant ratio, injection rate, treatment pressure, choke sizes, well spacing, and plug and perf versus sliding sleeves completions. Theloy (2014) addresses each of these topics and notes that more aggressive completions (more fracture stimulation stages) result in high productivity. Geologic factors include reservoir quality (matrix porosity and permeability), reservoir thickness, oil and water saturations, hydrocarbon generation potential, source rock maturity, overpressure, structure and regional stress regime, natural fractures, mechanical stratigraphy, amount of migration, and types of traps. Theloy (2014) also addresses each of these topics. Geologic factors such as source rock maturity, overpressure, reservoir quality, and thickness generally outweigh technological factors.

Utilizing the (oil/oil + water) ratio from longer-term production data is a quick method, developed by Theloy (2014), to identify sweet spot areas characterized by high productivity in the Bakken play. The first 90 days of production (oil/oil + water) is a useful indication of productivity and sweet spots. Figure 20 illustrates areas that produce more oil than water based on this production. The areas of highest oil-to-water production are Elm Coulee, the Billings Nose area, Parshall–Sanish, the Nesson anticline, and the Antelope anticline area.

Theloy (2014) mapped out estimated ultimate recovery (EUR) for the middle Bakken (Figures 21 and 22). Figure 22 illustrates by area EURs for wells drilled from 2010 to 2011. The best EURs are in the Sanish–Parshall area with 632,000 bbl of oil per well (MBO) per well. The Fort Berthold area is the second best with

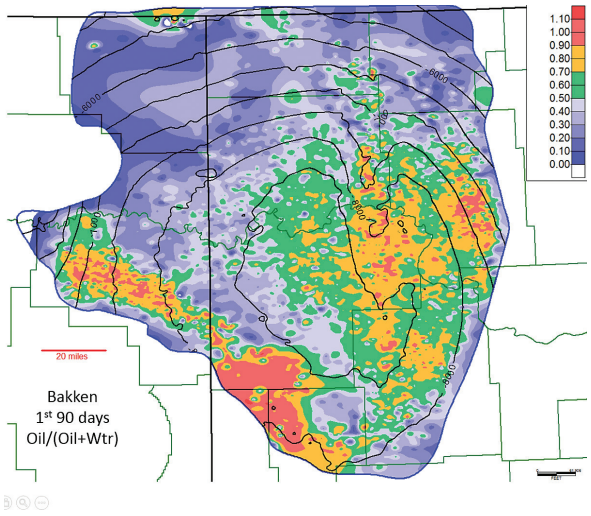

Figure 20. Bakken first 90 days of production: oil/(oil + water). Sweet spot areas with low water production are the warmer colors.

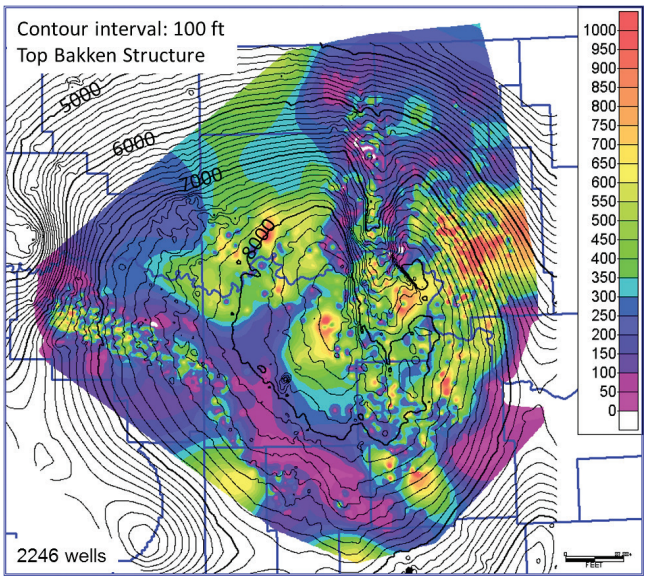

Figure 21. Bakken estimated ultimate recovery map (EUR). Note areas of low production along flanks of the Nesson anticline (suggest migration out of these areas). From Theloy (2014).

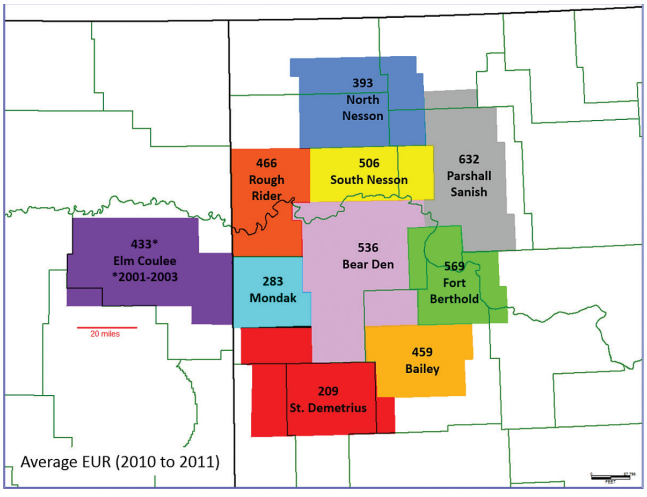

Figure 22. Average EUR 2010 to 2011 by area (thousand bbl). With exception of Elm Coulee, the average EUR was calculated from wells drilled between 2010 and 2011. From Theloy (2014).

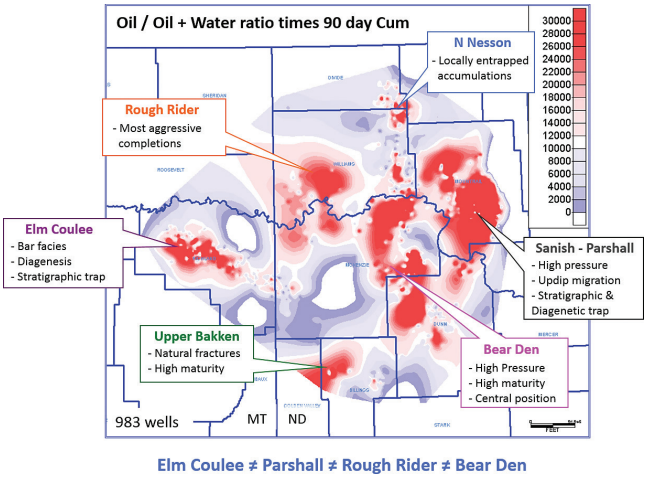

Figure 23. Bakken producing sweet spot areas. The accumulation is a continuous accumulation but individual sweet spot areas result from different causes. From Theloy (2014).

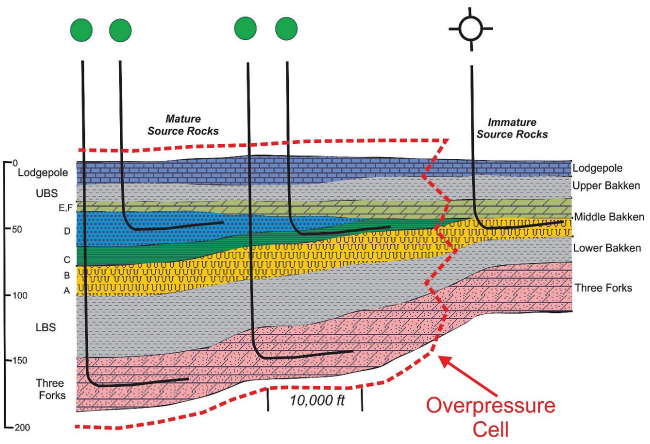

Figure 24. Stratigraphic cross section across Sanish and Parshall fields. Horizontal wells target middle Bakken facies C, D, and E. Stratigraphic thinning in the middle Bakken contributes to the trapping mechanism for the field. Note how facies C and D pinch-out to the east. Modified from Whiting (2010).

569 MBO per well. This is followed by the Bear Den (536 MBO per well) and South Nesson (506 MBO per well). Next is the Bailey area at 459 MBO per well. The updip eastern margin of the Bakken production is in an area of overpressuring (discussed later in this article). The crest of the Nesson anticline is a moderately producing area, which relates to structural controls on productivity (393 MBO per well). Consequently, the flanks of the anticline are a poorly producing area due to partial migration and depletion of hydrocarbons (updip). The poorest-producing areas are St. Demetrius (at 209 MBO per well) and Mondak (slightly better at 283 MBO per well) in the southern part of the basin. The poor production in these areas is probably related to the thinness of the middle Bakken and poor reservoir quality. Elm Coulee has an EUR per well of 433 MBO, which was calculated for the 2001–2003 time period that coincided with the onset of field development. Note that at this time, multistage fracture stimulation was not being performed in the field.

Figure 23 summarizes the various Bakken producing areas and reasons production differs from area to area. In general, structure, stratigraphy, and pore pressure are key ingredients to good production. Figure 24 is an illustration showing factors at Sanish and Parshall thought to be important to production. These factors include source bed maturity, overpressure, and stratigraphic pinchouts of units in an updip direction (Coskey and Leonard, 2009).

PRONGHORN

The Pronghorn is the basal member of the Bakken Formation and unconformably overlies the Three Forks (Figure 3) (LeFever et al., 2011). Johnson (2013) subdivided the Pronghorn into four lithofacies, which are—from bottom to top—PH-1) heavily bioturbated fine-grained sandstone, PH-2) burrowed dolomitic silty mudstone with storm deposits, PH-3) skeletal lime wacke- to packstone, and PH-4) shale with siltstone and sandstone laminations. The Pronghorn shows an overall deepening- and fining-upward character (Bottjer et al., 2011).

The subtidal deposits of the Pronghorn overlie unconformably the Three Forks Formation, and usually, a lag of rip-up clasts and abundant pyrite is developed in the basal portion. The contact between the Pronghorn and the lower Bakken shale is interpreted as a transgressive surface of erosion (Bottjer et al., 2011; LeFever et al., 2011; Johnson, 2013), marking the Pronghorn as lowstand deposits. Johnson (2013) recognized a transgressive surface within the upper part of the Pronghorn, and it may be possible that more than one surface exists or that the vertical position of the surface varies depending on the location in the basin.

The Pronghorn ranges in thickness from a zero edge to over 50 ft (15 m) (Figure 25). Much of the Pronghorn interval may be derived from the Cedar Creek anticline area where the Three Forks and Pronghorn are absent due to erosional truncation (Figures 7–9).

THREE FORKS FORMATION

The name Three Forks shales was used by Peale (1893) for beds resting between the Jefferson Formation and Madison Limestone for outcrops near Three

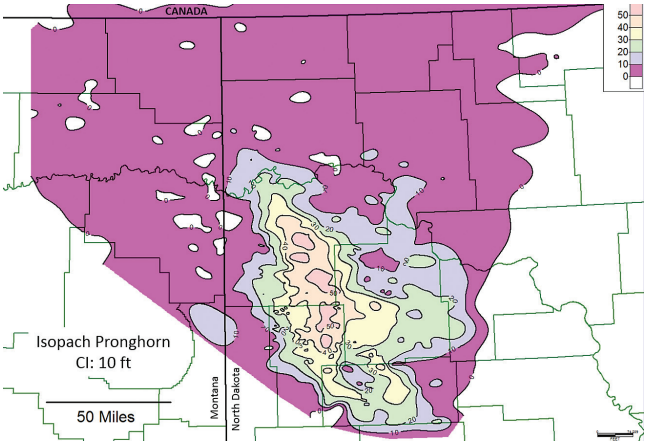

Figure 25. Isopach map of Pronghorn interval. The thickness ranges from a wedge-edge to over 50 ft (15 m). This largely dolomitic interval may largely be derived from erosion of Paleozoic units on the Cedar Creek anticline.

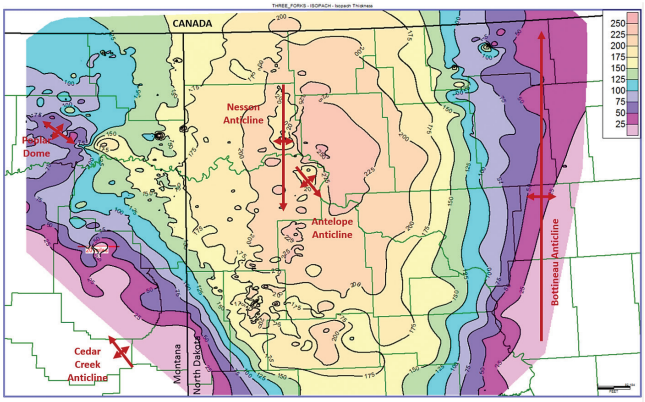

Figure 26. Isopach of total Three Forks interval. The Three Forks ranges in thickness from a wedge-edge to over 225 ft (69 m). Structural features control the thickness patterns seen on this map. Active structures during deposition include the Cedar Creek, Poplar, Nesson, and Bottineau anticlines. The thickest Three Forks area is east of the Nesson anticline.

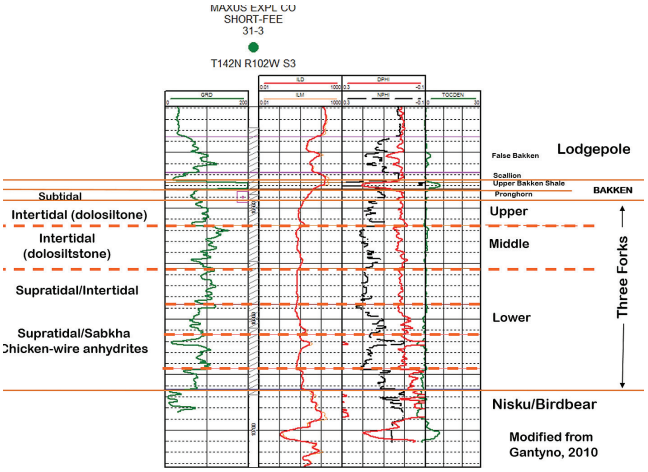

Figure 27. Well log display of the Bakken and Three Forks from the Maxus Short-Fee 31-3 (Sec. 3, T142N, R102W). GRD = gamma ray; ILD and ILM = resistivity curves; NPHI = porosity; DPHI = density porosity; TOCDEN = calculated TOC from density log. Modified from Gantyno (2011).

Forks, Montana (Sandberg, 1965). The name was later changed to Three Forks Formation by Haynes (1916). Sandberg (1965) published a detailed measured section of the Three Forks at its type section near Logan, Montana.

Sandberg and Hammond (1958) described the original Three Forks type section in the Mobil Producing Company No. 1 Solomon Bird Bear well, Sec. 22, T149N, R91W, Dunn County, North Dakota, using a clastic classification scheme. Poor preservation of the original type section core led to the selection of a new standard reference section for the Three Forks in the EOG Resources #2-11H Liberty well, Sec. 11, T151N, R91W, Mountrail County, North Dakota.

The Three Forks ranges in thickness from less than 25 to over 250 ft (8 to over 76 m) in the mapped area (Figure 26). Thickness patterns are controlled by paleostructural features such as the Poplar Dome, Nesson, Antelope, Cedar Creek, and Bottineau anticlines. Thinning and/or truncation occurs over the crest of the highs, and thickening of strata occurs on the flanks of the highs.

Many subdivisions have been proposed for the Three Forks (Berwick, 2008; Bottjer et al., 2011; LeFever et al., 2011; Gantyno, 2011; Gutierrez, 2014; Webster, 1984; Dumonceaux, 1984). For example, Gantyno (2011) subdivided the Three Forks into six units (Figure 27). For the sake of simplicity, the interval will be subdivided into three units in this chapter (upper, middle, and lower). These subdivisions are illustrated by Figure 27. The extents of each unit decreases upwards, with the lower Three Forks showing the largest areal distribution and the upper Three Forks showing the smallest areal distribution. This in part is due to the unconformity at the top of the Three Forks.

X-ray diffraction (XRD) mineralogy for the Three Forks is illustrated in Figure 28. The Three Forks is an argillaceous, silty to very-fine-grained, dolostone throughout. The formation becomes anhydritic toward the base. The hematite content increases in the middle and lower Three Forks, whereas the pyrite content increases in the upper Three Forks. Small amounts of halite also show up in an XRD analysis of the formation showing the high salinity of the formation. Often,

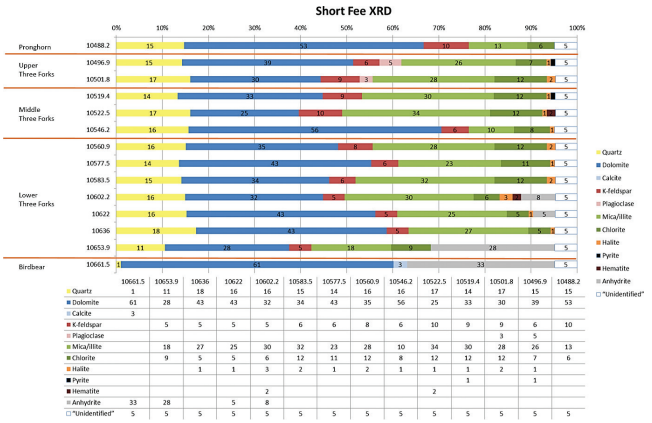

Figure 28. X-ray diffraction data (XRD) for the Three Forks Formation from the Maxus Short-Fee 31-3 (Sec. 3, T142N, R102W) well. Uppermost data are from the Pronghorn interval and lowermost data are from the Birdbear. Note the presence of dolomite, illite, and chlorite throughout the Three Forks. Note also the presence of evaporites (anhydrite and halite) in the Three Forks interval.

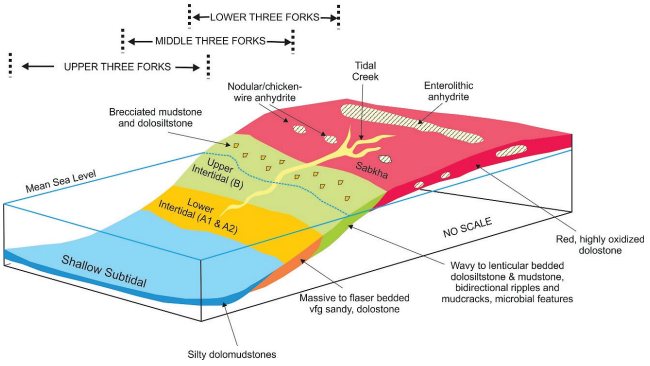

Figure 29. Three Forks schematic depositional model. Approximate settings for lower, middle, and upper Three Forks shown. Anhydrites mainly found in lower Three Forks. Modified from Berwick (2008), Gantyno (2011), and Franklin and Sonnenberg (2012).

halite crystals will precipitate on slabbed core surfaces (post slabbing). Halite beds are not reported to occur in the Three Forks, which may be a result of local dissolution. Salt hoppers are present in outcrops in central Montana.

The lower and middle Three Forks is known for its red color. The presence of hematite gives the Three Forks its red color. The hematite occurs as a thin coating around grains. The source of the hematite, as in most red bed sequences, is probably diagenetic. The source of hematite is generally intrastratal dissolution of detrital silicates such as hornblende, augite, olivine, chlorite, biotite, and magnetite (Tucker, 2001). The Three Forks has a large percentage of chlorite in its composition. The source of the chlorite is unknown but may be from volcanic arcs to the west. The red color comes from the oxidizing diagenetic environment. Only a small amount of iron, 0.1%, is sufficient to impart a red color. If reducing conditions prevail, the iron will be in a ferrous state and impart a green color. Secondary alteration of the red color takes place when reducing solutions penetrate into red sediments. This commonly occurs along porous beds, fractures, and so on. The upper Three Forks has a distinct green color in mudrock intervals, which may be an alteration of a previous red color.

Most of the previous workers in the Three Forks have interpreted the depositional environment to be subtidal to supratidal (Figure 29) (Dumonceaux, 1984; Berwick, 2008; Gantyno, 2011; Bottjer et al., 2011; LeFever et al., 2011; Gutierrez, 2014). Overall, the Three Forks represents a water-deepening cycle with more coastal and inland sabkha deposits in the lower Three Forks, and intertidal deposits in the middle and upper Three Forks.

Lower Three Forks

The deposits of the lower Three Forks reflect mainly a low-energy, supratidal sabkha setting in dry, evaporative climate conditions. The very fine grain sizes of sediments and the abundance of anhydrite set the lower Three Forks deposits apart from the overlying units. Anhydrite occurs as massive, argillaceous mosaic anhydrite or as distinctive beds, stringers, and nodules within a mudstone matrix. The precipitation of anhydrite is interpreted to have occurred coevally with sedimentation or at very early stage of diagenesis. The dolomitic claystones within the lower Three Forks are either reddish-brown or green in color, and both variations can occur in close juxtaposition to each other. The dolomudstones contain minor amounts of silt and are typically noncalcareous, hard, fissile, and well cemented. Usually, the mudstones are structureless to faintly laminated. Other sedimentary structures include compaction-loading features, dewatering structures, distortion around anhydrite nodules and granule-sized clasts, as well as mud cracks, syneresis cracks, and brecciation. The breccias contain clay and dolomudstone fragments floating in a matrix-supported fabric. Common cementing agents are anhydrite, dolomite, and pyrite in disseminated form (Gantyno, 2011; Franklin and Sonnenberg, 2012).

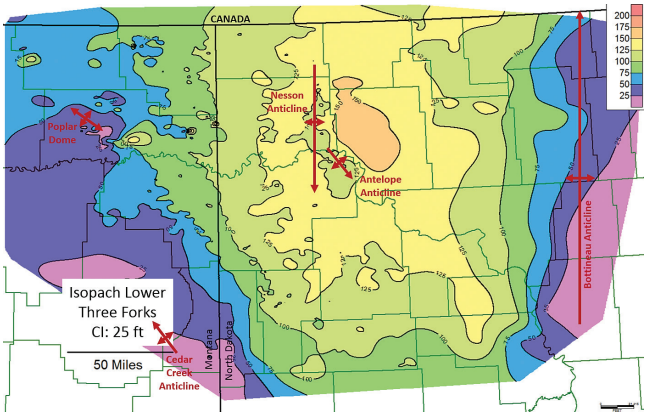

Figure 30. Isopach lower Three Forks. Thickness ranges from less than 25 to over 150 ft (8 to over 46 m) in mapped area. Thickest area is east of Nesson Anticline. Thinning occurs on Poplar, Nesson, Cedar Creek, and Boutineau anticlines.

The lower Three Forks ranges in thickness from less than 25 to over 150 ft (8 to over 46 m) in the mapped area (Figure 30). The thickest area is east of the Nesson anticline. Thinning of the lower Three Forks occurs toward the flanks of the basin.

Middle Three Forks

The middle Three Forks ranges in thickness from 20 to 60 ft (6 to 18 m) across the mapped area (Figure 31). Thinning occurs towards the flanks of the Williston Basin.

The middle Three Forks consists of beds of anhydritic, calcareous, argillaceous dolostone, silty dolostone, and sandy argillaceous dolostone. Generally, the unit is very fine grained, and grain size decreases upward. The unit is similar to the upper Three Forks, with an overall shallowing upward sequence followed by a water deepening event (dolomudstone).

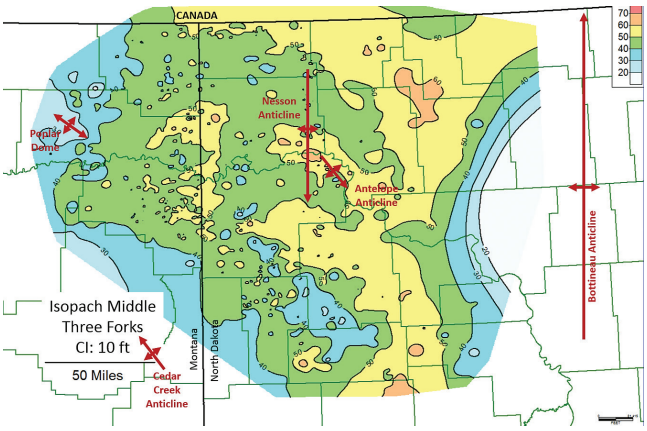

Figure 31. Isopach map of middle Three Forks. Thickness ranges from less than 20 to over 60 ft (6 to over 18 m) in mapped area.

The middle Three Forks is dominated by chaotic and brecciated facies. Two types of brecciated fabrics occur in the middle Three Forks, including matrix-supported and clast-supported breccia. The abundance of mud-supported breccia may be due to storm events (Bazzell, 2014). Original sedimentary structures such as parallel and ripple laminations are rarely preserved due to the high degree of brecciation and soft-sediment deformation (including dewatering structures).

A laminated facies often occurs near the base of the middle Three Forks. This facies consists of thin- to thick-bedded (millimeter to centimeter scale) alternating layers of mudstones and dolomitic siltstones.

The top of the middle Three Forks is a massive (possibly burrowed), structureless, subtidal mudstone. This unit is referred to as the RT marker bed and is 2 to 20 ft (0.6 to 6 m) thick. The unit is dominated by clay-sized material with silt-sized quartz and dolomite. The average composition of this upper unit is 38% dolomite, 30% clay, 27% quartz, and 2% pyrite.

Upper Three Forks

The upper Three Forks is dominated by silt-sized and some very-fine-grained sandstones and dolomite and has low permeabilities and porosities. The upper Three Forks ranges in thickness from a wedge edge to over 40 ft (12 m) in areas east of the Nesson anticline (Figure 32). The unit thins toward the margins of the depositional basin because of erosional truncation. On logs, the unit is difficult to separate from the overlying Pronghorn.

The upper Three Forks is evolving into a significant resource play in the Williston Basin. To date, over 2880 wells (including the older wells at Antelope) have been completed in the upper Three Forks (Figure 30). The upper Three Forks consists largely of pinkish-tan silty dolostones that are interbedded with green chloritic, dolomitic mudstone (Figure 33). A variety of facies have been reported in the upper Three Forks, ranging in depositional environment from subtidal to supratidal (Dumonceaux, 1984; Berwick, 2008; Gantyno, 2011; Bottjer et al., 2011). Typical sedimentary structures include parallel to subparallel laminations, uni- and bidirectional ripple cross-laminations, mudcracks,

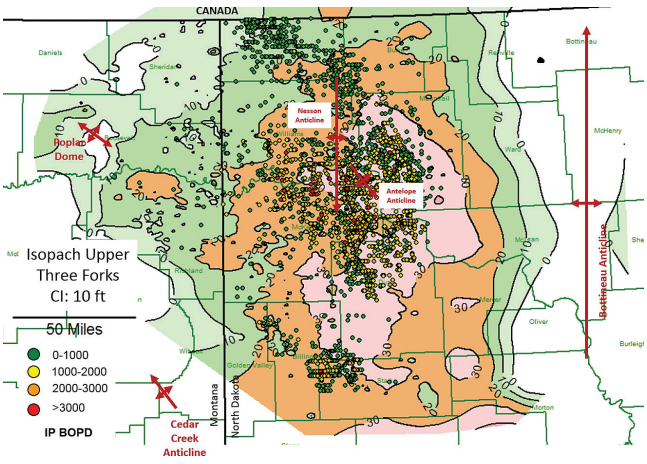

Figure 32. Isopach map upper Three Forks. Thickness ranges from a wedge-edge to over 30 ft (9 m). Thinning occurs towards Poplar dome and the Cedar Creek anticline. The vast majority of Three Forks wells are drilled in this interval. The colored dots indicate Three Forks initial production (see legend).

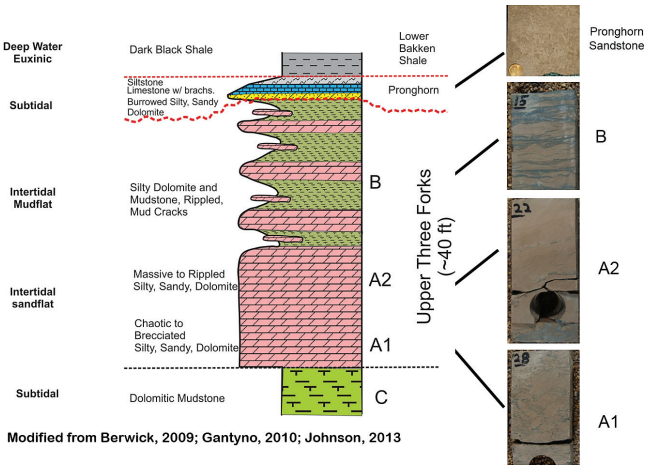

Figure 33. Schematic of upper Three Forks showing facies, core photographs, and interpreted depositional environment. Tidal environments dominate the upper Three Forks. Modified from Berwick (2008) and Gantyno (2011).

syneresis cracks, and soft sediment deformation. Deposition is a shallowing upward succession ranging from subtidal to upper intertidal. The Pronghorn member of the Bakken sits unconformably on the Three Forks.

The facies in the upper Three Forks is shown by Figure 33. The basal upper Three Forks (A1 and A2) is a sandy to silty dolostone unit that overlies the green mudstone facies of the middle Three Forks. The unit ranges in thickness from 10 to 25 ft (3 to 8 m). The mineralogic composition of the basal upper Three Forks is 57% dolomite, 29% quartz, 10% clay, and 2% pyrite. The unit can be subdivided into two subfacies, A1 and A2. The lower A1 facies is mottled, possibly burrowed, and characterized by soft sediment deformation that resembles dewatering structures. Upward-directed dewatering features are present. The overlying A2 is laminated to massive, silty dolostone. Some ripple and wavy laminations are present in the unit. The A1 and A2 are interpreted as shallowing upward succession. The B facies shown in Figure 33 consists of interlaminated to interbedded green dolomitic mudstone and pinkish-tan silty dolostones. The green mudstones constitute 30 to 70% of the unit. Sedimentary structures are uni- and bidirectional ripple cross-laminations, double clay drapes, mudcracks, syneresis cracks, scour surfaces, soft sediment deformation, and rare intraclast conglomerates. The intraclast conglomerates may form in small tidal channels, by storm events, or by evaporite dissolution.

THREE FORKS PRODUCTION

The original discovery at the Antelope field in 1953 established the upper Three Forks as a viable reservoir in the Williston Basin. The upper Three Forks remained fairly dormant until recently drilled horizontal wells began again to indicate its large potential.

The North Dakota Industrial Commission (NDIC) has recently estimated that the Three Forks will have recoverable reserves of 1.9 billion bbl of oil across much of the Williston Basin (Nordeng and Helms, 2010). The Three Forks play coincides with the Bakken play, which adds significantly to the reserves across the basin. The USGS mean technologically recoverable resource estimate for the Three Forks is 3371 billion bbl of oil, 3.5 tcf of gas, and 281 million bbl of natural gas liquids (Gaswirth et al., 2013).

Three Forks production is shown by Figure 6. The current cumulative total is 263,448,155 bbl of oil and 294,728,845 MCFG. Figure 34 illustrates the first 90 days' production (oil/oil + water) for the Three Forks and low water producing areas. The southern Nesson anticline and areas east of the Nesson anticline show the highest oil-to-water ratio.

RESERVOIR PROPERTIES: BAKKEN AND THREE FORKS

Measured core porosity and permeability are very low in the Bakken, Sanish, and Three Forks reservoirs (<10% porosity and <0.1 md permeability) in the Williston Basin, so productivity is assumed to be due to natural and artificial fracturing. The reservoirs generally require advanced technology to get them to

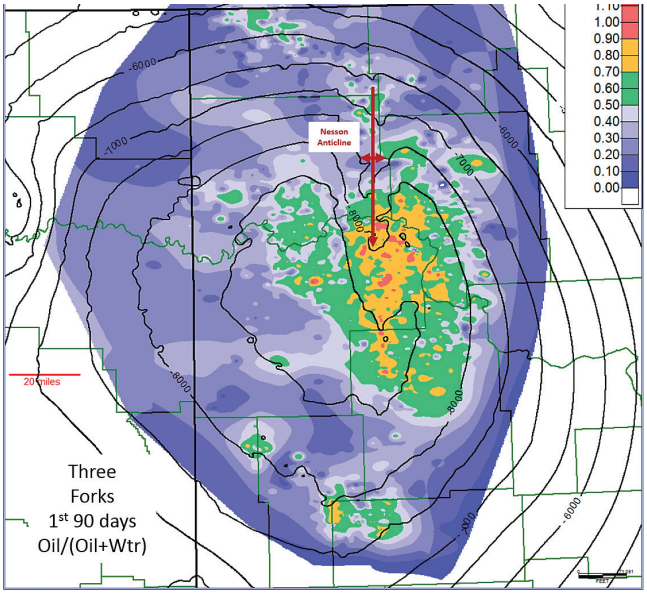

Figure 34. Three Forks production map for the first 90 days: oil/(oil + water). The warm colors (green to red) indicate wells which produce more oil than water. The cool colors (blue) indicate wells that produce more water than oil. The best production is associated with the Nesson anticline and areas to the east of the Nesson. After Theloy (2014).

produce (fracture stimulation and horizontal stimulation). For this reason, they should be considered to be technology reservoirs. Natural fractures in some areas (e.g., the Billings Nose area and Antelope field) are sufficient for vertical well production.

A core analysis from the Whiting Braaflat 11-11H (Sec. 11, T153N, R91W) provides the following information. The Scallion member of the Lodgepole has an average porosity of 2.3% and average permeability of 0.12 md (most permeability plugs had visible fractures). Average grain density is 2.7 gm/cc. The middle Bakken has average porosity of 6.7% and average permeability of 0.33 md (including plugs with visible fractures). Excluding core plugs with fractures, the average permeability number drops to 0.028 md. Average grain density in the middle Bakken is 2.7 gm/cc. The Three Forks has an average porosity of 7.6% and average permeability of 1.1 md (including core plugs with visible fractures). The average permeability excluding the plugs with fractures is 0.23 md. Average grain density in the Three Forks is 2.8 gm/cc. Most of the visible fractures in the core are horizontal. The Braaflat 11-11H (Figure 11) was completed as a horizontal well in the middle Bakken for 2669 BOPD and 1968 MCFGD. The well has a cumulative production of 359 million bbl of oil and 232 MMCFG.

Measured core porosity and permeability are also very low in the Bakken shale, Pronghorn, and Three Forks reservoirs at the Antelope field. The core analysis from the Duncan Rose #1 (Sec. 33, T15N, R94W) provides the following information. The lower Bakken shale has porosities of 3.8% and permeabilities of 0.01 md. The Pronghorn (formerly known as the Sanish) has porosities ranging from 6 to 9% and permeabilities ranging from 0.08 to 0.33 md. The upper Three Forks has porosities ranging from 8.3 to 10.6% and permeabilities ranging from 0.01 to 0.18 md. One foot of Three Forks 10,609–10,610 reported a permeability of 6.88 md, but this is interpreted to be due to a horizontal fracture.

LOWER AND UPPER BAKKEN SHALES

The upper and lower shale members are potential source rocks and are lithologically similar throughout much of the basin (Dow, 1974; Webster, 1984). The shales predominantly contain type II kerogens but may also contain some type I and type III (Sonnenberg, 2010b, Sonnenberg et al., 2011a, 2011b, 2001c, Jin, 2013) (Figure 35). The shales are potential source beds for the Bakken, Three Forks, and Lodgepole formations (Meissner et al., 1984; Sonnenberg, 2011; Longman et al., 2014). The shales are dark gray to black, hard, siliceous, slightly calcareous, dolomitic, pyritic, and massive to fissile, and they generally either break along horizontal fractures or with conchoidal fractures (Figures 36 and 37). Detrital silt grains are disseminated throughout the shale interval as scattered grains. Some discontinuous laminae of silt grains

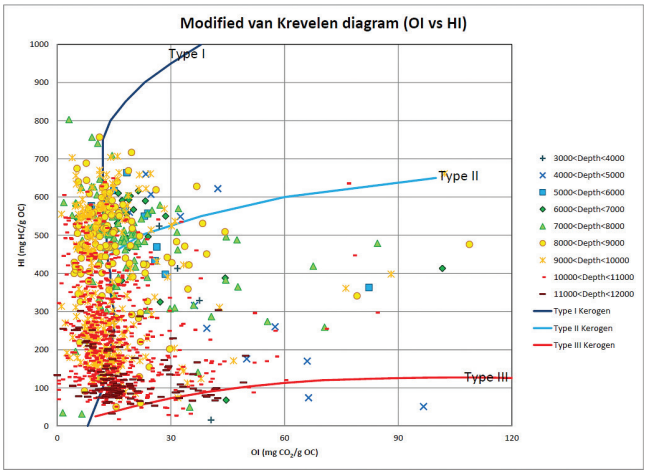

Figure 35. Modified van Krevelen diagram for the Bakken Formation of Williston Basin. Published data from Webster (1984) and Price et al. (1984). Majority of samples indicate a Type I and II oil-prone kerogen (algal origin). Legend shows source rock data by depth interval; EC Vaira from Elm Coulee (only 2 data points available). HI is hydrogen index (S2/TOC). OI is oxygen index (S3/TOC). From Jin (2013).

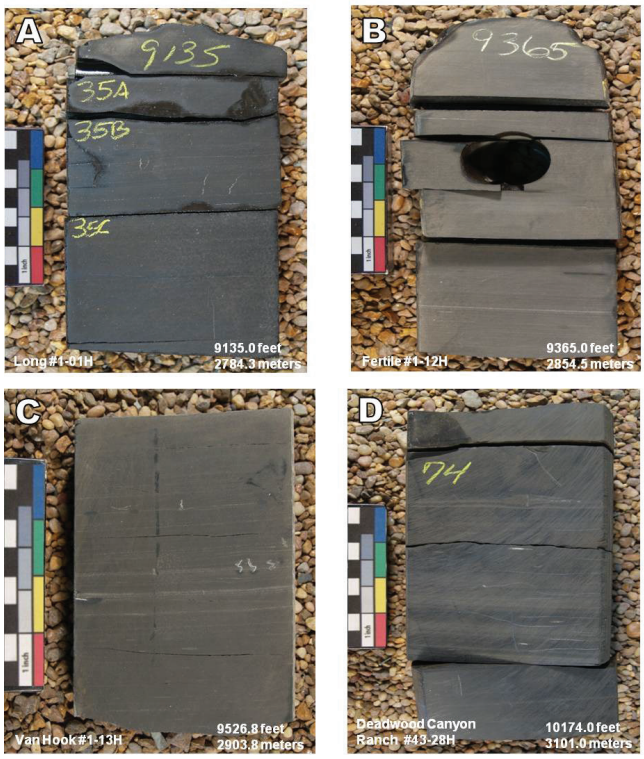

Figure 36. Core photos of facies G—organic rich pyritic brown/black mudstone. Photos A and B are from the upper Bakken shale, and photos C and D are from the lower Bakken shale. Small vertical fractures cemented by calcite and pyrite are visible in photo C.

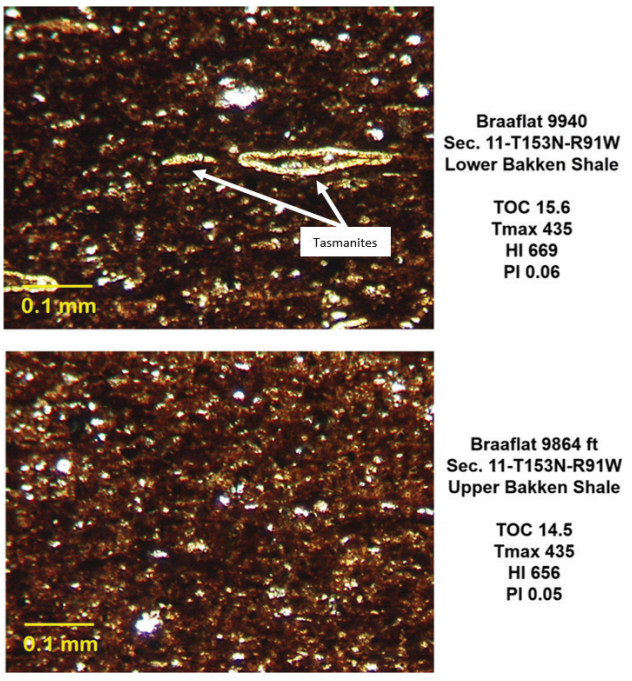

Figure 37. Thin section photomicrographs of upper and lower Bakken shales. Note abundance of Tasmanites in lower Bakken shale.

are present. The silt-sized material is probably eolian in origin. The shales contain radiolaria, conodonts, ostracodes, small cephalopods, small brachiopods, and *Tasmanites* (algae) fossils (Webster, 1984). The shales lack bioturbation but do contain flattened fecal pellets and lack evidence of bottom current transport except in the transitional foot to 3 ft (1 m) at the base and tops of the shales (Longman et al., 2014). The shales are dissimilar in that the upper shale lacks limestone and greenish-gray shale beds found locally in the lower shale (Pitman et al., 2001). The lower shale has a greater abundance of *Tasmanites*. Secondary pyrite occurs disseminated throughout the shale interval and as individual laminations and lenses. The shales consist of dark organic material, clay, silt-sized quartz, and some calcite and dolomite (both detrital and authigenic). The shale is kerogen rich in the deeper parts of the basin, and the organic material is distributed throughout. The Bakken kerogen is an amorphous kerogen inferred to be sapropelic, and the composition consists of 70 to 95% amorphous material, 0 to 20% herbaceous material, up to 30% coaly material (recycled opaque material), and 5% woody material (Webster, 1984). Because of the high hydrocarbon-generating capacity of the material determined from pyrolysis (>500 mg HC/g OC at shallow depths), Webster (1984) believes the amorphous material has an algal origin. Webster (1984) describes the total organic carbon content of the Bakken shales as averaging 11.3 wt.% in thermally mature areas of the basin. The shales average 15 to 20 wt.% total organic carbon (TOC) where thermally immature (Longman et al., 2014).

Schmoker and Hester (1983) derived an equation to calculate TOC content using bulk density logs. They derived the following equation for calculating TOC from bulk density: $TOC = (154{,}497/\rho) - 57.261$, where TOC is total organic carbon and ρ is the bulk density of the shale. Figure 11 illustrates the calculated TOC for the Braaflat 11-11H (Sec. 11, T153N, R91W) from the Sanish field. The calculated TOC is comparable to the actual measured TOC of 10 to 18 wt.%.

The upper and lower shale are interpreted to have been deposited in an offshore marine anoxic or oxygen-restricted environment during periods of sea-level rise (Price et al., 1984; Webster, 1984; LeFever et al., 1991; Pitman et al., 2001). The anoxic conditions may have resulted from a stratified hydrologic regime (Webster, 1984; Smith and Bustin, 1996, 2000). The stratified water column is envisioned as having an upper water layer that is well oxygenated and nutrient rich. High organic production occurred in this layer (probably planktonic algae). Following the death of the organisms, they sank through stagnant bottom waters and were deposited. Anoxic conditions are created by restricted circulation and in part

by destruction of organic matter by consuming organisms that remove oxygen and release hydrogen sulfide (Meissner et al., 1984; Webster, 1984). Anoxic conditions are indicated by the lack of benthic fauna and burrowing, as well as high TOC content. The Bakken may be part of continent-wide anoxic event that took place from late Famennian through Kinderhookian time (Meissner et al., 1984). The Bakken is correlative with the Woodford-Percha-Leatham-Sappington-Exshaw-Cottonwood Canyon source rock facies of the western Cordilleran and southern craton-margin geosynclines and the Antrim-Sunbury-New Albany-Chattanooga and equivalent source rock facies of the Appalachian geosyncline (Meissner et al., 1984).

The Bakken is not thermally mature throughout the Williston Basin. The shales are thermally immature in the eastern part of the basin and characterized on well logs by low resistivity (i.e., water-wet) (Figure 38). In the western Williston, the shales are characterized by high resistivity and thought to be oil-wet (Meissner, 1978). Hydrocarbons are nonconductive, which results in extremely high resistivities. Further evidence of the presence of hydrocarbon saturation comes from core analyses and also plots of pyrolysis data (i.e., production index versus depth plots or pyrolysis S1 versus depth plots) with depth (Price et al., 1984; Webster, 1984). These data clearly indicate that the Bakken shales are oil saturated where they have high resistivity. Wettability tests in the Bakken illustrate that the upper and lower shales are oil-wet while the Lodgepole, middle Bakken, and Three Forks intervals are water-wet (Cramer, 1986, 1991). Price (1999) and Price and LeFever (1992) noted the extremely high oil-to-water ratios associated with Bakken production, suggesting that most of the water has been displaced by hydrocarbon generation. The oil–water ratios are 200 to 800 bbl of oil to one bbl of water, with the mean being 300 bbl of oil to one bbl of water. The small amount of co-produced water may be dissolved in Bakken oil and exsolved during production, or it can be produced from the matrix of the reservoir rocks. Figure 38 illustrates the areas of high resistivities in the Bakken shales. The 100 ohm-m line is used as a cutoff value where generation has occurred.

Organic maturity has recently been modeled using the Time-Temperature Index (TTI) method by Nordeng and LeFever (2008) and Jin (2013). Their models suggest that organic maturity started approximately 100 Ma. Carlisle et al. (1992) suggest that hydrocarbon generation started in the early Cretaceous. Webster (1984) utilized TTI plots to conclude that oil generation began approximately 75 Ma (late Cretaceous).

Most of the oil generated in the Bakken black shales may have been expelled into the middle member of the Bakken or the upper Three Forks. Price and LeFever (1994) also presented evidence that most of the oil generated in the Bakken stayed in the Bakken and did not migrate into the overlying Madison Group. Earlier investigators thought the Bakken shales sourced reservoirs in the Bakken and entire Madison Group (Dow, 1974; Williams, 1974; Meissner, 1978).

The lower Bakken shale ranges in thickness from 0 to over 50 ft (0 to over 15 m) (Figure 39). The thickest area is a north–south trending area just east of the Nesson anticline. Slightly updip from the axis of the thick lies the greater Sanish–Parshall-Fort Berthold producing area. The lower Bakken shale is the main source bed for this sweet spot production area.

A plot of hydrogen index (mg HC/g OC) versus T_{max} °C for the lower Bakken shale illustrates Bakken source rock data that falls into immature, oil window, and

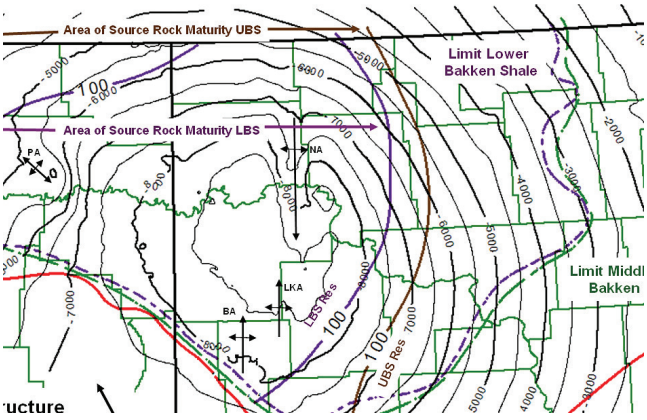

Figure 38. TStructure map on top of Bakken and limits of lower Bakken shale, middle Bakken, and upper Bakken shale across Williston Basin. Areas of source rock maturity for upper Bakken shale and lower Bakken shale are indicated by 100 ohm-m contour lines.

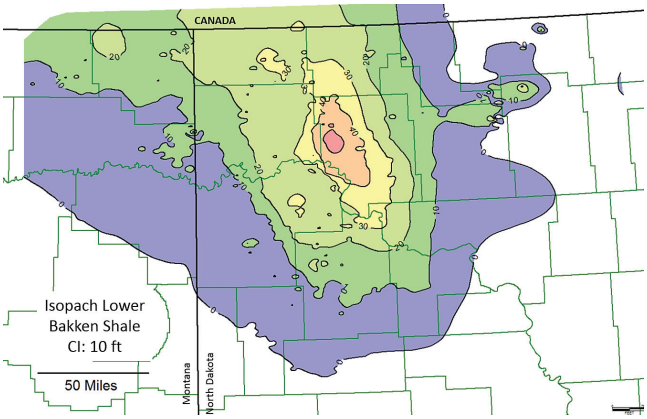

Figure 39. Isopach map of lower Bakken shale. Thickness ranges from a zero edge to over 50 ft (15 m).

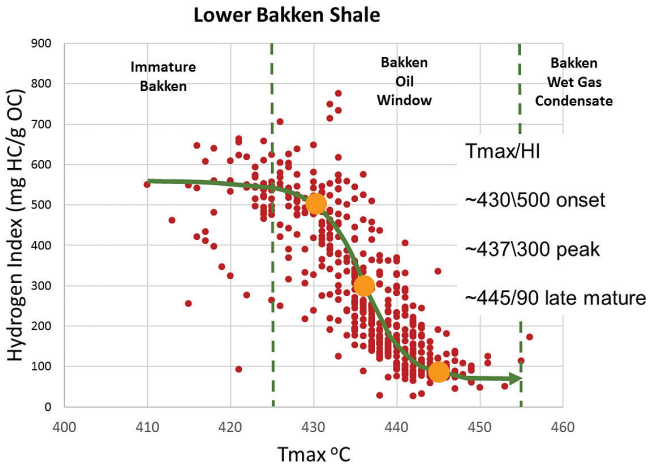

Figure 40. Hydrogen index versus T_{max} °C for the lower Bakken shale. Onset of intense hydrocarbon generation coincides with T_{max} values of 430° Celsius (806° Farenheit) and HI values of 500. Data are from the USGS (2016) and CSM Bakken (2015) data sets.

wet-gas condensate categories (Figure 40). The oil window ranges in value from 425 to 455 T_{max}. Onset of intense oil generation coincides with values of 500 HI and 430 for T_{max}. Peak generation is approximately 300 HI and 437 T_{max}. Late mature values are 90 HI and 445 T_{max}. These values can be mapped to illustrate mature and immature areas for the lower Bakken shale (Figures 41 and 42).

Figure 41 illustrates mapped T_{max} for the lower Bakken shale. These values are compared to the 100 ohm-m line taken from Hester and Schmoker (1985). The 100 ohm-m line coincides with T_{max} values of 425 to 430. The hot colors on Figure 40 are high geothermal gradient areas previously noted by Sonnenberg (2011a) and Jin (2013).

Figure 41 illustrates mapped HI values for the lower Bakken shale. These values are compared to

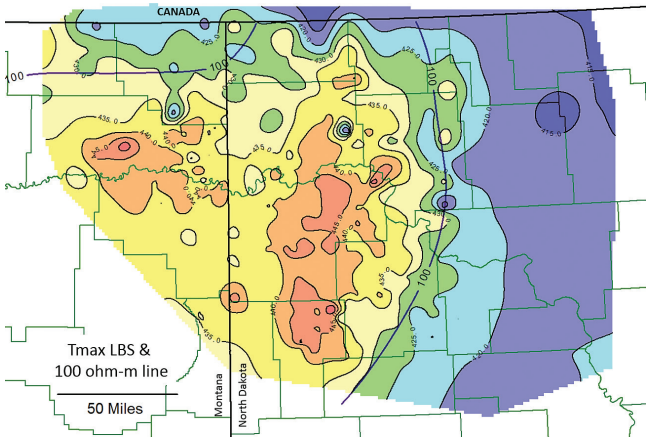

Figure 41. T_{max} values for lower Bakken shale (LBS). Also shown is the 100 ohm-m resistivity line for the lower Bakken shale (from Hester and Schmoker, 1985). The thermal mature areas of the lower Bakken shale are shown by the warmer colors. Immature areas are the blue colors. Data are from the USGS (2016) and CSM Bakken (2015) data sets.

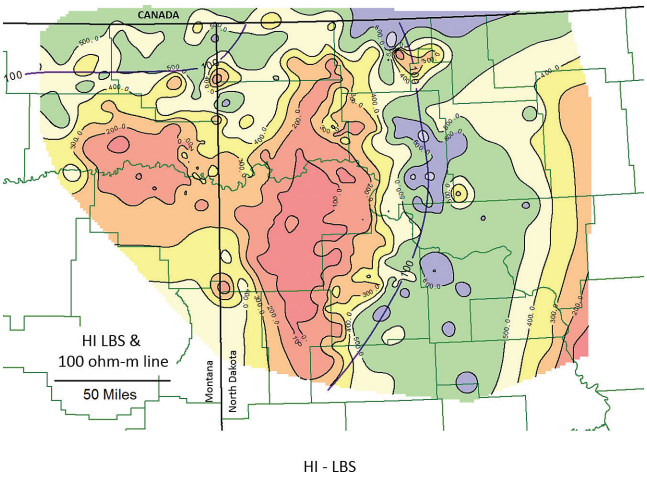

Figure 42. Hydrogen index (HI) contour map for the lower Bakken shale (LBS). Onset of generation is thought to occur at a HI number of 500. Data are from the USGS (2016) and CSM Bakken (2015) data sets.

the 100 ohm-m line taken from Hester and Schmoker (1985). The 100 ohm-m line approximately coincides with HI values of 500.

The upper Bakken shale is also an important source rock in the Bakken petroleum system (Figure 43). The upper Bakken shale ranges in thickness from 0 to approximately 25 ft (0 to ~8 m) in the mapped area. No obvious structural controls on thickness variations are suggested other than a Prairie salt dissolution-related thick shown in the southern part of the mapped area in Stark County. This anomalous area is also the area of prolific Lodgepole mounds.

A plot of hydrogen index (mg HC/g OC) versus T_{max} °C for the upper Bakken shale illustrates Bakken source rock data which falls into immature, oil window, and wet-gas condensate categories (Figure 44). The oil window ranges in value from 425 to 455 T_{max}. Onset of intense oil generation coincides with values of 500 HI and

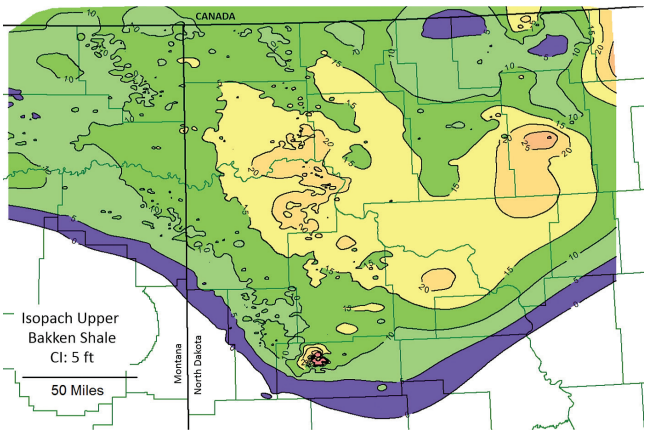

Figure 43. Isopach upper Bakken shale. The unit ranges in thickness from a wedge-edge to over 25 ft (7 m).

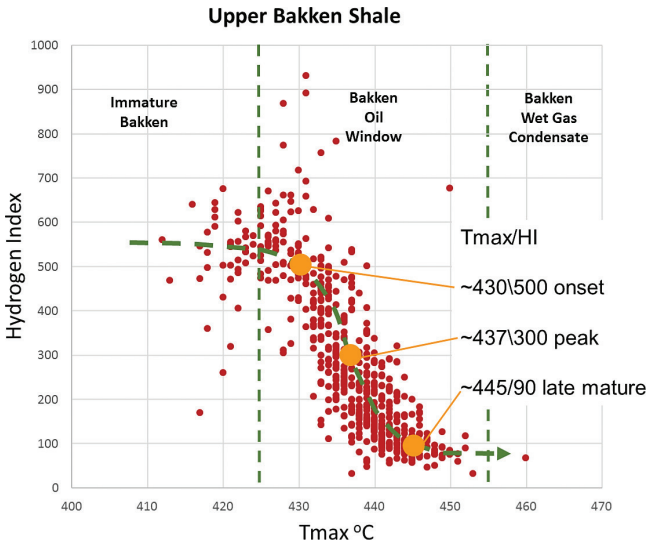

Figure 44. Hydrogen index versus T_{max} °C for the upper Bakken shale. Onset of intense hydrocarbon generation coincides with T_{max} values of 430° Celsius (806° Fahrenheit) and HI values of 500. Data are from the USGS Geochemistry Database (2016) and CSM Bakken Consortia data base (2015).

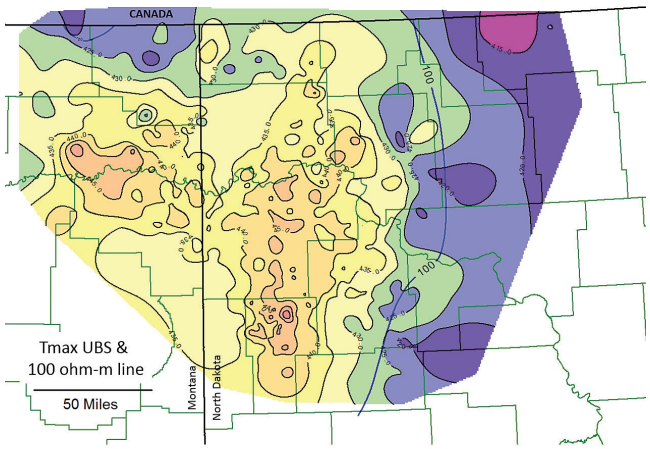

Tmax – UBS & 100 ohm-m line

Figure 45. T_{max} values for upper Bakken shale (UBS). Also shown is the 100 ohm-m resistivity line for the Upper Bakken Shale (from Hester and Schmoker, 1985). The thermal mature areas of the upper Bakken shale are shown by the warmer colors. Immature areas are the blue colors. Data are from the USGS Geochemistry Database (2016) and CSM Bakken Consortia data base (2015).

430 for T_{max}. Peak generation is approximately 300 HI and 437 T_{max}. Late mature values are 90 HI and 445 T_{max}. These values can be mapped to illustrate mature and immature areas for the upper Bakken shale (Figures 45 and 46).

Figure 45 illustrates mapped T_{max} values for the upper Bakken shale. Also shown is the 100 ohm-m resistivity line for the upper Bakken shale (from Hester and Schmoker, 1985). The thermal mature areas of the

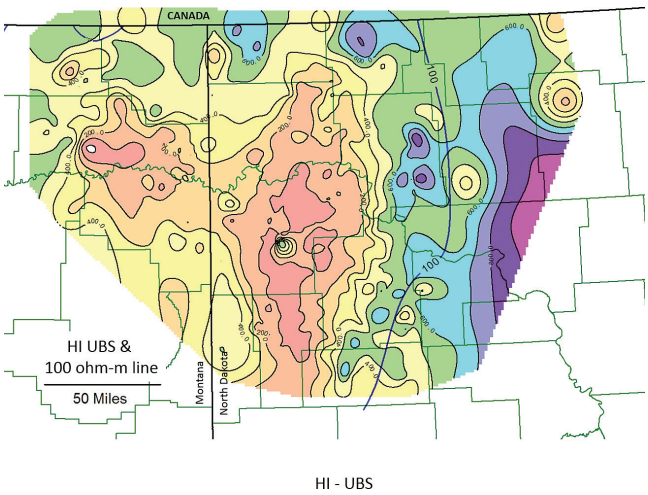

HI - UBS

Figure 46. Hydrogen index (HI) contour map for the upper Bakken shale (UBS). Onset of generation is thought to occur at a HI number of 500. Data are from the USGS Geochemistry Database (2016) and CSM Bakken Consortia data base (2015).

lower Bakken shale are shown by the warmer colors. Immature areas are the blue colors. The 100 ohm-m line coincides approximately with the 425 T_{max} contours.

Figure 46 shows a contoured HI map for the upper Bakken shale. These values are compared to the 100 ohm-m line taken from Hester and Schmoker (1985). The 100 ohm-m line approximately coincides with HI values of 500 to 600. The warm colors (yellow to red) are thermally mature areas, and the cool colors (light blue to purple) are thermally immature areas.

Although there is general agreement between different means to map thermally mature areas (resistivity versus HI versus T_{max}), the best correlations exist with T_{max} and resistivity.

BAKKEN AND THREE FORKS OILS

The oil produced from the Bakken and Three Forks reservoirs is different from oil produced from Madison reservoirs (Jarvie, 2001; Jiang et al., 2001; Lillis, 2013). Bakken-reservoired oils and Madison-reservoired oils are different based on a number of factors, including biomarker geochemistry. The Bakken-reservoired oils have high diasterane/sterane values, indicating argillaceous source rocks; the Madison-reservoired oils have low pristane/phytane and diasterane/sterane values and high norhopane/hopane values, indicating sourcing from carbonate rocks.

Bakken oils are moderate to high gravity (26 to 46° API), have low sulfur contents (less than 0.35 wt.%), and low pour points (average –25° Fahrenheit [–32° Celsius]). Madison oils have higher sulfur contents (0.2 to over 3.6 wt.%) and higher pour points (average 38 ° Fahrenheit [3° Celsius]).

RESERVOIR PRESSURE

Reservoir pressure in the Bakken is regarded as overpressured with pressure gradients exceeding 0.5 psi/ft (Figure 47) (Sonnenberg, 2010b). A new pressure map for the Bakken petroleum system was generated by Theloy (2014). The map is based on 92 BHP (bottom-hole pressure) and DFIT (diagnostic fracture injection test) data points, including six additional hydrostatic points at the eastern margin as well as six data points for the Sanish–Parshall area. High overpressures are found in large parts of the central basin and the Parshall area in the east, where gradients exceed 0.7 psi/ft. Elm Coulee has a pressure gradient around 0.55 psi/ft. Parshall is reported to have a gradient of 0.74 psi/ft. The area west of the Nesson anticline has pressure gradients of 0.6 to 0.7 psi/ft. Pressure gradients in Montana are generally in the 0.5+ psi/ft range.

A plot of pressure versus depth for Bakken and Three Forks data is shown in Figure 48 (from Theloy, 2014). Onset of oil generation is extrapolated to approximately 8400 ft (2560 m). In general, the Three Forks is slightly higher pressured than the Bakken. Parshall data points suggest that the Parshall field is

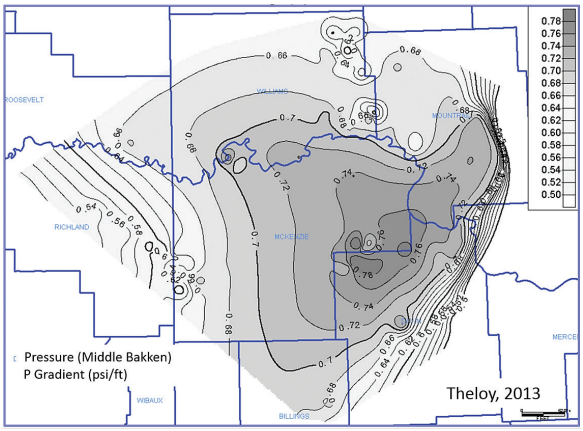

Figure 47. Pressure data for the middle Bakken reservoir. The map is based on 92 BHP (bottom-hole pressure) and DFIT (diagnostic fracture injection test) data points, including six additional hydrostatic points at eastern margin as well as six data points for the Sanish–Parshall area. Parshall is reported to have a gradient of 0.74 psi/ft. High overpressures are found in large parts of the central basin and the Parshall area in the east, where gradients exceed 0.7 psi/ft. Elm Coulee has a pressure gradient around 0.55 psi/ft. The area west of the Nesson anticline has pressure gradients of 0.6 to 0.7 psi/ft. Pressure gradients in Montana are generally in the 0.5+ psi/ft range. From Theloy (2014).

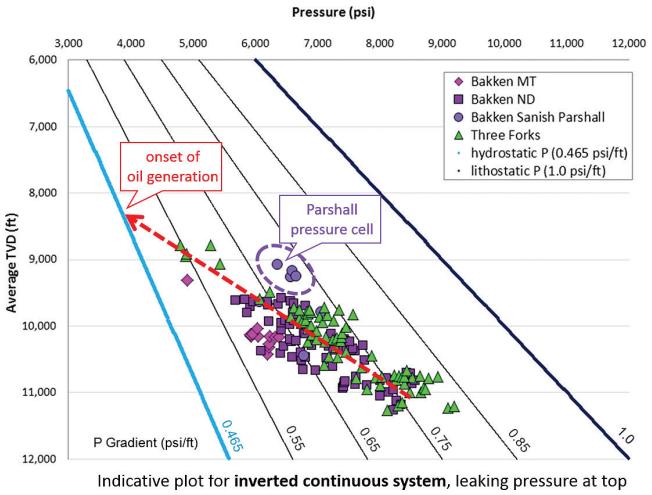

Figure 48. Pressure depth plot for Bakken and Three Forks using BHP and DFIT data points. The plot suggests onset of oil generation occurring at a depth of 8400 ft (2560 m). Data from the Parshall field plots off the main data trend suggesting a separate pressure compartment. The Three Forks appears to be slightly higher pressured than the Bakken pressures. From Theloy (2014).

a well-sealed pressure compartment. Data from Montana (mainly Elm Coulee and areas to the north) suggest more of a leaky seal.

Meissner (1978) described the role of overpressuring in the Bakken at Antelope and the creation of open tension fractures. The pressure gradient at Antelope is 0.73 psi/ft in the Bakken and upper Three Forks intervals (Folsom et al., 1959; Murray, 1968; Finch, 1969; Sonnenberg, 2010b). Normal pressures are found above and below the Bakken.

The abnormal pressures in the Bakken and Three Forks suggest that the oil generated in the Bakken petroleum system has largely stayed in the Bakken petroleum system. Lower pressures indicate dissipation of pressure in areas where migration has taken place.

A summary diagram illustrating areas of thermal maturity and overpressuring in the Bakken petroleum system is shown in Figure 49 (from Theloy, 2014).

FRACTURES

Fractures enhance the reservoir quality of the tight Bakken reservoir (Murray, 1968; Meissner, 1978; Pitman et al., 2001; Sonnenberg et al., 2011c; Theloy, 2014). Three types of fractures are reported to occur in the Bakken: (1) structural-related tectonic fractures, (2) stress-related regional fractures, and (3) diagenetic fractures associated with overpressuring due to hydrocarbon generation (Druyff, 1991; Carlisle et al., 1992;

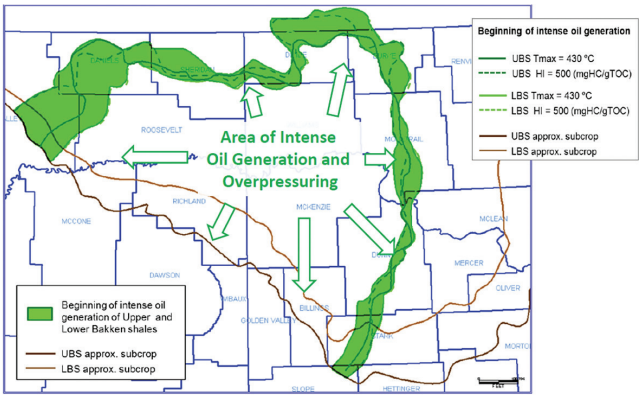

Beginning of intense oil generation based on Tmax and HI constraints of both Upper and Lower Bakken shales

Figure 49. Area of intense oil generation and overpressuring based on T_{max} and HI data. Subcrops of the upper and lower Bakken shales also shown. From Theloy (2014).

Price, 1999; Pitman et al., 2001; Hill, 2010). LeFever (1992) states that the best production comes from hydrocarbon-generated, related pervasive microfracturing within the Bakken, Three Forks, and Lodgepole combined with larger-scale fracturing (i.e., structural-related or stress-related regional fractures).

Fracturing of source rocks has been frequently discussed as a mechanism that enhances primary migration and increases the permeability of the source rock (Momper, 1980; Lempp et al., 1994). Fracturing observed in source rocks is commonly horizontal; however, oblique and perpendicular to bedding plane fractures also occur.

Structural-Related Tectonic Fractures

Structure-related fractures are associated with specific features like folds or faults (Stearns and Friedman, 1972). These types of fractures may pervade entire regions where similar structural features also are common. Changes in the structural trend, however, alter the trend of orientation of structure-related fractures. These fractures often occur in conjugate patterns. A complete conjugate pattern contains a left-lateral shear, a right-lateral shear, and an extension fracture.

Fractures associated with faults are assignable to the same stress state that caused the fault. The orientation of the fractures can be predicted from the orientation of the fault because they are miniatures of the fault. The width of the fracture zone is difficult to determine. The directional strike of the fracture trends is the same as the fault, so fluid movement direction and possible communication between wells can be predicted.

Fractures related to folding fall into two categories, hinge perpendicular and hinge parallel (Stearns and Friedman, 1972). The high rates of production at Antelope field suggest that the hinge-parallel type of fractures may be dominant in controlling production in this field.

Hinge-parallel and perpendicular fractures may also play roles associated with other anticlines and noses in the Williston Basin (i.e., Nesson, Cedar Creek, Poplar, Billings, and Little Knife anticlines).

Regional Fractures

Regional orthogonal fractures are common in little-deformed strata in many sedimentary basins (Lorenz et al., 1991). These fracture sets consist of a set of smooth, subparallel fractures, along with a more irregular set of cross-fractures. The fractures of the first set are considered to be systematic and parallel each other at very closely spaced intervals; fractures of the second set are nonsystematic and terminate against members of the first set. These fractures are important contributors to reservoir performance. The fractures are normal to bedding, occur throughout a basin, and are independent of local structure. The systematic fractures make good targets for deviated wells. The systematic fractures form during far-field compression and propagate in the plane of the maximum and intermediate compressive stresses. The fractures may form at depth in extension and parallel to the direction of regional horizontal tectonic compression.

Studies conducted on the regional stress field in the Williston Basin suggest a northeast–southwest orientation of the maximum horizontal stress (Zoback and Zoback, 1980; Narr and Burrus, 1984; Breig, 1988; Cramer, 1991; Whiting Petroleum, 2010; O'Brien et al., 2011; Sonnenberg et al., 2011c). Vertical fractures paralleling the maximum horizontal stress are thought to be the direction of open fractures (Figure 50). Natural fractures in the Mission Canyon in the Little Knife field trend in a general east–west direction, which is perpendicular to the trace of the Little Knife anticline. These fractures were related to the regional stress field. Oriented cores in the Elkhorn Ranch and Roosevelt field areas of the Billings anticline suggest that the maximum horizontal stress direction is N45E (Cramer, 1991). Multiwell interference testing in the Billings Nose area indicated restricted hydraulic communication exists between wells off the N45E trend. Natural fractures in the Mission Canyon at Big Stick field have a preferred orientation of N50°E. These fractures play a key role in Mission Canyon reservoir performance.

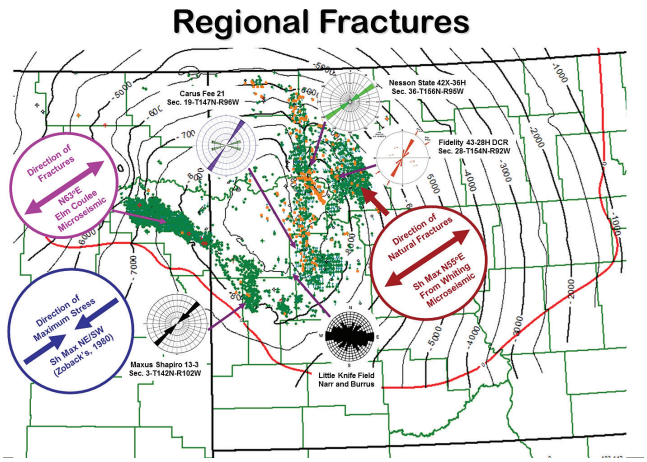

Figure 50. Regional fracture orientation based on literature, oriented core and microseismic data. Modified from Sonnenberg (2011b).

Microseismic data also supports the northeast–southwest orientation of regional fractures (Whiting Petroleum, 2010; O'Brien et al., 2011). In Parshall field microseismic surveys confirm a maximum horizontal stress direction of N55°E and for Elm Coulee N63°E.

Diagenetic Fractures

Microfracturing due to overpressuring of enclosed pore fluids is reviewed by Meissner (1978), Momper (1978), and Tissot and Welte (1984). The model proposed is that a large increase in pore pressure may be sufficient to overcome the capillary pressure or even exceed the mechanical strength of the rock and induce microcracking. These types of microfractures are restricted to deeply buried, compacted, low-permeability rocks. With thermal maturity, organic matter generates liquid or gaseous low-molecular-weight compounds. The mechanical strength of a rock is exceeded, and fracturing occurs if the internal fluid pressure in a rock or in local pressure centers inside the pores is greater than a factor of 1.42 to 2.4 over the hydrostatic pressure in the immediate surroundings (Tissot and Welte, 1984). Pressures that exceed normal hydrostatic and even lithostatic pressure are possible whenever massive generation of gas and oil from kerogen takes place.

The Bakken shales were probably indurated when hydrocarbon generation began (Dembicki and Pirkle, 1985). Fracturing, therefore, may be an important factor in the expulsion of oil generated in the Bakken shales.

Vertical and subhorizontal expulsion fractures have been reported in the Bakken shales in clay- and organic-rich intervals (Carlisle, 1991; Carlisle et al., 1992; Pitman et al., 2001; Vernik, 1994; Hill, 2010; Sonnenberg et al., 2011c; Theloy, 2014; Al Duhailan, 2014). Both micro- and macroexpulsion fractures have been observed (Carlisle et al., 1992). Carlisle et al. (1992), Pitman et al. (2001), and Price and Stolper (1999) discuss hydrocarbon generation resulting in superlithostatic pressures that could create the horizontal fractures. Price (1999) also discusses the model using early CO_2 generation and light hydrocarbons also creating high overpressures. The microexpulsion fractures have a "cracked-tip" morphology and have widths of 10 to 20 microns and lengths of approximately or ½ inch (1.3 cm) or longer. Connected vertical and horizontal macroexpulsion fractures also exist (Carlisle et al., 1992). These types of fractures are difficult to distinguish from small tectonic fractures, small-scale regional fractures, and bedding-plane partings.

ESTIMATES OF OIL GENERATED FROM BAKKEN SHALES

Numerous authors have estimated the amount of oil generated from the Bakken shales (Dow, 1974; Schmoker and Hester, 1983; Webster, 1984; Price, 1999; Meissner and Banks, 2000; Flannery and Kraus, 2006; Bohrer et al., 2008). Debate exists about how much oil has been generated and what formations have been sourced. Estimates of generated oil range from 10 to 500 billion bbl of oil. Different methodologies were used by various authors, resulting in the wide spread of estimates. The first estimate by Dow (1974) using an average of 4 wt.% TOC suggested 10 billion bbl of oil were generated. Webster (1984) calculated generation capacities to be 92 billion bbl of oil for North Dakota only based on the extent of thermal kerogen breakdown as observed on pyrolysis data. Schmoker and Hester utilized log-derived TOC and maturity (resistivity) data in their calculations and determined that 132 billion bbl of oil were generated. Price (1999) used an extensive data set to estimate generation of between 271 and 503 billion bbl of oil. More recent estimates (from 2000 to 2008) utilize computer mapping and modeling programs. Meissner and Banks (2000) estimated 32 billion bbl of generated oil. Flannery and Kraus (2006) used sophisticated computer modeling with extensive data input supplied by the North Dakota Geological Survey to estimate 300 billion bbl of generated oil. Most of the estimates are in excess of 100 billion bbl of oil generated in the Bakken petroleum system.

Oil generated in the Bakken shales is thought to have migrated into adjacent formations (Lodgepole and Three Forks) and into the middle Bakken member (Price and LeFever, 1994). And some of the generated oil stays within the Bakken shales. Thus much of the oil generated by the Bakken shales stays in the Bakken petroleum system reservoirs. The oils produced in the overlying upper Madison reservoirs are distinctly different from Bakken oils, and this suggests that they are self-sourced from the Madison (Jiang et al., 2001; Jarvie, 2001; Lillis, 2013). These reservoirs were previously thought to have been sourced from the Bakken shales (Dow, 1974; Meissner, 1978). The recovery factors for Bakken and Three Forks wells are often reported to be 3 to 10% of the oil in place (LeFever and Helms, 2006). The estimates of the amount of oil generated in the Williston Basin by the Bakken shales indicate a very large resource. How much of this resource can be recovered will be based on future technology and oil prices.

SUMMARY

The Bakken and Three Forks are an important tight oil resource play. The production in the Williston Basin is increasing dramatically because of the excellent results in recent drilling. The amount of technically recoverable oil has recently been estimated by Gaswirth et al. (2013) to be 7.3 billion bbl (3.7 from the Three Forks and 3.6 from the Bakken). New technology and enhanced recoveries may add to the number in the future. Total Bakken and Three Forks production to December 2014 was 1.289 billion bbl of oil and 1.3 tcf of gas from 12,051 wells (Figure 3). Thus the play is in its early stages. Production from both the Three Forks and Bakken is excellent. Both fracture and matrix permeability are important in the play.

Fracturing in the Bakken petroleum system occurs from a variety of causes: pore pressure, regional stress field, local structures (including salt dissolution features), and recurrent movement on basement fault systems. The regional stress field appears to play a significant role in how operators are orienting their laterals and overall production.

Many of the reservoirs in the Bakken petroleum system have low permeability. Productive areas or sweet spots are localized areas of improved reservoir permeability through natural fracturing or development of matrix permeability, or combination of both. Reservoir facies with matrix permeability are key ingredients to sweet spot areas.

REFERENCES CITED

Al Duhailan, M., 2014, Petroleum-expulsion fracturing in organic-rich shales: Genesis and impact on unconventional pervasive petroleum systems: Ph.D. theses, Colorado School of Mines, Golden, Colorado, 206 p.

Alexandre, C. S., 2011, Reservoir characterization and petrology of the Bakken Formation, Elm Coulee Field, Richland County, MT: M.S. thesis, Colorado School of Mines, Golden, Colorado, 159 p.

Bazzell, A., 2014, Origin of brecciated intervals and petrophysical analyses, the Three Forks Formation, Williston Basin, North Dakota, USA: M.S. thesis, Colorado School of Mines, Golden, Colorado, 140 p.

Berwick, B., 2008, Depositional environment, mineralogy, and sequence stratigraphy of the Late Devonian Sanish Member (upper Three Forks Formation), Williston Basin, North Dakota: M.S. thesis, Colorado School of Mines, Golden, Colorado, 262 p.

Blakey, R., 2005, Paleogeography and geologic evolution of North America: Northern Arizona University, Ron Blakey webpage, accessed March 15, 2009, http:jan.ucc.nau.edu/~rcb7/nam.html.

Bohrer, M., S. Fried, L. Helms, B. Hicks, B. Juenker, D. McCusker, et al., 2008, Bakken Formation resource study project: North Dakota Department of Mineral Resources Report, 23 p.

Bottjer, R. J., R. Sterling, A. Grau, and P. Dea, 2011, Stratigraphic relationships and reservoir quality at the Three Forks-Bakken Unconformity, Williston Basin, North Dakota, *in* J. W. Robinson, J. A. LeFever, and S. B. Gaswirth, eds., The Bakken-Three Forks petroleum system in the Williston Basin: Rocky Mountain Association of Geologists, p. 173–228.

Breig, J. J., 1988, Mississippian Mission Canyon reservoirs of the Billings Nose, Billings County, North Dakota, *in* S. M. Goolsby and M.W. Longman, eds., Occurrence and petrophysical properties of carbonate reservoirs in the Rocky Mountain Region: Rocky Mountain Association of Geologists, p. 357–369.

Canter, L., O. Skinner, and M. Sonnenfeld, 2009, Facies and mechanical stratigraphy of the middle Bakken, Mountrail County, North Dakota (abs): Rocky Mountain Section SEPM Luncheon, January 27.

Carlisle, W., 1991, The Bakken Formation of the Williston Basin: Deposition, maturation, and fracturing (abs.), *in* B. Hansen, ed., Geology and horizontal drilling of the Bakken Formation: Montana Geological Society, p. 89.

Carlisle, W. J., L. Dryff, M. Fryt, J. Artindale, and H. Von Der Dick, 1992, The Bakken Formation: An integrated geologic approach to horizontal drilling, *in* J. E. Schmoker, E. Coalson, and C. Brown, eds., Geologic studies relevant to horizontal drilling: Examples from western North America: Rocky Mountain Association of Geologists, p. 215–226.

Cobb, D., 2013, Characterization of thickness anomalies in the Bakken and Three Forks formations, North Central North Dakota, U.S.A.: M.S. thesis, Colorado School of Mines, Golden, Colorado, 196 p.

Coskey, R. J., and J. E. Leonard, 2009, Bakken oil accumulations: What's the trap?: AAPG Search and Discovery Article #90090, AAPG Annual Convention and Exhibition, Denver, Colorado, June 7–10, 2010, accessed September 22, 2016, http://www.searchanddiscovery.com/abstracts/html/2009/annual/abstracts/coskey.htm.

Cramer, D. D., 1986, Reservoir characteristics and stimulation techniques in the Bakken Formation and adjacent beds, Billings Nose area, Williston Basin, *in* S. Goolsby and M. W. Longman, eds., Proceedings from SPE Rocky Mountain Region Technical Meeting, Society of Petroleum Engineers, Paper No. 15166, p. 331–344.

Cramer, D. D., 1991, Stimulation treatments in the Bakken Formation: Implications for horizontal completions, *in* W. B. Hansen, ed., Geology and horizontal drilling of the Bakken Formation: Montana Geological Society, p. 117–140.

CSM Bakken Consortia data base, 2015, Source rock analysis data on Bakken wells Williston Basin: Unpublished source rock data from miscellaneous wells Williston Basin, Colorado School of Mines Bakken Consortia.

Dembicki, H., and F. L. Pirkle, 1985, Regional source rock mapping using a source potential rating index: AAPG Bulletin, v. 69, p. 567–581.

Dow, W. G., 1974, Application of oil-correlation and source-rock data to exploration in Williston Basin: AAPG Bulletin, v. 58, no. 7, p. 1253–1262.

Druyff, L., 1991, Reservoir properties of the Bakken shale (abs.), *in* W. B. Hansen, ed., Geology and horizontal drilling of the Bakken Formation: Montana Geological Society, p. 91.

Dumencaoux, G. M., 1984, Stratigraphy and depositional environments of the Three Forks Formation (upper Devonian), Williston Basin, North Dakota: M.S. thesis, University of North Dakota, 114 p.

Finch, W. C., 1969, Abnormal pressure in the Antelope Field, North Dakota: Journal of Petroleum Technology, July, p. 821–826.

Flannery, J., and J. Kraus, 2006, Integrated analysis of the Bakken petroleum system, U.S. Williston Basin: AAPG Search and Discovery Article #10105. Accessed December 15, 2008, http://www.searchanddiscovery.net/documents/2006/06035flannery/index.htm.

Folsom, C. B., C. Carlson, and S. B. Anderson, 1959, Geology of the Antelope Field: North Dakota Geological Survey Report of Investigation No. 32, 38 p.

Franklin, A. L., and S. A. Sonnenberg, 2012, Regional stratigraphic analysis of the Three Forks Formation, Williston Basin, USA: AAPG Search and Discovery Article #90142 © 2012 AAPG Annual Convention and Exhibition, accessed September 28, 2016, http://www.searchanddiscovery.com/abstracts/html/2012/90142ace/abstracts/frankl.htm.

Gantyno, A. A., 2011, Sequence stratigraphy and microfacies analysis of the late Devonian Three Forks Formation, Williston Basin, North Dakota and Montana, U.S.A.: M.S. thesis, Colorado School of Mines, Golden, Colorado, 201 p.

Gaswirth, S. B., K. R. Marra, T. A. Cook, R. R. Charpentier, D. L. Gautier, D. K. Higley, et al., 2013, Assessment of undiscovered oil resources in the Bakken and Three Forks formations, Williston Basin Province, Montana, North Dakota, and South Dakota: U.S. Geological Survey Report, accessed September 22, 2016, http://pubs.usgs.gov/fs/2013/3013/, 4 p.

Gent, V. A., 2011, Fourier analysis of the laminated facies of the middle Bakken Member, Sanish-Parshall Field, Mountrail County, North Dakota: M.S. thesis, Colorado School of Mines, Golden, Colorado, 135 p.

Gerhard, L. C., S. B. Anderson, and D. W. Fischer, 1990, Petroleum geology of the Williston Basin, *in* M. W. Leighton, D. R. Kolata, D. T. Oltz, and J. J. Eidel, eds., Interior Cratonic Basins: AAPG Memoir 51, p. 507–559.

Gerhard, L. C., S. B. Anderson, and J. A. LeFever, 1987, Structural history of the Nesson anticline, North Dakota, *in* M. W. Longman, ed., Williston Basin: Anatomy of a Cratonic Oil Province: Rocky Mountain Association of Geologists, p. 337–354.

Gerhard, L. C., S. B. Anderson, J. A. LeFever, and C. G. Carlson, 1982, Geological development, origin, and energy mineral resources of Williston Basin, North Dakota: AAPG Bulletin, v. 66, p. 989–1020.

Gutierrez, C., 2014, Stratigraphy and petroleum potential of the upper Three Forks Formation, North Dakota, Williston Basin, USA: M.S. thesis, Colorado School of Mines, Golden, Colorado, 180 p.

Hansen, W. B., and G. Long, 1991, Criteria for horizontal and vertical prospects in the Bakken Formation, Williston Basin, *in* W. B. Hansen, ed., Geology and horizontal drilling of the Bakken Formation: Montana Geological Society, p. 151–163.

Haynes, W. P., 1916, The fauna of the upper Devonian of Montana: Part 2. The stratigraphy and the Brachiopoda: Pittsburgh Carnegie Museum Annals, v. 10, p. 13–54.

Hester, T. C., and J. W. Schmoker, 1985, Selected physical properties of the Bakken Formation, North Dakota and Montana part of the Williston Basin: USGS Oil and Gas Investigations Chart OC-126, map scale 1:2,500,000, accessed September 22, 2016, http://ngmdb.usgs.gov/Prodesc/proddesc_5153.htm.

Hill, R., 2010, Bitumen filled fractures in the Bakken Formation and implications for gas shale systems: AAPG Search and Discovery Article #90108, AAPG International Convention and Exhibition, Calgary, Alberta, Canada, accessed September 22, 2016, http://www.searchanddiscovery.com/pdfz/abstracts/pdf/2010/intl/abstracts/ndx_hill02.pdf.html.

Jarvie, D. M., 2001, Williston Basin petroleum systems: Inferences from oil geochemistry and geology: Mountain Geologist, v. 38, no. 1, p. 19–41.

Jiang, C., M. Li, K. G. Osadetz, L. R. Snowdon, M. Obermajer, and M. G. Fowler, 2001, Bakken/Madison petroleum systems in the Canadian Williston Basin: Part 2. Molecular markers diagnostic of Bakken and Lodgepole source rocks: Organic Geochemistry, v. 32, p. 1037–1054.

Jin, H., 2013, Characterization for source rock potential of the Bakken shales in the Williston Basin, North Dakota and Montana: Ph.D. thesis, Colorado School of Mines, Golden, Colorado, 240 p.

Johnson, R. L., 2013, The Pronghorn member of the Bakken Formation, Williston Basin, USA: Lithology, Stratigraphy, and Reservoir Properties: M.S. thesis, Colorado School of Mines, Golden, Colorado, 166 p.

Kowalski, B., 2010, Quantitative mineralogic analysis of the middle Bakken member, Parshall Field, Mountrail County, North Dakota: M.S. thesis, Colorado School of Mines, Golden, Colorado, 126 p.

Kowalski, B. L., and S. A. Sonnenberg, 2011, Mineralogic analysis of the middle Bakken member, Parshall Field area, Mountrail County, North Dakota, *in* J. W. Robinson, J. A. LeFever, and S. B. Gaswirth, eds., The Bakken-Three Forks petroleum system in the Williston Basin: Rocky Mountain Association of Geologists, p. 102–126.

LeFever, J., 2006, Oil production from the Bakken Formation: A short history: North Dakota Geological Survey Newsletter, v. 32, no. 1, p. 1–6.

LeFever, J., 2007, Evolution of oil production in the Bakken Formation: RMS-AAPG Meeting and North Dakota Industrial Commission Geologic Investigation 49: NDIC website PowerPoint presentation, accessed December 15, 2008, https://www.dmr.nd.gov/ndgs/bakken/Papers/Petroleum%20Council%202004.ppt.

LeFever, J. A., 1992, Horizontal drilling in the Williston Basin, United States and Canada, *in* J. W. Schmoker, E. B. Coalson, and C. A. Brown, eds., Geological studies relevant to horizontal drilling: Examples from Western North America: Rocky Mountain Association of Geologists Guidebook, p. 177–198.

LeFever, J. A., 2008, Isopach of the Bakken Formation: North Dakota Geological Survey Geologic Investigations No. 59, Bakken Map Series: Sheet 1-5, scale: 1:1,000,000.

LeFever, J. A., and L. Helms, 2006, Bakken Formation reserve estimates: North Dakota Geological Survey website, accessed December 15, 2008, https://www.dmr.nd.gov/ndgs/bakken/newpostings/07272006_BakkenReserveEstimates.pdf, 6 p.

LeFever, J. A., and R. LeFever, 2005, Distribution of salts in the Williston Basin, North Dakota: North Dakota Geological Survey Report of Investigations no. 103, 41 p., two plates.

LeFever, J. A., R. LeFever, and S. Nordeng, 2011, Revised nomenclature for the Bakken Formation (Mississippian-Devonian), North Dakota, *in* J. W. Robinson, J. A. LeFever, and S. B. Gaswirth, eds., The Bakken-Three Forks petroleum system in the Williston Basin: Rocky Mountain Association of Geologists, p. 11–26.

LeFever, J. A., C. D. Martiniuk, E. F. R. Dancsok, and P. A. Mahnic, 1991, Petroleum potential of the middle member, Bakken Formation, Williston Basin, *in* J. E. Christopher and F. Haidl, eds., Proceedings of the Sixth International Williston Basin Symposium: Saskatchewan Geological Society, Special Publication 11, p. 76–94.

Lempp, C., O. Natau, U. Bayer, and D. Welte, 1994, The effect of temperature on rock mechanical properties and fracture mechanisms in source rocks: Experimental results: Society of Petroleum Engineers Paper No. 28039, p. 147–154.

Lillis, P. G., 2013, Review of oil families and their petroleum systems of the Williston Basin: Mountain Geologist, v. 50, no. 1, p. 5–31.

Longman, M., K. Kocman, and L. Wray, 2014, Petrography of the Bakken black "shales" in the eastern Williston Basin of North Dakota: AAPG Datapages/Search and Discovery Article #90193, Rocky Mountain Section AAPG Annual Meeting, Denver, Colorado, July 20–22, accessed September 22, 2016, http://www.searchanddiscovery.com/abstracts/html/2014/90193rms/abstracts/1956989.html.

Lorenz, J. C., L. W. Teufel, and N. R. Warpinski, 1991, Regional fractures I: A mechanism for the formation of regional fractures at depth in flat-lying reservoirs: AAPG Bulletin, v. 75, p. 1714–1737.

Martiniuk, C. D., 1991, Regional geology and petroleum potential of the Bakken Formation, southwestern Manitoba, *in* B. Hansen, ed., Geology and horizontal drilling of the Bakken Formation: Montana Geological Society, p. 43–67.

Meissner, F. F., 1978, Petroleum geology of the Bakken Formation, Williston Basin, North Dakota and Montana, *in* D. Estelle and R. Miller, eds., The economic geology of the Williston Basin, 1978 Williston Basin Symposium, September 24–27, Montana Geological Society, p. 207–230.

Meissner, F. F., and R. B. Banks, 2000, Computer simulation of hydrocarbon generation, migration, and accumulation under hydrodynamic conditions: Examples from the Williston and San Juan Basins, USA: AAPG Search and Discovery Article #40179, accessed December 15, 2008, http://www.searchanddiscovery.net/documents/2005/banks/index.htm?q=%2Btext%3Ameissner.

Meissner, F. F., J. Woodward, and J. L. Clayton, 1984, Stratigraphic relationships and distribution of source rocks in the Greater Rocky Mountain Region, *in* J. Woodward, F. F. Meissner, and J. L. Clayton, eds., Hydrocarbon source rocks of the Greater Rocky Mountain Region: Rocky Mountain Association of Geologists Guidebook, p. 1–34.

Momper, J. A., 1978, Oil migration limitations suggested by geological and geochemical considerations: AAPG Course Notes 8, Physical and chemical constraints on petroleum migration, B1–B60.

Momper, J. A., 1980, Oil expulsion: A consequence of oil generation: American Association of Petroleum Geologists slide/tape series, produced by Science-Thru-Media Co., New York, New York.

Murray, G. H., 1968, Quantitative fracture study: Sanish Pool, McKenzie County, North Dakota: AAPG Bulletin, v. 52, no. 1, p. 57–65.

Narr, W., and R. C. Burruss, 1984, Origin of fractures in Little Knife Field, North Dakota: AAPG Bulletin, v. 68, no. 9, p. 1087–1100.

Nordeng, S. H., 2009, The Bakken petroleum system: An example of a continuous petroleum accumulation: North Dakota Department of Mineral Resources Newsletter, v. 36, no. 1, p. 19–22.

Nordeng, S. H., and J. LeFever, 2008, The Bakken: A question of maturity: 16th Annual Williston Basin Petroleum Conference, April 28–30, North Dakota Geological Survey, PowerPoint presentation, accessed December 15, 2008, https://www.dmr.nd.gov/ndgs/wbpc/wbpc2008.asp.

Nordeng, S.H., and L. D. Helms, 2010, Bakken Source System, Three Forks Formation Assessment: Department of Mineral Resources, North Dakota Industrial Commission, accessed September 27, 2016, https://www.dmr.nd.gov/ndgs/bakken/bakkenthree.asp.

O'Brien, D. G., R. T. Larson, R. C. Parham, B. L. Thingelstad, W. W. Aud, R. A. Burns, et al., 2011, Using real-time downhole microseismic to evaluate fracture geometry for horizontal packer-sleeve completions in the Bakken Formation, Elm Coulee Field, Montana: Society of Petroleum Engineering Paper 139774, 22 p.

Parker, J. M., 1967, Salt solution and subsidence structures Wyoming, North Dakota, and Montana: AAPG Bulletin, v. 51, no. 10, p. 1929–1947.

Peale, A. C., 1893, Paleozoic section in the vicinity of Three Forks, Montana: U.S. Geological Survey Bulletin 110, 56 p.

Peterson, J. A., and L. M. MacCary, 1987, Regional stratigraphy and general petroleum geology of the U.S. portion of the Williston Basin and adjacent areas, *in* M. W. Longman, ed., Williston Basin: Anatomy of a cratonic oil province: Denver, Colorado, Rocky Mountain Association of Geologists, p. 9–43.

Pitman, J. K., L. C. Price, and J. A. LeFever, 2001, Diagenesis and fracture development in the Bakken Formation, Williston Basin: Implications for reservoir quality in the middle member: U.S. Geological Survey Professional Paper 1653, 19 p.

Price, L. C., 1999 (unpublished), Origins and characteristics of the basin-centered continuous reservoir unconventional oil-resource base of the Bakken Source System, Williston Basin: Unpublished, accessed September 22, 2018, http://www.undeerc.org/Price/.

Price, L. C., T. Ging, T. Daws, A. Love, M. Pawlewicz, and D. Anders, 1984, Organic metamorphism in the Mississippian-Devonian Bakken shale North Dakota portion of the Williston Basin, *in* J. Woodward, F. F. Meissner, and J. C. Clayton, eds., Hydrocarbon source rocks of the greater Rocky Mountain Region: Denver, Colorado, Rocky Mountain Association of Geologists, p. 83–134.

Price, L. C., and J. A. LeFever, 1992, Does horizontal drilling imply a huge oil-resource base in fractured shales? *in* J. W. Schmoker, E. B. Coalson, and C. A. Brown, eds., Geologic studies relevant to horizontal drilling: Examples from Western North America: Rocky Mountain Association of Geologists, p. 199–214.

Price, L. C., and J. A. LeFever, 1994, Dysfunctionalism in the Williston Basin: the mid-Madison/Bakken petroleum system: Bulletin of Canadian Petroleum Geology, v. 42, no. 2, p. 187–218.

Price, L. C., and K. Stolper, 1999, Evidence and causes of super-lithostatic fracturing, *in* L. C. Price, ed., Origins and characteristics of the basin-center continuous-reservoir unconventional oil-resource base of the Bakken Source System, Williston Basin: Unpublished, accessed May 6, 2010, http://www.undeerc.org/Price/.

Rogers, M. H., and W. A. Mattox, 1985, Solution of Devonian Prairie Formation salt: Seismic recognition and exploration implications, *in* R. R. Gries and R. C. Dyer, eds., Seismic exploration of the Rocky Mountain Region: Rocky Mountain Association of Geologist Guidebook, p. 137–142.

Rogers, M., and W. Mattox, 1985, Solution of the Devonian Prairie Formation salt: Seismic recognition and exploration implications, in R. R. Gries, ed., Seismic exploration of the Rocky Mountain Region: Rocky Mountain Association of Geologists, Boulder, Colorado, U.S.A., p. 137–141.

Sandberg, C. A., 1965, Nomenclature and correlation of lithologic subdivisions of the Jefferson and Three Forks formations of southern Montana and northern Wyoming: U.S. Geological Society Bulletin 1194-B, 18 p.

Sandberg, C. A., and C. R. Hammond, 1958, Devonian system in Williston Basin and central Montana: AAPG Bulletin, v. 42, p. 2293–2334.

Schmoker, J. W., and T. C. Hester, 1983, Organic carbon in Bakken Formation, United States portion of Williston Basin: AAPG Bulletin, v. 67, no. 12, p. 2165–2174.

Simenson, A., 2010, Depositional facies and petrophysical analysis of the Bakken Formation, Parshall Field, Mountrail County, North Dakota: M.S. thesis, Colorado School of Mines, Golden, Colorado, 198 p.

Simenson, A. L., S. A. Sonnenberg, and R. M. Cluff, 2011, Depositional facies and petrophysical analysis of the Bakken Formation, Parshall Field and Surrounding Area, Mountrail County, North Dakota, *in* J. W. Robinson, J. A. LeFever, and S. B. Gaswirth, eds., The Bakken-Three Forks petroleum system in the Williston Basin: Rocky Mountain Association of Geologists, p. 48–101.

Smith, M. G., and M. Bustin, 1996, Lithofacies and paleoenvironments of the upper Devonian and lower Mississippian Bakken Formation, Williston Basin: Bulletin of Canadian Petroleum Geology, v. 44, no. 3, p. 495–507.

Smith, M. G., and M. Bustin, 2000, Late Devonian and early Mississippian Bakken and Exshaw Black shale source rocks, Western Canada Sedimentary basin: A sequence stratigraphic interpretation: AAPG Bulletin, v. 84, no. 7, p. 940–960.

Sonnenberg, S. A., 2010a, Focusing on the Bakken: The Bakken petroleum system of the Williston Basin: Harts Magazine, July, p. 4–20.

Sonnenberg, S. A., 2010b, Abnormal pressure analysis in the Bakken Formation, Williston Basin: A key to future discoveries (abs.): 2010 Annual AAPG Meeting Abstracts, p. 242, accessed September 22, 2018, http://www.searchanddiscovery.com/pdfz/abstracts/pdf/2010/annual/abstracts/ndx_sonnenberg.pdf.html.

Sonnenberg, S. A., 2011, TOC and pyrolysis data for the Bakken shales, Williston Basin, North Dakota and Montana, *in* J. W. Robinson, J. A. LeFever, and S. B. Gaswirth, eds.,

The Bakken-Three Forks petroleum system in the Williston Basin: Rocky Mountain Association of Geologists, p. 308–331.

Sonnenberg, S. A., V. James, C. Theloy, and J. F. Sarg, 2011a, Middle Bakken facies, Williston Basin, USA: A key to prolific production: AAPG Annual Convention and Exhibition, Houston, Texas, Poster Session Presentation, Search and Discovery Article #50449, April 10–13, accessed September 22, 2016, http://www.searchanddiscovery.com/abstracts/html/2011/annual/abstracts/Sonnenberg3.html.

Sonnenberg, S. A., H. Jin, and J. F. Sarg, 2011b, Bakken mudrocks of the Williston Basin, world class source rocks: AAPG Annual Convention and Exhibition, Houston, Texas, Poster Session Presentation, Search and Discovery Article #80171, April 10–13, accessed September 22, 2016, http://www.searchanddiscovery.com/abstracts/html/2011/annual/abstracts/Sonnenberg2.html.

Sonnenberg, S.A., J. A. LeFever, and R. J. Hill, 2011c, Fracturing in the Bakken petroleum system, Williston Basin, *in* J. W. Robinson, J. A. LeFever, and S. B. Gaswirth, eds., The Bakken-Three Forks petroleum system in the Williston Basin: Rocky Mountain Association of Geologists, p. 393–417.

Sonnenberg, S. A., and A. Pramudito, 2009, Petroleum geology of the giant Elm Coulee Field, Williston Basin: AAPG Bulletin, v. 93, no. 9, p. 1127–1153.

Sperr, J. T., 1991, Exploration models for Bakken Reservoirs: Williston Basin, North Dakota and Montana, *in* B. Hansen, ed., Geology and horizontal drilling of the Bakken Formation: Montana Geological Society, p. 143–149.

Stearns, D. W., and M. Friedman, 1972, Reservoirs in fractured rock: AAPG Bulletin, p. 82–106.

Stroud, J., 2010, The role of the lower Lodgepole Formation in the Bakken petroleum system, Billings Nose, North Dakota: M.S. thesis, Colorado School of Mines, Golden, Colorado, 104 p.

Theloy, C., 2014, Integration of geological and technological factors influencing production in the Bakken play, Williston Basin: Ph.D. thesis, Colorado School of Mines, Golden, Colorado, 223 p.

Tissot, B. P., and D. H. Welte, 1984, Petroleum formation and occurrence (2nd ed.): Berlin, Heidelberg, New York, and Tokyo, Springer-Verlag, 699 p.

Tucker, M. E., 2001, Sedimentary petrology: Malden, Massachusetts, Blackwell Publishing, 262 p.

U. S. Geological Survey Geochemistry Database, 2016, Geochemistry Database: Energy Resources Program Geochemistry Laboratory Database (EGDB), U.S. Geological Survey, accessed September 28, 2016, http://energy.usgs.gov/GeochemistryGeophysics/GeochemistryLaboratories/GeochemistryLaboratories-GeochemistryDatabase.aspx.

Vernik, L., 1994, Hydrocarbon generation induces microcracking of source rocks: Geophysics, v. 59, no. 4, p. 555–563.

Vickery, J. O., 2010, Lithofacies, mineralogy, and ichnology of the Bakken Formation (Mississippian and Devonian), Williston Basin, Montana and North Dakota, USA: M.S. thesis, Colorado School of Mines, Golden, Colorado, 254 p.

Webster, R. L., 1984, Petroleum source rocks and stratigraphy of the Bakken Formation in North Dakota, *in* J. Woodward, F. F. Meissner, and J. C. Clayton, eds., Hydrocarbon source rocks of the Greater Rocky Mountain Region: Denver, Colorado, Rocky Mountain Association of Geologists, p. 57–81.

Weimer, R. J., 1980, Recurrent movement of basement faults: A tectonic style for Colorado and adjacent areas, *in* H. C. Kent and K. W. Porter, eds., Colorado Geology: Rocky Mountain Association of Geologists Guidebook, p. 23–35.

Whiting Petroleum, 2010, Current corporate information, December 2010: accessed December 23, 2010, http://www.whiting.com/investor-relations/presentationsand-media-events/.

Williams, J. A., 1974, Characterization of oil types in Williston Basin: AAPG Bulletin, v. 58, p. 1243–1252.

Zoback, M. L., and M. Zoback, 1980, State of stress in the conterminous United States: Journal of Geophysical Research, v. 85, no. B11, p. 6113–6156.